MC 2015 Göttingen

September 6–11, 2015

Georg-August-University Göttingen/Germany

GEORG-AUGUST-UNIVERSITÄT GÖTTINGEN

© Daniel Schwen • wikimedia org/Alciro Theodoro da Silva • goettingen.de

Microscopy Conference

Organizer

DGE DEUTSCHE GESELLSCHAFT FÜR ELEKTRONENMIKROSKOPIE

DGE – German Society for Electron Microscopy e. V.

PROCEEDINGS

www.mc2015.de

MC 2015 Proceedings

Life Sciences (LS)

Joint Session (JS)

PL01
Optical microscopy: the resolution revolution

S. W. Hell[1, 2]

[1]Max Planck Institute for Biophysical Chemistry, Göttingen
[2]German Cancer Research Center (DKFZ), Heidelberg

hell@nanoscopy.de

Throughout the 20th century it was widely accepted that a light microscope relying on conventional optical lenses cannot discern details that are much finer than about half the wavelength of light (200-400 nm), due to diffraction. However, in the 1990s, the viability to overcome the diffraction barrier was realized and microscopy concepts defined, that can resolve fluorescent features down to molecular dimensions. In this lecture, I will discuss the simple yet powerful principles that allow neutralizing the limiting role of diffraction [1, 2]. In a nutshell, feature molecules residing closer than the diffraction barrier are transferred to different (quantum) states, usually a bright fluorescent state and a dark state, so that they become discernible for a brief period of detection. Thus, the resolution-limiting role of diffraction is overcome, and the interior of transparent samples, such as living cells and tissues, can be imaged at the nanoscale.

1. Hell, S.W. Far-Field Optical Nanoscopy. *Science* 316, 1153-1158 (2007).
2. Hell, S.W. Microscopy and its focal switch. *Nature Methods* 6, 24-32 (2009).

PL02
X-ray imaging at the nanoscale

T. Salditt[1]

[1]Institut für Röntgenphysik, Universität Göttingen, Göttingen

tsaldit@gwdg.de

X-rays deeply penetrate matter and thus provide information about the functional (interior) architecture of complex samples, from biological tissues and cells to novel composite materials. However, this potential of hard x-rays in view of penetration power, high spatial resolution, quantitative contrast, and compatibility with environmental conditions has to date not been fully developed, mainly due to significant challenges in x-ray optics. With the advent of highly brilliant radiation, coherent focusing, and lens-less diffractive imaging this situation has changed. We show how nano-focused coherent x-ray synchrotron beams can be used for scanning as well as for full field holographic x-ray imaging. The central challenge of inverting the coherent diffraction pattern is discussed. Different reconstruction algorithms are presented, from holographic techniques to ptchography, a phase retrieval approach adapted from electron microscopy, which has proven extremely useful in x-ray imaging [1].

Following an introduction to the basic concepts of lensless x-ray imaging, different recent examples of biological imaging are presented, ranging from bacterial [1,2] and eukaryotic cells [3], to the level of tissue and organs [4].

In particular, we show how holographic projection images recorded by using the quasi-point source of an x-ray waveguide can be inverted to quantitative two and three dimensional images of the object, see Fig.1. The experimental and conceptual aspects of image formation, object reconstruction, contrast transfer function and resolution will be discussed, and illustrated by different examples.

1. K. Giewekemeyer,et al. *Quantitative biological imaging by ptychographic x-ray diffraction microscopy*, PNAS 107 (2), 529 (2010)
2. R. N. Wilke, M. Priebe,M. Bartels,K. Giewekemeyer, A. Diaz, P. Karvinen, T. Salditt
Hard X-ray imaging of bacterial cells: nano-diffraction and ptychographic reconstruction
Optics Express 20, 19232-19254 (2012)
3. M. Bartels, M. Krenkel, J. Haber, R. N. Wilke, and T. Salditt
X-Ray Holographic Imaging of Hydrated Biological Cells in Solution
Phys. Rev. Lett. (2015), 114, 048103
4. M. Krenkel, A. Markus, M. Bartels, C. Dullin, F. Alves, T. Salditt
Phase-contrast zoom tomography reveals precise locations of macrophages in mouse lungs
Sci. Rep. (2015), 5, 09973

PL03
PICO: chromatically corrected TEM and its applications

J. Mayer[1,2], J. Barthel[2], L. Houben[2], M. Beigmohamadi[1,2], R. D.-Borkowski[2], K. Urban[2]

[1]Central Facility for Electron Microscopy, RWTH Aachen University, Aachen, Germany
[2] Ernst Ruska-Centre for Microscopy and Spectroscopy with Electrons, Research Centre Juelich, Juelich, Germany

mayer@gfe.rwth-aachen.de

The invention of aberration correctors has revolutionized the development of TEM and STEM instrumentation. Only shortly after the development and installation of the first TEM with a corrector for the spherical aberration [1], commercial instruments with aberration correctors are now offered by all major manufacturers. In order to provide a platform for these novel developments and based on the experience with the first aberration corrected TEM [2-4], Research Centre Juelich and RWTH Aachen University have jointly founded the Ernst Ruska-Centre for Microscopy and Spectroscopy with Electrons (ER-C) [5]. At the Ernst Ruska-Centre we have recently installed the FEI Titan 60-300 PICO. PICO is a fourth-generation transmission electron microscope capable of obtaining high-resolution transmission electron microscopy images approaching 50 pm resolution in the C_C- and C_S-corrected mode at 300 keV. It is currently one of only two microscopes in the world capable of chromatic aberration correction [6-8].

In the present contribution we will report on the initial results obtained with the PICO instrument (Fig. 1b). In the PICO instrument, HRTEM images can be obtained with simultaneous correction of the spherical and the chromatic aberration. Furthermore, a spherical aberration corrector also exists in the illumination system for Cs-corrected STEM imaging. The blurring caused by the chromatic aberration C_c is proportional to the energy spread ΔE and inversely proportional to the primary electron energy E:

$$d_c = \frac{1}{2} C_c \frac{\Delta E}{E} \theta$$

where θ represents the aperture angle. The benefits of chromatic aberration corrected imaging are thus particularly large for HRTEM imaging at low accelerating voltages and for energy filtered (EFTEM) imaging with large energy window width. In the present contribution we will focus on these two applications and will present results from our recent work [9, 10], Fig. 1b.

1. M. Haider, H. Rose, S. Uhlemann, E. Schwan, B. Kabius, and K. Urban, Nature 392 (1998) 768.
2. M. Lentzen, B. Jahnen, C.L. Jia, K. Tillmann, and K. Urban, Ultramicroscopy 92 (2002) 233.
3. C.L. Jia, M. Lentzen, and K. Urban, Science 299 (2003) 870.
4. C. L. Jia, K. Urban, Science 303 (2004) 2001.
5. http://www.er-c.org
6. B. Kabius, P. Hartel, M. Haider, H. Müller, S. Uhlemann, U. Loebau, J. Zach, and H. Rose, J. Electron Microsc. 58 (2009) 147.
7. H. Rose, Philos.Trans.R.Soc.A: Math.Phys.Eng.Sci. 367(2009)3809–3823.
8. M. Haider, P.Hartel, H.Müller, S.Uhlemann, J.Zach, Microsc.Microanal. 16(2010)393–408.
9. K. Urban, J. Mayer, J. Jinschek, M. J. Neish, N. R. Lugg, and L. J. Allen, PRL 110, 185507 (2013)
10. J. Barthel and A. Thust, Ultramicroscopy 134(2013)6–17.

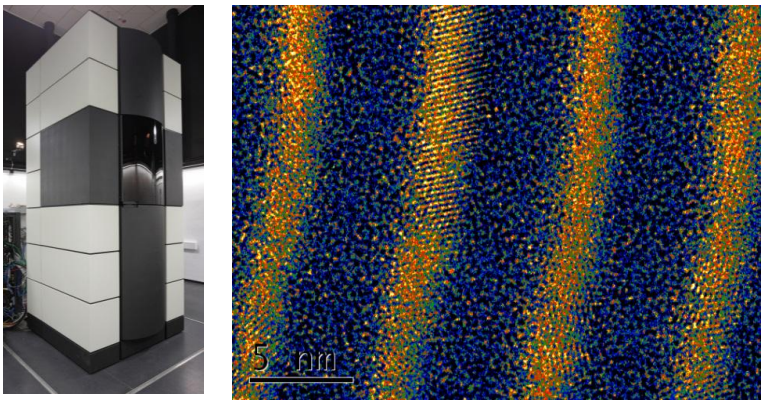

a **b**

Figure 1. The PICO instrument and an EFTEM map of the Si distribution in a multi-quantum-well solar cell.

ERL01

Three-dimensional atomic structure determination using electrons

J.-M. Zuo[1,2]

[1]Dept of Materials Science and Engineering, University of Illinois, Urbana-Champaign, UK
[2]Frederick Seitz Materials Research Laboratory, University of Illinois, Urbana-Champaign, UK

jianzuo@illinois.edu

Many technologically important materials possess complex nanostructures and structure dependent properties that require three-dimensional (3D) structure determination. Transmission electron diffraction (TED) and the related imaging are appropriate techniques for 3D nanostructure determination because they are highly sensitive to local atomic structure. Compared to X-ray diffraction, the small interaction volume in TED allows for high spatial resolution. However, because of the material dependent strong electron-matter interaction, a general approach to 3D structure analysis is still a challenge. Here. I will describe three approaches based on coherent electron diffraction, electron imaging and scanning electron nanodiffraction.

Traditionally, TED is performed either by using parallel beam illumination with the help of a selected area aperture for selected area electron diffraction (SAED) or by using a focused beam for convergent beam electron diffraction (CBED). For large crystals, accurate measurement of structure factor amplitudes and phases enables 3D reconstruction of electron potential or charge density and thus a direct visualization of chemical bonds [1]. For individual nanostructures, coherent electron nanodiffraction can be performed in a modern TEM instrument using a parallel electron beam of nanometers in diameter with help of an additional condenser lens (minilens) [2, 3]. Phasing of the electron diffraction pattern overcomes the microscope resolution limit and enables diffraction limited imaging[2]. For 3D analysis of nanostructures, there is a need to record multiple diffraction patterns or images by tilting the sample. With the 3D dataset, developments in reconstruction algorithms show that it is possible to reconstruct the atomic structure of an isolated small nanostructure[4, 5].

For atomic resolution imaging, recent advances in aberration correction enable the use of a larger condenser aperture than the conventional STEM[6]. The large aperture provides a reduced depth of focus and improved depth sensitivity. Together with the small electron probe (1 Å or less), this technique allows depth sectioning at high lateral resolution following the same principle as optical sectioning. Using an annular dark field (ADF) detector for Z-contrast imaging, several research groups have demonstrated 3D imaging of nanoparticles or detection of single atoms with a depth resolution of several nanometers, screw dislocations and interfacial atoms[7-10]. At the length scale of hundreds of nm, TEM based scanning electron nanodiffraction (SEND) technique is a promising technique for determining complex nanostructures at the resolution of few nm. In SEND, diffraction patterns are recorded by scanning the beam using the built-in TEM deflection coils and automatic camera readout[11]. In a conventional TEM with a LaB6 source, SEND can be performed in low dose mode using electron beams of ~2 nm in full-width at half-maximum (FWHM) and 0.1 pA or less in beam current[12]. Electron diffraction pattern indexing is achieved by a combination of correlation analysis of the recorded diffraction patterns, diffraction peak search and peak indexing using both length and angle information. By coupling with a tomographic holder, SEND can be performed with large sample tilts and thus the opportunity for the determination of 3D nanostructures at nanometer resolution with crystallographic information (Figure 1) [13].

1. J.M. Zuo, et al., Nature, 401 (1999) 49-52.
2. J.M. Zuo, et al., Science, 300 (2003) 1419-1421.
3. J.M. Zuo, et al., Microscopy Research and Technique, 64 (2004) 347-355.
4. X. Lu, et al., Ultramicroscopy, 149 (2015) 64-73.
5. M.C. Scott, et al., Nature, 483 (2012) 444-447.
6. H. Rose, Philos. Trans. R. Soc. A-Math. Phys. Eng. Sci., 367 (2009) 3809-3823.
7. A.Y. Borisevich, et al., Proc. Natl. Acad. Sci. U.S.A., 103 (2006) 3044.
8. W. Gao, et al., Nano Letters, 15 (2015) 2548-2554.
9. H.L. Xin, D.A. Muller, Journal of Electron Microscopy, 58 (2009) 157-165.
10. H. Yang, et al., Nature communications, 6 (2015) 7266.
11. J. Tao, et al., Physical Review Letters, 103 (2009) 097202.
12. K.-H. Kim, et al., Micron, 71 (2015) 39-45.
13. This work was supported by DOE BES (DEFG02-01ER45923) with contributions from Yifei Meng, Wenpei Gao and Xiangwen Lu.

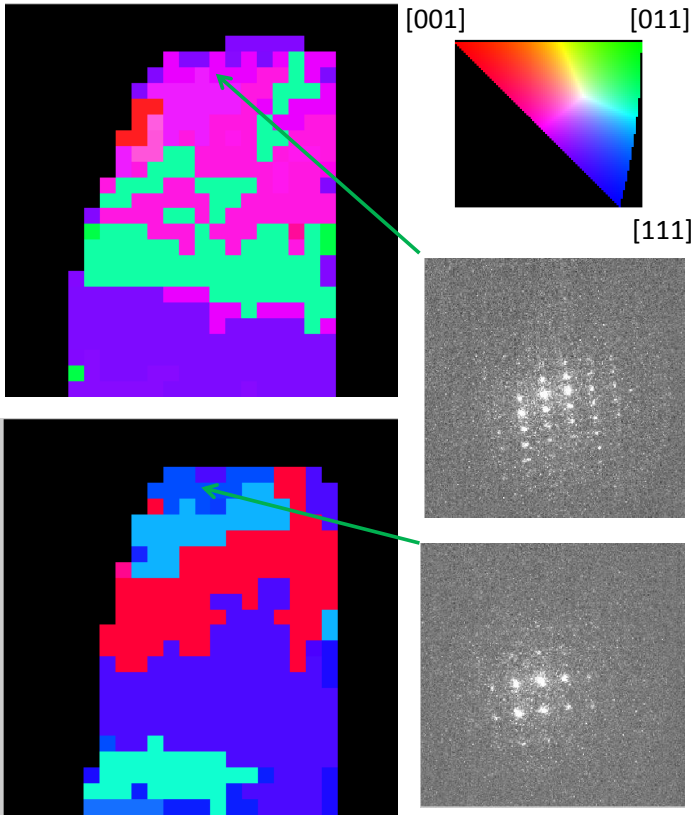

Figure 1. Orientation maps obtained from a high entropy alloy ($Al_{0.5}CoCrCuFeNi$) at two orientations of 30 degrees apart. The sample was first fabricated into a needle shape using FIB. SEND was performed using 25x25 sampling points over 240x240 nm^2 using an electron probe of 8 nm in FWHM The diffraction patterns were indexed using software developed at University of Illinois and colored according to the inverse pole figure at top-right corner. Two individual experimental diffraction patterns are shown on left.

ERL02
Doing structural biology in-situ – from molecules to cells

J. Plitzko[1], J. Briggs[2]

[1]Max Planck Institute of Biochemistry, Department of Molecular Structural Biology, Martinsried, Germany
[2] European Molecular Biology Laboratory Heidelberg, Structural and Computational Biology, Heidelberg, Germany

plitzko@biochem.mpg.de

We are experiencing a huge change in the role of the electron microscope in structural biology. This change is based on recent advances in imaging technology, particularly direct electron detection. Spectacular structures are being solved at near-atomic resolution by cryo-EM and there's more to come. The next challenge is to apply cryo-EM to study protein complexes and other biological objects within their native environment. Many supra- and macromolecular assemblies involved in key cellular processes cannot be studied in isolation; their function is so deeply rooted in their cellular context that it is impossible to isolate them without disrupting their structural integrity. Hence, it is highly desirable to study them in situ, within the virus or cell in which they perform their function.

Here, we will present our approaches towards in situ structural biology, - capturing three-dimensional structure at high resolution, unaltered by sample preparation. We will give an overview on recent advances in sample preparation, data collection and data processing, including technology for FIB milling, correlative light and electron microscopy, phase plate imaging and direct electron detection. We will present applications of these developments to determine biological structures in situ.

HRL
Exit wavefunction reconstruction – current status and future prospects

A. I. Kirkland[1]

[1]Department of Materials, University of Oxford, Oxford, UK

angus.kirkland@materials.ox.ac.uk

Exit wavefunction reconstruction is now firmly established as an important computational method for extracting quantitative information from high-resolution TEM images. The essence of the method is to seek solutions that invert the forward high-resolution phase contrast imaging process to recover the complex wavefunction at the exit surface (or other location) of the specimen from a suitably conditioned dataset of real image intensities.

This approach was originally proposed by Schiske [1] and subsequently extended by the groups of van Dyck and co-workers in Antwerp [2] and Saxton and Kirkland [3] in Cambridge using different input image geometries. For the former a series of axial images was used to extend the directly interpretable resolution limit from that set by the limits of spherical aberration to that imposed by partial coherence, whereas the latter used a tilt azimuth dataset, which enabled super-resolution beyond the axial limit.

This lecture will firstly review the historical development of this approach detailing the key electron optical and detector developments that enabled its practical application. I will also discuss the parallel developments in accurate aberration measurement which are required to suitably define the restoration filters used, with respect to approximations in the forward imaging process.

Subsequently, I will discuss the opportunities and advantages of combining electron-optical aberration correction and exit wave restoration with reference to selected materials problems.

Finally, I will discuss recent advances in which the restored wavefunction can be used to directly infer 3D structural data from local (atomistic) variations in the phase for weakly scattering objects and propose ways in which this could be extended to more general strong objects.

1. Schiske P. (1973). In Hawkes P. (Ed.), Image Processing and Computer Aided Design in Electron Optics, London: Academic Press, p. 82.
2. van Dyck D. & Coene W. (1984). Ultramicroscopy 15, 29–40.
3. Kirkland A.I., Saxton W.O., Chau K.L., Tsuno K. & Kawasaki M. (1995).Ultramicroscopy 57, 355–374.

PL04
Electron waves – reality shrouded in mystery

H. Lichte[1], F. Börrnert[1], B. Einenkel[1], A. Lenk[1], A. Lubk[1], F. Röder[1], J. Sickmann[1], S. Sturm[1], K. Vogel[1], D. Wolf[1]

[1]Triebenberg Laboratory, Technische Universität Dresden, Dresden, Germany

Hannes.Lichte@Triebenberg.de

Ernst Ruska wanted to overcome the Abbe-limit of resolution by microscopy, instead of light waves, using electrons, which he, in early days, considered as particles. As he writes in his memoirs [1], he was heavily disappointed to learn from the theoretician Houtermans that also electrons have to be described by waves. But he was much relieved finding out that the de Broglie-wavelengths of his electrons were by far smaller than atoms. So he could go on dreaming about imaging atomic details in solids. Of course, the concept of electron waves was well known under theoreticians, but not so popular with experimentalists. This is evident from the sentence “The reader need not fear that we will speak much about electron waves in this book....” by Brüche und Scherzer in [2]. In 1949, Scherzer brought the concept of electron waves to full awareness of electron microscopists in that he showed that atoms have to be considered phase objects, and hence the objective lens has to be operated at Scherzer focus, in order to obtain optimum phase contrast [3]. By this paper, he also gave birth to the description of image transfer in electron microscopy by means of the wave transfer function.

Irrevocably and convincingly, electron waves were revealed by means of electron biprism interference introduced by Möllenstedt and Düker in 1954 [4]. In the subsequent years, together with many coworkers, Möllenstedt showed the basic phenomena of electron interference as well as the fundamental phase shifting effects by electric and magnetic fields. Subsequently, electron holography, developed as a special way of pixelwise evaluating the interferometrical data, allows reconstructing amplitude and phase images of the electron wave. With the complete wave in the computer, all thinkable wave optical tools are applicable by numerical image processing for aberration correction and extraction of the object properties quantitatively. Since conventional phase contrast is rather poor – and even poorer with aberration correctors -, in particular the access to the phase-shifts has pioneered novel insight into solid state structures and properties.

At medium resolution with details larger than about 2 nm, the aberrations of the electron lenses can be neglected, and hence the reconstructed wave agrees with the object wave. Thus, the reconstructed phase distribution can directly be interpreted in terms of the object. This is the basis for achieving perfect phase contrast in focus without staining hence for determining

- Mean Inner Potentials in solids
- Functional potentials such as drift-diffusion potentials across pn-junctions
- Electric potentials across interfaces
- Trapping of charges at surfaces and interfaces
- Electric potential distributions in charge-modulated structures
- Magnetic fields in and around magnetic structures down to a nanoscale
- Magnetic leakage fields at structural inhomogeneities
- Ordering of magnetic nanoparticles
- Mechanical strain

and others. All these details are significant parts of the object structure, since they determine the functionality, e.g. in semiconductors and magnetics, and hence are indispensable for a comprehensive understanding of their properties.

At atomic resolution, because of the aberrations, amplitude and phase of the reconstructed wave differ considerably from the object wave and hence cannot be interpreted directly. First, the aberrations have to be corrected by appropriate processing. Then, both in amplitude and phase, lateral resolution can be achieved as high as determined by the information limit offered by the TEM used for recording the hologram. The resulting phase images allow details of the atomic structure to be revealed, such as

- Atomic potentials
- Difference of atomic numbers of different constituents
- Number of atoms in an atomic column

Recent developments

- Holographic Tomography. The phase signal represents the 2D-projection of the object structure integrated along the electron path. To obtain full 3D-information, the methods of holography and tomography are combined: A tilt series of holograms is recorded, from which the corresponding 2D-phase image series is reconstructed. Following tomographic procedures, from these 2D-images the 3D-representation is reconstructed, which allows uniquely determining 3D electric potential distributions and magnetic fields as well as elastic and inelastic attenuation coefficients.
- In situ Holography. The better the performance, the more object details contributing to the phase shift have to be considered. For example, electric phase shift variations may result from Mean Inner Potentials (MIP), thickness variations, e.g. by preferential etching, local variations of MIP at defects, boundaries, e.g. due to strain, surface states trapping charges, surface reconstruction, surface adsorption, doping, intended or unintended (impurities), electric polarization, etc. Therefore, we have to strengthen in-situ experiments where only the parameter of interest is varied, and a hence a better defined insight in solid state science is gained and used for a more detailed and accurate modeling of the substance under investigation.
- Inelastic Holography. By inelastic processes, coherence with respect to the elastic electrons is destroyed. However, the electron wave “newborn” by an inelastic event, such as excitation of a plasmon, has an appreciable area of coherence of about 30nm diameter in the object. This was measured by inelastic holography in an EFTEM path of rays. Strictly speaking, due to entanglement of the electrons with the object, these phenomena can only be described correctly by density matrices, which incorporate the propagation of coherence through the TEM.

In summary, one can say that, after 60 years of development, electron holography is an established method for comprehensive wave optical characterization of solids including their intrinsic electromagnetic fields. The performance, essentially restricted by quantum noise, allows atomic resolution both laterally and in signal. Lateral resolution of 0.08nm is reached in the holographically reconstructed wave. Phase resolution presently is about $2\pi/200$ at 0.1nm resolution, allowing detection of the electric field around the nucleus of single atoms. Any improvement of electron microscopes, such as of lateral resolution and of brightness of the electron gun, will enhance the capabilities of this unrivalled method for nanocharacterization. Therefore the new achievements such as the aberration corrector and electron sources with highest brightness will improve also the holographic analysis of smallest details in solids. And, we now have to learn dealing with density matrices describing the real world. Intrinsically, no science is ever settled!

1. E. Ruska, Acta Historica Leopoldina 12 (1979), p.33
2. E. Brüche und O. Scherzer, Geometrische Elektronenoptik, Springer 1934
3. O. Scherzer, Journal of Applied Physics 20 (1948), 20
4. G. Möllenstedt und H. Düker, Die Naturwissenschaften, Band 42 (1954), 41

PL05
Watching things fail: in-situ electron microscopy of fracture and flow

B. Kapelle[1], B. Roos[1], G. Richter[2], A. Kelling[1], C. Meckenhäuser[1], F. Süß[1], C. A. Volkert[1]

[1]Institute of Materials Physics, Georg August University, Göttingen, Germany
[2]Max-Plank-Institute for Intelligent Systems, Stuttgart, Germany

volkert@ump.gwdg.de

Deformation and fracture are complex and highly non-equilibrium processes which determine the strength of materials. Gaining insights into the mechanisms which control these dynamic processes requires dynamic methods. This presentation will describe in-situ electron microscopy studies of deformation and fracture in nanoscale specimens where we have been able to perform dynamic observations at length scales down to Angstroms and times scales between 0.1 seconds and several hours.

Our studies on deformation have been primarily focused on tensile loading of high quality Au nanowires using in-situ testing in the TEM and the SEM, where we observe the creation of dislocations by surface nucleation. Both the evolution of the defect morphology and the stress-strain behavior of the 20 nm to 300 nm diameter nanowires have been studied. We show that surface structure, stress state, and initial defects are more important in determining the deformation mode in nanoscale samples than the actual sample size. We also discuss evidence for reversible dislocation storage and the role of dislocation nucleation in the deformation of bulk metals.

Our studies on fracture have focused on crack propagation in nanolaminates, where we attempt to decipher the roles of surfaces and interfaces by propagating cracks parallel and perpendicular to the layer interfaces. We can directly observe the extent of the plastic zone in the TEM, which allows a qualitative connection between plasticity, fracture toughness values, and the selection of the crack propagation path. Furthermore, we observe changes in the crack path with layer thickness that we attribute to a size-dependent flow stress. The implications of such size dependent effects on the fracture toughness of nanocomposites will be discussed.

PL06
3D electron microscopy for cell biology

P. Walther[1]

[1]Central Facility for Electron Microscopy, Ulm University, Ulm, Germany

paul.walther@uni-ulm.de

We adapted and explored protocols for 3D imaging of electron microscopic samples. These are serial sectioning transmission electron microscopy (TEM); scanning transmission electron microscopy (STEM) tomography; and focused ion beam/scanning electron microscopy (FIB/SEM) tomography. With these methods relatively large volumes such as organelles or whole cells can be analyzed at resolutions of a few nm within a reasonable expenditure of time. These methods close the gap between 3D light microscopy and serial block-face SEM on the one hand side, and cryo-TEM single particle analysis on the other hand side.

The classic method is serial sectioning and imaging the same area in all sections. Another method is TEM tomography that involves tilting a section in the electron beam and then reconstruction of the volume by back projection of the images. When the scanning transmission (STEM) mode is used, thicker sections (up to 1 µm) can be analyzed [1, 2]. The third approach presented here is focused ion beam/scanning electron microscopy (FIB/SEM) tomography, in which a sample is repeatedly milled with a focused ion beam (FIB) and each newly produced block face is imaged with the scanning electron microscope (SEM). This process can be repeated ad libitum in arbitrary small increments. Resolution of this approach is considerably improved, when the secondary electron signal is used [3].

The most important prerequisite for all imaging approaches is adequate specimen preparation. We used cryo-fixation (high-pressure freeing), freeze substitution and plastic embedding. This method provided very reproducible results, what is essential when structural questions from the biomedical field need to be answered. Examples are host – pathogen interactions and analysis of the networks of intermediate filaments and amyloid fibers.

1. Hohmann-Marriott et al. (2009) Nanoscale 3D cellular imaging by axial scanning transmission electron tomography. Nat Methods. 6, 729-31
2. Höhn et al. (2011) Preparation of cryofixed cells for improved 3D ultrastructure with scanning transmission electron tomography. Histochem Cell Biol. 135, 1-9.
3. Villinger et al. (2012) FIB/SEM-tomography with TEM-like resolution for 3D imaging of high pressure frozen cells. Histochem Cell Biol 138, 549-556.

Functional Materials (magnetic, ferroelectric, ferroic, uperconducting, electronics)

MS1.001
Interpretation of holographic phase shifts from polar interfaces, ferroelectric nanostructures and charged dielectric materials

M. Beleggia[1,2]

[1]Center for Electron Nanoscopy, Technical University of Denmark, Lyngby, Denmark
[2]Helmholtz-Zentrum Berlin für Materialen und Energie, Berlin, Germany

mb@cen.dtu.dk

Electron holography experiments carried out on polar materials have proven extremely challenging [1,2]: contrary to ferromagnets, where the electron beam is affected by the magnetization, polarization alone is invisible to phase-sensitive techniques. The origin of this fundamental difference can be traced back to the Lorentz force: magnetic deflections are proportional to the B-field, of which M is an integral part, while electric deflections are proportional to the E-field; an electric field might as well be generated by bound polarization charges if present, but with a non-linear and, in a sense, non-local relationship as polarization charges may be very far away from the illuminated region of the sample. Moreover, the absence of magnetic monopoles combined with quantization of angular momentum, which applies only to spins and not to electric dipoles, results in screening/depolarizing effects manifesting themselves very differently in magnetic and electric polar materials.

In nanoparticles made of materials that are ferroelectric in bulk form, the polarization is suppressed by its own depolarization field [3]. To preserve P below a certain critical size, screening of the depolarization field must occur. Screening can be internal --redistribution of mobile charges in metallic or oxygen-vacant insulating ferroelectrics-- or external in case of embedment in a dielectric or metallic matrix. However, if the screening is 100% effective the internal electric field vanishes entirely, giving rise to no observable holographic signal. A trade-off needs to be found between screening capacity and magnitude of the resulting polarization that maximizes the residual internal field producing observable phase shifts. This trade-off will be discussed, highlighting realistic and achievable experimental conditions that may facilitate the success of holography experiments on ferroelectric nanostructures.

An omnipresent complication when interpreting holographic signals from nanoparticles originates from beam-induced charging. A poorly conductive object tends to charge positively upon irradiation due to secondary electron generation. When the object is supported by a conductive substrate, image charge effects will produce an overall dipole field from a charge object, i.e. with the same expected character as the stray field from polarization. As a result, separating charging and polarization is extremely challenging, and can be accomplished only by proper modelling and careful measurement strategies.

In case of polar interfaces [4], for example a ferroelectric layer sandwiched in between dielectrics, or heterostructures involving charge-layered oxide materials such as LaAlO3 in contact with doped or undoped SrTiO3 where a 2D electron gas may emerge, determining whether or not we can expect a phase shift is a difficult task. In addition to self-depolarization, particularly strong in parallel-plate-capacitor situations, we need to handle the band structure relaxation bringing extra mobile charges into the picture: charge transfer may occur even with insulators, if band bending is so severe that the chemical potential dips into their valence band. A test scenario involving two ferroelectrics with different bulk polarizations, with and without chemical potential shift will be presented to illustrate the complexity of the problem, and to provide an initial framework for the interpretation of holographic signals from polar interfaces.

1. D. Szwarcman et al., Phys. Rev. B 85, 134112 (2012)
2. M.J. Polkin et al., Nature Materials 11, 700 (2012)
3. C. Phatak et al., Phys. Rev. B 89, 214112 (2014)
4. N. Nakagawa et al., Nature Materials 5, 204 (2006)

Functional Materials (magnetic, ferroelectric, ferroic, uperconducting, electronics)

MS1.002
Study of spontaneous skyrmion and room temperature helimagnetic phase in Mn-Pt-Sn Heusler material by Lorentz TEM and differential phase contrast (DPC) microscopy

J. Wild[1], A. K. Najak[2,3], S. S. P. Parkin[3], C. Felser[2], J. Zweck[1]

[1]Universität Regensburg, Fakultät für Physik, Regensburg, Germany
[2]Max Planck Institute for Chemical Physics of Solids, Dresden, Germany
[3]Max Planck Institute of Microstructure Physics, Halle, Germany

johannes1.wild@ur.de

Magnetic skyrmions are particle like two-dimensional topologically stable spin textures. They were theoretically predicted by T. Skyrme over 25 years ago [1] and experimentally first observed six years ago [2]. Skyrmions can be found mostly in a particular class of chiral magnets with ordering temperatures below room temperature and are in most cases stabilized by external magnetic fields. They can be moved by low currents what makes them interesting for use in new storage devices like in the recently proposed race track memory device [3]

We present the first observation of skyrmions at zero field, so called spontaneous skyrmions, in Mn-Pt-Sn Heusler alloy. These skyrmions are extremely stable for fields from zero to more than 2 T, in a temperature range between 130 to 160 K. Additionally we observe a helimagnetic phase for low temperatures and for high temperatures up to 400 K.

The in-plane induction of the spin textures were measured by means of Lorentz transmission electron microscopy (LTEM) and differential phase contrast (DPC) microscopy. In LTEM a defocus-series was taken and the phase shift calculated by the transport of intensity equation (TIE). The direction and strength of the relative induction was then calculated from the phase shift. This method is quite common for studies of skyrmions in the TEM [4-5]. It has been demonstrated that DPC is capable to measure different micromagnetic structures in a STEM [6], too. DPC microscopy is operated in scanning TEM (STEM) mode while the deflection of the focused electron beam is measured by a four segment detector. The relative in-plane induction vector is calculated from the beam deflection at each pixel. To our knowledge we show the first study of skyrmions and helical phase with DPC microscopy.

Figure 1A shows a overfocused LTEM image taken at 300 K at zero magnetic field, the TIE analysis of this area is depicted in figure 1B. With application of magnetic fields the helimagnetic stripes increase their periods to more than 150 nm, at 0.25 T the periodicity becomes larger than 150 nm and transfers into a collinear FM spin state. At low temperatures we observe rather inhomogeneous stripes with irregular periodicity between 50 nm to 150 nm and a large numbers of dislocations. The application of magnetic field induces a similar effect as that at 300 K. We found that discreet skyrmions start appearing in addition to the magnetic stripes around 125 K like shown in Figure 2. With increasing temperature the material completely transfers into the skyrmion phase at $T \approx 135$ K and remains unchanged for magnetic fields up to 0.5 T like shown in figure 2. Surprisingly, we also observe skyrmions for a magnetic field of 2 T. The skyrmion phase disappears completely at 160 K.

We demonstrated the experimental realization of a spontaneous skyrmion ground state and a room temperature helimagnetic ordering in an acentric class of Heusler material. We could image the magnetic structures with LTEM and TIE and realized the first observation of these structures with DPC microscopy.

1. Skyrme, T. H. R. Nucl. Phys. 31, 556-569 (1962).
2. Mühlbauer, S. et al. Science 323, 915-919 (2009).
3. S. S. P. Parkin et al. Science 320, 190 (2008).
4. Yu, X. Z. et al. Nature 465, 901-904 (2010).
5. Seki, S. Science 336, 198-201 (2012).
6. T. Uhlig. Phys. Rev. Lett. 93(4) 047203 (2004).

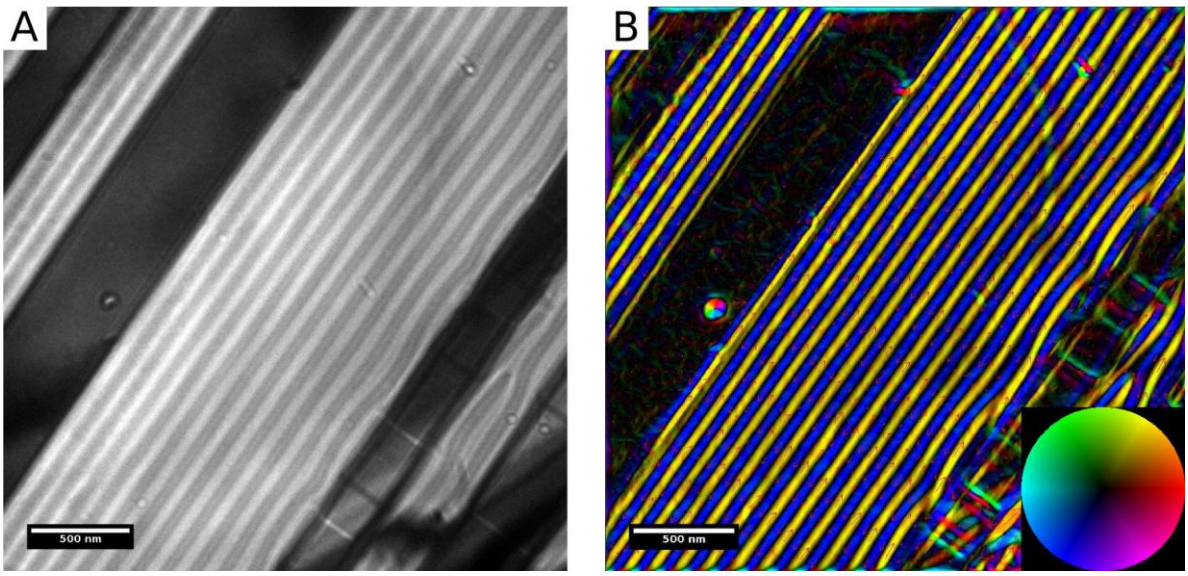

Figure 1. (A) Room temperature overfocus LTEM image showing the stripe modulation of the magnetic structure. (B) Reconstructed TIE image from under-, in- and overfocused LTEM images. The color at each magnetic stripe corresponds to the spin directions as demonstrated in the color wheel in the inset.

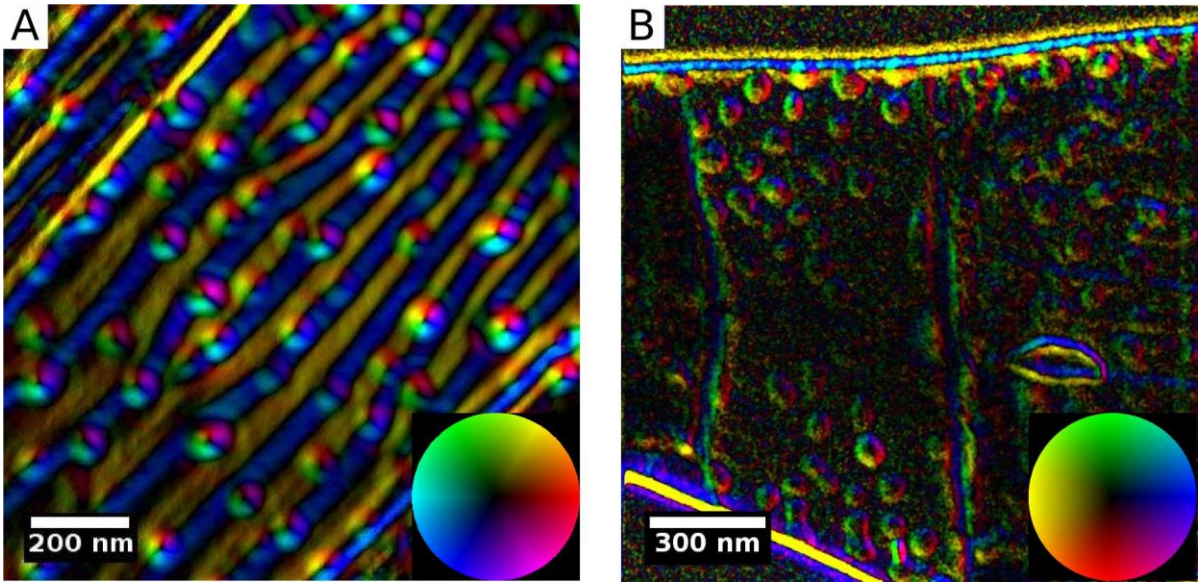

Figure 2. Relative in-plane induction of skyrmions and helical phase reconstructed by LTEM and TIE (A) and measured with DPC microscopy (B).

Functional Materials (magnetic, ferroelectric, ferroic, superconducting, electronics)

MS1.003
TEM studies on $RMnO_3$ multiferroic materials

Q. H. Zhang[1], G. T. Tan[2], L. J. Wang[1], L. Gu[1], A. Hirata[3], M. W. Chen[3], C. Q. Jin[1], Y. Yao[1], Y. G. Wang[1], X. F. Duan[1], R. Yu[1]

[1]Institute of Physics, Chinese Academy of Sciences, Laboratory for Advanced Materials & Electron Microscopy, Beijing, China
[2]Beijing Normal University, Department of Physics, Beijing, China
[3]Tohoku University, 3. WPI Advanced Institute for Materials Research, Sendai, Japan

rcyu@aphy.iphy.ac.cn

Multiferroic materials, displaying simultaneously ferromagnetism and ferroelectricity, have recently attracted growing interest due to their intriguing physical properties and potential applications.[1,2] In this presentation, we show our transmission electron microscopy results of $RMnO_3$ multiferroic materials. Using state-of-the-art aberration-corrected annular-bright-field and high-angle annular-dark-field scanning transmission electron microscopy, we investigated the structure of multiferroic vortex domains in $YMnO_3$ at atomic scale. Two types of displacements were identified among six domain walls; six translation-ferroelectric domains denoted by α+, γ−, β+, α−, γ+ and β−, respectively, were recognized, demonstrating the interlocking nature of the anti-vortex domain. We found that the anti-vortex core is about four unit cells wide. We reconstructed the vortex model with three swirling pairs of domain walls along the [001] direction. Two types of 180 degree domain walls, i.e., the transverse and the longitudinal domain walls are identified, which is in consistency with the interlock between ferroelectric and structural translation domain wall predicted previously [3]. These wall structures are different from the polarization inversion in conventional ferroelectrics. These results [4-6] are very critical for the understanding of topological behaviors and unusual properties of the multiferroic vortex. In addition, we found a new ferroelectric phase induced by oxygen vacancy ordering. We proposed a proper structure model and examined its correctness.

1. A. J. Freedman and H. Schmid, Magnetoelectric Interaction Phenomena inCrystals, Gordon and Breach:London (1975).
2. G. Srinivasan, E. T. Rasmussen, B. J. Levin, and R. Hayes, Phys. Rev. B, 65 (2002) 134402.
3. T. Choi, Y. Horibe, H. T. Yi, Y. J. Choi, W. D. Wu, and S. W. Cheong, Nat. Mater. 9 (2010) 253.
4. Q. H. Zhang, L. J. Wang, X. K. Wei, R. C. Yu, L. Gu, A. Hirata, M. W. Chen, C. Q. Jin, Y. Yao, Y. G. Wang, X. F. Duan, Phys. Rev. B (R), 85 (2012) 020102.
5. Qinghua Zhang, Guotai Tan, Lin Gu, Yuan Yao, Changqing Jin, Yanguo Wang, Xiaofeng Duan, Richeng Yu, Scientific Reports, 3 (2013) 2471.
6. Qinghua Zhang, Sandong Guo, Binghui Ge, Peng Chen, Yuan Yao, Lijuan Wang, Lin Gu, Yanguo Wang, Xiaofeng Duan, Changqing Jin, Banggui Liu, and Richeng Yu, J. Am. Cer. Soc., DOI: 10.1111/jace.12747.

Functional Materials (magnetic, ferroelectric, ferroic, superconducting, electronics)

MS1.004
Microstructural investigation of ultra-low fatigue in NiTiCu shape memory thin films by transmission electron microscopy

J. Strobel[1], T. Dankwort[1], C. Chluba[2], R. Lima de Miranda[2], W. Ge[3], M. Wuttig[3], E. Quandt[2], L. Kienle[1]

[1]Technical Faculty, CAU Kiel, Synthesis and Real Structure, Kiel, Germany
[2]Technical Faculty, CAU Kiel, Inorganic Functional Materials, Kiel, Germany
[3]University of Maryland, Materials Science, College Park, MD, United States

just@tf.uni-kiel.de

Their unique mechanical properties make the implementation of shape memory alloys (SMAs) highly desirable in a wide range of fields; the shape memory effect is the basis of modern solid state actuators as well as self-expanding cardiovascular stents, whereas superelasticity enables medical implants such as orthodontic arch wires and tools for minimally invasive surgery. [1] For future technologies like solid-state cooling or artificial heart valves the superelastic effect has to be cycled repeatedly and continuously for millions of cycles, which so far has been rendered impossible by pronounced fatigue in all available SMAs. Among these, NiTi-based alloys are the most studied and employed representative. The standard route towards lower fatigue was alloys with an equiatomic composition between Ni and Ti lattice positions to reduce the fraction of precipitates as much as possible. [2] Recently, however, a novel NiTiCu-based SMA has been discovered which exhibits ultra-low fatigue even after millions of cycles, even though it contains a high fraction of 54 at% Ti. This alloy represents the starting point on the way to reveal how SMAs in general can be tailored for long cycle stability. Extensive transmission electron microscopy (TEM) studies have been performed on these NiTiCu thin films to understand what the high fatigue-resistance is enabled by.

We present evidence that the Ti-containing precipitates are indeed crucial for this behavior: by forming epitaxial interfaces with the phase-changing matrix they mediate the complete phase transformation from B19 martensite to B2 austenite and back. [3] This completeness makes sure that no residual martensite can accumulate during back-and-forth transformation, which would ultimately lead to functional fatigue. It is assured by a preferential epitaxial coupling of Ti2Cu-type grains to austenite instead of martensite. The strain induced by the interfaces caters for the complete back transformation to austenite upon removal of mechanical load; investigations indicate the back transformation originates at these strained interfaces that always seem to incorporate an austenite-like transition layer of a few nanometer thickness. (Fig. 1) The strained epitaxial intergrowth is facilitated by the potential formation of several epitaxial interfaces for one precipitate yielding a high probability of epitaxial coupling for each individual martensite grain. Investigations were hampered by pronounced beam sensitivity of the samples. On multiple occasions a deterioration of B19 reflection has been observed (Fig. 2) which we interpret as a beam induced phase transformation to the B2 phase.

1. T. Duerig, A. Pelton, and D. Stockel , "An overview of Nitinol medical applications," *Materials Science and Engineering A*, vol. 273, pp. 149-160, 1999.
2. K. Otsuka and X. Ren, " Physical metallurgy of Ti-Ni-based shape memory alloys," *Progress in Materials Science*, vol. 50, pp. 511-678, 2005.
3. C. Chluba, et al., "Ultra-low fatigue NiTiCu shape memory alloy films," *submitted to Science*, 2014.

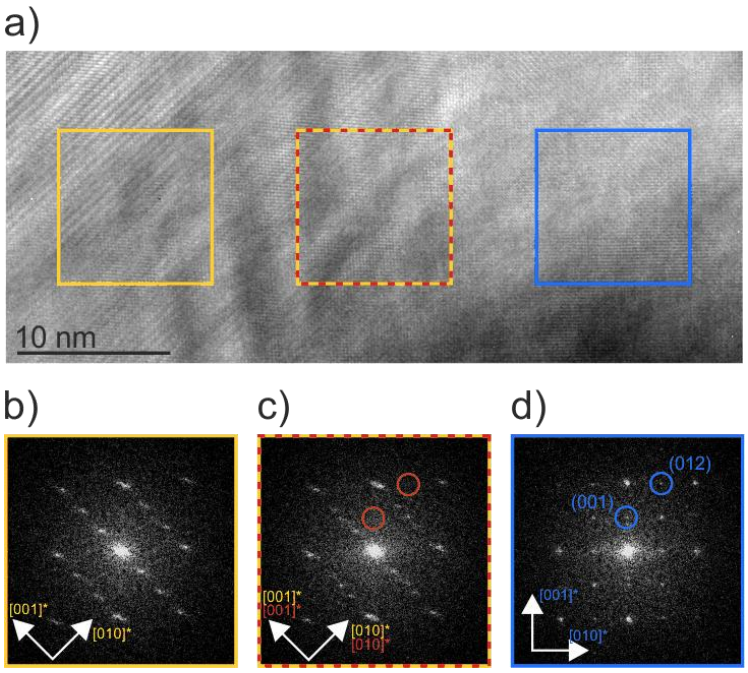

Figure 1. a) HRTEM micrograph of a Ti_2Cu-martensite interface. Colored squares indicate areas where the FFTs depicted in b) - d) have been calculated. b) FFT of Ti_2Cu, d) FFT of B19, zone axes are both 100. c) FFT of the indermediate region exhibiting a lack of characteristic B19 reflections (red circles) indicating that the structure rather resembles B2 austenite.

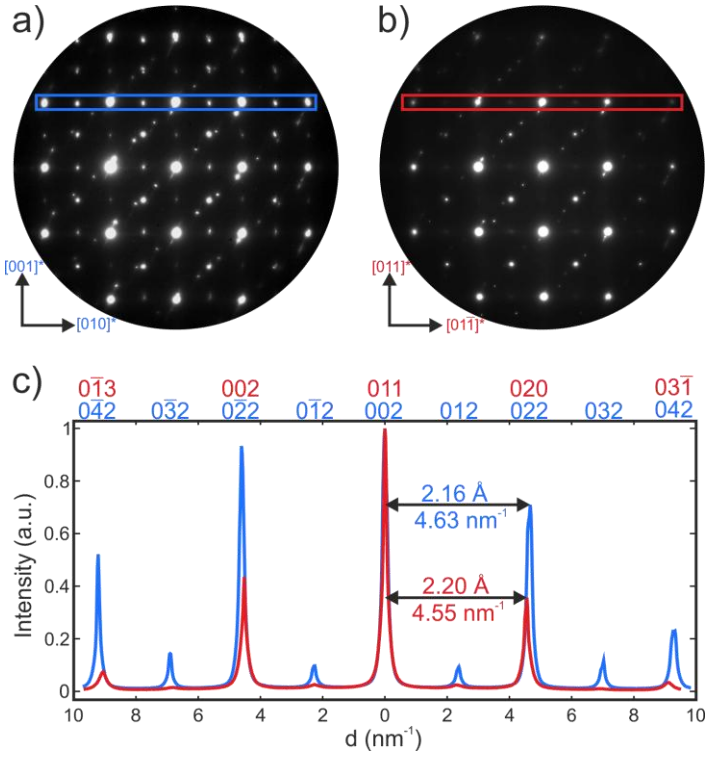

Figure 2. Diffraction patterns of region initially containing martensite. a) SAED of 100 B19. The characteristic (012) peaks are clearly visible. b) The same sample region after several minutes of exposure with a parallel e-beam. The reflections that are both visible in B2 and B19 are still present, but the characteristic 012B19 peaks have almost vanished, indicating that a phase transformation to B2 (ZA 100) has been induced. c) Profile along the colored rectangles in a) and c) proving the extenuation of 012B19 peaks and a slight increase in lattice parameter as expected for a B19-B2 phase transformation. Intensities have been normalized to 002B19/011B2 peak intensity.

Functional Materials (magnetic, ferroelectric, ferroic, superconducting, electronics)

MS1.005
Atomic structure and local chemistry of Sr-δ-doped La_2CuO_4 multilayers using aberration-corrected analytical STEM

Y. Wang[1], W. Sigle[1], D. Zhou[1], F. Baiutti[1], G. Logvenov[1], G. Gregori[1], G. Cristiani[1], J. Maier[1], P. A. van Aken[1]

[1]Max-Planck-Insititute for Solid State Research, Stuttgart, Germany

y.wang@fkf.mpg.de

Superconductivity in copper oxides arises when a parent insulator compound is doped beyond some critical concentration [1]. In the case of La2CuO4 (LCO), high-Tc superconductivity is obtained either by substituting La3+ with Sr2+ or by inserting interstitial O2- [2]. At internal interfaces, the enhancement of the superconducting critical temperature is influenced by the interfacial structure [3]. Recently, by using atomic layer-by-layer oxide molecular beam epitaxy (MBE), we have fabricated Sr-δ-doped LCO multilayered structures on LaSrAlO4 (LSAO) substrate, in which some atomic planes of LaO were intentionally substituted by SrO. By varying the spacing between the LCO and SrO layers high-*Tc* superconductivity (~ 40 *K*) was obtained [4]. In this study we focus on the detailed and quantitative scanning transmission electron microscopy (STEM) analysis in combination with energy-dispersive x-ray (EDX) analysis and electron energy-loss spectroscopy (EELS).

For the present contribution, we combine atomic-resolved quantitative STEM imaging with analytical STEM-EELS/EDX analysis to understand the occurrence of high-*Tc* superconductivity at Sr-δ-doped LCO interfaces with respect to the local lattice and oxygen octahedral distortion, as well as cation and electron hole redistribution. STEM investigations were performed using a JEOL JEM-ARM 200F scanning transmission electron microscope equipped with a cold field emission electron source, a DCOR probe corrector, a 100 mm2 JEOL Centurio EDX detector, and a Gatan GIF Quantum ERS electron energy-loss spectrometer.

Figure 1a shows a cross-sectional high-angle annular dark-field (HAADF) STEM image of Sr-δ-doped LCO multilayers, revealing that LCO and the LSAO substrate exhibit perfect epitaxy and show no local structural defects at the -δ-doped interfaces. From the HAADF image intensity, we can clearly see that the atomic column intensity in Sr-δ-doped region is lower than in pure LCO, due to the difference in the atomic number of La and Sr (ZSr=38, ZLa=57). The average image intensity profile in growth direction shows that at the Sr-δ-doped region the image intensity has a relatively sharp drop of intensity followed by a slowly increasing intensity pointing to an asymmetric Sr distribution. Atomic-resolved HAADF and ABF images, which were simultaneously acquired at the Sr-δ-doped region, are presented in Figs. 1b and 1c. In these images, all the atomic columns (La/Sr, Cu, O) have been resolved. The local lattice and copper-apical-oxygen distortions were quantitatively evaluated by image analysis and the association between these distortions and the superconductivity will be discussed.

A detailed study on the redistribution of Sr and of electron holes at the interface was performed by a combination of atomic-resolved STEM-EELS/EDX. The Sr-*L* EDX and Sr-L2,3 EELS (Fig.2 a) line-scan profiles show that Sr is redistributed over a few layers in LCO and has an asymmetric concentration profile. The electron holes across the Sr-δ-doped interfaces were characterized by analysis of the O-*K* near-edge fine structure, as presented in Figs. 2b and 2c. A comparison of the Sr and electron holes profiles suggests a rather complex charge rearrangement mechanism which account for the occurrence of the high-*Tc* superconductivity. [5]

1. P.A.Lee *et al.*, Rev.Mod.Phys. **78** (2006) 17
2. B.O.Wells *et al.*, Science **277** (1997) 1067
3. A.Gozar *et al.*, Nature **455** (2008) 782
4. F.Baiutti *et al.*, submitted (2015)
5. The research leading to these results has received funding from the European Union Seventh Framework Program under Grant Agreement No.312483 (ESTEEM2). U. Salzberger is particularly acknowledged for TEM specimen preparation.

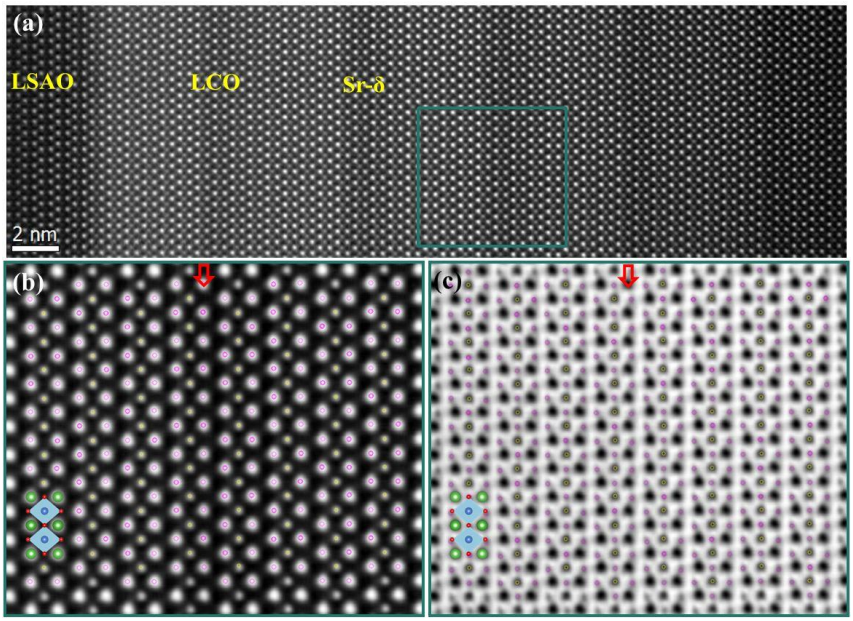

Figure 1. (a) HAADF image of Sr-δ-doped LCO multilayers epitaxially grown on a LSAO substrate. Simultaneously acquired (b) HAADF and (c) ABF images of one Sr-δ-doped region, on which the atomic columns have been marked for quantification of the lattice and copper-apical-oxygen distortions.

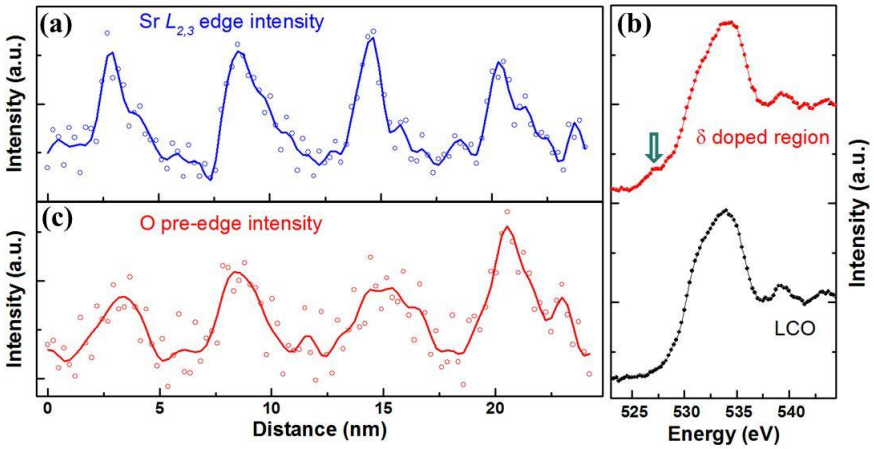

Figure 2. (a) Integrated Sr-$L_{2,3}$ EELS line profiles across 4 Sr-δ-doped regions. (b) O-K edge from a Sr-δ-doped region and from LCO. (c) Integrated O-K pre-edge intensity profile across 4 Sr-δ-doped regions.

Functional Materials (magnetic, ferroelectric, ferroic, superconducting, electronics)

MS1.P006
Energy diffractive imaging and spectroscopy of ferromagnetic $La_{0.7}Ba_{0.3}MnO_3$ thin films for resolving magnetic properties

X. Li[1], I. Verjoiu[1], P. A. van Aken[1]

[1]Max Planck Institute for Solid State Research, Stuttgart, Germany

xiaoyan.li@is.mpg.de

The development of quantitative magnetic characterization techniques down to the atomic scale promises a further progress in nanotechnology, such as for high density data storage. A reliable method to perform the magnetism measurement at such high spatial resolution is based on electron magnetic circular dichroism (EMCD) in a transmission electron microscope (TEM) - a novel method first developed by Schattschneider et al. in 2003 [1, 2]. Recently, an attractive technique of utilizing an astigmatic electron probe within a *C*s-corrected scanning electron transmission microscope (STEM) was proposed by Rusz et al. [3], showing great potential for measuring EMCD with atomic resolution. Their calculation reveals that it is possible to obtain the EMCD signal in the transmitted beam directly without the necessity of producing electron vortex beams. The crucial feature is the relation between crystal structure, magnetic symmetry of the sample, and distribution of the phase in the electron beam. A certain amount of aberration should be introduced to obtain the required phase symmetry of the electron beam and to measure the non-zero EMCD signal in the transmitted beam. This magnetic signal reaches its maximum intensity (~1%) when the beam is passing directly through an atomic column, and drops dramatically when the beam is shifted away from the column (shift > ½ FWHM of the beam). Practically, by simply taking the difference of in-column and off-column spectra, or of different atomic columns with opposite magnetic moments (in anti-ferromagnetic materials), the EMCD signal can be extracted at the atomic scale.

In our work, we are aiming at obtaining the EMCD signal with atomic resolution experimentally. The work is firstly carried out on the La0.7Ba0.3MnO3 (LBMO) ferromagnetic thin films where the magnetism is provided by Mn. Since the properties of perovskite materials are closely related to their structures, the preliminary STEM study was carried out using a JEOL ARM200F under aberration-corrected conditions to gain insight into the structural and chemical nature of the thin film. The high-angle annular dark-field image in Fig. 1a shows a cross-sectional view of a perovskite SrRuO3 (SRO)/LBMO/SRO multilayer heterostructure on SrTiO3 substrate, where no structural defects are observed. Further atomically resolved EELS-based elemental mapping of Ti, La, Ba, Mn are acquired across the thin film, as shown in Fig. 1b, demonstrating a sharp non-diffusing interface between LBMO and its neighboring SRO layers. The electronic structure of Mn was probed across the LBMO layer by means of high-energy resolved ELNES at the Mn-L2,3 edges (Fig. 1c). The ELNES spectra extracted from the interfaces show the same features as the ones within the layer, indicating a well-defined homogeneous chemical structure of Mn. These low-defect microstructures can explain the good magnetic property of LBMO at such low thickness (2.5 μB/Mn). In future, EELS spectrum images with sub-Å pixel size will be recorded under aberrated probe conditions, together with accurate measurements of the aberrations, expecting for a possibly reliable EMCD signal [4].

1. C. Hebert, P. Schattschneider: Ultramicroscopy **96** (2003) 463
2. P. Schattschneider et al.: Nature **441** (2006) 486
3. J. Rusz, J.-C. Idrobo and S. Bhowmick, Phys. Rev. Lett. **113** (2014) 145501
4. The research leading to these results has received funding from the European Union Seventh Framework Programme [FP7/2007-2013] under grant agreement n°312483 (ESTEEM2). XL gratefully acknowledges Dr. Yi Wang for the introduction and support with the microscopic investigations

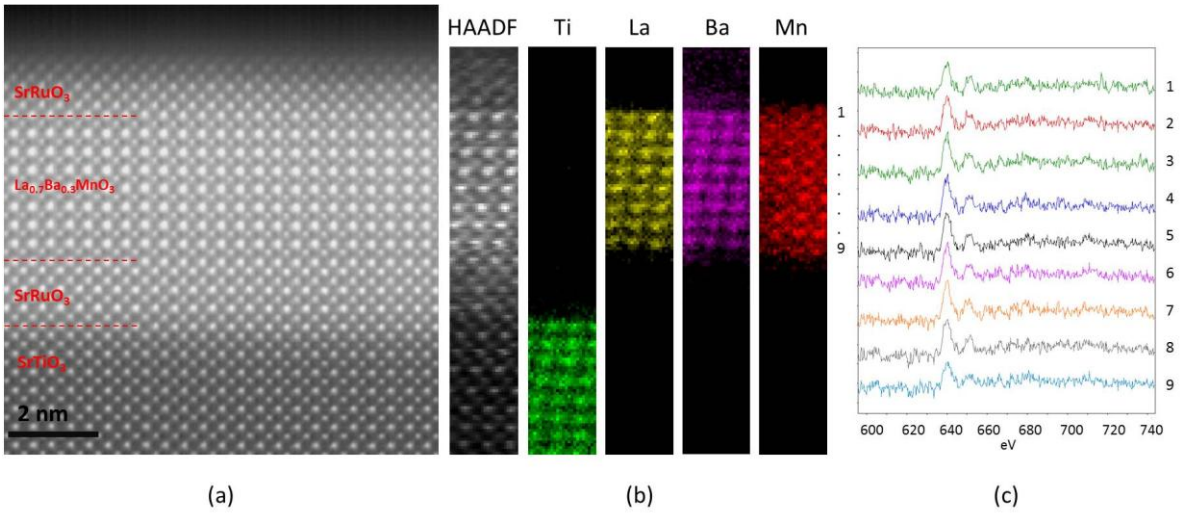

Figure 1. (a) STEM-HAADF image of the $La_{0.7}Ba_{0.3}MnO_3$ ferromagnetic thin film. (b) STEM-HAADF image and corresponding STEM-EELS elemental maps of Ti, La, Ba, Mn for the heterostructure. (c) EELS spectra of Mn $L_{2,3}$ extracted from every atomic layer of Mn.

Functional Materials (magnetic, ferroelectric, ferroic, superconducting, electronics)

MS1.P007
Magnetic structure of magnetite nanoparticles studied by electron holography

K. Vogel[1], S. Sturm[1], D. Wolf[1], E. Rosseeva[2], M. Helminger[2], H. Cölfen[2]

[1]Technische Universität Dresden, Institut für Strukturphysik, Dresden, Germany
[2]University of Konstanz, Department of Chemistry, Konstanz, Germany

karin.vogel@triebenberg.de

Electron holography is a powerful tool for investigation of magnetic specimens because the phase of the electron wave is sensitive to magnetic fields within or around the sample. Here, we apply off-axis electron holography for characterizing the magnetic structure of magnetite nanoparticles. The particles had been synthesized to mimic the structure and properties of magnetite crystals in magnetotactic bacteria. These bacteria contain magnetite nanocrystals arranged along a chain within the bacteria. The magnetization of the nanocrystals is nearly parallel to the axis of the chain, as shown by electron holography [1]. The aim of our studies is to check whether the synthesised magnetite nanoparticles show similar properties like the “natural” magnetite crystals within the bacteria.

The magnetite nanoparticles were synthesized using a precipitation method by slow addition of iron (II) sulfate solution to an aqueous solution containing the mixtures of potassium hydroxide and potassium nitrate (oxidizing agent). The synthesis was performed under nitrogen atmosphere. The resulting product was washed several times with degassed Milli-Q water and a drop of this suspension was placed on a TEM-grid.

For the holographic investigations we used a Philips CM200 TEM equipped with a Lorentz lens and an electrostatic biprism. The Lorentz lens allows investigating magnetic samples under virtually field-free conditions. The objective lens can be used to change the magnetization direction in the particles. After choosing a suitable chain of magnetite particles (Fig. 2a), the Fischione dual tilt tomography holder model 2050 was rotated to align the chain perpendicular to the tilt axis. Then, the specimen was tilted to +75 degree to achieve a large component of the magnetic field along the chain by switching on the objective lens. After a few seconds the objective lens was switched off, the holder was tilted back to zero, and the hologram was acquired under field-free conditions. To reverse the magnetization direction, the procedure was repeated with the specimen tilted to an angle of -75 degree.

From the holograms the complete electron wave in amplitude and phase was reconstructed. Figs. 1a and 1b show reconstructed phase images of the magnetite chain after exposition to external magnetic fields H in opposite direction. By comparing the phase profiles in Fig. 1c, it becomes evident that the magnetization direction in the chain has changed when the external magnetic field was reversed. Since the phase shift is not only influenced by the magnetic induction B, but also by the mean inner (electric) potential, we have to separate its magnetic and electric parts. This can be done by calculating half the difference and the sum of the two phase images shown in Figs. 1a and 1b. The separated magnetic phase contribution is shown in Fig. 2b. From the gradient of the magnetic phase, we obtained the induction map shown in Fig. 2c. The white lines in the map are lines of equal phase shift and correspond to the field lines of the projected B-field. The induction map reveals that the magnetization in the particles is aligned along the chain and the magnetic flux is closed by the stray field. The deviations in the lower part of the chain will be a subject of further investigation. Furthermore we will analyze the morphology of the magnetite particles using TEM tomography.

1. Dunin-Borkowski, R. E.; McCartney, M. R.; Frankel, R. B.; Bazylinski, D. A.; Posfai, M. & Buseck, P. R. Science, 1998, 282, 1868-1870.
2. We acknowledge the financial support from the European Union under the Seventh Framework Programme under a contract for an Integrated Infrastructure Initiative. Reference 312483 - ESTEEM2

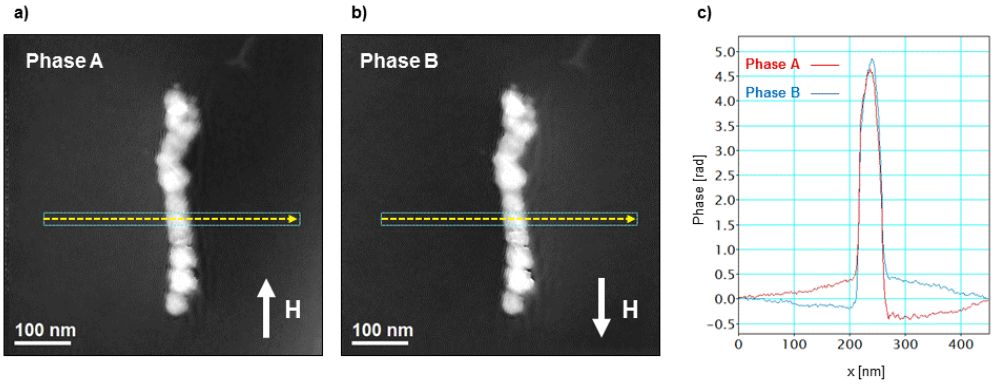

Figure 1. a), b) Phase images of a chain of magnetite particles. The arrows indicate the direction of the external magnetic field H. **c)** Phase profiles across the chain and the polymer support.

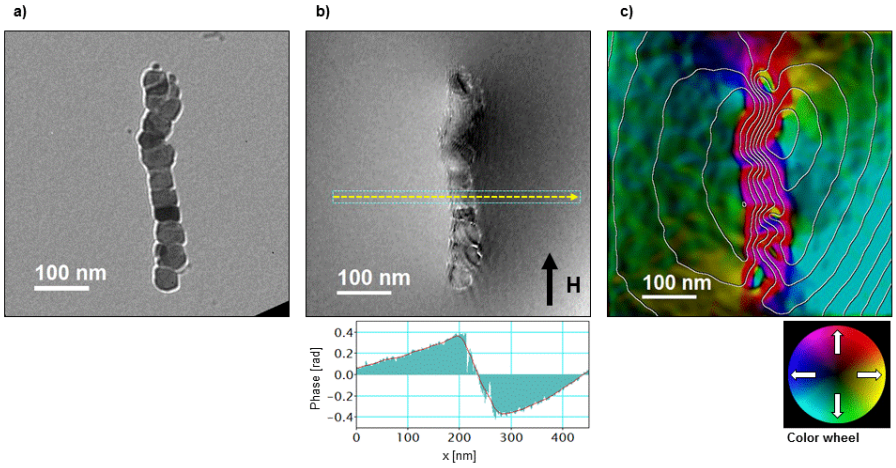

Figure 2. a) TEM image of the magnetite chain. **b)** Magnetic phase contribution separated from the phase image shown in Fig. 1a. **c)** Color-coded magnetic induction map obtained from the gradient of the magnetic phase image. The color wheel indicates the direction of the magnetic induction.

Functional Materials (magnetic, ferroelectric, ferroic, superconducting, electronics)

MS1.P008
Cross-sectional TEM preparation of ZnO nanospikes for fundamental 3D defect analysis

N. Wolff[1], V. Hrkac[1], J. Ditto[2], D. Smazna[3], R. Adelung[3], L. Kienle[1]

[1]Institute for Materials Science, Christian-Albrechts-Universität zu Kiel, Synthesis and Real Structure, Kiel, Germany
[2]University of Oregon, Department of Chemistry and Materials Science Institute, Oregon, United States
[3]Institute for Materials Science, Christian-Albrechts-Universität zu Kiel, Functional Nanomaterials, Kiel, Germany

niwo@tf.uni-kiel.de

A new concept for the realization of innovative magnetic field sensors with a limit of detection (LOD) smaller than 1 pT is based on the piezotronic read-out over a Schottky barrier of ZnO based magnetoelectric composites. Amongst morphology and doping concentration the ZnO crystal orientation and defects play a decisive role for the piezotronic properties, since they influence e.g. the conductivity and the height of the Schottky barrier. For monitoring such real-structure property relations, a three dimensional defect characterization is required. However, the strongly textured morphology inhibits wide-angle tilting experiments in TEM, and cross-sectional preparation of the one dimensional ZnO nanospikes is complicated by charging effects in FIB.

ZnO nanospikes prepared by the flame transport synthesis (FTS) method [1] have been subject of detailed plane-view investigations so far. Superposition twinning in nanospikes was investigated as an intrinsic real structural feature looking along [2-1-13] direction [2]. The observed twin boundary (TB) of a buried minority component is specified to be (2-1-11). Here, sophisticated cross-sectional preparation of ZnO nanospikes is achieved for the first time by selectively embedding them in amorphous carbon and subsequent cut and lift-out routine using the focused ion beam (FIB) technique. A novel shadowing technique was applied for careful thinning using the silicon substrate as a protective layer in order to minimize abrasion to the carbon film. Cross-sections of ZnO nanospikes are investigated using high resolution TEM. Closer inspection of the nanostructure (see Fig.1) reveals two common TB junctions. The TB junctions can be assigned to [2-1-10]/(01-13) and [2-1-10]/(01-11) having angles between the (0001) planes of 63.3° and 57°, respectively. Further, stacking mismatches and vacancies can be identified.

1. Mishra, Y. K., Kaps, S., Schuchardt, A., Paulowicz, I., Jin, X., Gedamu, D., Freitag, S., Claus, M., Wille, S., Kovalev, A., Gorb, S. N. and Adelung, R., Fabrication of Macroscopically Flexible and Highly Porous 3D Semiconductor Networks from Interpenetrating Nanostructures by a Simple Flame Transport Approach. Part. Part. Syst. Charact., 30, (2013), 775.
2. Hrkac, V.; Kienle, L.; Kaps, S.; Lotnyk, A.; Mishra, Y. K.; Schürmann, U.; Duppel, V.; Lotsch, B. V.; Adelung, R."Superposition twinning supported by texture in ZnO nanospikes," *J. Appl. Cryst.*, 46, (2013), 396.

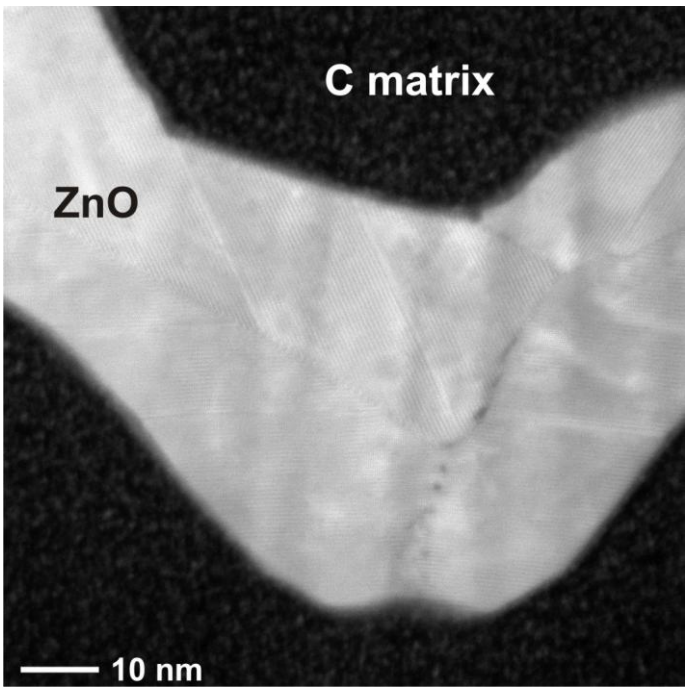

Figure 1. Exemplary cross-section of ZnO nanostructure in C matrix.

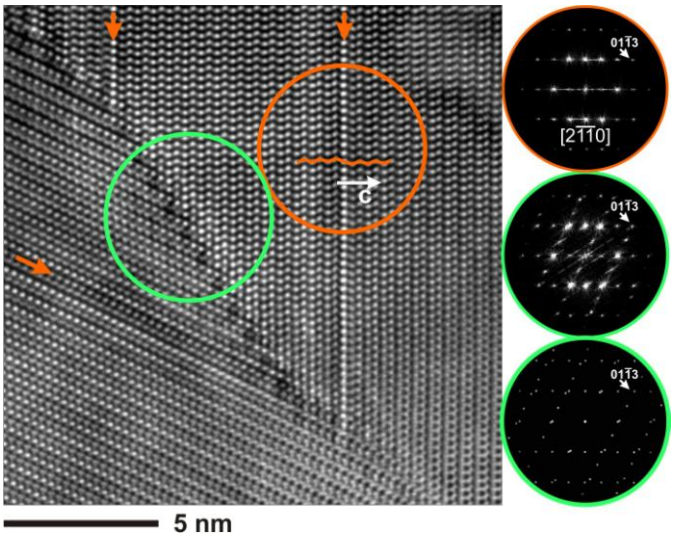

Figure 2. HRTEM micrograph of the cross-section presented in Fig.1. Stacking mismatches are indicated by arrows. (orange) FFT of area containing a basal-plane stacking fault in [2-1-10] zone axis orientation. (green) [2-1-10]/(01-13) TB junction, FFT and kinematic simulation by superposition (rotation by 63.3°).

Functional Materials (magnetic, ferroelectric, ferroic, superconducting, electronics)

MS1.P009
Lorentz microscopy of laser-induced vortex formation in microstructures

T. Eggebrecht[1], J. G. Gatzmann[2], V. Zbarsky[3], S. Schäfer[2], C. Ropers[2], M. Münzenberg[3], K. Samwer[1]

[1]I. Physikalisches Institut, Georg-August-Universität, Göttingen, Germany
[2]IV. Physikalisches Institut, Georg-August-Universität, Göttingen, Germany
[3]Grenz- und Oberflächenphysik, Ernst-Moritz-Arndt-Universität, Greifswald, Germany

teggebr@gwdg.de

For many years magnetic microstructures have been used for storing data in the hard drive industry. Several new methods were developed in order to save bits faster and with higher density in space.We present one of these potential methods in this work.

To produce magnetic microstructures, we show the focused ion beam method on thin Si3N4 membranes. Magnetically soft CoFeB thin films are capable to achieve a predictable long-range magnetic order.

Thereby, we are able to investigate single magnetic vortices caused by shape anisotropy in single elements. We used a modified transmission electron microscope (TEM) to introduce a laser beam, which can be positioned on the sample. The laser system facilitates single femtosecond pulses and the Lorentz imaging mode of the TEM provides a direct observation of change in magnetization. After excitation with a single pulse, we see a reversing in rotation of vortices to the opposite.

Furthermore, we examine the dependence on shape and size of the microstructures of this process. We acknowledge support by the DFG via SFB 1073.

Functional Materials (magnetic, ferroelectric, ferroic, superconducting, electronics)

MS1.P010
The synthesis and characterization of the hexagonal ferrite $Sr_3Co_2Fe_{24}O_{41}$

W. Salazar González[1], D. A. Landinez Tellez[1], L. C. Moreno[2], J. W. Sandino del Busto[1]

[1]Universidad Nacional de Colombia, Física, Bogotá, Colombia
[2]Universidad Nacional de Colombia, Química, Bogotá, Colombia

wsalazarg@unal.edu.co

The hexagonal ferrite Sr3Co2Fe24O41,also known as Sr3Co2 Z, is a material member of the ferrites' family, presenting high ferromagnetic properties at room temperature given for the crystal structure[1]. Due to their properties, this hexaferrite has become potentially important for technological applications, e.g. data storage material, components in devices that work in gigahertz frequencies, electric and magnetic sensors[2].In this work, the Z ferrite is synthesised by Pechini procedure[3].This procedure has as stages: formation of chelates of ions by using citric acid (C_6 H_8 O_7); formation of an organic ester by addition of ethylene glycol (C2H6O2) and subsequently polymerization by heating. This last one produces the basic material to obtain the searched phase for posteriors successive annealing temperatures. In this work annealing of 850°C, 1150°C and 1200°C were employed in order to obtain the single phase Z. Single phase characterization was carried out by XRD using *Cukα* radiation. Figure 1 shows results of XRD in samples annealed to 850°C and 1150°C. There was found coexistence of several phases of ferrites, such like M, Z ferrite and spinel.

The characterization using secondary and backscattering electrons in SEM showed homogeneous size and shape as well as a uniform material contrast (Figure 2). Besides, EDX analyses provide information about chemical composition showing the effectiveness of Pechini methods in the synthesis of Sr3Co2Z. Electron holography phase images of the specimens are reconstructed. Micrographs shows magnetic fields outside of a crystal (Figure 3) which is correlated with SAED indicating preferential orientation of the induced magnetization at room temperature respect to the crystal orientation.

Additional characterization techniques were applied to correlate the last results with the magnetoelectric properties, Electric characterization of Sr3Co2Z was made through measurements of electric polarization and magnetic magnetization was made by magnetization taken using a magnetic susceptometer.

The present study shows the manufacture process of hexaferrites by Pechini and results using several characterization techniques in order to know if the pure phase Z were obtained. The presence of magnetoelectric properties and their correlation with crystalline structure and domains structures was studied in detail.

1. Y. Kitagawa, Y. Hiraoka, T. Honda, T. Ishikura, H. Nakamura, y T. Kimura, «Low-field magnetoelectric effect at room temperature», *Nat. Mater.*, vol. 9, n.º 10, pp. 797-802, oct. 2010.
2. R. C. Pullar, «Hexagonal ferrites: A review of the synthesis, properties and applications of hexaferrite ceramics», *Prog. Mater. Sci.*, vol. 57, n.º 7, pp. 1191-1334, sep. 2012.
3. Pechini M. P. US Patent 3,3306,97. 1967. — www.google.com/patents/about? id=D3sfAAAAEBAJ&dq=3,330,697 (reference date: 30.03.2015).

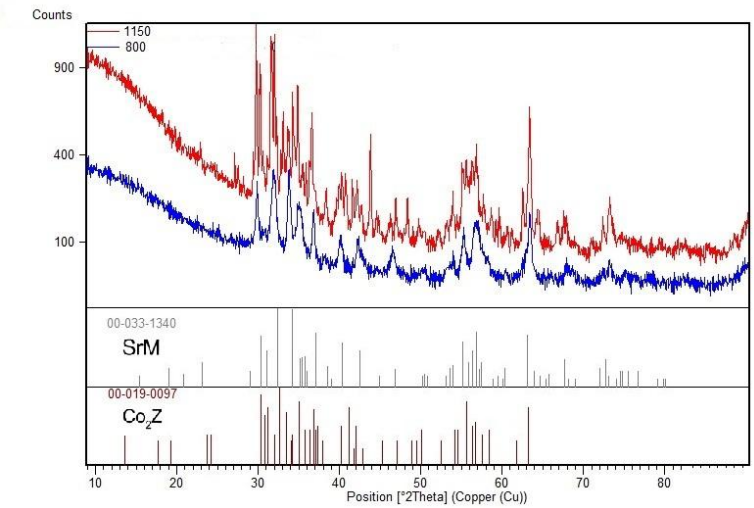

Figure 1.XRD patterns for the sample fired at various temperatures

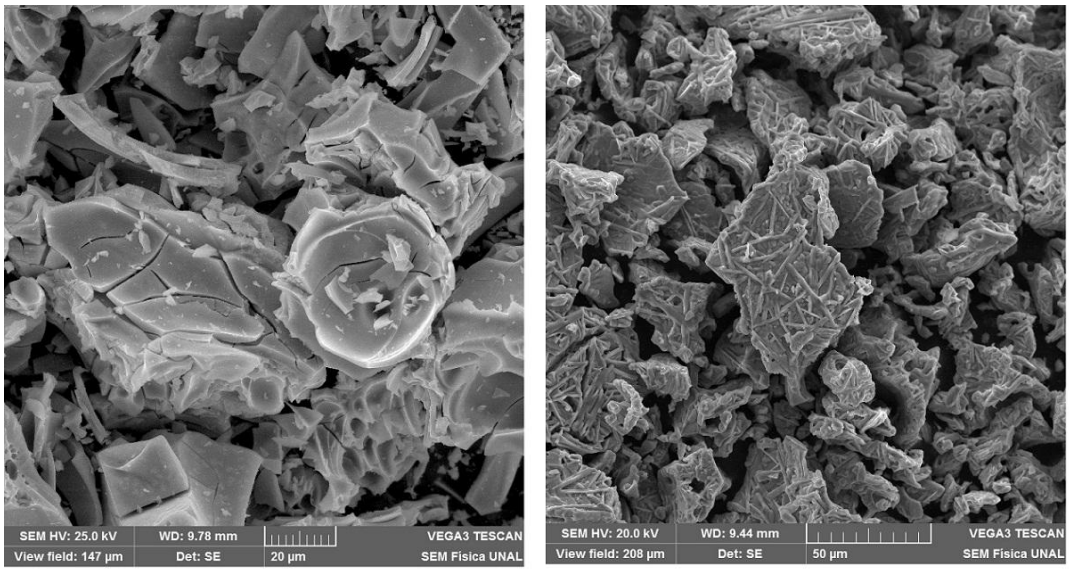

Figure 2. SEM Micrograph of samples to left: 850°C and right: 1150°C

Figure 3. Holographic phase micrograph showing the magnetic phase shift outside of a grain.

Functional Materials (magnetic, ferroelectric, ferroic, superconducting, electronics)

MS1.P011
In-situ TEM study of $Ge_{(8-n)}Sn_nSb_2Te_{11}$

D. Häußler[1], T. Dankwort[1], L. Kienle[1], C. Koch[2], W. Bensch[2], D. C. Johnson[3]

[1]University of Kiel, Insitute for Materials Science, Kiel, Germany
[2]University of Kiel, Institute for Anorganic Chemistry, Kiel, Germany
[3]University of Oregon, Eugene, United States

dih@tf.uni-kiel.de

The increasing disposability of smaller and less expensive computers and analogous improvements in computing power since several decades have resulted in the ability to share and to store information for an increasing amount of people. Consequently, a permanently increasing quantity of information must be stored more quickly on even smaller devices. So-called phase-change materials (PCM), based, e.g., on pseudo-binary compounds of (GeTe)x(Sb2Te3)y feature excellent prerequisites for applications in this field. They largely fulfill the needs for commercial use, viz. [1] high reflectivity contrast, cyclability, long-term stability, and fast crystallization speed. Inter alia, they are suitable to be switched reversibly between the amorphous and the metastable state connected with a pronounced contrast in optical and electric properties [2]. This way, those compounds can be used as a Blu-ray disc material as in disc players the switching between both states is accomplished by a focused laser beam and proceeds in the range of nanoseconds.

The crystalline structure of PCM devices based on Ge-Sb-Te phases is assigned to a distorted NaCl-type. The amount of vacancies is fixed by the ratio of GeTe and Sb2Te3 [3]. Structural details of the amorphous phase of PCMs are still not well understood, despite intense experimental and theoretical research.

The mechanisms which lead to the lowest energy structures in these compounds were identified as strain energy release by the formation of superlattice structures along hexagonal [0001] direction and by maximizing of the number of Te atoms surrounded by three Ge and three Sb atoms and Peierls-type bond dimerization [4]. The intrinsic vacancies form ordered planes perpendicular to the stacking direction, which separate the GST building blocks. Furthermore, the volume expansion of the metastable phase is a consequence of Coulomb repulsion between the Te atoms located in adjacent blocks.

The TEM investigations, in parts assisted by *in-situ* heating, held for a modified compound of GST 8211. Sn is used to substitute Ge with the intention to improve properties like increasing the optical and electrical contrast and to attain fast data transfer rates and a fast erasability. Amorphous, stoichiometric thin films with composition of Ge8-nSnnSb2Te11(n=2, n=4) and thicknesses

In *in-situ* heating experiments a crystallization dominated grain growth starting at 130 °C is found. At this temperature, diffuse scattering was observed in electron diffraction patterns of particular zone axes, which implies short range order phenomena unknown for PCMs so far. Close to 160 °C, *in-situ* heating experiments indicate that the short range ordering is altered to an ordered structure with so called vacancy layers which is consistent with similar results from measurements of *ex-situ* heated samples. Further, a certain plateau in the resistance measurements is observed in this temperature region that is brought into connection with these nanoscopic results.

1. Wuttig, M., Nat. Mater. **4** (2005) 265.
2. Bensch, W., and M. Wuttig, Chem. unserer Zeit **44** (2010) 92.
3. Buller, S. et al., Chem. Mater. **24** (2012) 3582.
4. Da Silva, J. L. F. et al., Phys. Rev. B **78** (2008) 224111.

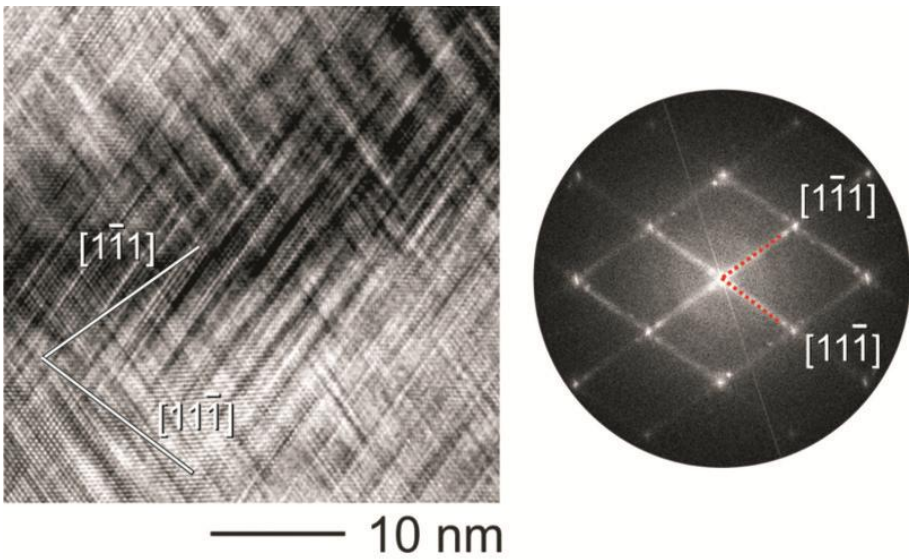

Figure 1. Left: HRTEM image taken after treatment at 130° C. Rigth: Appendent Fourier transform.

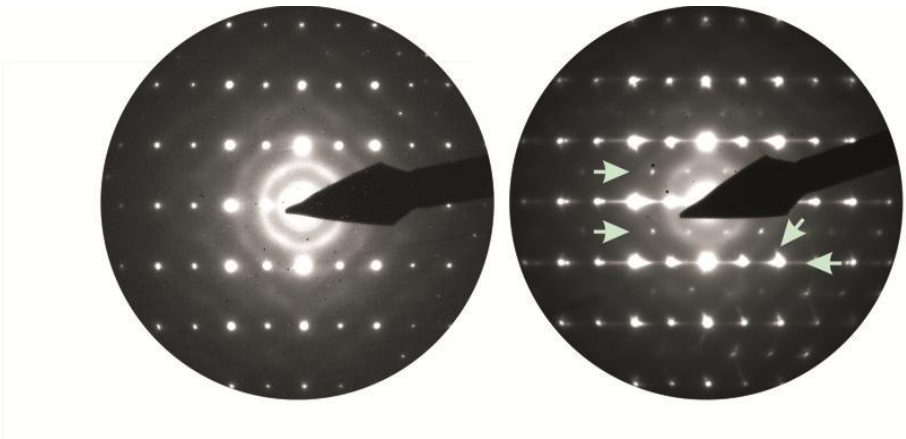

Figure 2. $(211)_c$ SAD patterns taken at 130° C (left) and 160° C (right), respectively. Arrows point to differences.

Functional Materials (magnetic, ferroelectric, ferroic, superconducting, electronics)

MS1.P012
Atomic-scale interface investigations of NdVO3 thin films

Y. E. Suyolcu[1], Y. Wang[1], W. Sigle[1], G. Logvenov[1], E. Benckiser[1], B. Keimer[1], P. A. van Aken[1]

[1]Max Planck Institute for Solid State Research, Stuttgart, Germany

suyolcu@is.mpg.de

Complex oxide materials exhibit a wide range of ionic and electronic phenomena. Their crystal structures (mostly perovskite or its derivatives) are highly adaptable to changes in composition and this compatibility provides the opportunity of synthesizing them in different forms, such as ultrathin films and/or heterostructures. The oxide heterostructures show extraordinary electronic properties which do not exist in bulk forms and the emergent phenomena occurring at the interfaces of these heterostructures are fascinating [1]. Perovskites with ABO3 stoichiometry and heterostructures of them have been in high demand for many years. The interest attributed to perovskites is also related to the wide variety of physical properties, such as the Mott transition, colossal magnetoresistance, ferroelectricity etc. Orthovanadates with the RVO3 stoichiometry (R=Y or trivalent rare earth metals) are of importance which show multiple orbital and magnetic ordering transitions as a function of temperature [2].

In the present study, detailed investigations on (Nd,La)VO3 (NVO) thin films using analytical scanning transmission electron microscopy (STEM) techniques were performed. The film was grown on NdGaO3 (NGO) substrate by pulsed laser deposition. For determining the structural quality and the elemental distribution across the interface, a JEOL ARM 200CF STEM operated at 200 kV and equipped with a cold field-emission electron source, a probe Cs corrector (DCOR, CEOS GmbH), a large-solid-angle JEOL Centurio SDD-type EDX detector, and a Gatan GIF Quantum ERS spectrometer was used. High-angle annular dark-field (HAADF) imaging and electron energy-loss spectroscopy (EELS) were performed atprobe semi-convergence angles of 20 mrad and 28 mrad, respectively.

NVO exhibits an orthorhombic structure with the space group Pbnm and with lattice parameters a = 0.5461 nm, b = 0.581 nm, and c = 0.7762 nm. Figure 1a and 1b show the structural model projected along the [001] direction and the atomically resolved HAADF image whose contrast is related to the atomic number contrast, respectively. The interface is found to be coherent and no structural defects are found. For an overview of the elemental distribution through the interface, EELS and EDX line scans were conducted. In Fig. 2 an EDX line-scan profile is presented, which exhibits relatively smooth and sharp changes of the signals along the growth direction. Furthermore, cation intermixing at the interface between the substrate and the thin film was proved by atomically resolved EEL spectrum imaging (Fig. 3).

1. Hwang, H. Y. et al., Nature Materials,11, 103-113, 2012.
2. Reehuis et al., Physical Review B, 73, 094440, 2006.
3.The research leading to these results has received funding from the European Union Seventh Framework Programme [FP7/2007-2013] under grant agreement n°312483 (ESTEEM2)

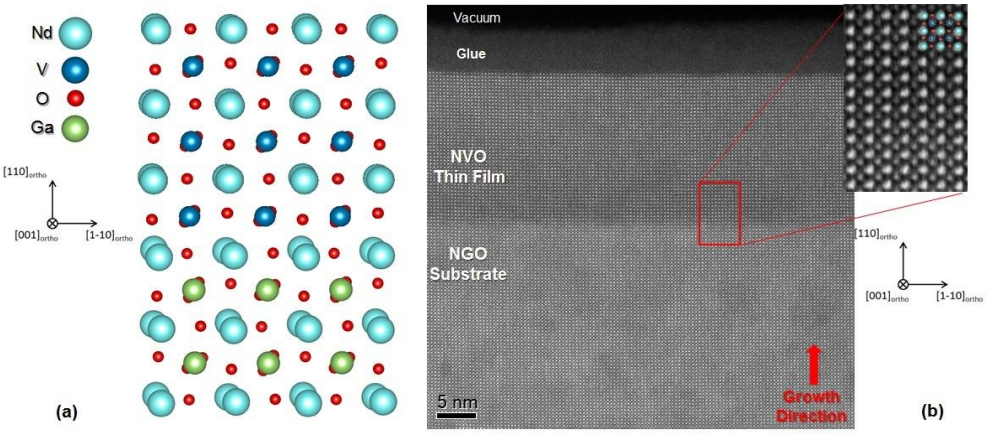

Figure 1. a) Structural model and b) STEM HAADF image showing the interface NVO thin film and NGO substrate.

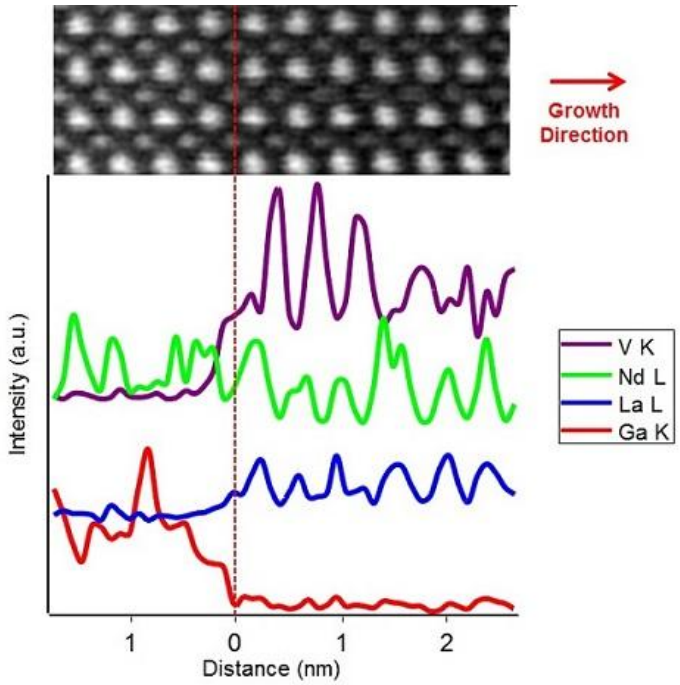

Figure 2. EDX line-scan profile showing the elemental distribution across the interface.

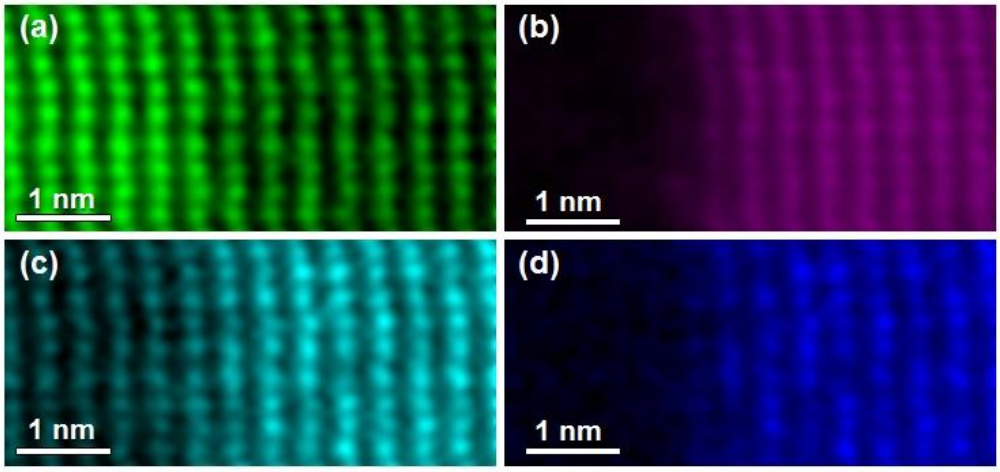

Figure 3. Chemical maps making use of the a) Nd-M5,4, b) V-L3,2, c)O-K, and d) La-M5,4 edges.

Functional Materials (magnetic, ferroelectric, ferroic, superconducting, electronics)

MS1.P013
Cathodoluminescence SEM-imaging of perovskite solar cell absorber layers

B. Förster[1], S. Förster[2], M. Ritter[2]

[1]University of Bayreuth, Macromolecular Chemistry I, Bayreuth, Germany
[2]University of Bayreuth, Physical Chemistry I, Bayreuth, Germany

beate.foerster@uni-bayreuth.de

Perovskite solar cells are among the most promising recent developments in solar technology. Device efficiencies have rapidly increased to more than 20%. These solar cells are based on perovskite absorbers such as CH3NH3PbX3, where X is a halide such as Br- or I-. They have band gaps in the range of 1.9 - 2.3 eV depending on the halide content. The absorber matrix is most commonly prepared by solution processing involving spin-coating of the precursors followed by evaporation and annealing, during which a thin crystalline perovskite layer is developing. An issue for these preparation methods is the resulting layer inhomogeneity, which strongly affects the device efficiency.

Using cathodoluminescence imaging at a scanning electron microscope (SEM-CL) we are able to determine spatial inhomogeneities of crystalline lead perovskite layers. Interestingly, the studies provide fundamental insights into the perovskite crystallization process. We observe the evolution of perovskite nanorods and nanosheets from small 6nm nanoparticles before three-dimensional crystals are finally emerging. The results provide important insights into how to direct perovskite crystallization to obtain suitable absorber layers for high device efficiency.

Functional Materials (magnetic, ferroelectric, ferroic, superconducting, electronics)

MS1.P014
Perovskite ferroelectric oxide nanostructures: fabrication, structural characterization and physical properties

H. Wu[1], L. Li[1], S. Zhou[1], J. Zhu[1], Z. Liu[2], X. Zhu[1]

[1]Nanjing University, School of Physics, Nanjing, China
[2]Nanjing University, Department of Materials Science and Engineering, Nanjing, China

xhzhu@nju.edu.cn

Perovskite ferroelectric oxide nanostructures are one of the most widely investigated functional nanomaterials, which have received considerable attention due to their novel size-dependent properties and miniaturization of ferroelectric-based electronic devices. In this work, we report on the fabrications of perovskite ferroelectric BaTiO3 and Pb(Zr0.53Ti0.47)O3 (PZT) nanostructures, and their structural characterization and physical properties are also characterized. By pulsed laser deposition method ferroelectric BaTiO3 nanostructured films were grown on Si substrates coated by nanoporous alumina membranes (NAMs) with an average pore size of 20 nm, and metal Pt nanowires were embedded in NAMs as a part of the bottom electrode. Similarly, PZT nanostructures were also fabricated on the Si substrates (coated with NAMs) by using sol-gel spin coating. The dielectric measurements demonstrated that the dielectric constant of the BaTiO3 nanostructured films with a thickness of 170 nm, was decreased slowly from 400 to 350 as the measured frequency increasing from 103 Hz to 106 Hz, and that the dielectric loss was increased slowly from 0.029 to 0.036 in the low frequency range from 103 Hz to 105 Hz. Polarization-electric field hysteresis loop indicated that the remanent polarization and the coercive field of the BaTiO3 nanostructured films were 17 μC/cm2 and 175 kV/cm, respectively. The dielectric constant of the sol-gel derived PZT nanostructured films with a thickness of 25 nm was decreased quickly from 860 to 100 as increasing the frequency in the range below 104 Hz, and then remained almost constant of 100 as further increasing the frequency up to 106 Hz. The dielectric loss peak observed near 4000 Hz was originated from the resonant absorption effect of the space charges. The polarization-electric field hysteresis loops of the sol-gel derived PZT film with a thickness 100 nm showed that the remnant polarization of the PZT nanostructured films was 50 μC/cm2 and coercive field of 500 kV/cm. Cross-sectional TEM images showed that the BaTiO3 and PZT nanostructured films contacted directly with the bottom electrode (metal nanowires), and the interface between them exhibited some degree of waviness. Both selected area electron diffraction and high-resolution TEM images confirmed that the BaTiO3 nanostructured films were the tetragonal phase with a perovskite structure. After post-annealing and crystallization of the BaTiO3 nanostructured films, some Pt nanowires became branches at their ends due to the re-growth of the Pt nanowires. A suitable post-annealing temperature is the critical processing parameter of fabricating ferroelectric ordered nanostructures as considering a trade-off between the ordered metal nanowires within NAMs and the crystallinity of ferroelectric nanostructured films.

Thin Films, Coatings, Interfaces and Surfaces

MS2.015
Analysis of composition and strain in semiconductor nanostructures by quantitative STEM using HAADF intensity, angular multi-range analysis and imaging STEM

A. Rosenauer[1], K. Müller-Caspary[1], M. Schowalter[1], T. Grieb[1], F. F. Krause[1], T. Mehrtens[1]

[1]Univeristät Bremen, Institut für Festkörperphysik, Bremen, Germany

rosenauer@ifp.uni-bremen.de

In this contribution we demonstrate application of quantitative STEM methods to measure composition and strain in semiconductor layers.

The image intensity in high-angle annular dark field (HAADF) STEM images shows a strong chemical sensitivity. As it is also influenced by specimen thickness, crystal orientation as well as characteristics of illumination and detector a standard-free quantification of composition requires a comparison with accurate image simulation, for which we use the frozen lattice approach of the STEMsim program taking the non-uniform detector sensitivity into account. Experimental STEM intensity is normalized with respect to the incident electron beam. To check the accuracy of simulated data we compared measured STEM intensity as function of the specimen thickness with simulation. For GaAs we found an accuracy that allows for the measurement of specimen thickness with an accuracy of approximately 5 nm for specimen thicknesses below 120 nm. To estimate the accuracy for small specimen thickness Van Aert et al. [1] used the atom counting method to experimentally obtain a relation between STEM intensity and number of atoms which also showed excellent agreement with simulation.

For the quantification of a STEM image (Fig. 1a) it is subdivided into Voronoi cells in which the intensity is averaged (Fig. 1b). Analysis of composition in a ternary semiconductor layer such as $In_xGa_{1-x}N$ requires measuring the specimen thickness in regions with known composition by comparison with the simulated STEM intensity. Interpolation of the obtained thickness into the layer with unknown composition yields the thickness map (Fig. 1c). Finally, specimen thickness and STEM intensity are compared with simulations computed as a function of composition resulting in a map of In-concentration *x* (Fig. 1d). In alloys containing atoms with different covalent radii (e.g. In and Ga) static atomic displacements occur, which are computed with empirical potentials and included in the simulation. For InGaN, the evaluated composition is compared with atom probe tomography (APT) using InGaN layers with high In concentration as applied in green laser diodes. The results of the STEM measurement are in excellent agreement with composition profiles obtained by APT [2]. As examples of application we demonstrate measurement of segregation efficiency in InGaAs layers buried in GaAs and quantification of few atomic percent of nitrogen in GaNAs. We also show that a combination of measurement of strain and HAADF image intensity can be used to determine both compositions x and y in quaternary $In_xGa_{1-x}N_yAs_{1-y}$.

Acquiring two STEM images of the same area with different angular ranges of the detector yields two sources of information which can be exploited, e.g. to evaluate specimen thickness and composition independently. This is demonstrated in Fig. 2 for GaNAs/GaAs.

As properties of semiconductors such as band gap energy and mobility of charge carriers are governed by strain, it is important to be able to measure strain accurately. In this context, STEM has the disadvantage of scan noise caused by positioning errors of the electron beam. This can be avoided by combining STEM illumination with conventional STEM imaging using an aberration corrected objective lens. This new imaging STEM (ISTEM) mode neither contains scan noise nor is it influenced by the source size. In addition, it has the advantage of spatial resolution beyond the diffraction and information limits [3].

1. S. Van Aert et al., Phys. Rev. B **87** (2013) 064107
2. T. Mehrtens et al., Appl. Phys. Lett. **102** (2013) 132112
3. A. Rosenauer, F.F. Krause et al. Phys. Rev. Lett. 113 (2014) 096101

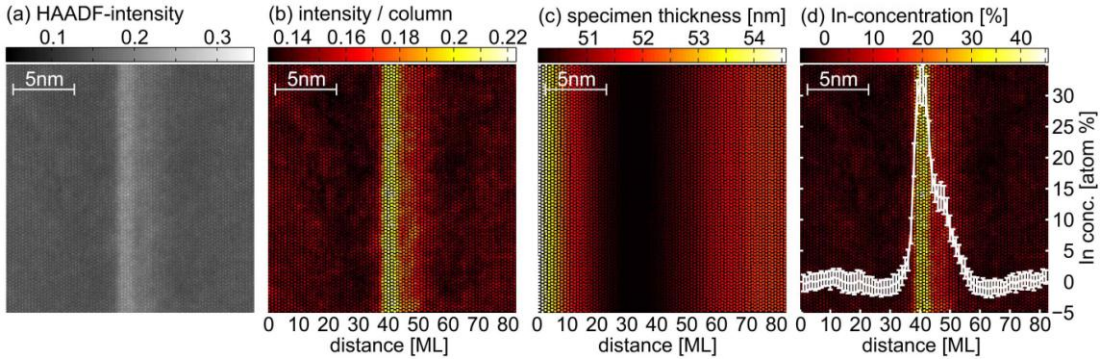

Figure 1. (a) HRSTEM image of an InGaN/GaN heterostructure, (b) intensity of Voronoi cells, (c) evaluated map of the specimen thickness and (d) resulting In-concentration.

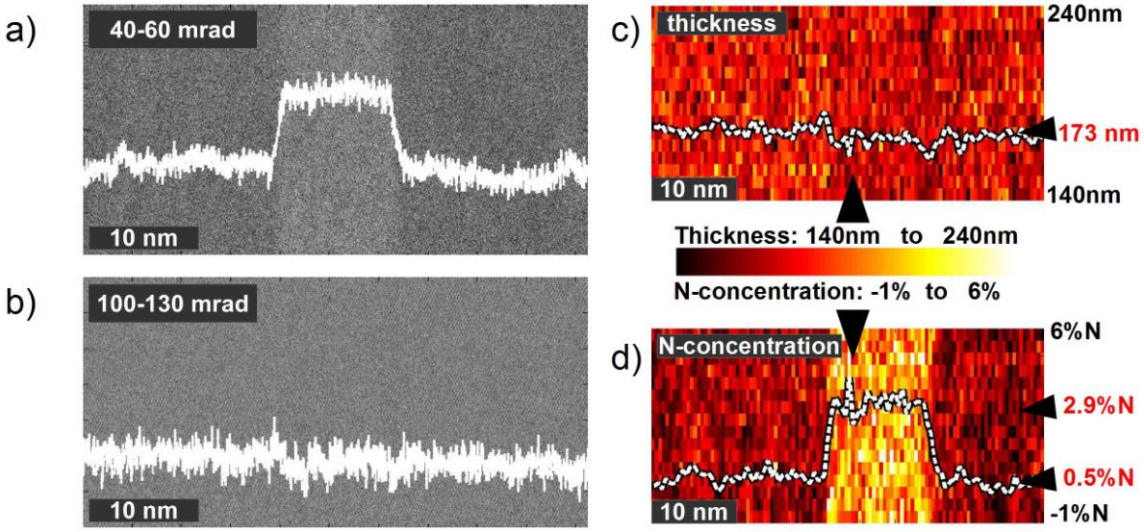

Figure 2. (a) STEM image acquired with an angular range of the detector of 40-60 mrad showing the GaNAs layer in the center. (b) The image acquired at 100-130 mrad does not show chemical sensitivity. Comparison with image simulation carried out for the two ranges of collection angle yields (c) the specimen thickness and (d) the N-concentration.

Thin Films, Coatings, Interfaces and Surfaces

MS2.016
Atomic-scale recognition of surface structure in the intercalation of Ti_3C_2X by aberration-corrected scanning transmission electron microscopy

X. Shen[1], X. Wang[1], Y. Gao[1], R. Yu[1], Z. Wang[1], L. Chen[1]

[1]Chinese Academy of Sciences, Institute of Physics, Beijing, China

xshen@aphy.iphy.ac.cn

MXenes represent a large family of functionalized two-dimensional (2D) transition-metal carbides and carbonitrides. However, most of the understanding on their unique structures and applications stops at the theoretical suggestion and lack of experimental support. Herein, the surface structure and intercalation chemistry of Ti_3C_2X are clarified at the atomic scale by aberration-corrected scanning transmission electron microscopy (STEM) and density functional theory (DFT) calculations. As shown in Figure 1, the STEM studies show that the functional groups (e.g., OH^-, F^-, O^-) and the intercalated sodium (Na) ions prefer to stay on the top sites of the centro-Ti atoms and the C atoms of the Ti_3C_2 monolayer, respectively. Besides, double Na-atomic layers are found within the Ti_3C_2X interlayer upon extensive Na intercalation via two-phase transition and solid-solution reactions. In addition, aluminum (Al)-ion intercalation leads to horizontal sliding of the Ti_3C_2X monolayer. On the basis of the STEM observations, the previous monolayer surface model of Ti_3C_2X is modified as shown in Figure 1. DFT calculations using the new modeling help to understand more about their physical and chemical properties. These findings enrich the understanding of the MXenes and shed light on future material design and applications.

1. Xuefeng Wang, Xi Shen, Yurui Gao, Zhaoxiang Wang, Richeng Yu, and Liquan Chen, J. Am. Chem. Soc., 137 (2015) 2715.

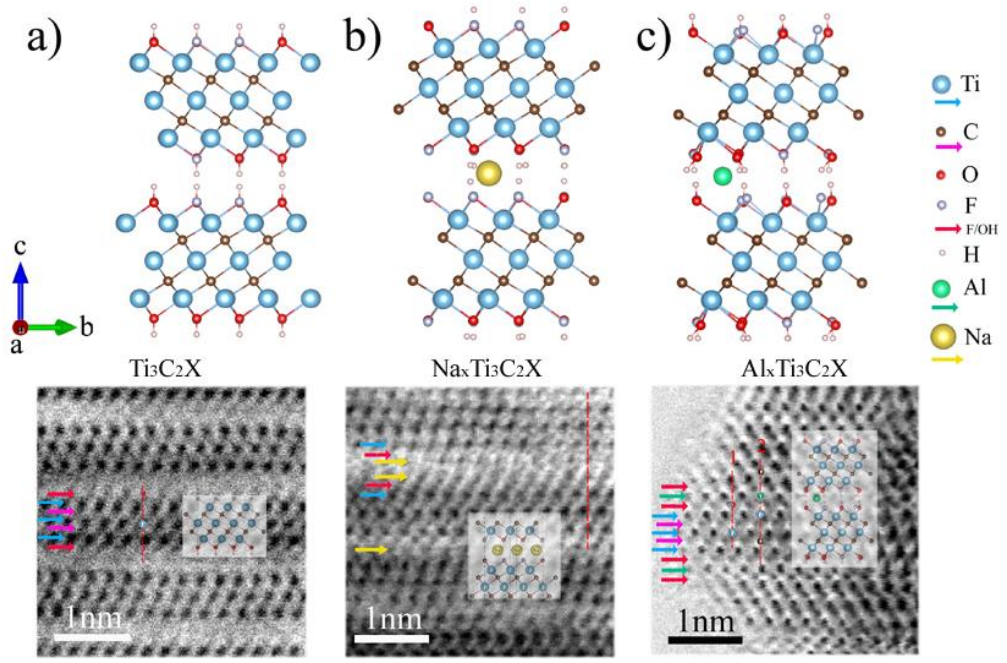

Figure 1. Optimized geometries of Ti_3C_2X (a), $Na_xTi_3C_2X$ (b), $Al_xTi_3C_2X$ (c) from cross-sectional view and corresponding ABF images.

Thin Films, Coatings, Interfaces and Surfaces

MS2.017
Analysis of threading dislocations in three-dimensional Ge crystals grown on (001)-Si substrates

Y. Arroyo Rojas Dasilva[1], M. Rossell[1], P. Groening [2], F. Isa[3], T. Kreiliger [3], H. von Känel[3], G. Isella [4], R. Erni[1]

[1]EMPA, Swiss Federal Laboratories for Materials Science and Technology, Electron Microscopy, Dübendorf, Switzerland
[2]EMPA, Swiss Federal Laboratories for Materials Science and Technology, Advanced Materials and Surfaces, Dübendorf, Switzerland
[3]ETH, Solid State Physics Laboratory, Zurich, Switzerland
[4]Politecnico di Milano, 4L-NESS and Department of Physics, Como, Italy

yadira.arroyo@empa.ch

Differences of lattice parameters and thermal expansion coefficients between Ge and Si, Ge/Si heterostructures present several problems such as high dislocation density, wafer bowing and cracks. One viable way to solve these problems is to grow dense arrays of three- dimensional Ge crystals on deeply patterned Si wafers by Low Energy Plasma Enhanced Chemical Vapor Deposition (LEPECVD) [1]. By using this innovative approach, epitaxial and thermal strains can be confined close to the heterointerface. Previous studies have shown that mainly high density of threading dislocations (TDs) is present in this system [2]. TDs along the [001] growth direction have been also observed with Burgers vector (*b*) of b=1/2<110> and edge character. In this work, we show a detailed TEM dislocation analysis in Ge pillars grown on patterned Si substrates.

Figure 1 shows a dark field (DF) image of a Ge Pillar under g=(2-20). The analysis of the dislocations evidences that the majority of the dislocations are 60° TDs with b=1/2<110> ending at the sidewalls of the pillars. TDs with line direction along [001] are also observed, they have b=1/2[1-10] and b=[001] with edge and screw character ending at the top surface.

Figures 2a and 2d show plane view HAADF-STEM images of the edge dislocations with b=1/2[110] and b=1/2[1-10]. According to our observations, these dislocations are indeed composed of two edge TDs and not just one as inferred from cross sectional analysis. The distance between them (0.5-1.5 nm) is too small to be identify from the image in Figure 1. These kind of dislocations are always present in the pillars as two parallel TDs (*DI* and *DII* in Fig. 2) with the same (G I) or perpendicular (GII) *b*.

The strain field analysis of the two groups of dislocations is performed using GPA (Geo- metrical Phase Analysis) on STEM images of Figure 2 in order to observe the strain interac- tion between the pairs of TDs. Figures 2b and 2e show the experimental ε_{xx} and ε_{xy} strain fields of GI and GII respectively. The color scale indicates that the strain ranges from -20% to 20%.The largest strain is found close to the core, while the strain decays with the distance from the core. The strain fields shows that in the core of theTDs the compressive region has negative values due to the extra half plane, whereas positive values are in the tensile region. The experimental strain maps are compared with simulations using the anisotropic elastic theory. For the TDs of GI, the strain map shows butterfly shapes in good agreement with the experimental one. The interaction of these dislocations is found in the compressive region from *DI* and the tensile region from *DII* where compressive and tensile areas are smaller due to the partial annihilation of the strain fields. For the TDs of GII, the simulated strain field matches very well with the experimental one, having partial annihilation from the tensile region of *DI* and compressive region from *DII*.

In summary, the majority of dislocations in the Ge pillars are TDs with b=1/2<1-10>. They are ending at the sidewalls of the pillar except for the edges TDs with b=1/2[1-10] and b=[001]. Atomic scale images show that the edge TDs are found to come in pairs, they are close to each other with the same or perpendicular b=1/2<110>. The strain fields inter- action of these dislocations show good matching with the simulated using the anisotropic theory. The observation of such dislocation pairs in Ge has not been documented before. The reason for the formation and their impact on the physical properties of the Ge pillars are subject of future investigations.

1. C.V. Falub and etal. *Science*, 335(6074):1330-1334, 2012.
2. A. Marzegalli and etal. *Advanced Materials*, 25(32):4408-4412, 2013.

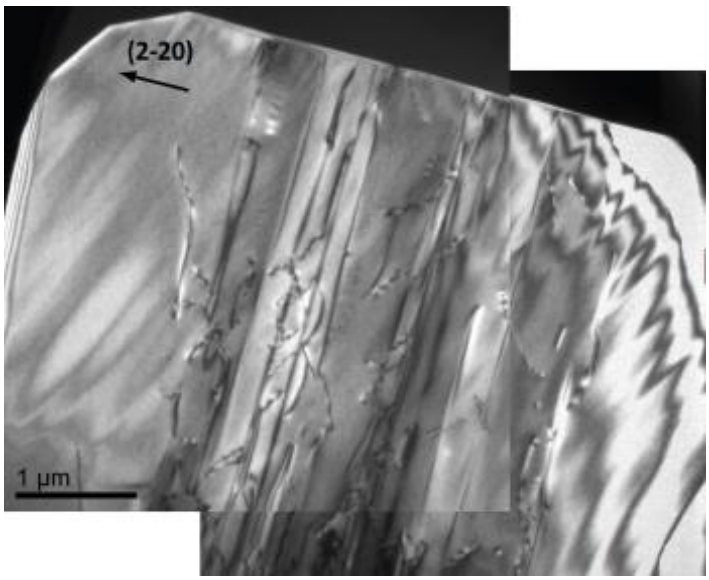

Figure 1. DF image of the top of a Ge pillar with TDs.

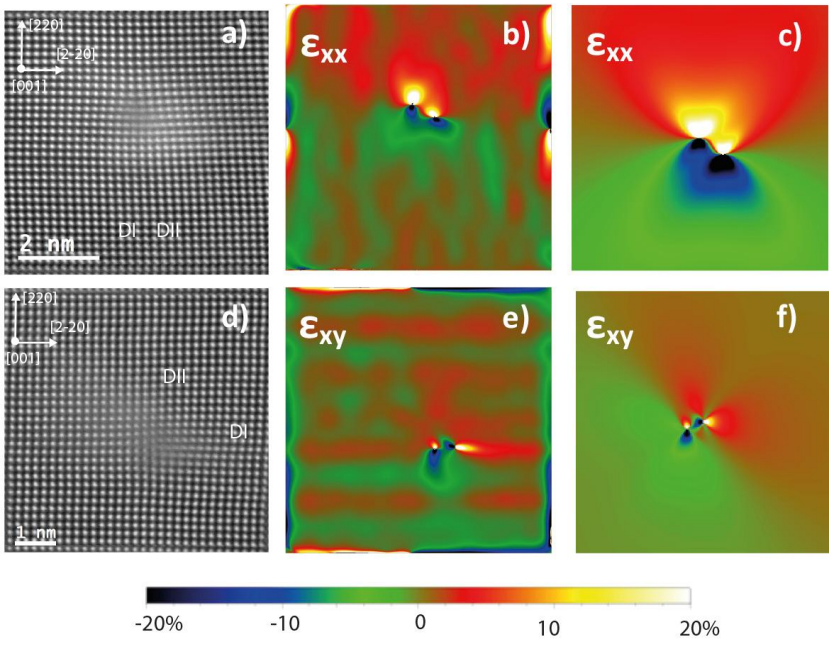

Figure 2. Parallel edge TDs with b=1/2< 110 >. a) STEM image from GI, b) experimental ε_{xx} strain field (GI), c) simulated ε_{xx} strain field from GI, d) STEM image from GII, e) experimental ε_{xy} strain field (GII) and f) simulated ε_{xx} strain field from GII.

Thin Films, Coatings, Interfaces and Surfaces

MS2.018
EFTEM investigation of low temperature synthesized $AlYB_{14}$ thin film

Y. T. Chen[1,2], O. Hunold[1], J. Mayer[3,2], J. Schneider[1]

[1]RWTH-Aachen University, Materials Chemistry, Aachen, Germany
[2]RWTH-Aachen University, Central Facility for Electron Microscopy, Aachen, Germany
[3]Forschungszentrum Juelich, Ernst Ruska-Centre for Microscopy and Spectroscopy with Electrons, Juelich, Germany

y.chen@fz-juelich.de

Energy filtered transmission electron microscopy (EFTEM) with high resolution is performed on low temperature synthesized $AlYB_{14}$ thin film. Equipped with a Cs-Cc achro-aplanat image corrector, the FEI Titan 50-300 PICO microscope has been used to identify elemental distribution of boron with atomic resolution.

Boron-rich solids with icosahedral strucutre exhibit outstanding mechanical properties[1], such as high melting point, hardness, and Young's modulus. According to both calculation and experiments, it is a promising material for the industry of wear resistance applications [1,2]. However, synthesizing crystalline XYB_{14}, where X and Y are metals, is challenging both with respect to the incorporation of impurities and the required synthesis temperature: 1400 °C.[4] The sample is synthesized with high power pulsed magnetron sputtering (HPPMS). The plasma generated with HPPMS contains significant fractions of ionized film forming species. These ions can be utilized to enhanced surface diffusion and hence enhance adatom mobility. The growth temperature is 675 °C, which is 725 °C below the typical bulk synthesis temperature. Orthorhombic AlYB14 (space group Imma) contains boron-icosahedra with five-fold symmetry, as shown in Figure 1. Here we report the synthesis of AlYB14 (space group Imma) based on HRTEM as the HRTEM image is consistent with the model for the (100) orientation.

With the help of both chromatic (Cc) and spherical (Cs) aberration correction, atomic resolution of EFTEM map can be achieved. The advantage is significant for the identification of boron icosahedron structure due to the unique distribution of high density boron. $AlYB_6$ with body-centered symmetry (bcc) can be identified with high contrast in both zero loss image and boron map, as shown in Figure 2. However, $AlYB_{14}$ can only be observed in boron K-edge map but absent in zero loss image, owing to the high-density boron matrix which reduce the contrast in the bright field image. The result demonstrates the importance of chromatic aberration correction in the EFTEM imaging enabling the phase identification of AlYB14 (space group Imma).

1. D. Emin, J. Solid State Chem. **179** (9), 2791 (2006).
2. Y. Lee and B. N. Harmon, J. Alloys Compd. **338** (2002).
3. B. A. Cook, J. L. Harringa, T. L. Lewis, and A. M. Russell, Scripta Mater. **42** (2000).
4. M. M. Korsukova, T. Lundström, and L.-E. Tergenius, J. Alloys Compd. **187** (1992).

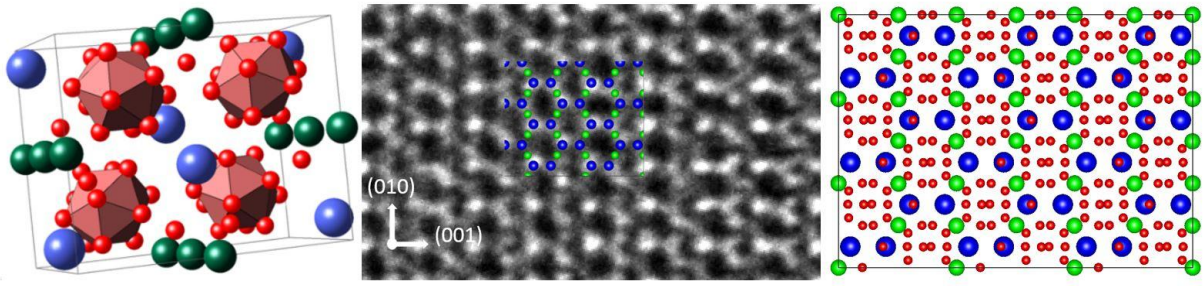

Figure 1 ● Y ● Al ● B

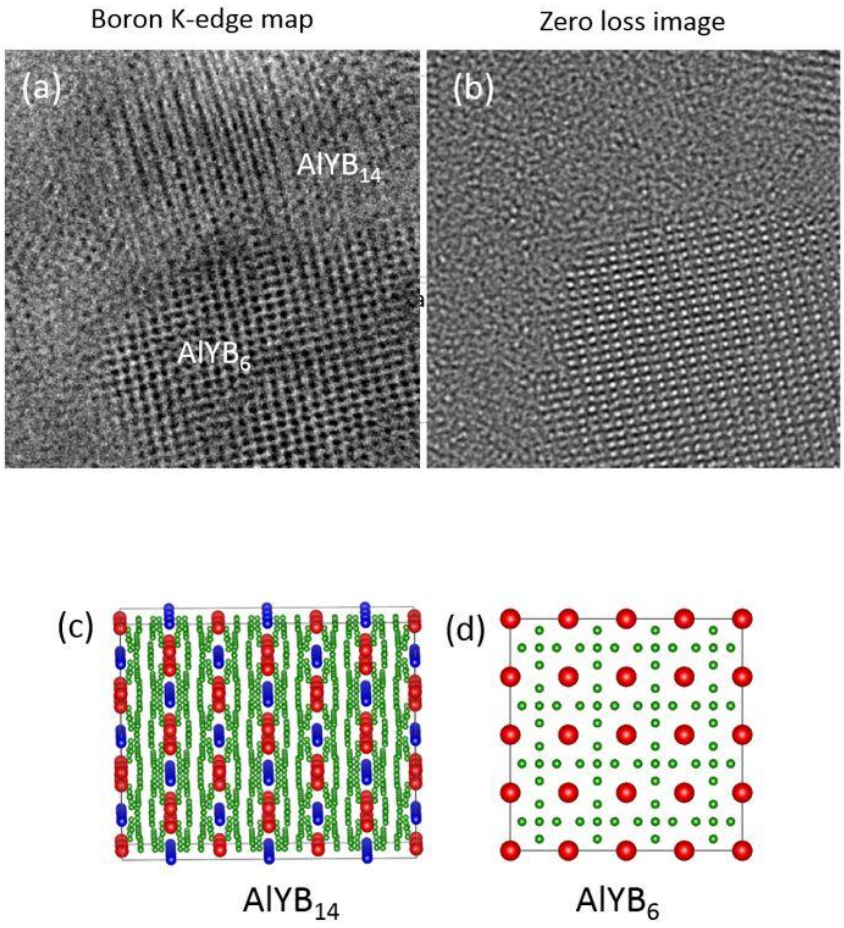
Boron K-edge map
Zero loss image
(a)
(b)
AlYB14
AlYB6
(c)
(d)
AlYB14
AlYB6

Thin Films, Coatings, Interfaces and Surfaces

MS2.019
Plasmons in topological insulator Bi_2Se_3 unravelled by swift electrons

N. Talebi[1], C. Özsoy Keskinbora[1], H. M. Benia[2], C. Koch[3], P. van Aken[1]

[1]Max Planck Institute for Solid State Research, Stuttgart Center for Electron Microscopy, Stuttgart, Germany
[2]Max Planck Institute for Solid State Research, Nanoscale Science, Stuttgart, Germany
[3]Universität Ulm, Institut für Experimentelle Physik, Ulm, Germany

talebi@is.mpg.de

Materials crystallizing in tetradymite structure are fascinating, since at their bandgap just near to the Fermi level they sustain time-reversal-invariant topological effects, which appears in exceptional electronic surface states captured in the so-far investigated mass-less Dirac cones [1]. Another characteristic of tetradymites is caused by the huge uniaxial electric anisotropic behaviour of the material. It has been shown that tetradymites and in particular Bi_2Se_3 and Bi_2Te_3 belong to the naturally rare class of hyperbolic materials [2] in the visible frequency range, with a smooth transition from elliptical to hyperbolic dispersion by marching over the frequency of excitation. Fig. 1a shows the permittivity of Bi_2Se_3 obtained using the generalized spectroscopic ellipsometry technique reported in ref. [2]. Since the Bi_2Se_3 structure is composed of hexagonal quintuple layers, the permittivity in the plane of the quintuples (a-b plane, as shown at the inset of figure 1 (a)) is different from the normal permittivity component parallel to the c-axis. Interestingly, at the energies lower than E = 1.06 eV, both the permittivity components are positive, and the material in overall behaves like a dielectric. At the energy range of , the vertical component of the permittivity becomes negative while the lateral component is positive, and finally for energies above E = 1.92 eV the vertical and lateral permittivity components hold the exactly vice versa signs. Due to this interplay between the metallic and dielectric response, Bi_2Se_3 can be a proper case for studying the plasmonic excitations in hyperbolic materials, with different bulk dispersion characteristics.

Here, utilizing electron energy-loss spectroscopy (EELS) and energy-filtered transmission electron microscopy (EFTEM) we experimentally investigate the plasmonic modes of Bi_2Se_3 nanostructures, using the Zeiss SESAM microscope [3]. Fig. 1b shows the acquired EFTEM images for a Bi_2Se_3 nanoprism particle, with the thickness of 30 nm. The very interesting observation is the bright intensities for the EELS signal almost at all the energy ranges from 0.8 eV up to 4 eV, while at higher energies the contribution of surface plasmon modes are more evident (compare the EFTEM images at the energies 1.2 eV and 3.6 eV). Interestingly, even at the energy of E=0.8 eV in which the material is totally dielectric, the excitation of an edge mode is apparent, which is due to the excitation of Dyakonov waves [4]. In fact, in contrast to the surface plasmon modes which are excited at the interface of a metallic and dielectric structure, Dyakonv waves are observed at the surface of highly anisotropic materials like Bi_2Se_3.

We furthermore theoretically investigate the surface waves and edge plasmon dispersions, both analytically and numerically [5], in order to obtain more understandings of our experimental observations. [6]

1. H. J. Zhang et al.: *Nature Phys.* **5** (2009) 438
2. M. Esslinger et al.: *ACS Photon.* **1** (2014) 1285
3. N. Talebi et al.: *Langmuir* **28** (2012) 8867
4. M. I. Dyakonov: *Sov. Phys. JETP* **67** (1988) 714
5. N. Talebi: *New J. Phys.* **16** (2014) 053021
6. NT gratefully acknowledges the Alexander von Humboldt Foundation for financial support. The research leading to these results has received funding from the European Union Seventh Framework Programme [FP7/2007-2013] under grant agreement n°312483 (ESTEEM2).

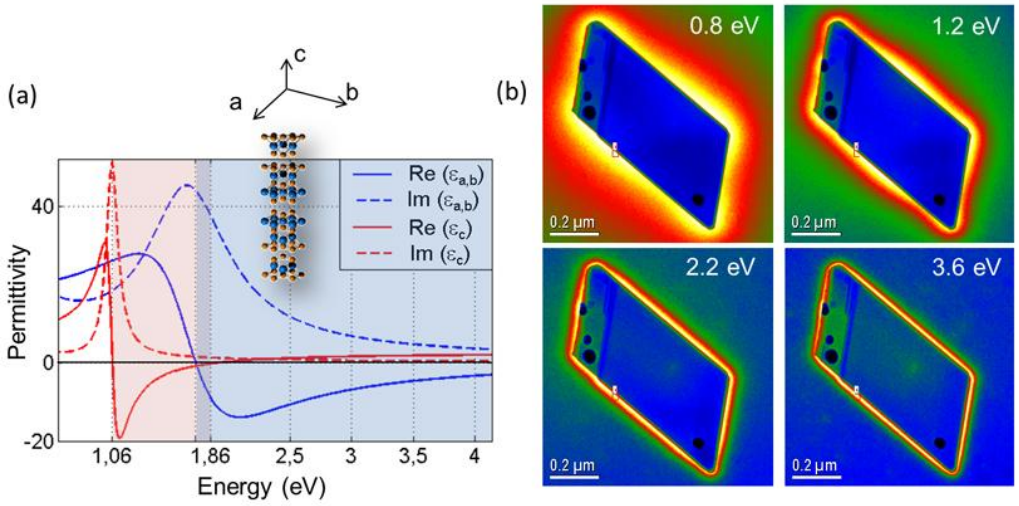

Figure 1. (a) Bi_2Se_3 permittivity at visible frequency range, (b) EFTEM images showing the mode profile of localized plasmons excited in a Bi_2Se_3 nanoparticle.

Thin Films, Coatings, Interfaces and Surfaces

MS2.020
Probing the physical properties of nanomagnets at the atomic scale

D. Pohl[1], A. Surrey[1,2], S. Schneider[1,2], B. Rellinghaus[1]

[1]IFW Dresden, Institute for Metallic Materials, Dresden, Germany
[2]TU Dresden, Institut für Festkörperphysik, Dresden, Germany

d.pohl@ifw-dresden.de

Magnetic nanoparticles and nanostructures have a huge application potential in a large variety of novel technologies. In order to provide for the desired magnetic or magneto-electronic functionalities, such nanomagnets are usually alloys (rather than pure elements), whose compositions are tuned in order to concurrently optimize their chemical, thermal and - of course - magnetic properties. All of the latter properties are in turn intimately correlated to the crystal structure of these nanoscopic materials entities. While both the thermodynamic equilibrium structure and phase stability of bulk materials are solely related to the volume, they become increasingly modified by the influence of surfaces at small sizes due to the enhanced surface-to-volume ratio. Evidently, a thorough understanding of the atomically resolved structure both in the volume and at the surfaces is mandatory in order to fully understand the structure-property relations of nanomaterials. Modern aberration-corrected transmission electron microscopy (TEM) has thus become an indispensable tool to determine these structures with ultimate spatial resolution. Unfortunately, the same interaction between the high energy electrons and the sample that allows for the high resolution imaging of the structures of interest may also lead to alterations of the surface atomic arrangement (see fig. 1b) and hereby to a modification of the very object of interest [1]. As a consequence, single-shot imaging techniques that minimize the impact of the imaging electron beam on the sample are required. The inherent reduction of experimentally derived data may, however, be compensated for by combining the experimental TEM investigations with molecular dynamics, Monte Carlo and HR-TEM contrast simulations, respectively.

In the present talk, these methods are used to explore the atomically resolved structure and phase stability of nanoparticles of binary metallic alloys such as FePt, CuAu, or FeNi. Here, Au nanoparticles serve as an elemental reference. Due to a variety of different particle morphologies, different types of surfaces are present and can be controlled [2]. It will be shown that the near-surface lattice relaxation frequently observed in alloy particles is indicative of a segregation of those alloy constituents, which have the lowest surface energies, to the particle surface [3-5]. Fig. 1a exemplarily highlights the surface-near lattice expansion in icosahedral FePt nanoparticle. This finding illustrates the limited applicability of bulk phase diagrams for nanoscopic objects. The potential of novel approaches to locally determine not only the structure but also the magnetic properties of nanomagnets by measuring the electron magnetic circular dichroism (EMCD) utilizing both plane electron waves [6] and electron vortices [7,8] will be exemplified for the case of $L1_0$-ordered FePt nanocubes. The latter techniques open the horizon for the local correlation of the physical properties of nanoscopic objects with their atomically resolved structure in-situ in the electron microscope.

1. A. Surrey, D. Pohl, L. Schultz, and B. Rellinghaus, Nano Lett. 12 (2012) 6071-6077.
2. D. Pohl, A. Surrey, B. Rellinghaus and L. Schultz, Appl. Phys. Lett. 101 (2012) 263105.
3. D. Pohl, U. Wiesenhütter, E. Mohn, L. Schultz, and B. Rellinghaus, Nano Lett. 14 (2014) 1776-178
4. D. Pohl, F. Schäffel, M.H. Rümmeli, E. Mohn, C. Täschner, L. Schultz, C. Kisielowski, and B. Rellinghaus, Phys. Rev. Lett. 107 (2011) 185501
5. B. Bieniek, D. Pohl, L. Schultz and B. Rellinghaus, “The effect of oxidation on the surface-near lattice relaxation in FeNi nanoparticles”, J. Nanopart. Res. 13 (2011) 5935-5946.
6. P. Schattschneider et al., Nature 441 (2006) 486-488.
7. J. Verbeeck et al., Nature 461 (2010) 301-303.
8. D. Pohl et al., Ultramicroscopy 150 (2015) 013907

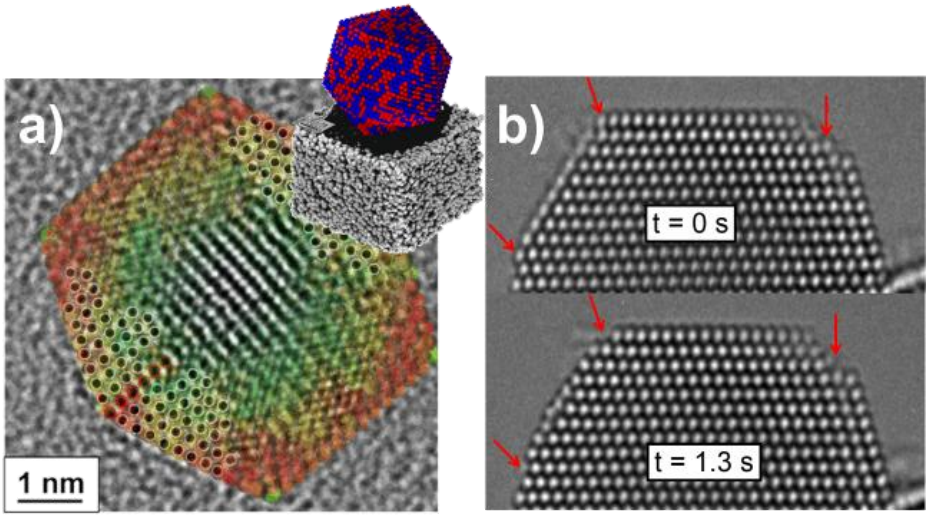

Figure 1: Determining local properties from HRTEM images. a) HRTEM image of a FePt icosahedron overlaid with a false color illustration of the simulated lattice strain. b) Time sequence of the surface diffusion on Au nanoparticles.

MS2.P021
Self assembled monolayer on DC sputtered nanostructured rutile TiO_2 platform for bisphenol A detection

K. K. Reza[1], N. Singh[1], M. A. Ali[1], V. V. Agrawal[1], A. M. Biradar[1]

[1]National Physical Laboratory, Biomedical Instrumentation Section, New Delhi, India

kamilreza@gmail.com

A biosensor platform comprising of the functionalized sputtered rutile nanostructured titanium dioxide ($nTiO_2$) for rapid detection of estrogenic substance (bisphenol A) has been proposed. The direct current (DC) sputtering of titanium (Ti) on glass substrate has been converted to ordered nanostructured TiO_2 film via oxidation. The nanostrucured TiO_2 surface was functionalized with self assembled monolayer (SAM) of 3-aminopropyltriethoxysilane (APTES) and glutaraldehyde. The enzyme molecule, tyrosinase (Tyrs) has been covalently immobilized on the surface of APTES modified nanostructured TiO_2 film. To investigate the crystalline structure and surface morphology of functionalized $nTiO_2$/Ti electrode, the X-ray diffraction, scanning electron microscopy, atomic force microscopy and Fourier transform infrared spectroscopy have been carried out. This impedimetric biosensor exhibits a comparable sensitivity (361.9 kΩ/μM) in a wide range of detection (0.01-1.0 μM) and a response time of 250 s for bisphenol A (BPA) monitoring. This novel manufacturing process for $nTiO_2$ film is cheap, practical and safer for functionlization with SAM and glutaraldehyde to improve the biosensor efficacy. The strong protein absorption capability of the $nTiO_2$ surface demonstrates an excellent electrochemical biosensor and could be useful for the detection of other phenolic compounds.

1. WHO. 2012. Endocrine disrupters and child health.
2. Oliveira, E. M., Beyer, S., Heinze, J., 2007. Bioelectrochem. 71, 186-191
3. Ali, M. A., Srivastava, S., Solanki, P. R., Agrawal, V. V., John, R., Malhotra, B. D., 2012. Appl. Phys. Lett. 101, 084105

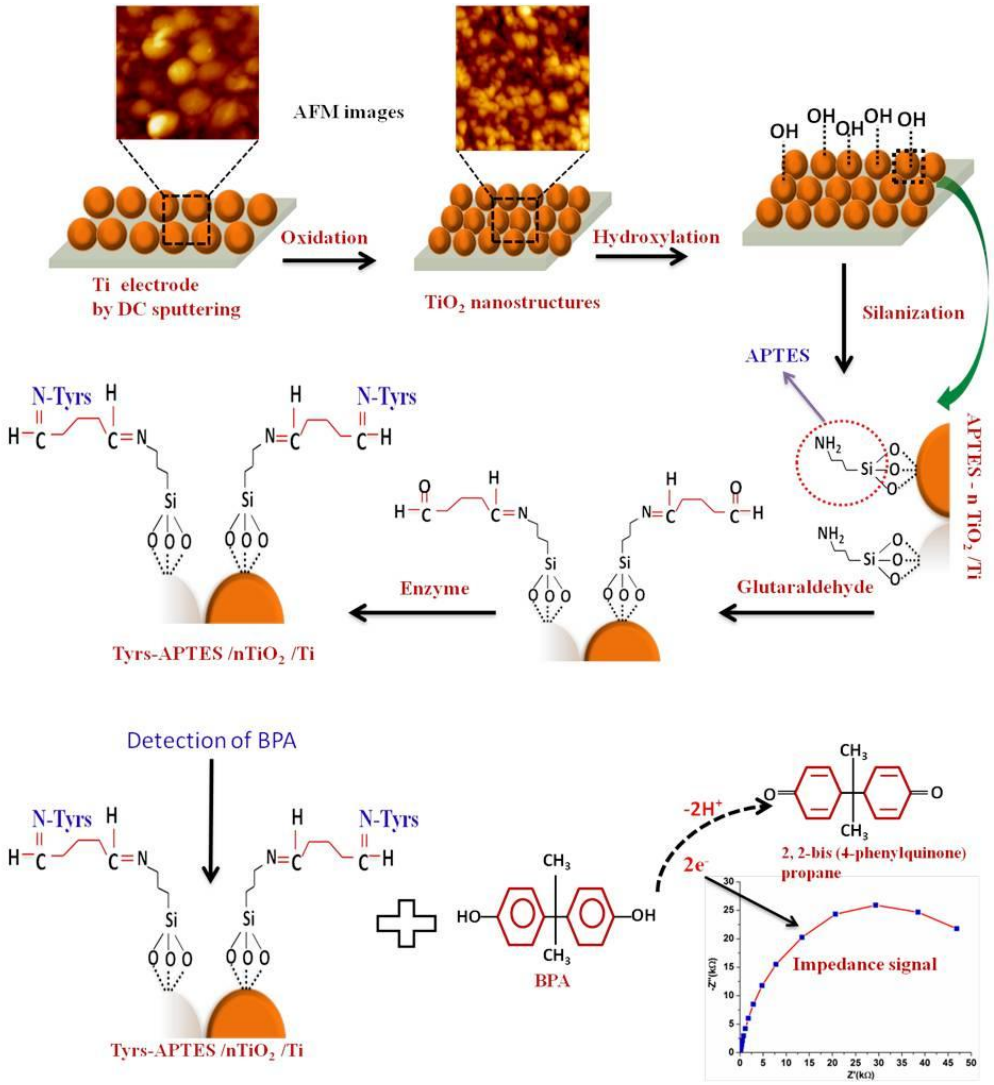

Figure 1. Schematic representation of self assembled DC sputtered nanostructured rutile TiO_2 platform detection of estrogenic substance.

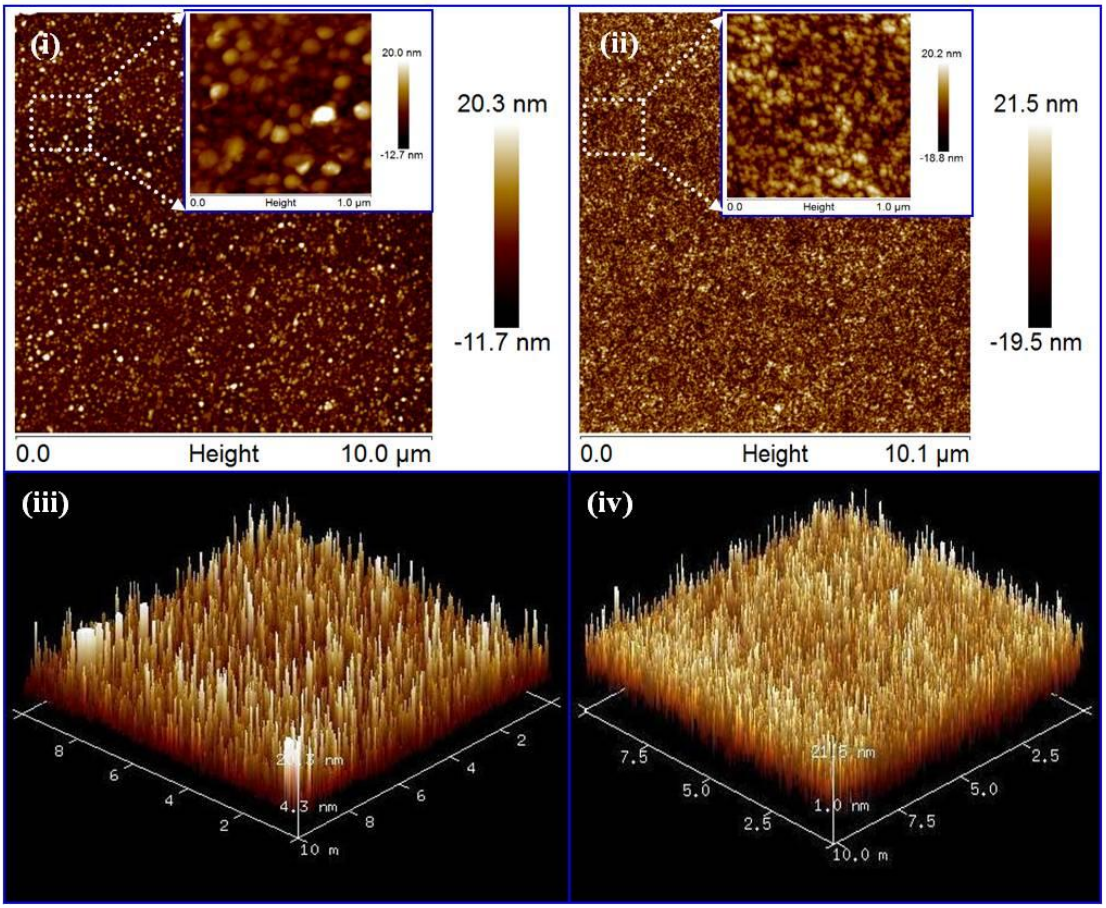

Figure 2. (i) AFM images of Ti film, inset zoom image of Ti film, (ii) AFM images of $nTiO_2$ film, inset zoom image of $nTiO_2$ film, (iii) 3D image of Ti film, (iv) 3D image of $nTiO_2$ film, (v) and (vi) histogram plots for average size of Ti and $nTiO_2$ particles, respectively.

Thin Films, Coatings, Interfaces and Surfaces

MS2.P022
Combined HR(S)/TEM and EDX characterization of nanostructured metal/semiconductor superlattices

M. Garbrecht[1], J. L. Schroeder[1], B. Saha[2], T. D. Sands[3], J. Birch[1]

[1]Linköping University, Thin Film Physics Division, Linköping, Sweden
[2]University of California at Berkeley, Department of Materials Science and Engineering, Berkeley, CA, United States
[3]Virginia Tech, 3. Bradley Department of Electrical and Computer Engineering And Department of Materials Science and Engineering, Blacksburg, VA, United States

magnus.garbrecht@liu.se

We present a detailed analysis on the quality and microstructure of various metal/semiconductor superlattices employing HR(S)/TEM (high-resolution (scanning)/transmission electron microscopy) imaging and spectroscopic methods on as-deposited and annealed samples.

Epitaxial metal/semiconductor superlattices are known to be promising candidates for microelectronic compounds in electronic, photonic, and plasmonic devices, but are also of interest for applications as hard coatings, and in thermoelectric materials [1]. The crystalline quality of the superlattices, in terms of their defect density, phase purity, interface roughness, and stoichiometry of the individual layers, plays a crucial role with respect to the physical properties and thus the applicability of such superlattice stacks. It was recently shown that metal/semiconductor superlattices based on (Al,Sc)N as the semiconductor component can be grown epitaxially with low-defect densities by magnetron sputtering on [001]MgO substrates [2].

We moreover reported on phase formation and thermal stability in as-deposited and long-time annealed cubic TiN/(Al,Sc)N superlattices employing - among other techniques - a combination of HR(S)/TEM and EDX (energy dispersive x-ray spectroscopy) mapping [3]. Figure 1 shows a HAADF(high-angle annular dark-field)-STEM overview micrograph of a TiN/(Al,Sc)N superlattice as well as EDX mapping of as-deposited, 24 h, and 120 h annealed (both at 950 °C) superlattices. The intermixing of the TiN and (Al,Sc)N layers with increased annealing time becomes apparent, giving insight into diffusion processes between the layers.

Figure 2 shows a typical HRTEM micrograph of an improved cubic (Ti,W)N/(Al,Sc)N superlattice stack [4]. The inserted FFT demonstrates the quality of epitaxial growth. More superlattice variations like e.g. (Hf,Zr)N/ScN were grown and analyzed as well.

All experiments were conducted at Linköping's image- and probe-corrected and monochromated FEI Titan^3 60-300 microscope equipped with a Gatan Quantum ERS GIF, high-brightness XFEG source, and Super-X EDX detector, operated at 300 kV [10].

1. T. D. Sands, C.J. Palmstrøm, J.P. Harbison, V.G. Keramidas, N. Tabatabaie, T.L. Cheeks, Y. Silberberg, *Stable and epitaxial Metal/III-V semiconductor heterostructures*, Mater. Sci. Rep. **5**: 98-170, 1990.
2. B. Saha, S. Saber, G.V. Naik, A. Boltasseva, E.A. Stach, E.P. Kvam, T.D. Sands, *Development of epitaxial AlxSc1-xN for artificially structured metal/semiconductor superlattice metamaterials*, Phys. Status Solidi B, 252, **2**, 251-259, 2015.
3. J. L. Schroeder, B. Saha, M. Garbrecht, N. Schell, T. D. Sands, and J. Birch, *Thermal stability of epitaxial cubic-TiN/(Al,Sc)N metal/semiconductor superlattices*, J. of Mater. Sci., **50**: 3200-3206, (2015).
4. B. Saha, Y. R. Koh, J. Comparan, S. Sadasivam, J. L. Schroeder, M. Garbrecht, J. Birch, D. Cahill, T. Fisher, A. Shakouri, and T. D. Sands, *Thermal Conductivity Through (Ti,W)N/(Al,Sc)N Metal/Semiconductor Superlattices*, submitted, (2015).
5. We acknowledge the Knut and Alice Wallenberg (KAW) Foundation for the Electron Microscope Laboratory in Linköping.

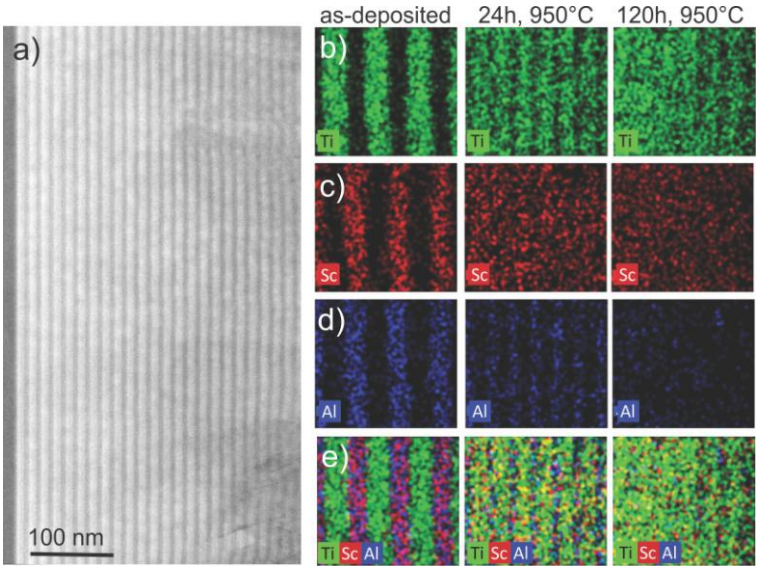

Figure 1. (a) Overview HAADF-STEM micrographs of an as-deposited TiN/(Al,Sc)N superlattice. Individual elemental (b-d) and combined (e) EDX maps of Ti, Sc, and Al demonstrate the intermixing of atomic species with increased annealing time [3].

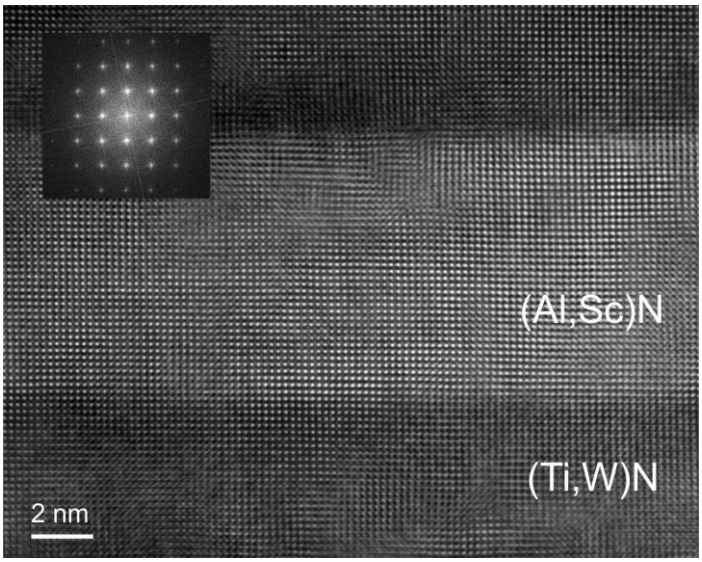

Figure 2. HRTEM micrograph of a (Ti,W)N/(Al,Sc)N superlattice stack, demonstrating the epitaxial quality of growth.

Thin Films, Coatings, Interfaces and Surfaces

MS2.P023
Theoretical study of precision and accuracy of strain analysis by nano-beam electron diffraction (SANBED)

C. Mahr[1], K. Müller-Caspary[1], T. Grieb[1], T. Mehrtens[1], M. Schowalter[1], F. F. Krause[1], D. Zillmann[1], A. Rosenauer[1]

[1]University of Bremen, Institute of Solid State Physics, Bremen, Germany

mahr@ifp.uni-bremen.de

Measurement of lattice strain is important to characterise semiconductor nanostructures. As strain has large influence on the electronic band structure, methods for measurement of strain with high precision, accuracy and spatial resolution in a large field of view are mandatory. In this contribution we present a theoretical study of precision and accuracy of measurements of strain from series of convergent-beam electron diffraction (CBED) patterns acquired while a focussed beam is scanned across the sample. According to Bragg's law, distances between diffraction discs depend on the local lattice parameter. Thus, information about strain can be derived by comparing distances between discs at different positions of the scanning electron probe. Strain analysis by nano-beam electron diffraction (SANBED) [1] provides high spatial resolution of 0.5 nm - 0.7nm in a field of view of several hundreds of nanometres. A precision of σ = 0.08% has been reported from experiments [1] and an enhancement can be achieved using electron beam precession. In this case the precision reaches 0.02% [2], also confirmed by simulation (Fig. 1).

In experiment, the precision of the method can be determined from the standard deviation of measured values in unstrained parts of the sample. The accuracy, which is the deviation between the measurement and the actual strain, can hardly be determined experimentally, because usually the actual strain is unknown. Hence we analysed accuracy and precision of SANBED by evaluation of simulated series of CBED patterns. The simulations of experimentally investigated well-known samples [2, 3] account for thermal diffuse scattering using the frozen-lattice approach [4] and for the modulation-transfer function of the image recording system.

We found that close to interfaces between parts of the specimen with different strain, the accuracy of the measurement decreases due to so-called 'halos' in the simulated CBED patterns (Fig. 2), which are caused by a variation of strain within the area of the sample covered by the electron beam. This halo effect can be explained by considering the probe formation process, as illustrated in Fig. 3.

In the scanning mode of a transmission electron microscope the incident electron wave can approximately be described as the inverse-Fourier transform of the condenser aperture. Hence, the electron beam is not only focussed in one point and high spatial frequencies of the inverse-Fourier transformed aperture can leak in parts of the specimen with different lattice plane distance. As the lattice plane distance of the illuminated crystal defines the diffraction angle and thus the position of the discs in the diffraction pattern, parts of the circular edge of the aperture function are shifted with respect to the remaining inner part of the aperture, forming the halo. We show that the halo effect can theoretically be minimised by using condenser apertures without sharp edges.

1. K. Müller and A. Rosenauer et al., Microsc. Microanal. **18** (2012), p. 995.
2. J.-L. Rouviere et al., Appl. Phys. Lett. **103** (2013), p. 241913.
3. T. Mehrtens et al., Ultramicroscopy **131** (2013), p.1.
4. D. v. Dyck, Ultramicroscopy **109** (2009), p. 677.

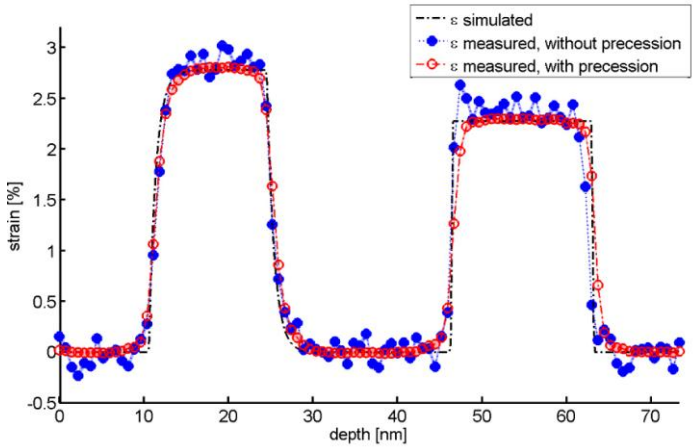

Figure1. Improvement of measurement of strain using electron beam precession. The red (open circles) and the blue (filled circles) curve show the evaluation of simulations with and without precession, respectively.

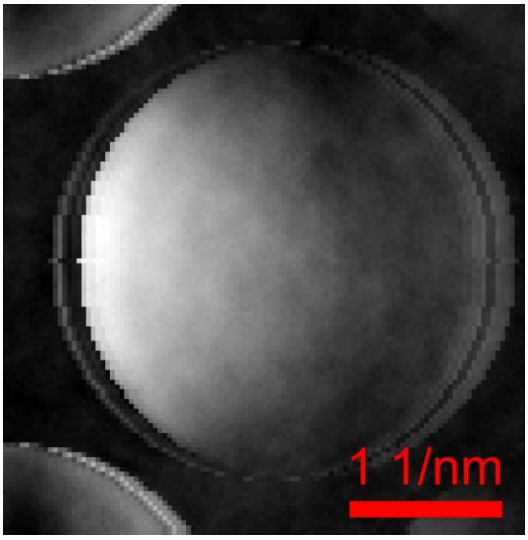

Figure 2. Halo at the 004-diffraction disc in a CBED pattern simulated at an interface between parts with different lattice plane spacing. In addition to the disc a bright ring appears at its left-hand side and interferences are visible in the right part.

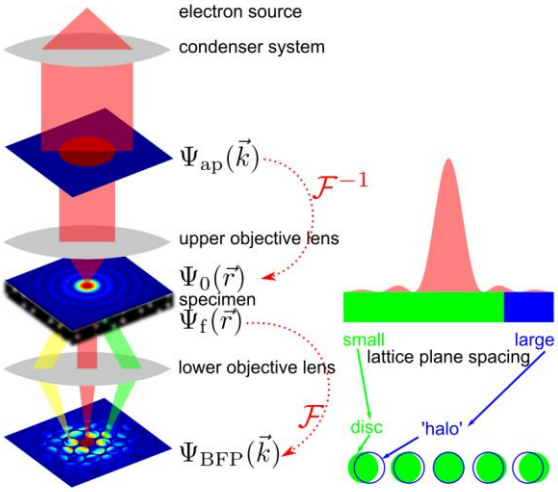

Figure 3. Origin of observed halos. Left: Formation of CBED patterns. The shape of the probe is given by the inverse-Fourier transform of the condenser aperture function. Right: Positioned at an interface between parts with different lattice plane spacing an outer part of the probe illuminates an area with different lattice parameter. Thus parts of the circular edge of the aperture function are shifted with respect to the inner part, forming the halo.

Thin Films, Coatings, Interfaces and Surfaces

MS2.P024
Atomic arrangement at antiphase boundaries connecting ZrO_2 pillars in ZrO_2-$La_{2/3}Sr_{1/3}MnO_3$ pillar-matrix structures

D. Zhou[1], W. Sigle[1], M. Kelsch[1], H.- U. Habermeier[1], P. A. van Aken[1]

[1]Max Planck Institute for Solid State Research, Stuttgart Center for Electron Microscopy (StEM), Stuttgart, Germany

d.zhou@fkf.mpg.de

Self-assembled vertically aligned nanocomposite thin films with two immiscible components hetero-epitaxially grown on single crystal substrates [1-4] have attracted tremendous research interest due to the advantages of utilizing both component functions and tuning material properties with high interface-to-volume ratio, hetero-epitaxial strain, or modifying the cation valence state. Anomalous magnetic anisotropy and modifications to the electric transport properties of $La_{2/3}Sr_{1/3}MnO_3$ (LSMO) have been reported to be achieved by introducing non-magnetic ZrO_2 pillars [5-7]. Whereas up to now, only macroscopic properties of ZrO_2-LSMO pillar-matrix systems (charge transport and magnetism) have been studied, microscopic properties at the atomic level were not studied at all.

Here we use high-angle annular dark-field (HAADF) imaging, annular bright-field (ABF) imaging, and electron energy-loss spectroscopy (EELS) in aberration-corrected scanning transmission electron microscopy (STEM) to reveal the structure, composition and valence state at atomic resolution for the pillar-matrix interface region and antiphase boundaries (APB) connecting adjacent ZrO_2 pillars with emphasis on antiphase boundaries connecting adjacent pillars. Details about the pillar-matrix interface region can be found in our previous report [8].

Atomic resolution EEL spectrum imaging (SI) reveals substantial interdiffusion at the ZrO_2-LSMO interface with Mn replacing Zr in ZrO_2 (thus stabilizing the cubic or tetragonal phase) and Zr replacing Mn atoms in LSMO. Charge balance requires the combination of Mn valence state change and oxygen vacancy formation which are observed to segregate at the interface.

As one way to relax the strain generated from the misfit of two components, three types of APBs were found connecting adjacent pillars, all exhibiting segregation of Mn. The crystal lattices on either side of the APB wall are displaced by an antiphase shift as can be seen in Figure 1, which includes two types of APBs. The Mn valence state in the APBs was found to be the same as in the matrix. The APB wall planes are either {110} or {310}. The arrangement of heavy and light elements is revealed by simultaneously acquired HAADF and ABF images, as shown in Figure 1c,d, and EELS spectrum imaging. The role of the pillars and APBs regarding elastic strain will be discussed.

The spin, charge, and orbital ordering in LSMO are extremely sensitive to local structural and elemental variations. Thus, our results provide a basis for understanding the origin of these properties [9].

1. Chen, A. P.; Bi, Z. X.; Hazariwala, H.; Zhang, X. H.; Su, Q.; Chen, L.; Jia, Q. X.; MacManus-Driscoll, J. L.; Wang, H. Y. Nanotechnology **2011,** 22, (31).
2. Imai, A.; Cheng, X.; Xin, H. L. L.; Eliseev, E. A.; Morozovska, A. N.; Kalinin, S. V.; Takahashi, R.; Lippmaa, M.; Matsumoto, Y.; Nagarajan, V. Acs Nano **2013,** 7, (12), 11079-11086.
3. Zheng, H.; Zhan, Q.; Zavaliche, F.; Sherburne, M.; Straub, F.; Cruz, M. P.; Chen, L. Q.; Dahmen, U.; Ramesh, R. Nano Lett **2006,** 6, (7), 1401-1407.
4. Liu, H. J.; Chen, L. Y.; He, Q.; Liang, C. W.; Chen, Y. Z.; Chien, Y. S.; Hsieh, Y. H.; Lin, S. J.; Arenholz, E.; Luo, C. W.; Chueh, Y. L.; Chen, Y. C.; Chu, Y. H. Acs Nano **2012,** 6, (8), 6952-6959.
5. Gao, Y. Z.; Zhang, J. C.; Fu, X. W.; Cao, G. X.; Habermeier, H. U. Prog Nat Sci-Mater **2013,** 23, (2), 127-132.
6. Jin, Y.; Yao, X. C.; Jia, R. R.; Cao, S. X.; Zhang, J. C. J Supercond Nov Magn **2013,** 26, (5), 1621-1624.
7. Gao, Y. Z.; Zhang, J. C.; Cao, G. X.; Mi, X. F.; Habermeier, H. U. Solid State Commun **2013,** 154, 46-50.
8. Dan Zhou, W. S., Eiji Okunishi, Yi Wang, Marion Kelsch, Hanns-Ulrich Habermeier and Peter A. van Aken. APL Materials **2014,** 2, (12), 10.
9. The research leading to these results has received funding from the European Union Seventh Framework Program [FP/2007-2013] under grant agreement no 312483 (ESTEEM2).

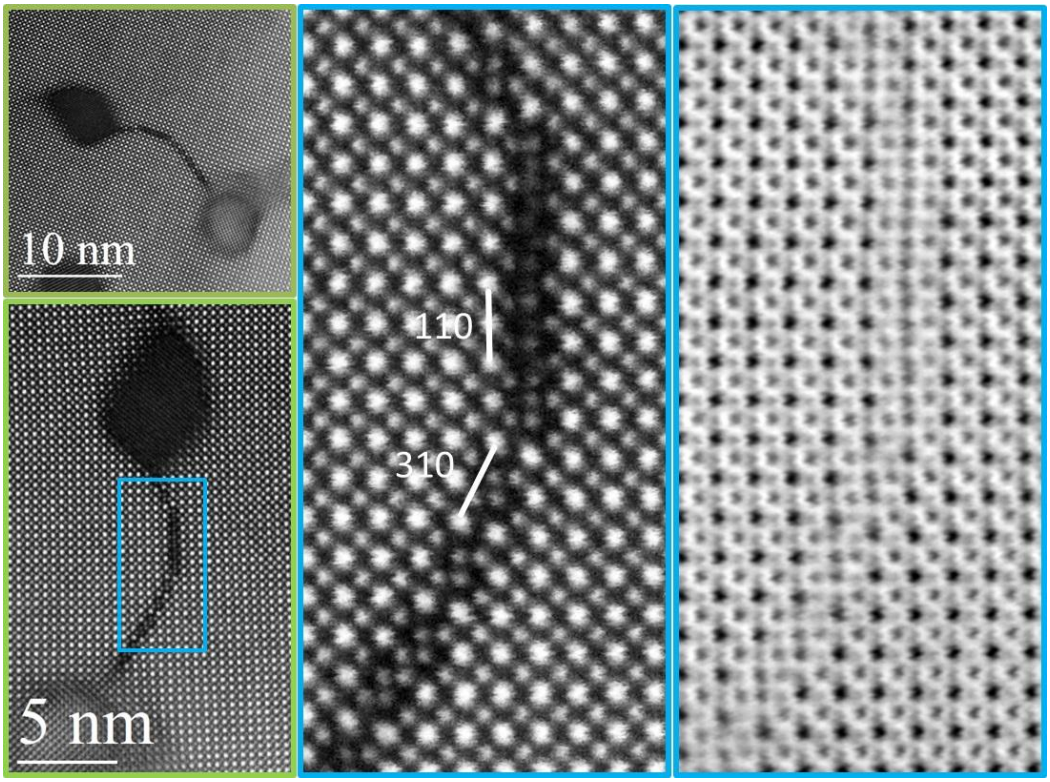

Figure 1. (a) HAADF image of a plan-view 80 mol% LSMO-20 mol% ZrO_2 sample showing two ZrO_2 pillars connected by APBs. (b) Magnified image of the boundary region shown in (a). Simultaneously acquired (c) HAADF and (d) ABF image of the region marked in blue in (b) including APBs with {110} and {310} boundary planes, respectively.

MS2.P025
Observing the morphology of single layered embedded silicon nanocrystals grown on temperature-stable TEM membranes

C. Kübel[1,2], S. Gutsch[3], J. Laube[3], D. Hiller[3], M. Zacharias[3]

[1]KIT, INT, Eggenstein-Leopoldshafen, Germany
[2]KIT, KNMF, Eggenstein-Leopoldshafen, Germany
[3]Albert-Ludwigs-University of Freiburg, IMTEK, Freiburg, Germany

christian.kuebel@kit.edu

Silicon nanoparticles potentially enable new applications in silicon based optoelectronics and photovoltaics. Single and multiple layers of Si rich oxides and oxyinitrides with varying Si excess concentrations can be deposited by PECVD [1] followed by subsequent high temperature annealing to induce phase separation into silicon nanoparticles embedded in a SiO_2 matrix. The optical and electrical properties of the ensembles of silicon nanoparticles are strongly influenced by structural properties such as size distribution, separation distance and density regardless of the application. However, the standard approach for structural characterization of these Si nanocrystal/SiO_2 superlattices by TEM is carried in cross-section only revealing the presence of multilayer stacks [2], but no detailed information on the Si nanocrystal network inside the superlattice can be obtained this way.

As an alternative, we used TEM compatible high temperature stable SiN membranes to investigate the morphology and size distribution of single layers of Si nanocrystal ensembles prepared by precipitation of a silicon-rich oxide layer sandwiched between two SiO_2 diffusion barriers [3]. In this way size distribution, shape and areal density of the Si nanocrystals can be accessed in plane-view by energy-filtered TEM without a need for further specimen preparation. However, care has to be taken to operate under low-dose conditions as electron beam exposure of the silicon oxides results in the formation of silicon nanocrystals both when operating the TEM at 80 and 300 kV as investigated in a number of dose series (Fig. 1).

Using this unique low-dose plane-view approach, we demonstrate how the nanocrystal size distribution develops depending on precipitation layer thickness and stoichiometry (Fig. 2). At low Si excess, isolated single crystalline Si particles with low density are observed indicating an incomplete phase separation. An increase of Si excess leads to larger Si particles near SiO_x=0.4 and we find a transition point, where the isolated Si particles merge into a continuous network. In addition, we study the influence of annealing conditions and find negligible differences that are indicative of fast phase separation on the timescale of seconds and significantly slower particle growth due diffusion processes. These results are crucial to understand processing conditions, doping and transport properties of Si nanocrystals embedded in dielectrics.

1. Laube et al. JAP, 116, 223501.
2. Hartel et al., Thin Solid Films (2011) 520, 121-125.
3. Gutsch et al., Beilstein J. Nanotechnology, accepted

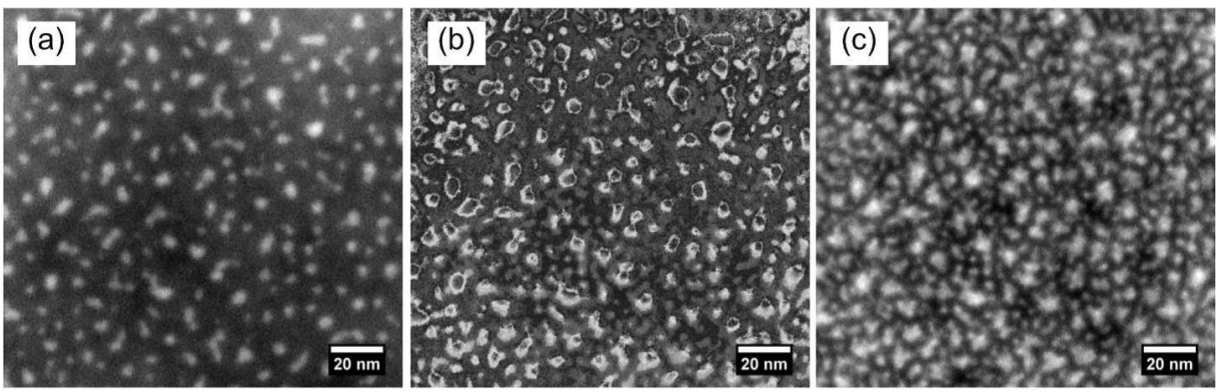

Figure 1. EFTEM images of 2 nm SiO_2/4.5 nm $SiO_{0.64}$/2 nm SiO_2: (a) image in fresh area, (c) after extended exposure to the electron beam and (b) XOR image of (a) and (c) highlighting the difference between the two as denoted by white regions. The nanoparticles grow in size and even new ones are created (from Ref. [3]).

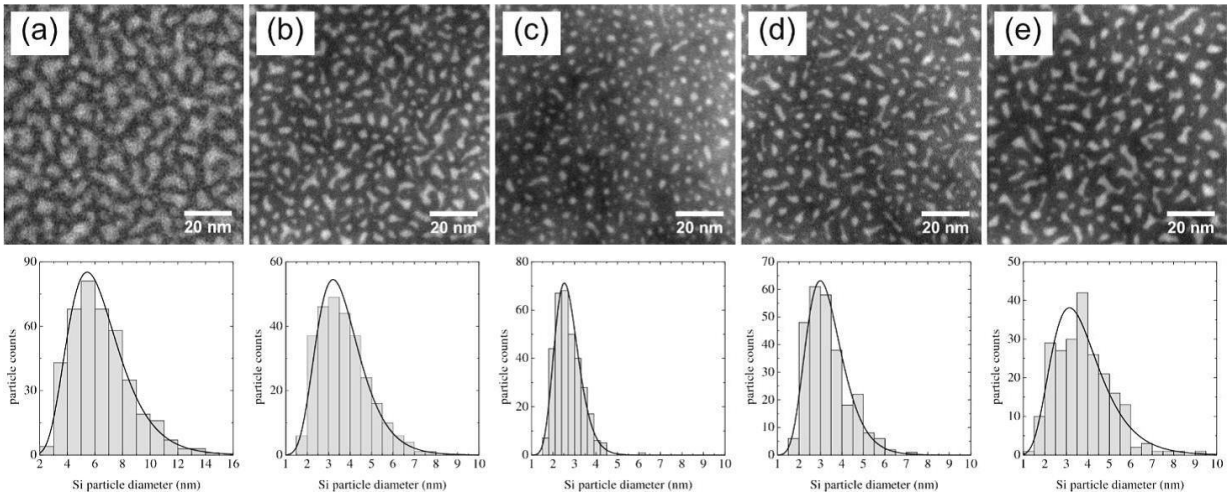

Figure 2. Low-dose EFTEM images and corresponding Si NC size distributions: (a) 10 nm $SiO_{0.93}$, (b) 4.5 nm $SiO_{0.93}$, (c) 3.5 nm $SiO_{0.93}$, (d) 3.5 nm $SiO_{0.85}$, (e) 3.5 nm $SiO_{0.64}$ (from Ref. [3]).

MS2.P026
Si diffusion and precipitation in Al during the Al-induced layer exchange (AlILE) process

S. M. Kraschewski[1], F. Niekiel[1], B. Butz[1], F. Gannott[2], B. Birajdar[1], J. Zaumseil[3], E. Spiecker[1]

[1]Universität Erlangen-Nürnberg, Lehrstuhl für Mikro- und Nanostrukturforschung & Center for Nanoanalysis and Electron Microscopy (CENEM), Erlangen, Germany
[2]Universität Erlangen-Nürnberg, Lehrstuhl für Polymerwerkstoffe (LSP), Erlangen, Germany
[3]Universität Heidelberg, Institute for Physical Chemistry, Heidelberg, Germany

simon.m.kraschewski@fau.de

Al-induced layer exchange (AlILE) is a promising route to fabricate polycrystalline Si (c-Si) seed layers from amorphous Si (a-Si) at low temperature. The process makes use of the phenomenon of metal-induced crystallization and is characterized by a layer exchange in a stack of a-Si/Al on glass substrate at temperatures in the range of 180-550 °C (Figure 1a). According to the current understanding of the process atomic Si diffuses into the Al layer where it becomes oversaturated and forms crystalline precipitates [1]. The precipitates grow laterally thus replacing the Al which is “pushed up” into the original a-Si layer [2]. In order to obtain c-Si layers with large grain size (up to 100 µm) in-diffusion and nucleation of Si in the Al layer have to be controlled which can be achieved by adding a thin AlOx barrier layer in between the Al and a-Si layers.

Cooling a partly reacted AlILE sample leads to formation of secondary c-Si nuclei in the unreacted regions resulting from high Si supersaturation in Al at lower temperatures, as shown in the light microscopy (LM) image Figure 1b). However, a certain distance d around the primary c-Si nuclei remains free of secondary nuclei. This phenomenon was first observed by Schneider et al. [1] who showed via in situ LM that the width d of this “depletion region” is the larger the faster the cooling while the density of secondary nuclei increases. Based on these observations Sarikov et al. [3] presented a model of the ALILE process in which it is assumed that already at annealing temperature the Si content in the Al layer is considerably higher than expected from the bulk Si/Al phase diagram. However, until now no analytical SEM/TEM studies have been performed in order to verify this model.

Performing analytical TEM measurements of Si concentration in the Al layer of slowly cooled and quenched samples will allow proving the model and investigating the diffusion process of Si during the AlILE process. For analytical TEM a FEI Titan Themis³ 300 equipped with a Super X detector and a Gatan Quantum GIF is used. In addition to ALILE sample annealed and quenched ex situ in a vertical oven, in situ heating and quenching experiments are carried out using a DENSsolutions TEM heating system, providing a quenching speed of up to 430 K/s in the used temperature regime.

Figure 2 shows results of a preliminary SEM EDXS study on ex situ cooled and quenched samples. According to these findings the precipitation of secondary nuclei can be completely suppressed by fast quenching.

1. J. Schneider et al., J. NON-CRYST SOLIDS 352, (2006)
2. B. Birajdar et al., PHYS STATUS SOLIDI 5, (2011)
3. A. Sarikov et al., J NON-CRYST SOLIDS 352, (2006)
4. The authors gratefully acknowledge financial support by the German Research Foundation (DFG) via the research training group GRK 1896 “In situ microscopy with electrons, X-rays and scanning probes” and the cluster of excellence EXC 315 “Engineering of advanced materials”.

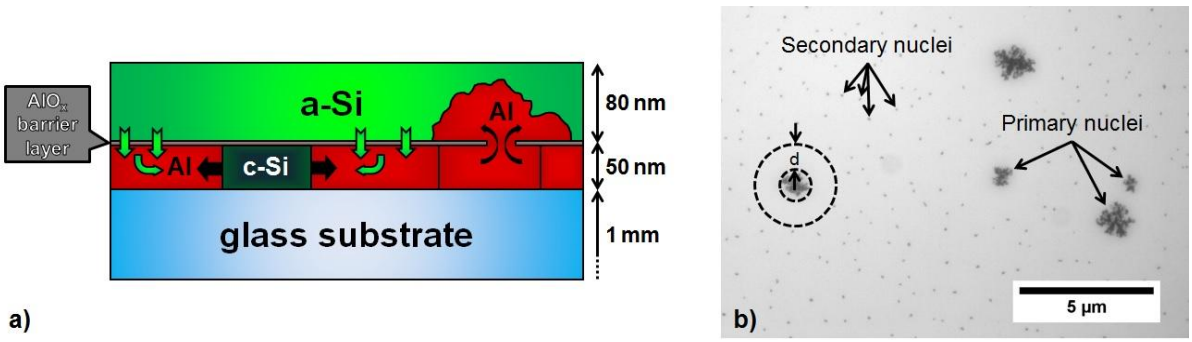

Figure 1. a) Schematic showing the elementary processes that occur during the AlILE (see text), b) LM image of a partly reacted AlILE sample after heat treatment at 450 °C: During cooling secondary c-Si nuclei formed in the unreacted regions except in a “depletion region” of width d around the primary c-Si nuclei.

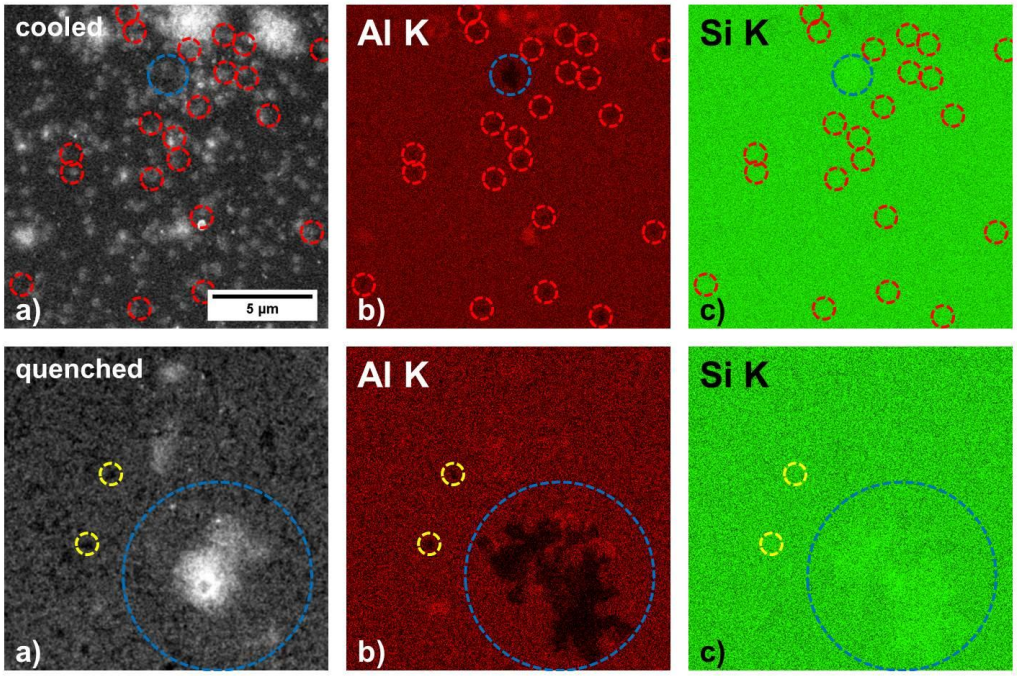

Figure 2. Plan-view SEM-EDXS investigation of a cooled (top row) and quenched (bottom row) AlILE sample after heat treatment at 420-425 °C for 7-10 min: a) BSE SEM images with corresponding b) Al-K and c) Si-K elemental maps from EDXS. Primary and secondary c-Si nuclei are indicated by blue and red circles, respectively. Because of the Si content in the glass substrate the Si map c) is hardly interpretable. Secondary nuclei only appear in the slowly cooled sample. Possible candidates for secondary nuclei (yellow circles) in the quenched sample turn out to be defects according the corresponding BSE SEM image. Pushed-up Al appears bright in the Al-K mappings.

Thin Films, Coatings, Interfaces and Surfaces

MS2.P027
SEM/EDX for the determination of thin film porosity: application to mesoporous TiO_2 layers

E. Ortel[1], R. Kraehnert[2], F. Galbert[2], V.- D. Hodoroaba[1]

[1]BAM, 6.8 Surface Analysis and Interfacial Chemistry, Berlin, Germany
[2]Technical University of Berlin, Berlin, Germany

erik.ortel@bam.de

Various applications such as automotive catalysts, photocatalysis and sensors rely on thin coatings with high active surface area. The development of new and improved coatings requires in-depth understanding of the film morphology and texture. Especially the film porosity is a key parameter to identify structure-property relationships in applications. However, an accurate porosity determination of thin porous coatings is a challenging. In this contribution we present and discuss a new approach for determining the porosity of films by X-rays at SEM.

The mass coverage of layers can be calculated by the film analysis software STRATAGem [1] from EDX determined *k*-values (the ratio of normalized intensity between unknown sample and standard) based on the well known Pouchou and Pichoir approach.[2] The high accuracy of STRATAGem results has been proven for various layered materials.[3-5] We present an approach for determination of the porosity by a combined SEM/EDX/STRATAGem analysis. From the STRATAGem-derived mass coverage and the coating thickness as determined by cross-section SEM micrographs, the average density of the film can be obtained. In a second step, the porosity can be calculated from the measured porous film density and the literature value for the pore walls bulk density. The complete approach is sketched in Figure 1.

The general procedure to determine the porosity is demonstrated on thin mesoporous TiO_2 films on Si wafer substrates. The TiO_2 films were synthesized by a template-assisted synthesis route, which provides a scalable model system with tunable porosity, see Figure 2.[6] EDX spectra of these films were measured at beam voltages of 7, 10, 15, 20, and 30 kV by using a high-throughput SDD EDS detector which enables a time-efficient analysis. Polished bulk of pure Ti and Si served as standard references. Oxygen was quantified by stoichiometry as well as by using a pure SiO_2 reference. The resulting *k*-values were verified by WDX analysis. The calculated mass coverage was independently validated by weighing and by ICP-OES of dissolved coatings. To determine the film thickness, the TiO_2 films were cleaved and the resulting cross-section was imaged with a SEM.

The measured *k*-values for Ti Ka and Si Ka in dependence on the beam voltage and the corresponding fitted curves calculated by STRATAGem are shown in Figure 3a for a porous 180 nm thick TiO_2 film. Figure 3b visualizes the resulting mass coverage values for all beam voltages. The scattering of the individual mass coverage values at different voltages reflects the robustness of the model.

An excellent agreement was obtained between the mass coverage calculated by STRATAGem and the mass coverage determined by weighing and ICP-OES of the same film. The increasing porosity of the thin TiO_2 films illustrated in Figure 2 could be calculated quantitatively by the new approach. The validation and traceability of the porosity results will be discussed. These combined SEM/EDX/STRATAGem analyses demonstrate a unique tool for non-destructive examination of the porosity of thin porous films.

1. Stratagem version 2.6, SAMx, 4, rue Galilée, 78280 Guyancourt, France
2. J.-L. Pouchou, Mikrochim Acta **138** (2002), p. 133.
3. V.-D. Hodoroaba et al., Surf. Interface Anal. **44** (2012), p. 1459.
4. M. Procop et al., Anal. Bioanal. Chem. **374** (2002) p. 631.
5. F. Galbert, Microsc. Microanal. **13** Suppl. 3 (2007) 96.
6. E. Ortel et al., Small **8** (2012), p. 298.

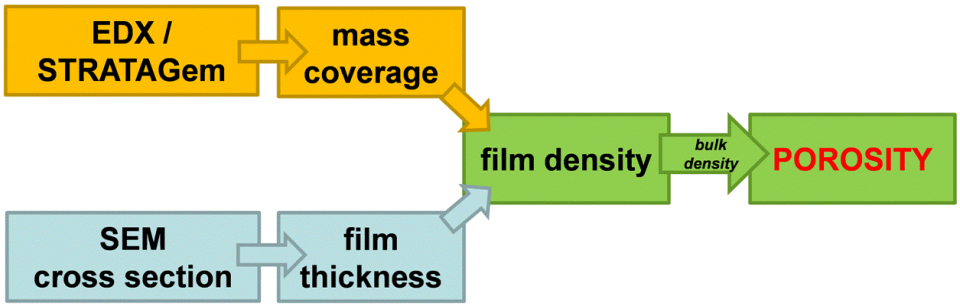

Figure 1. Illustration of the approach for the determination of the porosity of thin films by EDX/SEM analysis.

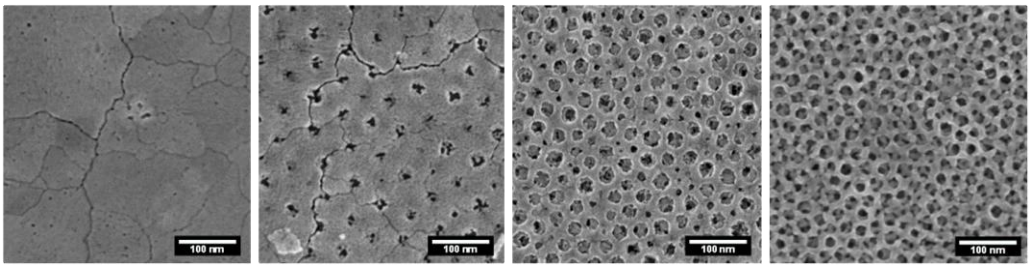

Figure 2. Top-view SEM micrographs of TiO_2 films synthesized with increased amount of a mesopore template, which results in an increase of the void fraction, i.e. film porosity (from left to right).

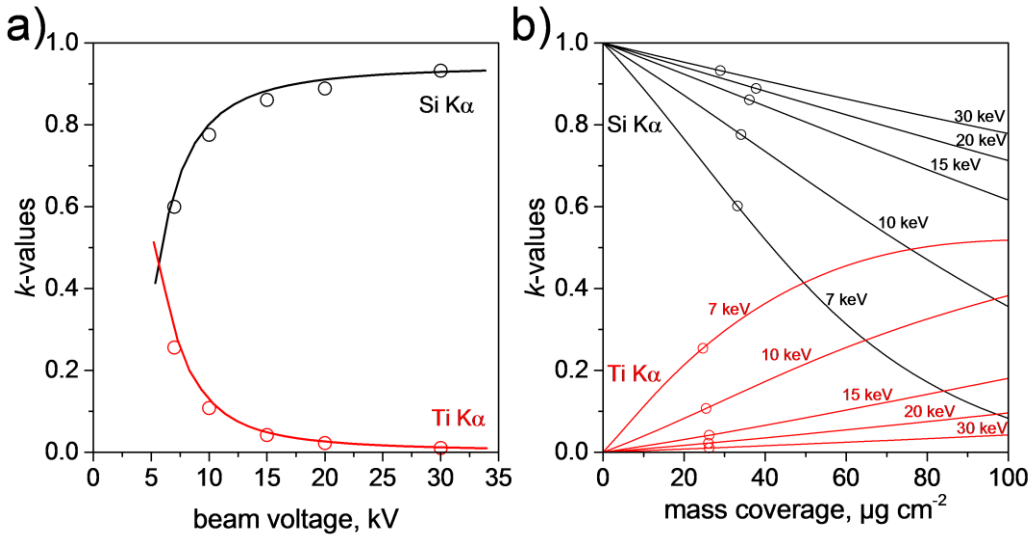

Figure 3. a) *k*-values versus beam voltage for Ti Ka (red) and Si Ka (black); the markers represent the measured values, the curves are fitted to the *k*-values. b) *k*-values of Ti Ka and Si Ka versus calculated mass coverage at each beam voltage.

Thin Films, Coatings, Interfaces and Surfaces

MS2.P028
TEM investigations of GaAs/Si nanostructures

R. Kozak[1], I. Prieto[2], M. D. Rossell[1], R. Erni[1], O. Skibitzki[3], T. Schroeder[3], H. von Känel[2]

[1]EMPA, Electron Microscopy Center, Dübendorf, Switzerland
[2]ETH Zürich, Laboratory for Solid State Physics, Zürich, Switzerland
[3]IHP, Frankfurt (Oder), Switzerland

roksolana.kozak@empa.ch

Monolithic heterogeneous integration of different semiconductors (Ge, Si_xGe_{1-x}, GaAs, etc.) on a Si chip is a promising area of research with a high potential to design new miniaturized structures (pillars, quantum dots, nano-wires, -tips, etc.) with tailored optoelectronic and photonic characteristics (higher carrier mobilities and saturation velocities, quasi-direct and direct bandgaps), which can find application in lasers, ultrafast transistors or photodetectors [1, 2]. In this work we present submicron sized GaAs crystals selectively grown by metal organic vapor phase epitaxy on Si pillars and tips (for example, as shown in the Fig. 1a). Growth on substrate nanopatterns eliminates threading dislocations similar to “aspect ratio trapping” in submicron trenches and pits [3]. It may even prevent plastic strain relaxation by misfit dislocations in contrast to the growth of thin films on planar substrates (Fig. 1b) by taking advantage of the compliant substrate effects [4]. Consequently, it is important to explore local atomic defects at the GaAs/Si interface and their evolution with changing shape/size of the substrate pattern and to analyze the residual elastic strain of grown crystals by means of state-of-the-art transmission electron microscopy (TEM) techniques.

The demand for thin and site specific TEM samples, which are constant in thickness and free of artifacts, makes specimen preparation of these nontrivial materials extremely challenging. Conventional cross-section and FIB lamella preparation methods have been applied and compared. The obtained high-resolution TEM images permit geometrical phase analysis (GPA), which can be used for lattice mismatch and strain characterization [5]. First results of interface studies for GaAs/Si nanostructures will be presented.

1. C.V. Falub et al., *Science* **335** (2012) 1330-1334.
2. A.G. Taboada et al., *Appl. Phys. Lett.* **104** (2014) 022112.
3. J.G. Fiorenza et al., *ECS Trans.* **33** (2010) 963-976.
4. P. Zaumseil et al., *J. Appl. Phys.* **112** (2012) 043506.
5. M. J. Hÿtch et al., *Ultramicroscopy* **74** (1998) 131-146.

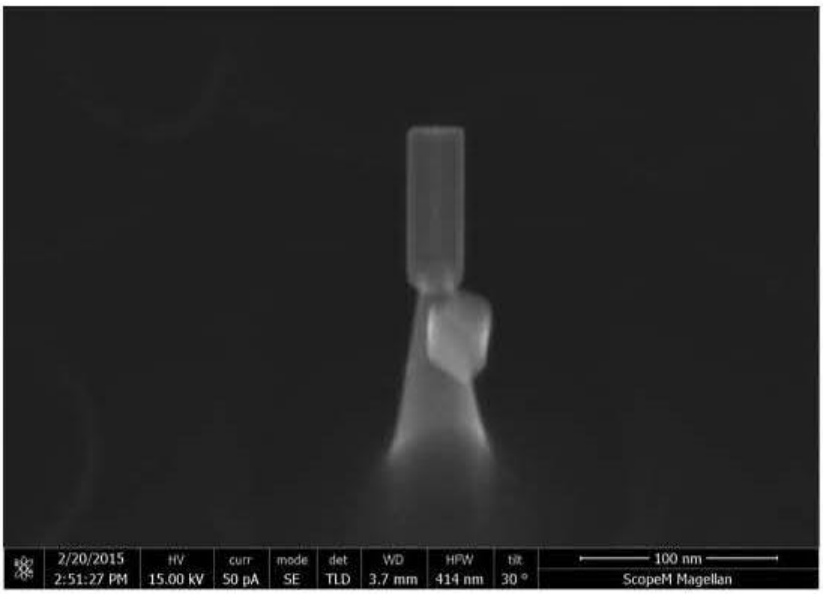

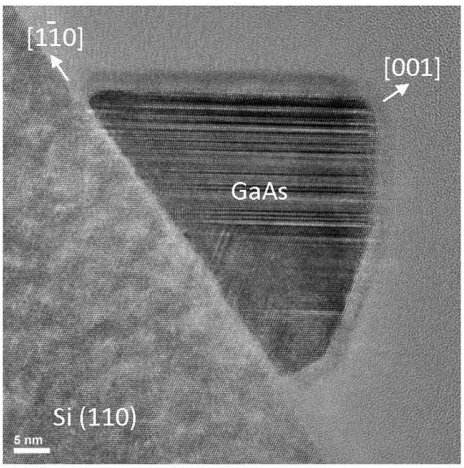

Thin Films, Coatings, Interfaces and Surfaces

MS2.P029
Interface study of CrN (VN, TiN) films on MgO and Al_2O_3 substrate using C_S-corrected HRTEM

Z. Zhang[1], G. Gehm[2]

[1]Erich Schmid Institute, Austrian Academy of Sciences, Leoben, Austria
[2]Max-Planck-Institut für Eisenforschung, Düsseldorf, Germany

zaoli.zhang@oeaw.ac.at

Transition metal nitrides have found wide-spread applications in the cutting- and machining-tool industry due to their extreme hardness, thermal stability and resistance to corrosion. The increasing demand of these nitrides requires an in-depth understanding of their structures at the atomic level. This has led to some experimental and theoretical researches [1-6]. The films used in this study were deposited by reactive direct current magnetron sputtering of a Cr/V/Ti metal target in an Ar+N_2 atmosphere at a constant total pressure of 1 Pa, a target power of 6 kW, and a temperature of 350°C. A TEM/STEM JEOL 2100F operated at 200 kV and equipped with an image-side C_S-corrector and a Gatan imaging filter (Tridiem) was utilized for characterizing the film structure.

In this paper, we will present some recent results on the atomic and electronic structures of metal nitride thin films (CrN, VN and TiN) on MgO and Al_2O_3 substrate (**Fig.1**a and **Fig. 1b**) using advanced TEM techniques, such as C_S-corrected HRTEM/STEM, EELS/EDXS, quantitative atomic measurement and electron diffraction analysis as well as theoretical calculations. Interfacial detailed atomic and electronic structures are revealed and compared. Interface induced phenomena between nitride films and substrates are unveiled [2,3].

Particular study on the effect of N defects in the metal nitride (CrN) film has led to some interesting conclusions. Ordered nitrogen (N) vacancies were often found to well distribute at the {111} planes. Combining independent image analysis, such as atomic displacement/strain measurement using geometrical phase analysis, and spectrum analysis by examining the low loss and core loss, fine structure analysis, some generalized conclusions are drawn, which are: (i) a relationship between the lattice constant and N vacancy concentration in CrN is established [5], (ii) the change of ionicity in CrN crystal with the N vacancy concentration is shown; (iii) Particularly, a direct relationship between electronic structure change (L_3/L_2 ratio) and elastic deformation (lattice constants) in CrN films has been experimentally derived, revealing that the elastic deformation may lead to a noticeable change in the fine structure of Cr-$L_{2,3}$ edge, i.e. L_3/L_2 ratio (shown in Fig.2). The experiment demonstrates an indirect approach to acquire electronic structure changes during the elastic deformation.

The effect of randomly distributed defects in the films has been explored in a quantitative way using quantitative electron diffraction, combined with HRTEM and EELS analysis. Some quantitative relations are established.

1. R. Daniel *et al*, Acta Materialia **58**(2010), p. 2621.
2. Z. L. Zhang, *et al* Physical. Review B **82(**R)(2010) p060103-4
3. Z. L. Zhang, *et al* Journal of Applied Physics, 110(2011)p043524-4
4. Z.L. Zhang *et al* Physical Review B **87** (2013) p014104.
5. T.P. Harzer, *et al* Thin Solid Films 545 (2013) p154-160
6. A.S. Botana *et al* Physical Review B **85**(2012), p. 235118
7. Gabriele Moser and Herwig Felber are gratefully acknowledged for their help with sample preparation, thanks are given to Dr.Hong Li for *ab-initio* calculations. Thank Dr. Rostislav Daniel and Christian Mitterer in Montanuniversität Leoben, Leoben, Austria for delivering the materials.

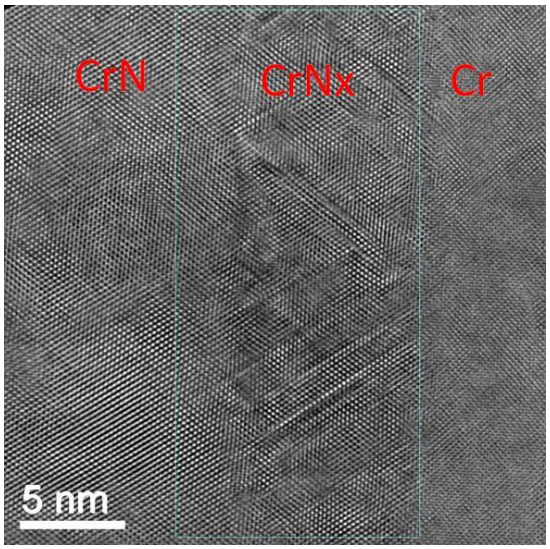

Figure1. Left: HRTEM image of the CrN and Cr films on MgO substrate, a defective layer between Cr and CrN, which originates from the ordered N vacancies. Right: HRTEM image of CrN film on Al_2O_3 substrate, viewing along [1-10] CrN and [01-10]Al_2O_3.

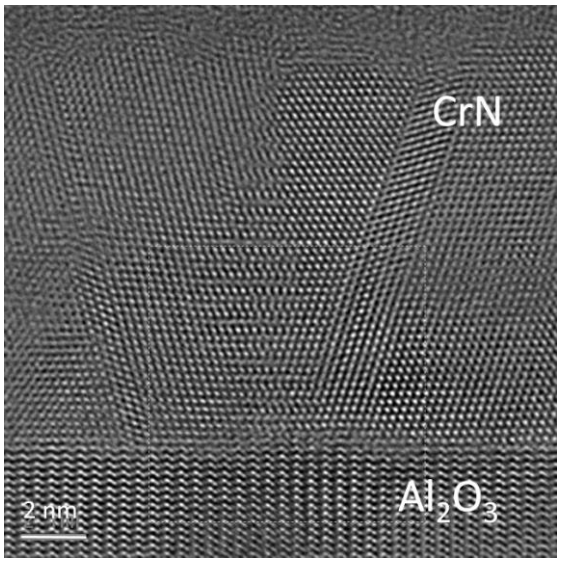

Figure 2. Variation of the white- line ratio (L3/L2) in Cr with the lattice constant of CrN

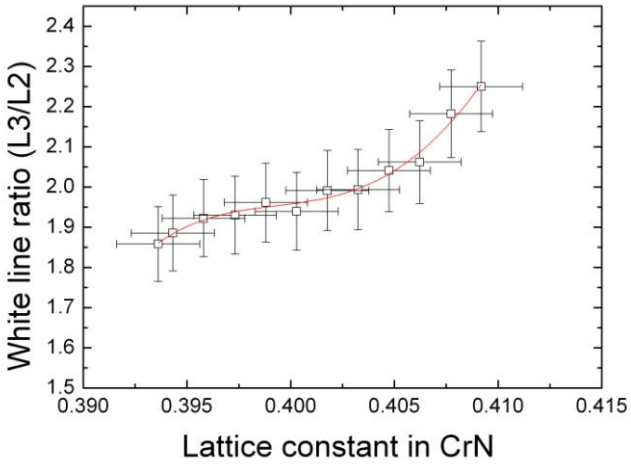

Thin Films, Coatings, Interfaces and Surfaces

MS2.P030
TEM analysis of Cr_2AlC coatings

A. Obrosov[1], S. Weiss[1], M. Naveed[1]

[1]BTU Cottbus - Senftenberg, Physical Metallurgy and Materials Technology, Cottbus, Germany

obrosale@tu-cottbus.de

In the last years, $M_{n+1}AX_n$ (MAX) phases came into focus of functional thin film research.MAX phases represent a family of ternary carbide or nitride compounds of the general formula: $M_{n+1}AX_n$, (MAX), where n = 1, 2, 3; M is an early transition metal; Ais an A Group (Group IIIA or IVA) element; and X is either carbon and/or nitrogen. In the current study Cr_2AlC coatings with 3 different substrate bias voltages V_s (60V, 90V and 120V) have been deposited on 30x15x3 mm Inconel 718 as well as silicon wafer by DC magnetron sputtering. Microstructural analysis was performed using scanning electron microscopy. Crystallite size of the films, preferential orientation and growth mode of the coatings were analyzed by means of transmission electron microscopy. The phase composition of the coatings was determined using X-ray diffraction technique (XRD). In this work discussion has been focused on the microstructural development of coatings due to variations in substrate voltage.

Thin Films, Coatings, Interfaces and Surfaces

MS2.P031
From zirconia to yttria — sampling the YSZ phase diagram using sputter-deposited thin films

T. Götsch[1], M. Stöger-Pollach[2], L. Mayr[1], B. Klötzer[1], S. Penner[1]

[1]University of Innsbruck, Institute of Physical Chemistry, Innsbruck, Austria
[2]Vienna University of Technology, University Service Center for Transmission Electron Microscopy (USTEM), Vienna, Austria

thomas.goetsch@uibk.ac.at

YSZ is one of the most extensively studied and most versatile materials due to its high mechanical strength, thermal stability and chemical inertness. Also, it features a high ionic conductivity, making it the ideal electrolyte for applications such as chemical sensors or intermediate-temperature solid oxide fuel cells (IT-SOFCs). Hence, the amount of works regarding YSZ thin films is vast; however, most of these films are produced with electrolyte layers in mind, which means that the thicknesses are either too high or the films are stuck to a substrate, preventing the application of transmission electron microscopy without further preparation steps.

Hence, in this work, the goal was to prepare epitaxially-grown, chemically homogeneous yttria-stabilized zirconia thin films ("YSZ") of various compositions (0% yttria (i.e. pure ZrO_2), 3%, 8%, 20%, 40% and 100% yttria (i.e. Y_2O_3)) by direct-current sputtering onto a single-crystalline NaCl(001) template at various temperatures, resulting in unsupported thin films after floating off NaCl in water.

A combined methodological approach, employing microscopy techniques (high-resolution (analytical) transmission electron microscopy (TEM) and atomic force microscopy (AFM)) as well as spectroscopical methods, such as surface-sensitive (angle-resolved) X-ray photoelectron spectroscopy (XPS), is utilized to fully characterize the prepared thin films. As an example, Figure 1 showcases a TEM bright field image as well as the corresponding selected area electron diffraction (SAED) pattern of "3YSZ", i.e. YSZ with 3 mol% yttria. This image indicates that the specimen contains cubic zirconia (albeit, in the target itself, it is monoclinic, indicating that a phase transformation takes place during the sputtering process), featuring a high ordering attributable to epitaxial growth with a [001] zone axis, as well as polycrystalline (cubic) yttria.

For 8YSZ (8 mol% yttria), for which the diffraction pattern also reveals that the film grows mainly in a [001] zone axis if deposited above 493 K, no Y-enrichment in surface- or bulk-regions takes place (see Figure 2 for an EFTEM image corroborating this). In fact, the Y-content of the sputter target is preserved in the thin films.[1]

Analysis of the plasmon region in electron energy-loss (EEL) spectra for the 8YSZ sample, seen in Figure 3, indicates a defective nature of the as-deposited films, which can be suppressed by post-deposition oxidation at 1073 K. This, however, induces considerable sintering, as deduced from transmission electron micrographs and surface morphology measurements by AFM.

1. T. Götsch; L. Mayr; M. Stöger-Pollach; B.Klötzer; S. Penner. *Appl. Surf. Sci.* **2015,** *331,* 427-436

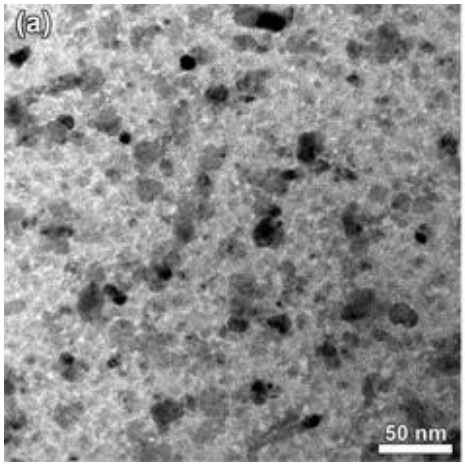
(a)
50 nm

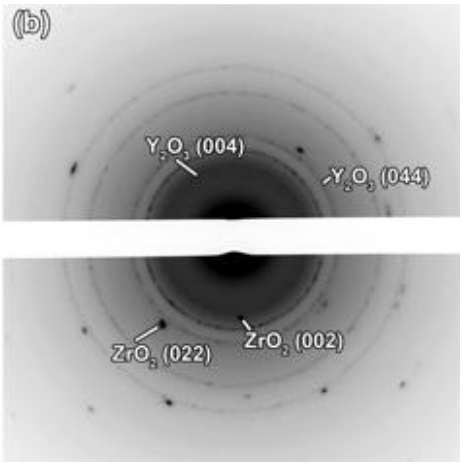
(b)
Y_2O_3 (004)
Y_2O_3 (044)
ZrO_2 (022)
ZrO_2 (002)

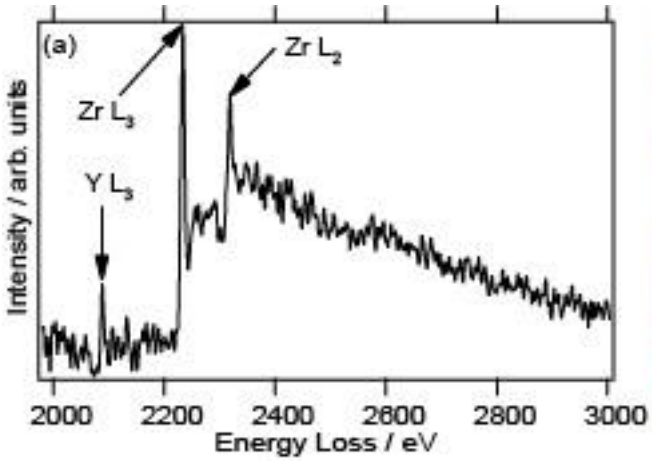
(a)
Zr L_3
Zr L_2
Y L_3
Intensity / arb. units
2000
2200
2400
2600
2800
3000
Energy Loss / eV

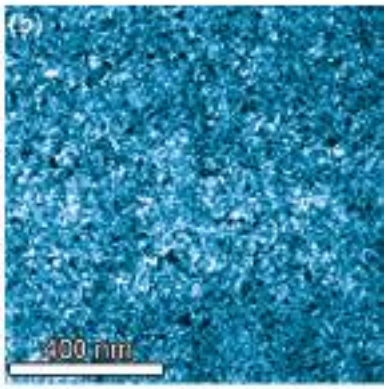
(b)
100 nm

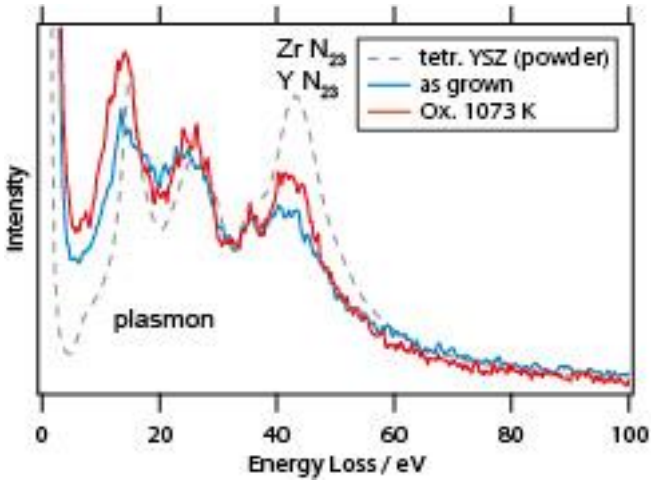
Zr N_{23}
Y N_{23}
tetr. YSZ (powder)
as grown
Ox. 1073 K
Intensity
plasmon
0
20
40
60
80
100
Energy Loss / eV

Thin Films, Coatings, Interfaces and Surfaces

MS2.P032
Nature and roughness of steels effect on intermetallic compounds obtained by galvanization

Y. Benarioua[1]

[1]M'sila University, Mechanical Engeneering, M'sila, Algeria

benariouayounes@yahoo.fr

In the last few years, the use of galvanization coating as material treatment to improve notably the chemical properties of steel parts has shown a large and extensive development. Zinc and some of its alloys have a number of characteristics that make it well suited for use as a protective coating against the corrosion of steel substrates under severe atmospheric conditions. The coating of galvanization offers in general case a cathodic protection to the ferrous materials. Because of these excellent characteristics, galvanization coatings are expected to be used for different protective applications fields. The aim of this research work is to study the effect of nature and roughness of steel substrates on intermetallic compounds of coatings obtained by galvanization. Steels substrates to be coated in this case are used in agriculture field as tubes and irrigation elements in pivot.

The specimens of steels witch prepared point of view roughness were initially degreased, picked in an aqueous solution containing 16% H_2SO_4 and fluxed in an aqueous solution of ZnCl2 and 2NH4Cl. After these three steeps of preparation, steels substrates were dipped into the galvanizing bath. For immersion time of 10 min, the coating of galvanization was carried out in the galvanizing bath at a temperature of about 460°C. The samples of steel were then quenched immediately in water upon removal from the bath in order to preserve the structure existing at the end of the galvanizing reaction.

During the galvanization process, the chemical reactions that take place between the steel and bath of zinc give rise to the formation of different intermetallic. Thus, three phases of Gamma, Delta and Zeta are produced as superposed layers on the steel substrate. Theses metallic compounds have been coated then by an outer layer of Eta phase. These intermetallic compounds produced by technological parameters of galvanization process have been characterized.

The structure was analyzed by X-ray diffraction witch has revealed the phases of Eta-Zn, Zeta-$FeZn_{13}$, $Delta_k$-$FeZn_7$, and $Delta_p$-$FeZn_{10}$. The morphology and thickness of phases formed the coatings were then observed by optical and scanning microscopy. The Gamma-phase observed by microscopy appears as a thin layer with a planar interface between the steel substrate and the Delta-phase layer. This last phase present a columnar morphology as a result of a preferred growth perpendicular to the interface in a direction along the basal plan of coating structure. Adjacent to Delta- phase, Zeta- phase appears and grows in a columnar morphology. Continued growth of these inter layers occurs rather than the formation of new outer layer of Eta- phase is formed.

The hardness of coatings was measured with a Vickers hardness tester with a low indentation load. The hardness profile performed on cross-section of steel sample was then characterized in this study. We notice that the d-phase present an elevated hardness compared to the substrate and the other phases of Zeta-FeZn13 and Eta-Zn.

Thin Films, Coatings, Interfaces and Surfaces

MS2.P033
Interaction of hydrogen with titanium-dioxide/palladium bilayers studied by HR-STEM EELS

M. Bongers[1], V. Roddatis[1], C. Nowak[1], A. Pundt[1]

[1]Institut für Materialphysik, Göttingen, Germany

mbongers@ump.gwdg.de

Catalysts are important in many chemical reactions to increase the amount of the reaction product per time, the so-called turnover rate. Two frequently used hydrogenation catalysts are Palladium (Pd) and Platinum (Pt). Supported by an oxide, these metal catalysts show increased turnover rates, for example in the water gas shift (WGS) reaction (CO + H2O → CO2 + H2) or the hydrogenation of carbon monoxide [1, 2]. The strongest increase in turnover rate was observed for titanium dioxide (TiO_2) [2]. Therefore, the metal/support interface is expected to be a very important parameter.

High resolution scanning transmission electron microscopy (HR-STEM) with electron energy loss spectroscopy (EELS) allows investigation of the density of states (DOS) above the Fermi level (E_F) at TiO_2/Pd interfaces. As suggested by Kobayashi et al. [3], the DOS is expected to change under hydrogen atmosphere. To get insight into the enhanced turnover rates, the energy states are investigated as a function of (a) distance from the metal/semiconductor interface and of (b) H_2 pressure.

Rutile-TiO_2/Pd double layers were prepared by reactive magnetron sputter deposition in oxygen atmosphere. The double layers reveal an epitaxial growth, and therefore, a high crystallinity, a low interface roughness, and a low stress state. Hence, they are suitable for the suggested HR-STEM EELS investigations because the influence of microstructural contributions is small, as shown in Fig. 1a. Cross-sectional TEM-lamellas were prepared by the focused ion beam (FIB) lift-out method, followed by Ar^+ ion milling. For observation during in-situ hydrogen gas loading, a FEI Titan environmental TEM (ETEM) 80-300 equipped with C_s-image corrector and beam monochromator was used.

The Ti-$L_{3,2}$ energy edges are sensitive to changes in the DOS above the Fermi energy (E_F). Therefore the Ti-L edges (Fig. 1) were examined with HR-STEM EELS line scans. Measurements reveal an increase in the energy edge onset in the presence of hydrogen. The results also suggests a strong influence of hydrogen on the DOS of TiO_2 close to the interface. An increase of the intensity ratio of the Ti-L_3 and Ti-L_2 edge indicates a change in valency. Additionally, an increase in the intensity ratio of the fine structure peaks *a* and *b* indicates a relative occupancy change of the t_{2g} and e_g levels, therefore supporting the argument of a changed valency.

1. D.C. Grenoble, M.M. Estadt, Journal of Catalysis 67 (1981) 90
2. M. Vannice et al., Journal of Catalysis 79 (1983) 70
3. H. Kobayashi et al., Surface Science 304 (1994) 393
4. Fischer, J. Appl. Phys. 41 (1970) 3561
5. Financial support by the DFG via SFB1073-C06 and DFG-PU131/9-1 is gratefully acknowledged.

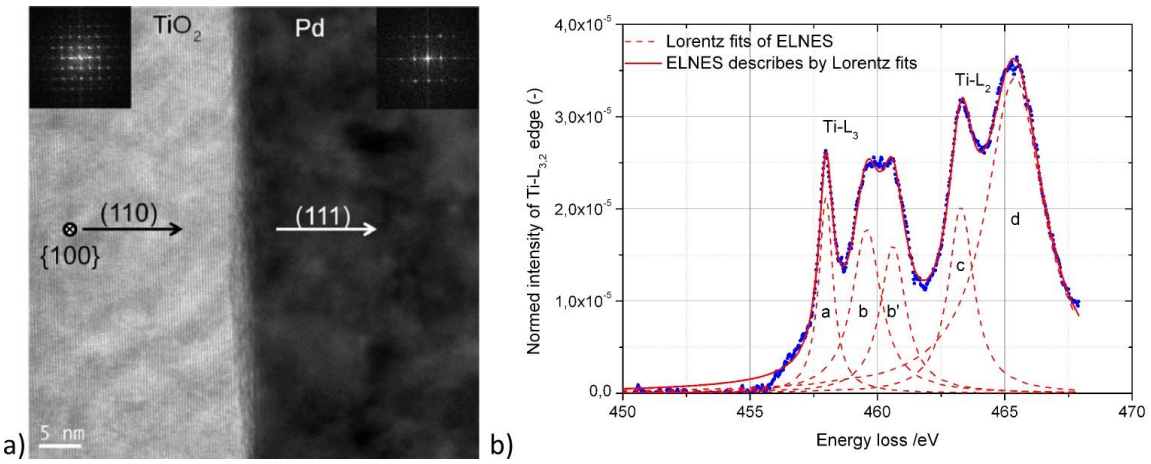

Figure 1. a) Bright-field TEM micrograph of TiO_2/Pd lamella in FEI Titan ETEM, the top left and right black boxes show the FFT of each layer. Single crystalline layers can be found. b) Example of a background corrected and normed Ti-$L_{3,2}$ ELNES as observed by the FEI Titan ETEM. Lorentz fitting (dashed lines) successfully describes the features in the Ti-$L_{3,2}$ electron loss near edge structure (ELNES) (right). The fine structure splitting in *a*, *b*, *b'* (L_3) and *c*, *d* (L_2) results from the distorted TiO_2 octahedron [4]. A beam monochromator was used when EELS spectra were recorded.

Thin Films, Coatings, Interfaces and Surfaces

MS2.P034
Local octahedral rotations and octahedral connectivity in epitaxially strained $LaNiO_3/LaGaO_3$ superlattices

H. Qi[1], M. Kinyanjui[1], J. Biskupek[1], D. Geiger[1], E. Benckiser[2], H.- U. Habermeier[2], B. Keimer[2], U. Kaiser[1]

[1]University of Ulm, Central Facility of Electron Microscopy, Electron Microscopy Group of Materials Science, Ulm, Germany
[2]Max Planck Institute for Solid State Research, Stuttgart, Germany

haoyuan.qi@uni-ulm.de

For ABO_3 perovskites, octahedral rotations and distortions couple strongly to the functional properties [1]. However, in short period perovskite superlattices, the characterization of the octahedral behavior remains challenging due to the local structural variations of the BO_6 octahedra. By using aberration-corrected high-resolution transmission electron microscopy (AC-HRTEM), we investigated the local octahedral rotations in a [(4 unit cell (u.c.)// 4 u.c.) ×8] $LaNiO_3/LaGaO_3$ (LNO/LGO) superlattice grown on a (001) $SrTiO_3$ (STO) substrate. The atomic models of bulk LNO and STO as well as the simulated images in [110] projection are shown in Fig. 1. Due to NiO_6 octahedral rotations, the projected oxygen positions shift up and down about the horizontal Ni-Ni line forming zigzags in the projections of NiO_2 layers. To quantify the zigzags, i.e. rotational magnitudes of NiO_6, we have defined an angle θ whose value is mainly determined by the magnitudes of [100] and [010] rotations, i.e. α and β.

Figure 2(a) and 2(c) represent the experimental AC-HRTEM images acquired across the substrate-superlattice interface and near the superlattice surface, respectively. The measured structural parameters θ, d_{001} and d_{-110} are shown in Fig. 2(b) and 2(d). The octahedral behavior varies along the growth direction even though the superlattice is coherently strained. As marked between the yellow lines in Fig. 2(a) and 2(b), near the substrate, octahedral rotations about [100] and [010] axes in the superlattice are suppressed due to the octahedral connectivity -rotational magnitudes and patterns- between the NiO_6 and TiO_6 octahedra. Away from the substrate the magnitudes of [100] and [010] rotations are enhanced as a response to substrate-induced tensile strain. As shown in Fig. 2(c) and 2(d), near the surface of the superlattice, the [100] and [010] rotational magnitudes of NiO_6 and GaO_6 relax to the bulk values of LNO and LGO, respectively. Our results indicate that the response of octahedral rotations to epitaxial strain in superlattices is significantly different from that in thin films.

1. H.Y. Hwang, Y. Iwasa, M.Kawasaki, B. Keimer, N.Nagaosa and Y. Tokura, Nat. Mater. **11**, 103 (2012).

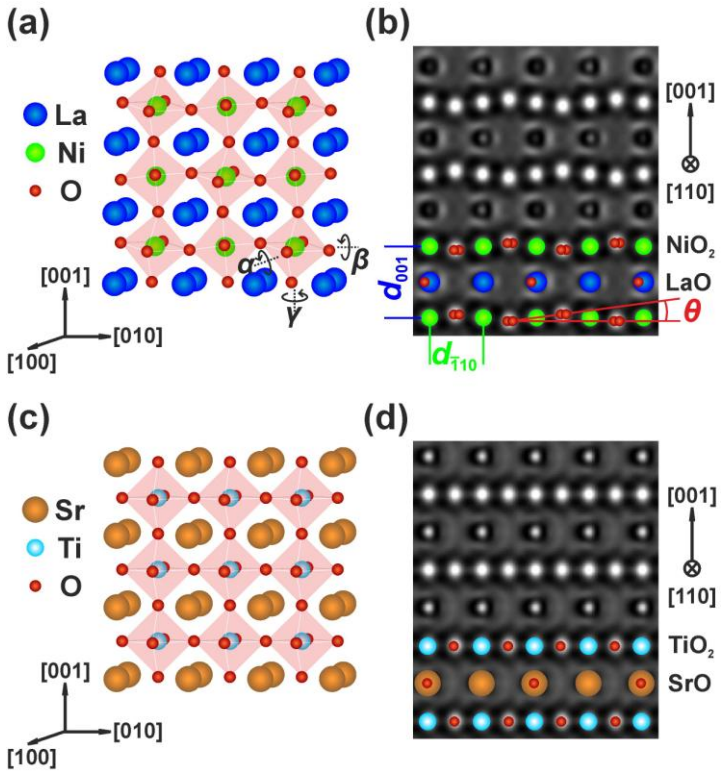

Figure1. (a) Atomic model of bulk LNO. (b) Simulated 300 kV AC-HRTEM image of bulk LNO in [110] projection. The identities of the atomic columns are indicated on the simulation. (c) Atomic model of bulk STO. (d) Simulated 300 kV AC-HRTEM image of bulk STO in [110] projection.

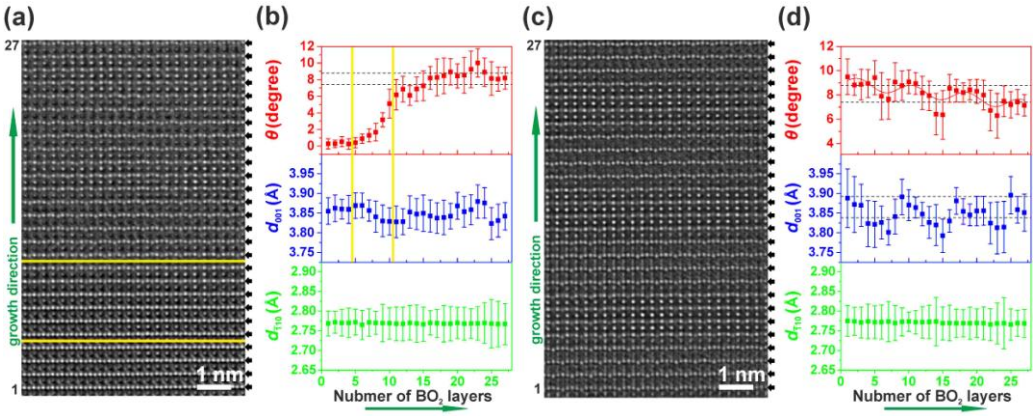

Figure 2. 300 kV AC-HRTEM images in [110] projection across the substrate-superlattice interface (a) and near the superlattice surface (c). The images were acquired using negative C_s imaging (NCSI) conditions with C_s ~ -15 µm and defocus ~ +5 nm (i.e. overfocus). Average background subtraction filtering was applied to remove noise. The BO_2 layers are marked by the black arrows. Numbering of the BO_2 layers starts from the bottom of each image and increases in the growth direction. (b) and (d) present measured structural parameters θ, d_{001} and d_{-110} from (a) and (c), respectively. Each data point is the average over a distance of ~10 nm in one BO_2 layer with the error bar representing the standard deviation. The dashed lines represent the bulk values of LNO and LGO ($\theta_{bulk,\ LNO}$ = 7.4°, $\theta_{bulk,\ LGO}$ = 8.8°, $d_{001,bulk\ LNO}$ = 3.838 Å, $d_{001,\ bulk\ LGO}$ = 3.892 Å). The STO-LNO interfacial region is highlighted between the yellow solid lines in (a) and (b). The curve in the top panel of (d) serves as guide to the eye to emphasize the oscillation of θ. Growth directions are indicated by the green arrows.

Thin Films, Coatings, Interfaces and Surfaces

MS2.P035
Microstructure of a steel-alumo-sol-coating- system after heat treatment in an oxyfuel atmosphere

I. Dörfel[1], M. Nofz[1], R. Sojref[1], M. Mosquera Feijoo[1], N. Wollschläger[1], A. Kranzmann[1]

[1]Bundesanstalt für Materialforschung und -prüfung BAM, Berlin, Germany

ilona.doerfel@bam.de

Coatings on substrates are instruments to avoid or reduce corrosion and modification of the substrate material during its use. So, protective coatings can cause prolongation of the lifetime, the increase of operation temperature or the extension of the application range of metallic substrates. Alumina coatings are one kind of prospects to produce protective layers. Such coatings can be fabricated by a sol-gel- process with the advantage of only marginal surface pretreatment of the substrate.

Here in the framework of the European project POEMA (Production of Coatings for New Efficient and Clean Coal Power Plant Materials), the commercial power plant steel P92 (9 % Cr) was coated and tested. The uncoated steel forms protective scales of Cr-rich oxides during its use in air and non-protective mixed oxides and iron oxides during its use in water vapor containing flue gas [1]. Substrates of P92 were dip-coated by an ethanolic Boehmite sol. The samples were heat treated at 650°C for 30 minutes in air to get a well adherent alumina coating (sample 1) and tested for 300 h at 650 °C in an oxyfuel combustion test atmosphere (1 bar, 60 CO_2+ 30 H_2 + 2 O_2 + 1 SO_2 +7 N_2 [Vol%], flow rate $3x10^{-2}$ m/s) (sample 2) which simulates the flue of a modern oxygen/fuel fired power plant.

For the microstructural characterization by TEM methods, TEM samples were produced as cross sections normal to the sample surfaces and normal to metallographic cuts of these samples by using the in situ lift out method by a FIB Quanta 3D. The FIB lamellae were investigated at 200 kV by an analytical STEM JEM 2200FS equipped with an Omega-type energy filter. Special effort was spent to characterize the microstructure of the oxidation zone near the interface to the steel and especially to the identification of the oxidation products of that region by EDX spectroscopy, TEM, STEM, HREM and energy filtered nano beam diffraction.

In this work the as-prepared samples (sample 1) are compared with the samples tested under oxyfuel conditions (sample 2).

Sample 1 shows the equational effect of the alumina coating on the roughness of the rippled surface of the steel substrate. Between the substrate and the coating itself islands of a narrow oxidation zone, consisting of two regions exist. Their part near the substrate is rich in chromium oxide the upper part near the coating is mixed of chromium oxides and chromium iron oxides. The sample is coated twice by alumo-sol, both sublayers are porous.

The sample 2 shows a closed oxidation zone consisting of two parts. Mainly the part near the steel is very inhomogeneous. Beside Cr_2O_3, cubic spinel, and Cr_3O_4 also mixed oxides with iron and manganese are present. The upper part of the oxidation zone is a mixture of Fe-and Al-oxide with either Al or Fe rich parts. In the corrosion reaction zone inward diffusion of carbon and sulfur took place. Sulfur was detected in the alumina part of the coating as well as in the oxidation zone. In the latter sulfur is found in combination with manganese. In sample 2 both sublayers of the alumina coating are porous.

As result of the tests under oxyfuel conditions two protective features for the substrate can be detected: i) the formation of a stable chromium and mixed oxide zone and ii) the alumina coating as a second barrier for outward iron diffusion.

1. S.R.J. Saunders, M. Monteiro, F. Rizzo, Progress Mat. Sci.**53** (2008) 775-837

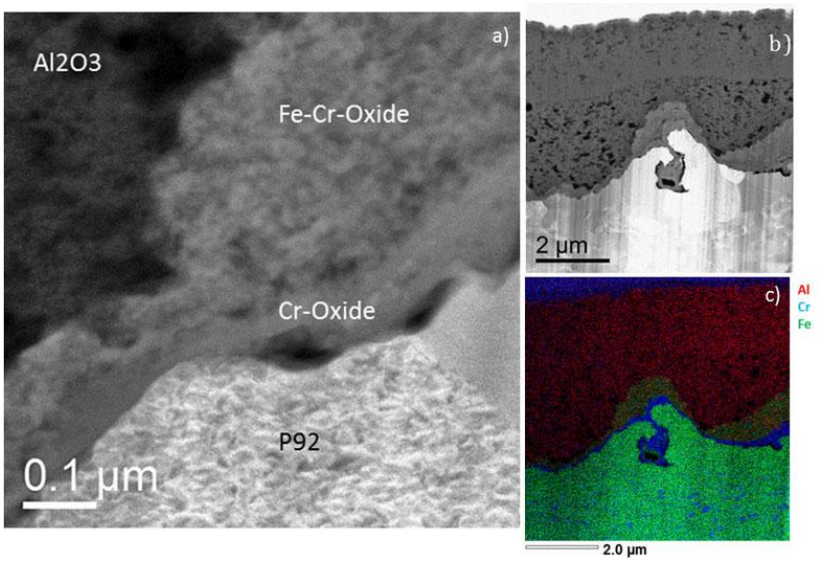

Figure1. Sample 1, a) STEM high angle annular dark field (HAADF) image, showing an island of the oxidation zone at the interface between steel and coating. b) STEM HAADF image of the rippled steel surface with an island of the oxidation zone and the two alumina coating sublayers. c) Elemental map of the same region.

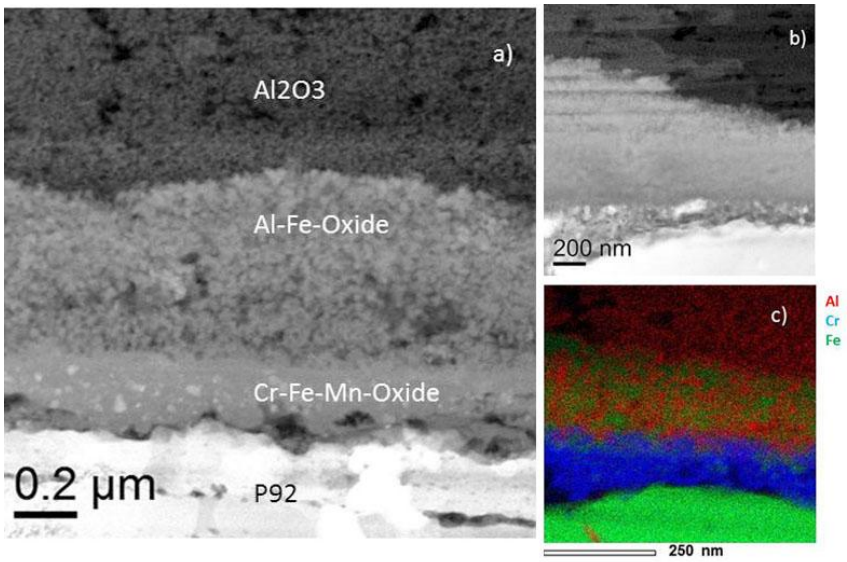

Figure 2. Sample 2, a) STEM HAADF image, showing the oxidation zone between alumina and steel. b) STEM HAADF image of details of the oxidation zone. c) Elemental map of the corresponding region.

Thin Films, Coatings, Interfaces and Surfaces

MS2.P036
Microscopical study of polymeric coating degradation used as a protective layer on glass

V. Petranova[1], J. Valach[1], V. Kocour[1]

[1]Institute of Theoretical and Applied Mechanics AS CR, v.v.i., Prague, Czech Republic

petranova@itam.cas.cz

Building materials and decorative elements composing facades and walls are one of the most exposed parts of the buildings. Impact of aggressive environment especially in the big cities can induce degradation of such materials and finally lead in complete destruction [1]. This study is part of the project concentrated on the development of transparent resistant polymeric coating protecting precious medieval glass mosaic of the 'Last judgment' situated on the portal of. Vitus Cathedral on Prague Castle [2].

Samples of glass slides partially dip-coated with thin *(about ten micrometers)* protective polymer layer with silica addition were aged using water steam. The first sample 0T was referential while the other samples 1T, 2T, 3T, 4T, 5T and 6T were subsequently removed from the ageing process after week (e.g. sample 2T - after two weeks etc.). According to number of weeks sample was exposed to accelerated weathering, it is marked as nT, where n indicates number of week in chamber, reference, i.e. Unweathered sample was marked 0T. To reveal the structural and chemical changes in detail scanning electron microscopy was used. The samples were examined in the MIRA II LMU SEM (Tescan corp., Czech Republic) equipped with energy dispersive X-ray detector (Bruker corp., Germany). Accelerating voltage was set on 15 kV for glass surface investigation and on 7 kV for polymeric coating investigation to ensure low penetration depth of primary electrons and thus better mapping of surface topography. To quantify structural changes image analysis in MATLAB and ImageJ environment was performed on secondary electron (SE) micrographs reflecting surface topography.

Based on microscopic observations the referential sample 0T didn't show any structural changes. Attack of water steam treatment on the polymer coating was clearly visible after three weeks ageing - on the 3T sample shallow pits with size ranging between 50-100 µm were developed. The percentage ratio of pits in the analyzed area 1.84 x 1.84 mm of 3T sample was 15.3 % and also in the subsequent samples the ratio values approximated to 15 % of the analyzed area (4T - 15.8 %, 5T - 16.9 % and 6T - 14.1 %). Moreover the depth of pits in 4T, 5T and 6T increased. Total degradation of polymer occurred in the surrounding of impurities which settled before polymer application on the glass surface (Fig. 1c). Chemical changes in polymer weren't observed.

Contrary to the coating, degradation of glass slide become apparent only after one week of weathering (sample 1T). The glass degraded also chemically. With increasing time of water steam ageing glass surface was covered by newly-formed crystals composed mainly of Ca, Si and Na (Fig.2). Based on image analysis of 6.31 x 6.31 mm sample areas the percentage ratio of newly-formed phases was for 2T - 17.3 %, for 3T - 25.9 %, for 4T - 42.7 % and for 5T - 52.8 %. In the sample 5T and 6T the glass showed broken structure (Fig. 3). Unfortunately it wasn't possible to perform image analysis and calculate the percentage ratio of newly-formed crystals in the most degraded 6T sample because of significantly broken structure causing the inappropriate signal intensity distribution.

1. Fort R., de Buergo M.A., Gomez-Heras M., Vazquez-Calvo C.: Heritage, Weathering and Conservation, CRC Press, ISBN 978-0415412728, (2006).
2. Valach J., Kocour V., Černý M.: Investigation of Optical Properties of Protective Layer for Glass Medieval Mosaic of Last Judgement from St. Vitus Cathedral in Prague, The 23rd International Congress on Glass, ISBN 978-80-904044-3-4, (2013).
3. The research was supported by the Ministry of Culture (project no. #DF12P01OVV017).

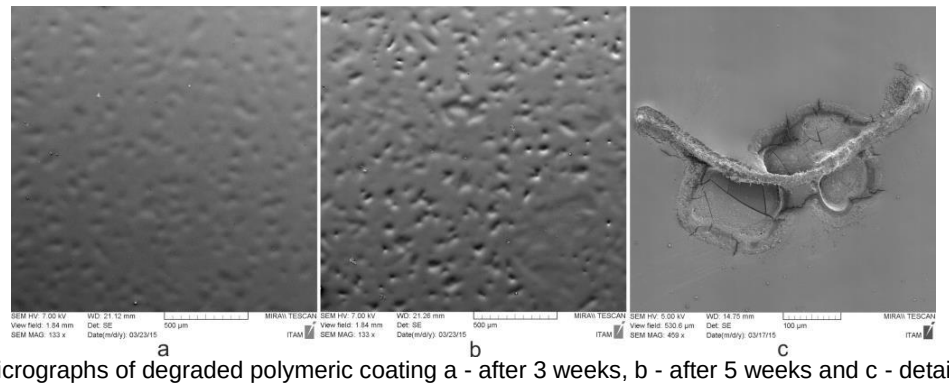

Figure 1. SE micrographs of degraded polymeric coating a - after 3 weeks, b - after 5 weeks and c - detail of total degradation “tunneling” around impurity.

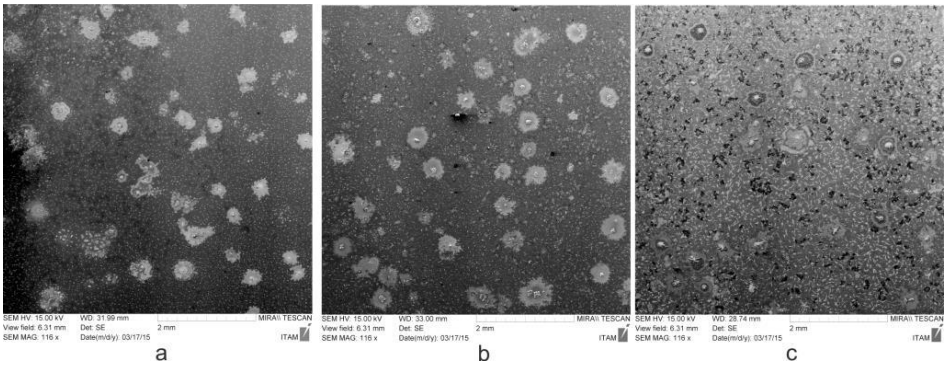

Figure 2. SE micrographs of degraded glass a - after 2 weeks, b - after 3 weeks and c - after 5 weeks

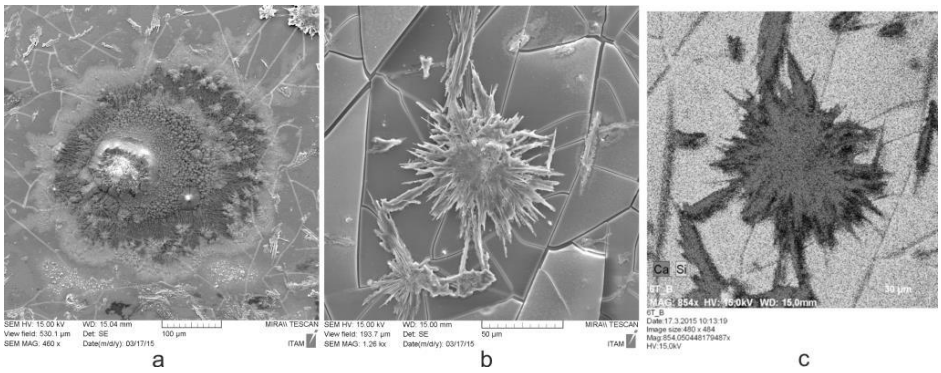

Figure 3. a and b - detail of newly formed crystallization products on degraded broken glass surface, c - element map of crystal phase

Thin Films, Coatings, Interfaces and Surfaces

MS2.P037
Microscopic examination and electrochemical study of light harvesting complex of photosystem II deposited on screen-printed graphite electrode

P. Piotrowska[1], Ů Kowalewska[2], M. Łazicka[1], M. Maj-Żurawska[3], J. Grzyb[4], M. Garstka[1]

[1]University of Warsaw, Faculty of Biology, Metabolism Regulation, Warsaw, Poland
[2]University of Warsaw, Faculty of Biology, Plant Anatomy and Cytology, Warsaw, Poland
[3]University of Warsaw, Faculty of Chemistry, Laboratory of Theoretical Basis of Analytical Chemistry, Warsaw, Poland
[4]Polish Academy of Sciences,Institute of Physics, Laboratory of Biological Physics, Warsaw, Poland

p.piotrowska@biol.uw.edu.pl

Development of various kinds of electrochemical sensors based on screen-printed carbon materials is due to the increased demand for cheap sensors useful in environmental analysis [1]. Carbone electrode used in our study was produced with laboratory-blended carbon paste composed of graphite particles and polymer binder with appropriate additives for better screen-printing production. Graphite electrode (GE) was activated by simple electrochemical surface treatment method in three electrode system with silver reference electrode (Fig. 1). Porous and hydrophobic graphite electrode surface with activated functional groups is good support for biomaterial such as proteins.

Screen-printed graphite electrode was modified with Light Harvesting Complex of Photosystem II (LHCII) and used as multilayer bioreceptor to construct photo-biosensor. LHCII is small (25 kDa) membrane protein and binds 22 molecules of chlorophyll and 4 molecules of xanthophyll. This complex is destined for absorbing light and transfer excitation towards the reaction centers [2]. LHCII interaction with the carbon surface involve physical adsorption by hydrophobic and electrostatic forces between the protein and solid phase. Graphite as positively charged material gives high probability of self-assembly of negative charged LHCII complexes on electrode surface[3].

Immobilized multilayer of LHCII chemically cross-linked by glutaraldehyde was examined by scanning electron microscopy (SEM) (Fig. 2) and atomic force microscopy (AFM) (Fig. 3). Properties of bioelectrode (LHCII-GE) were studied by electrochemical and fluorescence techniques.

SEM imaging of cross sectional semiconductor LHCII-GE showed diverse penetration of porous graphite dependent on potential applied to electrode. Moreover, the aggregation state of LHCII (monomeric and trimeric forms or large aggregates) and interactions of proteins with lipids influence the structure of bioreceptor at electrode surface.

AFM topography indicated also that LHCII was deposited on the graphite electrode. Scanning was done in tapping mode in a liquid cell. Analysis of average height of LHCII-GE under different electrochemicall potential applied provided information about self-organization of the bioelectrode outer surface.

Electrochemical behavior of LHCII complexes deposited on the electrode was investigated with cyclic voltammetry and differential pulse voltammetry. Chronoamperometric measurements during illumination show changes of photocurrent in relation to applied potential and LHCII aggregation state.

Our study is helpful to future construction of one-use photo-biosensor for environmental analyses.

The project granted on the decision number DEC-2013/09/B/NZ1/01111 by the National Science Centre, Poland.

1. Gang Cui, Jae Hyun Yoo, Joung Su Lee, Jina Yoo, Jung Hee Uhm, Geun Sig Cha and Hakhyun Nam: Analyst, (2001) 126: 1399-1403
2. Janik E, Bednarska J, Zubik M, Puzio M, Luchowski R, Grudzinski W, Mazur R, Garstka M, Maksymiec W, Kulik A, Dietlerd G, Gruszecki WI; Plant Cell (2013) 25: 2155-2170
3. Morio Nagata, Yutaka Amao, Hideki Hashimoto and Mamoru Nango; ACS Macro Letters 1 (2012) 296−299

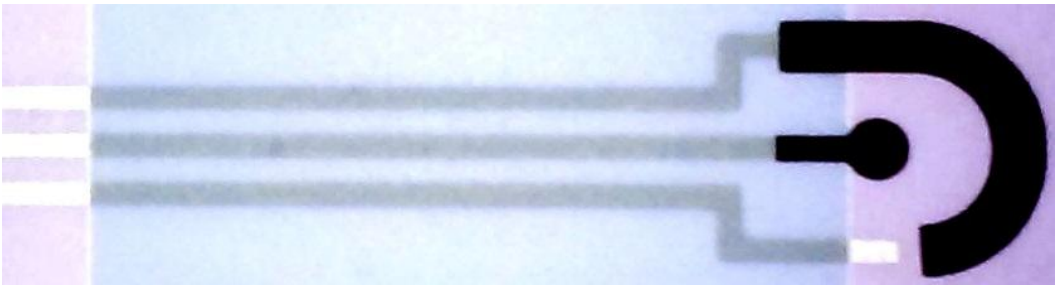

Figure 1. The screen-printed graphite three-electrode system.

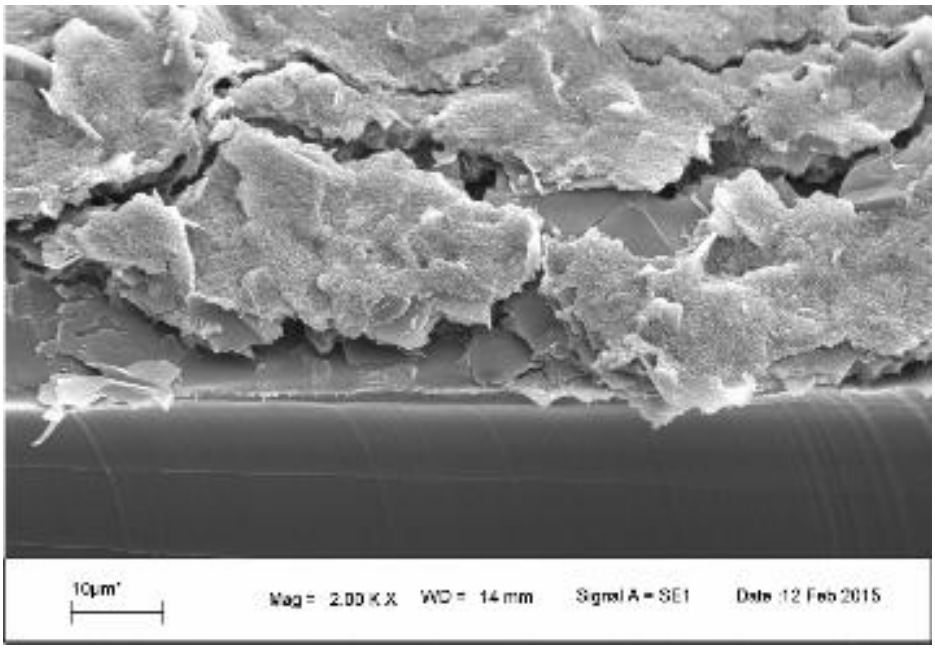

Figure 2. SEM cross sectional image of the screen-printed graphite electrode.

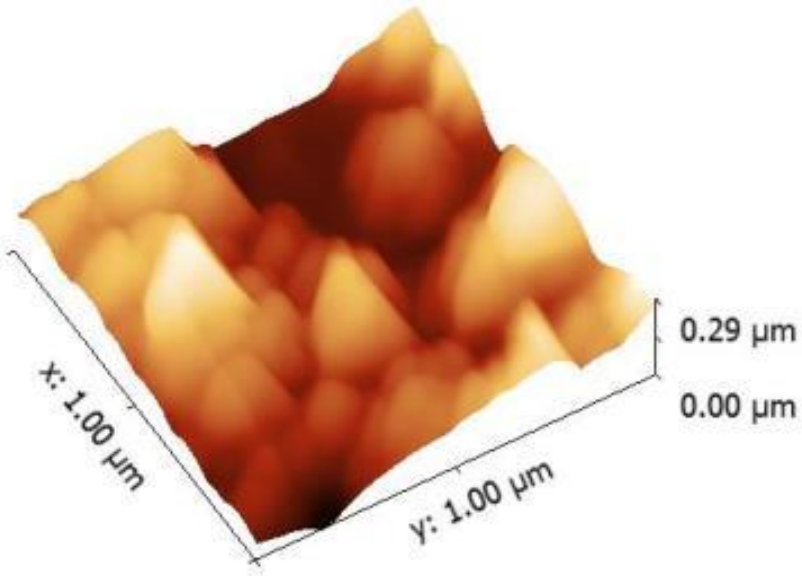

Figure 3. AFM images of the screen-printed graphite electrode surface.

Thin Films, Coatings, Interfaces and Surfaces

MS2.P038
Structural defects of La-based perovskite superlattices grown by PLD and MBE

A. Mark[1], F. Wrobel[1], G. Logvenov[1], E. Benckiser[1], W. Sigle[1], B. Keimer[1], P. van Aken[1]

[1]Max Planck Institute for Solid State Research, Stuttgart, Germany

a.mark@fkf.mpg.de

Transition metal oxide superlattices with controlled layer characteristics show a variety of interesting phenomena, the details of which depend on the layering parameters. For example, the magnetic behaviour and conductivity of $LaNiO_3$ can be tuned by controlling the layer thickness and by selecting appropriate intervening layer materials. Various methods for growing controlled superlattice structures exist, a favourite has been pulsed laser deposition (PLD), but molecular beam epitaxy (MBE) is now also popular because of the controlled deposition rate and the flexibility allowed by the use of individual element sources. In theory, this allows composition control to the level of individual atomic layers. The PLD process requires higher temperatures and pressures than MBE. It also involves significantly higher energies for the impinging particles, which has potential implications for interface roughnesses.

In this study a direct comparison has been made between two $LaNiO_3$-$LaAlO_3$ (LNO-LAO) superlattices grown on a $(LaAlO_3)_{0.3}(Sr_2TaAlO_6)_{0.7}$ (LSAT) substrate, one by PLD and the other by oxide MBE. The two samples are nominally identical, with 8 repetitions of 4-unit-cell LNO/4-unit-cell LAO bilayers. The PLD was carried out in a 0.5 mbar oxygen atmosphere and the samples were subsequently annealed in a 1.0 bar oxygen atmosphere. The MBE samples were grown and subsequently cooled in an atmosphere of 2.5 x 10-5 mbar ozone. Annealing was not performed. We report here the results of TEM investigations of the structures of the two samples.

Investigations were done in an aberration-corrected JEOL JEM-ARM200F TEM at 200kV. They revealed that the PLD grown sample had a sharp interface at the substrate and few perpendicular faults but the layer interfaces were not entirely flat. The layers appeared wavy, with the irregularities in one layer affecting the layer above. These irregularities were generally on the order of a one unit cell shift or an increase in the layer thickness. The MBE grown sample also showed a sharp interface at the substrate. The subsequent interfaces were flatter than in the PLD sample. The more visible difference was that the MBE sample had a series of faulted areas, previously described as 3D Ruddlesden-Popper faults [1].

Since it is known that the perfection of a superlattice has a bearing on its performance it is important that defects be characterized and their origins understood. These results discuss the characterization; future work will focus on the origins of the defects from the different growth processes. [2]

1. E. Detemple *et al.*: J. Appl. Phys. **112** (2012) 013509
2. The research leading to these results has received funding from the European Union Seventh Framework Program [FP/2007-2013] under grant agreement no 312483 (ESTEEM2).

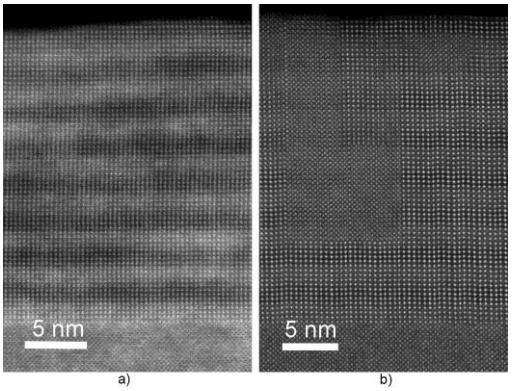

Figure 1. HAADF images of LNO-LAO superlattices on a LSAT substrate grown by a) PLD and b) oxide MBE.

Thin Films, Coatings, Interfaces and Surfaces

MS2.P039
Electron microscopy investigations of self-supported cobalt-substituted ZnO materials as remarkably stable electrocatalysts for water oxidation

C. Göbel[1], J. Pfrommer[1], S. Selve[1], D. Berger[1], M. Driess[1]

[1]TU Berlin, Department of Chemistry, Berlin, Germany

caren.goebel@tu-berlin.de

Zink oxide doped with cobalt (Co:ZnO) is a crystalline semi-conductor with a band gap of 3.3 eV at room temperature showing a high p-type conductivity and high hole density [1]. In this context, Co:ZnO might be interesting as sustainable and regenerate energy sources for any process using water as a hydrogen source in a (photo)electrochemical cell. Here, a unique cobalt-substituted zinc oxide (Co:ZnO) (pre)catalyst powder has been synthesized by low-temperature solvolysis of molecular heterobimetallic $Co_{4-x}Zn_xO_4$ (x=1-3) precursors [2]. For analysis of the electrocatalytic properties of the high Co doped Co:ZnO precatalyst, the powder was electrophoretic deposited (EPD) onto fluorinated tin oxide electrodes (FTO) (Fig. 1a). To get a deeper insight of the material under catalytic conditions, thin lamellas of the EPD layers were prepared by focused ion beam (FIB) before and after electrochemistry (Fig. 1b). The micro- and nanostructure, particle size, crystallinity and crystallographic phases were observed by HR-TEM.

SEM-FIB investigations confirmed the formation of relatively homogeneous Co:ZnO films fully covering the FTO substrate and build out of loosely packed particles. HR-TEM investigations of the deposited greenish powder layer before electrochemistry revealed a polydisperse sample consisting of particles with different sizes (20 to 200nm) and morphologies (rounded shape, plate-like hexagonal habitus). All particles show some contrast inhomogeneity (defects, small pores). Selected area electron diffraction (SAED) pattern of different particles could be indexed according to the wurzite-type ZnO structure ($P6_3mc$). EDX-analysis on individual particles confirms a high amount of incorporated Co within the ZnO lattice. Additionally, the green powder could be identified by powder X-ray diffractometry as also only wurzite-type ZnO with a Co content of about 30% in the Co:ZnO phase. The deposited Co:ZnO film after electrochemistry shows a brownish colour and is composed of small Co:ZnO particles. Few very large (ca. 1 µm) microcrystalline CoO particles (*Fmm*) are growing as a side product more originated from the starting powder. Close examination of the small nanocrystalline Co:ZnO particles with HR-TEM revealed the formation of an amorphous hull around the crystallites after oxidative conditioning (Fig. 1c) that was not present at the as-prepared Co:ZnO after the EPD process. EDX-analysis of the small Co:ZnO particles shows that they still contain large amounts of Co, although some Co leaching was observed. The amorphous Co-rich hydroxide-oxidic self-supported water-oxidation electrocatalyst performs at very low overpotentials (512 mV at pH7; 330 mV at pH12), while chronoamperometry shows a stable catalytic current over several hours (Fig. 1a). In summary, we have developed a novel and effective way to prepare a very stable heterobimetallic catalyst for water oxidation. The Co:ZnO EPD-material consists of particles characterized by an amorphous hydroxyoxylated CoZn overlayer formed in-situ and self-supported on crystalline Co:ZnO particles. As a result, the amorphous water oxidation catalyst overlayer and the crystalline Co:ZnO support are remarkably well-integrated.

1. A.C. Tuan, J.D. Bryan, A.B. Pakhomov, V. Shutthanandan, S. Thevuthasan, D.E. McCready, d. Gaspar, M.H. Engelhard, J.W.Rogers, Jr., K. Krishnan, D.R. Gamelin, S.A. Chambers, *Phys. Rev. B* **2004**, 70, 054424.
2. J. Pfrommer, M. Lublow, A. Azarpira, C. Göbel, M. Lücke, A. Steigert, M. Pogrzeba, P. W. Menezes, A. Fischer, T. Schedel-Niedrig, M. Driess, Angew. Chem. **2014**, 126, 1-6.

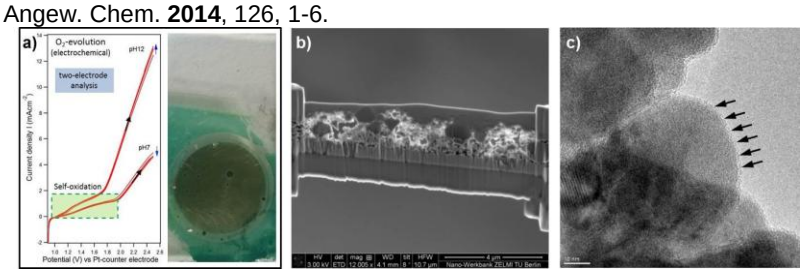

Figure 1. a) Two-electrode current-potential plot showing the self-oxidation of the Co:ZnO EPD layer (left), photograph of the Co:ZnO film on a FTO substrate as prepared (green) and after 6 h of water oxidation (brownish) b) FIB prepared cross section of the Co:ZnO EPD layer deposited on FTO glas after electrochemistry c) HR-TEM image of a Co:ZnO particle of the FIB layer after electrochemistry featuring a thin amorphous surface layer.

Thin Films, Coatings, Interfaces and Surfaces

MS2.P040
Aberration-corrected STEM study of polar and non-polar epitaxial GaN thin films produced by ion-beam nitridation of Ga droplets on different substrate materials

D. Poppitz[1], A. Lotnyk[1], J. Gerlach[1], B. Rauschenbach[1]

[1]Leibniz Institute of Surface Modification, Physical, Leipzig, Germany

david.poppitz@iom-leipzig.de

Gallium nitride (GaN) is a widely used semiconductor material in optoelectronics applications. To increase the emission of GaN based devices, the crystalline quality of polar and non-polar GaN thin films has to be improved. Furthermore, to make the material more interesting for applications, choosing cheaper substrate materials for epitaxial growth of GaN thin films or reducing the thickness of GaN films is mandatory.

In the present work, heteroepitaxial GaN thin films were grown by hyperthermal nitrogen ion-beam post-irradiation of pre-deposited gallium (Ga) droplets. The Ga droplets were deposited by a thermal effusion cell in a self-designed UHV chamber. The chamber is equipped with a hollow anode ion-beam source for supplying hyperthermal nitrogen ions with a maximum kinetic energy of 25 eV [1]. 6H-SiC(0001), Al_2O_3(0001), Al_2O_3(-1102) and γ-$LiAlO_2$(100) were used as substrate materials. The substrate temperature was kept constant at 630 °C during the ion beam irradiation. Our previous investigations showed a complete transformation of Ga droplets into coalesced epitaxial GaN thin films [2]. The growth mechanism was also proposed (Fig. 1 [1]). In this work, the microstructure of GaN thin films deposited by ion-beam nitridation of Ga droplets is studied. The special focus of this study is on the detailed structural characterization of the GaN thin films grown on different substrates by Cs-corrected STEM.

TEM specimens were prepared by FIB. Afterwards, the TEM lamellae were further treated by a focused low-energy argon ion milling [3,4]. With this, defects and ion implantations during the FIB process could be removed and a specimen thickness of approximately 30 nm was routinely achieved. STEM investigations were performed with a Titan^3 G2 60-300 probe Cs-corrected TEM operated at 300 kV.

Fig. 2 shows SEM images of a GaN thin film deposited on 6H-SiC(0001) substrate material before (Fig. 2a) and after the ion beam nitridation (Fig. 2b). The Ga droplets are transformed to a nearly coalesced GaN thin film with flat surface (Fig. 2c). Grain boundaries are formed between the crystallites. The HAADF-STEM overview image in Fig. 3 shows a GaN thin film with homogeneous film thickness. In the HRSTEM images in Fig. 4 domains of two different polytypes of GaN are seen. Fig. 4a shows a domain of z-GaN and Fig. 4b presents a domain of w-GaN. In both cases the film growth starts with a few monolayers of w-GaN until the film growth changes to z-GaN or stays as w-GaN until the deposition is stopped [4]. However, the crystalline quality of GaN films grown on other substrate materials is different compared to the GaN deposited on 6H-SiC. A higher density of defects like grain boundaries, stacking faults and cubic inclusions was identified. Nevertheless, coalesced GaN films were formed on all substrate materials. Additionally, crystallites with a 20° rotation of the c-axis were found in GaN films deposited on Al_2O_3(0001) substrates. The results of the present work show the formation of homogeneous epitaxial GaN thin films with polar and non-polar orientations even when the growth process starts with single Ga droplets.

1. L. Neumann, J. W. Gerlach, B. Rauschenbach, Thin Solid Films 520 (2012) 3936.
2. J. W. Gerlach, T. Ivanov, L. Neumann, T. Höche, D. Hirsch et al., J. Appl. Phys. 111 (2012), 113521.
3. A. Lotnyk, D. Poppitz, J. W. Gerlach, B. Rauschenbach, APL. 104 (2014) 071908.
4. D. Poppitz, A. Lotnyk, J. W. Gerlach et al., Micron (2015) http://dx.doi.org/10.1016/j.micron.2015.03.006
5. The financial support of the European Union and the Free State of Saxony (LenA Project; Project No. 100074065) is greatly acknowledged.

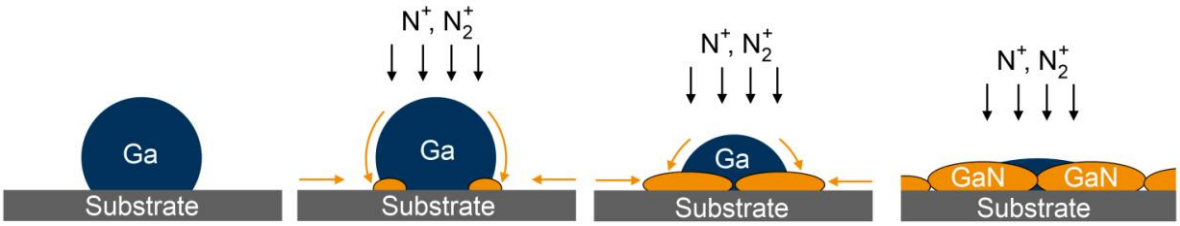

Figure 1. Growth mechanism of GaN thin films by ion beam nitridation of Ga droplets proposed by *Gerlach et al.* [1].

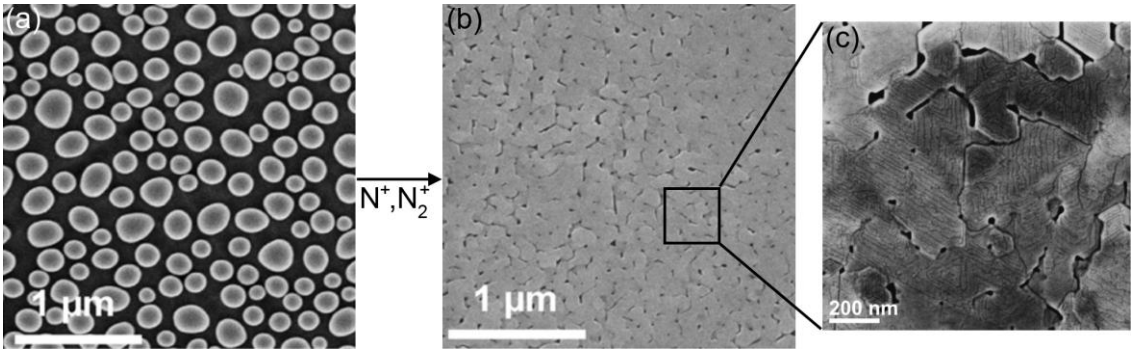

Figure 2. (a) SEM images of Ga droplets on a 6H-SiC(0001) substrate (a). (b)-(c) GaN thin film after ion beam nitridation process.

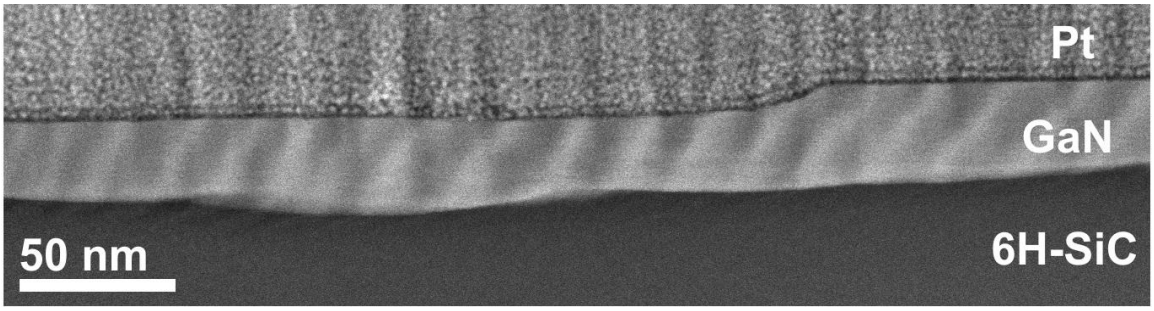

Figure 3. HAADF-STEM image of a GaN thin film grown on 6H-SiC(0001).

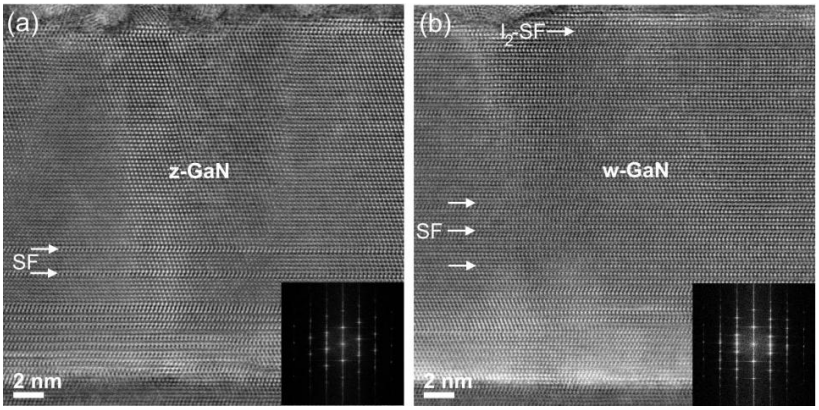

Figure 4. (a)-(b) HAADF-HRSTEM images of GaN thin film grown on 6H-SiC(0001). The film consists of z-GaN and w-GaN domains with basal plane stacking faults (SF).

Thin Films, Coatings, Interfaces and Surfaces

MS2.P041
Characterization of HgCdTe-CdTe-GaSb thin-film structures via focused ion beam microscopy and electron backscatter diffraction analysis

G. Neusser[1], M. Sieger[1], C. Kranz[1], W. Lei[2], R. Gu[2], J. Antoszewski[2], L. Faraone[2], B. Mizaikoff[1]

[1]University of Ulm, Institute of Analytical and Bioanalytical Chemistry, Ulm, Germany
[2]The University of Western Australia, School of Electrical, Electronic and Computer Engineering, Crawley, Perth, Australia

gregor.neusser@uni-ulm.de

In the present study electron backscatter diffraction (EBSD) analysis was evaluated as a rapid alternative method to transmission electron microscopy (TEM) investigations for determining the quality of HgCdTe-CdTe-GaAs (GAMCT) and HgCdTe-CdTe-GaSb (GSMCT) thin-film structures. Next to their utility as long-wave (mid-infrared; 3-20 µm) detector materials, our research team has recently demonstrated excellent wave guiding properties in this spectral regime, which requires a detailed characterization of the material interfaces for tailoring the optical properties[1]. Although TEM provides a higher resolution than EBSD, TEM investigations are time consuming, limited to small areas and require the preparation of high quality, electron transparent TEM samples. Sample preparation for EBSD studies by focused ion beam (FIB) treatment and the actual EBSD measurement are significantly more efficient (i.e., few hours) depending on size and composition of the sample. Using an EBSD camera (here, Digiview 4 by EDAX), a speed of 150 analyzed pixel per second was achieved with next generation cameras being even faster. Hence, mapping an area with dimensions of 7.65µm x 11.41µm at a step width of 30 nm (i.e., 112,420 pixel) can be performed in less than 15 min.

Prior to the EBSD measurements, a facet perpendicular to the layer structure was prepared at the edge of the sample via FIB milling at 30kV. The amorphous layer at the surface resulting from the FIB treatment was minimized using an acceleration voltage of the ion beam at 5 kV during the final polishing step. For comparison, EBSD measurements were also performed at naturally cleaved facets.

During the preparation of facets from GaAs or GaSb via FIB treatment, Ga-enriched droplets usually deposit at the sample surface (Fig.1A, and black regions in Fig.2A). This problem can be avoided by adding XeF_2 as a reactive gas during FIB milling. However, it was shown that XeF_2appears to affect CdTe such that no useful EBSD patterns were obtained. Therefore, the preparation of such facets at cryogenic conditions was investigated for avoiding droplet formation/deposition, as shown by M.C. Dolph et al.[2].

Local variations in lattice orientation are evident in the finally obtained color scale Kernel misorientation maps highlighting changes in misorientation up to 1.5° (Fig.2). Immediate changes in lattice misorientation are evident at the boundaries of the different phases for samples prepared via FIB treatment, while cleaved samples only reveal smooth transitions. Detailed studies on the differences between FIB treated and naturally cleaved facets are currently in progress for detailing the effects of FIB treatment on the sample structure. Finally, thus obtained findings are highly relevant for TEM measurements as well, since appropriate samples are frequently prepared via FIB milling of TEM lamellas.

1. X. Wang, J. Antoszewski, G. Putrino,W. Lei, L. Faraone, B. Mizaikoff (2013): “Mercury-Cadmium-TellurideWaveguides - A NovelStrategyfor On-Chip Mid-Infrared Sensors.” Analytical Chemistry, 85,10648−10652
2. M.C. Dolph, C. Santeufemio (2014): "Exploring cryogenic focused ion beam milling as a Group III-V device fabrication tool." Nuclear Instruments and Methods in Physical Research Section B: beam Interactions with Materials and Atoms, V328, pp. 33-41

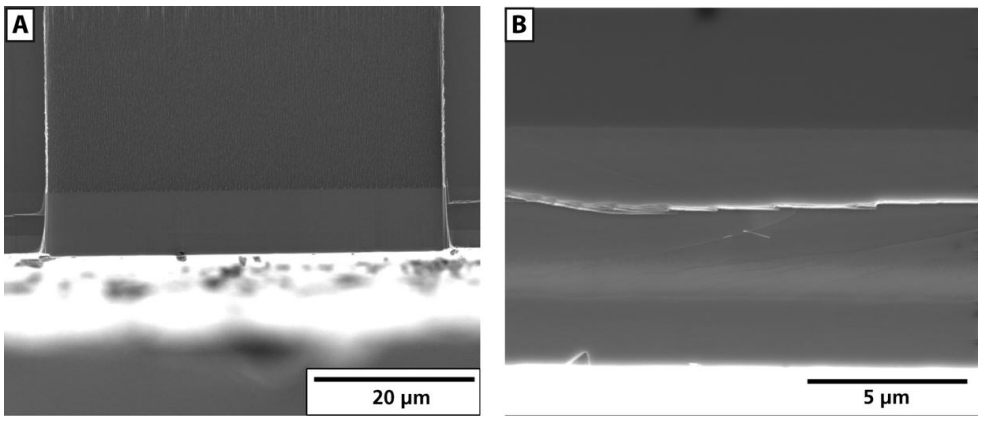

Figure1. Secondary electron images of the facets prepared by (A) FIB milling, and (B) cleaving.

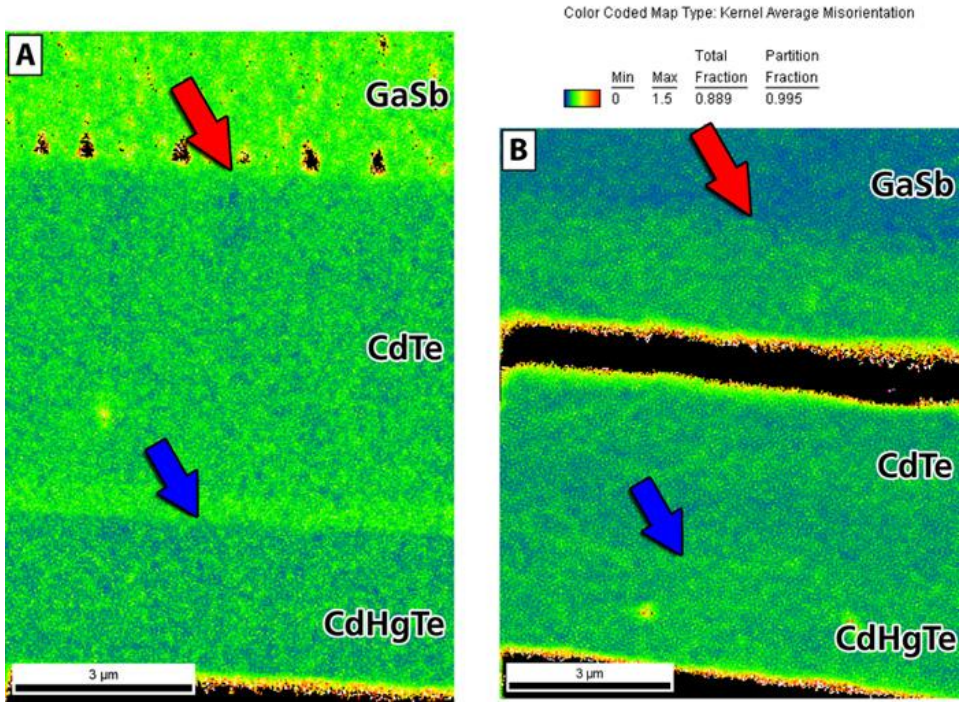

Figure 2. EBSD maps recorded at the facets prepared by FIB milling (A), and by cleaving (B) illustrating the Kernel average misorientation; borders between the layers are marked by arrows: GaSb and CdTe- red arrow; CdTe and CdHgTe- blue arrow

Thin Films, Coatings, Interfaces and Surfaces

MS2.P042
Understanding light emission and reflection in spherical submicron-mirror arrays by confocal microscopy

E. R. Spada[1], G. T. Valente[1], R. M. Faria[1], F. E. G. Guimarães[1]

[1]USP, São Paulo, Brazil

guimaraes@ifsc.usp.br

In recent years, there has been a growing interest in the interactions of fluorophores with metallic surfaces or particles, which can greatly extend the realm of fluorescence microscopy and its applications. The design of metallic surfaces in order to tailor and control the local electromagnetic environment in the vicinity of an emitter can yield an overall improvement in the fluorescence properties. The emission properties of molecules, such as the natural decay time and quantum efficiency, can be dramatically modified and improved by presence of metals. This work focused on the confocal microscopy characterization of an ultrathin polymeric film deposited on a periodic network of copper and cobalt submicron-mirrors. The mirror arrays were fabricated on tin-doped indium oxide (ITO) by electrochemical deposition through colloidal masks of PS spheres having nominal diameter of 456 and 756 nm. Polyfluorene (PFO) films with thicknesses around 6 nm were deposited on the metallic cavity surface by spin-casting and used as an emitting probing layer. We observed that metallic interactions in the near-field modify the PFO emission properties in ways not seen in classical fluorescence experiments in both spectral and life time (FLIM) imaging modes. Confocal microscopy in the reflectance mode, Scanning Electron Microscopy (SEM) and Atomic Force Microscopy (AFM) were also used to characterize the mirror structural properties prepared with different filling-in factors. The homogeneity and regularity of the electrochemical process could be measured by the planarity of terraces between the spherical mirror structures and by the circular symmetry of the emission profile (Fig. 1). Calculations of the reflectance and the emission profiles are in accordance with geometric optical laws, as well as with the excitation and collection of the emitted light of a uniform PFO film along the spherical mirrors when the microscope point spread function is considered. However, the major impact of the metallic mirrors on the PFO photophysics was revealed by fluorescence lifetime images (Fig. 2a and 2c). The FLIM image contrast revealed a strong change of decay time along the periodic mirror array, which is directly reflected in the modulation the emission intensity (Fig. 2b and 2d). Calculations (color solid lines) demonstrated that both emission efficiency and decay time are affected by the change of the coupling between the resonant plasmonic interaction and the emission field of the excited PFO molecule under influence along the spherical metallic surface.

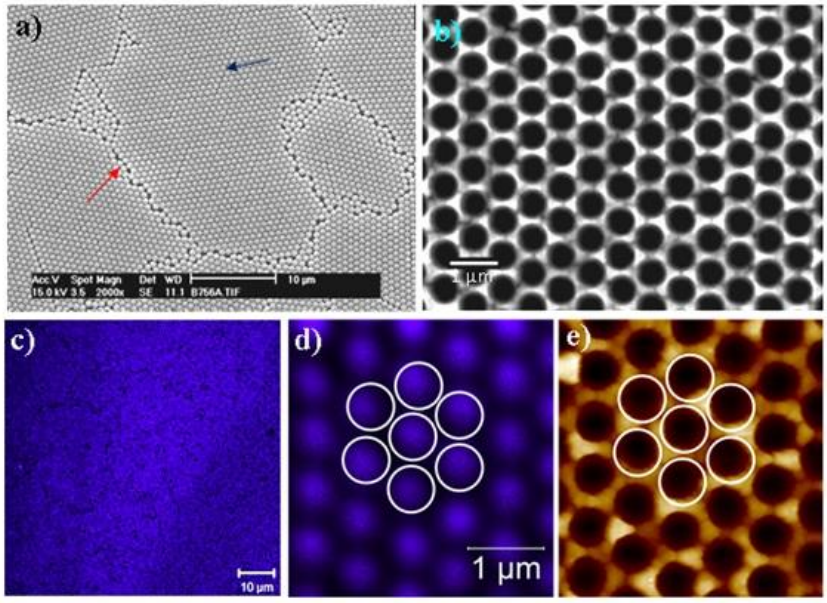

Figure 1. a) SEM viewgraph of a colloidal mask; b) SEM image of copper mirrors; c) Confocal spectral image.

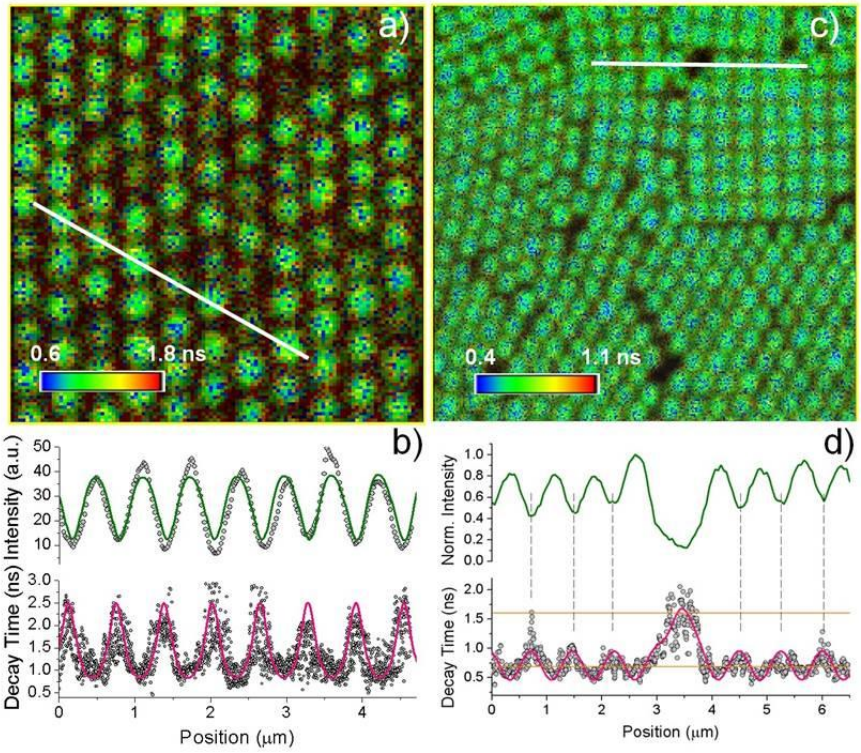

Figure 2. a) and b) FLIM images of mirror arrays containing a deposited PFO film; c) and d) Emission intensity and decay time evaluated along the periodic mirror array of a FLIM image (white lines).

Thin Films, Coatings, Interfaces and Surfaces

MS2.P043
Temperature and magnetic field dependent Raman microscopy on $(La_{0.65}Pr_{0.45})_{0.7}Ca_{0.3}MnO_3$

S. Merten[1], O. Sharpoval[2], B. Damaschke[1], V. Moshnyaga[1], K. Samwer[1]

[1]I. Physikalisches Instiut Universtität Göttingen, Göttingen, Germany
[2]IIEN, Academy of Science of Republic Moldova, Chinisau, Moldova, Republic of Moldova

basti@merten-web.de

Mixed valence manganites are still in the focus of fundamental research due to their rich phase diagramm with different electronic and magnetic phases. Crucial for the understanding oft he physics of manganites ist he strong electron-phonon coupling due to the Jahn-Teller effect. Here we report on a detailed Raman study of $(La_{0.65}Pr_{0.45})_{0.7}Ca_{0.3}MnO_3$ (T_c = 195 K) thin films. To assign the observable Raman modes, we performed polarized Raman spectroscopy at room temperature (λ = 532 nm, P = 1.2 mW). We observed four pronounced modes at 235 cm^{-1}, 434 cm^{-1}, 485 $^{cm-1}$ and 609 cm^{-1}. The 485 cm^{-1} and 609 cm^{-1} mode can be assigned to an anti-stretching and stretching mode, respectively, due to the Jahn-Teller effect in agreement with previous work [1]. The JT modes show a pronounced maximum at T_c (fig. 1). Furthermore, the magnetic field dependent Raman spectra show a similar behaviour near T_c as the temperature dependent spectra. Far below T_c no magnetic field effect is observable. We showed a correlation between the temperature as well as magnetic field dependent Raman spectra and the metall-insulator transition and the collosal magnetoresistance. Financial support from DFG, SFB 1073 (TP B04) is acknowledged.

1. M. N. Iliev, M. V. Abrashev et al., Phys. Rev. B, Vol. 57 (p.2872), 1998; M. N. Iliev, M. V. Abrashev et al., Phys. Rev. B, Vol. 73 (p.064302), 2006

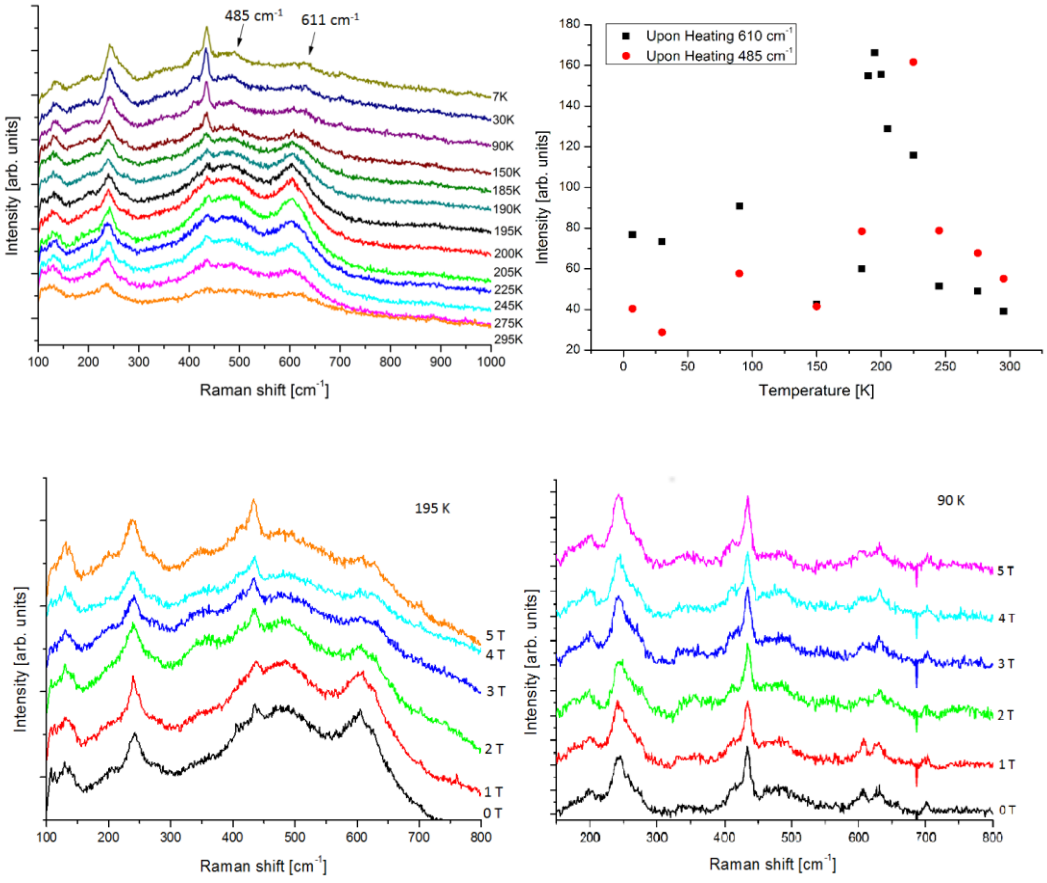

Thin Films, Coatings, Interfaces and Surfaces

MS2.P044
Analysis of crystallographic orientation dependence of low energy SEM contrast associated with the hexagonality of silicon carbide

K. Ashida[1], Y. Kutsuma[1], N. Ohtani[1], T. Kaneko[1]

[1]Kwansei Gakuin University, Nanotechnology for Sustainable Energy, Sanda City, Japan

dsv00027@kwansei.ac.jp

A potential of low energy SEM with primary electron energy (E_p) less than 2.0keV is demonstrated for a surface sensitive semi-quantitative imaging tool by characterizing crystallographic orientation dependence of the contrast from the surface of single crystalline silicon carbide (SiC) with different hexagonality such as 4H- and 6H-SiC {0001}. It is revealed that the structural difference associated with the length of Si-C stacking sequence is reflected to the crystallographic orientation contrast from the topmost surfaces within a range of 1.0nm in depth. The exchange of Si- and C-site in an identical crystal structure is here to be concerned with material contrast (*Z*-contrast).

SEM crystallographic orientation contrast has been qualitatively investigated in a relatively high E_p regime above 10keV, where the SEM contrast is interpreted based on Bragg condition within an interaction volume of the primary electron (PE) determined by high E_p penetration depth (a few tens of nm). Regarding a low E_p regime below 2.0keV, there have been few reports so far dealing with SEM crystallographic orientation contrast. In general, such a low energy SEM with a shallow penetration depth of PE can offer improved surface sensitivity (a few nm) and enhanced *Z*-contrast for low materials ($Z < 20$) [1]. In order to verify these feasibilities in applying the low E_p regime, it is important to prepare a sample having a well-defined crystal structure with a shallow marker layer beneath the surface to estimate the PE penetration depth.

Single crystal 4H- and 6H-SiC can fulfil this requirement because they have hexagonal sites in the center of their respective unit cells (1.0nm for 4H, 1.5nm for 6H in *c*-axis) functioning as the marker layers with different depth from the surfaces, where the stacking sequence of Si-C bilayer is turned over at the hexagonal sites. Furthermore, the contribution to *Z*-contrast can also be considered by comparing two different polar faces: (0001) Si- and (000-1) C-terminated faces. In this study, in order to investigate the low energy (< 2.0keV) SEM contrast dependence on the crystallographic orientation beneath the surface within a range of 1.0nm and on surface terminating atomic species, SEM image brightness and contrast related to tilting angle θ and rotation angle Φ was precisely investigated by utilizing step-controlled 4H- and 6H-SiC {0001}.

Figs.1 (a) and (b) show 1.0keV SEM images taken at different tilt angles from 4H-SiC (0001) stepped surface by using a conventional E-T detector. The step heights of those surfaces were confirmed to be the half of the 4H unit-cell (0.50nm) by an AFM measurement shown in Fig.1 (c). This observed clear contrast at 1.0keV was decreased with increasing E_p and then almost vanished at 10keV. Since the PE penetration depth is increased with E_p, the SEM contrast taken at 1.0keV is originated from the crystallographic orientation just beneath the surface [Fig.1 (d)] less than 1.0nm in depth. Furthermore, the dependence of the SEM image brightness on the rotation angle Φ was precisely evaluated as shown in Fig.2 (a). It is revealed that the image brightness represents a clear 3-fold rotational symmetry of 4H-SiC, which is well reproduced by a multiple scattering cluster theory [Fig.2 (b)] used for modelling 0.50 - 2.0keV electron diffraction patterns [2].

1. J. Cazaux, J. Appl. Phys. **112**, 084905 (2012).
2. I. I. Pronin, *et al*., Prog. Surf. Sci. **59**, pp. 53-65 (1998).

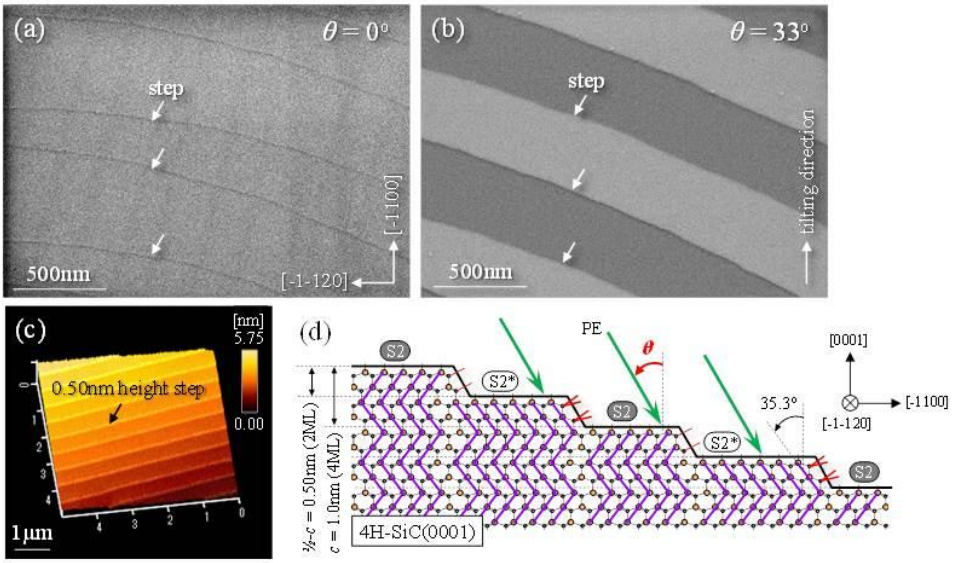

Figure1. (a) and (b) 1.0keV SEM images taken at different tilt angle (0^o and 33^o) from 4H-SiC (0001) stepped surface by using a conventional E-T detector. (c) AFM topographic image representing the step height of 0.50nm. (d) Physical geometry of PE and crystallographic orientation beneath the surface.

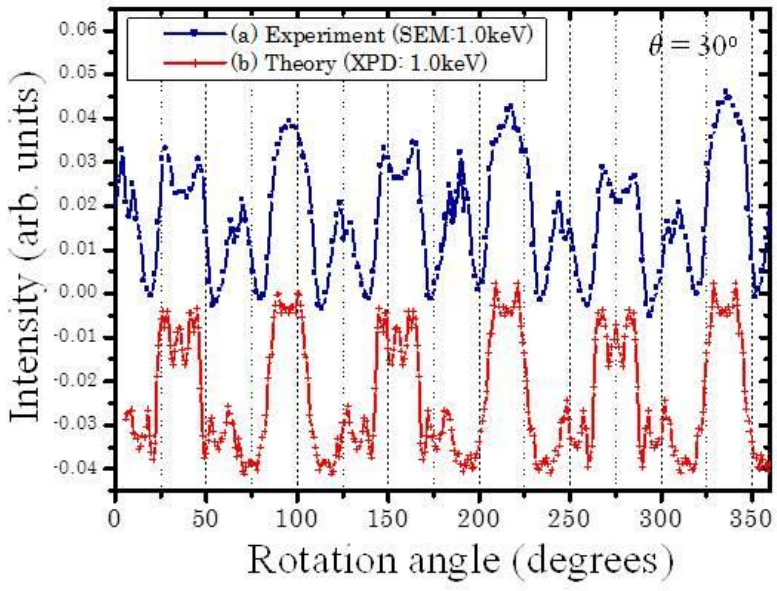

Figure2. (a) SEM image brightness plotted as a function of rotation angle taken at 1.0keV with keeping the tilting angle at 30^o. A base line is subtracted after the image analysis. (b) Theoretical curve at electron energy of 1.0keV and tilting angle of 30^o calculated by using a multiple scattering cluster theory.

Thin Films, Coatings, Interfaces and Surfaces

MS2.P045
An experimental study of the photoelectron work function change of silver-based contacts induced by Arcing in Airφ

A. Mohamed[1,2,3]

[1]National Preparatory School for Engineering Studies, Physics, Rouiba, Algeria
[2]Laboratoire "Arc Electrique et Plasmas Thermiques", CNRS, Aubière Cedex, France
[3]Department of Physics, Faculty of Sciences, University of Boumerdes (UMBB), Boumerdes, Algeria

akbim656@gmail.com

The influence of industrial conditioning (polishing, mechanical shocks and electrical arcs in air) on the microstructure, the composition, and the morphology of contact pastilles made of pure silver [Ag (99.999%)], silver-nickel alloy [Ag-Ni (60/40)], silver-tungsten alloy [Ag-W (50/50)], and silver-tungsten carbide [Ag-WC (50/50)] was investigated. The microstructure, physical properties and electronic emission behavior of pure silver Ag and silver-metal alloys (Ag-Me), for both virgin and arced electrical contacts, were studied.

Contacts were mounted in a contactor working repeatedly on air (laboratory atmosphere). When submitted to 500 opening electric arcs, the electron work function of an electromechanically conditioned contact Ag-Ni (60/40), measured photoelectrically by using Fowler's method of isothermal curves, is φ= (4.50 ±003) eV at room temperature, while for virgin Ag contacts, it was (4.30 ±003) eV. The increase in the EWF is due to the progressive inclusion of silver oxide in the Ag contact surface during arcing in air. The conditioned (500 arcs) silver-metal alloys studied in this work exhibit the same electronic emission behavior, namely arcing in air increases their EWF. We demonstrated that the electromechanical conditioning by successive electrical arcs affects the surface characteristics such as microstructure, roughness and photoelectron work function.

The observations made by a Scanning Electron Microscope (SEM) and the microanalyses made by an Energy Dispersive Spectrometer (EDS) of the cathode surfaces show the surface composition evolution of these contacts used under industrial conditions, and give some proofs of the various observed phenomena.

Thin Films, Coatings, Interfaces and Surfaces

MS2.P046
Correlation of atomic and electronic structure of manganite-titanite junctions to electric transport properties

B. Ifland[1], P. Peretzki[2], B. Kressdorf[1], M. Seibt[2], C. Jooss[1]

[1]University of Goettingen, Instiute of Materials Physics, Goettingen, Germany
[2]University of Goettingen, IV. Physical Institute, Goettingen, Germany

bifland@ump.gwdg.de

The efficiency of single junction solar cells based on semiconductor materials is mainly determined by transmission and thermalization losses. In strongly correlated oxides the excitation of the quasiparticles depends on the interaction between spin, charge, orbital and lattice degrees of freedom. These interactions may offer new mechanisms to overcome the above limitation, i.e. by slowing down the charge carrier thermalization time. Also for perovskite materials the existence of long living states of small polarons is reported [1].

This represents the general motivation for our studies of photovoltaic properties of pn-junctions made of perovskite manganite and titanate. Therefore two model systems are analyzed. One pn-heterojunction prepared by depositing an epitaxial thin film of p-doped $Pr_{0.67}Ca_{0.33}MnO_3$ (PCMO) on n-doped $SrTi_{0.998}Nb_{0.002}O_3$ (STNO) single crystal substrates via ion beam sputtering. For the second model system a pn-homojunction of nominal p- and n-doped PCMO (x=0.33, x=0.95) is prepared via pulsed laser deposition. Because of the high doping levels, the width of the space charge layer is only of the order of a few nanometers. Therefore, it is necessary to ensure a high quality of the interface with respect to structural and chemical properties.

TEM analysis shows an atomically sharp interface with a very small dislocation density and a B-site interdiffusion only on a length scale of a few unit cells. High resolution STEM images in combination with EELS spectra taken across the interface provides information of the local electronic structure. For the PCMO-STNO junction the conduction band changes its symmetry across the interface from states dominated by Mn e_g O2p hybridization on the manganite side to state dominated by Ti t_{2g} orbitals on the titanate side. Consequently, the orbital overlap of both states at the interface may be small. This may be the origin of an interfacial energy spike seen by electric characterization of the junction. [2] At the present state the main photovoltaic effect is only caused by the UV part of illumination with a Xe lamp, which can be attributed to polaron interband transitions in the PCMO. Probably this small orbital overlap limits the separation of IR induced excited carriers. Therefore, conclusions for a pn-junction with improved orbital overlap at the interface will be presented in form of a PCMO-PCMO homojunction.

We thank the German Research Society for funding through CRC 1073.

1. P. Grossmann, I. Rajkovic, R. Moré, J. Norpoth, S.Techert, C. Jooss, K. Mann, Rev. Sci. Instrum. 83, 053110 (2012)
2. G. Saucke, J. Norpoth, D. Su, Y. Zhu, Ch. Jooss, Phys. Rev. B 85 (2012) 165315.

Energy-Related Materials and Materials for Information Technology

MS3.047
Microscopic analysis of thin-film solar cells using correlative microscopy approaches and comparison with macroscopic device characterization

D. Abou-Ras[1]

[1]Helmholtz-Zentrum Berlin, Berlin, Germany

daniel.abou-ras@helmholtz-berlin.de

Thin-film solar cells consist of polycrystalline layer stacks. In spite of the corresponding high density of extended structural defects, power-conversion efficiencies of more than 20 % have been reached when using polycrystalline $Cu(In,Ga)Se_2$, CdTe, or $CH_3NH_3Pb(I,Cl)_3$ absorber layers. Indeed, the average grain sizes in these thin films are found to be well below 1 µm, at layer thicknesses of 0.5-10 µm. This situation demands in-depth investigations on how the microstructure, not only grain boundaries, but various extended structural defects, influences the photovoltaic performance.

The present contribution will give an overview of various electron and scanning-probe microscopy techniques to be applied, on identical positions, in order to first of all obtain relationships of microstructural, compositional, electrical, and optoelectronic properties of extended structural defects at micrometer to subnanometer scales. For CdTe and $Cu(In,Ga)Se_2$ solar cells, the extended structural defects feature atomic reconstructions of the atomic planes/lines adjacent to the defects. For the case of (random) grain boundaries (GBs), always different changes in composition for different GBs were found [1], which agrees well with the corresponding GBs analyses by correlative electron backscatter diffraction (EBSD), electron-beam-induced current (EBIC), cathodoluminescence, and scanning Kelvin-probe force microscopy. In contrast, for twin boundaries, stacking faults, and dislocation cores, only few, specific cases for the atomic reconstruction can be identified.

These results can be correlated with macroscopic device characterization. It was possible to establish EBIC measurements of solar cells at applied bias, using a lock-in amplifier. From the changes in the space-charge region width at varying the applied bias, we were able to estimate values for the net doping in various absorber layers. These values agree well with results from complementary capacitance-voltage analyses. For future work, it is planned to perform EBIC at applied bias in combination with EBSD at GBs.

Finally, the present contribution will also give insight into ways of controlling microstructure during the thin-film growth, employing real-time, in-situ X-ray diffraction and fluorescence analysis in combination with ex-situ materials characterization.

1. D. Abou-Ras, et al., Adv. En. Mater. 2 (2012) 992-998.
2. The author would like to acknowledge funding by the Helmholtz Virtual Institute VI-520 “Microstructure Control for Thin-Film Solar Cells”, collaborations with various project partners, as well as with the companies Carl Zeiss Microscopy, Oxford Instruments, and point electronic GmbH. Special thanks are due to various colleagues at HZB for providing the solar-cell specimens, the specimen preparation, as well as technical support at the microscope.

Energy-Related Materials and Materials for Information Technology

MS3.048
Analysis of electronic inhomogeneities in CIGS thin film solar cells by VEELS and holography

D. Keller[1,2], S. Buecheler[1], P. Reinhard[1], E. Snoeck[3], C. Gatel[3], M. D. Rossell[2], R. Erni[2], A. N. Tiwari[1]

[1]Empa, Laboratory for Thin Films and Photovoltaics, Duebendorf, Switzerland
[2]Empa, Electron Microscopy Center, Duebendorf, Switzerland
[3]CEMES, CNRS , Toulouse, France

debora.keller@empa.ch

Thin film solar cells based on Cu(In,Ga)Se_2 (CIGS) absorber layers have shown high efficiencies of more than 21 % despite the polycrystalline structure of CIGS. However, the electronic loss mechanisms in the bulk, at grain boundaries and interfaces are still not well understood. Due to the inhomogeneous composition of CIGS, it is supposed that also the electronic properties vary in CIGS. The positions of the conduction and valence band edges are directly correlated with the local composition of CIGS and thus, a variation of e.g. the Cu- or Ga-content causes local variations of the band gap (E_g) and the electronic structure. Furthermore, doping atoms, impurities and charge accumulations at structural defects may lead to additional fluctuations in the band structure. As a consequence, the transport of charge carriers and therefore the solar cell's efficiency is adversely affected [1].

In order to gain a deeper understanding on how such nanoscale inhomogeneities influence electronic loss mechanisms in CIGS solar cells, valence electron energy loss spectroscopy (VEELS) and electron holography (EH) were applied: VEELS allows for probing local E_g variations in CIGS and EH is a promising tool to gain knowledge about local potential fluctuations. However, VEELS suffers from limited energy resolution and several additional factors that may disturb the spectrum (radiation losses, thickness effects). EH is limited by the phase resolution and factors such as thickness effects and diffraction contrast. Hence, the reliability, accuracy and precision of the two techniques need to be carefully considered to ensure a proper interpretation of the results. In this work, advantages and limitations of VEELS and EH for local electronic characterization in CIGS are discussed.

In Fig. 1, a cross-section DF-STEM image of a CIGS solar cell is shown (a) and an example of the E_g variation across a CIGS layer (b), measured by VEELS on two different microscopes. As the E_g of CIGS varies within 1.0 - 1.7 eV depending on its composition, a high energy resolution and a sufficiently high signal-to-noise ratio (SNR) are required to ensure reliable data processing. While the precision, which is achieved by the cold FEG is mainly limited by the energy resolution, the SNR is the limiting factor for the monochromator in the present measurements. Hence, both VEELS experiments suffer from limited precision. However, the E_g variation in CIGS can still be accessed and the observed variation agrees well with the expectations based on the compositional variation, i.e. an increase of the E_g within Ga enriched and Cu depleted regions.

Fig. 2 shows the phase variation on a CIGS solar cell (a), measured by off-axis EH, and the DF-STEM (b) and BF-STEM (c) images of the same region. The phase shift is linearly correlated with the specimen thickness and the total potential variation, which is a sum of variations in the electrostatic potential, the mean inner potential (MIP) and distortions, such as electrical fields (charging) or diffraction contrast. Fig. 2 (d) shows the thickness variation measured (i) by the phase profile normalized by the MIP and (ii) by the DF-STEM intensity profile normalized by the density of atoms and their atomic numbers. In absence of distortions and MIP fluctuations, the difference between the two curves reveals the contributions of electrostatic potential variations. However, in case of CIGS, the effect of compositional variations on the MIP however needs to be taken into account to allow a reliable interpretation.

1. J.H. Werner et al., Thin Solid Films **480-481**, 399 (2005).
2. D. Keller et al., Microsc. Microanal. **20**, 1246 (2014).

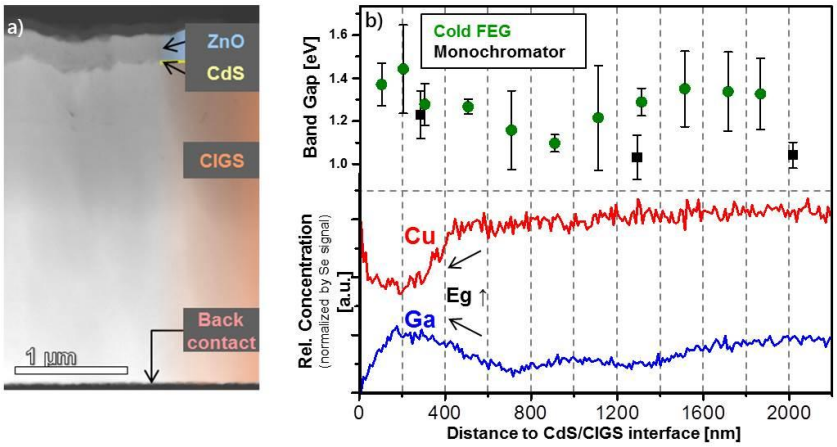

Figure 1. (a) Cross-section DF-STEM image and (b) E_g variation across the CIGS layer measured by VEELS. The values obtained by the monochromator stem from the same data setting as described in [2]. Below, the corresponding Cu and Ga concentration, measured by EDX, are shown.

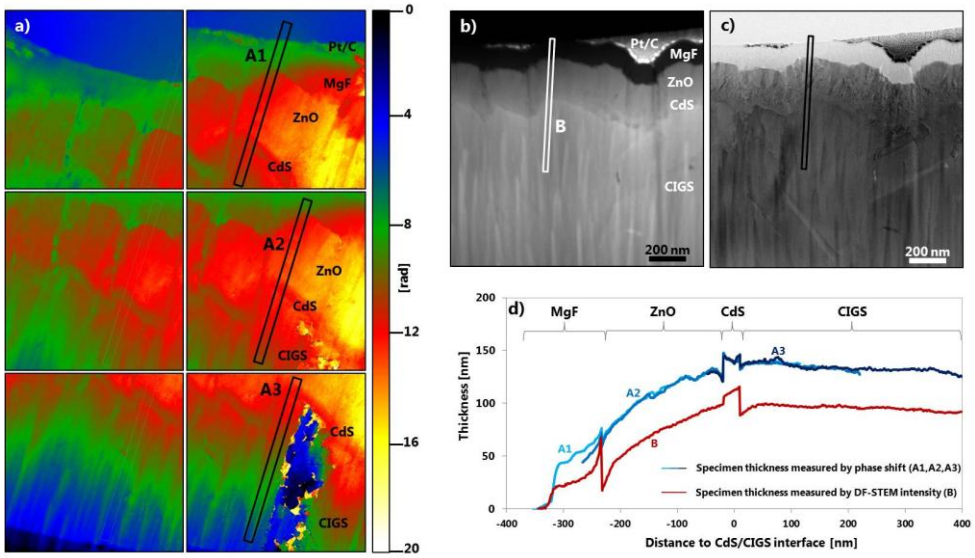

Figure 2. (a) Extracted phase images from off-axis holograms. (b) DF-STEM and (c) BF-STEM images of the same region. Corresponding thickness profiles (d), measured by DF-STEM and EH.

Energy-Related Materials and Materials for Information Technology

MS3.049
Revealing the nanocomposite structure of binary and ternary bulk heterojunction solar cells using energy-filtered TEM

S. Fladischer[1,2], T. Ameri[2], C. J. Brabec[2], E. Spiecker[1]

[1]Center for Nanoanalysis and Electron Microscopy, Universität Erlangen-Nürnberg , Erlangen, Germany
[2]Institute of Materials for Electronic and Energy Technology, University Erlangen-Nürnberg, Erlangen, Germany

stefanie.fladischer@fau.de

Organic photovoltaics is one of the most promising technologies for low cost energy production with the advantages of semi-transparency, flexibility and solution processing. The limited absorption spectrum of organic semiconductors can be overcome by a novel concept of ternary organic solar cells. In this concept the spectral sensitivity is enhanced by adding infrared sensitizers to the host system consisting of a wide bandgap polymer blended with fullerene derivatives. Various types of sensitizers such as low bandgap polymers, small molecules, dyes or nanoparticles are used in single bulk-heterojunction (BHJ) solar cells to enhance light harvesting properties as well as the power performance.[1] The presence and concentration of sensitizers decisively influences the nanocomposite structure of the active layer, which is an important parameter for the performance of the ternary solar cell. Thus in this work the nanocomposite structure of ternary solar cells is investigated using analytical transmission electron microscopy (TEM).

We started the characterization of binary blends before progressing to ternary blends. A widely used material combination for BHJ solar cells consists of the wide bandgap polymer P3HT in combination with the fullerene PCBM as electron acceptor. For TEM investigations plan view specimens of the pure materials and the blend were fabricated using the doctor blading technique.

Figure 1a shows a TEM zero-loss filtered bright field (BF) image of the P3HT:PCBM film. Due to the similarity of P3HT and PCBM regarding the chemical composition and the formation of a homogeneously thin film, the contrast in the TEM BF image is uniform and no significant structures can be seen. Thus conventional imaging techniques are not sufficient to identify and distinguish the two materials in this blend.

Electron energy-loss spectrometry (EELS) and energy filtered TEM (EFTEM) investigations were performed to elucidate the nanocomposite structure of the blend. Reference EEL spectra of the pure materials are shown in Figure 1b for P3HT and PCBM in the low loss region depicting respective plasmon peaks and their different energies. The high loss region containing the elemental information (ionization edges) as well as the low loss region containing the plasmonic information were used for the characterization of the blend. Based on EFTEM images elemental maps were determined for sulfur, which is found only in P3HT, and carbon which appears in the two materials in different contents (C_{P3HT} = 40.0 at%, C_{PCBM} =81.8 at%). The elemental maps of sulfur and carbon are depicted in Figures 1d and f, representing P3HT and PCBM, respectively. Furthermore EFTEM images in the plasmonic region were acquired and are shown in Figures 1c and e. The EFTEM image using 19 ± 4 eV depicts P3HT and the EFTEM image using 30 ± 4 eV depicts PCBM. When comparing the plasmonic images with the elemental maps it can be clearly seen that the signals representing P3HT and PCBM respectively are in good agreement and that the material distribution is complementary to each other. Thus the nanocomposite structure of the blend could be reliably and consistently analyzed using both the plasmonic and the elemental information.

EELS and EFTEM investigations will be used in a similar way like presented here for the case of P3HT:PCBM to determine the microstructure of ternary solar cells.

1. T. Ameri, P. Khoram, J. Min, C.J. Brabec, *Adv. Mater.* 25 (2013) 4245-4266
2. Financial support by the Marie Curie Initial Training Network (ITN) within the European Union's Seventh Framework Programme (Grant agreement no. 607585, OSNIRO) and by the German Science Foundation (DFG) via the Cluster of Excellence EXC 315 "Engineering of Advanced Materials" is gratefully acknowledged.

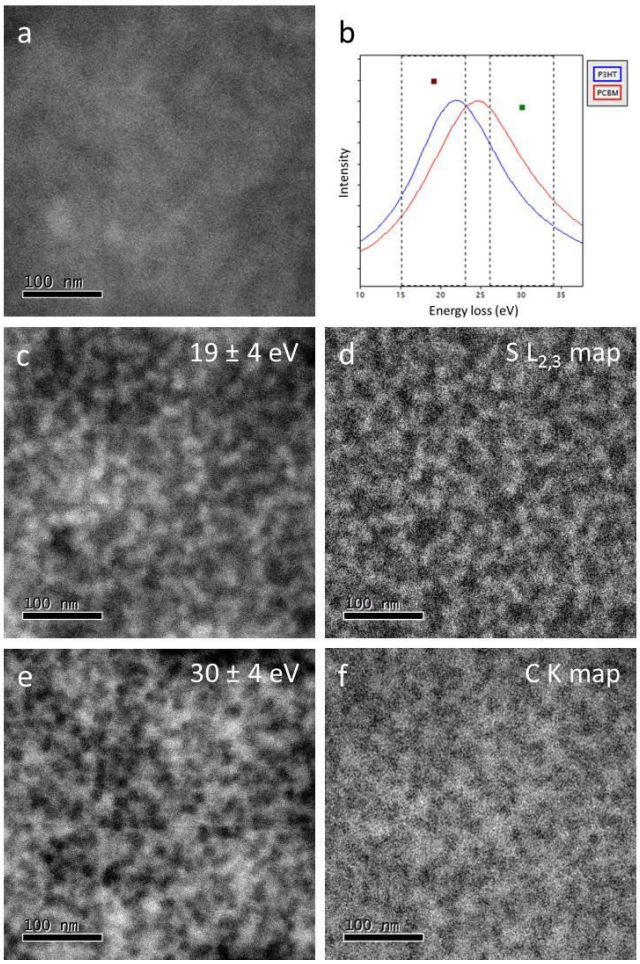

Figure 1: TEM zero-loss filtered BF image of the P3HT:PCBM blend (a), EEL spectra of pure P3HT and PCBM films in the low loss region (b), EFTEM images in the plasmonic region (c, e) and corresponding elemental maps of sulfur and carbon (d, f) of the P3HT:PCBM blend.

Energy-Related Materials and Materials for Information Technology

MS3.050
Analyzing the morphology of perovskite solar cells using nanobeam diffraction and electron spectroscopic methods

A. K. Kast[1,2,3], I. Wacker[4], G. Benner[5], L. Veith[4], D. Nanova[2,3,6], M. Agari[7], W. Hermes[7], P. Erk[7], W. Kowalsky[2,3], R. R. Schröder[1,2,4]

[1]Universitätsklinikum Heidelberg, CryoEM, CellNetworks, BioQuant, Heidelberg, Germany
[2]Innovationlab GmbH, Heidelberg, Germany
[3]TU Braunschweig, Institut für Hochfrequenztechnik, Braunschweig, Germany
[4]Universität Heidelberg, Centre for Advanced Materials, Heidelberg, Germany
[5]Carl Zeiss Microscopy GmbH, Oberkochen, Germany
[6]Universität Heidelberg, Kirchhoff-Institut für Physik, Heidelberg, Germany
[7]BASF SE, Ludwigshafen, Germany

anne.kast@bioquant.uni-heidelberg.de

Organometal trihalide perovskite materials, such as $CH_3NH_3PbI_3$ (MAPbI), have become of great interest for use in solar cells with their remarkable power conversion efficiencies and cost-efficient, solution-based processing. Solar cells based on these materials are fabricated similar to dye-sensitized solar cells: A mesoporous TiO_2 scaffold is infiltrated by the perovskite absorber. The materials distribution within this mesoporous layer can be visualized using e.g. electron energy-loss spectroscopic methods [1, 2]. Although information about the excitable electronic states and thus material distribution can be derived using these spectroscopic methods, detailed information on the structure of the material cannot be acquired.

In this study we use (Scanning) Transmission Electron Microscopy ((S)TEM) to correlate STEM Electron Energy-Loss Spectroscopy (EELS) and Nanobeam Diffraction (NBD). Figure 1 shows a STEM image of the investigated sample. Two points where quasi-simultaneously spectrum (Fig. 2 a, c) and diffraction pattern (Fig. 2 b, d) were acquired are marked red and green. The spectrum allows us to classify spot 1 (red) as TiO_2 and the diffraction pattern shows that it is present in crystalline form, while spot 2 (green) is of perovskite nature, also present in crystalline form.

Many measurements of this form were done on a focused ion beam (FIB) prepared lamella of a perovskite solar cell device. We found that areas containing perovskite-based material are present in both crystalline and amorphous form, the later presumably organometallic halogenoplumbate. NBD and STEM EELS measurements show that crystalline areas correlate with the appearance of a signal in the low-loss region of the EEL spectrum at about 7-8 eV loss, which is not present in amorphous regions.

1. M. Pfannmöller et al. Nano Lett. 11, 3099-3107 (2011).
2. D. Nanova et al. Nano Lett. 14, 2735-2740 (2014).
3. Financial support by the German Federal Ministry of Education and Research (FKZ 03EK3505J/L/K, FKZ 13GW0044, FKZ 13N10794) is gratefully acknowledged.

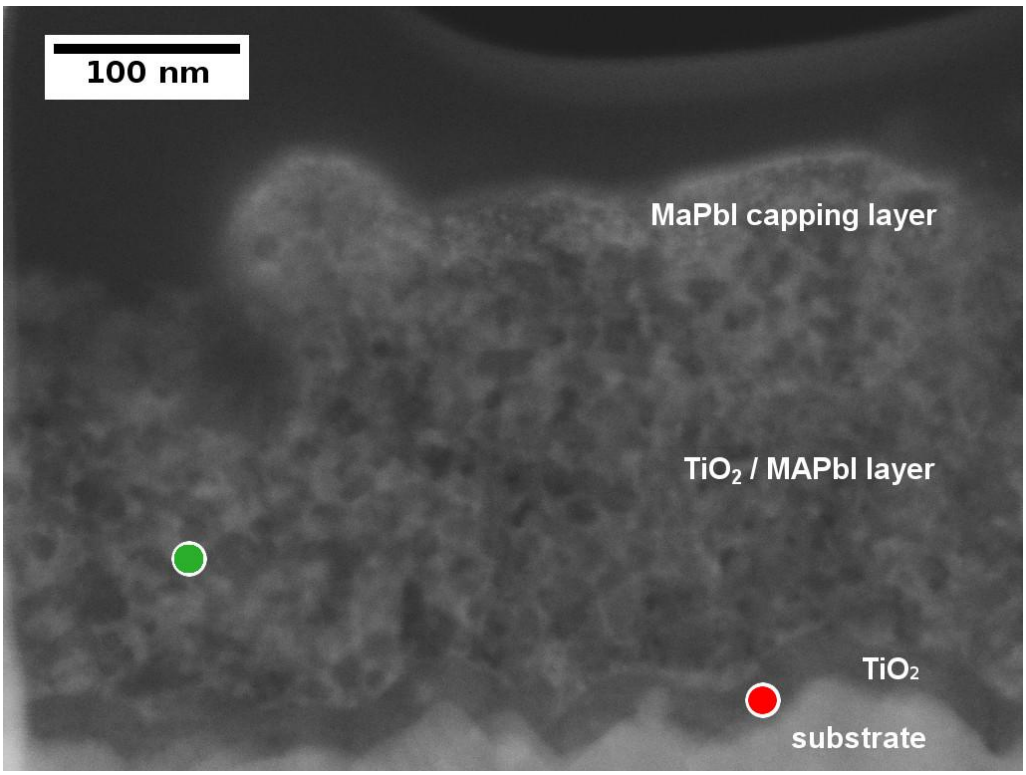

Figure 1. - STEM image of investigated cross-section. Two spots where quasi-simultaneously EELS and NBD data was acquired are marked in red and green. The respective spectra and diffraction patterns can be seen in Fig. 2 (red) and Fig. 3 (green).

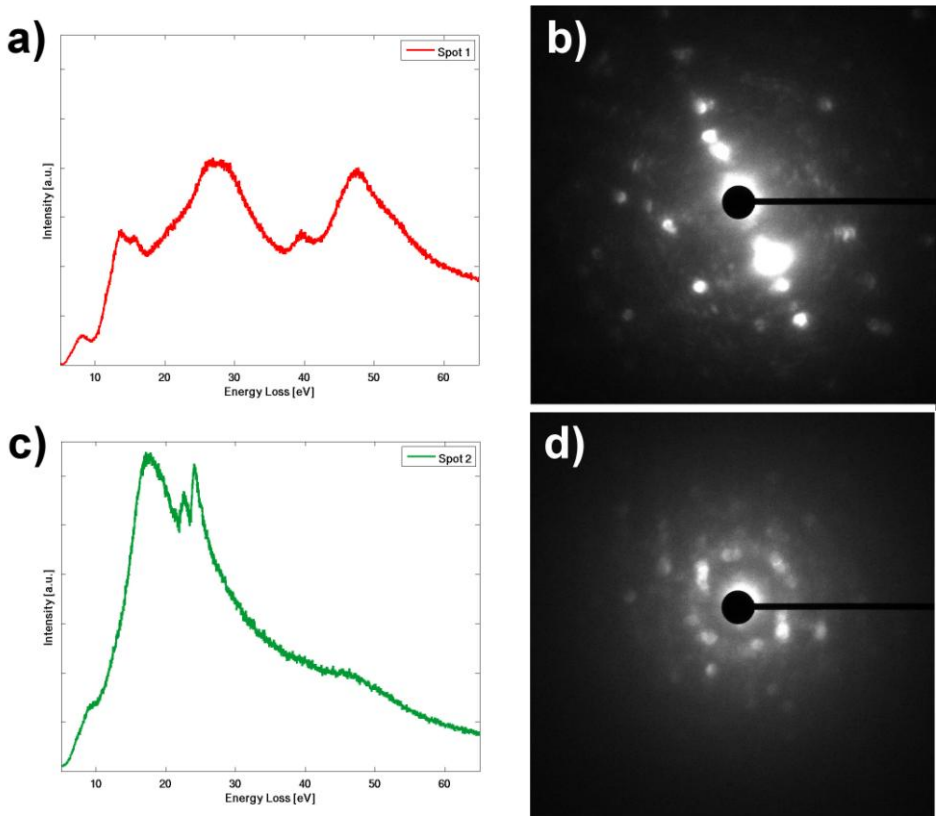

Figure 2. - Quasi-simultaneously acquired electron energy-loss spectrum (a) and diffraction pattern (b) of spot 1 (marked by red circle in Fig. 1), which can be identified as crystalline TiO_2. c) and d) show the acquired data for spot 2 (marked by green circle in Fig. 1), which can be identified as crystalline perovskite-based material.

Energy-Related Materials and Materials for Information Technology

MS3.051
Interfacial properties of ceria films on yttria-stabilized zirconia

H. Schmid[1,2], K. Song[3], P. Longo[4], E. Gilardi[1], G. Gregori[1], K. Du[3], J. Maier[1], P. A. van Aken[1]

[1]Max Planck Institute for Solid State Research, Stuttgart, Germany
[2]JEOL Germany GmbH, Munich, Germany
[3]Shenyang National Laboratories for Materials Science, Shenyang, China
[4]Gatan Inc., Pleasanton, CA, United States

vanaken@is.mpg.de

Ceria (CeO_2) and yttria-stabilized zirconia (YSZ) are two promising electrolyte materials used in solid oxide fuel cells due to their high ion conductivities. Theory predicts that the formation energy of oxygen vacancies is considerably decreased at free surfaces and internal interfaces. Oxygen vacancies are expected to segregate at the interfaces and thus might provide an easy path for rapid ion conduction.[1] The aim of the present work is to obtain insights into the structure and chemistry of interfaces between ceria films and YSZ substrates. Analytical scanning transmission electron microscopy (STEM) is the method of choice for a comprehensive materials characterization in terms of structure and chemistry down to atomic levels.[2] In the present study high-resolution structural and electron spectroscopic imaging (ESI) were performed in an advanced TEM/STEM system (JEOL JEM-ARM200F).

Continuous epitaxial films of pure and Gd-doped ceria were grown by pulsed laser deposition respectively on (111) and (100) YSZ substrates showing a cube-on-cube orientation relationship. No reaction layers or secondary phases were identified at the interfaces. The film-substrate lattice mismatch of ≈ 5.3% is accommodated by periodically spaced misfit dislocations observed at the interface with extra atomic planes in the YSZ substrate[3]. Electron energy-loss spectroscopy (EELS) line scans across the interface clearly reveal $Ce^{4+} \rightarrow Ce^{3+}$ reduction in narrow interface regions by utilizing valence sensitive Ce-M [4,5] energy-loss near-edge fine structures (ELNES) features (Fig. 1a-c). EELS spectrum images were recorded across whole ceria films including interface and surface regions. Atomic column-resolved ESI were acquired in selected regions of interest across ceria-YSZ interfaces. The setup used in these experiments provides an image resolution of about 110 pm in high-angle annular dark-field (HAADF) STEM imaging (Fig. 2a,d), and a probe current of 140 pA for EELS-ESI at an energy resolution of ca. 0.5 eV. Multiple linear least-squares (MLLS) fitting enables a unambiguous visualization of the $Ce^{4+} \rightarrow Ce^{3+}$ reduction at interfaces (Fig. 2b,e) and free surfaces. No noticeable differences were observed in systems with Gd-doped ceria films with up to 10 at.% Gd. In both doped and undoped samples a reduced interface region of about 1.2 ± 0.1 nm width was observed (Fig. 2c,f). Similarly, a reduced Ce^{+4-x} region was observed at the interface between the Ce oxide film and a metallic Cu capping. Assuming charge balance, the presence of Ce^{+3} ions is seen as evidence of oxygen vacancy formation in narrow interface regions.

In summary, it is concluded that advanced analytical TEM/STEM methods, i.e. high-resolution HAADF-STEM imaging in combination with EELS spectroscopic imaging enable the elucidation of local non-stoichiometry, which is crucial not only for understanding charge transport mechanisms in these hetero-structured materials, but also for understanding the catalytic properties of ceria. [3,4]

1. M. Fronzi *et al.*: Phys. Rev. B **86** (2012) 085407
2. H. Schmid, E. Okunishi and W. Mader: Ultramicroscopy **127** (2013) 76
3. K. Song *et al.*: APL Materials **2** (2014) 032104
4. KS and PvA acknowledge funding from the PhD student exchange program between the Max Planck Society and the Chinese Academy of Sciences and the Natural Sciences Foundation of China (Grant No. 51221264). The research leading to these results has received funding from the European Union Seventh Framework Program [FP/2007-2013] under grant agreement no 312483 (ESTEEM2).

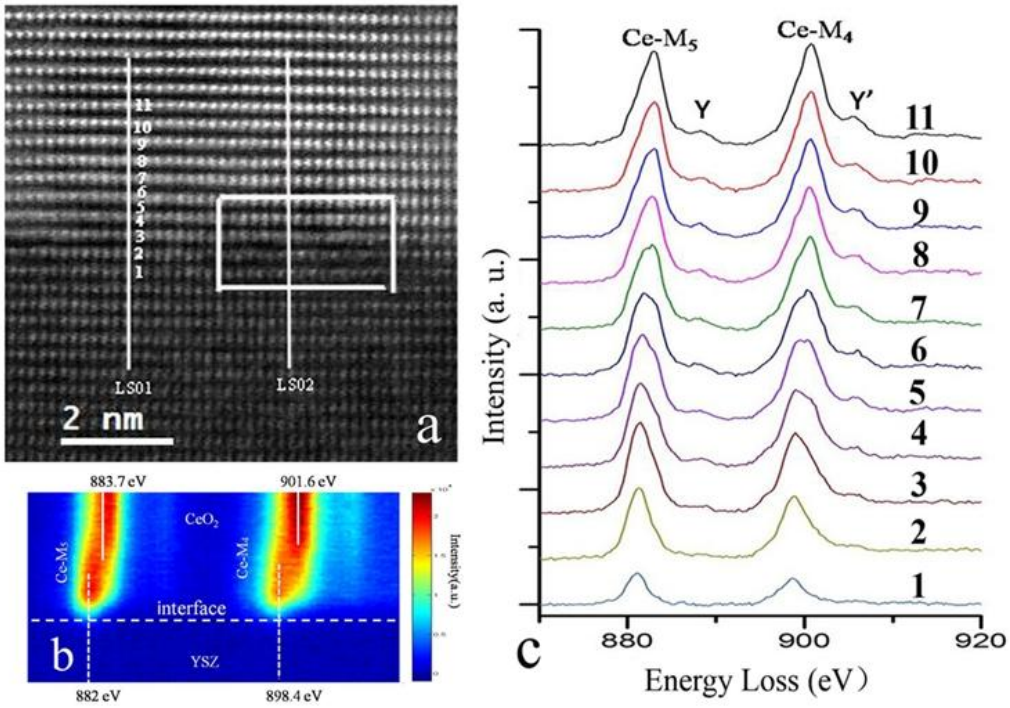

Figure 1. (a) Schematic HAADF-STEM image showing the position of the EELS line scans across the CeO_2/YSZ (111) interface. Line-scan 01 (LS01) went across regions between misfit dislocations and line-scan 02 (LS02) across the misfit dislocation core. (b) EELS spectrum image from LS01. (c) EELS spectra extracted from the spectrum image acquired along LS01, which illustrate the change of the Ce-$M_{4,5}$ edge from the bulk to the interface.

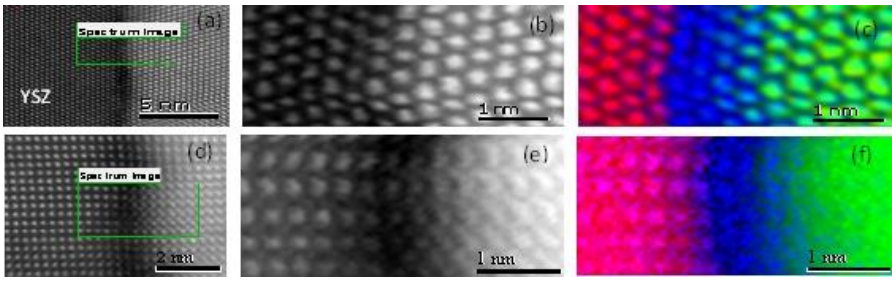

Figure 2. (a) and (d) STEM-HAADF images of the interface structure between undoped (a-c) and 10at.% Gd-doped (d-f) cerium-oxide film and YSZ substrate. (b) and (e) STEM-ADF survey images indicating the area of EELS spectroscopic imaging; (c) and (f) RGB overlay images obtained by MLLS fitting indicating Ce reduction in both interface layers (Zr red, Ce^{3+} blue, Ce^{4+} green).

Energy-Related Materials and Materials for Information Technology

MS3.052
Microstructure of $La_{0.58}Sr_{0.4}Co_{0.2}Fe_{0.8}O_{3-\delta}$ (LSCF) - $Gd_{0.2}Ce_{0.8}O_{2-\delta}$ (GDC) - $Y_{0.16}Zr_{0.84}O_{2-\delta}$ (YSZ) cathode/electrolyte interfaces in solid oxide fuel cells (SOFCs)

V. Wilde[1], H. Störmer[1], J. Szász[2], E. Ivers-Tiffée[2], D. Gerthsen[1]

[1]Karlsruher Institut für Technologie (KIT), Laboratorium für Elektronenmikroskopie, Karlsruhe, Germany
[2]Karlsruher Institut für Technologie (KIT), Institut für Angewandte Materialien – Werkstoffe der Elektrotechnik, Karlsruhe, Germany

virginia.wilde@student.kit.edu

Concerning future solid oxide fuel cell (SOFC) applications, high efficiency at low operating temperatures and long lifetime are essential. Therefore careful selection of materials is needed, especially regarding physical and chemical compatibility of the different components. For the electrolyte, Y_2O_3-stabilized zirconia (YSZ) is still state of the art. Moreover, mixed ionic-electronic conducting perovskites such as LSCF have been shown to be a highly performing cathode material [1]. Yet at SOFC operating temperatures, $La_{0.58}Sr_{0.4}Co_{0.2}Fe_{0.8}O_{3-\delta}$ (LSCF) is not compatible with YSZ, forming an insulating $SrZrO_3$-layer (SZO) which considerably reduces the efficiency of the cell [2, 3]. One idea of overcoming this problem is the incorporation of a Gd_2O_3-doped ceria (GDC) diffusion-barrier interlayer between YSZ and LSCF to prevent chemical reaction. This actually enhances the performance of SOFCs, however, upon fabrication (sintering) at 1200 °C, GDC-YSZ interdiffusion takes place, hence inducing formation of a low conducting Gd- and Ce-rich interdiffusion layer [4].

Aim of the present study is a detailed microstructural characterization of the LSCF-GDC-YSZ interfaces after different thermal pre-histories using conventional und analytical (scanning) transmission electron microscopy ((S)TEM). Especially the influence of the GDC sintering temperature on microstructural development is studied.

Symmetric cell samples were fabricated by screen-printing a GDC layer on YSZ substrates followed by sintering at 1100 °C, 1250 °C or 1400 °C, respectively. The LSCF was also screen-printed and sintered at 1080 °C.The samples with different GDC sintering temperatures will be denoted as GDC1100, GDC1250 and GDC1400.

TEM characterization was performed after GDC sintering (i.e. before LSCF deposition), after LSCF sintering and after electrical characterization at application-relevant temperatures (500 - 800 °C). The elemental distribution was determined by energy dispersive X-ray spectroscopy (EDXS) in a FEI Osiris ChemiSTEM transmission electron microscope.

Fig. 1 shows the Gd- and Sr-elemental distributions and corresponding composition line profiles across the interface region between GDC and YSZ of an electrically characterized sample of a)-c) GDC1100, d)-f) GDC1250 and g)-i) GDC1400. It is clearly visible in Fig. 1a) that two additional layers were formed between GDC and YSZ in GDC1100. The layer adjoined to the GDC layer (denoted by 1 in Figs. 1b,c) contains Sr and Zr in an equal percentage (Fig. 1c), indicating SZO formation. The second layer next to YSZ contains Ce and Gd (Fig. 1b) as well as Zr and Y (Fig. 1c). However, the GDC sintering temperature strongly influences the morphology of these two layers. In particular, higher sintering temperatures obviously reduce SZO formation. While there is a continuous SZO layer in GDC1100, SZO is formed in a network-like structure in GDC1250 (Fig. 1d) and only “channels” consisting of SZO are found in GDC1400 (Fig. 1g). Moreover, the width and the chemical composition of the second layer changes with higher GDC sintering temperature. While this layer is only ~300 nm thick in GDC1100, it has a width of over 1 µm in GDC1400 and the Ce content increases considerably (Figs. 1b,e,h).

The study gives new insights into material interactions at the interfaces in SOFCs and the effect of thermal treatment on microstructure. This improves the understanding of correlation between fabrication parameters and efficiency of SOFCs.

1. A. Mai et al, Solid State Ionics **176** (2005), 1341
2. A. Mai et al, Solid State Ionics **177** (2006), 1965
3. L. Kindermann et al, Solid State Ionics **89** (1996), 215
4. A. Tsoga et al, Ionics **4** (1998), 234

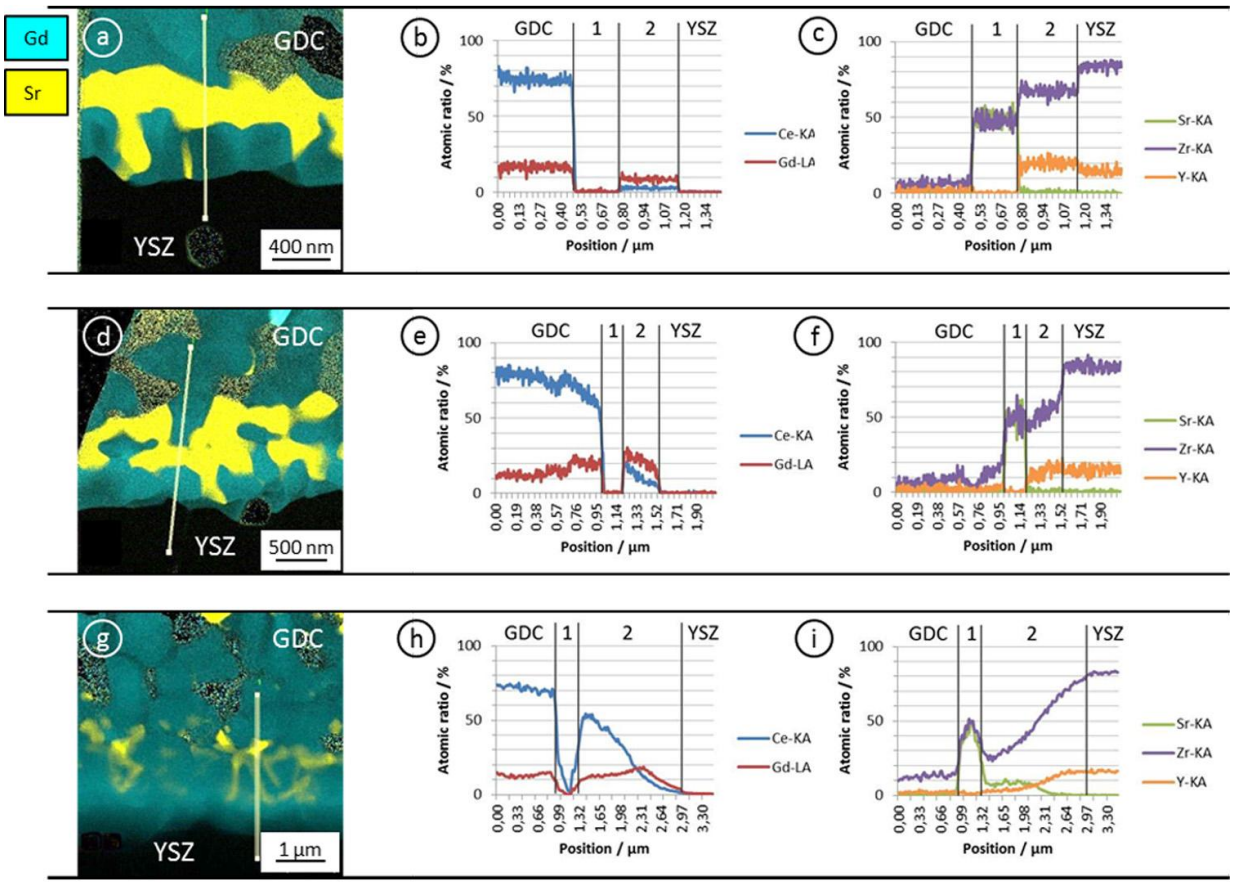

Figure 1. a) Color-coded Sr- and Gd-distribution of GDC1100 with b),c) corresponding composition line profiles across the interface. The two additional layers 1 and 2 between YSZ and GDC are marked by lines. d) Sr- and Gd-distribution of GDC1250 with e),f) corresponding composition line profiles, g) Sr- and Gd-distribution of GDC1400 with h),i) corresponding composition line profiles.

Energy-Related Materials and Materials for Information Technology

MS3.053
Nanostructured oxide thermoelectrics for high-temperature energy harvesting

A. Feldhoff[1], B. Geppert[1], M. Bittner[1]

[1]Leibniz University Hannover, Institute of Physical Chemistry and Electrochemistry, Hannover, Germany

armin.feldhoff@pci.uni-hannover.de

In the thermoelectric effect, an entropy current drives an electric current. Depending on the sign of the Seebeck coefficient α of the material, both currents are parallel or anti-parallel. The electric serial connection of n-type (α < 0) and p-type (α > 0) semiconducting legs with their contacts being alternatingly hot and cold, allows constructing thermoelectric modules, which can make use of the entropy current running from “hot” to “cold” for energy harvesting [1-3]. These solid state devices, which have no moving part, directly convert thermal energy (heat) into electric energy. If applied at high temperature, established thermoelectric materials suffer from thermal degradation in presence of atmospheric oxygen. This brings semiconducting oxides on the stage. These oxides, however have to be trimmed for their thermal conductivity to be coupled preferentially to the flow of charge carriers (e.g. electrons or holes) and not to the propagation of charge-less excitations of the solid (e.g. phonons). In this context, nanostructured oxides, which can be obtained via proper sintering and annealing procedures, are of high relevance to hinder the free propagation of phonons. Some ground-breaking nanostructured oxides have been made by us and have been investigated by high-resolution transmission electron microscope (HRTEM), selected area electron diffraction (SAED), energy-dispersive x-ray spectroscopy (EDXS) and electron energy-loss spectroscopy (EELS). An example is given in Fig. 1 by the transmission electron microscope analysis of $Ca_3Co_4O_9$-derived nanostructured oxide ceramic. Microstructure-property relationships have been established.

1. A. Feldhoff, Thermoelectric material tensor derived from the Onsager - de Groot - Callen model, Energy Harvesting and Systems, doi: 10.1515/ehs-2014-0040.
2. A. Feldhoff, B. Geppert, A high-temperature thermoelectric generator based on oxides, Energy Harvesting and Systems 1 (1-2) 69-78 (2014).
3. B. Geppert, D. Groeneveld, V. Loboda, A. Korotkov, A. Feldhoff, Finite-element simulations of a thermoelectric generator and their experimental validation, Energy Harvesting and Systems, doi: 10.1515/ehs-2015-0001.

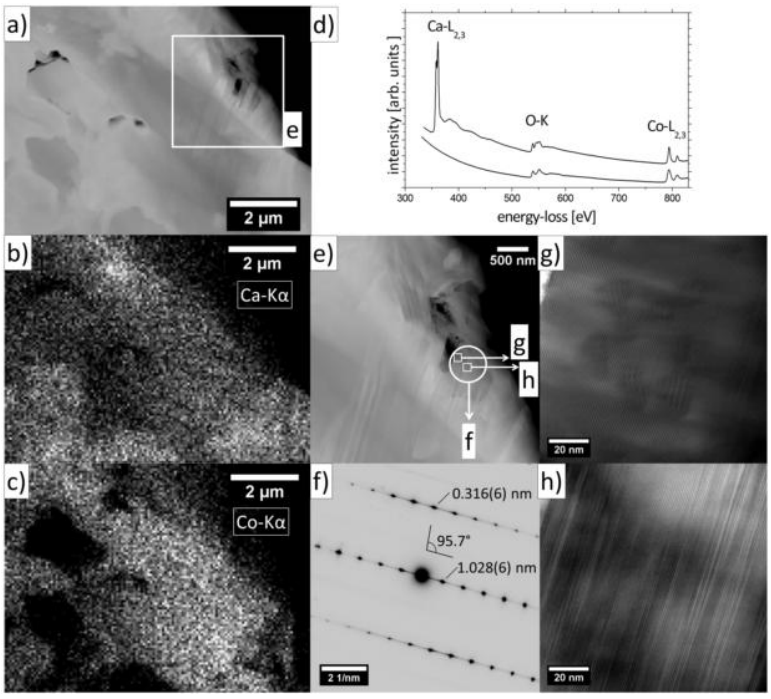

Energy-Related Materials and Materials for Information Technology

MS3.P054
Mapping the propagation of excitons through organic and inorganic light harvesting nano composites

A. Weber-Bargioni[1]

[1]Lawrence Berkley National Laboratory, Molecular FOundry, Berkeley, United States

awb@lbl.gov

Here we present unprecedented insight into the local exciton transport through organic and inorganic semiconducting nano building block assemblies using state of the art near field optics, hyperspectral mapping, and Field Effect Transistors to control the exciton transport electronically.

Controlling individual excitons and their deliberate movement through a material will provide the access to a new parameter space for the development of next generation light harvesting materials. E.g. with such control the captured energy in form of an excitons could be transported to predetermined sites in the material where the energy can be efficiently harvested. Nano materials have in principle the potential to realize this vision since the material property determining electronic structure can be tuned via geometry, material composition, interfaces and environment. However, the lack of spatial resolution has so far prevented the insight needed to develop engineering rules for the nm world to control the transport of optically excited electronic states at their native length scale.

To study the local exciton transport we use optical antennae to locally excite our sample optically and map spatially independent the energy flow by detecting either the local photo luminescence or the local photo current. We use this approach to study exciton transport through three model systems: Inorganic nano wires, 2-D assemblies of inorganic nano crystals, and through organic PV materials.

First we will present our results on exciton transport and local exciton properties in InP nanowire system and demonstrate that the local exciton recombination velocity is mediated by charge puddles on nanowire surfaces. CdSe Quantum Dot assemblies are another excellent absorber material system for light harvesting purposes. We determined exciton transport length through well ordered 2-D films of CdSe Nano Crystals of 80 nm and 120 nm for the 1-D case, mediated by Foerster Resonance Energy Transfer (FRET). To develop a better understanding of FRET between quantum dots (which is still not really understood) we used a graphene Field Effect Transistor to study FRET between individual quantum dots and graphene. In this device we can systematically tune with high precision the distance between graphene and quantum dot and the electronic structure of the exciton adsorber (graphene), while building the currently smallest light switch in the world.

Exciton diffusion is also a key hurdle for the systematic development of Organic Photo Voltaic. We used our techniques to directly measure the exciton diffusion length in polymer (P3HT) and small molecule (rubrene) organic photo voltaic materials and show a crystallinity dependent exciton diffusion length that correlates to the OPV dedvice power conversion efficiency. Furthermore we have evidence that local electric field gradient can modify the exciton diffusion length in organic semiconductors, where the exciton binding energy is large (1 eV) and the transport is mainly mediated by tunneling processes.

Energy-Related Materials and Materials for Information Technology

MS3.P055
Electron microscopic characterization of yttrium-doped BSCF ceramics

L. Grünewald[1], M. Meffert[1], H. Störmer[1], L.- S. Unger[2], S. F. Wagner[2], E. Ivers-Tiffée[2], D. Gerthsen[1]

[1]Karlsruher Institute of Technology (KIT), Laboratory for Electron Microscopy (LEM), Karlsruhe, Germany
[2]Karlsruher Institute of Technology (KIT), Institute for Applied Materials - Materials for Electrical and Electronic Engineering (IAM-WET), Karlsruhe, Germany

lukas.gruenewald@student.kit.edu

Perovskite-type mixed ionic-electronic conductors with chemical structure ABO_3 are widely studied materials for oxygen separation. $(Ba_{0.5}Sr_{0.5})(Co_{0.8}Fe_{0.2})O_{3-\delta}$ (BSCF) has shown promising oxygen permeation properties. However, at operating temperatures between 700 °C and 900 °C, a decline of oxygen permeation flux is observed due to the decomposition of the cubic perovskite phase into a secondary phase with hexagonal symmetry [1,2]. This decomposition is accompanied by a change in the valence state of the Co-cations [3]. Moreover, an additional secondary phase with plate-like morphology was identified which contains lamellae of the cubic, hexagonal and a $Ba_{n+1}Co_nO_{3n+3}(Co_8O_8)$ ($n \geq 2$) phase [3]. Furthermore, cobalt-oxide precipitates are observed. Since the decomposition of the cubic phase is most likely due to a varying B-site cation oxidation state, doping of BSCF with a monovalent B-site cation with suitable ionic radius is considered to increase the stability of the cubic phase. Tests with various doping elements (Zr, Y) were promising [4, 5] and especially Y-doping improves phase stability as it suppresses cobalt-oxide and plate-like phase formation. The remaining traces of the hexagonal phase are confined to grain-boundary regions, suggesting that an increase in grain size will be advantageous regarding the volume fraction of secondary phases. In addition, higher doping concentrations of up to 10 at% might further improve phase stability.

In this study the impact of grain size on secondary phase formation for 10 at% Y-doped (BSCF10Y) and undoped BSCF was studied. The BSCF sintering temperature was varied between 1050 and 1200 °C to produce samples with different grain sizes. Subsequently, samples were annealed at 700 - 800 °C for 240 h to simulate typical operating conditions and quenched in water to conserve the phase composition. Ex-situ characterization was performed by scanning and transmission electron microscopy. Details of the sample preparation procedure for scanning electron microscopy are outlined in [4].

Figure 1 shows SEM micrographs of two undoped BSCF samples sintered at (a) 1050 and (b) 1150 °C and after annealing at 700 °C. The homogeneous grey-scale in the image represents the cubic phase whereas hexagonal and plate-like/cobalt-oxide phases are depicted by dark and bright contrast, respectively. Since secondary phase nucleation originates at grain boundaries, the samples with larger grain sizes show, as expected, less secondary phase formation, especially in the grain interior (Fig. 1b). BSCF10Y samples annealed at 700 °C show only a small fraction of secondary phases, especially plate-like and cobalt-oxide phases (Fig. 1c). The BSCF10Y sample with largest grain-size annealed at 800 °C did not display any secondary phases at all (Fig. 1d). It has to be noted though, that BSCF10Y grain sizes were considerable smaller compared to pure BSCF after sintering under identical conditions, indicating a decrease in sintering activity due to Y-doping. Valence-state determination of the multivalent cations Fe and Co in BSCF and BSCF10Y using electron energy loss spectroscopy revealed identical oxidation states of 2.8+ (Fe) and 2.3+ (Co), respectively [6] in doped and undoped samples. It is therefore assumed that Y with a fixed valence state of 3+ will most likely increase the oxygen stoichiometry. Since the Y-cation has a higher ionic radius compared to Fe- and Co-cations, a certain fraction of the Y-cations might be located on the A-site of the cubic perovskite lattice. Hence, atomic location enhanced microanalysis as described by Taftø and Spence [7] was performed. Applying this method, A-site Y-dopant occupancies between 0,55 and 2,5 at% were found.

Y-doping impedes the transition from cubic to hexagonal and is therefore suitable for stabilizing BSCF. Even though B-site substitution was intended some Y was found on the A-site which can be attributed to its large ionic radius.

1. Švarcová et al., Solid State Ionics 178 (2008) p. 1787
2. C. Niedrig et al., Solid State Ionics 197 (2011) p. 25
3. P. Müller et al., Chem. Of Mat. 25 (2013) p. 564
4. S. Yakolev et al., Appl. Phys. Lett 96 (2010) p. 254 101
5. P. Haworth et al., Sep. and Purif. Technol. 81 (2011), p. 88

6. P. Müller et al, Microsc. Microanal 19 (2013) p. 1595
7. J. TaftØ and J. Spence, Science 218 (1982) p. 49
8. We acknowledge funding by the Deutsche Forschungsgemeinschaft.

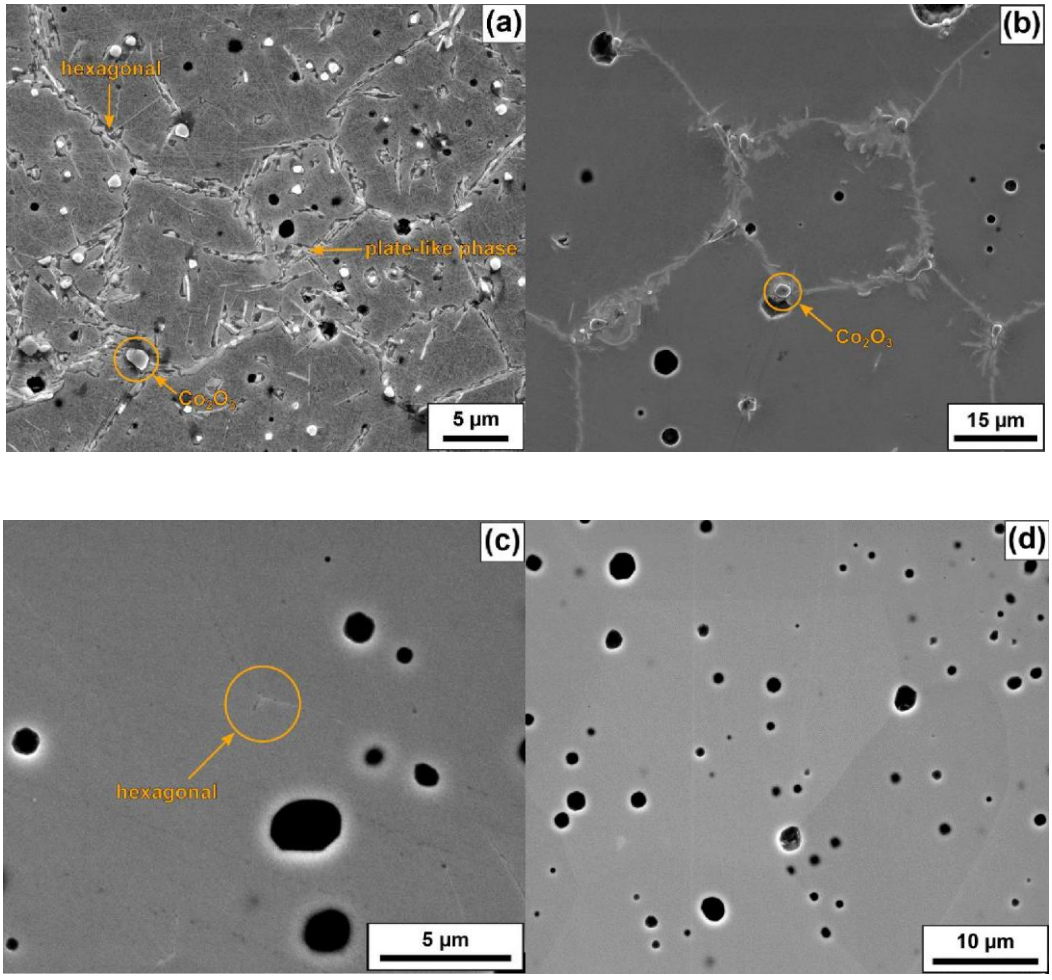

Figure 1. 15keV secondary-electron SEM images of undoped BSCF sintered at (a) 1050° C and (b) 1150°C and annealed at 700 ° C. BSCF10Y sintered at 1200 °C and annealed at (c) 700 °C and (d) 800 °C.

Energy-Related Materials and Materials for Information Technology

MS3.P056
$Cu_{2-x}Se$ phase in $Cu(In,Ga)Se_2$ thin-film solar cells by means of HR-STEM and EELS

E. Simsek[1], Q. M. Ramasse[2], D. Abou-Ras[3], R. Mainz[3], A. Weber[3], H.- J. Kleebe[4], P. A. van Aken[1]

[1]Max Planck Institute for Solid State Research, Stuttgart, Germany
[2]SuperSTEM, STFC Daresbury Laboratories, Daresbury, United Kingdom
[3]Helmholtz Zentrum Berlin, Berlin, Germany
[4]Technische Universität Darmstadt, Darmstadt, Germany

simsek@is.mpg.de

$Cu(In,Ga)Se_2$ (CIGSe) thin-film solar cells are of great interest with their high power-conversion efficiencies. They can achieve efficiencies over 21% [1] when produced by the multi-stage co-evaporation technique [2]. In the first stage In and Ga are deposited under Se atmosphere. In the second stage Cu is deposited under Se atmosphere, and the sample becomes Cu-rich ([Cu]/([In]+[Ga]) >1) at the end of the process. This temporary Cu-rich composition is necessary for the recrystallization, grain growth and defect annihilation of the thin film [3-5]. However, the Cu-rich composition forms a secondary phase, $Cu_{2-x}Se$, which is a degenerate p-type semiconductor and can be detrimental for the device performance [6]. Therefore, it is important to consume the remaining $Cu_{2-x}Se$ phase during the third stage. In, Ga and Se deposition at the third stage shifts the overall composition towards a single Cu-poor ([Cu]/([In]+[Ga]) phase.

In this study we focused on the non-consumed $Cu_{2-x}Se$ phase in Cu-poor CIGSe thin-films produced at low temperatures (430°C). We have observed $Cu_{2-x}Se$ planes at grain boundaries (GB) and also within individual grains as a separate phase using high-resolution scanning transmission electron microscopy (HR-STEM) in combination with electron energy-loss spectroscopy (EELS). HR-STEM analyses show that the Se sublattice continues through the CIGSe matrix and $Cu_{2-x}Se$ phase at the GB without any interruption, which is an indication of the coherency of these two phases. There are also publications discussing the coherency of the Cu_xSe phase and chalcopyrite $CuGaSe_2$, $CuInSe_2$ and CIGSe [6-8].

The high angle annular dark field (HAADF) image of two grains oriented in different directions and the GB between them is shown in Figure 1a. The upper grain is oriented in <110> and the bottom grain is oriented in an unknown direction, therefore the atomic columns cannot be resolved by HR-STEM. Figure 1b shows the simultaneous HAADF image acquired during spectrum image acquisition. Figure 1c is the corresponding red-green-blue (RGB) composite image, a color coded combination of the Se, Cu and In elemental maps (Fig. 1d-f) extracted from the EEL spectrum image, showing the CIGSe matrix and the $Cu_{2-x}Se$ phase formed at {112} planes.

This contribution gives insight about the $Cu_{2-x}Se$ phase in CIGSe thin-film solar cells with sub-atomic resolution. It helps to explain the formation mechanism and the effect of the secondary phase on the solar-cell performance of the CIGSe thin films.

1. ZSW press release 12/2014, 2014
2. Gabor, A. et al., Appl. Phys. Lett. 65/2, 198-200, 1994
3. Barreau, N. et al., Acta Mater. 58/17, 5572-5577, 2010
4. Rodriguez-Alvarez, H. et al., Acta Mater. 61/12, 4347-4353, 2013
5. Nishiwaki, S. et al., J. Mater. Res. 14/12, 4514-4520, 1999
6. Nadenau, V. et al., Solid State Phenomena 67-68, 397-402, 1999
7. Wada, T. et al., J. Maters. Res., 12-6, 1456-1462, 1996
8. Yan, Y. et al., Mat. Res. Soc. Symp. Proc. 668, H6.10.1-6, 2001
9. The work was supported in part by Helmholtz Virtual Institute HVI-520 “Microstructure Control for Thin-Film Solar Cells”. The research leading to these results has received funding from the European Union Seventh Framework Program [FP/2007-2013] under grant agreement no 312483 (ESTEEM2). SuperSTEM is the UK National Facility for Aberration-Corrected STEM, funded by EPSRC.

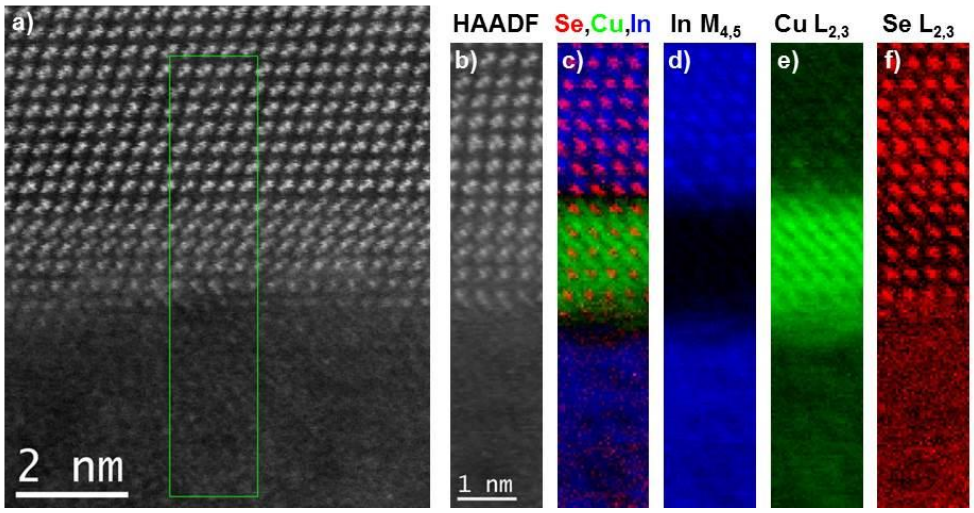

Figure 1. (a) HAADF image of two grains and the GB. (b) Simultaneous HAADF image acquired during spectrum image acquisition. (c) Corresponding red-green-blue composite image shows Se, Cu and In, respectively. (d), (e), (f) Elemental distribution maps extracted from the spectrum image acquired.

Energy-Related Materials and Materials for Information Technology

MS3.P057
Atomic-resolution Cs-corrected STEM investigation of metastable $Ge_2Sb_2Te_5$ phase change thin films

A. Lotnyk[1], S. Bernütz[1], X. Sun[1], M. Ehrhardt[1], B. Rauschenbach[1]

[1]Leibniz Institute of Surface Modification, Physical, Leipzig, Germany

andriy.lotnyk@iom-leipzig.de

Phase change materials (PCM), such as Te-based $Ge_2Sb_2Te_5$ (GST), are of high interest due to their technologically eminent optical and electronic properties. The GST material is known from optical memory applications (DVD-RAM) [1] and can be also used in non-volatile next generation random access memory (PCRAM). The operation principle of PCMs based devices is based on ultrafast reversible transformation between the amorphous and crystalline metastable phases. The metastable GST phase has a cubic NaCl structure with the 4(a) site being occupied by Te and the 4(b) site being randomly occupied by Ge and Sb with 20% of vacancies. Recently, EXAFS data showed that Ge and Sb atoms in the GST lattice are off-centre displaced resulting in a net dipole moment [2]. Thus, the GST exhibits also ferroelectric properties. However, an ordered GST lattice at 4(b) site based on HRTEM images was also proposed [3]. In addition, ab-initio calculations suggested that the metastable GST consists of two well-defined 3D repeated units (Te-Ge-Te-Sb-Te- (I) and -Te-Sb-Te-Ge- (II)) possessing rock-salt symmetry with highly ordered and layered vacancy positions [4]. Moreover, the GST lattice with coexisting of octahedral and tetrahedral Ge sites was also reported [5]. Thus, the atomic arrangements in the GST lattice are not well-understood and still under discussion. In addition, there are no reports on direct imaging of metastable laser crystallized GST phase by e.g Cs-corrected HRSTEM. Since detailed knowledge of real structure of PCMs is the key for understanding of fast crystallization speed and property contrast of PCMs, we aim in this work to study the atomic structure of metastable GST phase by an atomic-resolution Cs-corrected STEM combined with image simulations in order to reveal directly the atomic arrangements in GST lattice.

Metastable GST phase was obtained by laser irradiation of amorphous GST films. The specimens for STEM studies were prepared by a combination of FIB and focused low-energy Ar ion milling. Atomic-resolution STEM (HRSTEM) studies were performed with a probe Cs-corrected Titan^3 G2 60-300 microscope operated at 300 kV.

HAADF-HRSTEM images of metastable GST lattice in [001] and [110] viewing directions are shown Fig. 1 and Fig. 2, respectively. The calculated lattice parameter of 0.605±0.004 nm match the GST lattice parameter (0.6029 nm) reported by XRD reasonably well. In addition, shorter and longer Ge/Sb-Te distances were identified from extensive image analysis. This indicates off-centered locations of Ge/Sb atoms in the GST lattice. Analysis of intensity maxima on 4(b) site reveals some deviations in the peak intensities and is therefore a result of random distribution of Ge, Sb, and vacancies within the GST lattice. No confirmation on existing of tetrahedral Ge atoms was found from low-angle ADF-HRSTEM (Fig. 3). This was also proved by image simulations (Fig. 4).

In conclusion, our results show that the metastable GST phase is described by an ordered sublattice at 4(a) site and disordered sublattice at 4(b) site where only a distorted octahedral atomic arrangement of atoms exist without layered ordering of vacancies [6].

1. M. Wuttig, N. Yamada, Nature Mater. 6, 824 (2007)
2. A.V. Kolobov, P. Fons, A.I. Frenkel, A.L. Ankudinov et. al., Nature Mater. 3, 703 (2004)
3. Y. J. Park, J. Y. Lee, M. S. Youm, Y. T. Kim, H. S. Lee, J. Appl. Phys. 97, 093506 (2005)
4. Z. Sun, J. Zhou, R. Ahuja, PRL 96, 055507 (2006)
5. X.Q. Liu, X. B. Li, L. Zhang, Y.Q. Cheng et al., PRL 106, 025501 (2011)
6. U. Ross, A. Lotnyk, E. Thelander, B. Rauschenbach, APL 104, 121904 (2014)
7. The financial support of the European Union and the Free State of Saxony (LenA project; Project No. 100074065) is greatly
8. We thank Mrs. A. Mill for assistance in the FIB preparation.

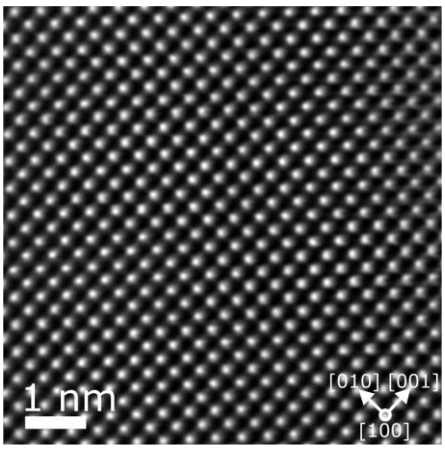

Figure 1. HAADF-HRSTEM image of GST lattice viewed along [001] zone axis

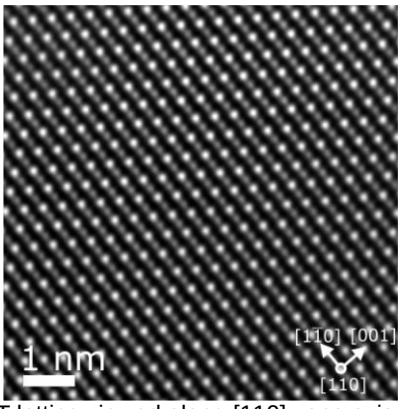

Figure 2. HAADF-HRSTEM image of GST lattice viewed along [110] zone axis.

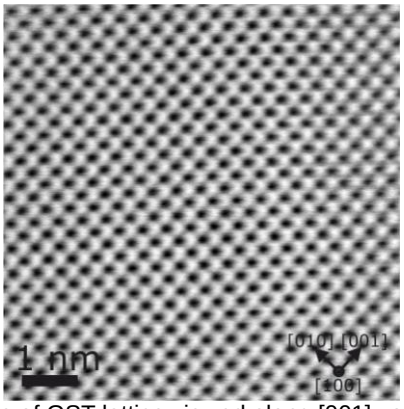

Figure 3. Low-angle ADF-HRSTEM image of GST lattice viewed along [001] zone axis.

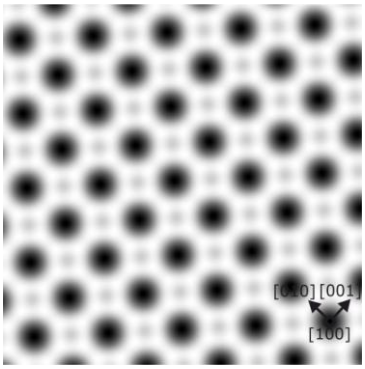

Figure 4. Simulated low-angle ADF-HRSTEM image assuming the locations of Ge atoms on tetrahedral sites.

Energy-Related Materials and Materials for Information Technology

MS3.P058
Elucidation of mechanism of selective Mg_2Cu formation at low temperature in Mg/Cu super-laminate composites

K. Tanaka[1], D. Kuniyama[2], S. Ikeuchi[3], R. Kondo[2], H. Takeshita[2]

[1]National Institute of Advanced Industrial Science and Technology (AIST), Research Institute of Electrochemical Energy, Osaka, Japan
[2]Kansai University, Faculty of Chemistry, Materials and Bioengineering, Osaka, Japan
[3]Kansai University, Graduate School of Science and Engineering, Osaka, Japan

koji.tanaka@aist.go.jp

Magnesium is expected as one of hydrogen storage materials owing to the advantages such as light weight, great crustal abundance,inexpensiveness, and high hydrogen storage capacity of 7.6 mass% to form MgH_2 [1]. However, MgH_2 is too stable to desorb hydrogen under moderate conditions because of its high standard formation enthalpy of -76 kJ(mol H_2)$^{-1}$, and a reaction of Mg to H_2 gas is sluggish. Thus, various Mg-based alloys and compounds have been investigated to improve the rate and to lower the temperature of hydrogen desorption [2-7]. We have applied accumulative roll bonding (ARB) followed by initial activation to the formation of intermetallic phase Mg_2Cu, where alloying Mg with transition metals such as Cu is effective for the improvement of thermodynamic and kinetic properties of hydrogenation and dehydrogenation [4, 6], and ARB is responsible for the acceleration of hydrogenation and dehydrogenation [8, 9].The improvement of kinetic properties of hydrogenation and dehydrogenation [8], its relations with microstructures [9, 10], the formation mechanism of micro/nano-structures through competitive reactions during initial hydrogenation [11], and the effect of initial structures of Mg/Cu super-laminate composites (SLCs) on kinetic properties of hydrogenation and dehydrogenation [12] have been reported in previous papers for Mg_2Cu-H_2 system. Through these investigations, it is found that alloying Mg with Cu to form Mg_2Cu occurred at low temperatures below 453 K selectively during heating process of initial hydrogenation. In this study, we will discuss alloying mechanism at low temperature in Mg/Cu SLCs.

Mg/Cu SLCs were prepared by ARB using a conventional two-high rolling mill [7]. Those were annealed at several temperatures below 453 K for several durations till 30 days. Micro/nano-structures of Mg/Cu SLCs were examined with SEM, and distortion and crystalline size were estimated by XRD. The thickness of the formed Mg_2Cu in annealed Mg/Cu SLCs was estimated from SEM images, and then activation energy and frequent factor were calculated.

Fig. 1 (a), (b), and (c) are reflected electron images taken at 1 kV. : (a) As-rolled, (b)453 K, 3 h, (c) 453 K, 30 d (720 h). As shown in fig. 1 (a), contrast of grains is seen in Cu, although contrast of distortion in Mg. It is clearly seen in fig. 1 (b) and (c) that Mg_2Cu was formed and grew during annealing, and surprisingly contrast of distortion in Mg did not disappear even at 453 K for 30 d (720 h). XRD measurement also showed Mg was distorted, although Cu was not distorted. Calculated activation energy and frequent factor of Mg/Cu SLCs respectively are 107 ± 6 kJmol^{-1} and 2.3 x 10^{-6} m^2s^{-1}, although those of Mg-Cu diffusion couples are 156 ± 10 kJmol^{-1} and 1.5 x 10^{-3} m^2s^{-1} [13], respectively. The growth constant at 453 K of Mg_2Cu in Mg/Cu CSLs of 1.0 x 10^{-18} m^2s^{-1} is much larger than that of Mg-Cu diffusion couples of 1.5 x 10^{-21} m^2s^{-1}. It can be considered that large amount of vacancies and dislocations introduced by sever plastic deformation of ARB enables alloying Mg with Cu to form Mg_2Cuat low temperature in Mg/Cu SLCs.

1. J. F. Stampfer, Jr., C. E. Holley, Jr., and J. F. Suttle, J. Am. Chem Soc. 82 (1960), 3504-3508.
2. S. Orimo et al., Acta Mater. 45 (1997), 331-341.
3. G. Liang et al., J. Alloy. Compd. 305 (2000), 239-245.
4. J. J. Reilly and R. H. Wiswall, (1967) Inorg. Chem. 6 (1967), 2220-2223.
5. J. J. Reilly and R. H. Wiswall, Inorg. Chem. 7 (1968), 2254-2256.
6. A. Karty et al., J. Appl. Phys. 50 (1979), 7200-7208.
7. T. T. Ueda et al., J. Alloy. Compd. 386 (2005), 253-257.
8. N. Takeichi et al., J. Alloy. Compd. 446-447 (2007), 543-548.
9. K. Tanaka et al., J. Mater. Sci. 43 (2008), 3812-3816.
10. K. Tanaka et al., Mater. Trans. 55 (2014), 1122-1128.
11. K. Tanaka et al., J. Alloy. Compd. (2015), DOI : 10.1016/j.jallcom.2015.01.196.
12. K. Tanaka et al., J. Alloy. Compd. 580 (2013), S222-S225.
13. K. Nonakaet al., Mater. Trans., JIM 36 (1995), 1463-1466.

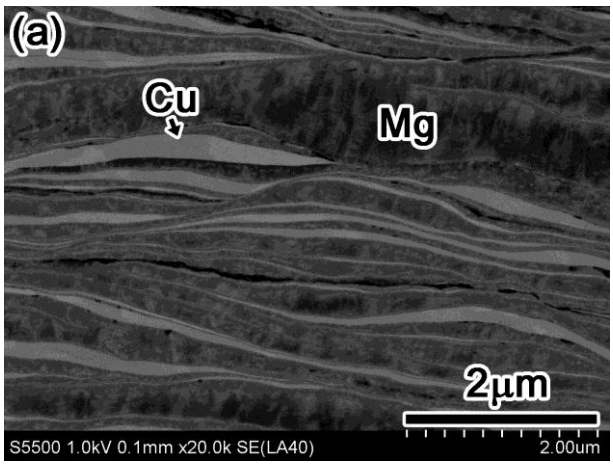

Figure 1. Reflected electron images taken at 1 kV. : (a) As-rolled, (b)453 K, 3 h, (c) 453 K, 30 d (720 h).

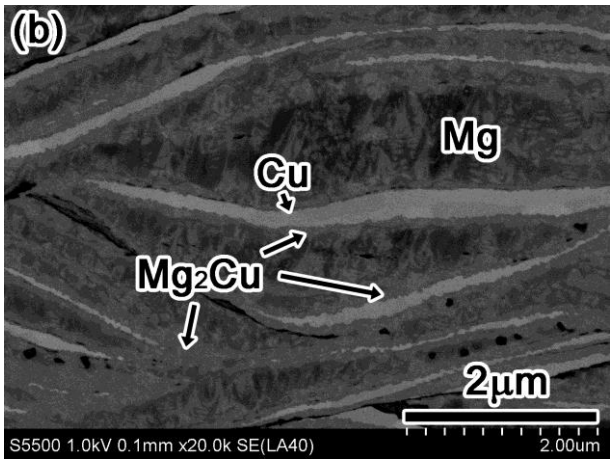

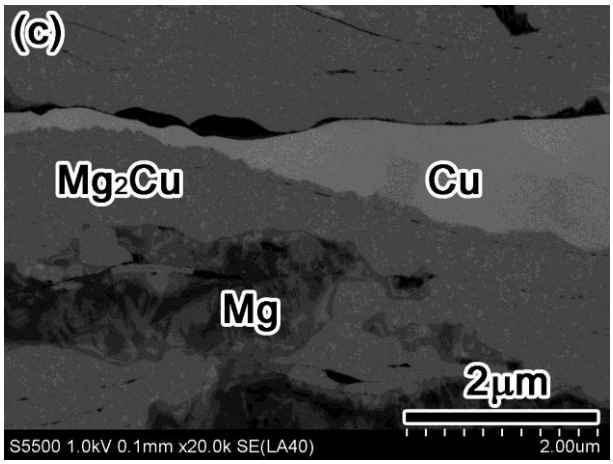

Energy-Related Materials and Materials for Information Technology

MS3.P059
Electron microscopy study of $CuInS_2$ solvothermally synthesized with l-Cysteine

A. Frank[1], A. S. Wochnik[2], C. Scheu[1]

[1]Max-Planck-Institut für Eisenforschung, Nanoanalytik und Grenzflächen, Düsseldorf, Germany
[2]Ludwig-Maximilians-Universität München, Chemie, München, Germany

a.frank@mpie.de

Over the last years research on renewable energy sources increased. Due to growing need in energy and as a consequence environmental pollution sources of “clean” energy supply are needed. Besides wind energy photovoltaic seems to be a promising solution because the energy of the sun is nearly inexhaustible.[1]

Copper indium disulfide, $CuInS_2$, is a promisingly material for photovoltaic applications. It offers a direct band gap of 1.5 eV combined with a high absorption coefficient of 10^5 cm^{-1}.[2] Furthermore it is possible to tune its type of conductivity dependent on the chemical composition.[3] Due to the high variety of possible nanostructures $CuInS_2$ can be used not only in inorganic solar cells but also as electrode in dye-sensitized solar cells. In combination with other materials (e.g. titanium dioxide, TiO_2) it is also used for solar-driven hydrogen evolution (water splitting). In terms of inorganic solar cells the combination of $CuInS_2$ with TiO_2 is also very interesting. Generally speaking, the combination of two nanostructured materials offers many advantages like for example an enhanced interface area for charge carrier separation as well as an enhanced light scattering due to nanostructuring. Despite this the migration distances to reach the interface of the charge carriers are decreased.[4]

In this work $CuInS_2$ is synthesized via a solvothermal process and analyzed via electron microscopy. Precursor salts are dissolved in ethanol and the sealed Teflon-lined autoclave is heated at 150 °C for 18 hours. Depending on which substrate (e.g. fluorine-doped tin oxide, FTO, or TiO_2 nanowire arrays) is used the obtained films differ in morphology. These nanostructures are analyzed with regard to crystallographic properties, nanostructure, chemical composition and optical properties. Primarily electron microscopic techniques like scanning and (scanning) transmission electron microscopy (SEM and (S)TEM, respectively) and spectroscopic methods are used.

With the above mentioned synthesis approach $CuInS_2$ crystallizes in the tetragonal Chalcopyrite modification as proven by X-ray diffraction (XRD). Both used substrates (FTO, TiO_2) are suitable for the solvothermal growth of $CuInS_2$. The chemical composition of the as-prepared samples is analyzed mainly with energy-dispersive X-ray spectroscopy. For different used ratios of the precursor salts the film composition is nearly stoichiometric whereas the film thickness increases. SEM images (Figure 1(a), (b)) display the surface and a cross section of the as-prepared samples for a medium concentration of precursors on FTO. The films consist of agglomerated nanoparticles and spread uniform all over the substrate. All the films show a good optical behavior over the whole visible range. TEM investigations confirm the formation of a crystalline film with good covering of the substrate (Figure 1(c)). Electron diffraction confirms the tetragonal Chalcopyrit crystal structure. Additionally, the reaction between only copper and sulfur precursor in ethanol was studied to confirm the reduction of Cu^{2+} to Cu^{+} which occurs during the synthesis of the films. The solid, grey product gives XRD reflections of a Cu-cysteine-complex which was also described by Dokken et al.[5] The resulting product was analyzed in TEM with electron energy loss spectroscopy (EELS, Figure 2). S L_{23} and Cu L_{23} edges in the obtained EELS spectra prove the formation of a Cu_xS phase when compared to literature data.[6] Further investigations will focus on the growth of $CuIn_2$ films on the different substrate with special regard to interfaces between $CuInS_2$ and FTO or TiO_2.

1. Morton, *Nature* **2006**, *443*, 19.
2. Tell, at al., *Physical Review B* **1971**, *4*, 2463.
3. Yukawa, et al., *Thin Solid Films* **1996**, *286*, 151.
4. Nanu, et al., *Advanced Functional Materials* **2005**, *15*, 95.
5. Dokken, et al., *Inorganica Chimica Acta* **2009**, *362*, 395.
6. Hofer, et al., *Ultramicroscopy* **1987**, *21*, 379.

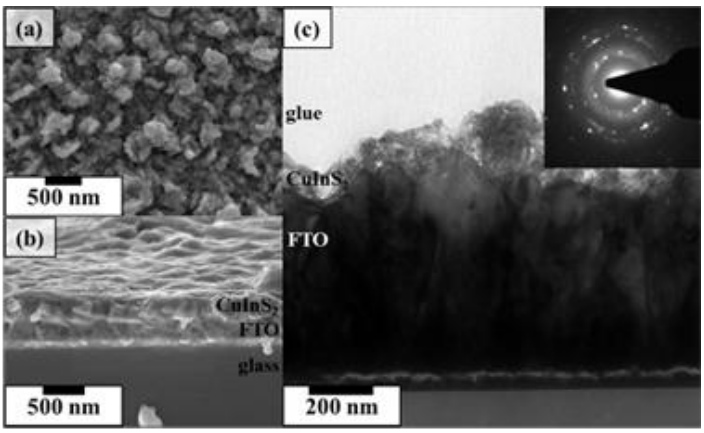

Figure 1. (a) and (b) SEM images of the as-prepared $CuInS_2$ films on FTO substrate. (a) shows the typical surface morphology of the samples, (b) the accordingly SEM cross section. (c) TEM image of the $CuInS_2$ film on FTO. The electron diffraction pattern indicates the formation of $CuInS_2$ in the tetragonal Chalcopyrite structure.

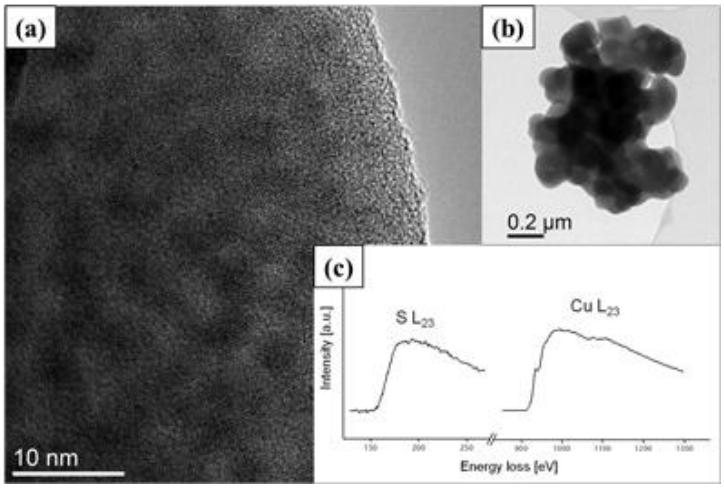

Figure 2. (a) and (b) TEM images of the reaction product with only copper and sulfur precursors in ethanol. (c) EELS spectra taken from this product. S L_{23} and Cu L_{23} edges indicate the presence of Cu_xS.[6]

Energy-Related Materials and Materials for Information Technology

MS3.P060
Beam stability and bonding behavior of a novel BeP_2N_4 compound determined by HRTEM and EELS

T. Dennenwaldt[1], J. Ciston[2], U. Dahmen[2], W.- Y. Ching[3], F. Pucher[4], W. Schnick[4], C. Scheu[5]

[1]EPFL, CIME, Lausanne, Switzerland
[2]Molecular Foundry, NCEM, Berkeley, United States
[3]University of Missouri–Kansas City, Department of Physics and Astronomy, Kansas City, United States
[4]LMU Munich, Department of Chemistry, Munich, Germany
[5]Max-Planck Institut für Eisenforschung GmbH, Nanoanalytic and Interfaces, Düsseldorf, Germany

teresa.dennenwaldt@epfl.ch

Nitride materials offer many possible applications in optoelectronics as a wide-band gap semiconductor, and also exhibit excellent mechanical performance in extreme environments due to their high strength, hardness, and stability at elevated temperatures [1]. Recently, the hard phenakite-type BeP_2N_4 has been synthesized via the multi-anvil high-pressure/high-temperature method [2]. This compound is isoelectronic and isostructural to β-Si_3N_4, which transforms under high pressure into the ultrahard spinel-type γ-Si_3N_4. In the present work the structure of the phenakite-type BeP_2N_4 was analyzed with high-resolution transmission electron microscopy (HRTEM) and electron energy loss spectroscopy (EELS) concerning its electron beam stability and bonding behavior [3]. The stability under electron bombardment was investigated at acceleration voltages of 80 and 300 kV using a Titan (S)TEM 80-300 keV (FIG. 1). Light elements like Be can be knocked out or displaced quickly by the electron beam. This was also detectable in HRTEM studies conducted at 300 keV. Experiments using similar conditions but operating the microscope at 80 keV revealed a much higher stability even up to 1,000 s. Electron diffraction experiments confirmed that the compound is crystalline exhibiting the phenakite-type structure. A HRTEM image and its corresponding diffraction pattern taken in [210] direction are given in FIG. 2. The electronic structure of the compound was determined by analyzing the edge onsets, relative peak positions and shapes of the Be-K, P-$L_{2,3}$ and N-K electron energy-loss near-edge structures (ELNES) (FIG. 3). The experimental ELNES (acquired with and without monochromator) were compared to density functional theory (DFT) calculations [3,4]. The detection of light elements like Be is challenging due to their low atomic number and easy removal under electron bombardment. The monochromated ELNES of the Be-K-, P-$L_{2,3}$-, and (partly) N-K-edges showed excellent agreement with the DFT calculations. Be and P are tetrahedrally coordinated whereas N is threefold coordinated exhibiting four different sites in the phenakite-type structure. The combination of high-energy-resolution EELS with DFT calculations enables a facile investigation of new structure types such as the hypothetical ultrahard spinel-type BeP_2N_4 compound in the future. Furthermore, materials with ultralight elements can be analyzed which is important for their further development.

1. W. de la Cruz et al., Opt. Mater. 25 (2004) 39.
2. F.J. Pucher et al., Chem. Eur. J. 16 (2010) 7208.
3. T. Dennenwaldt et al., Microsc. Microanal. 20 (2014) 664.
4. W.-Y. Ching et al., Phys. Rev. B 83 (2011) 155109.
5. The authors acknowledge support of the NCEM and NIM.

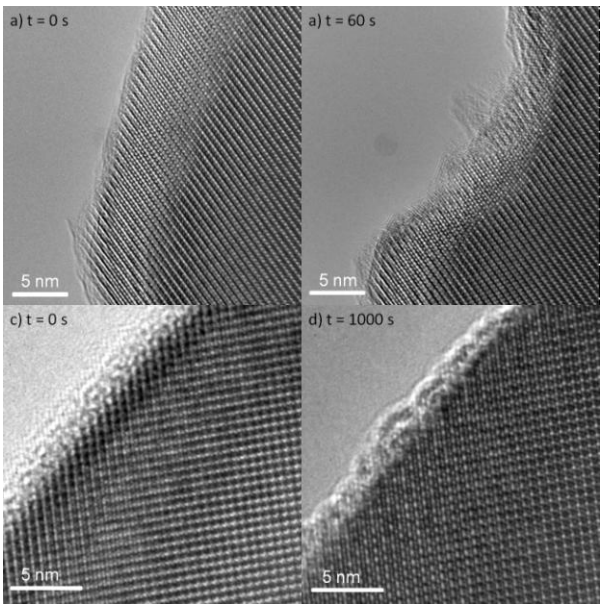

Figure 1. Beam damage study of the phenakite-type BeP_2N_4 phase [3], (a) nominal 0 s irradiation time at 300 kV, (b) 60 s irradiation time at 300 kV, (c) nominal 0 s irradiation time at 80 kV and (d) 1,000 s irradiation time at 80 kV. No severe damage can be observed after irradiating the sample for a longer time at 80 kV. Please note the different scale bars.

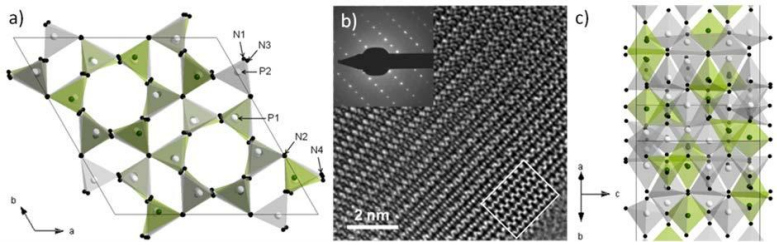

Figure 2. Crystal structure of the phenakite-type phase with BeN_4 tetrahedra highlighted in green, and PN4 tetrahedra in gray. (a) Structure viewed along [001], (b) HRTEM image of the phenakite-type BeP_2N_4 seen along the [210] direction with an enclosed simulated image and the corresponding diffraction pattern and (c) atomic arrangement of the phenakite-type phase viewed along [210]. The images are taken from [3].

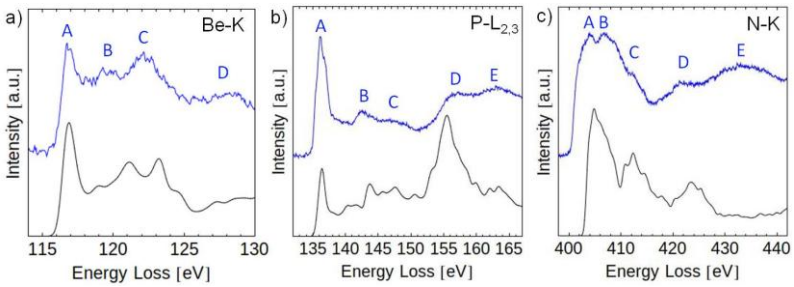

Figure 3. Calculated [4] (black) and experimental EEL spectra [3] (green without and blue with monochromator) of the phenakite-type BeP_2N_4 showing the Be-K (a), P-L_3 (b), and N-K edges (c).

Energy-Related Materials and Materials for Information Technology

MS3.P061
Multi-scale investigations of 3D TSV stacks using X-ray, electron and ion microscopy

M. Löffler[1], J. Gluch[1,2], J. Wolf[3], E. Zschech[1,2]

[1]Technische Universität Dresden, DCN, Dresden, Germany
[2]Fraunhofer Institute IKTS-MD, Dresden, Germany
[3]Fraunhofer IZM-ASSID, Dresden, Germany

markus.loeffler@tu-dresden.de

Advanced packaging processes and the resulting 3D products challenge process and quality control. To characterize 3D stacked chips for failure analysis, imaging and analytical techniques over several length scales are required [1]. Non-destructive characterization techniques such as X-ray imaging and X-ray computed tomography (XCT) are especially well suited for this task. The observation of features with sizes spanning from millimeters over micrometers down to several 10 nanometers allows to identify regions of interest for high resolution electron and ion microscopy. In particular, the initial sub-micron XCT steps allow to image the whole sample without any processing to identify peculiarities on the µm scale. Since sub-micron XCT and nano XCT are very useful techniques with a promising prospect for the future, we focus on the capabilities of two lab-based XCT tools with sub-micron resolution (Zeiss Versa) and with 50 nm resolution (Zeiss Ultra).

We demonstrate the capabilities for nondestructive imaging of multi-die stacks with Cu TSVs and AgSn microbumps. TSV etch profiles, major copper filling defects, small voids in Cu TSVs and variable solder flow are clearly visualized. An analysis of microbumps allows to evaluate geometrical features (shape, position) and intermetallic phases [2]. The full 3D imaging provides important information regarding the respective process steps (process control) and the product quality (quality control) and allow to select a region-of-interest for further analysis. Since deviations from the targeted geometry and defects are difficult to locate precisely from a two-dimensional image, X-ray computed tomography has to be applied to obtain a 3D digital version of the sample, which can be virtually sliced in arbitrary directions.

In a further step, the region-of-interest is studied with high resolution electron and ion microscopy. The analytical capabilities in the electron microscope allow for a mapping of the composition of the microbump solder material, including the determination of intermetallic phases, and for a determination of the crystallographic orientation of Cu grains in the TSV. The copper texture is important for the stress distribution in the silicon environment of the TSV [3], and therefore, for performance and reliability of the 3D-stacked chips.

1. E. Zschech, et al., Proc. IEEE IMAPS, San Diego/CA (2014)
2. E. Zschech, et al., Pan Pacific Microelectronics Symposium, Kauai 2015
3. V. Sukharev et al., IEEE Trans. Device Mater. Reliab. 9, 20 (2009)

Figure1. left: 3D representation of the full chip stack, middle: virtual slice through a small section of the whole chip stack, obtained from sub-micron XCT, right: virtual slice through a TSV and solder bump, obtained from two stitched nanoXCT

Energy-Related Materials and Materials for Information Technology

MS3.P062
Screening one-dimensional defects in GaN HEMTs by (S)TEM

A. Graff[1], M. Simon-Najasek[1], S. Hübner[1], F. Altmann[1]

[1]Fraunhofer Institute for Mechanics of Materials IWM, Halle, Germany

andreas.graff@iwmh.fraunhofer.de

Epitaxial layers of III- V semiconductors are used in electronic high power and high frequency applications. Especially GaN semiconductors are of growing importance due to the wide gap and the high electron mobility. Wafers for GaN microelectronics often consist of epitaxial grown GaN films on substrates like Al2O3, SiC or Silicon. Buffer layers are used to accommodate the lattice mismatch between the substrate and the GaN. Defects perpendicular to the interface remain, reaching the GaN surface. Nevertheless these GaN wafers are used to produce electrical devices like high mobility transistors (HEMT) by making source, drain and gate contacts. The ohmic source and drain contacts are produced by alloying the GaN with metals. Whereas the gate contact modulating the conductivity of the two dimensional electron gas has a metal semiconductor interface. The size of the HEMT depends on the intended frequency and power. For high frequency communication applications the gate length is about some 100 nanometers. In this case study some of the transistors showed an unusual high leakage current after processing. To find the cause for the locally increased leakage current the whole GaN substrate underneath the gate was investigated to find structural abnormalities. Large and relative thick electron transperant lamellas are investigated to identify crystal defects. For these samples the best (S)TEM imaging parameters have to be identified.

A large (50µm x 8µm) and thick (700nm) TEM lamella was prepared by FIB (Zeiss, NVision) containing half of the gate structure (Figure 1). The lamella was mounted by in situ lift out on a special TEM grid (Kleindiek, lift out shuttle). The TEM and STEM investigations were performed at 300kV (FEI, Titan 60-300). For STEM a standard HAADF detector was used.

Different techniques were evaluated to visualize threading defects in the thick GaN underneath the metallic gate. To get an overview of the defect distribution weak beam conditions were chosen. The GaN was oriented in the [-1100] direction which is perpendicular to the gate structure of the (0001) wafer material. Due to the thickness of the TEM cross section and the high mass thickness of the GaN bright field images show weak contrasts for the defects. Multiple scattering from the relative thick sample is blurring the images. Energy filtering in the zero loss could not increase the contrast significantly. STEM imaging with high camera length allows coherent scattered electrons to hit the HAADF detector and the defects are visible. The contrast of the dislocations could be optimized by increasing the camera length from angular dark field (ADF) to angular bright field (ABF) (Figure 2). To discriminate for different types of defects the thick TEM sample was systematically tilted with respect to the beam direction. For the tilted sample the ABF images gave the clearest contrast for the defects (Figure 3). Dislocations with screw and edge components could be distinguished by analyzing different two beam conditions.

STEM angular bright field techniques could be helpful to analyze one-dimensional defects in thick TEM samples. The structural results of this study were compared with leakage current localization techniques to find a correlation between the type of crystal defect and the local current density.

Acknowledgement: This work was performed as part of the research project “InnoDiaLE” funded by the Federal County of Saxony-Anhalt (project number 6060249005).

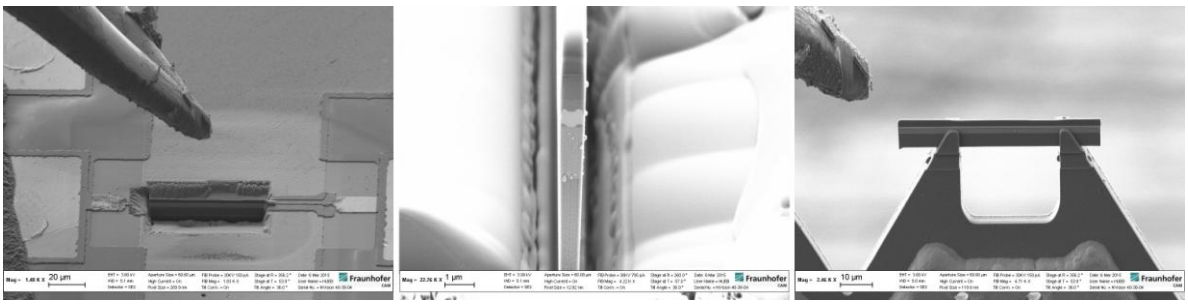

Figure 1. Left: SEM image of a large TEM lamella out of the gate region of a HEMT transistor. Middle: Cross section image of the lamella in containing the gate (Thickness about 700nm). Right: Sample mounted on special clamp holder by active gripper.

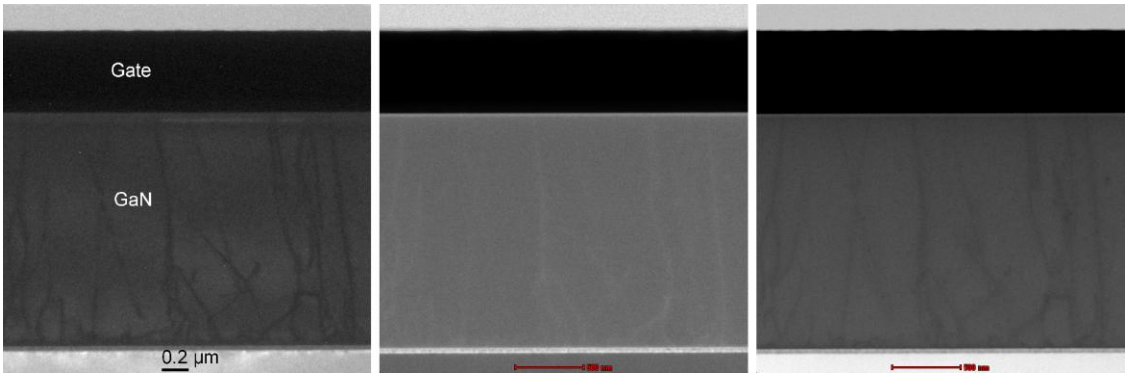

Figure 2. Left: TEM bright field image of the GaN with dislocations under weak beam conditions. Middle: STEM ADF image under same conditions. Right: STEM ABF image [-1100] beam direction.

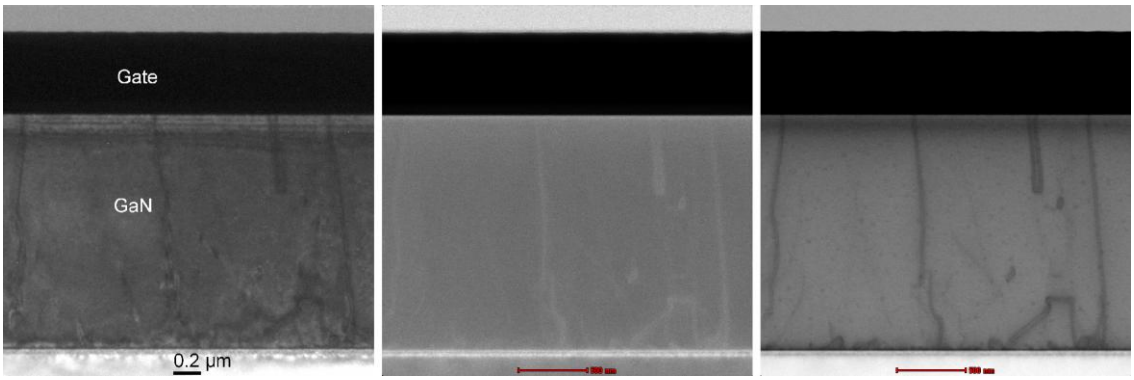

Figure 3. Left: Bright field image of the GaN with dislocations under two beam conditions (diffraction vector (0002)). Middle and Right: STEM ADF and ABF images under same conditions.

Energy-Related Materials and Materials for Information Technology

MS3.P063
Nanoconfined $LiBH_4$ for solid state hydrogen storage studied by analytical (S)TEM

A. Surrey[1,2], C. Bonatto Minella[3], N. Fechler[4], L. Schultz[1,2], B. Rellinghaus[1]

[1]IFW Dresden, Institute for Metallic Materials, Dresden, Germany
[2]TU Dresden, Institut für Festkörperphysik, Dresden, Germany
[3]Karlsruhe Institute of Technology, Institute of Nanotechnology, Eggenstein-Leopoldshafen, Germany
[4]Max Planck Institute of Colloids and Interfaces, Dept. of Colloid Chemistry Research Campus Golm, Potsdam, Germany

a.surrey@ifw-dresden.de

The complex hydride $LiBH_4$ is regarded as a promising material for solid state hydrogen storage because it contains 18.5 wt.% of H_2. However, its thermodynamic stability and its sluggish kinetics have hindered, so far, its utilization in stationary or mobile applications. In addition, the re-hydrogenation of its desorption products is promoted only under high temperatures and high pressures (600°C under 350 bar of hydrogen [1]). The dehydrogenation of bulk $LiBH_4$ occurs above 400°C and it can involve the evolution of diborane (B_2H_6) and very stable reaction products such as LiH and closoborane species (e.g. $Li_2B_{12}H_{12}$) might be formed in dependence of the experimental conditions used. The nanoconfinement of hydrides in porous scaffolds was shown to be a powerful tool to improve significantly their thermodynamic and kinetic properties. Within such pores, the material may lose its long range order and become amorphous. Nanoconfined $LiBH_4$ in activated carbon, carbon aerogels, ordered mesoporous carbon or carbon nanotubes has much lower desorption temperatures and an improved reversibility. However, all these scaffolds have the disadvantage of being either expensive or difficult to make.

In this study, we present the results for $LiBH_4$ nanoconfinement by melt infiltration within novel micro- and mesoporous scaffolds, which are synthesized by salt templating - a simple and sustainable technique that allows for the synthesis of a large variety of porous materials [2]. Therein nanoconfined $LiBH_4$ desorbs hydrogen in the range of 200°C to 350°C (see Fig. 1) without the evolution of B_2H_6 (not shown here). Re-hydrogenation is achieved at 300°C and 100 bar hydrogen (although partial) which are milder conditions in comparison with the bulk material. Transmission electron microscope (TEM) techniques were employed to investigate the nanoconfined hydride. Since the material is sensitive to moisture, a vacuum transfer holder was used to minimize the contact to air. The electron microscope is operated at an acceleration voltage of 80 keV to avoid beam damage of the carbon matrix. HRTEM and electron diffraction did not reveal any crystallinity. Since the specimen contains only light elements the scattering angles are small. Hence, STEM bright field imaging is very useful to image the specimen with a high contrast (see Fig. 2). EELS reveals the presence of boron within the pores of the carbon scaffold, however, lithium is very difficult to detect, because of the overlap of the Li-K absorption edge with a strong plasmonic signal. A spectrum image of the melt infiltrated sample is shown in Fig. 3. Boron is homogeneously distributed all over the investigated area with a concentration of 8±2 at.% relative to carbon (minimum 2%, maximum 22%). The boron and carbon elemental maps are complementary. Therefore, it can be concluded that regions of low carbon content are indicative for agglomerations of boron filled pores. The desorbed sample shows no B or LiH phase segregation and no ejection of crystalline LiH as reported in reference [3], which could explain the partial achieved reversibility. However, a change in the surface morphology is observed after dehydrogenation. The pores of the dehydrogenated sample are covered by a dense amorphous layer that also contains boron. In order to acquire more information on the sorption mechanism of confined $LiBH_4$, in-situ TEM heating will be performed, which allows to study the behavior of the hydride and its desorption products at high temperatures at the nanoscale.

1. Omiro et al., J. Alloys Compd. 2005, 404, 427-430.
2. Fechler et al., Adv. Mater. 2013, 25, 75-79.
3. House et al., J. Phys. Chem. C 2014, 118, 8843-8851.

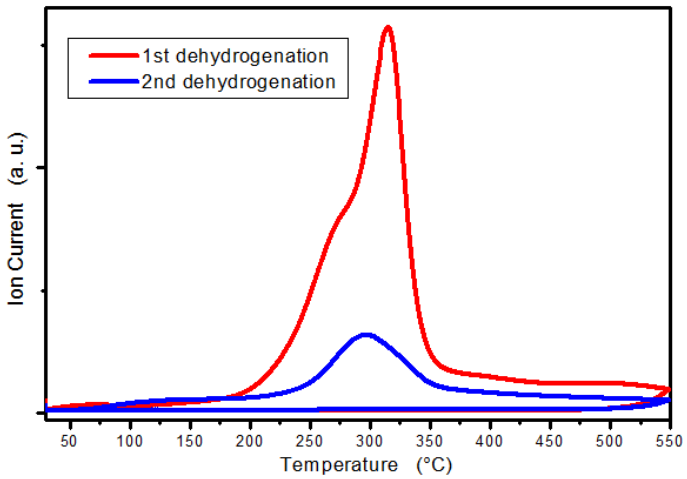

Figure 1. Hydrogen mass spectrometry for the first dehydrogenation (red curve) and the second dehydrogenation (blue curve) after re-hydrogenation of the melt infiltrated $LiBH_4$.

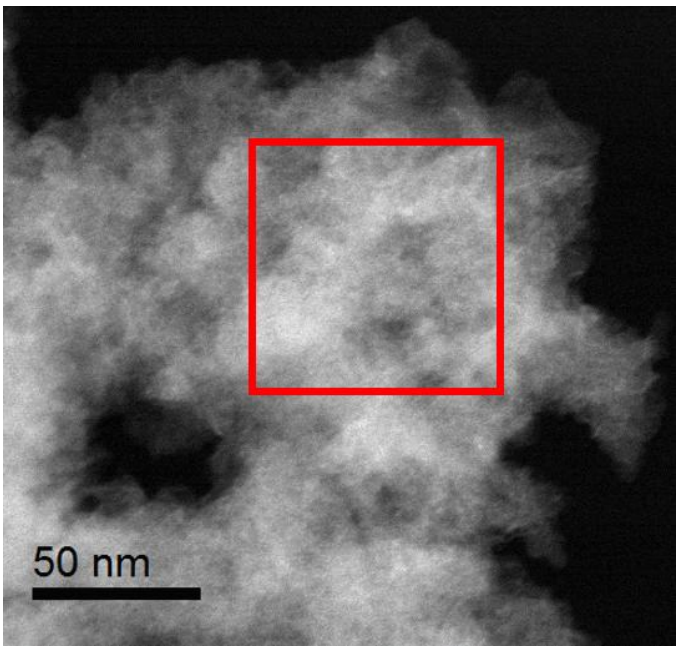

Figure 2. Bright field STEM image of melt infiltrated $LiBH_4$ within the porous carbon scaffold. The red square indicates the area of the spectrum image of Fig. 3.

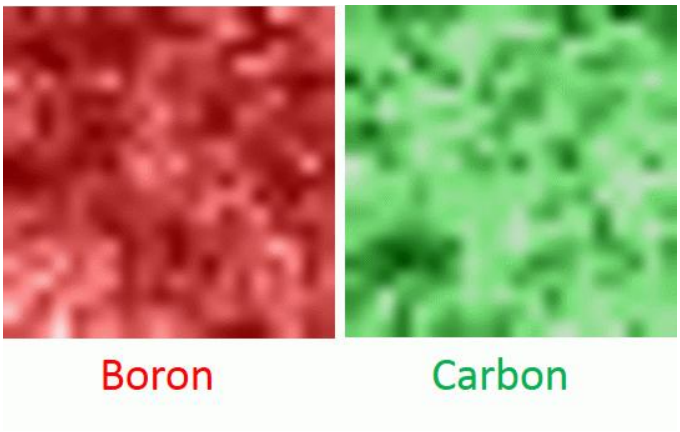

Figure 3. Spectrum image of the area marked in Fig. 2. The areal density of boron is displayed in red, of carbon in green.

Energy-Related Materials and Materials for Information Technology

MS3.P064
Microstucture and phase analysis of lithium-ion-battery (LIB) cathode materials

T. IJsselstein[1], H. Störmer[1], J. Costard[2], E. Ivers-Tiffée[2], D. Gerthsen[1]

[1]Karlsruher Institute of Technology (KIT), Laboratory for Electron Microscopy (LEM), Karlsruhe, Germany
[2]Karlsruhe Institute of Technology, Institute for Applied Materials - Materials for Electrical and Electronic Engineering (IAM-WET), Karlsruhe, Germany

tim.ijsselstein@partner.kit.edu

Lithium-ion battery (LIB) technology is the key enabler of energy storage and electric propulsion today. However, so far, state-of-the-art Lithium-ion batteries have not fully met the requirements of energy density, power density, extended lifetime and safety for automotive applications. Therefore, research activities focus on novel negative and positive electrode materials or novel electrolytes. $Li(Ni_{1/3}Mn_{1/3}Co_{1/3})O_2$ (NMC) with layered structure is one of the most promising cathode materials, due to its high operating voltage and high power or energy density [1]. However, there is still a lack of understanding the correlation between microstructure and elemental composition on cell performance and ageing. Usually, X-ray diffraction (XRD) is the standard technique for structure analysis, but lacks high spatial resolution and fails to detect nm-sized regions of secondary phases.

In this study, pristine and aged NMC cathodes from commercial high energy and high power cells were investigated by transmission electron microscopy (TEM). TEM Sample preparation was performed using the focused-ion-beam method. Information on the structural properties was obtained by electron diffraction. Elemental distributions were determined by EDXS mappings in the scanning transmission electron microscopy (STEM) mode utilizing a FEI OSIRIS ChemiSTEM operated at 200 kV and using the ESPRIT software (Bruker)

Figure 1 shows SEM micrographs of a (a) pristine and (d) aged NMC cathode. The cathode material consists of polycrystalline spherical primary particles. The individual NMC crystallites are between 200 nm and 2 µm in size. To ensure reliable statements upon possible differences in composition, EDXS mappings were acquired by selecting crystallites close to the edge of the primary particle and within the core. The elemental mapping and the cation ratio along a linescan of the pristine (b,c) and aged (e,f) NMC material is also given in Figure 1. Quantification for Ni, Mn and Co was performed considering C and O for background subtraction. The elemental composition is very homogeneous and can be determined within the measuring error to 50 at% Ni, 30 at% Mn and 20 at% Co, irrespective of position of the NMC crystallites (edge or core) as well as irrespective if pristine or aged material is considered. Moreover, no segregation of one cation towards the NMC grain surface is detected, indicating that there is no degradation of the cathode performance due to long-distance compositional changes. Figure 2 shows SAED micrographs of the (a) pristine (a) and aged NMC material, superimposed with SAED simulations performed by JEMS (red dots). The SAED patterns of the pristine material can be assigned to a layered structure with hexagonal symmetry (space group R-3m) [2]. Slight changes in symmetry occur for the aged material (Figure 2(b)) indicating structural changes in cation arrangement upon charging and de-charging of the material which could be, however, not be assigned to the layered R-3m structure or any spinel structure. It is assumed that the measured degradation of LIB performance is associated with a change in crystal symmetry, hampering Li intercalation.

1. K.C Kam et al. *J. Electrochem. Soc*. 159 (2012) A 1383.
2. O. Dolotko et al. J. Power Sources 255 (2014) 197.

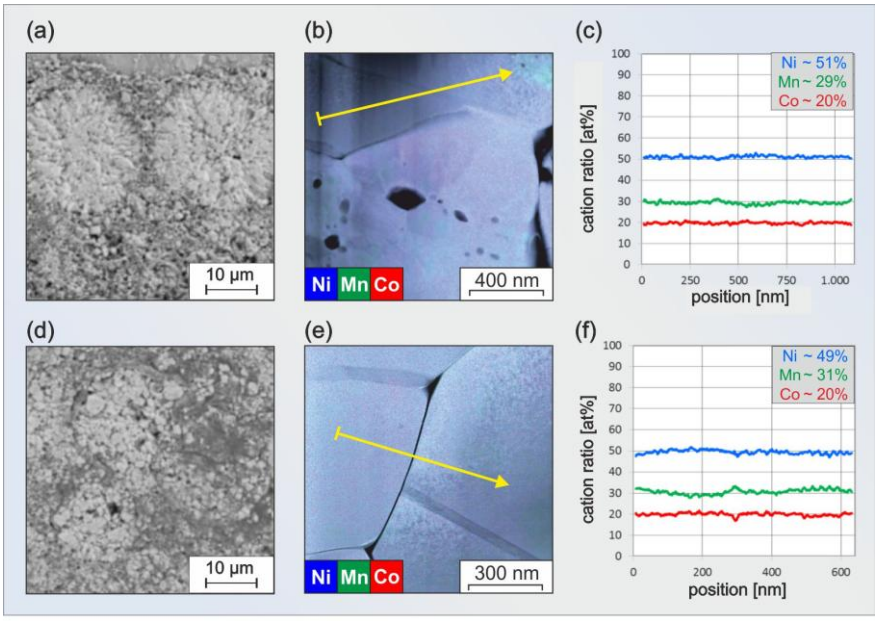

Figure 1. SEM micrographs of NMC primary particles in (a) pristine and (d) aged LIB cathodes. (b) – (f) EDXS elemental mapping and cooresponding quantified cation ration (linescan) of individual NMC crystallites within the (b,c as received and (e,f) aged material. The composition is homogeneous and no difference between pristine and aged material is measurable.

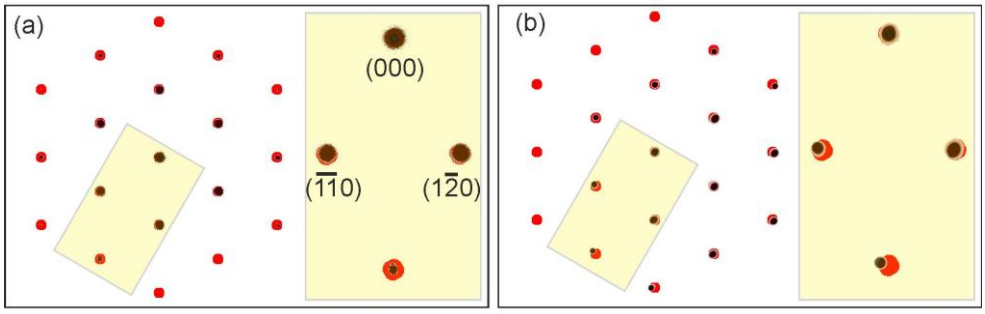

Figure 2. Simulated (red dots) and experimental SAED pattern of (a) pristine and (b) aged NMC material. The SAED pattern of the pristine material can be assigned to the [110] zone axis of the layered structure (space group R-3m). Upon ageing the symmetry changes, no unambiguous assignment to the layered or spinel structure is possible.

Energy-Related Materials and Materials for Information Technology

MS3.P065
Structure and stability of epitaxial multilayered superlattices of Bi_2Te_3 and Sb_2Te_3 thermoelectric thin films

T. Dankwort[1], A.- L. Hansen[1], M. Winkler[2], J. Ditto[3], J. D. Koenig[2], D. C. Johnson[3], W. Bensch[1], L. Kienle[1]

[1]Christian-Albrechts-Universität zu Kiel, Kiel, Germany
[2]Fraunhofer-Institut für Physikalsche Messtechnik (IPM), Freiburg, Germany
[3]University of Oregon, Eugene, United States

t.dankwort@gmail.com

Epitaxial multilayer superlattices of Bi_2Te_3 and Sb_2Te_3 were reported to exhibit outstanding thermo-electric figure of merit (ZT) of 2.4 at room temperature making them ideal candidates for applications such as low-temperature thermo-electric power generators [1]. However, the initially reported high-quality superlattices could not be reproduced and a thorough investigation of structural and physical properties is missing. Here we report our attempts to reproduce superlattices with stacking sequence of 1nm Bi_2Te_3 and 5 nm Sb_2Te_3 using molecular beam epitaxy. The process can be easily adjusted to produce any other desirable stacking sequence, which allows one to investigate the influence of the stacking sequence on electrical and thermal conductivity.

BaF_2 substrate material was used to promote the growth of expitaxial films. HAADF-STEM images of cross sections from the 1 nm Bi_2Te_3 / 5 nm Sb_2Te_3 superlattices show the formation of two distinct types of intergrowth structures. First a structure that's straight and parallel to the surfaceand in the vicinity of threading dislocations a second bowed structure (see fig. 1). HRSTEM images reveal that the bowed structure is due to a step-like intergrowth of Bi_2Te_3 which might be the result of edge dislocations.

To investigate the thermal stability of the obtained superlattices *in situ* and *ex situ* heating experiments were performed by TEM and XRD. Heating the sample *ex situ* for 200 °C resulted in a significant reduction of the superlattices most prominently at sides where bowed superlattices were expected leading to the assumption that the bowed superlattices show enhanced diffusivity. A reason might be facile diffusion paths along threading dislocations and an enhanced diffusivity along the *a* and *b* direction in comparison to straight superlattices where diffusion in *c* direction is the dominating process (see fig. 2). *In situ* TEM heating experiments validated these assumptions.

1. Venkatasubramanian, R. R.; Siivola, E.; Colpitts, T.; O'Quinn, B. *Nature* **2001**, *413*, 597.

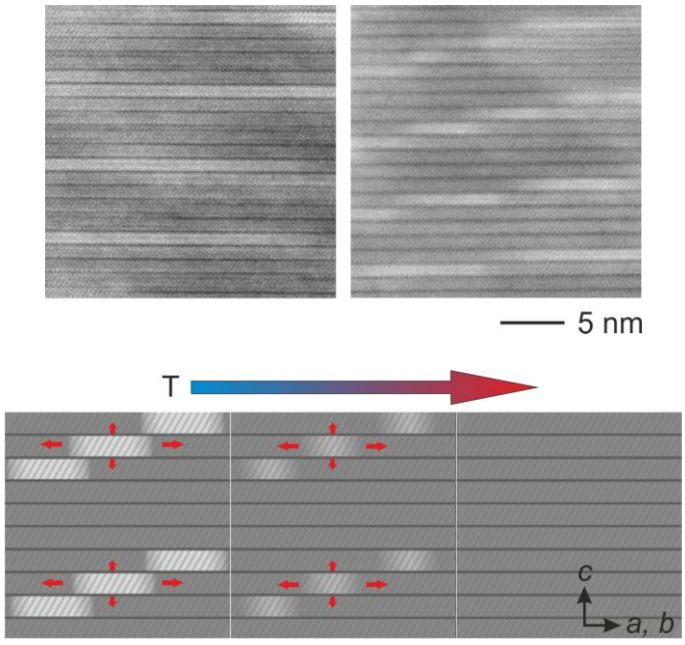

Energy-Related Materials and Materials for Information Technology

MS3.P066
Cs-corrected STEM characterisation of textured and epitaxial Ge-Sb-Te thin films

U. Ross[1], A. Lotnyk[1], E. Thelander[1], B. Rauschenbach[1]

[1]Leibniz Institute of Surface Modification , Physical, Leipzig, Germany

ulrich.ross@iom-leipzig.de

Phase change materials, such as Ge-Te-Sb (GST) alloys, are characterized by rapid, reversible crystallization behaviour from the amorphous state, accompanied by a large change in technically relevant material properties. Examples include changes in reflectivity for optical storage media and electrical resistivity for non-volatile resistive memory devices [1]. Highly-oriented thin films have recently become a focus of interest for their improved electrical switching behaviour, combining stable fast cycling of set-reset states with lowered threshold switching current requirements [2]. In addition, reports on thermoelectric properties in GST phase [3] and ferroelectic switching in metastable GST [4] warrant close inspection of the local crystalline atomic environment.

In this work, we study the thin-film growth of $Ge_2Sb_2Te_5$ produced by PLD on BaF_2(111) and Si(111). The $Ge_2Sb_2Te_5$ phase was chosen for its well-known phase change behaviour between amorphous, metastable cubic and stable layered hexagonal structure. A series of samples on both substrates at deposition temperatures between 85 and 280 °C was investigated. X-ray diffraction experiments indicated a particular epitaxial texture growth in the chosen temperature range [5].

The investigation was carried out using a FEI Titan³ G2 60-300 kV probe Cs-corrected TEM operated at 300 kV. The specimens for high-resolution STEM studies were prepared by a combination of FIB and focused low-energy Ar^+ ion milling [6] with argon ions at energies between 900 and 300 eV, thus minimizing residual damage and surface amorphization and resulting in foil thicknesses ~25 nm.

A comprehensive comparison of EDX measurements (Fig. 1) reveals a strong deviation in chemical composition at deposition temperatures above 200 °C. This can be explained by the preferential desorption of Ge during deposition and leads to additional disorder in compositions that do not match a preferred stoichiometry $Ge_2Sb_2Te_5$.

Cs-corrected HRSTEM images (Fig. 2) display the evolution of lattice disorder and phase transformation between cubic and hexagonal structure. The observed structures vary by degree of vacancy ordering, layer orientation and symmetry transition from cubic to hexagonal phase. At low and intermediate temperatures, a preferential growth of twin-domain rich columnar grains was found, while at high temperatures the layered epitaxial growth of GST is accompanied by characteristic stacking disorder that serves to accommodate residual strain due to interface topography. In addition, quantitative evaluation of the HAADF contrast shows a partial chemical ordering in the mixed Ge/Sb sublattice at high temperatures, as would be expected from the ideal bulk phase, yet contained within the stacking disordered structure. Lastly, close inspection of the GST-Si interface (Fig. 3) reveals the particular importance of vacancy layering for this growth behaviour. A Van-der-Waals gap immediately above the Te-rich surface serves to accommodate misfit strain.

We are therefore able to illustrate a thin film growth of GST alloys with an early onset of layered textured growth and a notable resilience to epitaxial lattice mismatch.

1. S. Raoux, W. Wełnic, D. Lelmini Chem. Rev. (2010) 110: 240
2. R. E. Simpson, P. Fons, A. V. Kolobov et al. Nature Nanotechnology (2011) 6, 501
3. T. Rosenthal, M. N. Schneider et. al. Chem. Mater. (2011) 23: 4349
4. A. V. Kolobov, D. J. Kim et.al. APL Materials (2014) 2(6): 066101
5. E. Thelander, J. W. Gerlach, U. Ross, A. Lotnyk, B. Rauschenbach Appl. Phys. Lett. (2014) 105: 221908
6. U. Ross, A. Lotnyk, E. Thelander, B. Rauschenbach Appl. Phys. Lett. (2014) 104: 121904
7. The financial support of the European Union and the Free State of Saxony (LenA project; Project No. 100074065) is greatly acknowledged. We thank Mrs. A. Mill for assistance in the FIB preparation.

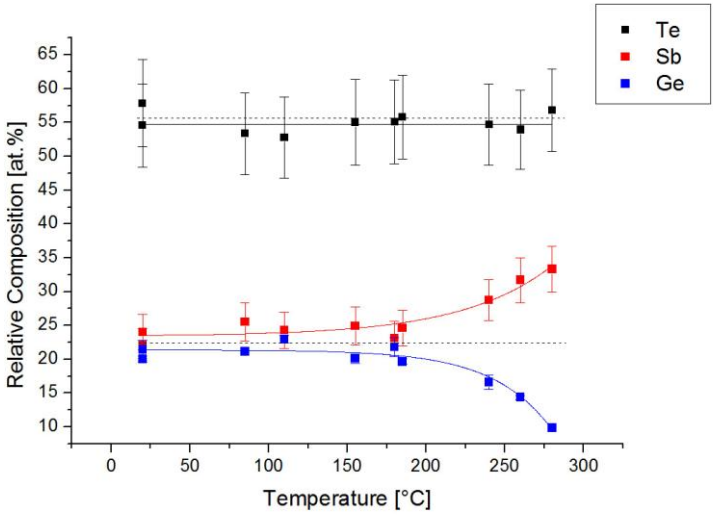

Figure 1. Comparison of chemical compositions from EDX measurements.

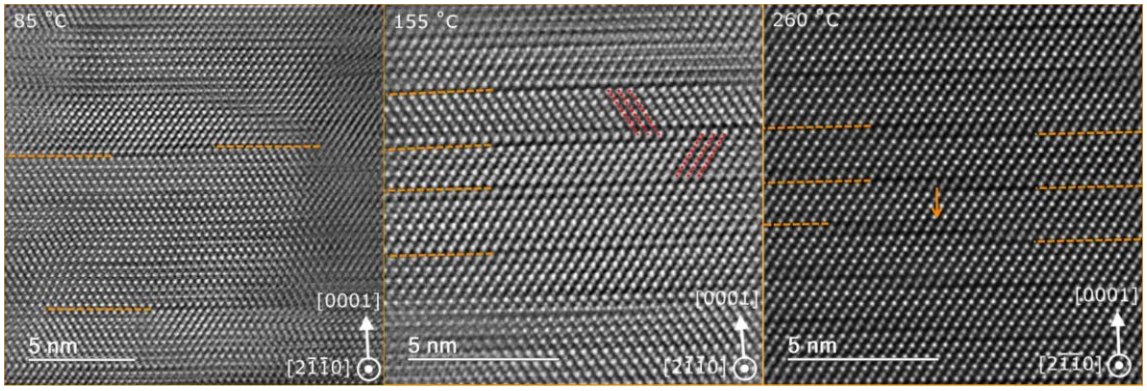

Figure 2. HAADF-STEM images of samples deposited onto BaF_2.

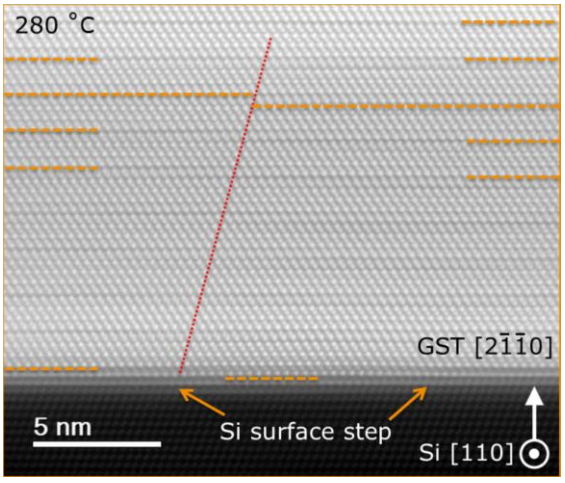

Figure 3. STEM image of GST-Si(111) interface.

Energy-Related Materials and Materials for Information Technology

MS3.P067
Influence of persistent resistance changes on structure and chemical composition of metal-$Pr_{1-x}Ca_xMnO_3$-metal thin film heterostructures observed in situ by TEM EELS

T. Kramer[1], M. Scherff[1], O. Janik[1], J. Hoffmann[1], C. Jooss[1]

[1]Georg-August-Universität Göttingen, Institut für Materialphysik, Göttingen, Germany

tkramer@ump.gwdg.de

Resistive switching phenomena are observed in many metal-oxide-metal thin film heterostructures. Application of an external voltage of the order of one volt between the facing metallic top and bottom electrode can change the initial virgin state resistance of the heterostructure to a high resistance state (HRS) or a low resistance state (LRS). The induced resistance change is persistent, i.e. the HRS or LRS remains after removing the applied bias. In order to microscopically explain the resistance changes, various models have been proposed, e.g., Mott transitions [1], Schottky barrier effects [2], trapping controlled space charge limited currents [3], or especially electro-chemical effects related to migration of oxygen cation vacancies [4,5]. In the latter case different types of distribution of the oxygen deficient regions are discussed. There are observations of a filamentary mechanism [6] or a concentration of oxygen vacancies near the top electrode [4].

We have selected the colossal resistance manganite $Pr_{1-x}Ca_xMnO_3$ (PCMO) sandwiched by precious metal electrodes (Pt, Au) as a model system for resistive switching. In this geometry PCMO provides two different types of switching which differ in polarity and magnitude. For PCMO a switching mechanism which is based on a redox reaction with the top electrode is known. In this case applying a positive bias at the top electrode induces an agglomeration of oxygen vacancies at the interface to the top electrode resulting in a HRS [4]. This switching polarity appears for non-precious top electrode materials. For precious metals oxides an inverted polarity in resistive switching is observed [7]. We suggest an oxygen vacancy migration in the PCMO layer from bulk to the interface with the top electrode as mechanism for this behaviour.

In order to observe the oxygen vacancy distribution we have done lateral resolved electron energy loss spectroscopy at Mangenese L-edge and Oxygen K-edge. The Intensity Ratio of Mn L3 and L2 peak changes with Mn valency [8] which are set in context to oxygen content by means of oxygen deficient bulk samples(see fig 2A). An even more sensible but not systematically observed probe for oxygen deficiency is the oxygen K-edge. Changes in oxygen content influences many features of the edge, e.g. intensity of the K_A, K_B and K_C feature or the position of the onset ([4] and see fig 2B).

The examined heterostructures were fabricated by Ion Beam Sputtering and patterned by means of a Focused Ion Beam system to two different geometries. On the one hand we have made “tooth like” lamellas (see fig 1A) used for electric stimulation in TEM experiments using a sample holder with a piezo-controlled nanotip.

To prevent contact resistance of the tip we have additionally designed a special set up of a lamella which is layed over a hole in SiN grid (see fig 1B). Electric contact is made via gold contacts made by optical lithography and a special TEM holder with electric lead through.

We will show investigations of structural and chemical responses on electrical stimulation corresponding to different resistance states. For this purpose we use a FEI Titan 80-300 ETEM [9]. It is equipped with an imaging aberration corrector and a high-resolution Gatan Imaging Filter (GIF), allowing experiments with sub-1Å resolution. The monochromator enables electron energy loss spectroscopy with 0.2 eV energy resolution.

1. R. Fors, et al, Phys Rev. B 2005
2. Ch. Jooss et al, Phys. Rev. B 2008
3. A. Odagawa et al, Phys. Rev. B 2004
4. H.S. Lee et al, Sci Rep 2013
5. Z. Liaoet al, J. appl. Phys. 2012
6. Y. Yang et al Sci Rep. 2013
7. J.-L. Gang et al Chen, Chin Phys Lett 2010

8. M. Varela et al, Phys Rev B 2009
9. We kindly acknowledge the funding of the State of Lower Saxony and the DFG

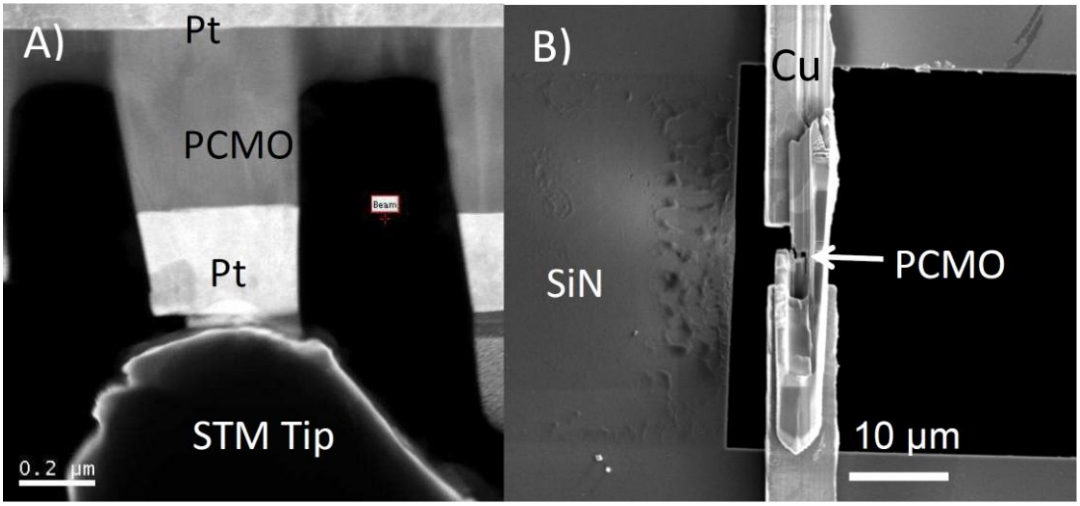

Figure 1. A) STEM ADF image of a contacted tooth for in situ EELS measurement B) SEM image of tipless set up prepared by FIB.

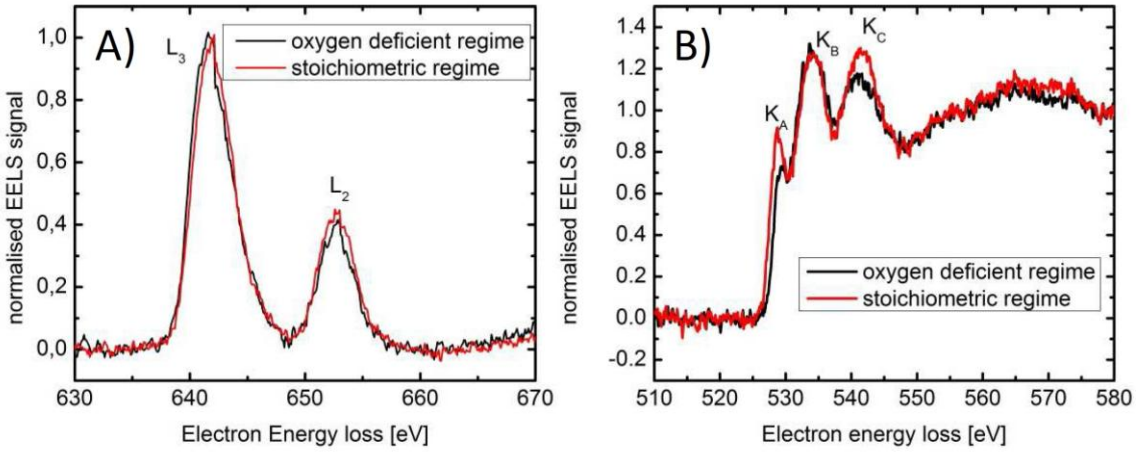

Figure 2. Comparison of EELS spectra of Mn L-edge and Oxygen K-edge of regimes in the same sample with and without oxygen deficiency; A) Background, Hartree-Slater corrected and normalized Mn L-edge: the integrated intensity ration L_3/L_2 is significantly higher in the oxygen deficient regime; B) Background corrected and normalized oxygen K edge: significant changes in intensity of K_A and K_B, as well as in position of the onset

Energy-Related Materials and Materials for Information Technology

MS3.P068
The formation of Si nanocrystals induced by CW laser annealing of silicon-rich silicon oxide

N. Wang[1], T. Fricke-Begemann[2], P. Peretzki[1], J. Ihlemann[2], M. Seibt[1]

[1]Georg-August-Universität Göttingen, IV. Physikalisches Institut, Göttingen, Germany
[2]Laser-Laboratorium Göttingen e.V, Department of Nanostructures, Göttingen, Germany

wang@ph4.physik.uni-goettingen.de

Crystalline silicon is not regarded as an adequate material for optical applications as it is an indirect-band gap semiconductor. One route to tailor optical properties of Si is the use of low-dimensional Si systems, whose optical properties have been related to various effects among which quantum confinement is the most obvious.[1,] Strong focus has been on the formation of nc- Si from Si-rich oxides (SiO_x, x~1) which decompose into the stable SiO_2 and nc-Si. Several methods are at hand that are suitable to transform SiO_x to nc-Si embedded in SiO_2, including thermal annealing[3] and annealing using pulsed laser sources[4]. Recently phase separation into SiO_2 and nc-Si using CW laser irradiation has been demonstrated for free-standing SiO_X films[5,6]. In this case, the preparation of free-standing films prevents the dissipation of heat to the substrate and ensures temperatures up to 1600°C and an efficient phase transition. In this work, we employ CW laser annealing at 405 nm wavelength to form nc-Si in SiO_x layers on a SiO_2 substrate and get a very strong structural effect during phase separation. Fused silica substrates are coated with a 530nm thick Si monoxide (SiO_x) layer by ion beam sputtering. CW laser irradiation is applied along a line by moving the sample during exposure to the laser beam, which is focused to a spot size of ~6 µm. The power of the laser is varied from 15 mW to 50 mW and the SiO_x surface is purged with nitrogen gas. Optical characterization yields strong photoluminescence signals from the irradiated areas in addition to damage formation at high laser power. For TEM investigations, focused ion beam (FIB, FEI Nova NanoLab 600) has been used to prepare cross-section samples. TEM analyses have been performed at 200kV in a Philips CM200 FEG-UT. Typical observations are summarized in Fig. 1 showing dark-field images obtained from a sample after irradiation at a laser power of 40mW. The low-magnification overview (top) shows the SiO_2 substrate (1), the SiO_x layer (2) with nc-Si indicated by the dashed lines and a highly damaged region (3). The details provided in the bottom images furthermore show the highly damaged region. Fig. 2 presents a HRTEM image showing nc-Si particles embedded in the amorphous Si oxide matrix. Chemical analysis using energy-dispersive x-ray spectrometry (EDX) is summarized in Fig. 3. The bright-field STEM image on the top left shows the main regions. The reduced total number of Si-K and O-K counts shown on the right hand side clearly shows that materials has been removed from region (3). The oxygen-to-Si ratio (bottom left) reveals regions (1) and (2) to be close to SiO_2 and SiO in composition, respectively, while the porous part (region 3) is close to SiO_2 implying that the oxygen depletion could not prevent oxidation of surface-near regions during laser irradiation. The chemical composition of the surface region might also be caused by thermodiffusion due to the laser generated temperature gradient, which is assumed to drive Si nanoclusters formed in the center of the laser beam to outer regions. Fig. 4 summarizes a systematic study of the power dependence of the thickness of the porous layer as measured by TEM. It is clearly seen that a critical laser power between 30 and 35mW exists, below which a damage-free laser irradiation is possible. Control experiments for laser powers of 30 and 25mW show that optically active Si-particles can be formed inside Si-rich SiO_x on SiO_2 substrates without the formation of porous surface-near regions.

1. W. L. Wilson et al., Science 262, 1242 (1993).
2. L. Pavesi, R. Turan (eds.): Si Nanocrystals - Fundamentals, Synthesis and Applications, Wiley VCH, Weinheim (2010).
3. B. Hinds et al., J. Vac. Sci. Technol. B Vol. 16, No. 4 (1998).
4. N. Tomozeiu, Appl.Surf. Sci. 253, 376 (2006).
5. L. Khriachtchev et al., Journal of Applied Physics, 108, 124301(2010).
6. T. Nikitin et al., Journal of Applied Physics, 111, 124302 (2012).
7. L. Khriachtchev, J. Electrochem. Soc. 159, K21 (2012).

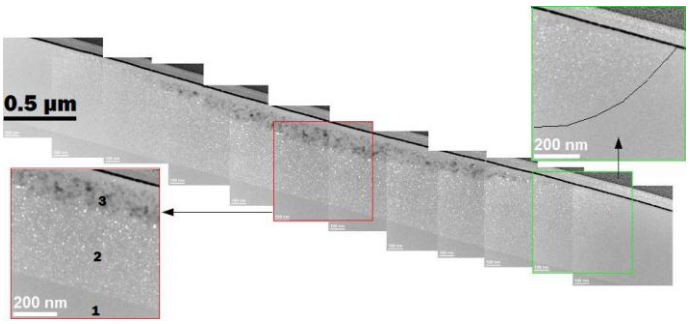

Figure 1. Conical dark-field image of a sample irradiated at 40 mW power.

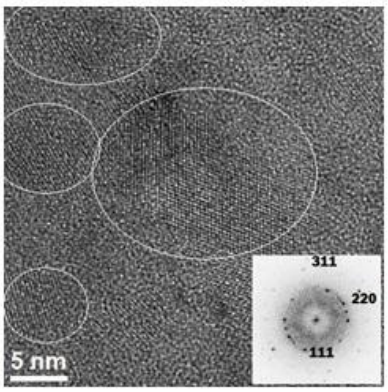

Figure 2. High-resolution image showing nc-Si embedded in amorphous Si oxide.

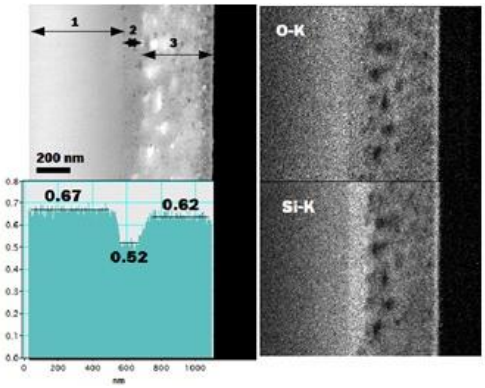

Figure 3. STEM and EDX analysis (for details, see text).

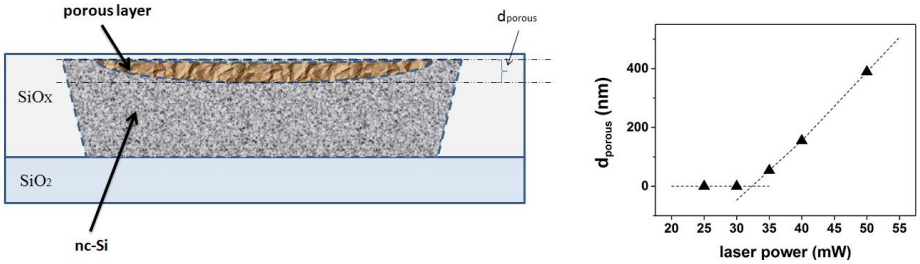

Figure 4. Dependence of damage formation on laser power. Left: schematic presentation of the sample microstructure showing the thickness d_{porous} of the damaged region. Right: experimental data of d_{porous} vs. the laser power.

Energy-Related Materials and Materials for Information Technology

MS3.P069
Structure determination of microcrystalline oxonitridosilicates and oxonitridoimidophosphates by combination of TEM and synchrotron methods

L. Neudert[1], F. Pucher[1], D. Durach[1], O. Oeckler[2], W. Schnick[1]

[1]LMU Munich, Department of Chemistry, Munich, Germany
[2]University Leipzig, IMKM, Leipzig, Germany

lukas.neudert@campus.lmu.de

Oxonitridosilicates doped with rare earth elements are important luminescence materials for phosphor-converted LEDs and the precise knowledge of their crystal structures is crucial to understand the properties. Yet, often the materials are obtained as microcrystalline samples that do not contain crystals suitable for conventional X-ray structure determination and the structures are often too complex for straightforward structure analysis using powder data. The same is true for many complex tetrahedral frameworks such as zeolites or oxonitridoimidophosphates. The latter are obtained by high-pressure synthesis which typically yields micro- or nanocrystallites. The situation is even more complicated if the samples are inhomogeneous. The combination of TEM and X-ray diffraction using microfocused synchrotron beams is an ideal approach to obtain precise structure data in such cases as exemplified in this contribution by two typical new compounds.

The structure of the oxonitridoimidophosphate $AlP_6(O,NH)_3N_9$ consists of a network built up from $P(O,N)_4$ tetrahedra whose topological arrangement is represented by the point symbol $\{3.6^5\}$ (Figure 1 left). $AlP_6(O,NH)_3N_9$ is the first oxonitridoimidophosphate that contains only one type of trivalent cation. In the microcrystalline sample obtained in a multi-anvil press at 6 GPa, electron diffraction (SAED) and EDX spectroscopy revealed lattice parameters and a chemical composition that did not match any known compound. A crystallite found by TEM was investigated with microfocused synchrotron radiation which yielded a first structure model. The presence of O was further evidenced by EELS. Superstructure reflections confirmed by SAED patterns and additional HRTEM investigations added important information to the X-ray diffraction study.

The new yellow phosphor $BaLa_3Si_5O_2N_9:Ce^{3+}$ crystallizes in a novel interrupted 3D network built up from SiN_4 and SiN_2O_2 tetrahedra (Figure 1 middle). Again, SAED and EDX proved that an unknown compound was present. Both methods were used in order to pre-characterize a crystallite for microfocus diffraction. In addition, Z-contrast (STEM-HAADF) images revealed direct structure information (heavy atom sites) and further showed real structure effects such as anti-phase domains specified by the anti-phase vector p = 1/4*b* along the anti-phase boundary (Figure 1 right). HRTEM imaging and corresponding simulations confirm the refined structure model. The distribution of elements with lacking scattering contrast such as O/N and Ba/La on mixed occupied sites were further analyzed by bond-valence sum calculations.

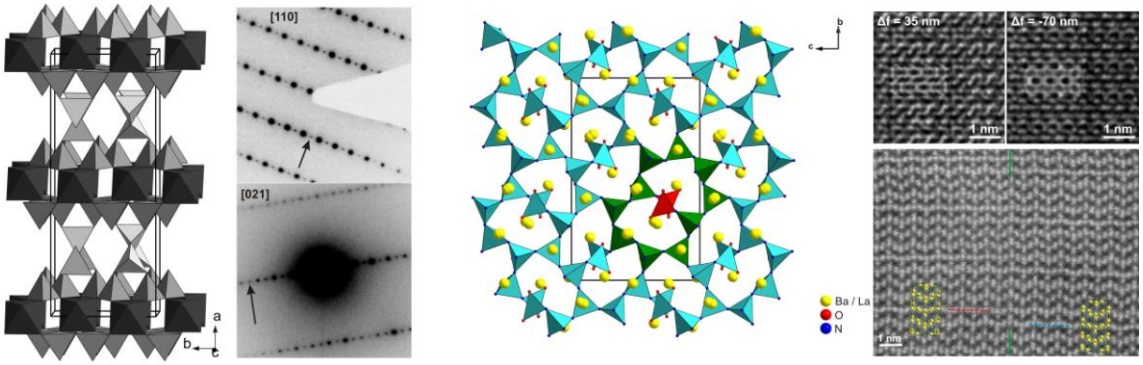

Figure1. left: structure of $AlP_6(O,NH)_3N_9$ (projection along [001], $Al(O,N)_6$ octahedra dark gray, $P(O,N)_4$ tetrahedra light gray) and SAED patterns with weak superstructure reflections (highlighted with black arrows),middle: structure of $BaLa_3Si_5O_2N_9:Ce^{3+}$ (projection along [100]), right: HRTEM images with simulations (insets) and STEM-HAADF images indicating anti-phase boundary (green lines).

Metals, Alloys and Intermetallics

MS4.070
Hierarchical microstructure of ferritic superalloys

C. Liebscher[1], V. Radmilovic[2], U. Dahmen[3], M. Asta[4], G. Ghosh[5]

[1]Max-Planck Institut für Eisenforschung GmbH, Structure and Nano-/Micromechanics of Materials, Düsseldorf, Germany
[2]University of Belgrade, Nanotechnology and Functional Materials Center, Belgrade, Serbia
[3]Lawrence Berkeley National Laboratory, National Center for Electron Microscopy, Berkeley, United States
[4]University of California, Berkeley, Department of Materials Science and Engineering, Berkeley, United States
[5]Northwestern University, Department of Materials Science and Engineering, Evanston, United States

liebscher.ch@gmail.com

The increasing needs for energy security, sustainable energy resources and reduced emission of carbon dioxide are the driving forces for the development of new processes and materials for energy generation. Promising alternatives for material replacements of nickel-based superalloys in ultra-supercritical steam turbines are precipitation strengthened ferritic superalloys [1,2].

A new class of ferritic alloys with hierarchical microstructure will be presented, were the bcc-Fe matrix is strengthened by coherent, two-phase $L2_1$-Ni_2TiAl / *B2*-NiAl precipitates. Electron diffraction, diffraction contrast imaging and aberration corrected high-resolution transmission electron microscopy (TEM) techniques are applied to study the underlying phase transformation pathways leading to the hierarchical microstructure. The early stages of microstructural evolution are investigated in the as-quenched condition and the subsequent solid-state aging heat treatment. Two alloy systems with varying Ti level of 2 and 4 wt.% are investigated.

For the alloy with 2 wt.% Ti, spherical *B2*-NiAl precipitates are forming in the bcc-Fe matrix following rapid solidification. In the course of the aging heat treatment at 700 ºC for 10 h the $L2_1$-ordered Ni_2TiAl phase is nucleating exclusively within the *B2*-NiAl primary precipitates. The corresponding microstructure is exhibiting three types of hierarchy: (i) A structural hierarchy due to chemical ordering with a chemically disordered matrix of bcc-Fe (A2), the nearest-neighbor (NN) ordered *B2*-precipitates (NiAl-type) and the next nearest-neighbor (NNN) ordered $L2_1$-precipitates (Ni_2TiAl-type) within *B2*, (ii) A dimensional hierarchy with a continuous bcc-Fe matrix coherently embedded *B2*-precipitates with a size range of 60-200 nm and the coherent precipitate substructure of $L2_1$-phase and dimensions of 15-20 nm. (iii) A spatial hierarchy where *B2*-precipitates are embedded in the bcc-Fe matrix and $L2_1$-precipitates nucleate and grow only within B2-precipitates. In addition, it is verified that the interface between *B2* and $L2_1$ is coherent and adopts a diffuse interface profile [3].

By increasing the overall Ti content to 4 wt.%, $L2_1$-Ni_2TiAl precipitates are forming in the bcc-Fe matrix after the quench. An internal network of ½<100> antiphase domain boundaries (APB) is revealed within the Ni_2TiAl-precipitates by diffraction contrast imaging. After solid-state aging for 3 h at 700 ºC the wetting of initial APBs by the *B2*-NiAl phase is confirmed using aberration-corrected STEM. The *B2* wetting layer is growing in width to ~7 nm after aging for 10 h at 700 ºC. The interfacial alignment for the corresponding phases is observed to be in a cube-on-cube orientation [4].

Figure 1 shows a comparison of the two-phase precipitate structure of the alloys with 2 and 4 wt.% Ti after 10 h of aging at 700 ºC. The underlying images are elemental maps of Fe (blue), Ni (red) and Ti (green) obtained by energy-filtered TEM.

1. Sun Z, Liebscher CH, Huang S, Teng Z, Song G, Wang G, Asta M, Rawlings M, Fine ME, Liaw PK. Scr Mater 2013;68:384.
2. Vo NQ, Liebscher CH, Rawlings MJS, Asta M, Dunand DC. Acta Mater 2014;71:89.
3. Liebscher CH, Radmilovic VR, Dahmen U, Vo NQ, Dunand DC, Asta M, Ghosh G. Acta Mater 2015, accepted.
4. Liebscher CH, Radmilovic V, Dahmen U, Asta M, Ghosh G. J Mater Sci 2012;48:2067.

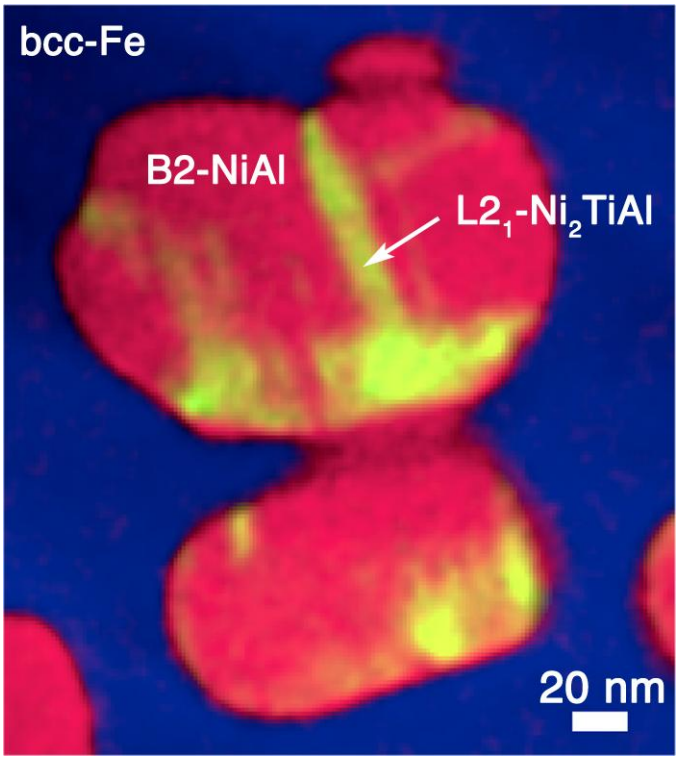

Figure 1. Two-phase precipitate structure after aging for 10 h at 700 ºC for the alloy with a) 2 wt.% Ti and b) 4 wt.% Ti. The underlying images are elemental maps of Fe (blue), Ni (red) and Ti (green) obtained by the three-window method utilizing the Fe-L_{23}, Ni-L_{23} and Ti-L_{23} edges respectively.

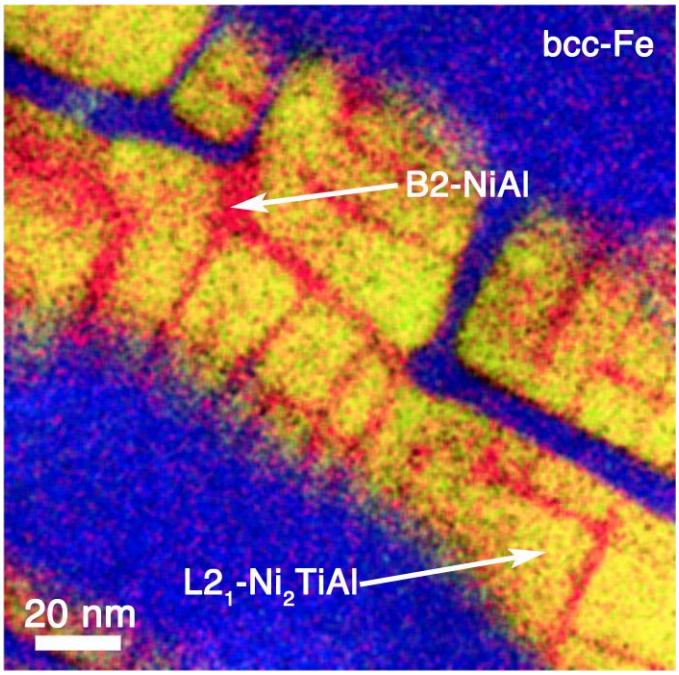

Metals, Alloys and Intermetallics

MS4.071
Observation of deformation induced redistribution of chromium and carbon in bearing steel

A. Diederichs[1], A. Schwedt[1], D. Park[1], M. Herbig[2], J. Mayer[1]

[1]Gemeinschaftslabor für Elektronenmikroskopie, Aachen, Germany
[2]Max Planck Institut für Eisenforschung, Düsseldorf, Germany

diederichs@gfe.rwth-aachen.de

Dissolution of carbides and formation of nanocrystalline structures in steels is a known degradation phenomenon in technical applications such as steel rail tracks [1], where the material is exposed to cyclic loading and fatigue. Similar features have been observed in the surrounding of nanocrystalline white etching areas (WEA) that form in 100Cr6 bearing steel used in wind turbines [2]. The reason behind formation of white etching areas in bearing steels and the role of the carbide degradation is not well understood, since the load situation in bearings is complicated and the characterization of the degraded microstructure and the movement of carbon and alloying elements from the carbides into the white etching areas is a challenging field for conventional microscopy techniques.

Electron-microscopy investigations with SEM and TEM of nanocrystalline structures in 100Cr6 bearings provide information about the behaviour of carbides under high loads and cyclic stress and show indications for a deformation induced dissolution. The analysis of dissolving carbides and recrystallized grains inside the WEA can give new information about loads and temperatures within WEA. The inhomogenous distribution of chromium within WEA as a result of deformation induced carbide dissolution has been revealed, but no differences in lattice parameters have been found with diffraction analysis for the different microstructures within WEA. (cf.fig.1)

Atom probe has been applied on pre-investigated regions as a promising technique for a spatially resolved compositional analysis, which was able to show the redistribution of carbon and the alloying elements on the atomar scale within the nanocrystalline WEA. Atom probe investigations of different regions within WEA show the formation carbon cell structures (cf.fig.2), which seem to match with observed grain sizes in WEA. It has been demonstrated, that the dissolution of carbides plays a role in the formation of WEA in bearing steels, since the carbides are the source for the WEA stabilizing carbon.

1. [TAK10] Takahashi, J., K. Kawakami, and M. Ueda. "Atom probe tomography analysis of the white etching layer in a rail track surface." *Acta Materialia* 58.10 (2010): 3602-3612.
2. [WES13] West, O. H. E., et al. "Application of Complementary Techniques for Advanced Characterization of White Etching Cracks." *Practical Metallography* 50.6 (2013): 410-431.

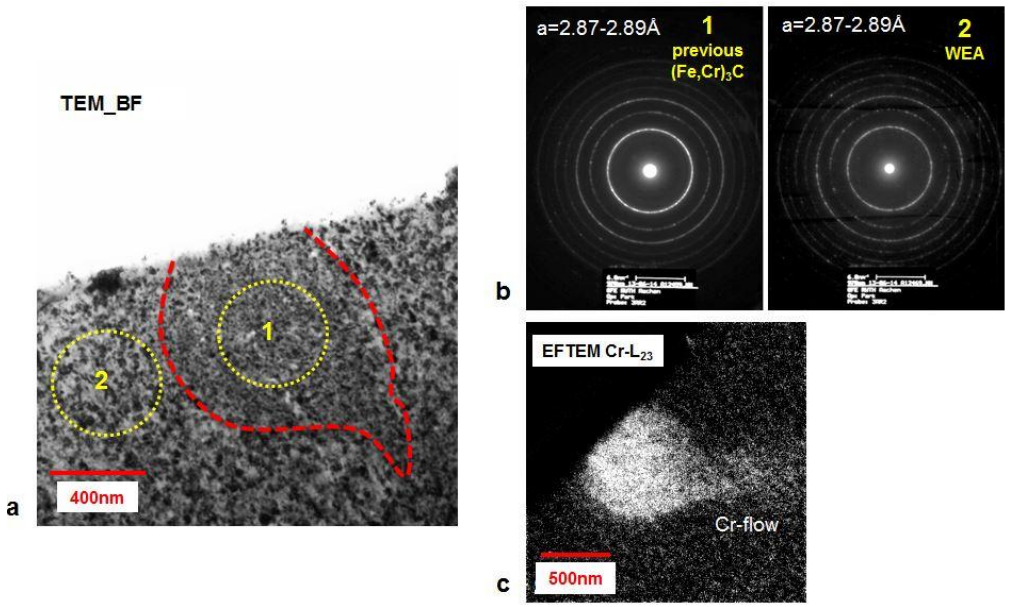

Figure 1. a) TEM Bright Field image of a previous carbide (marked in red) within the nanocrystalline WEA, regions for diffraction analysis are marked in yellow. b) Diffraction patterns of region 1 and 2 marked in a). A significant difference in the lattice parameter can not be observed. c) Magnified Cr-EFTEM Mapping of the previous carbid shows a smear flow of chromium.

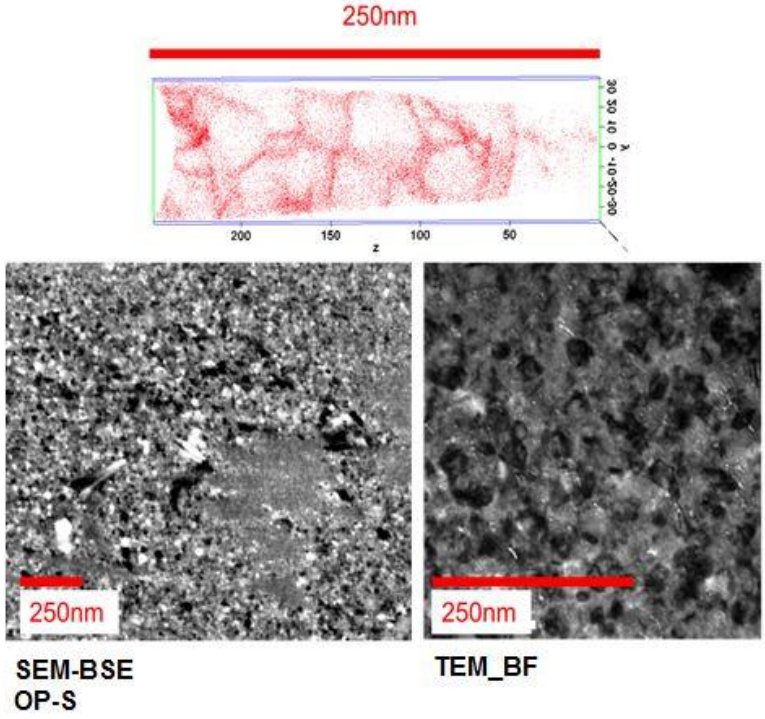

Figure 2. top: reconstruction of an atom probe measurement for a nanocrystalline WEA. Carbon atoms are shown in red and seem to be segregated in cells of different sizes. bottom left: SEM orientation contrast image shows different grain sizes within a WEA. bottom right: TEM Bright Field image shows fine grains within a nanocrystalline WEA.

Metals, Alloys and Intermetallics

MS4.072
Imaging nanostructured materials using STEM diffraction mapping

C. Gammer[1,2]

[1]University of Vienna, Vienna/Austria, United States
[2]Lawrence Berkeley National Laboratory, Berkeley, CA, United States

christoph.gammer@univie.ac.at

Conventional TEM is routinely used to study structural properties of metallic materials with nanometer resolution by combining diffraction and imaging techniques. Alternatively, ADF-STEM uses a converged scanning beam and an annular detector and can be used to image defects in metallic materials using diffraction contrast [1]. Still, in both TEM and STEM the possible images that can be formed are limited by the physical shapes and sizes of the apertures or detectors.

The present work shows that acquiring a STEM diffraction map can overcome these limitations by creating a rich diffraction-based dataset that can be analyzed in multiple ways after the experiment [2]. The main practical limitation for STEM diffraction mapping is the speed of the electron detector. Therefore, a Gatan K2 IS direct detection camera operating at a frame rate of 400 f/s is used. To evaluate the large datacube, custom DigitalMicrograph scripts were written. In order to demonstrate the technique, a precipitation strengthened and creep deformed ferritic alloy with a complex microstructure is used. The microstructure consists of a bcc-Fe matrix and smaller B2-NiAl precipitates. Figure 1 shows the experimental setup. An ADF-STEM is acquired (cf. Fig. 1a) and in addition a diffraction pattern is recorded for every probe position. By calculating the mean intensity for a virtual aperture at each probe position, a virtual dark-field image is reconstructed. In the present case, selecting a superlattice reflection reveals the ordered precipitates in the alloy (cf. Fig. 1b). Once the dark-field image is obtained, a virtual selected area aperture can be placed in any region of the image and the respective diffraction pattern is calculated by summing all diffraction patterns from that region. Fig. 1c shows the diffraction pattern corresponding to an ordered precipitate. The major advantage is that arbitrarily shaped virtual apertures can be designed according to the underlying crystal structure in order to optimize the image contrast. Examples of such virtual apertures will be presented.

The dataset acquired by STEM diffraction mapping contains very rich information on the local structure of the material and can not only be used for phase or orientation mapping but can even be used to generate strain maps by measuring the distance between diffracted peaks [3]. STEM diffraction mapping is well suited to measure nanoscale strain in metallic materials as it does not rely on a field of view with a single well-aligned zone axis condition. The application to highly defected materials will be presented, where strain mapping techniques based on high-resolution or diffraction contrast would fail. STEM diffraction mapping can also be combined with in-situ microscopy. It will be demonstrated how novel fast electron detectors enable real-time collection of diffraction maps at sufficient speeds to carry out diffraction mapping during continuous in-situ deformation.

It is envisioned that the recent interest in large data paired with novel ultrafast detector development will enable collecting multiple signals in parallel and generating multiple quantitative images after the experiment.

We acknowledge support by the Austrian FWF [J3397], and the Molecular Foundry, Lawrence Berkeley National Laboratory, U.S. Dept. of Energy Contract #DE-AC02-05CH11231.

1. P. Phillips, M. Brandes, M. Mills and M. DeGraef. Ultramicroscopy 111 (2011) 1483.
2. C. Gammer, V.B. Ozdol, C.H. Liebscher and A.M. Minor. Ultramicroscopy (2015) in press.
3. V.B. Ozdol, C. Gammer, M.C. Sarahan and A.M. Minor. Microsc. Microanal. 20 Suppl.3 (2014) 1046.

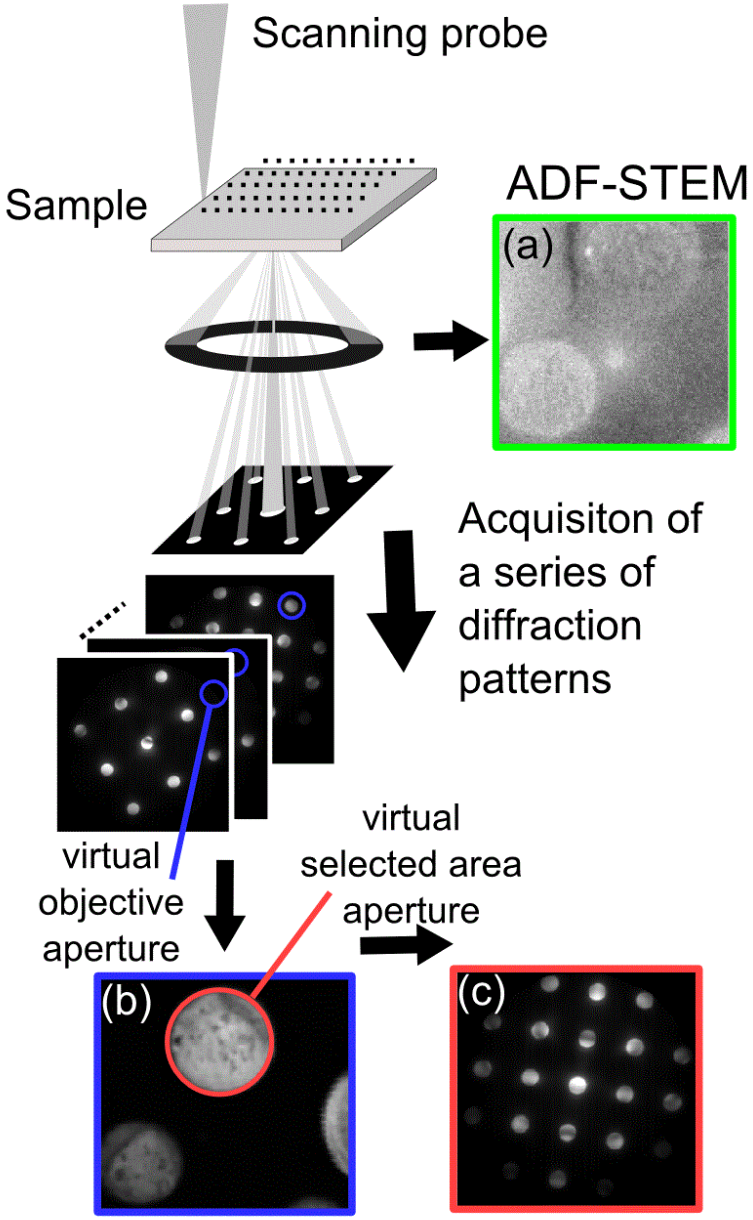

Figure 1. STEM diffraction mapping: (a) An ADF-STEM image is acquired and a diffraction pattern is recorded for every probe position. (b) By calculating the mean intensity in a virtual objective aperture (blue circle) for every probe position, a virtual dark-field image is reconstructed. (c) Selecting a certain area in the image and summing all corresponding diffraction patterns allows setting a virtual selected area aperture.

Metals, Alloys and Intermetallics

MS4.073
High-resolution in-situ study of metadislocation motion in the complex metallic alloy T-AlMnFe

M. Heggen[1], M. Feuerbacher[1]

[1]Forschungszentrum Jülich GmbH, Ernst Ruska Centre, Jülich, Germany

m.heggen@fz-juelich.de

Complex Metallic Alloys (CMAs) represent a large group of crystalline intermetallics comprising some hundreds of known phases in various alloy systems. They are characterized by the presence of icosahedral atom coordination, large lattice constants, and a correspondingly large number of atoms per unit cell, typically ranging between a few tens and some thousands [1]. CMAs have attracted increasing research interest and exceptional properties have been found [e.g. 2]. Several CMAs also show unusual plastic properties, the occurrence of new mechanisms of plastic deformation and novel defects [3]. Most prominent among those novel defects are metadislocations [3,4]. Metadislocations are exceptionally complex defects as they involve several hundreds of atoms in their core. They are partial dislocations which are not associated to conventional planar defects but to slabs of a structurally transformed complex phase or a certain number of so-called phason planes. Metadislocations were observed in several CMA phases like e_6- and e_{28}-AlPdMn [3,4], $Al_{13}Co_4$ [5,6], T-AlMnFe, and T-AlMnPd [7,8].

In this contribution, we present a high-resolution in-situ microstructural analysis of metadislocation motion in the CMA phase T-AlMnFe. A focussed-ion-beam specimen was heated in-situ using a MEMS based double-tilt heating holder (DENSsolutions, Delft, NL). Metadislocation motion occurs due to thermally-induced stresses at above 600°C. The in-situ analysis shows that metadislocation motion takes place along the [1 0 1] direction as a two-step process involving discrete unit-cell jumps. The in-situ work is supplemented by ex-situ analysis of the metadislocation-core and stacking-fault structure using aberration-corrected high-angle annular dark field scanning transmission electron microscopy (HAADF-STEM). The observed deformation mechanism is closely related to previously observed deformation mechanisms in the CMA phases T-Al-Mn-Fe and T-Al-Mn-Pd, which are based on the movement of a metadislocation core mediating strain and separate escort defects [7]. Upon deformation, the escort defects move ahead and locally transform the T-phase structure for accommodation of the dislocation core (Figure 1 b). Dislocation core and escort defects leave a slab of a modified structure which can be interpreted as a stack of stacking faults. Different types of metadislocations with Burgers vectors scaled by the irrational number tau are found [8]. They are associated to two, four and six planar faults, respectively. This mechanism implies the coordinated movement of hundreds of atoms per elementary step. Another very comparable mechanism involving metadislocation and escort defect motion was recently found in the complex phase o-$Al_{13}Co_4$ [5,6]. Here, two types of dislocations with six and four stacking faults are found, respectively.

1. K Urban, M Feuerbacher, J. Non Cryst. Sol. **334** (2004), p. 143.
2. M Armbrüster et al., Nature Materials **11** (2012), p. 690.
3. M Feuerbacher, M Heggen, „Dislocations in Solids: Metadislocations“ Vol 16. ed. J.P. Hirth and L. Kubin, (Elsevier, Amsterdam) p. 110.
4. H Klein, M Feuerbacher, P Schall, K Urban, Phys. Rev. Lett. **82** (1999), p. 3468.
5. M Heggen, M Feuerbacher, Mat. Res. Lett. (2014) DOI: 10.1080/21663831.2014.882869.
6. M Heidelmann, M Heggen, C Dwyer, M Feuerbacher, Scripta Materialia (2015) 98, p. 24.
7. M Heggen, L Houben, M Feuerbacher, Nature Materials **9** (2010), p. 332.
8. M Heggen, L Houben, M Feuerbacher, Acta Mater. **59** (2011), p. 4458.

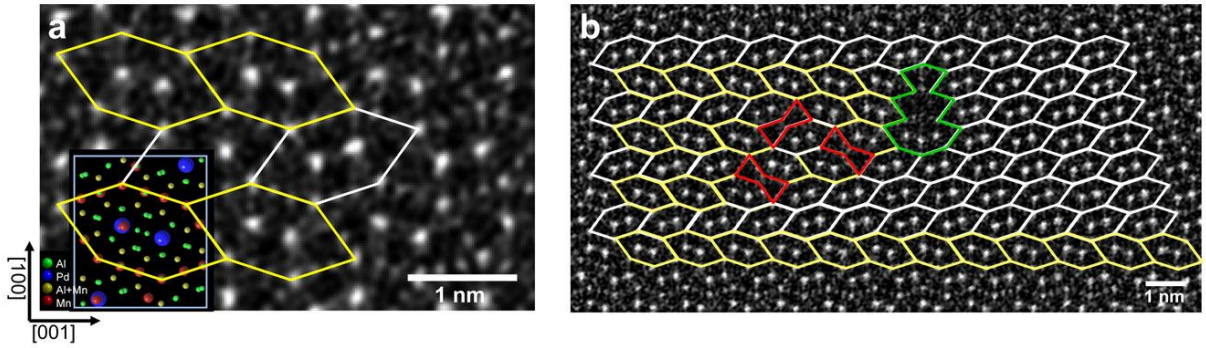

Figure 1. a) HAADF-STEM micrograph and model of T-AL-Mn-Pd along (0 1 0). The orthorhombic structure can be divided into structural subunits (white and yellow rhombs). b) Metadislocation in the T-phase. The dislocation core (green polygon) is escorted by three additional defects (red polygons). Upon movement, they leave a slab of a modified structure (parallelly oriented white rhombs) [7].

Metals, Alloys and Intermetallics

MS4.074
Probing structural order in a deformed metallic glass by fluctuation electron microscopy

V. Schmidt[1], H. Rösner[1], M. Peterlechner[1], P. Voyles[2], G. Wilde[1]

[1]Westfälische Wilhelms-Universität Münster, Institute of Material Physics, Münster, Germany
[2]University of Wisconsin-Madison, Materials Science and Engineering, Madison, United States

vitalij.schmidt@uni-muenster.de

Metallic glasses exhibit superior mechanical properties like high hardness or wear and corrosion resistance. However after a large elastic regime they are prone to catastrophic failure especially under tensile load. This motivates an interest in understanding the deformation behavior. For temperatures well below the glass transition and at high strains the plastic flow is restricted to narrow areas that are termed "shear bands". They are associated with a structural changes (free volume) compared to the surrounding matrix due to shear localization. Thus modifications of the local short- or medium-range order (SRO, MRO) are expected in shear bands.

Melt-spun and subsequently cold-rolled $Al_{88}Y_7Fe_5$ ribbons were prepared for transmission electron microscopy (TEM) by electro-polishing. The thin foils exhibit shear bands with contrast changes along their propagation direction observed by high angle annular dark-field scanning TEM (HAADF-STEM) [1].

In order to study directly the structural changes associated with the contrast variations in shear bands, fluctuation electron microscopy (FEM) has been used to characterize the deformed metallic glass samples by analyzing sets of nanobeam-diffraction patterns. The variance of the individual diffraction patterns was extracted from azimuthal profiles as shown in figure 1. The resulting profiles give a measure for the SRO/MRO present in the different shear band segments. From the same sets of diffraction patterns virtual dark-field images are generated to estimate the size of the ordered regions in real space. Such an image is shown for the dark shear band in figure 2. The obtained results reveal a complex stsructural variety within the shear bands of a given material that is discussed concerning the underlying physical mechanisms that govern shear band initiation as well as slip along existing shear bands.

1. H. Rösner, M. Peterlechner, C. Kübel, V. Schmidt, and G. Wilde, Ultramicroscopy **142**, 1 (2014).
2. T. L. Daulton, K. S. Bondi, and K. F. Kelton, Ultramicroscopy **110**, 1279 (2010).

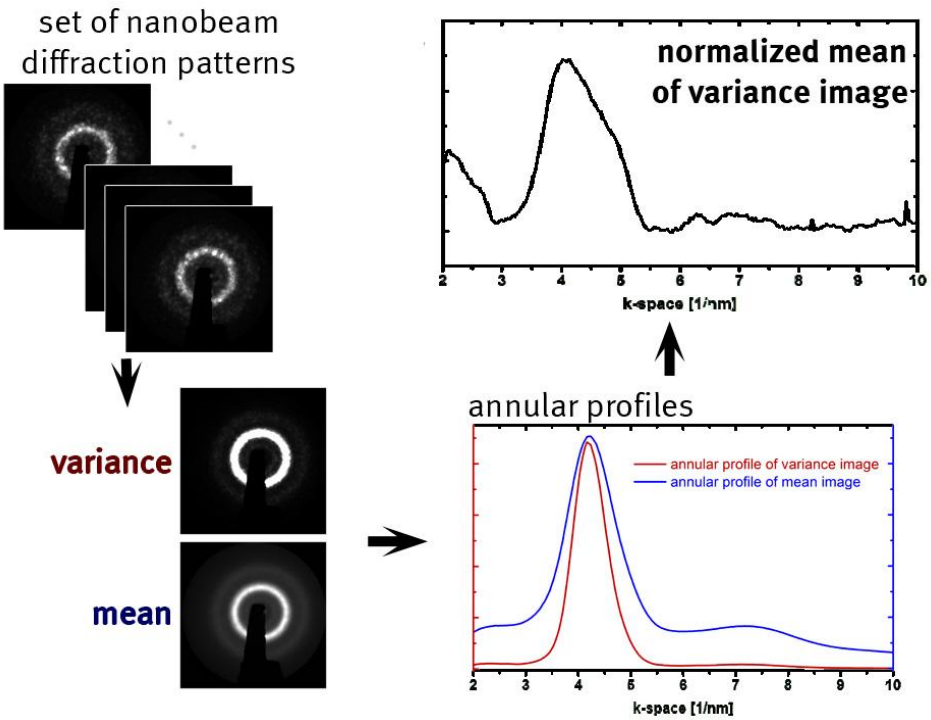

Figure 1. Scheme of the procedure to calculate the normalized mean of variance image as described by Daulton, Bondi and Kelton [1]. From the set of nanobeam diffraction patterns we calculate pixel by pixel a variance as well as a mean image. Afterwards the annular profile is extracted and the by dividing the variance by the mean squared we obtain the normalized mean of variance image.

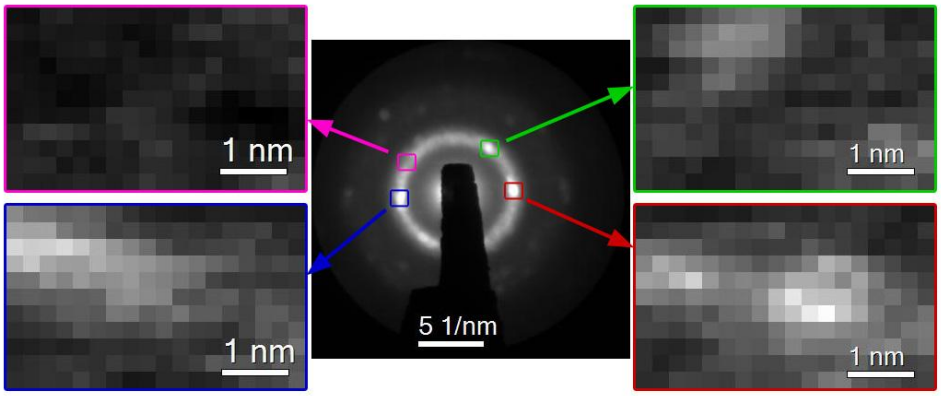

Figure 2. Virtual dark-field images extracted from the mean (central image) of a set of diffraction patterns of a dark shear band. The diffraction pattern shows an amorphous phase with brighter reflections indicating MRO. The regions of interest are indicated in k-space by the colored boxed. The colors of the frames indicate the related virtual dark field images.

Metals, Alloys and Intermetallics

MS4.075
Grain boundary density determined from simulated HAADF-STEM

Y. Buranova[1], H. Rösner[1], S. V. Divinski[1], G. Wilde[1]

[1]Westfälische Wilhelms-Universität Münster, Institut für Materialphysik, Münster, Germany

buranova.yulia@gmail.com

Grain boundaries have a significant impact on a wide range of physical properties of polycrystalline materials due to their specific atomic structure. It is assumed that the grain boundary excess volume plays an important role since it can directly be related to the grain boundary energy and has thus a significant influence on the transport and thermodynamic properties (diffusion/segregation). The excess volume of different GBs was calculated but not measured so far [1-2].

In the present study, we describe an approach to determine the density changes from simulated HAADF-STEM images of individual GBs and subsequently to calculate the corresponding excess volume. For this purpose, symmetrical tilt GBs with zone axes along the [100], [110] and [111] directions have been generated using molecular dynamics simulation (applying the LAMMPS software [3]) which were taken as input for the simulation of HAADF-STEM images using the Kirkland code [4, 5]. Parameters of transmission electron microscope (Zeiss Libra 200FE) were employed for the micrographs simulation.

It was found that the reduced local mass-density change, $\Delta\rho/\rho$, is proportional to the change of the corresponding intensities of the HAADF-STEM signal (Fig. 1):

$$\Delta\rho/\rho=\Delta\langle I\rangle/(\langle I\rangle)=(\langle Igb\ \rangle-\langle I\rangle)/(\langle I\rangle)=(I(x)-Io\ (x))/(Io\ (x)\ )\quad (1)$$

where ρ is the mass-density of a defect-free crystal area, $\langle I\rangle$ is the average intensity of the HAADF-STEM image of a low-indexed zone axis corresponding to a defect-free area of the grain interior and $\langle I_{gb}\rangle$ is the averaged intensity of a GB area. $I(x)$ and $I_0(x)$ are smooth functions, fitted to the given intensity plot. Using equation (1) the relative GB densities, $\Delta\rho/\rho$, have been calculated from the ratios of the GB area and grain interiors intensities. The results are displayed in Fig.2. The maximal relative density change for a high-angle GB has been estimated to be about 5%. For small misorientation angles, this value tends to zero. The relative density change is roughly proportional to the misorientation angle up to a misorientation of about 15°.

1. HB Aaron, GF Bolling, Surf. Sci. 31 (1972) p. 27.
2. D Wolf, Scripta Metall. 23 (1989) p. 1913.
3. S Plimpton, J Comp Phys. 117 (1995) p.1
4. DL Olmsted, SM Foiles, EA Holm Acta Mater. 57 (2009) p. 3694.
5. EJ Kirkland: Advanced computing in electron microscopy. 2nd ed. New York, Springer (2010).

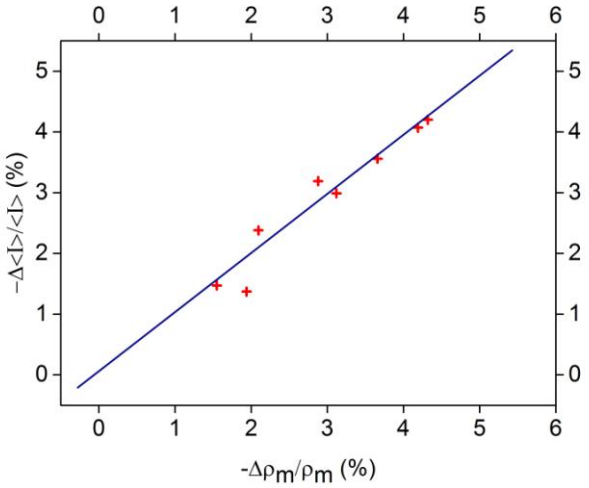

Figure 1. The intensity change of the HAADF-STEM images, $\Delta\langle I\rangle/\langle I\rangle$, as a function of the corresponding mass density. The solid line corresponds to the dependence $\Delta\langle I\rangle/\langle I\rangle=\Delta\rho_m/\rho_m$.

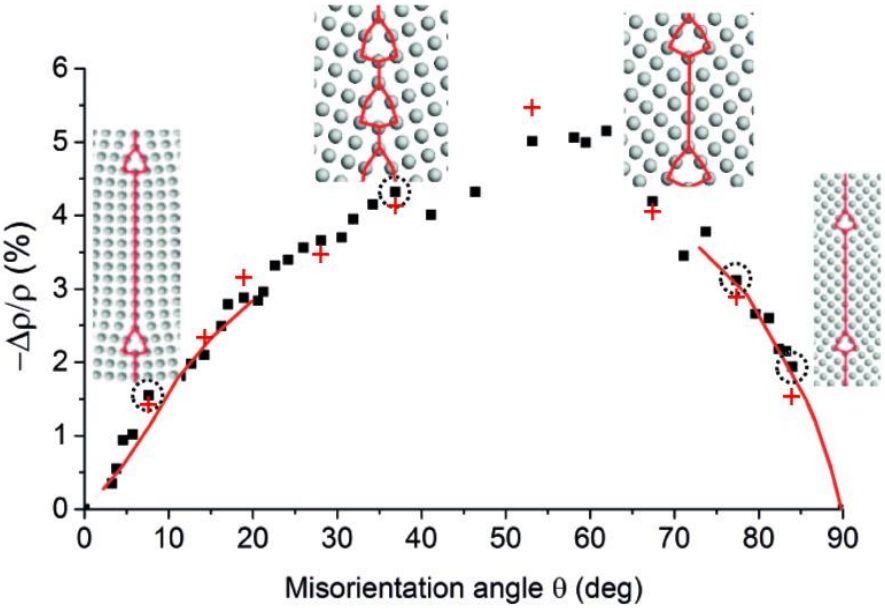

Figure 2. Relative GB density, Δρ/ρ, versus the misorientation angle, θ, for different types of symmetrical [100] tilt GBs measured from MD simulations (black squares) and from simulated HAADF-STEM images (red crosses). Solid lines represent the least squares fits to the data points. The structures of selected GBs (encircled symbols) are shown as insets.

Metals, Alloys and Intermetallics

MS4.076
Correlative microscale and atomic scale characterization of individual defects and interfaces in Ni-base superalloys

J. Müller[1], E. Spiecker[1]

[1]Institute of Micro- and Nanostructure Research, Erlangen, Germany

jul.mueller@fau.de

High resolution investigations generally lack the information of how defects or interfaces were integrated in the microstructure before TEM sample preparation making the significance of such investigations often questionable. The present work introduces an innovative focused ion beam (FIB) preparation method which overcomes this problem. As illustrated in figure 1 for the case of a dislocation, identification of the defect in a conventional TEM sample is followed by site-specific preparation of an ultra-thin FIB cross section containing the same defect in end-on orientation for high resolution analysis. Following this procedure the microstructure can be investigated on a larger scale by conventional TEM or STEM to identify and select individual characteristic dislocations. After preparation of the thin cross-section sample, the core configuration of the same dislocation can then be analyzed on atomic scale.

The feasibility of the procedure is demonstrated with two applications: (i) the investigation of the atomic core structure of a pre-characterized superdislocation in a creep-deformed Ni-base superalloy (figure 2 a,c)) and (ii) the analysis of the interface width of a γ/γ' interface in an undeformed Ni-base superalloy (figure 2 b,d).

In the first case conventional diffraction contrast and large angle convergent beam electron diffraction (LACBED) (not shown) revealed that the superdislocation is of type <100>(cf. Ref. [1]). Afterwards, the sample has been cut in a way as indicated by the red rectangle to obtain an ultra-thin lamella suitable for high resolution imaging of the dislocation core in end-on orientation. It was found that the dislocation core comprises two 60° dislocations with non-equal Burgers vectors of type 1/2<110> which are expected to jointly shear the γ'-phase by a combined glide and climb process [2].

In the second example the width of a γ/γ' interface has been investigated. Even for very thin samples high resolution studies often overestimate the interface width due to projection effects resulting from local inclination of the interface. To minimize such projection effects an interface which is well-aligned along the <010> direction was chosen beforehand in a plan-view sample (fig. 2b) by accurate correlation of the microstructure images to the <100> zone axis diffraction pattern (not shown). After FIB preparation the interface width has been measured from a HRSTEM image (fig. 2d). The analysis revealed that the structural transition from the γ- to the γ'-phase is extremely sharp and takes place within one unit cell of the fcc crystal structure.

The authors gratefully acknowledge financial support by the German Research Foundation (DFG) through the collaborative research center SFB-TR 103 (project A7) and the research training group 1229. They further thank Leonardo Agudo for providing TEM samples.

1. J. Müller, G. Eggeler, E. Spiecker, Acta Mater. 87, 34 (2015)
2. G. Eggeler, A. Dlouhy, phys. stat. sol. (a) 149, 349 (1995)

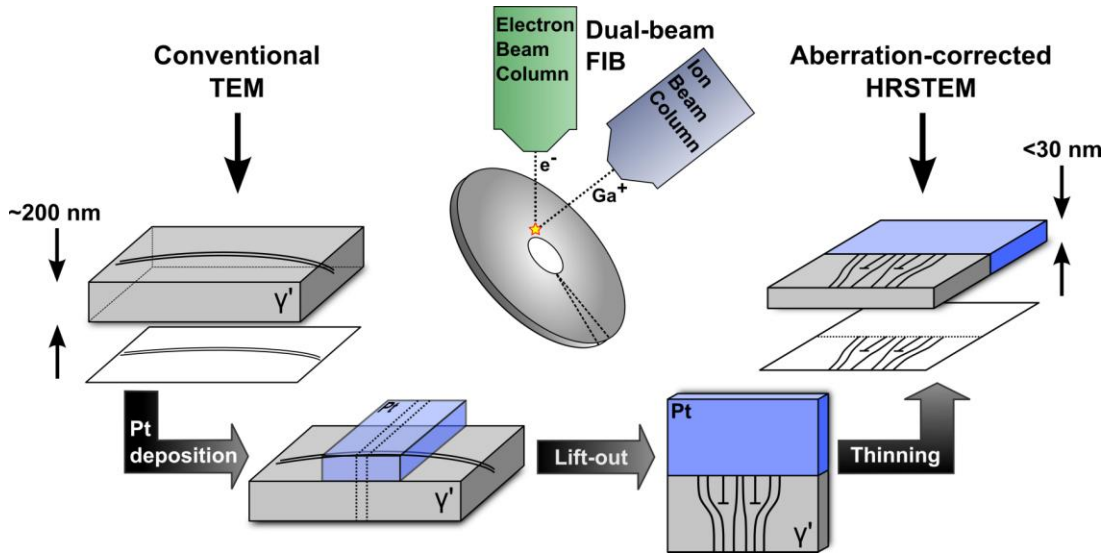

Figure 1. Illustration of the general procedure for preparation of an ultra-thin TEM lamella from a conventional TEM foil for a combined microscale and atomic scale characterization of extended defects (example of dislocation).

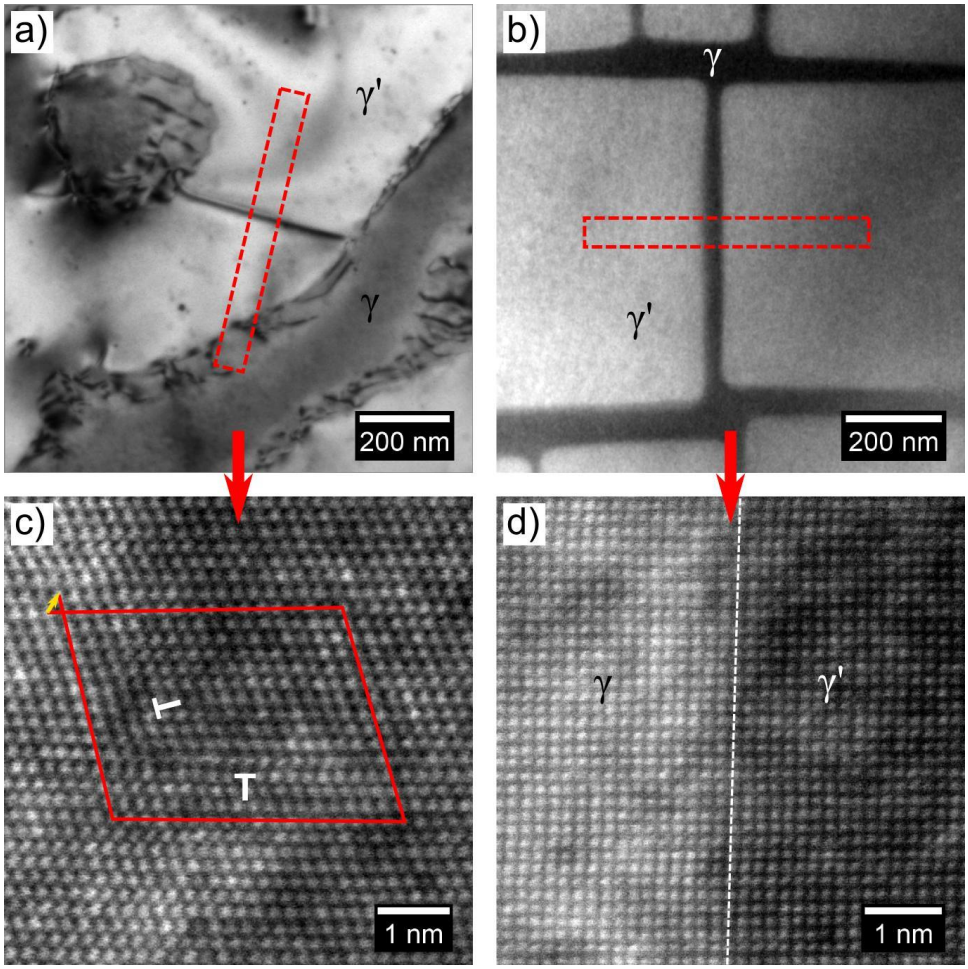

Figure 2. Application of the technique: a, c) Conventional TEM image ofsuperdislocation in a plan-view sample and HRSTEM image of the core structure of the same dislocation after site-specific cross-section preparation. b, d) Identification of a well-aligned γ/γ' interface by conventional TEM and HRSTEM analysis of the interface width with minimized projection effects.

Metals, Alloys and Intermetallics

MS4.P077
In-situ observation of grain growth in nanocrystalline palladium during heating using ACOM-STEM

K. K. Neelisetty[1], A. Kobler[1], K. Chakravadhanula[1], T. Scherer[1,2], H. Hahn[1], C. Kübel[1,2]

[1]KIT, INT, Eggenstein-Leopoldshafen, Germany
[2]KIT, KNMF, Eggenstein-Leopoldshafen, Germany

christian.kuebel@kit.edu

Nanocrystalline metals exhibit exceptional strength and fatigue properties compared to their coarse grained counterparts. However, they are limited by the thermal stability of their microstructure, which leads to significant grain growth already at room temperature for high purity metals. In order to develop strategies to retain their grain size, we are trying to understand the grain growth mechanisms active at small grain sizes.

As a model system we are investigating the grain growth in nanocrystalline palladium thin films by in-situ heating in a transmission electron microscope (TEM) as a powerful tool to directly image the dynamic changes during temperature induced grain growth. The grain growth is monitored in-situ using automated crystal orientation mapping (ACOM) to not only follow grain size and shape changes but to also get information about the crystallographic relationship between grains [1]. Thin films of ~ 50 nm nanocrystalline Pd were synthesized using magnetron sputtering and transferred onto an Aduro heating chips. Mapping the grain orientation in an area with more than a thousand grains in the initial state with a resolution of 1.5 nm allowed for a statistically meaningful analysis of the grain orientation, presence of twins, grain rotation and grain boundary migration with temperature (Fig. 1). Evaluation of the obtained maps was performed using MATLAB with a modified version of the Mtex tool box providing information about the local misorientation between neighboring grains, CSL boundary distribution, especially coherent and incoherent twin boundaries, twin density, average grain size, texture of grains, and the number of neighbors of selected growing grains . A global analysis of the orientation maps is in good agreement with experiments on bulk samples, exhibiting development of growth twins and a transition from an initial (111) orientation to a (100) dominated orientation during heating to about 1/3 T_m. More detailed information on the role of twin boundaries during grain growth as well as the effects of grain boundary curvature and grain boundary character will be discussed in the presentation.

1. A. Kobler, A. Kashiwar, H. Hahn, C. Kübel, Ultramicroscopy, 2013, 128, 68-81.

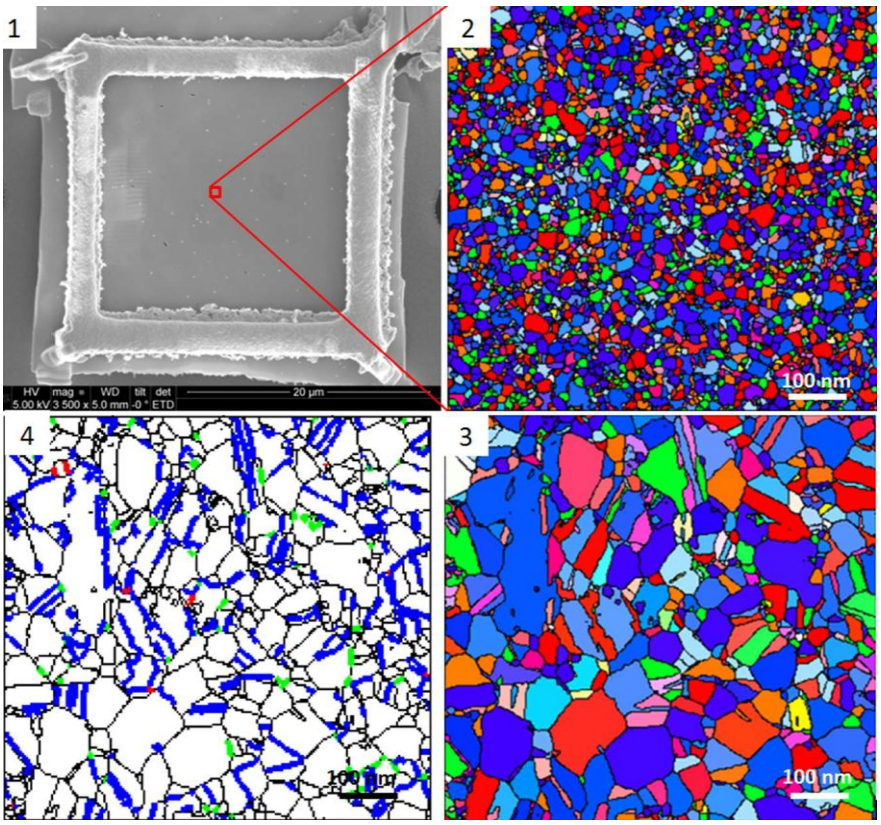

Figure 1. (1) nc Pd thin film with Au transfer frame on the MEMS heating device, (2-3) ACOM maps at early and final stage of heating, (4) grain boundary map at the final heating stage with incoherent (green), coherent (blue) S3 and S9 (red) boundaries indicated.

Metals, Alloys and Intermetallics

MS4.P078
Microstructure evolution in a 2618A aluminium alloy during ageing

C. Rockenhäuser[1], B. Skrotzki[1]

[1]Bundesanstalt für Materialforschung und -prüfung (BAM), Fachbereich 5.2 Experimentelle und modellbasierte Werkstoffmechanik, Berlin, Germany

christian.rockenhaeuser@bam.de

The aluminium alloy 2618A is an Al-Cu-Mg alloy which is part of the 2xxx series of age-hardenable alloys. These materials are designed for long-term operation in transportation and aerospace industries. The desired properties, e.g. creep behavior, hardness, and damage tolerance, are controlled by the distribution of fine precipitates formed within the matrix. However, the strength of the material declines during exposition to elevated temperatures due to the overageing of the S'-phase precipitates (Al_2CuMg) and the conversion of the S'-phase into the stable equilibrium S-phase [1]. A quantitative model of the overageing process at application relevant temperatures would be desirable for accurate predictions of component lifetime made from the 2618A alloy.

To systematically investigate the overageing process due to coarsening a) the precipitate phases (S' or S) have to be identified and b) the precipitate size distribution has to be determined at the initial stage (peak hardened alloy in the T6 condition) and at different artificially aged stages of ageing. To this purpose samples were fabricated from circular blanks and aged at different temperatures and times. To study the precipitate size distribution, cross-section samples were investigated using dark-field transmission electron microscopy (DFTEM). Preliminary investigations of the initial stage (T6 condition) are shown below (Figs. 1-3).

The Al_2CuMg precipitates were selectively imaged by DFTEM. The precipitates form as rods along the $_\alpha$ direction of the α-Al matrix. Therefore, the sample was oriented in the $[001]_\alpha$ direction for the TEM investigations. Fig. 1 shows a selected area diffraction pattern of the investigated sample area. The reflections of the oriented matrix are clearly visible. The streaks caused by the rod shaped precipitates lie in between the matrix reflections. These were selected to acquire dark-field images as indicated by the circle in Fig. 1. A dark-field image of the Al_2CuMg precipitates is shown in Fig. 2. The rods which are oriented along the $_\alpha$ direction and penetrate the image plane result in a roughly circular contrast. The longer line shaped contrasts are caused by rods oriented orthogonal to the incident electron beam and look similar to the precipitates in the 2618 alloy investigated by Nový et al. [2,3]. In order to evaluate the precipitate radii this contrast was removed by Fourier filtering the image. The filtered image was then used to evaluate the number and radii of the precipitates. The distribution of the precipitate radii is shown in Fig. 3. The maximum number of particles is clearly distinguishable at a 4 nm radius and quickly declines to higher radii. The high number of precipitates with radii of 0.5 nm and 1 nm is caused by artifacts arising from the analysis of the image contrast. The contrast caused by the precipitates not oriented parallel to the optical axis is not completely filtered out by Fourier filtering. Therefore, very small areas of contrast similar to the contrast of the Al_2CuMg rods oriented along the optical axis remain. These are falsely identified as rods with small diameters. Hence, the high number of precipitates with a radius of 1 nm and smaller should be neglected.

The analysis of dark-field images of the T6 condition shows that the method is viable to evaluate precipitate size distributions. Additional investigations of artificially aged samples (heat treatments and creep tests) are suitable to deliver data for a quantitative description of the coarsening process.

1. M.J. Styles et al., Acta Materialia **60** (2012) p6940.
2. F. Nový et al., J. Alloy Compd. **487** (2009) p146.
3. F. Nový et al., Int. J. Mat. Res. **103** (2012) p688.

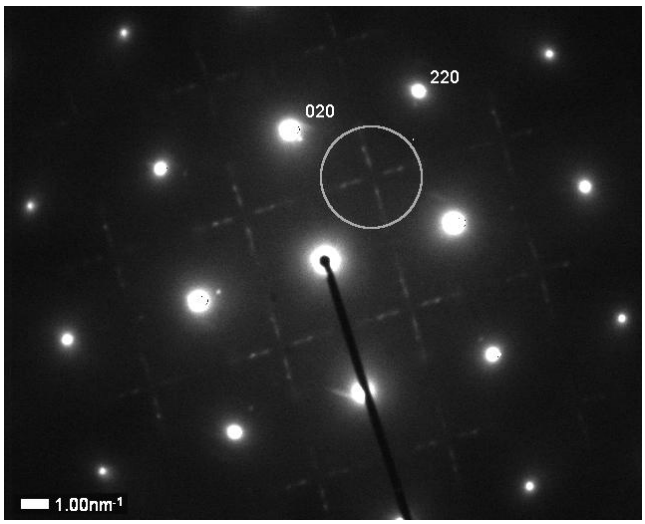

Figure 1. SAED pattern of the investigated sample area. The circle indicates the position of the objective aperture for dark-field imaging.

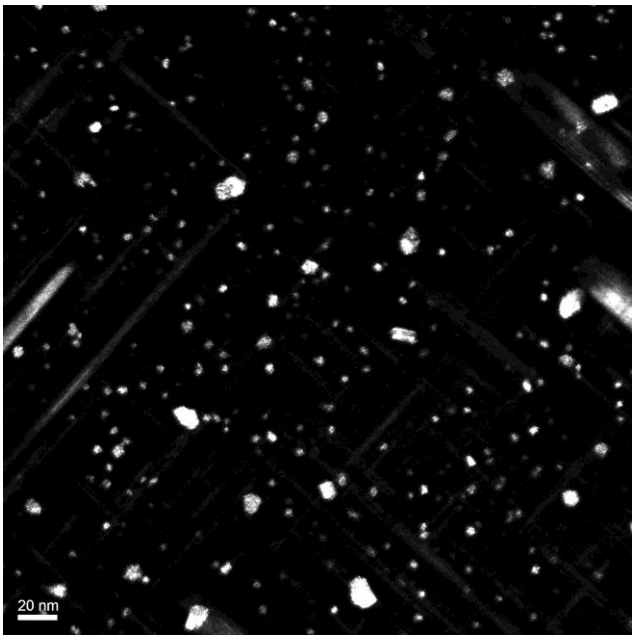

Figure 2. Dark-field image of the precipitates with the matrix oriented along the $[100]_{\alpha}$ zone axis.

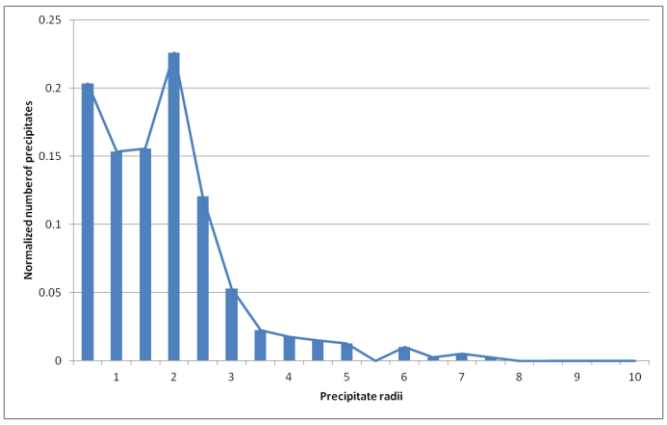

Figure 3. Normalized number of precipitates vs. precipitate radii

Metals, Alloys and Intermetallics

MS4.P079
Microstructure and order in NiPt3

A. S. Sologubenko[1], B. Schönfeld[2], M. Engelke[3]

[1]Swiss Federal Institute of Technology, Scientific Center for Optical and Electron Microscopy (ScopeM), Zürich, Switzerland
[2]Laboratory for Metal Physics and Technology, Material Science, Zürich, Switzerland
[3]DGS Druckguss Systeme AG, St. Gallen, Switzerland

alla.sologubenko@scopem.ethz.ch

While Ni_3Pt with $L1_2$ and NiPt with $L1_0$ structure are well established in the Ni-Pt system [1], the reported $NiPt_3$ phase with $L1_2$ structure [2, 3] is much less studied. Recently, Schönfeld et al. [4, 5] observed a sharp drop in electrical resistivity and the concurrent appearance of superstructure reflections upon long-time ageing of a $NiPt_3$ single crystal. With a maximum of 0.50(4) at 613 K, the Bragg-Williams long-range order parameter η was surprisingly far below 1, the value for a fully ordered state. No microscopic reasons for this low value were reported so far. Moreover, in a diffuse scattering experiment on Ni-87.8 at.% annealed at 603 K, a cigar-like diffuse scattering pattern was detected around *h*00 superstructure positions of the L12 structure [5]. This was unexpected as, only plate-like patterns in diffuse scattering are known for alloys that have an intermetallic phase with the L12 structure.

Therefore in the present work, complex studies by X-ray scattering and transmission electron microscopy of a Ni-75 at.% Pt single crystal were concentrated on two goals : (i) the direct estimation of the order-disorder transition temperature by following the long-range order parameter η and (ii) the microstructure analysis of selected ordering states to provide an understanding of the evolution of η and the peculiar scattering pattern around superstructure positions.

TEM/STEM study revealed that the long-range ordered L12-phase appears in form of precipitates (Figure 1a-c) that reach at most 12 nm in size at the highest order state. The very small domains are present in the matrix even at the as-quenched state and grow upon annealing. The two-beam bright field and weak-beam dark field micrographs acquired with g=010 as a second strong reflection (Figure 1a,b) They are coherent with the matrix, but tend to arrange along dislocations. Stacking faults spanning the domain boundaries appear within the domains at some stage of ordering. In the advance order state, APB within the domain were also detected.

High amount of strain due to the heterogeneous coherent microstructure up to the very end of the ordering reaction is responsible for the low value of order parameter. Figure 1d shows the saturation of the increase of the Bragg-Williams long-range order parameter upon isothermal annealing at 613 K as a function of time towards the maximal detected value 0.56. At higher temperatures, the h reduced abruptly. As no compositional variation was discovered in any compositional line profiles (in EDX-STEM with a probe size of 0.8 nm), no reference to disperse order [6, 7] in Ni-75 at.% Pt is revealed. The large strain and/or low energy costs for planar faults are evidenced by the presence of stacking faults the number of which increased with ageing time. Whether the cigar-shaped pattern around superstructure positions still stems from the less-ordered matrix or whether it originates from the natural abundance of 2:1 between APB of type II over type I when the ordered regions were brought in contact, still awaits confirmation.

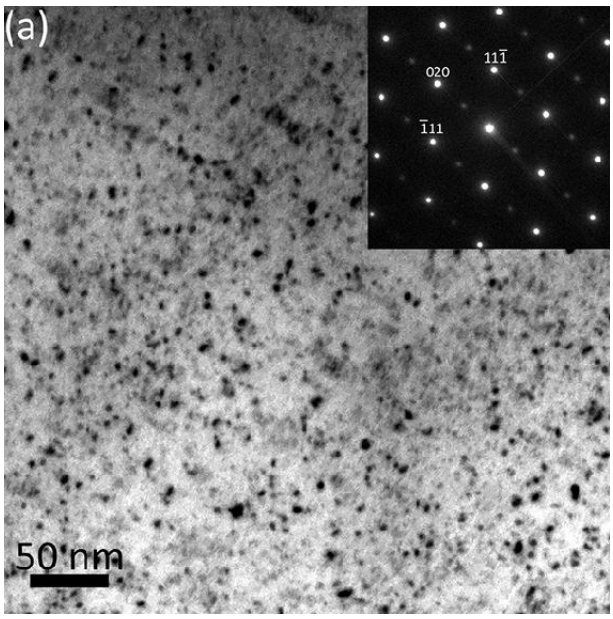

Figures 1. Two-beam bright field micrograph acquired close to [101] zone axis orientation with the g=020 as a second strong reflection. The insert shows the corresponding diffraction patterns acquired in the exact zone axis orientation.

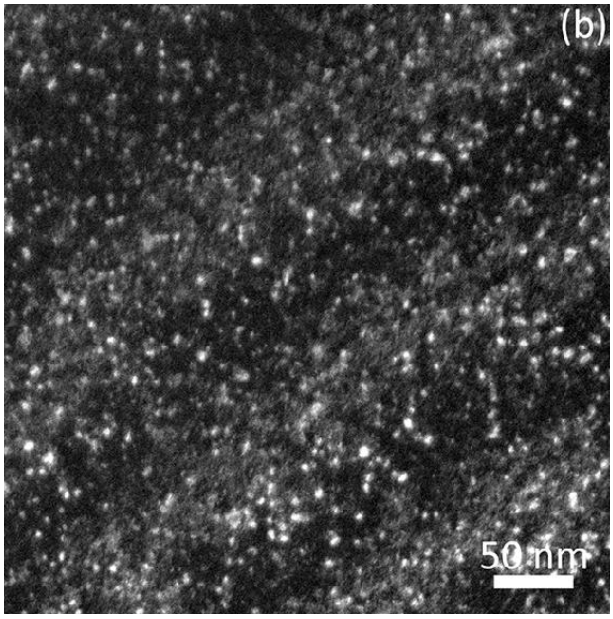

Figures 2. Weak-beam dark field micrograph acquired from the same area as in (a).

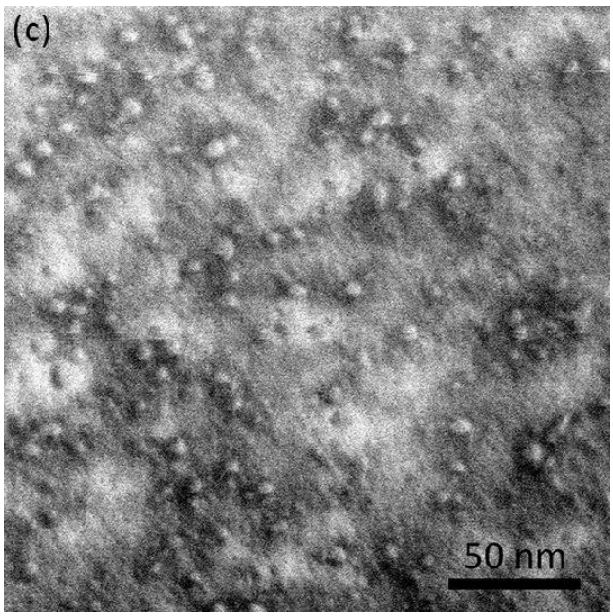

Figures 3. HAADF-STEM micrograph acquired with the specimen in the two-beam condition close to [101] zone axis orientation with g=020.

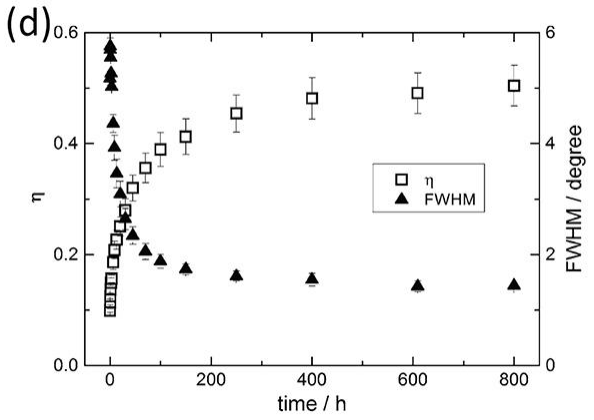

Figures 4. Integrated and normalized intensities around 300 and 330 positions acquired from the specimen annealed for different times at 613 K.

Metals, Alloys and Intermetallics

MS4.P080
TEM study of recrystallization at heterogeneous interfaces of ARB processed aluminum laminates

M. Cieslar[1], M. Poková[1], J. Veselý[1], M. Zimina[1]

[1]Charles Univwersity in Prague, Faculty of Mathematics and Physics, Prague, Czech Republic

cieslar@met.mff.cuni.cz

New technologies of components assembling in car and aircraft industries and requests on improved mechanical and corrosion properties of metallic materials in the packing industry activate the utilization of highly innovative and unconventional manufacturing processes. In addition a growing need in the decrease of fabrication costs and the limitation of the waste material in metal-forming processes results in the combination of non-traditional materials with modern casting methods and non-standard shaping. Also in the sheet-forming industry, where sheets and strips serve as semi-finished products for further processing, the established manufacturing technologies must be redesigned in order to fulfill new demands on the material formability, strengths, high temperature sagging resistance etc.

Incorporating twin-roll casting (TRC) and accumulative roll bonding (ARB) into a manufacturing process creates a new class of sheet materials with a high solid solution supersaturation and ultrafine grained structure. Nevertheless, low ductility of ARB materials significantly limits not only their production but also their applicability. Therefore superior properties including improved ductility can be reached when a material with a bimodal grain-size distribution is used. A composite multilayer sheets from commercial TRC Al (Al99.99) and AlMg3 (in wt.%: 2.6 Mg, 0.39 Mn, 0.3 Fe and 0.2 Si) alloy with up to 64 alternating layers of Al/AlMg3 were prepared. A significant grain fragmentation and refinement were observed in both types of material. Pronounced dynamic recovery and recrystallization result in a formation of equiaxed grains of submicron size in Al layers (Fig. 1) while only well-defined elongated subgrains without any sign of recrystallization appear in the AlMg3 material (Fig. 2).

Processes occurring at newly formed interfaces between the two materials at higher annealing temperatures were studied by TEM. Post-mortem observations have shown that recrystallization and grain growth begin in Al-layers. Growing grains can locally penetrate the original interface between Al and AlMg3 layers (Fig.3). In-situ TEM observations have confirmed this tendency. It is shown that mainly diffusion of Mg and Mn atoms enhanced by high annealing temperatures is responsible for this phenomenon.

1. The financial support of the project GAČR P107-12-0921 is gratefully acknowledged.

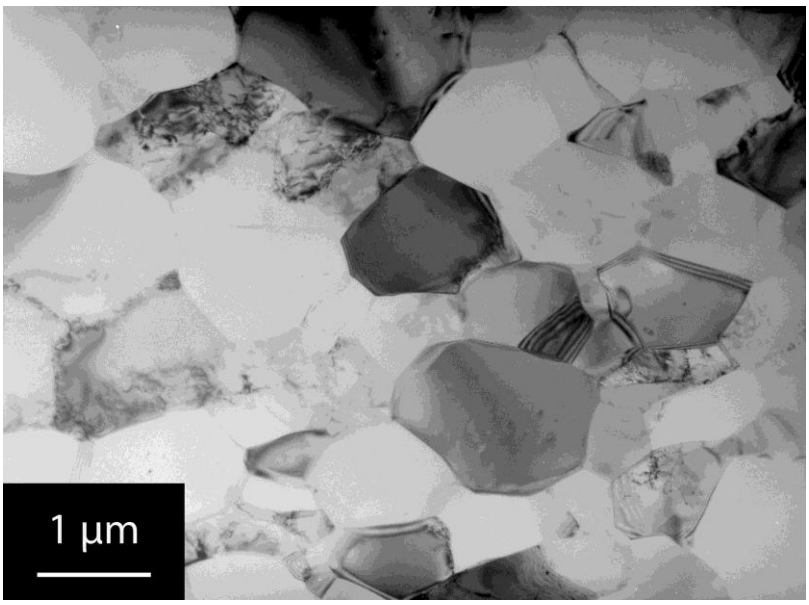

Figure 1. Grains in Al layer after 6 ARB cycles

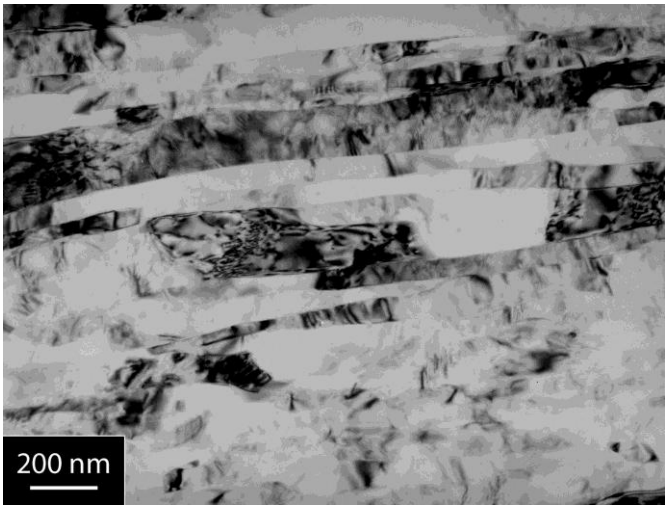

Figure 2. Flat subgrains in AlMg3 layer after 6 ARB cycles

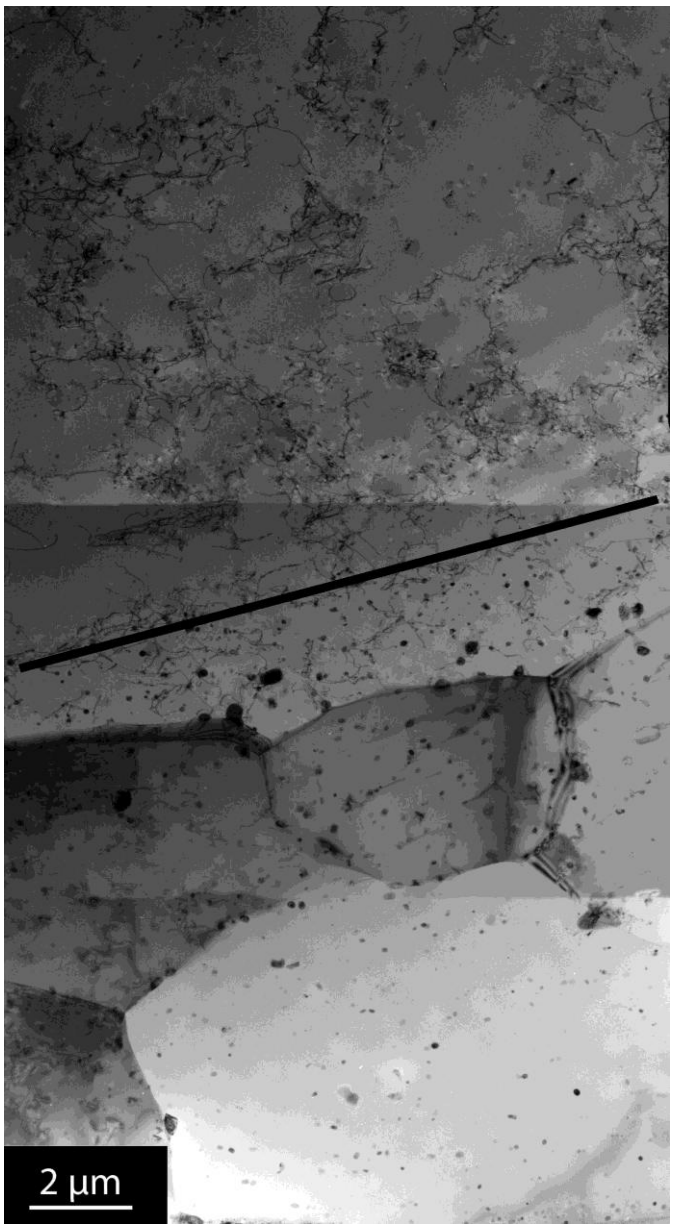

Figure 3. Original interface (marked by a black line) between Al (upper part) and AlMg3 (bottom part) layers after 6 ARB cycles and annealing at 480 °C.

Metals, Alloys and Intermetallics

MS4.P081
Structure analysis of Al-Co-Ni quasicrystal approximant using combination of HAADF STEM and 3D electron diffraction tomography

P. Oleynikov[1], T. Seki[2], K. B. Yoon[3], E. Abe[2], O. Terasaki[1,4]

[1]Stockholm University, Stockholm, Sweden
[2]University of Tokyo, Department of Materials Science & Engineering, Tokyo, Japan
[3]Sogang University, Department of Chemistry, Seoul, Korea, Republic of
[4]KAIST, Graduate School of EEWS, Daejeong, Sweden

peter.oleynikov@mmk.su.se

Analyzing the crystal structure of approximants is of vital importance in deriving structural information of building units (or basic clusters) and their arrangements toward decagonal quasicrystals (DQCs) [1]. The acquired knowledge is important for further hyper-space modeling. Since approximants are periodic crystals, conventional single-crystal X-ray diffraction could be applied to analyze their atomic structure. However, the task becomes quite challenging when it comes to the case of approximants, for example Al-Co-Ni [2]. These approximants often have very large unit cells with lattice constants of over a few tens of Ångströms [2]. A recent study also suggests that, except for the solved case of [2], it is often very difficult to grow single crystals having coherent crystallinity within the width of the incident X-ray beam. It is therefore desirable if the crystal structure can be assessed using electron diffraction from a sub-micron sized crystal domain.

The aim of this study is to assess the possibility of taking the advantage of 3D Electron Diffraction Tomography (3D EDT) [3] in order to solve the crystal structure of the Al-Co-Ni approximant (orthorhombic, proposed s.g. *Pba*2, a ~ 99Å, b ~ 64Å, c = 8.2Å). Automated 3D EDT is a fast and efficient technique that has been developed by us [3]. It can be used for fast 3D reciprocal space scanning with a given fine step (0.01° - 0.1°) using conventional transmission electron microscopes.

The crystal structure of the individual sub-micron single crystal was determined from the 3D EDT data collected in conventional selected area electron diffraction (SAED) mode using EDT-COLLECT software package [3] on JEOL JEM-2100 FEG CTEM equipped with a single high tilt holder (+/-50°) and Gatan UltraScan 1000 CCD (2048*2048). The acquired data set contains 2160 unique electron diffraction patterns (exposure 0.5 sec/frame). Reciprocal space coverage was ~105°. The recorded frames were processed using the EDT-PROCESS software package [3] and assembled into a corresponding 3D volumetric representation of reciprocal space (Fig. 1). The reflections with odd *l*-indices are much weaker than those with even *l*-indices. In present work we treated the structure having *c* = 4.1Å. The crystal structure was partially determined (Fig. 2) using the direct methods software Sir2011 [4] from the integrated intensities extracted by EDT-PROCESS program. We have compared the solution with a model obtained from the HAADF STEM image. Most of Ni/Co-atom positions and partially occupied Co/Al positions were determined from the 3D EDT data and are identical to the STEM model (205 and 220 respectively). Some Al-atoms are missing in the structure solution from the electron diffraction data.

In this work we show that combination of HAADF STEM and 3D EDT as very powerful techniques which offers a facile and systematic way to study complex crystal structures. The authors would like to thank the following people and organizations [5].

1. E. Abe, Chem. Soc. Rev. **41** (2014) pp. 6787-6798.
2. S. Hovmöller *et al*, Phil. Trans. R. Soc. A **370** (2012) pp. 2949-2959.
3. M. Gemmi and P. Oleynikov, Z. Kristallogr. **228** (2013), pp. 51-58.
4. M.C. Burla *et al*, J. Appl. Cryst. **45** (2012), pp. 357-361.
5. We kindly acknowledge Swedish Research Council (VR, 1486801), JEOL Ltd., Japan, Knut and Alice Wallenberg Foundation (3DEM-NATUR) and BK21Plus, Republic of Korea.

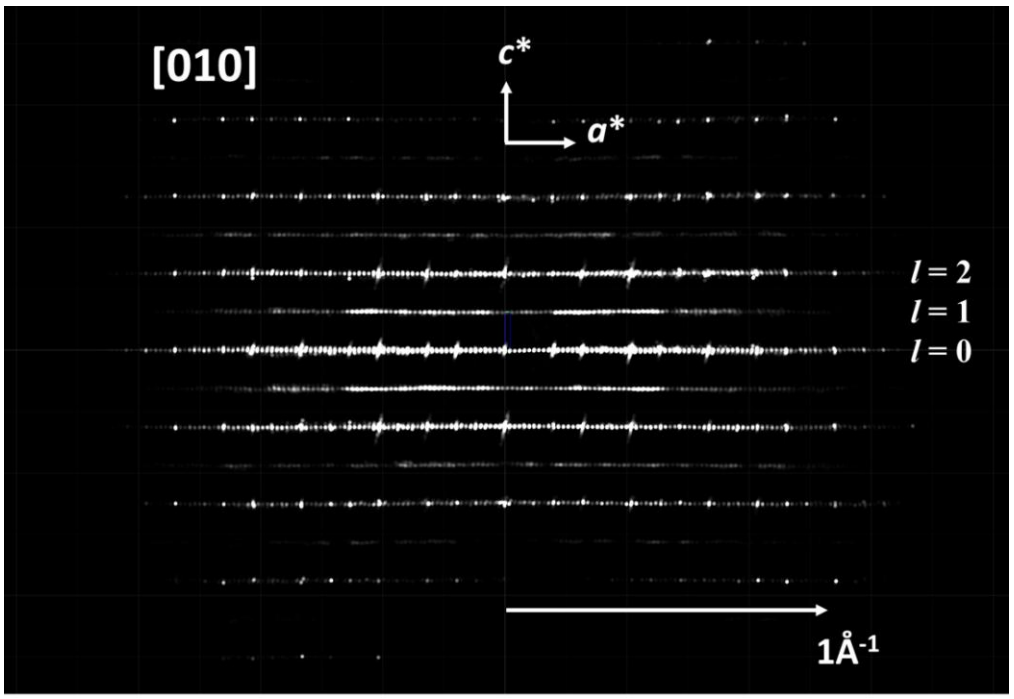

Figure 1. Reconstructed 3D reciprocal space seen along 010 direction.

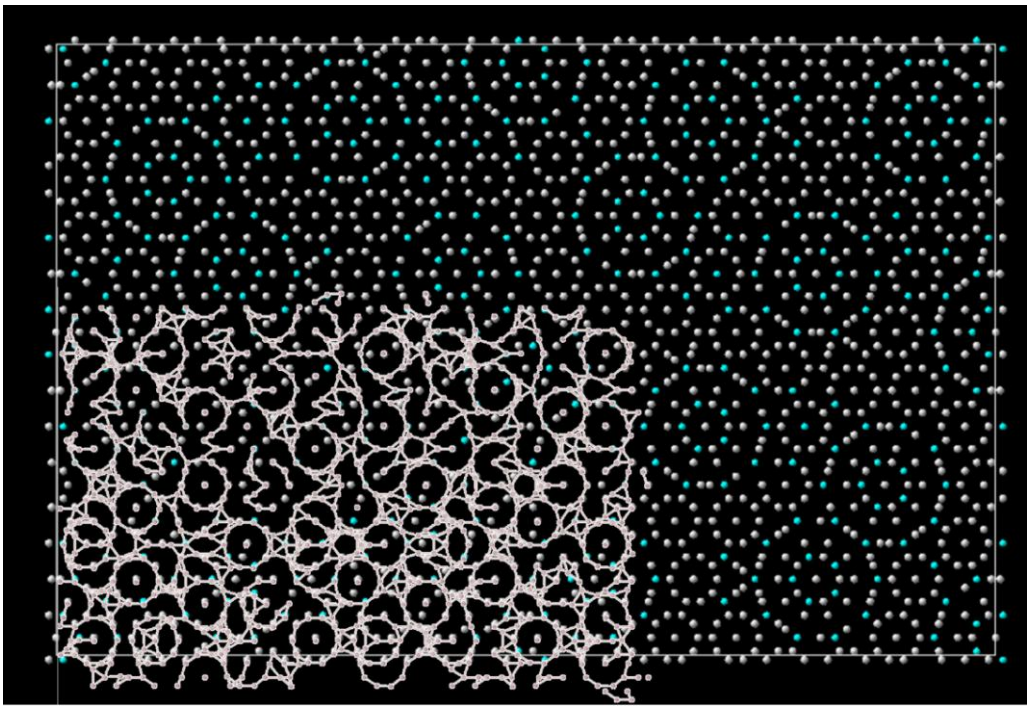

Figure 2. The HAADF STEM model (blue - Co-atoms, grey - Al-atoms) and an overlay of the structure model obtained using direct methods.

Metals, Alloys and Intermetallics

MS4.P082
On the physical nature of planar faults which form during creep in the γ'-phase of a CoNi-base single crystal superalloy

Y. M. Eggeler[1], J. Müller[1], M. S. Titus[2], A. Suzuki[3], T. M. Pllock[2], E. Spiecker[1]

[1]Friedrich Alexander University Erlangen-Nürnberg, Centre for Nanoanalysis and Electron Microscopy (CENEM), Erlangen, Germany
[2]University of Carlifornia Santa Barbara, Materials Department , Santa Barbara, United States
[3]Gneral Electric, Global research Centre , Niskayuna, United States

yolita.eggeler@fau.de

Ni-base single crystal superalloys are unique because they can withstand mechanical loads at temperatures up to 90% of their melting point. They are used for first stage blades of advanced gas turbines [1]. Their creep strength is associated with a two phase γ/γ' microstructure consisting of γ'-cubes with $L1_2$ crystal structure separated by thin fcc γ-matrix channels. In 2006, Sato et al. [2] discovered the same type of microstructure in a Co based alloy. This was the starting point for research on single crystal Co-based superalloys which are promising because Co exhibits an even higher melting point than Ni. The original CoAlW-system suffered from a low γ'-solvus temperature. This was improved by adding Ni, Cr and Ta [3] to the base alloy. Co- and CoNi-base single crystal superalloys show a pronounced tendency to form planar faults [4]. However, the mechanisms of fault formation are not fully explored yet.

The present study addresses the formation of planar faults during the early stages of creep in a single crystalline CoNi-base superalloy. For this purpose interrupted [001] tensile creep specimens after 300 MPa/900 °C creep to 0.5 % strain [5] have been investigated. Samples with [010] foil normals reveal the presence of planar faults that extend over multiple contiguous γ' precipitates and show a characteristic APB/SISF/APB configuration whereby superlattice intrinsic stacking faults (SISFs) are fully embedded within antiphase boundaries (APBs) [6]. In order to understand the physical nature and formation mechanism of such shear bands the terminating planar faults and dislocations have been investigated in a (001) sample cut perpendicular to the tensile axis (Figure 1). The TEM dark field image (a) taken with the g(010) superlattice reflection shows the presence of a SISF and, connected to that, an APB whereas the bright field image (b) obtained under two-beam condition for g(-311) (close to [103] zone axis) reveals the two partial dislocations terminating the SISF (leading partial) and separating the two planar fault from each other (trailing partial), respectively. The intrinsic nature of the SISF has been confirmed by fringe contrast analysis of g(020) bright field and dark field images as well as by HRTEM combined with geometric phase analysis (GPA) of similar stacking faults oriented edge-on in a [011] sample. Diffraction contrast analysis in combination with large angle convergent beam electron diffraction (LACBED) unambiguously show that the leading and trailing partials are of type a/3<112> and a/6<112>, respectively. The whole shear band that creates the APB/SISF/APB planar fault configuration in multiple contiguous γ' precipitates is thus of type a/2<112>. This is in contrast to the classical a<112> shearing mechanism observed in Ni-based superalloys where a second pair of partials re-establishes the order [7].

While the SISFs stay on the {111} glide plane the APBs tend to deviate from this plane towards energetically favorable {100} orientations (Figure 1a). This is expected to be a result of APB migration at creep temperatures driven by energy minimization. This proposal could be confirmed by *in situ* heating experiments (Figure 2) which directly show APB migration and {100} facetting at temperatures above 850 °C.

1. R. C. Reed, Superalloys, Camebridge University Press, 2006.
2. J. Sato et al., Science (2006), vol. 312, p. 90.
3. K. Shinagawa et al., Mater. Trans (2008), vol. 49, p. 1474
4. A. Suzuki et al., Acta Mater. (2008), vol. 56, p. 1288
5. Y. M. Eggeler et al., Acta Mater. (2014), vol. 77, p. 352
6. Y.M. Eggeler et al., Proc. Microscopy Congress MC2013, Regensburg, Germany (2013).
7. C. M. F. Rae et al. , Mater. Sci. Eng. A (2001), vol. 300, p. 125
8. The authors gratefully acknowledge financial support within the DFG collaborative research center SFB-TR 103 (project A7) and the NFS DMREF Grant DMR 1233704.

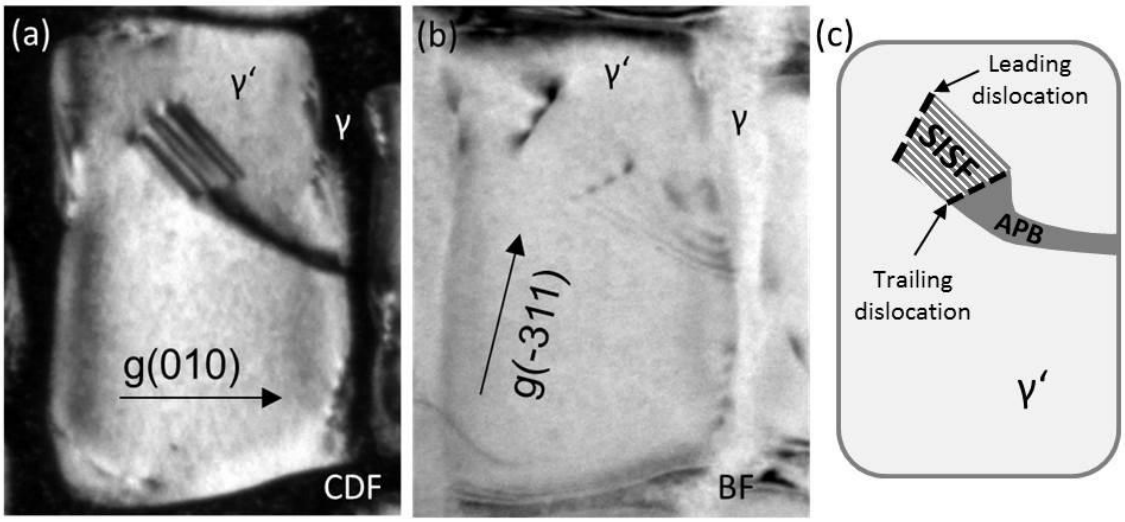

Figure 1. Conventional TEM images of planar faults and dislocations terminating a a/2<112> shear band in a CoNi-base superalloy. a) Centred dark field (CDF) image using g(010), showing the presence of a stacking fault and, connected to that, an APB. b) Bright field image taken under two-beam condition for g(-311), revealing the partial dislocations terminating the planar faults. c) Schematic describing the observed shear band.

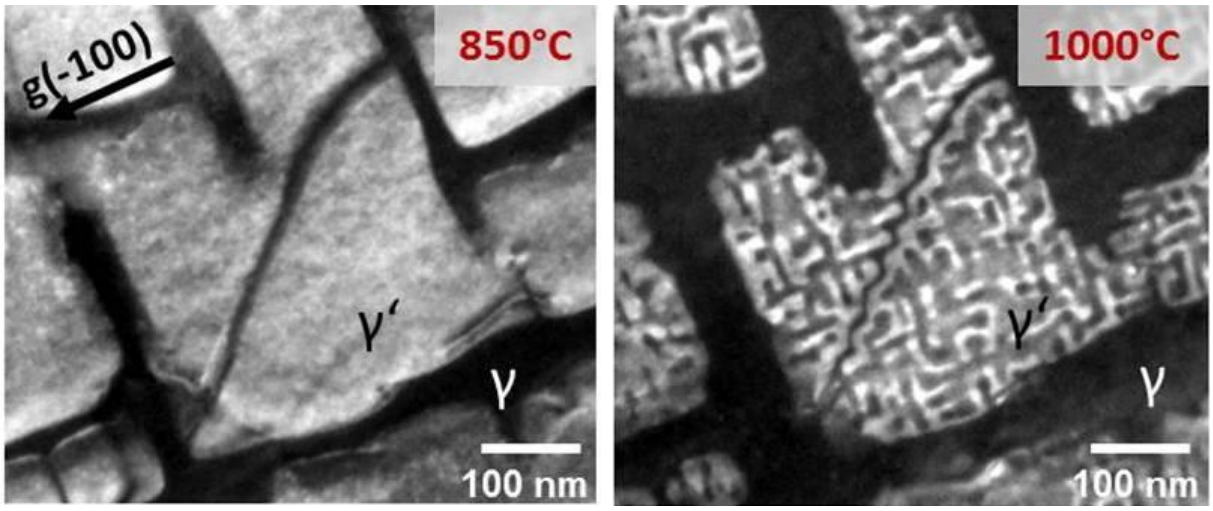

Figure 2. *In situ* TEM heating experiment showing that an APB that migrates from {111} towards energetically favourable {100} planes above temperatures of 850°C.

Metals, Alloys and Intermetallics

MS4.P083
Structural heterogeneities in thin foils of CuZr based bulk metallic glasses

S. Noisternig[1], C. Müller[1], C. Gammer[1], C. Ebner[1], H.- P. Karnthaler[1], C. Rentenberger[1]

[1]University of Vienna, Physics of Nanostructured Materials, Vienna, Austria

stefan.noisternig@univie.ac.at

Bulk metallic glasses (BMG) are amorphous materials with no long-range order. Still, topological and chemical short-range or medium-range order is expected to occur. The unique atomic structures of BMG lead to interesting physical and mechanical properties that make them useful for potential applications. In order to obtain structural information transmission electron microscopy (TEM) methods as electron diffraction or fluctuation electron microscopy can be applied. In all cases thin TEM specimens are of advantage to obtain interpretable results. It is the aim of the present work to show that in very thin areas of a CuZr-based BMG structural heterogeneities compared to the bulk sample can occur.

BMG of $Cu_{36}Zr_{48}Al_8Ag_8$ were prepared by centrifugal casting. Both as-cast samples and samples deformed by rolling were prepared by grinding, dimpling and ion milling to TEM foils. In addition, samples were also thinned by electropolishing using a solution of 33% nitric acid and 66% methanol. The TEM foils were studied in a Philips CM200 operating at 200kV. Selected area electron diffraction (SAED) patterns of the BMG were acquired from areas of different thickness using a Gatan Orius CCD camera. The apertures used select areas with a diameter of 300 or 1200 nm. In addition, energy dispersive X-ray (EDX) spectra were taken to obtain information on the chemical composition.

Figure 1 shows the SAED pattern of $Cu_{36}Zr_{48}Al_8Ag_8$ BMG taken from different areas of a wedge shaped TEM foil prepared by the multiple step procedure including ion-milling. In the thinnest area next to the edge of the sample two closely spaced diffuse diffraction rings (A, B) are present in the SAED pattern (cf. Fig. 1(a)). With increasing thickness a third diffuse ring (C) emerge between A and B and becomes dominant (cf. Fig. 1(b,c)). This change of the SAED pattern is summarized in Fig. 1(d) showing the intensity profiles. The integration along rings was carried out using the PASAD software [1]. The intensity maxima of the peaks A, B and C are at about 3.6, 4.7 and 4.3 nm^{-1}, respectively. It should be mentioned that (i) EDX spectra at thinner areas reveal enhanced oxygen content compared to thicker areas and (ii) the position of peak A can be correlated to that of amorphous zirconia. In the literature, double diffraction rings at similar positions as in Fig. 1(a) were observed in a $Cu_{32}Zr_{51}Al_9Ni_8$ alloy [2]. These double rings emerge from a single very broad peak during in-situ heating and are attributed to the formation of compositional and structural heterogeneities in thin films upon annealing. Contrary, in our case local heating of the thin area during ion-milling can be excluded since double rings are also observed in SAED patterns of thin films prepared by electropolishing.

Based on our results, it is concluded that in CuZr-based BMG thin foils structural heterogeneities in the form of three different structures (dependent on the distance to the surface) are present: (i) oxidized amorphous zirconia (peak A) at the surface, (ii) amorphous CuZr structure (peak B) affected by the surface layer (less Zr content) and (iii) amorphous bulk CuZr structure (peak C). The shift of peak position B to C by a change of the Zr content is supported by experimental data of CuZr based BMG [3].

1. C. Gammer, C. Mangler, C. Rentenberger, H. P. Karnthaler, Scr Mater 63, 312 (2010).
2. L. He et al., Thin Solid Films 561, 87 (2014).
3. X. Wang et al., Acta Mater 59, 1037 (2011).
4. We kindly acknowledge the support from the Austrian Science Fund (FWF): [I1309, P22440, J3397].

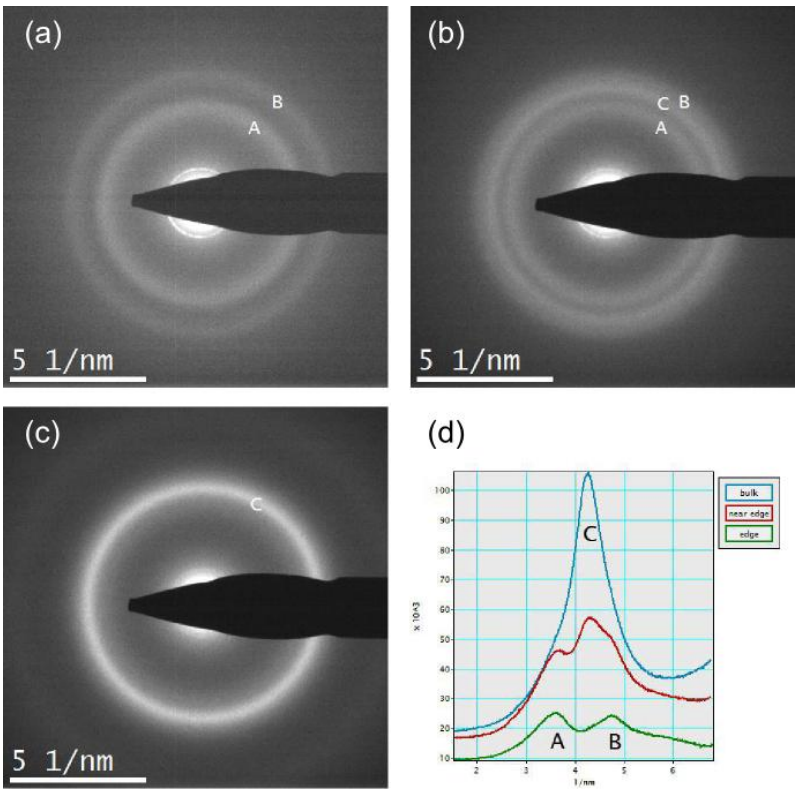

Figure 1. (a) Diffraction pattern of $Cu_{36}Zr_{48}Al_8Ag_8$ bulk metallic glass taken at the edge of the wedge shaped TEM foil shows double rings indicated A and B. (b, c) With increasing distance from the edge (increasing thickness) a strong third ring appears. (d) Intensity profiles obtained by integration along diffraction rings. Peak C lies between peak position A and B.

Metals, Alloys and Intermetallics

MS4.P084
Structure and phase composition hydrogenated zirconium

D. Litvinov[1], A. Pshenichnikov[1], J. Stuckert[1], M. Walter[1], J. Aktaa[1]

[1]KIT, Eggenstein-Leopoldshafen, Germany

litvinov@kit.edu

Electron back scattered diffraction (EBSD) analysis with scanning electron microscopy were applied to study structure and phase composition of Zr hydrogenated from gaseous phase. The pure Zr samples were hydrogenated up to different hydrogen content under the temperatures of 500, 600, 700 and 800 °C.

The most often detected δ - zirconium hydrides have face-centred crystal structure with zirconium atoms at the face-centred sites and hydrogen atoms occupying tetrahedral interstitial sites. At the room temperature (see Figure 1), there are three stable hydride phases with composition of ZrH (tetragonal γ - phase), $ZrH_{1.66}$ (cubic δ - phase) and ZrH_2 (tetragonal ε - phase) which are formed due to increase in the hydrogen concentration in the material. The tetragonal γ - phase is considered to be metastable and is shown in brackets in phase diagram in Figure 1. The β - phase of Zr is cubic and exists only at high temperature. After the cooling there is always β → α + δ martensitic type of transformation happened.

In Figure 2, EBSD phase maps (a), (c), (e) and orientation maps (b), (d), (f) of samples 1 (a-b), 2 (c-d) and 3 (e-f) from Figure 1 fabricated under the same temperature of 600 °C, but with different hydrogen content are shown. All maps in Figure 2 are combined with EBSD quality maps in the background.

After hydrogenation in α - region of the phase diagram in the sample 1 only δ - hydrides are detected. As it is shown in Figures 2a-b, the hydrides look in most of the cases like needles and grow from the grain boundary into the grain (intra-granular) that marked by ellipses. The detailed analysis of microtexture shows that intra-granular δ - hydrides grow parallel to the basal plane with relation: $\{0001\}_\alpha \parallel \{111\}_\delta$. However, some δ - hydrides are arranged between Zr grains (inter-granular) that marked by arrows in Figures 2a-b.

After hydrogenation of the sample 2 in (α + β) - region of the phase diagram and the following cooling, a mixed structure is observed. In Figure 2c-d, one part of the structure is similar to the structure of the sample 1, fabricated from α - region of phase diagram: δ - hydrides inside (marked by ellipses) or between (marked by arrows) Zr grains. The second part of the structure results from the β → α + δ martensitic type of transformation (marked by rectangles). In these areas, the local hydrogen concentration, probably, was enough to build β - phase at the high temperature. In the sample 2, also very small part of γ - hydrides is detected (marked by dashed arrow).

Hydrogenation in β - region of the phase diagram with the following cooling (Figures 2e-f) leads to the mix of the martensitic structure of the rests of zirconium (marked by rectangles), with very small part of γ - hydrides (marked by dashed arrows), and additional large grains consisting of δ - hydrides and mainly with intra-granular γ - hydrides (marked by rings). The tetragonal distorted intra-granular γ - hydrides have nearly the same orientations as the surrounding cubic δ - hydrides. The difference between two tetragonal and cubic lattices of these hydrides is very small. Note that γ - phase was observed at different hydrogen content. The fraction of γ - hydrides increases with hydrogen content, that is in consistence with X-ray diffraction measurements performed in [1].

It can be concluded, that the structure of hydrogenated Zr is strongly dependent on the point of the phase diagram, where the hydrogenation of samples is aborted and cooling started. For the first time the metastable γ - hydride phase is detected on EBSD - map, which shows its place and spatial distribution in the bulk of hydrogenated Zr.

1. A. Pshenichnikov, J. Stuckert, M. Walter, Microstructure and mechanical properties of Zircaloy-4 cladding hydrogenated at temperatures typical for loss-of-coolant accident (LOCA) conditions, Nuclear Engineering and Design 283 (2015) 33-39.

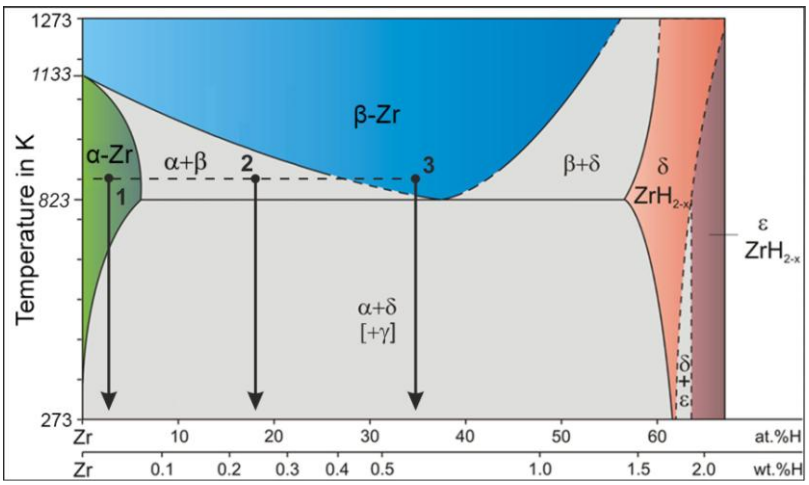
1273
1133
823
273
Temperature in K
β-Zr
α-Zr
α+β
2
3
1
β+δ
δ
ZrH2-x
ε
ZrH2-x
α+δ
[+γ]
δ+ε
Zr
10
20
30
40
50
60
at.%H
Zr
0.1
0.2
0.3
0.4
0.5
1.0
1.5
2.0
wt.%H

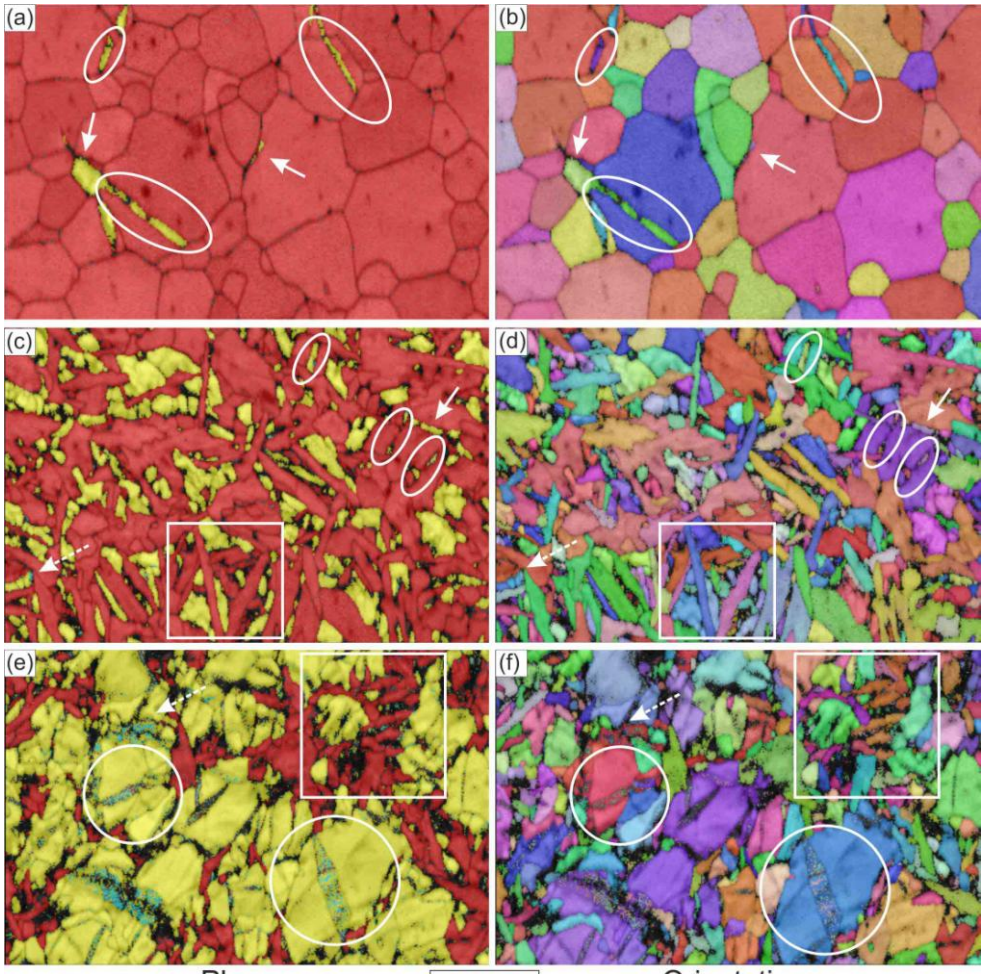
(a)
(b)
(c)
(d)
(e)
(f)
Phases
- α-Zr - hexagonal
- γ–ZrH - tetragonal
- δ–ZrH1.6 - cubic
5 μm
Orientations
[001]
α-Zr
[110]
[210]
[001]
[010]
[001]
γ–ZrH
[100]
δ–ZrH1.6
[111]
[101]

Metals, Alloys and Intermetallics

MS4.P085
Interaction of Ni-15at.%W alloy with carbon foil during spark plasma sintering

A. Ukhina[1], D. Dudina[1], B. Bokhonov[1], V. Mali[2], A. Anisimov[2]

[1]Institute of solid state chemistry and mechanochemistry SB RAS, Novosibirsk, Russian Federation
[2]Lavrentyev Institute of Hydrodynamics SB RAS, Novosibirsk, Russian Federation

auhina181@gmail.com

Carbon foil usually used in the practice of Spark Plasma Sintering (SPS) to protect the graphite die and punches from the chemical action of the sample is a source of graphitic carbon, the presence of which can affect the composition of the subsurface layers of the sintered material. In the present work, we prepared a Ni-15at.%W alloy by mechanical alloying of elemental powders. Sintering of this mixture by SPS and the influence of carbon from the foil on the microstructure of the compact were studied. Carbonyl nickel powder and tungsten powder were mechanically alloyed in a planetary ball mill for 50 min. The powders were consolidated by SPS at a temperature of 900ºC for 5 min to produce the compact samples. Based on scanning electron microscopy of polished cross-sections and X-ray diffraction phase analysis, we will discuss the phase composition of the sintered compacts as well as their morphological and structural characteristics.

It was shown that carbon diffuses into the volume of the Ni-W compacts to form carbides WC and Ni_2W_4C (Fig. 1). WC formed near the interface between the carbon foil and the compact. The thickness of the WC-containing layer was about 100 μm. In the center of the sample, particles of the Ni_2W_4C phase were found. The distribution of the Ni_2W_4C particles followed a pattern such that their preferential formation along the former boundaries between the agglomerates of the mechanically milled powder is suggested, considering faster diffusion of carbon along these paths compared to the bulk of the powder agglomerates.

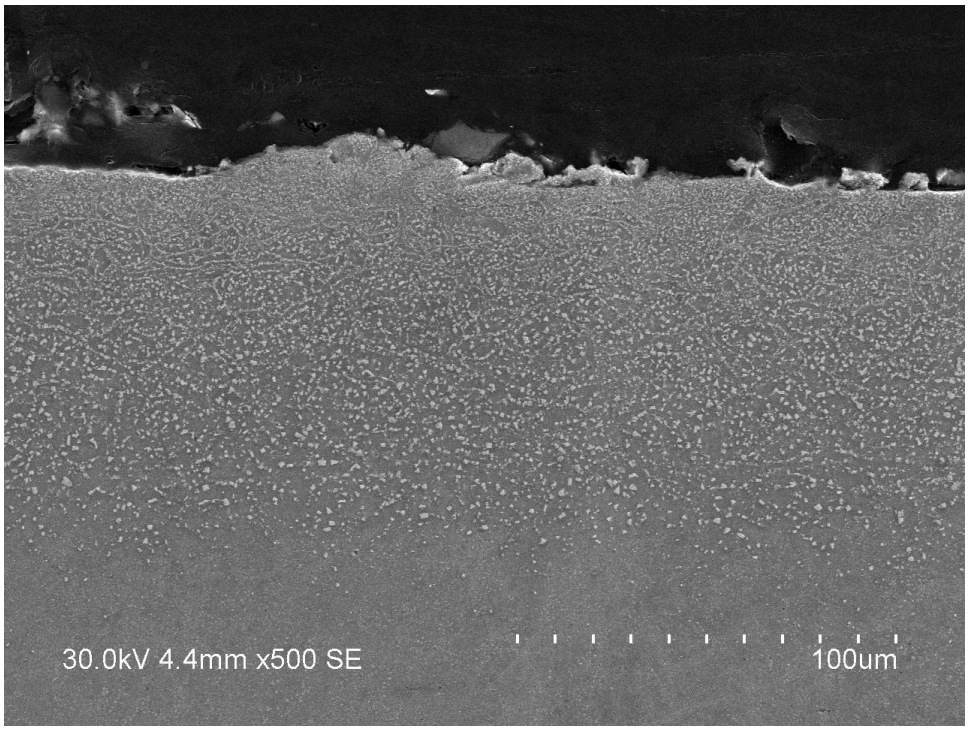

Figure 1. Microstructure of the Ni-15at.%W sample consolidated by SPS in contact with carbon foil (cross-section).

Metals, Alloys and Intermetallics

MS4.P086
EBSD-measurements of high shear zones of aluminium alloy AA6060

I. Driehorst[1,2], C. Fahrenson[1,2,] V. Sanabria[2]

[1]TU-Berlin, Berlin, Germany
[2] University, Center for Electron Microscopy, Berlin, Germany

Iryna.driehorst@tu-berlin.de

In this paper the microstructure of the friction-induced high shear zone (HSZ) of aluminium alloy AA6060 has been investigated using electron backscatter diffraction (EBSD). The HSZ is a part of the friction boundary layer and is characterized by a grain refinement. At first EBSD parameters for the characterization of the strong deformed microstructure were optimized. Following the limiting degree of deformation of the HSZ for feasible EBSD measurements was determined.

Friction experiments with aluminium alloy AA6060 were carried out using an axial friction test. Small cylinders with initial diameter of 7.8 mm and length 10.5 mm were extracted from homogenized cast billets of aluminium alloy. The specimens were heated up inside a steel liner for 20 minutes and set up by two counteracting stems with a constant strain rate of 0.0006 s^{-1}. The stems were fixed and the liner was pulled down 5 mm with constant slide speeds of 0.1 mm/s and 50 mm/s. Around 90 s after each friction test the specimens were quenched in water. The experiments were carried out at 300 °C, 400° C and 500 °C respectively (Sanabria, 2014). Each specimen was longitudinally sectioned and then submitted to standard metallographic preparation procedures. Finally the specimens were electrolytically polished to be analyzed with EBSD.

The microstructure of the HSZ was investigated using a Hitachi S-2700 tungsten filament SEM equipped with a NORDLYS II EBSD detector from HKL Technology, Hobro, Denmark. For the analysis CHANNEL5 software from HKL Technologywas used. The specimens were examined at an acceleration voltage of 20 kV and probe currents in the range of 1.5 to 2 nA. The investigations covered the cross section area of approximately 360x400 μm^2 and the step size was chosen between 0.1 and 0.5 µm with respect to the expected grain size.

At 500°C and 400°C and both sliding speeds good EBSD patterns of the microstructure of the HSZ (Fig. 1) were obtained. At 500°C and high sliding speed the recrystallization of strong deformed microstructure of the HSZ was observed. At 300°C and both sliding speeds only weak EBSD patterns were observed. The high plastic deformation could cause the multiplication of dislocations and generate the grain refinement (Humphrey, 2004) and possibly strong deformation of crystal lattice.

In order to improve the hit rate in this case a variation of Hough space resolutions and the number of detecting bands will be investigated.

1. Humphreys, F.J., Hatherly, M., 2004, Recrystallization and related annealing phenomena, Elsevier, Second edition, Oxford, U.K.
2. Sanabria, V., Müller, S., Reimers, W., 2014. Microstructure evolution of the friction boundary layer during extrusion of AA 6060, 11th International conference on technology of plasticity, ICTP 2014, 19-24 October 2014, Nagoya Congress Center, Nagoya, Japan

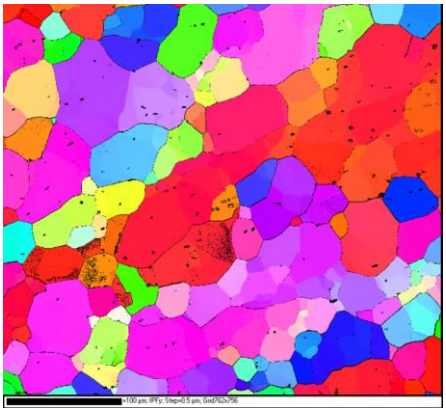

Metals, Alloys and Intermetallics

MS4.P088
Nanostructural characterization of magnetron sputtered Fe - Au thin films

U. Schürmann[1], C. Zamponi[2], T. Jurgeleit[2], E. Quandt[2], L. Kienle[1]

[1]Institute for Material Science, University Kiel, Synthesis and Real Structure, Kiel, Germany
[2]Institute for Material Science, University Kiel, Inorganic Functional Materials, Kiel, Germany

usc@tf.uni-kiel.de

Composites consisting of iron and gold are of relevance for biodegradable implant materials. Freestanding multilayer films were fabricated using magnetron sputtering technology and sacrificial Cu layer. These thin films were annealed for 2 hours at 685 °C and 850 °C in a vacuum furnace, respectively to homogenize the multilayer samples. The micro- and nanostructure was investigated by X-ray diffraction (XRD), energy dispersive X-ray spectroscopy (EDX) and transmission electron microscopy (TEM) (FEI Tecnai F30 STwin TEM (300 kV, field emission gun (FEG) cathode, spherical aberration coefficient C_S=1.2 mm). Cross-sectional lamellae of the films were prepared by focused ion beam (FEI Dualbeam Helios Nanolab) sectioning and milling. High angle annular dark field (HAADF)-STEM and EDX elemental mapping (Si/Li detector, EDAX) were performed on these samples to receive detailed information about the microstructure via Z-contrast imaging and to investigate the Fe and Au distribution.

The pristine sample shows bilayers of pure Au (10 nm) and pure Fe (700 nm). A columnar growth of the Fe perpendicular to the bilayers is visible, cf. broad irregularly shaped stripes in Figure 1(a). After annealing the multilayered microstructure converts into a new multiphase system consisting of an iron matrix and two different kinds of gold morphologies: segregations along grain boundaries and nanosized core-shell like precipitates. For the sample annealed at 685 °C for 2 hours the multilayer structure starts to disappear while the columnar growth of the Fe layers persists (Figure 1 (a)). After 2h at 850 °C the columnar microstructure of the Fe layers has vanished and isometric grains with sizes ranging from 2 µm to 7 µm can be found. Only a few gold precipitates are distributed inside the iron grains while the predominant amount of the gold segregates along the grain boundaries. This segregation of gold along the iron grain boundary is a result of the favored diffusion along grain boundaries and also depending on the lattice relations between the fcc structure of the Au and the bcc structure of the Fe. The gold precipitates show unusual and unexpected conformations. Nanosized gold structures with the shape of iron-filled tubes can be found as well as core-shell particles (Figure 1(c)). These morphologies can be explained by surface wetting and the mutual temperature depending solubility of Au and Fe in each other. The initial segregation of Au along the grain boundaries leads to the arrangement of precipitates shaped like triangles (Figure 1(b)). EDX elemental maps confirm the Au and Fe distribution.

1. C. Zamponi, U. Schürmann, T. Jurgeleit, L. Kienle, E. Quandt, Int. J. Mat. Res., 106(2), 103-107 (2015)
2. The authors want to thank the DFG for the financial support.

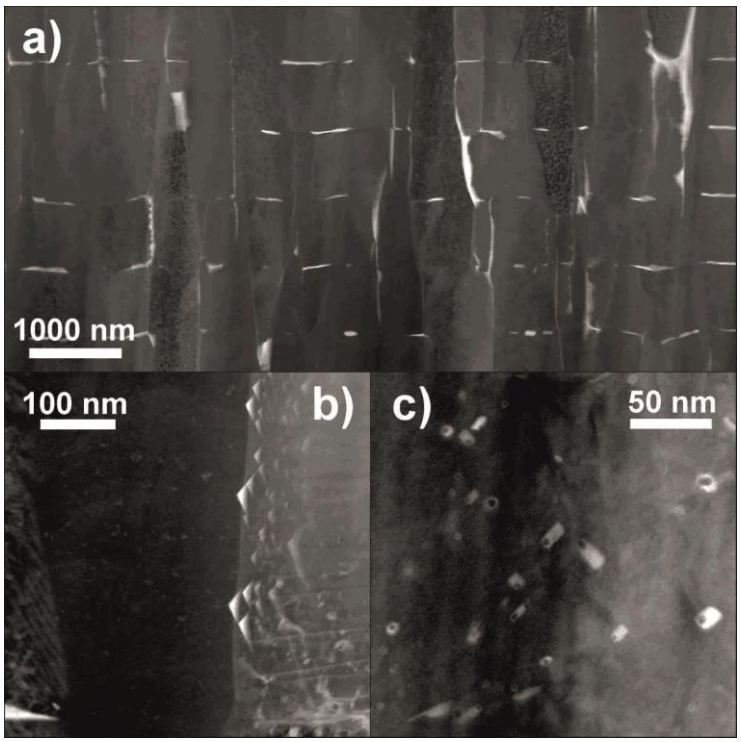

Figure1. HAADF-STEM images of the cross-sectional Fe-Au samples; Au: bright contrast, Fe: dark contrast. a) + b) Sample after heating at 685 °C. Distribution of the Au along the initial layer and at the grain boundaries of Fe. At higher magnification the segregation as triangle-shaped precipitates along the grain boundaries is visible. c) After heating to 850 °C iron-filled gold tubes and core-shell nanoparticles can be found.

Metals, Alloys and Intermetallics

MS4.P089
Texture analysis of thermo-mechanical treated steels by EBSD and X-ray measurements

M. Frerichs[1], H. Klein[1], K. Techmer[1]

[1]University of Göttingen, Department of Crystallography, Göttingen, Germany

mathias.frerichs@stud.uni-goettingen.de

Important anisotropic properties e.g. strength, plasticity of technically used materials depend on their crystallographic structure and on the specific phases (e.g. precipitations) which are formed during thermal treatment of the base-material.One of the most important products are niobium (Nb) micro-alloyed High Strength Low Alloy (HSLA) steel grades which are widely used in civil construction, automobile and line pipe applications.

The texture and microstructure of several micro-alloyed HSLA-Steels with low carbon contents (~0.05 wt %) were studied by EBSD (Electron Backscatter Diffraction), conventional X-ray diffraction and high-energy synchrotron radiation in order to detect some differences in micro-, meso- and macro-scales.

The calculations of the texture analyses were made on the basis of the orientation distribution function (ODF) using the harmonic method after Bunge [1]. In particular some interest lay on the determination of the Gaussian spread width used in EBSD-analysis. The magnitude of this spread influences distinctly the intensity of the texture. A comparison of the ODF from X-ray or synchrotron measurements will help to find reliable spread values for EBSD-analyses.

Rolled metals exists frequently show a texture gradient in the thickness [2]. A determination of this gradient will be often difficult or even impossible using conventional X-ray methods or high-energy synchrotron radiation because of the high penetration depth and the low local resolving power of the radiation. In contrast, electrons have a low penetration and a high local resolution [3]. This allows on the one hand the determination of a present texture gradient easily, even with the microstructure of the sample. On the other hand X-ray and synchrotron based methods enable a complete analysis of macroscopic anisotropic properties of a material [1].

Some texture results from the examined steels from EBSD, X-ray and synchrotron experiments will be given and discussed.

1. H.J. Bunge (1982): Texture Analysis in Material Science. Butterworths, London 1982.
2. D. Raabe and K. Lücke (1992): Texture and Microstructure of Hot Rolled Steel. Scripta Met. et Mat., **26**, 1221-1226.
3. V. Randle (1992): Microtexture Determination and its Applications. The Institute of Materials, London.

Metals, Alloys and Intermetallics

MS4.P090
carbon elemental mapping and phase analysis of TRIP steel

Y. Tanaka[1], M. Nagoshi[2]

[1]JFE Steel Corporation, Steel Research Laboratory, Chuo-ku Chiba, Japan
[2]JFE Steel Corporation, Steel Research Laboratory, Kawasaki, Japan

yuji-tanaka@jfe-steel.co.jp

Steel is an important material for industry because it covers wide range in mechanical strength and formability. This is achieved by controlling its microstructure. Phase transformation from austenite to ferrite during product process strongly governs its microstructure. TRansformation Induced Plasticity (TRIP) steel is one of the advanced high strength steel with excellent formability. It has a complex microstructure of mixing of a meta-stable austenite and stable ferrite phase. It is known that volume fraction of austenite is a good parameter to explain its elongation. Many efforts have been paid to obtain high amount of meta-stable austenite phase in a final product[1]. One strategy is to condense carbon element into austenite phase because it decreases Gibbs free energy of the system if it condenses to austenite phase at lower temperature.

From analytical point of view, it is a challenging problem to characterize a microstructure of a TRIP steel. One of the difficulties is phase identification in sub-micron meter scale. Recent development of a combination of FE-SEM and EBSD technique has been widely adapted to this field. The other difficulty is detecting trace carbon element using a microscope. Recently EPMA or 3DAP techniques were used to investigate carbon distribution in a steel[2]. However SEM-EDS has not been widely used for this purpose. EDS is said to be not good at detecting light element. In addition, electron beam produces contamination and it disables trace carbon analysis.

In this study, we investigated microstructure of a TRIP steel using SEM-EBSD and EDS. The total carbon content of the TRIP steel was less than 0.3 mass%. The steel specimen was mirror polished and conducted for EBSD analysis. EBSD measurement was performed at acceleration voltage 15kV using Carl Zeiss Supra55VP thermal FE SEM. After EBSD phase mapping, the specimen was repolished slightly to remove the contamination layer formed during EBSD measurement. The specimen and SEM chamber were cleaned by plasma generator to remove residual materials or gas which can become an origin of a contamination. SEM chamber was vacuumed below 10^{-7} Pa. EDS elemental mapping was performed on the same area of EBSD analysis with acceleration voltage 5kV. This voltage was selected to improve the spatial resolution of EDS mapping and SNR. SDD with 30mm^2 detection area were used for EDS analysis.

Figure 1a-c show SE image, EBSD phase map and carbon mapping respectively. The darker area in EBSD map represents martensite phase. Martensite is stable phase with middle concentration of carbon. We found that the carbon mapping was well correspond to SEM and EBSD phase map. It is clear that austenite contain larger amount of carbon than that in ferrite or martensite. The averaged carbon content in austenite was estimated from XRD peak shift of austenite. It evaluated as 0.7mass%. Carbon content in ferrite phase was estimated as almost 0% from a calculation of a phase diagram. Figure 2 shows the spectra from the area of ferrite, martensite and austenite. Though carbon was detected from ferrite phase due to unavoidable contamination, careful specimen preparation and large area SDD enabled us to distinguish the difference less than 1mass% carbon content in a steel with mapping technique. The combination of EBSD and EDS C mapping clarified the location and carbon enrichment of austenite in a complex microstructure.

1. K. Sugimoto, M. Tsunezawa, T. Hojo and S. Ikeda: ISIJ Int., 44(2004) 1608.
2. Y. Toji, G. Miyamoto and D. Raabe: Acta. Mater., 86(2015) 137.

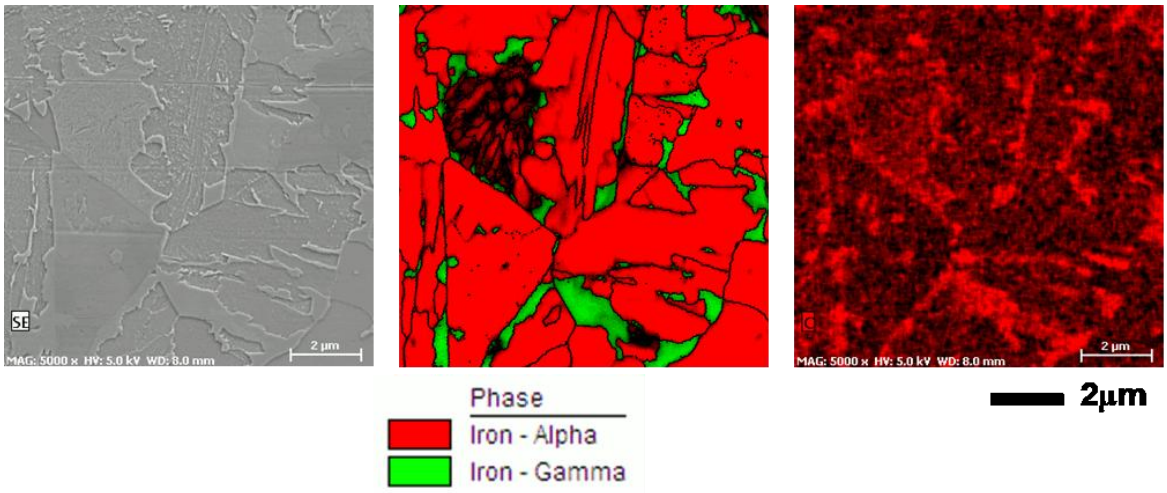

Figure 1. a) SE image b) EBSD phase map and c) EDS C map of the TRIP steel.

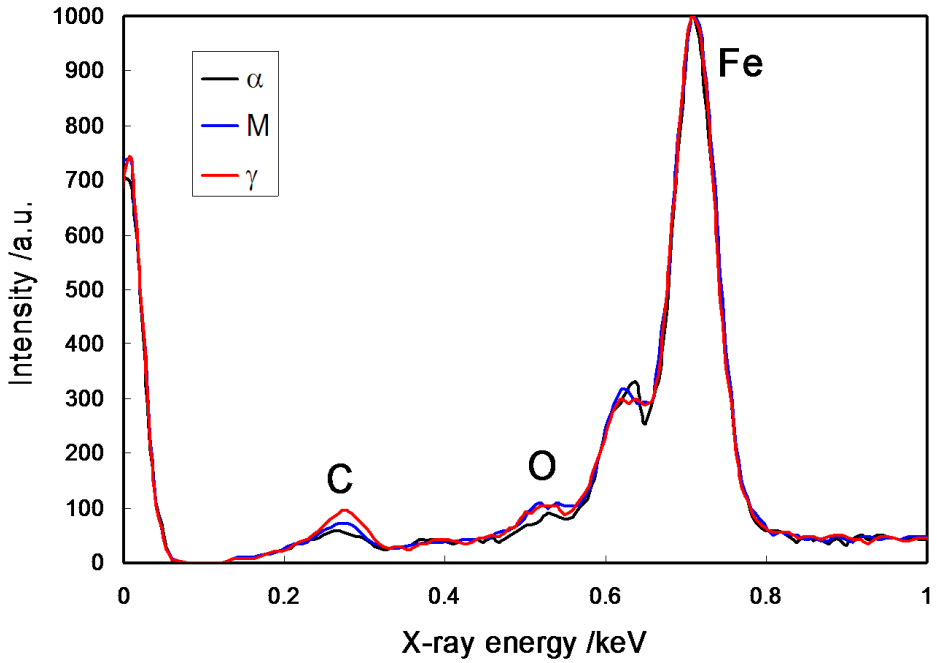

Figure 2. Energy dispersive spectra from ferrite, martensite and austenite phase.

Metals, Alloys and Intermetallics

MS4.P091
Multimodal analysis of phases formed by reaction diffusion in binary Fe-Al system

J. Čupera[1], V. Jan[1]

[1]Faculty of Mechanical Engineering, Brno University of Technology, Department of Material Science and Engineering, Brno, Czech Republic

cupera@fme.vutbr.cz

This work deals with identification possibilities for very fine microstructure phases formed by reaction diffusion in binary Fe-Al system. The Fe-Al samples were prepared by low-pressure cold spray technique using heated air (temperature 300 °C, pressure 1.5 MPa) as working gas. Pure Fe and Al powders mixtures were deposited on aluminium substrate. Prepared deposits were subsequently annealed isothermally at temperatures in range from 250 °C to 750 °C for two hours in protective argon atmosphere. Thereafter, phase composition and structure were examined on standard metallographic polished samples.

The samples of FeAl elemental mixture in the form of solid cuboids 8x8x4mm were annealed at temperatures from 500 °C up to 750 °C. The general interest in these samples lies in the fact that by solid state or liquid-solid diffusion new intermetallic material with open porous structure is formed. However, the microstructure of the material is generally composed of fine grains or mixtures of phases, where identification of these phases by standard methods is difficult.

First of all, the Energy Dispersive Spectroscopy - EDS (point analysis and line analysis of diffusion interfaces) and (bulk) X-ray diffraction - XRD were used. Because of too small size of the individual phase particles, the X-ray Diffraction was inconclusive. Very fine lamellar structure of two different intermetallic compounds begins to form at temperature of 650°C and a new problem with EDS chemical analysis for phase identification of the phases analysis arise too. The reason of this problem is that we face physical or/and spatial resolution limits of EDS. This problem can be solved by technique with better spatial resolution like Electron backscatter diffraction - EBSD and Low Voltage Backscatter Electron (LVBSE) imaging as additional tool. Both these methods have a spatial resolution of several nanometres and existing results from more conventional methods can be enriched with new details.

The diffusion profiles between individual metal particles in samples annealed at temperature 500 °C and 600 °C were analysed by EDS line and point analysis. Newly formed particles exclusively of the Al5Fe2 phase were identified in the material after annealing at temperature of 500 °C. Annealing at 600 °C further created FeAl and FeAl2 phases [1]. For higher annealing temperatures where complex microstructures with very fine features had evolved, EDS line and point analysis for diffusion profiles and EBSD analysis for phase analysis of the fine lamellar structures were used. For this lamellar microstructural mixture of phases the stable phase diagram and XRD data were obtained. However the data were unsufficient to identify the phases. Here EBSD was used to identify and the phase types.

Main result of this work is the proof of concept in the ability to identify very fine mixed microstructures and phases in annealed binary Fe-Al system by combination of several methods which allows overall improvements and overcomes the limits of individual analytical SEM methods.

1. JAN, Vít, ČUPERA Jan, CIZEK Jan: On the search for producing intermetallics by diffusion reaction of cold spray bulk deposits. *Surface and Coatings Technology*. 2014. DOI:10.1016/j.surfcoat.2014.12.011.
2. NETME CENTRE project CZ. 1.05/2.1.00/01.0002 ED0002/01/01, Czech; Grant Agency under the project GACR 13-35890S and OPVK project n.: CZ.1.07./2.3.00/20.0197 are acknowledged.

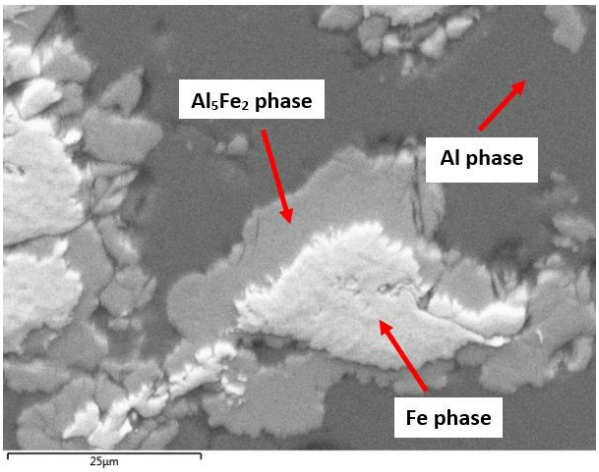

Figure 1. Microstructure and detail of Fe-Al interphase after 2h annealing at 550 °C.

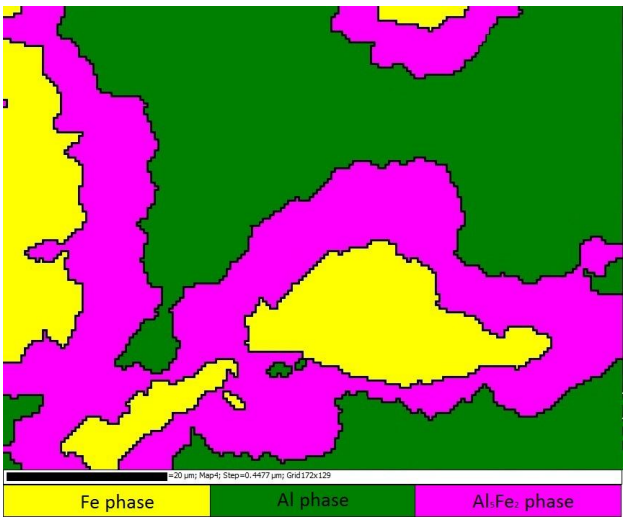

Figure 2. Reconstructed EBSD map of Fe-Al interphase after 2h annealing at 550 °C.

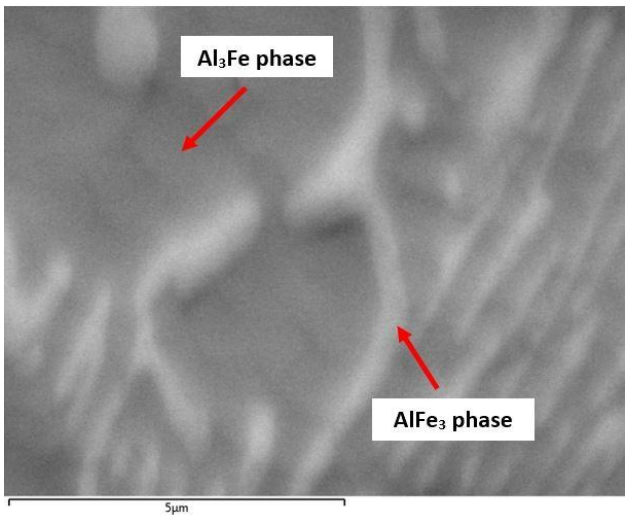

Figure 3. Microstructure and detail of Fe-Al interphase after 2h annealing at 750 °C.

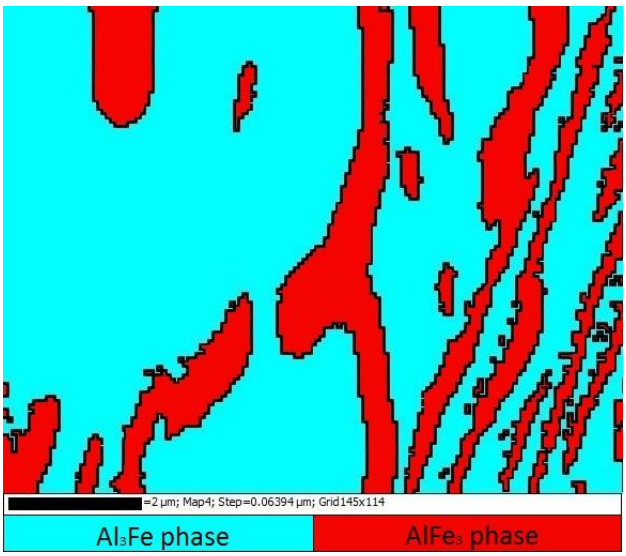

Figure 4. Reconstructed EBSD map of Fe-Al interphase after 2h annealing at 750 °C.

Metals, Alloys and Intermetallics

MS4.P092
Dissimilar welds in the system: SA533-E309L-E308L-alloy 82-alloy 182-SB168

L. Zamora Rangel[1], J. A. Aguilar Torres[1], L. Diaz Perez[1], A. Sandoval Jomenez[1]

[1]ININ, Materials of Technology, Lerma, Mexico

luis.zamora@inin.gob.mx

In some BWR reactors, has been reported to occur stress corrosion cracking (SCC) in dissimilar metal welds, which was used as filler nickel alloy 182. This filler metal is used in binding structures internal support core and connecting to the outside of the reactor vessel of a BWR. The support plate of the envelope is installed in the bottom of the reactor pressure vessel (RPV). This supports the reactor core to maintain the function of the insertion of the control rods and to guide the primary coolant flow. Consists of nickel alloy plates 600 joined by longitudinal welds basis and whose circumferential filler alloy is 82 and 182. The most notable design is a type of supporting plate, with support legs and Central Laguna Verde has this design [1].

These welds in an oxidizing atmosphere and under tension such as a BWR reactor, are prone to SCC over time during service operation. However, its effects may attenuate some controlling variables from the same manufacture of welding.

To the welding system under study, Fig. 1, two plates, the steel vessel SA533 and SB168 other (alloy 600), whose dimensions were 9.50 x 5.50 x 0.75 inches and 9,96 x 9.40 x 0.532 inches, respectively. For application of the coating on the vessel steel plate SA533 E309L and E308L electrodes were employed by SMAW welding process; for connecting it with inconel plate electrodes were used ERNiCr3 by GTAW welding process for the root and then for filling the coated electrodes ENiCrFe3 by SMAW process [2]. The welding parameters are shown in Table 1. The non-destructive (END) assays such as visual inspection, liquid penetrant and manual pulse-echo ultrasound, applied during each of the stages of manufacture system and end welds made of Fig. 1. The welding system was applied metallography technique to display the microstructures obtained. Additionally, Vickers Microhardness measurements were performed using a Shimadzu microhardness mark on the base metal, the heat affected zone and welding processes performed by applying a load of 50g for 10s.

The result of the application of NDT in the SA533-E309L-E308L-Alloy 82-Alloy 182-SB168 system based on the criteria of ASME Code, was in all cases, which showed no relevant indications [2]. The interfaces microstructures obtained are shown in Fig 2. In the obtained microstructures can be observed that the base metals present their characteristic structures: bainite and austenite for SA533 and SB168, respectively. Microstructures obtained with other filler present acicular dendrites towards the interface areas with discrete particles of chromium carbide and iron [3]. The values obtained, depending on the distance between welds, and base material in the HAZ of each welding process is shown in Fig. 3. The initial microhardness SA533 steel base materials was in the range of 263-308 HV, high values for this steel, and increased to the value of 355 HV in the HAZ; average hardness value for E309L-E308L interface was 200 HV; for E308L-alloy 182 interface of 206 HV and alloy 182-SB168 equal to 199 HV interface; all values are characteristic of these joints [4].

1. TR-105696-R9 (BWRVIP-03), 2006, Rev. 9: “BWR Vessel and Internals Project, Reactor Pressure Vessel and Internals”. EPRI, Palo Alto, CA, 1013394.
2. Code ASME 2010.
3. Scarberry R., Pearman S., Crum J. 1976, Precipitation reactions in Inconel alloy 600 and their effect on corrosion behavior”, Corrosion, V. 32, No. 10, pp.401-406.
4. Zamora L., et al. 2014, “Microstructure of Dissimilar Welding: Carbon Steel A36 and Austenitic Stainless Steel E309L-E308L”, 18TH International Microscopy Congress, Prague, 7-12 September 2014.

Figure 1. SA533-E309L-E308L-Alloy 82-Alloy 182-SB168 system.

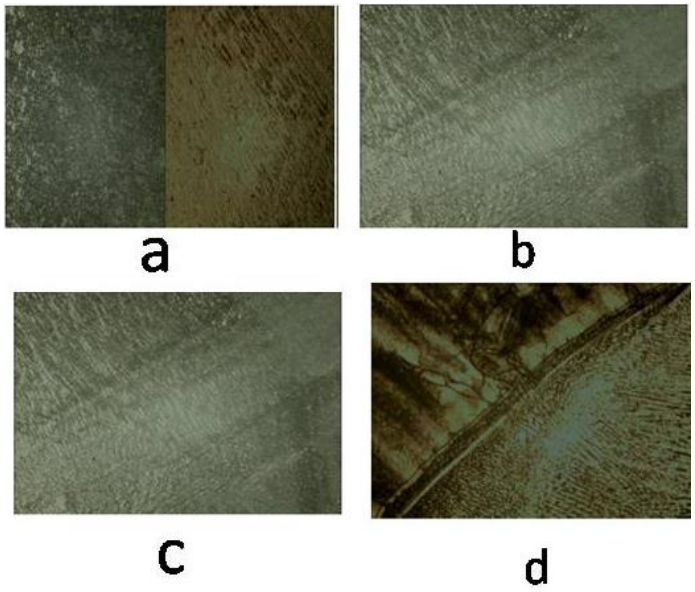

Figure 2. Interfaces microstructures: (a) SA533-E309L, 100X; (b) E309L-E308L, 100X; (c) E308L-Alloy 182, 100X; and (d) Alloy 182-SB168, 100X.

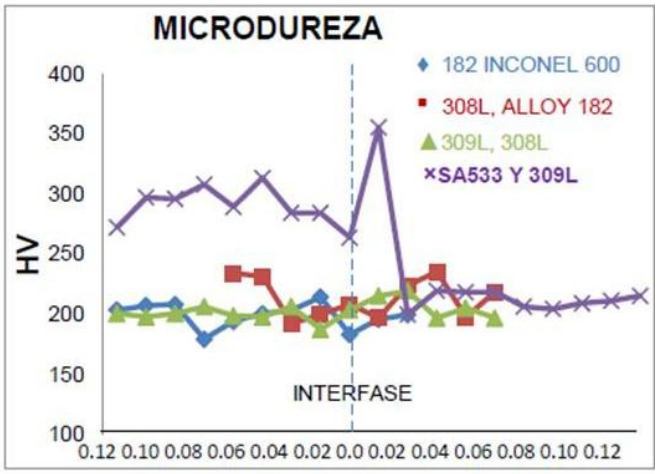

Figure 3. Profile of Microhardness at interfaces.

Step	Process	Electrode	Current	Voltage	Speed	Notes
1 Layer	SMAW	E309L, 3/32"	75 A	22-26 V	6.50 in/min	Cladding
2 Layers	SMAW	E308L, 3/32"	75 A	22-24 V	6.50 in/min	Cladding
1 Bead	GTAW	ERNiCr3, 1/8"	120 A	15 V	1.98 in/min	Welding root
10 Beads	SMAW	ENiCrFe3, 3/32"	75 A	22-25 V	5.50 in/min	Butt welding filler

Figure 4. Welding parameters.

Metals, Alloys and Intermetallics

MS4.P093
TEM analysis of planar defects in creep deformed single crystal cobalt-base superalloys

M. Lenz[1], Y. M. Eggeler[1], C. Zenk[2], S. Neumeier[2], M. Göken[2], P. Wollgramm[3], H. Buck[3], G. Eggeler[3], E. Spiecker[1]

[1]Institute of Micro- and Nanostructure Research, Department for Material Science & Engineering, Erlangen, Germany
[2]Institute of General Material Properties, Department for Material Science & Engineering, Erlangen, Germany
[3]Ruhr-Universität Bochum, Institute for Materials, Bochum, Germany

malte.lenz@fau.de

Co-based superalloys with a composition of Co-9Al-9W exhibit a stable γ/γ' microstructure at 900°C [1]. This microstructure appears to be identical to the microstructure of the well known Ni-base superalloys, which are used for first stage blades in gas turbines and therefore may provide similar or better mechanical high temperature properties. Further work on improving the simple ternary system showed, that adding Ni increases the γ' phase field and most importantly the γ'-solvus temperature [2]. In addition, Ta increases the high temperature strength [3] and Cr improves the high temperature corrosion resistance [4,5]. Based on these findings a new single crystalline Co-based superalloy, referred to as ERBOCo-1, was cast, heat treated and subsequently creep deformed in tension and compression.

In the present study we use conventional transmission electron microscopy (CTEM) to study the evolution of microstructure during tensile and compression creep. After the heat treatment the ERBOCo-1 alloy exhibits cuboidal γ' precipitates coherently embedded in a solid solution γ (fcc) matrix. The precipitates have an average edge length of 700 nm and a projected area fraction of 85%, see Figure 1. The cuboidal shape is a result from the combination of elastic anisotropy of the single crystal and the tendency to keep the elastic strain energy at a minimum.

After [001] tensile creep (850°C, 400 MPa) up to a plastic strain of 5%, SEM images show directional coarsening and coalescence of the precipitates. TEM images of samples which were prepared from miniature tensile and compressive specimens with a foil normal parallel to the tensile axis, show a high density of stacking faults in the γ/γ' microstructure.

The stacking faults were characterized by contrast analysis of bright field (BF) and centered dark field (CDF) images, using two beam conditions of fundamental reflections (see Figures 2 and 3). Comparing the fringe contrasts in BF (symmetric fringe contrast) and CDF (asymmetric fringe contrast), the inclination direction of the stacking faults and their physical nature (intrinsic or extrinsic) can be determined. Applying this method to different locations in the specimen, shows, that the numbers of observed super intrinsic (SISF) and super extrinsic stacking faults (SESF) are similar indicating low fault energies.

The direction of the Burgers vectors of the partial dislocations creating the stacking faults are characterized by the g·b invisibility criterion. Special attention is paid to the formation of new partial dislocation reaction events forming during creep.

The present analysis contributes to a better understanding of the deformation processes which govern the tensile and compression creep properties of new Co base superalloys. Further work is required to study geometrical features of planar faults and to describe the interactions of SISFs and SESFs. The microscopic observations can be compared to computer predictions.

1. Sato et al., Science **312**, (2006).
2. Shinagawa et al., Materials transactions, **49** (2008).
3. Suzuki et al., Acta Materialia, **56**, (2008).
4. Klein et al., Corrosion Science, Volume **53(9),** (2011).
5. Klein et al., Corrosion Science Volume **53(5)**, (2011).
6. The authors gratefully acknowledge the DFG priority program SFB-TR 103 for financial support.

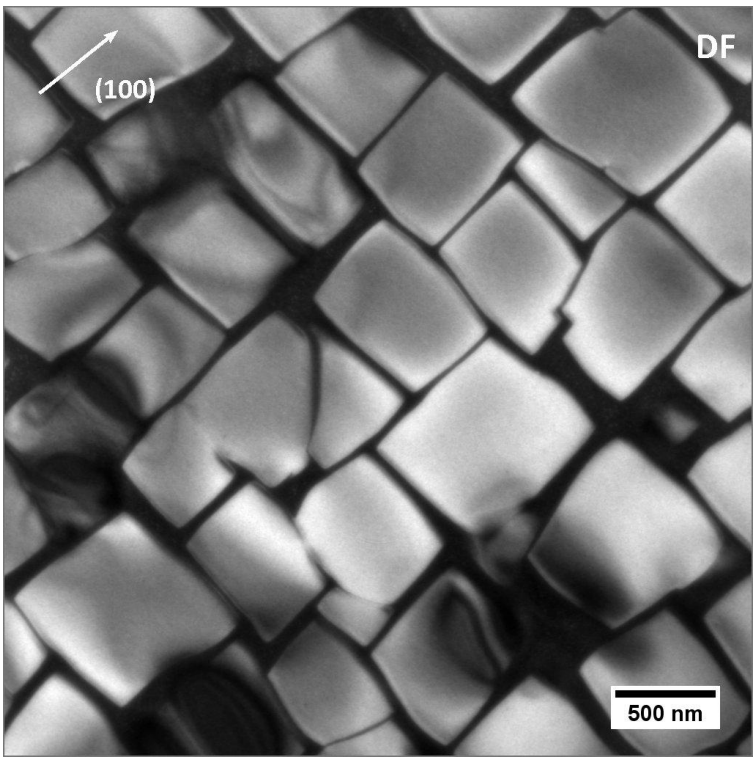

Figure 1. DF-micrograph of the heat treated undeformed ERBOCo-1 single crystal. The average edge length is 700 nm and projected area fraction of the γ´- precipitates is 85%

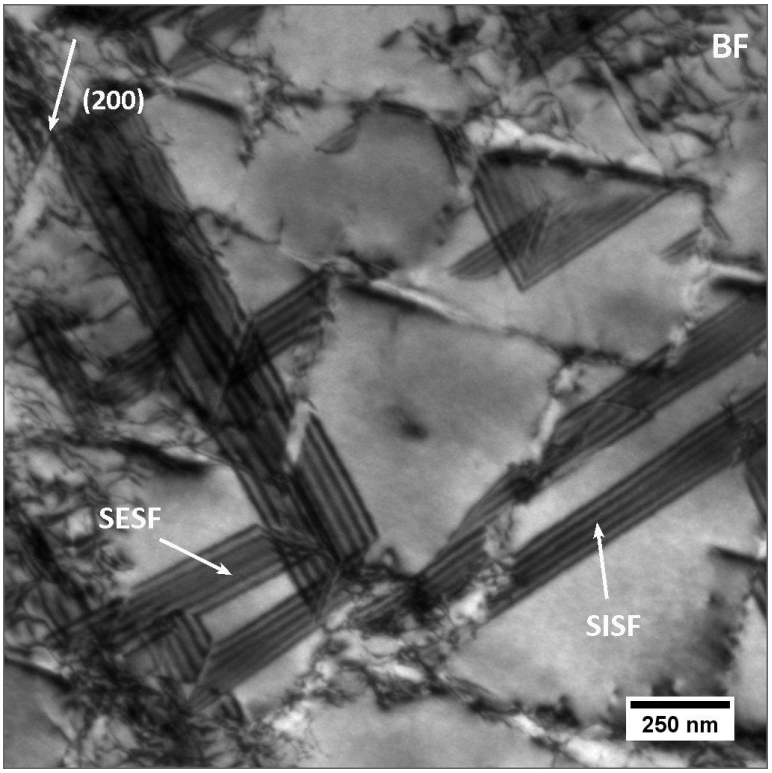

Figure 2. BF-micrograph (g=(200)) of 5% tensile deformed ERBOCo-1 single crystal. Stacking faults are only present in the ordered L12-structure of the γ´- precipitates.

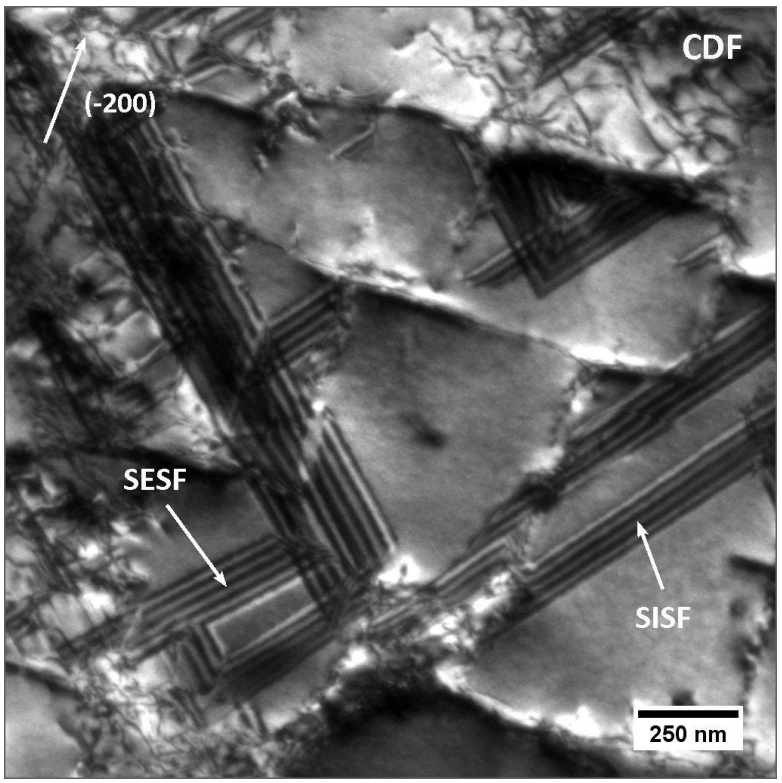

Figure 3. CDF micrograph (g=(-200)) of an arrangement of stacking faults. The asymmetric contrast in CDF allows a distinction between SISFs and SESFs.

Metals, Alloys and Intermetallics

MS4.P094
Analytical study of Z-phase precipitation in long term aged 9%Cr ferritic alloy

M. Klimenkov[1], U. Jäntsch[1], J. Hoffmann[1], M. Rieth[1]

[1]Karlsruhe Institute of Technology, Institute for Applied Materials - Applied Materials Physics, Eggenstein-Leopoldshafen, Germany

michael.klimenkov@kit.edu

High-performance reduced-activation ferritic-martensitic steels (EUROFER 97) with 9%Cr (WMnVTa) content have been envisaged for application as a structural material for operations at up to 650°C in future fusion reactors as well as in Generation IV fission reactors [1]. The steel exhibits several properties required for such applications: reduced void swelling, good resistance to radiation damage, high mechanical strength even at high temperatures, and reasonable ductility. To study long-term thermal stability of EUROFER, the material was annealed in the range from 400° to 650° for up to 70000 h. Thermal stability of the EUROFER97 microstructure is achieved by the formation of $M_{23}C_6$, TaC, and VN precipitates on the grain and lath boundaries [1]. Annealing at 600°C for several tens of thousands of hours leads to the formation of a Z phase which might influence the mechanical properties of the steel. Transmission Electron Microscopy (TEM) with Electron Energy Loss Spectroscopy (EELS) has been used for identification and to study the morphology, structure, and chemical composition of new precipitates formed during long-term thermal treatment.

As precipitates in ferritic steels can have a contrast similar to that of the matrix, they can only be studied using analytical imaging. Fig. 1 shows a distribution of main compositional elements in a specimen annealed at 600°C for 35000 h, which was obtained using EDX elemental mapping. The investigated area is marked by a square in the HAADF image (Fig. 1). The Fe map reveals the location of all secondary-phase precipitates. Cr distribution reflects the location of $M_{23}C_6$ precipitates and the Z phase. The smaller precipitates of $M_{23}C_6$ type have a size that varies from 50 nm to 120 nm and a higher Cr concentration than the larger, faceted Z-phase (up to 700 nm in size). Ta and V are present in small precipitates of MX type (VN and TaC [1]) as well as in the Z-phase. Based on these analytical results, it was found that the Z-phase can be differentiated well from other phases, which also may contain Cr, V, and Ta or a combined composition of these elements [2]. Fig. 2 presents a coloured map of these three compositional elements. Cr concentration is high in $M_{23}C_6$ precipitates, which is indicated by the red colour, the Ta map in blue colour reflects the location of TaC precipitates, and V in yellow colour shows the distribution of the few VN precipitates. The Z-phase is imaged in light blue and light green colours as a combination of these elements (Fig. 2). EELS and EDX spectra reflecting the chemical composition of the Z-phase are presented in Fig. 3. Pronounced N-K edge at 405eV, V-$L_{2,3}$ edge at 516eV and Cr-$L_{2,3}$ edge at 565eV are visible in the EELS. As tantalum shows a weak and smooth EELS $M_{4,5}$ edge at 1750eV it was detected using EDX.

TEM investigation of precipitates in EUROFER 97 after long-term thermal treatment at 550°C reveals the formation of Z-phase precipitates with (CrTaV)N composition.

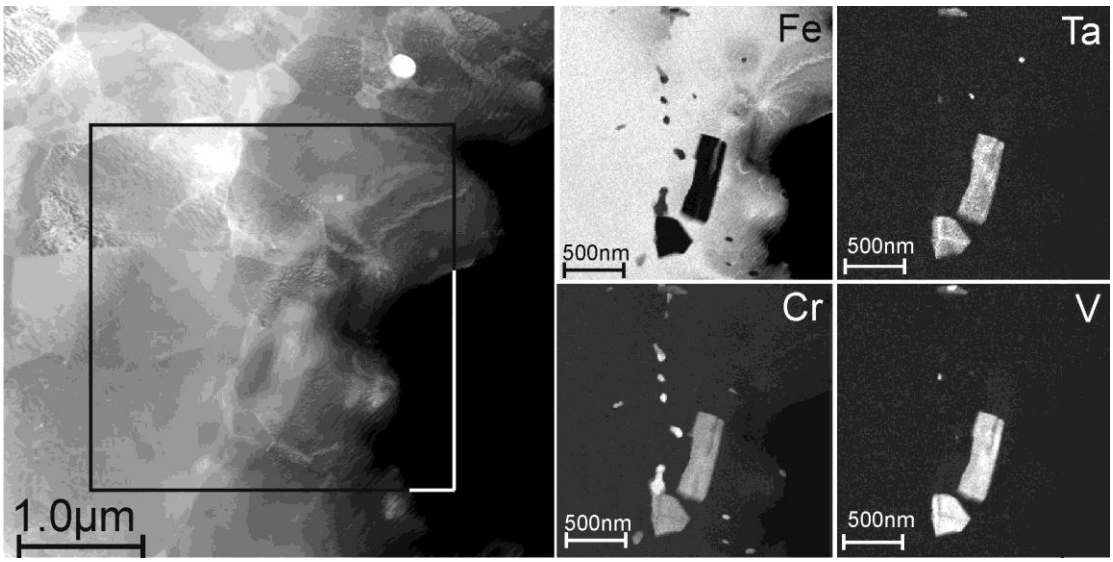

Figure 1. HAADF image of an area on the specimen edge and Fe, Cr, Ta, and V elemental maps.

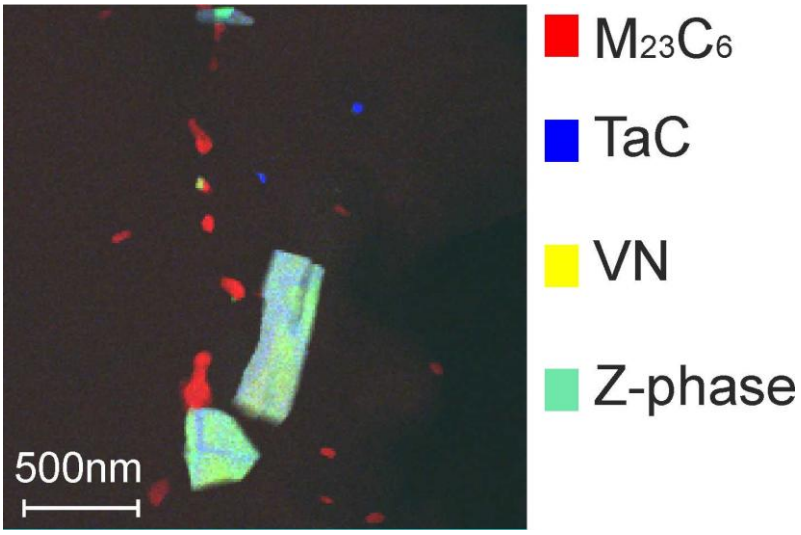

Figure 2. Colour mix image of Cr, Ta, and V maps.

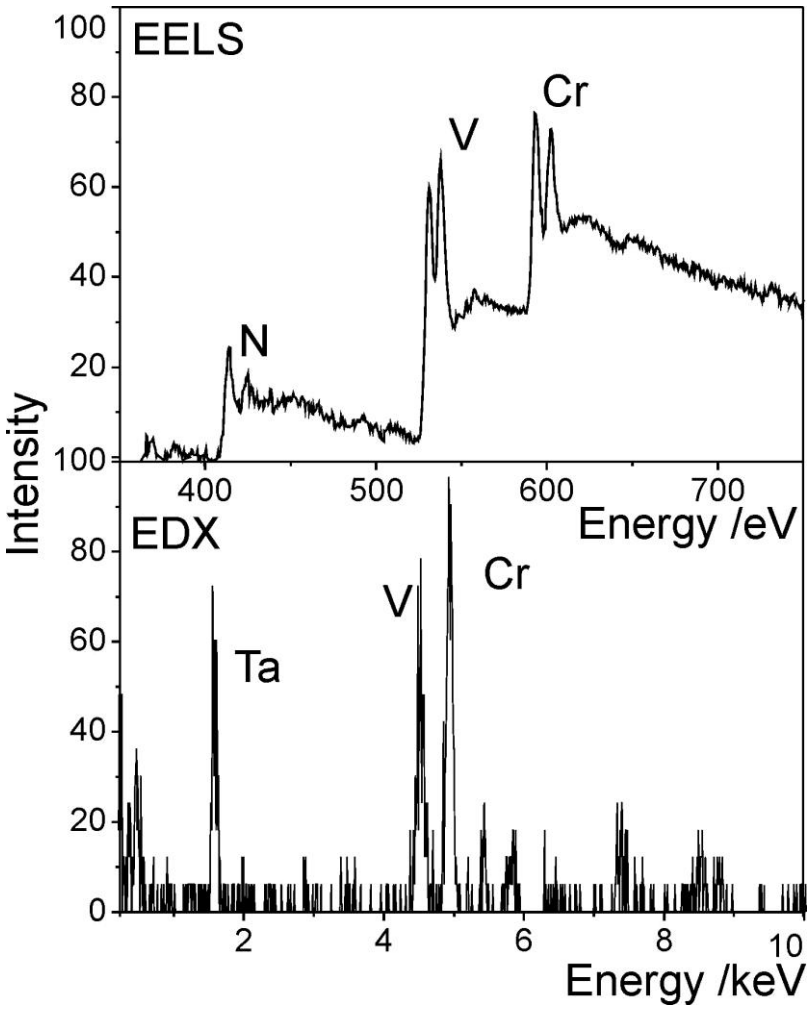

Figure 3. EDX and EELS spectra revealing the composition of the Z-phase.

Metals, Alloys and Intermetallics

MS4.P095
Influence of solution treatment on the microstructure and properties of Cu-0.8Cr and CuFe2 alloys

A. Urbańczyk-Gucwa[1], I. Bednarczyk[1], M. Jabłońska[1]

[1]Silesian University of Technology, Faculty of Materials Science and Metallurgy, Katowice, Poland

anna.urbanczyk-gucwa@polsl.pl

Copper alloys are recognizable as a prime materials in the so-called eco-project revolution, because these materials have a good combination of strength and electrical conductivity. Cu-0.8Cr and CuFe2 alloys in comparison with pure copper are mainly recognizable as a precipitation-hardenable electric engineering material. These properties can be improved by using modern methods of severe plastic deformation to produce ultrafine grained or nano -grained structures. From literature [1] is know, that metallurgical processes are very complicated and require high precision during melting and casting of alloys, since susceptibility to oxidation processes is high. In order to reduce the oxygen content in the cast alloy and improve the mechanical properties, is applied phosphorus, which have a better chemical relation with oxygen than with copper. For this reason gives the dissolution of oxygen in the liquid copper [2]. However the effect of phosphorus addition on the microstructure and precipitation process is not well understood. Increase of solution temperature can cause oxidation of the Cu alloys and increase in thickness of oxide layer. The preferred temperature of solution with the short times for Cu-0.8Cr and CuFe2 alloy is 1000 ± 10ºC [3-5]. In structure of Cu-0.8Cr and CuFe2 alloys after solution a large amount of precipitates of Cr and Fe are visible respectively. In this work the influence of solution treatment parameters on microstructure and properties have been investigated to eliminate the structural effects resulting from previous technological treatments and homogenous structure in the whole volume of the obtained material.

Cu-0.8Cr (C18200), and CuFe2 (C19400) alloys were prepared by melting and alloying in an open- air induction furnace. The billets were hot forged at temperature of 750ºC and next rolled with using intermediate annealing at temp. 700ºC for about 10 min. In the final, the material was rolled to obtain desired dimensions. Samples were subjected to heat treatment by solution at 1000ºC for 1, 3 and 12 hours with water cooling. Structural analysis of Cu-0.8Cr and CuFe2 alloys were performed using a light microscopy and a scanning transmission electron microscopy.

The increase of the time solution for Cu-0.8Cr and CuFe2 alloys effectively reduces structural defects. The structures of alloy is more homogeneous after 12h of solution in 1000ºC, than after 1h of solution in 1000ºC (Figure 1,3). Figure 3 shows SEM/EDS results of Cr particle analysis. Figure 4 shows chemical composition of Fe, P- rich precipitates in the CuFe2 alloy which are spherical in shape. In our investigation has been shown, that chemical composition of these particles is similar to reported in literature and this composition is suitable for Fe3P phase [6].

1. Rdzawski. Z.: Miedź stopowa. Wyd. Politechniki Śląskiej, Gliwice 2009
2. Górny Z.: Miedź i jej stopy o wysokiej konduktywności. Instytut Odlewnictwa, Kraków 2011
3. Rdzawski Z., Stobrawa J., Głuchowski W.: Structure and properties of CuFe2 alloy. Journal of Achievements in Materials and Manufacturing Engineering, Vol. 33 Issue 1, 2009, p.7-18
4. Stobrawa J., Rdzawski Z., Głuchowski W., Malec W.: Microstructure evolution in CRSC processed strips of oCuCr0.6 alloy. Journal of Achievements in Materials and Manufacturing Engineering, Vol. 38 Issue 1, 2010, p.195-202
5. Wei K., Wei W., Wang F., Bo Du Q., Aleksandrov I., Hu J.: Microstructure, mechanical properties and electrical conductivity of industrial Cu-0.5%Cr alloy processed by severe plastic deformation. Materials Science and Engineering A 528 (2011) 1478-1484
6. Jeong E., Han S., Goto M., Kim S.: Effects of thermo-mechanical processing and trace amount of carbon addition on tensile properties of Cu-2.5Fe-0.1 alloys. Materials Science and Engineering A 520 (2009) 66-74

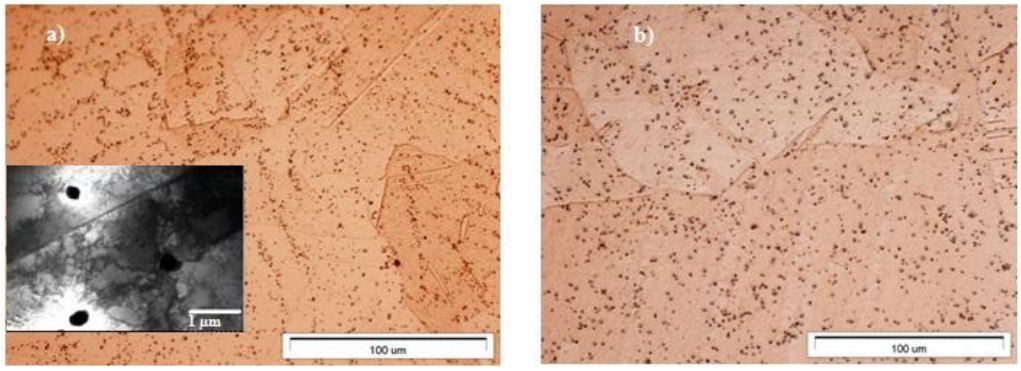

Figure 1. Microstructure of Cu-0.8Cr alloy after heat treatment by solution at temperature of 1000ºC: a) for 1 h, b) for 3 h.

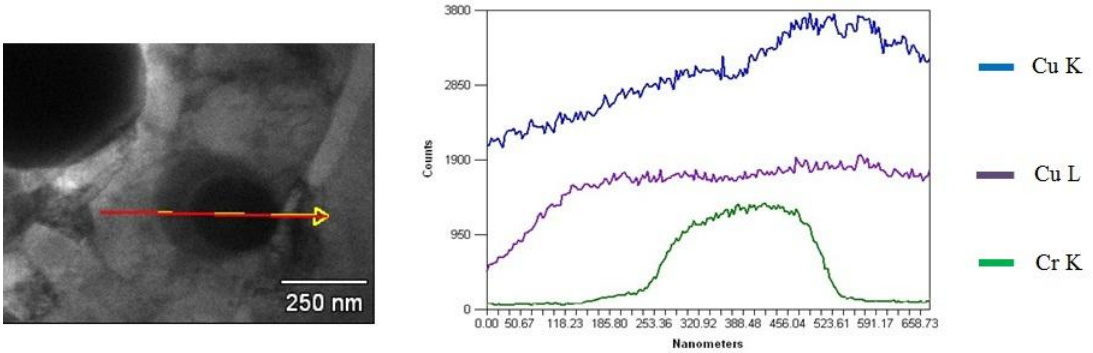

Figure 2. STEM/EDS analysis of particle in Cu-0.8Cr alloy after solution treatment at 1000ºC/1 h.

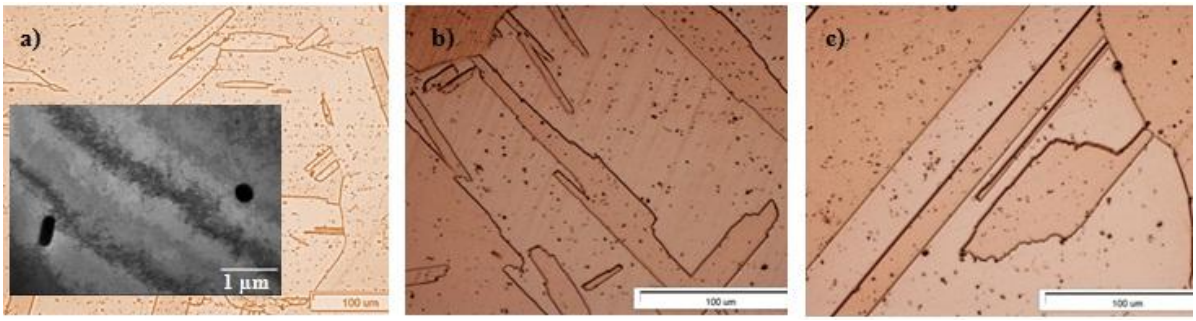

Figure 3. Microstructure of CuFe2 alloy after heat treatment by solution at temperature of 1000ºC:a) for 1 h, b) for 3 h c) 12 h

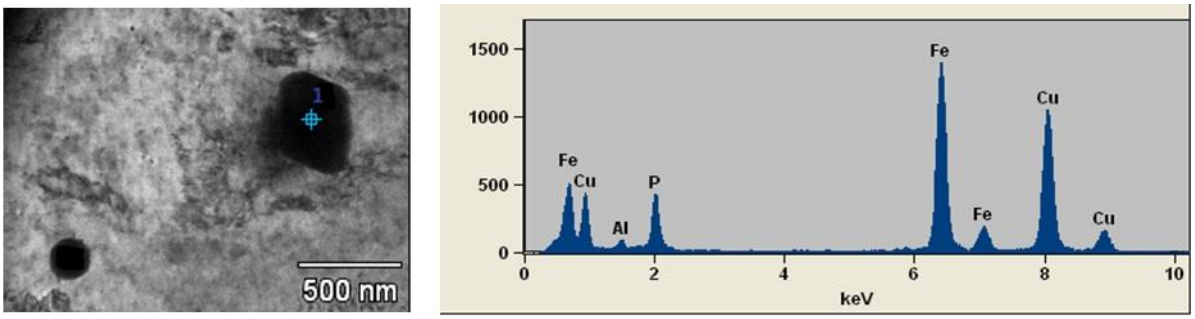

Figure 4. STEM- EDS spectra of particle in the CuFe2 alloy after solution treatment at 1000ºC/1h

Metals, Alloys and Intermetallics

MS4.P096
Deformation microstructures in AlMg5 and CuFe2 alloys after severe plastic deformation by rolling with cyclic movement of rolls

I. Bednarczyk[1], A. Urbańczyk-Gucwa[1]

[1]Silesian University of Technology, Faculty of Materials Science and Metallurgy, Katowice, Poland

iwona.bednarczyk@polsl.pl

A lot of the scientific investigations is focused on the research of new materials with a high efficiency and new technologies for their production. Nano-grained and ultrafine-grained alloys are interesting because they have better mechanical and physical properties than the materials with micrometer grained structure [1-5]. Severe plastic deformation (SPD) is an effective tool for producing nano-grained and ultrafine-grained alloys. The most widely used SPD methods are: equal-channel angular pressing (ECAP), high pressure torsion (HPT), cyclic extrusion compression (CEC), accumulative roll bonding (ARB). The effectiveness of these methods has been revealed for a number of materials based on aluminum, copper, titanium and other [3]. Recent work has demonstrated, that one of the methods which can be used for SPD processing is rolling with cyclic movements of rolls (RCMR). This original method of deformation has been patented in Poland. The rolled strip is deformed by reducing the height and additionally is affected by movement of the material layers in a direction perpendicular to the main direction of rolling. By repeating this procedure, very high strains have been introduced into material and significant structural refinements has been achieved. Scheme of the RCMR method was shown in Figure 1**.**

The microstructural investigations were performed for CuFe2, AlMg5 alloys. These alloys have quite a high mechanical properties and for this reason, the technological applications of these alloys are significant. In literature, there is lack of information about how the RCMR processing influence on refinement structure of CuFe2, AlMg5 alloys. Therefore, in this study, RCMR process was adopted to microstructural analysis of these alloys.

Before deformation the alloys were subjected to a solution treatment at 1000ºC/1h for CuFe2 and a temperature of 550°C/12h for AlMg5 with cooling in water. The RCMR process was performed using parameters such as: amplitude of transverse movement of rolls - A=1.6 [mm], frequency of transverse movement of rolls- f = 1 [Hz], rolling reduction - ε_h= 80 [%], and the rolling rate v was 1 [rpm]. Microstructural analysis were performed using a HITACHY (scanning transmission electron microscopy (STEM) technique. The detailed quantitative investigations of the ultrafine-grained structures were performed using "MET-ILO" software.

The deformed microstructures of alloys are mainly characterized by dislocation tangles structures with small misorientation angles (Figure 2a, Figure 3a)**.** It was also presented grains/subgrains with size < 1µm (Figure 2b,c and 3 b,c). In analyzed microareas, the occurrence of large misorientation angles between the formed ultrafine grains have been detected (Figure 2b, Figure 2b) **(**Figure 2c, Figure 3c)**.**

1. Richert M., Leszczyńska-Madej B., Richert J., Boczkal S.: Wpływ intensywnych odkształceń na strukturę aluminium i jego stopów. Rudy Metale Nieżelazne 2010, t.55, Nr.5, pp. 284÷291
2. Wei K. and all.: Microstructure, mechanical properties and electrical conductivity of industrial Cu-0,5%Cr alloy processed by severe plastic deformation. Materials. Science. and Engineering. A528, 2011, pp.1478-1484
3. Lewandowska M.: Wytwarzanie materiałów nanokrystalicznych metodą wyciskania hydrostatycznego. Obróbka Plastyczna Metali 2006, t. XVII Nr.4, pp. 9÷13
4. Skorupka J., Rodak K.: Zmiany struktury w stopie AlMg5 po dużym odkształceniu plastycznym. Rudy Metale Nieżelazne 2013, R58 Nr. 3, s. 143÷148
5. Cyganek Z., Rodak K., Grosman F.: Influence of rolling Influence of rolling process with induced strain path on aluminium structure and mechanical properties; Archives of Civil and Mechanical Engineering, 2012, p.15

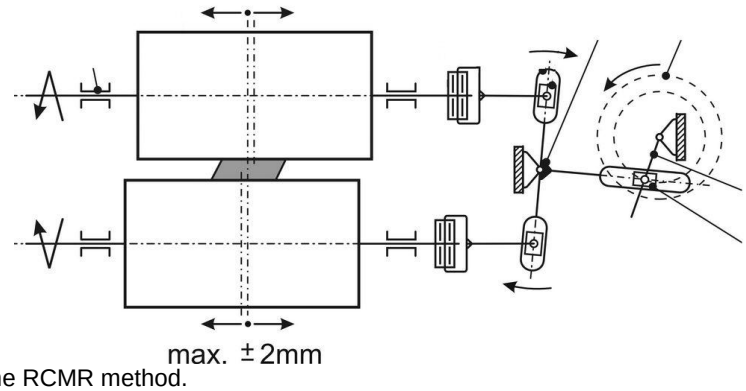

Figure 1. Scheme of the RCMR method.

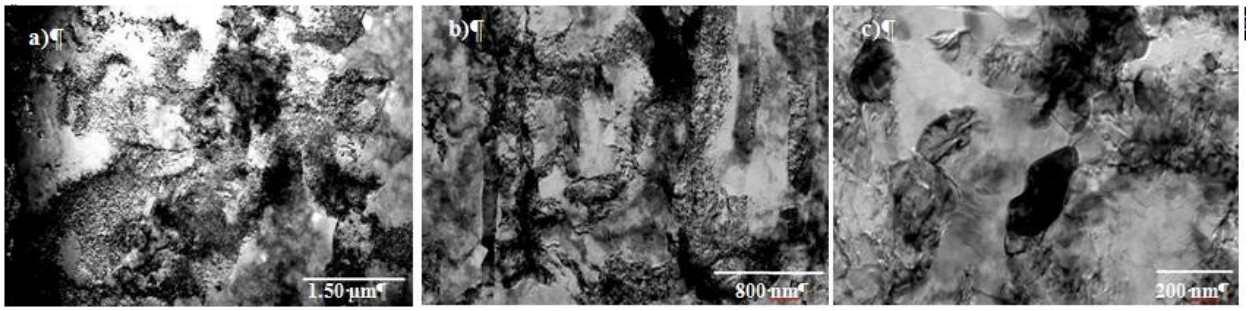

Figure 2. Substructure of AlMg5 alloy after RCMR deformation with the parameters: e_h = 80%, f = 1 Hz, A = 1.6 mm, v = 1 rpm.

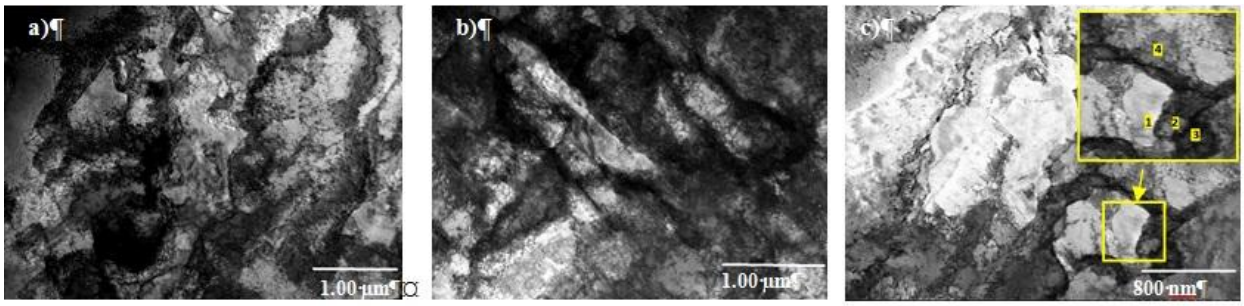

Figure 3. Substructure of CuFe2 alloy after RCMR deformation with the parameters: ε_h = 80%, f = 1 Hz, A = 1.6 mm, v = 1 rpm. Numbers 1-4 in fig.3c. correspond to diffraction patterns 1-4 for grains/subgrains.

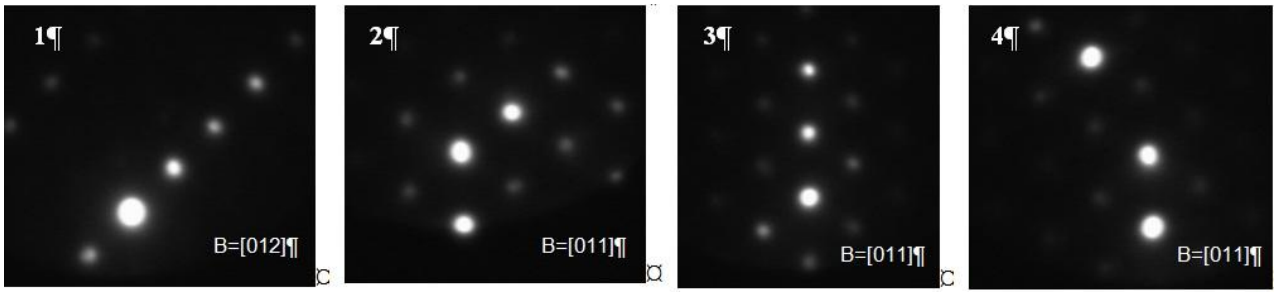

Figure 4. Diffraction patter from Fig.3c

Soft Matter, Polymers, C-Based Materials

MS5.098
Properties of carbon-based objects with low-voltage high-resolution transmission electron microscopy

U. Kaiser[1]

[1]Central Facility of Electron Microscopy, Group of Electron Microscopy of Materials Sciences, Ulm University, Ulm, Germany

ute.kaiser@uni-ulm.de

We report on structural and electronic properties of carbon-based objects obtained by analytical low-voltage aberration-corrected high-resolution transmission electron microscopy (AC-HRTEM).

We first demonstrate the presumptions which need to be taken into consideration for image interpretation. We show that for high-resolution imaging at low voltages the contribution of inelastic scattering must be taken into consideration [1]. For energy-filtered images of low-Z materials at low voltages, the contributions of elastic and inelastic scattering to the image intensity cannot be separated from each other because the inelastic scattering amplitudes are influenced by elastic scattering, and vice versa [2]. We moreover demonstrate our simple approach to correct for the antisymmetric residual aberrations in a HRTEM image by image post-processing [3]. As signal-to-noise is limited, we show an approach to work with noisy images [4], to sandwich beam-sensitive objects in-between two graphene layers [5,6], and to get graphene clean of residual contaminations [7]. The exchange of the isotopes of the molecules (deuterium instead of hydrogen) also enhances the stability against knock-on damage independent on the voltage [8].

In the application part we discuss how to change the properties of graphene by self-interstitials [9] and report on the discovery of new structures in-between [5,10] and on graphene [11,12] (see the Figure). We show that by exchanging hydrogen by chorine it is possible to image a chorine molecule in near-atomic resolution [13].

Moreover, we show that the monochromatic low-energy electron beam enables the acquisition of EELS spectra with exceptionally low background noise. In addition to the energy of electronic excitations, information on the momentum transfer can be obtained in the analytical TEM. We determine the dispersion behaviour for π and π+σ plasmons in free-standing single-layer graphene and multilayers as benchmark experiments confirming earlier calculations [14].

1. Z. Lee, J.C. Meyer, H. Rose, U. Kaiser, Ultramicroscopy 112 (2012) 39.
2. Z. Lee, H. Rose, R. Hambach, P. Wachsmuth, U. Kaiser, Ultramicroscopy 134 (2013)102.
3. O. Lehtinen, D. Geiger, Z. Lee, M. B. Whitwick, M.-W. Chen, A. Kis and U. Kaiser, Ultramicroscopy (2014) doi:10.1016/j.ultramic.2014.09.010
4.Z. Lee, H. Rose, O. Lehtinen,J. Biskupek, U. Kaiser, Ultramicroscopy 145 (2014) 3.
5. G. Algara-Siller, N. Severin, S. Y. Chong, T. Björkman, R. G. Palgrave, A. Laybourn, M. Antonietti, Y. Z. Khimyak, A. V. Krasheninnikov, J. P. Rabe, U. Kaiser, A. I. Cooper, A. Thomas and M. J. Bojdys Angewandte Chemie 53(29) (2014) 7450.
6. G. Algara-Siller, S. Kurasch, M. Sedighi, O. Lehtinen and U. Kaiser, Appl. Phys. Lett. 103 (2013) 203107.
7. G. Algara-Siller, O. Lehtinen, A. Turchanin, U. Kaiser, Appl. Phys. Lett. 104 (2014) 153115.
8. T. W. Chamberlain, J. Biskupek, S. T. Skowron, P. A. Bayliss, E. Bichoutskaia, U. Kaiser, A. N. Khlobystov, Small 11 (2014) 510.
9. O. Lehtinen, N. Vats, G. Algara-Siller, P. Knyrim and U. Kaiser, Nano Lett., 2015, 15 (1), 235
10. G. Algara-Siller, O. Lehtinen, F. C. Wang, R. R. Nair, U. Kaiser, H. A. Wu, A. K. Geim, I. V. Grigoriev Nature 519 (2015) 443.
11. B. Westenfelder, J. Biskupek, J. Meyer, S. Kurasch, X. Lin, F. Scholz, A. Groß, U. Kaiser, Scientific Reports 5 (2015) 8891.
12. O. Cretu, H.-P. Komsa, O. Lehtinen, G. Algara-Siller, U. Kaiser, K. Suenaga and A. V. Krasheninnikov, ACS Nano 8, (2014) 11950.
13. A. Markevich, S. Kurasch, O. Lehtinen, O. Reimer, N. Hohlbein, X. Feng, K. Möllen, A. Turchanin, A. N. Khlobystov, U. Kaiser, and E. Bichoutskaia submitted.
14. P. Wachsmuth, R.Hambach, G. Benner and U. Kaiser, Phys. Rev. B 90 (2014) 235434.

15. This work is supported by the German Research Foundation (DFG) and the Ministry of Science, Research and Arts (MWK) of the state Baden- Wurttemberg within the Sub-Ångstrøm Low-Voltage Electron Microscopy project (SALVE) and by the DFG in the frame of the SPP graphene.

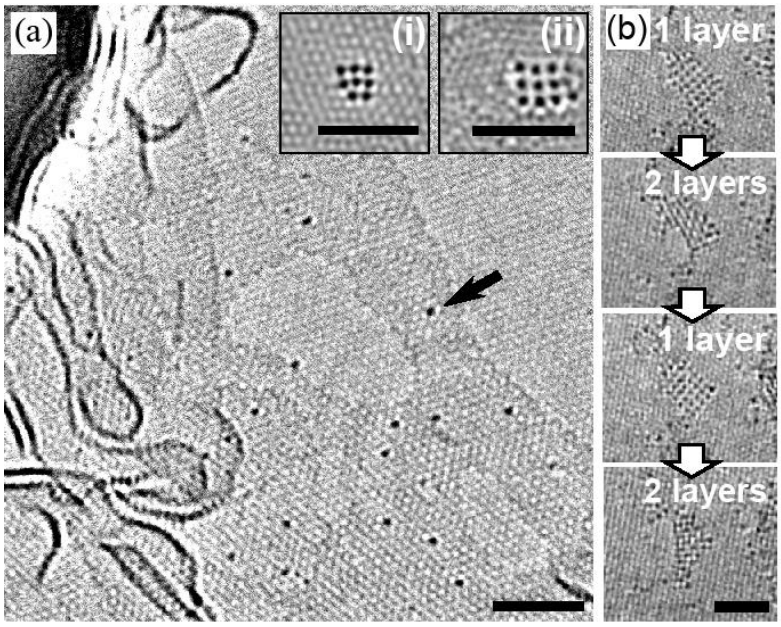

Figure 1. (a) 80 kV HRTEM image of graphene at elevated temperature. The arrow marks a mobile Au atom embedded in graphene and the inserts show small Au clusters. (b) HRTEM images of single and double layer of AuC-clusters in a NaCl-crystal structure [11] (scale bars: 1 nm)

Soft Matter, Polymers, C-Based Materials

MS5.099
Nanomorphology of organic solar cells imaged by low-energy STEM

D. Gerthsen[1], M. Pfaff[1], E. Müller[1]

[1]Karlsruhe Institute of Technology (KIT), Laboratory for Elecron Microscopy, Karlsruhe, Germany

gerthsen@kit.edu

Scanning transmission electron microscopy at electron energies below 30 keV (low-keV STEM) is a promising technique for materials analysis. Low-keV STEM images can be taken in a relatively inexpensive scanning electron microscope equipped with a STEM detector. The resolution for thin samples can approach the minimum electron-beam diameter, about 1 nm in state-of-the-art scanning electron microscopes, which is sufficient for solving many questions in materials science and biology. Knock-on damage at these low electron energies is largely avoided. For the optimization of the imaging conditions, the primary electron energy E_0 and the detection angle range can be easily varied without major microscope realignment. Low-keV high-angle annular dark-field (HAADF) STEM is particularly sensitive with respect to compositional variations because the mean square scattering angle is $\sim Z^2/E_0^2$ with the atomic number Z [1]. Despite of these advantages, only little dedicated work on low-keV STEM in scanning electron microscopes has been performed up to now, e.g. [2]. Another advantage is that low-keV STEM image intensities can be well modelled by Monte-Carlo simulations which facilitates, *e.g.*, the determination of sample thickness provided that the composition is known, the proper type of scattering cross-section is used and the properties of the STEM detector are taken into account [3].

The high chemical sensitivity of low-keV HAADF STEM can be exploited to image absorber layers of organic solar cells where the distribution of donor and acceptor phases determines their efficiency. This is exploited for a bulk heterojunction blend consisting of Poly(3-hexylselenophene) (P3HS):[6,6]-phenyl-C_{61}-butyric acid methyl esther ($PC_{61}BM$). Fig. 1 shows for comparison an in-focus 200 keV bright-field TEM and a 15 keV HAADF STEM image of a P3HS:$PC_{61}BM$ absorber layer with ~ 100 nm thickness. The uniform image intensity in the TEM image (Fig. 1a) does not allow any conclusions on the distribution of the two different phases whereas the 15 keV HAADF STEM image shows pronounced contrast variations. It is noted that the TEM contrast can be improved by defocusing the objective lens but this will strongly degrade the resolution if structures in the 10 nm range must be imaged. For further contrast interpretation of Fig. 1b the HAADF STEM intensity for P3HS and $PC_{61}BM$ was calculated as a function of E_0 for a sample thickness of 100 nm according to the model outlined in [1]. The intensities are normalized with respect to the intensity of the incident electron beam. Fig. 2 demonstrates that the HAADF STEM intensity depends strongly on E_0. For 15 keV, P3HS displays bright contrast compared to $PC_{61}BM$ indicating that P3HS occurs in elongated needle-like structures which are embedded in $PC_{61}BM$ (cf. Fig. 1b).

Fig. 2 suggests that the same HAADF STEM intensity for $PC_{61}BM$ and P3HS occurs at 8 keV and inverted contrast at lower E_0. This behavior is indeed observed in the HAADF STEM images in Fig. 3 taken at different E_0 which confirms 100 nm sample thickness in this case. The determination of E_0 at minimum contrast and contrast inversion can be exploited for sample thickness determination because minimum contrast depends on the local sample thickness.

Low-keV HAADF STEM is in general well suited for the study of soft matter samples where electron scattering is generally weak and only small differences between the material density and atomic number exist. Further electron optics development for scanning electron microscopes will improve the resolution of the technique and even atomic-scale resolution is conceivable in the future [4].

1. M. Pfaff *et al.*, J. Microscopy **243** (2011), 31.
2. P.G. Merli *et al.* Appl. Phys. Lett. **81** (2002), 4535.
3. T. Volkenandt *et al.*, Microsc. Microanal. **20** (2014), 111.
4. We acknowledge funding by the German Research Foundation (DFG) and provision of samples by M.F.G. Klein, A. Colsman and U. Lemmer (Light Technology Institute, KIT).

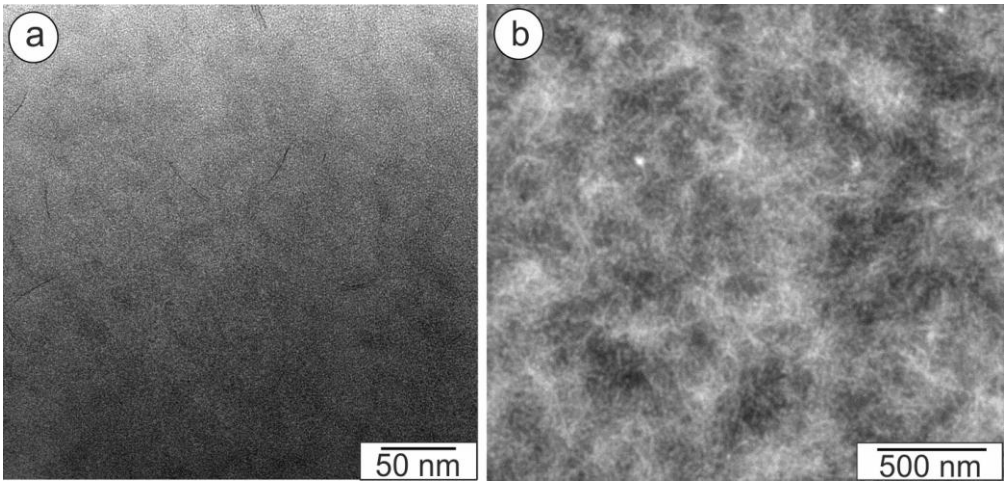

Figure 1. a) In-focus 200 keV bright-field TEM image and b) 15 keV HAADF STEM image of a P3HS:$PC_{61}BM$ absorber layer with ~ 100 nm thickness.

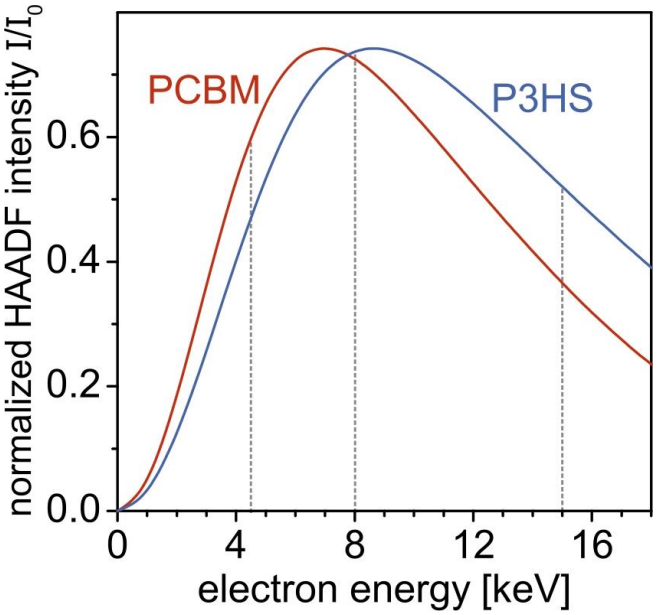

Figure 2. Calculated normalized HAADF STEM intensity for P3HS and PCBM as a function of E_0 for a sample thickness of 100 nm. Dashed lines mark E_0 at which the HAADF STEM images in Fig. 3 were taken.

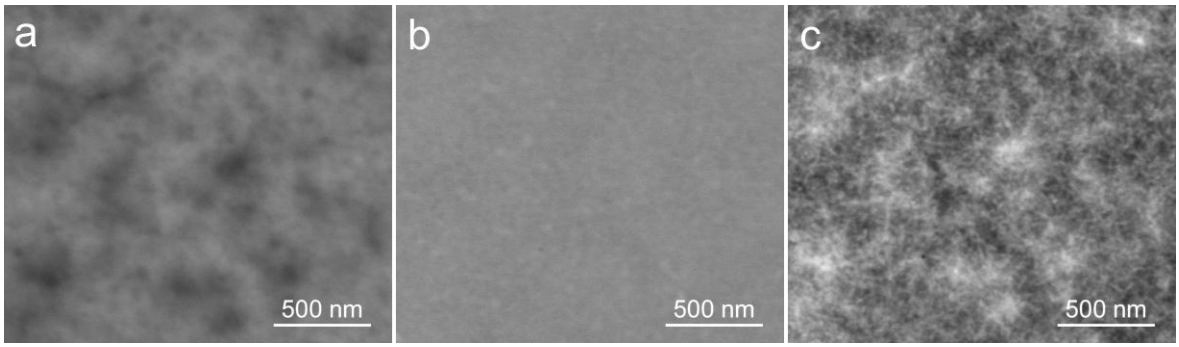

Figure 3. HAADF STEM images of a P3HS:$PC_{61}BM$ absorber layer taken with a) E_0 = 4.5 keV, b) E_0 = 8 keV and c) E_0 = 15 keV.

Soft Matter, Polymers, C-Based Materials

MS5.100
In-situ TEM study of the formation of fullerene-like cages on metal surfaces

F. Ben Romdhane[1], J. A. Rodriguez Manzo[2], A. Andrieux-Ledier[3], F. Fossard[3], A. Hallal[4], L. Magaud[4], J. Coraux[4], A. Loiseau[3], F. Banhart[1]

[1]Institut de Physique et de Chimie des Matériaux de Strasbourg, Département de surface et interface, Strasbourg, France
[2]University of Pennsylvania, Department of Physics and Astronomy, Philadelphia, United States
[3]Laboratoire d'Etude des Microstructures, ONERA-CNRS, Chatillon, France
[4]Institut Néel , Grenoble, France

ferdaous.benromdhane@ipcms.unistra.fr

Since their discovery in 1985, fullerenes have been the subject of only few electron microscopy studies due to their susceptibility to electron irradiation. The formation of fullerene molecules, in particular under realistic conditions, could hardly be observed at high spatial resolution. A large range of sizes of these cages exists, limited at the lower end by C_{20}, which is a dodecahedron composed of 12 pentagons. Not only its regular shape (it is a fundamental platonic polyhedron) but also its large curvature and hybridization between sp^2 and sp^3 make C_{20} a most interesting nanoparticle. Until now, only few studies reported the synthesis of C_{20} due to its instability and reactivity. Isolated cages of C_{20} haven't been observed to date by electron microscopy.

Here we report the first observation of the nucleation and growth of spherical carbon cages with a diameter of approximately 3.6 Å [1]. The experiments were carried out *in-situ* in a transmission electron microscope (TEM) by using a heating stage. The samples were prepared on few-layer graphene suspended on standard Cu grids for electron microscopy. Different transition metal layers (Co, Fe, Ru) with thickness of 5 nm were deposit by sputtering onto the graphene layers. After an initial heating and cooling cycle of the samples, small carbon cages appeared on the graphene layers around the periphery of metallic nanoparticles. The contrast of the cages in TEM images at high resolution is comparable to the appearance of C_{60}, except the much smaller size. The cages always appeared as aggregates. The prerequisite for the nucleation of the cages was an uncovered metal surface. The cages persist after cooling to room temperature. The identification of the elemental composition of the observed cages was carried out by taking EEL spectra using a monochromated microscope with an energy resolution of 0.2 eV. To relate the observed contrast in the TEM images to fullerene-like clusters, image simulations of polymerized and unpolymerized C_{20} were carried out by using the EMS (Electron Microscope Simulator) simulation program. The observations are in accordance with the simulated images of polymerized C_{20} molecules.

The nucleation of the cages can be explained as a solid-state growth process where carbon atoms are diffusing through the bulk of the metallic nanoparticles at high temperature and segregate on the surface. Since the C_{20} cages are less stable than larger fullerenes, their formation should be driven by kinetics under non-equilibrium conditions. Due to their large curvature and inherent reactivity, the cages tend to polymerize. The EELS shows a small p* peak, indicating a hybridization state between sp^2 and sp^3 as it is expected for graphitic layers with high curvature.

1. F. Ben Romdhane, J. A. Rodríguez-Manzo, A. Andrieux-Ledier, F. Fossard, A. Hallal, L. Magaud, J. Coraux, A. Loiseau, F. Banhart. "The formation of the smallest fullerene-like carbon cages on metal surfaces", submitted

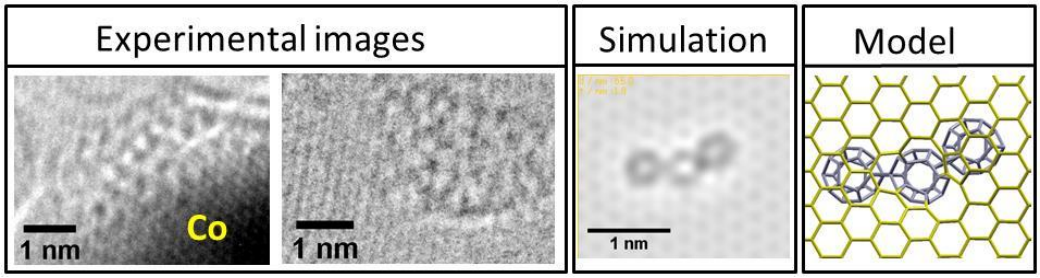

Soft Matter, Polymers, C-Based Materials

MS5.101
Microscopic evaluation of high-quality graphene oxide from wet-chemical synthesis

B. Butz[1], C. Dolle[1], S. Eigler[2], E. Spiecker[1]

[1]Universität Erlangen-Nürnberg, Institut für Mikro- und Nanostrukturforschung, Erlangen, Germany
[2]Universität Erlangen-Nürnberg, Lehrstuhl für Organische Chemie II, Erlangen, Germany

benjamin.butz@fau.de

Wet-chemical synthesis of monolayer graphene, that is utilized, e.g., to deposit percolated functional layers with well-defined properties, remains challenging. Per se, common exfoliation routes result in a mixture of graphene flakes with varying lateral dimensions and especially thicknesses, ranging from a monolayer up to a few ten layers. Hence, the resulting graphene product has to be fractioned by ultracentrifugation for further processing. An alternative but very promising route is to prepare percolated graphene layers from microparticulate, monolayer graphene oxide (GO) flakes, which can efficiently be derived from graphite by oxidation treatment. However, due to the harsh conditions during that reaction, the resulting GO is generally highly defective and exhibits reduced far-range order of the underlying carbon framework [1,2]. Due to the unintended release of carbon upon oxidation, the high density of atomic point defects may even cause recrystallization (nm-sized sub-grains separated by small-angle grain boundaries) or nm-scale holes, strongly limiting the performance of the derived graphene after reduction.

Recently, the oxidation to GO was substantially improved to almost overcome the loss of carbon atoms from the graphite sheets [3]. The obtained graphene after reduction of the GO bears charge carrier mobilities exceeding 2000 cm^2/Vs, which correlate to very low point-defect densities of around 0.01% for the best quality GO flakes [4].

Here, we present the detailed study on the microstructure and chemistry of the as-prepared GO by comprehensive TEM imaging and spectroscopy at 80 kV. The integrity of the underlying carbon framework of those GO flakes was proven by high-resolution TEM analyses (Fig. 1a). To address more detailed questions concerning the molecular structure of the material; meaning the distribution of functional groups and their bonding states, sample synthesis was further improved with respect to the minimization of unintended residuals on the GO. By the application of complementary X-ray/electron energy-loss spectroscopy (EELS) and energy-filtered TEM we were already able to identify most of the significant contamination sources. Figure 1b exemplarily shows the distribution of oxidized silicon, the main fraction of the amorphous residuals present in Fig. 1a. Prospectively, emphasis will be put on the understanding of electron-beam induced modifications of the original GO including the release of oxo-functionalities. That will give insight into the reduction mechanism of GO.

1. K. Erickson et al., Determination of the Local Chemical Structure of Graphene Oxide and Reduced Graphene Oxide, Adv. Mater. 22 (2010) 4467-4472
2. D. Pacilé et al., Electronic properties and atomic structure of graphene oxide membranes, Carbon 49 (2011) 966-972
3. S. Eigler et al., Graphene oxide: a stable carbon framework for functionalization, J. Mater. Chem. A 1 (2013) 11559-11562
4. S. Eigler et al., Wet Chemical Synthesis of Graphene, Adv. Mater. 25 (2013) 3583-3587
5. The authors gratefully acknowledge financial support by the German Research Foundation (DFG) within the framework of the SFB953 and the Cluster of Excellence EXC 315.

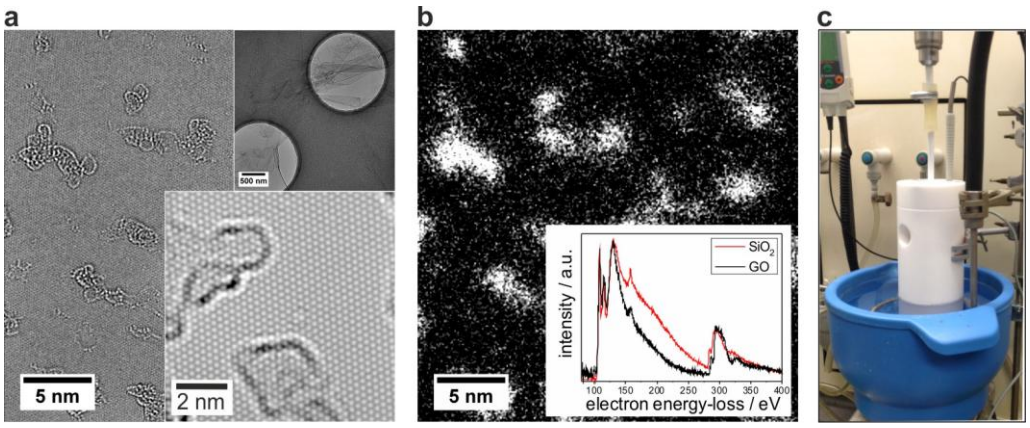

Figure 1. a) Inset (upper right): GO flakes after synthesis and deposition onto Quantifoil TEM support. HRTEM reveals intact carbon framework of the underlying sheet as well as amorphous residuals after release of functional groups. b) Si distribution by energy-filtered TEM (same area as a)). Inset shows EEL oxidation-state analysis of those SiO_x residuals. c) Teflon reactor developed for improved synthesis.

Soft Matter, Polymers, C-Based Materials

MS5.102
Investigating beam-damage effects on the polymer P3HT by electron diffraction and EELS at room temperature and LN_2 cryo-conditions

P. Kükelhan[1], A. K. Kast[1,2], Y. Vaynzof[3,4], R. R. Schröder[1,2,4]

[1]Universitätsklinikum Heidelberg, CryoEM, BioQuant, CellNetworks, Heidelberg, Germany
[2]Innovationlab GmbH, Heidelberg, Germany
[3]Universität Heidelberg, Kirchhoff-Institut für Physik, Heidelberg, Germany
[4]Universität Heidelberg, Centre for Advanced Materials, Heidelberg, Germany

pirmin.kuekelhan@bioquant.uni-heidelberg.de

Organic photovoltaic (OPV) is a promising future technology given its potential advantages like cost-efficient production and printability [1]. Many efficient materials have been studied over the past years and new record efficiencies of 12 % have been reported [2], In order to improve device efficiencies further, understanding of the interplay between absorber and acceptor materials in solar cells is crucial, thus calling for methods of morphological analysis. Transmission Electron Microscopy (TEM) coupled with Electron Energy-Loss Spectroscopy (EELS) can help to visualize material distributions [3], giving insight into properties such as phase separation, material interfaces and crystallinity. Since these carbon-based materials, much like biological samples, are extremely sensitive to irradiation [4], minimizing beam-damage is a necessity. Besides approaches using low electron doses and micro-dose focusing, cryo electron microscopy, as known from the life sciences, also decreases the damage of organic materials during irradiation.

In this work, the influence of LN2 cryo-conditions on electron diffraction and EELS measurements is investigated and compared to measurements performed at room temperature. The absorber polymer Poly(3-hexylthiophene-2,5-diyl) (P3HT) was chosen, since it is one of the most-researched materials in the field of OPV and thus very well understood [5]. P3HT in its regioregular (RR) form crystallizes very well [6], making it an optimal sample to investigate structural damage. Diffraction patterns of a sample of P3HT RR as-cast, acquired at room-temperature (a) and at cryo-conditions (b) can be seen in figure 1. The corresponding radial profiles in fig. 1c (RT) and 1d (cryo) confirm what can already be deduced from the patterns: cryo-conditions preserve the structural order of the polymer. The rings are of higher intensity and much sharper in fig. 1b than in 1a, where the diffuse signals suggest more amorphous regions. Along with the structural order of the polymer chains, the electronic properties are also damaged by electron irradiation. This can be studied by acquiring beam-damage series of EELS data. P3HT, being an organic semiconductor, shows a characteristic peak at about 2.6 eV, which can be attributed to the HOMO-LUMO transition. Fig. 2 shows how the low-loss region of the spectrum of P3HT RR changes during electron irradiation. The peak at 2.6 eV rapidly decreases and is blue-shifted before the characteristic signals for this solar cell material disappear completely.

Preliminary results suggest that the damage mechanism of characteristic spectral features of P3HT in the electron beam depends on sample temperature.

1. Gaudiana et al., Nature Photonics 2, 287 - 289 (2008)
2. Heliatek, press release, 16.01.2013
3. Pfannmoeller et al., Nano Lett., 11, 3099-3107 (2011)
4. Egerton et al., Micron 43, 2-7 (2012)
5. Dang et al., Adv. Mater., 23, 3597-3602 (2011)
6. Korovyanko et al., Phys. Rev. B, 64, 235122 (2001)
7. Financial support by the BMBF (FKZ 03EK3505K, FKZ 13N10794) is gratefully acknowledged.

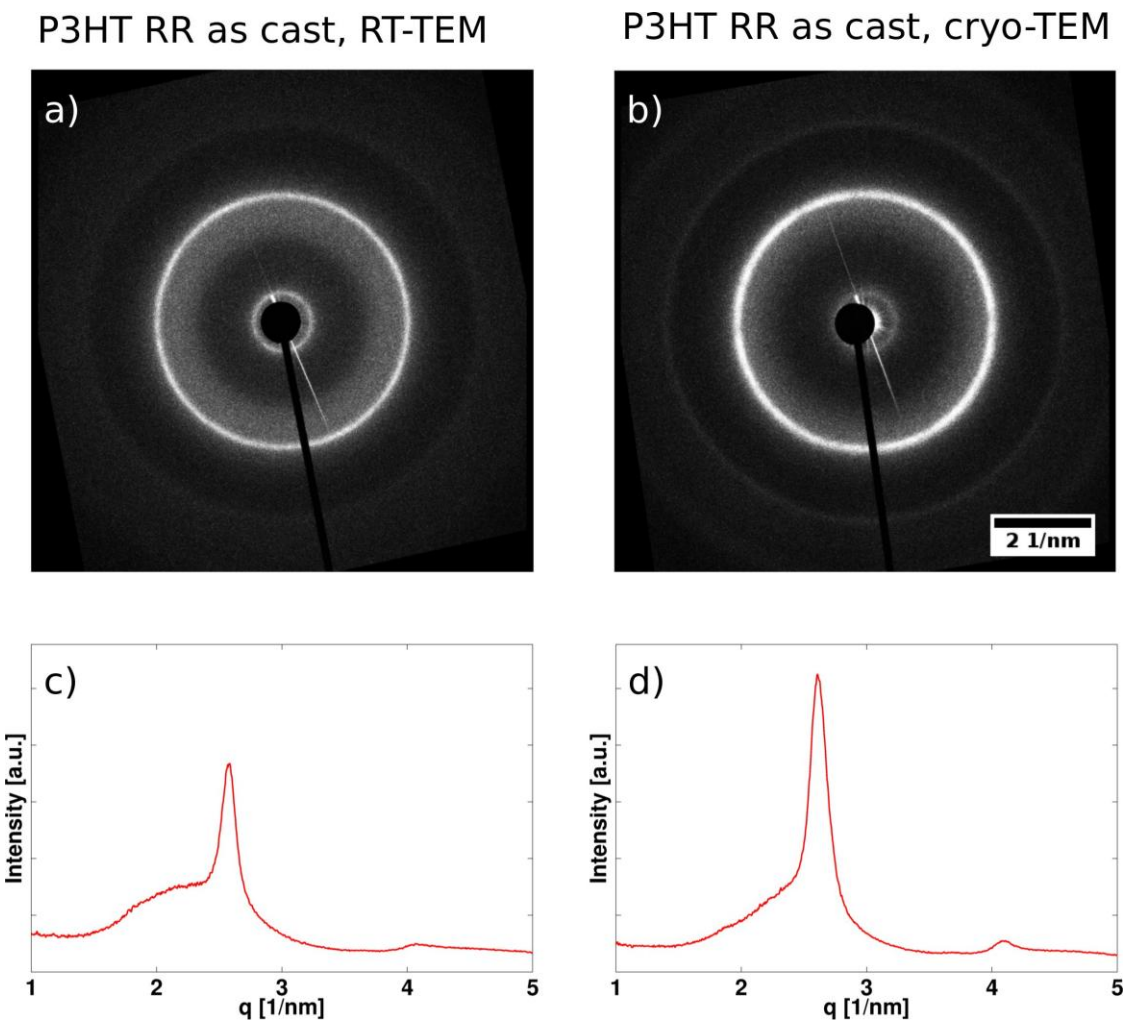

Figure 1. Diffraction pattern of P3HT RR as-cast acquired at room temperature (a) and cryo-conditions (b) at a dose of 680 e/sqnm. The corresponding radial profiles are shown in (c) and (d). The diffuse ring in (a) points to a higher number of amorphous regions. This can also be deduced from the radial profile. The more pronounced rings at cryo-conditions suggest less damage to the structural order during the exposure.

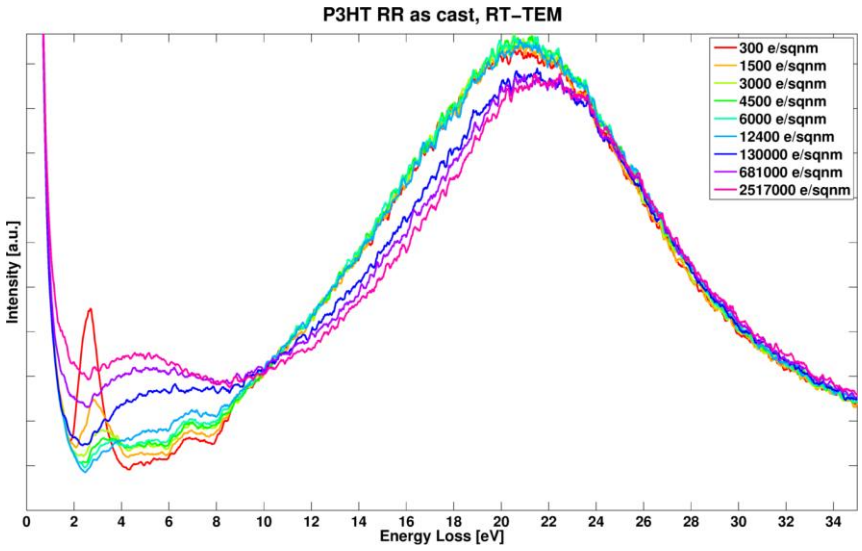

Figure 2. EELS dose series of P3HT RR as cast acquired at room temperature. The fast loss of the peak at 2.6 eV, representing the HOMO-LUMO transition, indicates the damage to the electronic structure of the absorber.

Soft Matter, Polymers, C-Based Materials

MS5.103
Self-organization of noncovalent systems in aqueous medium - updates on construction and destruction

H. Weissman[1]

[1]Weizmann Institute of Science, Organic Chemistry, Rehovot, Israel

haim.weissman@weizmann.ac.il

Supramolecular polymer systems are of primary importance for creating multifunctional adaptive materials as their structure and function can be reversibly controlled in situ. We will present our work on self-assembled nanostructures in aqueous media based on perylene diimide amphiphiles (PDI), whose structure was studied using cryogenic TEM and SEM. We used cryo-TEM and spectroscopic methods to study dynamic behavior of self-assembly of various systems thus gaining mechanistic insights about self-assembly and nano-crystallization. Some of our systems show photofunction and multiple stimuli-responsiveness, including reversible supramolecular depolymerization in situ through aromatic charging, which enables switching of mechanical properties and optical functions. Another system utilizes hierarchical supramolecular interaction for the formation of unique nanospirals (Figure 1) in aqueous solutions.

1. Kossoy, Elizaveta; Weissman, Haim; Rybtchinski, Boris. Bending Nanofibers into Nanospirals: Coordination Chemistry as a Tool for Shaping Hydrophobic Assemblies**.** *Chem. Eur. J.* 21, 166-176., (2015).
2. Elisha Krieg, Haim Weissman, Eyal Shimoni, Alona Bar On (Ustinov), Boris Rybtchinski. Understanding the Effect of Fluorocarbons in Aqueous Supramolecular Polymerization: Ultrastrong Noncovalent Binding and Cooperativity. *J. Am. Chem. Soc.* 136, 9443-9452., (2014).
3. Yaron Tidhar, Haim Weissman, Dmitry Tworowski, Boris Rybtchinski. Mechanism of Crystalline Self-Assembly in Aqueous Medium: A Combined Cryo-TEM/Kinetic Study**.** *Chem. Eur. J.* 20, 10332-10342, (2014).
4. Jonathan Baram, Haim Weissman, Yaron Tidhar, Iddo Pinkas, and Boris Rybtchinski. Hydrophobic Self-Assembly Affords Robust Noncovalent Polymer Isomers. *Angew. Chem. Int. Ed.* 53, 4123-4126, (2014).

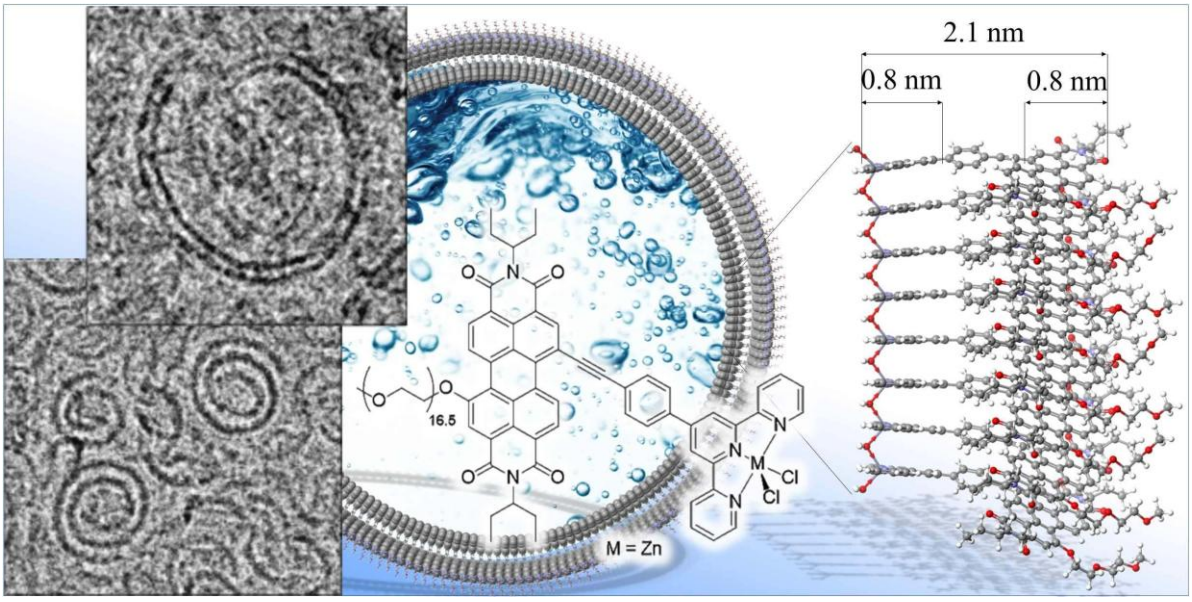

Figure 1. Cryo-TEM images of nanospirals in water/THF mixture made from amphiphilic PDI derivative that binds metal ions. Upon zinc or cobalt binding curling is induced by water bridges between the metallic centers.

Soft Matter, Polymers, C-Based Materials

MS5.P104
X-ray imaging of a drying colloid particle

K. Cho[1], I. G. Hwang[1], J. S. Park[2], J. H. Kim[2], J. Lim[3], B. M. Weon[1]

[1]Sungkyunkwan University, School of Advanced Materials Science and Engineering, Suwon, Korea
[2]Advanced Photonics Research Institute, Gwangju Institute of Science and Technology, Gwangju, Korea
[3]Beamline Division, Pohang Light Source, Pohang, Korea

kun_cho@outlook.com

When colloidal fluids dry, tracking liquid surfaces around a single colloid particle is difficult with conventional imaging techniques. Here we show that X-ray microscopy in the Pohang Light Source is very useful in tracking liquid surfaces during drying processes of colloidal fluids in real time. We demonstrate that when contact angles between colloid and liquid films decrease, drying rates of colloidal drops clearly increase. This result is helpful to improve understanding of drying processes that is relevant to inkjet printing, painting, and nanoparticle patterning.

1. This research was supported by Nano·Material Technology Development Program through the National Research Foundation of Korea(NRF) funded by the Ministry of Science, ICT and Future Planning.(2009-0082580)

Soft Matter, Polymers, C-Based Materials

MS5.P105
Curvature asymmetry in water coalescence

S. J. Lim[1], B. Gim[2], K. Fezzaa[3], B. M. Weon[1]

[1]Sungkyunkwan University, SKKU Advanced Institute of Nanotechnology, Suwon, Korea
[2]Korea Advanced Institute of Science and Technology (KAIST), Department of Bio and Brain Engineering, Daejeon, Korea
[3]Advanced Photon Source, Argonne National Laboratory, X-ray Science Division, Argonne, United States

sj-lim@hotmail.com

Curvature of a curved surface is an important element of fundamental phenomena. In particular, the driving force in hydrodynamics of liquids originates from curvature and surface tension. Here we study on water coalescence of different-sized drops with asymmetry curvature through direct observations using X-ray microscopy and numerical simulations. Asymmetry curvature between drops would play an important role in coalescence dynamics. This result helps understanding of symmetry breaking in curvature on hydrodynamics, which is applied in diverse field.

1. This work (NRF-2013R1A22A04008115) was supported by Mid-Career Researcher Program through NRF grant funded by the MEST (South Korea) and also was supported by Sungkyun Research Fund, Sungkyunkwan University, 2014. This research was supported by Nano·Material Technology Development Program through the National Research Foundation of Korea(NRF) funded by the Ministry of Science, ICT and Future Planning.(2009-0082580)

Soft Matter, Polymers, C-Based Materials

MS5.P106
Viscoelastic phase separation process and the development of micro and nano morphologies in epoxy based blends: a microscopy study

S. Thomas[1]

[1]Mahatma Gandhi University, Kottayam, International and Inter University Centre For Nanoscience and Nanotechnology, Kottayam, India

sabupolymer@yahoo.com

Phase separation in general could be either by diffusion or by diffusion and hydrodynamic flow. A new model has been suggested recently to follow the phase separation process in dynamically asymmetric mixtures composed of fast and slow components. This new model is often called the ***viscoelastic phase separation process*** due to the fact that viscoelastic effects play a dominant role in the phase separation process [1-6]. The dynamic asymmetry can be induced by either the large size difference (mol.wt) or the difference in glass-transition temperature between the components of a mixture or blend. The mol.wt difference often exists in complex fluids, such as polymer solutions, polymer blends, micellar solutions, colloidal suspensions, emulsions, and protein solutions. The Tg differences, can exist in any mixtures. In dynamically asymmetric mixtures, phase separation generally leads to the formation of a long-lived `interaction network' (a transient gel) of slow-component molecules (or particles), if the attractive interactions between them are strong enough. Because of its long relaxation time, it cannot catch up with the deformation rate of the phase separation itself and as a result the stress is asymmetrically divided between the components. This leads to the transient formation of network like or sponge like structures of a slow-component-rich phase and its volume shrinking [4]. In the present talk we present our new results on the viscoelastic phase separation process in epoxy/SAN and epoxy/ABS blends [1-4]. Epoxy resin is often blended with high molecular weight thermoplastics to generate micro structured morphologies for the better impact performance. These systems are very ideal to follow the viscoelastic phase separation process on account of their mol.wt and Tg differences. We have looked at the phase separation process in these blends by various techniques such as optical microscopy, scanning electron microscopy, transmission electron microscopy, atomic force microscopy, and small angle laser light scattering. The dynamics of phase separation has been carefully followed by optical microscopy and laser light scattering. In most cases the system undergo spinodal decomposition and the viscoelastic phase separation was prominent at higher concentration of the thermoplastic phase where phase inversion occurs [1-6]. The particle in particle morphology (secondary, ternary and quaternary phases), IPN type of structures and unusual shrinkage have been examined as a result of the viscoelastic phase separation process [1, 4]. All these phenomena have been carefully quantified and co-related with the viscoelastic phase separation process.

1. P. Jyotishkumar, J. Pionteck, C. Ozdilek, P. Moldenaers, U. Cvelbar, M. Mozetic, S. Thomas, ***Soft matter accepted.***
2. P. Jyotishkumar, C. Ozdilek, P. Moldenaers, C. Sinturel, A. Janke, J. Pionteck, and S. Thomas, ***J. Phys. Chem. B.*, 2010, 114, 13271-13281.**
3. P. Jyotishkumar, J. Koetz, B. Tierisch, V. Strehmel, R. Häßler, C. Ozdilek, P. Moldenaers, and S. Thomas, ***J. Phys. Chem.B.*, 2009, 113, 5418-5430.**
4. J. Jose, K. Joseph, J. Pionteck, and S. Thomas, ***J. Phys. Chem. B.*, 2008, 112, 14793-14803.**
5. X. Zhong, Y. Liu, H. Su, G. Zhan, Y. Yu, and W. Gan, ***Soft Matter*, 2011, 7, 3642-3650.**
6. H. Tanaka, ***Adv Mater.*, 2009, 21, 1872-1880.**

Soft Matter, Polymers, C-Based Materials

MS5.P107
Application of TEM techniques for microstructural characterization of perfluoropentacene grown on graphene

R. Felix[1], K. I. Gries[1], T. Breuer[1], G. Witte[1], K. Volz[1]

[1]Philipps-Universität Marburg, Marburg, Germany

rocio.felix@physik.uni-marburg.de

Organic semiconductors (OSCs) are up-and-coming in research and industry due to their potential applications in electronic devices such as organic field-effect transistors (OFETs) and light-emitting diodes (OLEDs). The OSC that we investigated was perfluoropentacene (PFP, $C_{22}F_{14}$), which is the perfluorinated version of the well-known OSC pentacene ($C_{22}H_{14}$). PFP adopts a triclinic arrangement with the P1 space group in the bulk and it exhibits high electron mobilities (n-type OSC). As substrate for PFP deposition, we used graphene, whose sp^2-hybridized carbon adopts a two-dimensional hexagonal arrangement; it has attracted a remarkable interest during the last ten years due to its great mechanical and electronic properties [1-3].

The packing of OSCs typically falls between a herringbone (HB, edge-to-face) and π -stacking (face-to-face) ordering. However, π-stacking is considered to be the superior motif because the increased physical overlap of the π-orbitals may lead to increased electronic overlap and higher carrier mobility [4]. Therefore, considerable research effort has been made to modify the molecular packing of OSCs from HB to π-stacking.

It is known that molecular orientation and ordering of different organic semiconductors depend on substrate interaction and substrate roughness. Until now, PFP has been widely studied on different substrates such as halides [5], SiO_2 [6] or Ag (111) [7] and it was always found to grow in a HB motif. But, Salzmann et al [8] reported a vertically π-stacked growth of PFP films on graphene-coated quartz substrate by combining X-ray diffraction (XRD) methods with theoretical structure modeling.

With our study, we intend to go much further, since transmission electron microscopy (TEM) is a powerful tool that allows us to obtain images and diffraction patterns at the same position, unlike XRD, that provides precise information about lattice constants and crystal structure, but it can hardly determine in plane ordering of small structures. Therefore, in contrast to all reports so far, we show the arrangement and crystal orientation of PFP grown on graphene using TEM techniques. Our characterization was carried out by bright field (BF) and dark field (DF) TEM, selected area electron diffraction (SAED) patterns and high angular annular dark field (HAADF)-scanning TEM (STEM).

Thereby, we report a characteristic growth of PFP in islands with distinct faceting (see figure 1) where the orientation is induced by the graphene layer. The diffraction pattern of this π-stacked PFP (figure 2) confirms the proposed orientation by Salzmann [8], and besides, it shows a coincidence between some graphene and PFP reflections. When we correlate the SAED patterns with the BF pictures, it is possible to see that the edges of the islands are created by certain planes ((-7 8 2) and (-40 -1 5)) whose angles are connected with specific reflections of SAED patterns. These planes are the most favourable ones which can form the island edges, as can be seen in the crystal model of figure 3.

Summarizing, with this study we provide, for the first time, an evidence for the epitaxial relation of PFP grown on graphene showing the suggested alignment of PFP with the graphene lattice along its [001] direction by using different TEM techniques.

1. Geim, A. K. Science 324, 1530-1534 (2009)
2. Lee, C. et al. Science 321, 385-388 (2008)
3. Castro Neto, A. H. et al. Rev. Mod. Phys. 81, 109-162 (2009)
4. Chang Y.C. et al. J. Org. Chem. 73, 4608-4614 (2008)
5. Breuer, T. et al. Phys. Rev. B 83, 155428 (2011)
6. Haas, B. et al., J. Appl. Phys. 110, 073514 (2011)
7. Duhm, S. et al., Phys. Rev. B 81, 045418 (2010)
8. Salzmann, I. et al., ACS Nano 6, 112, 10874-10883 (2012)

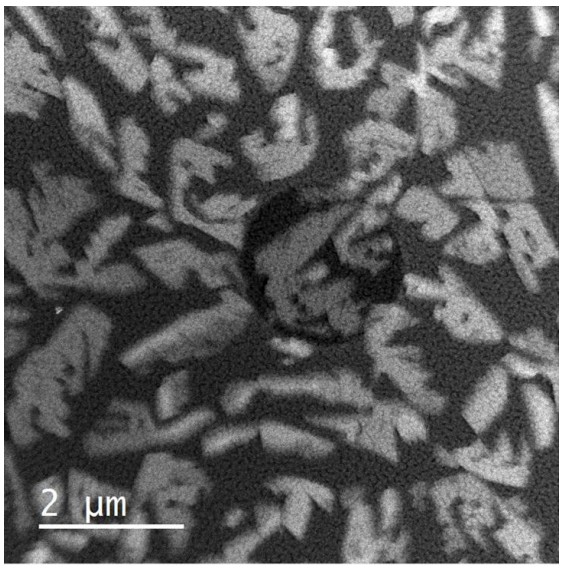

Figure 1. HAADF-STEM micrograph where the characteristic edges of the islands are visible.

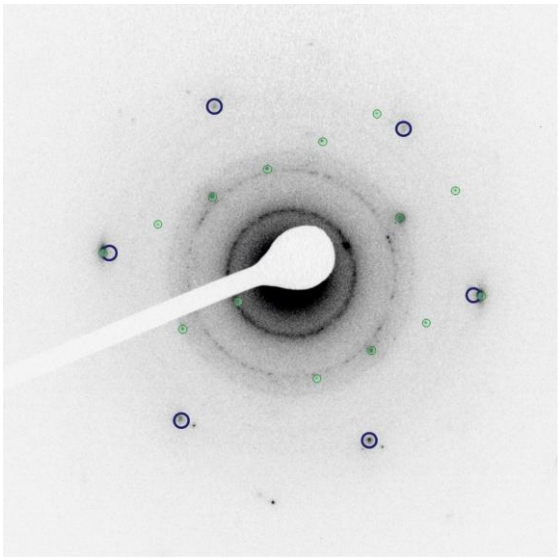

Figure 2. Experimental SAED pattern of a PFP island grown on graphene, where green and blue reflections belong to PFP and graphene layer, respectively.

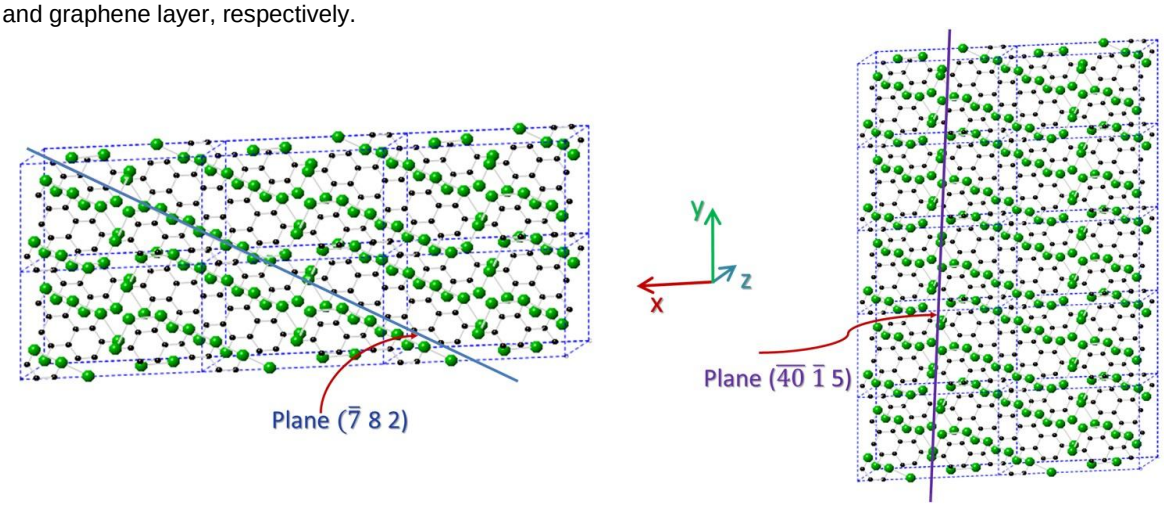

Figure 3. Crystal model of PFP unit cells with (-7 8 2) (left) and (-40 -1 5) (right) planes in normal viewing direction to (001) plane.

Soft Matter, Polymers, C-Based Materials

MS5.P108
TEM and EELS studies of new carbon structures obtained from C_{60}

E. Tyukalova[1,2], B. Kulnitskiy[1,2], I. Perezhogin[1], M. Popov[1,2], A. Kirichenko[1], V. Blank[1,2]

[1]Technological Institute for Superhard and Novel Carbon Materials, Russian Federation
[2]Moscow Institute of Physics and Technology (State University), Moscow, Russian Federation

tyukalova@phystech.edu

In the present work, transmission electron microscopy (TEM) and electron energy loss spectroscopy (EELS) were used to examine C_{60} samples synthesised under various processing conditions. The first group of samples was obtained under pressure of approximately 5 GPa and at high temperature (1000°C). The second group was obtained under high pressure with a shear deformation (20 GPa without a catalyst and 6-7 GPa with CS_2 catalyst [1]) or under high pressure with laser pulse heating [2]. Samples were obtained using unique equipment: a high-pressure diamond anvil cell (DAC) and shear diamond anvil cell (SDAC). The aim of this work is to characterize the structures of the materials synthesized from C_{60}, and to explain the role of synthesis conditions in the formation of final product. Electron Microscopy studies were performed on JEM-2010 microscope equipped with the GIF Quantum EELS-spectrometer.

Fig. 1a shows the typical high-resolution image of a sample from the 1st group. The diffuse elongated arcs present on the Fourier transform (inset) correspond to the structural fragments with slightly disoriented planes composing an angle from 65° to 85°.

The samples from the 2nd group sometimes also yield spot reflections in the diffraction patterns (Fig 1b, inset) (apart diffuse ring). Interplanar distances correspond to the fullerite lattice (a ≈1.417 nm) or distorted fullerite lattice (reduced a ~ 1.30 nm).

Fig. 2 shows the EELS spectra of our samples. According to literature data, EELS spectra of fullerite C_{60} contains a number of characteristic peaks at 284 eV, 292 eV, 298 eV and 300 eV. It should be noticed that there are a small peaks near 287 eV that correspond to the presence of molecular structure of C_{60} [3].

The EELS spectra recorded from the 1st group of samples (high temperature) are similar to the spectrum of graphite. The obtained spectra have the most intense peak at 292eV (same as in amorphous carbon or graphite), while for fullerite such peak is at 300eV. Similar deviation was previously observed after irradiation of a fullerene with an intense electron beam [4]. This was due to the formation of «defected graphitic network» [5], which is the destruction of spherical C_{60} fullerene molecules.

The EEL spectra from the 2nd group (higher pressure) have characteristics of the fullerite spectrum. In particular, there is a small peak at 287eV; positions and heights of the peaks at 292 eV, 298 eV, 300 eV within the accuracy of our measurements coincide with the same parameters of the peaks in the spectrum of the initial fullerite.

Thus, after the treatment the molecules of fullerene remain in the sample, and chemical bonds in the resulting structure have essentially the same character as in the initial fullerene (relative amount of bonds responsible for the C_{60} polymerization is insignificant).

We propose the following interpretation of our experimental results. High pressure treatment of the C60 leads to its polymerization alongdirection [2] and decrease of fullerence fcc-lattice parameter. Further increase of pressure along with shear deformation (or increase of a temperature) leads to particular (or complete) destruction of C60 molecules and formation of new carbon structure (with graphite-like fragments) which is shown in fig. 1 with EEL in fig. 2a.

1. M. Popov *et al*. *Carbon*, 76 (2014) 250.
2.M. Popov *et al*.*J. Appl. Phys.*, 115 (2014) 153506.
3.A.J. Papworth*et al*. *Phys. Review*, 64, 4 (2000) 5509.
4. P. L. Hansen *et al*. *Chemical physics letters*, 181, 4 (1991) 367.
5. M.A.Tamor and C.H.Wu. *J. Appl.Phys*., 67 (1990) 1007.

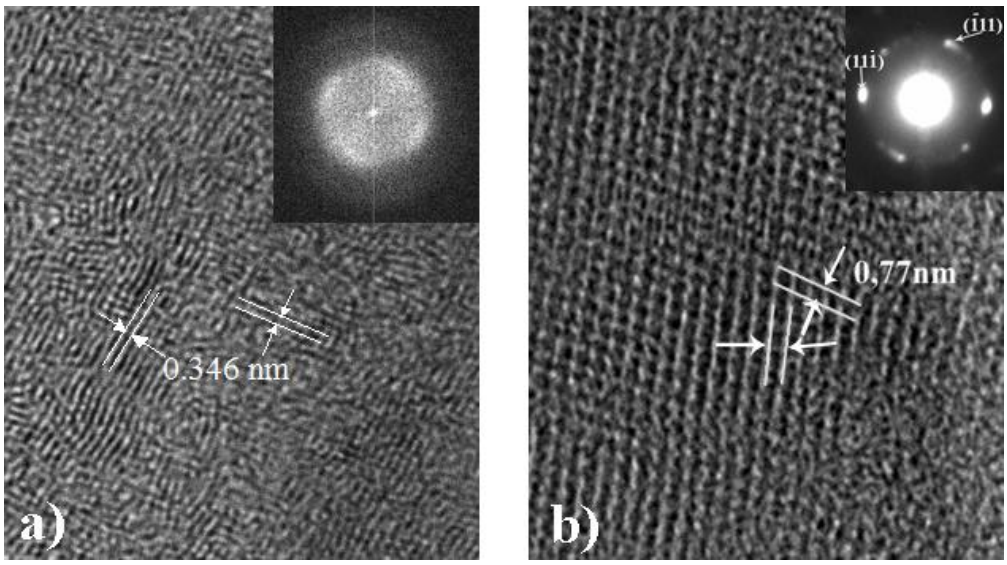

Figure 1. a) HRTEM image of the disordered phase (inset - Fourier transform). Internplanar distances are 0.346 nm, the interplanar angle is in the range of 65°-85°. b) HRTEM image from a sample in the 2nd group (inset - corresponding diffraction pattern). The diffraction corresponds to the [101] zone-axis of non-distorted fullerite lattice with a≈1.34 nm.

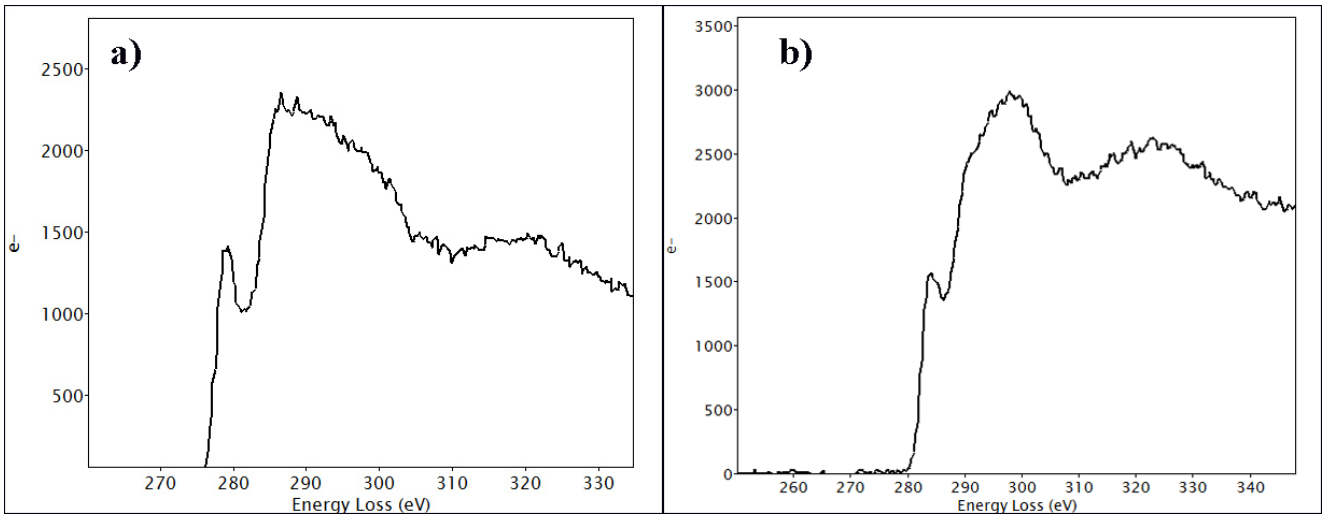

Figure 2. a) EELS spectrum of the 1st samples group (high temperature) and b) spectrum of the 2nd samples group.

Soft Matter, Polymers, C-Based Materials

MS5.P109
SEM image analysis of CNT interconnect vias

Y. Abe[1], A. Vyas[1], R. Senegor[1], C. Yang[1]

[1]Santa Clara University, Center for Nanostructures, Santa Clara, CA, United States

yuu.abe@gmail.com

Carbon-based nanostructures such as carbon nanotubes (CNTs) and carbon nanofibers (CNFs) are candidate materials for next-generation integrated circuit technologies due to their high current-carrying capacities and excellent electrical, thermal, and mechanical properties [1,2]. Since the total resistance of a via depends on the number of conductive CNTs inside the via, it is important to investigate not only the characteristics of the via but also the individual CNTs inside the via [3]. In this paper, we report the use of a SEM imaging technique to detect defective CNT vias and identify CNTs contributing to the conducting process.

We have designed and fabricated test devices for vertical CNT interconnect vias [4]. A cross-sectional schematic of via test devices is presented in Fig. 1. A bottom-up process using plasma-enhanced chemical vapor deposition (PECVD) for CNT growth was used to mitigate the difficulty in high-aspect-ratio device fabrication.

Figs. 2 (a) and (b) show the secondary electron (SE) images of CNT vias at 30 kV and 0.5 kV acceleration voltages, respectively. To extend our previous work on via characterization [4.5], we identify detection mechanisms based on observations of beam-induced specimen charging. 30 kV SE image shows a strong geometry contrast around the via edges. In comparison, 0.5 kV SE image has a clear voltage contrast from the potential wall created by the SEs and the small resistance between the ground plane and the surface. Thus this voltage contrast suggests the failure of the observed via, most likely caused by current stressing.

Figs. 3 (a) to (d) show high-magnification SE images of a CNT via using 30 kV, 1 kV, 0.5 kV, and 0.1 kV acceleration voltages, respectively. At the spot indicated, the contrast becomes weaker at 0.5 kV and 0.1 kV, since higher-energy incident electrons have longer penetration depth, and the electrons reaching the embedded CNTs relax the charging of the surrounding dielectric residue due to electron beam-induced conduction [6, 7]. This result suggests that low-energy imaging is effective in observing unexposed CNTs below the top via surface.

In summary, SEM imaging of defective structures in fabricated CNT vias has been presented. The voltage-contrast imaging is shown to be effective in identifying failed vias, while low-energy imaging is a viable technique to observe unexposed CNTs. The use of these imaging techniques is potentially valuable for via characterization and for eventual functionalization of CNT via interconnects.

1. T. Saito, T. Yamada, D. Fabris, H. Kitsuki, P. Wilhite, M. Suzuki, and C.Y. Yang, "Improved contact for thermal and electrical transport in carbon nanofiber interconnects," Applied Physics Letters, vol. 93, 102108 (1-3), 2008.
2. M. S. Dresselhaus, G. Dresselhaus, and P. Avouris, “Carbon nanotubes: synthesis, structure, properties, and applications,” Springer, Berlin, 2001.
3. M. Nihei, A. Kawabata, T. Hyakushima, S. Sato, T. Nozue, D. Kondo, H. Sshioya, T. Iwai, M. Ohfuti, and Y. Awano, “Carbon Nanotube Via Technologies for Advanced Interconnect Integration,” *Extended abstracts of Conference on Solid State Devices and Materials*, vol. 2006, pp. 140-141, September 2006.
4. C. Zhou, A.A. Vyas, P. Wilhite, P. Wang, M. Chan, and C.Y. Yang, “Resistance Determination for Sub-100nm Carbon Nanotube Vias,” IEEE Electron Device Letters, vol. 36, 71-73, 2015.
5. P. Wilhite, A.A. Vyas, Jason Tan, Jasper Tan, T. Yamada, P. Wang, J. Park, and C.Y. Yang, “Metal-nanocarbon contacts,” Semiconductor Science and Technology, vol. 29, 054006 (16pp), 2014.
6. M. Suzuki, Y. Ominami, T. Sekiguchi, and C. Y. Yang, “Secondary electron imaging of embedded defects in carbon nanofiber via interconnects,” Applied Physics Letters, vol. 93, 263110 (1-3), 2008.
7. Y. Homma, S. Suzuki, Y. Kobayashi, M. Nagase, and D. Takagi, “Mechanism of bright selective imaging of single-walled carbon nanotubes on insulators by scanning electron microscopy,” Applied Physics Letters, vol. 84, 1750-1752, 2004.

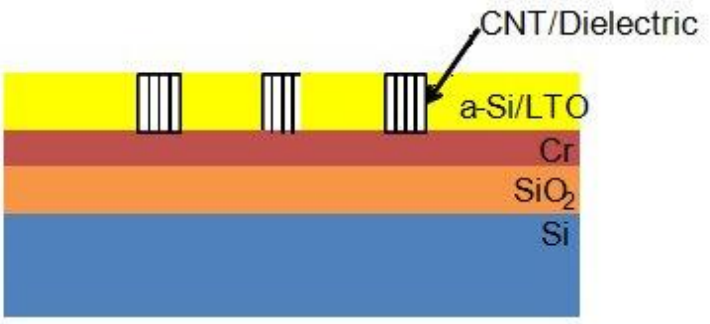

Figure 1. Cross-sectional schematic of CNT vias

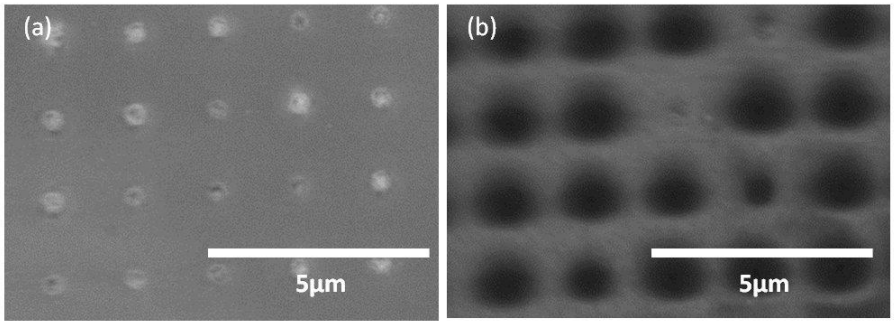

Figure 2. Top-view SEM images of CNT vias with (a) 30 kV and (b) 0,5 kV electron acceleration voltages. 0,5 kV image reveals a voltage contrast from the potential wall created by the SEs and the small resistance between the ground plane and the surface. The images with less contrast in (b) correspond to failed vias.

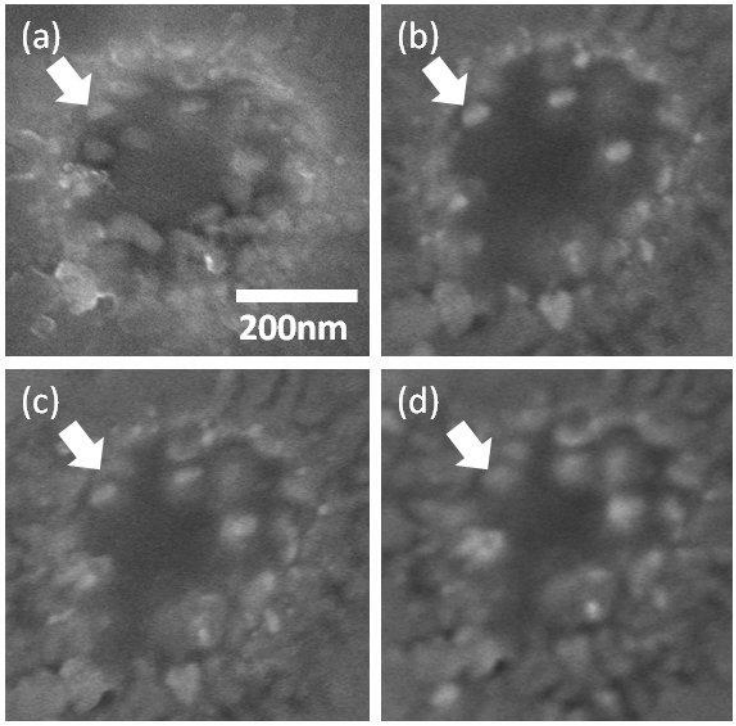

Figure 3. High-magnification top-view SEM images with (a) 30 kV, (b) 1kV, (c) 0,5kV, (d) 0,1 kV electron acceleration voltages for the same CNT via. The contrast in die area indicated by the arrow is weaker at 0,5 kV and 0,1 kV, since lower-energy incident electrons have shorter penetration depths, thus unable to relax the charging of the dielectric embedding the CNTs.

Soft Matter, Polymers, C-Based Materials

MS5.P110
Formation of square ice by confinement of water between graphene layers

G. Algara-Siller[1], O. Lehtinen[1], F.- C. Wang[2], R. R. Nair[3], U. Kaiser[1], H.- A. Wu[2], A. K. Geim[3], I. V. Grigorieva[3]

[1]Ulm University, Group of Electron Microscopy of Materials Science, Ulm, Germany
[2]University of Science and Technology of China, Department of Modern Mechanics, Hefei, China
[3]University of Manchester, School of Physics and Astronomy, Manchester, United Kingdom

gerardo.algara-siller@uni-ulm.de

The properties of graphene render it a perfect substrate for TEM investigations of organic or inorganic nanomaterials [1]. Encapsulation of radiation sensitive samples between graphene layers provide protection against electron beam induced damage [2-4].

Furthermore, graphene layers have been used as windows and confinement for in-situ experiments in liquid cells [5].
In our experiments we confined water between graphene layers by drop casting. The sample preparation is as follows: graphene grown on copper by CVD was transferred to TEM grids, on one grid a drop of DI water was cast and the other grid was placed on top of the drop and let to dry. During drying the two graphene layers came into contact squeezing out most of the water but numerous water pockets remained between, sealed by the graphene layers. These water pockets were imaged by HRTEM at 80 kV in an aberration-corrected FEI TITAN 80-300 in room temperature conditions [6].

Our results show that the graphene-confined water is constituted by crystallites. The structure of these crystallites exhibited a square lattice with a lattice constant of 2.83 A. The structural characterisation of the crystallites was obtained using different TEM techniques, i.e. HRTEM, SAED and EELS. Confirmation that the formed square lattice is made of water, hence -square ice-, was obtained by EELS measurements around the Oxygen K edge. Through sequential imaging of the sample it was observed, among other atom dynamics (e.g. crystal coalescence), that the square ice crystal increased and decreased its number of layers. Contrast analysis on these images indicate that the square ice varied from one to maximum three layers. The stacking configuration of the square ice was determined with the help of image calculations, that is the square ice stacks in an AA configuration.

The structure and formation of a square ice phase was theoretically investigated using molecular dynamics simulations of water in graphene capillaries. The results estimated that the pressure exerted on the water molecules by the graphene layers, van der Waals pressure, is above 1 GPa and that this pressure is a key component for the formation of square ice.

1. R.S. Pantelic, J.C. Meyer, U. Kaiser, H. Stahlberg. Solid State Communications 152 (2012).
2. N. Mohanty, M. Fahrenholtz, A. Nagaraja, D. Boyle, V. Berry. Nano Letters 11 (2011).
3. R. Zan, Q.M. Ramasse, R. Jalil, T. Georgiou, U. Bangert, K.S. Novoselov. ACS Nano 7 (2013).
4. G. Algara-Siller, S. Kurasch, M. Sedighi, O. Lehtinen, U. Kaiser. Applied Physics Letters 103 (2013).
5. J.M. Yuk, J. Park, P. Ercius, K. Kim, D.J. Hellebusch, M.F. Crommie, J.Y. Lee, A. Zettl, A.P. Alivisatos. Science 336 (2012)
6. G. Algara-Siller, O. Lehtinen, F.C. Wang, R.R. Nair, U. Kaiser, H.A. Wu, A.K. Geim, I.V. Grigorieva. Nature 519 (2015)
7. We acknowledge the financial support by the DFG and the state Baden-Württemberg in the frame of the SALVE project and by the DFG in the frame of the TR21 CO.CO.MAT.

Soft Matter, Polymers, C-Based Materials

MS5.P111
Numerical correction of residual anti-symmetric aberrations in single high resolution images of weakly scattering 2D-objects using image Cs-corrected TEM

O. Lehtinen[1], D. Geiger[1], Z. Lee[1], M. B. Whitwick[2], M.- W. Chen[2], A. Kis[2], U. Kaiser[1]

[1]University of Ulm, Ulm, Germany
[2]Ecole Polytechnique Federalede Lausanne, Lausanne, Switzerland

ossi.lehtinen@gmail.com

Modern transmission electron microscopes (TEM), equipped with image Cs-corrector [1], allow nowadays atomic resolution also at lower accelerating voltages [2], e.g. at 80kV, where 2D-structures like graphene can be investigated below the knock-on damage limit [3].

In practice, the hardware aberration correction (AC) can be performed only to a limit imposed by the measurement accuracy and the adjustment precision of the correcting elements, and starts to drift immediately after ending the procedure [4], resulting in residual aberrations. Special techniques, which allow the reconstruction of the image wave like off-axis electron holography, can be used to remove numerically in post-processing the coherent residual aberrations, if these can be estimated properly [5].

In this paper we present an easy alternative way for post-image aberration correction for weak phase objects (WPO). The method is based on applying to the Fourier transform of the recorded image intensity a phase plate with the opposite anti-symmetric wave aberration and subsequently Fourier inverting this intermediate result [6].

The correction of the residual coherent anti-symmetric aberrations like axial coma (B_2), three-fold astigmatism (A_2) and other anti-symmetric aberrations of higher orders, using "conventional AC-HRTEM images" is possible. At 80kV, graphene can be considered from this point of view as WPO, where also other 2D materials like $MoSe_2$ fulfill to some extend this criterion. The method has been applied to experimental AC-HRTEM images of single-layer graphene and $MoSe_2$ resulting in images with strongly reduced residual low-order aberrations, and consequently with significantly improved interpretability. It will be shown that residual aberrations such as A_2 and B_2 can generate undesired artifacts in HRTEM images and open room for possible misinterpretations of the structure (see fig.1 and 2).

Alternatively, this method can be used to study the influence of anti-symmetric aberrations on the HRTEM images of weakly scattering objects or to estimate by trial and error the residual aberrations in these images.

1. M. Haider et al., Ultramicroscopy75 (1998), p.53.
2. U. Kaiser et al., Ultramicroscopy 111, (2011), p.1239.
3. A. Zobelli et al., Phys Rev B, 75 (24) (2007), p. 245402.
4. J. Barthel, A. Thust, Ultramicroscopy 134 (2013), p. 6.
5. D. Geiger et al., Microsc. Microanal. 14, (2008), p.68.
6. O. Lehtinen et al., Ultramicroscopy 151 (2015), p. 130.

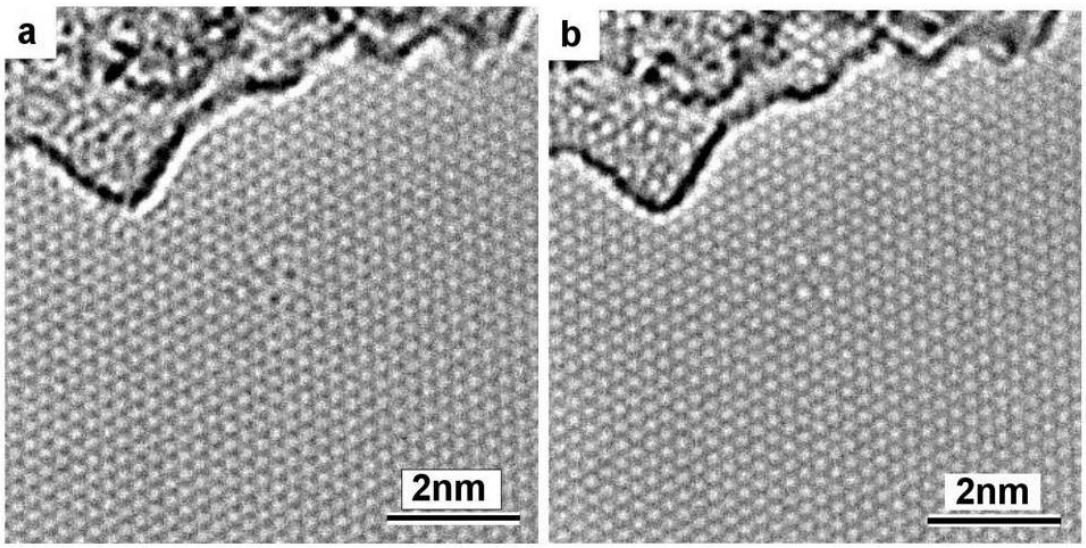

Figure 1. An experimental test with an intentionally introduced large A_2 aberration. (a) AC-HRTEM image of a point defect in graphene with A_2 set to 1.0 ±0.1 µm/48° (as measured by the corrector software). (b) Recovered image after correcting for 1.0 µm/41.5° of A_2. The imaged structure/defects are obviously easier to interpret.

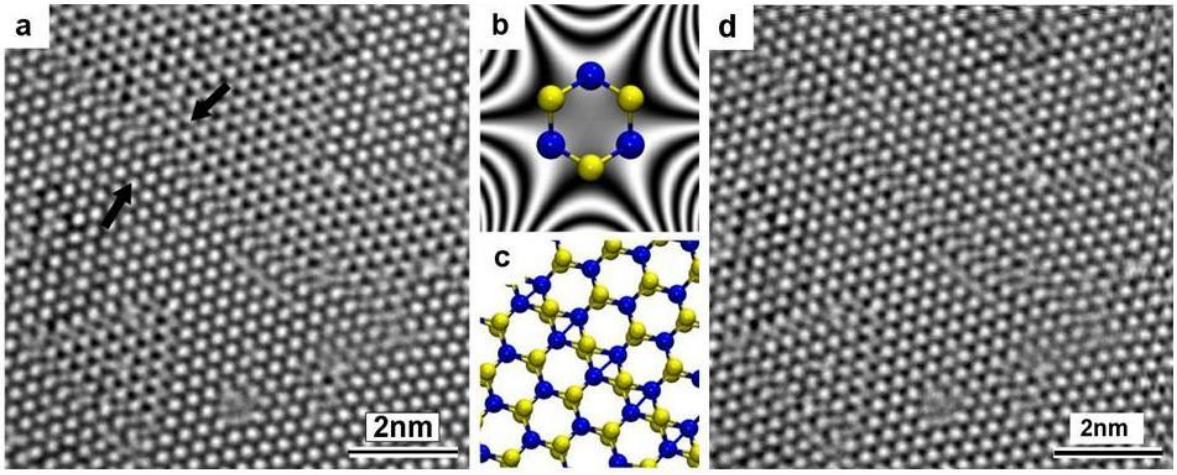

Figure 2. Experimental AC-HRTEM images of mirror-twin boundaries in single-layer $MoSe_2$ suffering from residual aberrations. (a) Due to residual aberrations, the lattice has a completely different appearance on the opposite sides of the boundaries. Compare, for example, the two areas marked by the arrows. Also this effect can be explained by alignment of the $MoSe_2$ lattice with residual A_2 (b) and by the swapping of the Mo and dual Se sites in the three-fold symmetric lattice when crossing the boundary (c where the dark atoms represent Mo and light atoms Se, with two Se atoms always residing on top of each other). The reversal of the lattice results in the accentuation of different sublattices in these regions. (d) The AC-HRTEM image after correction (A_2 = 75 nm/15°). The $MoSe_2$ lattice has identical appearance on both sides of the mirror-twin boundary as expected for an aberration-free image.

Soft Matter, Polymers, C-Based Materials

MS5.P112
AFM characterization of dexamethasone sodium phosphate loaded bovine and porcine erythrocyte ghosts

I. Kostić[1], K. Bukara[1], B. Vasić[2], V. Ilić[3], A. Stančić[3], R. Gajić[2], B. Bugarski[1]

[1]University of Belgrade, Faculty of Technology and Metallurgy, Department of Chemical Engineering, Belgrade, Serbia
[2]University of Belgrade, Institute of Physics, Belgrade, Serbia
[3]University of Belgrade, Institute for Medical Research, Belgrade, Serbia

ikostic@tmf.bg.ac.rs

In this study, atomic force microscopy (AFM) analysis was applied to gain insight into the morphology of dexamethasone sodium phosphate (DEXP) loaded bovine and porcine erythrocyte ghosts, as novel bio-derived drug delivery systems, recently described [1].

In order to identify possible alterations induced by DEXP, controlled (sham encapsulated) and DEXP-encapsulated erythrocyte ghosts were prepared for AFM measurements as described in Kostić et al. [2]. Topographic AFM measurements were performed in the semi-contact mode under ambient conditions using the NTEGRA Prima system from NT-MDT (NT-MDT Co. Moscow, Russia). Simultaneously with the topographic measurements, the phase lags of the AFM cantilever oscillations were recorded thus forming AFM phase images. NSG01 probes from NT-MDT with a typical tip curvature radius of about 6 nm and a typical force constant of 5 N/m were used. Topographic images were processed using the instrument-equipped software by the plane subtraction or by the fitting with the first order lines, while the raw data was used for the phase images. For the calculation of the root-mean-square (RMS) of the surface roughness, only cell surfaces were selected from AFM images and then RMS was directly generated by the instrument software, using a total of 15 cell measurements for each preparation.

Figs. 1 and 2 present results of the AFM morphological analysis for DEXP loaded bovine and porcine ghosts, respectively, where three dimensional topographic images ((a1) and (b1)) and height cross-section ((a2) and (b2)) along the selected lines are given. During moving of AFM probe along sample surface, both amplitude and phase of the AFM cantilever oscillations are influenced by topographic features. In the vicinity of sharp steps in the topography, AFM phase changes abruptly, and it can be used to visualize better the edges of membrane invaginations. The phase images of ghosts are shown in Figs. 1 (a3) and 2 (b3) for sham and DEXP loaded bovine ghosts, respectively, and in Figs. 2 (a3) and 2(b3) for sham and DEXP loaded porcine ghosts, respectively. The phase lag of the AFM cantilever across ghosts' surfaces is represented by a bright contrast. On the contrary, dark features inside ghosts' surfaces represent the edges of membrane invaginations, since these parts correlate with the maximal phase lag of AFM cantilever in comparison with the ghosts' surfaces. The surface of sham encapsulated bovine ghost is observed to be rich in membrane invaginations with RMS value of 17.2±1.4 nm. The applied process of DEXP encapsulation caused minor, but statistically insignificant ($p>0.05$) decrease in RMS value for the surface roughness which was 15.9±2.8 nm. When it comes to DEXP loaded porcine ghosts, detected increase in surface roughness implied more pronounced defects in erythrocyte ghosts' morphology. RMS value for the surface roughness amounted 30.0±5.4 nm and 34.26±7.5 nm for sham and DEXP encapsulated porcine ghosts, respectively ($p>0.05$). The AFM topography images and calculated RMS showed no additional effect of DEXP itself on the morphology of the ghosts carriers. Nonetheless, AFM analysis indicated significant morphological difference between bovine and porcine erythrocyte ghosts (with or without encapsulated drug, $p<0.05$); this could influence the other distinct properties and performances of two investigated kind of ghosts as drug carriers.

1. Kostić I.T., Ilić V.Lj., Đorđević V.B. Bukara K.M., Mojsilović S.B., Nedović V.A., Bugarski D.S., Veljović Đ.N., Mišić D.M., Bugarski B.M., *Colloids Surf B* 122 (2014) 250-259.
2. Kostić, I.T., Bukara, K.M., Ilić, V.L., Ralević, U.M., Bugarski, B.M.: "Preparation of erythrocyte ghosts from slaughterhouse blood for AFM observation", -*Proceedings of the 18th International Microscopy Congress*, Prague, Czech Republic 2014, ID-1-P-1470.

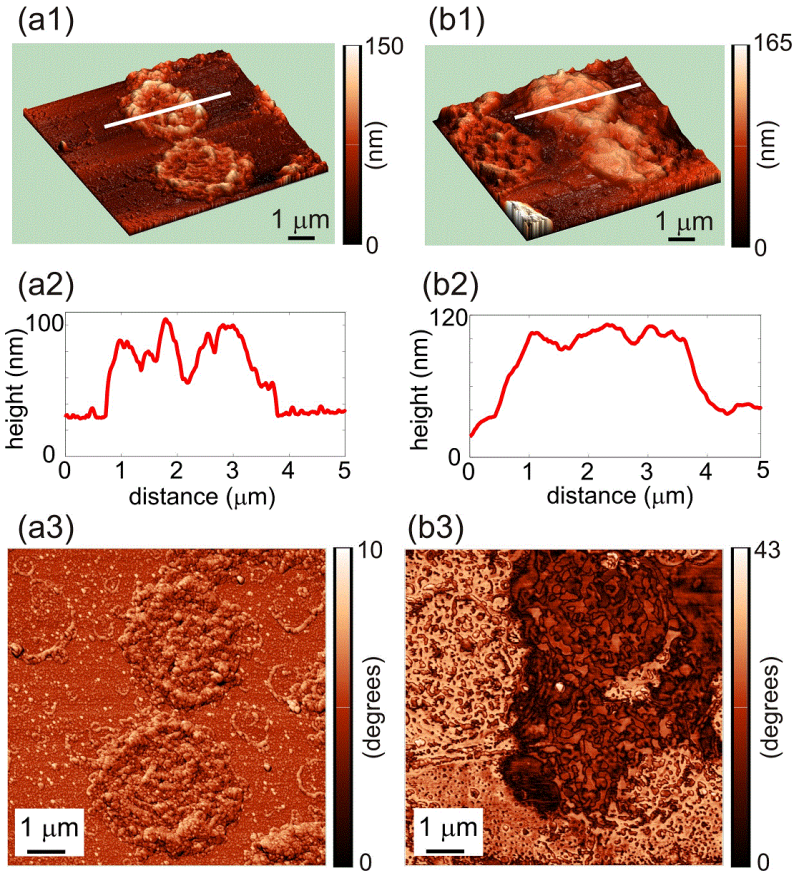

Figure 1. AFM analysis of (a) sham and (b) DEXP encapsulated bovine erythrocyte ghosts

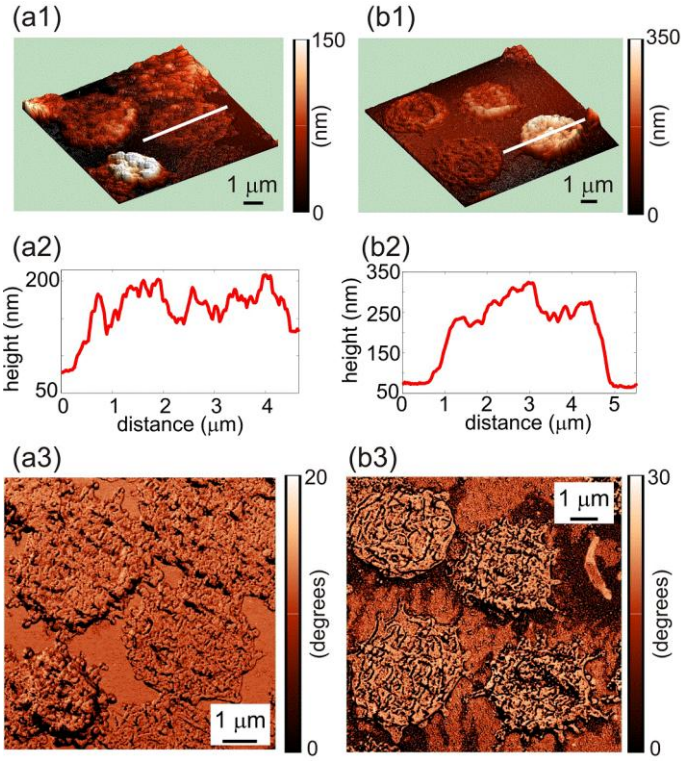

Figure 2. AFM analysis of (a) sham and (b) DEXP encapsulated porcine erythrocyte ghosts

Soft Matter, Polymers, C-Based Materials

MS5.P113
Characterisation of graphitisation process in ion implanted diamond

S. Rubanov[1], V. Popov[2], V. Antonov[2], L. Safronov[3], I. Kupriyanov[3], Y. Pal'yanov[3]

[1]University of Melbourne, Bio21 Institute, Melbourne, Australia
[2]Rzhanov Institute of Semiconductor Physics, Novosibirsk, Russian Federation
[3]Sobolev Institute of Geology and Mineralogy, Novosibirsk, Russian Federation

sergey@unimelb.edu.au

In the last decade ion-beam induced amorphisation of diamond with following graphitisation via high temperature annealing has attracted significant interest due to ability to fabricate device structures containing two stable structural forms of carbon: diamond and graphite. The main advantage of this approach consists in the possibility of creating conductive contacts and electrodes or buried conductive structures in high quality diamond substrates without additional lithographic or growth processes. Diamond-graphite-diamond heterostructures are interesting material for device applications in optoelectronics, photonics and quantum informatics.

In the present work process of graphitisation of ion beam induced amorphous layers in diamond was studied by means of conventional and high resolution transmission electron microscopy (TEM). High pressure high temperature (HPHT) synthetic (111) diamond substrates (Ib type) were used in this study. To create buried amorphous layers diamond samples were implanted with 50 keV H_2^+ ions to fluences of $(3\div13)\times10^{16}cm^{-2}$. Also, diamond substrates were implanted with 120 keV N^+ ions to a fluence of 3.5×10^{16} cm^{-2} through the masks fabricated on the diamond surface using photo-lithography technique. This allowed to create conductive contact areas upon thermal annealing. Next, diamond samples were annealed at high temperatures (HT) in the range 1200-1300^o C at vacuum pressure (VP, 10^{-3} Pa) or high pressure (HP, 4-8 GPa).

TEM study showed that after vacuum pressure annealing the amorphous areas were converted into fine grain polycrystalline graphite with predominant orientation of graphite (002) plains normal to the specimen's surface. Also, the swelling of implanted areas was evident. This swelling is a result of conversion of diamond sp^3 bonds into graphitic sp^2, with corresponding density reduction. For high pressure high temperature annealing TEM imaging together with selected area diffraction pattern have shown that amorphous region were converted into single crystal graphite. The graphene planes were parallel to the surface or (111) diamond lattice planes. The interface between graphite and diamond was found sharp without any visible transition region. Thus, ion implantation with following high pressure high temperature allows obtaining epitaxial graphite layers inside bulk diamond.

Soft Matter, Polymers, C-Based Materials

MS5.P114
In situ TEM/STEM visualization of metal stained amphoteric core/shell microgels

T. Caumanns[1], A. Gelissen[2], A. Schmid[2], J. Mayer[1], R. Walter[2]

[1]RWTH Aachen University, Central Facility For Electron Microscopy, Aachen, Germany
[2]RWTH Aachen University, Institute For Physical Chemistry, Aachen, Germany

caumanns@gfe.rwth-aachen.de

More than ever polymer science focuses on complex molecular structures and supramolecular assemblies. Microgels are responsive polymer materials and structures, which can be manipulated in e.g. charge or size by external parameters like pH or temperature variation. The investigated microgels are soft particulate polymer networks that can be dispersed in an aqueos medium. They reveal unique features providing new opportunities to develop smart bio-inspired materials. In contrast to rigid colloidal particles, which lack the possibility to adapt their size and shape to enviromental requirements, microgels have switchable properties of form and function that makes them very useful in a wide range of e.g. biological sciences and medical applications. They combine properties of dissolved macromolecules with those of colloidal particles. In the present work, thermoresponsive microgels were studied in their ambient enviroment by *in situ*-experiments in TEM/STEM.

Microgels with core-shell architecture were obtained by precipitation polymerization. First a particle was synthesized and purified before a shell was synthesized on top by the seed and feed method. Core and shell have oppositely charged copolymers to create a two compartment amphoteric microgel system, that is alternately stained with gold and magnetite nanoparticles. [1], [2]

In our studies, these microgels were observed by *in situ*-TEM in liquid environment. In the experiments, a thin layer of liquid was embedded between two hermetically sealed, electron transparent Si_3N_4-windows. The used holder is an *in situ*-liquid cell holder manufactured by Hummingbird Company and the microscope is a Zeiss Libra 200FE with an acceleration voltage of 200 kV. The resolution is mainly limited by the thickness of the liquid. To increase the contrast, an energy filter window of about 100 eV is inserted at the most probable energy loss, which reduces the background scattering of the solvent. A big challenge is to focus and get sufficient resolution because of the high mobility of the almost freely moving particles through the liquid.

1. J, Dockendorff, M. Gauthier, A. Mourran, M. Moller, Macromolecules (Washington, DC, US), 41 (2008) 6621.
2. A. Pich, S. Bhattacharya, Y. Lu, V. Boyko, H.-J. P. Adler, Langmuir 20 (2004) 10706.
3. The authors kindly acknowledge the financial support through the SFB 985 through the DFG.

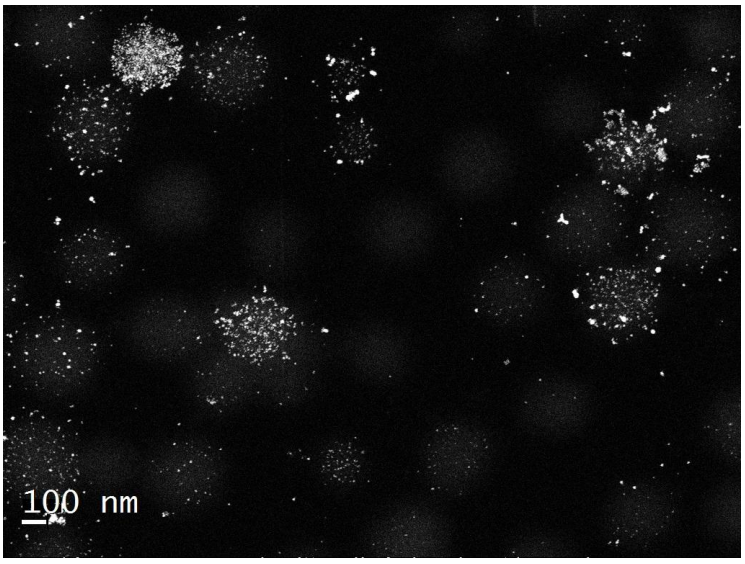

Figure 1. *in situ* STEM HAADF of a core shell microgel. The core is stained with gold NPs. The microgels are sticking to the window; that helps to focus to the particles.

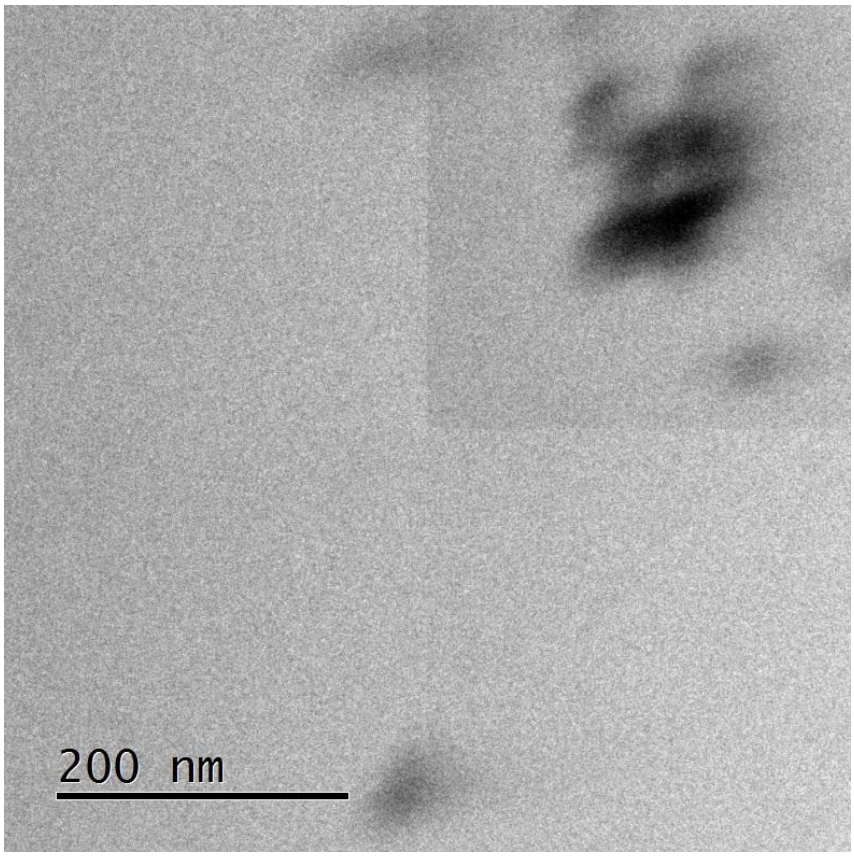

Figure 2. A comparable most probable loss filtered bright field *in situ* TEM image. The resolution decreases tremendously.

Soft Matter, Polymers, C-Based Materials

MS5.P115
TEM investigation of multi-walled hollow fibres produced by tri-axial electrospinning

I. Letofsky-Papst[1,2], B. S. Okan[3], J. S. M. Zanjani[4], M. Yildiz[4], Y. Menceloglu[4], W. Grogger[1,2]

[1]Institute for Electron Microscopy and Nanoanalysis, University of Technology, Graz, Austria
[2]Graz Centre for Electron Microscopy, Graz, Austria
[3]Sabanci University Nanotechnology Research and Application Center, SUNUM, Istanbul, Turkey
[4]Sabanci University, Faculty of Engineering and Natural Sciences, Istanbul, Turkey

ilse.papst@felmi-zfe.at

Hollow structured nanofibers with exceptional properties such as low density, high specific surface area, and tuneable surface properties have found essential applications as catalyst supports, drug delivery systems, and membranes. Different production techniques were reported for production of hollow structured fibers. In a first approach, conventional electro-spun polymeric fibres utilized as template followed by coating the electro-spun fabric and removal of the template were used to fabricate hollow structured fibers with different wall materials [1]. The limiting factors of this method are complexity in coating and efficiency of the template removing processes. Second method is the co-axial electrospinning process, where core-shell fibres are produced by using two different solutions followed by a selective removal of the core material which also results in hollow structured fibres [2]. Herein, multi-axial electrospinning technique was employed to produce hollow structured fibers with different wall materials in single step process without any post treatments. In the fabrication process of multi-axial electro-spun nanofibers, a strong electric field is applied between a nozzle containing concentric tubes allowing for the extrusion of different fluids to tip of the nozzle and grounded metallic plate as a collector [3]. The diameter, surface morphology and layered structure of multi-walled hollow electro-spun fibres are controlled by tailoring the solvent properties, degree of miscibility of solutions, polymer concentration, applied voltage, electrospinning distance, and flow rate [4].

Morphological investigations on layer formation and hollowness of fibers were performed by acquiring TEM images using a monochromated TF20 TEM, Schottky cathode, operated at 200 kV. The samples were prepared by embedding the fibres into epoxy resin and subsequently cut in the ultramicrotome.

In order to be able to show that the hollowness and structural integrity of the fibers can be controlled, we have investigated tri-axial electro-spun fibers using two different outer layer polymers, namely PMMA and PS while keeping the inner layer material the same, PAAm. The TEM image in Figure 1a) shows a PMMA/PAAm hollow fiber with a diameter of about 330 nm, where the inner part - corresponding to a hollow core - is about 125 nm in diameter. The fiber (500 nm in diameter) in Figure 1b) shows that using PS as an outer layer instead of PMMA leads to an increase of the inner diameter up to 260 nm.

From these results we can conclude the diameter of hollowness can be adjusted by changing the type of polymer in the outer layer. This controllability can provide an easy encapsulation of functional materials with different viscosities if required, and increase the life-time of encapsulated materials through circumventing leakage.

1. M. Bognitzki, H. Hou, M. Ishaque, T. Frese, M. Hellwig, C. Scharte, et al: Adv. Mater (Weinheim, Ger) 12(9) (2000), 637-640.
2. D. Li, Y. Xia: Nano Lett. 4(5) (2004), 933-938.
3. E. Ozden-Yeniguan, E. Simsek, Y.Z. Meneceloglu, C. Atilgan: Pysical Chemistry Chemical Physics, 15 (2013), 17862-17872
4. J.S.M. Zanjani, B.S. Okan, I. Letofsky-Papst, M. Yildiz, Y.Z. Meneceloglu: Europ. Polymer Journal, 62 (2015), 66-76.
5. The authors gratefully acknowledge financial support from the Scientific and Technical Research Council of Turkey (TUBITAK) Project No: 112M312/COST MP1202 HINT project and thank to European Union within the 7th Framework Program [FP7/2007-2013] under grant agreement no. 312483 (ESTEEM2).

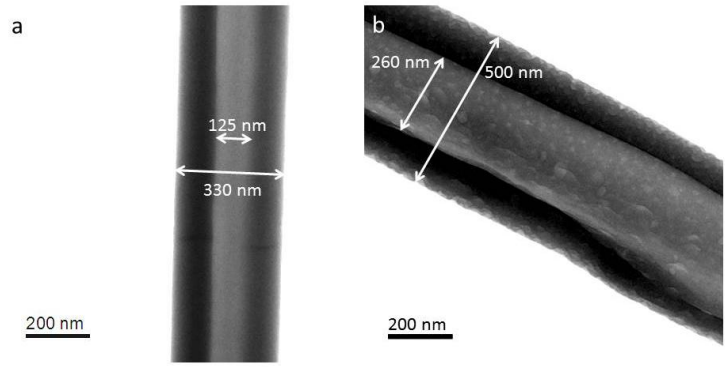

Figure 1. a) TEM image of PMMA/PAAm multi-walled hollow fiber; b) TEM image of PS/PAAm multi-walled hollow fiber.

Soft Matter, Polymers, C-Based Materials

MS5.P116
High resolution transmission electron microscopy of molecules on graphene

N. Vats[1]

[1]Max Planck Institute for Solid State Research, Stuttgart Centre for Elctronmicroscopy, Stuttgart, Germany

n.vats@fkf.mpg.de

The quest for fully transparent sample support for high-resolution transmission electron microscopy (HRTEM) has been fulfilled by introduction of single-layer graphene (SLG) [1]. Apart from its excellent electrical and mechanical properties [2], its one atom thick single crystalline structure consisting of carbon atoms forms the basis of its unmatched superiority compared to other sample support for specimens in HRTEM. Also, SLG as sample support enables specimen to be imaged as if it's free standing. Introduction of spherical aberration correctors (C_s) in modern TEMs coupled with low acceleration voltage permits characterization of radiation-sensitive specimens including biological at atomic resolution.

The aim of the present work is to perform structural and chemical analysis of organic, inorganic and organometallic molecules deposited on single-layer graphene using HRTEM and to understand different adsorption mechanism such as chemisorption or physisorption that governs the binding of molecule to the surface of deposition. This involves careful and systematic interdisciplinary co-operation at various level of experiment, which includes:

a) Preparation of ultra-clean free-standing SLG [3].

b) Highly controlled and clean deposition of molecules using techniques such as thermal evaporation in vacuum and mass filtered electrospray ion-beam deposition (ES-IBD) [4].

c) Setting up proper imaging (low-dose) condition during HRTEM acquisition.

Results comprising of above mentioned approaches will be presented.

1. Nair, R. R. et al. *Applied Physics Letters* 97 (2010): 153102.
2. Geim, A. K. *Science* 324 (2009): 1530-1534.
3. Longchamp, J-N. et al. *Journal of Vacuum Science & Technology B* 31 (2013): 020605.
4. Rauschenbach, S. et al. *Small* 2 (2006): 540-547.
5. Dubey, G. et al. *Journal of the American Chemical Society* 136 (2014): 13482-13485.

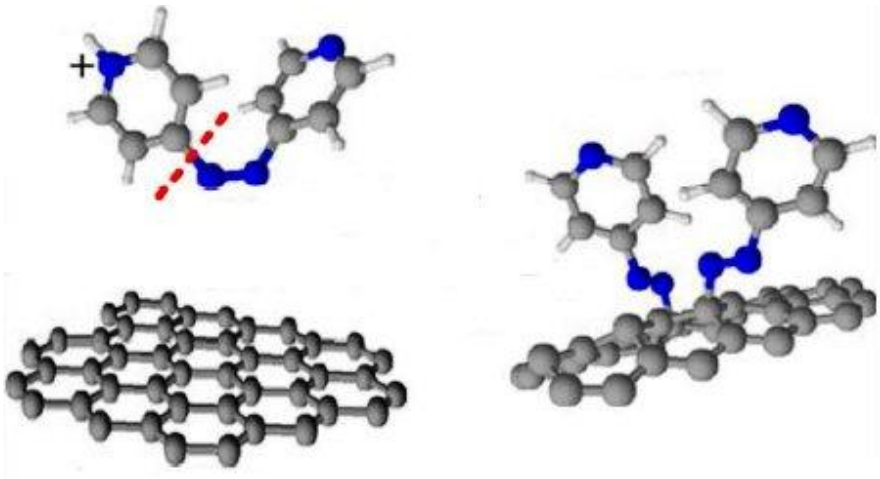

Figure 1. Represents an example of highly controlled and clean deposition process where, azopyridinium molecule is deposited on CVD-grown ultra clean SLG via reactive landing [5] mechanism which results in azopyridly-functionalized graphene.

Soft Matter, Polymers, C-Based Materials

MS5.P117
Phage-controlled assembly of organic-inorganic multilayered nanostructures

P. Moghimian[1], V. Srot[1], D. Rothenstein[2], S. J. Facey[2], L. Harnau[3], B. Hauer[2], J. Bill[2], P. A. van Aken[1]

[1]Max Planck Institute for Solid State Research, StEM, Stuttgart, Germany
[2]University of Stuttgart, Stuttgart, Germany
[3]Max Planck Institute for Intelligent Systems, Stuttgart, Germany

moghimian@is.mpg.de

Biomimetic synthesis of organic-inorganic composites is of great importance in nanoscience and has been extensively explored using self-assembly approaches.[1] Construction of ordered and defect-free nanostructures is a necessity for the fabrication of next generation optical and electronic devices.[2] The Ff class of inoviruses (filamentous phages, e.g. M13 phages) has been subject of intensive studies due to their self -assembling nature,[3] and due to the fact that they are highly stable and can tolerate a wide range of temperatures and pH values.[4] In this study, a liquid crystal system was used for the construction of a highly ordered composite material from wild-type (WT) filamentous M13 phages and zinc oxide (ZnO). First, WT M13 phages were deposited from a viral solution on amorphous carbon (a-C) and silicon dioxide (SiO_2) films in order to investigate the interactions between the phages and substrate surface. When the phages were immobilized on the SiO_2 surface, the trend of the system was toward the formation of an isotropic phase. However, viral particles show a high degree of alignment along a common axis on a-C surface as per nematic liquid crystalline model. The M13-phage particles were found to have a high affinity for incorporation into a closely-ordered pattern onto a-C surface (Fig. 1).[5] Such patterns can further function as templates to nucleate highly uniform inorganic layers and to construct organic-inorganic multilayers in an alternating fashion. According to these findings, we prepared organized viral films deposited from a viral solution on carbon-sputtered silicon wafers using convective assembly method as a viral-scaffold for the ordered synthesis of ZnO nanoparticles from a ZnO deposition solution.[6] Using scanning electron microscopy (SEM) and transmission electron microscopy (TEM), we show that ZnO nanoparticles are templated and ordered over a micrometer length scale (Fig. 2). We report that the formation of directionally immobilized arrays of viruses assists the controlled and oriented mineralization of inorganic nanomaterials such as ZnO.[7]

1. S.-W. Lee and A. M. Belcher, *Nano Lett.*, 2004, **4**, 387-390.
2. S. W. Lee, C. B. Mao, C. E. Flynn and A. M. Belcher, *Science*, 2002, **296**, 892-895.
3. A. S. Khalil, J. M. Ferrer, R. R. Brau, S. T. Kottmann, C. J. Noren, M. J. Lang and A. M. Belcher, *Proceedings of the National Academy of Sciences*, 2007, **104**, 4892-4897.
4. Z. Niu, M. Bruckman, B. Harp, C. Mello and Q. Wang, *Nano Res.*, 2008, **1**, 235-241.
5. P. Moghimian, V. Srot, D. Rothenstein, S. J. Facey, L. Harnau, B. Hauer, J. Bill and P. A. van Aken, *Langmuir*, 2014, **30**, 11428-11432.
6. P. Atanasova, D. Rothenstein, J. J. Schneider, R. C. Hoffmann, S. Dilfer, S. Eiben, C. Wege, H. Jeske and J. Bill, *Adv. Mater.*, 2011, **23**, 4918-4922.
7. Financial support by the DFG for funding SPP 1569 is gratefully acknowledged. The research leading to these results has received funding from the European Union Seventh Framework Programme [FP7/2007-2013] under grant agreement n°312483 (ESTEEM2).

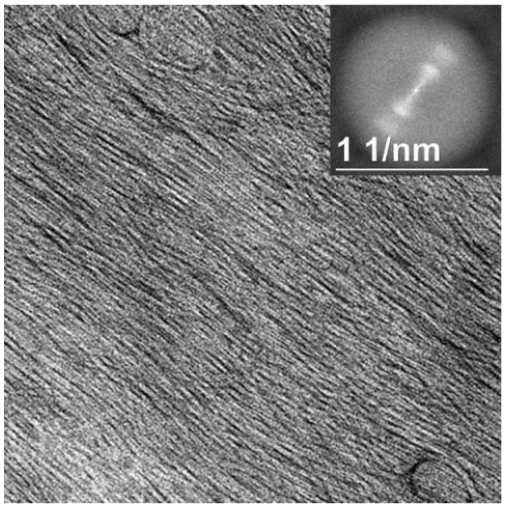

Figure 1. Bright-field TEM image of WT M13 phages highly oriented on a-C support film from a droplet of M13 viral solution (3.5×10^{14} pfu/mL). The inset shows the 2D Fourier-transformed image with an intensity profile in a narrow and elongated ellipse perpendicular to the direction of alignment.

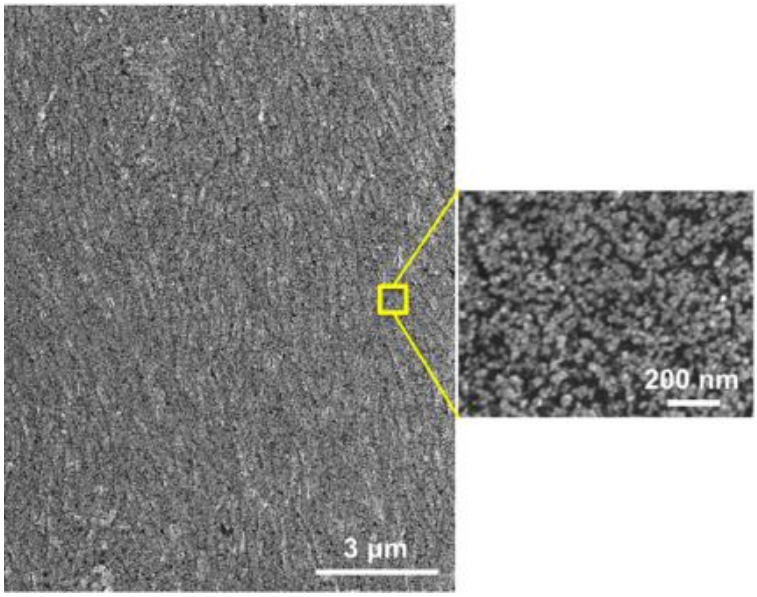

Figure 2. Plan-view SEM image of mineralized ZnO nanoparticles on highly oriented film of M13 phages immobilized on carbon-sputtered silicon wafer.

Soft Matter, Polymers, C-Based Materials

MS5.P118
Ultrastructural peculiarities of the surgical sutures

P. Karakozov[1], I. Baibekov[1], B. Ibadov[1], D. Mardonov[1]

[1]Center of Surgery, Pathology, Tashkent, Uzbekistan

pkarakozov@yahoo.com

The spatial ultrastructure of a number of native (in vitro) surgical sutures with their knots used in surgery has been examined. Interaction between synthetic materials and biological tissues in various periods after their implantation into man and experimental animals (in vivo) were also studied. The methods of scanning and light microscopy of stained histological and half-thin sections were used.

It was found that initial microstructural characteristics of homogenous by composition and apparentlysimilar synthetic materialssignificantly differ, especially after their implantation in biological organism. Various defects of the samples, which have undergone to mechanical or biochemical influences, are discovered before and after implantation. The degree of these defects and their nature were rather individual and depended on the type, composition of the synthetic material and manufacturer.

Moreover, these defects are revealed at very beginning stages of their application, before even sutures used. As a rule, it is a disintegration of suture fibres of different degree or the damages of their surface integrity. These processes much more marked in the knots where they took the range from minor deformation to total destruction and were followed by inescapable suture dehiscence.The most vulnerable subjects, in terms of disintegrative processes, are the braided absorbable sutures, while the least - the synthetic monofilaments.Stability and strength of the knot sizably depend on tightness of suture loops and durability of loops form. The suture surface microrelief and elasticity play notable role. From this position braded multifilament sutures have advantage before monofilament.

In case when sutures directly contact with blood flow, the surface microrelief and physical-chemical characteristics are the source for thrombosis or microthrombosis before suture integrates with biological tissues.

The study of the coated braided or silicone treated sutures reveals that when knotting these materials deform the sutures surfaces with formation of numerous lumps of different sizes and shapes. Exactly in these areas, in early postoperative period, fibrin deposition with further thrombi or microthrombi formation was observed as well as at the places of sutures surface damages. Knot dimension and linear size are important in cardiovascular surgery as source of thrombi. The braided suture knots approximate to flattened sphere, monofilament knots - to cylinder or cone.

By contrast to the obvious convenience of their usage, the visualization of their three-dimensional structure reveals flaws, which may serve as a source of complications. The nature of interactions of artificial materials and the recipient tissues, and their integration into the cardiovascular or other biological system directly depend on the structure of used threads and their electrostatic characteristics**.**

The initial defects or damages decrease the period of sutures adequate functioning, increase the degree or risk of their destruction and raising specific for implants complications, including local and common hemodynamic disturbances, thrombosis and microthrombosis. Meanwhile the best results demonstrate synthetic monofilaments. The study of the thread cuts reveals that braided sutures form different degree fringe which is absent in monofilaments. The braided sutures faster and to greater extent integrate with biological tissueswhile monofilaments are encapsulated preserving their initial structure.

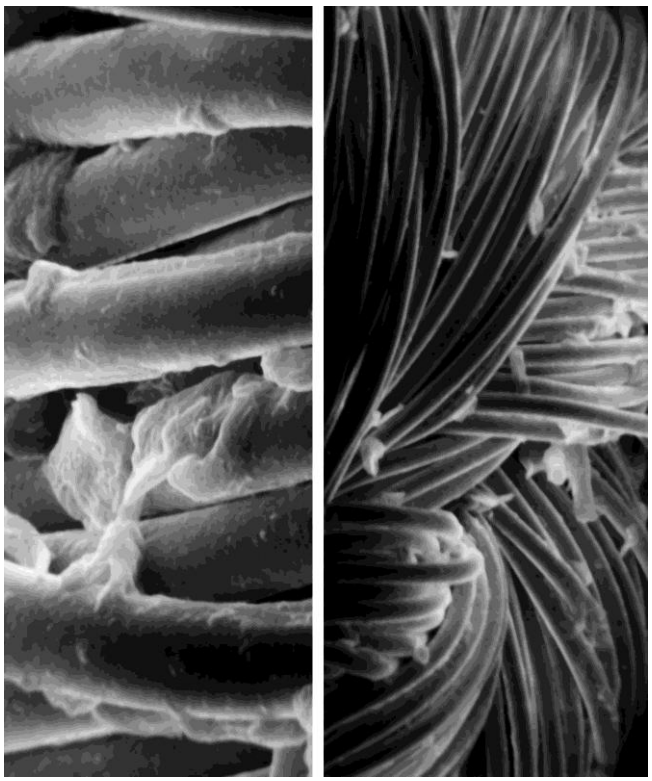

Figure 1. Original surgical suture ETHIBOND EXTRA. The knot surgace. SEM. x200, x1000.

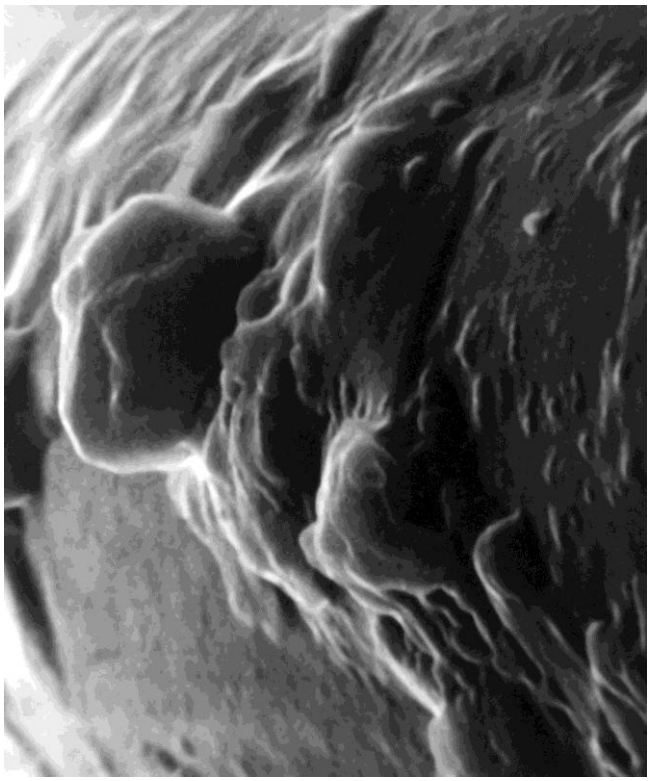

Figure 2. Original surgical suture ETHIBOND EXTRA. The knot surgace. SEM. x10000.

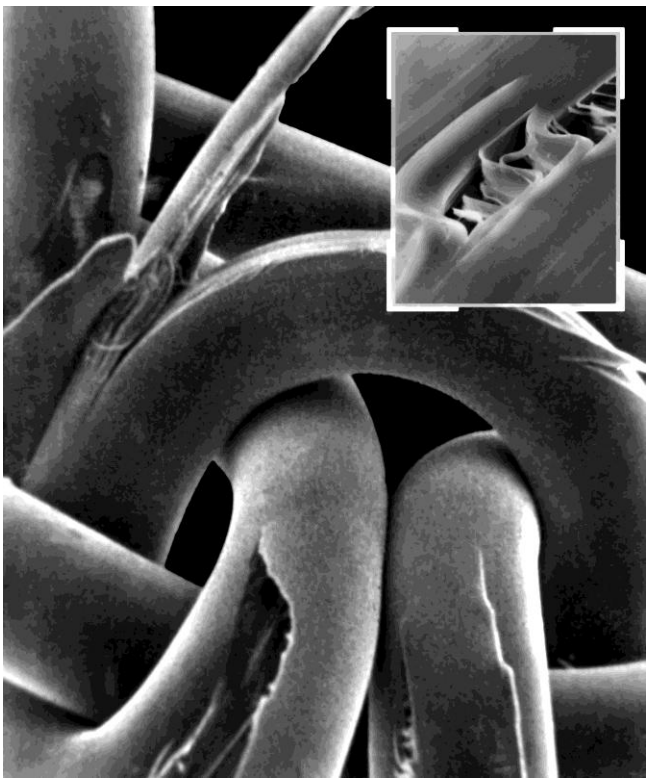

Figure 3. Original surgical suture BIOSYN. The knot surface. SEM. x60. Insert - the same. SEM. x600.

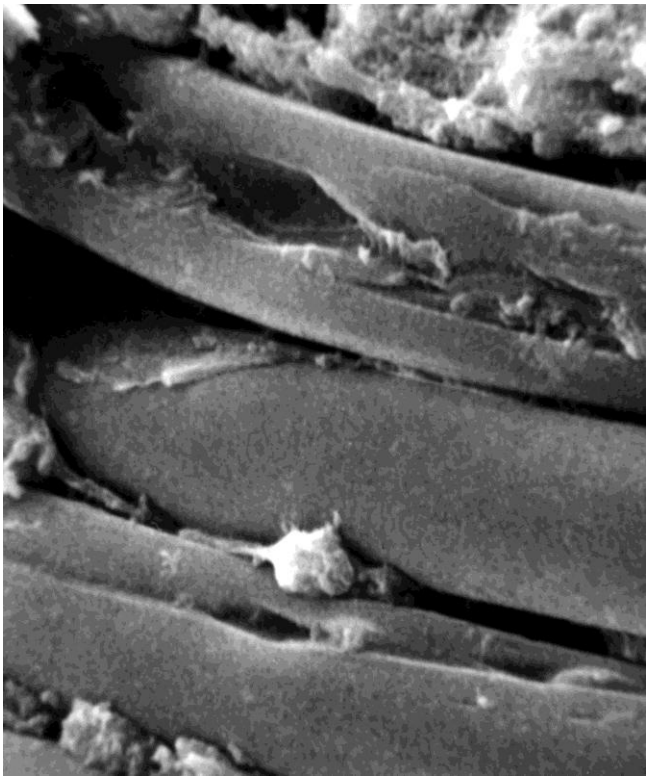

Figure. 4. Surgical suture SINTOFIL. 7 days after VSD repair. The knot surface. SEM. x1000.

Soft Matter, Polymers, C-Based Materials

MS5.P119
Synthetic materials in cardiovascular surgery – SEM visualization

P. Karakozov[1], B. Ibadov[1], I. Baibekov[1]

[1]Center of Surgery, Pathology, Tashkent, Uzbekistan

bakhromibadov@gmail.com

The three dimensional spatial ultrastructure of a number of the native synthetic materials used in cardiovascular surgery (in vivo) and in various periods after their implantation into man's and experimental animals' heart and vessels (in vitro) has been examined. Patches, prosthetic cardiac valves, vascular prostheses, endocardial electrodes, coronary stents, artificial heart ventricles, parts of pump oxygenators produced by different companies were studied. The methods of scanning and light microscopy of stained histological and half-thin sections were used.

It was found that initial structural characteristics of homogenous synthetic materials significantly differ especially after their implantation in the biological systems. In this process, various defects of above mentioned samples or their components, which have undergone to mechanical or biochemical influences, were discovered. The degree of these defects and their nature were rather individual and depended on the type and composure of the synthetic material. The advantages of these materials, from the point of view of their convenience in usage, sometimes become their drawbacks in studying their three-dimensional organization. The nature of interactions of artificial materials and the recipient tissues, and their integration into the cardiovascular system directly depend on structure of used implants.

Each of cardiovascular areas, which undergo to prosthetics, has its specific surface microrelief determining characteristic blood flow in this region. The change of this microrelief is one of the reasons that leads to change of local blood flow and promotes thrombi formation. Accordingly, surface microrelief of synthetic materials used, must approach the principle structure of replaced parts of cardiovascular system under reconstruction, to the greatest possible extent.

The initial defects or damages appearing in the process of the synthetic materials usage decrease the period of their adequate functioning, increase the degree or risk of their destruction and arising specific for implants complications, including local and common hemodynamic disturbances, thrombosis and microthrombosis.

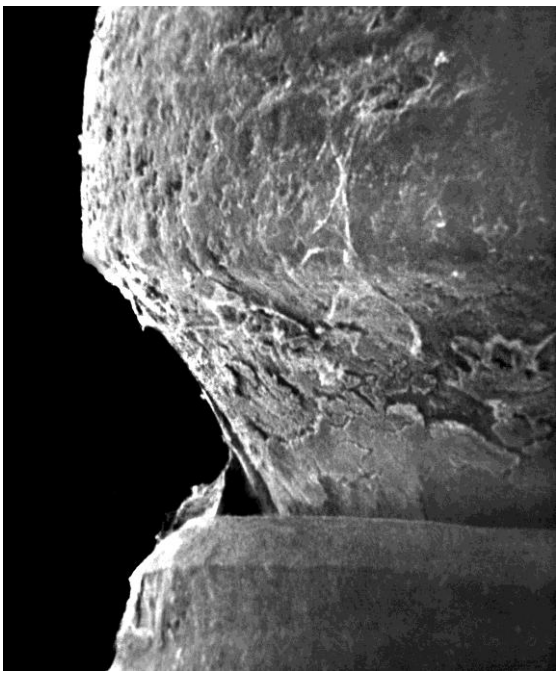

Figure 1. The head of intraventricular endocardial electrode. 7 days after implantation in man's right ventricle. The external surface. SEM. x100.

Figure 2. Ftorlon-lavsan knitted vascular prosthesis. 6 months after reconstruction of man's femoral artery. SEM. x60.

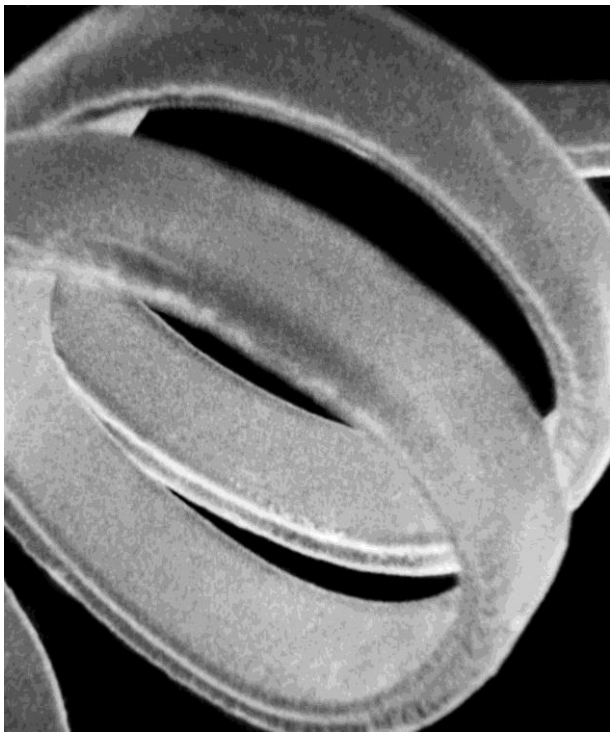

Figure 3. Original coronary artery stent. External and internal surfaces. SEM. x60.

Figure 4. Original cardiovascular patch. Teflon felt. SEM. x60.

Soft Matter, Polymers, C-Based Materials

MS5.P120
Scanning electron microscopy for polyurethane microcapsule detection

L. Stiebra[1], U. Cabulis[2], T. Vlcek[3]

[1]Riga Technical University, Institute of Technical Physics, Riga, Latvia
[2]Latvian State Institute of Wood Chemistry, Riga, Latvia
[3]Toseda s.r.o., Pardubice, Czech Republic

laurastiebra@gmail.com

Microencapsulation is a process in which around solid particles, liquids or molecular dispersions spherical shell from other material is made. Encapsulated substance is called core material, active agent or inner phase, whereas outer material - membrane, shell, coating or wall material. It is possible to obtain closed microcapsules with the size range between 100 nm and 100 µm.

Capsule membrane may have different characteristics. It can be one or multi-walled, with varied thickness, porosity, mechanical strength, size. These parameters are important for active agent release control - if capsule is broken it happens momentarily. However, if active agent is diffusing through shell wall, the release is gradual. Taking into account the specificities of walls making capsules, it can be inferred that they are influenced by mechanical force, temperature, chemical or biochemical reactions, pH, electric field etc. It should be kept in mind when analysing techniques and their conditions have been chose.

The variations of substances encapsulated and wall material is almost unlimited, as well as field of such microcapsule applications. It is possible to use them in agriculture, pharmacy, food, cosmetics, textiles, paints, adhesives and coatings, etc.

In this work through interphase polymerization two types of polyurethane shell microcapsules were synthesized - empty and filled with isophorone diisocyanate. It was done in order to obtain self-healing coating materials that can autonomously extend the lifetime of the surface material by restoring structural integrity after mechanical damages of paint and stops corrosion.

For microcapsule shell forming polyol (glycerol or 1,3-propanediol) and toluene diisocyanate was used. As a solvent cyclohexanone was taken, but as surfactant - gum arabic.

In order to evaluate morphology and surface features of microcapsules scanning electron microscope *SEM Tescan TS 5136 MM* with secondary electron detector and *VEGA TC* computer software was used. Before SEM image taking capsules were glued on aluminium specimen tables with adhesive tape. To provide electron conductivity, samples were sputter coated with gold using sputter coater *Emitech K550X*.

The images shows that despite vacuum environment in the SEM chamber microcapsules are not damaged and they remains nearly spherical. In Figure 1 “unfilled” polyurethane microcapsules are shown. Contrary to what we were expecting, microcapsules are not empty but filled with lots of smaller capsules. It is seen that both outer and inner surfaces are rough. The size distribution is uneven and the size of capsules is between 1 and 100 µm. Figure 2 shows with isophorone diisocyanate filled microcapsules and the presence of isocyanate is obvious. Because of little damages for some capsules it has reacted with air moisture and has became solid. The surfaces of these capsules unlike empty capsules are smooth and shell wall thickness is small. The average size of these capsules are between 20 and 50 µm.

With this work we have proved that it is possible to obtain spherical and good quality microcapsules using described above synthesis method. Scanning electron microscopy is a suitable detecting method and using appropriate conditions capsules maintains undamaged. With isocyanate filled polyurethane capsules have the potential to be industrially used in adhesives and coatings as self-healing additives.

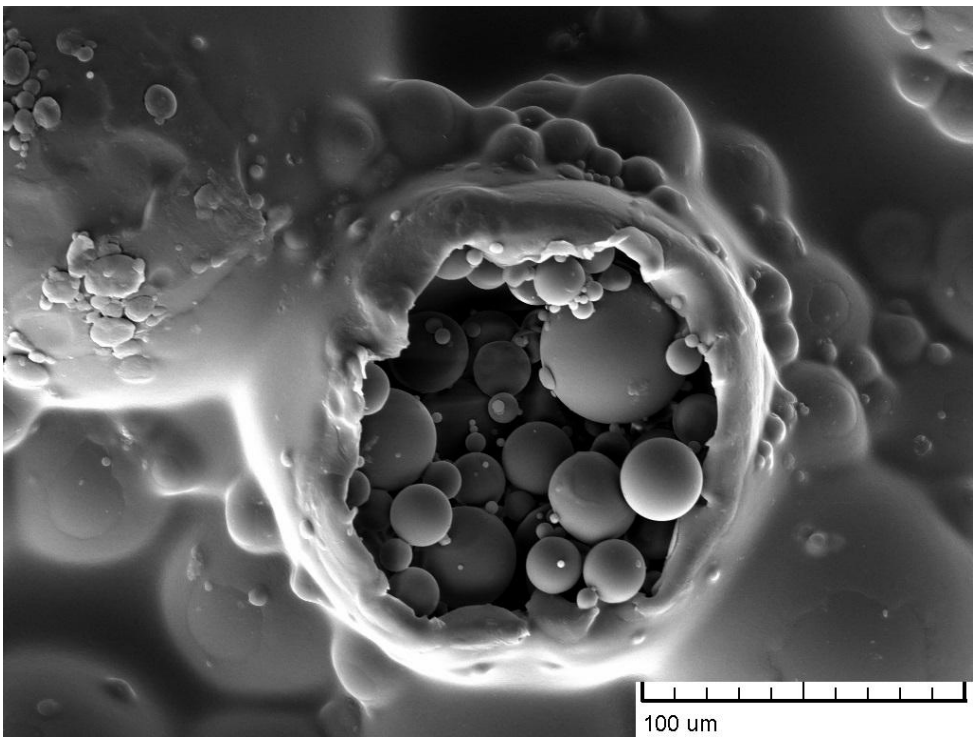
100 um

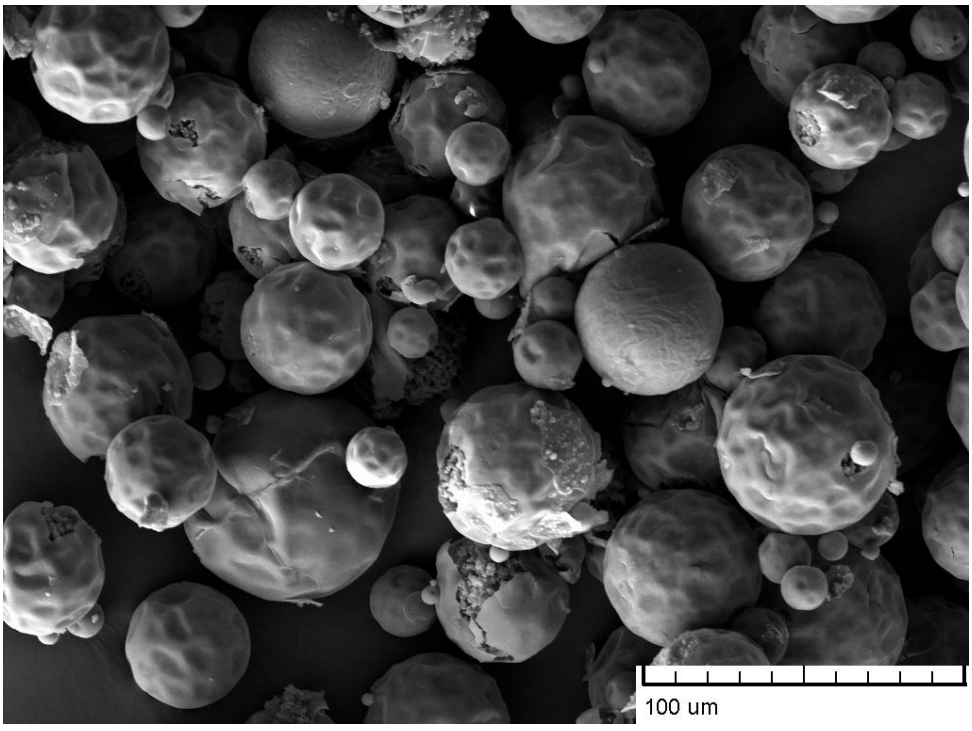
100 um

Soft Matter, Polymers, C-Based Materials

MS5.P121
TEM and SEM characterization of calcium phosphate platelets

C. Prietzel[1], I. Kovach[1], J. Koetz[1]

[1]University of Potsdam, Institute of Chemistry, Potsdam-Golm, Germany

claudia.prietzel@uni-potsdam.de

Calcium phosphates are the most important inorganic components of biological hard tissues, and several applications for calcium phosphates have been developed in the last decades, e.g. as bone repair material.

We present results of our studies of the calcium phosphate crystallization process in absence and presence of gelatin, chitosan, and gelatin-chitosan mixtures. Depending on the polymeric additives and the thermal treatment >600°C we get different aggregates of crystal platelets, e.g. ball-like supramolecular structures.

For the investigations of the supramolecular structure we used a scanning electron microscope S-4800 from Hitachi equipped with an energy dispersive X-ray detector (EDX) for the elemental analysis. The TEM investigations were carried out by using the high-resolution TEM JEM-2200FS (JEOL) operating at an acceleration voltage of 200kV. The sample preparation for the TEM investigation was done by dropping an aqueous suspension of the calcium phosphate on a carbon coated copper grid.

Figure 1 shows a SEM micrograph of the thermal treated gelatin-chitosan modified calcium phosphate. The ball-like super structures are formed by loosely packed calcium phosphate platelets. The dimension of the platelets is in the µm scale and the thickness is in the range of about 100nm. After thermal treatment (>600°C) they are stable in the electron beam in the TEM, and can be analyzed in more detail. Selected area diffraction patterns (SAD) and high-resolution TEM analysis show highly ordered crystalline structures. A HRTEM micrograph of one individual platelet is shown in figure 2 with a lattice plane distance of 0.334nm. This corresponds to {200} lattice planes of dicalcium phosphate. Additional powder X-ray diffraction (PXRD) analysis shows similarities with different calcium phosphate phases, i.e. dicalcium phosphate ($Ca_2P_2O_7$), and β-tricalcium phosphates (β-TCP, $Ca_3(PO_4)_2$) [1].

1. I. Kovach, S. Kosmella, C. Prietzel, C. Bagdahn and J. Koetz, Nano-porous calcium phosphate balls, Colloids and Surfaces B: Biointerfaces (2015) submitted

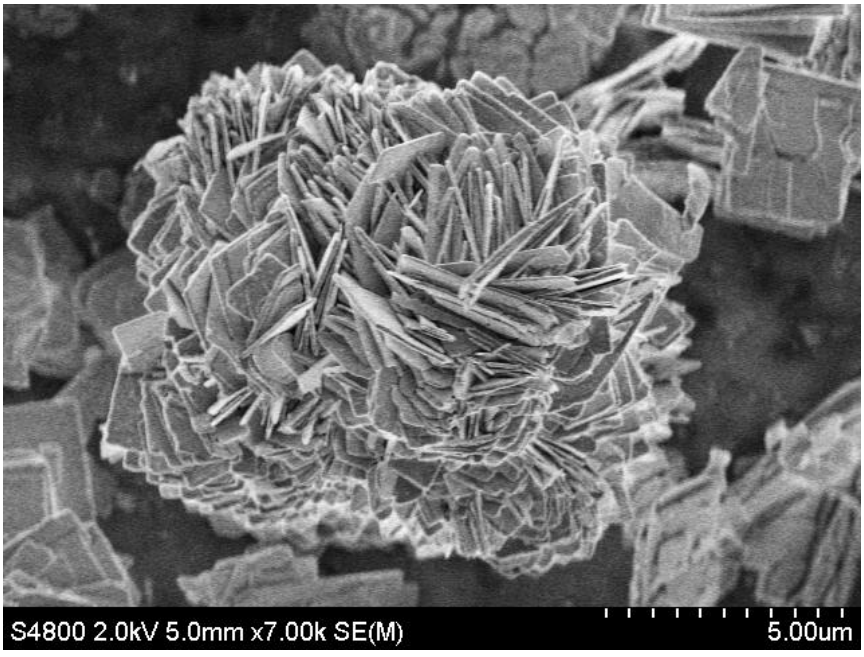

Figure 1. SEM micrograph of thermal treated gelatin-chitosan modified calcium phosphate platelets.

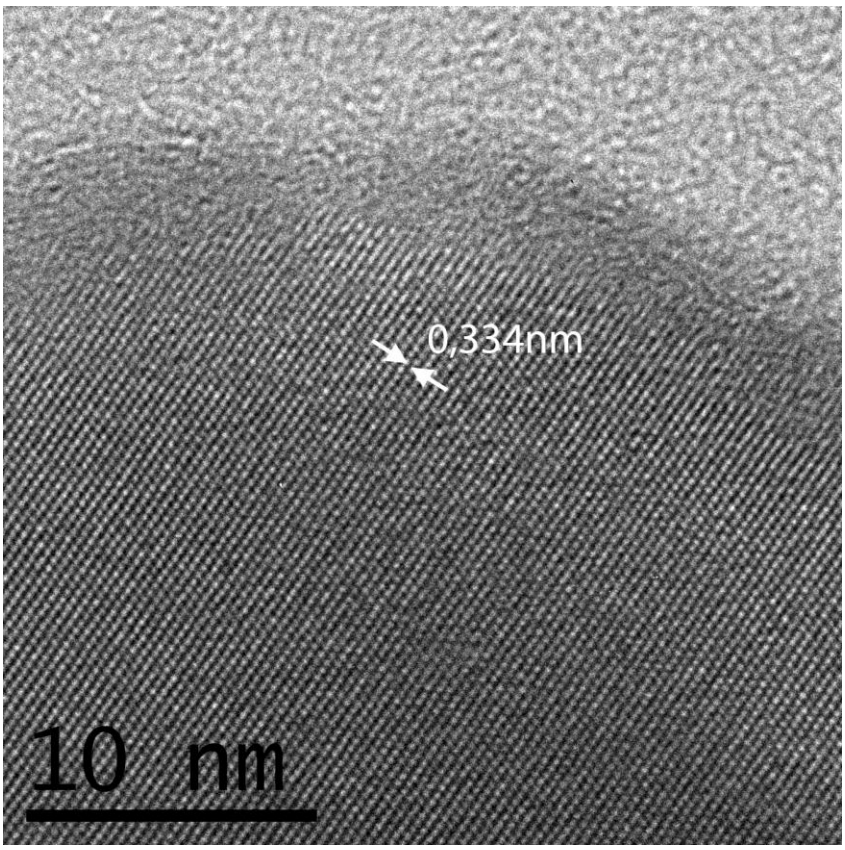

Figure 2. HRTEM micrograph of a thermal treated gelatin-chitosan modified calcium phosphate platelet.

Soft Matter, Polymers, C-Based Materials

MS5.P122
High resolution electron microscopy and Raman imaging of graphene-plasmonic interfaces

R. K. Biroju[1], P. K. Giri[2]

[1]Institute of Technology Guwahati, Centre for Nanotechnology, Guwahati, India
[2]Institute of Technology Guwahati, Department of Physics, Guwahati, India

giri@iitg.ernet.in

Graphene and related 2D materials and their hybrid nanostructures with 0D plasmonic nanoparticles (NPs) have received much interest due to their near field plasmonic effects in wide range of UV-vis-NIR wavelength, which are important for the photocatalysis and photonic applications.[1] However, high resolution microscopic studies of such hybrid nanostructures are challenging and thus less explored. We have fabricated large area single layer graphene (SLG) by chemical vapour deposition (CVD) technique and probed the in-plane and edge defects by high resolution transmission electron microscopy (HRTEM) and Raman imaging through quantitative analysis (see Fig. 1).[2-3] Further, the defective and defect free CVD graphene samples are physically functionalized with transitional metal (TM) thin films and nanoparticles (NPs) of gold (Au) and silver (Ag) and resonance Raman spectroscopy (RRS) and Raman imaging were carried out on the hybrid nanostructures, as illustrated in the Fig. 2. The spatial distribution of TM atoms and defect mediated interaction with graphene were investigated based on the RRS and localised surface plasmon resonance (LSPR) effects and it was correlated with the quantitative analysis from HRTEM imaging. Excitation wavelength dependent SERS and LSPR from graphene-TM hybrids before and after rapid thermal annealing (RTA) reveal the electron-phonon interaction on the graphene surface, which leads to the charge transfer from TM to graphene through in-plane defects. The graphene-TM hybrid system exhibit broadband absorption in the UV-vis-NIR region and this is significant for the reduction in the SERS signal, which was observed from the wavelength dependent Raman spectra and Raman mappings. The wide range of UV-vis-NIR absorption from the graphene-TM hybrids is very significant for the enhanced photocatalytic and photovoltaic applications of these novel hybrid structures.

1. Ferrari, A. C.; Bonaccorso, F.; Fal'ko, V.; Novoselov, K. S.; Roche, S.; Boggild, P. et al. Science and technology roadmap for graphene, related two-dimensional crystals, and hybrid systems. *Nanoscale* **2015,** *7* (11), 4598-4810.
2. Ding, M.; Tang, Y.; Star, A. Understanding Interfaces in Metal-Graphitic Hybrid Nanostructures. *The Journal of Physical Chemistry Letters* **2012,** *4* (1), 147-160.
3. Biroju, R. K.; Giri, P. K. Defect Enhanced Efficient Physical Functionalization of Graphene with Gold Nanoparticles Probed by Resonance Raman Spectroscopy. *J. Phys. Chem. C* **2014,** *118* (25), 13833-13843.

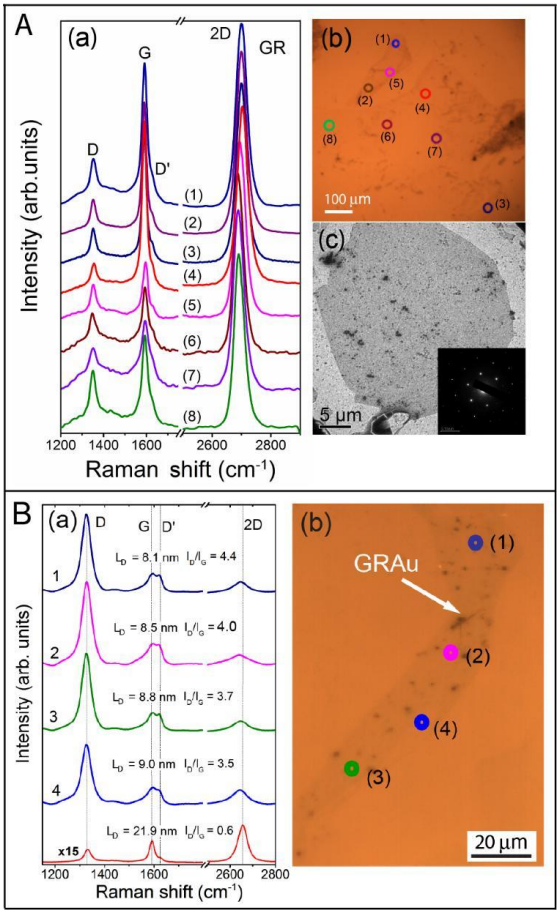

Figure 1: A. Raman fingerprint (λ_{ex}=514.5 nm) of CVD grown graphene (GR) transferred onto a Si/SiO_2 substrate, and (b) corresponding optical microscopy (OM) image showing the scanned area for each spectrum marked with a serial number. (c) TEM image of GR and corresponding SAED pattern of GR showing hexagonal lattice. **B.** (a) Position dependent Raman profiles of GR-Au and GR measured with λ_{ex}=632.8 nm. Inter-defect distance (L_D) at each position was calculated from the I_D/I_G intensity ratio. Note that the spectrum for the pristine graphene shown at the bottom is scaled up by a factor of 15 for comparison. (b) Corresponding OM image of scanning positions.

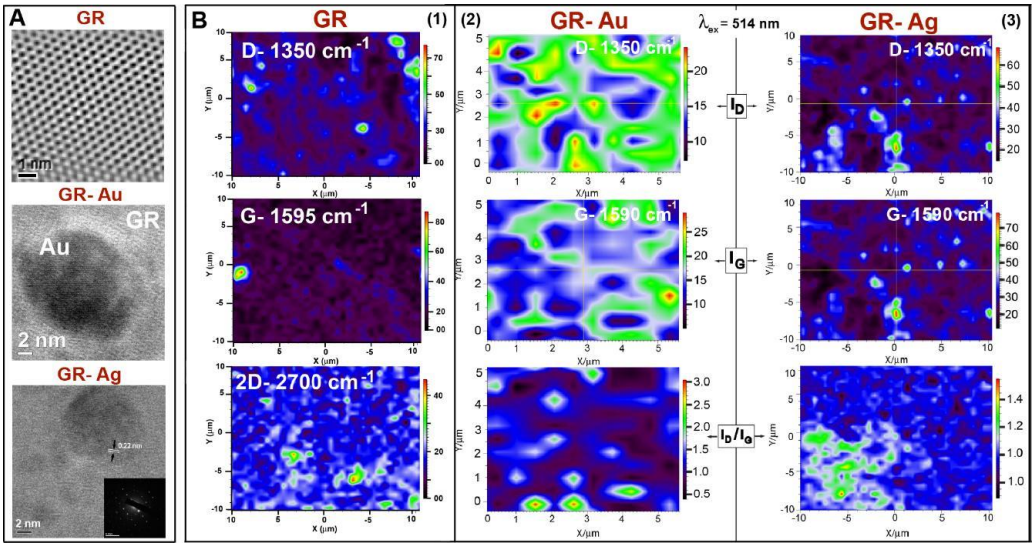

Figure 2: A. IFFT image of the single layer graphene showing hexagonal lattice and HRTEM images of Au and Ag embedded graphene layer and corresponding SAED pattern. **B. (1)** Spatial Raman mappings of CVD graphene showing D, G and 2D bands, which indicate the presence of BLG and FLG (Note that all the mappings are recorded on 10×10 μm^2 area at 514.5 nm laser excitation). Spatial Raman mapping of GR-TM hybrids showing the distribution of defects/ TM on the graphene layer. **(2-3)** The Raman mapping shown for the D, G bands and ratio of their intensities (I_D/I_G) for

GR-Au and GR-Ag samples, respectively. Note that the scanning area of the Raman mappings for GR-Au is 5×5 mm^2 and for GR-Ag 10×10 mm^2.

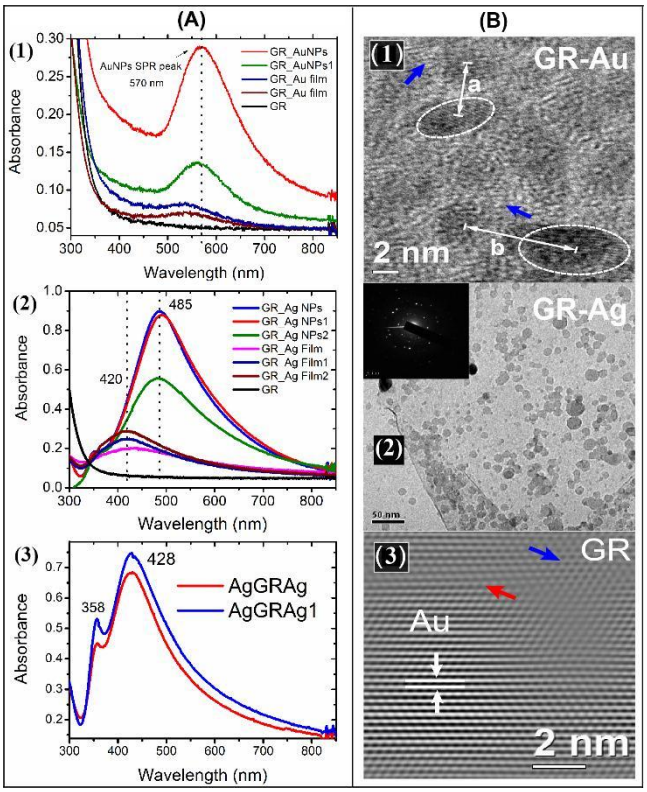

Figure 3: A. LSPR absorption from the graphene-TM hybrids: **(1)** GR-Au, **(2)** GR-Ag and **(3)** Ag-GR-Ag sandwich structure, before and after RTA process (Ag1). Note that the centres of LSPR absorption bands are denoted in nm unit. **B. (1)** HRTEM image of GR-Au showing the distance between two neighbouring Au NPs. **(b)** TEM image of GR-Ag after RTA, **(c)** IFFT lattice image showing the graphene and Au lattice fringes.

Nanoparticles, Nanostructured Materials, Catalysts

MS6.123
Watching catalysts in action

D. Gardini[1], P. M. Mortensen[2], C. D. Damsgaard[1], J. M. Christensen[2], T. W. Hansen[1], A. D. Jensen[2], J. B. Wagner[1]

[1]Technical University of Denmark, Center for Electron Nanoscopy, Kgs. Lyngby, Denmark
[2]Technical University of Denmark, Department of Chemical and Biochemical Engineering, Kgs. Lyngby, Denmark

jakob.wagner@cen.dtu.dk

The rate of catalyzed chemical reactions is in general very dependent on the actual state and geometry of the catalysts surface. This state and geometry are very often dependent on the actual chemical environment the solid-state catalyst is exposed to. Electron microscopy in general and transmission electron microscopy (TEM) in particular gives unmatched detailed insight of the local chemical and structural state of the nanostructured catalysts. Adding the possibility of controlling the gaseous atmosphere around the studied sample at elevated temperature gives a unique way of watching catalysts in action.

The formation and stability of molybdenum carbide based catalysts for hydrodeoxygenation (HDO) of bio-oil has been addressed by environmental TEM (ETEM) and *in situ* XRD. The active molybdenumo carbide has a strong tendency to oxidize at reaction temperature in presence of water (which is a product in the HDO reaction). The formation of Mo_2C from molybdenum oxide by carburization has been monitored by means of *in situ* XRD for further study in the ETEM. Gas-phase ETEM studies show that the active Mo_2C is fully embedded in an oxide layer during exposure to 300 Pa water vapour at 400˚C as shown in Figure 1. Preliminary studies involving co-feeding of 220 Pa CH_4 in addition to the water vapour indicate a preventing effect on the surface oxidation, increasing the stability of the molybdenum carbide catalyst.

Unfortunately, the conversion of gas species in the catalytic reaction are not directly observable in ETEM. However, in the case of the process involving solid reactants as in soot oxidation, it is possible to follow the catalytic reaction by imaging the process by means of ETEM and thereby give direct visualization of the chemical reaction.

Soot particles in the exhaust from diesel vehicles are likely to cause lung cancer and to affect the climate both locally and globally. Soot particles are therefore typically removed from exhaust gases by filtration through a ceramic filter. However, increased fuel consumption due to filter regeneration demands development of soot oxidation catalysts that can lower the regeneration temperature. The heterogeneously catalyzed soot oxidation is a gas/solid/solid interaction; hence, the contact between soot and catalyst is very important for the catalytic activity.

Here, we have monitored the soot oxidation by a silver catalyst *in situ* in the ETEM by ramping the temperature in 300 Pa oxygen at identical rates as used in temperature programmed oxidation experiments. Small Ag particles are observed to be highly mobile at an oxidation temperature of approx. 350˚C. The Ag particles travel throughout the soot partly oxidizing the carbon structures. A full oxidation of the soot is observed when the temperature reaches 700˚C. Snapshots of the *in situ* temperature programmed soot oxidation are shown in Figure 2.

The exact pressure and temperature are essential parameters when quantifying catalytic processes. However, measuring those parameters at the sample where the chemistry is taking place is often hindered by geometrical limitations in the ETEM. By addressing this issue by means of Computational Fluid Dynamics calculations of the temperature and pressure profiles in a differential pumped ETEM as used in the above examples we show a good correspondence between the pressure and temperature at the catalysts sample and the gauges monitoring the parameters in the experimental setup.

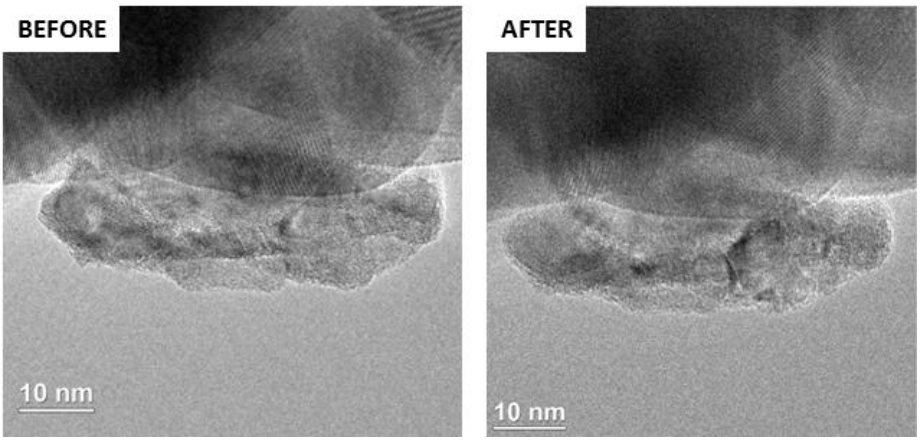

Figure 1. Molybdenum carbide based catalyst for HDO before and after exposure to H_2O at 400 ˚C.

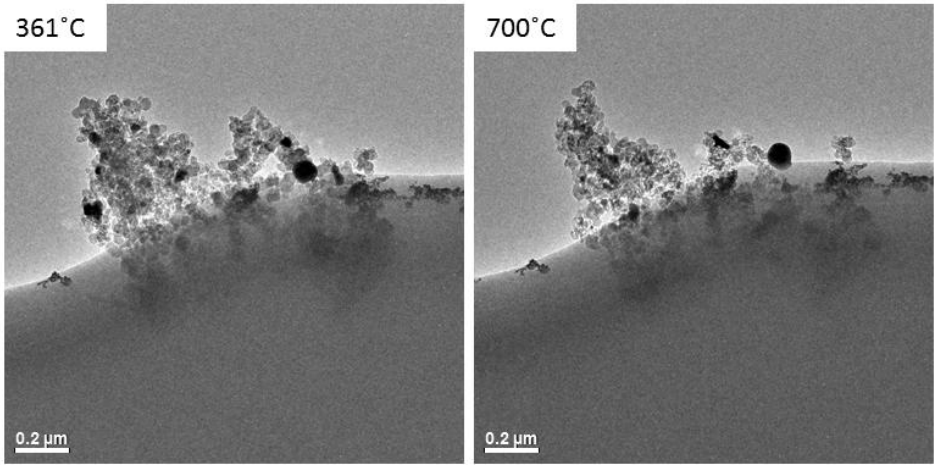

Figure 2. BF-TEM micrographs of in situ soot oxidation by a silver catalyst in the ETEM in tight contact condition. $P(O_2)$=300 Pa.

Nanoparticles, Nanostructured Materials, Catalysts

MS6.124
Imaging metal-organic framework materials (MOFs) and their interaction with metallic nanoparticles

S. Turner[1], M. Meledina[1], C. Wiktor[1], M. Filippousi[1], G. Van Tendeloo[1]

[1]EMAT - University of Antwerp, Physics, Antwerp, Belgium

stuart.turner@uantwerp.be

Metal-organic frameworks (MOFs) are a relatively new class of porous materials, consisting of metal ion centers linked together by organic linkers to create flexible, but crystalline porous networks. In recent years, MOFs have received a great deal of attention because of their high specific surface areas and pore volumes, applicable in gas (H_2) storage, catalysis, and photovoltaics.[1,2] For specific applications MOF crystals can be loaded with catalytically active materials like Pd, Au, Cu and Ru in the form of nanoparticles, small clusters or single atoms, leading to a heightened activity in e.g. olefin hydrogenolysis and methanol synthesis or with semiconductor nanomaterials like GaN or ZnO for improved optical properties.[2]

Structural characterization of this type of extremely delicate materials and their interaction with extra-framework guests remains extremely challenging. Most of the common characterization techniques like X-ray diffraction of nitrogen adsorption for this type of materials only offer global structural information, and cannot provide information on e.g. embedded nanoparticles. Transmission electron microscopy is ideally suited for this, as it can provide structural information down to atomic resolution. Improved TEM technology including low-voltage techniques, cooling holders, beam-blanking systems and fast-readout cameras nowadays do allow pore imaging of most types of MOFs.[3]

In this contribution, recent results on metal-loaded metal organic frameworks (Au@UiO-66 and Pt/Pd@MIL-101, Pd@COF-102)[4] characterized by aberration-corrected TEM and STEM, EDX mapping and electron tomography will be presented, and the limitations of the techniques applied to this type of materials will be discussed.

1. Turner S. et al. (2008) *Chemistry of Materials*, **20**, 5622-5627.
2. Meilikhov M. (2010) *EJIC, Eur. J. Inorg. Chem.,* 3701-371
3. Wiktor C. et al. (2012) *Microporous and Mesoporous Materials*, **162** 131-135.
4. Leus K. et al. (2015) *RSC Advances*, **5**, 22334-22342

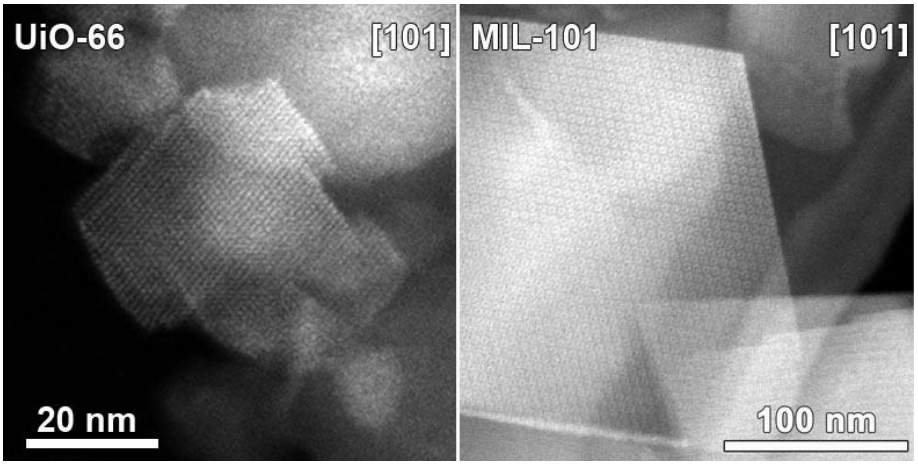

Figure 1. a) High resolution ADF-STEM images of UiO-66 (left, pore sizes of 8Å & 11Å) and MIL-101 (right, pore sizes of 29Å & 34Å), showing the framework pores can be imaged intact.

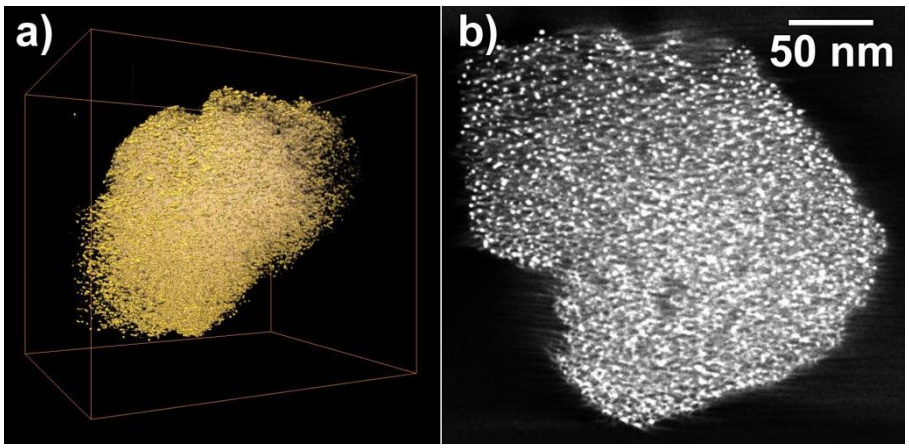

Figure 2. a) Tomographic reconstruction of Pd@COF-102, a Pd nanoparticle-loaded “organic” MOF. [5] The Pd nanoparticles are rendered in gold, the COF framework in soft off-white. b) Orthoslice through the three dimensional reconstruction of a loaded Pd@COF-102. The particles visible as white dots are clearly present in the whole crystals without any preferential distribution in size or position.

Nanoparticles, Nanostructured Materials, Catalysts

MS6.125
Direct imaging of octahedral distortion in a complex mixed molybdenum vanadium mixed oxide

T. Lunkenbein[1], F. Girgsdies[1], J. Noack[1], A. Wernbacher[1], M. Eichelbaum[1], A. Trunschke[1], R. Schlögl[1], M. G. Willinger[2]

[1]Fritz-Haber-Insitute of the Max-Planck-Society, Inorganic Chemistry, Berlin, Germany
[2]Max-Planck-Institut für Chemische Energiekonversion, Mühlheim (Ruhr), Germany

lunkenbein@fhi-berlin.mpg.de

"It would be very easy to make an analysis of any complicated chemical substance; all one would have to do would be to look at it and see where the atoms are. The only trouble is that the electron microscope is one hundred times too poor." With this statement R. Feynman has already highlighted the future importance of transmission electron microscopes (TEMs) in 1959. Nowadays Cs corrected TEMs are powerful enough to obtain point resolution below 50 pm.[1,2] However, direct imaging of light elements next to heavy elements remains complex. In probe corrected scanning transmission electron microscopy (STEM) recent developments tackle this challenge, resulting in the revival of the annular bright field (ABF) detector. In contrary to the contrast detected by the high angle annular dark field (HAADF) method, the ABF detector is also sensitive to light elements.[3,4]

Using the ABF detector, we investigated orthorhombic (Mo,V) oxides crystallized in a structure analog to the M1 structure (ICSD no. 55097) of MoVTeNb oxide. The obtained micrographs were compared with Rietveld refined X-ray diffraction (XRD) and electron paramagnetic resonance (EPR) data. Figure 1 shows an ABF image where the oxygen atoms brighten up. Furthermore we directly measured metal-oxygen bond angles and discussed the oxidation states of the metal centres. Our results prove Feynman´s prediction.

Seeing where the atoms are, generates in particular in heterogeneous catalysis a deeper understanding of the functionality of materials on the way towards tailor-made catalysts.

1. Erni R, Rossell MD, Kisielowski C, Dahmen U, *Phys. Rev. Lett.* 2009; 102: 096101.
2. Takayanagi K, Kim S, Lee S, Oshima Y, Tanaka T, Tanishiro Y, Sawada H, Hosokawa F, Tomita T, Kaneyama T, Kondo Y, *J. Electron Microsc.* 2011; 60: S239-S244.
3. Batson PE, *Nat Mater* 2011; 10: 270-271.
4. Findlay SD, Shibata N, Sawada H, Okunishi E, Kondo Y, Ikuhara Y, *Ultramicroscopy* 2010, 110: 903-923.

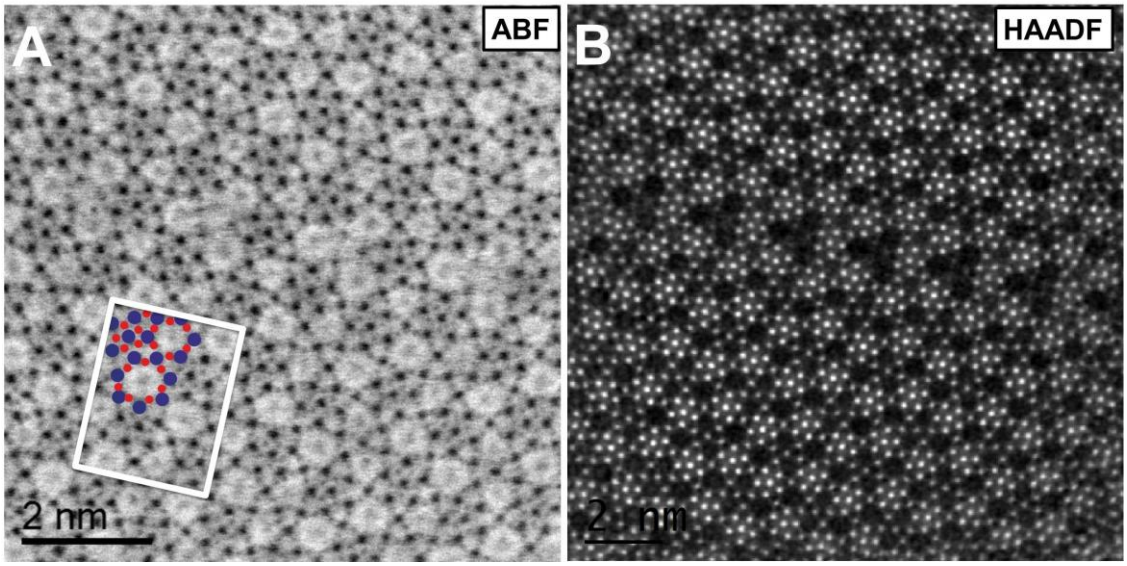

Figure 1. (A) ABF-STEM image of $(Mo,V)O_x$. The white rectangle displays the orthorhombic unit cell. Metal sites are highlighted blue and oxygen atoms are labeled red. (B) Corresponding HAADF image.

Nanoparticles, Nanostructured Materials, Catalysts

MS6.126
Principles of transmission electron microscopy of nanoparticles in liquid and application in biology and materials science

N. de Jonge[1,2]

[1]INM - Leibniz Institute for New Materials, Saarbrücken, Germany
[2]Saarland University, Physics Department, Saarbrücken, Germany

niels.dejonge@inm-gmbh.de

Electron microscopy traditionally studies solid samples with (sub-)nano scale resolution in a vacuum environment. But for many research questions it would be highly desirable to be able to study the samples in a functional environment. Of particular relevance is the imaging of nanomaterials and biological samples (e.g. proteins, DNA, cells) in liquid [1]. We have developed a new technology to image specimens in a micrometers-thick liquid layer [2]. A specimen, for example, an eukaryotic cell, or an assembly of nanoparticles, is placed in a microfluidic chamber with electron transparent windows of silicon nitride (SiN), and then imaged with scanning transmission electron microscopy (STEM), see Fig. 1A. This so-called Liquid STEM approach is capable of visualizing nanoscale materials of high atomic number (Z) in low-Z liquids, resulting from the Z contrast of STEM. The spatial resolution depends on the microscope settings, the used materials, the location of the nanomaterials in the liquid, and the liquid thickness. For example, gold nanoparticles can be imaged with a resolution as high as 1 nm on top of a liquid layer of 4 micrometers thickness [3]. The same principle of STEM detection can be used for environmental scanning electron microscopy (ESEM), whereby a thin water layer is maintained in equilibrium with saturated water vapor (Fig. 1B).

In the area of biology, Liquid STEM presents a new methodology to study the distribution of individual proteins and their assembly into protein complexes [4]. Gold nanoparticles or fluorescent quantum dots are used as specific protein labels and provide contrast in the liquid layer containing a whole cell. It is readily possible to study thousands of labels on dozens of cells as a consequence of the absence of the traditional extensive sample preparation associated with electron microscopy. With Liquid STEM we have acquired statistics about the stoichiometric distribution of the epidermal growth factor receptor [5]. It is also possible to study nanoparticle uptake in live cells using the microfluidic chamber [6].

Liquid STEM sheds new light on the behavior of nanoparticles in liquid. Dynamic STEM is capable of recording movies of flowing nanoparticles. It was discovered that nanoparticle movement in close proximity of the supporting silicon nitride (SiN) membrane is three orders of magnitude slower than what was expected on the basis of Brownian motion for a bulk liquid [7], pointing to the existence of a layer of highly ordered liquid at the membrane. The growth of gold dendrites can readily be observed [8], see Fig. 2. Depending on the exact liquid conditions, nanoparticles grow, dissolve in the liquid, or agglomerate. Understanding these parameters is essential for the interpretation of these experiments in a liquid environment.

1. de Jonge, N., Ross, F.M., Nat Nanotechnol 6, 695-704, 2011.
2. de Jonge, N., et al., Proc Natl Acad Sci 106, 2159-2164, 2009.
3. de Jonge, N., et al., Ultramicroscopy 110, 1114-1119, 2010.
4. Peckys, D.B., de Jonge, N., Microsc Microanal 20, 189-198, 2014.
5. Peckys, D.B., et al., Sci Rep 3, 2626: 1-6, 2013.
6. Peckys, D.B., de Jonge, N., Nano Lett 11, 1733-1738, 2011.
7. Ring, E.A., de Jonge, N., Micron 43, 1078-1084, 2012.
8. Kraus, T., de Jonge, N., Langmuir 29, 8427-32, 2013.

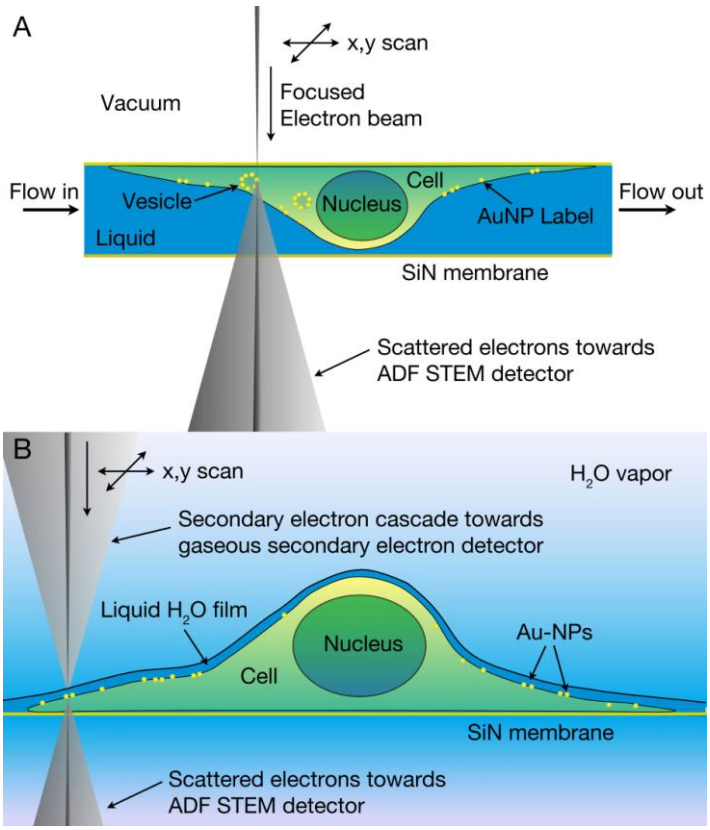

Figure 1. Principles of Liquid STEM. A sample, for example, an eukaryotic cell is grown on a supporting SiN membrane. Proteins labeled with gold nanoparticles reside in the plasma membrane. Imaging is done by scanning a focused electron beam over the cell. Transmitted electrons are recorded with the STEM detector located beneath the sample. (A) The cell is fully enclosed in a microfluidic chamber with two SiN windows for STEM. (B) The cell is maintained in a saturated water vapor atmosphere, while a thin layer of water covers the cell for Liquid STEM using ESEM. Reprinted with permission from [4]. Copyright 2014 Cambridge University Press.

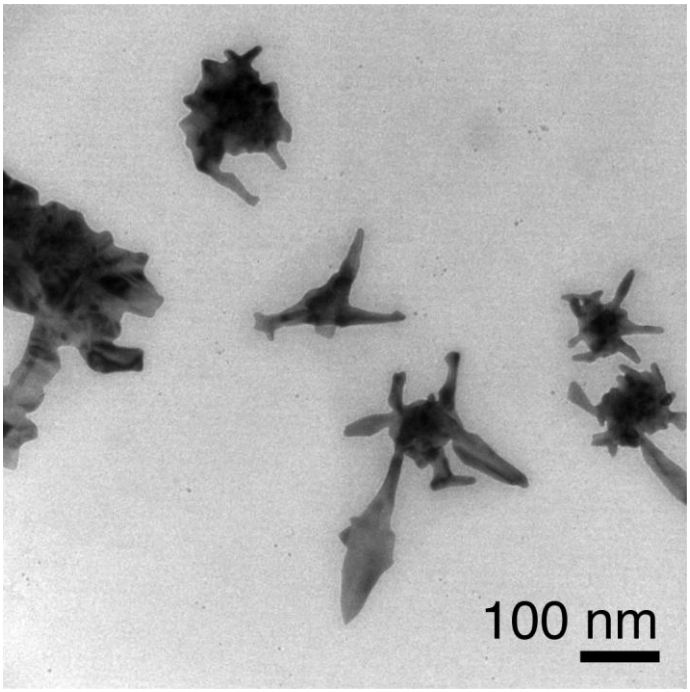

Figure 2. Gold nano-dendrites grown in-situ using Liquid TEM. Reprinted with permission from [8]. Copyright 2013 American Chemical Society.

Nanoparticles, Nanostructured Materials, Catalysts

MS6.127
Variation of the core atomic structure of thiolated $(Au_xAg_{1-x})_{312\pm55}$ nanoclusters with composition from aberration-corrected HAADF STEM

N. Jian[1], R. Palmer[1]

[1]University of Birmingham, School of Physics & Astronomy, Birmingham, United Kingdom

nxj203@bham.ac.uk

Nanoclusters are attracting considerable attention because of their unique physical, chemical and catalytic properties.[1]Small, alloy nanoclusters are of increasing interest due to their distinctive size and composition-dependent effects,[2] which suggest potential applications in catalysis, optics, engineering and electronics. In recent years, research on the synthesis of alloy nanoclusters has demonstrated impressive size and composition control, from sub-10nm AuAg alloy nanoparticles to size-selected monolayer-protected alloy nanoparticles $Au_{25-n}Ag_n(SR)_{18}$, $Au_{144-n}Ag_n(SR)_{60}$, etc.[3-6] Thus the atomic structures of alloy nanoclusters need to be investigated in order to establish the structure-property correlation in these systems. Here we present an investigation of the core atomic structure of thiolated $(Au_xAg_{1-x})_{312\pm55}$ nanoclusters as a function of composition (x) by using aberration-corrected HAADF STEM combined with multislice electron scattering simulations of the STEM images.[7] Three structural motifs are considered: icosahedral, fcc, and Ino-decahedral. A combination of integrated HAADF STEM intensity and diameter measurements is used to "fractionate" the deposited sample according to varying metal core size and composition.[8] Our results show that the atomic structure of thiolated $(Au_xAg_{1-x})_{312\pm55}$ nanoclusters are dependent on the composition: most Au-rich cluster structures are fcc, while most Ag-rich clusters are icosahedral and in between a corresponding variation is found. The ino-decahedral structure was only found in clusters with larger than 30% Au. The results should be relevant to the catalytic application of this new class of nanosystems. We believe that the experimental approach employed also has much potential to investigate the size, composition, and atomic structures of other binary nanostructures.

1. Schmid, G.; Bäumle, M.; Geerkens, M.; Helm, I.; Osemann, C.; Sawitowski, T. Current and Future Applications of Nanoclusters. *Chem. Soc. Rev.* **1999**, *28*, 179-185.
2. Ferrando, R.; Jellinek, J.; Johnston, R. Nanoalloys: From Theory to Applications of Alloy Clusters and Nanoparticles. *Chem. Rev.* **2008**, *108*, 845-910.
3. Li, Y.; Wang, Z. W.; Chiu, C.-Y.; Ruan, L.; Yang, W.; Yang, Y.; Palmer, R. E.; Huang, Y. Synthesis of Bimetallic Pt-Pd Core-Shell Nanocrystals and Their High Electrocatalytic Activity Modulated by Pd Shell Thickness. *Nanoscale* **2012**, *4*, 845-851.
4. Kumara, C.; Aikens, C. M.; Dass, A. X-ray Crystal Structure and Theoretical Analysis of Au25−xAgx(SCH2CH2Ph)18 − Alloy. *J. Phys. Chem. C* **2014**, *5*, 461-466.
5. Kumara, C.; Dass, A. (AuAg)144(SR)60 Alloy Nanomolecules. *Nanoscale* **2011**, *3*, 3064-3067.
6. Hostetler, M.; Zhong, C.; Yen, B. K. H.; Anderegg, J.; Gross, S. M.; D., E. N.; Porter, M.; Murray. Stable, Monolayer-Protected Metal Alloy Clusters. *J. Am. Chem. Soc.* **1998**, *7863*, 9396-9397.
7. N. Jian and R. E. Palmer, *J. Phys. Chem. C*, 2015, 150325132914007.
8. N. Jian, C. Stapelfeldt, K.-J. Hu, M. Fröba, and R. E. Palmer, *Nanoscale*, 2015, **7**, 885-888.

Nanoparticles, Nanostructured Materials, Catalysts

MS6.128
Electron diffraction study of metallic iron-rich Fe/Sc nanoglasses

X. Mu[1], D. Wang[1,2], C. Wang[1], A. Fischer[1], J. Ivanisenko[1], C. Kuebel[1,2], H. Hahn[1]

[1]Karlsruhe Institute of Technology, Institute of Nanotechnology, Eggenstein-Leopoldshafen, Germany
[2]Karlsruhe Institute of Technology, Karlsruhe Nano Micro Facility, Eggenstein-Leopoldshafen, Germany

xiaoke.mu@kit.edu

Nanoglasses are produced by compaction of nanometer-sized amorphous particles under an ultra-high pressure [1]. Small angle X-ray scattering and positron annihilation studies [2] give evidence that nanoglasses prepared by compaction of $Fe_{25}Sc_{75}$ and $Fe_{90}Sc_{10}$ nanoparticles contain nanometer-sized amorphous cores with high atomic density (comparable to rapidly-quenched) and amorphous interfacial regions with a substantially lower atomic density. The reduced atomic density in the interfacial regions is most likely responsible for the drastic property changes. Most surprisingly, a ferromagnetic behavior at room temperature is found for a $Fe_{90}Sc_{10}$ nanoglass, while the non-compacted primary particles and a rapidly-quenched ribbon are paramagnetic at room temperature [3].

In order to explain the magnetic behavior of nanoglasses, the atomic structure of the interfacial region needs to be known. One of the important tools to characterize disordered structures is the atomic radial distribution function (RDF). The RDF gives the probability to find certain atomic pairs as a function of the pair separation and consequently, contains the structural information in the short and medium range [4]. Electron diffraction, including the high signal to noise ratio structural information at large scattering angles, can provide high resolution RDF in real space. Figure 1 schematically demonstrates the procedure of RDF calculation: initially, the structure information is extracted from the electron diffraction pattern and followed by Fourier transformation to the RDF.

In this work, iron-rich Fe/Sc nanoglasses were produced by two different methods: (i) compaction of 6-8 nm-sized amorphous $Fe_{85}Sc_{15}$ particles produced by inert gas evaporation/condensation at 6 GPa [5]; (ii) ultrahigh vacuum (UHV) deposition of high momentum (HM) glassy $Fe_{80}Sc_{20}$ clusters with 1000 atoms per cluster at different kinetic energies. The experimental RDFs (figure 2, left) show that the 6 GPa compacted nanoglass (red) and the UHV-HM (1200 eV) deposited nanoglass (black) possess distorted short-range ordering (compared to α-iron). Moreover, the drastically attenuated features in both RDFs at ranges longer than 12 Å are an indication for the average dimension of the smallest ordered substructures in both nanoglasses. A decreased shoulder at 2.75 Å (red arrow in figure 2, right) of the RDF of the HUV-HM deposited sample implies a reduced population of the 1^{st} Fe—Sc and 2^{nd} Fe—Fe pairs due to a higher impact energy in comparison to the inert-gas condensation. Further molecular dynamic simulation is planned to gain a full understanding of the glassy structure, especially in the interfacial region.

1. Jing J, Krämer A, Birringer R, Gleiter H, Gonser U. J Non Cryst Solids 1989;113:167.
2. Fang JX, Vainio U, Puff W, Würschum R, Wang XL, Wang D, Ghafari M, Jiang F, Sun J, Hahn H, Gleiter H. Nano Lett 2012;12:458.
3. Witte R, Feng T, Fang JX, Fischer a., Ghafari M, Kruk R, Brand R a., Wang D, Hahn H, Gleiter H. Appl Phys Lett 2013;103:073106.
4. Cockayne DJH. Annu Rev Mater Res 2007;37:159.
5. Birringer R, Gleiter H, Klein H-P, Marquardt P. Phys Lett A 1984;102:365.

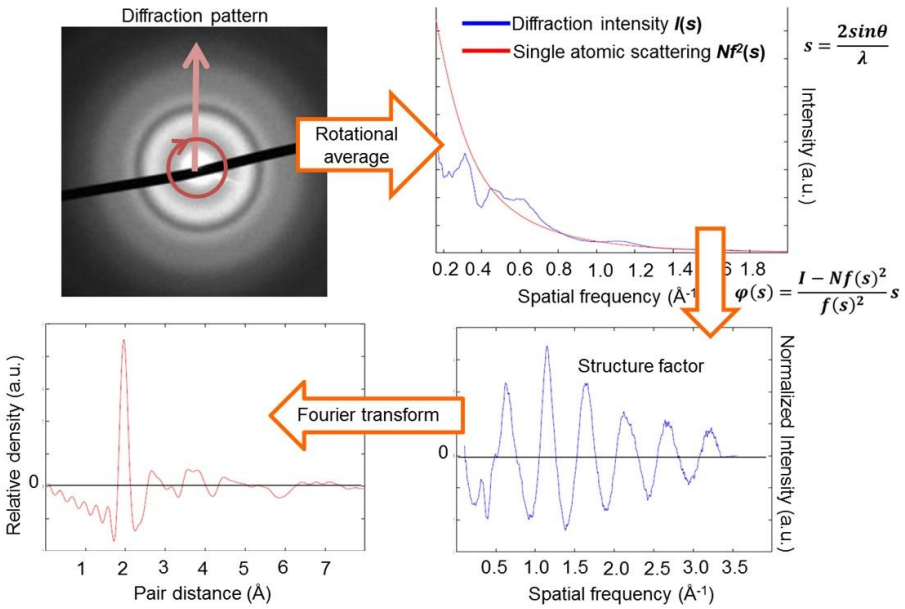

Figure 1. Schematic demonstration of RDF calculation from a diffraction pattern.

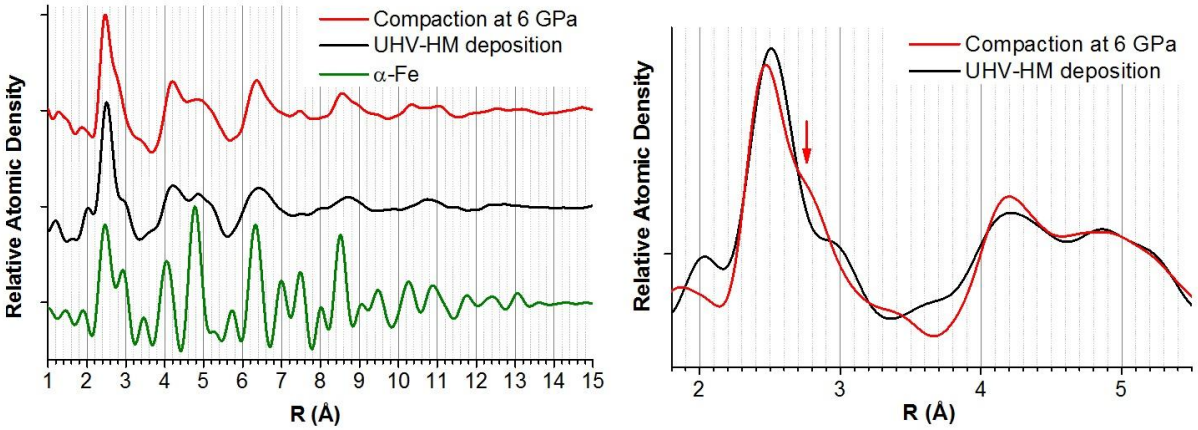

Figure 2. Left: RDF of compacted nanoglass at 6 GPa (red) and RDF of UHV-HM (1200 eV) deposition film (black) as well as a simulated RDF of α-iron. Right: enlarged short-range scope of the left RDFs for the first and the second nearest atomic pairs, i.e. the 1st and 2nd coordination shells.

Nanoparticles, Nanostructured Materials, Catalysts

MS6.P129
Real-space imaging of plasmonic modes of gold tapers by EFTEM and EELS

W. Sigle[1], N. Talebi[1], S. Guo[1], M. Esmann[2], S. F. Becker[2], R. Vogelgesang[2], C. T. Lienau[2], P. A. van Aken[1]

[1]Max-Planck-Institut für Festkörperforschung, Stuttgart Center for Electron Microscopy, Stuttgart, Germany
[2]Carl von Ossietzky Universität Oldenburg, Institut für Physik, Oldenburg, Germany

sigle@is.mpg.de

Plasmonic nanoparticles have been extensively studied in the literature due to their ability of supporting localized surface plasmon modes.

Here, we study three-dimensional single-crystalline gold tapers by electron energy-loss spectroscopy. Such tapers have been shown capable of nanolocalizing the optical energy at their apices by effectively converting surface plasmons propagating along the shaft into localized plasmons at the apex[1]. Notably, only rotationally symmetric modes - i.e. with angular momentum number m = 0 - can provide a smooth and diffraction-free transfer of energy to the apex[2]. The full picture of an optical taper, however, requires also consideration of all higher-order angular momentum orders (m = 1, 2,…).

We show that for sufficiently large local taper radii the projection of the local angular momentum along the electron trajectory leads to an activation of the parallel wave vector selection rule. This in turn results in a hyperbolic resonance condition for locally excitable optical modes.

The variation of these modes as a function of distance from the apex is displayed in Fig.1. The (m = 0)-mode shows up as a highly broadband mode at the very apex. In Fig.2 energy-filtered images showing the spatial distribution of these modes are shown[3].

1. M. Stockman, Phys. Rev. Lett. **93** (2004) p.137404.
2. M. Esmann *et al.*, Beilstein J Nanotech. **4** (2013) p.603.
3.The research leading to these results has received funding from the European Union Seventh Framework Program [FP/2007-2013] under grant agreement no 312483 (ESTEEM2).

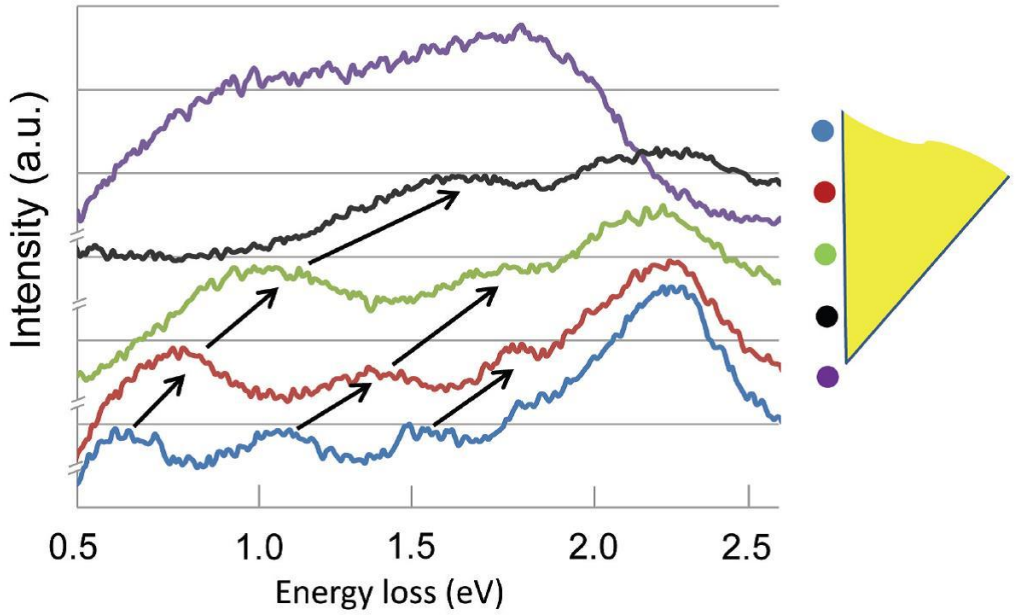

Figure 1. EELS spectra for electron impact at the apex (purple) and at distances of 275 nm (black), 504 nm (green), 733 nm (red), and 962 nm (blue) from the apex. The spectra are shifted vertically for clarity. The zero-loss-peak contribution was subtracted from the individual spectra by using a power-law fit.

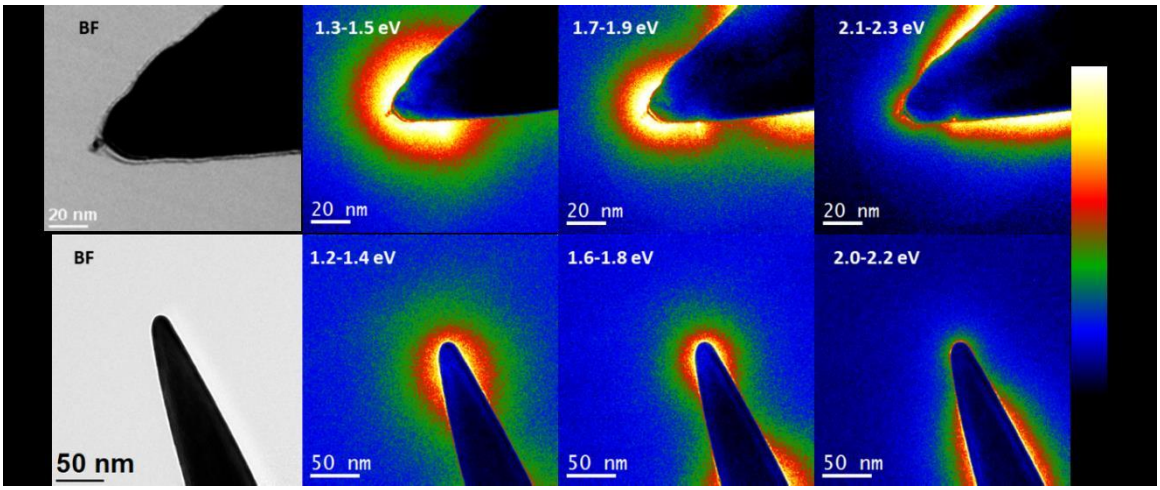

Figure 2. Bright-field image and EFTEM images of conical Au tapers with an opening angle of (a) 35° in the energy-loss interval from 1.3 to 2.3 eV and of (b) 15° in the energy-loss interval from 1.2 to 2.2 eV. The color bar on the right symbolizes the energy-loss probability which is a measure of the *z*-component of the excited electric field.

Nanoparticles, Nanostructured Materials, Catalysts

MS6.P130
Microscopy study on the compatibilising action of nanoclay in natural rubber(NR)/nitrile rubber (NBR) elastomer blend nanocomposites

H. Joseph Maria[1], S. Thomas[1,2], K. Joseph Maria[1,2], C. Mathew[1,2]

[1]Mahatma Gandhi University, Priyadarshini Hills P. O. Kottayam, Kerlala, India -686 560, International and Inter University Centre For Nanoscience and Nanotechnology,, Kottayam, India
[2]Mahatma Gandhi University, Kottayam., School of Chemical Sciences, Kottayam, India

hannavidhu@gmail.com

The need of production of novel materials with the best cost/performance balance is increasing and the scope of mixing the existing polymers to produce a new material with required properties is on demand. Thus research based on the study of polymer blends and polymer-filler composites is extensive for improving their processing capabilities and reducing the product costs. Natural rubber (NR)/nitrile rubber (NBR) elastomer blend nanocomposites were prepared by using organically modified nanoclay as the compatibilizer. The effect of the compatibilizing action was investigated by focusing on the morphological properties using transmission electron microscopy, scanning electron microscopy etc. Morphology of the polymer nanocomposites is related to all other properties. The intercalated and exfoliated clay platelets in the elastomer blend nanocomposites exhibited good improvement in the material properties compared to gum blend composition. The X-ray diffraction data and high resolution transmission electron microscopy give insight in to the clay exfoliation and intercalation and its localization. It was observed that the properties were improved with good dispersion of clay in the polymer blend system. The effect of preparation method also was found to influence the dispersion of the nanoclay which in turn affected the final properties.

Nanoparticles, Nanostructured Materials, Catalysts

MS6.P131
Tailoring the structures and the activities of porous carbon supported ultra-small Ru nanoparticles

D. Wang[1], A. Villa[2], C. Chan-Thaw[2], G. Veith[3], L. Prati[2]

[1]Karlsruhe Institute of Technology, Institite of Nanotechnology and Karlsruhe Nano Micro Facility, Eggenstein-Leopoldshafen, Germany
[2]Università di Milano, Dipartimento di Chimica, Milan, Italy
[3]Oak Ridge National Laboratory, Materials Science and Technology Division, Oak Ridge, United States

di.wang@kit.edu

Supported noble metal catalysts, such as Ru, Pd or Pt are highly active in catalytic conversion of biomass derived platform molecules into high-valued products. Recently Ru-based catalysts have shown high activity in both liquid phase oxidation of aliphatic alcohols [1] and in hydrogenation of levulinic acid [2]. By controllable synthesis methodology, the structures of nanocatalysts can be designed towards specific activity and selectivity for the reaction of interest. In addition, the support may influence the structure of metal particles on it and consequently the activity and selectivity of the catalyst. Carbon represents an ideal support for liquid phase application where typically mild temperatures are used. Carbon has several advantages such as being stable in both acidic and basic environments and easily tunable surface chemistry. In this presentation, we report a synthesis by incipient wetness method and structural characterization by TEM for Ru nanocatalysts supported on two types of carbon supports, ordered mesoporous carbon (OMC) and activated carbon (AC), respectively. The catalysts were tested in hydrogenation of levulinic acid and the influence of the tailored structure on the activity is discussed.

OMC was prepared by carbonization of a polymer gel derived from Pluronic F127 as reported in [3]. For the incipient wetness process, solid $RuCl_3$ is dissolved in water and the solution is then added to the supports (AC or OMC), with the volume of the solution equal to the volume of the pores in the support. The catalysts were reduced in H_2 at 300°C for 2h. For both Ru/AC and Ru/OMC the final ruthenium loading is 1 wt. %. The catalysts were examined in an image aberration corrected FEI Titan 80-300 electron microscope by using STEM, HRTEM and electron tomography.

The incipient wetness procedure produced highly dispersed small Ru nanoparticles. The median particle size is 1.2 nm for Ru/OMC and 1.5 nm for Ru/AC. The size distribution for Ru/OMC is narrower than that for Ru/AC due to more agglomeration on the AC support. STEM tomography has clearly shown that Ru particles are mostly situated inside the pores of OMC support with measured pore size around 8.5 nm. In contrast, the Ru particles were not impregnated into the pores of activated carbon support, which has a pore size around 2.5 nm. XPS has shown that activated carbon contains more hydroxyl and carboxyl functional groups. The high concentration of O species on the surface of AC could act as anchoring sites for Ru therefore limiting its diffusion into the pores. The preferred anchoring location of particles explains the difference in activity of the catalysts in hydrogenation of levulinic acid. On both catalysts, γ-valerolactone (GVL) was obtained as dominating product. The conversion after 1 hour reaction time is higher for Ru/AC than for Ru/OMC. The lower reaction rate in the case of Ru/OMC could be due to the location of the particles inside the pores, which makes the reactant mixture more difficult to access them. On the other hand, Ru/OMC exhibited excellent stability in recycling test, whereas Ru/AC lost activity continuously during the consecutive runs.

1. L. Prati, F. Porta, D. Wang, A. Villa, *Catal. Sci. Technol.* 2011; 1: 1624-1629.
2. A. Villa, C. E. Chan-Thaw, S. Campisi, C. L. Bianchi, D. Wang, P. G. Kotula, C.Kuebel, L. Prati, *PCCP*, 2015, DOI: 10.1039/C5CP00632E
3. Fulvio PF, Mayes RT, Wang X, Mahurin SM, Bauer JC, Presser V, McDonough J,Gogotsi Y, Dai S, *Adv. Funct. Mater.* 2011; 21: 2208

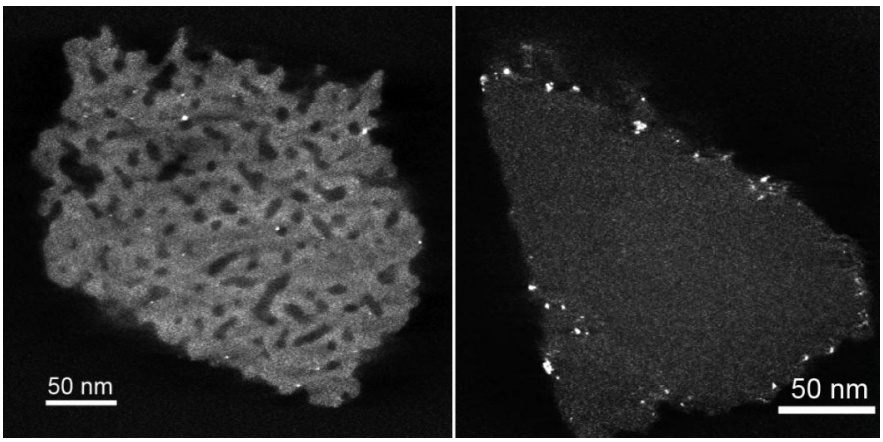

Figure 1. The representative cross section slices from STEM tomogram of Ru/OMC (left) and Ru/AC (right), respectively.

Nanoparticles, Nanostructured Materials, Catalysts

MS6.P132
Two-dimensional crystallization of P22 virus like particles

H. Yoshimura[1], E. Edwards[2], M. Uchida[2], K. McCoy[2], R. Roychoudhury[2], B. Schwarz[2], D. Patterson[2], T. Douglas[2]

[1]Meiji University, Physics, Kawasaki, Japan
[2]Indiana University, Chemistry, Bloomington, United States

hyoshi@meiji.ac.jp

Virus like particles (VLPs) are now well established a platforms for constructing functional biomimetic materials. The P22 VLP can be used as a capsule to sequester high concentration of enzymes within its cavity. Also, using several kinds of linkers between these active VLPs, an ordered assembly of coupled catalytic particles can be created. To achieve this, it is important to know the structure of VLP precisely. Here we report two-dimensional (2D) crystallization of bacteriophage P22 procapsid (PC), expanded form of PC, empty shell of PC, and enzymes incorporated PC for electron crystallography. The structure of P22 has been investigated only by single particle analysis of cryo-electron microscopy (EM) while similar bacteriophage HK97 was investigated both by cryo-EM and X-ray crystallography and has precise structure coordinate.

2D crystals of P22 were formed on a lipid monolayer at the water-air interface. Equal amount of zwitterionic lipid 1,2-dimyristoyl-*sn*-glycero-3-phosphocholine (DMPC) and cationic lipid 1,2-dimyristoyl-3-trimethylammonium-propane (DMTAP) was spread on a subphase containing 1% trehalose. P22 solution was injected from underneath the lipid monolayer and floated to the surface because of the density difference between the subphase and protein solution. After 15 hours, the lipid monolayer with adsorbed P22 was transferred to a holey carbon grid and was examined by electron microscopy. 2D crystals were obtained under subphase containing 100 mM NaCl, 10 mM MES (pH 5.0) and 1% trehalose. Crystallization ability was not depended on the form of the P22 VLPs, procapsid, expanded, or empty shell. And also enzymes incorporated did not influence the array formation.

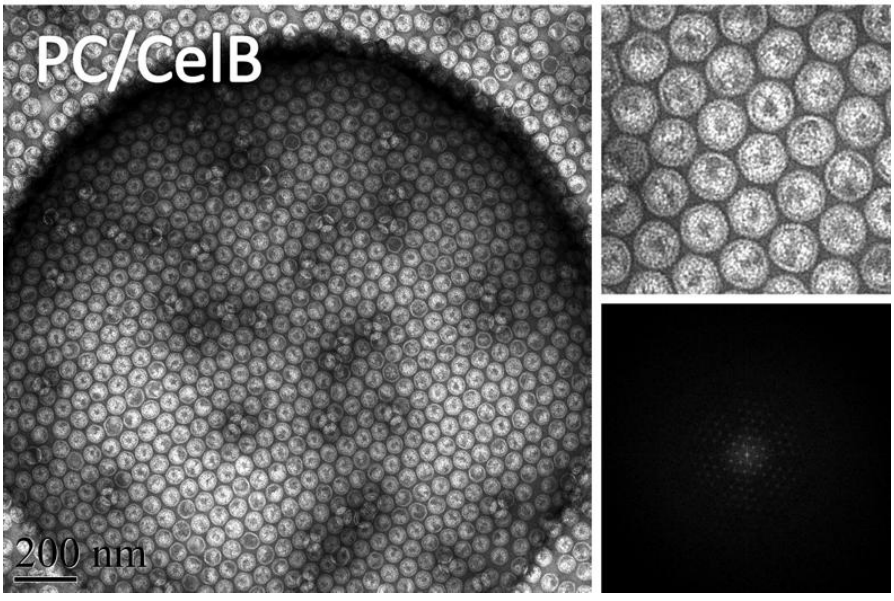

Nanoparticles, Nanostructured Materials, Catalysts

MS6.P133
Understanding and controlling atomic layer deposited TiO_2 on carbon-based nanomaterials: growth, structure and properties

Y. Zhang[1], C. Guerra-Nuñez[2], I. Utke[2], J. Michler[2], M. Li[3], H. G. Park[3], M. Rossell[1], R. Erni[1]

[1]EMPA, Swiss Federal Laboratories for Materials Science and Technology, Electron Microscopy Center, Dübendorf, Switzerland
[2]EMPA, Swiss Federal Laboratories for Materials Sci, Laboratory of Mechanics of Materials and Nanostructure, Thun, Switzerland
[3]ETH Zürich, Department of Mechanical and Process Engineering, Zürich, Switzerland

yucheng.zhang@empa.ch

Combining unique properties of the semiconductor TiO_2 and carbon-based nano-materials including carbon nanotubes (CNTs) and graphenes leads to enhanced performance for many important applications such as photocatalysis, solar cells, water splitting and nanoelectronics[1]. However, controlled deposition of thin conformal oxide films on CNTs and graphenes using atomic layer deposition (ALD) is still challenging as the early stages of nucleation and subsequent growth are not yet well understood. Here we adopted ALD to grow TiO_2 on multiwall nanotubes (MW-CNTs), and advanced transmission electron microscopy (TEM) techniques to characterize the structure and chemistry of the heterostructure[2,3]. The effect of deposition conditions, including temperature (60°C-240°C), number of ALD cycles (20-750), and surface pre-treatment of the MW-CNTs with oxygen plasma, on morphology, crystallinity and conformality of TiO_2 has been systematically studied through high-resolution TEM imaging and electron energy loss spectroscopy (EELS). As shown in Figure 1 and 2, by tuning the deposition conditions, controllable nucleation and growth of TiO_2 on CNT can be achieved, resulting in various morphology and crystallinity that may be suitable for different applications. Coalesced anatase TiO_2 conforming onto the MW-CNTs can be obtained with a growth temperature over 200°C. In addition, an ultra-thin (~5 nm) layer of anatase with high crystallinity and conformality on the CNTs is formed using a low temperature (60°C) ALD followed by annealing at a high temperature (400°C) in vacuum[4]. The correlation between the morphology of the heterostructures and their properties, in the context of solar energy, will also be discussed in this presentation.

1. Marichy, C. & Pinna, N. Carbon-nanostructures coated/decorated by atomic layer deposition: Growth and applications. *Coordination Chemistry Reviews* **257**, 3232-3253, doi:10.1016/j.ccr.2013.08.007 (2013).
2. Zhang, Y. C. *et al.* Growth and characterization of CNT-TiO2 heterostructures. *Beilstein Journal of Nanotechnology* **5**, 946-955, doi:10.3762/bjnano.5.108 (2014).
3. Zhang, Y. *et al.* Understanding and Controlling Nucleation and Growth of TiO2 Deposited on Multi-wall Carbon Nanotubes with Atomic Layer Deposition. *The Journal of Physical Chemistry C*, doi:10.1021/jp511004h (2015).
4. Zhang, Y. *et al.* Formation of Ultrathin Monocrystalline Anatase TiO_2-CNT Core-Shell Nanostructure. *to be submitted*

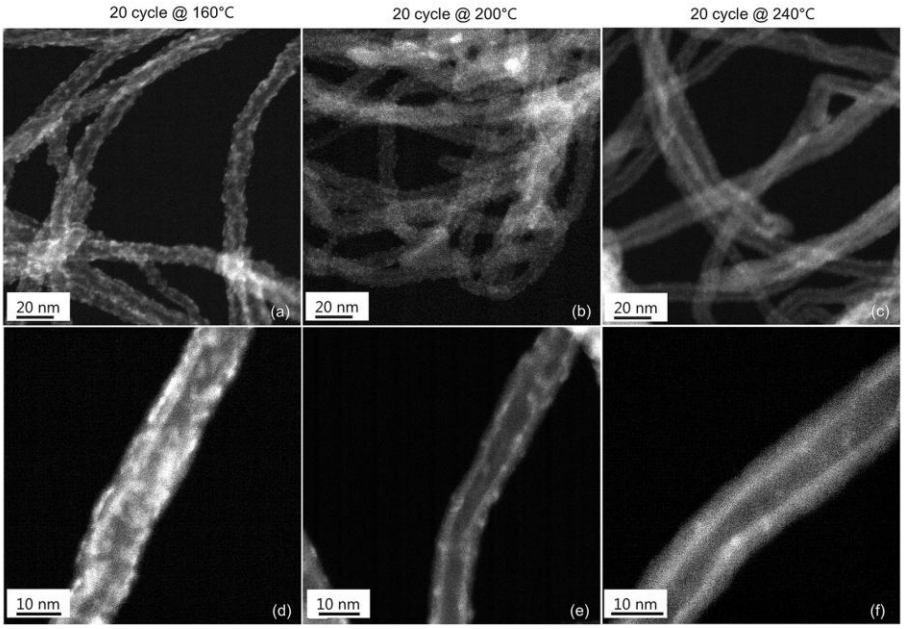

Figure 1. Nucleation of TiO_2 on MW-CNTs after 20 ALD cycles at different temperatures characterized with scanning TEM high angle annular dark field (STEM-HAADF) imaging. The top row shows an overview of the sample and the bottom row zooms in on individual CNTs. The nuclei densities decrease from 160°C to 240°C while the nuclei size remains similar.

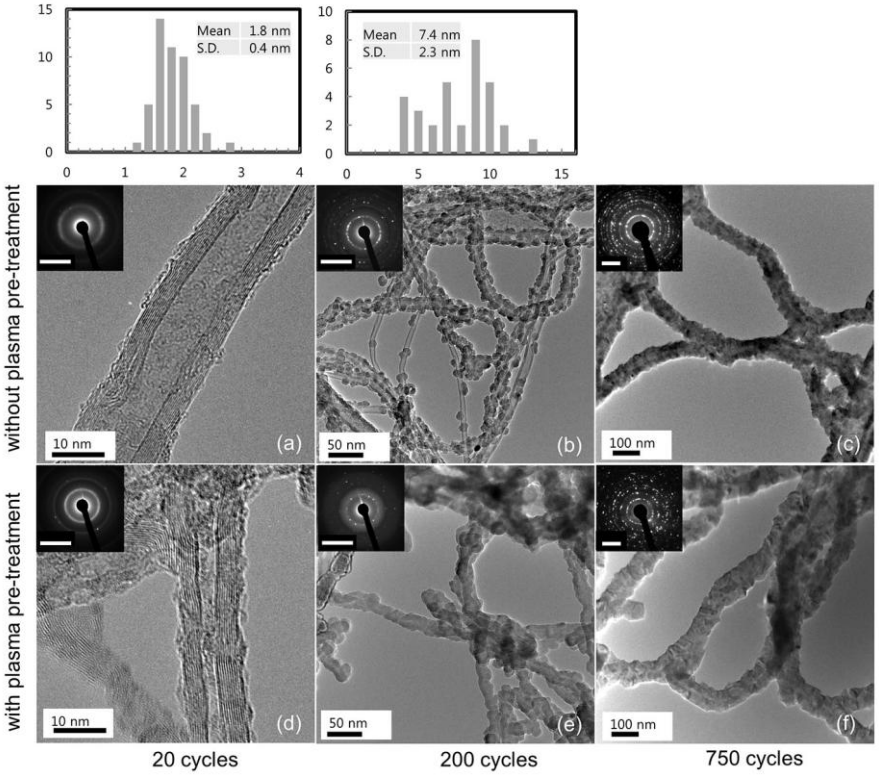

Figure 2. Growth of TiO_2 on MW-CNTs deposited at 200°C. (a), (b) and (c) are after 20, 200, 750 cycles respectively. (d), (e) and (f) are on the CNT pre-treated with O_2 plasma and subsequently deposited for the same cycles. The inset shows the selected area diffraction pattern (SADP) from the corresponding sample. The scale bar is 5 nm^{-1}. The top histograms are the size distributions of TiO_2 particles measured from the samples in (a) and (b) respectively. For the other samples, a coalesced layer is formed and hence similar measurement is not possible.

Nanoparticles, Nanostructured Materials, Catalysts

MS6.P134
Modular construction of Pt@TiO_2 core-shell nanoclusters for fuel cell catalysis and water splitting

C. E. Blackmore[1], N. V. Rees[2], R. E. Palmer[1]

[1]University of Birmingham, Nano Physics Research Lab, Birmingham, United Kingdom
[2]University of Birmingham , Chemical Engineering, Birmingham, United Kingdom

cew825@bham.ac.uk

Better, cheaper catalysts are a focus of study within today's research community given the critical challenges of low carbon energy supply and the storage of renewable energy as fuel. Currently Platinum is used as the principal catalyst within fuel cells: reducing the quantity of Platinum through nano-structuring or material replacement should improve the viability of the hydrogen economy [1]. Core-Shell Platinum-Titanium oxide (Pt@TiO_2) nano-clusters show promise for fuel cell catalysts [2,3] and for hydrogen generation through solar water splitting [4]. We report size-selected binary Pt@TiO_2 clusters [5] generated using a magnetron sputtering, gas condensation cluster beam source and imaged using a probe-corrected Scanning Transmission Electron Microscope (STEM) in High Angle Annular Dark Field (HAADF) mode [6]. Pt core-TiO_2 shell clusters have been produced with a size range from 2 nm (30 kDa) up to 5nm (120 kDa) with a mass resolution of 16. Remarkably, these clusters exhibit a preferred Pt core size of 30 ± 6 Pt atoms (1 nm), independent of the overall cluster size. For small clusters with mass below 55 kDa a single core is observed, whereas larger clusters exhibit 2 to 4 separate cores, increasing with size, indicating the modular assembly of core-shell monomers. Preliminary electrochemistry work indicates that these clusters are catalytically active for the hydrogen evolution reaction.

1. C. Zhong, J. Luo, B. Fang, B. Wanjala, P. Njoki, R. Loukrakpam, J. Yin, Nanotechnology. 21, (2010).
2. P. Jennings, B. Pollet, R. Johnston, PCCP. 14, 3134-9 (2012).
3. P. Jennings, B. Pollet, R. Johnston, J Phys Chem C. 116, 15241-15250 (2012).
4.M. Ni, M.Leung, D. Leung, K. Sumathy, Renew Sust Energ Rev 11, 401-425, (2007).
5. S. Pratontep, S.J. Carroll, C. Xirouchaki, M. Streun, R.E. Palmer, Rev Sci Instrum 76, 1-8 (2005).
6. C.E. Blackmore, N.V. Rees, R.E. Palmer, PCCP (2015), DOI: 10.1039/C5CP00285K

Nanoparticles, Nanostructured Materials, Catalysts

MS6.P135
Cycling behavior of Fe-doped ceria catalysts characterized by aberration-corrected imaging, electron energy-loss spectroscopy and in-situ heating

M. Meledina[1], S. Turner[1], V. Galvita[2], H. Poelman[2], G. B. Marin[2], G. Van Tendeloo[1]

[1]University of Antwerp, EMAT, Antwerp, Belgium
[2]Ghent University, Laboratory for Chemical Technology, Ghent, Belgium

maria.meledina@uantwerpen.be

The chemical looping process is based on multiple reduction/re-oxidation steps of metal oxides, functioning as oxygen carriers during the conversion of CO_2 and a hydrocarbon fuel to the chemical building block CO and H_2O. As the reduction/re-oxidation reactions are carried out at an elevated temperature of 600°C, one of the main problems in chemical looping is sintering of the metal oxide oxygen carrier. Iron-oxide doped ceria has presented itself as an excellent candidate for use as oxygen carrier, as it has both a high oxygen exchange capacity and the iron dopants are thought to enhance the resistance of the material ability to sintering. However, in order to confirm this, a detailed study of the morphology, structure and sintering behavior of FeO_x:ceria is necessary during all steps of the chemical looping process.

In this work, as-synthesized and chemical looping cycled ceria, 5 wt.% and 10wt.% FeO_x:CeO_2 materials were studied in detail by aberration-corrected HAADF-STEM imaging and spatially resolved electron energy-loss spectroscopy (EELS) (Fig. 1). Our results show that the undoped ceria material is reduced at the nanoparticle surface [1] and the presence of small voids within the material is confirmed. Doping with 5wt.% of iron leads does not lead to the formation of a separate iron-containing phase. The iron dopants are found to be present at the surface of the ceria material, and decorating the void walls [2]. Higher iron oxide doping leads to the formation of the separate Fe_2O_3 phase in the as-produced sample. In-situ heating TEM experiments allow to monitor the morphology changes during sintering, namely movement of the ceria vacancies, voids and sintering of the individual nanoparticles.

1. Turner et al., Nanoscale 2011, 3, 3385-3390.
2. Meledina et al Nanoscale 2015, 7, 3196-3204.

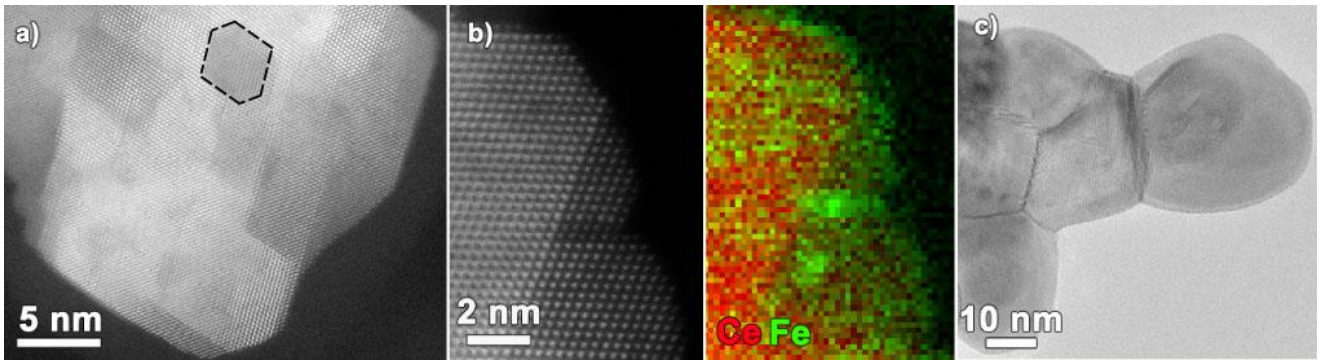

Figure 1. a) HAADF-STEM image of a ceria nanoparticle in the as-prepared 10wt.% Fe:ceria sample. Faceted voids are present (marked with dashed lines) inside the nanoparticle b) HAADF-STEM image together with EELS maps for Ce and Fe acquired for the as-prepared 10wt% Fe:ceria sample. Iron is enriched the surface of the ceria nanoparticles c) TEM-overview image of the 5wt% Fe:ceria sample after cycling. Sintering occurs with formation of grain boundaries between the particles.

Nanoparticles, Nanostructured Materials, Catalysts

MS6.P136
Metastability of the atomic structures of size-selected gold nanoparticles

D. Wells[1], G. Rossi[2], R. Ferrando[2], R. Palmer[1]

[1]University of Birmingham, NPRL, Department of Physics and Astronomy, Birmingham, United Kingdom
[2]INFM and IMEM/CNR, Dipartimento di Fisica dell'Università di Genova, Genova, Italy

dxw326@bham.ac.uk

Here we employ aberration-corrected electron microscopy and atomistic computer simulations to demonstrate the hierarchy of metastability in deposited, size-selected gold nanoparticles (clusters), an archetypal class of nanomaterials well known for the catalytic activity which only appears on the nanometer-scale. We show that the atomic structures presented by "magic number" Au_{561}, Au_{742} and Au_{923} clusters are "locked". They are in fact determined by the solidification which occurs from the liquid state early in their growth (by assembly from atoms in the gas phase) followed by template growth. It is quite likely that transitions from a locked, metastable configuration to a more stable (but still metastable) structure, as observed here under the electron beam, will occur during catalytic reactions, for example. [1]

More specifically, a magnetron sputtering, gas aggregation cluster source with lateral time-of-flight mass filter was used for production of the size-selected gold clusters. The nanoclusters were imaged using HAADF STEM and atomic structures identified by the simulation 'atlas' method [2]. In addition to this, stability of the clusters' atomic structure was assessed by video imaging during continuous irradiation with the STEM electron beam, and observation of the resulting structural transformations. These experiments showed that the most abundant decahedral structures transform into fcc structures; the decahedron is metastable with respect to fcc. An example of such a structural transformation is shown in figure 1. These results support the idea of template growth and show that even under slow growth formation conditions the proportion of structural isomers observed is not representative of the ground state, equilibrium structure. [1]

1. Wells, D., Rossi, G., Ferrando, R. and Palmer, R. E. Metastability of the atomic structures of size-selected gold nanoparticles. Nanoscale (2015) Advance Article.
2. Wang, Z. W. and Palmer, R. E. Determination of the ground-state atomic structures of size-selected Au nanoclusters by electron-beam-induced transformation. *Phys. Rev. Lett.* **108**, (2012).

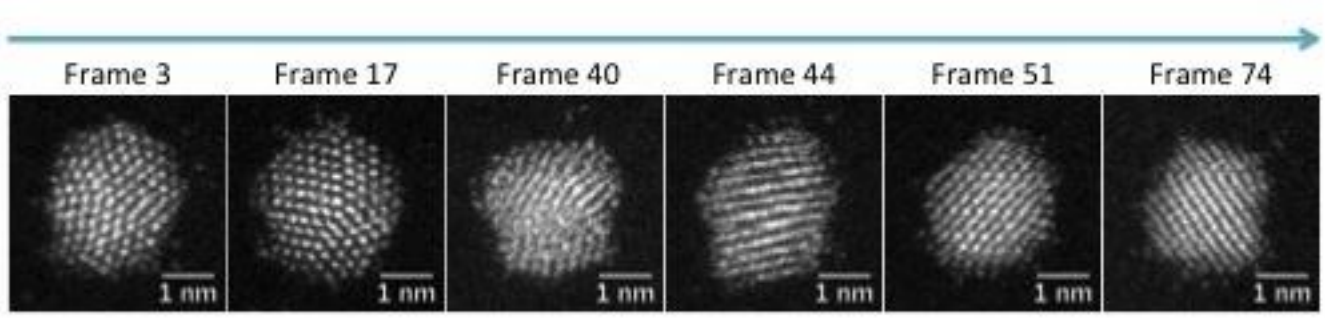

Figure 1. Structural transformation, from decahedron to fcc, of an Au_{561} cluster under continuous irradiation with the STEM electron-beam.

Nanoparticles, Nanostructured Materials, Catalysts

MS6.P137
Electron microscopy and spectroscopic studies of arbitrary shaped si nanocrystals decorated on vertical Si nanowires array

R. Ghosh[1], P. K. Giri[1]

[1]Indian Institute of Technology Guwahati, Department of Physics, Guwahati, India

g.ramesh@iitg.ernet.in

Large area, vertically aligned Si nanowires (NWs) grown by metal assisted chemical etching (MACE) have been attracting great deal of research interest due to their unique optical properties and wide range of applications in nanotechnology. During MACE process, self-grown Si nanocrystals (NCs) of different shapes and sizes are usually formed on Si NWs due to the side wall etching of Si NWs that results in porous like Si NWs. These Si NCs decorated Si NWs exhibit significantly different optical characteristics over the bulk Si including Raman shift, visible to near infra-red (NIR) photoluminescence (PL), ultralow reflectance and photocatalytic properties and these are being exploited in variety of applications, e.g., light emitting diodes, sensors, photocatalytic water splitting, high efficiency photovoltaic cells and other photonic devices.

We report on the fabrication of highly ordered arrays of micron-long Si NWs with diameter in the range 20-400 nm by MACE (Ag assisted) from single crystalline Si wafers at room temperature under different etching conditions and these NWs are covered with arbitrary shaped self-grown Si NCs due to the side wall etching. The formation mechanism and morphology of the Si NWs/ NCs are examined by using several microscopic techniques, e.g., atomic force microscopy (AFM), field emission scanning electron microscopy (FESEM) and high resolution transmission electron microscopy (HRTEM) (see Fig. 1). The vertical Si NWs decorated with ultrasmall Si NCs show tunable visible PL at room temperature (see Fig. 2). The light emission properties of these nanostructures are explained using quantum confinement effect in Si NCs. We observe a downshift and an asymmetric broadening of the first-order phonon mode in the Si NWs/NCs (see Fig. 2) and through quantitative analysis, the phonon confinement effect in the Si NCs is shown to be responsible for the observed downshift and asymmetric broadening. The Si NWs/NCs show ultralow reflectance in entire visible range and enhanced photocatalytic activity as compared to the bulk Si (see Fig. 3). This study demonstrates the efficacy of combined high resolution microscopy and spectroscopic tools to understand the unusual optical characteristics of the Si NCs/NWs. Since the fabrication process adopted here is very simple and robust, and the crystalline quality of the Si NWs and Si NCs is superior, it can be easily integrated into advanced optoelectronics and photonic devices for improved device performance.

1. Ramesh Ghosh, P. K. Giri, Kenji Imakita, and Minoru Fujii, ***Nanotechnology*** 25 (4), 045703 (2014).
2. Ramesh Ghosh, P. K. Giri, Kenji Imakita, and Minoru Fujii, ***J. Alloys Comp.*** *pp. 419-428* (2015), (Accepted, In Press).
3. Ramesh Ghosh, Arindam Pal, P. K. Giri, ***J. Raman Spectro.*** (2015), (Accepted).

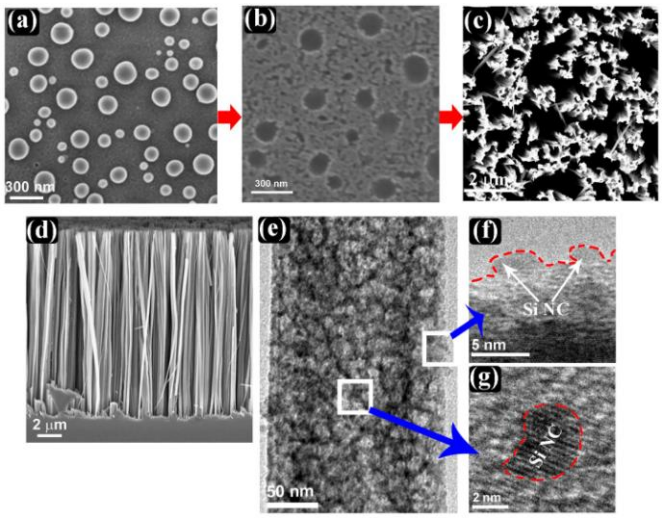

Figure 1. FESEM image of: (a) Ag nanoparticles (NPs) on the surface of the Si(100). (b) Initial stage of etching (after 30 sec) of Si wafer in HF and H_2O_2 solution. (c) Si NWs grown after 60 min etch of the Si wafer while (d) the corresponding FESEM cross-sectional image. (e) TEM image of an individual Si NW. (f) A magnified view of the Si NW and it is clear that the surface of the Si NWs is rough due to the presence of the arbitrary shaped Si NCs originating from the side wall etching of the NWs. (g) The HRTEM lattice image of a single Si NC and its shape is marked by dashed line.

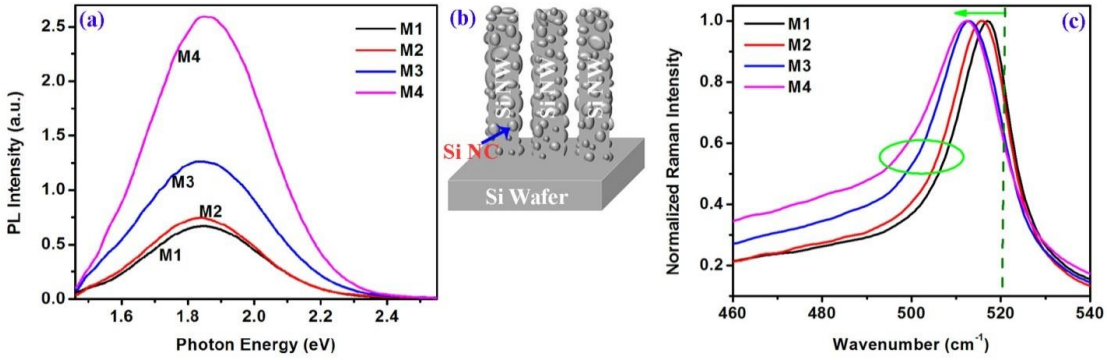

Figure 2. (a) PL spectra of different Si NW/NCs samples grown by the MACE (Ag assisted) in HF and H_2O_2 solution at room temperature for different time: 5 min (M1); 10 min (M2); 15 min (M3); 20 min (M4). (b) Schematic diagram of the Si NCs decorated Si NWs. (c) Comparison of the 1st order Raman spectra of different Si NCs/NWs samples. The arrow indicates the redshift and oval mark indicates the lower wavenumber asymmetry as compared to the bulk Si spectrum.

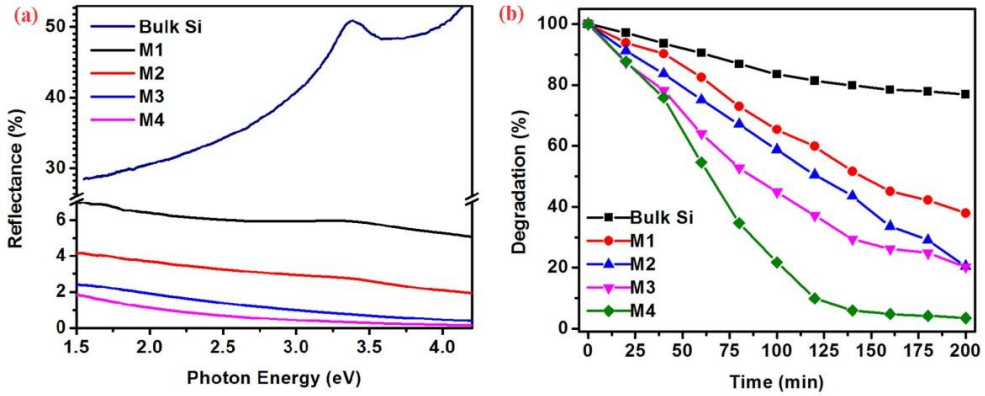

Figure 3. (a) Comparison of the reflectivity spectra of the Si NWs/NCs with that of the bulk Si. (b) Comparison of the photocatalytic degradation of Methylene Blue for different Si NCs/NWs samples as a function of time under visible light illumination.

Nanoparticles, Nanostructured Materials, Catalysts

MS6.P138
Electron microscopy study of aluminum nanoparticles with customized coatings manufactured via the flow-levitation method

A. Zhigach[1], I. Leipunsky[1], N. Berezkina[1], M. Kuskov[1], E. Afanasenkova[1], B. Kudrov[1], G. F. Lopez[2], O. Zhigalina[3]

[1]V.L. Talrose Institute for Energy Problems of Chemical Physics RAS, Moscow, Russian Federation
[2]Northeastern University, College of Professional Studies, Boston, Massachusetts, United States
[3]Shubnikov Institute for Crystallography RAS, Moscow, Russian Federation

yyleibe@gmail.com

The two most important challenges encountered during manufacturing of aluminum-metal nano-powders (Al NPs) are: (1) agglomeration susceptibility of the nanoparticles, and (2) high surface chemical activity which results on undesirable pyrophoric effects and adsorption of environmental species. These difficulties are effectively overcome through deposition of suitable nano-scaled chemical coatings on the surface of the aluminum nanoparticles before metal-to-metal bonds between them are formed during the synthesis process.

This research presents a detailed microscopic study and characterization of inorganic and organic coatings deposited on Al NPs manufactured via the Flow-Levitation (FL) method [1]. The FL-method is a versatile technique that allows concurrent in-situ deposition of customized coatings during the manufacturing of the metal nano-particles [2]. Distinctive features of this innovative technique are explained, in conjunction with concomitant processes to deposit the specialized coatings on the surface of the Al NPs.

Peculiar nanoparticle morphologies observed via scanning and transmission electron microscopy for different types of coating are depicted and scrutinized. The study focuses primarily on Al NPs with oxide, nitride, oxy-nitride, organic, silicon- and fluorine-organic coatings. Coating depositions for this study were performed via chemical reaction with oxygen gas, gaseous dry ammonia, and substances such as carbonic acids, perfluoroacetic acid, hexamethyldisilazane (Table 1). Coating thicknesses studied ranged from less than 1nm to more than 20 nm depending on the treatment parameters.

In addition to the electron microscopy techniques, characterization of the particles was performed via X-Ray energy-dispersion spectroscopy, X-Ray photoelectron spectroscopy and X-Ray diffraction analysis.

Analyses and characterization using transmission electron microscopy (TEM), high resolution TEM (HRTEM), scanning electron microscopy (SEM), and electron diffraction (ED) reveal that in all cases, the coated Al NPs present a clear “core-shell” structure with anearly-spherical metal core.

A few typical examples are shown in the figures below. Figure 1A illustrates the core-shell structure of Al NPs coated with a very dense and thin oxide film of essentially constant thickness. Figure 1B illustrates Al NPs with an organic coating showing an*inner* thin oxide layer of constant thickness, and the *outer* organic thick layer of variable thickness which in some places may be comparable to the diameter of the base metal nanoparticle.Figure 1C is an SEM image of Al NPs with a relatively thick aluminum oxide coating which typically show a well-developed“brain-like”surface relief consisting mainly ofirregular folds. Figure 1D illustrates an ED pattern of a multitude of Al NPs showing presence of metal (core) and oxide (shell).

Applicability of customized coated Al NPs is extensive in a wide variety of technical applications. The AL NPs subject of this study for example, were successfully used as fillers in high energy containing materials [3] and UHMW polyethylene-based heat conducting dielectrics [4].

1.A.N. Jigatch, M.L. Kuskov, I.O. Leipunskyet al. Synthesis of ultrafine metals, alloys and metal compounds via Guen-Miller method: history, state-of-the-art, prospects// Nanotechnologies in Russia, 2012, v. 7, № 3-4,28-37, Russian edition only.
2.A.N. Jigatch, I.O.Leipunsky, M.L. Kuskov et al. Synthesis of coatings on ultra-fine aluminum particles surface // Khimicheskaya Fizika (in Russian), 2002, v. 21, №4, pp. 72-78.
3. A. N. Zhigach,I.O. Leipunskii,N. G. Berezkina et al.Aluminized Nitramine-Based Nanocomposites: Manufacturing Technique and Structure Study // *Combustion, Explosion, and Shock Waves, Vol. 45, No. 6, pp. 666-677, 2009*
4. A. N. Zhigach, N. G. Berezkina, I. O. Leipunskii et al. Production of Nanosized Aluminum Powders and Their Application as Fillers for Composite Materials Based on Ultrahigh Molecular Polyethylene (UHMPE) // *Bulletin of the Russian Academy of Sciences. Physics, 2011, Vol. 75, No. 11, pp. 1488-1494*

Table 1. Typical coatings on Al nanoparticles.

Reactant	Coating composition
Dry oxygen O_2	Al oxide: "thin" (Fig. 1A) or "thick" (Fig. 1C)
Ammonia NH_3	Al (oxy)nitride
Acrylic acid CH_2=CH-COOH	Poly-acrylic
Tri-fluorine-acetic acid CF_3COOH	Fluorine-organic
Hexamethyldisilazane $(CH3)_3$-Si-NH-Si-$(CH_3)_3$.	Trimethyl-siloxane

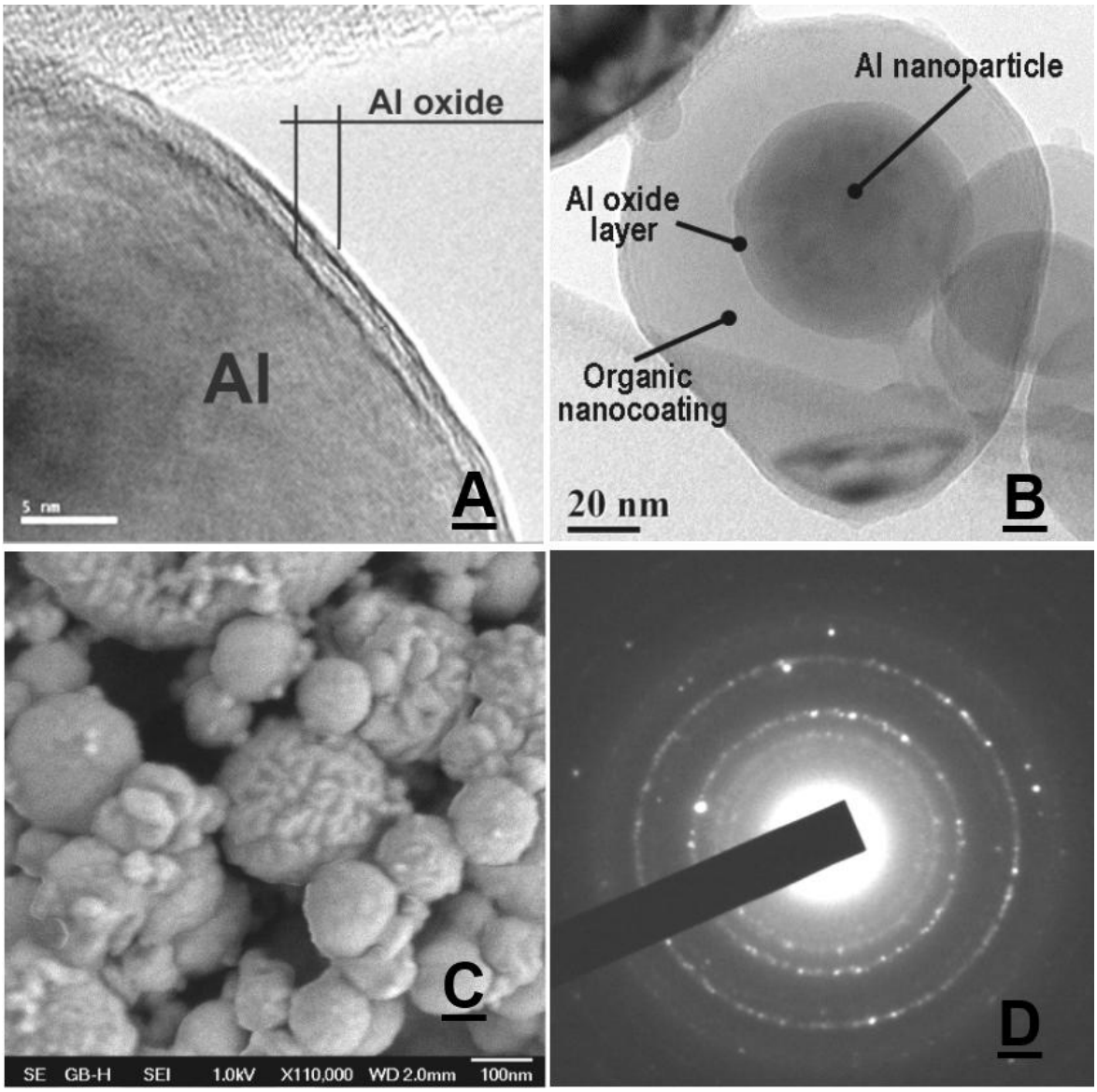

Figure 2. Aluminum nano-particles study: TEM images of the particles with "thin" aluminum oxide coating (A) and binary aluminium oxide – organic coating (B); SEM image of aluminum nanoparticles with "thick" aluminum oxide coating (C) and electron diffraction pattern of a multitude of such nanoparticles (D).

Nanoparticles, Nanostructured Materials, Catalysts

MS6.P139
Concurrent ordering and phase transformation in nanocrystalline $SmCo_7$

M. Seyring[1], X. Song[2], M. Rettenmayr[1]

[1]Friedrich Schiller University, Metallic Materials, Jena, Germany
[2]Beijing UT, Beijing, China

martin.seyring@uni-jena.de

Sm-Co alloys containing stabilized $SmCo_7$ phase possess a great potential for serving as advanced high temperature permanent magnets [1,2]. In the binary system, $SmCo_7$ is metastable and decomposes into the equilibrium phases Sm_2Co_{17} and $SmCo_5$, where the transition to Sm_2Co_{17} is an order-disorder transformation [3]. The order/disorder is attributed to the degree of the periodic arrangement of the Co pairs (dumbbells) in the lattice.

Stabilization of the binary $SmCo_7$ phase can be accomplished by nanostructuring [4]. In nanocrystalline $SmCo_7$ the complex concurrent processes of ordering and phase transformation are for the first time characterized on the atomic scale. The ordering transformation starts during annealing at 600°C for 30min and is fully accomplished after annealing at 700°C for 30min [5]. Crystallographic analysis of single nanograins by high-resolution transmission electron microscopy (HRTEM) and nanobeam electron diffraction (NBED) shows that when the metastable $SmCo_7$ (1:7) decomposes, the hexagonal Sm_2Co_{17} superstructure (2:17H) forms at first as precursor of the rhombohedral Sm_2Co_{17} superstructure (2:17R). For the ordering process, the evolution of the atom arrangement in the crystal structures is demonstrated by HRTEM in comparison with the projected crystal structure and the change in the corresponding Fourier diffractograms (Fig.1). Early stages of the phase transformation are visualized by highlighting specific superstructure domains in single nanograins using Fourier reconstruction of HRTEM images (Fig.2). From these reconstructions the fractions of the 2:17H and 2:17R superstructure phases were quantified for individual nanograins. A distinct correlation between the fraction of the superstructure phases and the grain size is found, showing unambiguously the grain size dependence of the phase transformation in the nanocrystalline alloy according to thermodynamic calculations [6].

The identified mechanism shows the grain size dependence of the concurrent ordering and phase transformation of 1:7 ® 2:17H ® 2:17R. The concept of a critical grain size for the phase transformation is experimentally confirmed with our high resolution study, and our findings facilitate the structural control of nanocrystalline materials.

1. Buschow, K. H. J. *Reports on Progress in Physics* 1991, *54*, 1123-1213.
2. Al-Omari, I. A.;Yeshurun, Y.;Zhou, J.; Sellmyer, D. J. *Journal of Applied Physics* 2000, *87*, 6710-6712.
3. Zhang, Z. D.;Liu, W.;Liu, J. P.; Sellmyer, D. J *Journal of Physics D-Applied Physics* 2000, *33*, R217-R246.
4. Zhang, Z. X.;Song, X. Y.;Xu, W. W.;Seyring, M.; Rettenmayr, M. *Scr. Mater*. 2010, 62, 594-597.
5. Zhang, Z. X.;Song, X. Y.; Xu, W. W. *Acta Mater.* 2011, *59*, 1808-1817.
6. Xu, W. W.;Song, X. Y.; Zhang, Z. X. *Appl. Phys. Lett.* 2010, *97*, 3.

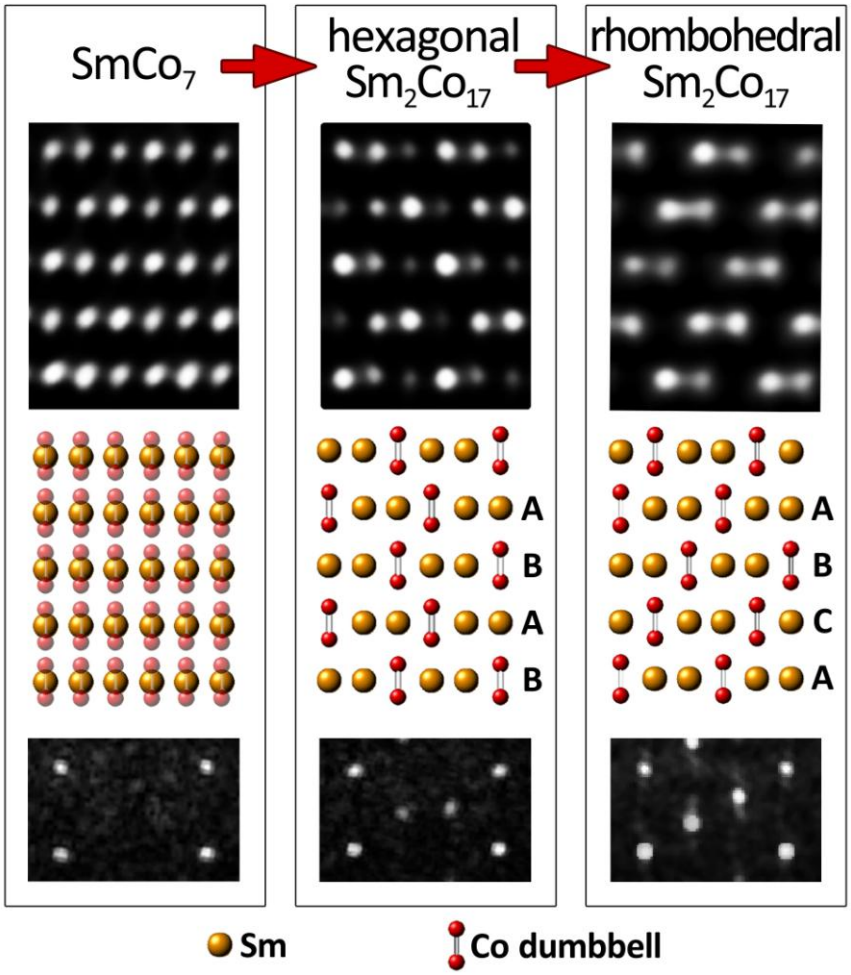

Figure 1: Evolution of the atomic arrangement during the concurrent ordering and phase transformation: representative HRTEM images (top), corresponding projected crystal structures (center) and Fourier diffractograms (bottom) for the disordered 1:7 phase as well as the 2:17H and 2:17R superstructure phases, respectively. A, B and C indicate the stacking sequence of atomic layers.

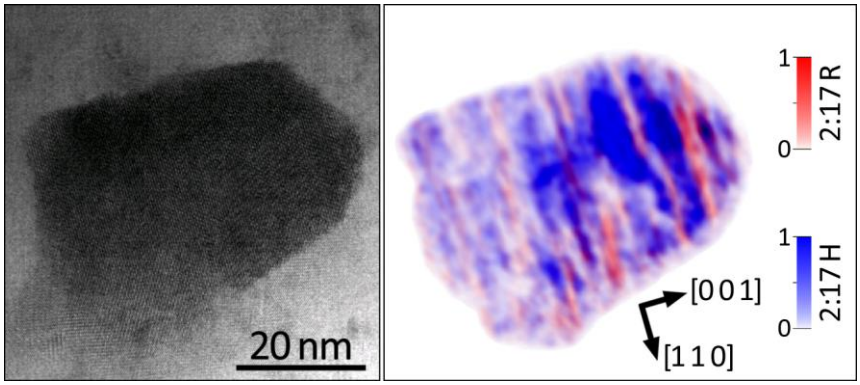

Figur.2. Highlighted superstructure domains in a nanograin with an area equivalent diameter of 49nm. The amplitude image visualizing the 2:17H and 2:17R domains (right) is generated by Fourier reconstruction of the corresponding HRTEM image (left).

Nanoparticles, Nanostructured Materials, Catalysts

MS6.P140
Segregation phenomena in rare-earth transition-metal nanoparticles

F. Schmidt[1], D. Pohl[1], L. Schultz[1], B. Rellinghaus[1]

[1]Leibniz Institute for Solid State and Materials Research, Dresden, Germany

f.schmidt@ifw-dresden.de

Rare earth transition metal (RE-TM) alloys, in particular $Nd_2Fe_{14}B$ and $SmCo_5$, are among the magnets that provide highest energy products and coercive fields and are therefore widely used as hard magnetic material in a large variety of applications [1,2]. Usually, these applications require macroscopic quantities and sizes, e.g., for stator/rotor magnets in electric motors and generators. Accordingly, there is a steady demand to enhance the magnetic properties of these hard magnets - a goal which is typically pursued by optimizing the grain boundary phases that effectively control the inter-granular coupling. These grain boundary phases in turn form through segregation from the individual grains.

The present study aims at investigating segregation phenomena in RE-TM nanoparticles which may easily serve as model materials for the grains in a bulk hard magnet. Particular attention is paid to the chemical (de-)composition and on the structure in the near-surface and near-interface areas in such particles.

Nd-Fe-B and Sm-Co nanoparticles were prepared by inert gas condensation in a commercially available nanoparticle deposition system (*Nanodep 60, Oxford Applied Research, OAR*). Prior to their deposition on an amorphous carbon film, the particles can be optically annealed in flight. This in-flight annealing is realized by means of a light furnace [3]. After their deposition, the particles are covered with a thin carbon layer using RF sputtering in order to suppress the oxidation of the particles. Structural and chemical characterization of the nanoparticles was conducted by aberration-corrected high resolution (scanning) transmission electron microscopy (HR-TEM, HR-STEM) using a *FEI Titan^3 80-300* microscope equipped with a C_S image corrector, energy dispersive x-ray spectrometry (EDXS) and electron energy loss spectrometry (EELS), respectively. For optimal contrast transfer over a wide range of spatial frequencies, negative spherical aberration imaging (NCSI) was used in HR-TEM mode [4]. The chemical investigations at atomic scale were conducted by means of local EELS measurements in STEM mode.

The nanoparticle size of both species, Nd-Fe-B and Sm-Co, lies between 5 and 15 nm, and in their as-prepared (unheated) state, the particles have nearly spheroidal shapes. Such unheated particles are found to be mostly amorphous with - if it all - only small crystalline centers. Upon in-flight annealing, however, the particles start to (re-)crystallize. Chemical analyses (EDX, EELS) reveal a comparably high degree of oxidation for the unheated nanoparticles and a lower degree of oxidation for the heated particles. HRTEM and STEM-EELS investigations of the unheated and heated Nd-Fe-B (Sm-Co) nanoparticles reveal a segregation of Nd (Co) towards the particle surfaces in both cases, which is mainly attributed to the different surface energies of the RE and the TM elements [5]. However, the annealed particles show a more pronounced Nd (Co) segregation than the unheated ones. Fig. 1 (a) shows as an example a representative STEM image of an in-flight annealed Nd-Fe-B nanoparticle, where a Fe-rich part of the particle can be clearly distinguished from the a Nd-rich part due to the difference in Z-contrast. Further STEM EELS analyses reveal that B preferentially occurs in Fe-rich vicinities within the particles (cf. Fig. 1(b)).

It will be shown with the help of model calculations that the observed segregation is indeed to be ascribed to differences in the surface energies of the alloy constituents.

1. Coey, J. M. D., J. Alloys Compd., 326(1-2), 2-6, 2001.
2. Gutfleisch, O., J. Phys D: Appl. Phys., 33(17), R157-R172, 2000.
3. B. Rellinghaus et al, IEEE Transactions on Magnetics 42, 3048, 2006.
4. M. Lentzen et al, Ultramicroscopy 92, 233, 2002.
5. F. Schmidt et al, J. Nanopart. Res. (2015), in print.

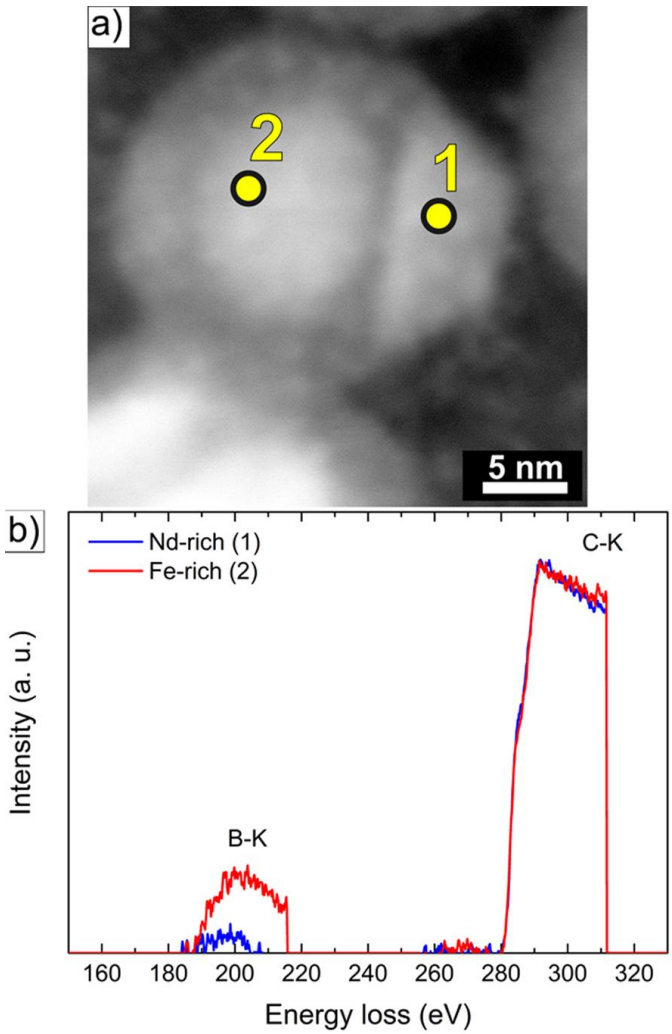

Figure 1. (a) HAADF STEM image of an optically annealed Nd-Fe-B nanoparticle that clearly reveals segregation. The two different parts of the nanoparticle can be clearly distinguished: On the right side (position 1), there is a Nd-rich part, and on the left side (position 2) the Fe-rich part as evidenced from local EELS measurements. (b) Normalized EEL spectra as obtained from positions 1 and 2. The B content is clearly higher in the Fe-rich part of the nanoparticle as compared to the Nd-rich part.

Nanoparticles, Nanostructured Materials, Catalysts

MS6.P141
Performance modification of granular FePt media by seed layer processing

S. Wicht[1,2], V. Neu[1], L. Schultz[1,3], O. Mosenz[4], V. Mehta[4], S. Jain[4], J. Reiner[4], O. Hellwig[4], D. Weller[4], B. Rellinghaus[1]

[1]Leibniz Institute for Solid State and Materials Research Dresden, Germany
[2]Technische Universität Dresden, IFWW, Dresden, Germany
[3]Technische Universität Dresden, Dresden, Germany
[4]HGST a Western Digital Company, San Jose, Germany

s.wicht@ifw-dresden.de

As a consequence of the continuously increasing amount of digitized information reliable high capacity data storage at ultimate densities is needed. At present, hard disk media with areal densities beyond 1TB/in² are envisioned. For this, granular films of $L1_0$-ordered FePt, grown on a highly textured MgO seed layer, are promising materials candidates due to their high magneto-crystalline anisotropy [1]. Here, the lattice mismatch between the MgO seed layer and the $L1_0$-FePt grains induces a preferred growth with the [001] magnetic easy axis perpendicular to the film plane. Nevertheless, the use of MgO provokes some drawbacks of which the relative misalignment between the local FePt grain relative to the underlying MgO seed crystal [2] is examined in this work. Therefore, Ar^+ ion irradiation of the MgO seed layer surface, prior to the deposition of FePt, is utilized to modify the FePt-MgO interface. The influence of this treatment on the structure and magnetic performance of the granular layer is investigated.

Atomic force microscopy (AFM), X-Ray diffraction (XRD) and aberration-corrected high-resolution transmission electron microscopy (HRTEM) in cross section and plan view geometries are used to explore the properties of the MgO seed layer, the granular FePt layer, and the interface between both. The results are then correlated with the magnetic properties as obtained from measurements using vibrating sample magnetometry (VSM) in fields of up to 14 T.

First AFM results of the uncovered MgO layers indicate a smoothening of the seed layer surfaces with enhanced irradiation times [3]. For the granular layers, this interface modulation results in an improved texture of the FePt grains as indicated by the increased FePt (001) and (002) Bragg peaks, at least for a moderate etching time of 4 s (Fig. 1). Further enhancing the Ar^+ ion irradiation, however, results in a decrease of these super structure peaks as well as the emergence of additional FePt (110) and (111) peaks. From HRTEM analysis in cross-sectional geometry (Fig. 2), it can be seen that this change in texture is accompanied by a modification of the grain morphology. Whereas for the untreated reference sample (a) mainly spheroidal grain morphologies occur, this changes to (b) columnar and (c) island-like shapes upon increasing the irradiation times to 4 s and 10 s, respectively. Furthermore, the amount of randomly oriented second layer particles as well as the degree of coalescence of primary deposited grains are enhanced.

The latter strongly affects the magnetic performance of the media which is observable in the magnetic measurements along the easy (EA, Fig. 3) and the hard axis (HA) direction of the granular films. For the EA curves the proceeding coalescence results in a reduction of the coercivity from 5.0 T to 2.6 T, since the grain boundary region forms the magnetic weakest part of the sintered particle which facilitates the magnetization reversal [4]. On the other hand, the contacts of regions with different easy axes orientations inside the sintered grains strongly degrades the magnetic texture of the film, which is observable by the enhanced HA remanence value.

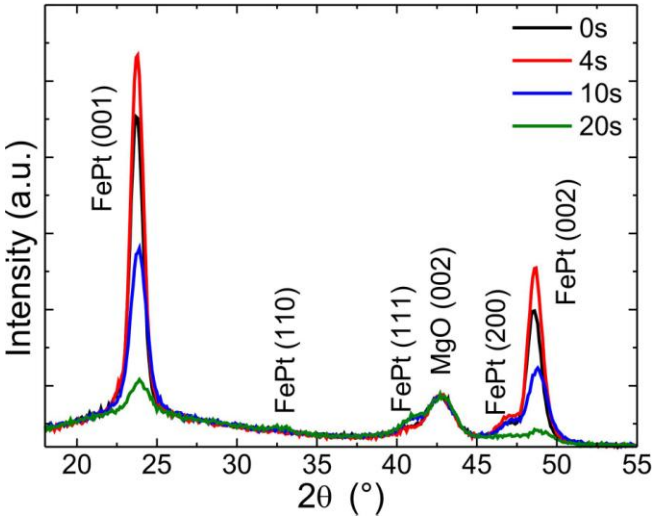

Figure 1. XRD patterns of four different granular FePt films grown on MgO seed layers that have been exposed to Ar^+ ion irradiation for 0, 4, 10 and 20 s, respectively.

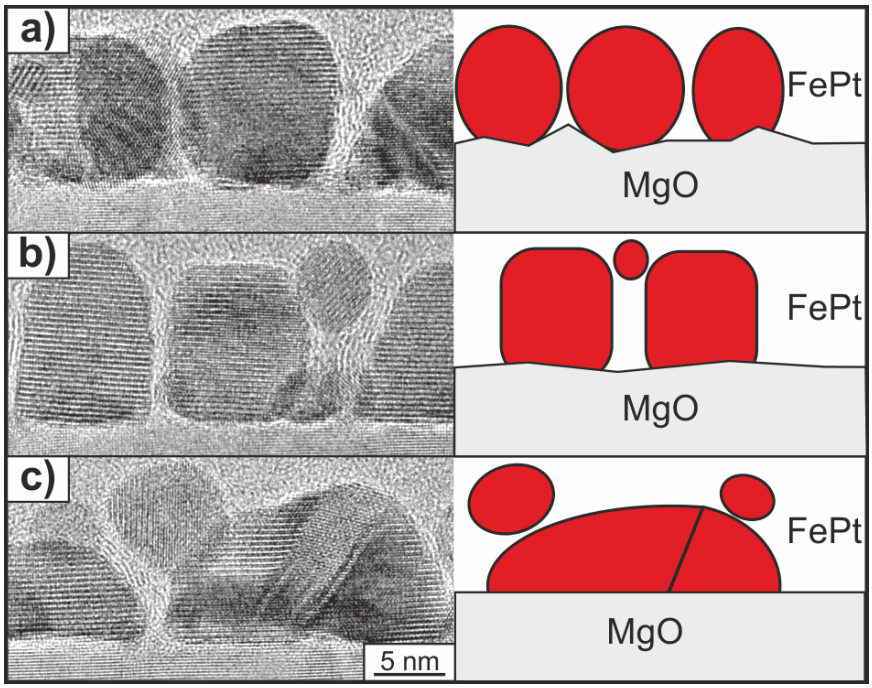

Figure 2. Cross-sectional HRTEM images of three granular FePt-C samples: a) reference sample without Ar^+ ion etching, b) after 4 s and c) after 10 s of irradiation. The schematic drawings on the right hand side illustrate the apparent changes in the particle morphology and structure.

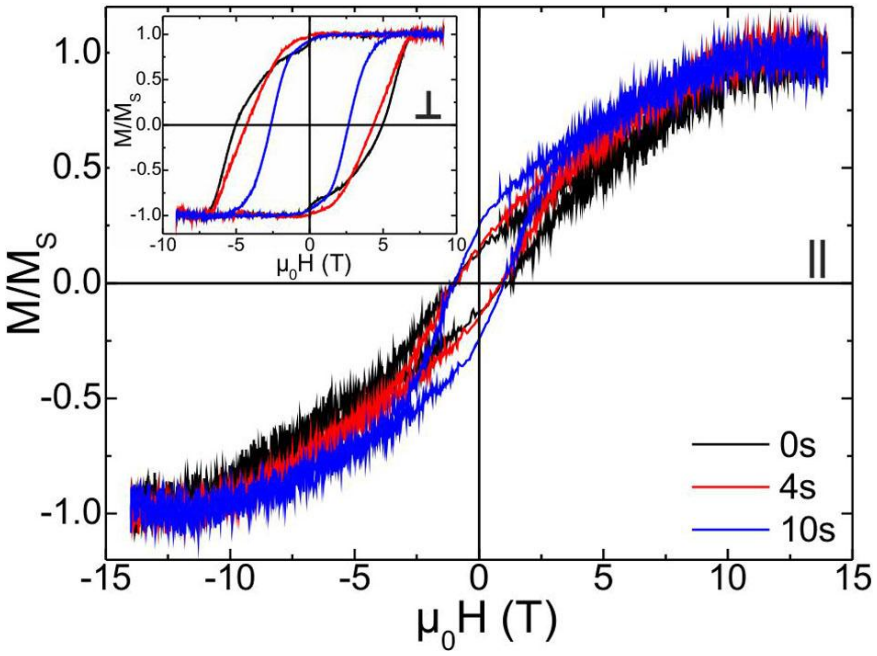

Figure 3. Hysteresis loops measured along the easy (out of plane, inlay) and a hard magnetic axis (in plane) of the granular film.

Nanoparticles, Nanostructured Materials, Catalysts

MS6.P142
Hybrid atomic structure of the Schmid cluster $Au_{55}(PPh_3)_{12}Cl_6$ resolved by aberration-corrected STEM

N. Jian[1], C. Stapelfeldt[2], M. Fröba[2], R. Palmer[1]

[1]University of Birmingham, School of Physics & Astronomy, Birmingham, United Kingdom
[2]University of Hamburg, Institute of Inorganic and Applied Chemistry, Department of Chemistry, Hamburg, Germany

nxj203@bham.ac.uk

The synthesis of the ligand-stabilized $Au_{55}(PPh_3)_{12}Cl_6$ cluster by Schmid and colleagues reported in 1981[1] was a significant event in the emergence of nanotechnology. Its unique size (1.4nm), stability and electronic properties drew a great deal of attention[2,3]. It was quickly seen as the basis of a future single electron transistor and potential building block of a nanostructured system[2-3]. However, the atomic structure of $Au_{55}(PPh_3)_{12}Cl_6$ has long remained a mystery, as the cluster resisted the crystallization which is needed to allow single-crystal X-ray diffraction analysis[4]. Here we report the atomic structure investigation of the $Au_{55}(PPh_3)_{12}Cl_6$ Schmid cluster with aberration-corrected scanning transmission electron microscopy (STEM) combined with multislice simulation of the STEM images.[5] Atom counting was employed, with size-selected clusters as mass standards, to "fractionate" the correct cluster size in the image analysis. Systematic structure analysis shows that a hybrid structure which includes both fcc and icosahedral features, predicted by density functional theory for bare Au_{55} clusters, best matches nearly half the clusters observed. Most other clusters are amorphous. Neither cuboctahedral and icosahedral structures were not found (contrary to previous assignments[6-8]), nor any Ino-decahedral structures. We believe our conclusions are consistent with all the previous, apparently contradictory structural studies of the Schmid cluster. The fusion of size-fractionation by the STEM mass balance method and atomic structure determination in the aberration-correction STEM is thus shown to be a powerful combination.

1. Schmid, G.; Pfeil, R.; Boese, R.; Bandermann, F.; Meyer, S.; Calis, G.; van der Velden. J. Chem. Ber. 1981, 114, 3634.
2. Schmid, G. *Chem. Soc. Rev.* **2008**, *37*, 1909-1930.
3. Chi, L.; Hartig, M.; Drechsler, T.; Schwaack, T.; Seidel, C.; Fuchs, H.; Schmid, G. *Appl. Phys. A Mater. Sci. Process.* **1998**, *190*, 187-190.
4. Pei, Y.; Shao, N.; Gao, Y.; Zeng, X. *ACS Nano* **2010**, *4*, 2009-2020.
5. N. Jian, C. Stapelfeldt, K.-J. Hu, M. Fröba, and R. E. Palmer, *Nanoscale*, 2014, **7**, 885-888.
6. Marcus, M.; Andrews, M. *Phys. Rev. B* **1990**, *42*, 3312-3316.
7. Benfield, R.; Grandjean, D. *J. Phys. Chem. B* **2001**, *105*, 1961-1970.
8. Vogel, W.; Rosner, B.; Tesche, B. *J. Phys. Chem.* **1993**, *97*, 11611-11616.
9. N. Jian, C. Stapelfeldt, K.-J. Hu, M. Fröba, and R. E. Palmer, *Nanoscale*, 2015, **7**, 885-888.

Nanoparticles, Nanostructured Materials, Catalysts

MS6.P143
Platinum doped cerium oxide layers on nitrogenated carbon: from primary microscopic study to fuel cell application

J. Lavkova[1,2], M. Dubau[2], V. Potin[3], I. Matolinova[2], V. Matolin[2]

[1]Universite de Bourgogne, Laboratoire Interdisciplinaire Carnot de Bourgogne, Dijon/France, Czech Republic
[2]Charles University, Department of Plasma and Surface Science, Prague, Czech Republic
[3]Universite de Bourgogne, Laboratoire Interdisciplinaire Carnot de Bourgogne, Dijon, France

jaroslava.lavkova@gmail.com

Platinum (Pt) is a versatile element in catalysis that efficiently mediates a multitude of chemical reactions. Unfortunately, Pt is a rare noble metal and its high price exceeding that of gold, limits large-scale applications. Therefore, not surprisingly, reducing amount of Pt is the major driving force in catalysis research. There are two strategies to tackle this challenge: to replace noble metal by others, less expensive materials; and to use platinum as efficiently as possible.

In this study, we handle both of them by growing extremely porous Pt-CeO_2 structures prepared by magnetron sputtering on amorphous carbon (a-C) and nitrogenated amorphous carbon films (CN_x) by carrying on our previous research[1]. The morphology and chemistry of the catalysts were locally investigated by using microscopy tools - the Scanning Electron Microscopy (SEM) and the Transmission Electron Microscopy (TEM) with associated techniques (EDX and EELS).

It is shown that the roughness of the layers is dependent on the deposition conditions, the amount of deposited material and the type of the carbon substrate. The change of these parameters results in growth of the mushroom-like (Fig. 1a) or noodle-like structures (Fig. 1b). By the optimization and the suitable combination of materials we can tune the morphology of the catalysts (Fig. 1c).

All structures are consisting of carbon base coated by crystalline cerium compounds doped by platinum. The crystallites of stoichiometric CeO_2 crystals were observed on the surface besides reduced Ce_2O_3 and Ce_7O_{12} close to the carbon substrate. Moreover, catalyst layer contains also CeC_2 particles and Pt-Ce alloys. With the higher content of Pt in the layer, the more metallic Pt crystals were found.

The results obtained by EELS spectroscopy are in agreement with crystallography. The cerium in state 3+ is occurring on the interface with carbon substrate and is continuously changing to Ce^{4+} in direction to the surface of the structure.

The knowledge of Pt-CeO_x growth on carbon substrates was applied to increase the porosity of commercial substrate used as GDL in fuel cells. The catalyst film was deposited on GDL with (Fig. 2b) and without (Fig. 2a) CN_x intermediate layer. The difference in structure and porosity is significant.

In our previous study was shown[2] that during magnetron sputtering of Pt-CeO_x layer the oxygen plasma forming in the chamber causes the etching of the carbon substrate. The different etching rate of a-C and CN_x[3] plays important role in the shape of the structure.

The extremely porous Pt-CeO_x structures prepared by magnetron sputtering on nitrogenated amorphous carbon are presented. By the suitable combination of deposition parameters and materials we are able to create promising constructions for fuel cell applications.

1. V. Matolin et. al, Langmuir 26, 12824-12831 (2010)
2. J. Lavkova et. al, Nanoscale 7, 4038-4047 (2015)
3. M. Dubau et. al, ACS Appl. Mater. Interfaces 6, 1213-1218 (2014)

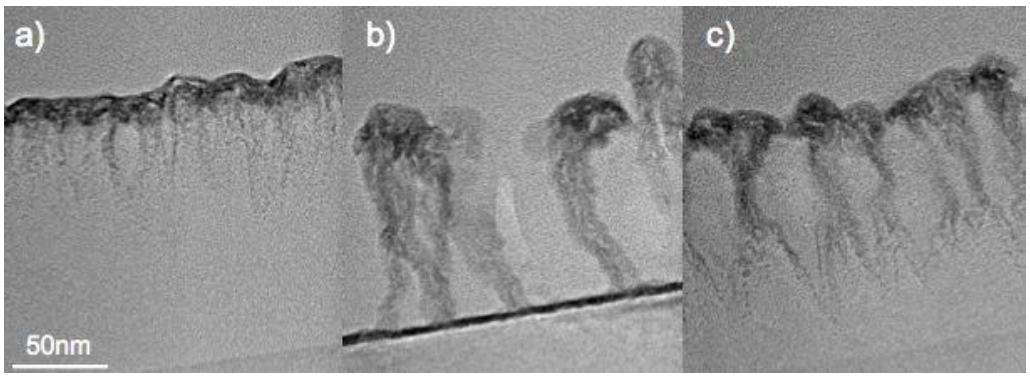

Figure 1. The Pt-CeO_x/a-C (a), Pt-CeO_x/CN_x (b) and Pt-CeO_x/CN_x/a-C (c) layers deposited on silicon.

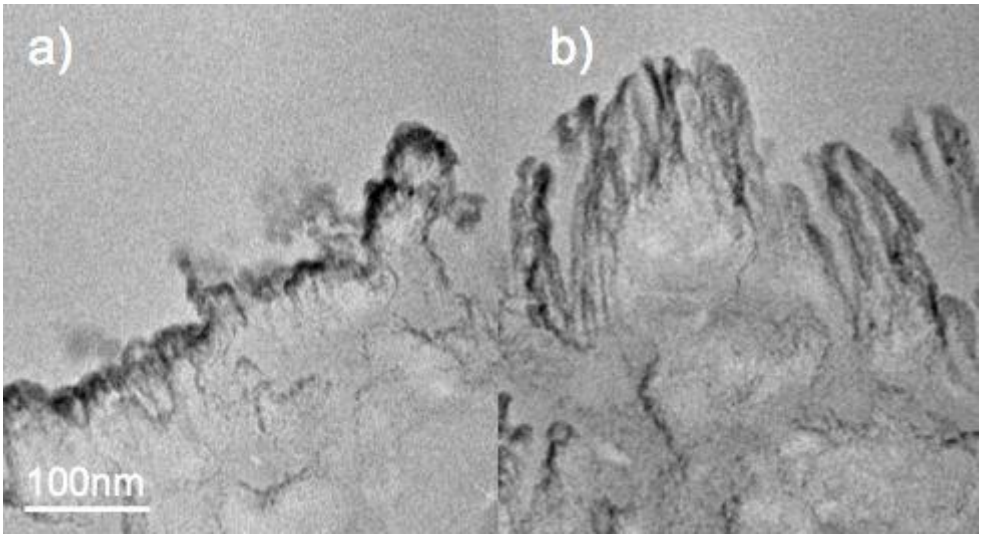

Figure 2. Pt-CeO_x/GDL (a) and Pt-CeO_x/CN_x/GDL (b).

Nanoparticles, Nanostructured Materials, Catalysts

MS6.P144
Structural and optical characterisation of h-BN layers

L. Schué[1,2], A. Pierret[1], F. Fossard[1], F. Ducastelle[1], J. Barjon[2], A. Loiseau[1]

[1]Laboratoire d'Etude des Microstructures, CNRS/ONERA, Chatillon, France
[2]GEMAC, Université de Versailles/CNRS, Versailles, France

frederic.fossard@onera.fr

Hexagonal boron nitride is a wide band gap semiconductor (~ 6.5 eV), which meets a growing interest for graphene engineering [1]. In particular electron mobility of graphene is shown to be preserved when graphene is supported by a h-BN film. We attempt to have a better comprehension of the optical and electronic properties of thin BN layers, in correlation with their structural properties and to better know how electronic properties of graphene can be impacted by underlying BN layers.

Until recently, these properties were poorly known due to both the scarcity of crystals and suitable investigation tools. This situation has changed thanks, first, to the development of dedicated cathodoluminescence (CL) experiments running at 5K and adapted to the detection in the far UV range [2] as displayed in figure 1, and second to the avaibility of high quality single crystals [3].

H-BN has been shown to display original optical properties, governed, in the energy range 5.2 - 6 eV, by strong Frenkel-type excitonic effects [2, 4]. In this work, we first investigate by CL the luminescence properties of hBN samples synthesized by three different processes (HPHT, PDCs and a commercial powder). We observe in CL spectra the same features of the S series, in the energy range 5.7 - 6 eV. This reveals the intrinsic origin of these excitonic recombinations unlike the D series previously attributed to excitons trapped on defects such as dislocations or grain boundaries and observed at lower energy (5.2 - 5.7 eV) [5].

Besides, thin hBN layers have been obtained by mechanical exfoliation from small crystallites of a commercial powder and single crystal. We performed CL measurements on several flakes with various thicknesses from 100L to 6L and observed a significant effect of the confinement on the luminescence of hBN, especially in the energy range 5.7 - 6 eV previously mentioned. Indeed, CL spectra exhibit S series with different features depending on the hBN thickness. This strongly suggests that this signal (S series) could arise from distinct contributions that we will discuss.

The research leading to these Framework Programme under grant agreement n°604391 Graphene Flagship results has received partial funding from the European Union Seventh

1. C.R. Dean et al. Nature Nanotechnology, 5, 722, (2010)
2. P. Jaffrennou el al., Phys. Rev. B, 77, 235422, (2008)
3. Y. Kubota et al., Science, 317, 932, (2007)
4. L. Museur et al., Phys. Stat. Sol. RRL, 5, 414, (2011)
5. A. Pierret et al., Phys. Rev. B, 89, 035214, (2014)

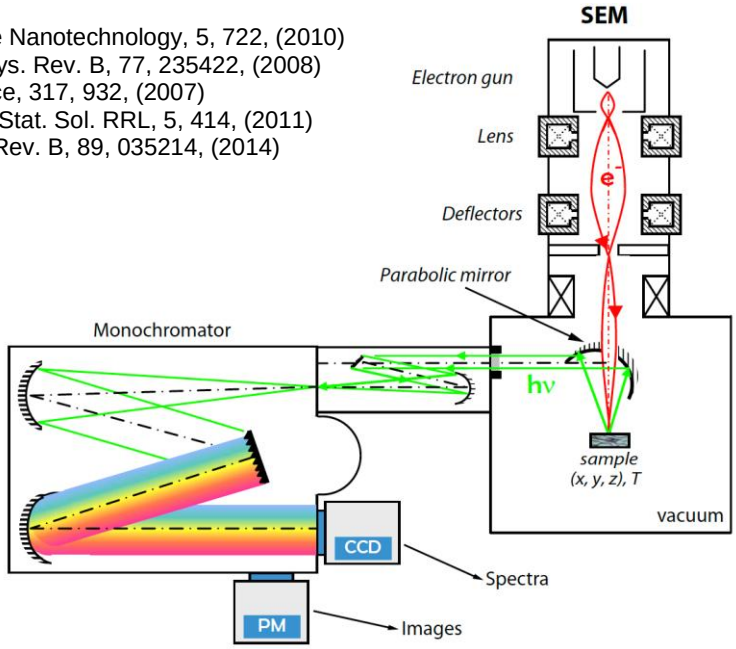

Nanoparticles, Nanostructured Materials, Catalysts

MS6.P145
Structure and chemistry of regular arrays of porous anodic aluminium oxide (AAO) and its thermal stability

M. Peterlechner[1], S. Ostendorp[1], G. Wilde[1]

[1]University of Muenster, Institut of Materials Physics, Muenster, Germany

martin.peterlechner@uni-muenster.de

Controlled anodisation of aluminium yields highly regular nano-pore structures, casually termed anodic aluminium oxide (AAO) membranes. AAO membranes can be utilised as templates to deposit a wide area of materials onto substrates as dots, wires or tubes. A recent review including a summary also of studies of the structure and chemistry of the pores and pore-walls is given in reference [1]. It was shown, that anions are incorporated in the AAOs and their distribution is not homogenous. The present study focuses on the analysis of AAOs made by three different electrolytes, with a particular focus on the chemistry and local structure, and their changes upon annealing.

Samples of AAO membranes with pore diameters of 40 to 200 nm were prepared in a two step anodisation procedure from high purity aluminium foils. Samples for transmission electron microscopy (TEM) were processed using an ultrasonic drill, dimpling and subsequently, ion-milling using a Gatan PIPS with acceleration voltages between 5 and 2 kV. A Zeiss Libra 200 FE with an in-column Omega filter was utilized to obtain conventional TEM and high-angle annular dark-field (HAADF) micrographs at 200 kV. A FEI Titan 80-300 was used to obtain nano-beam diffraction pattern (NBDP) and low-loss electron energy loss spectroscopy (EELS) data at 300 kV. Additionally, scanning electron microscopy (SEM) was carried out at 30 kV using thin TEM foils to test the influence of beam damage on the structure and to carry out energy dispersive X-ray (EDX) analysis. It should be noted, that charging effects of the insulating AAO structures could be strongly reduced by stacking the TEM samples between holey carbon grids.

Figure 1a shows a HAADF image, and 1b a diffraction pattern of an AAO membrane made in phosphoric acid. In the HAADF image pores are shown and the hexagonal pore wall structure is visible by bright contrast. A thickness variation induced by PIPS is visible in HAADF and detectable by EELS, running as stripes from top left to bottom right in Figure 1a. Some pore-walls run perpendicular to these PIPS stripes and show no detectable local thickness variation due to preferential edging. The chemical analysis shows a phosphorous depletion in the pore-wall, decreasing from 1.8 to 1.2 at.%. This is in agreement with only some previous works. Effects of beam damage and charging in spot mode and also in TEM mode are discussed. The HAADF Z-contrast of the pore-wall is increased, even though this region shows a depletion of the heavier element phosphorus (compared to Al and O). Line scans of NBDP show no evident indication for any structural difference between the pore and the pore-wall. Thus, the density difference between the pore and the pore-wall could be estimated and shows an increase of about 6 percent. Upon annealing at temperatures up to 900°C crystallisation occurs. The pore-walls crystallise at lower temperatures, followed by the pores. Figure 2 shows a diffraction pattern of an AAO made in phosphoric acid after annealing. Twelve aperture positions are indicated and their corresponding dark-field images show, that the pores are still amorphous while the pore-walls are crystallised. Thus, the slightly increased anion content of the pores thermally stabilised the AAO structure. Analogous findings are observed by beam induced crystallisation.

1. Lee, W. & Park, S. Porous anodic aluminum oxide: anodization and templated synthesis of functional nanostructures. Chem. Rev. (2014).
2. We kindly acknowledge the help of Di Wang and Christian Kübel at the Karlsruhe-Nano-Micro-Facility (KNMF) at KIT for help with the Titan experiments.

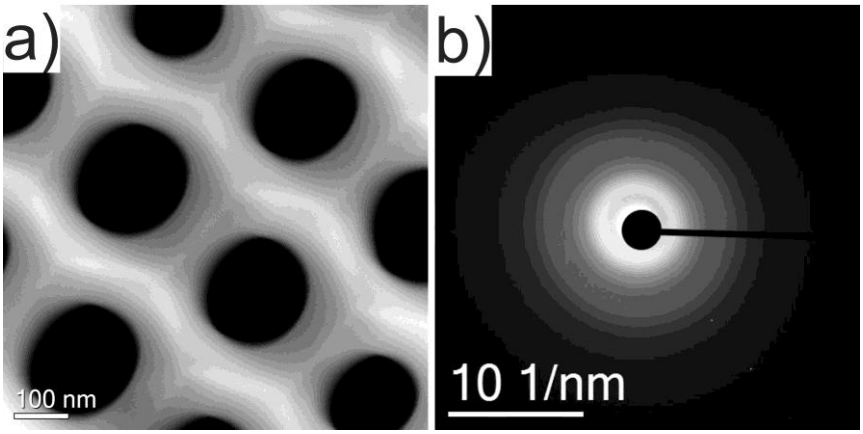

Figure 1. a) HAADF image of an AAO array (140 V, oxalic acid). **b)** The diffraction pattern shows a fully amorphous structure. In the HAADF image stripes arising by thickness variations induced by the PIPS sample preparation are visible. Pore-walls running perpendicular to the PIPS stripes show an increase in contrast arising due to a more dense structure.

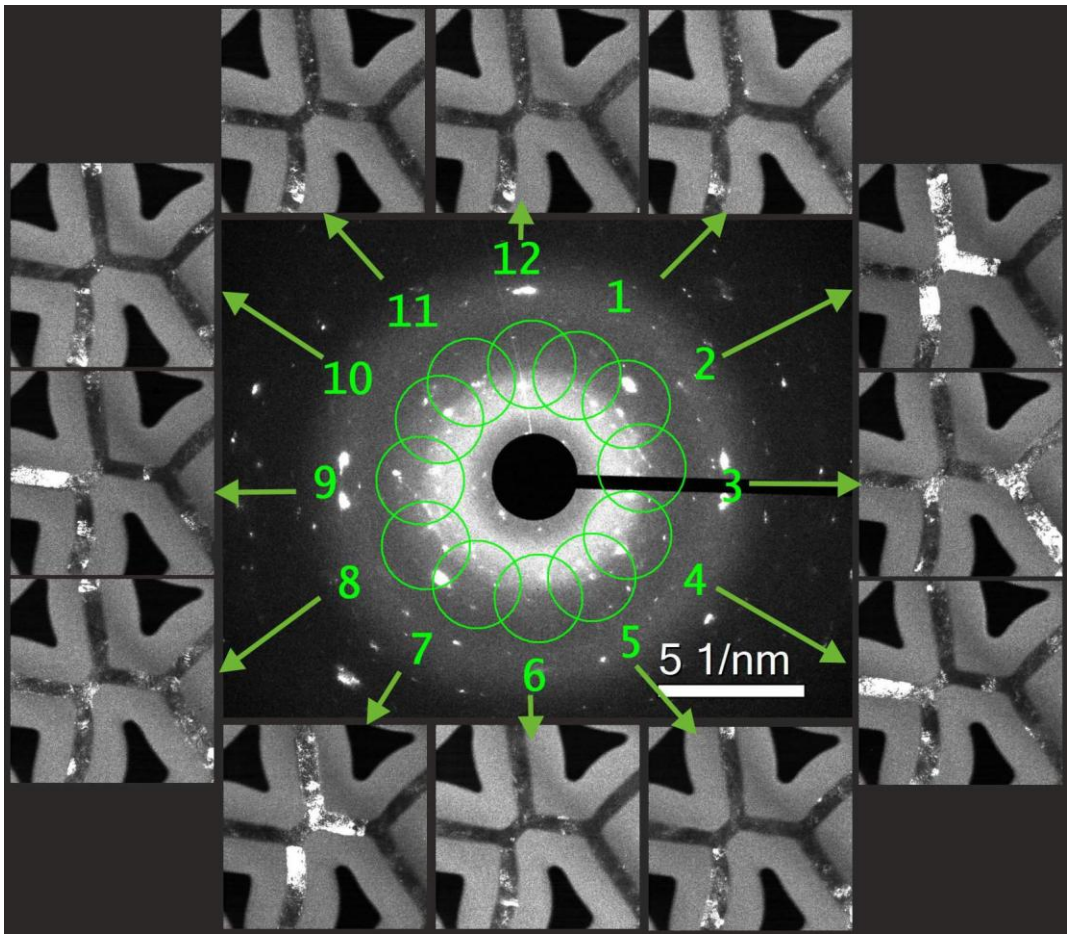

Figure 2. Energy filtered dark-field series of an annealed AAO (made in phosphoric acid, annealed at 900 °C, 3min, ~400 nm interpore distance). The used aperture positions are indicated and the corresponding dark-field images are shown. The pores are amorphous and the initially more dense pore-walls crystallised into elongated nanograins.

Nanoparticles, Nanostructured Materials, Catalysts

MS6.P146
Graphene research - a new era of microscopic methods for engineered graphene

S. Freitag[1]

[1]Carl Zeiss Microscopy GmbH, Munich, Germany

stefanie.freitag@zeiss.com

Graphene is two dimensional layer of carbon atoms and because of its high conductivity it has the potential to function as a conductor, a transistor, a quantum dot, a molecular switch or other devices. In the ability to transport heat, it outperforms all other known materials. Optically it is highly transparent but completely impermeable for any other atoms. That makes it promising for products LED´s and solar cells. Harder than steel and also showing a high elasticity, graphene unites several astonishing material properties. These are for example usable in ceramics and building material. Researcher where searching for more outstanding properties of graphene and doing research on the atomic scale for several years. Now a new era is coming up where researcher and companies are aiming for the final manufactured product.

Preparation methods, patterning procedures and interfacing methods were analyzed in this study.

Graphene was investigated after the preparation with a common adhesive tape and an uncleaned surface substrate and also with a special adhesive wafer foil and plasma cleaned Si substrate. The graphene flakes were analyzed with light microscopy (LM), electron microscopy (EM) and atomic force microscopy (AFM) by means of the correlative microscopy technique (CorrMic). In a second step it is investigated, how helium ion microscopy (HIM) is able to pattern graphene nano ribbons for band gap creation. For the third steps X-ray microscopy was used to analyze the final manufactured products.

The findings show that bright field microscopy can indicate the number of graphene layers and thickness if the graphene is on a thin optically resonant film [1,2,3]. There is a strong difference in contamination between the two preparation methods. Standard adhesive tapes leave residuals on the surface and the flake itself, which often are only resolved by high resolution microscopic techniques like SEM and especially AFM. Since a lot of investigation on graphene is only done by using optical microscopy, such contamination may cause false and/or misleading results.

In the SEM it was proven that the energy dispersive back scattered detector (EsB) allows to distinguish between single and multi-layer graphene [4]. By means of patterning and preparation of graphene nano ribbons with the helium ion microscope one can create bandgaps in graphene which are necessary for electrical devices. The investigations showed that the bandgap in a graphene ribbon increases as the ribbon width decreases [5].

Graphene quantum dots on the other hand can be imaged with cathodoluminescence (CL). The CL spectrum has its peak were the quantum dots change their shape from circular-to-polygonal-shape and their corresponding edge-state [6].

The STEM detector reveals structures of graphene that need more investigation to fully understand them. X-ray microscopy enables the analysis of for example ceramics, batteries and building material, so it allows the evaluation the final product that isn´t a 2D material anymore but has properties in 3D.

1. P. Blake *et al* , Appl. Phys. Lett. 91 (2007) 063124
2. Z. H. Ni *et al*, Nano Lett. 7 (2007) 2758
3. Y. Y. Wang *et al*, Nanotechnology 23 (2012) 495713
4. Iwona Joswik-Biala *et al*, Microsc. Microanal. 20 Suppl 3 (2014)
5. D.S. Pickard *et al*, Microscopy and Microanalysis 07/2012; 18(S2):800-801
6. Soo Seok Kang *et al*, Current Applied Physics 14 (2014) S111-S114

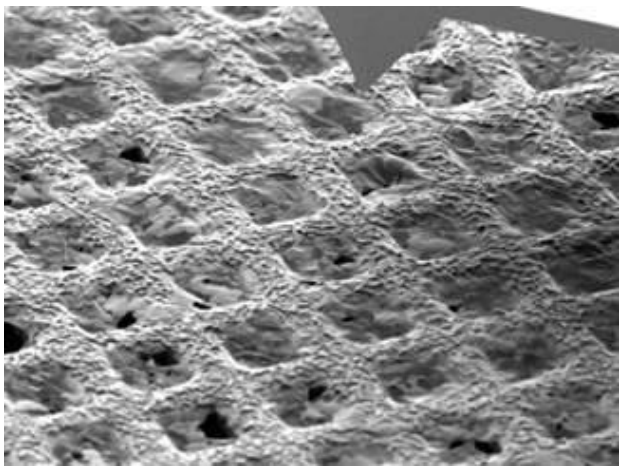

Figure 1. SEM with integrated AFM for hardness, stiffness, E modulus determination; Sample courtesy by Frank Hitzel, DME Nanotechnology GmbH, Braunschweig

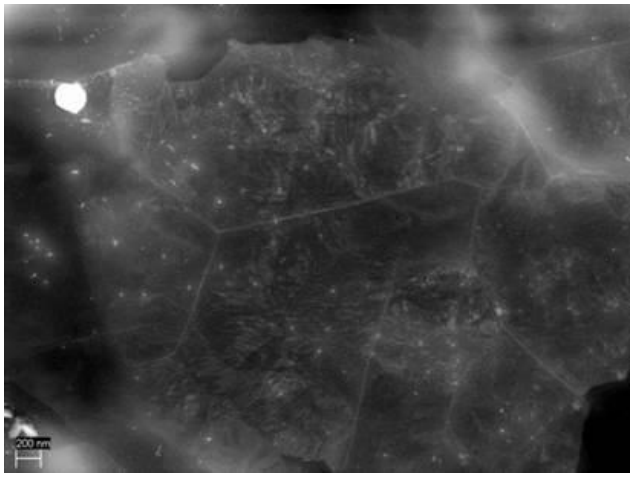

Figure 2. Graphene imaged in dark field mode with STEM detector; Sample courtesy by Kenneth Png, ZEISS Microscopy GmbH, Cambridge

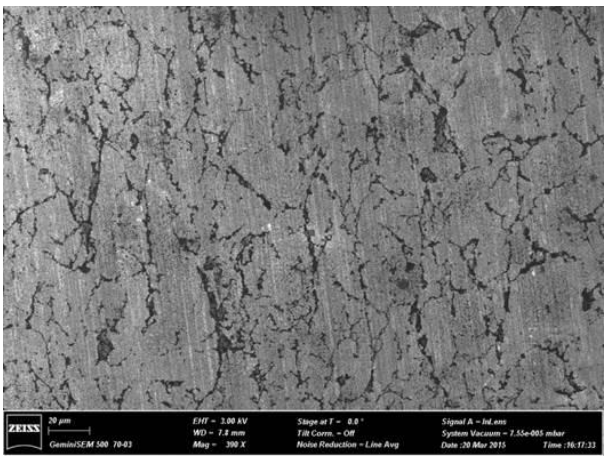

Figure 3. Imaging of Graphene on Sapphire for quality analysis of wrinkles in the layers; Sample courtesy by Markus Boese, ZEISS Microscopy GmbH, Oberkochen

Nanoparticles, Nanostructured Materials, Catalysts

MS6.P147
HAADF-STEM observation of nanoporous palladium-aluminium film fabricated by hot-water treatment

T. Harumoto[1], Y. Tamura[1], T. Ishiguro[1]

[1]Tokyo University of Science, Materials Science and Technology, Tokyo, Japan

taharumoto@rs.tus.ac.jp

Since nanoporous metals exhibit large surface-to-volume ratios, they have been applied to catalysts, sensors and fuel cell batteries. For analysing the morphology of such nanoporous metals, scanning electron microscopy (SEM) and transmission electron microscopy (TEM) are generally adopted. However, the resolution of SEM is insufficient in some cases and the diffraction contrast in TEM images brings difficulties to image analysis. Thus, an alternative observation method is required. In this study, high-angle annular dark-field scanning transmission electron microscopy (HAADF-STEM), which corresponds to Z-contrast, has been applied to nanoporous metal analysis.

Nanoporous palladium-aluminium film has been prepared from aluminium-palladium film using a hot-water-treatment.[1] In brief, aluminium-palladium film was sputter-deposited on substrate. After the deposition, the film was boiled in ultrapure water at 368 K for 110 minutes. It should be noted that since this method does not require strong acid or alkali, the nanoporous film was fabricated environmentally friendly as compared with the conventional dealloying methods.[2,3] HAADF images were acquired using STEM (HD-2300C; Hitachi High-technologies Co.) operated at 200 kV. The cross-sectional specimen was prepared using Ar ion milling.

Figure 1 shows cross-sectional bright-field (BF)-STEM and HAADF-STEM images of nanoporous palladium-aluminium film fabricated using the hot-water-treatment. It is clear from BF-STEM and HAADF-STEM images that the ligament/pore sizes of the nanoporous film were relatively small (~10 nm). However, the details nanoporous structure, such as a-few-nm pores, can be observed only on HAADF-STEM image. In addition, by comparison with BF-STEM image, HAADF-STEM image exhibits high contrast. This can be attributed to the characteristics of HAADF image, which relates to charge density and not to diffraction contrast.

In this study, nanoporous palladium-aluminium film has been fabricated by environmentally friendly method and observed using STEM. According to the comparison with BF-STEM image, HAADF-STEM image demonstrates enhanced contrast and is suitable for analysing nanoporous metals.

1. T. Harumoto, Y. Tamura and T. Ishiguro, “Ultrafine Nanoporous Palladium-Aluminum Film Fabricated by Citric Acid-Assisted Hot-Water-Treatment of Aluminum-Palladium Alloy Film”, AIP Advances, 5, pp.017146, 2015
2. W. C. Li and T. J. Balk, “Achieving Finer Pores and Ligaments in Nanoporous Palladium-Nickel Thin Films”, Scripta Mater., 62, pp.167-169, 2010
3. J. Schoop and T. J. Balk, “Engineering Defect-Free Nanoporous Pd from Optimized Pd-Ni Precursor Alloy by Understanding Palladium-Hydrogen Interactions During Dealloying”, Metall. Mater. Trans. A, 45A, pp2309-2314, 2014

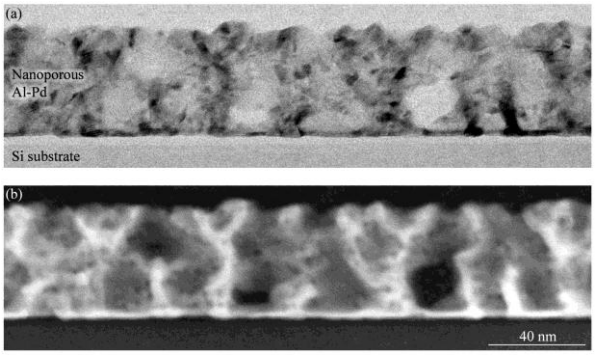

Figure 1. (a) BF-STEM and (b) corresponding HAADF-STEM images of the nanoprorous palladium-aluminum film fabricated by the hot-water treatment of aluminum-palladium film.

Nanoparticles, Nanostructured Materials, Catalysts

MS6.P148
Thermal behavior of carbon-coated lithium iron phosphate

F. Krumeich[1], O. Waser[2], S. Pratsinis[2]

[1]ETH Zürich, Laboratory of Inorganic Chemistry, Zürich, Switzerland
[2]ETH Zürich, Particle Technology Laboratory, Zürich, Switzerland

krumeich@inorg.chem.ethz.ch

$LiFePO_4$ is an attractive material for Li-ion battery applications as it shows high cycle stability and can be produced from low cost raw materials [1]. Unfortunately, the electric conductivity of $LiFePO_4$ is low and the diffusion of the Li ions along the one-dimensional channels of its olivine structure is slow. The diffusion limitation can be surmounted with smaller particle sizes while the conductivity can be increased either by doping or by embedding $LiFePO_4$ in a conductive matrix like carbon. A particularly promising approach is the generation of a core-shell structure in form of C-coated $LiFePO_4$ nanoparticles, in which carbon not only improves the conductivity between the electrochemically active particles but also protects the core from reacting with the electrolyte.

Carbon-coated $LiFePO_4$ nanoparticles were produced in an enclosed flame spray pyrolysis unit [2] and coated in-situ downstream by pyrolysis of C_2H_2 in an O_2-controlled atmosphere [3]. The thermal stability of this material was recently probed in ex-situ experiments [3]. After annealing in Ar/H_2 atmosphere at 700 °C for 4 h, the morphology and particle size are preserved while the same treatment at 800 °C leads to fusion of the core $LiFePO_4$ into larger particles being $LiFePO_4$ crystals according to XRD results. The carbon shells remain as empty spheres according toTEM [3]. To study this process in more detail, in-situ TEM was carried out now with a heating holder [4].

The TEM image of a large area recorded at RT (Figure 1a) shows $LiFePO_4$ nanoparticles with a diameter of ca. 10-60 nm, coated with carbon shells of a few nm thickness. Additionally, segregated carbon is visible between these core-shell particles, certainly further improving the electric conductivity of this composite. After heating the specimen in-situ up to 800 °C, TEM of the same area reveals drastic changes (Figure 1b). Most $LiFePO_4$ diffused out of the carbon shells sintering to larger particles of several 100 nm in diameter while leaving behind empty carbon spheres (Figures 1b and 2e,f). The investigation of selected areas at intermediate temperature stages reveals that most of these morphology changes occur only at temperatures above 700 °C (Figure 2). In particular, sintering of the $LiFePO_4$ particles is observed above 750 °C. In addition, crystallization of the core particles occurs around 400 °C as evidenced by electron diffraction and in accordance with in-situ X-ray powder diffraction results. [5]

1. C. H. Mi et al., J. Electrochem. Soc. **152** (2005) p. A483.
2. A. Teleki et al., Sens. Actuators B **119** (2006) p. 683.
3. O. Waser *et al.*, J. Aerosol Sci. **42** (2011) p. 657.
4. TEM investigations were performed at a Tecnai F30 (FEI) microscope operated at 300 kV using a Gatan 628 heating holder.
5. We thank the Scientific Center for Optical and Electron Microscopy of ETH Zurich (ScopeM) for support and M. Cantoni (CIME, EPFL Lausanne) for lending us the heating holder.

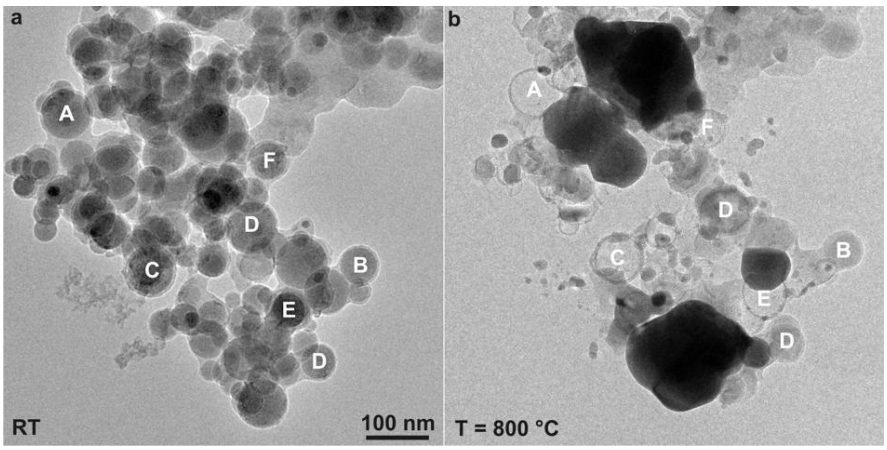

Figure 1. TEM images of the same area of carbon-coated $LiFePO_4$ at room temperature (a) and after in-situ heating to 800 °C (b). During the heating, empty carbon spheres (e.g., A and C) were developed and $LiFePO_4$ particles sintered together (e.g. above E and left of D in (b)). In spite of drastic changes, typical features allow one to recognize corresponding sites as indicated by the same letters in images (a) and (b).

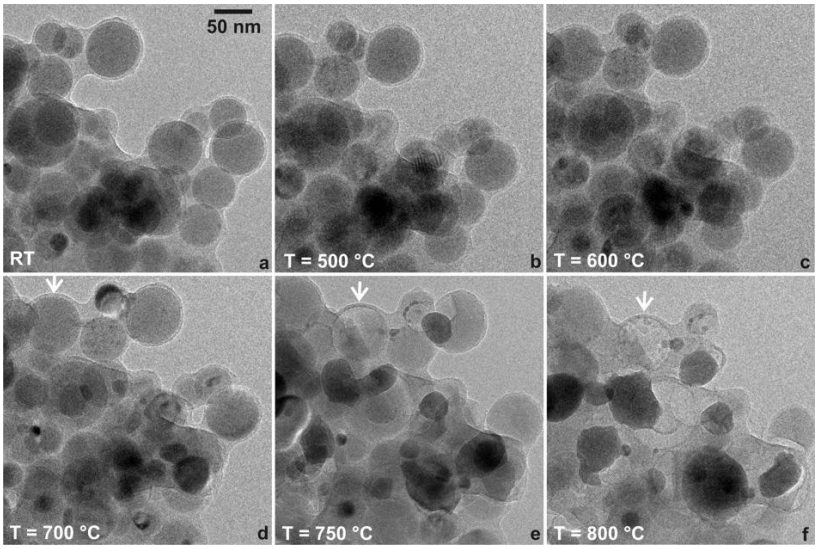

Figure 2. TEM images of the same area of the carbon-coated $LiFePO_4$ at room temperature (a) and after different stages of the in-situ heating experiment (b-f). Most changes − in particular the formation of empty carbon shells (an example is marked by arrows) and the particle growth − only occur at temperatures above 700 °C (d-f) which is in agreement with ex-situ measurements [3].

Nanoparticles, Nanostructured Materials, Catalysts

MS6.P149
Atomic-structure of twinning in nanocatalyst by aberration-corrected STEM

C. N. Hsiao[1], P. K. Chiu[1], Y. W. Lin[1], F. Z. Chen[1], J. L. A. Yeh[1]

[1]National Applied Research Laboratories, Instrument Technology Research Center, Hsinchu, Taiwan

0209347@narlabs.org.tw

The study of the connection between active site and defect of nanocatalyst is a rising field in nonotechnology [1,2,3]. Twinning in bimetallic heterogeneous nanocatalyst was investigated using HRTEM and aberration-corrected HRSTEM. The phase plates were calculated from the aberration coefficients of the measured probe tableau for various outer tilt angle of the optical axis and the accuracy required for the compensation of the various residual aberration coefficients in order to achieve sub-angstrom resolution with the electron optics system was evaluated up to the fifth order aberrations. It is found that the interplanar spacing of the Au-Pd nanoparticle (111) planes observed along the [110] zone axis was approximately 0.24 nm measured by HRTEM (Figure 1). In addition, the HRSTEM HAADF image demonstrated that the twin boundaries on the surfaces of heterogeneous nanoparticle catalyst at atomic scale (Figure 2). These defects are introduced during the growth to alleviate the internal stress and reduced strain energy which caused by the 4.6 % lattice mismatch of Au-Pd bimetallic system. This results the crystal transformation from fcc {111} to{110} and turn back to {111} on the surface of the nanocatalyst. The relevant displacement vectors b=a/6[112] of the partial dislocation (Shockey dislocation) from the stress release as the boundary of twin. This shift vector can be seen by the elementary cell on the close packed {111} plane. Furthermore, Twin boundaries could be regarded as the reactive sites of catalysts by causing steps to be formed on the nanoparticle surfaces. The atomic structural features might be possible to effect further application in the catalyst research.

1. J. P. Greeley, Active site of an industrial catalyst, Science, 336 (2012) 810-811.
2. M. Behrens, F. Studt, I. Kasatkin, S. Kühl, M. Hävecker, F. Abild-Pedersen, The Active Site of Methanol Synthesis over $Cu/ZnO/Al_2O_3$ Industrial Catalysts, Science 336 (2012) 893-897.
3. Q. Fu, H. Saltsburg, M. Flytzani-Stephanopoulos, Active nonmetallic Au and Pt species on ceria-based water-gas shift catalysts, Science 301 (2003) 935-938.

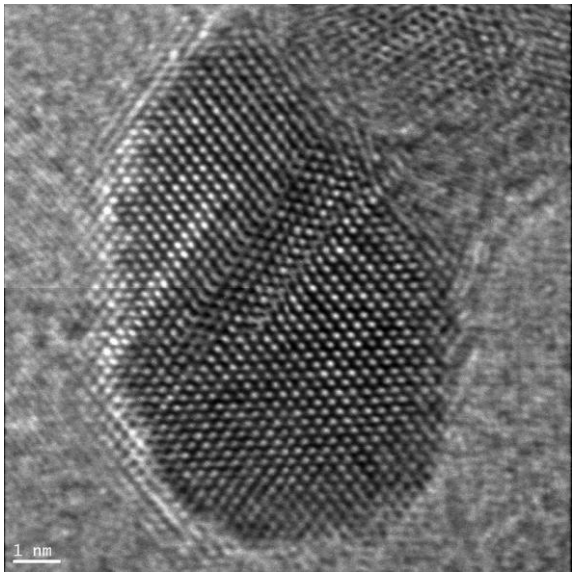

Figure 1. The HRTEM image of bimetallic heterogeneous nanoparticle catalyst.

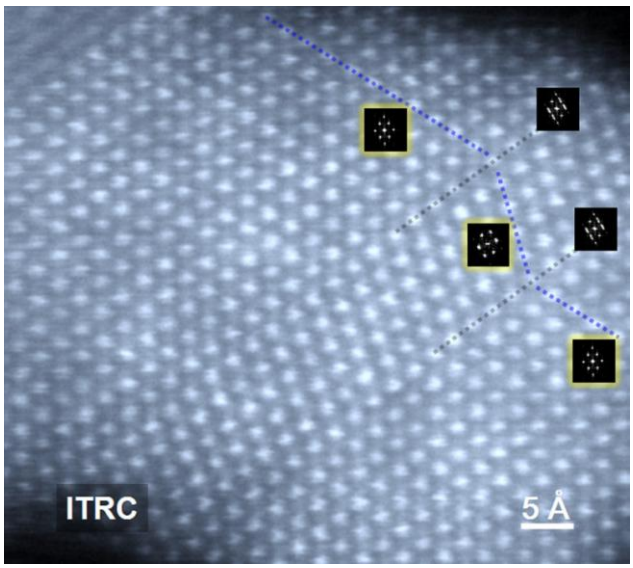

Figure 2. The HRSTEM HAADF image of bimetallic heterogeneous nanoparticles catalyst with twinning structure at atomic resolution.

Nanoparticles, Nanostructured Materials, Catalysts

MS6.P150
Atomic structure of monolayer-protected Au_{144} nanoclusters investigated by aberration-corrected STEM

J. Liu[1], N. Jian[1], R. E. Palmer[1]

[1]University of Birmingham, School of Physics & Astronomy, Birmingham, United Kingdom

jxl318@bham.ac.uk

To understand the atomic structure of the monolayer-protected clusters is essential to their original intriguing physical and chemical properties [1]. Single crystal X-ray crystallography is the best method to determine the total atomic structures [2]. However, due to the considerable difficulties of growing good quality single crystals, the utilisation of this technique is rather limited.

Aberration-corrected scanning transmission electron microscopy (STEM) is a powerful method to investigate the nanostructure of individual cluster [3]. Here we employ STEM combined with multislice simulations to investigate the atomic structure of MP Au clusters of nominal composition of $Au_{144}(SCH_2CH_2Ph)_{60}$. These clusters were "weighed" against size-selected clusters ($Au_{923\pm23}$) and fractionated. The fraction of clusters actually containing 144±5 Au atoms was assigned to the $Au_{144}(SCH_2CH_2Ph)_{60}$ clusters and compared with structural model simulations. Our statistical structure investigation shows that only about 11% of the clusters match the predicted pseudo-icosahedral structure [4], while the rest of the clusters are amorphous.

1. Ma, G.; Binder, A.; Chi, M.; Liu, C.; Jin, R.; Jiang, D.; Fan, J.; Dai, S.. Chem. Commun. 2012, 48, 11413-11415.
2. Jadzinsky, P. D.; Calero, G.; Ackerson, C. J.; Bushnell, D. A.; Kornberg, R. D. Science 2007, 318, 430-433.
3. Jian, N.; Stapelfeldt, C.; Hu, K.-J.; Fröba, M.; Palmer, R. E. Nanoscale 2015, 7, 885-888.
4. Lopez-acevedo, O.; Akola, J.; Whetten, R. L.; Grönbeck H.; Häkkinen H. J. Phys. Chem. C 2009, 144, 5035-5038.

Nanoparticles, Nanostructured Materials, Catalysts

MS6.P151
The structure of $Gd_2O_2(CO_3)$ and a-FeO(OH) hollow particles

R. Popescu[1], J. Jung-König[2], W. Beichel[2], C. Feldmann[2], D. Gerthsen[1]

[1]Laboratorium für Elektronenmikroskopie, Karlsruhe, Germany
[2]Institut für Anorganische Chemie, Karlsruhe, Germany

radian.popescu@kit.edu

Nanoparticles (NPs) stand out due to their unique properties as compared to the corresponding bulk materials. Beside the chemical composition, the specific NP properties are determined by their structure. In this work we study the structure of $Gd_2O_2(CO_3)$ and FeO(OH) HPs, which can be used as delivery system for drugs, dyes and catalysts [1].

For the structural and chemical characterization, high-resolution (HR) transmission electron microscopy (TEM) and high-angle annular dark-field (HAADF) scanning TEM (STEM) combined with energy-dispersive X-ray spectroscopy (EDXS) were used. NPs were prepared by a microemulsion approach [2] and deposited on an amorphous carbon film at room temperature. HRTEM was performed with an aberration-corrected FEI Titan^3 80-300 microscope at 80 kV and 300 kV and HAADF STEM/EDXS with an FEI Osiris ChemiSTEM at 200 kV.

HRTEM images of $Gd_2O_2(CO_3)$ NPs (Fig. 1a) demonstrate the hollow NP morphology, and the absence of lattice fringes indicates that hollow particles (HPs) occur in amorphous structure. However, illumination with 300 keV electrons for time intervals of 5 s results in the start of crystallization with the formation of small crystallites (Fig. 1b). Information on their structure is obtained by calculating the two-dimensional Fourier transform of HRTEM images, denoted as diffractograms. The region within the frame on Fig. 1b) is a single $Gd_2O_2(CO_3)$ monocrystal, as indicated by the good agreement between its diffractogram and the calculated diffraction pattern of bulk *hcp* $Gd_2O_2(CO_3)$ (space group $P6_3/mmc$, space group number 194) in the [421]-zone axis (Fig. 1c). This finding supports that the HPs are initially composed of amorphous $Gd_2O_2(CO_3)$. The chemical composition of HPs was determined using EDXS by scanning a rectangular area within single HPs (frame in Fig. 1d). The quantification of EDXS area scans of 44 different HPs using the Gd-L series and O-K line yields an average composition of $Gd_{30\pm4}O_{70\pm4}$, in agreement with the $Gd_2O_2(CO_3)$ composition, i.e. Gd_2O_5=$Gd_{29}O_{71}$. Further, EDXS line profiles through particles (e.g. line in Fig. 1d) are used to derive Gd- and O-concentration profiles (Fig. 1e). These profiles suggest a uniform distribution of Gd and O within HPs and yields a chemical composition of $Gd_{26\pm4}O_{74\pm4}$ in agreement with that of $Gd_2O_2(CO_3)$. Moreover, EDXS maps of the Gd (Gd-L_{a1}) (Fig. 1f) and O (O-K_{a1}) distributions (Fig. 1g), support the uniform distribution of Gd and O within HPs and their hollow morphology.

Fig. 1 h) shows the HRTEM image of a single FeO(OH) particle with a hollow morphology. The HP in Fig. 1h) is a FeO(OH) monocrystal, as suggested by the good agreement between its diffractogram and the calculated diffraction pattern of bulk orthorhombic a-FeO(OH) (goethite, space group Pbnm, space group number 62) in the [010]-zone axis (Fig. 1i). The quantification of EDXS area scans of 15 different HPs with the Fe-K and O-K lines results in an average chemical composition of $Fe_{32\pm4}O_{68\pm4}$, which corresponds well with the composition of FeO(OH), i.e. Fe_1O_2 = $Fe_{33}O_{67}$. Moreover, EDXS maps of Fe (Fe-K_{a1}) (Fig. 1k) and O (O-K_{a1}) (Fig. 1l) distributions measured from the HP shown on Fig. 1j), support the uniform distribution of Fe and O within HPs and their hollow morphology.

1. I.P. Kaur et al, Int. J. Pharm. 269 (2004), 1.
2. D. H. M. Buchold and C. Feldmann, Adv. Funct. Mater. 18 (2008), 1002.

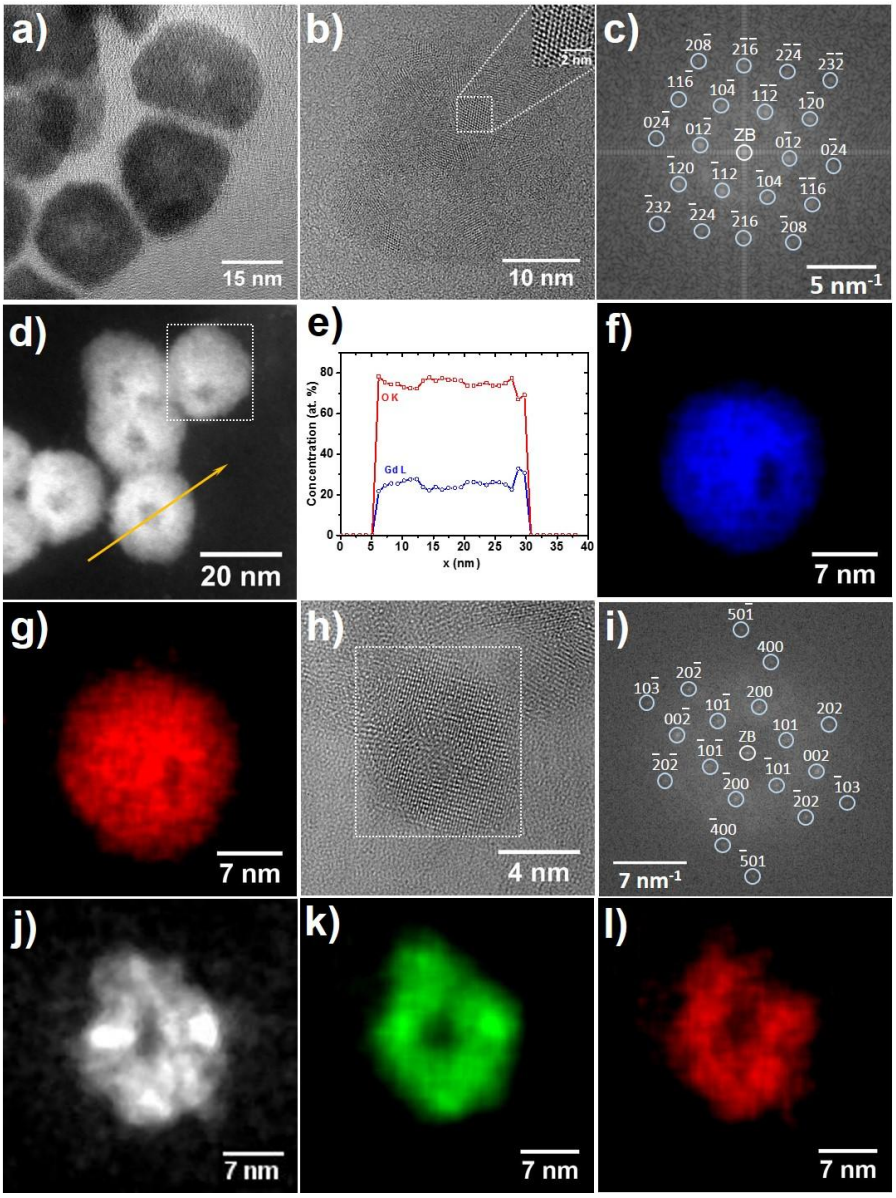

Figure 1. a)-g) $Gd_2O_2(CO_3)$ HPs: a)-b) HRTEM images, c) diffractogram of the square region in b) and calculated diffraction pattern with Miller indices for *hcp* $Gd_2O_2(CO_3)$ in the [421]-zone axis (blue circles). The white circle indicates the zero-order beam (ZB). d) HAADF STEM image with EDXS area (rectangle) and line-scan direction (orange line), e) Gd- and O-composition profiles along the line in d), f)-g) EDXS maps of the (f) Gd- and (g) O-distributions. **h)-l) a-FeO(OH) HPs:** h) HRTEM image, i) diffractogram of the whole HP in h) and calculated diffraction pattern with Miller indices for orthorhombic a-FeO(OH) in the [010]-zone axis, j) HAADF STEM image and corresponding EDXS maps of (k) Fe and (l) O distributions.

Nanoparticles, Nanostructured Materials, Catalysts

MS6.P152
Consistency and green synthesis of silver nanoparticles using (lavandulifilia) extract

F. Gholamhoseinpoor[1], M. Navaderi[2]

[1]Esfarayen, Iran, Islamic Republic of Iran
[2]Tehran, Iran, Islamic Republic of Iran

farnooshghp@yahoo.com

Abstract Biomolecules present in the extract can be used to reduce metal ions to nanoparticles synthesized in a green one-step process. The Byvzhn reduction of metal ions to the metal base, which is quite fast, easily performed at room temperature and pressure, and scaled up easily. Synthesis intermediates plant extracts environmentally benign. Reduction factors involved include water-soluble plant metabolites (eg alkaloids, phenolic compounds, terpenoids) and co-enzymes. Silver nanoparticles (Ag) with special focus on the synthesis plant. Extract a variety of (lavandulifilia) have been successfully used in the manufacture of nanoparticles. The purpose of this study was to evaluate the antioxidant properties of this plant and its ability to synthesize silver nanoparticles. (Lavandulifilia) leaves for the preparation of aqueous extract was used for this study. Silver nanoparticles with various techniques such as spectroscopy, UV-VIS, spectroscopy, FT-IR, X-ray diffraction (XRD), scanning electron microscopy (SEM) and transmission electron microscopy (TEM) was determined. Electron microscopic examination showed that the nanoparticles are spherical and uniformly distributed, and its size is 01-01 nm. X-ray diffraction pattern showed high purity silver nanoparticles centered cubic structure with a size of 81 nm. In addition, herbal extracts, live plants can be used for synthesis. The method of making nanoparticles using plant extracts were here. Scanning Electron Microscope (SEM) means the formation of silver nanoparticles. The results of TEM, SEM, FT-IR, UV-VIS and XRD confirmed that the leaf extract (lavandulifilia) can be synthesized silver nanoparticles. Keywords: leaves, silver nanoparticles. Scanning Electron Microscope (SEM). Biosynthesis of nanoparticles.

Nanoparticles, Nanostructured Materials, Catalysts

MS6.P153
Atomic scale in-situ studies of catalytic reactions between d-elemental clusters and carbon nanostructures inside SWNT

T. Zoberbier[1], J. Biskupek[1], U. Kaiser[1], T. Chamberlain[2], A. Khlobystov[2]

[1]Ulm University, Electron Microscopy of Materials Sciences, Ulm, Germany
[2]University of Nottingham, School of Chemistry, Nottingham, Germany

thilo.zoberbier@uni-ulm.de

Catalysis at the nanoscale plays an essential role in the fabrication, the transformation and the functionalization of carbon nanostructures. The control and efficiency of these processes largely depends on the morphologic properties of the catalyst as well as the metal specific chemical properties. However neither the catalytic mechanisms are understood on an atomic level nor is there a systematic understanding of fundamentals why different metal type deviate in their aptitude.

In our experiments aberration corrected HRTEM is used for atomically resolved in situ imaging of chemical reactions between a large range of d-elemental nanoparticles (~1 nm) and carbon inside SWNTs. This enables a detailed and systematic study of the processes characterizing the catalytic properties, aptitude and applications of different metals: formation of ordered carbon network in different morphologies, annealing and reorganization processes, ability to assimilate source material and disintegration of carbon structures. Further these investigations allow a study of the underlying metal-specific properties of Pi- and Sigma- bonding, metal-cohesive forces and solubility of carbon in the metal.

Nanoparticles, Nanostructured Materials, Catalysts

MS6.P154
Characterization of alkali modified Au catalysts on rutile for the conversion of CO_2 to propanol

C. R. Kreyenschulte[1], S. J. Ahlers[1], E. V. Kondratenko[1], M.- M. Pohl[1]

[1]Leibniz Institute for Catalysis, Rostock, Germany

carsten.kreyenschulte@catalysis.de

Using CO_2 as the basis for the synthesis of valuable chemicals has the chance to substitute fossil carbon sources. For this reason, the conversion of CO_2 with C_2H_4 and H_2 into 1-propanol over TiO_2-supported catalysts possessing Au nanoparticles has been investigated. The rutile-based catalysts showed superior performance to their anatase-based counterparts. Propanol selectivity is strongly improved when promoting Au/TiO_2 with either K or Cs. The highest selectivity of up to 99% propanol could be achieved with a certain amount of the promoter. With a further increase in its loading, the activity of the catalyst starts to decrease. For catalyst preparation and chemical characterization we refer to the according publications [1, 2].

Here we compare the morphology of these differently loaded catalysts to determine the influence of K and Cs on the structure and the behavior during reaction. For characterization we use a probe corrected JEOL ARM 200F equipped with a HAADF-detector and EDXS providing high resolution element sensitive contrast. Independently of the promoter concentration in the catalysts, the Au particles on the support show a variety of sizes comprising diameters of several nm down to agglomerations of a few Au atoms.

In the case of promoting the catalyst with Cs we observe a fine layering of heavier atoms on the support and on the gold particles (fig. 1a). Additionally decoration effects on the support (fig. 1b) and coverages of the gold particles (fig.1c) were observed. By EDXS, a weak Cs signal for these structures could be detected. Further analysis of this layer proved to be difficult due to the low amount of Cs in the specimen and an overlapping of the Cs-La and Ti-Ka peaks in the EDX spectrum.

The morphology of the K loaded catalyst is similar to the undoped Au/TiO_2 system (fig. 1d) and does not show an obvious covering of the support and on the particles visible in the HAADF micrographs. This behavior is to be expected due the similarity of the mass of K and Ti. However, the positions of the peaks in the EDX spectrum allow us to clearly identify the presence of K within the specimen. Considering the otherwise similar characteristics of the specimens, we assume the coating with heavier atoms in the Cs loaded specimen to be Cs and not e.g. finely distributed gold atoms.

The catalytic system presented here shows the advantages of using aberration corrected HAADF-imaging in combination with elemental analysis, however, also its limitations. Z-contrast provides for the detection of heavy elements on a support consisting of lighter elements but identification is less straight forward.

1. "Catalytic Role and Location of Cs Promoter in Cs-Au/TiO2 Catalysts for Propanol Synthesis from CO2, C2H4 and H2" S. J. Ahlers, M.-M. Pohl, J. Radnik, D. Linke, E. V. Kondratenko, submitted to Appl. Catalysis B
2. "Propanol formation from CO2 and C2H4 with H2 over Au/TiO2: Effect of support and K doping" S. J. Ahlers, R. Kraehnert, C. Kreyenschulte, M.-M. Pohl, D. Linke, E. V. Kondratenko, submitted to Catalysis Today

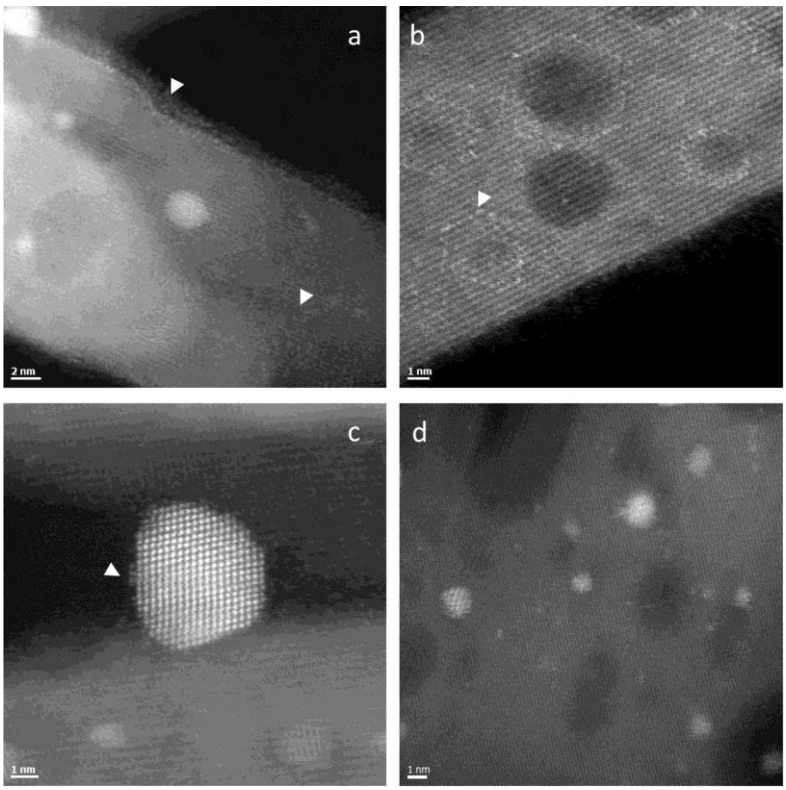

Figure 1. HAADF-image Cs doped and undoped Au at rutile; a: Cs-covered support with Cs single atoms (10 wt-% Cs); b: Cs decoration effects at steps (7wt-% Cs); c: first Gold particles with imperfect Cs shell at 4wt-% Cs; d: undoped Au at rutile; Arrows: Cs rich features

Nanoparticles, Nanostructured Materials, Catalysts

MS6.P155
Electron Beam induced deposition (EBID) as a novel tool for building plasmonic structures

C. Haverkamp[1], K. Höflich[1], S. Christiansen[1]

[1]Helmholtz-Zentrum-Berlin, Berlin, Germany

caspar.haverkamp@helmholtz-berlin.de

The electron beam induced deposition (EBID) permits highly precise fabrication of truly three-dimensional nanostructures of almost arbitrary shapes on any conductive substrate using metal-organic precursors. The EBID process makes use of the local decomposition of a typically metal-organic compounds as precursor gases (e.g. dimethyl-gold(III)-acetyl-acetonate) under the electron beam. A gas-injection system (GIS) inserts a precursor gas into the vacuum chamber of a scanning electron microscope (SEM), the precursor molecules which adsorb, desorb and diffuse at the substrate surface are locally decomposed by the secondary electrons created by interaction of the electron beam with the substrate. Because the interaction volume changes with the beam parameters the created geometries depend strongly on them. Parameters like beam intensity and acceleration voltage not only influence the shape of the structure but also material properties like the atomic composition. The structures that form during decomposition of the organo-metallic precursor gas contain a carbonaceous matrix in which single crystalline metallic nanocrystals of a few nanometers in diameter are dispersed.

One ideal field for application of this highly precise technique is the creation of nanostructures smaller than the wavelength of visible light. The investigation of interactions of electromagnetic waves with such sub-wavelength structures is topic of the intensely studied field of nano-optics. Since the EBID process allows to create structures with lateral dimensions below 15 nm with the freedom of arbitrary shapes EBID can be ideally used for the fabrication of plasmonic (after additional metal coverage) and metamaterial (as-deposited) nano-devices.

Nanoparticles, Nanostructured Materials, Catalysts

MS6.P156
Analysis of platinum-cobalt bimetallic nanoparticles in hollow carbon shells

A.- C. Swertz[1], G.- H. Wang[1], N. Pfänder[2], F. Schüth[1], C. Lehmann[1]

[1]Max-Planck-Institut für Kohlenforschung, Mülheim a. d. Ruhr, Germany
[2]Fritz-Haber-Institut der MPG, Berlin, Germany

swertz@kofo.mpg.de

PtCo bimetallic nanoparticles encapsulated in hollow carbon spheres (HCS) show a remarkably high activity as catalyst for the conversion of 5-hydroxymethylfurfural to 2,5-dimethylfuran. The synthesis of these particles follows a simple strategy with three major steps: Formation of platinum nanoparticles encapsulated in hollow polymer shells (Pt@HPS), introduction of cobalt ions to the polymer shells (Pt@HPS-Co^{2+}) and Carbonization of the shells and alloying of the bimetallic particles (PtCo@HCS).[1]

In this study the intermediates and products from this synthesis were analyzed using different electron microscopy methods like HR-TEM, HAADF-STEM and EDX elemental mapping. The aim of this study was to understand the reaction mechanism of the formation of PtCo@HCS. These results help to generalize the synthesis strategy for different noble and transition metals to synthesize a wide range of bimetallic catalysts. Furthermore this strategy could be used to syntherize trimetallic nanoparticles starting the reaction with two noble metals added to the polymer precursor or introducing two transition metals to the polymer shell.

1. Wang, G., Hilgert, J., Richter, F., Wang, F., Bongard, H.-J., Spliethoff, B., Weidenthaler, C., & Schüth, F., Nature Materials, 13, 293-300 (2014)

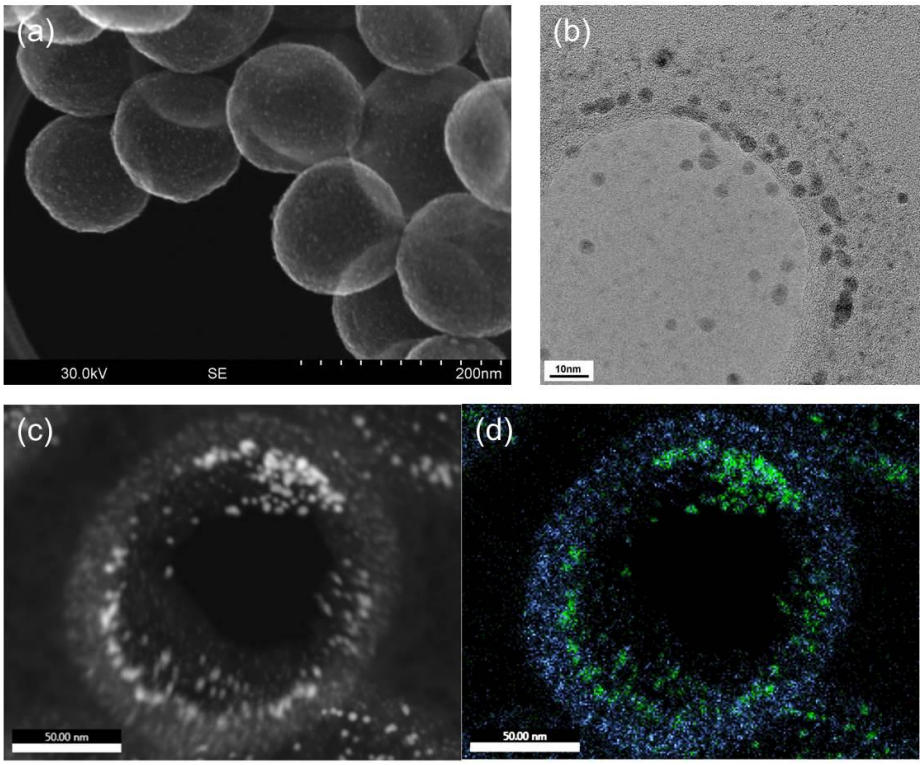

Figure 1. Micrographs of PtCo@HCS: SEM image (a), HR-TEM image (b), HAADF-STEM image (c) and corresponding Pt (green) and Co (blue) elemental map (d).

Nanoparticles, Nanostructured Materials, Catalysts

MS6.P157
3D structures of porous carbon materials with different pore size used as nanocatalyst supports

W. Wang[1], D. Wang[1], A. Villa[2], Z. Zhao-Karger[1], L. Prati[2], C. Kübel[1]

[1]Karlsruhe Institute of Technology, Institute of Nanotechnology, Eggenstein-Leopoldshafen, Germany
[2]University of Milan, Department of Chemistry, Milan, Italy

wu.wang@partner.kit.edu

Porous carbon materials are widely used as nanocatalyst supports due to high surface areas, hierarchical meso- or micro-porosity and tunable surface chemistry [1,2,3]. The porous structures of carbon can effectively influence the morphology and distribution of metal particles supported on them and therefore the catalytic behaviors such as activity, selectivity and resistance to deactivation [4,5]. In addition, the reactant transport properties through the pores are also dependent on the pore space morphology [6]. In present work, we use electron tomography to provide three dimensional (3D) information at nanometer scale for understanding the pore space morphology of different porous carbon support materials, including covalent triazine frameworks (CTFs), ordered mesoporous carbon (OMC) and commercial activated carbon (AC, from Norit), etc. Either HAADF STEM tomogram or TEM tomogram for these porous carbon materials are reconstructed from tilt series images in a tilting angle range above ±70°. Figure 1 shows an example of cross section slice of CTFs and OMC, in which small pores down to few nanometers are clearly visible. With further segmentation and chord length distribution (CLD) analysis, the surface areas, pore volumes and network structures are expected to be derived quantitatively. These quantitative data will be compared to BET measurement therefore offering in depth understanding of the supported nanocatalyst structures and their properties.

1. Rodríguez-reinoso F. Carbon N Y 1998;36:159.
2. Ryoo R, Joo SH, Kruk M, Jaroniec M. Adv Mater 2001;13:677.
3. Serp P, Corrias M, Kalck P. Appl Catal A Gen 2003;253:337.
4. Chan-Thaw CE, Villa A, Katekomol P, Su D, Thomas A, Prati L. Nano Lett 2010;10:537.
5. Ding J, Chan KY, Ren J, Xiao FS. Electrochim Acta 2005;50:3131.
6. Chan KY, Ding J, Ren J, Cheng S, Tsang KY. J Mater Chem 2004;14:505.

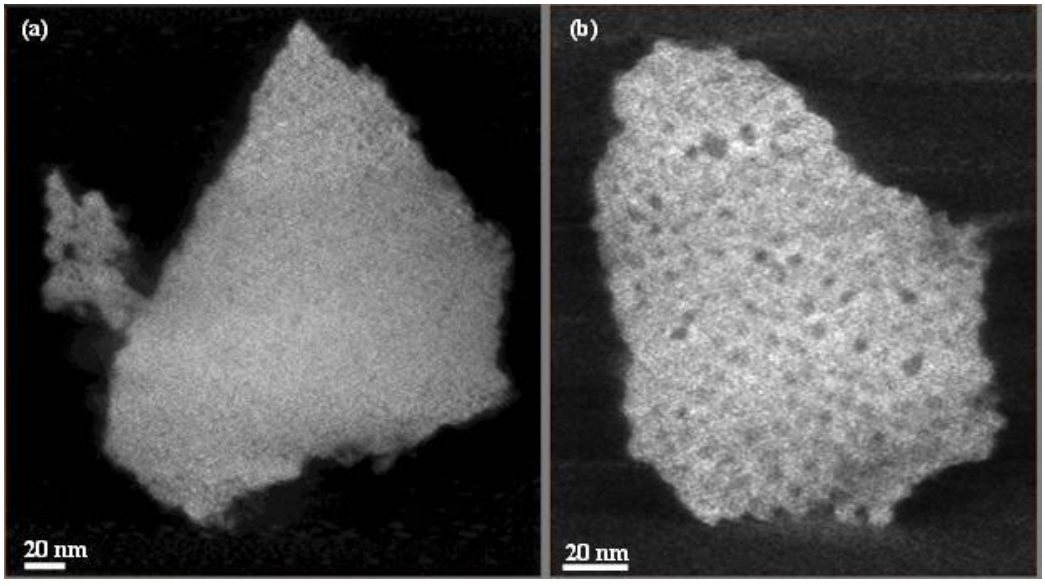

Figure 1. A cross section slice from reconstructed STEM electron tomogram of (a) CTFs and (b) OMC.

Nanoparticles, Nanostructured Materials, Catalysts

MS6.P158
SEM-EDS investigation of TiO_2 nanoparticles in sun lotions

M. Sysoltseva[1], R. Winterhalter[1], C. Scheu[2], H. Fromme[1]

[1]Bavarian Health and Food Safety Authority, Munich, Germany
[2]Max-Planck-Institut für Eisenforschung GmbH, Düsseldorf, Germany

marina.sysoltseva@lgl.bayern.de

Titanium dioxide (TiO_2) is widely used in sun lotions as a physical (mineral) filter to prevent skin damage from sun exposure, which may cause premature skin aging and skin cancer. The sunscreens may have a content of mineral filters up to 25%. If used in nanoparticle form, the TiO_2 does not leave a white film on the skin as does a sun milk containing micro-TiO_2 particle. Due to this property nano-TiO_2 has been increasingly used in sun lotions and sun milks since 1990. There is the possibility that a consumer is exposed to engineered nanoparticles by using such products. According to requirements of new Cosmetic Regulation No. 1223/2009 of the European parliament all nanomaterials which are present in cosmetic products shall be clearly indicated. Therefore, it is important to have analytical techniques, which would be sensitive enough to allow measurement, analysis and characterisation of small nanoparticles in a sun screen.

In this study electron microscopy techniques in combination with energy dispersive X-ray spectroscopy (EDS) have been applied for visualizing titanium dioxide from sun screen, determining the size, shape and aggregation of particles. Characteristics for the sun lotion are high fat content and matrix of high complexity. Different sample preparation methods were tested for imaging of TiO_2 in the sun lotion, such as applying sun lotion on silica wafer or carbon glue pad and defatting of the sample with hexane. The characterisation of titanium dioxide particles after these sample preparation was impossible. Therefore, a novel extraction method using methanol to remove organic components from the samples was developed which allowed not only the imaging of the nanoparticles but also determination of the chemical composition.

Six brands of sunscreen products with sun protection (SPF) factor between 30 and 50+ were investigated. Our results showed that all of these products contained titanium dioxide in the nanometer range (Fig.1). All samples included aggregates of round nano-TiO_2 particles. The size of primary titanium dioxide particles was between 20 and 40 nm. In the sun lotion (a) with SPF 50+ we found only a few small aggregates, so it was concluded, that it should have the smallest amount of titanium dioxide. In contrast, in the sun screen (f) with SPF 30 the largest aggregates of TiO_2 were observed.

Additionally, in the sample (a) diamond shaped particles were found (Fig.1a). They are app. 500 nm large and should be composed of an organic material because only C-Signal by SEM and EDS was observed.

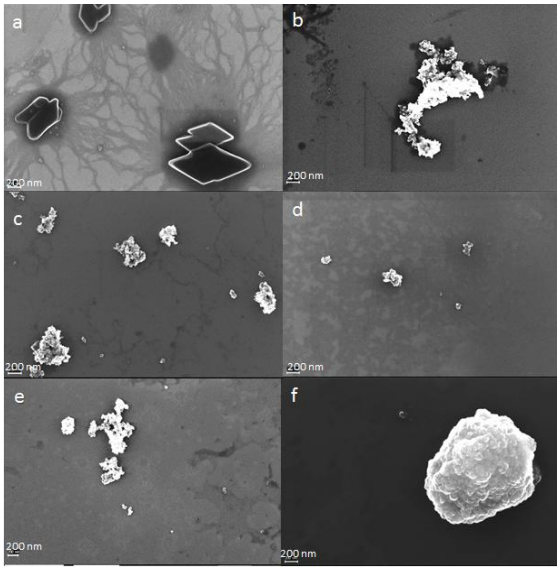

Figure 1. SEM images of particles from sunscreens after extraction: a) SPF 50+, b) SPF 50+, c) SPF 50, d) SPF 50+, e) SPF 50+, f) SPF 30.

Nanoparticles, Nanostructured Materials, Catalysts

MS6.P159
Electron microscopy study of Zn ultrafine particles manufactured via the flow-levitation method

A. Zhigach[1], I. Leipunsky[1], N. Berezkina[1], M. Kuskov[1], E. Afanasenkova[1], S. Gorbatov[1], O. Zhigalina[2], V. Zhigalina[2], D. Khmelenin[2], G. F. Lopez[3]

[1]V.L. Talrose Institute for Energy Problems of Chemical Physics RAS , Moscow, Russian Federation
[2]Shubnikov Institute of Crystallography, Moscow, Russian Federation
[3]Northeastern University, College of Professional Studies, Boston, Massachusetts, United States

yyleibe@gmail.com

Ultrafine Zn powders (Zn UFPs) are used in a wide variety of applications in medicine, engineering and science. Application success depends highly on structural characteristics and morphology of constituent nanoparticles which in turn depend on manufacturing factors present during the synthesis.

This work is a detailed microscopic study of structure, size and morphology of Zn particles that are manufactured via the Flow-Levitation (FL) method [1]. The FL method is a versatile evaporation-condensation technique that allows controlled and flexible variation of parameters involved during the synthesis of Zn particles, in particular, the flow character and type of carrier gas. The goal is to determine the influence of those parameters in the characteristics of the nanoparticles. Characterization and analyses of samples are performed using scanning electron microscopy (SEM), high resolution transmission electron microscopy (HRTEM) and electron diffraction (ED), energy-dispersion spectroscopy (EDX) and X-Ray diffraction (XRD).

Several Zn UFPs samples were synthesized under various fabrication conditions. Two general morphological types of Zn particles are observed: spheroidal and crystalline. The resulting shape is found to be strongly dependent on thermo-physical properties of the carrier gas and the mechanism of condensation.

Spheroidal particle formation is the result of a predominant “from vapor - to liquid” condensation followed by the liquid particles solidification. Observable flat or concave sections on the surface of spheroidal particles arise from shrinkage during solidification. A SEM image of a sample containing spheroidal (average size 0,5-1,2 μm) and crystalline (average size 0,2-0,3 μm) Zn particles is shown in Figure 1A.

Direct transition “from vapor - to solid phase” occurring at higher heat removal rates results in initial formation of hexagonal-plate-shaped particles followed by Zn vapors condensation on their solid surface forming crystals of different shapes such as hexagonal plates, prisms, equiaxial faceted crystals, etc.

Some crystalline particles have developed into angular “sandglass” shapes (average size 0.5 μm). They appear to start as a contact twin followed by epitaxial growth during the condensation (which may be accompanied by lamellar twinning) and ending with the formation of relatively large sandglass-shaped particles, in most cases laminated. Figures 1B and 1C shows two different samples of purely crystalline Zn particles (average size 0.2 μm). Irrespective of their final shape, all particles show crystal facets typical of hexagonal system with basal plane (0001). X-Ray diffraction analysis of dissimilar samples shows the same patterns of metallic crystalline Zn with small amounts of ZnO which counts for their oxidation in air. Electron diffraction analysis also showed the hexagonal crystalline phase of Zn particles irrespective of their morphology and the presence of small ZnO crystalline particles.

In order to study the fine structure of large size Zn particles (>1,5 μm), two large Zn particles of the same morphology but different orientation were cut using the focused ion beam (FIB) method, directly inside the microscope, on thin slices parallel to (0001) and (-12-10) planes. Figure 2 illustrates results of TEM and HRTEM studies. High resolution electron microscopy, filtering of images obtained, and Fast Fourier Transform (FFT) revealed a crystalline layer of ~10 nm thick on the particles surface which interplanar distance 2.75 Å corresponds to ZnO.

Analysis of electron diffraction patterns, and TEM and HRTEM images did not reveal structural differences between “large” and “small” Zn particles.

1. A.N. Jigatch, M.L. Kuskov, I.O. Leipunsky et al. Synthesis of ultrafine metals, alloys and metal compounds via Guen-Miller method: history, state-of-the-art, prospects // Nanotechnologies in Russia, 2012, v. 7, № 3-4, 28-37, Russian edition only.

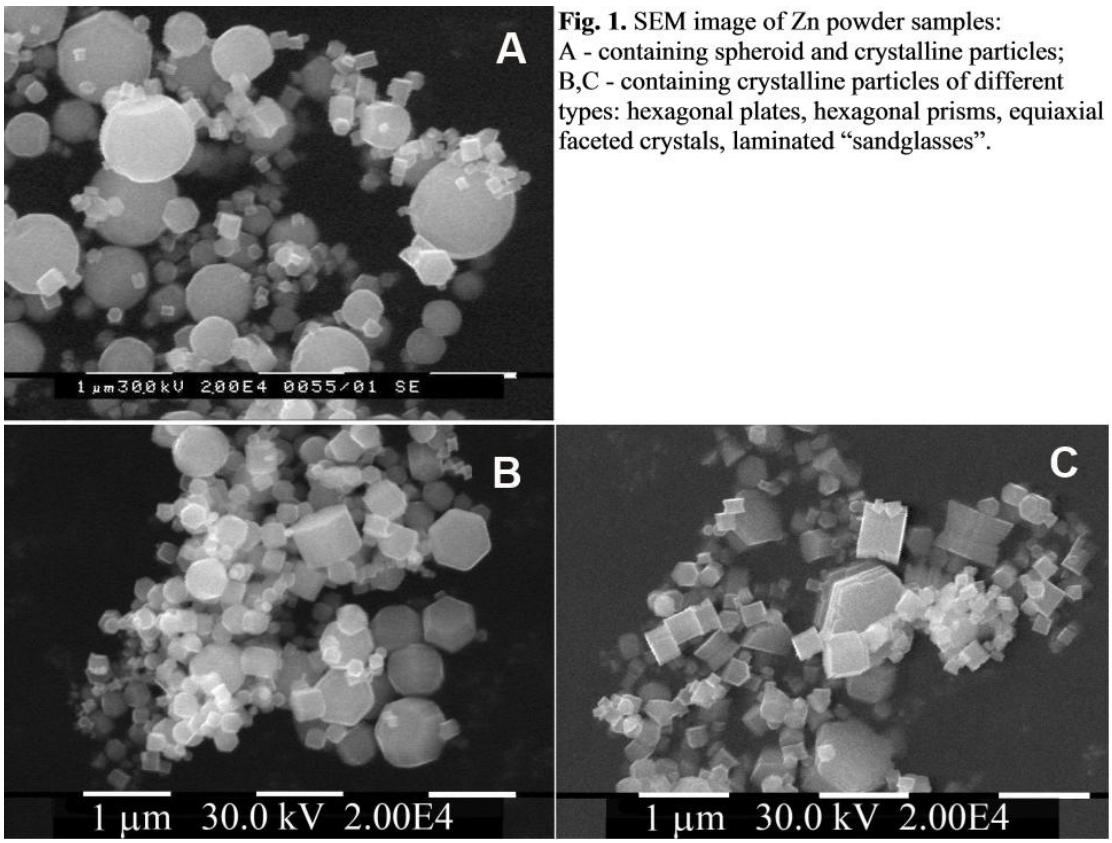

Fig. 1. SEM image of Zn powder samples:
A - containing spheroid and crystalline particles;
B,C - containing crystalline particles of different types: hexagonal plates, hexagonal prisms, equiaxial faceted crystals, laminated "sandglasses".

Figure 1. SEM image of Zn powder samples: A- Containing spheroid and crystalline particles; B,C – containing crystalline particles of different types: hexagonal plates, hexagonal prisms, equiaxial facted crystals, laminated "sandglasses!.

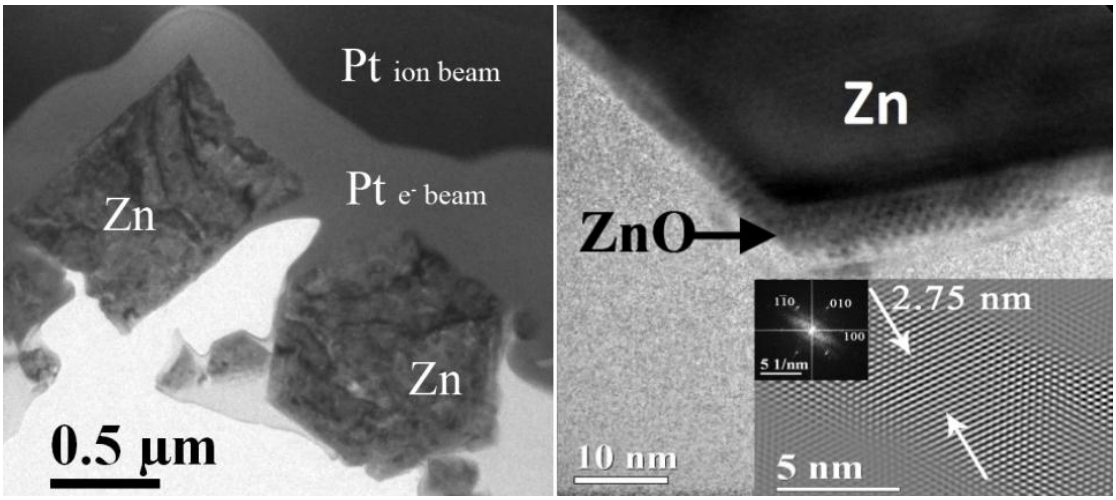

Figure 2. A – TEM image of thin slices of two typical "large" Zn particles cut parallel to (0001) and (1210) planes using FIB method directly inside the Helios NanoLab DualBeam microscope. B – HRTEM image of the cut particle. Insertions represent filtered HRTEM image and FFT pattern of the zinc oxide layer.

Nanoparticles, Nanostructured Materials, Catalysts

MS6.P160
Microstructural investigation of shaped fuel cell catalyst nanoparticles

M. Gocyla[1], M. Heggen[1], F. Dionigi[2], R. M. Arán-Ais[3], S. Kühl[2], V. Beermann[2], R. E. Dunin-Borkowski[1], P. Strasser[2]

[1]Forschungszentrum Jülich, Ernst-Ruska-Centre for Microscopy and Spectroscopy with Electrons and Peter Grünberg Institute, Jülich, Germany
[2]Technical University of Berlin, Chemistry, Chemical Engineering Division, Berlin, Germany
[3]Universidad de Alicante, Instituto de Electroquimica, Alicante, Spain

m.gocyla@fz-juelich.de

The sustainable storage and conversion of energy in fuel cells, Li air batteries and electrolyzers depends strongly on the use of high performance nanoparticle catalysts. The development of stable, highly active catalysts for the oxygen reduction reaction (ORR) at the cathodes of polymer electrolyte membrane fuel cells is a significant challenge. A promising approach to increase catalytic activity is the use of octahedral bimetallic nanoparticles. As a result of the presence of highly catalytically active (111)-oriented surfaces in Pt3Ni [1, 2], they are considered to be “dream electrocatalysts” for the ORR [3, 4]. Recent studies have uncovered an element specific anisotropic growth in octahedral PtNi nanoparticles, taking the form of Pt-rich frames and Ni-rich facets [5, 6]. ORR on such PtNi catalysts leads to preferential leaching of Ni from the particle surface, as well as to the loss of highly active (111)-oriented surfaces and a strong degradation in catalyst activity [5]. These and other theoretical and experimental studies have provided evidence for the strong dependence of catalyst performance on structure and composition and underlined the importance of careful microstructural and compositional analysis on the atomic scale.

Here, we present a detailed microstructural study of well-defined octahedral shaped binary PtNi, PtCo and ternary PtNiCo alloy nanoparticle catalysts, which are grown using different techniques and subjected to different chemical and thermal annealing steps. The particles are investigated using high-angle annular dark field (HAADF) imaging in probe-corrected FEI Titan scanning transmission electron microscopes (STEMs) and atomic-scale compositional analysis using electron energy electron-loss spectroscopy (EELS) and energy-dispersive X-ray (EDX) spectroscopy in an FEI ChemiSTEM equipped with a Super-X detector. The experiments are supplemented by *in situ* heating experiments performed under environmental conditions at up to 1 bar pressure using a MEMS-based static gas closed cell specimen holder (DENS solutions, Delft, NL).

Figure 1 shows HAADF images and EDX spectrum images records from the octahedral particles during a series of thermal annealing and acidic leaching experiments. Before leaching, structural anisotropy is observed, with Ni-rich (111)-oriented facets and a Pt-rich hexapod frame. After leaching, Ni has been preferentially removed, to leave a concave octahedral Pt-rich frame, which leads to strong degradation in catalytic performance. In order to understand the anisotropic growth behavior related to the deposition of the transition metal, various growth experiments were performed, involving the addition of Co as a third element or the replacement of Ni by Co. Specific structural features were found in the ternary catalyst; while the noble metal Pt is distributed in the catalyst in the same way as in the binary catalyst (i.e., in the form of a hexapod frame), the transition metals are nearly homogenously distributed in the facets of the octahedron, with Ni building an encasement around the octahedron.

1. H. A. Gasteiger, N. M. Markovic, Science 324, 48 (2009).
2. V. R. Stamenkovic, B. Fowler, B.S. Mun, G. Wang, P.N. Ross, C.A. Lucas, N.M. Marković, Science 315, 493 (2007).
3. M. K. Debe, Nature 486, 43 (2012).
4. G. Wu, K. L. More, C. M. Johnston, P. Zelenay, Science 332, 443 (2011).
5. L. Gan, C. Cui, M. Heggen, F. Dionigi, S. Rudi, P. Strasser, *Science*, 346, 6216 (2014).
6. Cui, C., Gan, L., Heggen, M., Rudi, S.,Strasser, P., *Nat. Mater.* 12, 8 (2013).

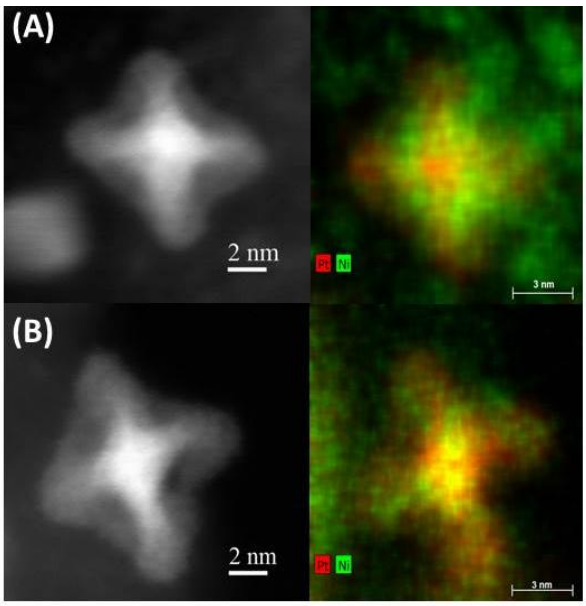

Figure 1. HAADF STEM images and EDX spectrum images of PtNi octahedral nanoparticles studied (A) before and (B) after acidic leaching, demonstrating an anisotropic compositional distribution and preferential leaching.

Nanoparticles, Nanostructured Materials, Catalysts

MS6.P161
Electron-phonon coupling in Au nanoclusters studied by ultrafast electron diffraction

D. Wells[1], R. E. Palmer[1], T. Vasileiadis[2], R. Ernstorfer[2]

[1]University of Birmingham, NPRL, Department of Physics and Astronomy, Birmingham, United Kingdom
[2]Max Planck Research Group, Department of Physical Chemistry, Berlin, Germany

dxw326@bham.ac.uk

We present first results of electron-phonon coupling measurements in size-selected Au nanoclusters using ultrafast (pump-probe) electron diffraction. The nanoclusters are produced with a magnetron sputtering, gas aggregation cluster source with lateral time-of-flight mass filter. The first measurements are focused on Au clusters with 923±23 atoms [1]; this size is located at the border between bulk and nano regimes based on ultrafast optical measurements [2]. Ultrafast diffraction provides the most direct probe to observe the response of the lattice to electronic excitations caused by femtosecond laser pulses. (Photoexcited) electron diffraction in particular is an ideal tool for studying nanostructures because of the much higher scattering cross-section in comparison with X-rays. Here the lattice temperature is probed by the decrease in *intensity* of the diffraction peaks due to the Debye-Waller effect (Fig. 1a) after the system is optically excited. In addition the peak *position* can be used as a probe of ultrafast thermal expansion with sub-picometer resolution (Fig. 1b). Our first findings suggest rapid heat transfer from the electronic to the lattice subsystem and demonstrate the ability of ultrafast diffraction to study photo-induced changes in nanostructured systems with sub-picometer sensitivity to structural changes.

1. Wang, Z. W. and Palmer, R. E., Phys. Rev. Lett. 108, (2012).
2. S. H. Yau , O. Varnavski , and T. Goodson**,** Acc. Chem. Res., 46 1506-1516 (2013).

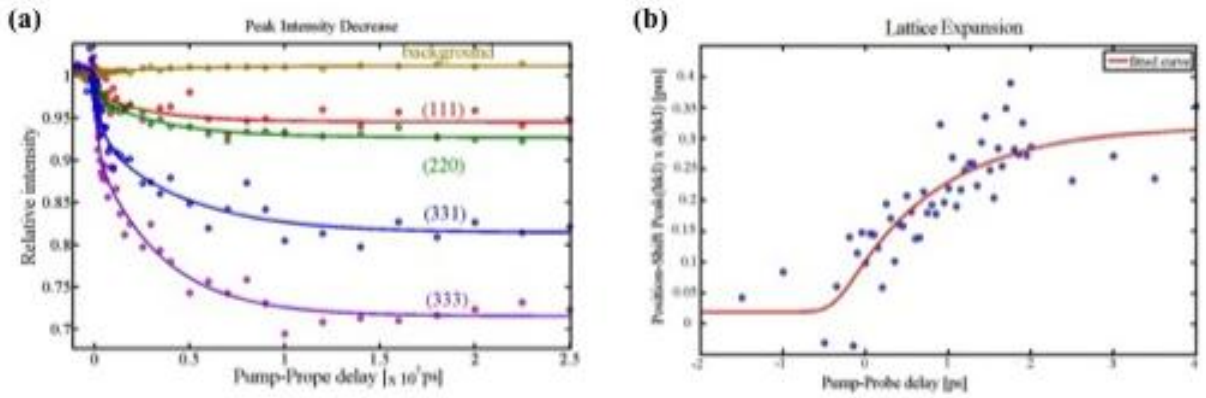

Figure 1. (a) Diffraction peak height decay due to the Debye-Waller effect. As temperature rises the mean atomic displacements increase and the structure deviates from the ideal crystalline lattice, causing the height of the diffraction peaks to decrease; (b) Lattice expansion calculated from the shrinkage of the diffraction rings. In the first few picoseconds (of pump-probe delay) an overall expansion of the nanocluster of less than half a picometer is observed.

Nanoparticles, Nanostructured Materials, Catalysts

MS6.P162
Pt diffusion dynamics on the formation Cr-Pt core-shell nanoparticles

J. Liu[1], G. Gupta[2], P. Iqbal[2], F. Yin[1,3], R. E. Palmer[1], S. Sharma[2], K. C. Leung[4], P. M. Mendes[2]

[1]University of Birmingham, School of Physics & Astronomy, Birmingham, United Kingdom
[2]University of Birmingham, School of Chemical Engineering, Birmingham, United Kingdom
[3]Shaanxi Normal University, School of Physics and Information Technology, Xi'an, United Kingdom
[4]The Hong Kong Baptist University, Department of Chemistry and Institute of Creativity, Hong Kong, Hong Kong

p.m.mendes@bham.ac.uk

Bimetallic nanoparticles are of wide interest due to the possibility to enhance or attain novel properties that cannot be reached in nanoparticles from pure metals[1]. Layered core-shell bimetallic Cr-Pt nanoparticles were prepared by the formation and later reduction of an intermediate Pt ion-containing supramolecular complex onto pre-formed Cr nanoparticles. The resultant nanoparticles were characterised by X-Ray diffraction analysis, transmission electron microscopy, X-ray photoelectron spectroscopy and aberration-corrected scanning transmission electron microscopy. The results are consistent with the presence of Pt diffusion during or after bimetallic nanoparticle formation, which has resulted in a Pt/Cr-alloyed core and shell. We postulate that such Pt diffusion occurs by an electric field-assisted process according to Cabrera-Mott theory, and that it originates from the low work function of the pre-formed oxygen defective Cr nanoparticles and the rather large electron affinity of Pt.

1. R. Ghosh Chaudhuri and S. Paria, *Chem Rev*, 2012, **112**, 2373-2433.
2. G. Gupta, P. Iqbal, F. Yin et al. Pt Diffusion Dynamics on the Formation Cr-Pt Core-Shell Nanoparticles, submitted.

Nanoparticles, Nanostructured Materials, Catalysts

MS6.P163
Synthesis and analysis of various compositions in the system Cu-In-S

G. Neubüser[1], E. Quiroga-Gonzáles[2], L. Nolte[1], W. Bensch[3], L. Kienle[1]

[1]University of Kiel, Institute for Materials Science, Kiel, Germany
[2]Meritorious Autonomous University of Puebla, Institute for Physics, Puebla, Mexico
[3]University of Kiel, Institute of Inorganic Chemistry, Kiel, Germany

gn@tf.uni-kiel.de

Photocatalysis represents - among other techniques - a promising and clean energy source. Hydrogen conversion from water is achieved by exposing the respective catalyst to sunlight; however, the efficiency of the material strongly depends on the width of the optical absorption spectrum. In order to enhance the efficiency, mixtures of ternary compounds in the copper indium sulfur system were investigated as e.g. CuInS2 is a well-known material for photovoltaic applications [1] and also presents photocatalytic activity for H2 production from water [2]. The mixtures of Cu-In-S compounds were obtained by controlled solvothermal syntheses.

Stoichiometric amounts of the pure elements in organic solvent were subjected to different temperatures and pressures to obtain three different phases $CuInS_2$ (C1), $CuIn_3S_5$ (C2) and $CuIn_7S_{11}$ (C3) and their mixtures. For chemical analysis as well as micro- and nanostructural investigations X-ray diffraction and energy dispersive X-ray spectroscopy measurements in addition to scanning and transmission electron microscopy techniques were employed.

At lower synthesis temperature the C1 phase (wurtzite-type) appeared as black solid consisting of microplates partially aligned in bunches of 3 to 5 plates with sizes up to 10 µm (see fig. 1). Higher temperatures induce the formation of red C2 nanosheets and C3, an orange fluff-like phase containing nanobelts. Especially C2 and C3 which crystallize in new structure types show unique nanostructural features. Tilting experiments in the TEM showed that C2 nanosheets exhibit a tendency to be bent and rolled up. The C2 nanosheets are built from overlapping layers which are rotated to each other (turbostratic disordering). This phenomenon results in characteristic anomalies in diffraction patterns (see fig. 2, zone axis [221]) and superposition phenomena in HRTEM micrographs. C3, the copper poorest phase, forms nanobelts showing a lamellar structure with some degree of bending along the belt. As C2 and C3 tend to appear next to each other C3 is possibly a product of C2 as enrolled edges separate to nanobelts. This has to be proven by further experiments involving EDX and high resolution TEM.

1. A. Goosens, J. Hofhuis, Nanotechnology 19 (2008) 424018.
2. L. Zheng, Y. Xu, Y. Song, C. Wu, M. Zhang, Y. Xie, Inorg. Chem. 48/9 (2009) 4003.

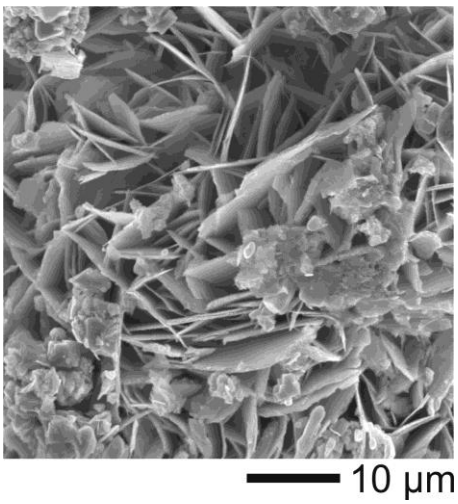

Figure 1. SEM image of the C1 phase showing partially parallel aligned microplates of composition $Cu_{1.3}InS_{2.3}$

Figure 2. ED image of the C2 phase showing multiple sets of reflexes of one zone rotated to each other indicating rotated layers

Nanoparticles, Nanostructured Materials, Catalysts

MS6.P164
The role of spatial resolved electron energy lost spectroscopy for the investigation of the mechanism of nanoparticle generation by laser irradiation in liquids

C. Schaumberg[1], M. Wollgarten[2], K. Rademann[1]

[1]Humboldt-Universität zu Berlin, Department of Chemistry, Berlin, Germany
[2]Helmholtz-Zentrum Berlin für Materialien und Energie GmbH, Institut Nanoarchitekturen für die Energieumwandlung, Berlin, Germany

christian.schaumberg@chemie.hu-berlin.de

Pulsed laser ablation in liquids (PLAL) and pulsed laser fragmentation in liquids (PLFL) have proved to be efficient routes to surfactant-free colloidal nanoparticles. Unfortunately little is known about the formation mechanisms of these particles. Investigations on some copper containing precursors revealed a major changes in the chemical composition during the laser irradiation while in other cases the chemical composition is preserved.[1,2] In order to get a deeper insights in the involved processes a thorough study of the generated nanoparticles is essential. Analytical transmission electron microscopy is hereby the most elegant approach to get information of the chemical composition on the nanometer scale.

In particular, we report on electron energy loss spectroscopy (EELS) measurements at the copper $L_{2,3}$ edge for the synthesized materials. For oxidized copper atoms the 3d orbitals are not completely filled. This gives rise to white lines in the EEL spectra as electrons may be exited from 2p orbitals to empty 3d orbitals. The strength of this effect varies with the electron density at the copper atoms.[3] Thus, it becomes feasible to determine the oxidation state of the copper atoms with good spatial resolution. Further information about the chemical environment of the copper atoms is revealed by measuring and modeling the electron loss near edge spectra (ELNES). These findings are complemented by elemental mappings obtained by energy filtered transmission electron microscopy (EFTEM) leading to new concepts for the underling mechanisms of PLAL and PLFL.

1. C. A. Schaumberg, M. Wollgarten, K. Rademann, J. Phys. Chem., 2014, 118 (37), 8329-8337.
2. C. A. Schaumberg, M. Wollgarten, K. Rademann, PCCP, submitted.
3. D. Shindo, K. Hiraga, A.-P. Tsai, A. Chiba, J. Electron Microsc., 42, 48-50 (1993).

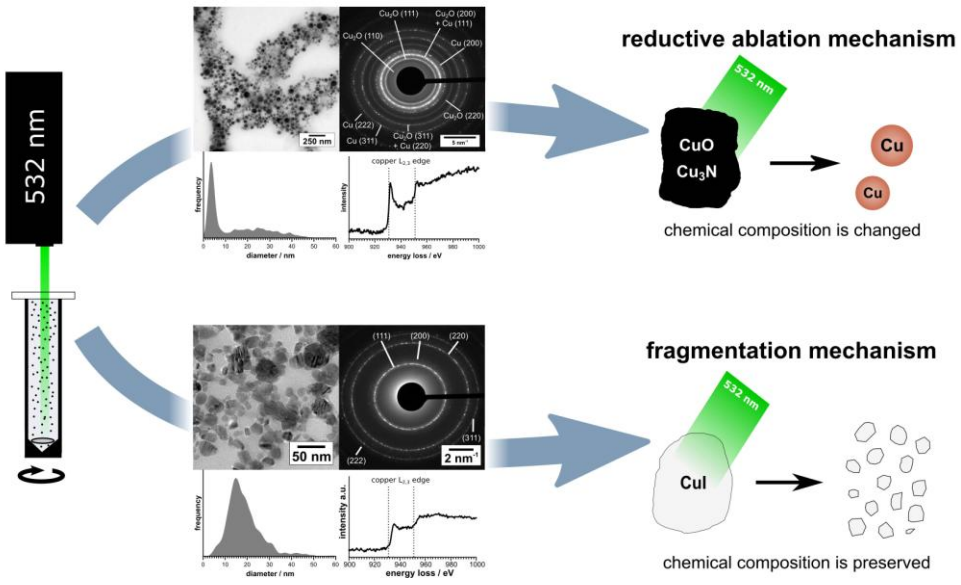

Nanoparticles, Nanostructured Materials, Catalysts

MS6.P165
Atomic-resolution TEM and spectroscopic investigations of indium gallium zinc oxide and indium iron zinc oxide nanowires

G. Schaan[1], H. K. Schmid[1,2], W. Mader[1]

[1]Rheinische Friedrich-Wilhelms-Universität Bonn, Institute of Inorganic Chemistry, Bonn, Germany
[2]JEOL GmbH, Eching bei München, Germany

gschaan@uni-bonn.de

Materials based on zinc oxide with additions of other metal oxides offer a broad range of applications such as varistors, transparent conducting oxides (TCOs), gas sensors and dye-sensitized solar cells. They have good semiconducting and optical properties at low costs and abundant availability.[1] In order to fully comprehend the physical properties of these materials, it is crucial to gain an understanding of the atomic arrangement and the formation mechanisms of their unique structural features: i.e. basal and pyramidal inversion domain boundaries (IDBs). Specifically, we aim to trace the process of distribution of different atomic species among these two IDBs.

ZnO nanowires (NWs) were grown on fused silica substrates by thermal evaporation utilizing a metal-seeded growth mechanism.[2] Doping the NWs with indium and gallium or iron was performed by spin-coating with solutions of indium nitrate and gallium nitrate or iron(III) acetylacetonate, respectively, in 2-methoxyethanol. For thermal decomposition of the solution droplets and subsequent reaction of the various oxide particles at the ZnO NW surface, the specimen was annealed inside a furnace at atmospheric conditions.

Conventional TEM bright field imaging was conducted in a Philips/FEI CM30 T microscope. High-angle annular dark-field (HAADF) and bright-field (BF) STEM imaging at high resolution as well as EELS and EDX spectroscopic imaging were performed using an advanced analytical TEM/STEM system (JEOL JEM-ARM 200CF equipped with a cold FEG and probe C_s corrector).[3]

The above-mentioned synthesis method yields ZnO NWs of different growth directions, among others. Conversion of these NWs to IGZO NWs proceeds quickly and throughout the entire structure (Fig.1). HAADF imaging reveals single-layer slabs of atomic columns with brighter Z contrast separated by domains with lower Z contrast and varying widths of 2 to 5 layers. Spatially-resolved EDS analysis proves these features correspond with In-decorated basal IDBs and ZnO domains containing Ga, respectively. 1D linescans perpendicular to the IDBs reveal only a slight intensity maximum for Ga close to the center of each domain. Furthermore, EELS analysis shows higher relative Ga concentration in domains consisting of only 2 layers (Fig. 2). This indicates that Ga is distributed almost evenly among all atomic layers inside a specific wurtzite domain. A mean chemical formula of $InGaO_3(ZnO)_3$ as estimated from the width of wurtzite-structure domains between basal IDBs corresponds well with quantitative EDS measurements.

The formation of IFZO is possible as well, but does not proceed as readily as in the case of IGZO. The overall relative contents of In and Fe are lower, and thus the nanostructures are more sparsely permeated with basal IDBs (Fig. 3). In sufficiently wide ZnO domains, Fe is not distributed evenly among all layers, but instead the cations form zigzag-shaped pyramidal IDBs spanning the entire domain. EDS elemental distribution maps reveal that In occupies octahedral sites in basal IDBs exclusively, while tetrahedral or trigonal-bipyramidal sites are decorated only with Fe and Zn (Fig. 4). Thus, both cations occupy those sites most suitable for them although the structure is not in thermodynamic equilibrium.

We conclude that both trivalent cations react with the ZnO NW where the basal IDB meets the surface. From there, the basal IDB grows into the bulk of the NW at a linear rate, while also constantly delivering dopant cations towards the root of the pyramidal IDB connected to its tip.

1. D. P. Norton *et al.*, *Mater. Today* **6** (2004), 34-40.
2. H. Simon, T. Krekeler, G. Schaan, W. Mader, *Cryst. Growth Des.* **13** (2013), 572-580.
3. H. Schmid, E. Okunishi. W. Mader, *Ultramicrosc.* **127** (2013) 76-84

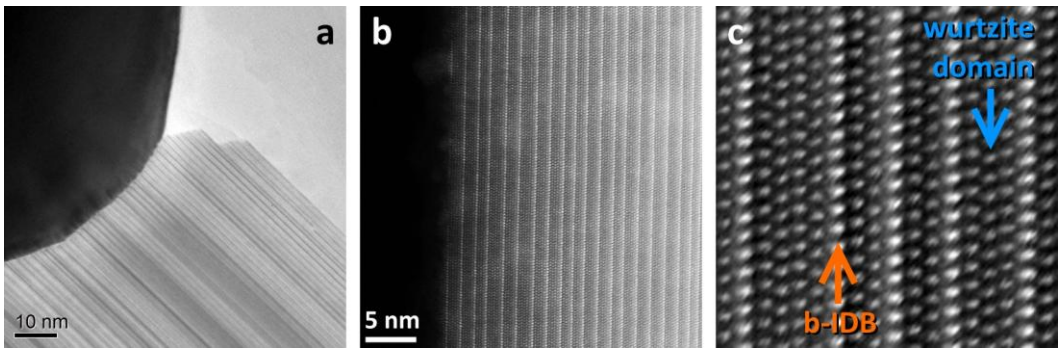

Figure 1. Conventional TEM BF (a) and HAADF-STEM (b, c) images of an IGZO nanowire in [2-1-10] orientation.

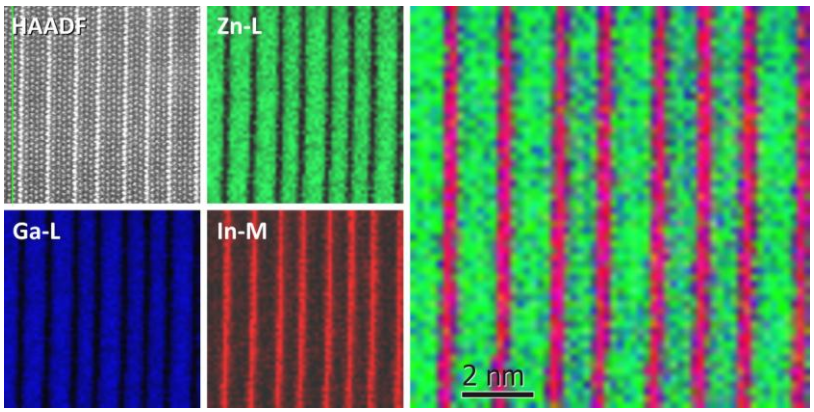

Figure 2. EELS elemental distribution maps and RGB overlay image of an IGZO nanowire.

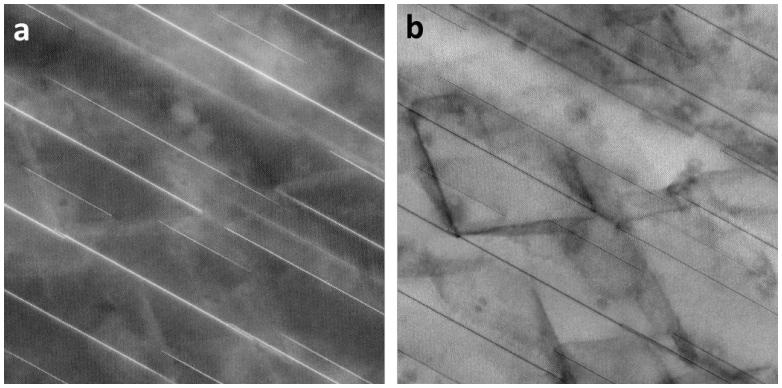

Figure 3. HAADF (a) and BF (b) STEM images of an IFZO nanowire in [2-1-10] orientation.

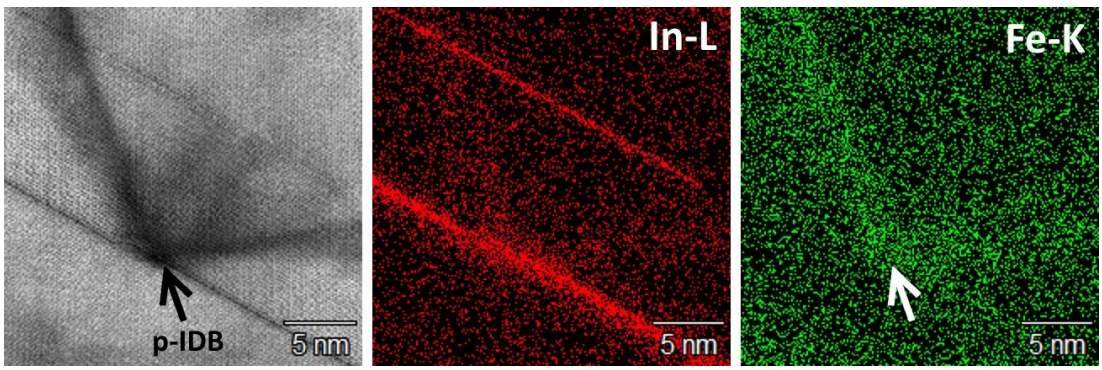

Figure 4. EDS-SIX elemental distribution maps of an IFZO nanowire.

Nanoparticles, Nanostructured Materials, Catalysts

MS6.P166
TEM study on hydrothermally synthesized $(SnO_2)_x(ZnO)_{1-x}$ powders

P. Kaya[1], I. G. Tuncolu[1], C. Aciksari[1], E. Suvaci[1], E. Özel[1], S. Rembeza[2], E. S. Rembeza[2], Y. Plotnikova[2], N. Kosheleva[2], S. Turan[1]

[1]Anadolu University, Material Science & Engineering, Eskisehir, Turkey
[2]Voronezh State Technical University, Department of Semiconductor Electronics and Nanoelectronics, Voronezh, Russian Federation

pkayamse@gmail.com

Transparent conductive oxides (TCO) are unusual materials that are not only electrically conductive but also optically transparent [1]. In recent years, TCO layers, based on doped and undoped ZnO and SnO_2, are technologically important thanks to their high visible transparency and good electrical conductivity. SnO_2, an n-type semiconductor with a direct band gap of 3.6-4 eV [2], is capable of emitting light when excited with suitable input energy. It has high exciton binding energy of 130 meV [3] and high thermal stability [4]. ZnO, another versatile n-type semiconductor has direct band gap (3.37 eV) and large exciton binding energy (60 meV) [5]. It is a well known fact that the TCO films have been widely used as transparent electrodes in various devices which include liquid crystal displays, solar cells, flat panel displays and LEDS. Transparent conducting materials are currently available in the marketplace such as indium tin oxide. Despite the rising cost and limited availability, the development of cheaper and more accessible films, such as doped SnO_2, is in high demand. In the present work, ZnO and SnO_2 powders were successfully synthesized with hydrothermal synthesis. ZnO powders were synthesized from the hydrous zinc nitrate ($Zn(NO_3)_4.6H_2O$) with ammonium hydroxide (NH_4OH) at pH 8.4 by hydrothermal synthesis at 100°C, 3 hours while SnO_2 powders were synthesized at 200°C from hydrous tin oxide, which was prepared by direct strike precipitation of $SnCl_4$ solution by adding NH_4OH solution at pH 9. Average primary particle size of agglomerated SnO_2 powder measured from transmission electron microscopy (TEM) image was about 3 nm (Fig. 1). On the other hand, average particle size of ZnO powder revealed from scanning transmission electron microscopy (STEM) image was about 4-6 µm in length (Fig. 2). In this study, formation mechanism of the synthesized powders is explained according to the TEM analyses.

1.Wager, J. F. (2003). Transparent electronics. *Science*, *300*(5623), 1245-1246.
2. A.Y. El-Etre, S.M. Reda, Characterization of nanocrystalline SnO2 thin film fabricated by electrodeposition method for dyesensitized solar cell application, Appl. Surf. Sci. 256 (2010) 6601-6606.
3. Sivasankar Reddy, N.M. Figueiredo, A. Cavaleiro, Nanocrystalline Au:Ag:SnO2 films prepared by pulsed magnetron sputtering, J. Phys. Chem. Solids 74 (2013) 825-829.
4. R. Anandhi, K. Ravichandran, R. Mohan, Conductivity enhancement of Zno: F thin films by the deposition of SnO2:F over layers for optoelectronic applications, Mater. Sci. Eng., B 178 (2013) 65-70.
5. K. Saravanakumar, B. Sakthivel, K. Ravichandran, Simultaneous doping of aluminum and fluorine on zinc oxide nanopowders using a low-cost soft chemical route, Mater. Lett. 65 (2011) 2278-2280.

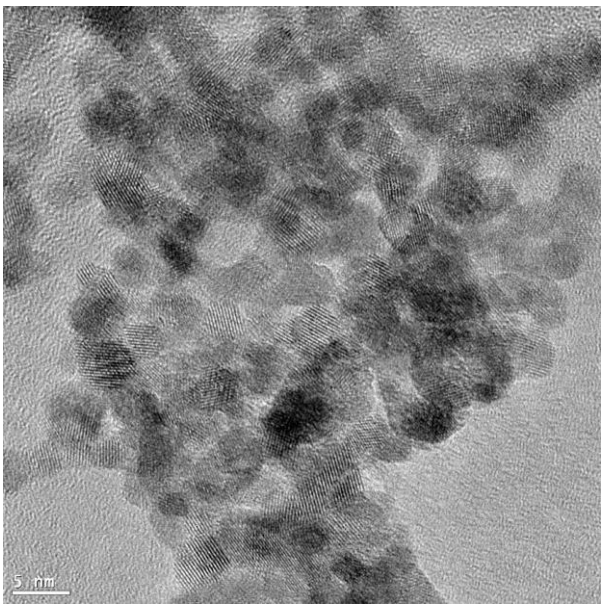

Figure 1. TEM image of SnO_2 powder

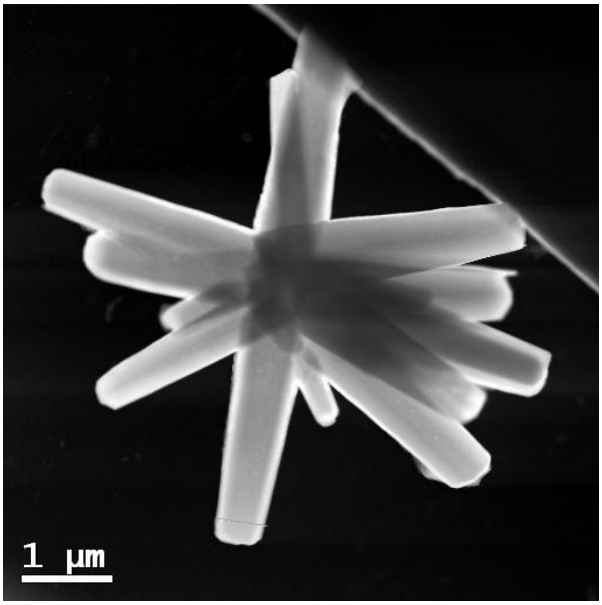

Figure 2. STEM-ADF image of ZnO powder

Nanoparticles, Nanostructured Materials, Catalysts

MS6.P167
Towards type-selective SWCNTs growth: comparative study on characterization techniques for an effective CVD process development

S. Motaragheb Jafarpour[1], M. Kini[1], S. Hermann[1], S. E.Schulz[1,2]

[1]Chemnitz University of Technology, Center for Microtechnologies, Chemnitz, Germany
[2]Fraunhofer Institute for Electronic Nano Systems, 09107 Chemnitz, Germany, Germany

saeed.jafarpour@zfm.tu-chemnitz.de

For direct integration of CVD grown SWCNTs in applications like FETs, it is of crucial importance to know the quality and composition of the material. Unfortunately for more advanced CVD process exploiting for instance multi-catalyst systems, it is in general a very time consuming procedure to access important details like content of amorphous or sp2/sp3 carbon as well as semiconducting to metallic ratio or even chiral distribution.

In search of an effective characterization method for CVD process developments, we performed a comparative study using several characterization techniques to investigate purity, structure and type of CVD grown vertically aligned SWCNTs (VA-SWCNTs). Therefore microscopic techniques such as AFM, SEM, and TEM as well as spectroscopic techniques like XPS, TGA, Raman spectroscopy and UV-Vis absorption spectroscopy were used. The advantage and disadvantage of these characterization techniques are balanced and a multi-technique approach is suggested to achieve a fast and reliable access to the essential information.

Nanoparticles, Nanostructured Materials, Catalysts

MS6.P168
In-situ structural characterisation of 2D nanomaterials incorporated into bioengineered materials

C. Hobbs[1], V. Nicolosi[1]

[1]CRANN, School of Physics, Trinity College Dublin, Dublin, Ireland

hobbsc@tcd.ie

This study uses the techniques of scanning electron microscopy (SEM) and transmission electron microscopy (TEM/STEM) to characterize gene-nanomaterial hybrids and assess their ability to be employed as non-viral delivery vectors. In addition, SEM and TEM characterize functional collagen-based scaffolds.

This study analyses the properties of nanohydroxyapatite (nHA) and layered double hydroxides (LDH) materials that can be used as non-viral gene delivery vectors. The former is a biocompatible, non-toxic calcium phosphate mineral which makes it a suitable candidate as a delivery platform[1]. On the other hand, LDHs are composed of brucite-like layers with a charge compensating anionic interlayer[2]. SEM and TEM provide an in-depth insight into how DNA structures interact with nano-materials and how they form hybrids for enhanced gene and drug delivery.

In addition, collagen-based scaffolds are functional implant materials capable of interacting with both stem cells and the immune system enabling tissue regeneration. The inclusion of nanomaterials such as nHA into collagen-based scaffolds result in a biocompatible structure which is osteoconductive, osteoinductive and mechanically superior[1]. Thus, it is required to characterize how these nanomaterials are physically and chemically patterned in the implant materials.

Fig. 1 presents the nHA images obtained using TEM. The nHA particles are found to have a spherical structure of diameter ~50nm. This result indicates that nHA is a good candidate for cellular transfection and further characterizes their potential use as a gene delivery vector. The current work of this study investigates how these nHA particles interact with DNA structures.

In relation to the Layered Double Hydroxides, both the SEM and TEM images present a well-defined hexagonal platelet-like structure of ~100nm, as presented in Fig. 2 and Fig.3. The size and layered structure of the LDHs provide promising results that they can be used as potential gene delivery vectors in relation to cellular transfection. Similarly, ongoing work of this study examines the recrystallization of LDH over time, including in-situ TEM analysis. In addition, DNA structures complexed to the layered structures will be studied using the techniques of STEM and diffraction studies.
The current study also presents TEM data of collagen fibrils, as seen in Fig. 4. The collagen fibrils were found to have a diameter of ~300nm. In addition, the collagen banding formation is evidently portrayed using TEM analysis.

Future work of this study aims to use the techniques of STEM, diffraction and electron energy loss spectroscopy (EELS) to characterize the patterning of these nanomaterials throughout the fibrils. This will ultimately lead to a further understanding of the enhanced features of these collagen-based scaffolds.

The use of SEM and TEM to characterize gene delivery vectors can provide further information to that of optical microscopy such as particle structure of complexes, gene-delivery efficacy and collagen-nanomaterial interaction. Also, it is evident that TEM techniques provide an accurate method of analysing collagen fibril structure. Furthermore, the techniques and applications of this study offer a demonstration of the overlap between materials science and the life sciences, and how they can be beneficial to both respective fields of research.

1. Curtin *et. al*, *Adv. Mater*. , **2012**, *24*, 749-754.
2. Xue Bi *et. al*, *Pharmaceutics*, **2014**, *6*, 298-332.
3. Shoulders *et. al*, Annu Rev Biochem, **2009**, *78*, 929-958.

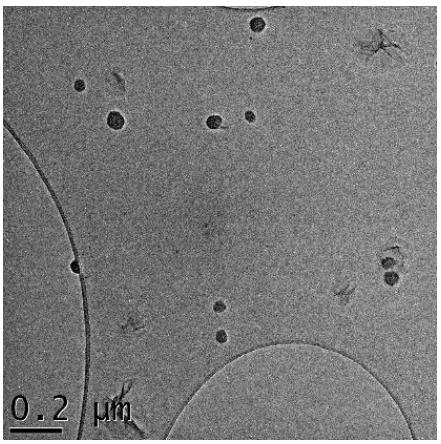
0.2 µm

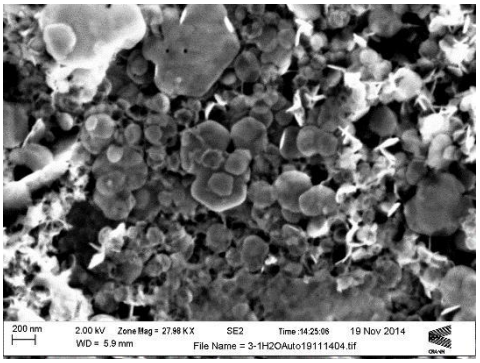
200 nm
2.00 kV Zone Mag = 27.98 K X SE2 Time :14:25:06 19 Nov 2014
WD = 5.9 mm
File Name = 3-1H2OAuto19111404.tif

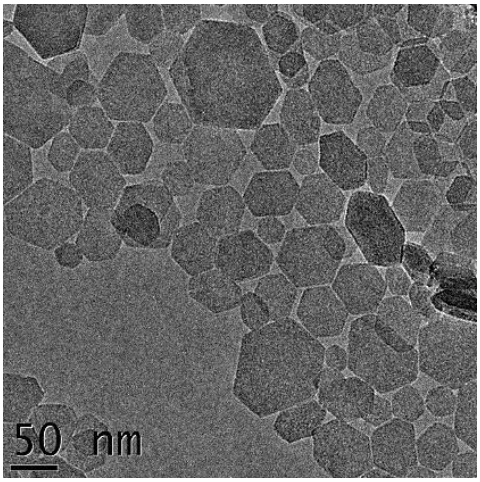
50 nm

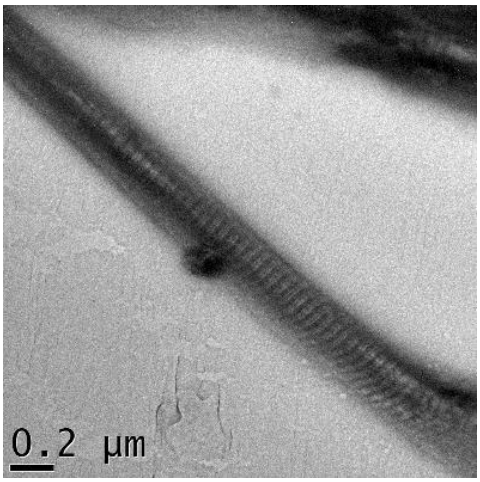
0.2 µm

Nanoparticles, Nanostructured Materials, Catalysts

MS6.P169
Micellar aggregates and immune stimulatingComplex (iscom) matrices from saponins of horse chestnut seeds

S. Schönfeldt[1], M. Rohde[2], C. C. Müller-Goymann[1]

[1]Institut für Pharmazeutische Technologie, Technische Universität Braunschweig, Braunschweig, Germany
[2]Helmholtz Centre for Infection Research, HZI, Central Facility for Microscopy, Braunschweig, Germany

s.schoenfeldt@tu-bs.de

For the first time, immune stimulating complexes (ISCOMs) have been described by Morein et al. in 1984 [1]. ISCOMs are nanoparticulate structures composed of Quillaja saponin (Quil A), cholesterol (Chol) and phospholipids (PC). Loaded with an antigen, ISCOMs showed immune stimulating properties. The complex is used as a vaccine adjuvant in order to induce a stronger immune response and longer protection. The key component of ISCOMs is the saponin Quil A, which has two hydrophilic parts and a lipophilic one. A lot of triterpenoid saponins form organized spherical structures (micelles) in aqueous solutions and intricate micellar aggregates [2]. Demana et al. presented a pseudo-ternary phase diagram of aqueous mixtures of Quil A, cholesterol and phospholipid with the percentage distribution of particulate structures [3].

Horse chestnut seeds contain 3 to 10 % triterpenoid saponins. The saponin extract contains more than 30 saponins referred to aescin or *β*-escin and has anti-inflammatory, vaso-constrictive and vaso-protective effects [4]. Aescin is an amphiphilic molecule that contains a hydrophilic (sugar components) and a lipophilic part (aglycon, Figure 1, left). In aqueous solutions, the formation of micelles (aescin micelles) was observed by transmission electron microscopy (TEM, Figure 2A). The aim of our study was to elucidate the effects of aescin on liposomal phosphatidylcholine/cholesterol dispersions. The specific stoichiometric mass ratio of the pseudo-ternary phase diagram of aqueous mixtures of Aescin:Chol:PC 6:2:2 is displayed in Figure 1, right.

The structural features of the resulting aggregates were determined by TEM. In this system, cage-like ISCOM matrices, α-helical matrices, ring-like and worm-like micelles were observed. Ring-like micelles (Figure 2B) revealed various sizes. The outer diameter varied from 15 nm up to 50 nm with an inner diameter from 2 nm up to 20 nm. Worm-like micelles had a width between 6 nm and 15 nm, whereas their size differed greatly with regard to single micelles and agglomerates thereof (Figure 2C). The α-helical matrix is one of the most stable natural conformations and includes a lot of worm-like micelles (Figure 2D). The length of the helices mainly depends on the number of interacting worm-like micelles, however, the width is equal. Different cage-like structures of the ISCOM matrices were determined: so-called tennis ball structure and icosahedron stump so-called football structure. The tennis ball structure is a geometric body with 20 surfaces, i.e., 12 equilateral, regular pentagons and 8 regular hexagons [5]. Four hexagons are connected with each other and are surrounded by twelve pentagons. In rectangular orientation to this arrangement, another row of four hexagons surrounded by pentagons arises. Every pentagon shares two edges with another pentagon and three edges with a hexagon. The football structure is a polyhedron consisting of a total of 32 surfaces, i.e., 12 equilateral, regular pentagons and 20 regular hexagons. Every pentagon is isolated and in each case five hexagons form a ring. The size of the ISCOM matrices were calculated based on the data of small-angle x-ray scattering by Pedersen et al. The outer diameters for the tennis balls are 38.1 ± 0.3 nm and for footballs 48.6 ± 0.4 nm [5].

The size of the present structures with aescin depends on the projection and ranges from 40 to 65 nm. The dominating structure is the football structure (Figures 2E, 2F).

Finally we confirm the interaction of saponins with cholesterol and phopholipids from liposomes as the major step for the formation of ISCOM matrices. Furthermore aescin was identified as a new key component of ISCOMs.

1. Morien, B. et al.: *Nature* **1984**,308: 457-460.
2. Chapagain, B.P., Wiesmann, Z.: *J Agric Food Chem* **2006**,54: 6277-6285.
3. Demana, P.H. et al.: *Int. J. Pharm.* **2004**,270: 229-239.
4. Sitori, C.R.: *Pharmacol. Res.* **2001**,44: 183-193.
5. Pedersen, J.S. et al.: *Biophysical J* **2012**,102: 2372-2380.

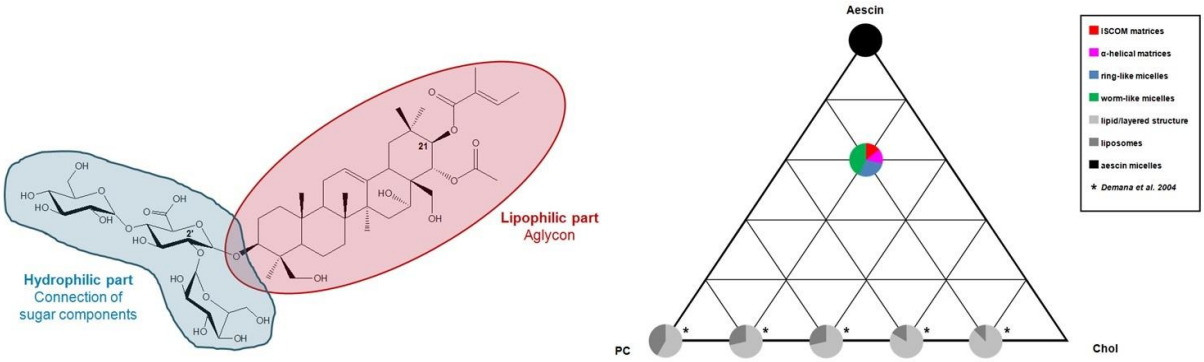

Figure 1. Aescin Ia ($C_{55}H_{86}O_{24}$, exact mass: 1130,55; *left*) and pseudo-ternary phase diagram of aqueous mixtures of aescin, cholesterol and phospholipid (*right*)

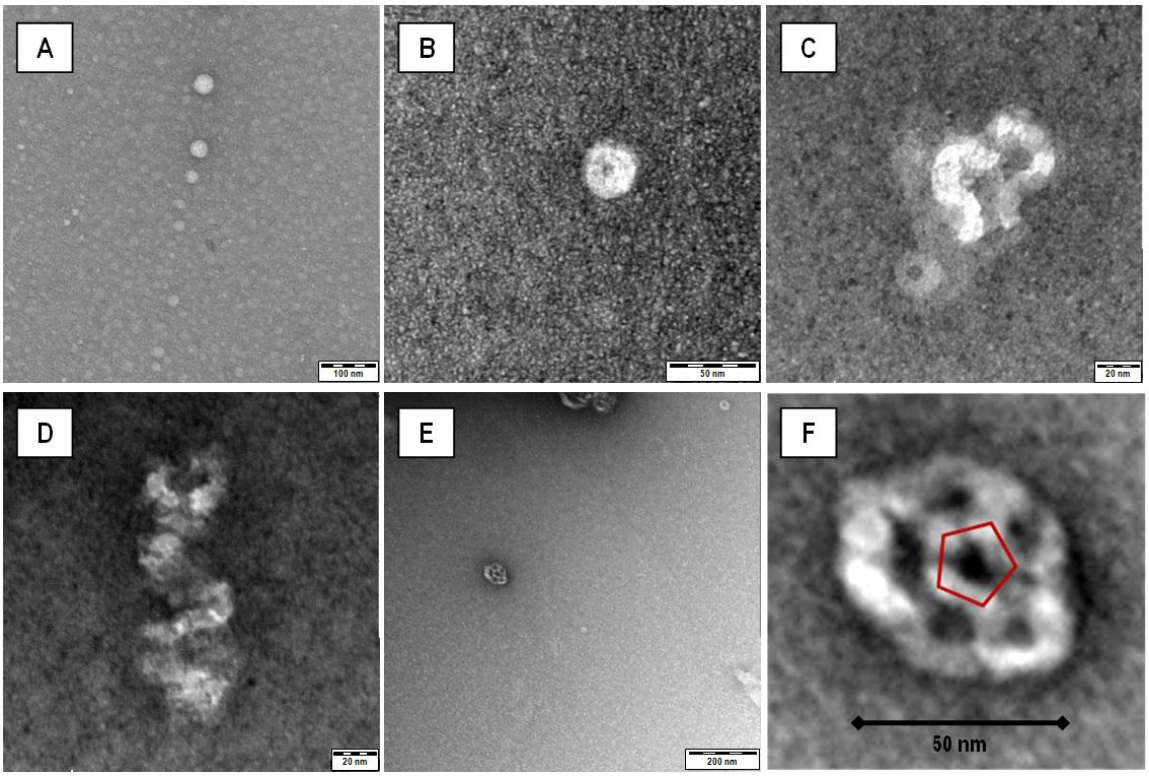

Figure 2. Transmission electron micrographs. Aescin micelles (A), ring-like micelles (B), worm-like micelles (C),α-helical matrices (D) and ISCOM matrices (E,F)

Nanoparticles, Nanostructured Materials, Catalysts

MS6.P170
Development of novel multimodal imaging probes and related methods for cellular labeling and tracking

E. Özliseli[1], S. Tadayon[2,3], D. Desai[2,1], N. Prabhakar[1,4], T. Gulin-Sarfraz[2,1], E. von Haartman[2,1], J. Teuho[3], J. Rosenholm[2,1]

[1]Åbo Akademi, Pharmaceutical Sciences Laboratory, Faculty of Science and Engineering, Turku, Finland
[2]Åbo Akademi, Laboratory of Physical Chemistry, Faculty of Science and Engineering, Turku, Finland
[3]University of Turku, Turku PET Centre, Turku, Finland
[4]University of Turku, Laboratory of Biophysics, Cell Biology and Anatomy, Turku, Finland

ezgi.ozliseli@abo.fi

Nanomedicine is one of the most active research areas in nanotechnology, where nanoparticles have been used for the prevention, diagnosis and treatment of diseases. The use of nanotechnology in medicine especially for drug delivery and cancer therapy has become widespread in recent years. At present, current technologies for tumor imaging are not efficient to acquire high-resolution images for evaluation of tumors at the microscopic level. Therefore, novel imaging probes developed based on nanoparticles offer highly efficient outcomes [3].

Multi-modal imaging which combines two or more imaging techniques has gained more attention recently in cancer diagnosis and treatment. Several imaging techniques have been developed to distinguish the disease such as such as computer tomography (CT), magnetic resonance imaging (MRI), ultrasound imaging, positron emission tomography (PET) and optical imaging. Nevertheless, none of them is efficient by itself without supportive information of other modality. Therefore, multimodal imaging presents a better understanding with taking advantages of different imaging modalities together [1,2].

In this project, nanoparticles with multi-modal imaging properties had been developed and evaluated for their ability to monitor cancer cells on cellular level with high resolution. CAM model was used for this purpose as *in vivo* model and cell viability and cellular uptake (i.e. cellular labeling efficiency) of fluorescent dye loaded mesoporous silica nanoparticles (MSNs), nanodiamond-mesoporous silica composites and MSN-based MRI contrast agents were evaluated for their feasibility as imaging probes. Pre-labelled MDA-MB-231 human breast cancer cells with nanoprobes were imaged with Stereo Microscopy, Confocal Microscopy and IVIS (*in vivo* imaging techniques) to track metastasis; and samples prepared in the same manner were scanned with MRI to attain accurate, detailed multimodal images.

1. Baker, M., 2010. Whole-animal imaging: The whole picture. Nature 463: 977-980.
2. Hellebust, A., Richards-Kortum, R. 2012. Advances in molecular imaging: targeted optical contrast agents for cancer diagnostics. Nanomedicine 7(3): 429-445.
3. Salata, O.V. 2004. Applications of nanoparticles in biology and medicine. Journal of Nanobiotechnology 2(3).

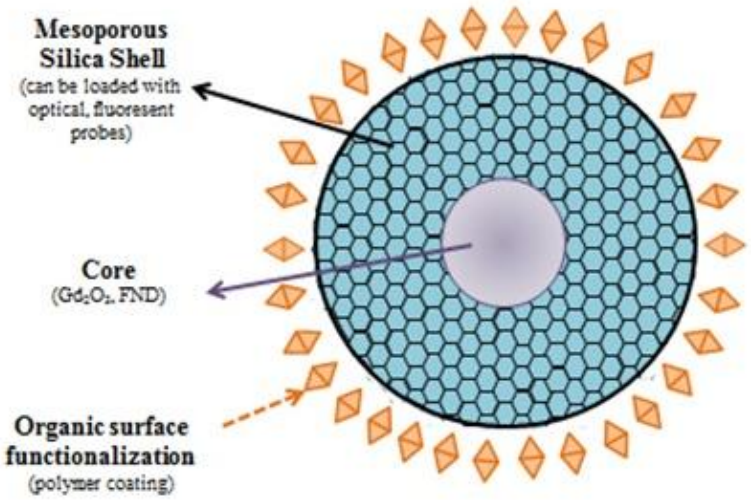

Figure 1. Schematic representation of a mesoporous silica core-shell design with a core exhibiting the imaging activity and a porous silica shell which can further carry molecular imaging probes.

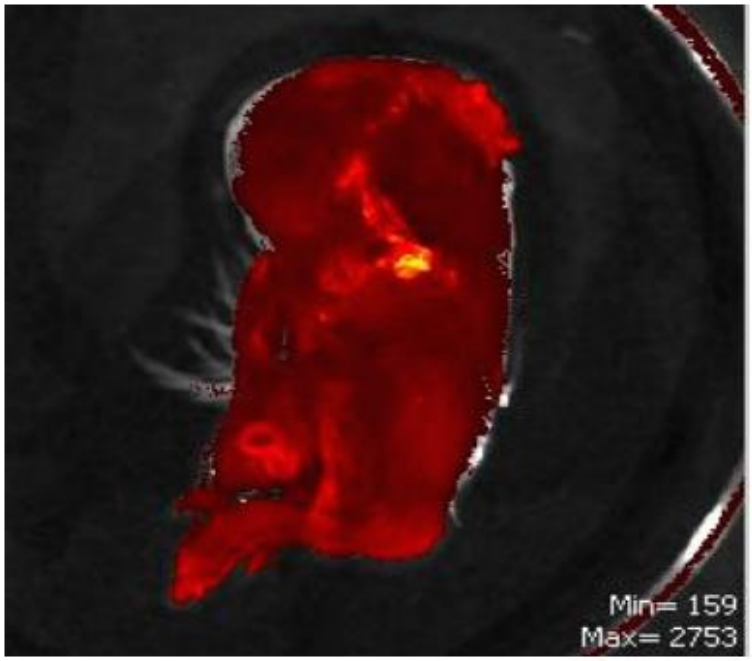

Figure 2. in vivo fluorescence imaging of chicken embryo incubated with cancer cells which are labeled with MSN:DiI. Bright spot shows the migration and subsequently accumulation of cells within the body.

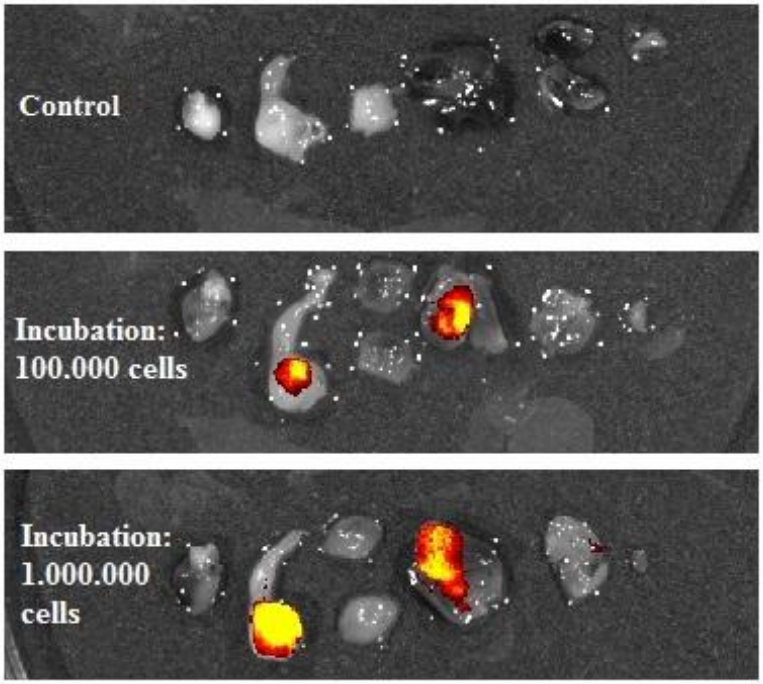

Figure 3. ex vitvo fluorescence image revealing metastasized cells labelled with nanoparticles and implanted on chicken embryo. Organs from left to the right: heart, intestine, lungs, liver, kidneys and spleen.

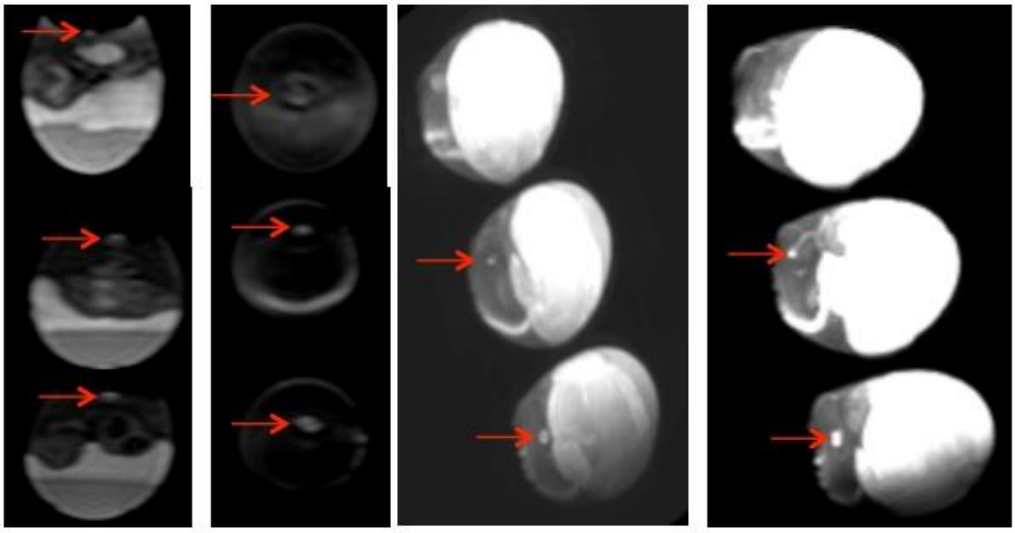

Figure 4. MRI of post-labelled with MSN:Gd(aca)3 in CAM model. Images were acquired by human MRI scanner. MSN:Gd(aca)3 was administrated on top of tumors. From top to bottom: Post-labelled 1X which received 30 µl of 5 mg/ml suspension of contrast agents one day prior to MRI and post-labelled 2X which received 30 µl of 5 mg/ml suspension of contrast agents two and one days prior consecutively.

Ceramics, Composites, Geomaterials, Archaeology

MS7.171
Electron microscopic investigation of hydrothermally grown rutile nanowires

A. Wisnet[1], S. B. Betzler[1], A. Folger[2], A. Frank[2], C. Scheu[2]

[1]Department of Chemistry, Ludwig-Maximilians-University, Munich, Germany
[2]Max-Planck-Institut für Eisenforschung GmbH, Düsseldorf, Germany

scheu@mpie.de
Keywords: TiO_2, hydrothermal growth, defects

TiO_2 is a semiconducting oxide which can be used in many applications such as paint, dental paste, watersplitting devices or in photovoltaics [1]. In many of these applications, nanostructured TiO_2 is used as it offers a high surface area and resulting in a high interface area when combined with other materials. The band gap depends on the crystal modification and amounts to ~3.0 eV for rutile and 3.2 eV for anatase. The opto-electronic properties are further influenced by the crystal size and defects.

In our work we have chosen a hydrothermal processing route to grow TiO_2 nanowires on fluorine-doped tin oxide substrates. Their morphology was studied by scanning electron microscopy and transmission electron microscopy. Analysis of the crystal structure and atomic arrangement was done by electron diffraction and high resolution S/TEM studies. The chemical composition was investigated by energy-dispersive X-ray spectroscopy and electron energy-loss spectroscopy.

The nanowires crystallize in the rutile modification and possess a facetted morphology with the main facets being the {110} facets [2]. The growth is parallel to the <001> direction with a truncated growth front formed by {111} and {001} facets. The nanowires have a single crystalline bottom, but with ongoing crystal growth planar defects occur which form the starting point of a defect cascade causing a finger-like structuring of the nanowire top (Figure 1). This is most likely caused by steric hindrance and electrostatic repulsion at the {001} facets [2]. Heating experiments performed at elevated temperatures revealed that the fingers at the nanowire top can be removed, but voids are formed within the nanowire interior as observed in electron tomography. However, when applied in nanostructured solar cells these voids have comparable little negative effect on the transport properties compared to the fingers [3].

1. X. Chen, S. S. Mao, Chem. Rev. 2007, 107, 2891.
2. A. Wisnet, S. B. Betzler, R. V. Zucker, J. A. Dorman, P. Wagatha, S. Matich, E.Okunishi, L. Schmidt-Mende, C. Scheu, Cryst. Growth Des., 2014, 14(9), 4658.
3. A. Wisnet, K. Bader, S. B. Betzler, M. Handloser, J. Weickert, A. Hartschuh, L. Schmidt-Mende, C. Scheu, J. A. Dorman., Adv. Funct. Mater. 2015, doi: 10.1002 /adfm.201404010.

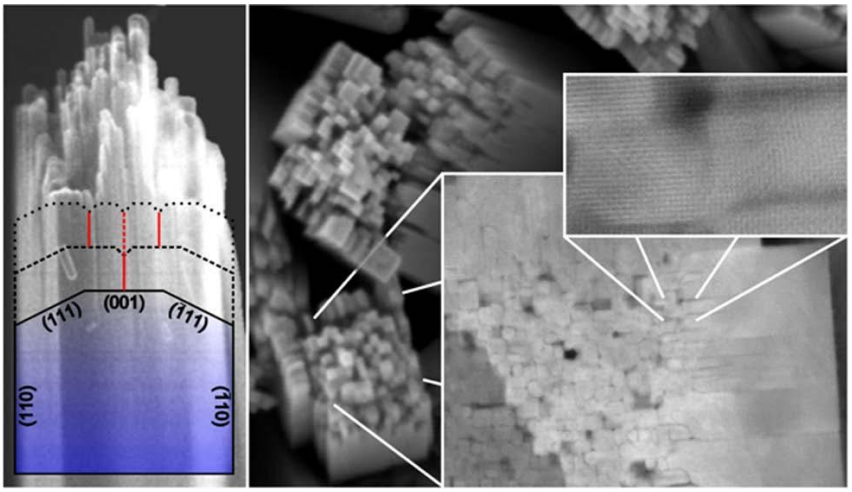

Figure 1. Electron microscopic investigation of hydrothermally grown rutile nanowires: Secondary electron STEM image (left), top-view SEM image (middle), cross-section STEM images (right). Figure taken from [2].

Ceramics, Composites, Geomaterials, Archaeology

MS7.172
Crystallization of glasses explored by cutting-edge TEM

C. Patzig[1], A. de Pablos-Martín[1], T. Höche[1]

[1]Fraunhofer IWM, Halle, Germany

thomas.hoeche@iwmh.fraunhofer.de

Glass-ceramics, i.e. glasses that underwent a controlled crystallization, are present in many areas of life, including zero-thermo-expansion cooktops, advanced telescopes, lasing and up-conversion materials. Their properties depend critically on tailoring their micro- and nanostructure. In order to pursue knowledge-based materials developments, an in-depth understanding of nucleation and crystallization mechanisms is crucial and among other techniques, cutting-edge TEM is capable of gaining deep insights.

In particular, nucleation and growth of crystals in non-isochemical systems, i.e. the precipitation of crystals with a composition different from the surrounding glassy matrix, is of high importance for understanding of the micro- and nanostructure of technically important glass ceramics. In particular, the spatial distribution of elements not incorporated in the growing crystal is of major importance.

Exemplified by numerous glass-ceramics examples ranging from lithia aluminosilicate (LAS), magnesium aluminosilicate (MAS), to oxyfluoride systems, non-isochemical precipitation is studied by EDXS mapping, nanodiffraction, ELNES analyses (in conjunction with spatially averaging XANES), and HRTEM / HRSTEM imaging.

One example will concern glasses of the composition 51.9 SiO_2·21.2 MgO·21.2 Al_2O_3·5.7 ZrO_2 that are exposed to a heat treatment in a two-step annealing process at 950° C and 1060° C. Upon annealing, volume crystallization results in high-strength glass-ceramics with a-quartz solid solution as main crystal phase and ZrO_2 and $MgAl_2O_4$ as secondary crystal phases (Fig. 1)[1,2]. Adding 2.5 mol% Y_2O_3 to the otherwise unaltered glass composition and applying the same heat-treatment scheme alters the course of crystallization totally (Fig. 2)[3,4]. In that case, no quartz or quartz solid solution at all is precipitating during devitrification of the glasses. Instead, only ZrO_2 as primary and $MgAl_2O_4$ as secondary crystal phases are found, whereas the residual glass becomes drastically enriched in Y_2O_3. Despite the total absence of quartz or quartz solid solution phases in the latter glass-ceramics, it was observed that the same annealing-induced increase in bending strength appears for both sample sets, suggesting that the existence of quartz in magnesium-alumosilicate glass-ceramics is not a prerequisite for excellent mechanical properties thereof. Based on a thorough characterisation of microstructural evolution, strengthening mechanisms for both sets of glass-ceramics will be discussed.

It will be demonstrated that advanced sample preparation routes along with TEM investigations of the spatial distribution of majority elements in glass-ceramics, nano diffraction, and spatially resolved ELNES helps understanding nucleation and crystal growth mechanisms in this important group of materials.

1. C. Patzig, Th. Höche, M. Dittmer, C. Rüssel, *Cryst. Growth Des.* **12(4)** (2012), 1556-1563.
2. C. Patzig, M. Krause, Th. Höche, M. Dittmer, A. Gawronski, C. Rüssel, Y. Hu, H. Ikeno, I. Tanaka, and G. Henderson, *J. Non-Cryst. Solids*, **384** (2014) 47-54.
3. A. Gawronski, C. Patzig, T. Höche and C. Rüssel*, CrystEngComm* **15** (2013), 6165-6176.
4. A. Gawronski, C. Rüssel, C. Patzig, and Th. Höche, *J. Mater. Sci.* ***50(4)*** (2015), 1986-1995.
5. This work was/is funded by the German Science Foundation, DFG, under contracts HO 1691/5-1 and HO 1691/6-1.

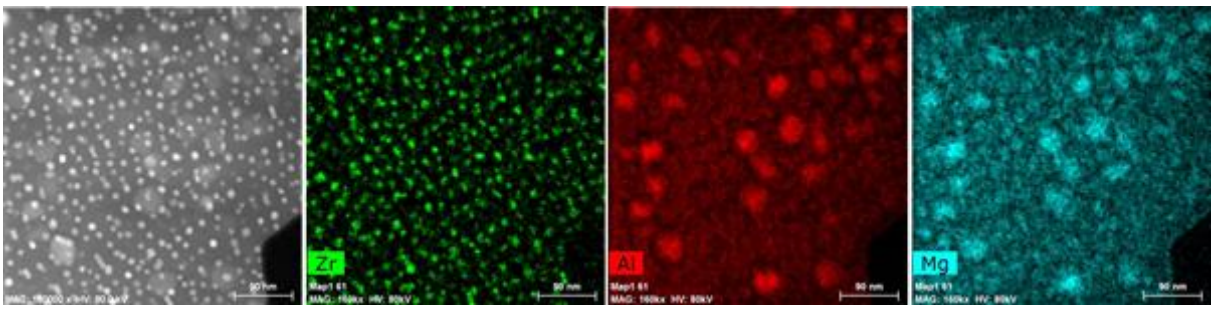

Figure 1. Energy-dispersive X-Ray maps (acquired in an FEI TITAN³ G2 80-300 equipped with a SuperX EDXS system) of an Y_2O_3-free, quartz-precipitating magnesium-alumosilicate glass-ceramics, showing the precipitation of spinel (Al-purple) from stuffed quartz solid solution grown on star-shaped ZrO_2 nucleation crystals.

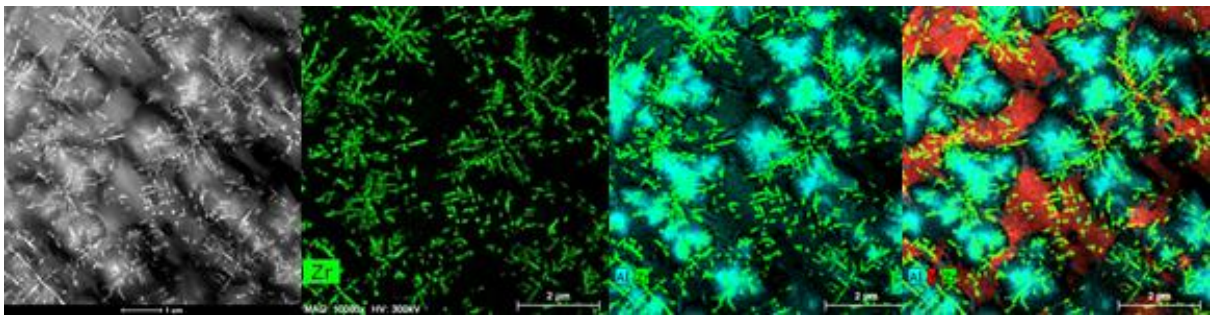

Figure 2. Energy-dispersive X-Ray maps of an Y_2O_3-containing, quartz-free magnesium-alumosilicate glass-ceramics, showing the growth of spinel (Al-purple) upon ZrO_2 (Zr-green), and the enrichment of Y_2O_3 in the residual glass (Y-red).

Ceramics, Composites, Geomaterials, Archaeology

MS7.173
Striking high iron enrichment in hard dental tissues of rodents inspected by analytical (S)TEM

V. Srot[1], U. Salzberger[1], B. Bussmann[1], B. Pokorny[2,3], I. Jelenko[2], P. A. van Aken[1]

[1]MPI for Solid State Research, Stuttgart Center for Electron Microscopy, Stuttgart, Germany
[2]ERICo Velenje, Ecological Research and Industrial Cooperation, Velenje, Slovenia
[3]Environmental Protection College, Velenje, Slovenia

v.srot@fkf.mpg.de

Biominerals produced by living organisms appear to be very diverse in composition and structure. Many of these biominerals are highly complex composite materials with superior physical and mechanical properties [1,2] that cannot be imitated in the laboratory. Unique masterpiece architectures, where organic matrix and inorganic crystalline or amorphous minerals are linked together are formed under conditions of moderate temperature, pressure and pH.

Rodents possess continuously growing opposing long pairs of incisors that are worn down by gnawing. The front surface of the incisors is enamel consisting of 96 wt% of inorganic material. The innermost part is softer dentine that forms the bulk of the teeth [3]. The surface of incisors of different rodent species shows characteristic orange-brown color and is identified with the presence of iron [4]. Based on electron microprobe analysis of the enamel surface of rat´s enamel, amount of iron (Fe) is 10-30 wt% [5].

In our study, the microstructure and the chemical composition of incisors of the feral coypu (*Myocastor coypus* Molina) were investigated in detail by using energy-dispersive X-ray spectroscopy (EDX) and electron energy-loss spectroscopy (EELS) combined with scanning transmission electron microscopy (STEM) imaging at high spatial as well as high energy resolution using VG HB501UX, Zeiss SESAM and JEOL ARM200F microscopes.

The layer with a variable thickness was uncovered on the outer surface of incisors which was not reported before in rodent teeth. According to our EDX and EELS investigations the outer surface layer is highly enriched in iron (Fe), with much higher concentration levels as reported in the literature. A bright-field (BF)-TEM image acquired from the interface between the Fe-rich surface layer (Fe-SL) and Fe-rich enamel (Fe-E) is shown in Figure 1a. Energy-filtered TEM (EFTEM) maps formed using the calcium (Ca) and iron (Fe) signals are shown in Figure 1b, yielding a relatively rough interface between Fe-E and Fe-SL. An annular dark field (ADF)-STEM image displaying the interface between Fe-SL and Fe-E is shown in Figure 2a. Within Fe-SL we surprisingly detected multiple iron-containing varieties. Studies of the electronic structure suggest that Fe is present in predominantly 3+ valence state. O-K energy-loss near-edge structures (ELNES) acquired from different positions within the Fe-SL suggests the presence of different intermixing levels between Fe phosphates and Fe oxide/hydroxide (Figure 2b). The function and incorporation of iron in many living organisms is still not unambiguously understood despite of wide occurrence of iron in nature. Our discoveries will greatly enhance the understanding and function of Fe in hard dental tissues at the nanometer-scale level.

1. U.G.K. Wegst and M.F. Ashby: Phil. Mag. **84** (2004) 2167
2. A.P. Jackson and J.F.V. Vincent: J. Mater. Sci. **25** (1990) 3173
3. B.A. Niemec in *Small animal dental, oral & maxillofacial disease*. Manson Publishing Ltd, London, (2010).
4. E.V. Pindborg, J.J. Pindborg, and C.M. Plum: Acta Pharmacol. **2** (1946) 294
5. A. Halse: Archs Oral Biol. **19** (1974) 7

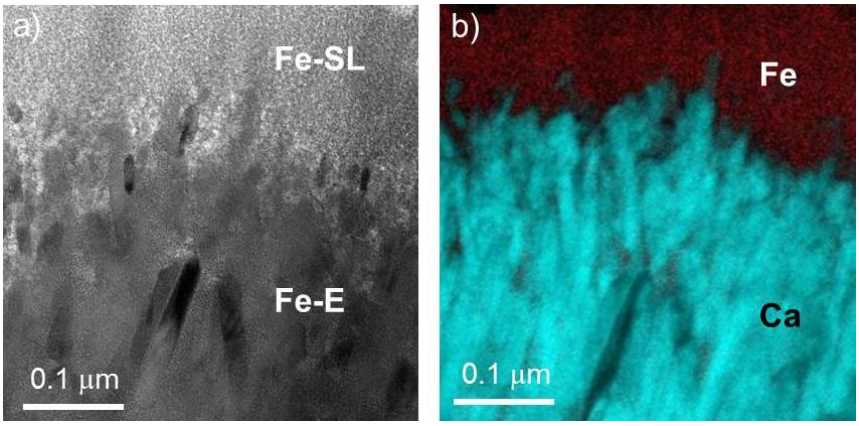

Figure 1. (a) BF-TEM image of a rough interface between Fe-SL and Fe-E. (b) Calcium (Ca) and iron (Fe) EFTEM maps to distinguish between Fe-SL and Fe-E, respectively.

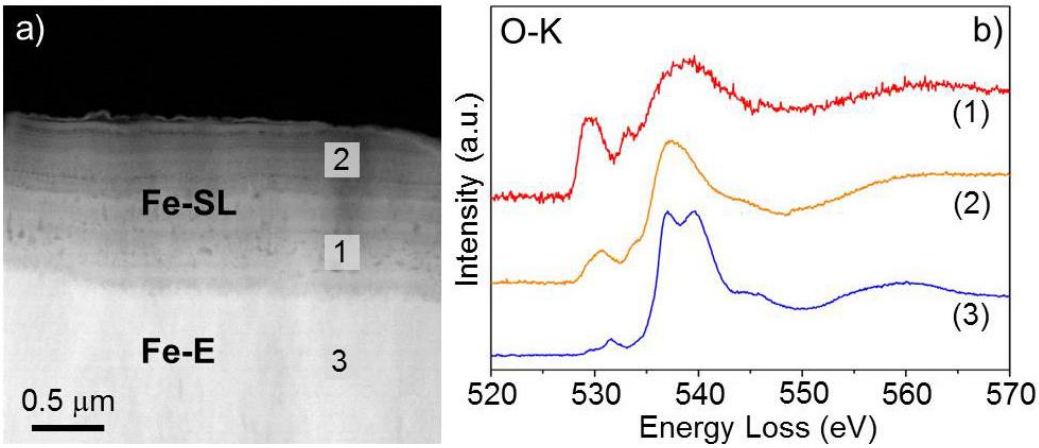

Figure 2. (a) ADF-STEM image of the interface between Fe-SL and Fe-E. (b) O-K edges acquired from positions within the Fe-SL and Fe-E indicated in (a).

Ceramics, Composites, Geomaterials, Archaeology

MS7.174
Atomic-scale characterization of interfaces in rutile/hematite intergrowths from Mwinilunga, Zambia

N. Daneu[1], N. Stankovic[1], A. Recnik[1]

[1]Jožef Stefan Institute, Department for Nanostructured Materials, Ljubljana, Slovenia

nina.daneu@ijs.si

Rutile/hematite intergrowths from Mwinilunga in Zambia are composed of up to several-centimeter-large euhedral hematite crystals covered by epitaxially grown reticulated rutile networks. The samples were studied down to the subnanometer-scale in order to resolve the complex sequence of topotaxial reactions that led to their formation (Rečnik et al. 2015). A simple morphological analysis indicated that rutile and hematite are met near the $_R\{101\}_R||_H\{110\}_H$ law, leading to 12 possible directions of rutile exsolution within a hematite matrix, where the c-axes of the rutile lamellae are tilted for ±2.78° from the $_H$ directions in hematite. Such orientation relationship results in 144 different incidences between the intergrown rutile crystals. All potential rutile-rutile interfaces can be classified into four categories: (1) non-crystallographic contacts at 60° and 120°, (2) {101} twin boundaries (TB) with incidence angles of 114.44° and their complementaries at 65.56°, (3) {301} TB at 54.44° with complementaries at 125.56° and (4) low-angle tilt boundaries at 174.44° and 5.56°. Except for the non-crystallographic contacts, all other rutile-rutile interfaces were confirmed in the Mwinilunga samples. Figure 1 shows five rutile lamellae exsoluted from the matrix in five different orientations and impinging at four contacts: two low-angle tilt boundaries (R1|R2 and R3|R4)), (101) TB (R6|R3) and (301) TB (R3|R2). Figure 2 shows a low-angle tilt boundary between two rutile domains, driven by topotaxial relation $\{170\}_H||\{401\}_R$. Small angular misfit between the rutiles is compensated by regular edge dislocations along the contact. In the perpendicular orientation, $[100]_H$, hematite host shows remnants of ilmenite lamellae in the vicinity of rutile exsolutions (Figure 3), an important indication of the high-T formation of the primary ferrian-ilmenite crystals. Another type of exsolution process was observed within the rutile, characterized by tripling the {101} rutile reflections (Figure 4). Unlike rutile exsolutions in hematite, hematite exsolutions in rutile form $\{301\}_R||\{030\}_H$ equilibrium interfaces due to a lower exsolution temperature. Bulk composition of our samples indicates that the ratio between ilmenite and hematite in parent ferrian-ilmenite crystals was close to $Ilm_{67}Hem_{33}$, typical for Fe-Ti rich differentiates of mafic magma (1050-1150°C). The presence of ilmenite lamellae indicates that the primary solid solution passed the miscibility gap at ~900 °C. Subsequent exsolution processes were triggered by surface oxidation of ferrous iron and remobilization of cations within the common oxygen sublattice. Based on nanostructural analysis of the samples, we identified three successive processes: (1) exsolution of ilmenite lamellae from the primary ferrian-ilmenite crystals (~900°C), (2) exsolution of rutile lamellae from ilmenite (~740°C) and (3) exsolution of hematite lamellae from supersaturated Fe-rich rutile, which served for diffusion of ferrous iron to the surface (<600°C). All observed topotaxial reactions are function of temperature and oxygen fugacity.

1. Rečnik, A., Stanković, N. and Daneu, N.: Topotaxial reactions during the genesis of oriented rutile/hematite intergrowths from Mwinilunga (Zambia). Contr Min Petr (2015) 169: 19.

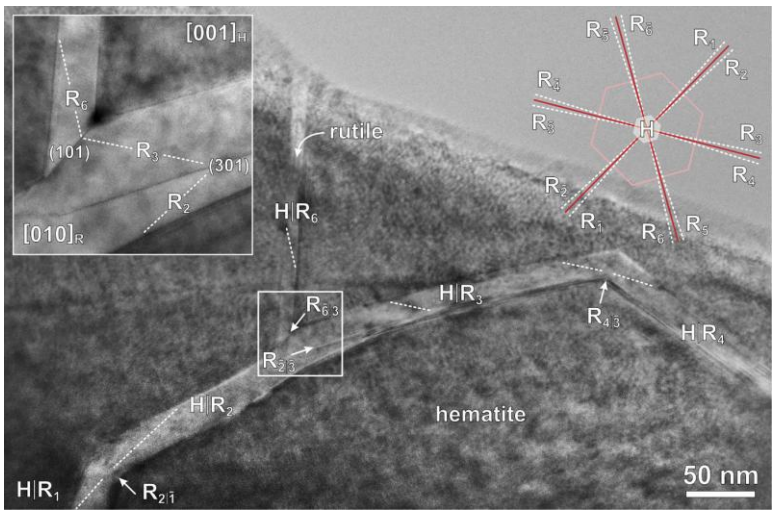

Figure 1. TEM image of rutile lamellae exsoluted in five orientations within hematite. The inset is a close-up of the two crystallographic-contacts, (101) and (301) TB.

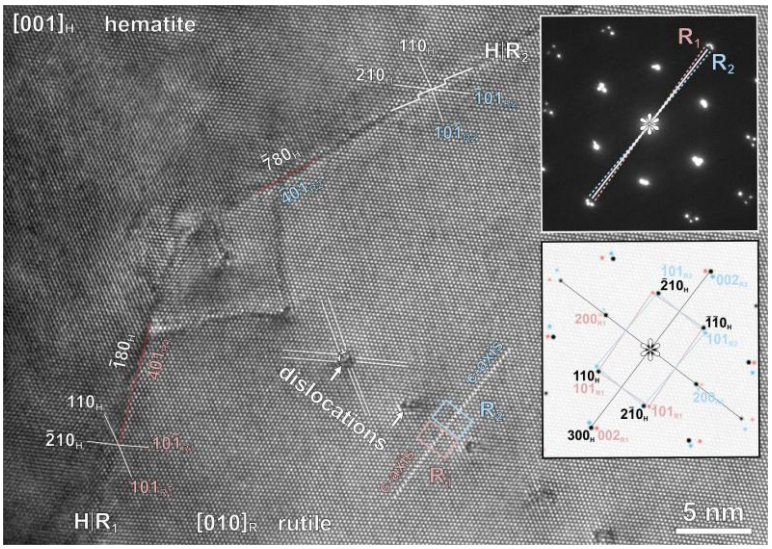

Figure 2. Structural analysis of a low-angle tilt boundary between two ruile domains and the rutile/hematite interface with the.

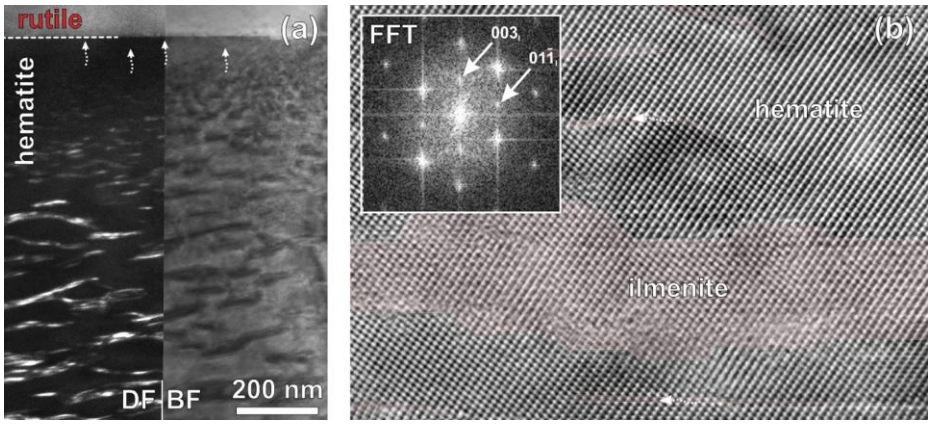

Figure 3. (a) DF/BF composite image of lens-shaped nanosized ilmenite precipitates. (b) HRTEM image of an ilmenite precipitate showing characteristic additional $(003)_I$ ilmenite reflections in the FFT pattern.

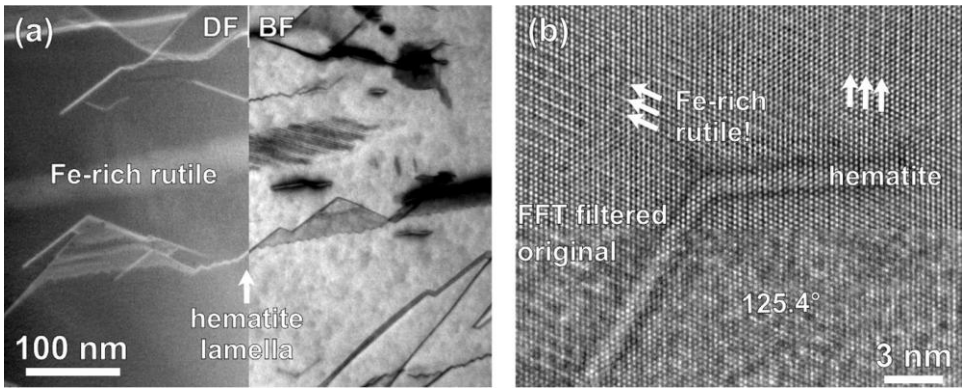

Figure 4. (a) DF/BF composite image of Fe-rich (hematite) exsolutions within rutile lamellae. (b) HRTEM image of hematite exsolution in rutile.

Ceramics, Composites, Geomaterials, Archaeology

MS7.175
Aberration corrected (S)TEM analysis of {001} platelets in natural diamond

J. Olivier[1], J. Neethling[1], M. Naidoo[2], T. Kroon[3]

[1] Centre for High Resolution Transmission Electron Microscopy, Port Elizabeth, South Africa
[2]University of the Witwatersrand, Materials Research Institute, DST-NRF Centre of Excellence in Strong Materials and School of Physics, Johannesburg, South Africa
[3]University of the Free State, Physics department, Bloemfontein, South Africa

jolivier@nmmu.ac.za

The exact nature and atomic structure of type {001} platelets in diamond is still largely unknown[1]. The platelets found in type Ia natural diamonds are known to contain nitrogen as impurity with electron energy loss spectroscopy (EELS) measurements indicating that the nitrogen content varies from between 6% to 61% of a monolayer in the platelet[1]. An early model of the platelet proposed that it consists of a double layer of nitrogen atoms[2]. Subsequently this model was substituted for a model containing a double layer of carbon atoms[3]. Later an asymmetry in the structure of the platelet as viewed along different <110> directions were observed experimentally which complicated matters further[4].

The generally accepted formation mechanism for the platelet is that of an interstitial aggregate process. However a recently proposed model by Miranda and co-workers suggests a microscopic structure of the platelets which is formed by a shearing process[1]. The model by Miranda et al. shows an atomic structure at the core of the platelet defect as a double layer of threefold coordinated sp^2 carbon atoms embedded in the sp^3 diamond matrix[1]. The model seems compelling as its structure would be different as viewed along different <110> type directions and according to the authors would be an energetically favourable mechanism of formation. However it has been met with contention due to its implications relating to the geo-history of type Ia natural diamonds.

This paper presents results from an atomic resolution (S)TEM and EELS study of the platelets. (S)TEM lamella was prepared using a FEI Helios Nanolab 650 focused ion beam (FIB) SEM. The prepared lamella was subsequently investigated in a double Cs-corrected JEOL JEM-ARM200F equipped with a GATAN Quantum Image Filter and operated at 200 kV.

Figure 1 shows a typical HAADF STEM image of a {001} platelet in the diamond as viewed edge on. Figure 2 shows an EEL spectrum obtained from the platelet confirming the presence of N. The HAADF STEM image of the platelet gives a clear indication of atomic positions which can be used to determine the platelet structure. An asymmetry in the platelet structure when viewed along two perpendicular <110> directions was also found. Results of an EELS spectrum imaging analysis across the platelet will be presented. This was done, as shown in Figure 2, to determine the presence and concentration of nitrogen within the platelet as well as to investigate the C-C bonding state across the platelet using the near edge fine structure of the C K-edge. The results found were in favour of an interstitial aggregate process of formation.

1. Miranda, C.R., Antonelli, A. and Nunes, R.W. (2004) Phys. Rev. Lett.93, 265502.
2. Lang, A.R. (1964) Proc. Phys. Soc. London,84, 871.
3. Humble, P. (1982) Proc. R. Soc. London, A381, 65.
4. Bruley, J. (1992) Phil. Mag. Lett.66, 47.
5. Neethling, J.H. *et al.* (2012) Proc. Microsc. Soc. South. Afr.42, 65.
6. Goss, J.P. *et al.* (2003) Phys. Rev. B67, 165208

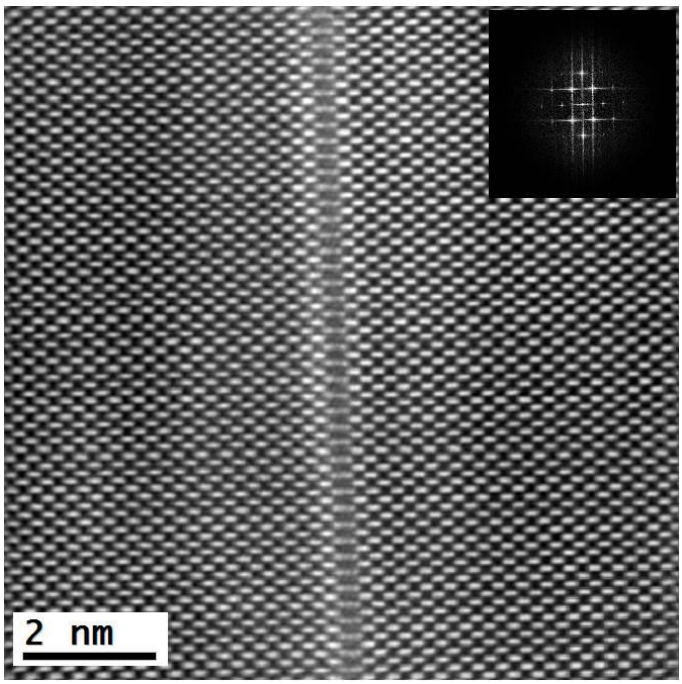

Figure 1. HAADF STEM micrograph of a platelet on the {001} plane of diamond viewed edge-on

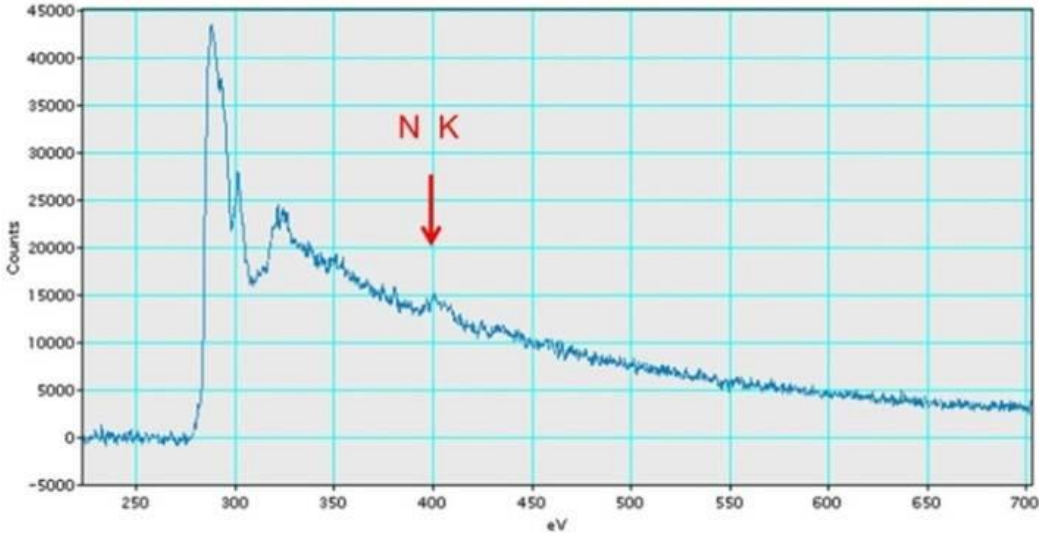

Figure 2. Electron energy loss spectrum showing the presence of N in the platelet

Ceramics, Composites, Geomaterials, Archaeology

MS7.176
Atomic structure and chemistry of dislocation cores at low-angle tilt grainboundary in $SrTiO_3$ bicrystals

H. Du[1,2], C.- L. Jia[1,3], L. Houben[1,3], V. Metlenko[4], R. A. De Souza[4], R. Waser[3,5], J. Mayer[1,2]

[1]Research Centre Juelich GmbH, Ernst Ruska-Centre for Microscopy and Spectroscopy with Electrons, Juelich, Germany
[2]RWTH Aachen University, Central Facility for Electron Microscopy (GFE), Aachen, Germany
[3]Research Centre Juelich GmbH, Peter Grünberg Institute, Juelich, Germany
[4]RWTH Aachen University, Institute of Physical Chemistry, Aachen, Germany
[5]RWTH Aachen University, Institute of Materials for Electrical Engineering, Aachen, Germany

h.du@fz-juelich.de

Dislocations in perovskite oxides have been found to have important impacts on their electronic and ionic transportation properties, which are believed to be related to the structure and chemistry of dislocation cores. For dislocation cores at a 6° low-angle [0 0 1] tilt grain boundaryin $SrTiO_3$, an embedded TiO_x rocksalt-like structure has been suggested [1], consistent with a deficiency of Sr. However, direct evidence supporting these suggestions has not been obtained up to now.

In this work [2], we reveal the atomic structure and chemistry of edge dislocation cores at a low-angle [0 0 1] symmetric tilt-boundary in $SrTiO_3$ bicrystals by imaging techniques of high-angle annular dark-field scanning transmission electron micro-scopy (HAADF-STEM) and electron energy loss spectroscopy (EELS) with an FEI Titan cube^3 60-300 (PICO) microscope operated at 80 kV.

At the tensional side of the dislocation cores, we have found extra HAADF signal peaks appearing at the positions of oxygen columns. By atomic-resolution EELS and EDX spectrum imaging, we have ascertained that these extra HAADF signal peaks are attributed to atomic columns containing Ti. Moreover, we have revealed evident depletion of Sr whereas enrichment of Ti at the tensional side of the dislocation cores, where the ELNES features of the Ti $L_{2,3}$ edge and the O *K* edge indicate a lower valence state of the Ti cations than the normal Ti^{4+}.

Our results provide direct experimental evidence for a local coordination of edge-sharing TiO_6 octahedra at the tensional side of the dislocation cores. The coordination is associated with the FCC TiO phase and its formation at the tensional side of the dislocation cores can be understood as the result of strain. Because the FCC TiO phase consisting of edge-sharing TiO_6 octahedra has a larger lattice constant (0.42 nm) than $SrTiO_3$ (0.39 nm), similarly, in the dislocation core, the formation of edge-sharing TiO_6 octahedra accommodates tensional strain, and thus lowers the system energy.

1. J.P. Buban, M. Chi, D.J. Masiel, J.P. Bradley, B. Jiang, H. Stahlberg, N.D. Browning, *J. Mater. Res.* 24 (**2009**) 2191-2199,
2. H. Du, C.-L. Jia, L. Houben, V. Metlenko, R. A. De Souza, R. Waser, J. Mayer, *Acta Mater.* 89 (**2015**) 344-351
3. This work has been supported by the Deutsche Forschungsgemeinschaft, Germany (SFB 917).

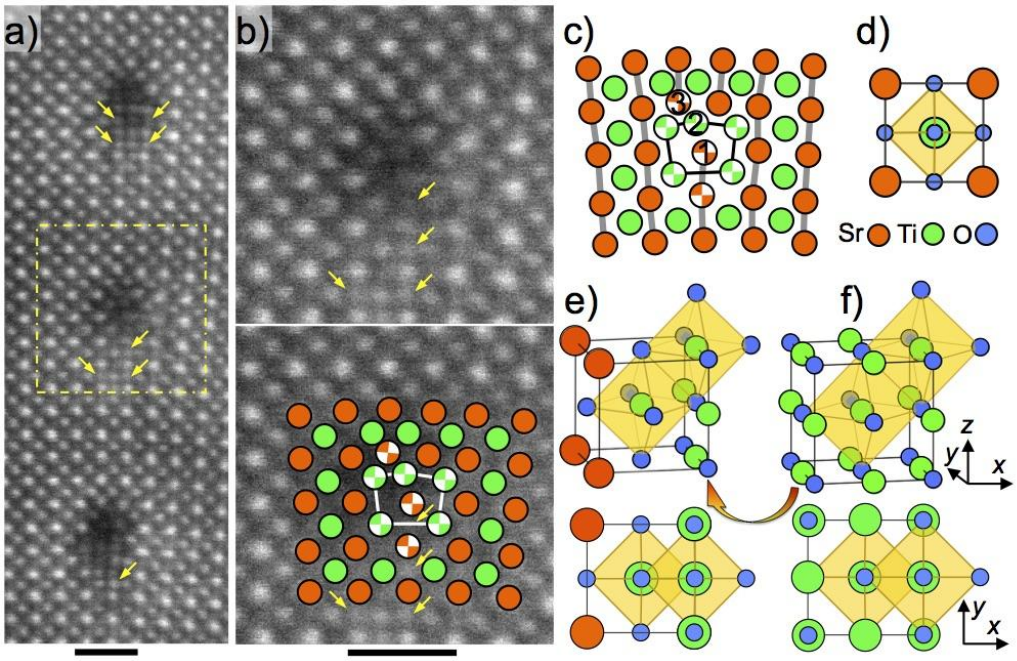

Figure 1. (a) An atomic-resolution HAADF image of three edge dislocation cores acquired at 80 kV acceleration voltage. At the tensional side of the dislocation cores, extra HAADF signal peaks are found at the position of oxygen columns as indicated by arrows. (b) A magnified view of the dislocation core marked by a square in the left panel, from which a simplified atomic model without the extra HAADF peaks was derived. (c) The simplified core-structural model, in which white sectors indicate the possible existence of under-occupancy and intermixing in the columns, and gray lines highlight the dissociation nature of the dislocation. (d) Unit cell of $SrTiO_3$. (e) Structural model associated with the extra HAADF peaks. (f) Unit cell of the FCC TiO. Scale bar: 1.0 nm.

Ceramics, Composites, Geomaterials, Archaeology

MS7.P177
Spinel exsolution from (Mg,Fe)O ferropericlase and habit controlling mechanisms

K. Marquardt[1], S. Jacobsen[2,1], N. Miyajima[1], G. Pearson[3], J. Harris[3]

[1]Universität Bayreuth, Bayerisches Geoinstut, Bayreuth, Germany
[2]Northwestern University, Department of Earth and Planetary Sciences, Evanston, United States
[3]University of Alberta, Department of Earth & Atmospheric Sciences, Alberta, Canada

katharina.marquardt@uni-bayreuth.de

(Mg,Fe)O is of geophysical importance being the second most abundant phase of the Earth's lower mantle. In addition, variously doped MgO is among the most widely used refractory materials employed in numerous high-temperature industrial and technological applications. Periclase (MgO) incorporates significant amounts of alumina at high temperature; below the solvus (~2000°C) $MgAl_2O_4$ spinel exsolves and is usually dispersed within periclase grains or along grain boundaries (Ghosh et al. 2004). In nature, incorporation of various trivalent cations (generally M^{3+} for Al^{3+}, Fe^{3+}, Cr^{3+}) in ferropericlase can lead to exsolution of e.g. magnesioferrite spinel, $(Mg,Fe^{2+})(M^{3+})_2O_4$, with implications for the oxidation state of the mantle (Wirth et al. 2014). The presence of exsolved spinel in (Mg,Fe)O affects the physical properties of the bulk material, e.g. strength (Ghosh et al. 2004). The change of interfaces between exsolved spinel and MgO from coherent to incoherent upon growth exhibits similarities to thin-film-substrate interfaces, where the extent of interfacial stress is compensated by regularly-spaced interface dislocations (Hesse and Senz 2004). With the goal to understand habit forms of exsolving phases, the formation of magnesioferrite precipitates from a natural ferropericlase $(Mg_{.83}Fe_{.17})O$ has been studied by transmission electron microscopy .We observe that areas free of linear defects are generally characterized by 20nm-sized spinel octahedra, evenly distributed in the ferropericlase matrix (Fig.1). However, in the presence of dislocation-like features, the magnesioferrite preferentially nucleates along these features. It appears the final shape of the resulting single-crystal spinels are controlled by pre-existing dislocations, in agreement with observations in another natural sample (Wirth et al. 2014). Linear dislocation features as thin as 10 nm are filled with spinel (Fig.2a-d). These linear features are spatially associated with surface features attributed to deformation. Our observations may explain previously observed exsolution microstructures of needle-like spinels in ferropericlase that form a "tweed" pattern (Otsuka et al. 2013), which we suggest also formed along pre-existing dislocations. We conclude from the habit and shape of spinel in this (Mg,Fe)O that exsolution nucleation sites are defect controlled, as opposed to lattice strain controlled in the defect-free regions or other known exsolution systems, e.g. spinodal decomposition in feldspars (Hartmann et al. 2008). The observation that dislocations act as nucleation sites for spinel exsolution and thus may control needle like growth might be used to control direction and shape of spinels in MgO-based refractories.

1. Ghosh a., Sarkar R, Mukherjee B, Das SK (2004) J Eur Ceram Soc 24:2079-2085.
2. Hartmann K, Wirth R, Markl G (2008) Contrib to Mineral Petrol 156:359-375.
3. Hesse D, Senz S (2004) solid state. 252:252-257.
4. Otsuka K, Longo M, McCammon C a., Karato SI (2013) Earth Planet Sci Lett 365:7-16.
5. Wirth R, Dobrzhinetskaya L, Harte B, et al. (2014) Earth Planet Sci Lett 404:365-375.

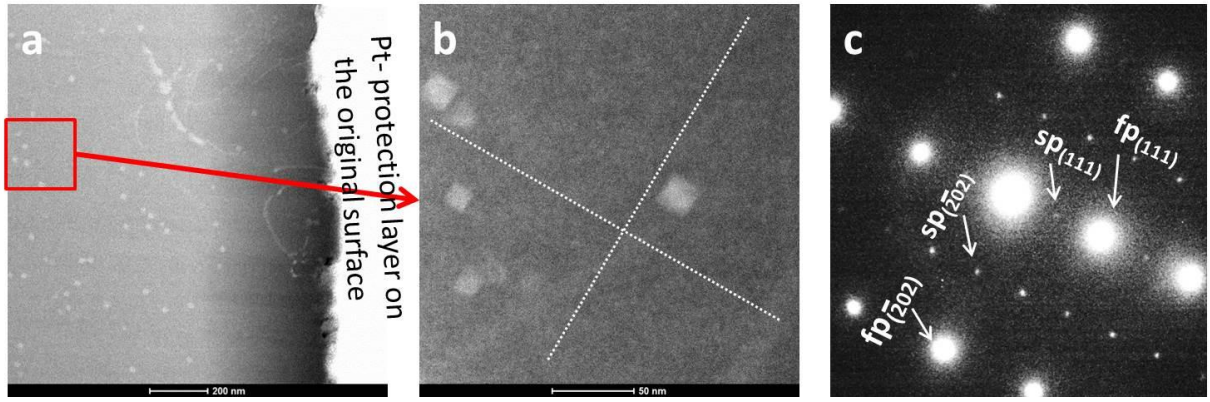

Figure 1. Spatial relation between matrix precipitates of spinel and elongated precipitates of spinel in ferropericlase. a,b) STEM image tuned to give z-contrast. b) Enlargement of the boxed region in a. c) SAD highlighting the intergrowth relation between ferropericlase and spinel.

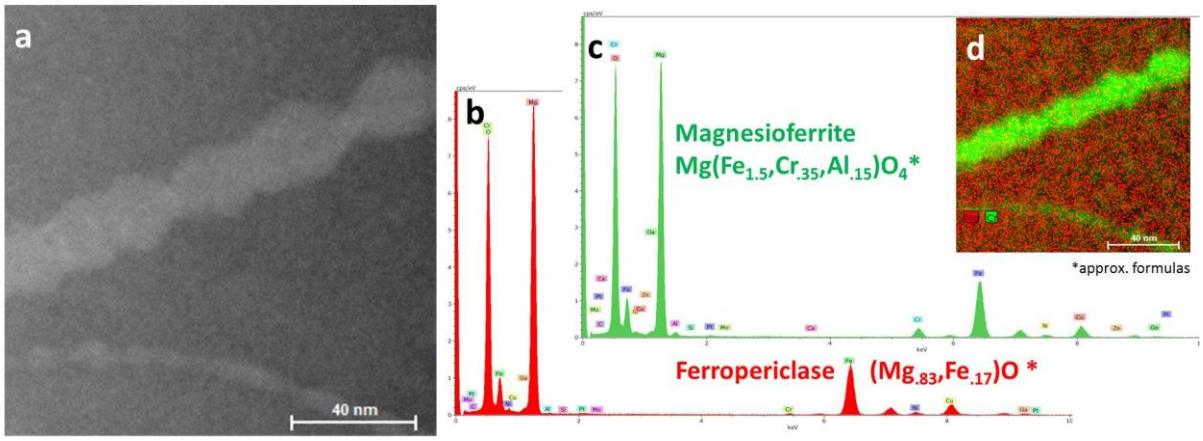

Figure 2. a) STEM image using Z-contrast conditions. The spinel linearly aligned along a 'dislocation like' feature. b) EDX-spectra of the ferropericlase matrix with the approximate composition inserted. c) EDX-spectra of the exsolved magnesioferrite (spinel structure) with the approximate composition inserted. d) EDX-map highlighting the regional distribution of elevated Cr-content (green) with the complementary distribution of Mg (red).

MS7.P178
Dielectric properties and atomic-scale microstructures of the cubic-pyrochlore phase in the system of Bi_2O_3-MgO-Nb_2O_5

X. Zhu[1], Y. Zhang[1], J. Zhu[1], S. Zhou[1], Z. Liu[2]

[1]Nanjing University, School of Physics, Nanjing, China
[2]Nanjing University, Department of Materials Science and Engineering, Nanjing, China

xhzhu@nju.edu.cn

The oxides of the pyrochlore family with general formula $A_2B_2O_7$ are predominantly cubic and ionic in nature, and their structures allow a wide variety of chemical substitution at the A and B sites, therefore, exhibiting a wide spectrum of physical properties such as dielectric, magnetic, optical and catalytic behaviors. There properties are normally controlled by parameters such as ionic sizes, polarizabilities of the ions, electronic configurations. In recent years, the cubic pyrochlore phase in the system of Bi_2O_3-MgO-Nb_2O_5 has been investigated as a promising dielectric material for low-temperature co-fired ceramic multilayered applications and tunable microwave dielectric components. In this work, single-phase pyrochlore-type ceramic samples of $Bi_{1.5}MgNb_{1.5}O_7$ (BMN) in the system of Bi_2O_3-MgO-Nb_2O_5 were synthesized *via* solid-state reactions, and their dielectric properties and microstructures were investigated by dielectric impedance spectroscopy, X-ray diffraction (XRD), Raman spectra, and high-resolution transmission electron microscopy (HRTEM). The dielectric permittivities (up to 1 MHz) were found to be ~ 140 at room temperature, while the dielectric loss tangents were about 0.003 at 100 kHz, respectively. The XRD patterns demonstrated that the synthesized BMN samples had cubic phase pyrochlore-type structure, which was also confirmed by electron diffraction patterns. The lattice parameter (*a*) of the unit cell in BMN wasmeasured to be 10.52 Å,which indicated that the density was about 91.4% of the theoretical one. The vibrational peaks observed in the Raman spectra of BMNsamplesalso confirmed the cubic phase pyrochlore-type structure of the synthesized BMN. The local nanoscale structural information of thesynthesized BMN was revealed by electron diffraction patterns and HRTEM images, and the relationship between the dielectric properties and microstructures is also discussed.

Ceramics, Composites, Geomaterials, Archaeology

MS7.P179
TEM investigations of Nextel™ 610 alumina fibers and of wound highly porous oxide (WHIPOX) ceramic matrix composites (CMCs)

M. Müller[1], J. Mayer[1]

[1]RWTH Aachen University, Central Facility for Electron Microscopy, Aachen, Germany

mueller@gfe.rwth-aachen.de

Oxide ceramics are widely used as structural materials for long-term high-temperature applications in oxidizing atmospheres. Monolithic ceramics are not suitable for many applications due to their brittle fracture behavior. This brittleness can be overcome by fiber reinforcement of ceramics [1]. The so called ceramic matrix composites (CMCs) show pseudoplastic behavior, if the fiber-matrix bonding is relatively weak [1]. If the interfacial bonds between fiber and matrix are strong cracks will go unimpeded through the interfaces which lead to a brittle fracture behavior of the composite [2]. Weak interfacial bonds, in contrast, induce a debonding at the interface which is followed by crack deflection, crack bridging, fiber fracture and/or fiber pullout [2]. These additional energy absorbing phenomena lead to enhanced fracture toughness compared to CMCs with strong interfacial bonds. Weak fiber-matrix-interfaces can be achieved e.g. by porous or low toughness fiber-coatings. A less expensively alternative is the use of a highly porous matrix instead of a dense matrix and a weak-fiber-matrix interphase [3]. In this work CMCs with Nextel™ 610 alumina-fibers (3M, St. Paul, MN) and a porous alumina-matrix, produced at the German Aerospace Center Cologne, so called WHIPOX (wound highly porous oxide) CMCs, were characterized by TEM-methods. The WHIPOX-material was manufactured by filament winding as described in [4]. Besides the sintering temperature also the matrix preparation method was modified. Thin cross sections of WHIPOX-samples embedded in an epoxy-resin and of Nextel™ 610 alumina fibers were prepared by Single or Dual FIB-technique. The lamellae were investigated at FEI Tecnai F20 operated at 200 kV and FEI Titan G2 80-200 CREWELEY which is equipped with a Super-X EDX system. For TEM investigation TEM BF images, HRTEM images, SAD patterns as well as STEM HAADF images, EDX-spectra and -mappings have been acquired experimentally. In addition STEM Tomography has been performed. As an example figure 1 shows a STEM HAADF image of an alumina matrix between two fibers of a WHIPOX CMC sintered at 1200 °C. The investigations have shown the presence of yttria stabilized zirconia (YSZ)-particle within the WHIPOX-matrix which influence the sintering activity. For this reason different WHIPOX-materials were produced, on the one hand without YSZ-particles and on the other hand with intentionally added YSZ-particles, and the resulting matrix-structures have been compared. It was found that YSZ-particles can influence the sinter degree and therefore also the interfacial bonds and fracture toughness of the composite. As expected a higher sintering temperature led to a higher sinter degree. Furthermore the presence and the diffusion of silicon and iron within Nextel™ 610 alumina fibers have been shown with the help of EDX-mappings. Figure 2 shows the STEM HAADF image of a fiber annealed at 800 °C and the Figures 3 and 4 are the corresponding EDX elemental mappings of silicon (Si) and iron (Fe)

1. K. K. Chawla: Composite Materials, Science and Engineering, Springer, New York, 2012.
2. K. K. Chawla:Ceramic Matrix Composites, Kluwer Academic Publishers, Boston, Dordrecht, London, 2003.
3. F. F. Lange, W. Tu, C.A. G. Evans, Mat. Sci. Eng. A 195 (1995) 145-150.
4. M. Schmücker, P. Mechnich, in: W. Krenkel (Ed.), Ceramic Matrix Composites, Wiley, Weinheim, 2008, pp. 205-229.
5. The authors kindly acknowledge the financial support through funding of the EU and North Rhine-Westphalia within the CeraMER-project and Yen-Ting Chen and Prof. Jochen M. Schneider, Materials Chemistry, RWTH Aachen University, for the help given in the investigations at FEI Titan G2 80-200 CREWELEY, Ernst Ruska-Centre, Jülich.

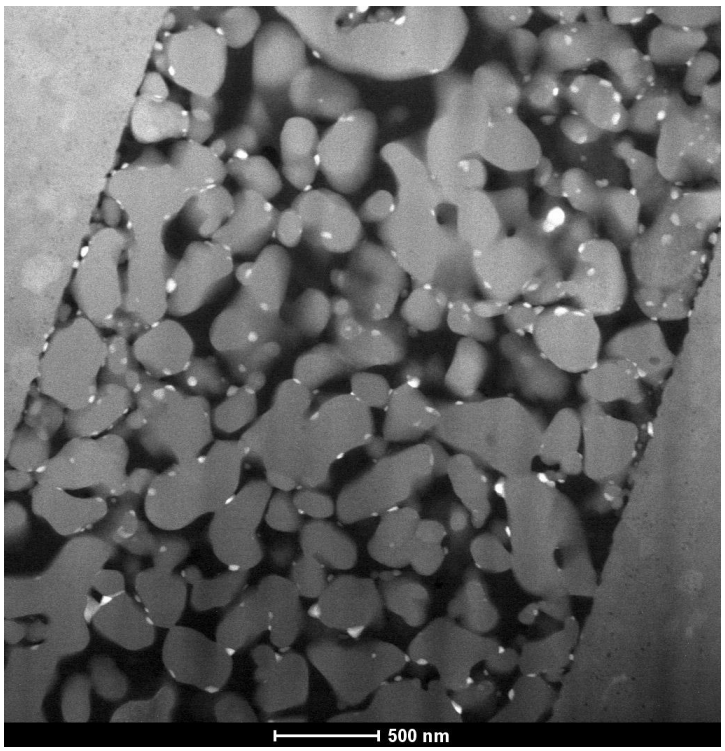

Figure 1. HAADF image of the alumina matrix area between two alumina fibers of a WHIPOX CMC sintered at 1200 °C.

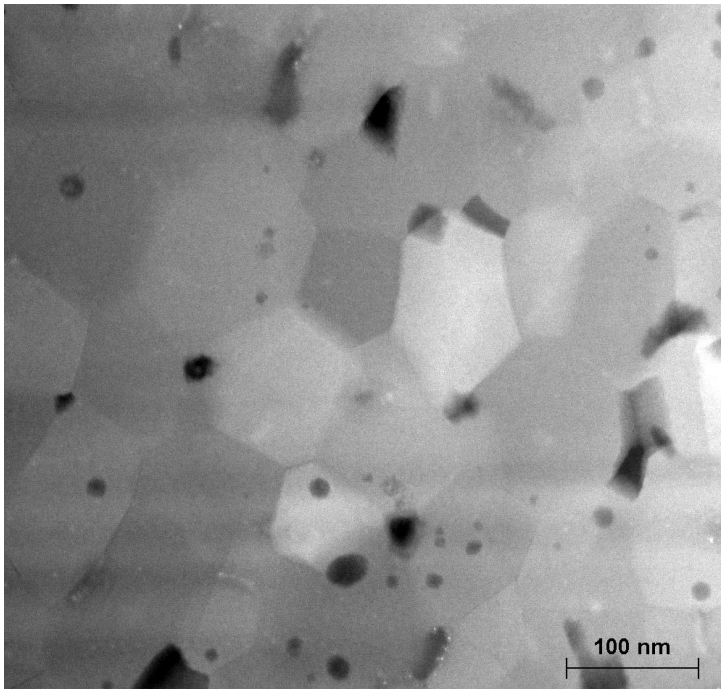

Figure 2. HAADF image of a Nextel^{TM} 610 alumina fiber annealed at 800 °C.

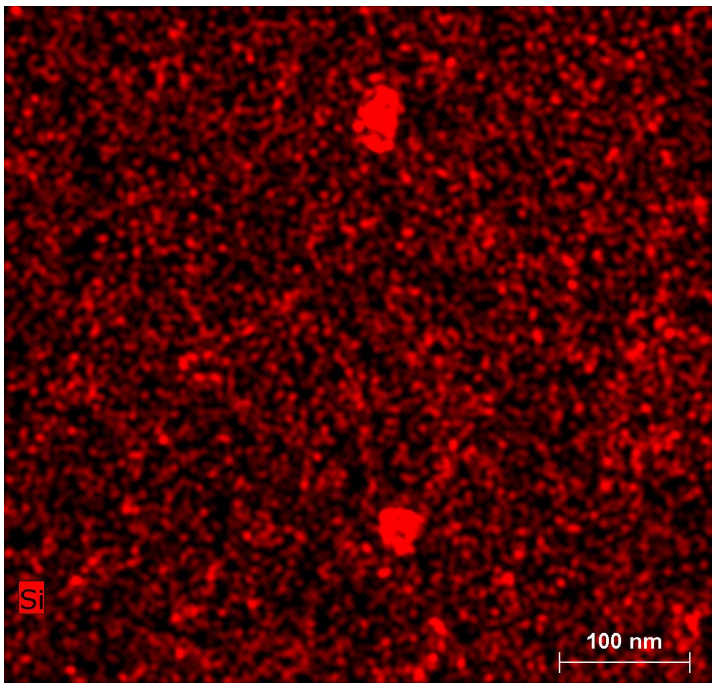

Figure 3. EDX elemental mapping of Si taken at the same place as the HAADF image in Figure 2.

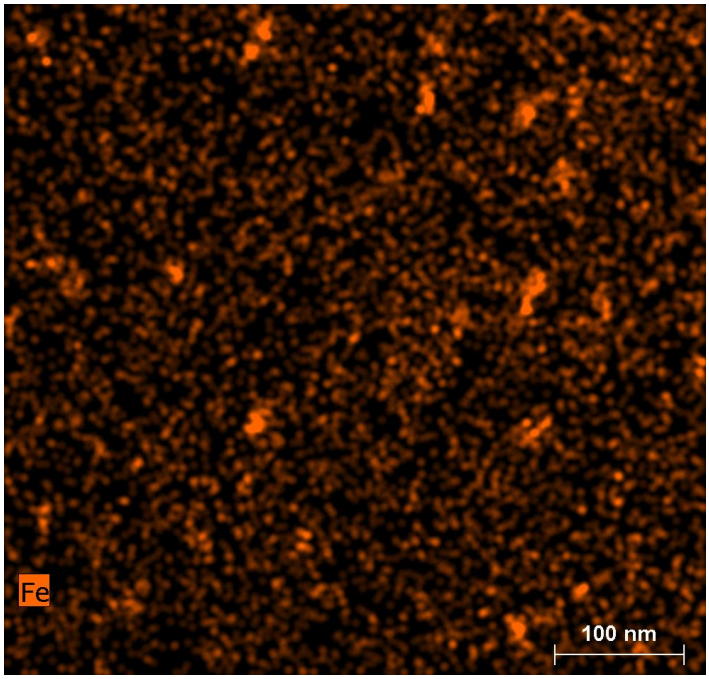

Figure 4. EDX elemental mapping of Fe taken at the same place as the HAADF image in Figure 2.

Ceramics, Composites, Geomaterials, Archaeology

MS7.P180
SEM/EDS/EBSD analysis of the bulk and finish of ceramic sherds recovered during San José de Moro Archaeology Program

D. Dietrich[1], T. Mehner[1], A. Dittes[1], D. Nickel[1], T. Lampke[1]

[1]Technische Universität Chemnitz, Oberflächentechnik/Funktionswerkstoffe, Chemnitz, Germany

dagmar.dietrich@mb.tu-chemnitz.de

Pre-Inca regional societies like Wari, dating from roughly A.D. 600 to 1100, who dwelt inland in the Andes betwixt the coastal cultures Moche and Nazca, were predominant cultures encompassing much of modern-day Peru and Bolivia. The agrarian society supported indigenous elites of impressive wealth, power, and organization. High status burials and most of the Late Moche Fine Line Ceramics have been recovered in San José de Moro throughout 10 years of excavation [1]. Additionally in this context, a large corpus of Wari and Wari-derived ceramic material has been found.

Fragments of the ceramic artifacts were subjected to scanning electron microscopy and energy-dispersive X-ray spectroscopy to determine the element composition and structure of the pottery core and its finish. The aim of the study is to provide additional indications for the procurement of the raw clays, the firing conditions and the applied decoration technique [2, 3]. Cross-sections of the body evidenced the bulk composition and distribution of Si, Ca, K, Mg, Fe and O in the mineral inclusions and the fired clay (as shown for example in Fig. 1a). The mineral characterization by EBSD proved the crystalline nature of numerous phases, but apart from quartz and iron oxides, the exact crystallographic identification failed due to weak diffraction patterns, varying composition of the feldspars, their micro granular aspect and the porosity of the body. Additionally, the rim region (bottom of Fig. 1 a) shows the cross-section of a paint layer indicating an enrichment of Ca and Fe. The mineral analysis will be accomplished by X-ray diffraction. EDS analysis of the surface with black, white, grey and red painted motifs (exemplified in Fig. 1 b-d) showed the elemental composition of the colors as basis for a detailed X-ray diffraction study of the mineral content of separated pigments. Furthermore, EDS cluster maps provide information about the chronological order of the application of the paint.

We greatly acknowledge L.J. Castillo Butters, La Pontificia Universidad Católica del Perú and R. Chapoulie, Université Bordeaux Montaigne for giving the opportunity to contribute to the study and providing the artifacts.

1. L. J. Castillo (2000) La precencia de Wari en San José de Moro. Boletin de Arqueologia PUCP, 4: 143-179.
2. A. Rohfritsch (2006) Céramiques Mochicas de la Vallée de Jequetepequue (Pérou) - Étude technique et physico-chimique d'exemplaires provenant de Dos Cabezas et San José de Moro, Master thesis, Université Michel de Montaigne Bordeaux 3.
3. N. Sharratt, M. Golitko, P.R. Williams, L. Dussubieux (2009) Ceramic Production During the Middle Horizon: Wari and Tiwanaku Clay Procurement in the Moquegua Valley, Peru. Geoarcheology 24 (6): 792-820.

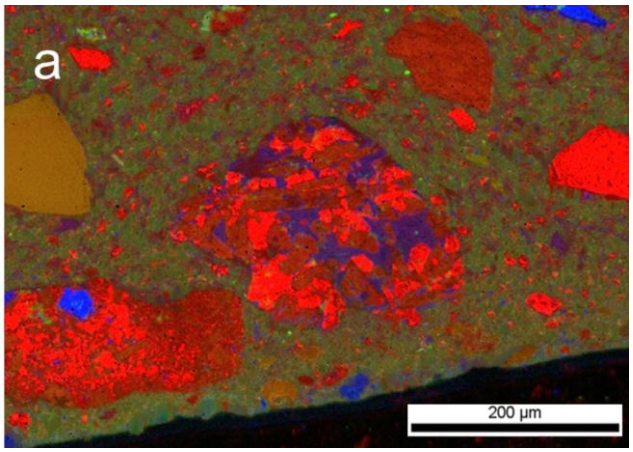

Figure 1. Analysis of Wari ceramic sherds: a) Element map (RGB: Si-Ca-Fe) of a cross-section of the artifact shown in the right of b), and c) SEM image and d) EDS cluster map of the surface of the artifact shown in the left of b).

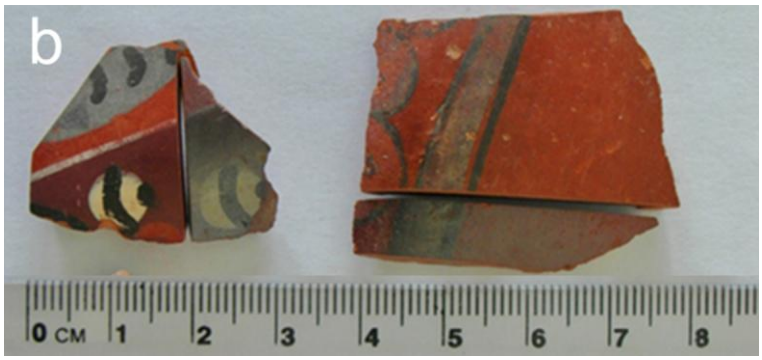

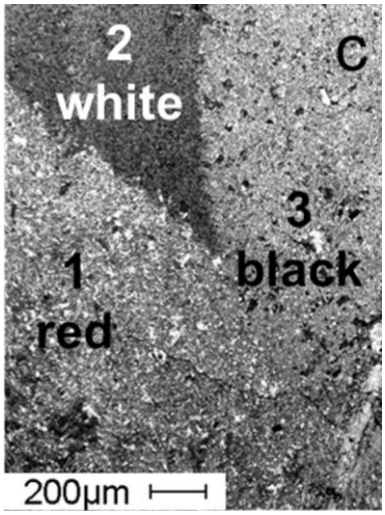

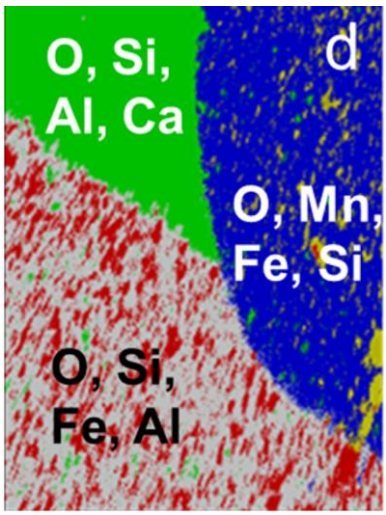

Ceramics, Composites, Geomaterials, Archaeology

MS7.P181
The Effect of alien additives on the characteristics and sturcture of $NiFe_2O_4$ spinel ceramics

Y. Liu[1]

[1]Northeastern University, Materials & Metallurgy, Shenyang, China

liuyh@smm.neu.edu.cn

The oxides MnO_2、TiO_2、V_2O_5 were added into the bulk materials during the course of synthesis $NiFe_2O_4$ spinel ceramics, and the effects of the various additives on sintering process and the properties of $NiFe_2O_4$ spinel were investigated.

The results show that the properties of the materials are significantly changed due to the addition of the three oxides. It is clear that the overall properties of the materials are enhanced due to the additive of MnO_2, such as the increase of density and electrical conductivity, enhancement of corrosion resistance capacity and improvement of bending strength. With the optimum amount of additive, bending strength and electrical conductivity of the specimens are improved by 53% and 15%, respectively, while the corrosion rate decreases to 36.6% of the materials containing Cu-Ni elements. The addition of V_2O_5 results in the slightly decrease of bending strength and density of the specimens while electrical conductivity is obviously improved and corrosion rate greatly decreases. Electrical conductivity is improved by 51.2% while the corrosion rate decreases to 45.6% in the presence of the optimum amount of additive. With the addition of ZrO_2, electrical conductivity slightly decreases and corrosion rate increases a little while bending strength is remarkably improved. Finally, bending strength with low levels of ZrO_2 addition is enhanced by 89.7%.

Ceramics, Composites, Geomaterials, Archaeology

MS7.P182
Self-assembly of functionalized magnetite nanoparticles to a super-crystalline nanocomposite

T. Krekeler[1], A. Dreyer[2], A. Feld[3], M. Ritter[1]

[1]Hamburg University of Technology, Electron Microscopy Unit, Hamburg, Germany
[2]Hamburg University of Technology, Institute of Advanced Ceramics, Hamburg, Germany
[3]University of Hamburg, Institute for Physical Chemistry, Hamburg, Germany

krekeler@tuhh.de

Composite materials are formed by combining two materials resulting in a new material with mechanical properties which surpass the individual components. Combined with the “smaller is stronger”[1] rule for nanosized structures, nanocomposites of inorganic (hard) and organic (soft) components of tooth enamel of vertebrates or the shell of abalone snails show highly improved toughness. The cause of this is that the “soft” proteins in these materials allow elastic deformation of the material resulting in higher overall durability. This approach can be transferred to other systems thus enabling novel materials with tailored physical properties. To fully understand the macroscopic mechanical properties, it is crucial to obtain proper knowledge of the microstructure of the new material.

In this work we describe the formation of a new nanocomposite material made of monodisperse magnetite nanoparticles with oleic acid as a linker. The round particles have a diameter of 17.6 +/- 1.6 nm and are covered with oleic acid during their synthesis[2]. After processing the particles by centrifugation and washing with solvents, the particles were uniaxially pressed with subsequent thermal treatment to induce crosslinking of the oleic acid molecules.

Because of the very small size distribution, large areas of face-centered cubic (fcc) packed nanoparticles are created during the pressing, forming super crystals of magnetite nanoparticles (Fig. 1). The size of these super crystalline domains can reach several microns and contain several hundred thousand individual particles.

After prolonged thermal treatment the particles show distinct facets and are still separated by 2 nm (Fig. 2) showing no sintering or grain growth. The distance of 2 nm corresponds to the molecule length of oleic acid of 19.7 Å, indicating an interweaving of the linker molecules. Electron diffraction on the close packed structures shows an intensity modulation with a fourfold symmetry on the diffraction rings of the (400) and (220) lattice spacing of magnetite (Fig. 3). This intensity modulation is a result of an alignment of the individual single crystalline particles. The reason for this alignment is assumed to be a maximization of packing density of the particles, which resemble truncated cubes after thermal treatment. The observed fcc packing in the thermally treated super crystals is attributable to the formation of the closed packed structure during the pressing of the initially round particles (Fig. 4). Never observed were the actual preferred spatial arrangement of primitive cubic for cube-shaped particles[3] or body-centered cubic (bcc) for truncated cubes[4]. This is assumed to be a consequence of oleic acid crosslinking during the early stage of thermal treatment resulting in a rigid matrix preventing any major rearrangement of the later facetted particles.

1. R. Maaß, Acta Materialia, 2009, 20, 5996-6005.
2. W. William, ChemComm, 2004, 2306-2307.
3. C. Friderichs, ZAAC, 2012, 638, 10, 1627.
4. Z. Quan, PNAS, 2014, 111, 25, 9054.

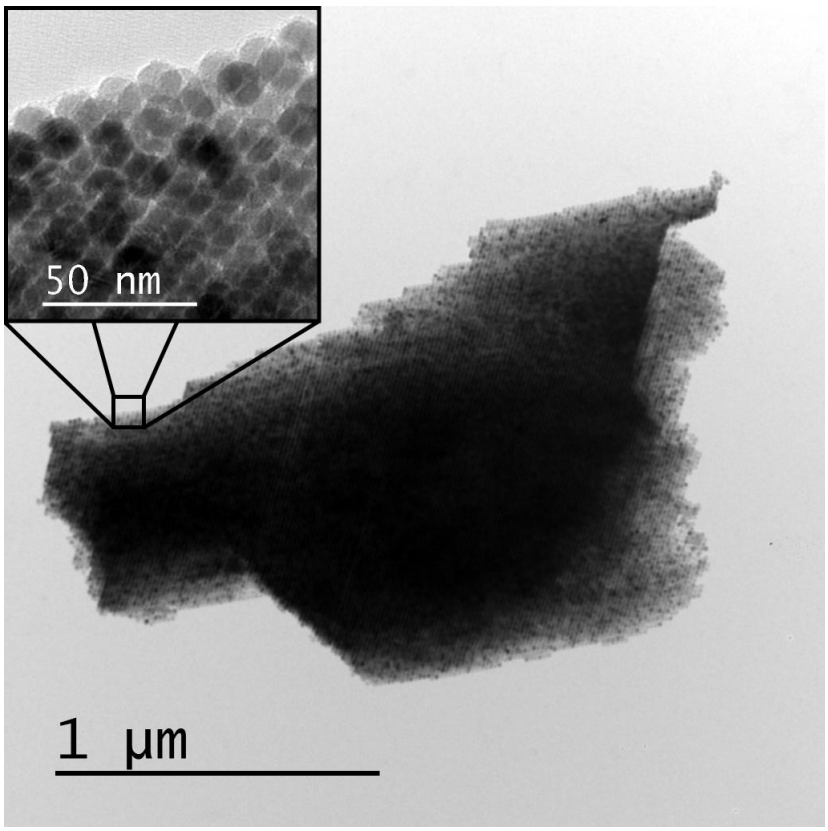

Figure 1. TEM BF-image of Fe_3O_4-oleic acid super crystal. Inset shows close packing of the nanoparticles.

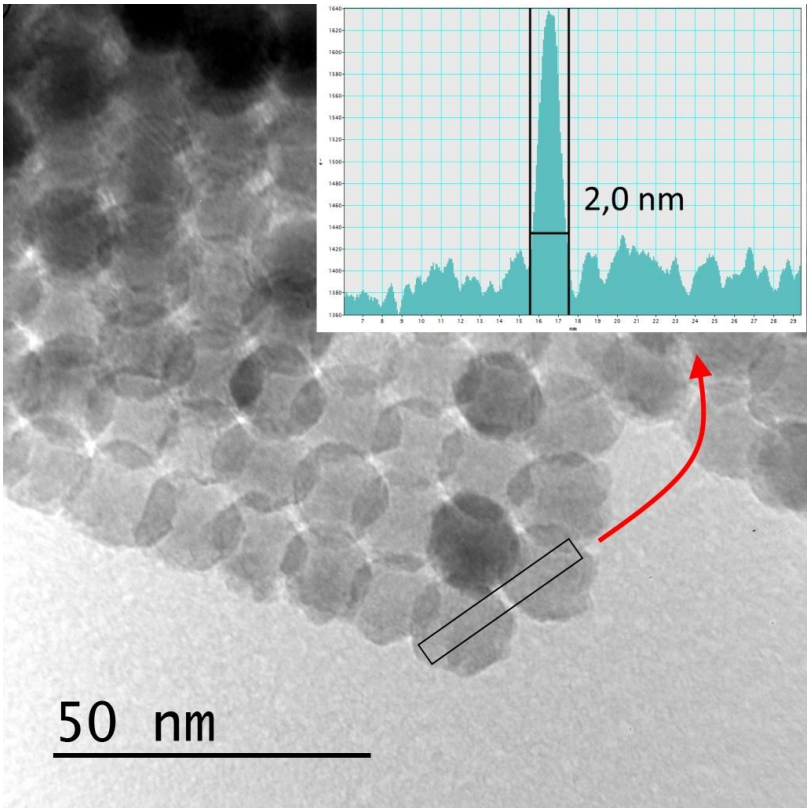

Figure 2. TEM BF-image of faceted Fe_3O_4 nanoparticles. Profile shows particle distance of 2 nm.

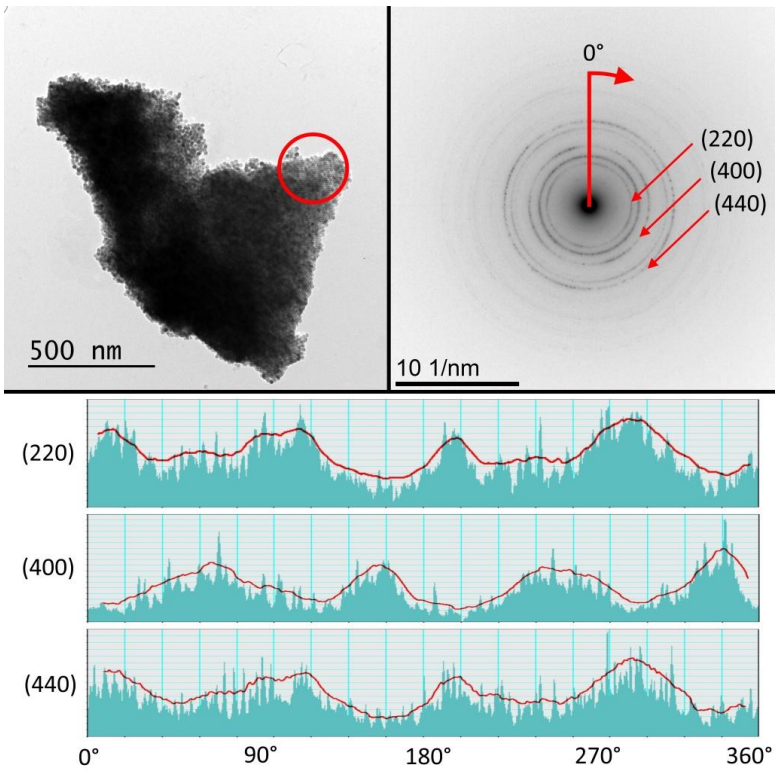

Figure 3. TEM BF-image of Fe_3O_4-oleic acid super crystal and SAED-Pattern of marked area. Profiles show surface plot of the (220), (400) and (440) diffraction rings. Averaged profile drawn in red.

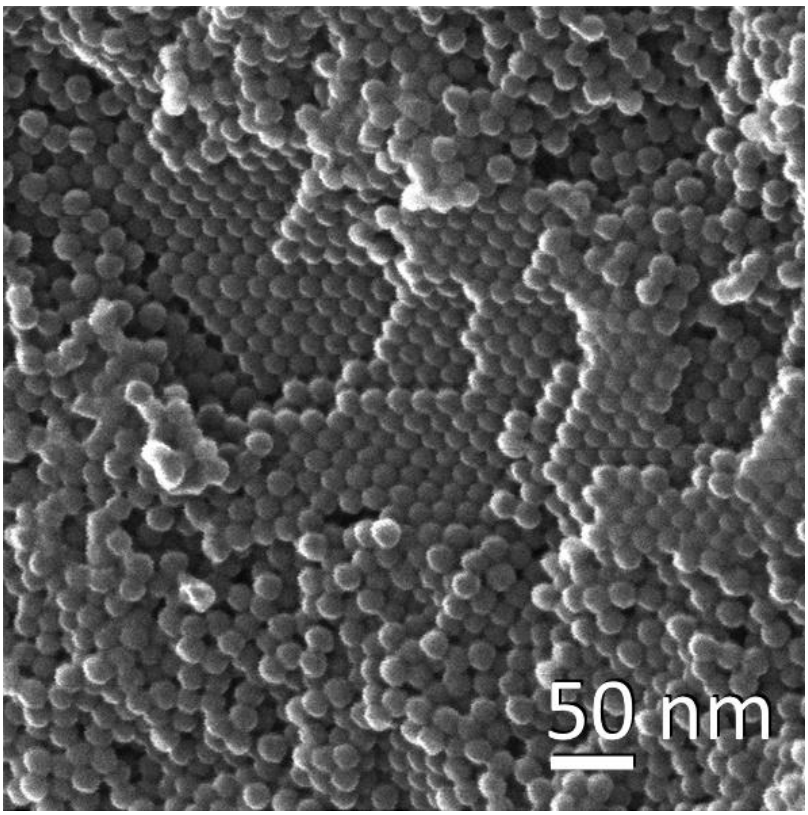

Figure 4. SEM-image of round shaped Fe_3O_4-oleic acid particles in a close packed structure before thermal treatment.

Advances in Instrumentation, Detectors, FIB and Preparation

IM1.001
Approaching the “lab in the gap”: first results from a versatile in-situ (S)TEM

F. Börrnert[1,2,3], H. Müller[2], M. Linck[2], A. Horst[5], A. I. Kirkland[5], B. Büchner[1,5], H. Lichte[1]

[1]Technische Universität Dresden, Dresden, Germany
[2]IFW Dresden, Dresden, Germany
[3]University of Oxford, Department of Materials, Oxford, United Kingdom
[4]CEOS GmbH, Heidelberg, Germany
[5]University of Oxford, Oxford, United Kingdom

felix.boerrnert@tu-dresden.de

In the past, the general development of microscopes was governed by the desire for ever higher resolution in the micrographs. This led to programs like the TEAM project resulting in as fantastic machines as the TEAM I microscope offering a resolving power of about half an Ångström in both TEM and STEM mode [1]. In this course, virtually all means were taken to increase the resolving power even if it put severe limitations to other aspects of microscope aided research. As the most prominent examples in (S)TEM serve the millimeter-sized pole piece gap and the few-Tesla-scale magnetic lens field the sample resides in. A recent survey of the DOE in the future needs of microscopy research resulted in a significant change of direction; besides multi-dimensional and ultrafast microscopy the “lab in the gap” approach has been identified as the most promising development in future electron microscopy [2]. To this end, the key development is increasing the space around the sample for multi-modal *in-situ* experiments.

In this contribution, we present a fully operational prototype transmission electron microscope offering a sample chamber with a 70 mm “pole piece gap” that is accessible through five arbitrarily usable ports ISO-K DN63 from several sides, see Figure 1. Additionally, the sample space is completely magnetic field free. Conceivable configurations are, for example, a tube with a diameter of slightly more than 60 mm could be driven horizontally through the entire microscope column; with a differential pumping system enabling operation in gaseous environments. Another example is the possible combination of a liquid helium continuous flow cryostat providing long-time stable low temperatures and mobile electrical probers for *in-situ* transport measurements on structures found and controlled *ad hoc* in the microscope.

To achieve a decent resolving power with this large sample space, the microscope is operated in a C_s corrected Lorentz mode for both conventional and scanning imaging mode. The resolving power of the instrument is about 1 nm in conventional imaging mode and better than 5 nm in scanning mode at 200 kV electron acceleration voltage [3]. An upgrade of the electron optics that enhances the microscope’s resolving power in conventional imaging mode to *ca.* 0.5 nm is planned for the near future. It is noteworthy that all of the alterations to the original state of the microscope, a double C_s corrected JEOL JEM-2010F, are fully reversible. To aid navigation on sample positions that are not electron transparent, *e. g.* for placing mobile probers on pre-processed contact pads, we installed a secondary electron detector. For the mapping of electric and magnetic fields at the nanoscale *via* off-axis electron holography, an electrostatic biprism is available.

For the design of new experiments to be performed inside the microscope, we built a testing rack with a copy of the microscope’s new sample chamber. Also, the rack has the same outer shape as the microscope with its peripherals, thus, all necessary attachments can be checked for collisions and space requirements.

The main area of research the microscope is planned for is solid state physics. Examples are *in-situ* characterization and manipulation of unconventional superconductors, magnetic nanostructures, and topological phenomena. However, this does not exclude any other experiment conceivable for this microscope.

The authors acknowledge financial support from the European Union under the Seventh Framework Programme under a contract for an Integrated Infrastructure Initiative (Reference 312483—ESTEEM2).

1. P. Ercius *et al*., Microsc. Microanal. 18 (2012), p. 676.
2. Report of the Basic Energy Sciences Workshop on the Future of Electron Scattering & Diffraction (2014), URL http://science.energy.gov/~/media/bes/pdf/reports/files/Future_of_Electron_Scattering.pdf.
3. F. Börrnert *et al.*, Ultramicrosc. (2015), DOI 10.1016/j.ultramic.2014.11.011.

Figure 1. Microscope with new sample chamber, test rack with sample chamber, and sample chamber on test rack viewed along electron beam direction

Advances in Instrumentation, Detectors, FIB and Preparation

IM1.002
The wave-particle duality of electrons demonstrated with sub-pixel resolution by recording off-axis electron holograms on a pnCCD direct detector

H. Ryll[1], M. Simson[2], C. Boothroyd[3], R. E. Dunin-Borkowski[3], C. Dwyer[3], R. Hartmann[1], M. Huth[1], S. Ihle[1], V. Migunov[3], K. Müller-Caspary[4], A. Rosenauer[4], J. Schmidt[1], H. Soltau[2], L. Strüder[1]

[1]PNSensor GmbH, Munich, Germany
[2]PNDetector GmbH, Munich, Germany
[3]Ernst Ruska-Centre for Microscopy and Spectroscopy with Electrons and Peter Grünberg Institute, Forschungszentrum Jülich, Jülich, Germany
[4]Universität Bremen, Bremen, Germany

henning.ryll@pnsensor.de

A direct demonstration of wave-particle duality is performed by detecting single electrons during the build-up of an electron holographic interference pattern on a pnCCD direct digital electron detector, similar to the first direct electron interference experiment conducted by Donati, Missiroli and Pozzi [1].

The pnCCD is a special type of a charge-coupled device (CCD), whose high signal-to-noise ratio enables the detection of single electrons in the energy range between 5 and 300 keV in the transmission electrons microscope (TEM). The pnCCD that was used for this and previous experiments has a format of 264×264 pixels with a pixel size of 48×48 µm² [2]. The full frame readout rate is 1000 frames per second with a readout noise of only 4 el.. The signal to noise ratio is 300:1 for a 5 keV TEM electron. In binning or windowing modes, the readout rate increases linearly. For example, 66×264 pixels are read out at 4000 frames per second.

For the present experiment, an off-axis electron hologram was recorded without a specimen in the field of view using an electron biprism, which was inserted into the trajectory of the electrons in the TEM. The electron rate was reduced such that on average less than one electron hit the detector in each frame, ensuring that individual electrons did not interact with one another. It could be assumed that there was only one electron present in the TEM during the integration time of 1 ms per frame. Each electron hitting the pnCCD is clearly visible, arriving at seemingly random positions on the detector. However, as expected from quantum mechanics, the integration of many frames reveals a typical interference pattern (Figure 1).

The capability to distinguish single TEM electrons from noise over a wide energy range enables further processing of the raw data to determine the point of entry (PoE) on the detector of each TEM electron with a resolution that is much higher than the physical pixel size. One method that can be used to determine the PoE is to calculate the center of gravity (CoG) of the intensity distribution of each TEM electron (referred to as the CoG method) and to use the CoG as the PoE. As experimental data and simulations show, the resulting distribution of x and y coordinates is not equal, as it should be, especially for the case of homogenous illumination. This effect has been described for strip detectors [3] and can be corrected either using a statistical approach (referred to as the Eta method here) or using models based on simulations. The theoretical difference between the actual PoE and the calculated PoE can be calculated using simulations. For electron energies below 80 keV, the full width at half maximum (FWHM) of the distribution of differences between the actual and calculated PoE is less than one pixel (60 keV: Cog: 0.42 pix, Eta: 0.28pix) (Figure 2a).

A comparison between images obtained using the three different methods (integrating intensity images and the Cog and Eta methods) shows an improvement in fringe visibility from 0.49 to 0.50 and 0.58, respectively (Figure 2d).

In conclusion, single electrons can be detected in the energy range from 5 to 300 keV. The position precision is significantly better than the pixel size using the CoG and Eta methods, leading to improved image quality.

1. O. Donati, G. F. Missiroli, G. Pozzi, Am. J. Phys. 44 (1973), p.639-644.
2. K. Müller, H.Ryll et al., Appl. Phys. Lett. 101 (2012), p. 2121101-2121104.
3. E. Belau, R. Klanner, G. Lutz, et al., Nucl. Instr. Meth. Phys. Res. (1983), p.252-260.

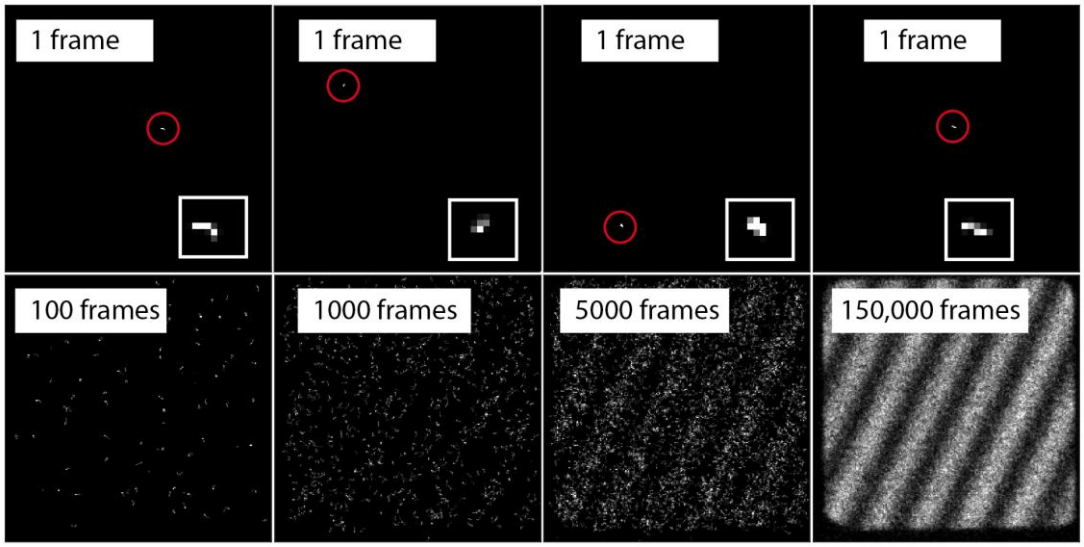

Figure 1. Single frames measuring single electrons in the TEM in the upper row. For better visibility, the electrons are highlighted with circles. The insets show magnified areas of the intensity distribution of each single electron. The integration of many such frames reveals an interference pattern in the images in the lower row.

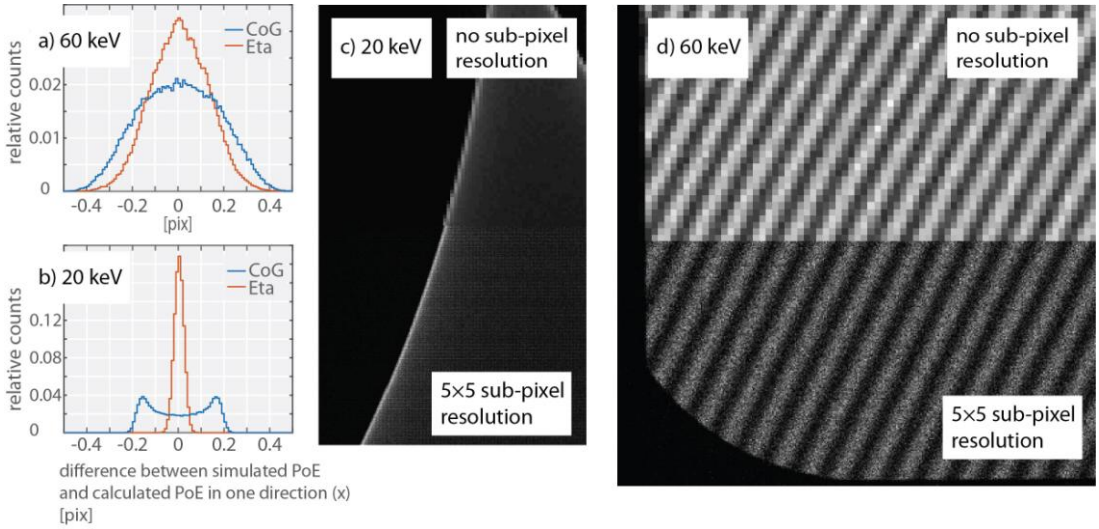

Figure 2. Distribution of the difference between the simulated point of entry (PoE) of TEM electrons and calculated PoE for the CoG and Eta methods for electron energies of 60 keV in a) and 20 keV in b). The pixel size is 48×48µm². A test image recorded using 20 keV electrons is shown in c). The upper half is obtained without and the lower half with 5×5 sub-pixel resolution. The image in d) displays interference fringes at an electron energy of 60 keV without and with 5×5 sub-pixel resolution, respectively.

Advances in Instrumentation, Detectors, FIB and Preparation

IM1.003
Development of low voltage cryo-electron microscope for simultaneous imaging of bright field, dark field STEM and SEM using unroofed frozen cells

J. Usukura[1]

[1]Nagoya University, Structural Biology Research Center, Nagoya, Japan

usukuraj@esi.nagoya-u.ac.jp

Cryo-electron microscopy has been used exclusively for single particle analysis of purified proteins. Recently, technical improvements on rapid freezing and cryo-sectioning such as CEMOVIS permitted structural analysis of organelle or macromolecules in cells. However, cryo-sections show quite low contrast due to few electron scattering, so that make a finding and a focusing of target much harder. In order to overcome such problem, we developed SEM based cryo-STEM that is able to take images on focus with less affect of contrast transfer function (CTF). Concomitantly, we employed unroofing techniques in preparation procedure, because interaction between cytoskeleton and membrane surface become observable on face. We succeeded simultaneous imaging of cryo-dark field and bright field STEM and secondary electron with extremely high contrast and accuracy.

NRK cells were cultured on the molybdenum mesh grid covered with carbon coated polyvinyl Formvar. Cultured cells were washed once with HEPE Ringer's solution and placed in KHMgE buffer for unroofing by weak sonication. Plunging them into liquid ethane using Leica EM GP quickly froze unroofed cells. Frozen samples were then brought into SU9000 SEM (Hitachi High-Technologies Co.) by using newly developed cryo-transfer holder.

Membrane cytoskeletons were observed well simultaneously in cryo-dark field and bright field STEM and secondary electron (SEM)(see attached figure). In particular, simultaneous SEM imaging was capable of evaluating sample condition and judging the irradiation damages how much the sample received irradiation damages while observing. On the other hand, the unroofing was developed originally for one of preparation methods in freeze-etching replica method. We improved and extended this technique further for cryo-electron microscopy to describe the cytoskeleton, because soluble components were washed away on unroofing. Expectedly, actin filaments and microtubules were found on the cytoplasmic surface of cell membrane with extremely high contrast. In the cortical area, the filaments often extended in parallel. In other regions, however, fine filaments extended in various directions on the membrane, while aggregating and dispersing at several points, which eventually divided the membrane surface into several domains. The images obtained in this way must therefore be comparable with freeze-etching results. Evidence confirmed by two different observation methods is very important for determining real structures.

This study was supported by the grant, "Development of Systems and Technologies for Advanced Measurement and Analysis" Program from the Japan Science and Technology Agency (JST) (to J. U.).

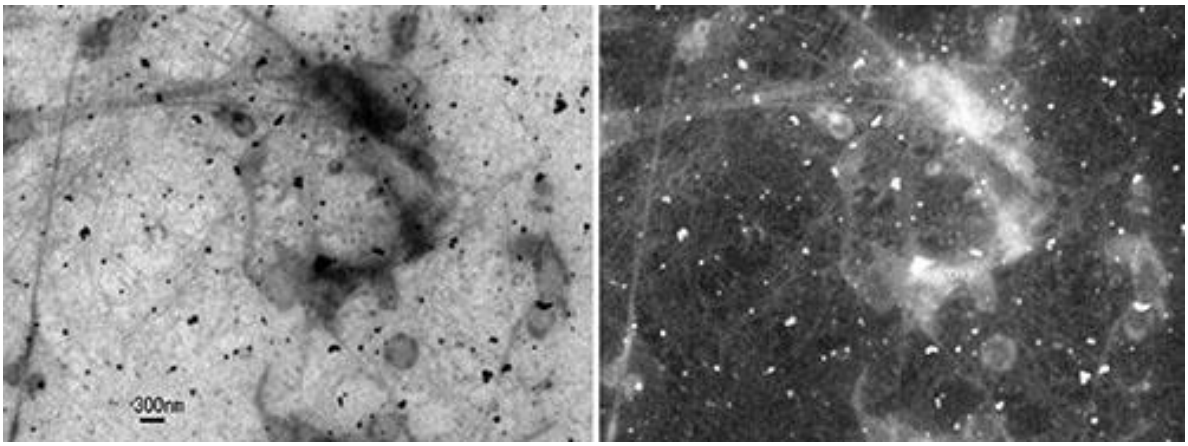

Advances in Instrumentation, Detectors, FIB and Preparation

IM1.004
Optical spectroscopy integrated with environmental scanning transmission electron microscopy: a comprehensive in-situ characterization

M. Picher[1,2,3], S. Mazzucco[2,3], S. Blankenship[2], R. Sharma[2]

[1]IPCMS, DSI, Strasbourg/France, United States
[2]NIST, CNST, Gaithersburg, MD, United States
[3]University of Maryland, Institute for Research in Electronics and Applied Physics, College Park, MD, United States

matthieu_picher@yahoo.fr

In situ imaging, using an environmental scanning transmission electron microscope (ESTEM), has been successfully used to reveal and understand the crucial chemical and physical processes occurring at the nanoscale in many important phenomena, e.g. oxidation/reduction, coalescence, Ostwald ripening, surface reconstruction, substrate/catalyst interaction, etc. However, the relevance of such ETEM studies, and the ability to derive quantitative information out of them, may be hindered if the following two questions cannot be satisfactorily answered: i) Is the probed area representative of the whole sample? And in particular, do high energy electrons alter the reaction mechanism? ii) What is the sample temperature under the gaseous environment?

Here, we present a unique instrument that helps to address both of these issues by allowing the collection of Raman data during high-resolution ESTEM observation. Such coupled measurements are made possible thanks to the insertion of a parabolic mirror in between the sample holder and the lower pole piece of the microscope (a 1.65 mm tall confined space). The mirror focuses the incoming laser on the sample and collects the scattered Raman photons. A set of optics then carries the Raman signal up to the spectrometer (see figure 1. c).

This new platform enables us to combine and compare the structural information and kinetics from micrometer-scale areas obtained by Raman spectroscopy with the local information collected by the ETEM at the nanometer-scale (near atomic). This system also permits us to simultaneously monitor the temperature of the probed material (at micrometer scale) by analyzing shifts in Raman peak frequency, which is especially helpful during environmental studies where the temperature can severely drop when gases are injected in the sample area.

Moreover, this versatile optical setup can also be used i) for cathodoluminescence and photoluminescence measurements (see figure 1 a&b) ii) as a heating source: the sample can be reproducibly heated up to 1000°C at 25 mW with a 532 nm laser, iii) to investigate light/matter interactions (the current 532 nm laser can be easily replaced by any IR/Vis/UV wavelength).

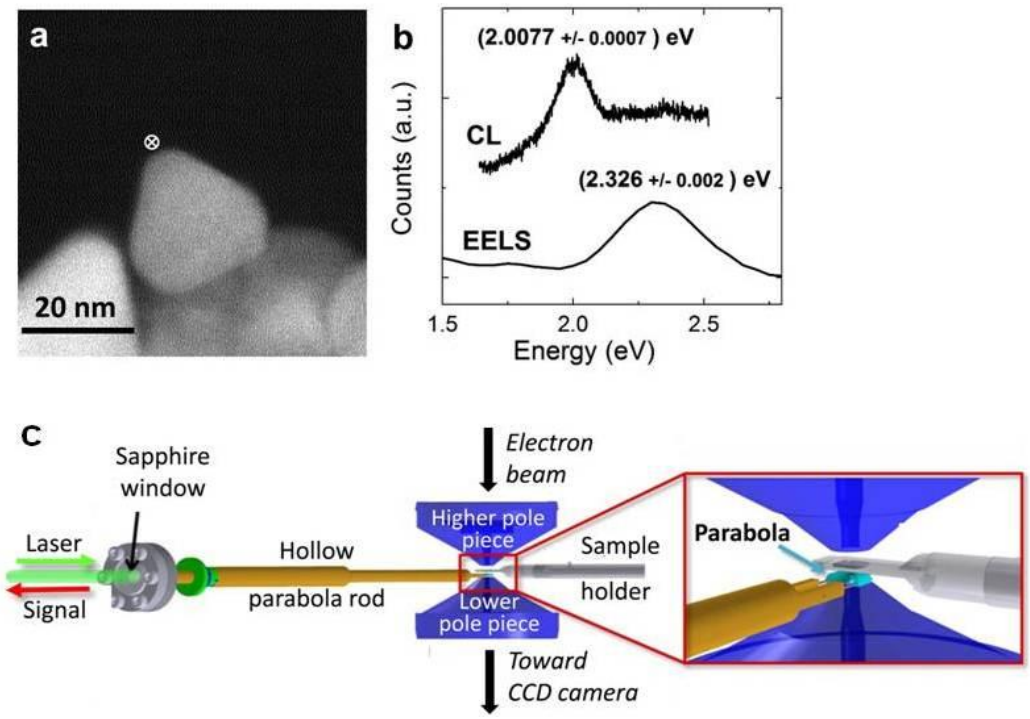

Figure 1. a) STEM image of a triangular gold nanoparticle b) Corresponding cathodoluminescence and EELS spectra. The probe is located on the top corner of the particle, as indicated by the white circular marker on a). c) Schematic view of the integrated optical spectroscopy system. The laser goes through the optical window and then is focused on the sample membrane after hitting the parabola located below the sample. The parabola also collects a portion (1.5 sr) of the photons emitted by the sample.

Advances in Instrumentation, Detectors, FIB and Preparation

IM1.005
MEMS-type microchips for biological samples investigation in electron microscopy

M. Krysztof[1], J. Dziuban[1], A. Gorecka-Drzazga[1], T. Grzebyk[1]

[1]Wroclaw University of Technology, Faculty of Microsystem Electronics and Photonics, Wroclaw, Poland

michal.krysztof@pwr.edu.pl

Biological sample holders in electron microscopy are known since the half of the last century. The idea is to separate the wet tissue from the high vacuum of the microscope by a very thin membrane transparent to electrons. Now this issue is studied again because of a dynamic development of MEMS technology. In literature there can be found several solutions of biological sample holders used in SEM and TEM.

The first example is a wet-tissue SEM [1] with a special made sample holder (fig. 1a) fabricated by means of precision mechanics. It gives very good images of untreated samples (fig. 1b). This technique is described as an alternative way of cancer diagnosis. The suspected tissue can be measured, without special preparations, within an hour from sampling. Moreover employment of electron microscopy in cancer research can give many new information about features of cancer [2]. Another system incorporates a closed microchip with a sample inside (fig. 1c) [3]. It is suited for high resolution TEM and gives very good images of bacteria enclosed in the chip (fig. 1d). A very interesting solution of a sample holder for TEM is a nanoreactor which contains microfluidic channel, SiN viewing windows and a Pt heater (fig. 2a,b,c). It is used for imaging the structural changes in a catalyser during the catalytic reaction in high pressure and high temperature (fig. 2d,e) [4].

We propose fabricating a microfluidic microsystem for observing living cells in SEM or in TEM (fig. 3). It contains a microfluidic channel for transporting the biological solution into the viewing window area and to the outlet, so after the imaging the sample can be subjected to other types of testing. The microsystem can be attached to a standard mounting device for SEM or TEM. In the SEM mode the electron beam passes through the membrane and generates the backscattered electron signal on the biological sample. This signal is measured by classical BSE detector. In TEM mode the electron beam passes through the first membrane, the sample and the second membrane and is detected by high resolution ccd camera. This kind of equipment can be adapted to image specific type of samples and to specific diagnosis techniques.

Proposed microsystems demand using classical electron microscopes which aren't always accessible, especially outside the specialized laboratory. That is why a miniature electron microscope would be an asset. In literature there are information about miniaturizing electron microscopes or its parts, like electron gun or electron optics column. All described solutions lacks a pumping system suitable for creating and maintaining vacuum in miniature devices. Recent works of our team resulted in fabricating of a vacuum micropump [5] which can be used in developing miniature electron microscope. We propose a concept of a fully integrated miniature MEMS-type transmission electron microscope (fig. 5). It contains an electron gun, an electronoptics column and a viewing window made of SiN membranes. It is connected with a miniature vacuum pump and integrated with a microsystem described above. Such miniature device can be used as a specialized diagnosis device. It can be movable so it can be used outside the specialized laboratory.

1. A. Nyska, et al., Toxicol Pathol, 32 (2004) 357-363.
2. J. A. Tucker, Ultrastruct Pathol, 24 (2000) 383-389.
3. Kuo-Linag Liu, et al., Lab Chip, 8 (2008) 1915-1921.
4. J. F. Creemer, et al., J. MEMS, 19 (2010) 254-264.
5. T. Grzebyk, et al., Sensors and Actuators A, 208 (2014) 113-119.

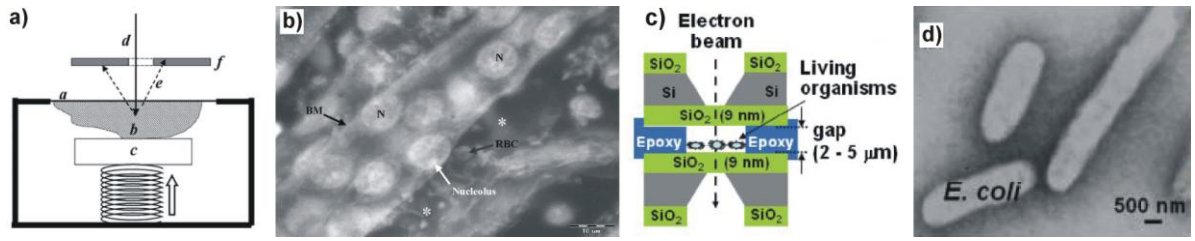

Figure 1. Scheme of a sample holder of a wet-tissue SEM (a), an image taken with this device (b) [1]. Scheme of a sample holder for TEM (c), an image of E.coli bacteria obtained with this device (d) [3].

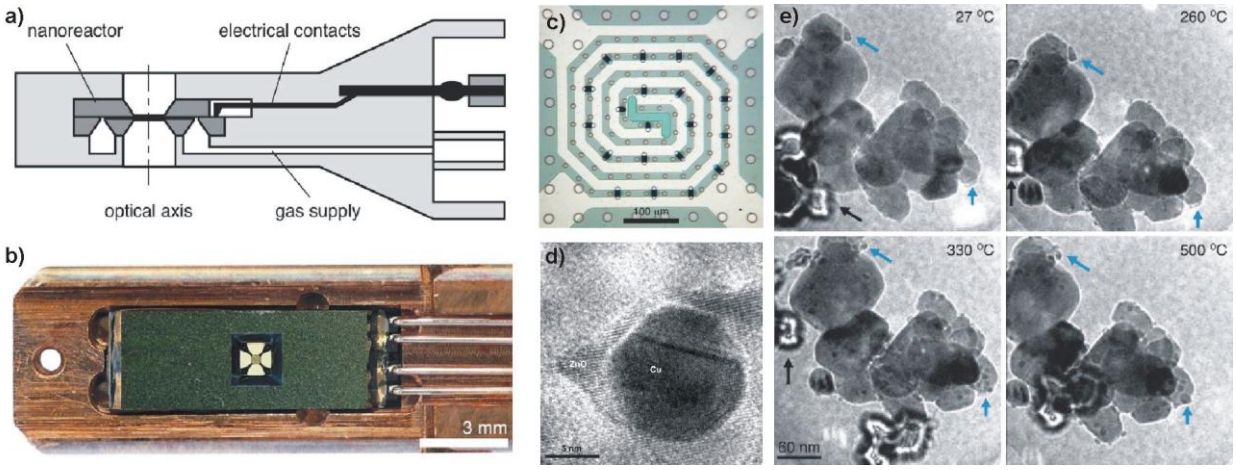

Figure 2. Scheme (a) and the view of a nanoreactor (b). A microscopic image of a nanoreactor structure with platinum heater and SiN viewing windows (c). High resolution image of Cu crystal on ZnO support (d). Images of CuO crystals on ZnO support during catalytic reaction (e) [4].

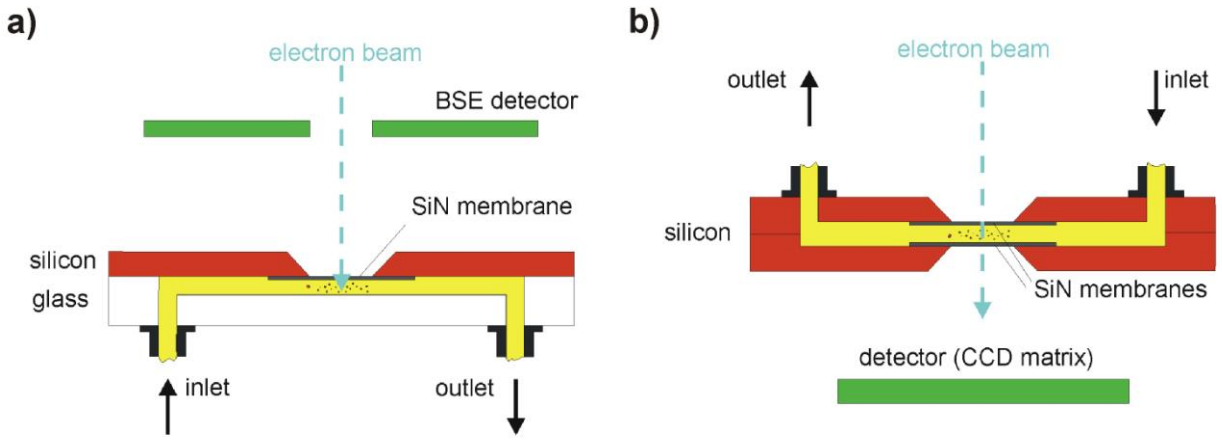

Figure 3. Schemes of microfluidic microsystems for SEM (a) and TEM (b).

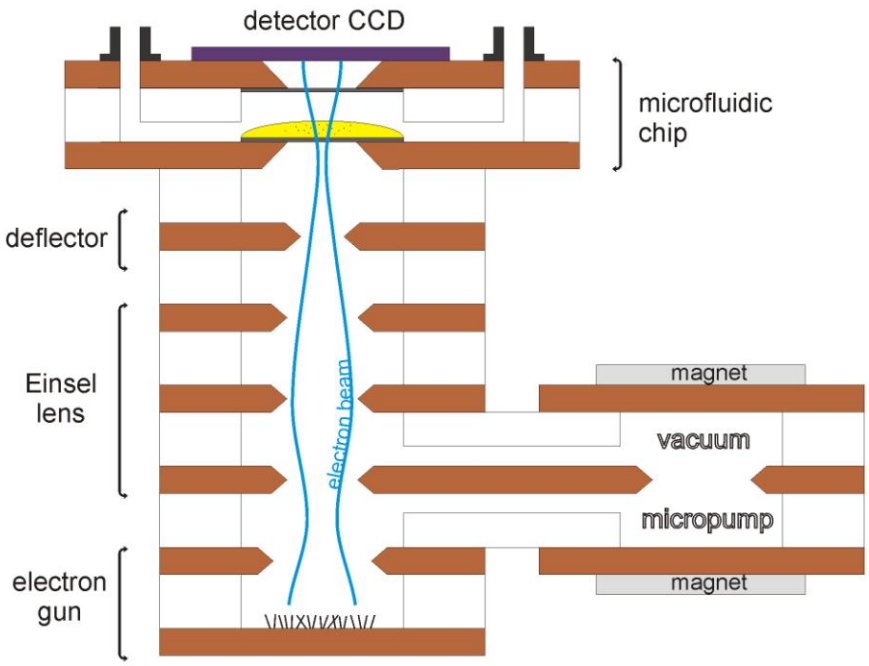

Figure 4. Scheme of a miniature MEMS-type transmission electron microscope.

Advances in Instrumentation, Detectors, FIB and Preparation

IM1.P007
Structural biology at the single particle level: imaging tobacco mosaic virus by low-energy electron holography

J.- N. Longchamp[1], T. Latychevskaia[1], C. Escher[1], H.- W. Fink[1]

[1]University of Zurich, Physics Institute, Zurich, Switzerland

longchamp@physik.uzh.ch

A milestone for structural biology would definitely be attained if methods and tools were available, that do away with averaging over an ensemble of molecules and thereby enable structural biology on a truly single molecule level. To obtain atomic resolution information about the structure of any individual biological molecule, entirely new concepts and technologies are needed. One approach of this kind is associated with the recent XFEL projects. Unfortunately, there are now strong indications that also here averaging over a large number of molecules will be inevitable in order to obtain images with a sufficiently high signal-to-noise ratio to enable numerical reconstruction of the diffraction pattern with atomic resolution [1].

Our approach to structural biology at the single molecule level is motivated by the experimental evidences that electrons with a kinetic energy in the range of 50-250eV are harmless to biomolecules [2, 3]. Even after exposing fragile molecules like DNA or proteins to a total electron dose of $10^6 e^-/Å^2$, more than six orders of magnitude higher than the critical dose in transmission electron microscopy, no radiation damage could be observed [2]. This, combined with the fact that the de Broglie wavelengths associated with this energy range are between 0.8 and 1.7Å, makes low-energy electron microscopy a candidate for structural biology at the single molecule level.

In our low-energy electron holographic setup (Figure 1), inspired by Gabor's original idea of inline holography [4, 5], a sharp tungsten tip acts as source for a divergent beam of highly coherent electrons [5]. Part of the emitted electron wave is elastically scattered off the object and hence is called the object wave, while the un-scattered part of the wave represents the reference wave. At a distant detector, the hologram, i.e. the pattern resulting from the interference of these two waves is recorded. A hologram contains the phase information of the object wave, and the object structure can thus be reconstructed unambiguously.

Here, we will report nanometer resolution imaging by means of low-energy electron holography of individual tobacco mosaic viruses (TMV) deposited onto ultraclean freestanding grapheme [6]. We will show that structural details arising from the helical structure of the viruses can be revealed and that the agreement between our images and an atomic model of TMV available from the protein database is remarkable (Figure 2). We will also describe our on-going efforts towards 2Å resolution by means of low-energy electron coherent diffraction imaging (CDI). By implementing a CDI experimental scheme for low-energy electrons, we could already image a 210nm freestanding region of graphene at 2Å resolution, revealing more than half a million of graphene unit cells at once [7].

1. J. W. Miao, H. N. Chapman, J. Kirz, D. Sayre, and K. O. Hodgson, *Annu. Rev. Biophys. Biomol. Struct.*, 2004, **33**, 157-176.
2. M. Germann, T. Latychevskaia, C. Escher, and H.-W. Fink, *Phys. Rev. Lett.*, 2010, **104**, 95501.
3. J.-N. Longchamp, T. Latychevskaia, C. Escher, and H.-W. Fink, *Appl. Phys. Lett.*, 2012, **101**, 93701.
4. D. Gabor, *Nature*, 1948, **161**, 777-778.
5. H.-W. Fink, W. Stocker, and H. Schmid, *Phys. Rev. Lett.*, 1990, **65**, 1204-1206.
6. J.-N. Longchamp, T. Latychevskaia, C. Escher, and H.-W. Fink, 2014.
7. J.-N. Longchamp, T. Latychevskaia, C. Escher, and H.-W. Fink, *Phys. Rev. Lett.*, 2013, **110**, 255501.

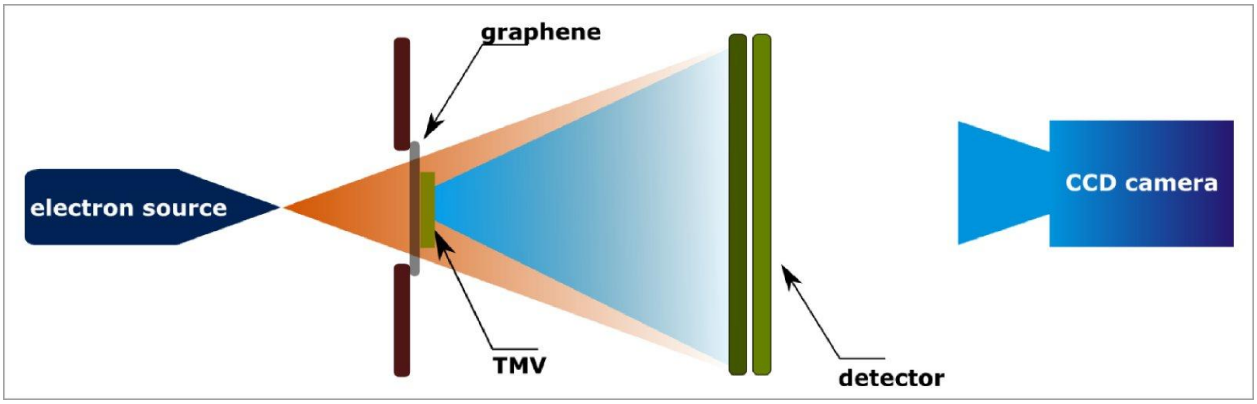

Figure 1. Scheme of the experimental setup of low-energy electron holography. The source-sample distance amounts to typically 100-1000nm, which leads to kinetic electron energies in the range of 50-250eV.

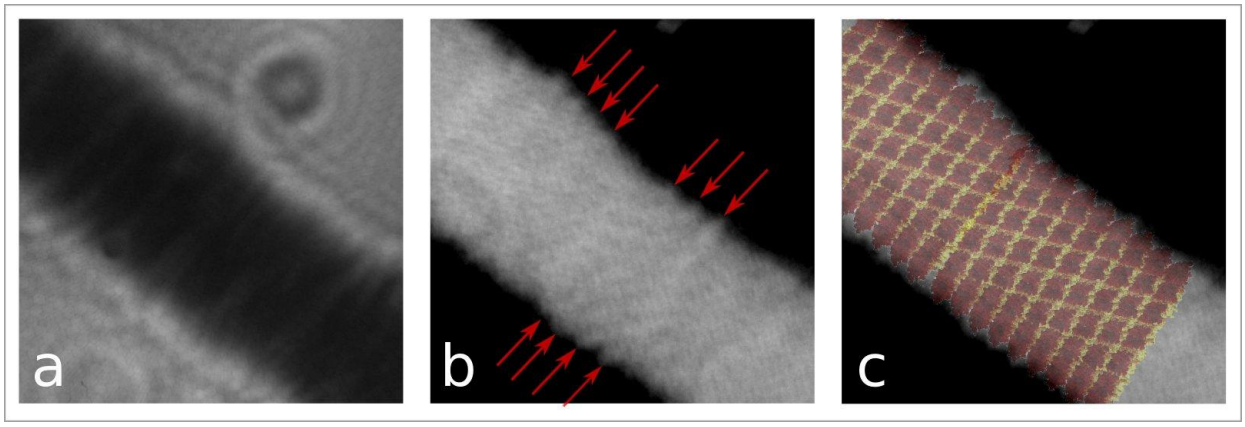

Figure 2. a High-magnification hologram of TMV recorded at 80eV. b Reconstruction of the shape of TMV from a, the red arrows mark the presence of details arising from the helical structure of TMV. c An atomic model for TMV is superimposed on the image presented in b.

Advances in Instrumentation, Detectors, FIB and Preparation

IM1.P008
Combination of FIB plan-view preparation and cross sectional STEM tomography to obtain 3D information on gallium containing structures within silicon

K. I. Gries[1], K. Werner[1], A. Beyer[1], W. Stolz[1], K. Volz[1]

[1]Philipps University Marburg, Faculty of Physics and Materials Science Center, Marburg, Germany

katharina.gries@physik.uni-marburg.de

Ga containing III/V-semiconductors grown epitaxially on Si (001) are suitable for many different applications (solar cells, light emitting diodes, lasers). Therefore these materials are of special interest. The growth of different Ga containing materials on Si were already studied by several groups [1,2], whereas the fundamentals of gallium deposition at low temperatures (20°C-500°C) have not been studied until now.

It is known that for GaN grown on Si melt-back etching of Si by Ga occurs [3]. Similar effects have also been recorded for GaP grown on Si [1]. Since the characteristics of the III/V layers are influenced by this effect, we analyzed the deposition of Ga on Si to get a deeper insight into the structures forming at the interface.

The growth was performed by metalorganic chemical vapor phase deposition (MOCVD) on nominally exact Si (001) substrates at 500°C using trimethylgallium as precursor.

Scanning transmission electron microscopic (STEM) investigations in combination with energy dispersive X-ray (EDX) spectroscopy of cross sectional samples revealed gallium containing structures reaching into the silicon [4]. These structures seem to exhibit a pyramidal structure forming facets on the Si {111} planes.

To get a deeper insight into the three-dimensional shape of these gallium containing structures, they have been also prepared in plan-view orientation. The conventional plan-view preparation including mechanical grinding followed by ion polishing is not suitable for these samples since the structures are sensitive to chemicals which are normally used during the preparation steps.

Therefore focused ion beam (FIB) plan-view samples based on the H-bar method [5] have been created avoiding any treatment with chemicals. A high angle annular dark field (HAADF) STEM image of such a sample is shown in Fig. 1 revealing a square shape of the structure in [001] direction.

Additionally, more knowledge on the three-dimensional shape of the gallium containing structures can be achieved performing STEM electron tomography measurements of cross sectional samples. Results of the reconstructed data are presented in Fig. 2. In [001] direction the square shape is again confirmed whereas in [100] and [010] directions a 90° angle at the base of the structure can be measured.

All these information obtained by the plan-view sample geometry and in combination with the electron tomography data lead to a confirmation of the pyramidal shape (Fig. 3) of the gallium containing structures and give important insight on the nanoscale processes occurring during melt-back etching of Si by Ga.

1. K. Volz et al., Journal of Crystal Growth 315 (2011) 37
2. Z. Liliental-Weber et al., Ultramicroscopy 30 (1989) 20
3. H. Ishikawa et al., Journal of Crystal Growth 189/190 (1998) 178
4. K. Werner et al., Journal of Crystal Growth 405 (2014) 102
5. K. J. O'Shea et al., Micron 66 (2014) 9

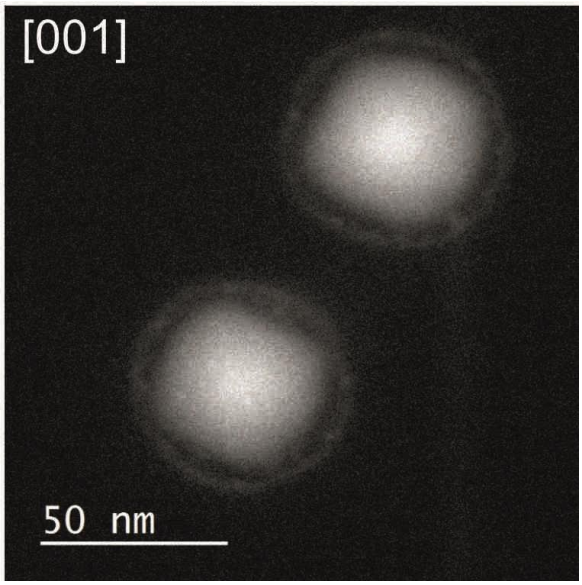

Figure 1. HAADF STEM image of a FIB plan-view prepared sample. The square shape of the gallium containing structures is clearly visible. The bright ring surrounding the structure is originated by the cap that is also visible in the reconstructed data in Fig. 2.

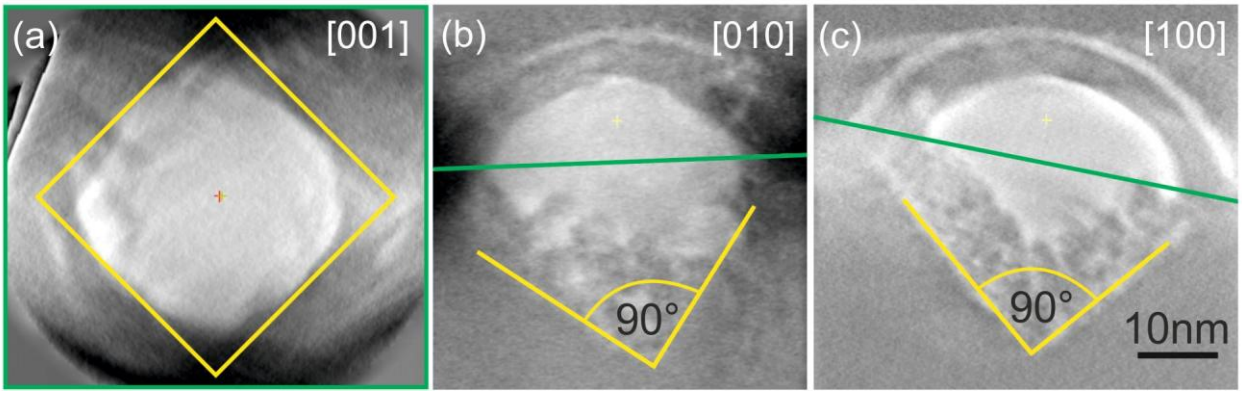

Figure 2. Reconstruction of the electron tomographic data of a gallium containing structure. The slice in (a) is oriented along the green lines that are drawn in (b) and (c).

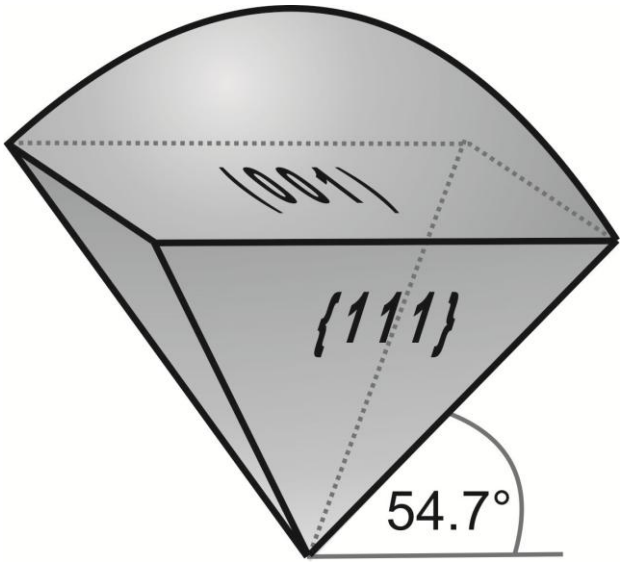

Figure 3. Model of the gallium containing structure. The pyramidal shaped structure reaches into the silicon.

Advances in Instrumentation, Detectors, FIB and Preparation

IM1.P009
Push-button variable pressure mode with in-lens detection and new objective lens in an FESEM

E. Essers[1], S. Meyer[1], D. Kirsten[1], W. Berger[1], R. Arnold[1], B. Gamm[1], V. Drexel[1], D. Preikszas[1], M. Rohm[1], L. Han[1], M. Albiez[1]

[1]Carl Zeiss Microscopy GmbH, Oberkochen, Germany

erik.essers@zeiss.com

The easiest way to image charging samples in an SEM, is to use the variable pressure (VP) mode, in which case secondary electron (SE) detection is performed with the help of a gas ionisation cascade. Since this creates gas scintillation and a strong increase in the number of SE, a gas scintillation detector or a collector electrode can be used for SE detection and yields similar signals.

Figure 1 shows a photograph of the newly developed, pneumatically retractable VP module, called NanoVP module. One switches between high vacuum and the VP mode by just pushing a button. A pressure limiting aperture is inserted and the working conditions are installed in about 60 seconds. With the retracted VP module, not only is high vacuum operation possible, but also the navigation on charging samples at 30 Pa gas pressure. In both cases the full field of view and arbitrary working distances can be used.

The detector arrangement for the VP mode is depicted in Figure 2, which shows a schematic cross section of the NanoVP module below the objective lens. For the first time ever, in-lens detection with scintillator-photomultiplier detectors is realized in the VP mode [1, 2].

For SE in-lens detection a voltage is applied between the specimen and the conical pressure limiting aperture (PLA), see Figure 2. This results in a gas ionisation cascade, which is symbolized by a cloud that is directed towards the conical PLA. There the SE enter the region with better vacuum and are accelerated by the electric field of the objective lens. In the objective lens, the magnetic and electric fields direct the SE to the in-lens detectors.

Besides an excellent signal-to-noise ratio (SNR), the SE in-lens detection with scintillator-photomultiplier detectors also provides additional information in the VP mode. Compared to other SE images in the VP mode, the SE in-lens images use different electrons and look quite different, as will be shown by direct comparison.

When the retractable VP module is combined with a newly developed objective lens, the nano-twin lens, the low-voltage performance is drastically improved for both the high vacuum and the variable pressure modes. The imaging properties of the nano-twin objective lens will be discussed in both modes regarding to resolution and detection efficiency.

The gas path length (GPL) of the primary electron (PE) beam is the crucial parameter that determines the scattering of the PE in the gas. Especially for low-voltage operation (≤ 3 keV) the GPL determines the SNR of the detector signal. For EDX the GPL determines the EDX resolution because of the skirt effect. Therefore the GPL has been drastically shortened compared to the former design. The resulting excellent low-voltage performance is demonstrated in Figure 3, where a heavily charging and strongly beam-sensitive sample [3] is imaged at 3 kV and 150 Pa with the gas scintillation detector. Moreover, the VP image of Figure 4 was taken at 1 kV and 30 Pa with the SE in-lens detector.

The setup and the detection principles will be explained in detail and first applications will be presented.

1. E. Essers, Optik **110**, Supplement 8: Proceedings, p. 47
2. E. Essers, Patents EP1068630B1, US6590210B1
3. Sample courtesy of Dr. Braun, Leibniz-Institute of Polymer Research Dresden

Figure 1. Photograph of the retractable NanoVP module (inserted below the newly developed nano-twin objective lens). The four-quadrant diode is used for BSE detection.

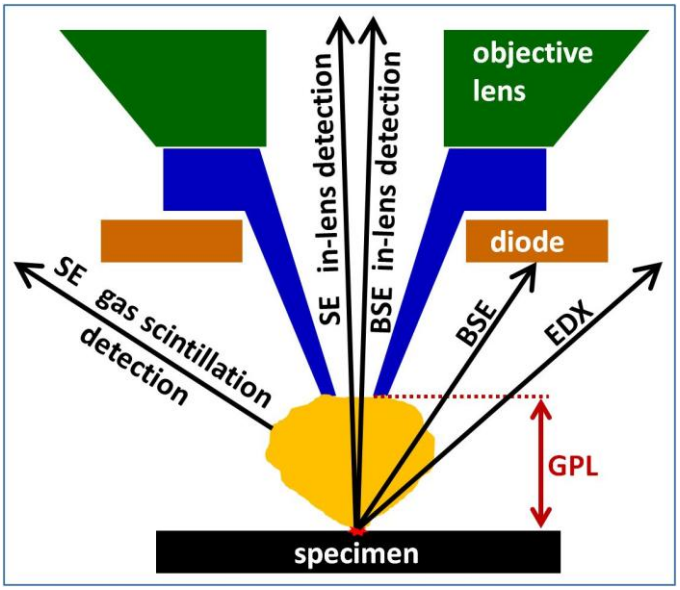

Figure 2. Schematic drawing of the detector arrangement in the variable pressure mode. All detectors can be used in parallel.

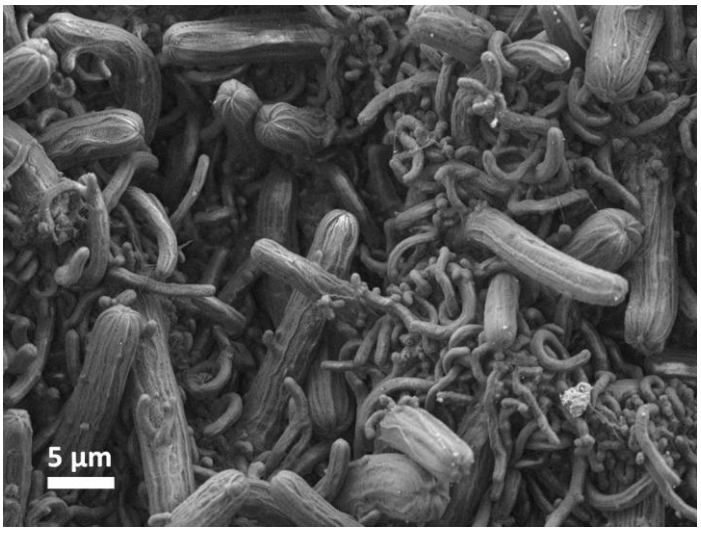

Figure 3. Fibrous polymer microstructures imaged at 3 kV with the gas scintillation detector and 150 Pa Nitrogen gas pressure. [3]

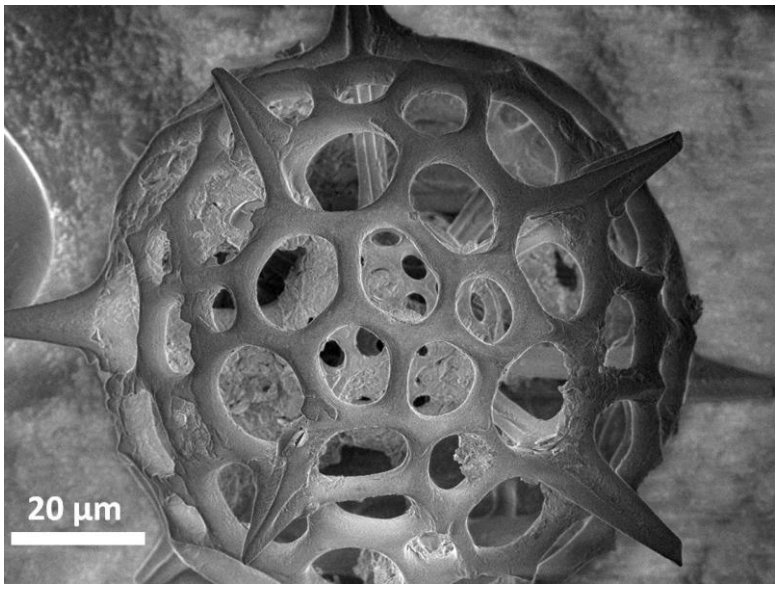

Figure 4. Radiolaria imaged at 1 kV with SE in-lens detection and 30 Pa Nitrogen gas pressure.

Advances in Instrumentation, Detectors, FIB and Preparation

IM1.P010
Study of phase and composition contrast of nanomaterials with LL-BSE imaging

X. Liu[1]

[1]Carl Zeiss Microscopy GmbH, Oberkochen, Germany

xiong.liu@zeiss.com

The surface and interface dominate the both materials properties and the performance of semiconductor devices with continuously shrinking the size and structure. The advanced nanofabrication technology is able to engineer well-defined materials structures down to a few nanometers. This requires scanning electron microscope (SEM) as a most conventional technical method in material characterization and analysis not only to visualize and resolve such nanostructures with the secondary electron imaging at a low landing energy to reveal real surface information but also to analyze the tiny compositional differences like doping contrast, oxidation states of elements, small phases, hybrids or function group in polymers etc., which are not available via the classical backscattered electron imaging or other Energy-dispersive X-ray spectroscopy methods. Although the classical backscattered electron (BSE) imaging are from the multiple inelastic scattering process which could provide density related contrast like channeling contrast at high landing energy, the backscattering coefficient shows non-linear behavior and get very complicated at low landing energy range[1].

In the conventional backscattering process (Rutherford scattering), the backscattered electrons are mainly from the scattering of the high energy primary electrons with the nucleus charge or inner electron shells of the material. In such a case the contrast or brightness of the BSE imaging scale with material density, atomic number (Z). However the scattering between the primary beam with the outer electron shells of the materials at low impact energy (below 2 kV) region is not any more negligible which even becomes more dominant where the surface plasma resonance and ionization loss could happen and contribute to in the total contrast mechanism [2]. Such backscattered electrons undergone a single inelastic scattering process with low energy loss are rebounded back along the primary electron beam which involve unique properties of the analyzed materials.

The unique electron beam booster inside the Gemini® column not only maintains the brightness of the primary electron beam but also reduced the aperture diffraction at low energy. The recently appeared new “Nano-Twin Lens” has a tremendous improvements in lens aberration correction and electron signal separation on the basis of the well-known Gemini® lens technology. The integration of the “Nano-Twin Lens” and beam booster technology means, on one hand a further reduction of the beam probe size for both low kV and high kV, and on the other, the dispersion of generated electron signals backward into the column has been enhanced. It means that the secondary electrons and backscattered electrons with a small energy and angle differences could be amplified and separated through the “Nano-Twin Lens” in real time and space without converting the signals or applying stage bias. The separated backscattered electrons undergoes energy filtering by an energy filtering grid and are projected back into the corresponding detector. The multiple inelastic scattered electrons could be filtered out by setting an appropriate threshold potential to the filtering grid. Only the backscattered electrons with a specific energy low loss (energy larger than the gird potential) could go through the grids window into the detector for imaging. At low landing energy condition, such backscattered electrons are called energy low loss backscattered electrons which bring some characteristic properties and scattering information of the specimen. This idea design allows microscopists to gain not only a better resolution but more unique contrast information in low kV applications.

Herein, we will present the band gap difference induced contrast in ZnO nanocrystals imaging (ref. Figure 1) and different phases ferrite, austenite, marensite in steel as shown in Figure2 by LL-BSE imaging.

1. L. Reimer, Scanning electron microscopy, 2nd edition. Springer-Verlag, 1998, Berlin Heidelberg New York.
2. H. Jaksch, Contrast mechanisms of low loss backscattered electrons in field emission SEM, EMAS conference, May 2011, France.

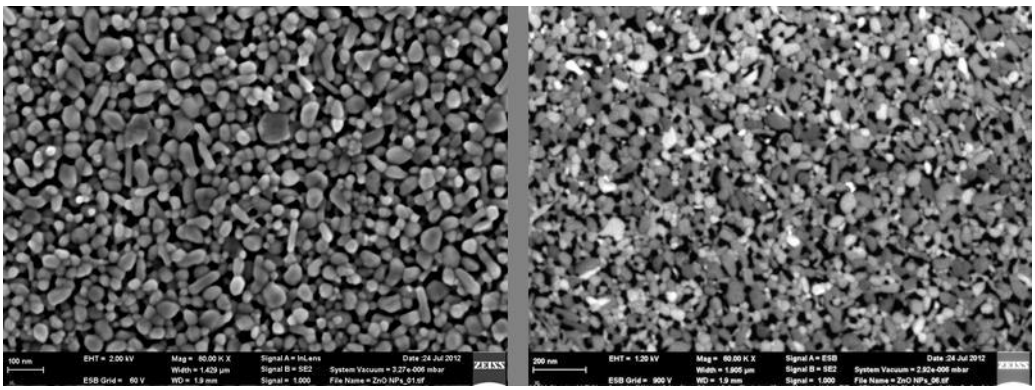

Figure 1. The SE1 image (left) and LL-BSE image (right) of the ZnO nanocrystals where the LL-BSE image is from the low loss BSEs with an energy between 800 and 900 eV.

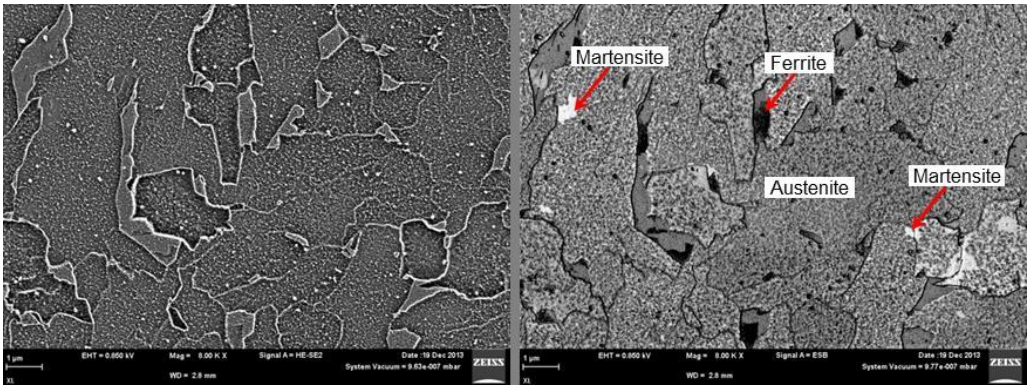

Figure 2. The SE1 image (left) and corresponding LL-BSE image (right) of a steel sample with polishing and chemical etching.

IM1.P011
Imaging and analysis with JEOL analytical atomic resolution microscopes

P. Wachsmuth[1]

[1]JEOL, Eching, Germany

wachsmuth@jeol.de

With more than 60 years of experience in research and development, JEOL is today one of the largest manufactures of electron optical systems.

With the two new atomic resolution microscopes (ARM), the JEM-ARM200F and JEM-ARM300F, JEOL recently introduced the first 200kV and 300kV transmission electron microscopes (TEM) developed from the ground up, aiming for an optimal integration of modern aberration correctors. State-of-the-art TEMs like the JEM-ARM300F are highly stable and provide a wealth of characterization methods such as high resolution STEM/TEM imaging, energy dispersion X-ray spectroscopy (EDS) or electron-energy loss spectroscopy (EELS), which are indispensable for the investigation and characterization of materials down to the sub-Angström scale.

In order to further push the analytical capabilities of these modern electron microscopes, JEOL also launched two new x-ray spectrometers: a new dual EDS system for TEMs and newly developed soft x-ray emission spectrometer (SXES) for scanning electron microscopes (SEM).

Advances in Instrumentation, Detectors, FIB and Preparation

IM1.P012
Fast STEM imaging with the pixelated pnCCD (S)TEM-camera

M. Simson[1], H. Ryll[2], R. Hartmann[2], M. Huth[2], S. Ihle[2], L. Jones[3], Y. Kondo[4], K. Müller[5], P. Nellist[3], R. Sagawa[4], J. Schmidt[2], H. Soltau[1], L. Strueder[2], H. Yang[3]

[1]PNDetector GmbH, Munich, Germany
[2]PNSensor GmbH, Munich, Germany
[3]University of Oxford, Oxford, United Kingdom
[4]JEOL, Tokyo, Japan
[5]University Bremen, Bremen, Germany

melanie.schulze@pndetector.de

Recording a two-dimensional image of the diffraction pattern (or parts of it) for each probe position in a two-dimensional STEM image results in a 4D-STEM data cube. For a typical STEM image of 256x256 probe positions, a total of 65,536 2D detector-plane images need to be recorded. With the pnCCD (S)TEM camera such a 4D data cube with a 264x264 pixel detector image for each probe position can be recorded in less than 70 s. This camera uses a direct detecting, radiation hard pnCCD with a readout speed of at least 1,000 full frames per second (fps) [1]. Several measurements have been performed to demonstrate the capability of this new camera for 4D-STEM imaging, among them strain analysis, magnetic domain mapping and most recently electron ptychography.

Electron ptychography has been described theoretically already in 1993 [2] but so far was limited experimentally by the low readout speed of existing cameras. In this technique, the intensity distribution in the bright field disk is recorded in 2D for each STEM probe position (Figure 1a). In an electron wave-optical approach the phase and amplitude information is extracted from the recorded intensity images. The reconstructed phase image shows enhanced image contrast compared to the conventional annular dark field image, especially for light elements (Figure 2). Measurements with the pnCCD (S)TEM camera were carried out using a JEOL ARM200-CF in order to investigate different samples with the ptychographic phase reconstruction technique. Simulations show that the phase reconstruction technique does not require the full camera resolution of 264x264 pixels [3]. The pnCCD camera can be used in windowing and binning modes to further increase the measurement speed. Different combinations were tested at up to 4,000 fps (4-fold binning in one direction, i.e. 66x264 pixels, see Figure 1c). A 512x512 STEM image can then be recorded in just over a minute.

Other 4D-STEM applications like strain analysis or magnetic domain mapping use the cameras's ability to precisely determine the exact position of the bright field disk on the detector. When traversing the sample the electron beam can be deflected due to different effects in the sample causing a movement of the positions of the diffraction disks. The advantage of using a 2D detector over conventional quadrant DPC detectors is the possibility to separate movements of the disk from intensity fluctuations inside it. Strain in the sample causes such movements of the diffracted beam and can be measured by 4D-STEM [4]. Imaging of magnetic fields inside the sample is possible using a Lorentz-like setup of the STEM, a 2D detector and analysis of the movements of the BF disk. Measurements demonstrating the technique with a nickel sample have been done.

Dark field measurements profit from using 4D-STEM as well. By adapting the camera length, the 2D diffraction pattern can be recorded. In an offline analysis different STEM images can be reconstructed by using different parts of the detector images corresponding to different parts of the scattered beam.

The pnCCD (S)TEM-camera promotes new techniques in STEM, with various fields of application benefiting from recording the two-dimensional detector image. With its direct detection, high readout speed and radiation hardness the pnCCD (S)TEM camera makes recording of large 4D data cubes in short times possible and enables new science.

1. H. Ryll et al., Microscopy and Microanalysis 19 (2013), p.1160-1161.
2. J.M. Rodenburg, B.C. McCallum, P.D. Nellist, Ultramicroscopy. 48 (1993) 304-314.
3. H. Yang et al., Ultramicroscopy. doi:10.1016/j.ultramic.2014.10.013
4. K. Müller et al., Appl. Phys. Lett. 101 (2012), p. 2121101-2121104.

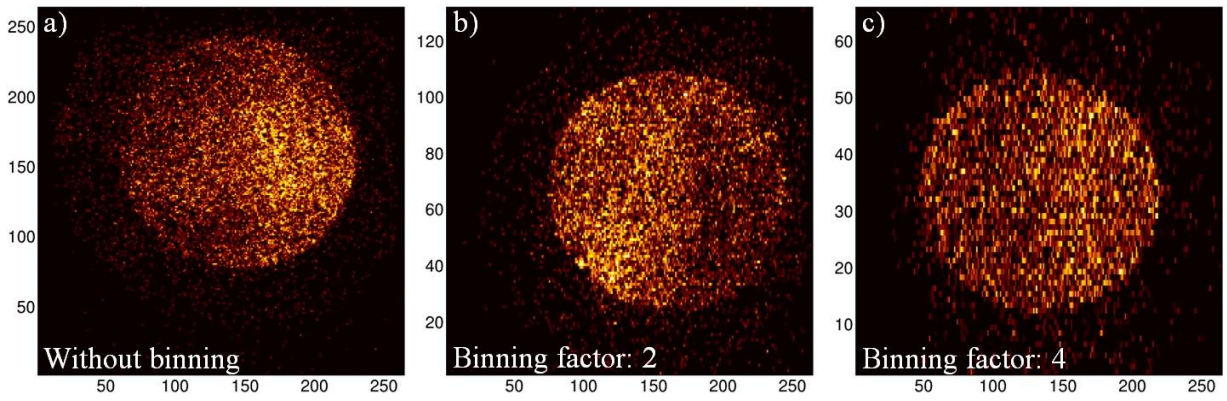

Figure 1. Examples of recorded single raw images of the bright field disk for individual probe positions in STEM. Images were recorded without binning (a), 2-fold binning (b) and 4-fold binning (c). Frame rates were 1,000, 2,000, and 3,000 fps, respectively. The intensity distributions in these images are analyzed to extract the phase information.

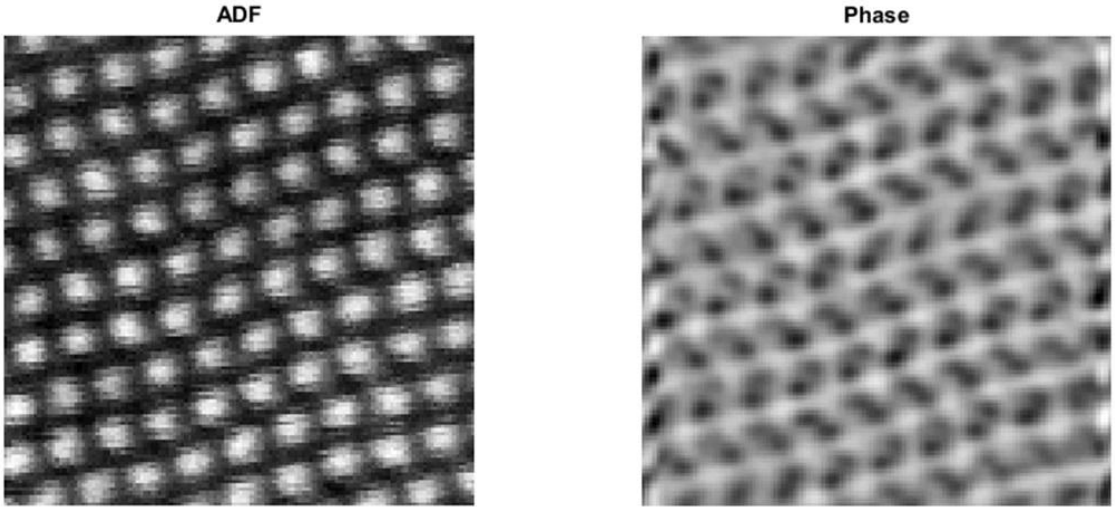

Figure 2. Comparison of the conventional annular dark field (ADF) image and the reconstructed phase of a GaN sample using a ptychography method. Pairs of Ga-N columns show in the reconstructed phase, but the N columns are nearly invisible in the simultaneously recorded ADF image. Images contain 128x128 probe positions recorded at a dwell time of 250 µs.

Advances in Instrumentation, Detectors, FIB and Preparation

IM1.P013
JEOL solutions for life sciences - from correlative microscopy to single molecules and tomography

E. Katzmann[1]

[1]JEOL GmbH, Eching, Germany

katzmann@jeol.de

JEOL (figure 1) is one of the largest manufacturer of electron optic systems and employs around 3000 people worldwide. Having a long tradition in manufacturing electron optic systems JEOL offers a wide range of solutions for life sciences. Starting from sample preparation tools like cross section polisher or ion slicer and going to correlative microscopy for scanning electron microscopes (SEM) with the SEM supporter software. For increased resolution different transmission electron microscopes (TEM, figure 2) with unique features as the in-column Ω energy filter combine the ease of use with superior data collection for every question to be solved in modern life sciences. Together with JEOL instruments several software solutions to automate data acquisition for single particle (JADAS) or tomography (TEMography) experiments are ready to be explored by the user.

Advances in Instrumentation, Detectors, FIB and Preparation

IM1.P014
IV characteristic and quantitative comparison of electroluminescence of a GaN based core-shell LED measured via point contacts inside a CL-SEM

J. Ledig[1], T. Schimpke[1,2], G. Scholz[1], F. F. Krause[3], M. Strassburg[2], A. Rosenauer[3], H.- H. Wehmann[1], A. Waag[1]

[1]Technische Universität Braunschweig, Institute of Semiconductor Technology and Laboratory for Emerging Nanometrology, Braunschweig, Germany
[2]OSRAM Opto Semiconductors GmbH, Regensburg, Germany
[3]University of Bremen, Institute of Solid State Physics, Bremen, Germany

j.ledig@tu-bs.de

Three dimensional light emitting diodes (LEDs) with a shell geometry around a columnar GaN core are supposed to have substantial advantages over conventional planar LEDs. The active area along the sidewalls of the GaN pillars can considerably be increased by high aspect ratios - leading to a lower current density inside the InGaN quantum well (QW) at the same operation current per substrate area. Due to the 3-dimensional (3D) shape, the electrical and optical characterization of such device structures is a substantial problem. In addition, a spatially resolved investigation is needed in order to discuss gradients along the structure and to optimize them regarding the device operation.

The investigated AlInGaN core-shell LEDs are grown by selective area metal organic vapor phase epitaxy on templates consisting of a patterned SiO_x mask layer on an n-type GaN layer on sapphire wafer. A manipulator setup inside a scanning electron microscope (SEM) has been used in combination with a cathodoluminescence (CL) system to characterize electro-optical properties of single 3D-LEDs. Electron beam induced current (EBIC) images obtained inside the SEM by contacting via the substrate and a tungsten probe tip, c.f. Figure 1, clearly prove, that a conjunct p-type shell is wrapped around the entire n-type column with an aspect ratio of about 8 forming a depletion region.

For each spectrum the electroluminescence (EL) is driven by a voltage source, enabled 500 ms prior to measuring the current. Subsequently the CCD parallel detector is started and the voltage source is disabled after a certain EL-exposure time. This EL-exposure time is dynamically adopted from 900 ms down to 5 ms which enhances the dynamic range of the optical setup. The spectra are corrected with respect to the spectral sensitivity of the optical system - including the collection optics, monochromator and the detector. Although the absolute sensitivity of the optical setup is not known, an insight to the external quantum efficiency (EQE) of the EL is possible by comparing different LEDs. A reliable adjustment of the samples (by about 10 µm) in the focus of the parabolic collection mirror was achieved by using the optical microscope image on the CCD parallel detector, in particular the light spots where smaller than the entrance slit.

The electro-optical measurement (IV and EL spectra) at several contact points along the structure was performed in an upward and backward sweep using a voltage source. The IV-hysteresis at each IV curve, c.f. Figure 3, is assigned to burn-in of the tip contact and have a small significance regarding the evaluated LI characteristic. The IV curves indicate that both the current spreading (low current regime) and a series resistance (high current regime) increase along the sidewall which is assigned to an increasing p-GaN layer thickness along the structure. A lamella from this sample was prepared by FIB milling, STEM investigations by HAADF imaging revealed the interfaces and a gradient in thickness of the shell layers along the height and are yielding the local composition of the $In_xGa_{1-x}N$ and $Al_xGa_{1-x}N$ layers. A wavelength shift of the QW emission by about 30 nm is observed along the structure height for both excitation methods (CL and EL, c.f. Figure 2 and 4); this is assigned to a gradient of the indium incorporation caused by changing local growth conditions. Those findings gave a valuable insight as the gradient can be reduced by altering the growth parameters.

1. We thank Dr. Uwe Jahn for support regarding optical characterization. The financial support of the European commission (GECCO) as well as the endorsement of the JOMC is acknowledged.

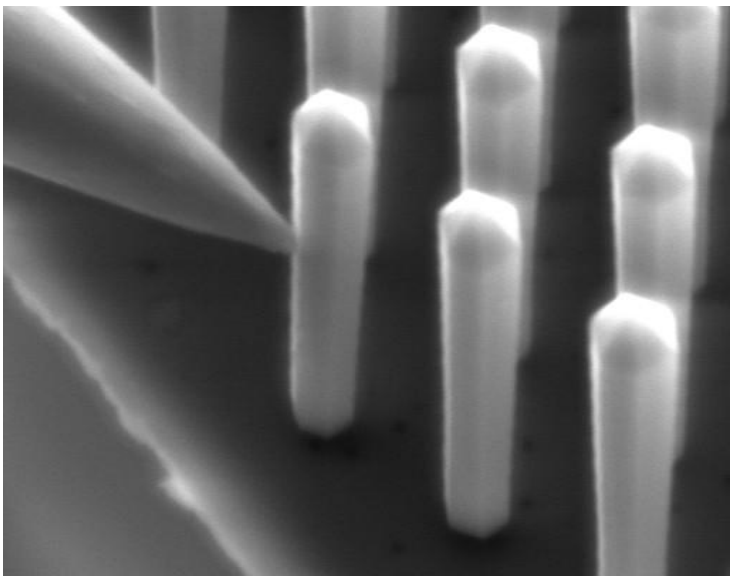

Figure 1. SE image of the core-shell LED contacted by a probe tip at the sidewall at a height of 5.6 µm (FOV = 11.4 µm, tilt = 30°, EHT = 15 kV).

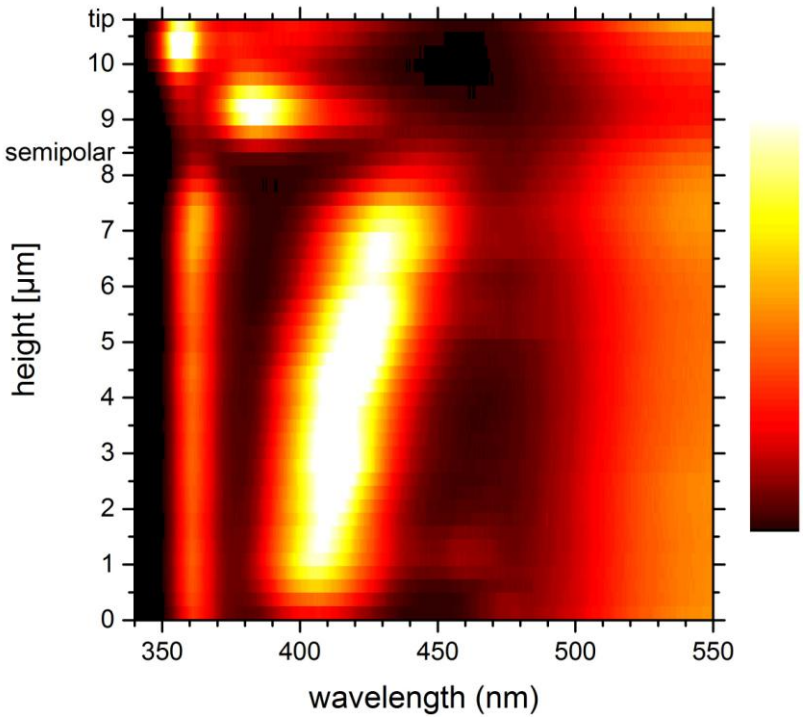

Figure 2. contour plot of the spectral CL intensity of a line-scan along a core-shell LED shown in (tilt = 30°, EHT = 10 kV) revealing the NBE, YL and QW emission.

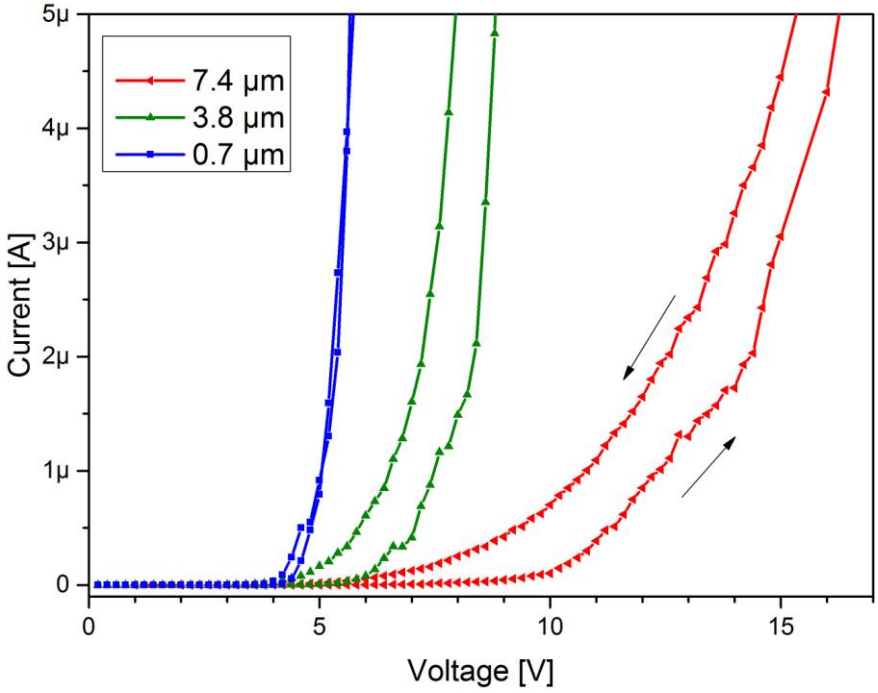

Figure 3. IV characteristics obtained at three contact points on the LED shown in Figure 1.

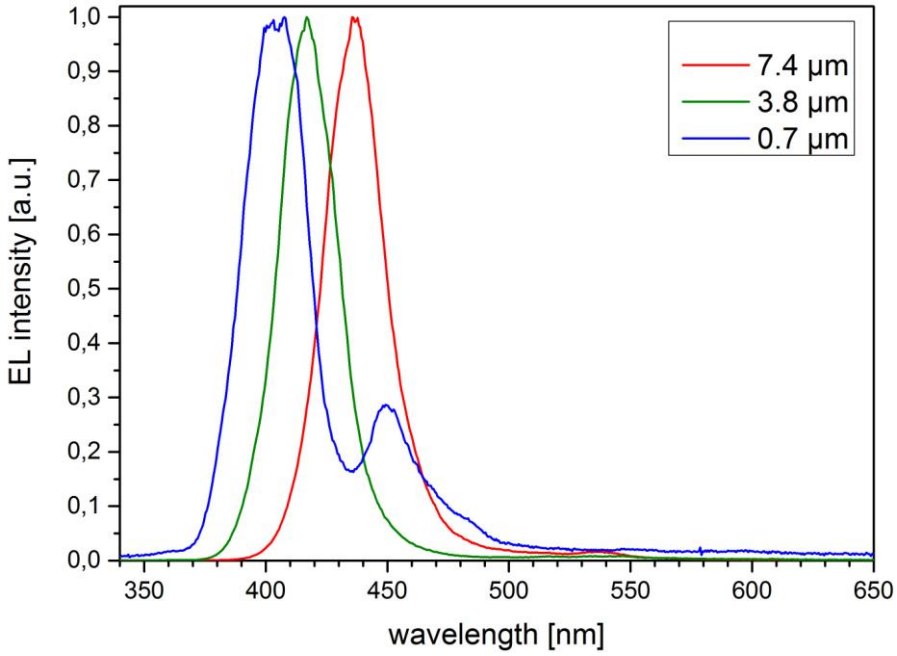

Figure 4. normalized EL spectra obtained at about 1 µA of three contact points on the LED shown in Figure 1.

Advances in Instrumentation, Detectors, FIB and Preparation

IM1.P015
The SPANOCH method: A key to establish aberration correction in miniaturized (multi)column systems?

R. Janzen[1], M. Haider[1,2], B. da Cunha[1,3]

[1]Karlsruher Institut für Technologie, Laboratorium für Elektronenmikroskopie, Karlsruhe, Germany
[2]CEOS GmbH, Heidelberg, Germany
[3]Carl von Ossietzky Universität, Oldenburg, Germany

info@dr-janzen.de

Unfortunately charged particle optics applications are usually limited by aberrations, especially by the chromatic and spherical aberration. In electron microscopy correctors are meanwhile commonly used. Nowadays charged particle optics finds its way into miniaturized applications. Whereas miniaturized columns including mini lenses exist, the commonly used correctors are too complex for a use in miniaturized single or multicolumn systems. Nevertheless the general principle of multipole based correctors may be transferred to such systems.

The key is the fact that a hole with n-fold shape within an aperture separating two electric fields with different strengths produces a superposition of a round lens field and a 2n-pole field (plus more or less higher order terms depending on the shape). In simple terms all that has to be done in order to use such multipole fields for reduction / correction of aberrations, is to pile up apertures with n-fold shaped holes on adequate voltages in a sophisticated way.

The method doing so will be denoted by SPANOCH (**S**ophisticated **P**ile of **A**pertures with **no**n- **c**ircular **H**oles) in the following, indicating that it uses apertures with non-circular holes in order to produce multipole fields (for correction purposes).

In 2008 an electrostatic analogue of the commonly used hexapole Cs-corrector was used in order to design a Cs-corrected extraction optics. This was used as a test setting within a ray tracing based computer simulation to demonstrate the SPANOCH concept and its proof of principle.

Here we describe our efforts to use SPANOC for correction of chromatic aberration.

For that purpose we took the Rose-Weißbäcker correction principle (See [1] and following explanations) of an electrostatic Cc-corrector and transferred it to SPANOCH. The Rose-Weißbäcker design is based on Scherzer's finding that neither rotationally symmetric nor quadrupole fields alone can produce negative chromatic aberration contributions but a superposition of both can. Scherzer derived a condition how to combine those types of fields in order to get maximum correction power. This demand for superimposed quadrupole and round lens fields makes the SPANOCH concept be predestined for building an electrostatic Cc-corrector. In our design strategy we use Scherzer's condition as an input. Thus it is fulfilled at any aperture a priori. The contours of the aperture holes are later on calculated out of equipotential lines of the superposition of the round lens fields and the quadrupole fields assigned to them by Scherzer's condition.

As in any quadrupole based Corrector design the (chromatic) aberration is corrected in two perpendicular sections subsequently. Therefore an astigmatic splitting (providing the first of a series of astigmatic intermediate images) is needed. In contrast to the conventional (Rose-Weißbäcker) design (and in accordance to our design rule) Scherzer's condition is fulfilled within the astigmatic splitting as well as within the stigmatic recombination. Thus these components become involved in the correction process. This leads to a simple corrector design: The entire corrector is built out of only 3 triplets of apertures with non-circular holes. The generic design contains the voltages of the apertures and the distances between them as degrees of freedom. Sensible values of those parameters are found by a numerical feedback loop taking care of the right symmetry conditions of the axial fundamental rays (see figure 1). We verified the correction by adding two round lenses (one at any end of the assembly) forming a telescopic imaging with variable magnification and showing that the chromatic aberration integral vanishes in the image plane for both sections.

1. Christoph Weißbäcker, Harald Rose: Electrostatic correction of the chromatic and of the spherical aberration of charged-particle lenses; Journal of Electron Microscopy 50 (5): 383-390 (2001)

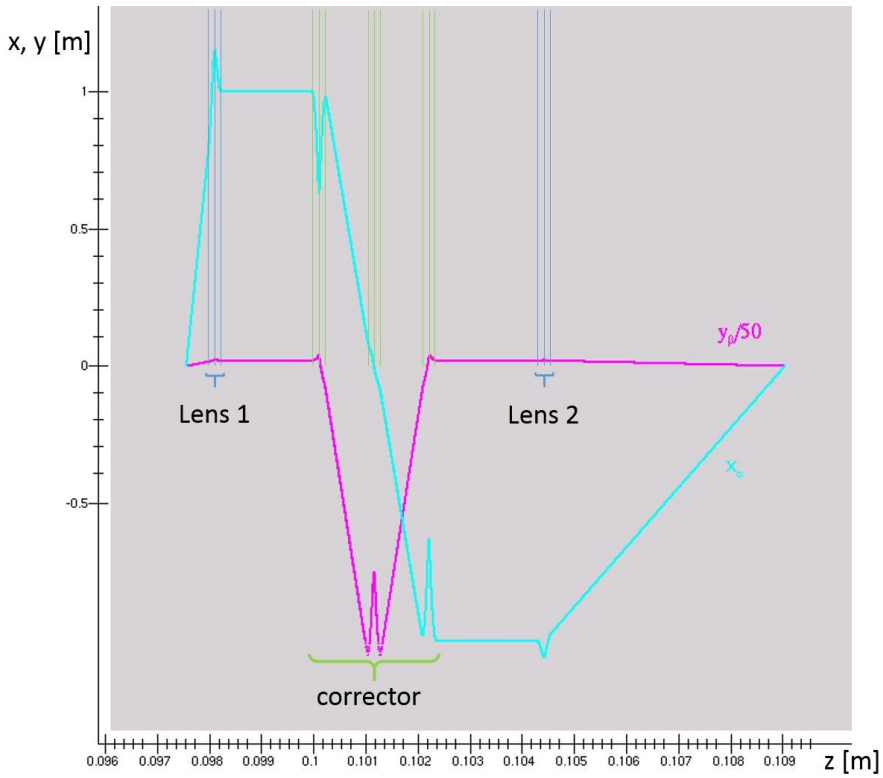

Figure 1. Position markers of apertures and sketch of the course of the axial fundamental rays within the SPANOCH Cc-Corrector embedded in a telescopic round lens duplet.

Advances in Instrumentation, Detectors, FIB and Preparation

IM1.P016
Crystal orientation mapping using ion image series: iCHORD

L. Cyril[1], D. Thierry[1], Y. Hui[1], B. Nicholas[2], D.- M. Armel[3], V. D. M. Bertrand[4], R. Christophe[5], E. Thierry[1]

[1]University of Lyon - INSA de Lyon - CNRS, MATEIS Laboratory, Villeurbanne, France
[2]University of Lyon - CNRS, ILM Laboratory, Villeurbanne, France
[3]University of Lyon - CNRS, INL Laboratory, Villeurbanne, France
[4]ENS of Lyon - CNRS, LGL Laboratory, Lyon, France
[5]University of Lyon - INSA of Lyon - CNRS, LIRIS Laboratory, Villeurbanne, France

cyril.langlois@insa-lyon.fr

Obtaining an orientation map of grains in a polycrystalline material is fundamental in materials science. Countless applications ranging from the study of metallic alloy recrystallization to the determination of grain boundary character in ceramics rely on a complete knowledge of a material's crystallographic features [1,2]. For all material properties where crystallographic texture plays an important role, it is crucial to have access to the orientation of the grains in the sample.

Generally, for grains at the micron scale, orientation maps are obtained by Electron Back Scattered Diffraction (EBSD) in a Scanning Electron Microscope (SEM). For various reasons, orientation maps with the EBSD technique can be challenging: material properties (conductive or not, preparation problems), geometrical setup (impossibility to collect the signal), pseudo-symmetry Kikuchi diffraction patterns, nano-sized structures, large area mapping, highly deformed samples, etc. In this context, it is worth investigating other means to map the crystallographic orientations of grains in polycrystalline samples.

Channeling contrast is a well-known phenomenon allowing grains of a polycrystalline sample to be distinguished, even if only one phase is present. Depending on the orientation of the crystallographic planes, the secondary and backscattered electron yields vary from one grain to the other, resulting in different intensities received by the detectors. For this reason, the contrast of each grain varies when the orientation of the sample is changed [3].

We show in this study how it is possible to use this channeling effect (with an electron or an ion beam) to obtain the three Euler angles characterizing the orientation at a given point of the sample surface. The main concept is to obtain an intensity profile at that point, to compare the intensity profile to a semi-empirical database of profiles and to find the best fit, i.e. the three Euler angles associated with this point. Comparing this method with EBSD measurements on the same area allowed us to determine the precision of the indexation, which is better than 5°. We discuss then the best way to obtain an intensity series, either by tilting or rotating the sample. The issue of acquisition time is also discussed. We conclude by evaluating the pros and cons of using ions or electrons for such indexation purposes.

1. Estimation of recrystallized volume fraction from EBSD data, J. Tarasiuk, Ph. Gerber and B. Bacroix, Acta Materialia (2002) 50 1467-1477
2. Characterization of the Grain-Boundary Character and Energy Distributions of Yttria Using Automated Serial Sectioning and EBSD in the FIB, S.J. Dillon and G.S. Rohrer, J. Am. Ceram. Soc. (2009) 92 1580-1585
3. Crystallographic orientation contrast associated with Ga+ ion channeling for Fe and Cu in focused ion beam method, Y. Yahiro, K. Kaneko, T. Fujita, W.-J. Moon and Z. Horita, J. Electron Microscopy (2004) 53 571-576

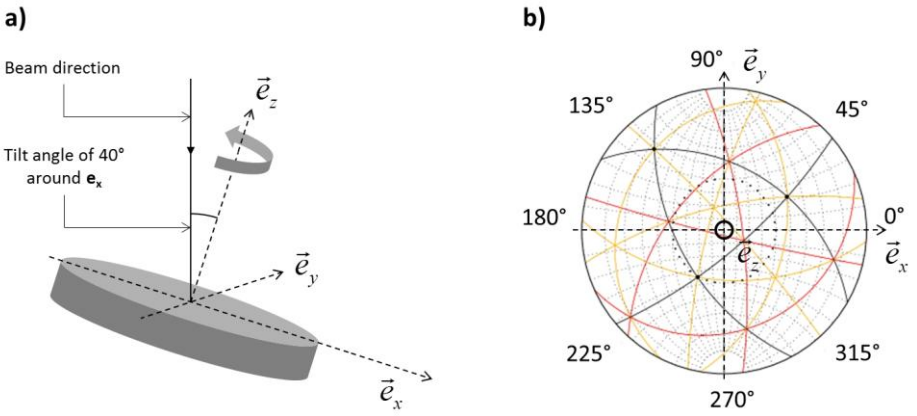

Figure 1. (a) Acquisition setup for iCHORD method (b) Stereographic projection of a grain + reference frame

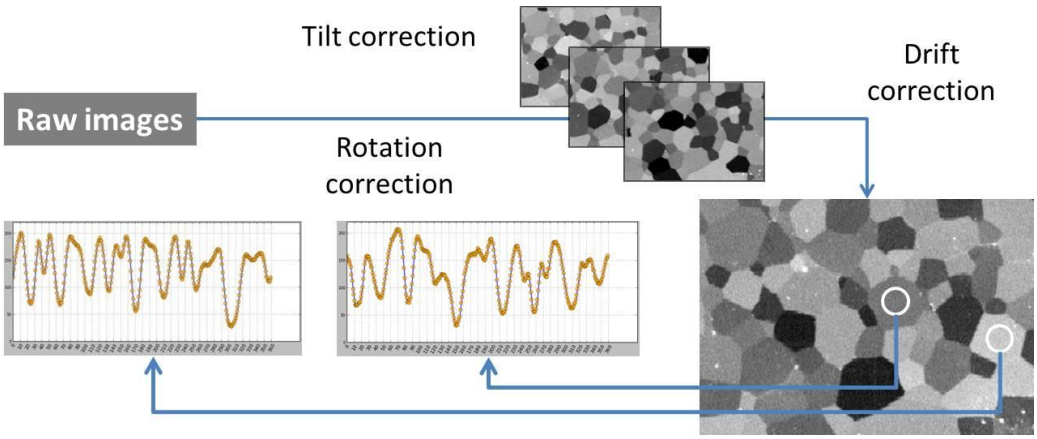

Figure 2. Image processing to obtain an intensity profile for the iCHORD method.

Figure 3. (a) iCHORD raw orientation map (b) EBSD orientation map on the same area -orientation averaging inside each grain (c) disorientation map between iCHORD and EBSD maps. Max disorientation = 4.8°.

Advances in Instrumentation, Detectors, FIB and Preparation

IM1.P017
A compact transfer lens design used for desktop electron microscope

W.- Y. Chang[1], F.- R. Chen[1]

[1]National Tsing Hua University, Engineering and System Science, Hsinchu, Taiwan

weiyu429@gmail.com

Spherical and chromatic aberrations are two of the most important lens aberrations for high resolutionelectron microscope. Rose proposed that a spherical aberration corrector can be made of two hexapoles together with transfer round lens doublet, and combined magnetic and electrostatic quadrupole lenses can be used as a chromatic aberration corrector [1]. In the former case, the role of the first transfer doublet (round lens) is to transfer the diffraction pattern to the corrector. The second transfer doublet is used to reverse the electron trajectory to cancel out the second-order aberrations induced by the hexapole. In the latter case, quadrupole lenses make the beam shape astigmatic in the x- and the y-directions and generate negative chromatic aberration in each direction. Normally, the physical dimension of a lens depends on the size of the coils. As shown in figure 1 (a) [2], in order to design a compact aberration corrector to fit into a commercial table-top scanning electron microscope, we design a spherical aberration corrector using the permanent magnets as transfer lens doublet, which has the rotation free property at the image plane. The magnetic field of a round lens usually can be modelled as a bell shape function [3]. As shown in equation 1, we can fit the magnetic field of permanent magnet lens by two bell shape functions of the inverse sign, each of which has a relative shift in the z-direction. The B_0 is the maximum field strength of the peak, z_0 is the peak positions of magnetic field relative to the center z=0, and the W is the FWHM of each peak.The result field distribution at 1200 Gauss is shown as a black line in figure 1 (b).The magnetic field of the permanent magnet is equivalent to that of the conventional round lens doublet.The solid red and green lines are the ray trajectory of focus and field rays, respectively, for the field strength at 1200 Gauss, while the dash lines depict corresponding ray trajectory for the case of the transfer lens at a specified field strength with a 5~10 percent deviation relative to those for 1200 Gauss.

The electron paraxial rays can be deduced by solving the differential equation ofparaxial path equations (2) [4].

The structure of Cs aberration corrector with permanent magnet transfer lens doublet and two hexapoles is given in the figure 2 (a). The permanent magnet transfer lens has a magnification M=-1. The two hexapole magnetic lenses locate at the coma free point as proposed by Rose. The total length of the aberration corrector is about 50mm. Again, the red and green solid lines are the calculated focus and field rays. Figure 2 (b) and figure 2 (c) shows the electron spot size aberration figure simulated by MEBS software for 15kV electrons. The electron spot size is about 20nm without the spherical corrector, but it is effectively reduced to 0.5nm by introducing the proposed aberration corrector.

As a result, it is clear, we can modify the electron ray by slightly adjust the field strength, and as shows in the solid red and green in figure 1 (b), it represents the ideal characters of a transfer lens. Rays parallel to the optical axis will also parallel to the optical axis after passing through the permanent magnetic lens, and rays come from the front focal point will again concentrate on the back focal point. We not only can reduce the total physical dimension, but can also correct the spherical aberration by using the newly developed Cs corrector. The final spot size due to spherical aberration is below 0.5nm.

Figure 1:(a) The construction of the permanent magnets transfer doublet, and (b) the magneticfield distribution at Bo=1200 Gauss (black line), the solid red lines are the focusing ray and the solid green lines are the field ray atBo=1200 Gauss. The dashed line shows the ray with 5~10 percent deviation relative to those for 1200 Gauss.

Figure2:(a) The proposed aberration corrector consists of two permanent magnet transfer lens doublet and two hexapole magnetic lenses locate at the coma free point where is at a distance of focal length f=7mm from the transfer lens. (b) The electron spot size without the Cs corrector is about 20nm. (c) The electron spot size with Cs corrector is about 0.5nm (Not in the same scale as Fig. 2 (b).

1. H. Rose, Nuclear Instruments and Methods, 187 (1981) 187-199
2. T. Iwaya, S. Kobori, T. Ohtaki, H. Hatano “SCANNING ELECTRON MICROSCOPE,” U.S. Patent: 2012,0211654, issued date Aug. 23, 2012

3.Glaser, W. , *Z. Phys.*, 117, 285 (1941).
4. Rose, Harald H. "Geometrical charged-particle optics." (2009).

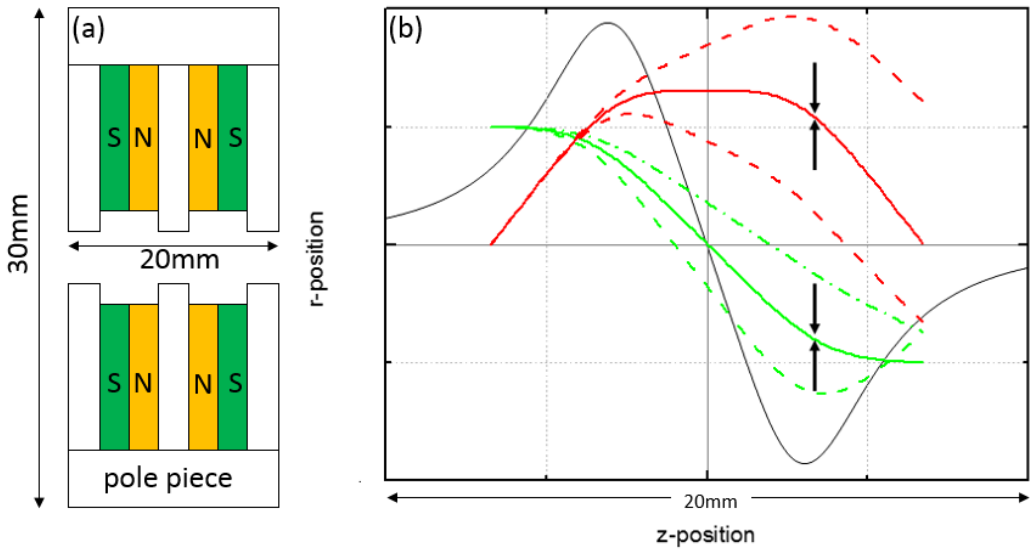

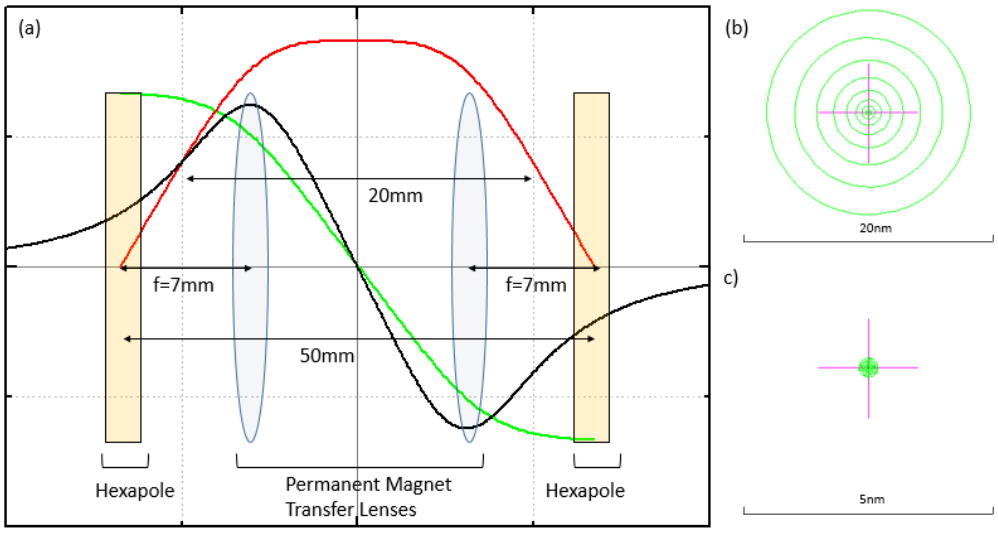

$$B(z) = \frac{B_0}{1+\left(\frac{z-z_0}{W}\right)^2} - \frac{B_0}{1+\left(\frac{z+z_0}{W}\right)^2} \qquad (1)$$

$$r''(z) + \frac{\eta}{8\Phi} B(z)^2 r(z) = 0 \qquad (2)$$

Advances in Instrumentation, Detectors, FIB and Preparation

IM1.P018
Ultra-high resolution FIB-SEM for semiconductors

J. Jiruše[1], M. Havelka[1], J. Polster[1], T. Hrnčíř[1]

[1]TESCAN Brno, s.r.o., Brno, Czech Republic

jaroslav.jiruse@tescan.cz

Combined ultra-fast FIB (Focused Ion Beam) with the plasma Xe ion source and the ultra-high resolution SEM (Scanning Electron Microscope) with the immersion electron optics is introduced to form a powerful tool for semiconductor industry.

Plasma Xe FIB has 50-times higher milling rate compared to traditional Ga ion FIB and eliminates conductive contamination of integrated circuits [1]. Therefore, it is useful for processing large volumes of compounds such as SiGe, (In)GaAs and (In,Al)GaN. Utilization was presented for preparation of large TEM lamella [2] or the first large-scale FIB tomography [3]. Until recently, Xe FIB had a lower resolution hindering its utilization for common Ga FIB applications. Improving the lateral resolution more than two times, we overcame this drawback.

Replacing the conventional electron optics of SEM with recently developed immersion electron optics and using a sophisticated detection system enable to reach an ultra-high resolution imaging at low electron beam energies. Detectors of backscattered electrons have increased detection limits and efficiency, thus able to detect in the complete range of electron energies 0.2-30 keV. This is advantageous for inspecting the semiconductor samples and integrated circuits just after preparation of their large cross-sections by Xe plasma FIB, see Figures 1 and 2. For observation with low-energy electrons sensitive to fine surface details, it is crucial to minimize the curtaining effect by tilting the sample in the course of FIB polishing. To take care of this unwanted effect, a special piezo manipulator was designed, so called the rocking stage.

FIB-SEM system can be equipped with a wide range of integrated analytical instruments like EDX, EBSD, TOF-SIMS, EBIC and even AFM reported previously [4]. TOF-SIMS analyzer benefits from Xe primary ions by better detection limit compared to Ga primary ions. Raman analysis in FIB-SEM [5] is also enabled here thus providing ultra-high resolution electron beam, ultra-fast milling Xe ion beam and finally photon beam in one instrument.

1. T Hrnčíř *et al,* Proceedings of 38th Int. Symp. for Testing and Failure Analysis ISTFA (2012), 26.
2. A Delobbe *et al,* Microsc. and Microanal. 20 (2014), 298.
3. T Hrnčíř *et al,* Microsc. and Microanal. 19 Suppl 2 (2013), 860.
4. J Jiruše *et al,* Microsc. Microanal. **18** Suppl 2 (2012), 638.
5. J Jiruše *et al,* Journal of Vac. Sci. Technol. B **32** (2014), 06FC03.
6. The research leading to these results has received funding from the European Union 7th Framework Program [FP7/2007-2013] under grant agreement n°280566, project UnivSEM.

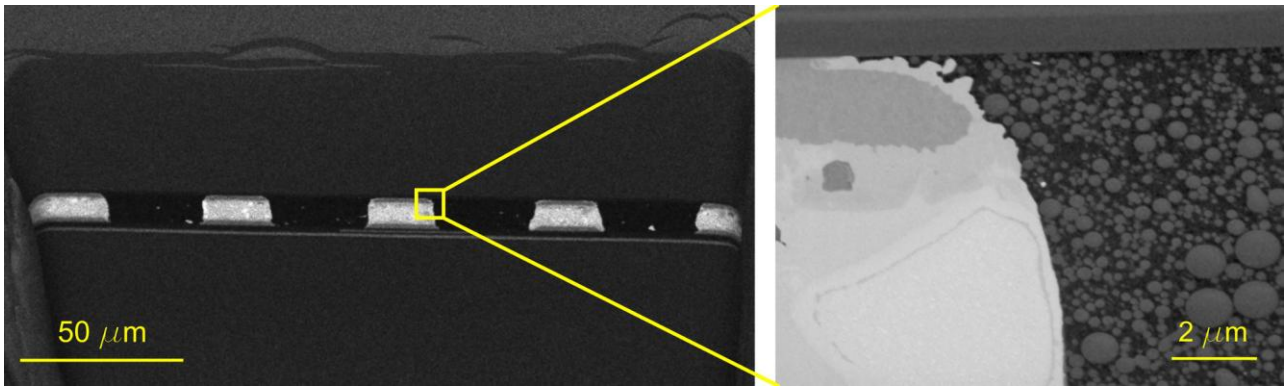

Figure 1. Image acquired by low-energy In-Beam BE detector with acceleration voltage 2 kV. Left: Large-area cross section through mold compound and Al bonding wires. Right: Detail on top edge of Al metal via, silicon layers and polysilicon filling.

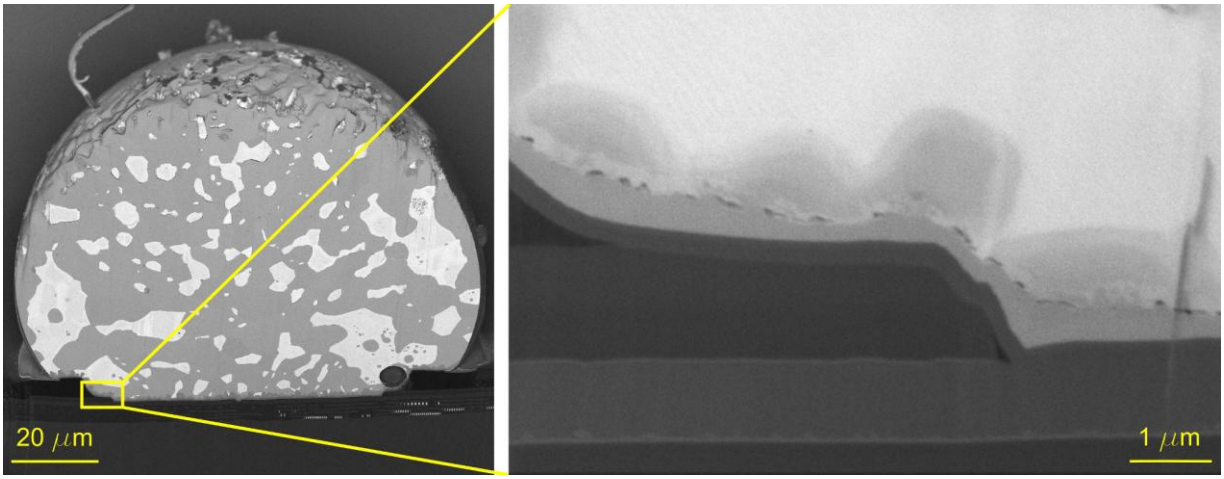

Figure 2. SEM image of the solder bump, cross-sectioned by plasma FIB, taken using low-energy In-Beam BE detector. Left: Large-area cross section of the solder bump. The electrical and mechanical connection between the die and the substrate is critical for the flip chip package functionality. Inside Sn bump material there is visible formation of Pb dendritic structure points (white islands) caused by e.g. too rapid cooling. Intermetallic compound (IMC), repassivation layer (polyimide), under bump metallurgy (UBM) and integrated circuit layers are clearly visible due to the high material contrast of In-Beam BE imaging.
Right: Detail of the bump at 1 keV showing cracks in intermetallic compound layer and delamination in repassivation layer. Sn - Pb island boundary is also clearly visible.

Advances in Instrumentation, Detectors, FIB and Preparation

IM1.P019
Imaging at low energies by a new scintillation BSE detector

J. Kološová[1], M. Havelka[1], M. Petrov[1], J. Jiruše[1], P. Horodyský[2]

[1]TESCAN Brno, s.r.o., Brno, Czech Republic
[2]CRYTUR, s.r.o., Turnov, Czech Republic

jolana.kolosova@tescan.cz

Low-energy scanning electron microscopy (SEM) is becoming the preferred instrumentation technique in many fields of research. Operating of SEM at low primary beam energies offers several advantages, like decreasing the depth of specimen radiation damage, clear visualization of non-conductive samples or better resolution of fine surface structures [1]. In the case of backscattered electron (BSE) imaging, working at low primary beam energies <2keV (and currents) puts high demands on the actual detector design because of the weak signal intensities. We will show results obtained with our recently developed new scintillation type BSE detector with enhanced sensitivity in the low energy region [2]. The detection limit of the detector was pushed down to 200 eV. A good collection efficiency together with the high light yield and short decay time of the scintillation material guarantee high signal to noise ratio even at high scanning rates and low probe currents. A typical field of application of the new detector is failure analysis in semiconductor industry. Low energies ensure a better depth resolution as the signal contains information only from the top layers and is not affected by the signal from the bulk, see Figure 1. Another application can be found in 3D analysis of resin-embedded biological samples. Low electron range is needed to prevent oversampling and radiation damage, and the charging artefacts must be avoided [3]. The detector was routinely used for serial block-face backscattered imaging of epoxy-embedded biological tissue and a variety of staining protocols for contrast enhancement were successfully tested, see Figure 2. Concerning uncoated non-conductive samples, undistorted artefact-free BSE images of highly charging samples were obtained through imaging at critical energy with drift-corrected frame accumulation, see Figure 3.

1. D.C. Bell and N. Erdman (Eds.) *Low Voltage Electron microscopy: Principles and Applications*, John Wiley and Sons, 2013
2. J. Kolosova *et al*, Proceedings of the 18th International Microscopy Congress, 2014
3.http://www.gatan.com/products/sem-imaging-spectroscopy/3view-system#publications(Gatan 3View application note)
4. http://sourceforge.net/projects/accord/

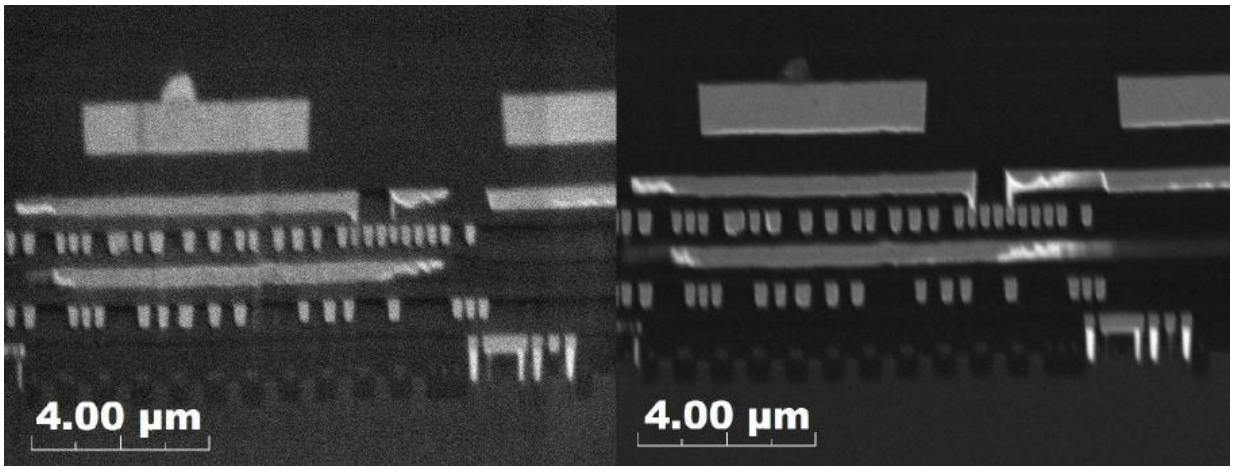

Figure 1: IC cross section imaged at 1 keV (left) and 5 keV (right) primary energies showing enhanced surface sensitivity at lower primary beam energies.

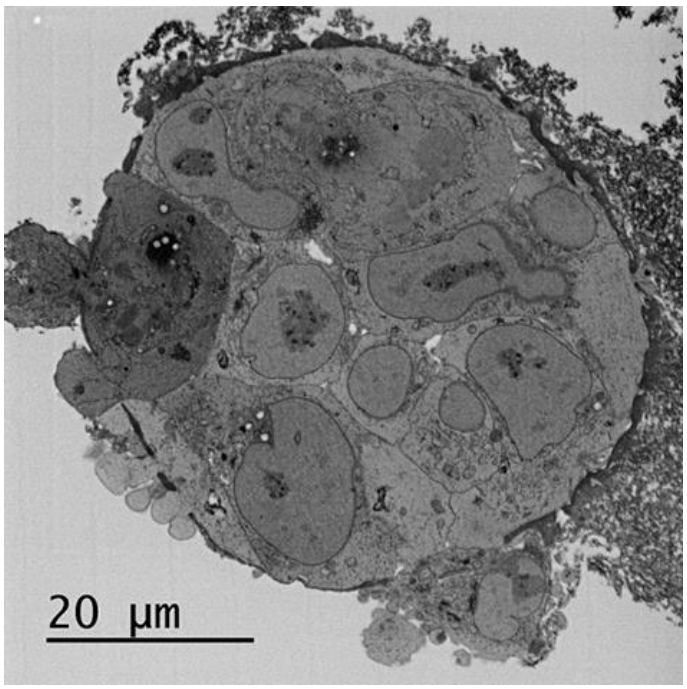

Figure 2: The human embryonic stem cell colony acquired during serial block-face imaging. Sample by courtesy of Department of Histology and Embryology, Faculty of Medicine, Masaryk University, Brno.

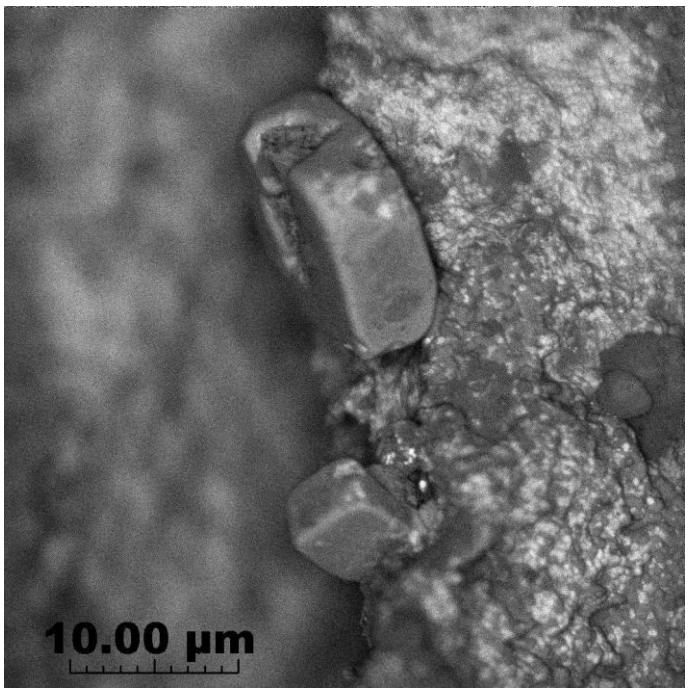

Figure 3: Uncoated Al2O3-ZrO2 laminate with KCl cubes. Imaging was done at 800 eV primary beam energy and 200 pA probe current. Drift-corrected frame accumulation was used [4].

Advances in Instrumentation, Detectors, FIB and Preparation

IM1.P020
SIMS on FIB instruments: a powerful tool for high-resolution high-sensitivity analytics at the nano scale

D. Dowsett[1], T. Wirtz[1], J.- N. Audinot[1], S. Eswara Moorthy[1], P. Philipp[1]

[1]Luxembourg Institute of Science and Technology, Advanced Instrumentation for Ion Nano-Analytics (AINA), Belvaux, Luxembourg

david.dowsett@list.lu

FIB-based instruments have become of increasing importance in materials and life sciences. They are an ideal tool for high resolution 2D and 3D imaging and for nanofabrication (nano-machining and deposition, etc.), yet their analytical capabilities are currently limited. By contrast, secondary ion mass spectrometry (SIMS) is an extremely powerful technique for surface analysis owing to its excellent sensitivity, good dynamic range, high mass resolution and its ability to differentiate between isotopes. Adding SIMS capability to FIB instruments offers not only the prospect of obtaining elemental information at much higher resolution than state-of-the-art SIMS instruments (limited only by the size of the probe-sample interaction ~10nm), but allows for a direct correlation of SIMS images with high resolution secondary electron images.

Past attempts of integrating mass spectrometers on FIB instruments were rather unsuccessful because of poor detection limits which were due to (i) low ionization yields of the sputtered matter, (ii) extraction optics with low secondary ion extraction efficiency, and (iii) mass spectrometers with a low duty cycles and/or transmission. In order to overcome these limitations, we have investigated using reactive gas flooding during FIB-SIMS and developed compact high-performance magnetic sector mass spectrometers with dedicated high-efficiency extraction optics.

In order to reach good detection limits when probing very small voxels in imaging applications, the ionization probability of the sputtered atoms and molecules needs to be maximized. When using typical ion species used in FIB-based instrumentation such as Ga or noble gases, the intrinsic yields are low compared to the ones found in conventional SIMS. Secondary ion yields have been maximised by using O_2 flooding for positive secondary ions and Cs flooding for negative secondary during the SIMS analysis. Compared to Ga or noble gas primary ion species without flooding, the ionisation probabilities have been increased by up to 4 orders of magnitude, which leads to detection limits varying from 10^{-3}-10^{-7} for lateral resolutions between 10 nm and 100 nm. Images recorded with poorer lateral resolution but excellent detection limit (e.g. 1 ppm @ 50 nm) can be correlated with secondary electron images recorded at high lateral resolution using Ga, He, Ne or electron beams, overcoming the trade-off between detection limit and smallest feature size. The SIMS add-on has been optimised for FIB-SIMS applications. The extraction optics have maximum efficiency without distorting the primary ion beam and are coupled to a specially designed compact magnetic sector mass spectrometer with a high mass resolution (M/DM>1000), full mass range (H-U) and detection of several elements in parallel.

Adding the analytical capabilities of SIMS to high resolution imaging and nanofabrication instruments paves the way for a new level of correlative microscopy, combining both high special resolution structural and high sensitivity elemental information. We will present the latest results from a number of different FIB based instruments, including the helium ion microscope.

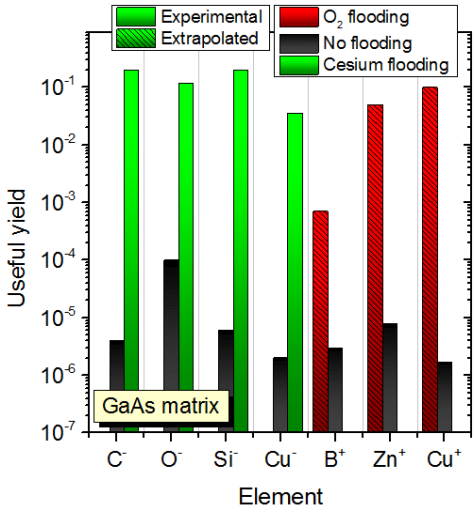

Figure 1: Enhancement of secondary ion yields using reactive gas flooding under Ga^+ bombardment

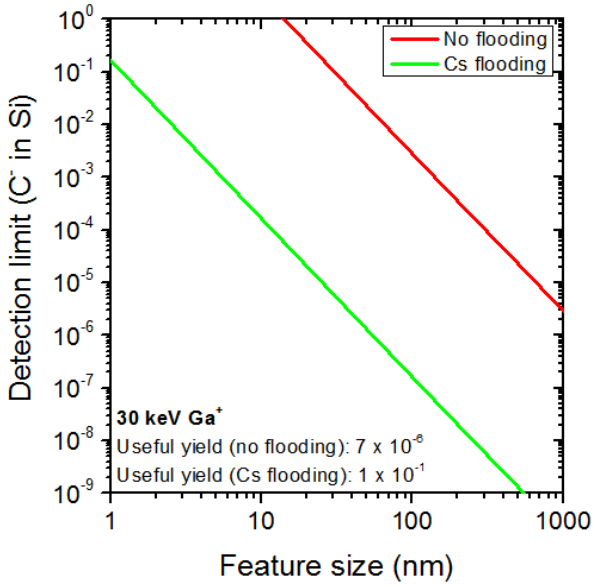

Figure 2: Detection limit using a Ga^+ FIB with and without Cs flooding vs. minimum feature size: example for the detection of C^-.

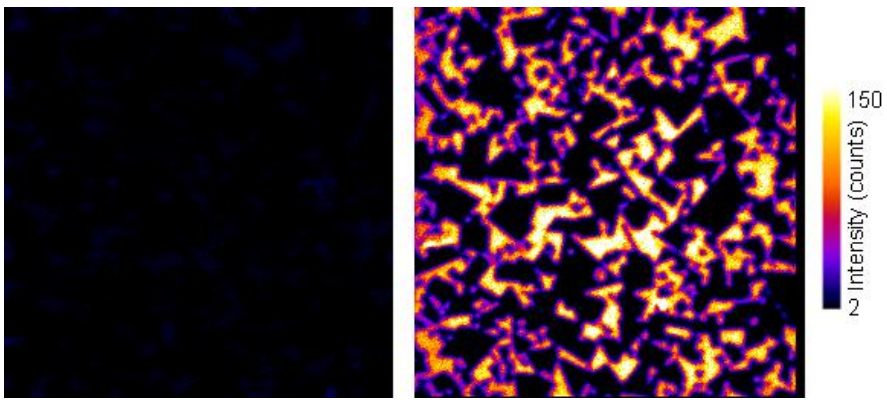

Figure 3: Co distribution in a tungsten carbide sample imaged by Ga^+ FIB-SIMS (field of view: 50x50 mm^2): (a) without O_2 flooding, (b) with O_2 flooding

Advances in Instrumentation, Detectors, FIB and Preparation

IM1.P021
Fast and easy automated TEM-lamella preparation

T. Volkenandt[1], G. Pavia[1], I. Schulmeyer[1], M. Kienle[1]

[1]Carl Zeiss Microscopy GmbH, Oberkochen, Germany

tobias.volkenandt@zeiss.com

Most people use a Focused Ion Beam (FIB) microscope to gain information from regions below the sample surface. One way to achieve this is to extract a small piece of sample material which can then be analyzed in a TEM (Transmission Electron Microscope), STEM (Scanning Transmission Electron Microscope) or a SEM (Scanning Electron Microscope) with STEM detector [1]. This process is called TEM lamella preparation. It can be time consuming and affords several preparation steps. If an operator planned to perform all these steps by hand, he would waste a lot of time watching the microscope and waiting for the individual tasks to finish before starting the next. This can be avoided by using automated software.

With its last generation of Crossbeam microscopes Zeiss introduced SmartFIB, a new software for FIB patterning. Of course SmartFIB is capable of all kinds of conventional milling, but also offers easy to use wizards for cross-section and TEM lamella preparation. The necessary user interaction is limited to choosing regions of interest and setting up parameters. SmartFIB takes care of the milling and can be left unattended. This allows multi-site preparation and overnight or weekend runs, providing the operator with a bunch of pre-prepared samples to continue working on.

The new TEM lamella wizard of SmartFIB consists of four main steps that are fully customizable to fit all needs. The first step is defining the region of interest and dimensions of the TEM lamella. In the second step the deposition of a protection layer can be setup with respect to thickness, margins and deposition material. The milling of the trenches is defined in the third step. It can be divided into several milling steps, like e.g. coarse, medium and fine. Each milling step can have its own FIB probe current, proximity and overlap. To minimize redeposition the milling steps can be split into loops and to assure a plane parallel final surface an additional stage tilt can be applied. The last main step is the cut-out. It can be adapted in terms of dimensions and shape. Remaining links are definable for both ends of the lamella or just one. This provides lift-out compatibility with any micro manipulator configuration. The complete lamella definition can be saved and imported again. After the job is set up it can be started either right away or transferred to a process list together with other milling jobs. At the time of exposure an advanced drift correction algorithm takes care of relocating the chosen sample positions and assures that the regions of interest stay in place especially during necessary tilting.

Figure 1 shows a screenshot of SmartFIB illustrating the variety of options in the TEM lamella wizard. The milling result can be seen in the background behind the schematic preview of the lamella milling objects. The milling time for such a TEM lamella can take between 10 and 60 minutes, depending on the sample material and chosen parameters. But during this time, no user interaction is necessary. After the process has finished, the TEM lamella is ready for lift-out and further polishing. The final polishing can be supported by live thickness measurements based on electron backscatter contrast. This assures precise preparation including end-point detection at a predefined thickness of the lamella. [2]

We illustrated the capabilities of the new SmartFIB software by Zeiss. SmartFIB offers workflow oriented wizards for TEM lamella preparation and comes with export/import functionality for fast and reproducible results. All tasks and layouts can be added to a process list which is processed automatically. No user interaction is needed during the exposure including GIS operations and stage tilting. SmartFIB is available for the new Crossbeam 540 and Crossbeam 340 microscopes.

1. LA Giannuzzi and FA Stevie, Micron **30** (1999), p. 197
2. R Salzer and L Lechner, Microscopy and Microanalysis **18** (2012), p. 654.

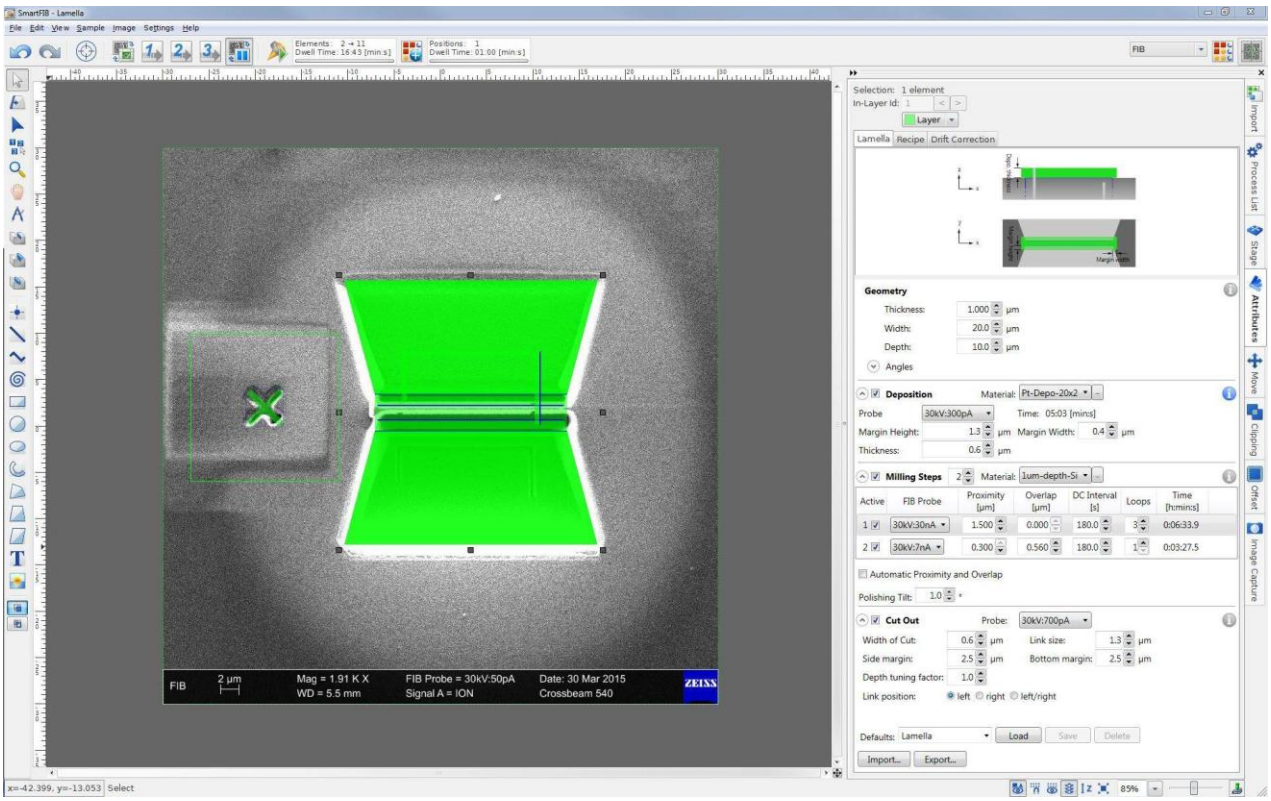

Figure 1. Screenshot of SmartFIB showing the TEM lamella wizard.

Advances in Instrumentation, Detectors, FIB and Preparation

IM1.P022
Automated image acquisition and particle classification in the MiniTEM instrument

I.- M. Sintorn[1,2], G. Kylberg[1], L. Haag[1], R. Nordström[1]

[1]Vironova AB, Stockholm, Sweden
[2]Uppsala University, Departement of Information Technology, Uppsala, Sweden

ida.sintorn@it.uu.se

The MiniTEM instrument is a recently introduced desktop-top low-voltage TEM with incorporated automatic image acquisition and analysis functionality. The microscope runs at 25 keV, which enables imaging of biological (negative stain and tissue sections) as well as inorganic samples prepared with standard methods. It is small, robust, requires only one standard wall socket, and can be hosted in any lab or office and easily moved The GUI is developed for Windows 8, and designed for a touch screen, allowing convenient manual moving around in the sample and changing magnification using pinch-zooming. The instrument has an integrated image processing and analysis library, which allows the user to design and apply analysis scripts. A graph based interface is used to create scripts which can be saved for future use and applied to multiple images, either acquired on the fly or manually acquired and stored in a folder.

Here, we illustrate how the MiniTEM instrument can be used to image, detect and classify virus particles in a highly automated manner. We designed an analysis script for automatic image acquisition followed by segmentation of possible virus particles in a specified size range. For the detected particles, characteristic measures are computed and a trained Random Forest classifier discriminates between Adenovirus, Rotavirus and debris (various non-virus objects present in the sample). This analysis script is shown in Figure 1. In the analysis we present here, 51 images were automatically acquired (with a pixelsize of 0.98 nm^2/pixel) and a total of 1702 particles were segmented and classified. Figure 2 shows an example image with the segmentation and classification result overlaid. The average classification error for the Random Forest classifier was computed to 4.52 % (77 particles out of 1702). Figure 3 shows the confusion matrix from the classification and the number of particles in each of the three classes.

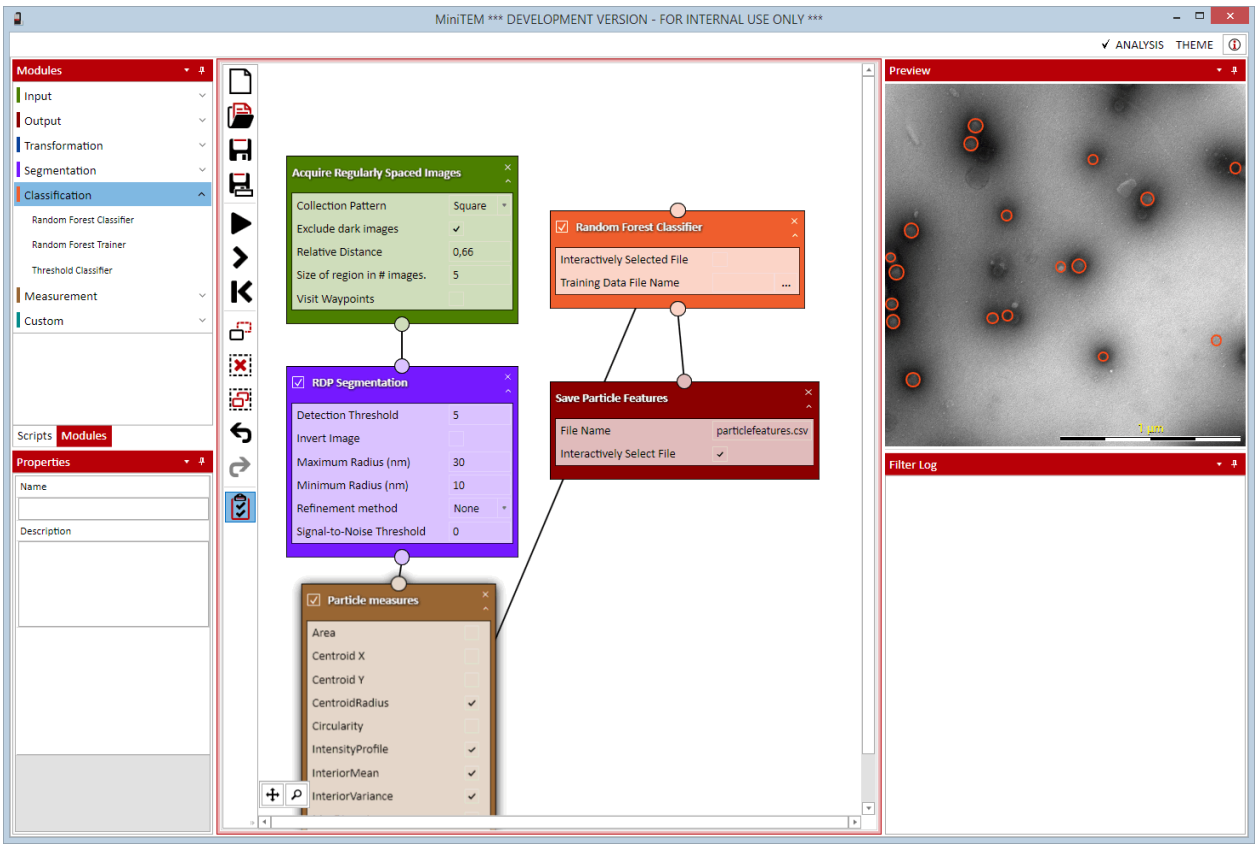

Figure 1. The MiniTEM GUI showing the acquisition, detection and classification.

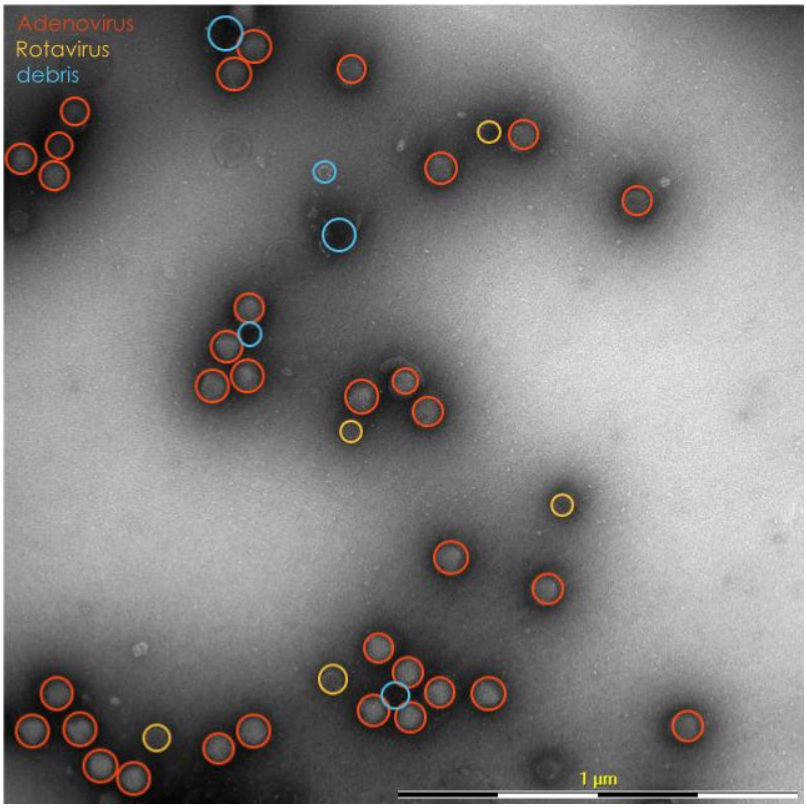

Figure 2. Example of one of the automatically acquired images with the resulting detection and classification.

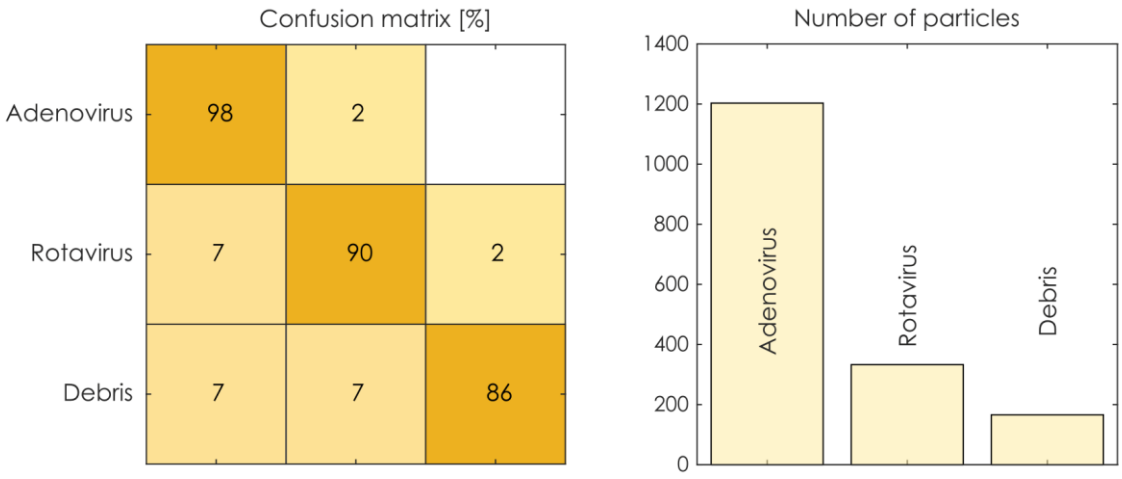

Figure 3. Confusion matrix from the classification.

Advances in Instrumentation, Detectors, FIB and Preparation

IM1.P023
Band-pass-filter for secondary electrons in ultra-high resolution SEM

I. Konvalina[1], F. Mika[1], I. Müllerová[1], S. Krátký[1]

[1]Institute of Scientific Instruments of the ASCR, v. v. i., Electron Microscopy, Brno, Czech Republic

konvalina@isibrno.cz

A Scanning electron microscope (SEM) is commonly equipped with a through-the-lens secondary electron detector (TLD). The detection system does not consist of just an Everhart-Thornley detector [1], but includes other electrodes. In addition, magnetic fields influence the trajectories of the signal electrons emitted from the specimen. The TLD detector works as a band-pass-filter for the special setup of potentials of electrodes inside the objective lens, the positive potential on the specimen regulates the energy window of the filter.

An energy filtered image contains additional information to that of an unfiltered one. The contrast of the filtered image is changed and new information about the topography and the material can be observed [2,3].

In order to confirm the band-pass-filter character of the TLD detector, we simulated many secondary electron (SE) trajectories with respect to their energy and angular distribution. The properties of the band-pass-filter were simulated for a working distance in the range of 1 mm to 3 mm and a primary beam energy from 1 keV to 10 keV. The 3D electrostatic field of the system was calculated by Simion [4], magnetic field and ray-tracing were done using EOD [5]. One example of simulated results is shown in Figure 1. The emission energy of SE detected by the TLD with taking into account the cosine distribution of emission is shown as a function of the positive sample bias. The blue curve (min) shows the lower threshold of the band-pass-filter, is clearly defined. However the upper threshold is not defined so easily. So we specify two upper borders, max_1 and max_2. The border max_1 means that TLD detector detects SEs in the whole range of emitted polar and azimuthal angles, but max_2 signifies that SEs emitted mainly with a high polar angles are detected.

The test sample with chromium and silver stripes on silicon substrate was used for the experiments. The energy spectrum of electrons emitted for both materials was simulated by using SW for Monte Carlo (MC) simulation of electron-specimen interaction in low-voltage SEM based on the Geant4 platform [6]. The primary beam energy was E_P = 1 keV and number of beam particles $N(E_P)$ = 50 000, were used in simulations. Results of MC simulations for SEs leaving the specimen are shown in Figure 2. The number of SEs emitted from chromium is higher than from silver for energies from 0 to 10.4 eV. However for energies higher than 10.4 eV more SEs are emitted from the silver specimen. The width of the stripe was 3 um in case of silver and 6 um for chromium. The thickness of both materials was 150 um. The designed pattern was manufactured by a combination of e-beam lithography, wet etching and lift-off technique.

The experiment was performed in the Magellan 400 SEM [7]. The micrographs of the sample were taken for positive potential on the specimen 0, 4, 8, 10, 12 and 24 V. For the potential 8 V on the sample the TLD detects mainly electrons with energies 4 to 7 eV, it means that SE yield of Cr is higher and the stripes are brighter than Ag (see Figure 3a). On the other hand for potential of 12 V, TLD detects energies from 8 to 11 eV, consequently the Ag stripes are now brighter (see Figure 3c).

1. T.E. Everhart and R.F.M. Thornley, J. Sci. Instr. 37 (1960), p. 246.
2. P. Kazemian, S.A.M. Mentink, C. Rodenburg, C.J. Humphreys, Ultramicroscopy 107 (2007), p. 140.
3. J. Cazaux, Journal of Electron Microscopy 61 (2012), p. 261.
4. D.A. Dahl, Int. J. Mass Spectrom. 200 (2000) p. 3.
5. J. Zlámal and B. Lencová, Nucl. Instr. Meth. Phys. Res. A 645 (2011), p. 278.
6. E. Kief, E. Bosch, J. Phys. D: Appl. Phys. 41 (2008) 215310.
7. http://www.fei.com/
8. The work is supported by the TA CR (TE01020118). The authors would like to thanks Dr. M. Unčovský (FEI Company, Brno, Czech Republic) for useful discussions.

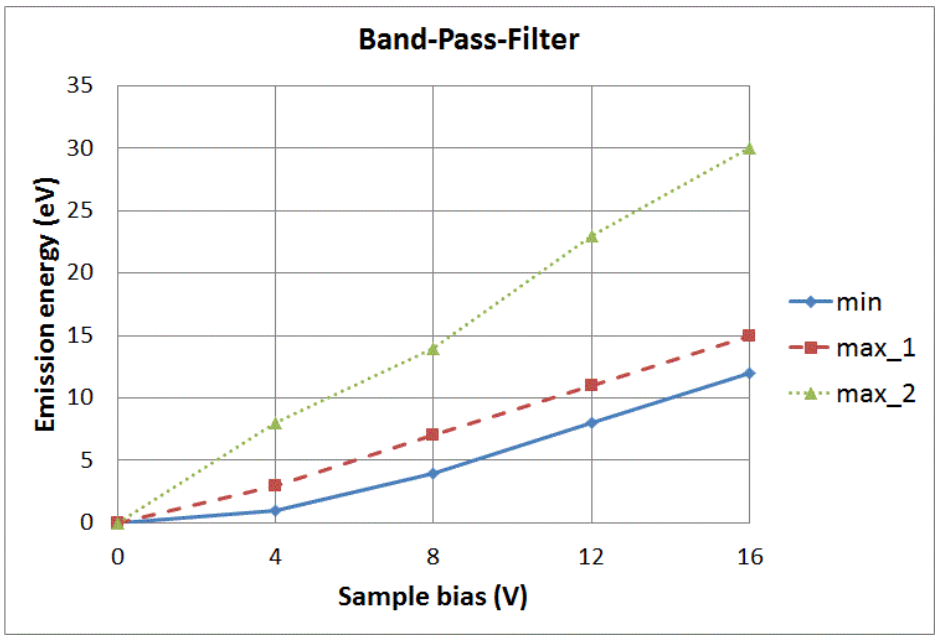

Figure 1. The emission energy of SE detected by the TLD as a function of the sample bias, working distance WD = 1 mm, primary beam energy E_P = 1 keV.

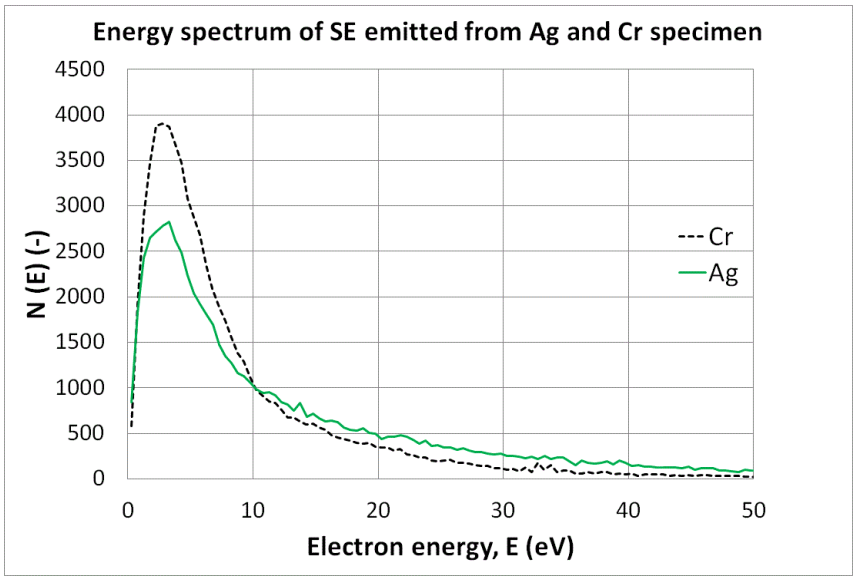

Figure 2. Simulated energy spectrum of secondary electrons for a chromium and a silver specimen, primary beam energy E_P = 1 keV.

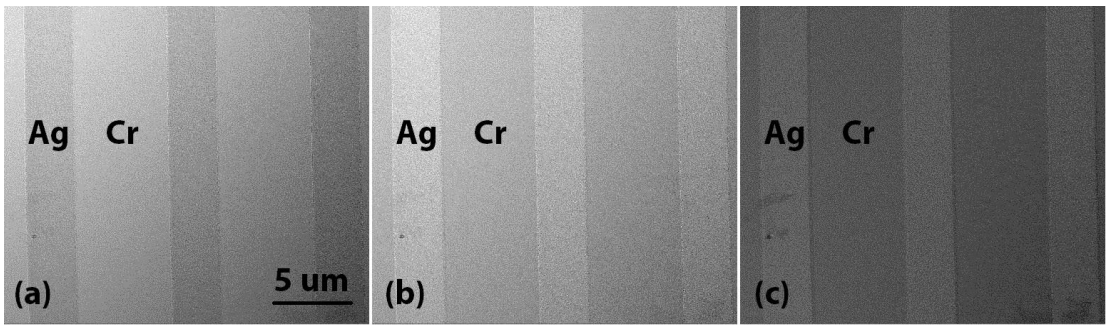

Figure 3. Ag (3 um)/Cr (6 um) stripes on silicon substrate, potential on the sample is 8 V (a), 12 V (b) and 24 V (c).

Advances in Instrumentation, Detectors, FIB and Preparation

IM1.P024
TEM sample preparation using the microPREP^{TM} laser tool

M. Krause[1], G. Schusser[1], P. Schumacher[2], T. Höche[1]

[1]Fraunhofer IWM, Halle, Germany
[2]3D-Micromac AG, Chemnitz, Germany

thomas.hoeche@iwmh.fraunhofer.de

Over the past fifty year, lasers have perpetuated to find new, often groundbreaking applications in science and technology. Among the latter are technologies for health care, telecommunication, welding (e.g. in automotive industry), and micromachining.

Microstructure diagnostics is increasingly confronted with the need to assess large areas or large depth inside 3D functional structures like through-silicon vias. Under such circumstances, the milling rates of Ga FIBs and even Xe plasma FIBs are insufficient. Remedy is found in the combination of laser micromachining (possessing a six orders of magnitude higher ablation rate than a Ga FIB) with FIB or ion broad-beam polishing.

In the commercially available microPREP^{TM} tool [1-3] (Fig. 1), the outstanding properties of an ultrashort pulsed laser can be utilized for microstructure diagnostics sample preparation: laser light consists of just photons (making the process inherently free of elemental contamination), extremely high energy densities can be focused in very small areas (ca. 12 µm), and the laser beam can be precisely positioned using deflection mirrors. By choosing the right laser, structure damage by local heating is reduced to well below a micron.

Exemplified for a sample to be investigated by transmission electron microscopy (TEM) and following a three-stage approach, a supporting basic structure is cut from the feedstock first. Second, the supported structure (see Figs. 2 to 4) is thinned down to a few micron of residual thickness and third, the supported and thinned structure is polished using an ion broad beam or by FIB machining. This way, multiple positions can be thinned at a desired position and handling of the samples is made easy by its robustness. As shown in Fig. 4, non-conducting sample can be readily machined as the laser is not afflicted by charging. Total laser machining times of well below 30 min are achieved and the advantages of the approach can be used not just for semiconductors and alloys, but also for coatings, and target preparation on the one-digit micron scale. Besides bulk samples, a new approach for the preparation of cross-sections will be presented further reducing the time to sample.

microPREP^{TM}, the all-new, patented laser-micromachining tool developed by 3D-Micromac is the first instrument to make fast, clean, and efficient laser ablation available for the preparation of samples for microstructure diagnostics. Besides TEM samples, micromachining of objects suitable for local electrode atom probe, micromechanical testing, X-ray tomography and microscopy as well as cross-sections for scanning electron microscopy is now at your fingertips.

1. M. Krause & Th. Höche, European Patent application EP 13 162 360.
2. Th. Höche, M. Krause, M. Ebert & U. Wagner: “A Novel Laser Tool for High-Volume Sample Preparation” Laser Technik Journal 1 (2015) 42-44.
3. M. Krause, M. Ebert, Th. Höche, & U.Wagner: „MicroPREP—A New Laser Tool for High-Throughput Sample Preparation” Proc. of ISTFA 2014, November 9-13, 2014, Houston, Texas, USA, p. 270-276.

Figure 1. 3D-Micromac's microPREP desktop workstation for laser-based sample preparation.

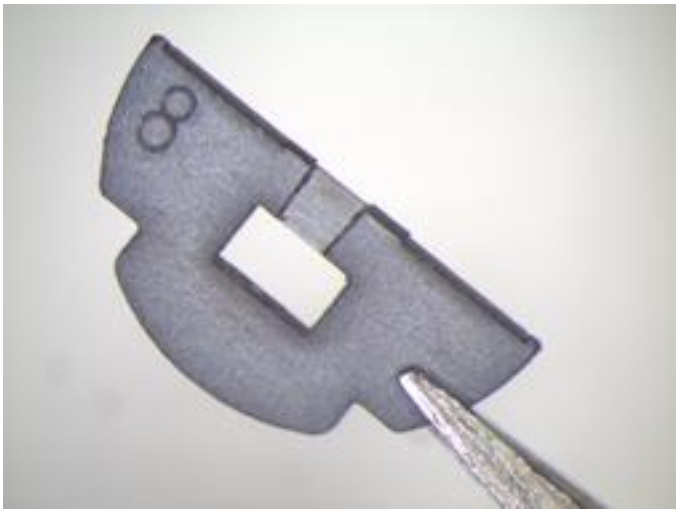

Figure 2. Basic TEM sample structure consisting of a rugged ring for save handling and a supported structure that is further thinned to eventually become electron transparent.

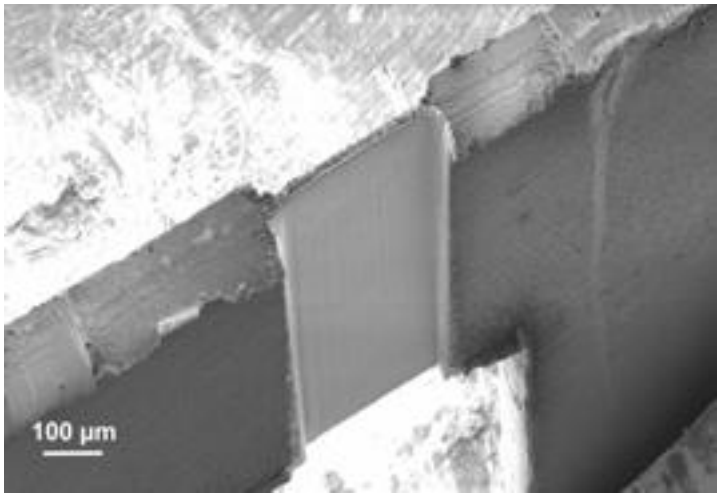

Figure 3. H-bar sample machined in Copper. In a very short time, very large, smooth and plane-parallel slabs can be made.

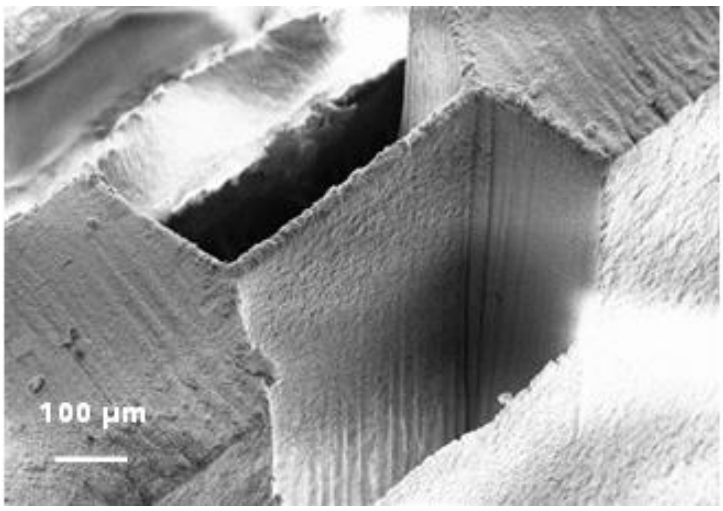

Figure 4. H-bar sample machined into sapphire. Since the laser is not susceptible to electrostatic charging and machining of at-the-wavelength-of-the-laser is viable, dielectrics can be easily machined.

Advances in Instrumentation, Detectors, FIB and Preparation

IM1.P025
Multi-channel solid state electron detectors for STEM and SEM

A. Liebel[1], M. Simson[1], R. Eckhardt[1], A. Niculae[1], H. Soltau[1], P. Holl[2]

[1]PNDetector, Munich, Germany
[2]PNSensor, Munich, Germany

andreas.liebel@pndetector.de

Imaging with electrons and elemental analysis with X-rays is the primary goal in SEM und STEM analysis. Modern microscopes need advanced detectors which are efficient and fast even under challenging imaging conditions. For Backscattered Electron (BSE) imaging in SEM or Scanning Transmission Electron Microscopy (STEM) imaging in TEM or SEM, silicon based solid state or scintillator detectors are used. The two major benefits of solid state detectors are the slim shape and the freedom in designing any preferred geometry. To capture all signals, the detector - typically a pin diode - should be large and also provide some partition of the detector area in order to distinguish between different electron scattering angles and get the most possible information from the sample. Therefore multi-channel electron detectors as shown in Figure are proposed for this purpose.

The size of the detector also determines the signal capacitance and thereby the speed and noise of the detector system. This value has to be reduced to achieve best performance. For optimized silicon detectors the sensor volume can be fully depleted by reasonable bias voltages (< 100 V) which decreases the detector capacitance down to a value of 3-15 pF per segment.

Further optimizations of the geometry of the detector design lead to an increase in collection efficiency. The sensitivity for small electron energies (e.g. 2-5 keV in SEM) can be improved by using advanced techniques for processing the detector entrance window which reduce the detector dead layer and therefore enhance the quantum efficiency. Moreover, the parasitic cable and connection capacitances have been decreased by a new preamplifier concept.

By all these measures signal rise times smaller 100 nsec are enabled for low to moderate detector gains with the optimized BSE detector. Figure 2 shows a measured signal rise time of approximately 80 nsec which was acquired by scanning over a sharp silicon edge. This short rise time leads to sharp images without any smearing effects even for pixel dwell times of 100 nsec as can be seen in Figure 3.

Even for very low signals as it is the case for soft matter or biological samples which need high gain amplification, fast data acquisition can be achieved by an alternative detector configuration. Hereby, instead of a pin diode, a multi-channel SDD which is operated in current readout mode can be used. This detector features signal capacitances below 1 pF and enables small signal rise times even at very high amplification (see Fig. 4).
In this contribution we will present the results of our measurements and compare different detector types and design proposals.

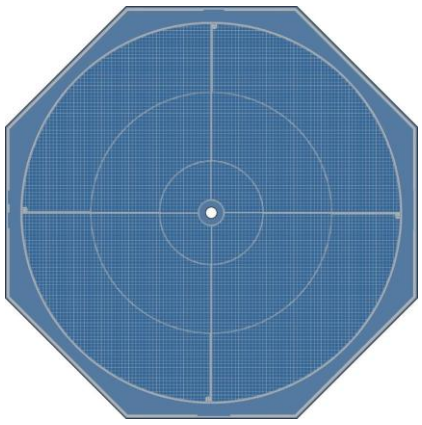

Figure 1. New 12 cell STEM detector with an outer diameter of 22 mm and a central hole of approx. 0.5 mm.

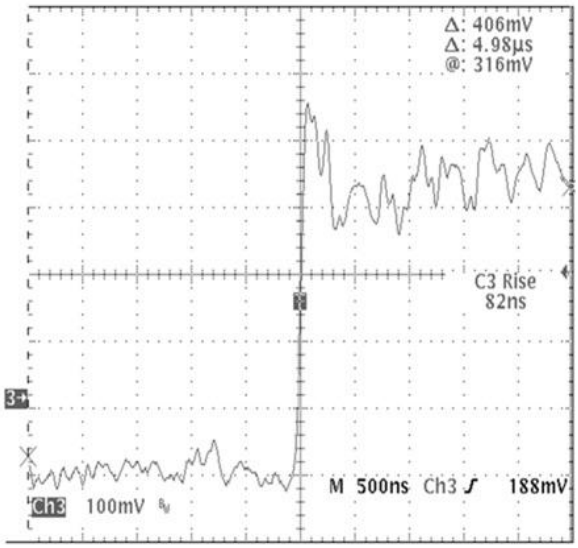

Figure 2. Signal rise time of approx. 80 nsec measured by scanning over a sharp silicon edge with the optimized BSE detector.

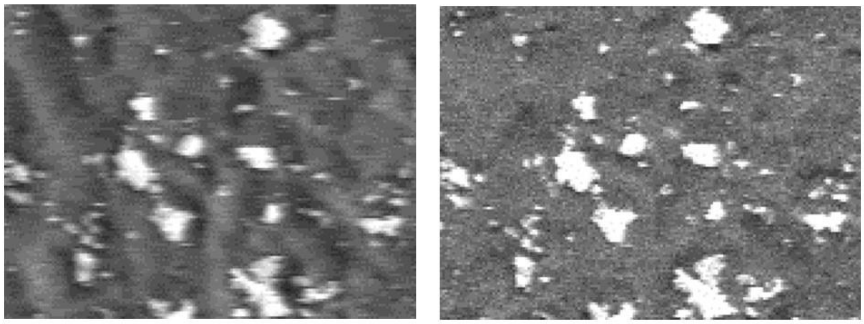

Figure 3. Comparison of two BSE image sections with 168 x 125 pixels taken at 100 nsec pixel dwell time. The left image was acquired with a conventional BSE detector with 250 nsec signal rise time and shows smearing in the scanning direction. The image on the right was taken with the optimized BSE detector featuring 80 nsec signal rise time and shows sharp details without smearing.

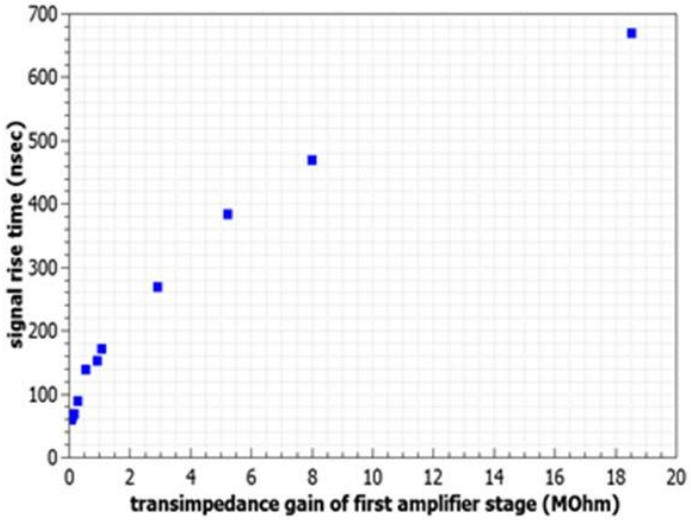

Figure 4. The measured rise time of the electron detector based on SDD technology is still <500 nsec at a very high gain of 10 MOhm as needed for weak signals which are typical for soft matter analysis. This is about 10 times faster than a conventional solid state BSE detector at similar gain.

IM1.P026
Monochromatizing without filtering using dynamic fields without bunching: a new concept for d-TEM illumination

R. Janzen[1], G. Schönhense[2]

[1]Karlsruhe Institut fur Technologie, Karlsruhe, Germany
[2] Institut für Physik, Johannes Gutenberg Universität Mainz, Mainz, Germany

info@dr-janzen.de

Commonly used monochromators are energy filters. The majority of the particles with undesired energies is removed. Thus the output current diminishes with increasing degree of monochromatization. Monochromators in the original meaning of the word that would affect the energy of the particles by an energy selective acceleration can only be realized by use of dynamic fields.

Dynamic field applications without exception involve a condition between the phase of the dynamic field and the entrance point of time of the particle into the field. If this condition is fulfilled, the dynamic field application works exactly. Unfortunately the width of the time interval where the condition is fulfilled is mathematically zero. Thus up to now dynamic field applications in charged particle optics limit themselves to a small time interval around the periodically recurring point of optimum phase where the condition is fulfilled to a good approximation. For that purpose bunches are formed around the optimum phase point. Unfortunately bunch forming suffers from Liouville's theorem: The product of the bunch length and the energy spread within it is a constant.

In this work a concept is presented that circumvents this dilemma. A circularly polarized standing wave deflects the charged particle beam to a rotating orbital feeding the particles into a propagating wave that rotates within a toroidal wave guide (see figure 1). The circular deflection supplies a time coding. The entrance point of time of any particle is locked to its azimuthal position. Provided that the deflecting field and the rotating propagating wave (denoted by working field in the following) are synchronized correctly the optimum phase condition is fulfilled exactly and constantly. Time uncertainty vanishes within the limits of technical & practical implementing of the concept. The working field may be cascaded. It can be used for a large variety of applications such as monochromatizing, spread inversion, time focusing (and not covered in this contribution: accelerating, pulse forming, spread amplification, and aberration correction). In the end the spiral orbital may be focused to an inverse circular deflector that undoes the action of the first circular deflector and thus leads the particles back to the original axis (see figure 2.).

A monochromator based on circular deflection was demonstrated to work by computer simulation assuming theoretically ideal TE10 mode microwaves as dynamic fields. The energy spread vanishes within the limits of technical & practical implementing of the concept without any loss of current.

Finally, a vision of a dynamic TEM illumination column based on circular deflection yielding equidistant monochromatic single-electron pulses will be presented. The latter concept makes use of plasmonic field emitters synchronized to the deflection and working fields.

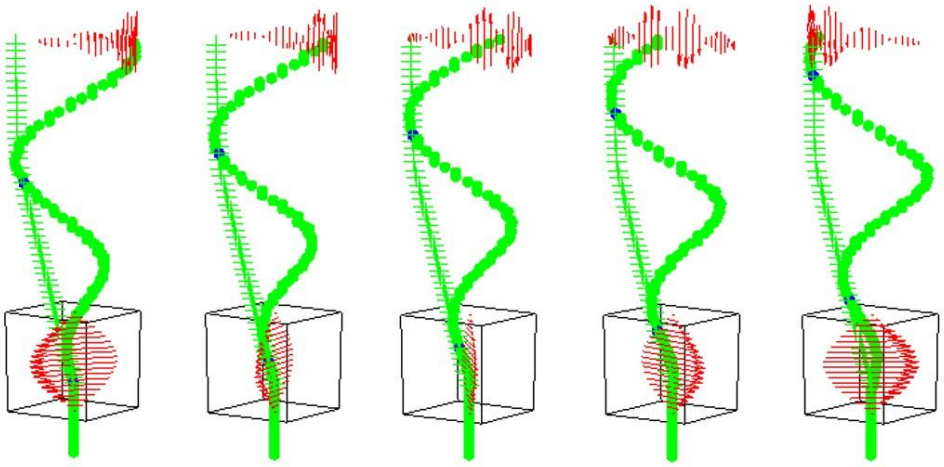

Figure 1. Five snapshots of an animated schematic drawing illustrating the principle of a typical circular deflection application. The circular deflector wave is a circularly polarized standing wave within a cubic resonator. The electric field vector (shown by the lower group of red arrows) rotates, always pointing perpendicularly to the direction of motion (which is in this figure assumed to point upwards) of the electrons (green). The working field is represented by the upper group of red arrows. It is a propagating wave that is rotating within a toroidal resonator (not shown).

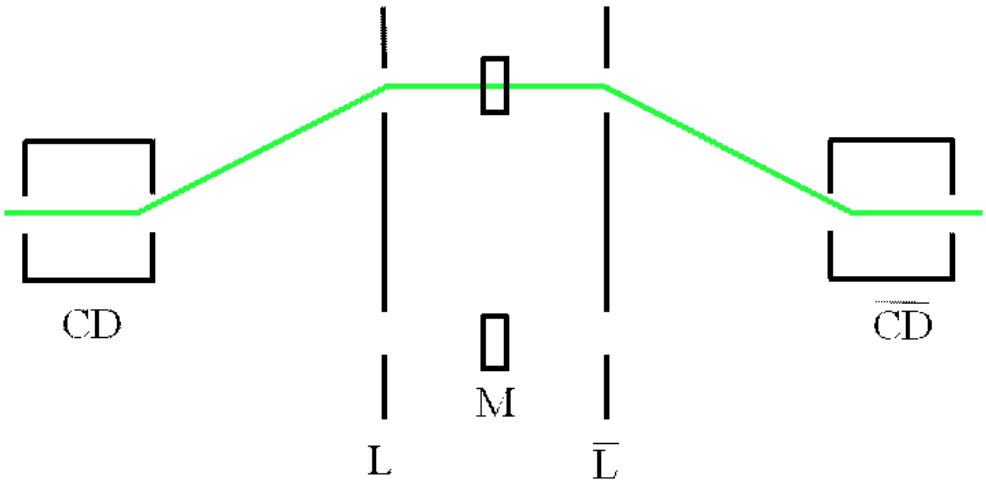

Figure 2. Schematic drawing (cross sectional view) of a simplified monochromator design based on circular deflection. Note that in difference to figure 1 the electrons are assumed to move from left to right. They are deflected by the circular deflector CD, focused by some lens like element L, monochromatized by the working field inside the toroidal resonator M, focused again and deflected by an 'undoing' circular deflector in the end.

Advances in Instrumentation, Detectors, FIB and Preparation

IM1.P027
Detecting compositional differences in nanomaterials with in-lens angular filtering

E. J. Vesseur[1], D. Phifer[1], P. Wandrol[1], D. Wall[1], A. Sandu[1]

[1]FEI Company, Eindhoven, Netherlands

ernst.jan.vesseur@fei.com

Scanning electron microscope characterization of nanomaterials requires low landing voltage to reduce beam penetration for the small feature size, and it also requires advanced detection that can separate material composition. To this end, SEMs with in-lens detection have been improving for years with a myriad of technologies relying on detector placement and a multitude of biasing schemes to force or limit electrons to or from detectors to achieve information selectivity. The newest electrostatic electron column for SEM from FEI enables exceptional in-lens & in-column angular filtering; showing unique nanomaterial topographic and composition information. This leads to efficient discrimination without the need for specific energy selection filters.

In low voltage SEM, the ability to capture important compositional information of nanomaterial composition is limited to narrow BSE energy bands. These specific BSE energies are difficult to define and setup in SEMs equipped with energy filtering bias (grid) systems [1]. On the other hand, information can be separated into topographic and compositional components when signal is collected from different angles, as is done for example using an in-chamber BSE detector based on a concentric ring diode arrangement [2]. Therefore with nanoparticle characterization the question of applying an angular filtering in the lens and column seems a reasonable approach to segment this signal without needing bias filtering. With this column design, detectors are optimally placed for collection of various angles through the use of simulations to optimize signal collection and understand what energy and angle is being collected by individual detectors. In-lens angular segmentation separates signals containing relevant information such that biased grid energy filtering can be avoided to separate nanomaterial composition at low voltage.

The electrostatic column design uses a biased column liner to decelerate the electron beam as it exits the electron column and the latest design includes detectors to collect signals of particular angular distributions [1]. As used for nanoparticle characterization, the bias on the column liner tube serves to attract and focus the signal towards particular places in the column leading to working distance “sweet spots” where the angle of collection will be optimized. This bias forms an electrostatic lens and filters the energy distributions by angle allowing clear separation of different information which can be collected on the various detector positions. By exploiting angular filtering for better topographic and compositional contrast we bring new flexibility in imaging nanoparticles and nanomaterials.

1. P.G. Merli et al., Ultramicroscopy 88 (2001) 139-150
2. T. Vystavel, Proceedings of XIVth Intnl. Conference on Electron Microscopy, 26-30 June 2011, Wista, Poland.

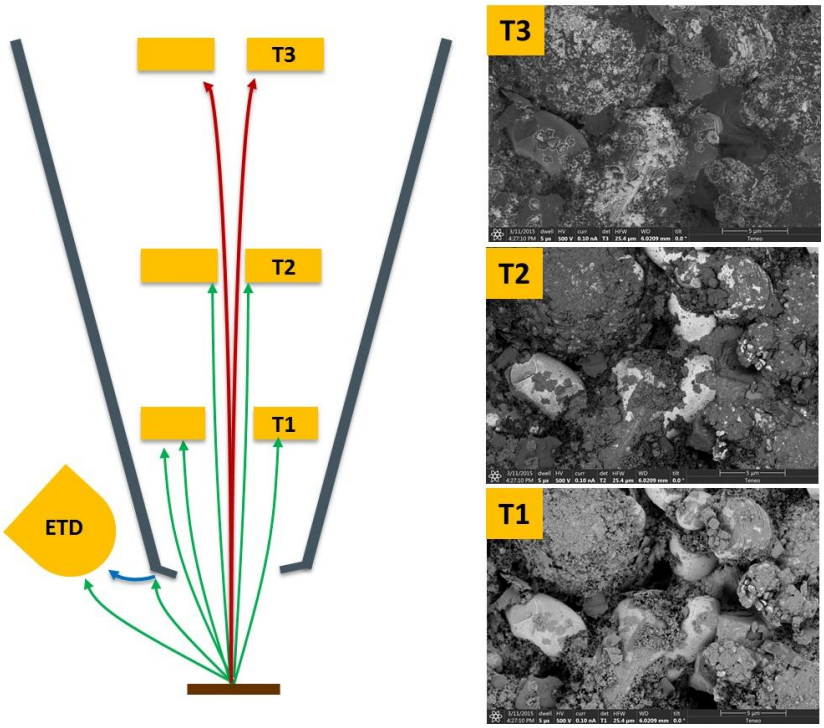

Figure 1. Exceptional information from Nanoparticles can be captured simultaneously from high, medium and low angles showing different information as the angular distribution from an electrostatic lens separates these signals without the need for an additional bias to capture both composition and topographic information. Sample is a Lithium ion battery cathode showing the bright Li particles and SEI layer and carbon nanoparticles imaged at 500V. Lithium ion battery cathode sample provided by Tomáš Kazda, Brno University of Technology.

Advances in Instrumentation, Detectors, FIB and Preparation

IM1.P028
Newest developments for low voltage STEM with in-lens cold FE-SEM

T. Sunaoshi[1], Y. Orai[1], H. Ito[1], S. Okada[1], T. Ogashiwa[1], M. Konno[1], K. Kaji[1], R. Schmidt[2]

[1]Hitachi High-Technologies Corporation, Hitachi Naka, Japan
[2]Hitachi High-Technologies Europe GmbH, Electron Microscopy, Krefeld, Germany

roland.schmidt@hht-eu.com

The need of high resolution STEM imaging at low accelerating voltages has been increasing in the field of soft material science due to the reduction of electron beam damage at low accelerating voltage and due to the larger scattering contrast when observing light and soft materials. Examples from nanotubes, graphene and polymers, in which the structural, elemental, and chemical nature was characterized, were reported [1-3]. Recently lattice fringe images of Pyrophylite at 7kV, Fig. 1, and of Si{222} at 30kV with reflection spot corresponding to 0.157nm were detected in the BF-STEM image and Fourier transform image, respectively [4].

In this talk/poster new developments are presented to further improve the resolution performance of the in-lens FE-SEM SU9000 at low accelerating voltage by the adaption of a deceleration holder, which reduces the SE resolution from 1.2nm to 0.8nm at 1kV. At the same time by the proper height of the deceleration field SE and BSE can be separated effectively with the Top SE detector and the Upper BSE detector, respectively, at landing voltages down to 100V. With an optional Top filter the energy of of BSE can be gradually cut to enhance Low Loss BSE contrast.

The analytical performance of this unique in-lens FE-SEM was complemented by a modified windowless EDX detector with 100mm² detector area allowing 1nm lateral EDX resolution in a compound semiconductor at 30kV. A post-column EELS system is presented, which was optimized for the high-speed elemental mapping of light elements at 30kV and below.

1. K.Suenaga , M.Koshino, Nature, vol.468, (2010), pp.1088-1090
2. U. Kaiser et al., Ultramicroscopy 111 (2011) 1239-1246.
3. O. Kamimura et al., Ultramicroscopy 110 (2) (2010) 130-133.
4. T. Sunaoshi et al., ICEM Prague (2014)

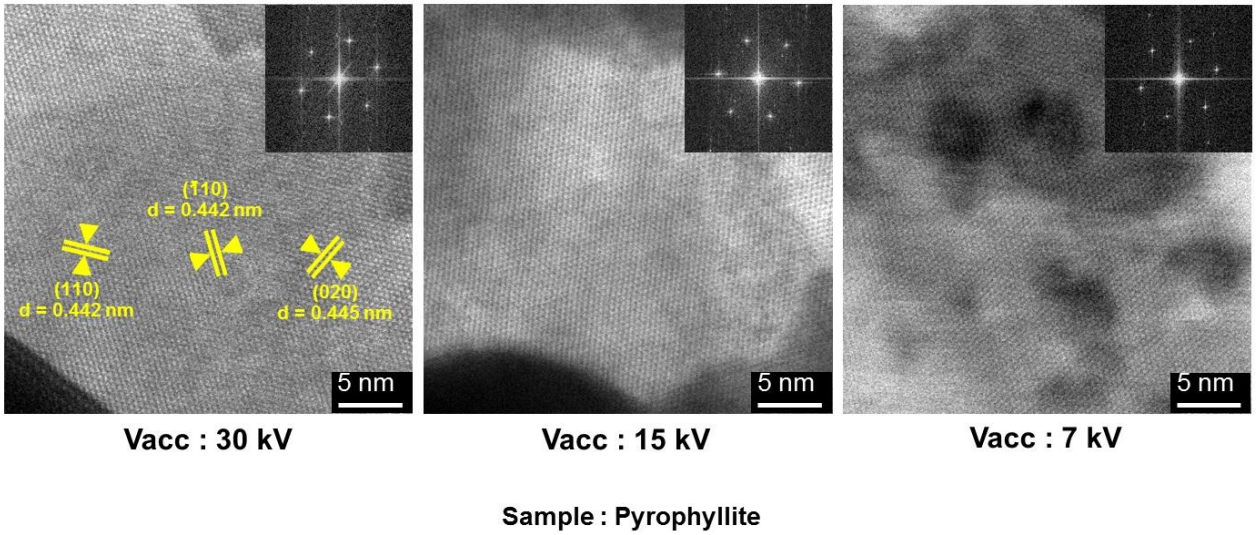

Figure 1. Lattice resolution images at 30kV, 15kV and 7kV

Advances in Instrumentation, Detectors, FIB and Preparation

IM1.P029
STEM strain measurement from a stream of diffraction patterns recorded on a pixel-free delay-line detector

K. Müller-Caspary[1], A. Oelsner[2], A. Rosenauer[1], P. Potapov[3]

[1]Universität Bremen, Bremen, Germany
[2]Surface Concept GmbH, Mainz, Germany
[3]GLOBALFOUNDRIES Dresden Module 1, Dresden, Germany

mueller@ifp.uni-bremen.de

Recent progress in nano-beam electron diffraction (NBED), ptychography and differential phase contrast microscopy [1] is based on the acquisition of a four-dimensional data set $I(x_p,y_p,x,y)$ with (x_p,y_p) the position of the STEM probe, (x,y) a coordinate in the recorded image/diffraction pattern and intensity I. Since the speed of conventional charge-coupled devices is limited, a major challenge is the development of fast detectors.

Here we present pilot experiments with a delay-line detector (DLD) mounted on an FEI Titan facility. As illustrated in Fig.1 the top of the DLD consists of a microchannel plate (MCP) stack that causes a cascade of secondary electrons for each 300keV electron impinging on the detector. The heart of the DLD are 2 meandering wires shown in blue and red in which each cascade causes electrical pulses travelling towards the ends of the wires. Depending on the incident position of the electron a characteristic time delay between the arrivals of the 2 conjunct pulses at the ends of a wire is measured with high accuracy, giving the coordinate of incidence perpendicular to the meander. By crossing two such delay-lines the point (x,y) and timetof incidence can be detected. Thus the DLD allows for both the recording of a continuous stream of single electron events processed by a time-to-digital converter (TDC) with a time precision in the picosecond range and the in-situ integration of the signal over a certain frame time to obtain conventional images. Note that no pixel raster is involved here. The two modes of operation are illustrated in the right part of Fig. 1.

To characterise the DLD, we determined the quantum efficiency (QE) as a function of the incident intensity as shown in Fig. 2. The QE takes values between 50% for 0.5x10^6 and 22% for 17x10^6 electrons/second for a homogeneous illumination of the detector. Moreover, the modulation transfer function was determined to 0.1 at Nyquist frequency.

Finally, we present strain measurements as in Fig. 3 for a GeSi/Si MOSFET for the [001] and [110] direction at a STEM raster of 100x100 pixels. In particular we observe 2 strain regimes inside the GeSi stressors owing to different Ge contents of 25% and 37%, as has been verified by quantitative STEM Z-contrast evaluations. In Fig.3a, strain ε_{yy} in [001] direction was measured from the position of the 004 reflection [2] whereas the 220 reflection was used for the lateral strain measurement of ε_{xx} in Fig.3b. In between the stressors, the gate channel exhibits compressive strain of up to 3% laterally and an expansion below 1% along [001]. Dwell times between 40 and 5ms have been used, corresponding to an acquisition of 10,000 diffraction patterns in 6.5 and 0.8min, respectively.

1. Nature Communications 5, 5653 (2014).
2. Microscopy and Microanalysis 18, 995 (2012).

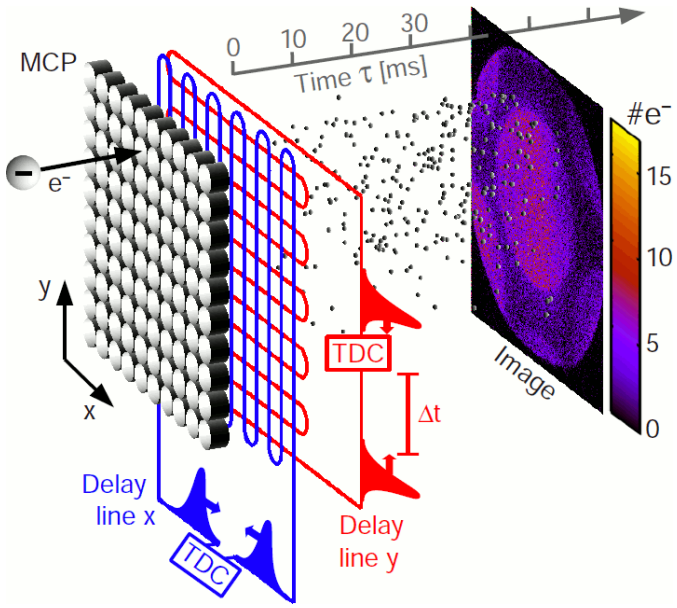

Figure 1. Schematic to illustrate the functional principle of the delay-line detector. An incident electron causes a cascade in the microchannel plate (MCP) stack, leading to pulses in the meandering delay-lines which are processed by a time-to-digital (TDC) converter. The time stream of single events can be recorded or integrated to conventional frames as shown here for an integration time of 40ms.

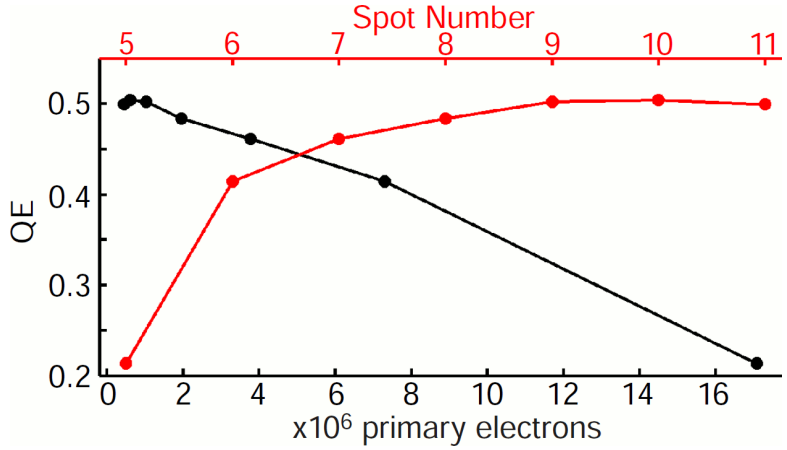

Figure 2. Quantum efficiency of the DLD as a function of the incident dose (black) (per second) measured from exposures to homogeneous illumination. The red curve shows the dependence on the Spot Number in an FEI Titan operated at 300kV in HRSTEM mode.

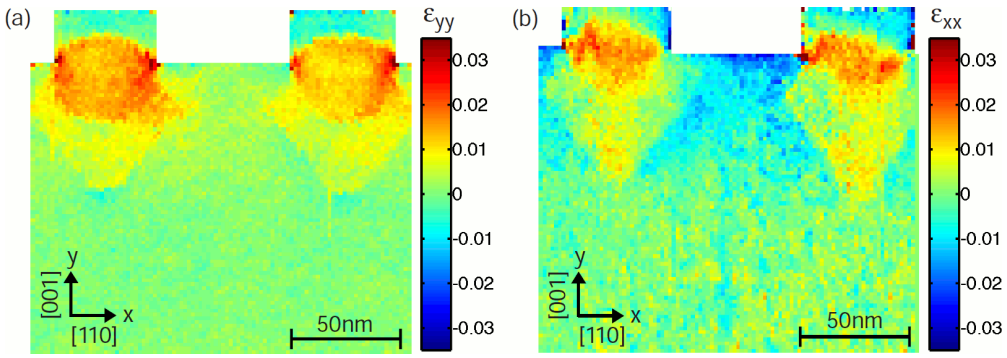

Figure 3. Maps for (a) vertical and (b) lateral strain in a Si-based MOSFET teststructure measured from the 004 and 220 reflection and 40ms dwell times, respectively. The GeSi stressors cause a compression of up to 3% along [110] and an expansion below 1% along [001] in the gate region.

Advances in Instrumentation, Detectors, FIB and Preparation

IM1.P030
Application of the EsB Detector in the low voltage scanning electron microscopy (LVSEM)

A. Garitagoitia Cid[1], R. Rosenkranz[2], E. Zschech[1,2]

[1]Technical University Dresden, Dresden, Germany
[2]Fraunhofer Institute for Ceramic Technologies and Systems - Materials Diagnostics (IKTS-MD), Dresden, Germany

aranzazu.garitagoitia@tu-dresden.de

In addition to high-resolution imaging, the detection of small differences in material composition is a challenge for the Low Voltage Scanning Electron Microscopy (LVSEM). During the last decade, LVSEM has been widely used thanks to the advances in electron gun design, aberration-corrected optics, as well as in the improvements in the sensitivity of recording images and in obtaining analytical information. However, little attention has been paid to detector testing or optimization [1, 2]. The use of the Energy selective Backscattered (EsB) electron detector benefits the performance of the microscope at lower primary beam voltages (E_p). With the EsB detector, it is possible to detect only electrons with a certain energy by controlling the grid bias. This energy window technique is based on a cut off of secondary electrons (SE) and backscattered electrons (BSE) with high or moderate energy loss. If the primary beam energy is decreased, then the interaction volume is smaller. For BSE imaging, it means that the low-loss BSEs are scattered on a near-surface region of the sample; a characteristic that is of special interest for studies of ultra-thin films and surfaces. Optimizing the parameters which most influence the LVSEM performance (E_p, EsB grid voltage and working distance) is a fundamental step to characterize the specimen, in order to obtain the desired material contrast. Figure 1 shows two BSE images of the same region of the polymer sample Acrylonitrile Butadiene Styrene (ABS), which has been stained with OsO_4. OsO_4 selectively reacts with the polybutadiene particles providing contrast with respect to the acrylonitrile-styrene matrix. On the left BSE image, bulk sample information is obtained with E_p = 5 kV and the homogeneous distribution of the polybutadiene particles in acrylonitrile-styrene matrix is visible. When the primary beam E_p is 1 kV (right image), then the surface of the specimen can be imaged thanks to the combination of lower E_p value and higher EsB grid voltage, revealing larger areas of polybutadiene with OsO_4 (brighter phase) at the surface of the specimen caused by shear forces during cutting the specimen.

Another advantage of LVSEM is the mitigation of sample damage. In the case of dense and porous organosilicate glass (OSG) thin films, which are used as insulating material with low permittivity in semiconductor industry, the glass network is densified during the electron beam/sample interaction which phenomenologically causes a significant shrinkage of the material [3]. A Carl Zeiss SEM/FIB system NVision40 with Gemini column and three types of detectors, the conventional Everhart-Thornley detector, the Inlense detector and the EsB detector was used for this investigation. By combining the advantages of using a lower E_p value with the EsB detector, the compositional contrast is increased and the shrinkage phenomena is significantly mitigated, as shown in Figure 2.

1. D. C. Bell, N. Erdman, *Low Voltage Electron Microscopy: Principles and Applications*, John Wiley & Sons, United Kingdom **2013**.
2. H. Schatten, J. B. Pawley, *Biological Low-Voltage Scanning Electron Microscopy,* Springer, USA **2008**.
3. H. Geisler, D. Chumakov, E. Zschech, Nanomechanical Probing Techniques, NanoS 01.08, 27-33, **2008**.
4. We kindly thank Carl Zeiss Microscopy GmbH, Oberkochen, Germany, for funding the investigations in the framework of the project “Untersuchungen zur Charakteristik und Applikation des EsB Detektors”. Constructive discussions with the Carl Zeiss Microscopy team, particularly with Markus Boese, are acknowledged. Additionally, we would like to thank Petr Formánek, Leibniz Institute for Polymer Research, Dresden, Germany, and Khashayar Pakbaz, SBA Materials Inc., Albuquerque/AZ, USA, for providing ABS polymer and porous OSG thin films samples, respectively.

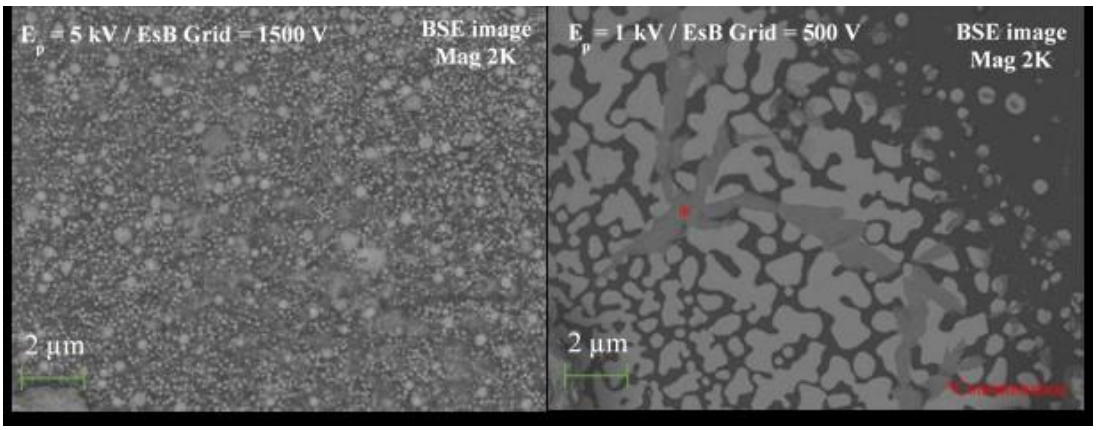

Figure 1. BSE images of the same sample region of the ABS polymer stained with OsO_4. On the left, bulk sample information is obtained at Ep = 5 kV and it shows homogenous distribution of spherical polybutadiene particles. At lower primary beam voltage (Ep = 1kV), the image on the right shows large areas of irregularly shaped polybutadiene with OsO_4 caused by mechanical deformation of the surface.

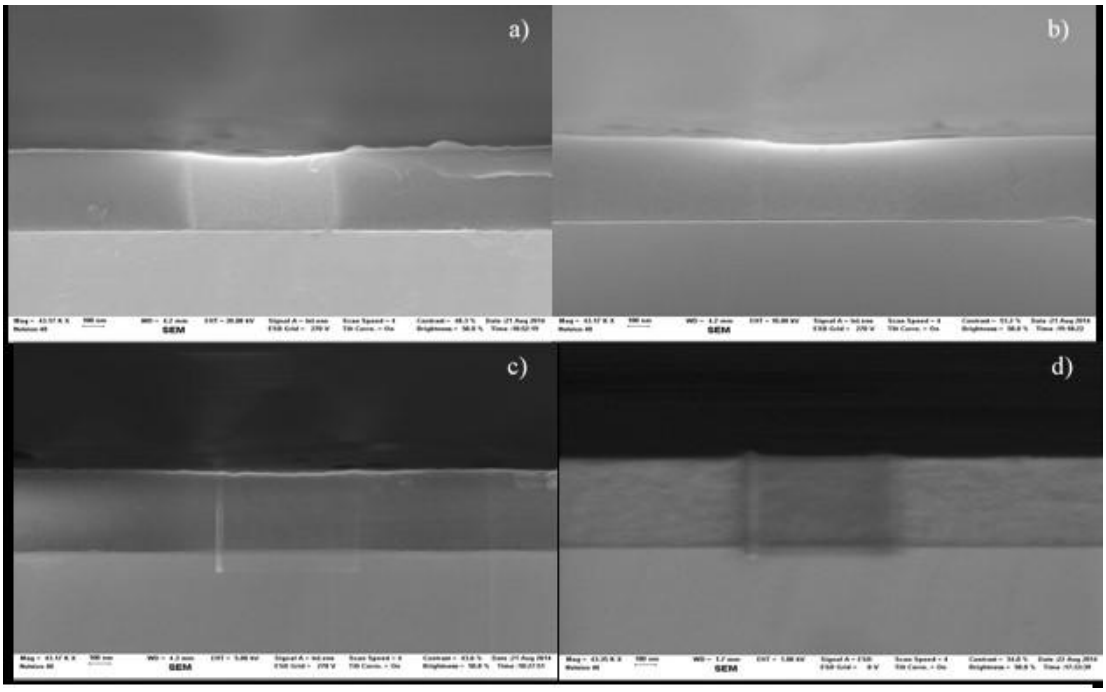

Figure 2. InLens images of shrinkage (a), (b), (c) in a OSG thin film on Si substrate after 3 min. scan with high magnification at E_p = 20, 10 and 5 kV, respectively. The EsB image (d) shows no shrinkage with E_p =1 kV.

Advances in Instrumentation, Detectors, FIB and Preparation

IM1.P031
Improvement of a stereology based morphometer

M. Hinderer[1], B. Wolf[1]

[1]Heinz Nixdorf-Lehrstuhl für Medizinische Elektronik , Technische Universität München, München, Germany

haecker@mytum.de

This paper deals with a well-proven method for analyzing potential malignant tissue samples in order to statistically confirm morphological findings. Instead of a qualitative interpretation of a possible symptom-determined effect on cells or tissues, quantitative data are obtained that can be processed. A stereological method based on “Buffon’s Needle” [1] is used to determine numerical values from tissue slices. The theoretical background for cell biology has been described by Weibel [2]. The circumference of a 2D structure taken from a cross-section through a volume corresponds to the surface and the enclosed area corresponds to the volume of the 3D topology. The relations of the surfaces and volumes of the ultrastructural components form the basis for decisive characteristics and classify tissue.

In 1985, Wolf [3] introduced his “Morphometer”, a semi-automatic device that supports counting, handling and calculating relations. An electrically conductive grid was placed on the printed TEM pictures or directly onto the screen (figure 1). Users had to retrace all the structures with a contact pen that was connected to a microcontroller. This allowed investigating a plurality of different tissues and gathering a great number of reference data. The advantage of this statistical method over conventional qualitative methods is that it can be used both by experts as well as non-experts due to the more or less straightforward tracing of structures. However, retracing all membranes, cell areas and sub-cellular components is extremely time-consuming.

The new system is based on Wolf’s Morphometer in order to be able to reuse all available reference data for classification. The key difference is a new user interface and automatic detection algorithms. The original Morphometer required manual detection of all surfaces as well as volumes by means of a pen whereas the new one is able to detect structures automatically. Due to great variations in the quality of the image and the tissue slices, it is not possible to detect the same structure in different TEM pictures reliably enough using only one algorithm. Our system is therefore a combination of automatic and manual detection with a pen on a touch screen. The user has to mark only the outline of the structures and no longer the entire area (figure 2).

On the basis of all the available reference data, we can say that the most decisive relations to distinguish between malignant and benign tissues are: nucleus to cell volume, heterochromatin to nucleus volume, surface of the cell membrane to volume of the cell, surface of the nucleus to volume of the nucleus and the number of mitochondria. For this reason, our new system is confined solely to these characteristics.

After the user has traced the cell envelope and the nucleus, the software automatically calculates the circumference, the area and the area of the heterochromatin. In addition, optionally the user can mark the mitochondria. In order to obtain a statistically representative characterization, the number of cells that have to be evaluated depends on various factors. The standard deviation is always shown and the user can finish the detection process when detection is sufficient. The new system enables very fast analysis of whole cell groups compared to the original Morphometer.

In order to gain a fully automated classification, the whole process (cutting, preparing and microscope) has to be improved. Especially the manner of cutting and preparing the tissue needs to be standardized.

1. A. Rezhd, “Buffon’s Needle Problem”, www.math.dartmouth.edu/archive/m20f11/public_html/RezhdoProj.pdf , Accessed March 24, Dartmouth College (US), 2015
2. L. Cruz-Orive and E. Weibel, “Recent stereological methods for cell biology: a brief survey”, Commentaries - The American Physiological Society, 1040-0605/90, 1990
3. B. Wolf, “Interaktive “On-Line”-Morphometrie mit dem TEM für Forschung und Diagnose“, In: Mikroskopie Elektronenmikroskopie, p. 16 - 22, GIT Verlag Ernst Giebeler, Darmstad, April 1984

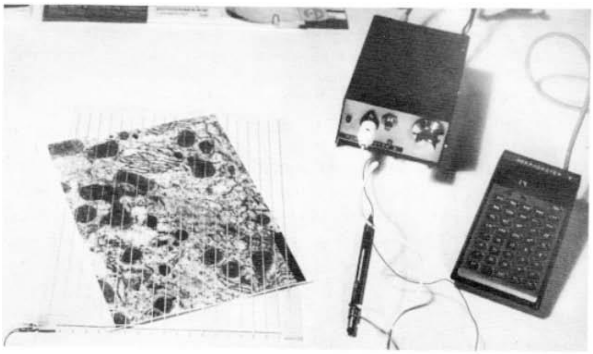

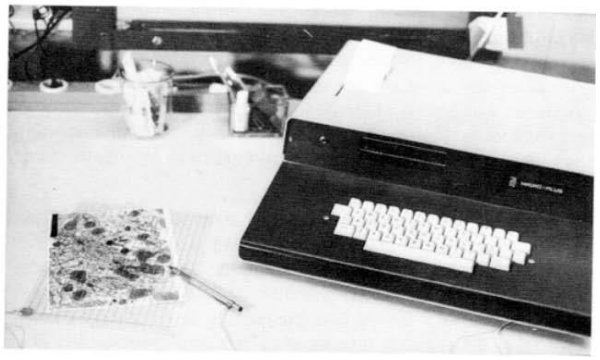

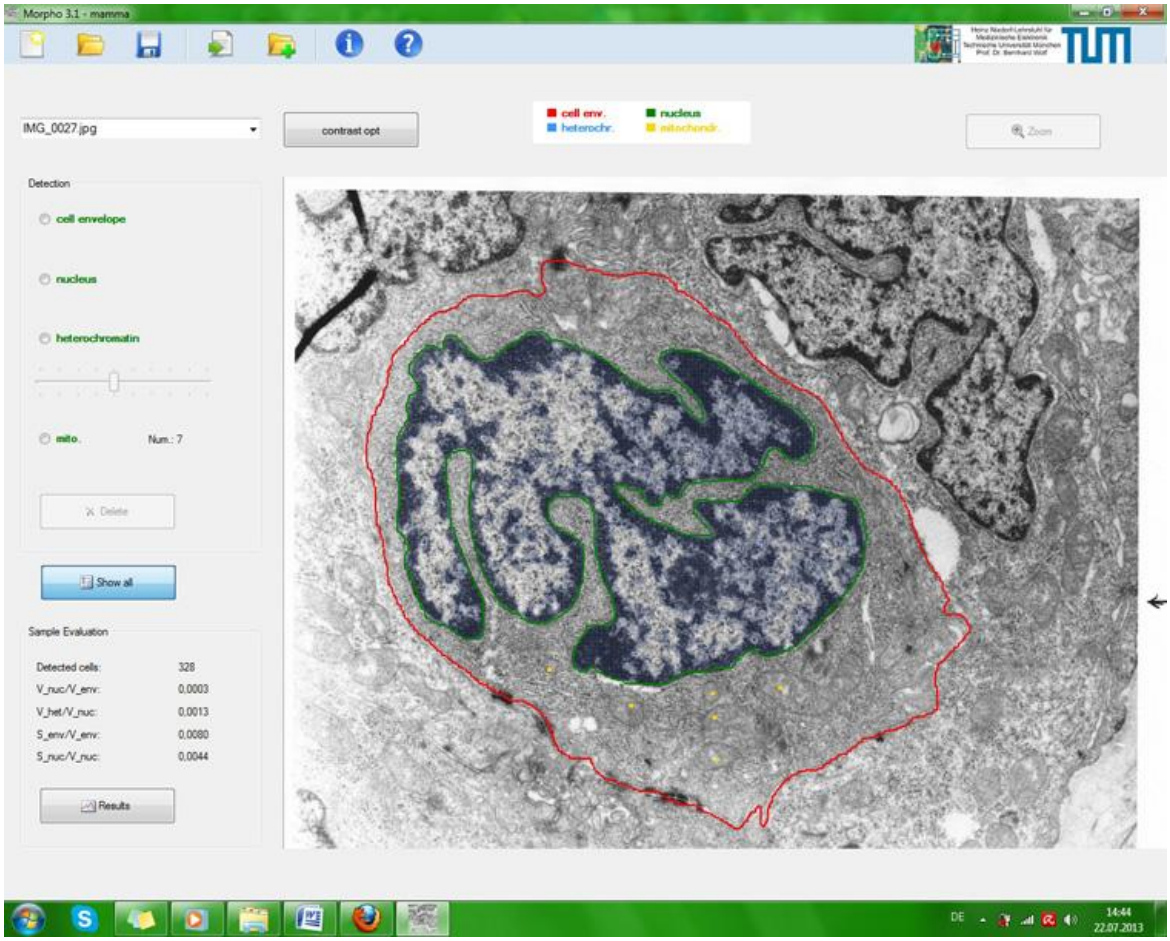
Morpho 3.1 - mamma
IMG_0027.jpg
contrast opt
cell env.
nucleus
heterochr.
mitochondr.
Zoom
Detection
cell envelope
nucleus
heterochromatin
mito.
Num.: 7
Delete
Show all
Sample Evaluation
Detected cells: 328
V_nuc/V_env: 0,0003
V_het/V_nuc: 0,0013
S_env/V_env: 0,0080
S_nuc/V_nuc: 0,0044
Results
DE
14:44
22.07.2013

Advances in Instrumentation, Detectors, FIB and Preparation

IM1.P032
EBSD sample preparation with high and low energy Ar milling

S. Kalácska[1], G. Varga[1], Z. Dankházi[1], Z. Radi[2], K. Havancsák[1]

[1]Eötvös Loránd University (ELTE), Department of Materials Physics, Budapest, Hungary
[2]Technoorg Linda Co., Budapest, Hungary

kalacska@metal.elte.hu

EBSD is a versatile tool providing grain size determination, orientation mapping, phase identification and 3D mapping. Since the EBSD information comes from a few tens of nanometers of the specimen surface regions the most critical issue of the EBSD measurement is the surface quality. The surface should be perfectly clean, free of amorphous or deformed surface layer and moreover it should be flat because of the shadowing effect. Lack of these factors can result either no or faded diffraction pattern.

As it is known, the usual mechanical grinding and polishing create an amorphous layer of (1-100) nm thickness on the surface. The commonly suggested colloidal silica polishment continues for hours and can embed residual polishing material in the surface grains. Electro-polishing of the surface can also be tried, but this is a difficult and complex procedure, nevertheless in some cases it cannot lead to the desired result.

In the last decades a new surface milling method is spreading. This is based on energetic ion beam milling; the underlying physical process is the sputtering. One direction of this method is the focused ion beam technique (FIB) with ion energies up to 30 keV. The other direction uses near parallel inert gas (usually Ar) ion beams with energy up to 10 keV.

In this poster we present a newly developed Ar ion sample milling apparatus and show how advantageously it can be utilized to produce high quality sample surface. Surface quality development on series of composite and ceramic samples was investigated using Technoorg Linda's SC-1000 SEMPrep Ar ion milling apparatus. The surface quality of samples was characterized by the image quality (IQ) parameter of the electron backscatter diffraction (EBSD) measurement. Ar ion polishing recipes have provided to prepare a surface appropriate for high quality EBSD mapping. The initial surfaces of samples were roughly grinded and polished. High quality surface smoothness could be achieved during the subsequent Ar ion polishing treatment. The optimal angles of Ar ion incidence and the polishing times were determined for several materials using a FEI “Quanta 3D FEG” SEM.

Advances in Instrumentation, Detectors, FIB and Preparation

IM1.P033
Low voltage TEM/STEM from 10 kV to 25 kV

E. Coufalova[1], M. Mynar[1], P. Stepan[1], M. Drsticka[1], V. Kolarik[1]

[1]DELONG INSTRUMENTS a.s., Brno, Czech Republic

eva.coufalova@dicomps.com

The application studies of new low voltage transmission microscope LVEM25, working at 10-25 kV are presented. The LVEM25 was designed on the basis of experience with the low voltage transmission electron microscopy at 5 kV [1,2], which is intended for the study of samples with low contrast (organic matters). Many aspects were optimized during design of the instruments:

1) Maintaining relatively low voltage to keep up high contrast.
2) The use of such energy, which would open the possibility to increase the resolution of the system to the area of atomic (molecular) resolution using the monochromatization of the primary beam and Cs correction in future.
3) Practical standpoints - reasonable dimensions, resistance to external influences.
4) Energy sufficient for the transmissivity of electrons through samples of "standard" thickness.

It turned out to be suitable to base such electron-optical system on the use of magnetostatic (the objective lens) and electrostatic (projection system) elements. For the above reasons, we have chosen a range of energy of 10-25 keV. This choice enables to maintain the concept of combination of electron-optical and light-optical magnification, which leads to a significant reduction of the dimensions of the unit and solving simultaneously the problem of TEM image digitalization. It emerged that the working energy of 25 keV is the highest possible energy, at which there is no degradation of the applicable high light-optical magnification due to scattering in the single crystal fluorescent screen.

Using light lenses with large numerical aperture (up to 0.95), we achieve a high collection efficiency of the light from the screen. Also, the level of the light signal is high enough at 25keV energy. We have verified that the electron-optical system can be operated in several modes: transmission (TEM) at 25 and 16 keV, scanning transmission (STEM) at 15 and 10 keV and diffraction at 25 and 16 keV.

The first experimental results confirm the assumptions obtained by electron-optical simulations, in particular the expected resolution in various modes.

It is further confirmed that the contrast inevitably decreases at the energy of 25 keV compared to the lower energies, however, it is still significantly higher than in the energy area of above 50 keV. Even thin sections for which there is no significant increase of chromatic aberration provide sufficient contrast in the image at this working energy. This brings the opportunity to study both stained and unstained samples at low radiation damage.

This version has been optimized for identification of viruses - samples prepared with negative staining and fixation. It allows mobility of the device, and is equipped with user friendly control system with a simple concept.

1. A. Delong, Electron Microscopy 1992, Vol.1, 79-82, 1992
2. L. F. Drummy et al, “Low-voltage electron microscopy of polymer and organic molecular thin films“, Ultramicroscopy, 99,pp. 247-256, 2004
3. The work has been supported by Eurostars Programme of EUREKA and European Community.

Figure 1. The body of MiniTEM on a standard desk

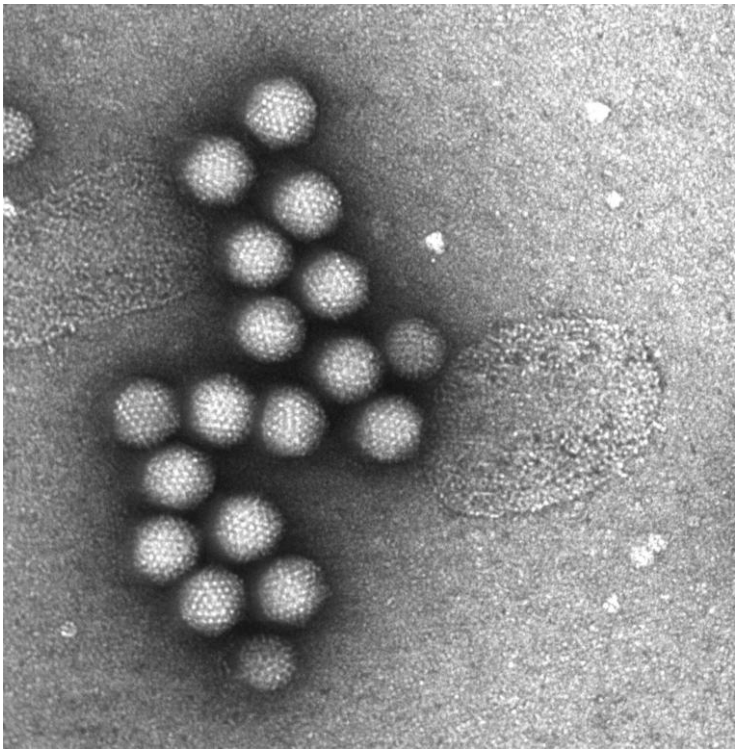

Figure 2. ATCC and rota viruses stained with 2%Uac in STEM mode at 10 keV

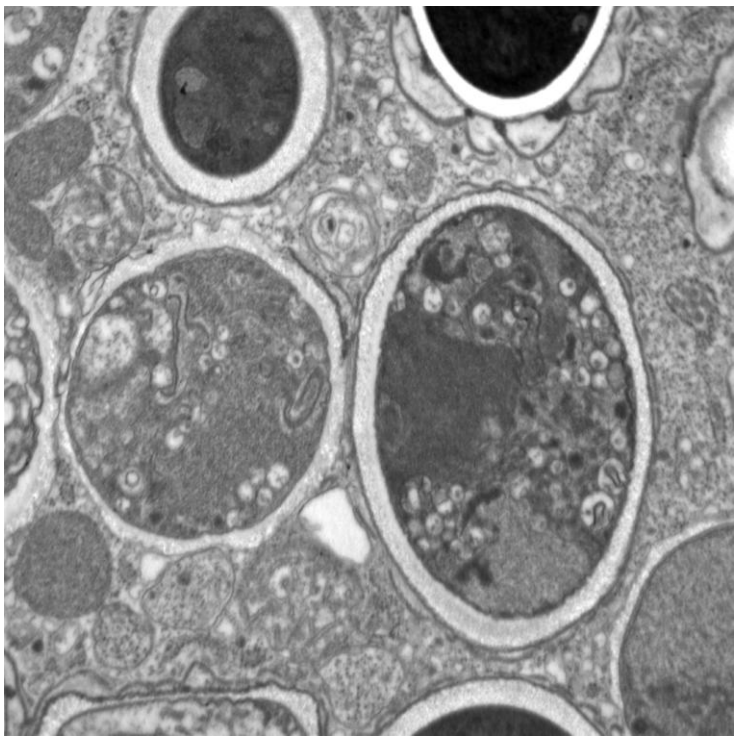

Figure 3. Microsporidie TEM 25 kV

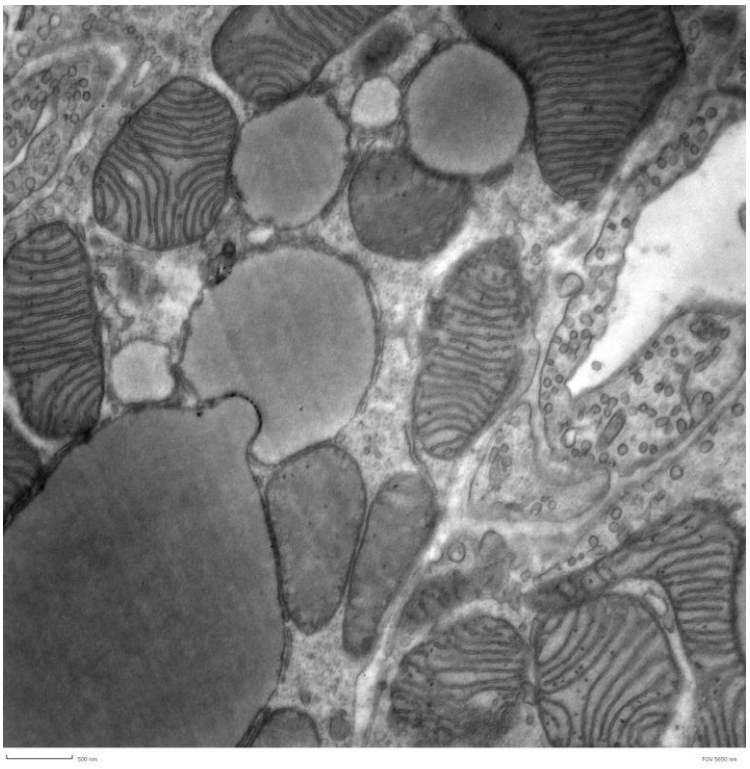

Figure 4. Brown Adipose tissue 90nm TEM 25 kV

Advances in Instrumentation, Detectors, FIB and Preparation

IM1.P034
Preparation of nanoporous gold for EBSD analysis

U. Haßlinger[1], K. Wang[2], Z. Qi[2], J. Weißmüller[2], M. Ritter[1]

[1]Hamburg University of Technology TUHH, Electron Microscopy Unit, Hamburg, Germany
[2]Hamburg University of Technology TUHH, Institute of Materials Physics and Technology, Hamburg, Germany

ritter@tuhh.de

Nanoporous metals often show novel properties that make them interesting for a variety of applications like catalysis or as actuators, due to their high surface area and small structure size. Frequently, information about the local crystal structure is required for a better understanding of this class of materials. High resolution orientation information can be provided by Electron Backscatter Diffraction (EBSD). Sample preparation for EBSD needs to provide a flat surface and introduce only little deformation. Usually, standard bulk sample preparation techniques do not produce satisfying results for nanoporous metals. Mechanical grinding and polishing, for example, often leads to massive deformation and densification of the ligament structure at the surface. Therefore, this study is aimed at finding an alternative bulk sample preparation routine for one of the most common nanoporous metals, nanoporous gold (npg). Typically, npg bulk samples are produced from AgAu alloy sheets or wires by removing the less noble silver electrochemically (dealloying). The original grain size of about 100 µm is conserved during the dealloying process and the created ligaments are of the size of a few nm, but larger ligament sizes can be tuned by subsequent heat treatment.

The first step of the preparation routine is the infiltration of the npg samples by a polymer to stabilize the ligament structure. However, polymer infiltration does not prevent densification and deformation of the ligaments completely, if the sample is prepared using mechanical grinding and polishing (figures 1 and 2). Although the size of the local orientation map (figure 2) is much smaller than the grain size, there are no dominant orientations visible. This improves significantly, if the samples are cut with an Ultramicrotome (UM), instead, in order to create the flat sample surface necessary for EBSD. The ligament structure appears to be largely intact at the cut surface (figure 3). In EBSD, the grain structure becomes visible because the preparation introduces considerably less orientation variation, as the local orientation map within one grain illustrates (figure 4). However, analysis of the orientation variation within several grains shows that the amount of surface deformation introduced by the Ultramicrotome is not negligible and strongly dependent on the grain orientation with respect to the cutting direction. Therefore, the deformed surface layer has been removed with a focused ion beam (FIB). As a result, the indexing of local crystal orientations in EBSD has improved significantly. The orientation variation within single grains is smaller and no longer grain orientation dependent.

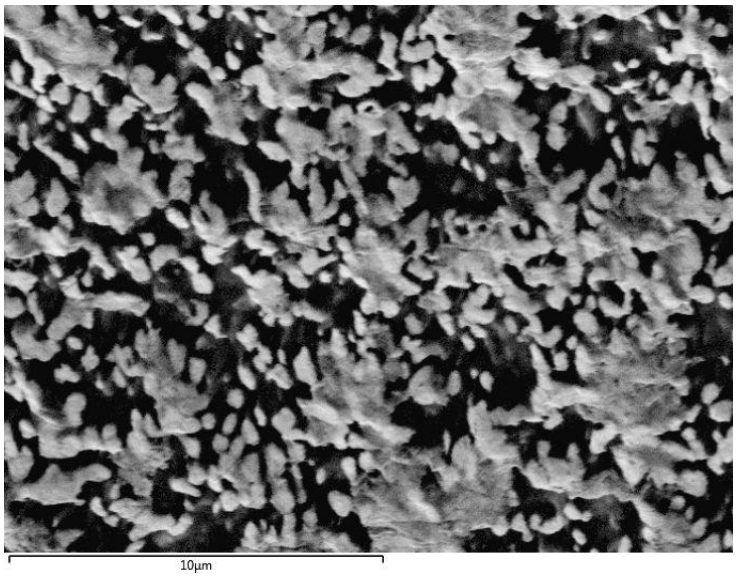

Figure 1. Scanning electron microscope (SEM) image of a polymer infiltrated nanoporous gold (inpg) sample (ligament size: ~260 nm) prepared by mechanical polishing and grinding

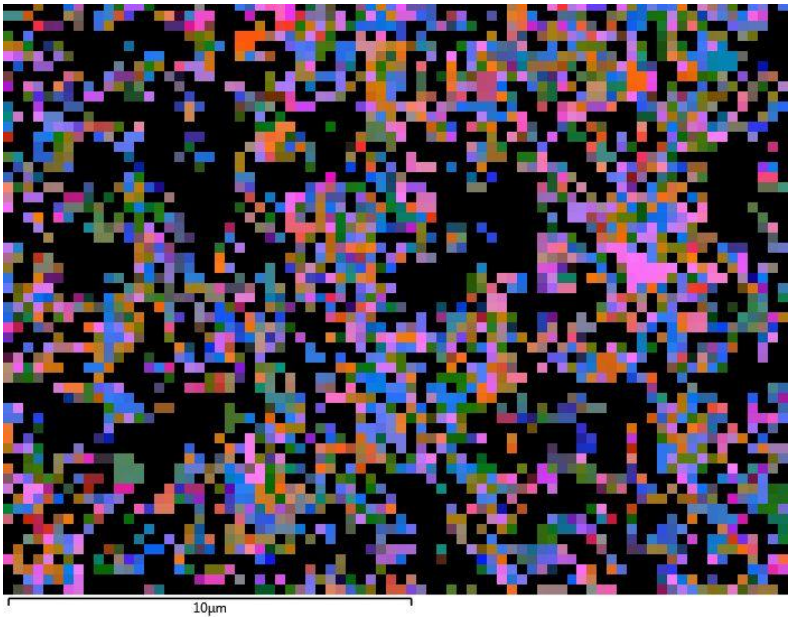

Figure 2. Local orientation map (Euler coloring) generated by EBSD (corresponding to figure 1)

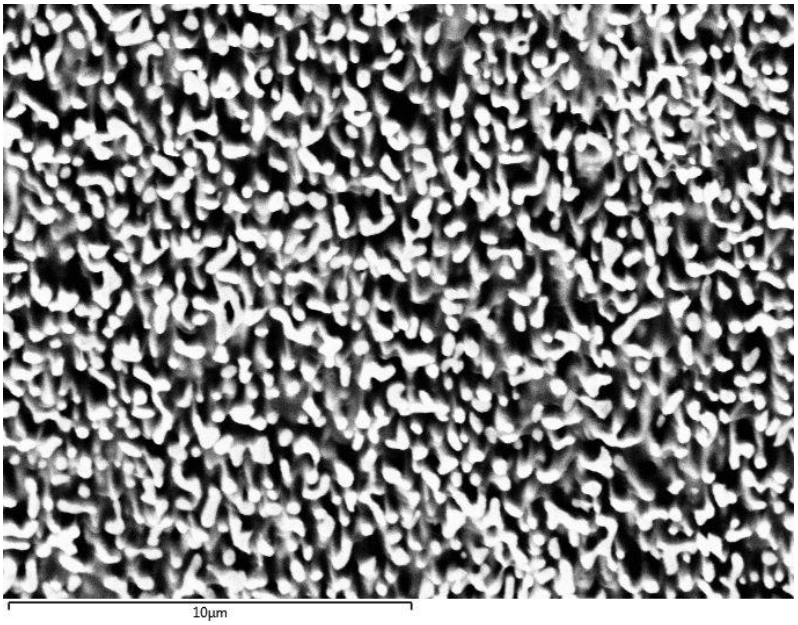

Figure 3. SEM image of a section within one grain of a polymer infiltrated npg sample (ligament size: ~260 nm) prepared by Ultramicrotomy

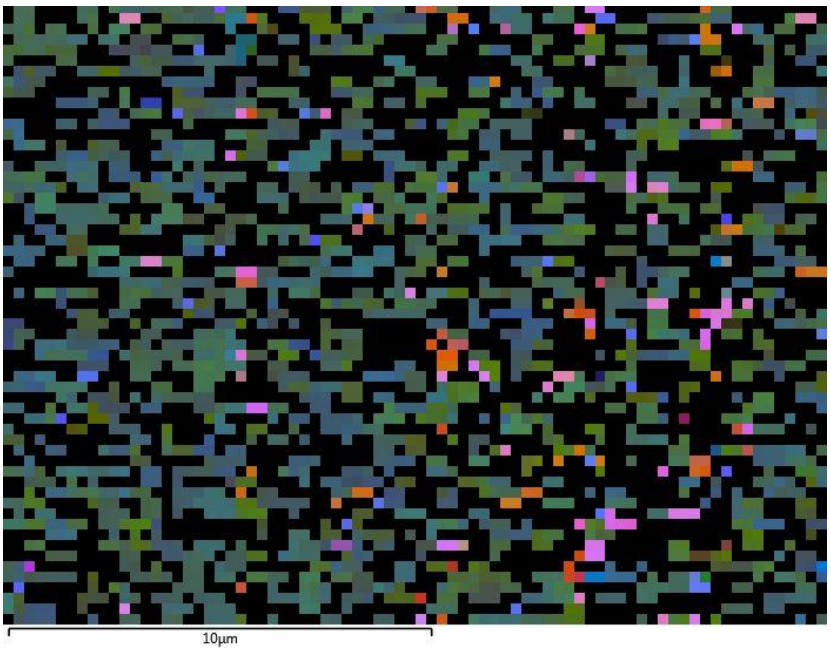

Figure 4. Local orientation map (Euler coloring) generated by EBSD (corresponding to figure 3)

Advances in Instrumentation, Detectors, FIB and Preparation

IM1.P035
Novel specimen-preparation routes for individual microsized particles for investigation by transmission electron microscopy

L. Berthold[1], M. Krause[1], T. Höche[1]

[1]Fraunhofer Institute for Mechanics of Materials IWM, Nanomaterials and Nanoanalytics, Halle, Germany

lutz.berthold@iwmh.fraunhofer.de

For imaging and analyses of small particles, microscopic fragments and other separated microscaled specimens in transmission electron microscopy (TEM), an efficient, fast, targetted, reliable and competitive method of preparation is necessary.

Using conventional methods, the preparation of cross-sections from such individual small samples to electron transparency is a complex and laborious task. In the standard approach, single particles/fragments are deposited by means of micro manipulator and fixed on a substrate (H) bar with a thickness of 80 to 100 µm. This assemblage of substrate and particles/fragments are then ion-beam thinned to residual thickness of just a few 100 nm.

In order to improve this preparation technique, a very fast and efficient preparation route was developed by combining laser milling with ion beam techniques. Using the all-new laser processing system microPREP[1-3] (3D-Micromac AG, Chemnitz, Germany, Fig. 1), a newly designed specimen-support platform with reduced residual thickness of the area for particles/fragments deposition can be readily prepared, Figs. 2-4.

Due to the reduced thickness, the processing time in a focused ion beam workstation is greatly reduced. Furthermore the substrate material is variable and therefore optimum conditions for analytical investigations (EDXS, EELS) in the TEM can be attained. On such cross sections of particles/fragments, the thickness of the latter as well as the morphology of layers, interfaces, artefacts, grain and crystal structure, morphology, chemical components etc. can be study down to the atomic scale.

Alternatively, wedge polishing of particles glued to the surface of a sacrificial wafer proved a very valuable way to get statistical information on a larger ensemble of pigments rather than details on individual particles.

Examples of samples prepared both ways will be shown after TEM characterization in our cutting-edge TEM (FEI TITAN³ G2 80-300).

1. M. Krause & Th. Höche, European Patent application EP 13 162 360.
2. Th. Höche, M. Krause, M. Ebert & U. Wagner: “A Novel Laser Tool for High-Volume Sample Preparation” *Laser Technik Journal* 1 (2015) 42-44.
3. M. Krause, M. Ebert, Th. Höche, & U.Wagner: „MicroPREP—A New Laser Tool for High-Throughput Sample Preparation” *Proc. of ISTFA 2014*, November 9-13, 2014, Houston, Texas, USA, p. 270-276.

Figure 1. microPREP tool for laser-based sample preparation (by 3D-Micromac AG, Chemnitz, Germany)

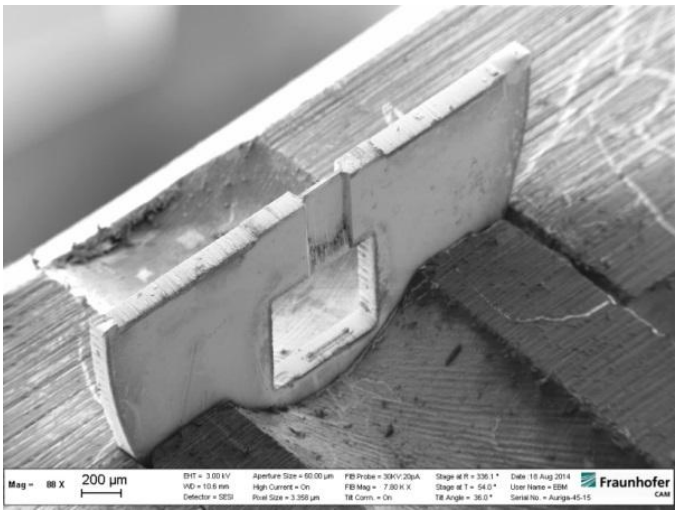

Figure 2. Laser-cut H-bar support prior to deposition of individual particles (scanning electron micrograph).

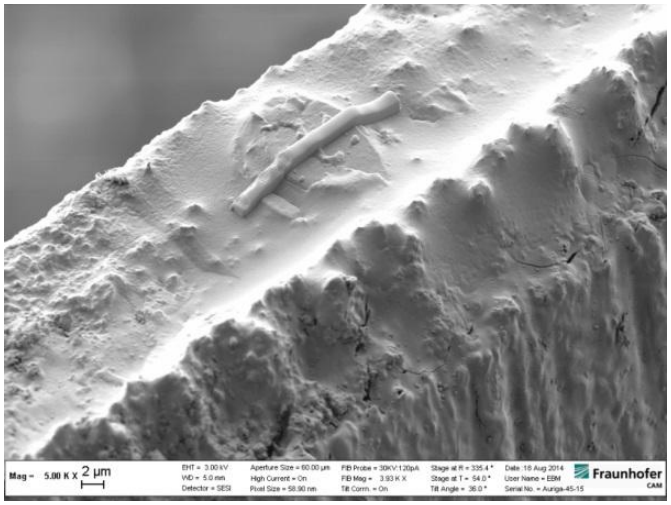

Figure 3. Pigment particles deposited and fixed on a support platform (scanning electron micrograph).

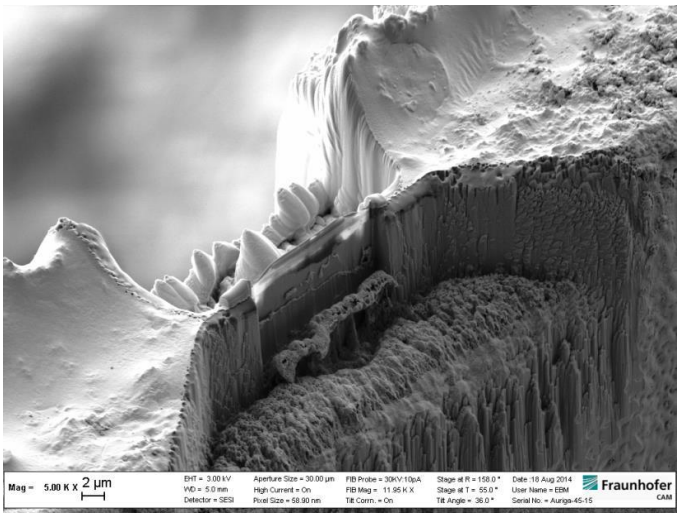

Figure 4. Ion-beam thinned pigment particles with electron transparency (scanning electron micrograph).

Advances in Instrumentation, Detectors, FIB and Preparation

IM1.P036
Nondestructive inspection of 4” wafers with 3D LED structures in a tilted view by EBIC and CL inside an FE-SEM

J. Ledig[1], S. Fündling[1], J. Hartmann[1], H.- H. Wehmann[1], A. Waag[1]

[1]Technische Universität Braunschweig, Institute of Semiconductor Technology and Laboratory for Emerging Nanometrology, Braunschweig, Germany

j.ledig@tu-bs.de

Three dimensional light emitting diodes (3D-LEDs) with a core-shell geometry are supposed to have substantial advantages over conventional planar LEDs.[1] The active area along the sidewalls of GaN pillars can be increased considerably by high aspect ratios - leading to a lower current density inside the InGaN quantum well (QW) at the same operation current per substrate area. The production of devices out of these 3D-LEDs will scale up to substrates with larger areas, generating a request for characterization techniques of local electro-optical properties with a high spatial resolution on different positions of the substrate (e.g. mapping and investigation of test features). As also subsequent device processing may be performed on a wafer scale non-destructive techniques should be applied..

Especially the 3D shape poses a challenge to the electrical and optical characterization of such device structures. In addition, a spatially resolved investigation is needed in order to discuss gradients along single structures and to optimize them regarding device operation. To investigate vertical features of 3D structures by an SEM, a tilted view is necessary; usually a spatially resolved imaging by conventional SEM signals (e.g. SE, CL) is carried out at about 30°.[2] By tilting a sample in conventional CL setups, only areas close to a non-concave edge can be placed in the optical focus.

We present results obtained with an FE-SEM which is equipped with SE, In-Beam SE, low-kV BSE, EBIC and monochromatic CL detection as well as a piezo controlled manipulator setup (c.f. Figure 1). A simultaneous use of all available detectors is possible, only the BSE detection is physically hindered by the optical setup whose focus is at a working distance of about 10.25 mm. A modified parabolic collection mirror enables measuring luminescence from planar samples in a tilted view up to 30° without a significant loss of collection efficiency. In addition, tilting the sample significantly enhances the collection efficiency of the SE detector due to its arrangement with respect to the CL mirror.

Thanks to the large chamber, a non-destructive characterization on each position of whole wafers up to 4” tilted to 30° is possible by EBIC and CL. An additional flange in the chamber door is used for feed throughs to the manipulator setup which can be mounted on different locations on the sample stage.

In addition, by changing the deflection parameters (e.g. rocking) the SEM allows a lateral scanning of the sample by the electron probe from slightly different angles. This enables a 3D imaging without moving (tilting) the sample (c.f. Figure 2) giving a fast and deeper insight to the morphology of features with high aspect ratios, e.g. the probe tip and 3D structures themselves, also during CL mapping.

1. Mandl, M. *et al.* Group III nitride core-shell nano- and microrods for optoelectronic applications. *Phys. Status Solidi RRL - Rapid Res. Lett.* **7,** 800-814 (2013).
2. Wang, X. *et al.* Growth and characterization of mixed polar GaN columns and core-shell LEDs. *Phys. Status Solidi* **5,** (2015).

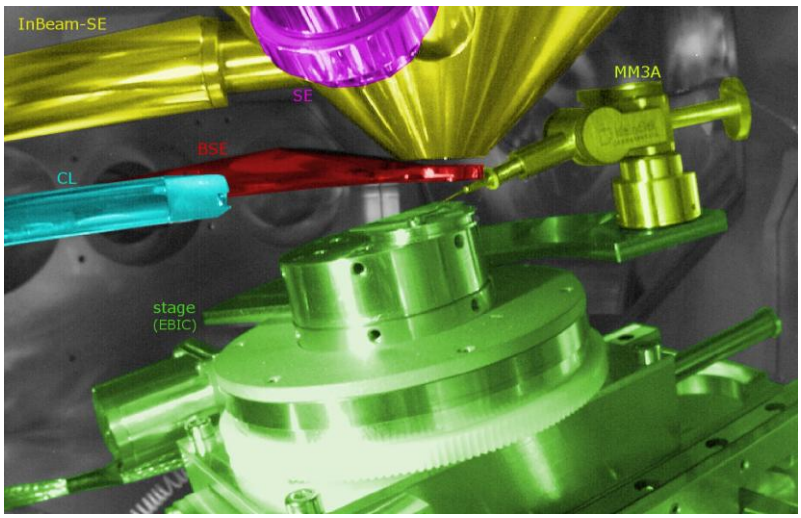

Figure 1. Colorized photo taken by the chamber-view camera highlighting the sample stage (green), manipulator (light green), modified parabolic mirror for light collection (cyan), BSE (red), in-Beam SE (yellow) and SE detector (magenta).

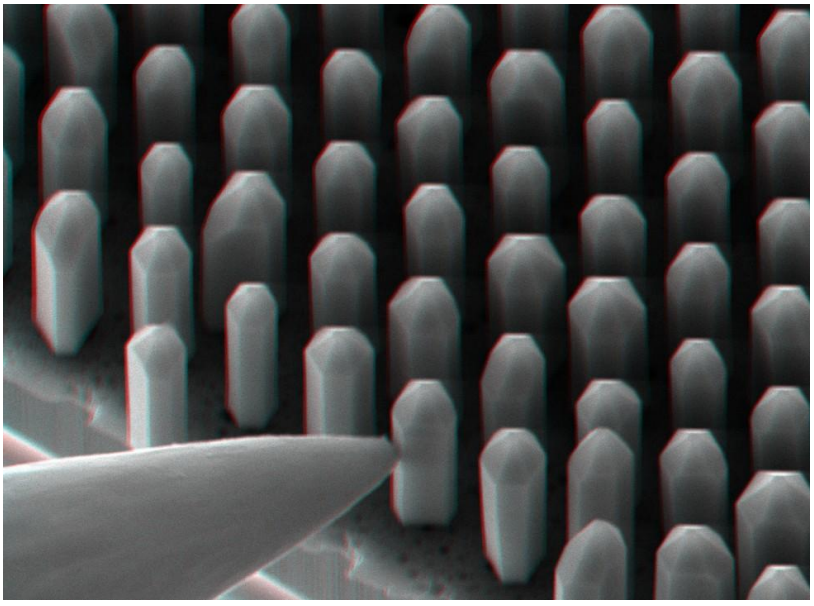

Figure 2. Stereoscopic SE image (color overlay) of a core-shell LED contacted by a probe tip (tilt = 30°, EHT = 15 kV, FOV = 19 µm)

Advances in Instrumentation, Detectors, FIB and Preparation

IM1.P037
Electrical characterization of Pt wires deposited by FIB

U. Hömpler[1], F. Kießling[1], T. Niermann[1], D. Berger[2], M. Lehmann[1]

[1]Technische Universität Berlin, IOAP, Berlin, Germany
[2]Technische Universität Berlin, ZELMI, Berlin, Germany

hoempler@physik.tu-berlin.de

A common technique for contacting specimen at the micrometer scale is the ion beam (IB) or electron beam (EB) induced deposition of Pt. Measurements showed different resistance behaviors of the Pt depending on the deposition methods [1]. The resistivity of IB deposited Pt (Pt_{IB}) is up to two orders of magnitude smaller than EB deposited Pt (Pt_{EB}). To investigate semiconductor devices it is necessary to know line and contact resistance of these Pt wires. For this reason we employ 4-wire and 2-wire sensing to characterize Pt wires deposited in slightly different ways [2,3].

Figure 1 shows one test structure consisting of conducting Au pads with a Ti adhesive layer on an insulting oxidized Si wafer. A 100 mesh 3 mm TEM grid (hole width 214 µm and bar width 40 µm) was used as mask. (160±10) nm Ti and (200±30) nm Au (figure 1c) were deposited on the wafer by thermal evaporation. By removing the mask, insulated contact pads were produced (figure 1a). The resistivity of the insulating SiO_2 layer is determined to > 10^3 Ωcm. Pads of a 2x2 matrix are contacted by Pt deposition (figure 1b). Two different procedures for deposition were investigated (FIB, FEI Helios Nanolab 600): only Pt_{IB} depositions on the specimen and Pt_{IB} deposition on a Pt_{EB} protection layer as commonly used in FIB to reduce the damaging by the ion beam.

The electrical characterization of the produced specimen is done at a point probe station with a Keithley SourceMeter (Model 2400). Figure 2 shows the ohmic behavior of the Pt wires by the linear slope at the IU-curve. The three Pt bars of a Pt wire are deposited in two different modes: all at once (parallel mode) or one after the other (serial mode). The higher resistivity in parallel mode is determined by process variations. The resistance of the Pt_{IB} wire does not depend on the sensing method indicating a negligible contact resistance between the wire and the pad. The high resistance of the 4-wire sensed Pt_{IB} wire on the Pt_{EB} layers and the even higher resistance for 2-wire sensing can be explained by an electrical bypass of the Pt_{IB} wire through the Au pad. This bypass is inefficient with the Pt_{EB} layer in between due to the 2-3 magnitude higher resistance of the Pt_{EB} [1] compared to the Pt_{IB}. Therefore the current is split in a part flowing through the Au pad and a part flowing through the Pt_{IB} wire.

The measured resistivity of IB deposited Pt of (0.750±0.150) mΩcm is in the same order as reported in the literature [1,4]. This resistivity is several magnitudes smaller than in semiconductors e.g. two magnitudes for GaN and therefore suitable for semiconductor measurements. Semiconductor devices with an Au pad on top should be contacted with sole Pt_{IB} as the semiconductor is protected by the Au and due to the high resistance of the Pt_{EB}.

1. R.M. Langford et al., Microelectronic Engineering 84 (2007) 784-788.
2. E. Stern et al., Applied Physics Letters 88 (2006) 053106.
3. A. Motayed et al., Journal of Applied Physics 100 (2006) 024306.
4. S. Smith et al., IEEE Transactions on Semiconductor Manufacturing, Vol. 16 No.2 (2003) 199-206.
5. We kindly acknowledge the support from the DFG within the Collaborative Research Center 787, project A4

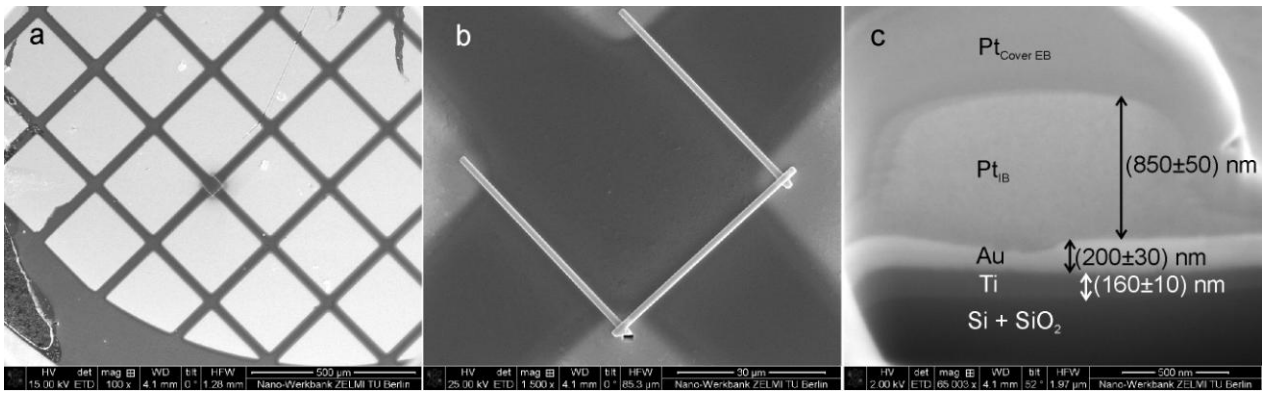

Figure 1. Test structure 1: a) an overview of the gold pad grid with the Pt deposition contacting a 2x2 pad area. b) The Pt deposition connecting the pads. The shadows around the Pt wires are a thin Pt layer deposited by secondary electrons. c) The measured thicknesses in the specimen with a covering protective Pt layer.

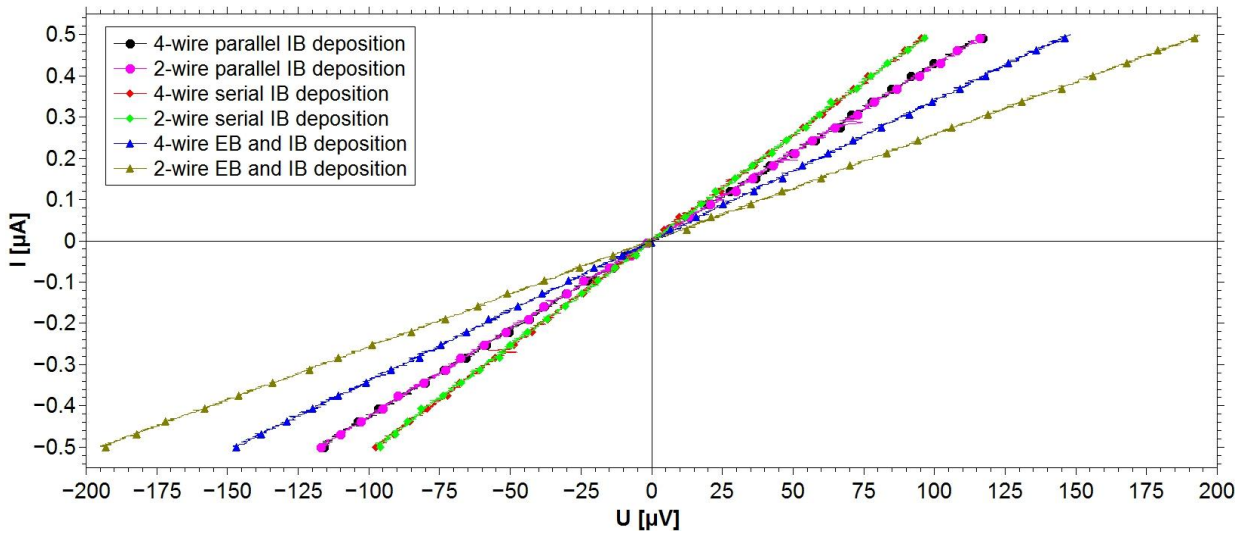

Figure 2. Comparison of 4-wire and 2-wire sensing of the test structures. In Pt_{IB} wires no contact resistance can be measured. Pt_{IB} wires on a Pt_{EB} layer exhibit a contact resistance.

Advances in Instrumentation, Detectors, FIB and Preparation

IM1.P038
Topographic contrast of HR-SEM

U. Gernert[1], D. Berger[1], M. Hemmleb[2]

[1]Technische Universität Berlin, Zentraleinrichtung Elektronenmikroskopie ZELMI, Berlin, Germany
[2]m2c microscopy measurement & calibration, Potsdam, Germany

ulrich.gernert@tu-berlin.de

State-of-the-art high resolution scanning electron microscopes (HR-SEM) have a multiple detection system that is optimized to analyse subtly element differences and thin surface layers with high sensitivity and high spatial resolution [1]. The purpose of this contribution is to investigate the remaining, but nevertheless in many applications very important, topographic contrast obtained with those specialised detection systems based on a Hitachi SU8030 SEM. As a test specimen we used spherical calottes that were produced on Si wafers by ion beam induced Pt deposition (FEI Helios NanoLab600). The diameter and the heights were chosen in that way that the surface inclination changes between 90° in the center and 45° at the edge [fig. 1]. After calibration of the deposition rate the spherical calottes are automatically produced by a script controlling the ion beam.

In conventional SEM, i.e. at low or medium magnification, the topographic contrast is high if a directional detector is used, e.g. a secondary electron (SE)-chamber detector or the differential signal of two opposite segments of a pole-piece backscattered electron (BSE)-detector [fig. 2]. Unfortunately, these detectors are not available in high resolution requiring a low acceleration voltage and a small working distance. Therefore, the inlens detectors have to be used. As an example fig. 3a shows the BSE-signal of the upper detector (i.e. the lower inlens detector of the SU 8030).

For the evaluation of the SEM image data, an advanced histogram method was implemented and applied. The histogram function represents the distribution of the mean gray values of concentric circles with different radius, starting from the centre to the maximum radius of the selected object in pixel steps. Fig. 3b shows the histogram related to fig. 3a. Obviously, the BSE-signal of the upper detectors shows inverted topographic information with a low contrast. This effect becomes even worse if the BSE-Signal of the top-detector is used. In addition, the histograms of the BSE-signals depend slightly on the working distance, as will it be discussed on the poster. In conclusion it is clear that the BSE signal of the inlens detectors is not suitable to analyse topographic contrast. The reasons are first that the inlens signal is not directional and second that the number of BSEs does not depend clearly on the surface inclination since not all high energy BSE are collected by the inlens detector for inclined surfaces.

Fig. 4a and 4b show the corresponding results for the SE-signal of the upper detector. Despite the detection geometry of the upper detector, the signal has fortunately a perfect rotational symmetry. Moreover the signal and the inclination contrast (i.e. the intersection of the electron beam with the inclined surface) shown by the histograms have proved to depend neither on the acceleration voltage nor on the working distance. Therefore it might be derived that the SE-signal of the upper detector is well suited for analysing the topographic contrast.

We also investigated the topographic contrast in the deceleration mode, which is widely used for the surface-sensitive analysis of specimens at low excitation energies. In the deceleration mode the contrast of the images of the spheres show no axial symmetry corresponding to the small deviations of the rotationally symmetry of the spheres themselves [Fig. 1]. Therefore the topography contrast is highest. Unfortunately the homogeneity of the deceleration field is influenced by the overall shape of specimen close to the feature of interest as well, disabling a quantitative analysis of the topography.

In conclusion it is recommended to use the SE-signal of the upper detector to analyse the topography since its contrast is highest and does not depend on the electron energy and the working distance.

1. Gernert U., Berger D., Physical background of multiple detection possibilities of the Hitachi SU8030 SEM, IMC2014 Prag,ISBN 978-80-260-6720-7
2. We kindly acknowledge financial support from the Deutsche Forschungsgemeinschaft DFG (INST 131/631-1).

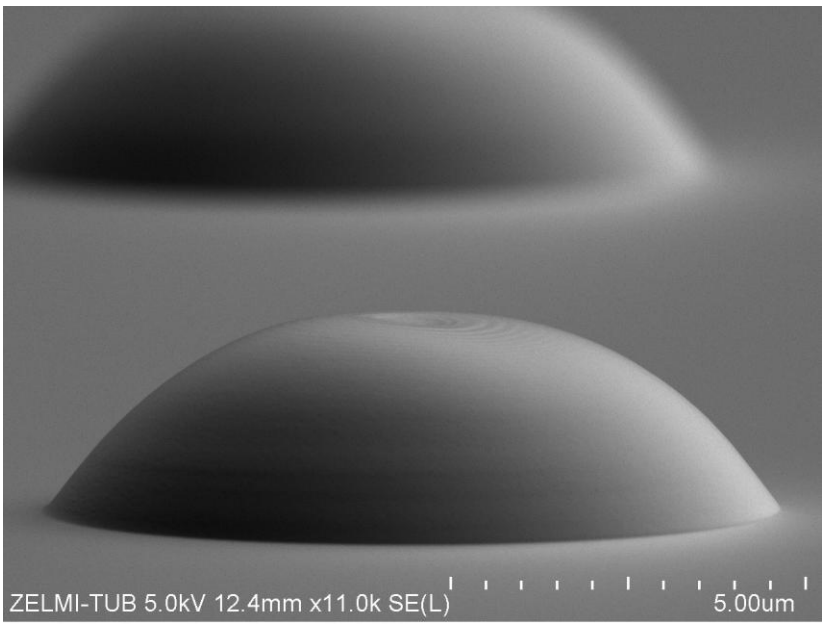

Figure 1. Test specimen imaged at 85°

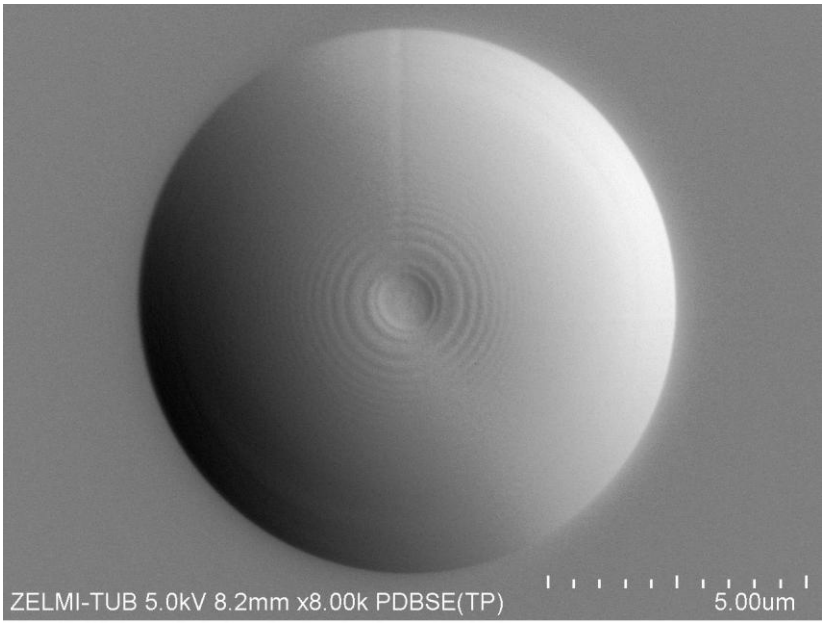

Figure 2. Differential signal of pole piece BSE-detector

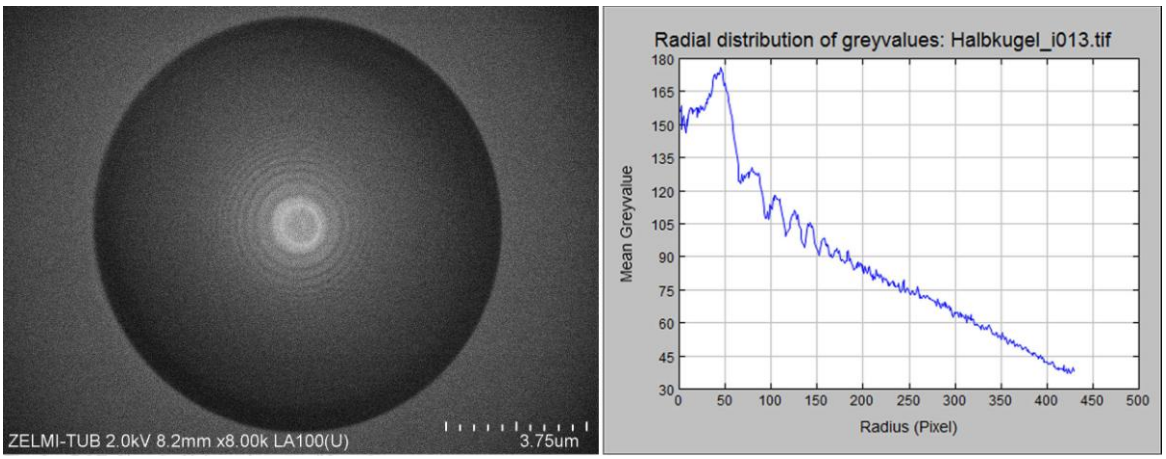

Figure 3. a) BSE-Signal of inlens detector (Upper); b) Radial distribution of intensity (integrated on circle rings)

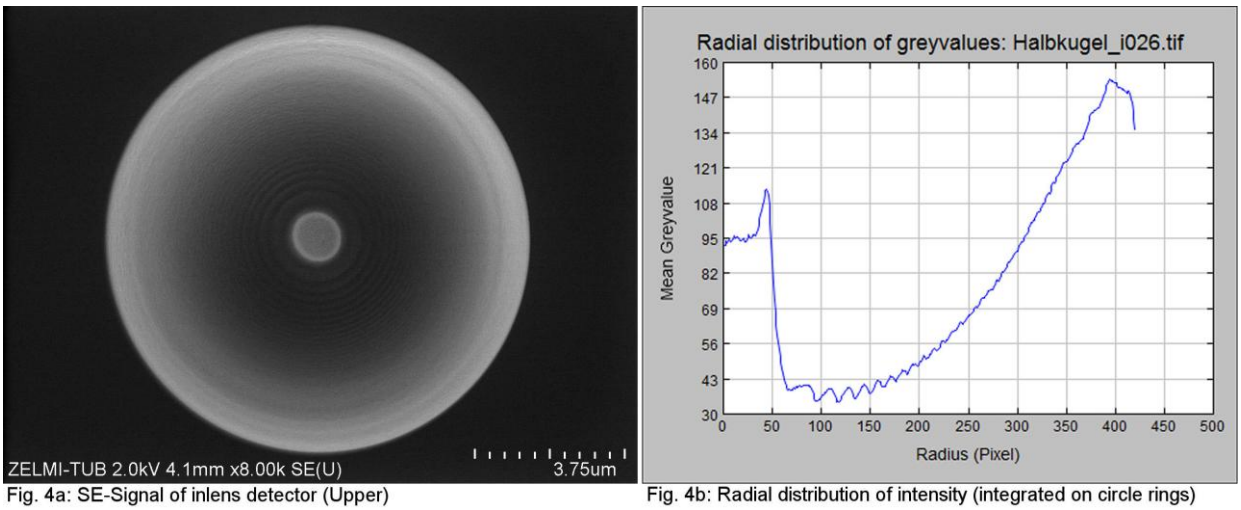

Fig. 4a: SE-Signal of inlens detector (Upper)

Fig. 4b: Radial distribution of intensity (integrated on circle rings)

Figure 4. a) SE-Signal of inlens detector (Upper); b) Radial distribution of intensity (integrated on circle rings)

Advances in Instrumentation, Detectors, FIB and Preparation

IM1.P039
Ultra performance liquid chromatography- mass spectrometry method for the simultaneous determination of pharmaceutical drugs in waste waters

Z. Alothman[1], S. Wabaidur[1]

[1]King Saud University, Riyadh, Saudi Arabia

zaothman@ksu.edu.sa

A highly sensitive Ultra Performance Liquid Chromatography−Mass Spectrometry method has been developed for the identification and simultaneous determination of various pharmaceuticals in industrial waste water samples. The analyzed waste water samples were collected from different industrial waste of Riyadh City, Saudi Arabia. The binary mobile phase was used a mixture of acetonitrile and 0.1% aqueous solution of formic acid at a flow rate of 0.4 ml min^{-1}. Identification and quantitation of the analyzed drug samples were carried out using mass spectrometer equipped with electrospray ionization source operated in negative ionization mode. The linear range of the proposed method was found to be in the range of 18-270 ng ml^{-1} for all drugs with limit of detection in the range of 1.25 to 1.89 ng ml^{-1}.

Advances in Instrumentation, Detectors, FIB and Preparation

IM1.P040
New approach of segmentation of FIB tomograms of porous carbon-rich materials

M. Mundszinger[1], J. Bernhard[1], U. Golla-Schindler[1], U. Kaiser[1]

[1]Universität Ulm, ZE Elektronenmikroskopie, Ulm, Germany

manuel.mundszinger@uni-ulm.de

Tomograms received from a focused ion beam (FIB) machine using the ion beam to slice the specimen and the electron beam to view the result are widely used in material sciences to gain quantitative information about the topography and composition of the specimen under investigation. With a single tomogram it is possible to determine the volume fraction and the surface of a selected element. After acquisition, the first step to generate the tomogram segmentation of the raw data. Segmentation of FIB tomograms of a porous material can, however, be very troublesome caused by the high depth of focus given by the scanning electron microscope. Thus the same graylevel can be obtained e.g. for the top and the bottom of a pore if both is in the range of the depth of focus, which can become the restricting hurdle for a reliable automatic or at least semi-automatic segmentation of the single picture and therefore of the whole tomogram. One possibility is to fill the pores with resin to decrease the insights in the sample structure. However, many resins are carbon-based and therefore this procedure only works fine as long as the sample does not contain carbon. But if the sample contains carbon, the sample-resin contrast will be very weak, if existent at all (Ender, 2012). One solution to this problem provides the Gas Injection System (GIS) in the FIB. The approach is to fill the pores during cutting with the FIB in situ with platinum. This procedure enables sufficient contrast in the SEM images (Eswara-Moorthy, 2014). However, this in-situ method is not suitable for every sample and is moreover time consuming and expensive.

Here we present a new way to face the problem associated with FIB-tomograms of porous materials with carbon-rich inclusions. For our method we use carbon-free industrial available coatings to avoid the loss of the carbon contrast in the SEM images. The used coating is a high-temperature coating from the Kager Industrieprodukte GmbH marked as Hie-Coat 840-C.

Our first experiments showed an insufficient wetting of coating and sample and consequently the obtained pore filling was not sufficient (see Figure 1 a). However, the wetting was strongly improved by hydrophilization using a plasma cleaner (Gatan Advanced Plasma System Solarus 950) when treated for 30s with a mixture of 50%/50% hydrogen and oxygen. After this treatment, the coating was put on the sample with a brush and air dried for 24 hours. The investigations were performed using a Zeiss NVision 40 Ar. In conclusion, the first results are promising. The contrast between the coating and the cathode material is good (see Figure 1), and the wetting was significantly improved (compare Figure 1 a with b). So, the use of a plasma cleaner for improved wetting seems to provide a cheap and exceptionally easy-to-handle routine for sample pre-preparation for porous carbon-rich materials.

1. Ender, M. a.-T. (2012). *Quantitative Characterization of LiFePO4 Cathodes Reconstructed by FIB/SEM Tomography.* Journal of The Electrochemical Society, 159, A972-980.
2. Eswara-Moorthy, S. K.-M. (2014). *An In Situ SEM-FIB-Based Method for Contrast Enhancement and Tomographic Reconstruction for Structural Quantification of Porous Carbon Electrodes.* Microscopy and Microanalysis, 20, 1576-1580.

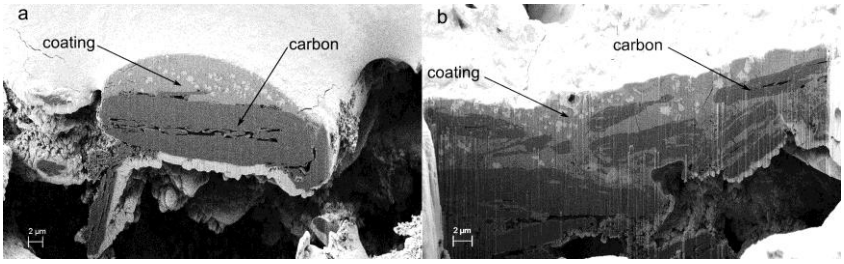

Figure 1. A porous battery material before (a) and after (b) treatment with the plasma cleaner. a: carbon cathode with the used coating on top without the plasma cleaner treatment. b: the same cathode after the treatment.

Advances in Instrumentation, Detectors, FIB and Preparation

IM1.P041
The Nanoworkbench: automated nanorobotic system inside of scanning electron or focused ion beam microscopes

E. Burkart[1], D. Peters[1], I. Burkart[1]

[1]Klocke Nanotechnik, Aachen, Germany

burkart@nanomotor.de

Many every day developments would not exist today without preparation, handling and assembly of materials under optical microscopes. There would be no wristwatch, no in vitro fertilization, no mini-gearbox, just to mention a few. These products depend on using toolsets like tweezers, knives, hooks, probes and several different measurement tools in combination with optical microscopes. But material properties and functionalities also depend on structure dimensions that are smaller than the wavelength of light.

The operators of SEM, FIB or Dual Beam systems generally work without toolsets. One reason for this is the disconnected closed loop operation between human eyes and hands that enable complex operations under optical microscopes without even thinking about it

The two main aspects of the new Nanoworkbech by Klocke Nanotechnik GmbH, the development of its Nanorobotics technology and the applications enabled by it, are described in this paper.

Aspect 1, development of the technology: In general the success of in-SEM/FIB Nanorobotics depends on the co-operation of several important modules in one global system. The main developments include:

- Nanomanipulators in automation, for movement of end-effectors and sample handling,
- Different end-effectors for nano- probing, cutting, cleaning, force distance or wear measurements,
  gripping, sorting or material preparation and processing,
- Automatic in-situ tip cleaning process
- Automatic 3D position detection of all tools and SEM/FIB
- A control of all tool and SEM/FIB sample stage positions in a common global coordinate system,
- SEM picture assisted haptic interface by “Live Image Positioning”,
- Modular design for fast configuration & teaching of nano-analytical or nano-handling processes.

With instantiating these technical demands the Nanoworkbench enables secure and easy usage of toolsets within SEM/FIB systems, for manual operation, for non-professional users and in high level of automation, e.g. for high throughput industrial processes, even as job-shop [1].

Aspect 2, development of a series of new applications in one system: Expanding the SEM/FIB to a material processing system and a nano-analytical workbench opens the door to many applications in all fields of research and development up to industrial production [5]. Several examples of these new interdisciplinary research and development fields will be described during the presentation.

A few examples of Nanoworkbench applications are highlighted in Figure 1. Although these examples may raise the impression of a review about different machines and their usage, this is not the case. Described is the development of the Nanoworkbench.

1. D. Morrant, EIEx Magazine of European Innovation Exchange, 1 (2009)
2. G. Schmid, M. Noyong, Colloid Polym Sci., (2008)
3. C.-H. Ke1, H.D. Espinosa, Journal of the Mechanics and Physics of solids, 53 (2005)
4. Seong Chu Lim, Keun Soo Kim, Kay Hyeok An, Dept. of Phys., Sungkyunkwan University, Korea (2002)
5. Supported by European Commission, IST and Ziel2.NRW

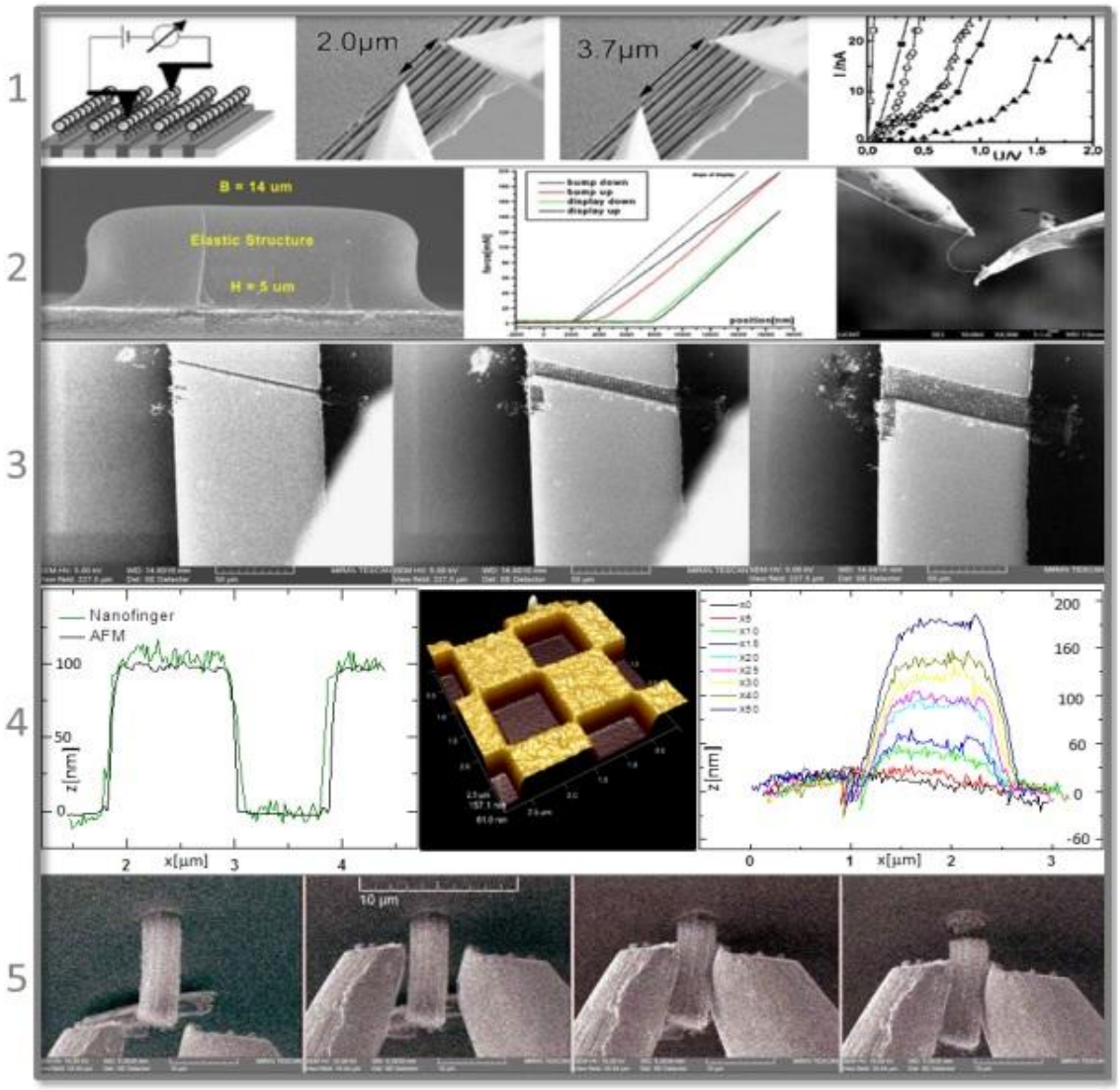

Figure 1.
(1)Nano-Probing: of Gold55-Clusters arranged in chains [2]: The electrical conductivity along these gold chains is measured over different distances and compared with the conductivity of bare gold wires.
(2)Nano-Tribology and similar measurements can be performed in high resolution [4]
(3)Nano-Cutting: fast milling of structures
(4)3D-Nanofinger: measurement of gold and EBID structures grown and measured in situ
(5)Particle-Sorting: Gripping of a rigid CNT bundle with high force and separation from the ground [3]

Quantitative Techniques and Image Simulation in TEM/STEM, SEM and Diffraction

IM2.042
Precise nanoparticle atom-counting using a minimum electron budget

S. Van Aert[1], A. De Backer[1], A. De wael[1], K. van den Bos[1], J. Gonnissen[1], G. T. Martinez[1]

[1]EMAT/University of Antwerp, Antwerp, Belgium

sandra.vanaert@uantwerpen.be

Quantitative annular dark field scanning transmission electron microscopy (ADF STEM) has become a powerful technique for nanoparticle atom-counting. Existing quantification methods treat ADF STEM images as numerical datasets from which unknown structure parameters are estimated by comparison with image simulations or by using parameter estimation based methods [1-4]. So-called scattering cross-sections are very sensitive for the number of atoms contained in an atomic column explaining its success in different applications [2-7]. However, when studying beam sensitive structures, the incoming electron dose needs to be optimised in order to balance sample damage and atom-counting precision. The questions are then how to retrieve most information from an ADF STEM image, how to optimise the experiment design, and how to derive the minimally required electron dose.

The cross-section approach quantifies the total intensity of scattered electrons atomic column by atomic column and has been shown to be robust to a wide range of imaging parameters including defocus, source size effects, and aberrations such as astigmatism [5]. Other performance measures include image intensities on a pixel by pixel basis and peak intensities. Comparison in terms of atom-counting precision suggests that scattering cross-sections perform equally well as image intensities and perform better than peak intensities [7]. A recent study answers the question why cross-sections are more sensitive to the number of atoms as compared to peak intensities. Figure 1 shows the increase of scattering cross-sections (left blue y-axis) and peak intensities (right green y-axis) as a function of the number of atoms for a Pt crystal viewed along the [110] zone axis. Whereas peak intensities saturate, cross-sections do not show this behaviour. This can be understood when analysing the electron wave function propagation through the crystal. Such analysis shows that when the electron probe is located at the core of an atomic column, the probe delocalises around 6 atoms. For off-column probe positions, the electrons get attracted to the core of the column at higher thicknesses. This explains why cross-sections, combining on- as well as off-column positions of the probe, capture atomic column information up to larger sample thicknesses as compared to peak intensities. In addition, a new electron channelling-based prediction model allows one to accurately predict cross-sections of mixed columns opening up possibilities to unscramble hetero-nanostructures in terms of number of atoms.

Theoretically computed error bars for the cross-sections are shown in Fig.1 for two different incident electron doses. For the highest electron dose, overlap of cross-sections for different numbers of atoms is absent allowing single-atom sensitivity. The use of a lower electron dose will inevitably result in counting errors. Such a computation thus allows one to predict the minimum electron dose needed in order to attain single-atom sensitivity for a given experimental setup. This minimum value can further be reduced when optimising the microscope settings. The principles of statistical detection theory allow one to quantify the probability of error for atom-counting [7]. Based on this expression, it can be shown that for very thin objects low angle ADF STEM is optimal and that for thicker objects the optimal inner angle increases as illustrated in Fig. 2.

In conclusion, the combination of the high sensitivity of scattering cross-sections and statistical experimental design in principle enables us to count atoms with single-atom sensitivity while keeping the electron dose low enough to study beam sensitive nanostructures. This will be illustrated using several experimental examples.

1. J M LeBeau et al., Nano Lett. 10 (2010), p. 4405.
2. S Van Aert et al., Nature 470 (2011), p. 374.
3. S Van Aert et al., Phys. Rev. B 87 (2013), p. 064107.
4. A De Backer et al., Ultramicroscopy 134 (2013), p. 23.
5. E et al., Ultramicroscopy 133 (2013), p. 109.
6. A De Backer et al., Ultramicroscopy 151 (2014), p. 56.
7. A De Backer et al., Ultramicroscopy 151 (2014), p. 46.

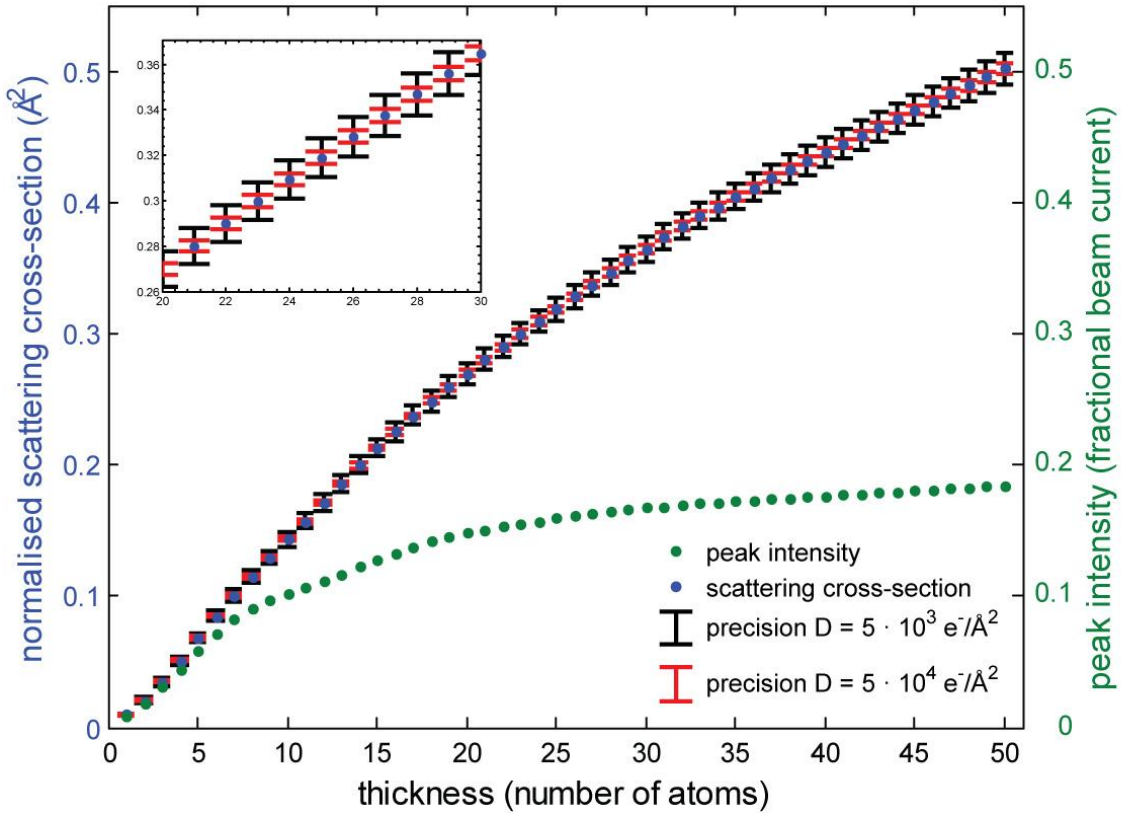

Figure 1. Scattering cross-sections (left blue axis) and peak intensity (right green axis) as a function of sample thickness for Pt in [110] zone axis. Theoretically predicted error bars are shown in black and red for two different incident electron doses.

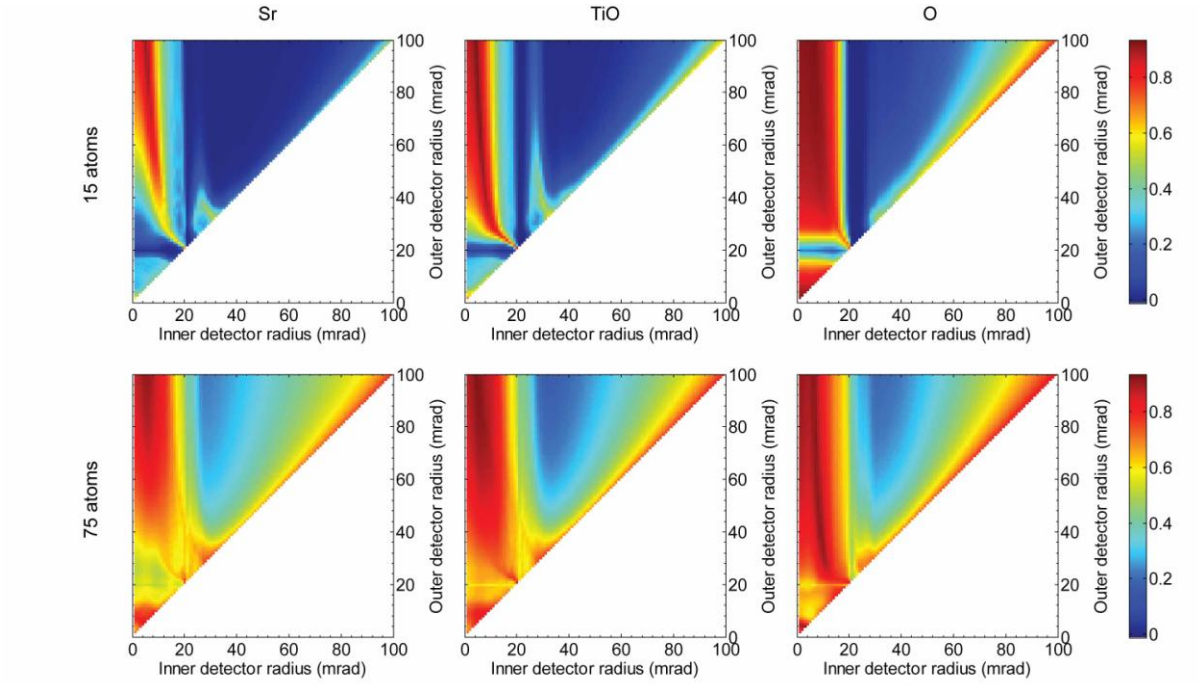

Figure 2. Probability of error as a function for inner and outer detector angle for the three different atomic columns in SrTiO3 for an electron dose of 105 electrons/Å2. The upper and lower rows show the results when the goal is to find the optimal setting when counting up to 15 and 75 atoms, respectively.

Quantitative Techniques and Image Simulation in TEM/STEM, SEM and Diffraction

IM2.043
Obtaining a high-precision match between simulation and experiment in HRTEM

J. Barthel[1], C.L. Jia[1], A. Thust[1]

[1]Ernst Ruska-Centre for Microscopy and Spectroscopy with Electrons, Forschungszentrum Jülich GmbH, Jülich, Germany

ju.barthel@fz-juelich.de

The introduction of aberration correction to high-resolution electron microscopy (HRTEM) almost two decades ago facilitated the access to atomic structure information in a revolutionary way and enabled numerous unprecedented materials science results [1]. By extending the usable regime of lateral resolution to one angstrom and below, HRTEM became sensitive enough to quantify details of the atomic structure such as lateral displacements, vacancy concentrations, or mixed site occupancies for elements with low and high atomic numbers, e.g. in Ref. [2].

Most of the works in this field rely on the capability of reproducing experimentally recorded images with images calculated numerically based on an assumed model of the object's atomic structure. In order to accurately deduce structural details from an HRTEM image on the atomic scale, a match between simulation and experiment should be achieved ideally on the same absolute intensity scale. This means that the images should show the same mean intensity, contrast, and pattern. The key to access the absolute intensity scale is the accurate knowledge about all parameters of the electron microscope which are relevant for the imaging process. This includes the calculation of the electron diffraction in the object, the transfer of the electron wave function from the object exit-plane to the image plane, and the registration of the image intensity distribution by the detector. Following this approach, the frequently reported huge mismatch of approximately a factor of 3 between simulation and experiment [3], also known as the 'Stobbs factor', is no longer found in recent experiments [4].

As an example a high-precision match of absolute image intensities for a thin MgO crystal is displayed in Fig. 1. The magnitude of the residual systematic discrepancy in this match is on the order of the statistical image noise. The available signal allows us to unambiguously count the number of atoms contained in one atomic column even for light elements such as magnesium and oxygen as demonstrated in Fig. 2. Furthermore, the location of an atomic column can be determined along the projected direction, which provides in combination with the atom counting the necessary information to reconstruct the three-dimensional shape of a nano-crystal from a single two-dimensional HRTEM image [5]. In this contribution we will describe the procedure used to achieve a high-precision match based on examples. We will also discuss several effects which could potentially contribute to small residual discrepancies such as thermal diffuse scattering, thermal magnetic field noise, and local variations of the sample tilt.

1. K.W. Urban, Science 321 (2008) p. 506.
2. C.-L. Jia et al., Microscopy and Microanalysis 19 (2013) p. 310.
3. M.J. Hÿtch and W.M. Stobbs, Ultramicroscopy 53 (1994) p. 191.
4. A. Thust, Physical Review Letters 102 (2009) 220801.
5. C.-L. Jia et al., Nature Materials 13 (2014) p. 1044.

Figure 1. High-precision match between an experimental image (a) and a simulated image (b) of a thin MgO crystal in [001] zone axis orientation. The images (a) and (b) have a contrast of about 0.109 and 0.105 relative to the vacuum mean level respectively. The residual difference image (c) exhibits very small systematic deviations and has a contrast of 0.022, which is comparable to the vacuum noise contrast of 0.013. All images are displayed using the same grey level scale denoted on the right with the vacuum mean level normalized to 1.

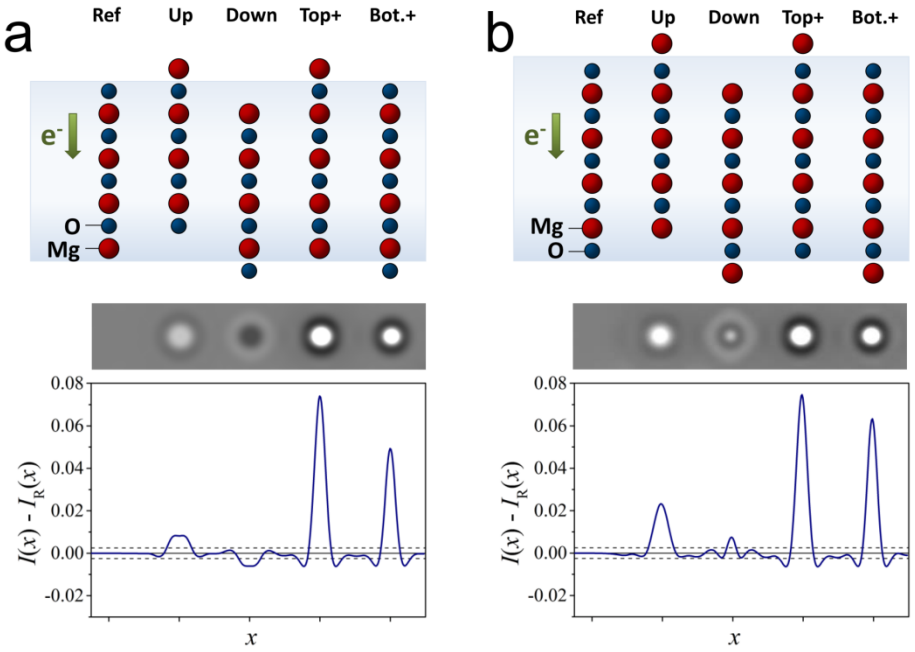

Figure 2. Simulation examples demonstrating the effect of elementary modifications in the atomic arrangement of individual [001] columns in an MgO crystal on the image intensity. The change of the image intensity distribution with respect to a reference column of (a) 8 atoms and (b) 9 atoms upon shifting the column by one atomic plane up or down, or by adding one atom to the top or to the bottom of the column is displayed in grey scale image stripes below. The plots at the bottom show horizontal line-scans through the difference images. The dashed lines in the plots indicate the uncertainty for measuring the peak height in an image due to noise.

.

Quantitative Techniques and Image Simulation in TEM/STEM, SEM and Diffraction

IM2.044
ISTEM : a novel incoherent imaging mode for ultra-high resolution beyond the classical information limit

F. F. Krause[1], A. Rosenauer[1], M. Schowalter[1], K. Müller-Caspary[1], T. Mehrtens[1]

[1]Universität Bremen, IFP, Bremen, Germany

f.krause@ifp.uni-bremen.de

It is well-known that TEM imaging with spatial incoherent illumination allows for an increased resolution and higher robustness towards chromatic aberrations compared to coherent illumination as used in conventional TEM (CTEM). This has been realised in scanning TEM (STEM) via reciprocity, which however suffers from other resolution-limiting factors such as scan noise or the finite extent of the electron source.

The ISTEM (Imaging STEM) method [Phys. Rev Lett. **113**, 096101(2014)] presented here constitutes a novel way for the realisation of incoherent imaging, which circumvents those problems. It combines STEM illumination with CTEM projection as illustrated in Fig. 1: A camera is used to acquire images formed by the focused electron probe scanning over the specimen. With the exposition chosen equal to the scan time, the resulting image corresponds to a sum over all probe positions. As different specimen positions are illuminated at different times, the corresponding intensities are summed up incoherently. ISTEM is therefore an incoherent imaging mode and benefits from the associated improvement of resolution.

The equivalence of the ISTEM illumination and CTEM with a largely extended and incoherent electron source can be rigorously shown within the mutual intensity formalism. From this, the gain of resolution can be intuitively understood in the limit of total incoherence, in which case the transfer is given by the autocorrelation of the coherent transfer function. The theoretical considerations also show that neither scan noise nor source size have any influence on ISTEM-images.

In simulative studies the capability of ISTEM to extend the point resolution beyond the diffraction limit, its robustness towards temporal incoherence and the resulting possibility to overcome the information limit are demonstrated. These calculations are confirmed by experimental ISTEM-micrographs of GaN in [11-20] and [1100] projection, as presented in Fig. 2, which are found in agreement with simulations. For the latter direction neighbouring Ga- and N-columns at a distance of only 63 pm are resolved despite an information limit of 83 pm of the image-corrected TITAN 80/300 G1 microscope used for the acquisition. The information limit is thereby clearly overcome by 24%.

A study comparing the results of strain-state analysis from simulated ISTEM images of a strained InGaAs-crystal with annular dark-field and bright-field STEM micrographs simulated for a probe-corrected microscope, promises a significant increase in precision for ISTEM compared to STEM, due to its immunity to scan noise and source size.

Thanks to the principle of reciprocity, ISTEM can be made equivalent to any STEM mode by appropriate choice of apertures, allowing the realisation of e.g. annular bright-field STEM, holding out the prospect of ultra-high resolution imaging of even lightest elements.

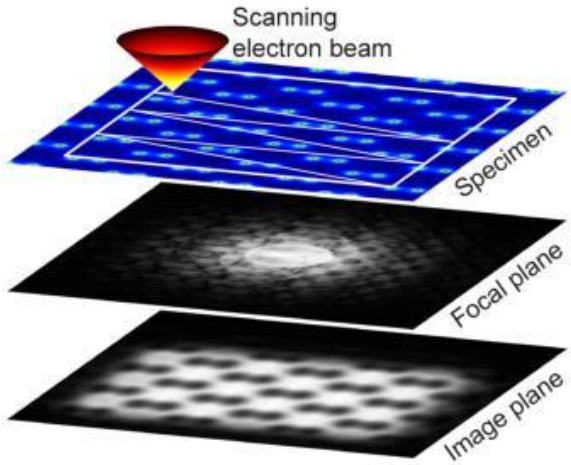

Figure 1. The principle of ISTEM: Incoherence is obtained by scanning the focussed probe over the specimen. The recording camera acquires one image per complete scan thereby summing up all images of individual probe positions.

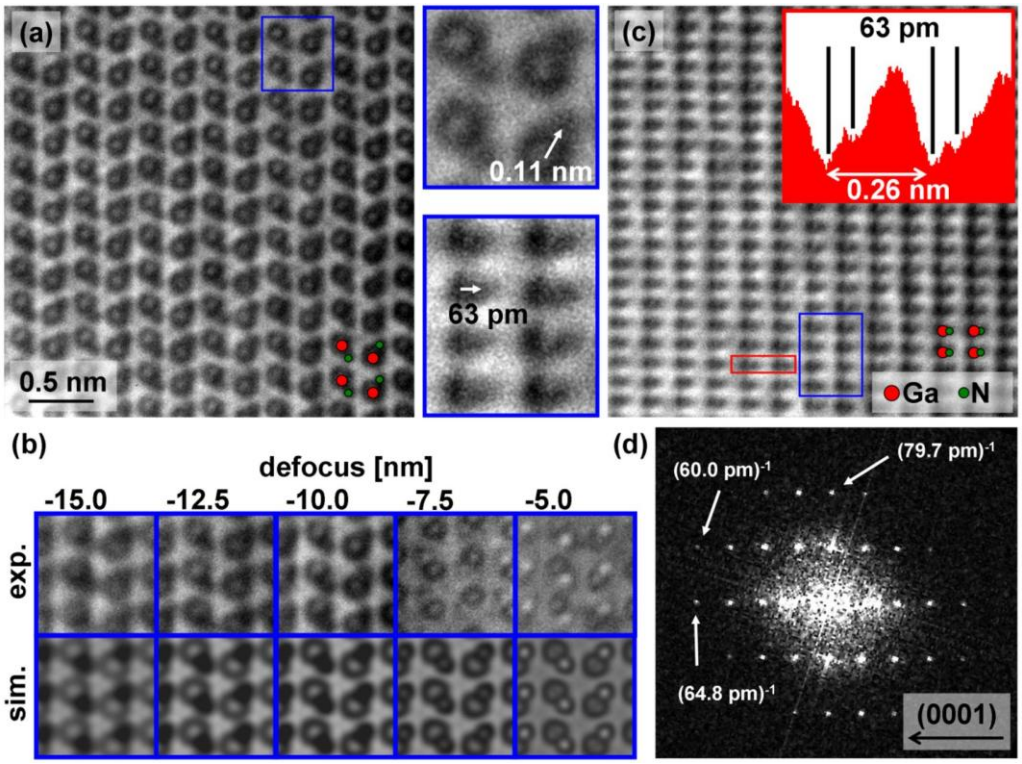

Figure 2. Experimental ISTEM-micrographs of GaN in [11-20] (a) and [1100] projection (c). The linescan was taken from the area framed red and clearly shows the resolved 63 pm dumbbells. (b) shows a comparison of an experimental and a simulated defocusseries for the [11-20] direction. The diffractogram (d) of the [1100] micrograph clearly extends to frequencies beyond the information limit of 83 pm.

Quantitative Techniques and Image Simulation in TEM/STEM, SEM and Diffraction

IM2.045
Retrieving depth-direction specimen variations in ferroelectric polarization and strain from TEM diffraction data using artificial neural network optimization

R. S. Pennington[1], C. T. Koch[1]

[1]Ulm University, Institute for Experimental Physics, Ulm, Germany

robert.pennington@uni-ulm.de

The current challenge for three-dimensional TEM characterization is retrieving specimen characteristics from along the beam direction.

We have developed an algorithm suitable for retrieving multiple different parameters from crystalline specimens, including strain and ferroelectric polarization, using artificial neural network many-parameter optimization [1] [2] [3]. Because our algorithm fully includes multiple scattering, it is ideal for thicker specimens; these calculations are feasible in part because our algorithm uses GPU computing hardware, providing substantial speedup [4]. Here, we focus on how both strain and ferroelectric polarization can be retrieved simultaneously using our algorithm on TEM diffraction data.

We use this example because convergent-beam electron diffraction (CBED) measurements of ferroelectric polarization in barium titanate by Tsuda et al. indicate a domain structure with a few-nanometer length scale; however, by using a thick specimen, each CBED pattern will map multiple domains [5]. Additionally, the unit cell can be in a tetragonal or cubic state, which influences the polarization states and can be modeled like strain [6]. Our algorithm is well-suited to retrieving simultaneously the ferroelectric polarization and strain in the specimen [1].

The results of applying our algorithm to simulated noisy CBED data are shown in Figures 1 and 2. This simulation modeled a 110 nm barium titanate specimen using 629 Bloch-wave reflections at 300 kV along a [100] zone axis, optimized assuming the 13 lowest-order reflections were measured and dividing the specimen into eleven 10 nm layers, with [111]-direction polarization and constant-volume tetragonal-to-cubic distortion as free parameters for each layer; 1681 pixels are used, as used in [1]. The initial specimen guess was unpolarized and reference-tetragonal [5]. Figure 1 shows the retrieved polarization values for all 11 layers; our algorithm retrieves the correct polarization values. Figure 2 shows the mean diffraction-intensity mismatch (for the 13 measured reflections) and the mean parameter error; our algorithm rapidly converges to the noise limit.

Our algorithm provides versatile three-dimensional characterization for crystalline specimens, as demonstrated by retrieving simultaneous strain and ferroelectric polarization for barium titanate.

1. R. S. Pennington and C. T. Koch, Ultramicroscopy 155, 42 (2015).
2. R. S. Pennington and C. T. Koch, Ultramicroscopy 148, 105 (2015).
3. R. S. Pennington, W. Van den Broek, and C. T. Koch, Phys. Rev. B 89, 205409 (2014).
4. R. S. Pennington, F. Wang, and C. T. Koch, Ultramicroscopy 141, 32 (2014).
5. K. Tsuda, A. Yasuhara, and M. Tanaka, Appl. Phys. Lett. 103, 082908 (2013).
6. K. Tsuda, R. Sano, and M. Tanaka, Phys. Rev. B 86, 214106 (2012).
7. The authors acknowledge funding from the Carl Zeiss Foundation and from the DFG (grant no. KO 2911/7-1).

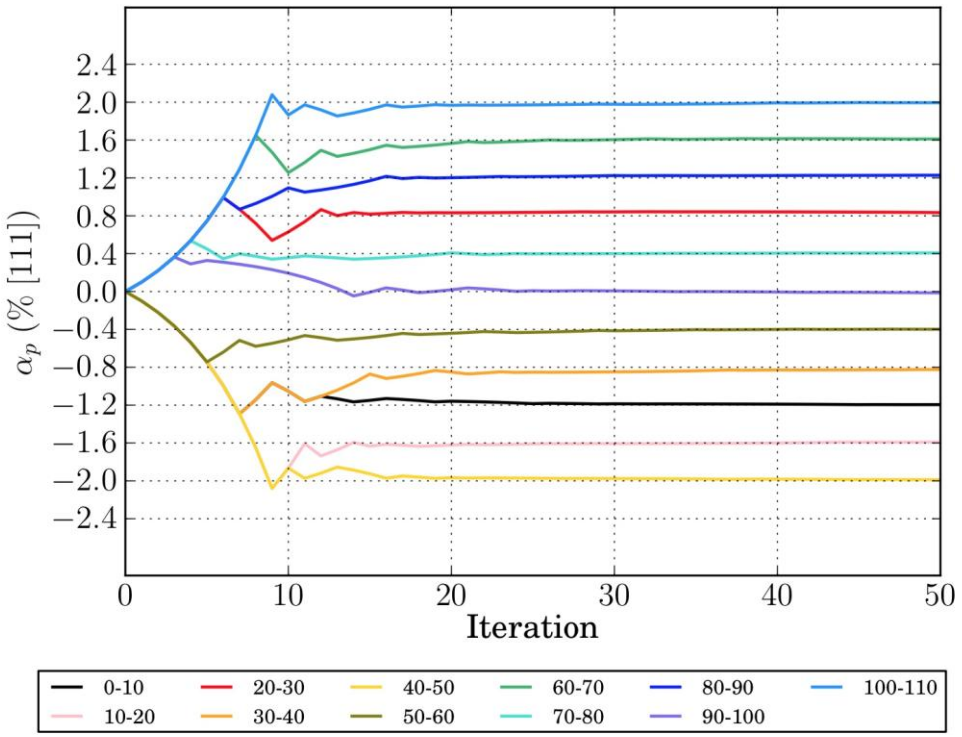

Figure 1. Polarization values retrieved for each layer in the simulated data; the true values of polarization are, due to a random sort, starting at the top surface (in percent of the unit-cell diagonal) [-1.2%, -1.6%, +0.8%, -0.8%, -2.0%, -0.4%, +1.6%, +0.4%, +1.2%, 0%, +2%].

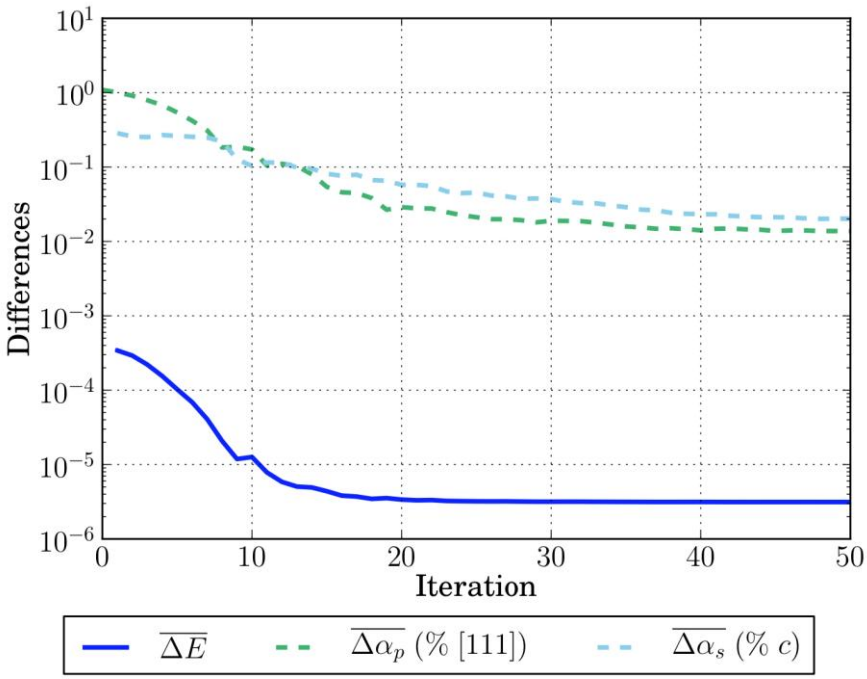

Figure 2. Mean intensity mismatch (black), and the mean parameter error for polarization (green) and strain (blue); true "strain" values are a reference tetragonal unit cell at the top and bottom surfaces [5], and a cubic unit cell in the middle, with equal intermediate steps between.

Quantitative Techniques and Image Simulation in TEM/STEM, SEM and Diffraction

IM2.046
Quantitative nano-beam electron diffraction: measuring strain and electric fields

T. Grieb[1], D. Carvalho[2], K. Müller-Caspary[1], M. Schowalter[1], C. Mahr[1], A. Beyer[3], A. Hyra[1], T. Ben[2], F. M. Morales[2], R. Garcia[2], K. Volz[3], B. Daudin[4], A. Rosenauer[1]

[1]University of Bremen, Institut für Festkörperphysik, Bremen, Germany
[2]University of Cadiz, Ciencia e Ingenieria de los Materiales, Cadiz, Spain
[3]Philipps University Marburg, Wissenschaftliches Zentrum für Materialwissenschaften, Marburg, Germany
[4]University Grenoble Alpes, Nanophysique et Semiconducteurs, Grenoble, France

grieb@ifp.uni-bremen.de

In epitaxially grown semiconductor-based devices, lattice strain and polarization fields influence growth and electronic performance. Strain can be introduced on purpose, e.g. to change the carrier transport in metal-oxide field-effect transistors (MOSFETs), or it is an unavoidable fact when growing e.g., a ternary material on a binary substrate. In polar materials, such as GaN, the growth of incorporated layers can be limited as polarization fields appear. For the proper design of such semiconductor structures, (quantitative) measurement of strain and electric fields on the nano scale is indispensable.

Lattice strain is often measured from HRTEM micrographs. This approach benefits from a high lateral resolution but has the obvious drawback of a small field-of-view. For measuring fields in TEM, electron holography is usually the method of choice [1]. This technique has the disadvantage that a phase shift from polarization fields can be overlain by other phase shifts, e.g., due to local changes in the chemical composition. In this contribution we show that nano-beam electron diffraction (NBED) can be used to measure both, strain and electric fields. To obtain the experimental results shown in the following, an FEI Titan 80/300 was operated at 300 kV in scanning TEM (STEM) mode.

For measuring strain only, the SANBED (strain-analysis by NBED [2]) method was used. Here, the electron beam is scanned over the specimen and for each scan point a diffraction pattern is recorded with a CCD camera (see Fig. 1a). A semi-convergence angle of 2.6 mrad was used to avoid an overlap of the Bragg discs. By using automatic routines, the disc positions are found in each diffraction pattern. From the relative change of the distance between the primary beam (000) and a second beam of choice (e.g. 004) over the scan, the relative change of the lattice parameter can be obtained. Fig. 1b shows the measured two-dimensional strain profile from scanning over a GaNAs layer along the [001] growth direction. The GaNAs layer is embedded in GaAs and has a nitrogen concentration of 1.1 %. The horizontal line shows the theoretical value of the strain (approx. 0.4 %), taking biaxial relaxation into account. Even for this low amount of strain, the profile reproduces the embedded GaNAs layer very accurately.

When scanning over an embedded AlGaN layer within polar AlN along [0001] growth direction, the primary-beam is shifted due to differences in the electric polarizations in AlN and AlGaN. From this shift the relative polarization field can be calculated if the specimen thickness is known. Fig. 2a shows the measured electric field from evaluating the shift of the primary beam when scanning over an AlGaN layer with a gallium concentration of 80% [3]. Additionally, the relative 0002-disc position was used to determine the strain. The strain profile is shown in Fig. 2b.

A clear drawback of this way of performing NBED is the need of non-overlapping discs, as the reduced convergence angle limits the spatial resolution in comparison to HRSTEM settings with semi-convergence angles of 9 mrad and more. We are tracking different ways of optimizing NBED [4]: In case of field measurements, recording the center-of-gravity (COG) of large STEM-diffraction patterns yields the momentum transferred to the STEM probe which can be related to the electric field [5]. In contrast to methods using a DPC detector (e.g. [6]), recording the COG is basically not affected by inhomogeneous disc illumination.

1. P.A. Midgley & R.E. Dunin-Borkowski, Nat. Mat. 8 (2009) 271.
2. K. Müller et al., Microsc. Microanal. 18 (2012) 995.
3. D. Carvalho et al., in preparation.
4. C. Mahr et al., submitted to Ultramicroscopy.

5. K. Müller et al., Nat. Comm. 5 (2014) 5653.
6. N. Shibata et al., Nat. Phys. 8 (2012) 611.

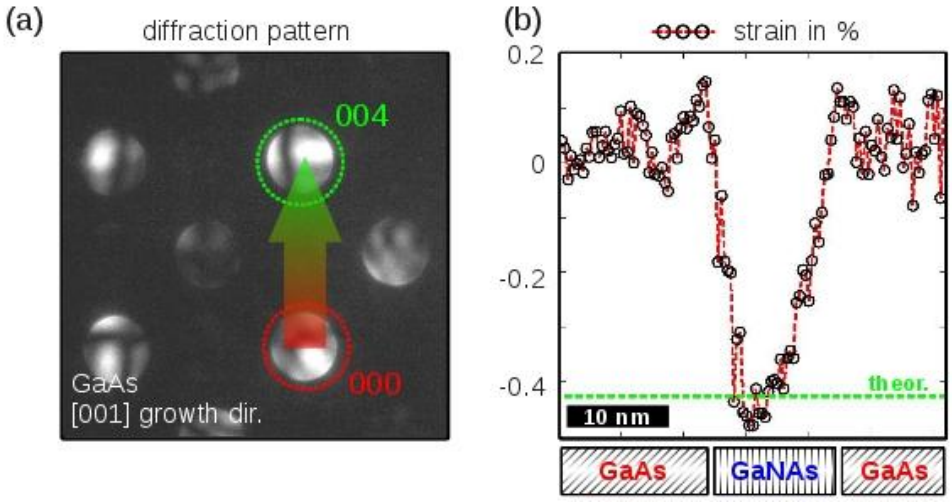

Figure 1. (a) Diffraction pattern for one scan point in SANBED. (b) Measured strain of a GaNAs layer in GaAs using the SANBED method.

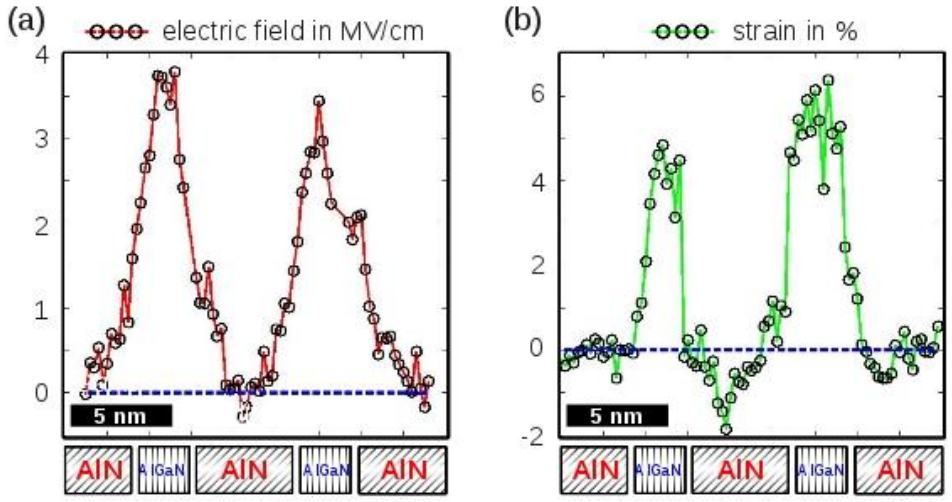

Figure 2. NBED investigation of an AlGaN layers in AlN. (a) Electric field from tracking the 000 disc and (b) strain from the distance between 0000 and 0002 disc.

Quantitative Techniques and Image Simulation in TEM/STEM, SEM and Diffraction

IM2.047
Diagonalization of the mixed dynamic form factor and its significance for the image calculation involving inelastic scattering

Z. Lee[1], R. Hambach[1,2], U. Kaiser[1], H. Rose[1]

[1]Universität Ulm, Ulm, Germany
[2]Friedrich-Schiller-Universität, Jena, Germany

zhongbo.lee@uni-ulm.de

The multislice algorithm, which is applied for HRTEM image calculation considering elastic scattering, has been extended to the image calculation considering inelastic scattering [1]. A simultaneous elastic- inelastic scattering event is modeled by the product of the incoming mutual coherent function (MCF) and the response of the sample, denoted by the mixed dynamic object transparency (MDOT). Both functions depend on 4D spatial coordinates. Therefore, a number of 4D Fourier transforms are required when propagating the MCF using multislice algorithm. In the case of a thick sample, the computation of 4D Fourier transforms can be very time-consuming. The MDOT is a variable is real space, and can be calculated by using 4D Fourier transform from a variable depending on the mixed dynamic form factor (MDFF), which is defined in reciprocal space [2].

In this work, we illustrate that by utilizing the method of matrix diagonalization, one can find a proper basis to represent the MDFF $S(\mathbf{q},\mathbf{q}',\Delta E)$ as well as the key element $S(\mathbf{q},\mathbf{q}',\Delta E)/(\mathbf{q}^2+\mathbf{q}_E^2)(\mathbf{q}'^2+\mathbf{q}_E^2)$ [2] required for image calculation involving inelastic scattering. With this method, not only a four-dimensional problem can be reduced to two-dimensional, but also the number of two-dimensional problems is minimized. For calculating low-voltage (20kV) HRTEM images of crystals, inelastic scattering needs to be involved [3]. One needs only one eigenvector for the approximation of the key element relating to the MDFF in the case. This can be a great advantage when one incorporates inelastic scattering into a multislice algorithm. A single inelastic scattering event results in a number of 4D mutual coherence functions, and instead of performing many 4D Fourier transforms, one only needs to perform the same number of 2D Fourier transforms. In the case of multiple inelastic scatterings, the number of generated mutual coherence functions increases exponentially, which indicates that the number of 4D Fourier transforms can be overloaded for the computer. Thus, the efficiency improvement through the 2D Fourier transforms allows us to study more complicated scattering problems.

1. H. Müller, H. Rose, and P. Schorsch, *Journal of Microscopy* **190**: 73-88 (1998).
2. H. Rose, *Optik* **45**:139-158 (1976).
3. Z. Lee, H. Rose, R. Hambach, P. Wachsmuth, U. Kaiser, *Ultramicroscopy* **134**: 102-1112 (2013).

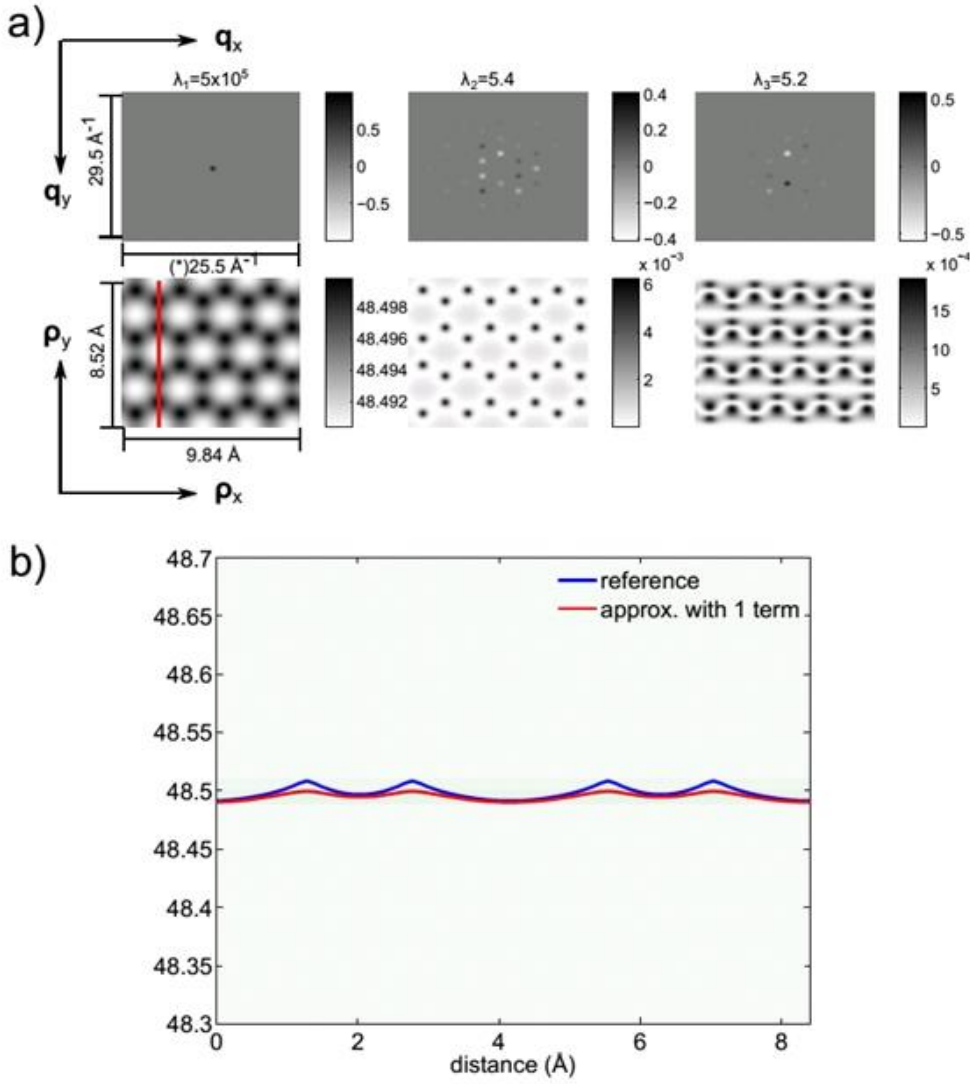

Figure 1. a)1st row: Real parts of the first three eigenvectors of the matrix $S(\mathbf{q},\mathbf{q}',\Delta E)/(\mathbf{q}^2+\mathbf{q}_E^2)(\mathbf{q}'^2+\mathbf{q}_E^2)$ for graphene assuming an energy loss of 10eV and an energy of 20keV for the incident electron. The corresponding eigenvalues are listed above each eigenvector. 2nd row: the images show the first three components of the MCF. b)The diagonal elements of the for graphene calculated with two methods - 4D Fourier transform without any approximation (blue curve) and 2D Fourier transform of one eigenvector corresponding to the largest eigenvalue obtained from matrix diagonalization (red curve). The difference between the two curves is negligible. However, the computational efficiency for the red curve is more than 1000 times of that for the blue curve.

Quantitative Techniques and Image Simulation in TEM/STEM, SEM and Diffraction

IM2.P048
Cation distribution in doped $(Ba_{0.5}Sr_{0.5})(Co_{0.8}Fe_{0.2})O_{3-d}$ ceramics using channeling enhanced micoanalysis

M. Meffert[1], H. Störmer[1], D. Gerthsen[1]

[1]Karlsruhe Institute of Technology (KIT), Laboratory for Electron Microscopy (LEM), Karlsruhe, Germany

matthias.meffert@kit.edu

Atom location by channeling enhanced microanalysis (ALCHEMI) as proposed by Taftø and Spence has been widely used for determining lattice sites of impurity atoms in various host crystals [1]. By comparing X-ray emission intensities for different specimen orientations of dopant and host elements with known lattice position, it is even possible to get quantitative results. However, the so-called ratio technique is susceptible to errors due to delocalization effects especially for weakly bound electrons. Over the years many improvements in terms of correction factors have been made in order to account for this issue [2]. Recently, it also has become possible to accurately calculate the orientation dependent inelastic scattering crosssection and compare these simulations with measured X-ray intensities to further boost reliability [3, 4].

Mixed ionic and electronic conducting perovskites like $(Ba_{0.5}Sr_{0.5})(Co_{0.8}Fe_{0.2})O_{3-d}$ (BSCF) are considered as promising materials for oxygen separation membranes. Yet, the inherent long-time instability of the cubic perovskite phase poses a major obstacle regarding general application. Decomposition of the cubic phase into various secondary phases at low temperatures (T < 840 °C) was attributed to the easily oxidizable B-site cation Co which changes its oxidation state according to the oxygen stoichiometry [5-8]. To inhibit valence changes B-site doping with monovalent transition metals was investigated with favorable effect especially for Y [9]. Even though B-site substitution is targeted Y may also be incorporated on the A-site of the cubic perovskite lattice.

Therefore the occupancy of Y and Sc B-site doped BSCF was studied by applying a refined ALCHEMI technique where simulated inelastic cross-sections were compared with measured X-ray intensities for different electron incident angles. For the measurement a FEI Osiris microscope with ChemiSTEM capabilities and a FEI Titan was utilized. To eliminate microscopic dependent parameters cross-section ratios were used instead of raw peak heights. Profiles were normalized to non-channeling intensities where no reflections are strongly excited. Good A-site channeling was observed for electrons propagating parallel to {111} planes. The projected atomic positions for a [112] zone axis is shown in Figure 1a where the {111} planes are highlighted by dashed lines.

Since Fe and Sr are exclusively located on the B-/A-site, this ratio shows a pronounced variation if the sample orientation is changed. Simulated profiles of the inelastic cross-section ratio of σ_{Sr}/σ_{Fe} for different sample thicknesses is given in Figure 1b as a function of the scattering vector. Since the channeling intensity strongly depends on the sample thickness, CBED was used to determine local sample thickness. As depicted in Figure 2a the variation σ_{Sr}/σ_{Y} in 10 at% Y doped BSCF is less pronounced compared to σ_{Sr}/σ_{Fe} indicating a non-exclusive B-site occupation for Y. The best match between simulation and experiment was achieved for 75 % B-site and 25 % A-site occupation (cf. Figure 2a). For lower dopant concentrations (1 - 3 at%) a higher percentage of up to 55 % was measured for A-site occupation.

In 3 at% Sc-doped BSCF, the Sc-K emission line is superimposed by the Ba-Ll line, which makes deconvolution essential. Deconvolution was done by subtracting a reference spectrum of undoped BSCF from the measured data. The best fit of the deconvoluted data set was achieved for exclusive B-site occupation (cf. Figure 2b).

The tendency for Y to occupy the A-site can be attributed to the comparatively large ionic radius. The ionic radius of Y is quite large (90 pm) compared to Fe and Co (54 - 74.5 pm depending on oxidation and spin-state) which makes A-site occupation possible whereas the ionic radius of Sc (74.5 pm) is close to that of Co and Fe.

1. J. Taftø and J. Spence, Science **218** (1982) p. 49
2. S. J. Pennycook, Ultramicroscopy **26** (1988) p. 239
3. W. Nüchter and W. Sigle, Philos. Mag. A **71** (1995) p. 165
4. M. P. Oxley and L. J. Allen, J. Appl. Crystallogr 36 (2003) p. 940
5. S. Švarcová et al., Solid State Ionics **178** (2008) p. 1787
6. M. Arnold et al., Chem. Mater. **21** (2009) p. 635
7. C. Niedrig et al., Solid State Ionics **197** (2011) p. 25
8. P. Müller et al., Chem. Mater. **25** (2013) p. 564
9. P. Haworth et al., Sep. Purif. Technol. **81** (2011) p. 88
10. We acknowledge funding by the Deutsche Forschungsgemeinschaft.

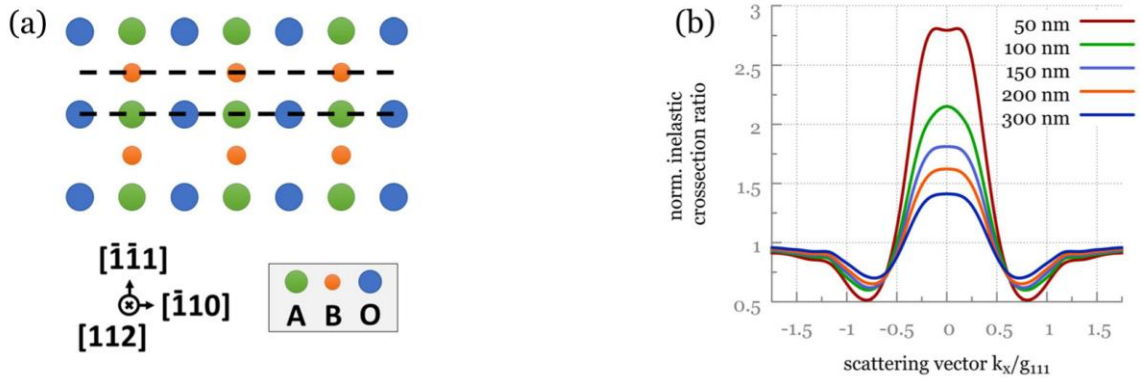

Figure 1. (a) Projected BSCF crystal structure along the [112] zone axis. The {111} planes used in this channeling experiment are highlighted by black dashed lines. (b) Simulated channeling profiles of σ_{Sr}/σ_{Fe} inelastic cross-section ratios as a function of the scattering vector for sample thicknesses between 50 and 300 nm and 300 keV electron energy.

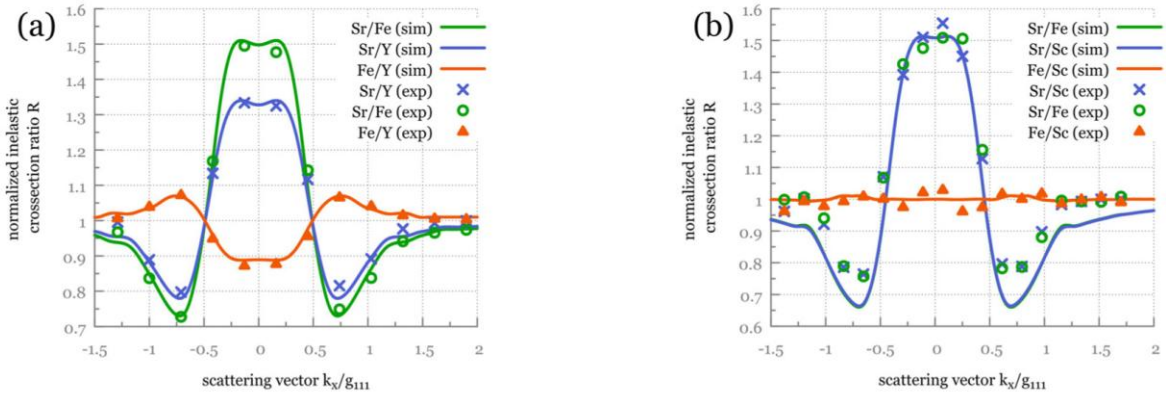

Figure 2. (a) Simulated (sim) channeling profiles for 10 at% Y-doped BSCF with 75% B-site occupancy and experimental (exp) data. (b) Channeling profiles for 3 at% Sc-doped BSCF with 100 % B-site occupancy.

Quantitative Techniques and Image Simulation in TEM/STEM, SEM and Diffraction

IM2.P049
Temperature dependence of HAADF-intensity: influence of disorder

T. Mehrtens[1], M. Schowalter[1], J. Borchardt[1], M. Grimme[1], K. Müller-Caspary[1], L. Hoffmann[2], H. Jönen[2], U. Rossow[2], A. Hangleiter[2], A. Rosenauer[1]

[1]Universität Bremen, Institut für Festkörperphysik, Bremen, Germany
[2]TU Braunschweig, Institut für Angewandte Physik, Braunschweig, Germany

mehrtens@ifp.uni-bremen.de

In the last decade, high-angle annular dark field-scanning transmission electron microscopy (HAADF-STEM) has gained more and more attention as it has some major benefits compared to conventional TEM. It provides a chemical sensitive image contrast that is easy to interpret and allows quantification of specimen thickness and composition [1]. The main contribution to the image intensity in HAADF-STEM is caused by thermal diffuse scattering (TDS) and Huang-scattering due to static atomic displacements (SAD) [2].

Compared to a perfect crystal, both effects (TDS and SAD) induce an amount of disorder into the system that allows scattering into higher angles and to angles that do not coincide with reciprocal lattice vectors.

In this contribution we have studied the influence of disorder on the temperature dependence of the HAADF-intensity. To this end, amorphous silicon and a crystalline GaN/InGaN heterostructure were analyzed for specimen temperatures varying between 77K and 623K.

For the amorphous Si sample no significant change of the HAADF-intensity was found (Fig. 1), while for the GaN/InGaN sample an increase of intensity has been observed for increasing specimen temperature (Fig. 2). Comparing InGaN and GaN it was found that the pure binary GaN is more affected by temperature as the ternary InGaN. Thus, the chemical contrast between GaN and InGaN is a function of temperature. Additionally, frozen phonon simulations were performed with the STEMsim program [3]. These simulations showed the same temperature dependence as found experimentally.

The different behavior of the three materials can be explained as follows. In wurtzite GaN each of the metal- and non-metal sublattices is occupied by only one atomic species (Ga or N). Due to the small atomic vibrations at low temperatures the amount of diffuse scattering to high angles is low as Ga and N atoms are close to their equilibrium crystal positions. Increasing specimen temperature leads to increasing atomic vibrations. Thus, atoms are more displaced from their equilibrium positions and diffuse scattering arises.

In InGaN indium and gallium share the metal sublattice. Due to their different covalent radii local strain fields are induced that result in a static disorder within the crystal. This static disorder is also present at low temperatures and thermal disorder contributes less to the total disorder. Therefore, the HAADF-intensity of InGaN is less affected by the specimen temperature.

For amorphous silicon, structural disorder is so high that increasing the specimen temperature has no influence on the amount of electrons scattered into higher angles.

1. Rosenauer et al., Ultramicroscopy **109**, 1171-1182 (2009)
2. Grillo et al., Physical Review B **77**, 054103 (2008)
3. Rosenauer and Schowalter, Springer Netherlands (2008)

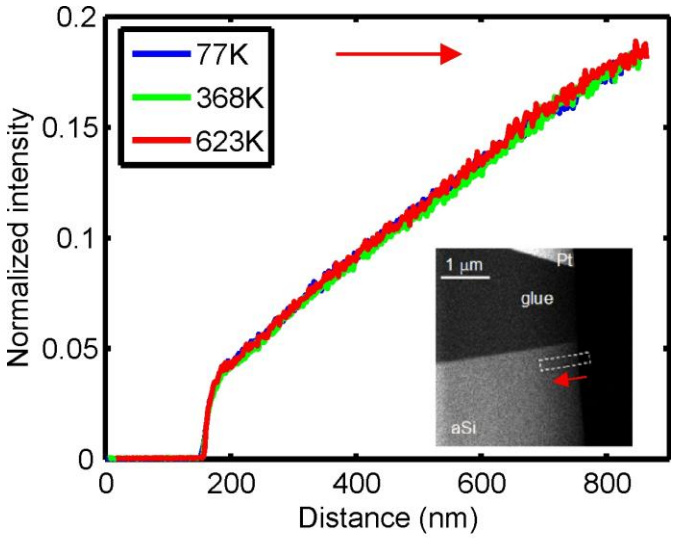

Figure 1. HAADF-STEM intensity profile of an amorphous silicon sample for different specimen temperatures. All linescans were performed at the same region indicated by the dashed rectangle in the inset. No significant change has been observed.

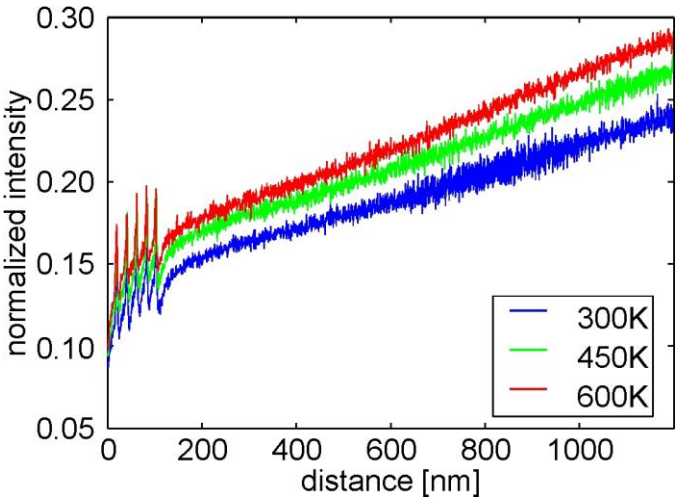

Figure 2. Intensity profile of a crystalline GaN/InGaN heterostructure. A well pronounced increase of the intensity is visible for higher temperatures.

Quantitative Techniques and Image Simulation in TEM/STEM, SEM and Diffraction

IM2.P050
Backscattered-electron SEM contrast of SiO_2 nanoparticles

T. Kowoll[1], E. Müller[1], D. Gerthsen[1]

[1]Karlsruher Institut für Technologie, Laboratorium für Elektronenmikroskopie, Karlsruhe, Germany

thomas.kowoll@kit.edu

Scanning electron microscopy (SEM) is frequently used for the characterization of nanoparticles (NPs) and imaging with backscattered electrons (BSE) is particularly interesting to reveal sample regions with different atomic number. However, the contrast of samples with complex geometries compared to flat bulk samples cannot be quantitatively described by common theoretical models [1] because they are not well suited for describing the scattering processes. In this work we will show that the BSE SEM contrast of SiO_2 NPs strongly depends on the atomic number Z of the substrate material and imaging parameters like the primary electron (PE) energy E_0 and working distance WD.

For this purpose SiO_2 NPs (Z = 10) with diameters from 50 nm to 110 nm were deposited on two different substrates. The first substrate is interesting for correlative SEM and light microscopy imaging and consists of glass slides coated by electrically conductive indium-tin-oxide (ITO) (Z = 24.25) with 180 nm thickness [2]. The second substrate type consists of amorphous (glassy) carbon (Z = 6), which is covered by only 20 nm ITO. A FEI Quanta 650 FEG equipped with a semiconductor BSE detector was used. To optimize the NP contrast, E_0 between 3 and 17 keV and WDs between 4 and 12 mm were tested. Monte Carlo (MC) simulations were performed with the Casino program [3] employing Mott cross-sections for comparison with the measured data. The baseline intensity I_{zero} was recorded with blanked electron beam. NP contrast was calculated by , where I_{NP} is the NP intensity and I_{BR} the substrate intensity. Fig. 1a,b show 5 keV BSE SEM images of SiO_2 NPs on the 180 nm ITO/glass substrate taken at WDs of 10 mm (Fig. 1a) and 4 mm (Fig. 1b). Although the same object is imaged, contrast inversion of SiO_2 NPs is observed. Fig. 1c shows a 5 keV BSE SEM image (WD = 10 mm) of SiO_2 NPs on 20 nm ITO/carbon substrate where NP contrast inversion is observed compared to the 180 nm ITO/glass substrate (Fig. 1a). The images in Fig. 1 indicate that simple interpretation of BSE SEM images in terms of the local Z value is not adequate for complex sample geometries.

NP contrast reversal was studied in detail by varying E_0 for WD = 10 mm. Fig. 2a presents measured and calculated C values. Contrast reversal occurs at ~4 keV for SiO_2 NPs on 20 nm ITO/carbon and at ~10 keV for NPs on 180 nm ITO/glass with in general low contrast at larger E_0 for this substrate. With the high electrical conductivity of the carbon substrate, the ITO thickness and its scattering contribution can be minimized allowing improved C at higher E_0 compared to the 180 nm ITO/glass substrate. The NP contrast for the latter substrate is close to zero for E_0 > 7 keV due to an overwhelming BSE contribution from ITO. Converging C values for low E_0 indicate a) that the PEs will not even penetrate through 20 nm ITO anymore and b) that contrast inversion is related to the ITO thickness. Fig. 2b shows NP contrast as a function of WD for E_0 = 5 keV. While the NP contrast for the 20 nm ITO/carbon substrate approaches zero with increasing WD, there is a contrast inversion for the 180 nm ITO/glass substrate at WD » 6 mm. We attribute this inversion to angular anisotropic BSE scattering, whereby the scattering angle range of collected BSEs is controlled by the WD. MC-simulations in general describe the NP contrast well.

Two unexpected effects were observed for BSE SEM contrast of SiO_2 NP on different substrates: a strong dependency on the substrate material, i.e. its atomic number, and a “geometrical” contrast inversion which can be controlled by the WD. Optimum NP contrast is obtained for small E_0 and WD values.

1. H. Niedrig, J. Appl. Phys., 53 (1982), pp. R15.
2. H. Pluk, et al., J. Microsc, 233 (2009), pp. 353-363.
3. P. Hovington, et al., Scanning, 19 (1997), pp. 1-14.

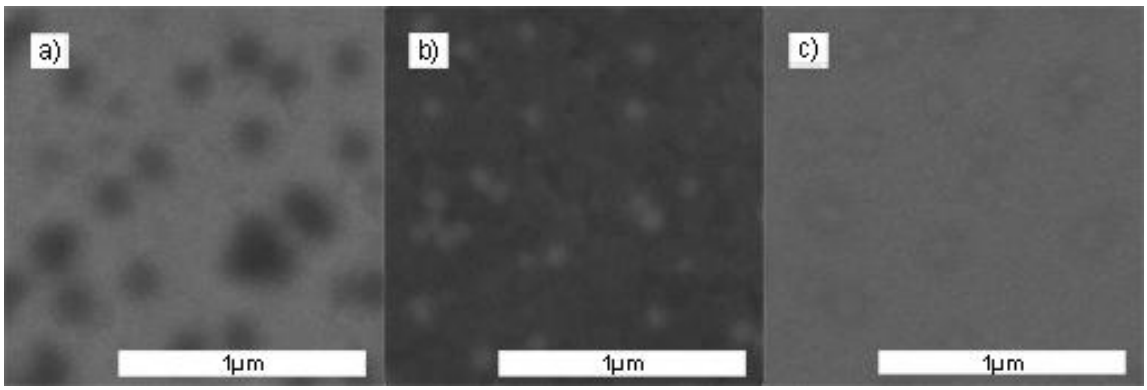

Figure 1. 5 keV BSE SEM images of SiO_2 NPs on a) 180 nm ITO/glass with WD = 10 mm, b) WD = 4 mm and c) on 20 nm ITO/carbon with WD = 10 mm.

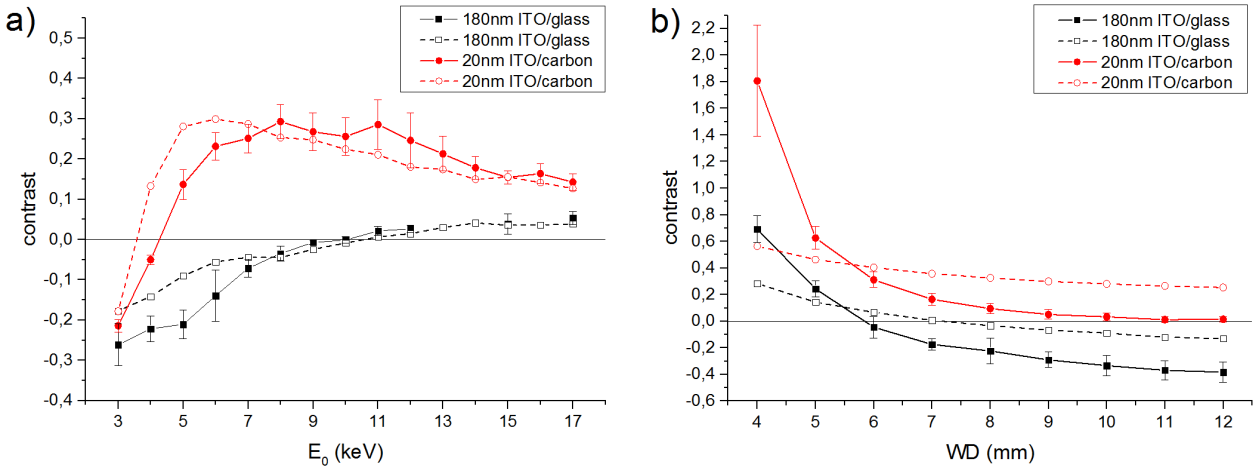

Figure 2. Measured (solid symbols) and simulated (empty symbols) contrast of SiO_2 NPs from BSE SEM images as a function of a) E_0 (WD = 10 mm) and b) WD (E_0 = 5 keV) on two different substrates (lines guide to the eye).

Quantitative Techniques and Image Simulation in TEM/STEM, SEM and Diffraction

IM2.P051
Quantification of sample thickness by low-energy scanning transmission electron microscopy

M. Hugenschmidt[1], E. Müller[1], D. Gerthsen[1]

[1]Karlsruhe Institute of Technology, Laboratory for Electron Microscopy, Karlsruhe, Germany

milena.hugenschmidt@student.kit.edu

For the quantification of information from electron microscopy images, it is often required to precisely know the local sample thickness *t*. Several techniques for the determination of *t* are already established. More recently, high-angle annular dark-field (HAADF) scanning transmission electron microscopy (STEM) at low primary electron energies ($E_0 \leq 30$ keV) came up as a promising technique [1-2]. It is based on the comparison of measured intensities of HAADF-STEM images with Monte Carlo (MC) simulations and can be applied to samples with known composition. However,the most suitable scattering cross-section (CS) to be used in the simulation must be determinedfor accurate sample thickness determination.

Wedge-shaped samples with a known thickness profile fabricated by focused-ion-beam (FIB) milling were used. STEM measurements were performed with aFEI DualBeam Strata 400S equipped with a semiconductor STEM-detector.

In this work we have analyzed electron CSs to be used in the simulations for HAADF STEM at E_0 between 10 keV and 30 keV on different sample (MgO Z=10, Ge Z=32 and Pd Z=46). The measured HAADF STEM intensities I_s were normalized with respect to the intensity of the incident electron beam I_{white} and the black level I_{black} according to

$I_{nor} = (I_s - I_{black})/(I_{white} - I_{black})$.

HAADF-STEM intensities simulated by the CASINO software [3] were normalized with respect to the number of simulated primary electrons. MC-simulations were performed by considering the screened Rutherford CS (SR-CS) and different Mott CSs (M-CS) implemented in the code.

Fig. 1a shows aHAADF STEM image of the STEM-detector, used for the determination of I_{white} and I_{black}. The innermost part of the HAADF-detector is bright, while the view on the much larger HAADF-segment is restricted by the polepiece. Fig. 1b shows a cross-section HAADF STEM image of a wedge-shaped MgO sample. The thickness of the sample increases from left to right. The arrow indicates an intensity line profile which is compared with simulated intensities.

Fig. 2 contains measured and simulated intensity line profiles of the normalized HAADF STEM intensity as a function of *t*. Simulated intensities on the basis of SR-CS and only two of the M-CS (by Interpolation and by Equation (Drouin and Gauvin) [4]) which fit best to the measurement are plotted. The maximum of I_{nor} shifts to lower *t* for lower E_0 and higher *Z.* Measured I_{nor} values are generally lower than simulated one due to uncertainties concerning I_{white} and the response of the detector. The best fit between experiment and simulations was determined by comparing the maxima positions of I_{nor}. For light materials (MgO) and high primary electron energies (30 keV), the M-CS is the best choice, for all other investigated E_0 and *Z,* the SR-CS better describes the measured data.

Adequate choice of CSs for MC-simulations facilitatesthickness determination for samples with known composition by comparison of experimental and simulated HAADF STEM intensities.However, further work is necessary to clarify the lower measured intensities in comparison with simulations [5].

1. P.G. Merli et al., *Ultramicrosc.*94 (2003), p. 89.
2. T. Volkenandt et al., *Microsc. Microanal.* 16 (2010), p. 604.
3. H. Demers et al., *Scanning* 33 (2011), p.135.
4. D. Drouin et al., *Scanning* 19 (1997), p. 20.
5. We acknowledge financing of the project by the German Research Foundation [DFG].

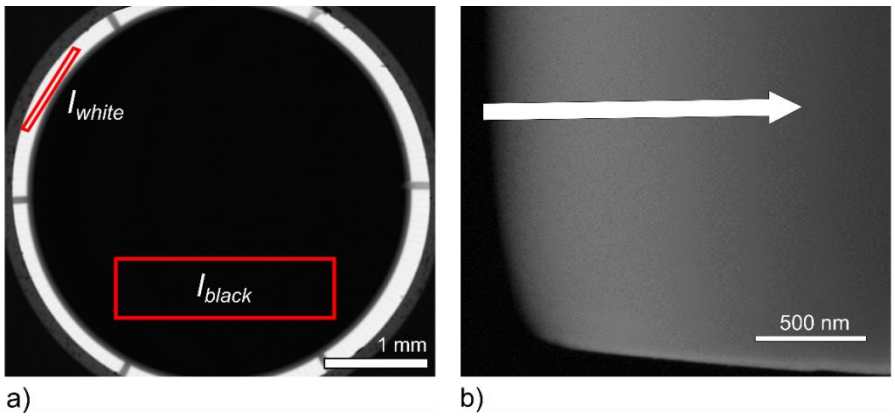

Figure 1. a) HAADF STEM image of STEM-detector. Marked areas illustrate I_{white} and I_{black} used for normalization of the measured HAADF STEM intensities. b) Cross-section HAADF STEM image of the MgO sample at 20 keV with indicated position of the line scan.

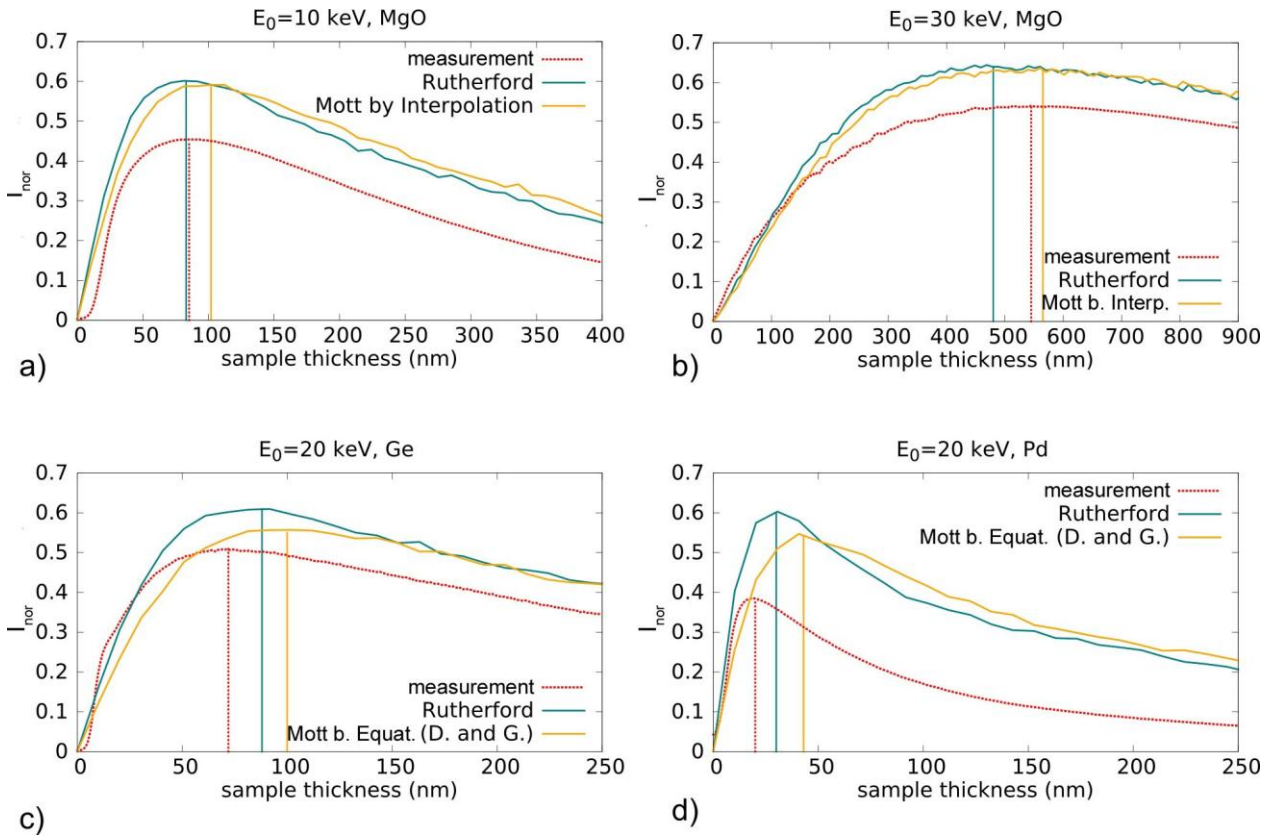

Figure 2. Simulated (SR-CS and most suitable M-CS) and measured I_{nor} for samples with different Z and E_0 with maxima indicated by lines. a) MgO, E_0 = 10keV, b) MgO, E_0 = 30keV, c) Ge, E_0 = 20keV, d) Pd, E_0 = 20keV.

Quantitative Techniques and Image Simulation in TEM/STEM, SEM and Diffraction

IM2.P052
Quantitative field measurements using differential phase contrast microscopy

J. Zweck[1], F. Schwarzhuber[1], J. Wild[1], V. Galioit[1], R. Schregle[1], M. Lohr[1]

[1]University of Regensburg, Physics, Regensburg, Germany

josef.zweck@ur.de

Differential phase contrast imaging is a STEM technique which uses an annular four-quadrant detector instead of the commonly used annular dark field detector to monitor minute deflections of the diffraction disk which are caused by electric and/or magnetic fields. If these fields are sufficiently homogeneuous, they cause a deflection of the evenly illuminated diffraction disk. From a simple deflection measurement of the beam disk it is possible to derive the strength of the local field, probed by the beam, if the specimen thickness is known.

For a quantitative treatment, it is first important to understand the range of linearity for the detector setup given. We derive this relation precisely, using a simple geometrical argumentation.

As usual in position sensitive detectors, if no deflection is present, the opposing sectors of the detector are illuminated evenly, their difference signal is zero (apart from noise contributions). If the diffraction disk is then shifted by a tiny amount, one sector receives less electrons, while the other one receives more. The minimum detectable deflection depends on the signal noise for the given situation. A computation (see fig.1) for a beam current density of 80 $\mu A/m^2$ and various dwell times shows that beam displacements down to 0.1 µm are measurable with a semiconductor detector. The standard deviations are indicated by dashed (1 sigma) and dotted (3 sigma) lines.

Finally, we report on a direct calibration of the beam deflection by using a specialized specimen holder (fig. 2). We implement a small condensor for electrostatic beam deflection. Figure 2 shows a fully assembled holder tip (a), an explosion view (b) and a photograph of the holder, showing the dimensions of the condensor used (c). The beam shift correlates linearly with the applied electric field as expected.

It is important to note that a measurement may not only measure the signal falling onto the detectors, as this signal may vary, if the beam intensity fluctuates with position, i.e. when the specimen's thickness varies or if locally a diffraction condition is met. To avoid misinterpretations, the measured signal has to be normalized with the total signal falling onto the detectors.

The talk will give quantitative figures for the least measurable deflection of the electron beam as a function of microscope parameters, which allows the experimenter to choose the parameters according to what he wants to measure. It will be shown that for usual specimen thicknesses of 50 nm electric field gradients in the range of 10 mV/nm are accessible, as well as intrinsic magnetic fields in the range of 50 mT.

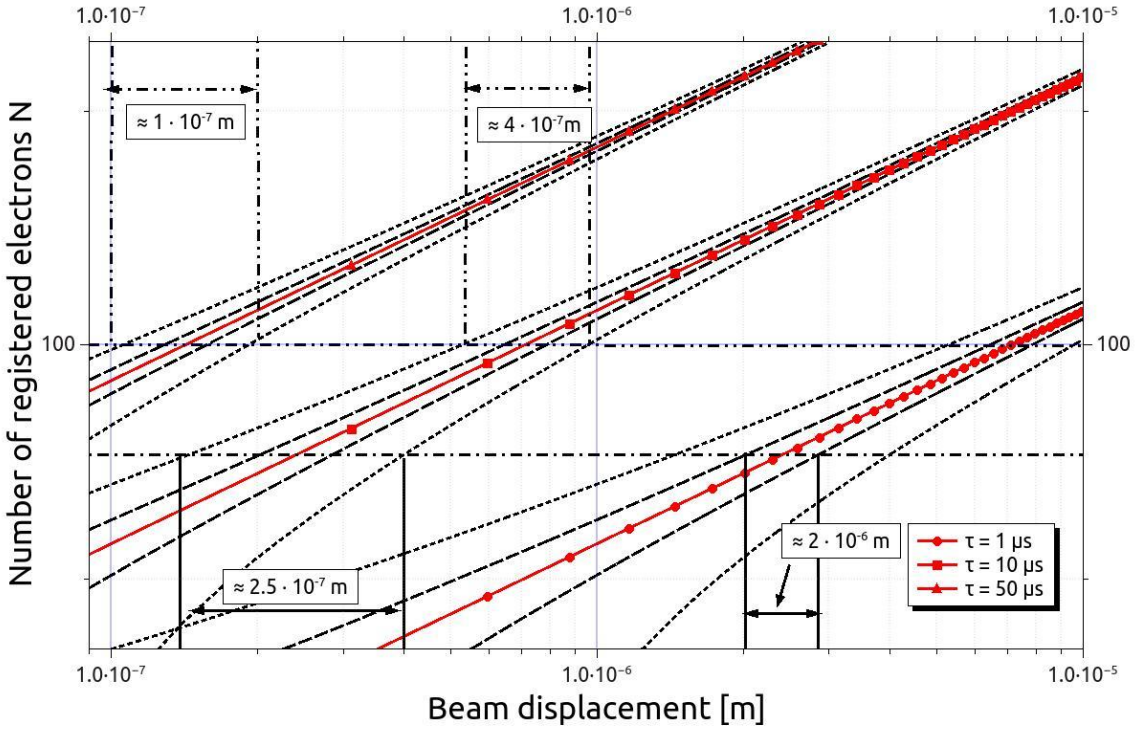
1.0·10⁻⁷
1.0·10⁻⁶
1.0·10⁻⁵
≈ 1 · 10⁻⁷ m
≈ 4 · 10⁻⁷m
100
100
≈ 2.5 · 10⁻⁷ m
≈ 2 · 10⁻⁶ m
τ = 1 µs
τ = 10 µs
τ = 50 µs
Number of registered electrons N
Beam displacement [m]

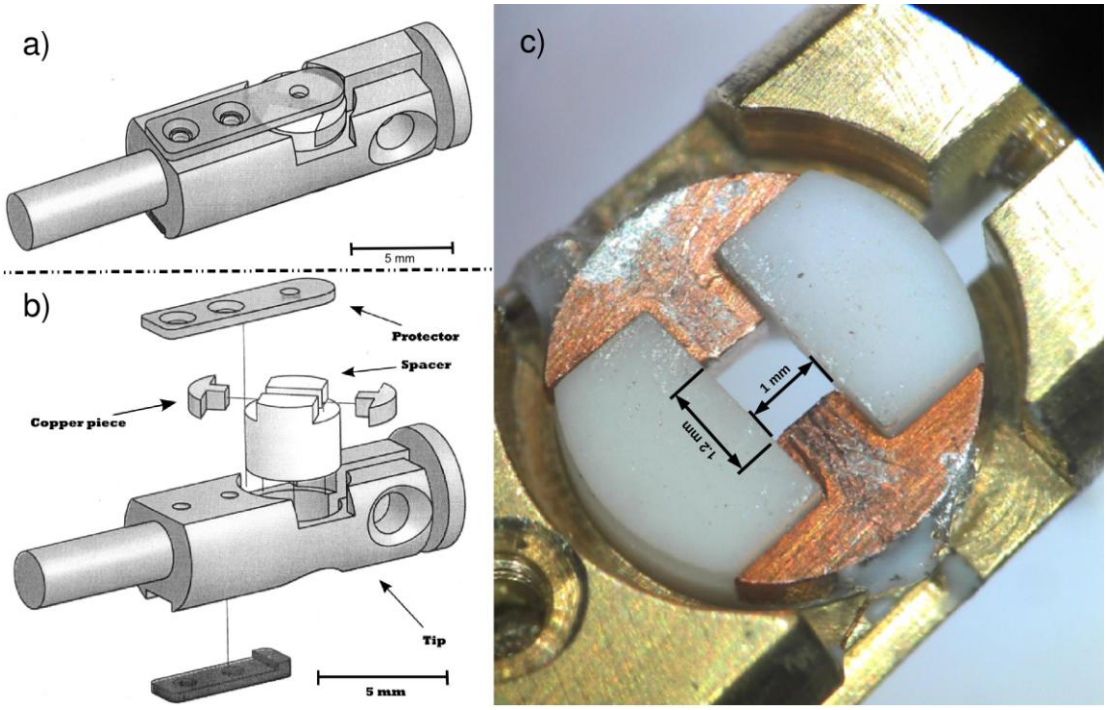
a)
5 mm
b)
Protector
Spacer
Copper piece
Tip
5 mm
c)
1 mm
1.2 mm

Quantitative Techniques and Image Simulation in TEM/STEM, SEM and Diffraction

IM2.P053
Refinement of crystal structure from LABED patterns

F. Wang[1], R. Pennington[1], C. T. Koch[1]

[1]Universität Ulm, Institut für Experimentelle Physik, Ulm, Germany

feng.wang@uni-ulm.de

Structure-factor refinement by quantitative convergent-beam electron diffraction (QCBED) [1] has been able to reveal the charge distribution responsible for the bonding between atoms [2].

However, in order to be able to fit a set of complex structure factors by comparing dynamical electron diffraction simulations to the contrast within CBED discs, the sample must typically be roughly 100 nm thick, and the lattice parameters should not exceed 1 nm.

Also, in order to extract the elastic scattering signal, it must be assumed that the incoherent background (mainly thermal diffuse scattering (TDS)) varies only slowly, an assumption that is not generally correct.

In contrast, large-angle rocking-beam electron diffraction (LARBED) [3] data (see, for example Fig. 1) can be acquired for arbitrarily large unit cell structures and reveals features that are clearly due to dynamical electron diffraction even at specimen thicknesses below 10 nm.

This makes structure factor refinement from nanocrystals possible.

As is common in QCBED work we write the scattering matrix S in the form S=exp(iTA), determining the excitation errors (diagonal of A) from the pattern geometry. We then reduce the problem to finding the factor T, which is acceleration voltage and specimen thickness related, and all the off-diagonal entries Ug-h in A, from a series of observed norms of entries in one column of S (the squared norms correspond to the diffraction intensities shown in the example pattern in Fig. 1). To efficiently solve such a nonlinear programming problem up to several hundreds of variables, a gradient-based iterative method is critical.

In this work, by accelerating the calculation of the expensive Bloch-wave simulation with Compute Unified Device Architecture (CUDA) dynamic parallelism, we developed a C++ program implementing a Homotopy optimisation algorithm to do the refinement, and apply this program on the experimental LARBED patterns of SrTiO3 successfully. We also illustrate the convergence and the fitted potential field, and compare the reconstructed diffraction intensity with the experimental one.

1. C. Deininger, G. Necker, J. Mayer, Ultramicroscopy 54 (1994) 15-30
2. J.-M. Zuo, M. Kim, M. O'Keefe, J.C.H. Spence, Nature 401 (1999) 49
3. C.T. Koch, Ultramicroscopy 111 (2011) 828 840
4. The authors acknowledge financial support by the Carl Zeiss Foundation and the DFG (Grant No. KO 2911/7-1).

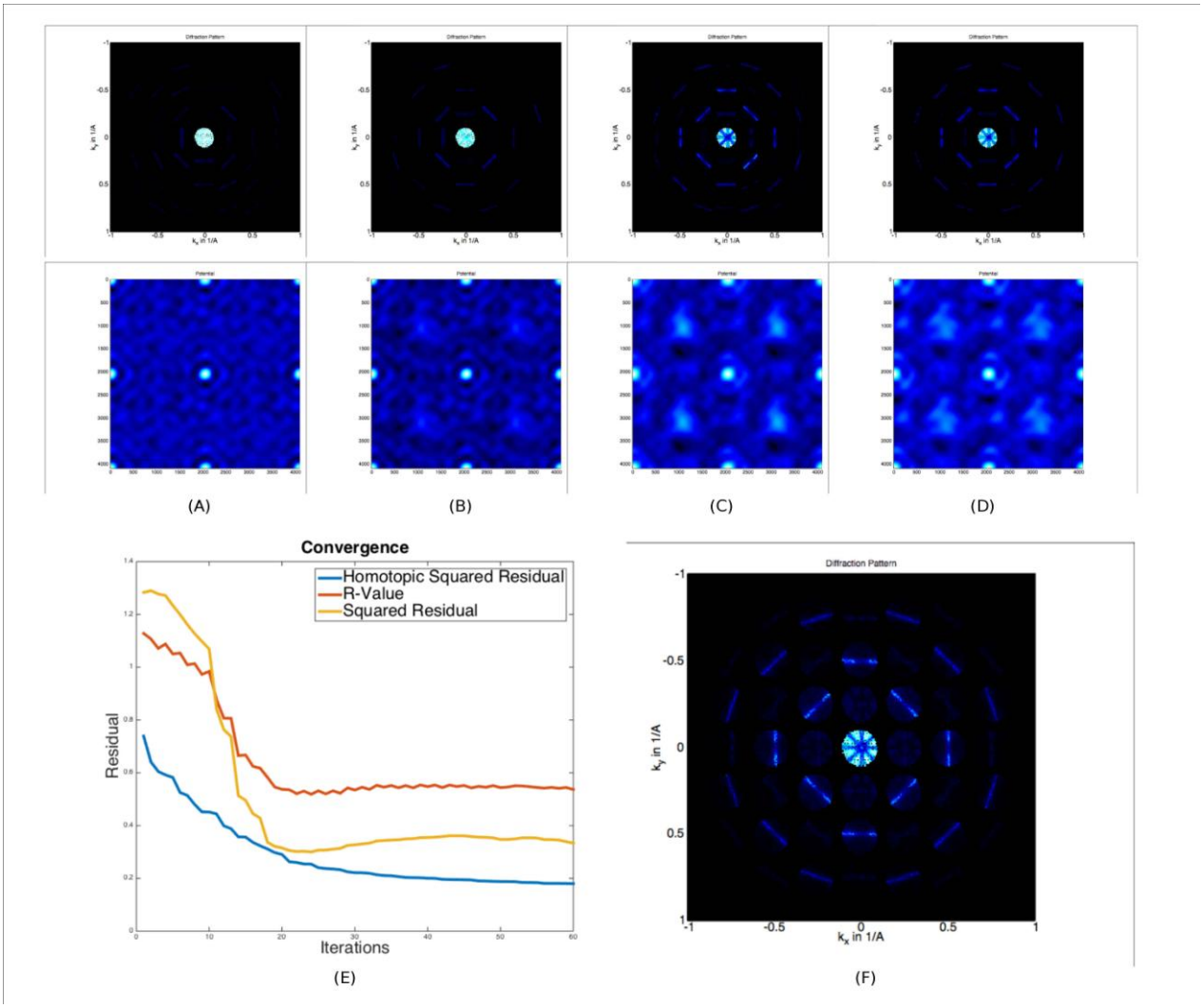

Figure 1. (A) Reconstructed potential field(lower) and diffraction pattern(upper) at the first step; (B) Reconstructed potential field(lower) and diffraction pattern(upper) at the 10th step; (C) Reconstructed potential field(lower) and diffraction pattern(upper) at the 20th step; (D) Reconstruction potential field(lower) and diffraction pattern(upper) at the 60th step; (E) Convergence curve for the refinement program, the red curve corresponds to the R-Value residual, the yellow one corresponds to squared residual and the blue one corresponds to homotopic square residual; (F) The experimental LARBED pattern obtained from a SrTiO3 specimen at 120KV, and the thickness for the specimen is about 15 nm.

Quantitative Techniques and Image Simulation in TEM/STEM, SEM and Diffraction

IM2.P054
Including backscattered electrons in the simulation of TEM images

C. Wacker[1], R. Schröder[1]

[1]Universitätsklinikum Heidelberg, CryoEM, CellNetworks, BioQuant, Heidelberg, Germany

christian.wacker@bioquant.uni-heidelberg.de

The successful realization of aberration corrected TEM allows atomic resolution at acceleration voltages as low as 20 kV [1]. Since most of the simulation algorithms have been developed to approximate imaging at much higher energies, the applicability of these algorithms must now be re-evaluated at lower energy scales. Previous studies [2-4] examined the scattering of the incoming electrons to high angles and its impact on the image formation process. To continue these investigations we present here a first quantitative study on the effects of backscattered electrons, which are usually neglected in simulation programs.

The time-independent Schrödinger equation provides a comprehensive description of elastic scattering. However, the high-energy approximation, which is commonly used to derive the multislice algorithm [5], neglects the effects of the backscattered electrons. Nevertheless, it has been shown that the multislice approach can be extended far beyond the limits of the high-energy approximation [6]. Thus, we developed a multislice algorithm that propagates transfer matrices instead of wave functions. This approach allows to track the signal of the backscattered electrons through the whole sample and enables the correct inclusion of all interference effects. As an example we simulated a 46.1 nm thick crystal of silicon [110] by taking into account the backscattering effects (Figure 1). For an acceleration voltage of 30 kV we found that the total intensity of the wave in forward direction is reduced by about 0.2 ‰ compared to a simulation without backscattering effects. Furthermore, we calculated the signal of the backscattered electrons for a single benzene molecule (Figure 2).

The underlying principles of this new multislice algorithm are valid for all acceleration voltages. However, its numerical implementation requires a minimal electron energy: Each pixel in Fourier space is associated with a certain transversal momentum. This momentum in turn corresponds to a kinetic energy. If this energy becomes larger than the total energy available the oscillating wave function in the direction of the optical axis is replaced by growing and falling exponential functions. Eventually, this results in ill-conditioned transfer matrices, that cannot be treated numerically. Hence, a minimal acceleration voltage is needed whose value depends on the Nyquist frequency. The described problem is not limited to simulations considering backscattering. It needs to be taken into account for all (multislice) algorithms that try to improve the high-energy approximation.

1. U. Kaiser, J. Biskupek, J.C. Meyer, J. Leschner, L. Lechner, H. Rose, M. Stöger-Pollach, A.N. Khlobystov, P. Hartel, H. Müller, M. Haider, S. Eyhusen, G. Benner, Ultramicroscopy 111 (2011) 1239-1246
2. C.Y. Cai, J.H. Chen; Micron 43 (2012) 374-379
3. W.Q. Ming, J.H. Chen; Ultramicroscopy 134 (2013) 135-143
4. C. Wacker, R.R. Schröder; Ultramicroscopy 151 (2015) 211-223
5. E.J. Kirkland, Advanced Computing in Electron Microscopy, Springer, 2010
6. J.H. Chen, D. Van Dyck; Ultramicroscopy 70 (1997) 29-44
7. Acknowledgment: CW gratefully acknowledges the Studienstiftung des Deutschen Volkes for a PhD scholarship.

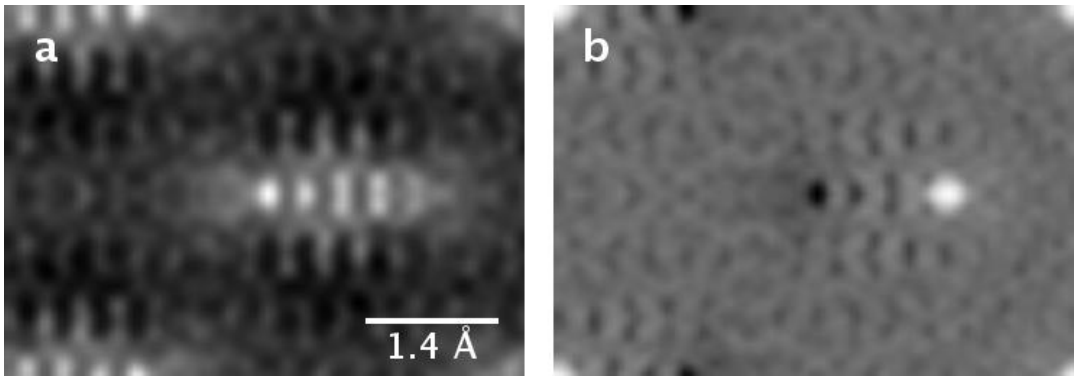

Figure 1. Elastic multislice simulation of 46.1 nm thick silicon [110] (acceleration voltage: 30 kV, pixel size: 0.06 Å). a) Exit wave function with backscattering effects included. b) Change of the exit wave function caused by the backscattered electrons (amplified by about 5000).

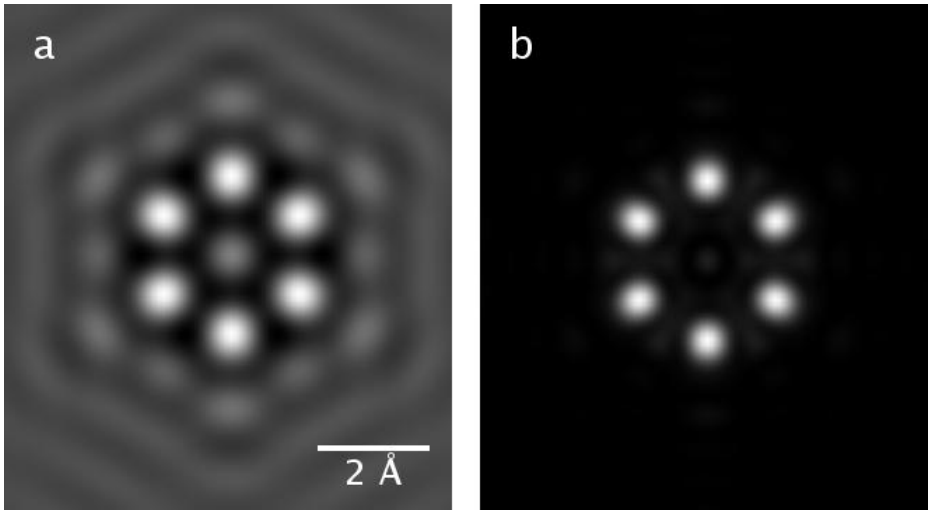

Figure 2. Elastic multislice simulation of a single benzene molecule (acceleration voltage: 20 kV, pixel size: 0.1 Å). Signal from the forward (a) and backward scattered (b) electrons. For both directions an aperture of 80 mrad has been included limiting resolution to about 1 Å. Note that the backscattered signal has been amplified by about 10^8.

Quantitative Techniques and Image Simulation in TEM/STEM, SEM and Diffraction

IM2.P055
Effects of small sample tilt on atomic column position determination in ABF-STEM imaging

D. Zhou[1], K. Müller-Caspary[2], W. Sigle[1], F. F. Krause[2], A. Rosenauer[2], P. A. van Aken[1]

[1]Max Planck Institute for Solid State Research, Stuttgart Center for Electron Microscopy (StEM), Stuttgart, Germany
[2]Institut für Festkörperphysik, Universität Bremen, Bremen, Germany

d.zhou@fkf.mpg.de

Annular bright field (ABF) imaging in scanning transmission electron microscopy (STEM), as illustrated in Figure 1, has intrigued research interest in recent years due to its capability of direct visualisation of light elements, such as Li, N and O [1,2]. Simultaneous acquisition of high-angle annular dark-field (HAADF) and ABF images combines both modes' capabilities and enables one to simultaneously visualize atoms of a large range of atomic numbers. The capability of direct visualisation of both heavy and light elements is important in the atomic-scale study of a great number of material systems. The arrangement of light elements around heavy elements, such as the tilt of oxygen octahedral in complex oxides or the oxygen sub-lattice at complex-oxide hetero-interfaces, is accessible at the atomic-scale [3]. To extract reliable atom positions directly from the images one has to assume that the maxima/minima positions in HAADF/ABF images precisely correspond to the atom positions.

In this work, we investigate the reliability of the atomic column position determination in ABF-STEM imaging, with special emphasis on the influence of small specimen tilt from the zone axis. A glance of sample tilt effect on ABF/HAADF imaging is presented in Figure 2 which is the simulated results on cubic ZrO_2. Small specimen tilt can occur by inaccurate tilting by the operator, but can also have intrinsic reasons such as in the case of static tilts of crystal planes or atom columns near crystal defects. Quantitative interpretation of both experimental HAADF and ABF images and simulation results reveals the complexity of the maxima/minima positions deviating from the supposed positions in HAADF/ABF images when a small amount of local sample tilt exists. The reasons leading to these results will be discussed with respect to basic imaging theory. Suggestions on how to improve the precision on the determination of the atom positions in ABF imaging will be proposed.

1. E. Okunishi, I. Ishikawa, H. Sawada, F. Hosokawa, M. Hori, Y. Kondo, Visualization of Light Elements at Ultrahigh Resolution by STEM Annular Bright Field Microscopy, Microsc Microanal, 15 (2009) 164-165.
2. S.D. Findlay, N. Shibata, H. Sawada, E. Okunishi, Y. Kondo, T. Yamamoto, Y. Ikuhara, Robust atomic resolution imaging of light elements using scanning transmission electron microscopy, Appl Phys Lett, 95 (2009).
3. R. Huang, H.C. Ding, W.I. Liang, Y.C. Gao, X.D. Tang, Q. He, C.G. Duan, Z.Q. Zhu, J.H. Chu, C.A.J. Fisher, T. Hirayama, Y. Ikuhara, Y.H. Chu, Atomic-Scale Visualization of Polarization Pinning and Relaxation at Coherent BiFeO3/LaAlO3 Interfaces, Adv Funct Mater, 24 (2014) 793-799.
4. The authors thank Prof. H.-U.Habermeier for providing the ZrO_2-LSMO sample and Marion Kelsch for preparing the plan-view TEM sample, both Max Planck Institute for Solid State Research. The research leading to these results has received funding from the European Union Seventh Framework Programme [FP7/2007-2013] under grant agreement n°312483 (ESTEEM2).

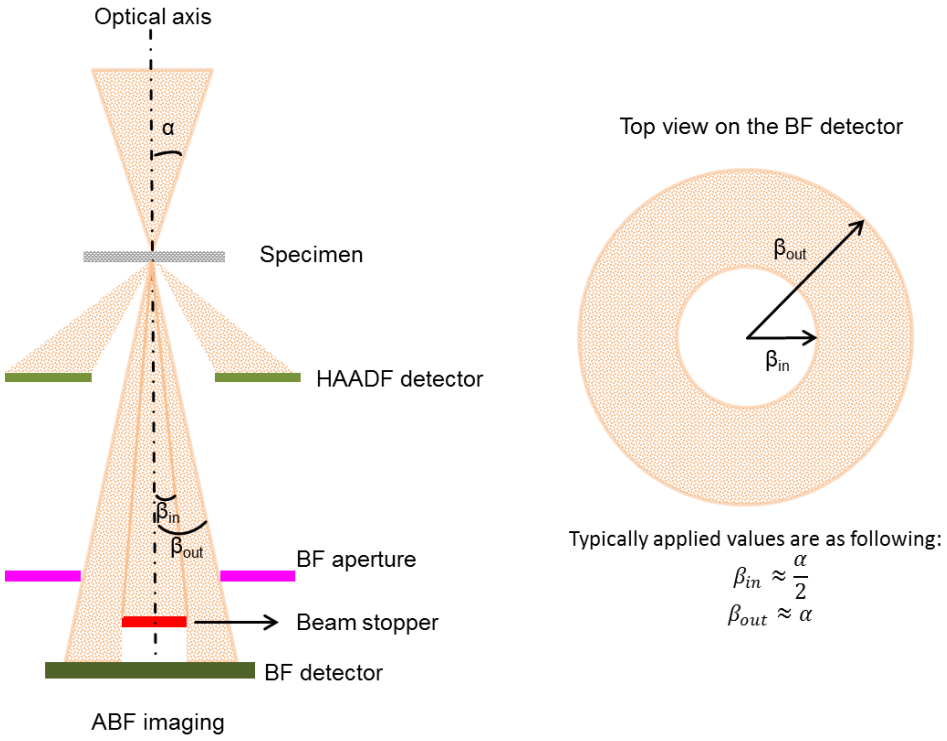

Figure 1. Schematic of the geometry for ABF imaging.

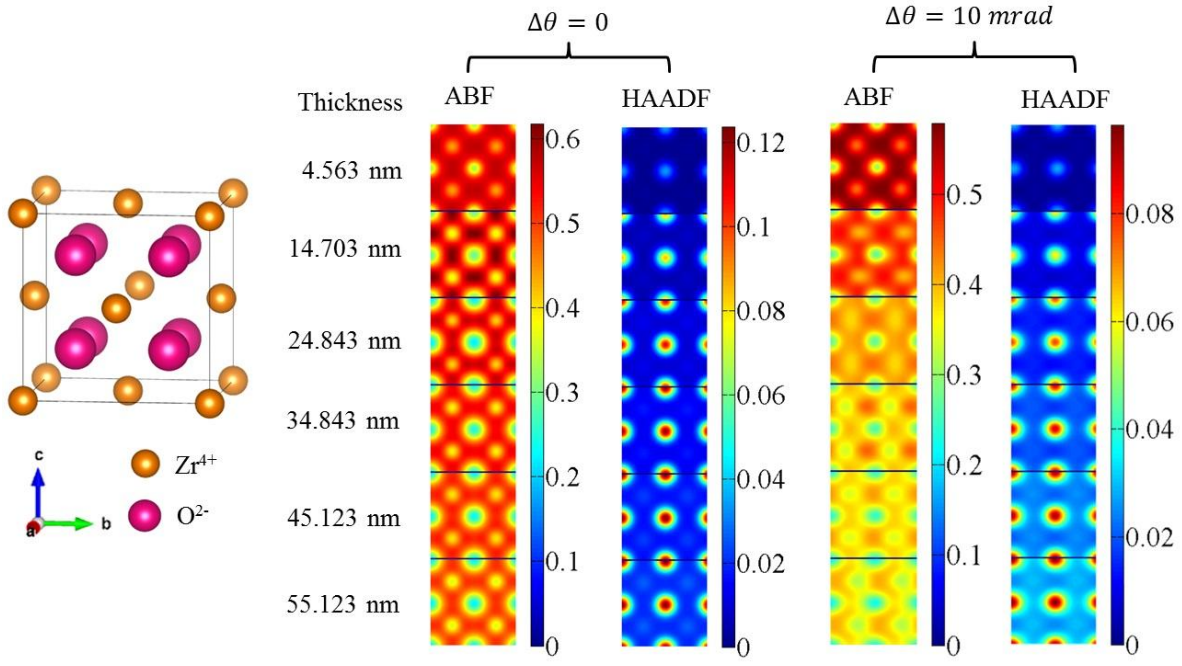

Figure 2. Visualization of the effect of sample tilt, where Δθ is the amount of the sample tilt, on the variation of the minima / maxima position in simulated ABF/HAADF images of cubic ZrO_2 (see structure at the left) for different thicknesses. The central and right ABF/HAADF images are simulated for 0 and 10 mrad, respectively.

Quantitative Techniques and Image Simulation in TEM/STEM, SEM and Diffraction

IM2.P056
Accurate shape and size determination of engineered NPs by electron microscopy (SEM, T-SEM, TEM, SAED)

E. Ortel[1], L. Pellutiè[2], F. Pellegrino[2], V. Maurino[2], J. Mielke[1], B. Powierza[1], I. Häusler[3], W. Österle[3], V.- D. Hodoroaba[1]

[1]BAM, 6.8 Surface Analysis and Interfacial Chemistry, Berlin, Germany
[2]University of Turin, Turin, Italy
[3]BAM, 5.1, Berlin, Germany

erik.ortel@bam.de

Engineered nanoparticles (NPs) are used as an active material in sensors, photovoltaics, photocatalysis, etc. Numerous publications have shown that particular facets of NPs dramatically influence their performance, e.g. in photocatalytic reactions with TiO_2 NPs [1, 2]. Therefore, information about the NP morphology expressed as area ratios of particular facets is highly demanded for the development of advanced nanomaterials.

The determination of the particle size distribution for spherical NPs is a task resolved rather easily by various techniques. However, measuring the morphology of individual NPs having complex 3D geometries like cubes, prisms or (bi)pyramids is challenging. Often, only time-consuming TEM and TEM-tomography experiments can resolve the 3D structure and facets of particles in the nanometer range accurately. We present new approaches based on i) top-view high resolution SEM and ii) in-depth view, transmission SEM (TSEM) for the determination of the full shape of facet-controlled NPs.

From top-view high resolution SEM (approach i) we could identify the 3D geometry and the individual facet boundaries of NPs. A computer-generated 3D skeleton was manually matched to these facet boundaries, thereby yielding the necessary parameters for a full 3D description of the NP shape. The evaluation of the NP shape from TSEM (approach ii) relies on an automatic image analysis: The 2D projection of the particles on the image plane depends strongly on their orientation with respect to the incident electron beam. Taking only those particles into account for which the 2D projection coincides with an assumed silhouette for standing or lying NPs on the substrate, the size of the corresponding NP facet can be determined. Due to automated image analysis, statistically relevant amounts of data could be generated quickly and lead to reliable estimates of the NPs facet size.

These general procedures to determine the NP shape is demonstrated on truncated bipyramidal TiO_2 anatase NPs. The TiO_2 NPs were synthesized by a ligand-assisted synthesis route, which provides a scalable model system with tuneable TiO_2 NP geometries [1, 2]. Figure 1 presents top-view SEM micrographs of TiO_2 anatase NPs. The truncated bipyramidal shape is clearly recognizable in Figure 1A. An enlarged part of A shows a single NP where individual facet boundaries can be identified (Figure 1B). A computer-generated 3D skeleton was matched to the facet boundaries which results in a full 3D description of the NP shape (Figure 1C). Figure 2 consists of TSEM micrographs of the truncated bipyramidal TiO_2 NPs whereas A) shows the original micrograph and B) the same micrograph with NPs considered for the evaluation of the NPs shape. The NPs marked in red and yellow were identified as standing upright and flat-lying NPs on the support, respectively (Figure 2B). Hence the corresponding NPs lengths and widths could be measured from the TSEM micrograph.

In order to validate the new methods and estimate the associated measurement uncertainties, TSEM images of randomly oriented bipyramidal particles with known dimensions were simulated and evaluated in the same way as the measured images. A good agreement was obtained between the known parameters and the evaluation results. Furthermore, for selected NPs, the obtained dimensions were confirmed by HRTEM/SAED measurements.[3]

1. C. Deiana et al., Phys. Chem. Chem. Phys. **15** (2013), p. 307.
2. C. Li et al., J. Am. Chem. Soc. **137** (2015), p. 1520
3. The research leading to these results has received funding from the European Union's Seventh Framework Programme (FP7/2007-2013) under grant agreements n°604577 (SETNanoMetro) and n°604347 (NanoDefine).

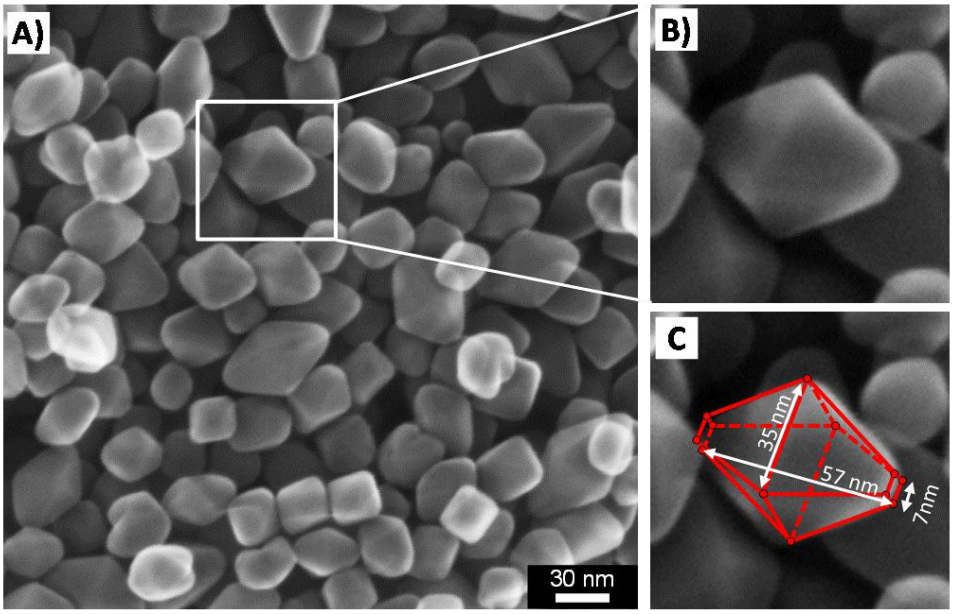

Figure 1. Top-view SEM micrographs of truncated bipyramidal TiO_2 NPs, A) overview, B) zoom-in on a single NP where individual facet boundaries can be identified, C) computer-generated 3D skeleton matched to facet boundaries.

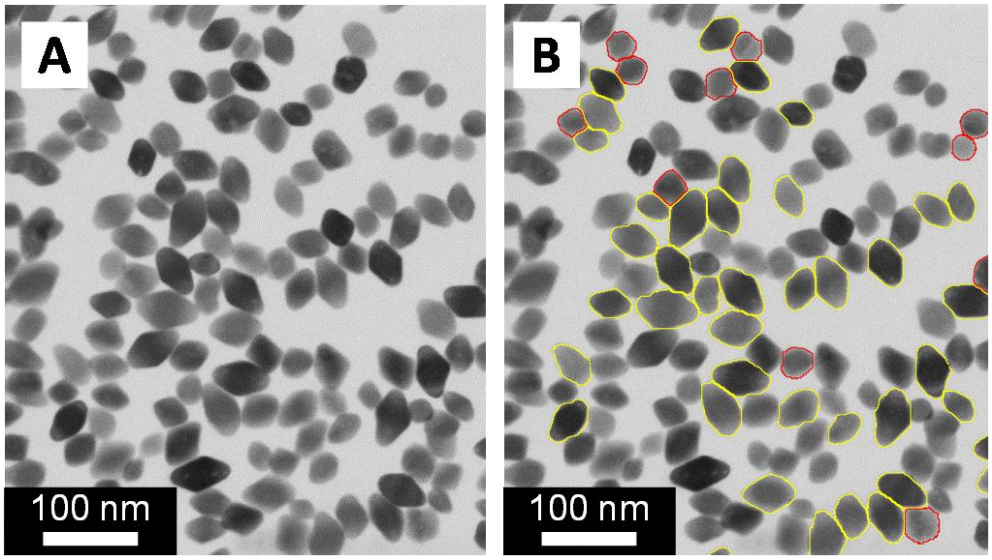

Figure 2. TSEM micrograph of truncated bipyramidal TiO_2 NPs, A) original micrograph, B) NPs considered for the evaluation of NPs widths (red boundaries) and lengths (yellow boundaries).

Quantitative Techniques and Image Simulation in TEM/STEM, SEM and Diffraction

IM2.P057
Two-dimensional misorientation mapping by rocking dark-field transmission electron microscopy

D. Tyutyunnikov[1], M. Mitsuhara[2], C. Koch[1]

[1]Ulm University, Institute of Experimental Physics, Ulm, Germany
[2]Kyushu university, Department of Engineering Sciences for Electronics and Materials, Kasuga, Fukuoka, Japan

dmitry.tyutyunnikov@uni-ulm.de

Transmission electron microscopy (TEM) is a powerful tool for investigating the atomic structure and morphology of nano- and micro-objects. A very large fraction of the specimen investigated by electron microscopists working in the field of materials science is crystalline. Crystal defects break the translational symmetry of the crystal and lead to elastic strain and changes of the orientation of the unit cell of the crystal in space. We are going to demonstrate a new technique which delivers precise two-dimensional maps of crystal orientation with high spatial resolution and large field of view. In contrast to conventional orientation mapping in polycrystalline materials [1, 2, 3], our approach only maps small deviations from a given zone axis, i.e. the crystal lattice misorientation. With this approach the local misorientation changes can be mapped with a precision of $< 0.1°$. The spatial resolution of this approach is limited by the size of the unit cell, since this determines the size of the objective aperture to be used for the experiment.

Our method is based on the analysis of one-dimensional rocking curves extracted from a tilt series of DF images for multiple reflections. Especially reflections with high Miller indices are preferred. DF images are recorded at slightly different specimen tilts, so that the tilt range will cover just a few degrees. The technique makes use of the fact that the contrast in DF images is typically very sensitive to the sample's orientation. The presented method relies of the strong DF contrast between locations in the specimen whose local crystal orientation is slightly different, leading to the well-known bend contours (see Fig. 1).

As it was shown in our previous work [4] the changes in the local crystal orientation can be extracted from the positions of the maxima in the rocking curves for all recorded reflections at a given specimen position. The DF tilt series data from multiple reflections thus allows us to retrieve accurate two-dimensional orientation maps. After properly subtracting the background in each of the different rocking curves the position of the maximum of the rocking curve is given by its first moment.

Once the positions of the rocking curve maxima are known, the determination of the crystal lattice misorientation may be considered a numerical optimization problem. Because at the specimen tilt angle corresponding to the maximum of the rocking curve the Bragg condition for that reflection should be precisely satisfied and thus the excitation error close to zero, the objective function to be minimized is simply the weighted sum of those squared excitation errors.

The reconstructed crystal lattice misorientation map determined in this way is shown in Fig. 2.

1. S.I. Wright and D.J. Dingley. Orientation imaging in the transmission electron microscope. Materials Science Forum, 273-275:209-214, 1998
2. H.H. Liu, S. Schmidt, H.F. Poulsen, A. Godfrey, Z.Q. Liu and J.A. Sharon and X. Huang. Three-dimensional orientation mapping in transmission electron microscope. Science, 332, 833-834 2011.
3. A. Morawiec, E. Bouzy, H. Paul and J.J. Fundenberger. Orientation precision of TEM-based orientation mapping techniques. Ultramicroscopy, 136,107-118, 2014.
4. Dmitry Tyutyunnikov, V. Burak Özdöl and Christoph T.Koch. Simultaneous orientation and thickness mapping in transmission electron microscopy. Ultramicroscopy, 150:37-43, 2014.

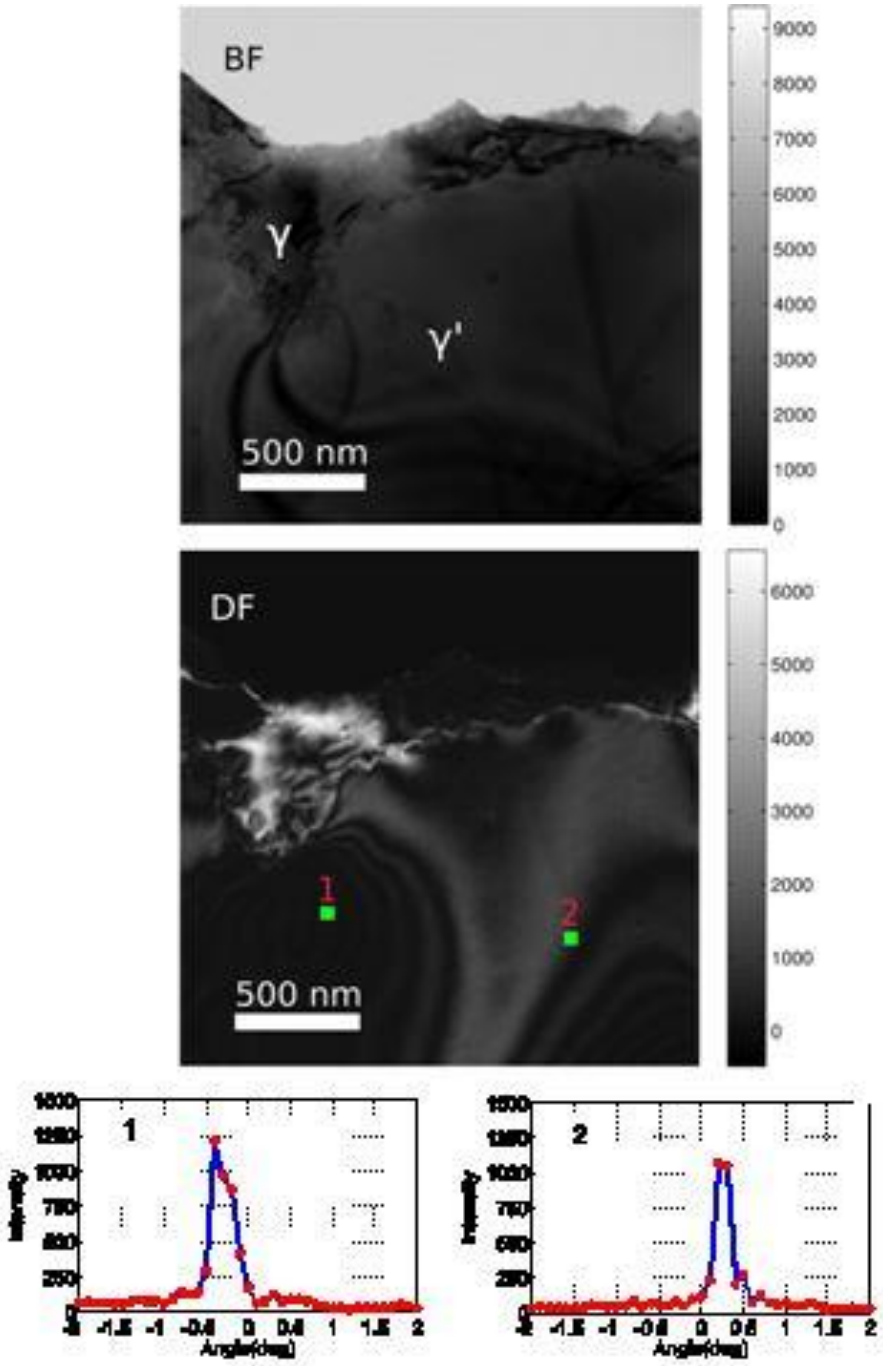

Figure 1. Top and Middle: One BF and one DF ([311], zone=[103]) image extracted from the respective tilt series used for this analysis. The material is the Ni-based super-alloy CMSX-4. Regions composed of the y and y' phases are identified. Bottom: rocking curves extracted from the data at the two positions indicated int the image above.

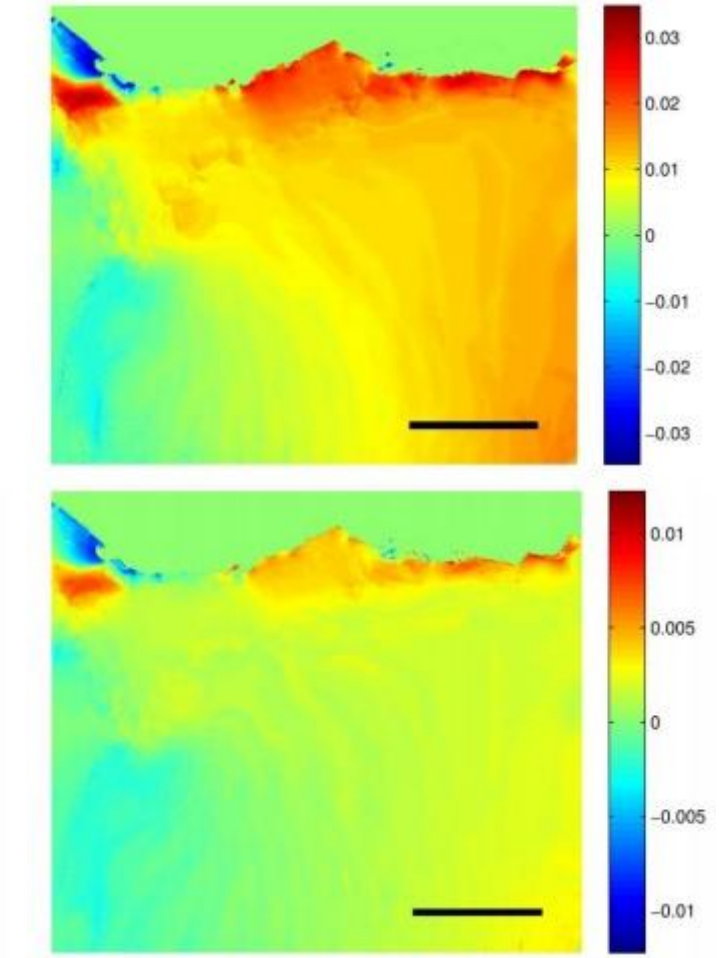

Figure 2. Top: k_x component of crystal lattice misorientation. Bottom: k_y component. The length of the black scale bar is 500 nm.

Quantitative Techniques and Image Simulation in TEM/STEM, SEM and Diffraction

IM2.P058
A software for the depictive representation of shape and bending of crystalline TEM samples from a series of dark field images as input data

M. Kuczyk[1], S. Schulze[1], M. Hietschold[1]

[1]Institut für Physik, Professur Analytik an Festkörperoberflächen, Chemnitz, Germany

martin.kuczyk@s2010.tu-chemnitz.de

Electron transparent TEM samples of crystalline material as obtained by mechanical polishing and ion milling are featured as more or less bended foils varying in their orientation at a micrometer length scale. This clearly stands out as interference fringes in dark and bright field TEM images. The bending results from internal strain in the sample, which might be introduced not only by sample preparation but also due to strain fields around defects or functional structures as well.

Usually methods of dark field microscopy are used to obtain information about sample orientation on a micrometer scale [1].

In this paper we work out a straightforward procedure to derive the imaged sample geometry from a series of dark field images taken from diffraction spots at small excitation errors. We implemented a method, in which the excitation errors as suggested by the image intensities in a set of dark field images define the orientation of the reciprocal lattice with respect to the Ewald sphere for every pixel of the imaged area in kinematic approximation (Fig. 1). For the experiments we used the 200kV High Resolution Transmission Electron Microscope (HRTEM) Philips CM 20 FEG, with an Imaging Energy Filter from Gatan (GIF) to obtain sets of dark field images of (110) orientated silicon samples.

In succession we were able to establish orientation maps of the sample (Fig. 2 - 3). Using an iterative algorithm we reconstructed a three dimensional model of the imaged sample area. Starting from one given pixel position the remaining sample surface coordinates for the adjacent pixels were deduced, using the known orientation data.

Due to the large diameter of the Ewald sphere for the TEM and the numerical approach in finding the orientation of the lattice at a micrometer length scale, the orientation maps and in consequence the reconstructed imaged sample geometries are not unique. As a result we distinguish two possible geometries (Fig. 4), which describe the bending of the foil into two opposite directions.

Such model representations of sample bending give illustrative insight in internal strain fields around functional structures introduced into semiconductor wafers for instance. Furthermore we plan on calculating the strain fields from those models (Fig. 4) to directly show the strain in the bended samples.

1. G. Wu, S. Zaefferer, Advances in TEM orientation microscopy by combination of dark-field conical scanning and improved image matching, Ultramicroscopy 109 (2009) 1317-1325

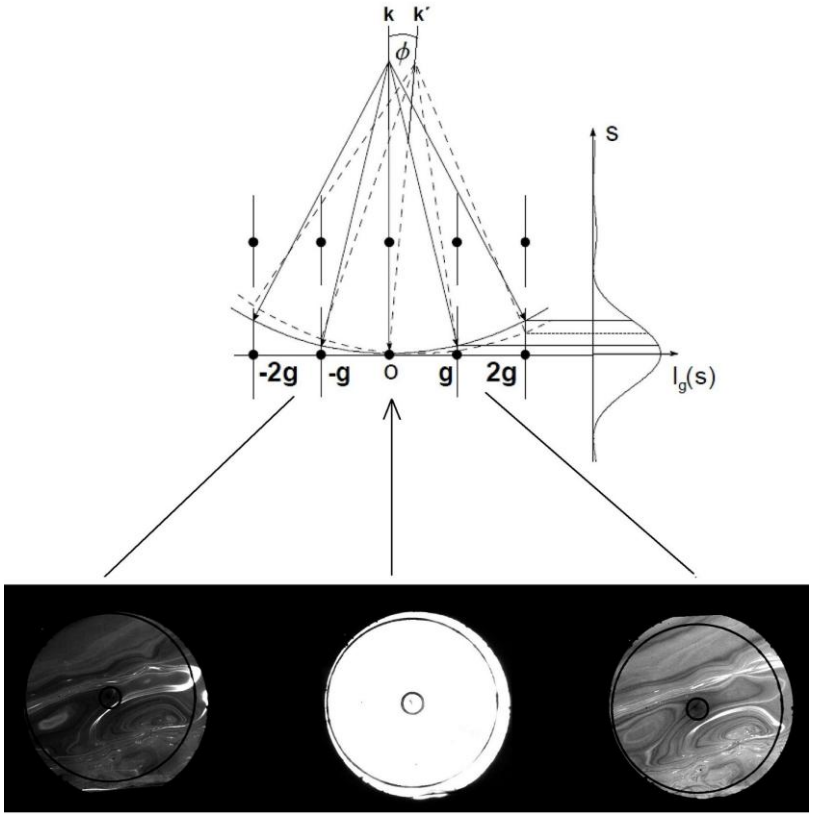

Figure 1. Sketch to show the influence of the excitation error *s* on the intensity *I* of different diffraction spots *g*. As seen below a smaller excitation error results in a brighter image.

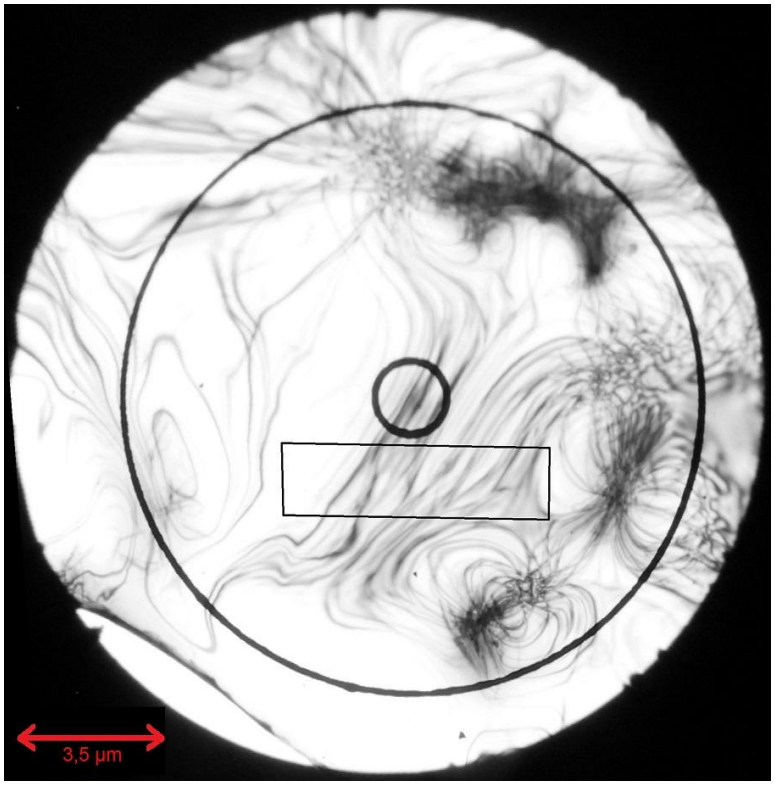

Figure 2. Bright field image of a silicon sample with a rectangular indicator frame for the analyzed sample area (6.5 µm x 1.2 µm)

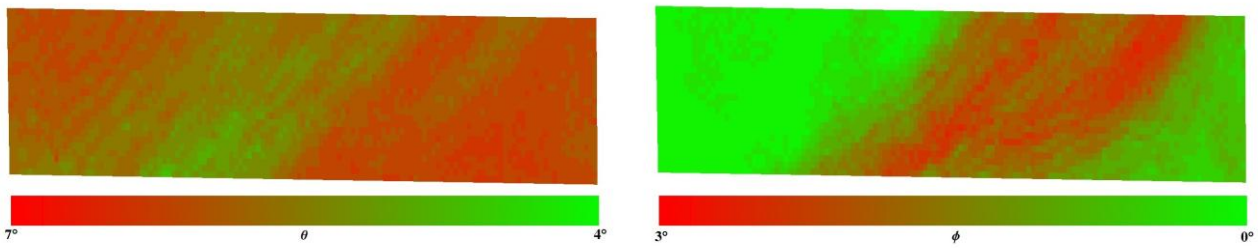

Figure 3. Orientation maps showing the deviation of the (110) orientation from the sample normal in the two Euler angles θ and φ for the sample field marked in Fig. 2

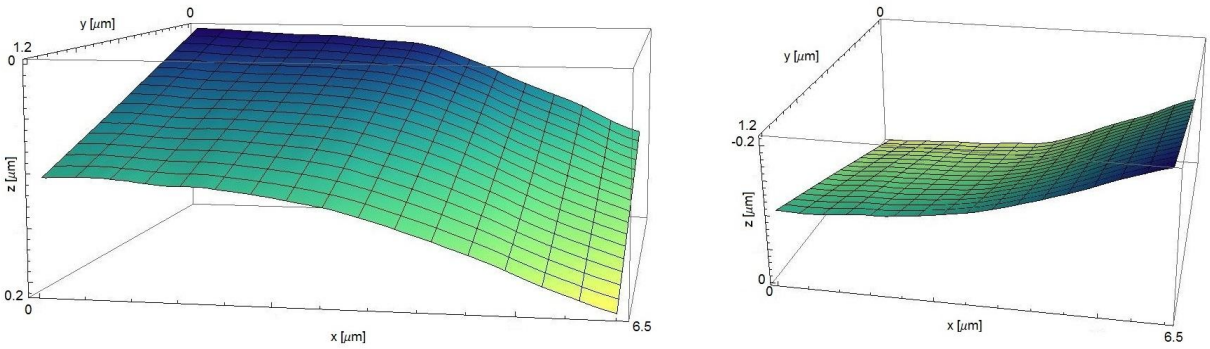

Figure 4. Ambiguity of the three dimensional models of the bended sample surface : the two possible solutions for the sample geometry

Quantitative Techniques and Image Simulation in TEM/STEM, SEM and Diffraction

IM2.P059
The energy dependent backscatter yield variations at low voltage and possible applications

M. Boese[1], K. Sempf[1,2], T. Alexander[1], Z. Fang[1]

[1]Zeiss Microscopy, Oberkochen, Germany
[2] Fraunhofer- IKTS, Dresden, Germany

markus.boese@zeiss.com

For imaging of nano-materials and composites it is often necessary to detect smallest compositional differences in these materials. Very often the nanostructure needs to be distinguishable from matrix or substrates in order to image it. The main advantage of material analysis at low Voltages is due to the reduced interaction volume of the primary beam. Benefit is here a higher resolution and the ability to gain surface sensitivity for better imaging conditions.

It is known, that under certain low Voltage conditions a contrast reversal occurs, showing high Z materials with dark contrast and light materials with bright contrast in the BSE image. In this study we investigate, how the change of the backscatter coefficient with changing primary energy can be utilized for gaining information in SEM backscattered imaging. In particular, if this can be used to gain material contrast for low voltage backscattered imaging compared to imaging conditions above 1-2 kV.

The primary energy dependency of the backscatter coefficient was described by Cazaux [1] using the empirical expression:

$h = a\,(1 \pm e^{-b\,Eo})$

The sign is + for low Z and - for the high Z elements. The parameters "*a*" and "*b*" were fitted to experimental values and a resulting characteristic is given for a range of different elements Z range from 4 to 80. The different slope for different elements is resulting from the different b values, whereas the a value is corresponding to the asymptotic value for higher Eo (>2-4 kV) [1].

Figure 1 shows the energy dependency of the yield, plotted for high Z and low Z elements. In general backscattering yield becomes lower for heavier elements going to low voltage and higher for lighter elements. The shape of the curve depends strongly on "*b*". The discontinuous change of this parameter enables us to produce some extra contrast for certain element combinations under low voltage imaging conditions. We can expect a raise in contrast up to 40% for imaging Ag and Cu at 300V (Fig. 1) compared to 10% contrast for primary energies higher than 2kV. (Note at high energy the backscatter yield is solely dependent on the "*a*" parameter)

For low Z the parameter "*b*" changes as well for different elements. But the contrast (difference between the Al and O yield in Fig. 1) is not changing as much. Here the advantage of low voltage applications is the higher signal itself due to the higher yields at low Voltage.

Experiments are carried out in a ZEISS Ultra 55 SEM equipped with an EsB detector capable of BSE detection in a sub 1kV regime. The GEMINI lens design enables the detection of backscattered electrons passing through the objective lens and then hit the EsB Detector positioned above the Inlens SE detector. A grid repels secondary electrons and can be used for energy filtered SEM Imaging [2]. Fig. 2 illustrates the low voltage imaging capabilities of this system. An example is given by a ceramic composite sample consisting of high Z and low Z phases. As shown in Fig 2 the low voltage BSE image is suitable to differentiate 5 different phases due to the leveling of the individual backscattering signal for high and low Z.

Further applications for the contrast enhancement at low voltage could be done on material systems like InGaAs, and Pb free solder containing different phases of Cu, Ag and Sn.

1. J. Cazaux, J. Appl. Phys 112 (2012), p. 84905.
2. H. Jaksch, EMC 2008 proceedings (2008), 1, 555

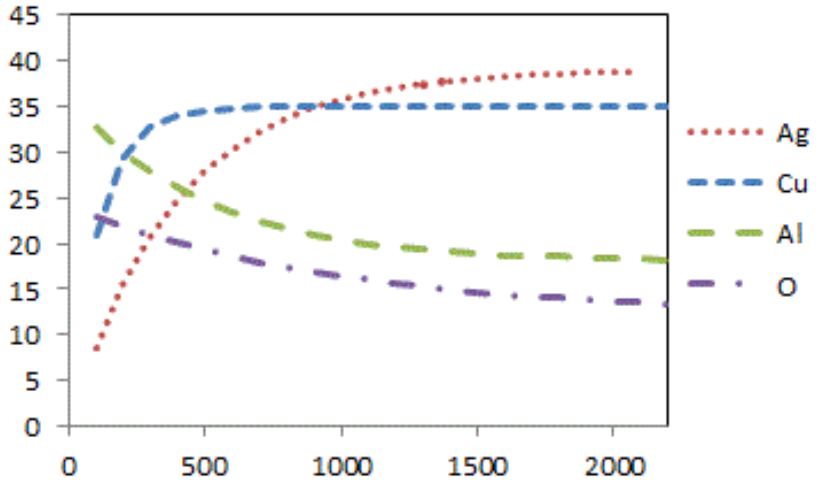

Figure 1. Energy dependency of backscatter yield h for high and low Z materials. The different slope of the curves can be utilized to gain contrast at low voltage imaging conditions.

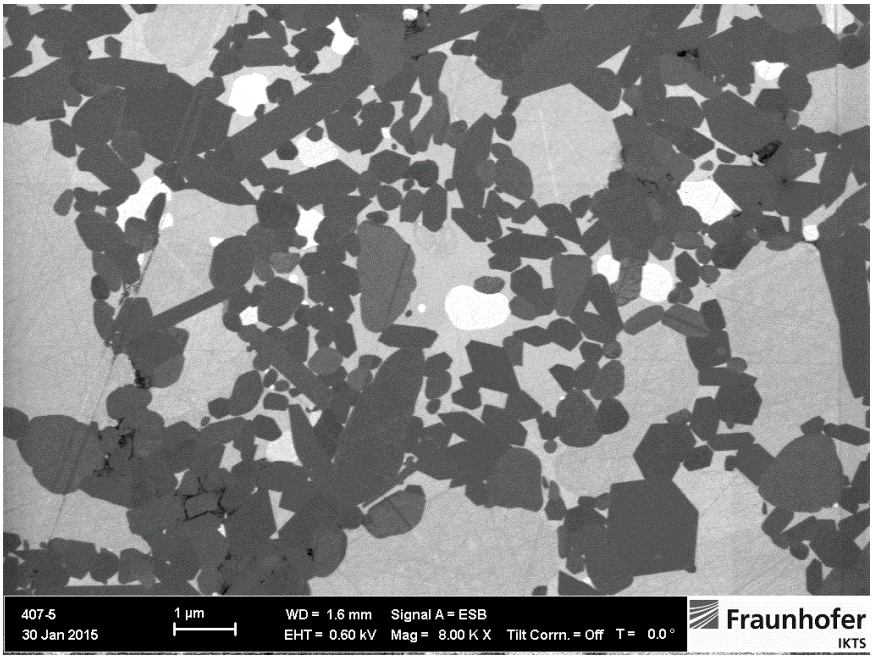

Figure 2. 5 different phases are distinguishable under low voltage conditions. Phases are: SiC, Si_3N_4, Y-Al-Si-oxinitride, $MoSi_2$, Mo_5Si_2.

Quantitative Techniques and Image Simulation in TEM/STEM, SEM and Diffraction

IM2.P060
Optimizing transmission Kikuchi diffraction setup with Monte Carlo simulations

N. Jöhrmann[1], M. Hietschold[1]

[1]TU Chemnitz, Chemnitz, Germany

nathanael.joehrmann@s2002.tu-chemnitz.de

Transmission Kikuchi Diffraction in a Scanning Electron Microscope is an interesting modification of Electron Backscatter Diffraction to get information about crystalline structures with high spatial resolution [1]. The achievable lateral resolution and the measurement time depend strongly on several parameters like sample thickness, sample tilt, acceleration voltage, working distance and detector position. Optimizing so many parameters experimentally would be very time consuming. Moreover, for each new sample material it might be necessary to choose a completely different set of parameters.

An alternative is to use Monte Carlo simulations to predict the influence of sample thickness, sample position and acceleration voltage on the detector signal, exposure time and expected lateral resolution. On the one hand, this helps already before sample preparation to decide if lateral resolution would actually improve significantly in comparison to normal Electron Backscatter Diffraction. If so, it can give a hint what sample thickness should be aimed for, to get optimal results.

On the other hand, it is possible to find suitable parameters for a given sample and get information about the expected lateral resolution. The first challenge in this case is to find out about the sample thickness. One method is to use the necessary exposure time of the detector together with the beam current and acceleration voltage. Because the exposure time decreases with increasing sample thickness d for sufficient thin samples, a comparison with simulations gives information about d. Another approach uses the background signal of a single Electron Backscatter Pattern, as is shown in Fig. 1 a) to d) for Pt-films with thicknesses reaching from 10 nm to 100 nm. The homogeneity of the detector exposure changes with sample thickness and can be described for example by the intensity center (red crosses in Fig. 1). This allows getting information about thickness in every measurement point of a mapping and therefore leads to a thickness map of the sample. Fig. 1 e) to h) shows the corresponding simulated beam spread for different Pt-film thicknesses, which relates with the lateral resolution. The latter is also influenced by acceleration voltage and sample tilt. Monte Carlo Simulations show, that the best lateral resolution is not necessarily to be expected for a tilt of 0°. That is because for electrons that actually hit the detector the path length through the sample can be decreased by slightly tilting the sample.

1. R. R. Keller und R. H. Geiss, Journal of Microscopy 245 (2011), pp. 245-251

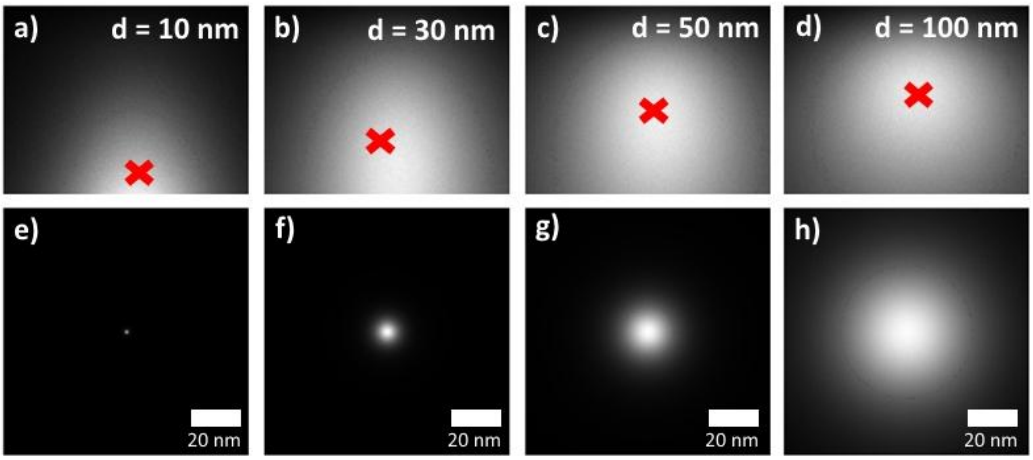

Figure 1. Monte Carlo Simulations for Pt-films with thicknesses from 10 nm to 100 nm; a,b,c,d) simulated background; e,f,g,h) corresponding beam spread

Quantitative Techniques and Image Simulation in TEM/STEM, SEM and Diffraction

IM2.P061
(S)TEM investigation of coherently strained (GaIn)(NAs) hetero-structures with respect to finite thickness effects

J. Münzner[1], A. Beyer[1], K. Volz[1]

[1]Philipps-Universität Marburg, Marburg, Germany

juergen.muenzner@physik.uni-marburg.de

(Scanning) Transmission electron microscopy ((S)TEM) offers the possibility to investigate material properties with atomic resolution, which became even more reliable in the last decade due to aberration correction.

A typical application is the investigation of the composition and structure of (multiple) quantum well (MQW) systems of different semiconductor crystals like (GaIn)(NAs) embedded in GaAs.

By changing the composition in multinary material systems, material properties like the band gap can be tailored precisely enabling various applications in the vast field of photonics.

Those hetero-structures can be grown epitaxially and coherently strained, which results in a change of the unit cell parameters called “tetragonal distortion”.

TEM can provide this information with atomic resolution and is well suited for low dimensional structures. However, the finite thickness of TEM samples changes the initial strain state of embedded structures. This redistribution of the internal strain energy might lead to wrong conclusions about material properties, when compared to bulk measurements with x-ray diffraction (XRD).

Strained semiconductor hetero-structures of (GaIn)(NAs)/GaAs MQWs on GaAs substrate were prepared in cross-section geometry and thinned down to electron transparency by conventional argon broad ion beam thinning.

The geometry and composition of the MQW structure is investigated with atomic resolution using an image- and probe-corrected (S)TEM (JEOL JEM-2200FS) in both modes.

TEM sample thicknesses are measured with electron energy loss spectroscopy and by comparing high angular annular dark field intensity of STEM with image simulations done with the STEMSIM [3] code.

The microscopic strain state is evaluated using the Geometric Phase Analysis (GPA) software [1] and compared with XRD data of the bulk structure. In order to compare the effect of elastic strain relaxation of the surface areas, the bulging out is measured with atomic force microscopy (AFM) on TEM samples.

Furthermore, a part of the actual TEM sample is sectioned with a focused ion beam (FIB) (JEOL JIB-4601F). These cross-sectional profiles of TEM samples are thinned and investigated by TEM strain mapping and thickness measurements (fig.1).

Utilizing this approach it is possible to investigate the profile of real TEM samples and the effect of elastic strain relaxation on TEM investigations in different model systems.

Additionally, a lattice matched MQW system is investigated to separate strain induced effects from preparational artifacts.

The COMSOL [2] package is used for modeling those TEM sample geometries and calculation of their strain state (fig.2).

The deviation of strain measurements in XRD and TEM can be explained by taking into account the finite thickness of TEM samples in the relaxation of coherently strained layers. Finite elements analysis is in good agreement with TEM investigations and can be used to calculate bulk properties from TEM measurements and reveal material properties at the nanoscale.

1. GPA, HREM Research Inc.
2. COMSOL Multiphysics® 4.3
3. A. Rosenauer, et al., Microsc. Of Semicond. Materials 2007, Springer Proceedings in Physics Vol 120, pp 170-172

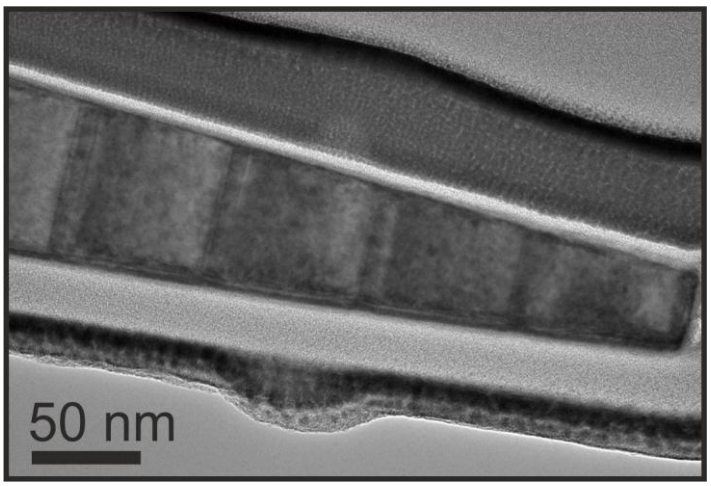

Figure 1. TEM overview of the cross-section of a actual TEM sample containing (GaIn)(NAs) QWs

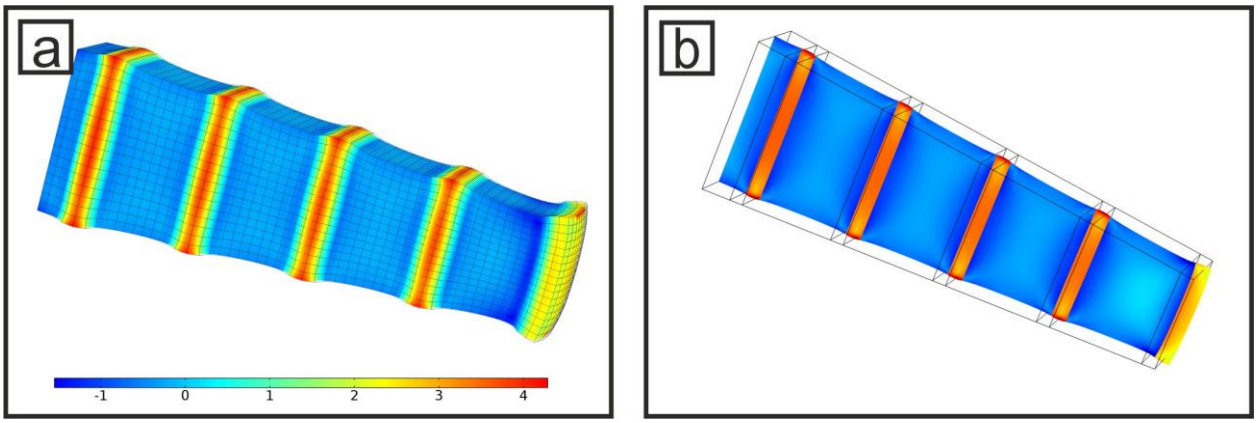

Figure 2. (a) COMSOL model of a TEM sample. The Magnitude of the tetragonal distortion is indicated by color. The bulding out at the surfaces is increased by a factor of ten. (b) A central slice through this model.

Quantitative Techniques and Image Simulation in TEM/STEM, SEM and Diffraction

IM2.P062
Charging in dependence on the accelerating voltage of free-supported films

U. Golla-Schindler[1], A. Oelschlägel[1], J. Bernhard[1], U. Kaiser[1]

[1]Group of Electron Microscopy of Material Science, Ulm, Germany

ute.golla-schindler@uni-ulm.de

One essential precondition for a successful characterization of material by using electron microscopy is a sufficient electronic conductivity. Insulating specimens can be charged by electron irradiation. For SEM and samples where R< t (R electron range and t sample thickness) it is well known that the total electron yield σ with $\sigma = \eta + \delta$ as the sum of the backscattering coefficient η and the secondary electron yield δ becomes larger than unity between two critical energies E_1 and E_2 (Figure 1a). The specimen becomes negatively charged when $\sigma < 1$ for $E>E_2$ and $E< E_1$. For $E_1 \leq E \leq E_2$ more electrons are emitted as secondary and back scattered electrons than primary electrons are stopped inside the specimen, which results in a positively charged specimen with a few volts. In this range insulating samples can be observed without charging effects [1]. For not too rough and homogeneous samples figure 1b show typical E_2 values depending on the specimen tilt. For free supporting films when R< t, the total electron yield becomes:

$\sigma = \eta + \delta_t + \delta_b + \tau$ where δ_t and δ_b are secondary electron yields at top and bottom of the sample, respectively and τ are transmitted electrons. Positive and negative charging for σ larger or smaller than unity is obtained in the same manner as for bulk samples, but a third critical energy E_3 can be defined where for increasing accelerating voltage $\sigma > 1$ and positive charging appears. In Figure 1c) calculated electron yields for free-supported formvar films in dependence on the mass thickness are presented, where the intersection with $\sigma = 1$ line gives the critical energies $E_{1,2,3}$,respectively.

In conventional TEM with accelerating voltages above 100 keV positive charging for not conductive samples can become the limiting factor. Therefore the reduction of the accelerating voltage down to 20 kV accessible in the SALVE microscope, should reduce positive charging and under specific circumstances enable to reach the critical energy E_3 . To obtain experimentally the critical energy E_3 we have implemented a transmission unit [2] in SEM which enables to determine the electron range R and the critical energies E_2, and E_3experimentally.

Figure 2 shows exemplary four images of an image series taken with increasing acclerating voltage a) below E_2 at 1.3 keV, b) start of negative charging at 1.4 keV, c) negative charged at 1.5 keV and d) behind E_3 at 2.1 keV. The specimen was a free supported formvar film on a conventional copper grid and the investigations were performed using a SEM/FIB NVISION 40.[5]

1. Reimer L., Golla U., Böngeler R., Kässens M., Schindler B., Senkel R. (1992) Charging of bulk specimens, insulating layers and free-supporting films in scanning electron microscopy. Optik 92 14-22
2. Kaiser, U., Biskupek, J., Meyer, J.C., Leschner, J., Lechner, L., Rose, H., Stoger- Pollach, M., Khlobystov, A.N., Harterl, P., Muller, H., Haider, M., Eyhusen, S. & Benner, G. (2011). Transmission electron microscopy at 20 kV for imaging andspectroscopy. Ultramicroscopy 111, 1239-1246.
3. Inventor of the Patent of Carl Zeiss SMT GmbH, Entwicklung und Prototypenbau eines STEM Detektors für ein Rasterelektronenmikroskop Rasterelektronenmikroskop: Patentnr.: DE 10211977, EP 1347490,US 2003/0230713 A1
4. Golla U., Schindler B. and Reimer L. (1994) Contrast in the transmission mode of a low-voltage scanning electron microscope. Journal of Microscopy 173 219-225
5. This work was supported by the DFG (German Research Foundation) and the Ministry of Science, Research and the Arts (MWK) of Baden-Wuerttemberg in the frame of the SALVE (Sub Angstrom Low-Voltage Electron microscopy and spectroscopy project).

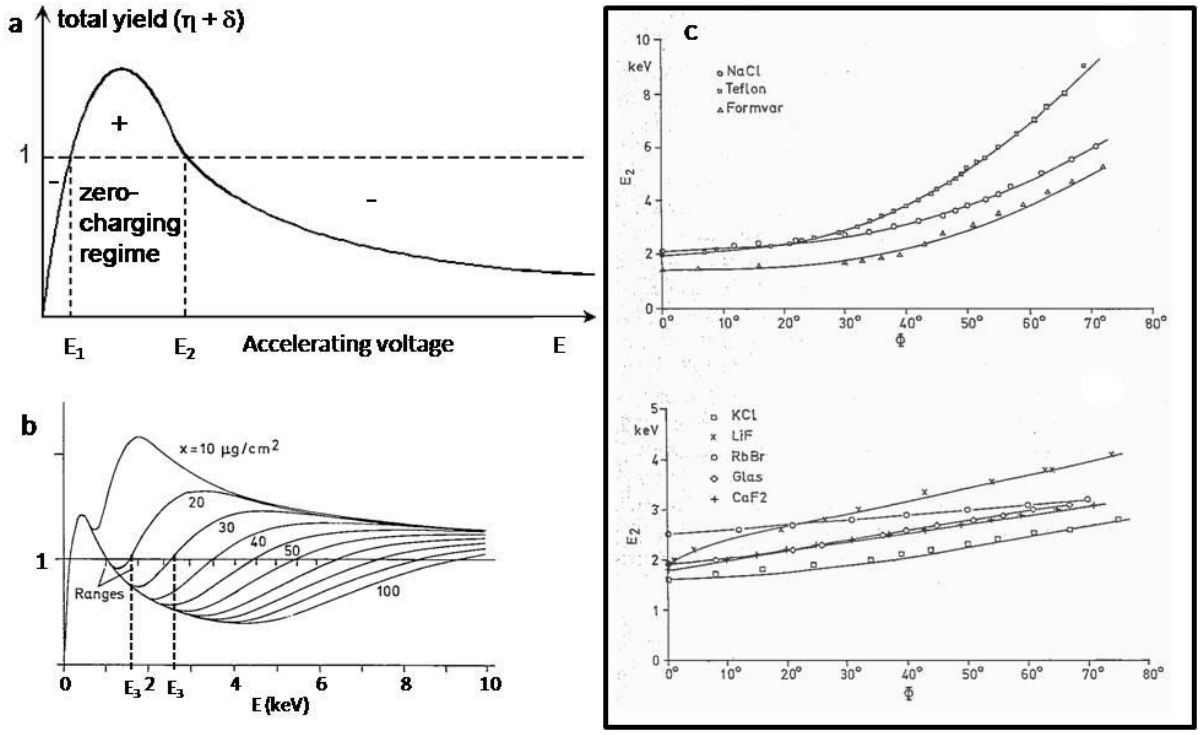

Figure 1. Total electron yield and critical energies $E_{1,2,3}$ a) schematic drawing of the total electron yield b) calculated total yield for free supported formvar films with varying thickness c) measurement of E_2 as function of tilt angle F for insulators and alkali halogenides.

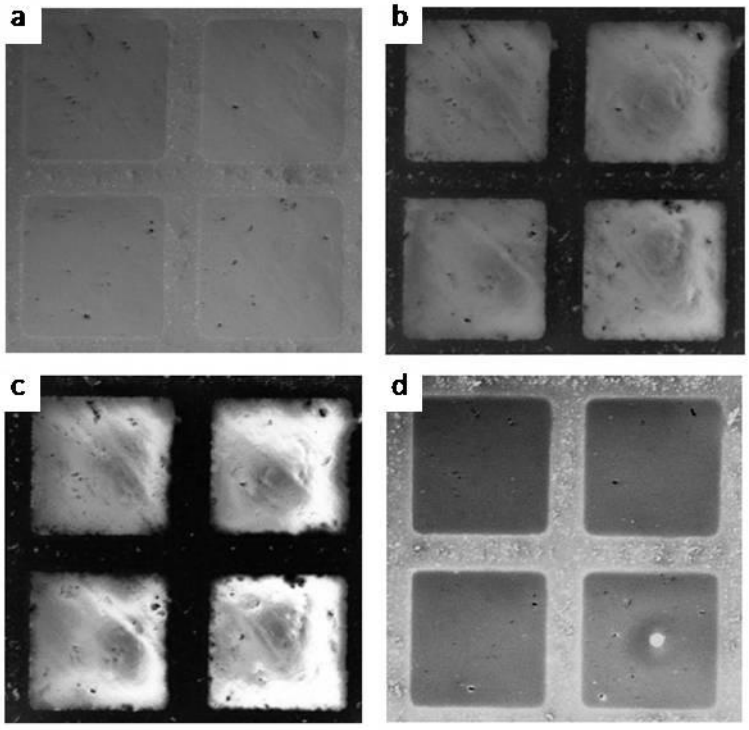

Figure 2. Charging of a free-supported Formvar film on cupper at different acceleration voltages in a SEM microscope a) 1.3keV b) 1.4keV c) 1.5keV d) 2.1keV.

Quantitative Techniques and Image Simulation in TEM/STEM, SEM and Diffraction

IM2.P063
Investigation of detector characteristics for quantification of HAADF-STEM images

M. Schowalter[1], F. F. Krause[1], T. Grieb[1], K. Müller-Caspary[1], T. Mehrtens[1], A. Rosenauer[1]

[1]Institute of Solid State Physics, Bremen, Germany

schowalter@ifp.uni-bremen.de

HAADF-STEM has gained considerable attention in recent years due to its applicability for atom-counting [Nanoletters **10** (2010), 4405] and composition determination [Ultramicroscopy **111** (2011), 1316]. Both methods rely on normalized intensity by $I_{norm}=(I-I_{back})/(I_{det}-I_{back})$, with I_{det} and I_{back} intensities on and offside the detector (Fig. 1a), which for instance can directly be compared with simulations.

Fig. 1a depicts an image of an amorphous Si wedge with normalized intensities. A linescan as indicated is shown as blue line in Fig. 1b. In the vacuum region the intensity is expected to be zero, but small negative values are observed. This can be attributed to the thresholding during the detector scan evaluation, which overestimates the amplifier offset. In Fig. 1c one can see that the offset intensity I_{amp} of the amplifier is significantly smaller than I_{back}. However, substituting I_{amp} for I_{back} in the normalization procedure yields positive values in vacuum (green line in Fig. 1b). This discrepancy is caused by accidental electrons impinging on the detector even if the beam is scanned in vacuum [Microscopy and Microanalysis **20** (2014), 99]. A histogram of a vacuum image showing the presence of accidental electrons is depicted in Fig. 1d.

We further studied the angular distribution of these accidental electrons. A series of vacuum images was recorded with varying outer detector angle. For each image a histogram of intensities was built and Gaussians were fitted to the amplifier peak as well as the peak corresponding to one electron. From the peak distance the single electron signal was determined. The number of accidental electrons then was determined by dividing the area below the one electron peak by the single electron signal. Fig. 2a shows the number of accidental electrons as a function of the outer detector angle, from which we derived the probability that an incoming electron is detected under a certain angle (Fig. 2b). We found that the number of electrons is decreasing up to a detection angle of 220 mrad. The reason for the stagnation of the number of electrons is an apparent cut-off of the diffraction pattern as depicted in Fig. 3a, which in addition is strongly distorted due to the imaging Cs-corrector.

To study the influence of distortions and sensitivity the semiconvergence angle was reduced by inserting a 7 mm aperture. Then the beam was scanned over the detector in diffraction mode by applying a series of beam tilts. The resulting detector scan is visualized in Fig. 3b, c for camera lengths of 196 mm and 301 mm. The effective sensitivity maps differ from the sensitivity that would be measured from a detector scan in imaging mode. However, the radially integrated sensitivity is quite similar for the 196 mm camera length, but is significantly differing at 301mm, where even a corona-like behavior was observed.

We also measured the single electron response of the detector. To this end, the intensity was reduced as far as possible and a series of detector scans was recorded. In regions of 4x4 pixels histograms were built and the single electron signal was determined as described above. The variation of the single electron signal over the detector is depicted in Fig. 4. The sensitivity is similar to the sensitivity that would be measured in a detector scan in image mode.

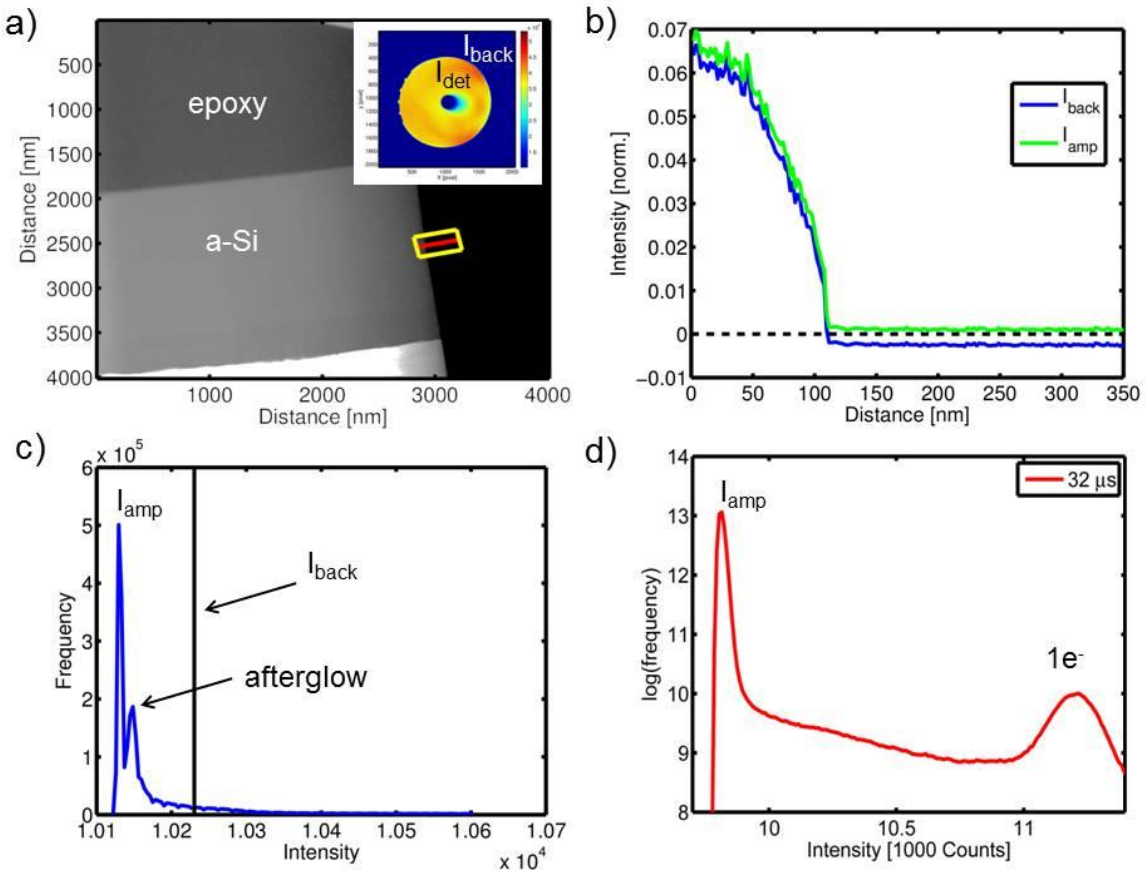

Figure 1. a) Normalized image of a wedge. b) Linescan indicated in part a. c) Histogram of the detector scan shown in a. The black vertical line indicates the position of the I_{back}. The second peak is due to an afterglow of the scintillator. d) Histogram of intensities of a vacuum image. Beside the amplifier peak a peak corresponding to one accidental electron per pixel is visible.

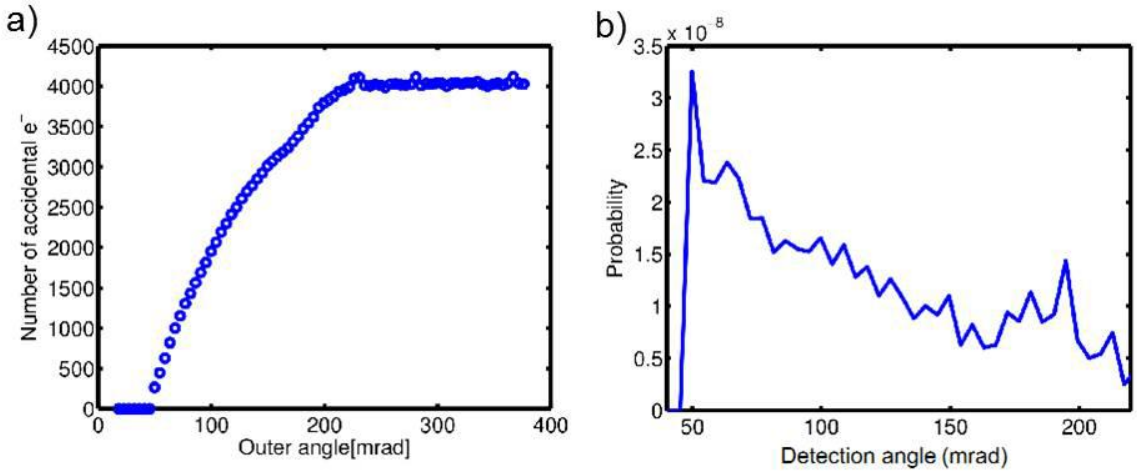

Figure 2. a) Number of accidental electrons as a function of outer detector angle. b) The probability of a beam electron to be detected under a certain angle decreases with the detection angle.

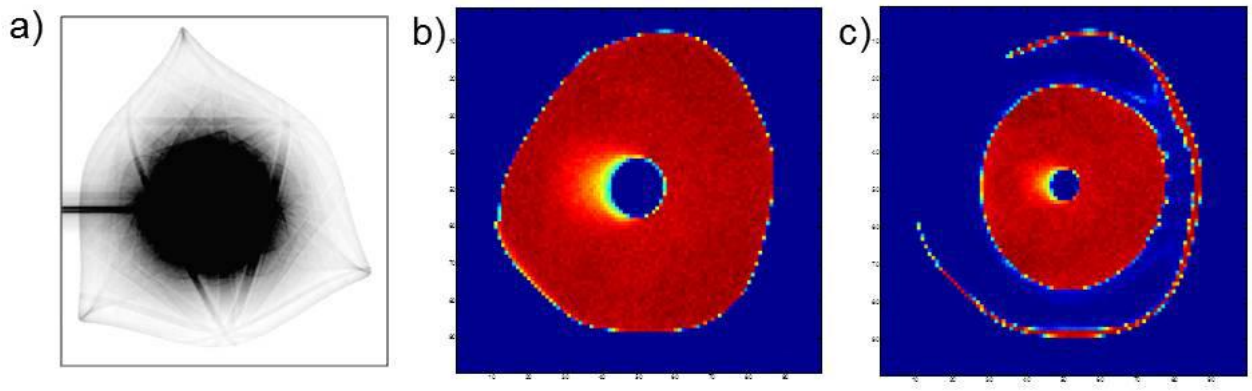

Figure 3. a) Diffraction pattern showing the cut-off. Detector scans taken by tilting the beam for 196 mm (b) and 301 mm (c) camera length.

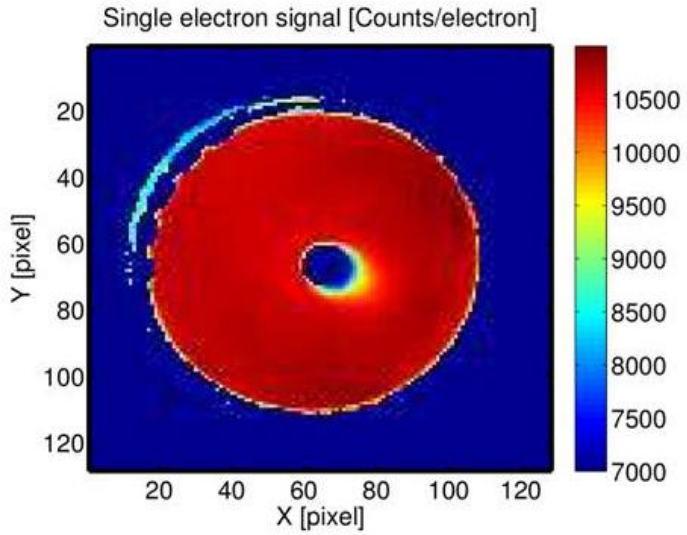

Figure 4. Single electron response of the detector.

Quantitative Techniques and Image Simulation in TEM/STEM, SEM and Diffraction

IM2.P064
Homogeneity and composition of MOVPE-grown AlInGaN: a multiprobe nanostructure study

F. F. Krause[1], M. Schowalter[1], J.- P. Ahl[2], J. Hertkorn[2], R. Egoavil[3], D. Tytko[4], P. P. Choi[4], T. Mehrtens[1], K. Müller-Caspary[1], D. Raabe[4], J. Verbeeck[3], K. Engl[2], A. Rosenauer[1]

[1]Universität Bremen, IFP, Bremen, Germany
[2]OSRAM Opto Semiconductors GmbH, Regensburg, Germany
[3]Univeriteit Antwerpen, EMAT, Antwerpen, Belgium
[4]Max-Planck-Institut für Eisenforschung, Düsseldorf, Germany

f.krause@ifp.uni-bremen.de

The quaternary material system AlInGaN has recently attracted attention for the construction of electronic and optoelectronic devices, benefitting from its additional compositional degree of freedom opposed to ternary materials, which allows e.g. polarisation-matched growth. The electronic properties of InAlGaN devices significantly depend not only significantly on the composition but also on the nanoscale compositional homogeneity of the alloy. The identification or exclusion of concentration fluctuations is hence of high interest, especially as the occurrence of indium-rich clusters has been reported for this material system [Phys. Rev. B **70**, 073202 (2004)].

Hence, a comprehensive multiprobe study of homogeneity and composition of such compounds is presented. Five AlInGaN layers with indium concentrations from 0 to 17 at.% and aluminum concentrations between 0 and 39 at.% grown by metal-organic vapor phase epitaxy (MOVPE) were investigated. Energy dispersive X-ray spectroscopy (EDX), high-angle annular dark field scanning transmission electron microscopy (HAADF STEM) and atom-probe tomography (APT) were employed.

EDX mappings reveal distributions of local concentrations which are in good agreement with random atomic distributions as depicted in Fig. 1 for one exemplary layer.

The homogeneity is hence further investigated with HAADF STEM by quantifying the agreement of the statistical distribution of atomic column intensities from experiment and of frozen-phonon multislice simulations of an ideal random alloy employing various statistical tests. The investigated samples are thereby found to be fully homogeneous with high significance as can also be seen in the histograms in Fig. 2. The statistical power of this test is validated by comparison to additional simulations for the case of indium-rich clusters with nanometer-scale dimensions, which show clear and significant deviation from the distribution of a random alloy. The investigations thus allow to rule out indium clustering in the sample on this scale.

Statistical analyses of APT reconstructions fully verify these results, as the distribution of detected ions in the reconstruction, as shown in Fig. 3, are found to agree with binomial distributions by the chi-square-test with high significance. The power of this test is demonstrated by using a reference sample containing known composition fluctuations, which was indeed found to be inhomogeneous with high significance. A broadening of the AlInGaN emission peak which has been observed in photoluminescence spectroscopy (PL) thus can be attributed solely to random alloy fluctuations.

Though HAADF STEM evaluation only allows for the reduction of possible combinations of indium and aluminum concentrations to the proximity of isolines in the two-dimensional composition space, the observed compositional ranges of composition are in agreement with the EDX and APT results within the respective precisions.

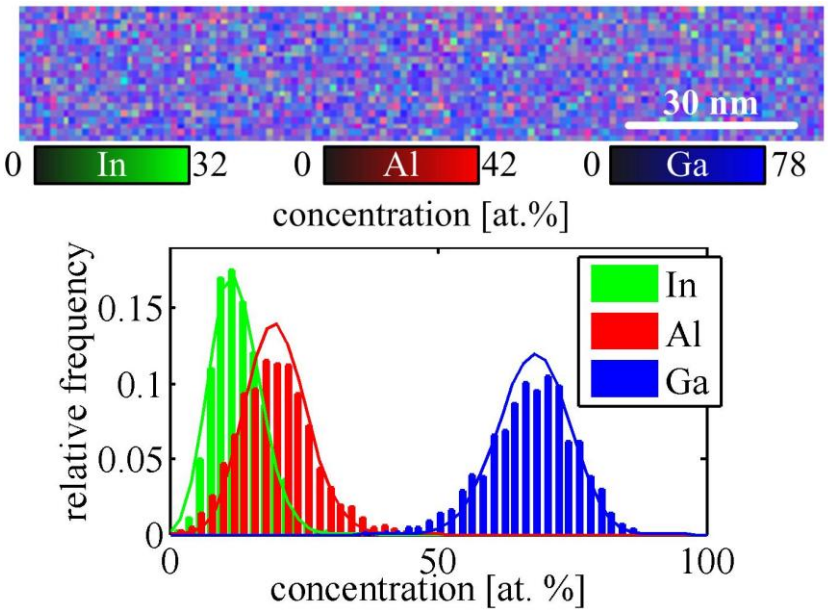

Figure 1. Top: Concentration map for the layer with the highest aluminum content obtained from EDX. Bottom: Histogram of the measured concentrations (bars) in comparison with a binomial distribution (solid curve).

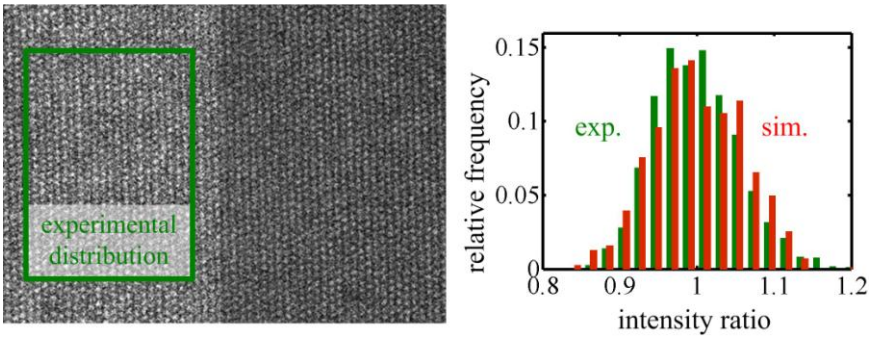

Figure 2. Left: Experimental STEM image with aluminum rich AlInGaN layer on the left. Right: Histogram showing the experimental distribution in green and the simulated distribution in red.

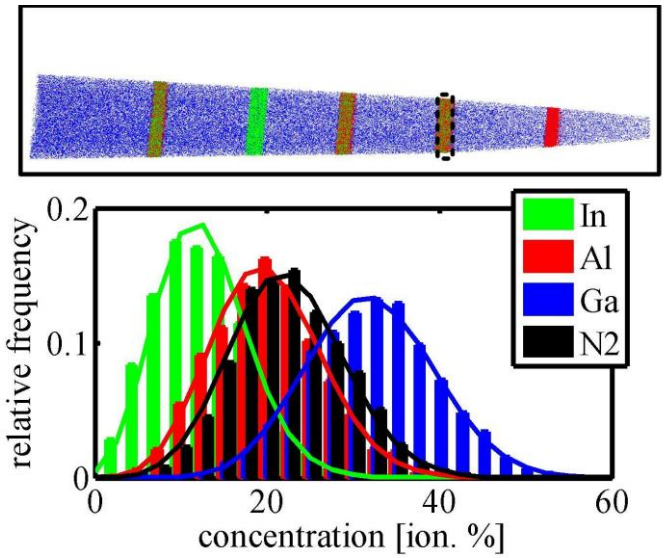

Figure 3. Top: Reconstruction of the APT tip sample. The investigated layer is marked. Bottom: Histogram showing the distributions of concentration in the marked volume (bars), which is found to be in significant agreement with expectations according to binomial distribution (solid curves).

Quantitative Techniques and Image Simulation in TEM/STEM, SEM and Diffraction

IM2.P065
Nanometrology with a TEM - determining the position of an amorphous interface

S. Majert[1], H. Kohl[1]

[1]Westfälische Wilhelms-Universität Münster, Physikalisches Institut, Münster, Germany

stephan.majert@gmail.com

With the miniaturization of components in computers and other electronic devices, the task of controlling the size of such components becomes more demanding. For the smallest components a Transmission Electron Microscope (TEM) can be used to measure the positions of interfaces with high resolution. However, the position of an interface is not always clearly discernible from a TEM image. To determine the position of an amorphous interface one often uses the mean value between the average intensities in the image domains on both sides of an estimated interface position [1]. The result is the interface position as it a appears on the TEM image, which may or may not be identical to the actual interface position in the specimen. To test whether the apparent interface position corresponds to the actual interface position in the specimen, we developed a multislice program to simulate TEM images of amorphous interfaces as found in cross-sectional preparations of semiconductor devices. With this program, we can compare the apparent interface position on the simulated TEM image with the actual position of the interface known from the atomic coordinates used in the simulation.

In [1], a specimen containing amorphous platinum, amorphous silicon dioxide and crystalline silicon was examined. Therefore we simulated a TEM image of this specimen. The results are shown in fig.1, with the red lines marking the actual interface positions. We find that the interface between the silicon crystal and the amorphous silicon dioxide can be clearly discerned from the TEM image. In addition, our simulations show that the crystal only marginally influences the image intensities at the position of the amorphous interface between platinum and silicon dioxide. We therefore neglected the crystal-amorphous interface and focused on simulating the interface between amorphous platinum and amorphous silicon dioxide.

Fig.2 shows the simulated TEM image of a Pt-SiO_2 amorphous interface where the actual interface is located at x=30.0Å. We define the apparent interface position as the point where the intensity has reached the mean value of the average intensity in the platinum and the average intensity in the SiO_2 image domain [1]. By plotting the average intensity parallel to the interface in a graph (fig.3), the apparent position of the interface (blue arrow) can be determined as x=31.2Å, which means that the apparent interface position deviates from the actual interface position by 1.2Å. This deviation stems from the different scattering behaviors of platinum and SiO_2.

1. G. Dai et al., Measurement Science and Technology 24 (2013) 085001. http://dx.doi.org/10.1088/0957-0233/24/8/085001
2. We thank Dr. G. Dai and Dr. G. Frase for valuable discussions.

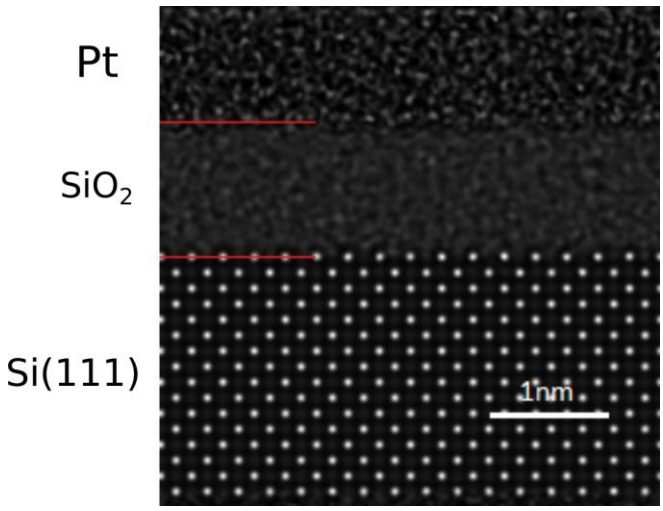

Figure 1. Simulated TEM image of a specimen containing amorphous platinum, amorphous SiO_2 and crystalline silicon. The actual interface positions are marked with red lines.

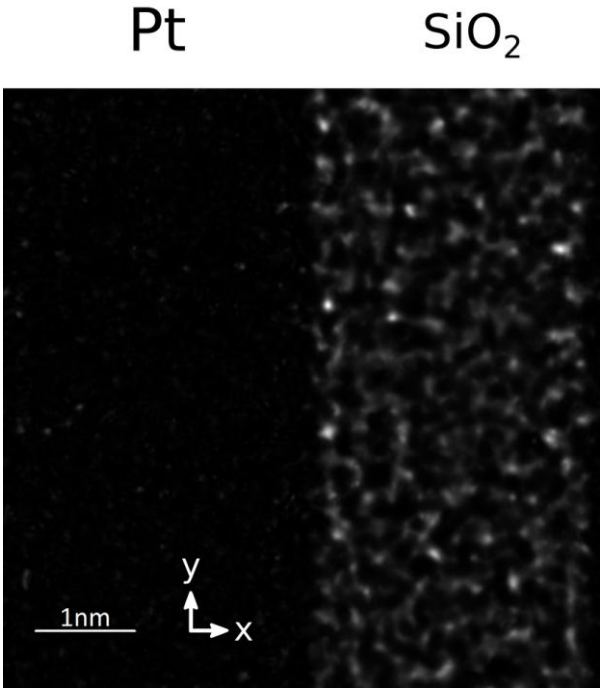

Figure 2. Simulated TEM image of a 50nm thick interface between amorphous platinum and amorphous SiO_2, assuming an aberration corrected microscope with an objective aperture half angle of 25mrad, an acceleration voltage of 300kV and spherical aberration coefficients of C_1 = 2Å, C_3 = -0.002mm and C_5 = 2.5mm.

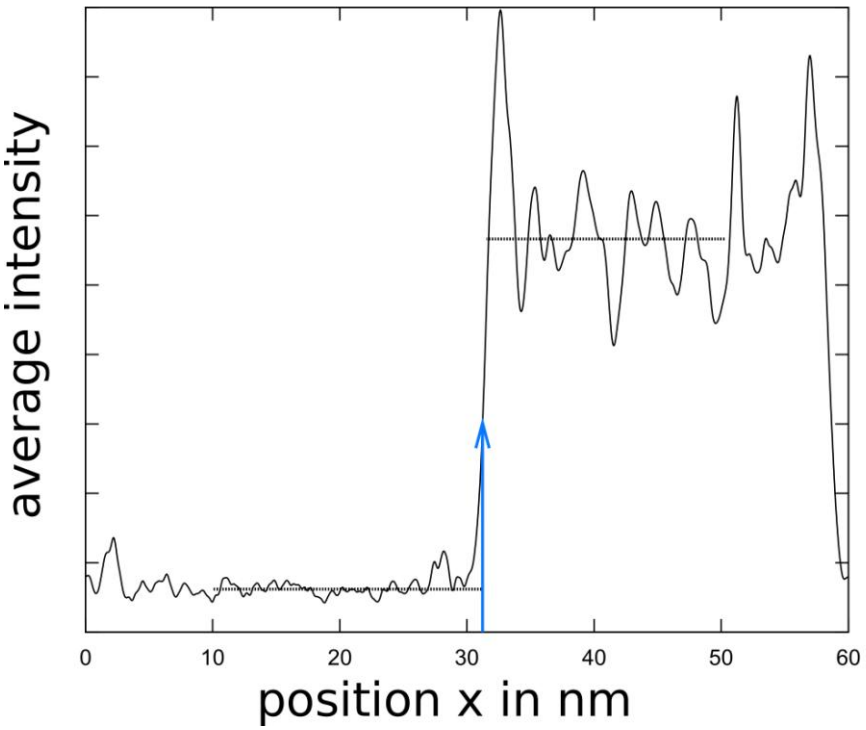

Figure 3. Intensity averaged along the y-direction in fig.2. The blue arrow marks the apparent interface position, whereas the actual interface is located at x = 30Å. The dashed lines show the average intensities in the Pt and SiO_2 image domain.

Quantitative Techniques and Image Simulation in TEM/STEM, SEM and Diffraction

IM2.P066
Retrieving low frequencies in exit-wave reconstructions from focal series through total-variation-like regularization of the error function

W. Van den Broek[1], X. Jiang[1], C. T. Koch[1]

[1]Ulm University, Ulm, Germany

wouter.vandenbroek@uni-ulm.de

It has long since been realized that the action of the objective lens in transmission electron microscopy or in optical microscopy can be undone, thus revealing the phase and amplitude of the electron or optical wave as it exits the specimen. Especially the phase information is of interest as it bears a close resemblance to the specimen's projected potential or refractive index.

Conventionally, this so-called exit-wave reconstruction uses a series of defocused images in a Gerchberg-Saxton-type algorithm [1]. These iterative algorithms come in many varieties, but all of them propagate the intermediate solution back and forth through the objective lens, while in some way enforcing the constraints that (*a*) in the lens' defocus planes, the wave amplitudes must equal the measured amplitudes and (*b*) waves that are back-propagated from the defocus planes to the object's exit plane must be equal. The solution's higher frequencies are readily retrieved, but the lower frequencies can take tens of thousands of iterations [2].

Recently, IDPS (inverse dynamical photon diffraction) was developed according to the principles of [3,4] to operate on optical data. IDPS is a 3D reconstruction algorithm that takes the propagation of the optical wave through the sample and the objective lens into account exactly. IDPS retrieves the phase by iteratively minimizing an error function through gradient descent optimization. In the remainder of this abstract, the object is restricted to one slice and is thus effectively 2D.

Since IDPS explicitly minimizes an error function, it becomes possible to regularize the solution by adding a regularization term, E_R, and thus select for alternate solutions with enhanced lower spatial frequencies.

In this abstract, E_R is set to the L1-norm of the result of the so-called DXDY and DR filters applied to the solution, in order to promote sparse edges. As a test case a focal series of unstained mouse tissue is chosen, recorded with an optical microscope. The wavelength is 0.55 µm, the numerical aperture is 1.20 and the focus values range from -4.4 µm to 4.4 µm with 0.22 µm steps.

DXDY implements the sum of the x- and the y-derivative, evaluated as central finite differences of 8^{th} order accuracy. This significantly reduces artifacts and the lower frequencies are retrieved better (Fig. 1). However, also a slight artificial ripple, overlaying the entire image, is observed.

This inspired the RD filter, which is composed of random but known values. The expectation value of the absolute value of this filter is approximately proportional to the local standard deviation of the image. Therefore, the RD filter can be thought of as a linear approximation to the total variation [5], which is known for selecting for solutions that are sparse in gradient-space. The RD filter yields results that are close to that of DXDY, but no ripple effect is observed since it is less likely to have a strong preferential direction (Fig. 1). [6]

1. RW Gerchberg and WO Saxton, Optik **35** (1972), p. 237.
2. C Ophus, T Ewalds, Ultramicroscopy 113 (2012), p. 88.
3. W Van den Broek, CT Koch, Phys. Rev. Lett. **109** (2012), p. 245502.
4. W Van den Broek, CT Koch, Phys. Rev. B **87** (2013), p. 184108.
5. EJ Candes et al., IEEE Transactions on Information Theory **52** (2006), p. 489.
6. The authors acknowledge the Carl Zeiss Foundation and the German Research Foundation (DFG, Grant No. KO 2911/7-1). The authors thank Carl Zeiss Microscopy GmbH and Carl Zeiss Corporate Research and Technology for providing the experimental optical microscopy data.

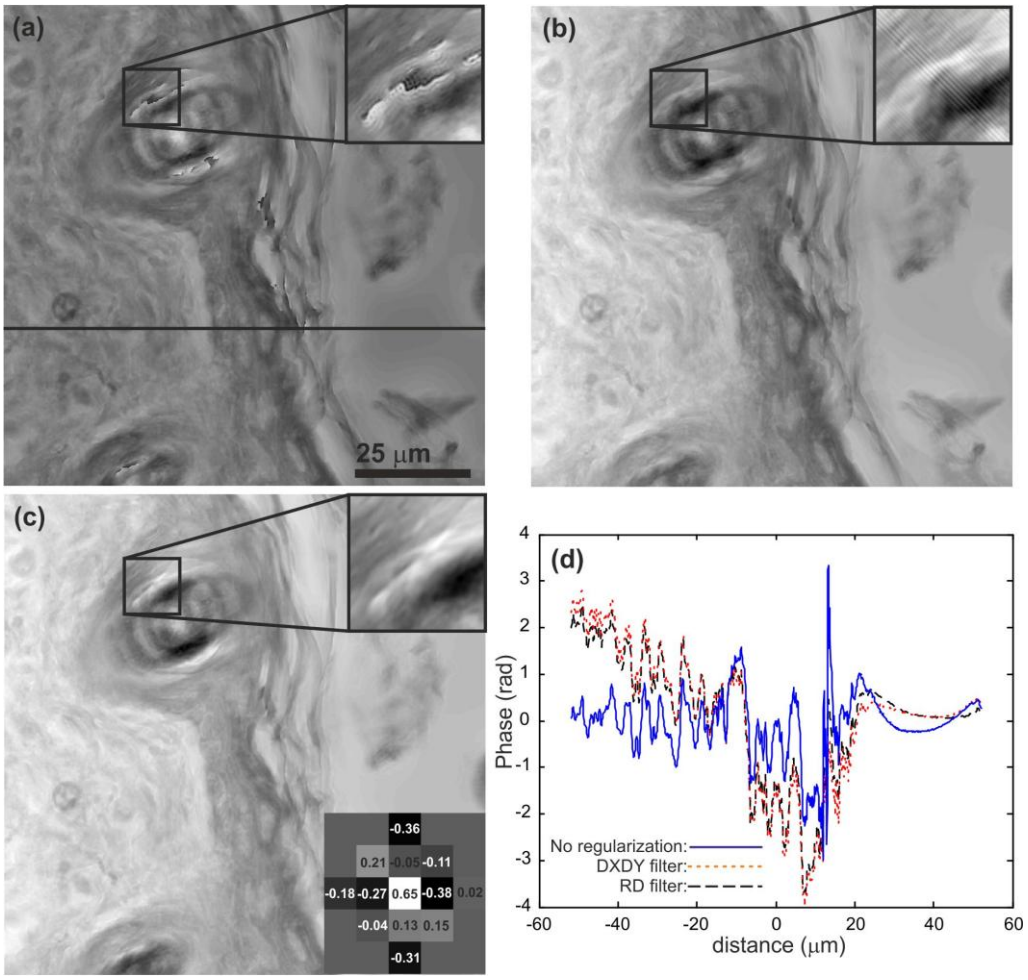

Figure 1. (*a*): Reconstructed phase without regularization (R factor: 3.5%), note the artifacts. (*b*): DXDY regularization (R factor: 3.4%), the artifacts of *a* have disappeared, but there is an overlaying ripple. (*c*): RD regularization (R factor: 3.3%), the ripple effect has disappeared, RD filter in the lower right. (*d*): Profiles along the line indicated in *a*.

Quantitative Techniques and Image Simulation in TEM/STEM, SEM and Diffraction

IM2.P067
Precession-based variable conical dark field-imaging for solving materials science problems

H. Kirmse[1], E. Steeg[1], S. Kirstein[1], J. Rabe[1]

[1]Humboldt-Universität zu Berlin, Institut für Physik, Berlin, Germany

holm.kirmse@physik.hu-berlin.de

Dark-field imaging is widely used in both, TEM and STEM mode. In STEM mode the beam is focused into a tiny probe scanned across the area of interest. A corresponding image provides essential information on defects and mass/thickness distribution. Crystalline nanoparticles (NPs) of different structure can be visualized independently of their orientation. In order to separate them, a technique performed in TEM mode is proposed here. Utilizing beam precession [1], conical dark-field imaging can be realized at any TEM by either an appropriate Digital Micrograph script [2] or by attaching an ASTAR system providing additional options like scanning nano-beam diffraction [3]. For this work a JEOL2200FS equipped with an ASTAR system was used.

When tilting the incident beam by α and inserting the objective aperture, the direct beam is blocked and electrons scattered into a certain angular interval can pass forming a dark-field TEM image (see Fig. 1a). The size of the objective aperture defines the angular resolution. In case of JEOL 2200FS used for this experiment and operated at 200 kV, the angular resolution is about 0.05° (0.44 mrad) for the smallest objective aperture. Hence, diffraction rings of an angular distance larger than this value can be separated. In Fig. 1a two diffraction rings are symbolized by dotted-dashed yellowish lines where only the inner one is allowed to enter the image plane. In order to collect all electrons scattered into a given angle in all azimuthal directions, the incident beam is fully precessed. In the resulting dark-field image all crystalline areas show up, from which electrons are diffracted into this ring. Exploiting the technique even further, the precession angle can be changed from 0° up to a maximum value of 3° (about 26 mrad). By this, different diffraction rings can be selected for gaining information on, e.g., the presence of different crystalline phases or areas with superstructure reflections.

For a proof of principle, Ag NPs deposited on a carbon support film were investigated. Diffraction patterns for increasing precession angle are shown in Fig. 1b. The yellow circles indicate the size and position of the objective aperture inserted for conical dark-field imaging. Carefully inspecting, e.g., the pattern for α = 0.19°, additional circles are seen (one is highlighted in green). The individual 220 reflections of Ag are forced by precession to move along these circles, having the same diameter like the centered bright circle of the direct beam. For α = 0.19° all 220 circles intersect within the area selected by the objective aperture. Hence, crystalline Ag NPs of different azimuthal orientations show up in the corresponding conical dark-field image of Fig. 1c. Similarly, NPs are seen for α = 0.13° due to intersecting 111 circles. Superimposition of both images (not shown) yields that none of the NPs contribute to both of them, which proves a statistical orientation distribution of the Ag NPs.

Applying a precession angle of α = 0.10° only electrons which are scattered thermally diffuse contribute to the image. Here, the image intensity is dominated by the carbon film. This is of big advantage for imaging of weak phase objects. For these, contrast is usually gained by a large defocus of about 1 µm leading to strong Fresnel fringes at interfaces. Another approach is to introduce an annular aperture at the back focal plane of the objective lens [4]. But utilizing conical dark-field imaging discussed here, a strong contrast is gained already for in focus condition and without limiting the functionality of the objective aperture.

1. R. Vincent, P.A. Midgley, Ultramicroscopy **53** (1994) 271
2. D. Zhang; P. Oleynikov, S. Hovmöller, X. Zou, Z. Krist. **225** (2010) 94
3. D. Viladot , M.Veron, M. Gemmi, F. Peiro, J. Portillo, S. Estrade, J. Mendoza, N. Llorca-Isern, J. Micr. **252** (2013) 23
4. F. Leroux, E. Bladt, J.-P. Timmermans, G. Van Tendeloo, S. Bals, Microsc. Microanal. **19** (2013) 629
5. Part of this work is supported by the DFG in the framework of CRC951 HIOS.

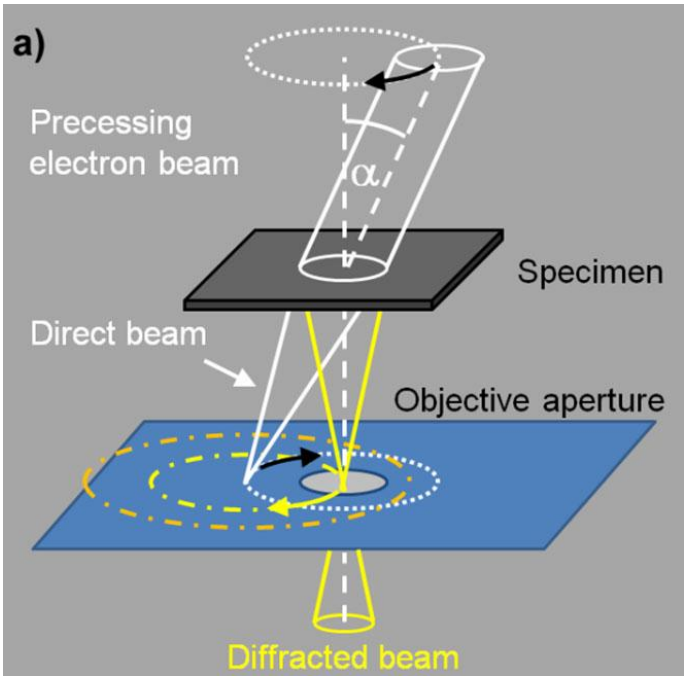

Figure 1. Precession-based variable dark-field TEM imaging: a) sketch of ray paths, b) series of diffraction patterns of Ag NPs on carbon support film for increasing precession angle α, c) series of dark-field images for increasing precession angle.

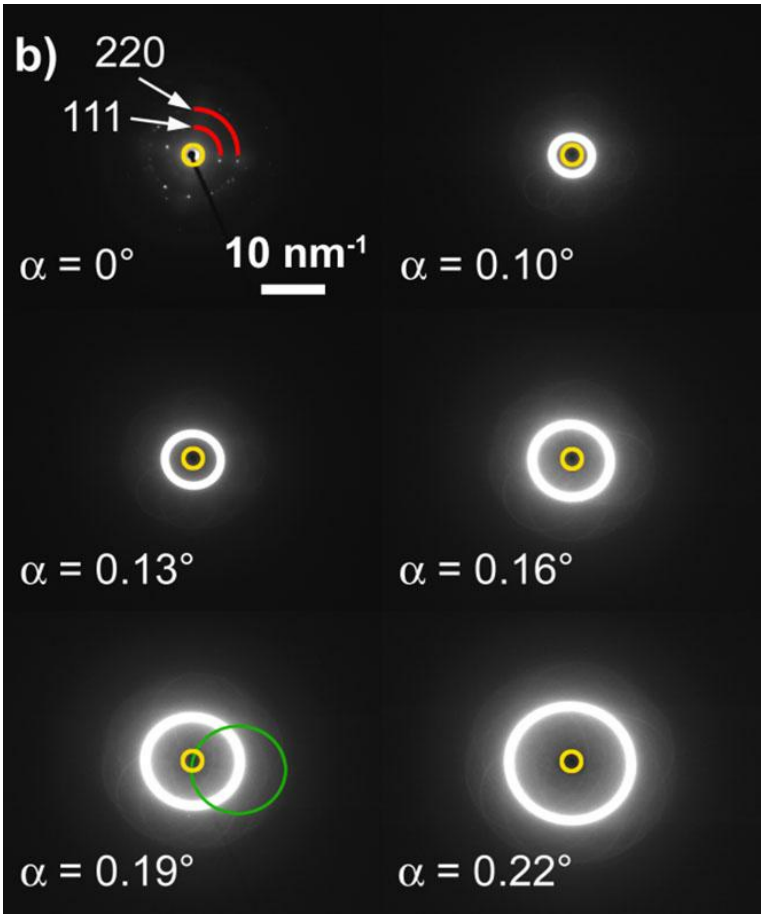

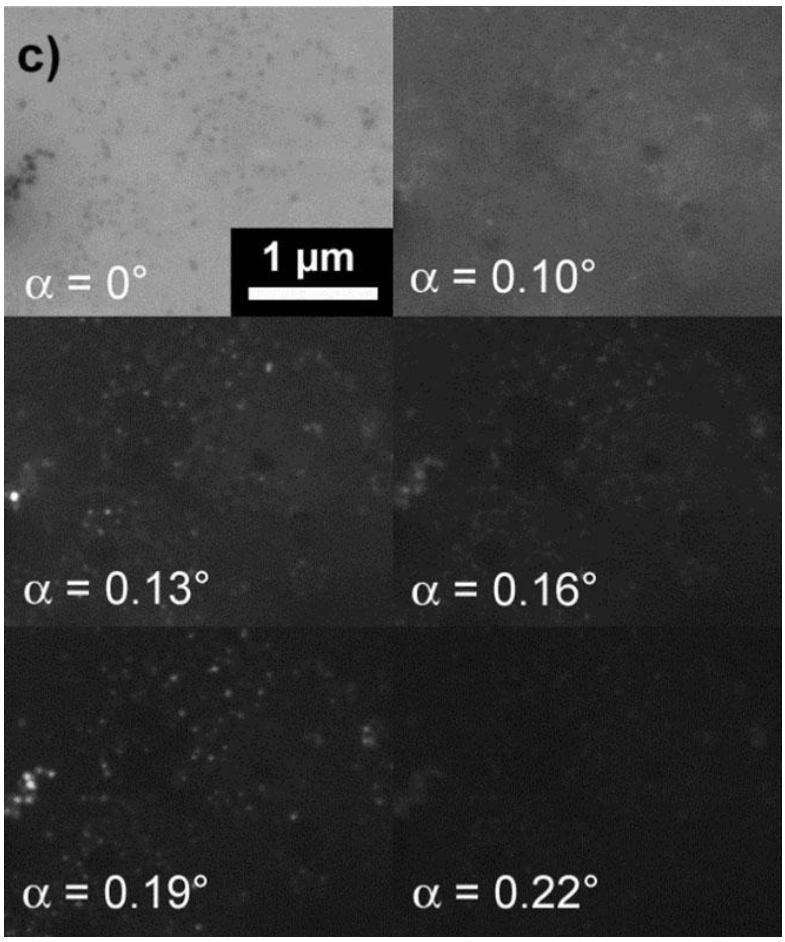
c)
1 µm
α = 0°
α = 0.10°
α = 0.13°
α = 0.16°
α = 0.19°
α = 0.22°

Quantitative Techniques and Image Simulation in TEM/STEM, SEM and Diffraction

IM2.P068
Illumination convergence semi-angle estimation using the inverse dynamical photon scattering framework

X. Jiang[1], W. Van den Broek[1], J. Müller[1], C. Koch[1]

[1]Ulm University, Experimental Physics, Ulm, Germany

xiaoming.jiang@uni-ulm.de

The influence of the illumination convergence semi-angle, α, on transmission electron microscopy (TEM) or optical microscopy can be modeled by a convolution of the intensity with a Gaussian whose width is a function of α and defocus [1]. When focus variation, or a focal series, is used for retrieval of the phase of the electron or optical exit wave, this effect cannot be ignored; especially in the optical case, where α can be much larger than in TEM. In this abstract α is estimated using the inverse dynamical photon scattering (IDPS) framework [2], which is based on the principles from [3, 4] , thus taking the propagation of the optical wave through the sample and the objective lens into account exactly. α is estimated simultaneously with the amplitude and the phase of the exit wave.

This method is demonstrated on data acquired on a Carl Zeiss AxioVert 200M optical microscope, fitted with an LED-based illumination system developed in-house (wavelength 525 nm). The wing of a fruit fly (drosophila) was mounted on a copper TEM-grid and used as a sample (experimental condition: defocus -70 - 70 µm with a step of 10 µm, numerical aperture 0.3, magnification 10×). Estimation with the conjugate gradient [5] and iRProp+ [6] algorithms yielded similar results: 7.96° and 7.79°, respectively.

The quality of the reconstructed phase was evaluated by normalized sum of squared difference (SSD) and the R factor. Fig. 1 plots the normalized SSD as a function of number of iterations. The R factors with and without simultaneous α-estimation are 4.28% and 5.98%, respectively. The difference in quality can also be directly observed: in Fig. 2 (b) the reconstructed phase with α-estimation resolves more details than the reconstructed phase assuming perfect spatial coherence in Fig. 2 (c); in Fig. 2 (f) the recorded image at zero defocus is compared to the images, (d) and (e), at zero defocus that are generated from the reconstructed phase. In conclusion simultaneous α-estimation improves the performance of the reconstruction.

1. CT Koch. Ultramicroscopy, 108(2008), p. 141.
2. W Vanden Broek, X Jiang, C Husemann and CT Koch. An abstract submitted in the same Conference Volume.
3. W Van den Broek and CT Koch. Physical review letters, 109(2012), p.245502.
4. W Vanden Broek and CT Koch. Physical Review B, 87(2013), p.184108.
5. SJ Wright and J Nocedal. Numerical optimization, Springer New York, 1999.
6. C Igel and M Hüsken. In Proceedings of neural computation (2000), p.115.

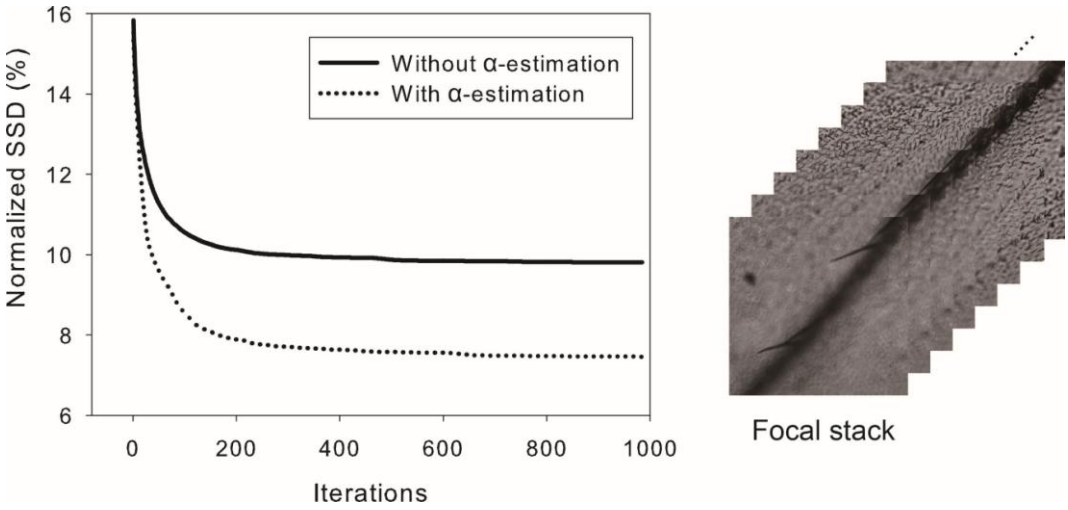

Figure 1. Normalized SSD with (dashed line) and without (full line) simultaneous α-estimation calculated from a focal stack of 15 images.

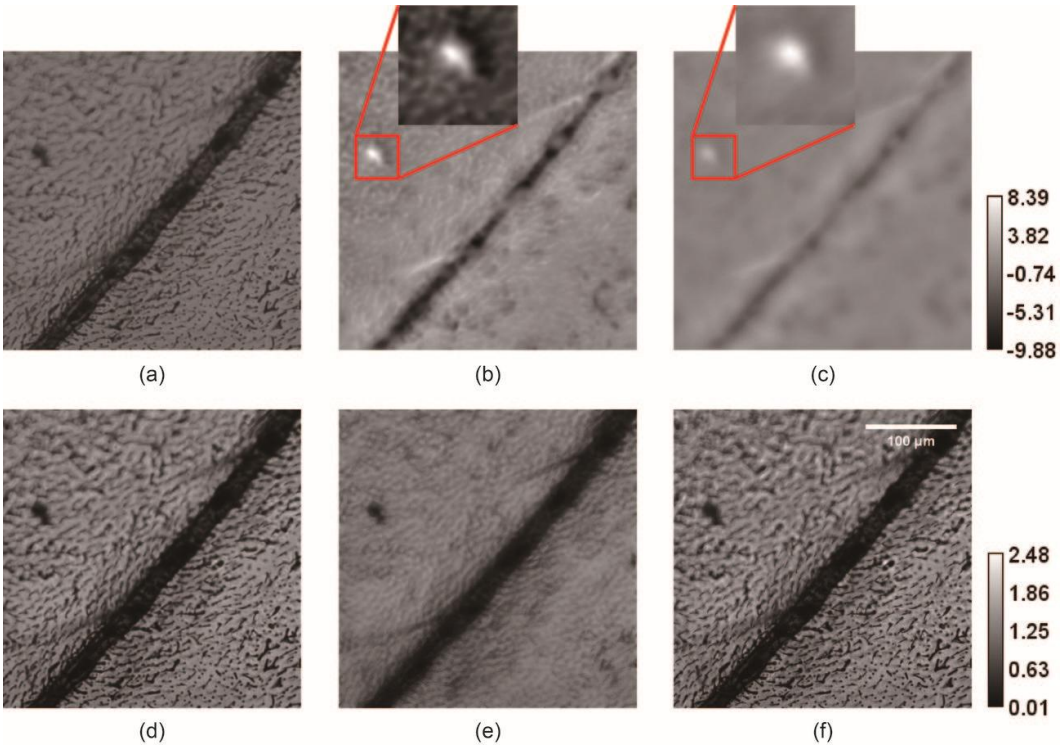

Figure 2. First row: (a) reconstructed amplitude with α-estimation, (b) phase with α-estimation, and (c) phase without α-estimation. Second row: (d) image generated from the reconstructed phase with α estimation, (e) without α-estimation, and (f) the measured image at zero defocus. (b) and (c) share the colorbar from the first row; (a), (d), (e) and (f) share the colorbar from the second row.

Quantitative Techniques and Image Simulation in TEM/STEM, SEM and Diffraction

IM2.P069
Calculations of elastic and inelastic scattering processes of relativistic electrons in oriented crystals

D. Hinderks[1], H. Kohl[1]

[1]Westfälisches-Wilhelms-Universität, Physikalisches Institut, Münster, Germany

dieter.hinderks@uni-muenster.de

Many modern electron microscopes operate at acceleration voltages up to several hundred kV. The accelerated electrons thus reach velocities approaching the speed of light. Therefore the scattering processes have to be treated relativistically. We focus on inelastic scattering in crystals.

In a non-relativistic treatment a periodic potential is used to describe the crystal. The periodic potential of a crystal provides Bloch waves as solutions of the Schrödinger equation. The scattering process is mathematically described using matrix elements between product states of such Bloch waves multiplied by the objects wave function [1].

We have extended this non-relativistic treatment to relativistic electrons. The Schrödinger equation is replaced by the relativistic Dirac equation. For a periodic potential the solution of the Dirac equation provides us relativistic four component Bloch waves (Fig. 1). Spin-up and spin-down electrons are described by two different four components of this wave function (Fig. 2). Inserting the periodic potential and Bloch wave ansatz into the Dirac equation we obtain equations which allow us to calculate the excitation coefficients and the Fourier coefficients of the wave function using a matrix diagonalization. Due to the four component wave functions we thus obtain four equations to calculate this coefficients. But only one of these equations yields a nontrivial solution, which is needed to diagonalize this matrix.The formalism is similar to the non-relativistic case. Using Fermis golden rule and separating the coordinates of the incident electron from those of the atom electrons, We can view the incident electrons as a perturbation which leads to a transition of the atomic electrons from an initial to a final state. In our approach we use the relativistic propagator theory where the atomic electrons are seen under the influence of a scalar and a vector potential generated by the fast incident electrons via their charge and current. Therewith we obtain an expression for the scattering matrix in first order Born approximation (Fig. 3).Retardation of the electro-magnetic field is automatically included in this relativistic treatment. This approach has previously been used for relativistic plane waves [2]. In our formalism we substitutione the plane waves by Bloch waves for crystalline materials. Consequently we have to evaluate the matrix elements considering different sums over reciprocal space and the different single relativistic Bloch waves.

1. A. Weickenmeier and H. Kohl, Phil. Mag. B60 (1989) 467.
2. R. Knippelmeyer et al.,Ultramicroscopy 68 (1997) 25-41.

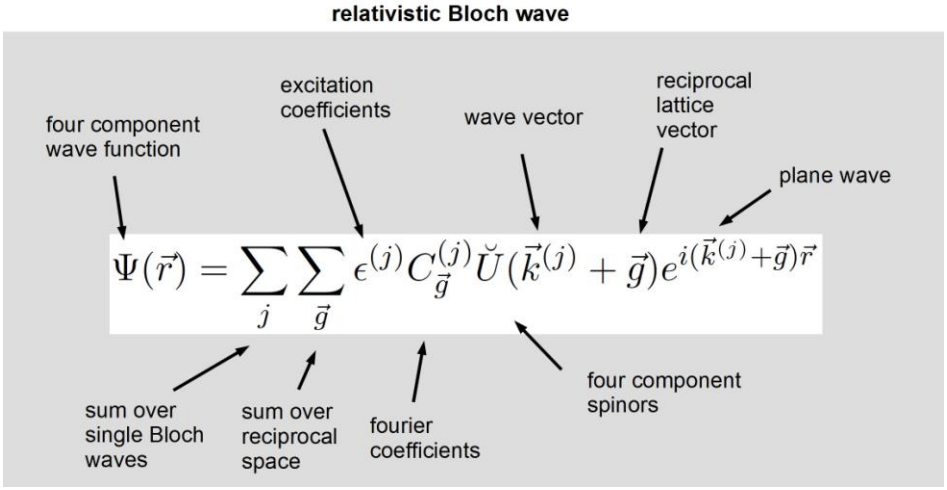

Figure 1. Relativistic Bloch wave.

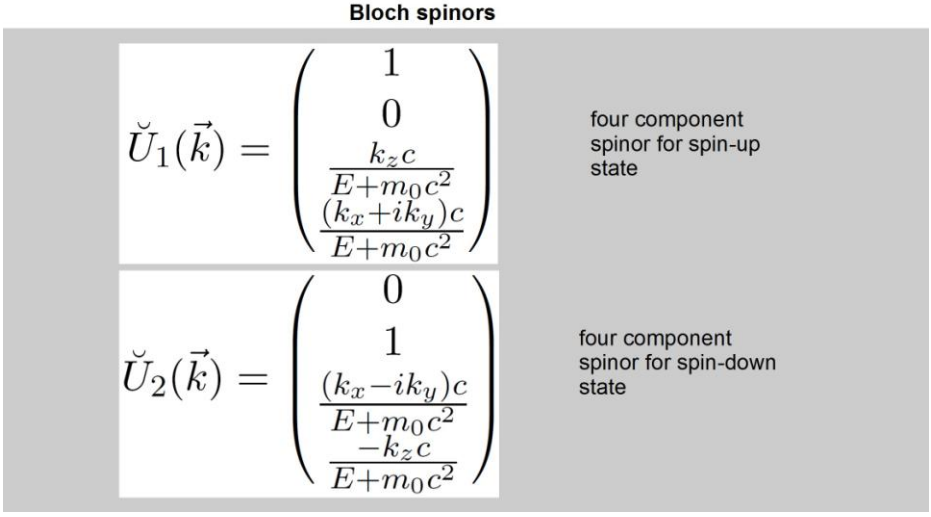

Figure 2. Bloch wave spinors.

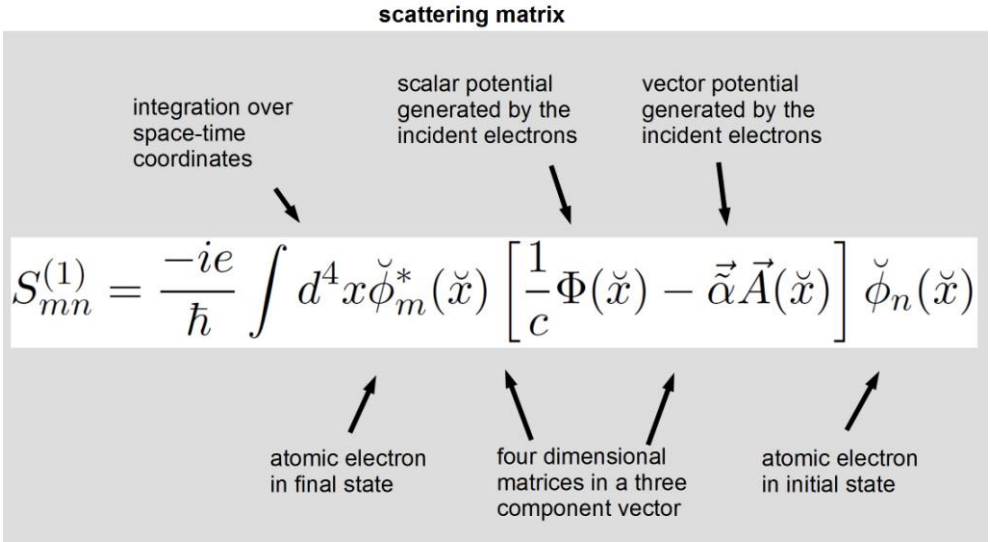

Figure 3. Scattering matrix.

Quantitative Techniques and Image Simulation in TEM/STEM, SEM and Diffraction

IM2.P070
Electron diffraction at semiconductor heterointerfaces and its implications to the holographic potentiometry of semiconductor devices

M. Narodovitch[1], T. Niermann[1], M. Lehmann[1]

[1]Technische Universität Berlin, Institut für Optik und Atomare Physik, Berlin, Germany

michaeln@physik.tu-berlin.de

The phase of an electron wave transmitted through a thin sample can be reconstructed in the transmission electron microscope (TEM) using electron holography. With the simple approach $\varphi(x,y) = \sigma \cdot V(x,y) \cdot t(x,y)$ (1) the local phase shift of the electron wave is determined by the average object potential along the electron beam at position (x,y) with local sample thickness t [1].

In a state-of-art TEM a good precision of the phase measurement can be achieved due to the superior signal-to-noise ratio. Nevertheless the accuracy of holographic potentiometry, i.e. the actual relationship between measured phase and the actually interesting physical quantities, is still limited by experimental uncertainties when evaluating the phase profile. Due to the effects like e.g. beam induced carrier redistribution and electron diffraction, this uncertainties concerns not only the sample thickness t but also the validity of the whole approach [2].

Especially when heterojunctions like e.g. multi quantum wells are mapped, a step-like change of the mean inner potential leads to electron diffraction at the heterointerface. In this contribution, we will show how an abrupt change of the object potential V affects the phase profile and we will analyze the systematic error when the phase is only assumed to be proportional to V according to equation (1). Furthermore, we will discuss the impact of the actual sample tilt and defocus.

As a model structure, a GaN / $Al_{20}Ga_{80}N$ heterojunction is chosen with a mean inner potential of 16.8 V and 16.3 V, respectively [3]. We use the high energy approximation of the Schrödinger equation to compute the exit wave, given a plane 300 kV incident wave [4]. Possible surface effects are neglected.

Figure 1 illustrates the simulation setup. The width W is defined as the 10 - 90% steepness of the potential step. The angle reflects a small tilt normally applied in the holographic experiment in order to obtain kinematic diffraction conditions. For the simulation of the actual focus plane we use the standard Fresnel propagator. Apart from that no further aberrations are simulated. The systematic error is defined as the difference between the given potential profile and the extracted potential profile using eq. (1).

Exemplary results for an untilted sample are shown in Figure 2. While the input potential profile changes only in a small area around the heterojunction (W = 0.25 nm), the phase profile of the exit wave appears to be broadened and shows considerable oscillations due to diffraction at the heterojunction. Assuming the potential profile to be proportional to the phase profile leads to a systematic error of up to 0.06 V in the vicinity of the 100 nm thick heterojunction. The error even increases when the sample becomes thicker. This error decreases when the sample is tilted or the steepness W is broaden.

All in all we show that the electron diffraction has a considerable influence to the holographic measurement if heterojunctions are mapped with a resolution better then 1 nm. For the evaluation of the local potential with eq. (1) a quantitative estimate of the expected error will be given. Especially when the second derivative of the potential profile is used for charge density mapping the expected error might distort the measurement significantly.

1. H. Lichte, M. Lehmann, Annu. Rev. Modern Physics 71 (2008) 016102
2. J. B. Park, T. Niermann et. al., Appl. Phys. Lett. 105 (2014) 094102
3. P. Kruse, M. Schonwalter, D. Laemon et. al., Ultramicroscopy 106 (2006) 105-113
4. De Graef, M. *Introduction to conventional electron microscopy.* Cambridge University Press (2003)
5. We kindly acknowledge support from the DFG within the Collaborative Research Center 787, project A4.

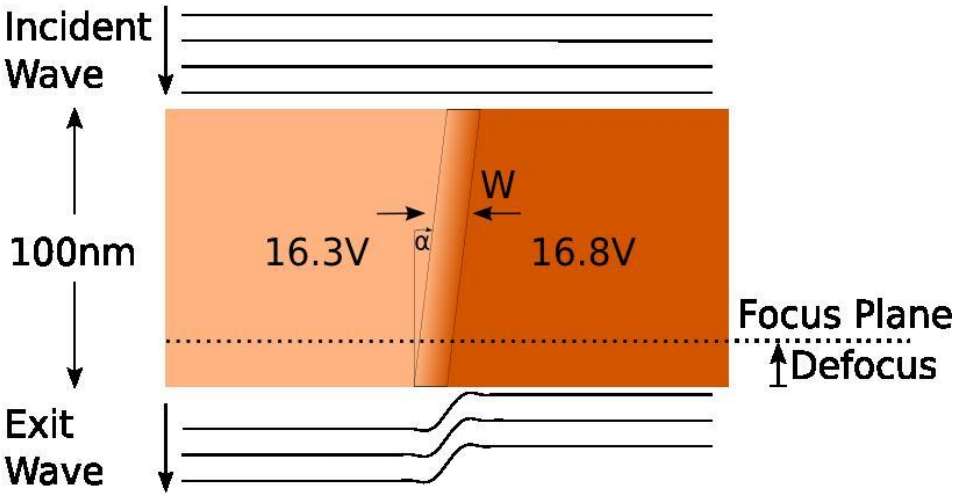

Figure 1. The simulation setup. A heterojunction is illuminated by a plane electron wave with an energy of 300kV. As the wave propagates through the sample the phase of the wave shifts depending on the material. Finally the wavefront leaves the sample and is imaged by an ideal imaging system.

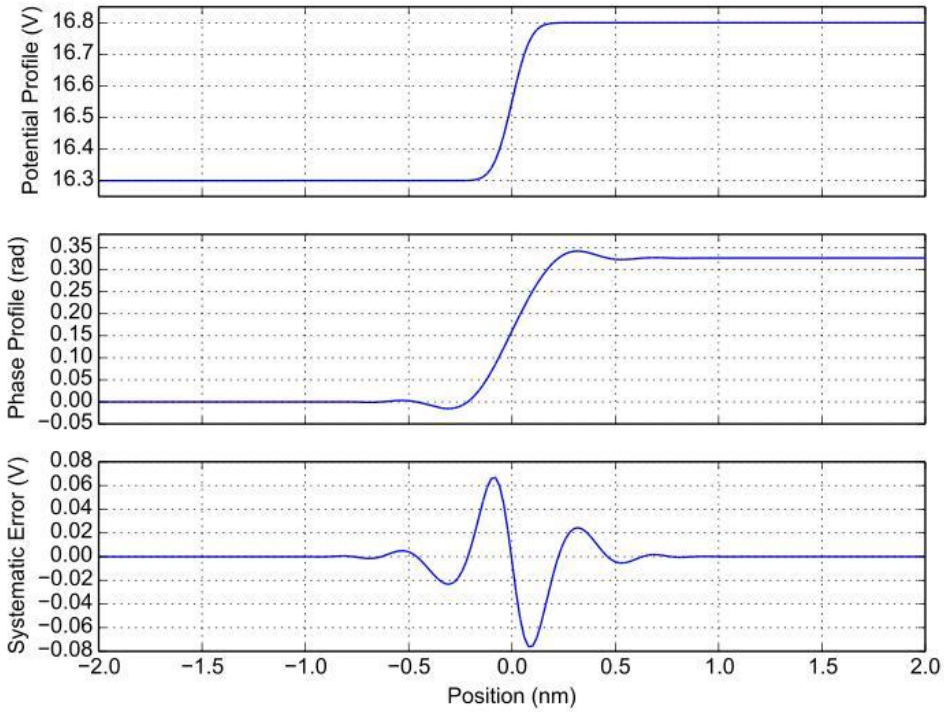

Figure 2. Simulation results for the case of an untilted (α=0°) 100nm thick sample. The input potential profile has a 10-90% width of W = 0.25nm. For the image of the phase profile the focus plane is set to the exit surface. Using the approach (1) a potential profile and finally the systematic error was computed from the phase profile.

Quantitative Techniques and Image Simulation in TEM/STEM, SEM and Diffraction

IM2.P071
Comparing thickness determination methods of TEM lamellas

M. Hartmann[1], J. Biskupek[1], D. Geiger[1], U. Kaiser[1]

[1]University of Ulm, Central Facility of Electron Microscopy, Electron Microscopy Group of Materials Science, Ulm, Germany

manuel.hartmann@uni-ulm.de

Exact thickness determination of TEM samples is a long pursued task (see e.g. [1]) and it is a necessity for quantitative image analysis. Therefore in this work we investigate the accuracy, reliability, thickness range and application to various materials by comparing different TEM methods such as convergent beam electron diffraction (CBED), electron energy loss spectroscopy (EELS) and mass thickness contrast in HAADF-STEM.

In practice, thickness measurement comparison implies the need of a reliable reference thickness, which can be determined by CBED or using a special well-known sample geometry. The commonly applied CBED t wo-beam condition method, as proposed by Kelly (1975) in [1] is only practicable for a thickness range up to 300 nm. Another method for thickness determination is the determination of the inelastic mean free path (IMFP) from EELS experiments. However, the IMFP requires calibration using CBED or parameterised models (e.g. [2, 3]) unless the thickness can be calculated via a well-known sample geometry. A third approach is the mass thickness contrast, which requires careful characterisation of the HAADF detector, image calculations and also the thickness calibration via a well-known sample geometry [4].

In our work, we applied a novel computer-aided cross correlation approach which determines specimen thickness by quantitative pattern matching of simulated CBED patterns with experimental ones. Simulated CBED patterns were calculated with the Bloch-wave simulation tool MBFIT [5]. Due to quantitative cross-correlation, an accuracy of 2% for silicon was achieved as shown in figure 1a-d. This method is stable against convergent angle variations, slight mis-tilts and bending of the sample. This simplifies much the experimental work-flow of CBED pattern acquisition. Moreover, we acquired for all CBED patterns corresponding EEL spectra and calculated the IMFP using parameterised models, and finally compared thickness determination using both approaches. In general, EELS determined thicknesses are higher than those from CBED. For comparison, we also applied HAADF-STEM thickness measurements [4] using a wedge shaped silicon sample. However, these results overestimated the wedge gradient up to a factor 2, the origin of this mismatch is still under investigation.

Also the IMFP was measured directly without applying parameterised models using small MgO nanocubes, as in this case the thickness could be measured in the image because of the cubic shape. The high accuracy that was finally achieved for thickness measurements using EELS and CBED techniques for identical samples (e.g. Si test sample) allowed indirect determination of the thickness of the amorphous layer as well. This is possible because CBED is, unlike EELS, only affected by the crystalline part of the specimen.

1. Kelly, P. M., Jostsons, A., Blake, R. G. and Napier, J. G. (1975), Physica status solidi (a) 31, 771-780.
2. Malis, T., Cheng, S. C. and Egerton, R. F. (1988), Journal of Electron Microscopy Technique 8, 193-200.
3. Iakoubovskii, K., Mitsuishi, K., Nakayama, Y. and Furuya, K. (2008), Microscopy Research and Technique 71, 626-631.
4. Rosenauer A. et al. (2009), Ultramicroscopy 109(9), 1171 - 1182.
5. Tsuda, K. and Tanaka, M. (1999), Acta Crystallographica Section A 55, 939-954.
6. Acknowledgement. We are grateful to Sabine Grözinger and Jörg Bernhard for TEM sample preparation, and to Dr. Thorsten Mehrtens and Prof. Andreas Rosenauer for assist and help with HAADF-STEM thickness measurements.

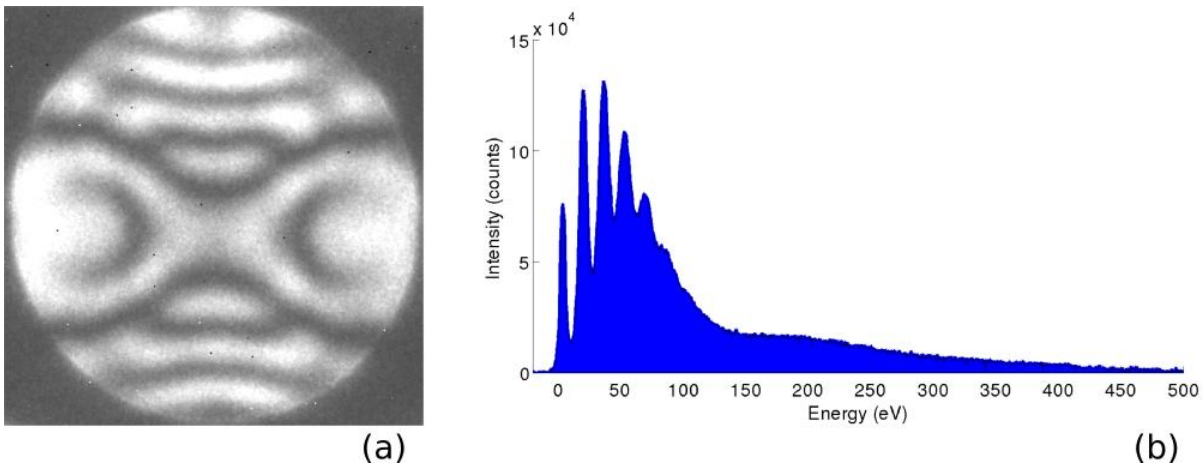

Figure 1. (a) Energy-filtered experimental CBED pattern of [110]-silicon at 300 kV. (b) EEL spectra obtained from the same sample position as the CBED pattern. Using the IMFP model from Iakoubovskii [3], the resulting thickness is 655 nm.

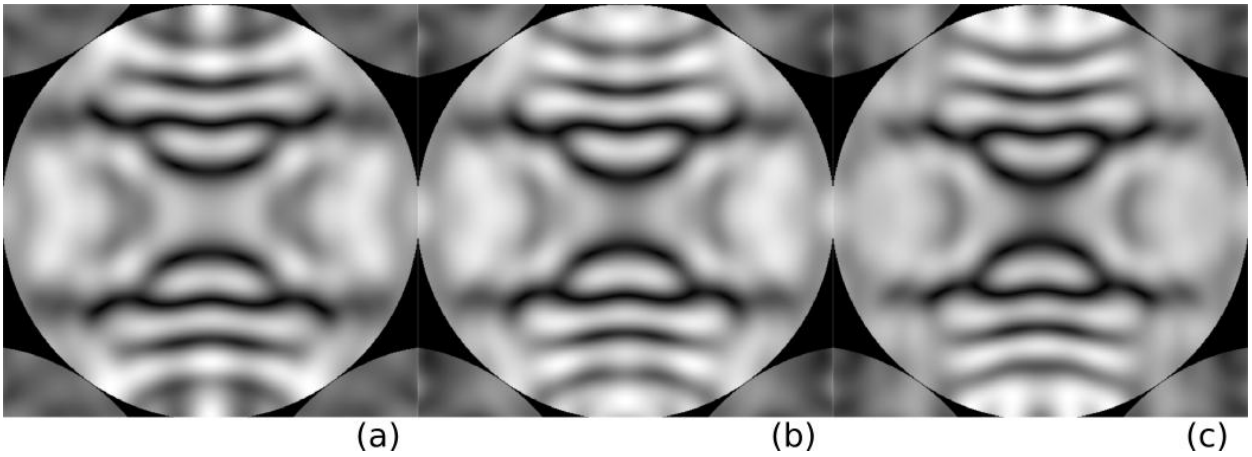

Figure 2. Simulated CBED patterns of [110]-silicon with thickness 575 nm (a), 595 nm (b) and 615 nm (c) at 300 kV. The experimental pattern (Figure 1a) matches to the simulated pattern with a thickness 595 nm using the novel computer aided quantitative pattern matching approach.

Quantitative Techniques and Image Simulation in TEM/STEM, SEM and Diffraction

IM2.P072
Influence of bulging due to elastic relaxation of thin TEM samples on HAADF intensities

L. Duschek[1], K. Jandieri[1], A. Beyer[1], J. Münzner[1], K. Volz[1]

[1]Philipps-Universität Marburg, Physics , Marburg, Germany

lennart.duschek@physik.uni-marburg.de

Transmission electron microscopy as well as scanning transmission electron microscopy (S)TEM is the method of choice concerning atomic resolution analysis of semiconductor devices. Often it is not possible to interpret the acquired experimental images directly without additional information of the structure. This may be either structural information of the multi-quantum-well (MQW) architecture or detailed knowledge of composition. Often, experimental data is compared to theoretical simulated images in order to extract quantitative data like atom distribution and local displacements. Thereto, HAADF (high angle annular darkf field imaging) in STEM can be used.

The first step of simulating electron microscopy images is to build a model and geometry of the sample. Since the modelling of real prepared TEM samples is very complex and therefore hardly possible, several assumptions have to be made to simplify the structure. To decide which assumption is acceptable and does not affect the final result, the influence of this specific assumption has to be studied carefully. For this purpose modelled test-systems are a good way to determine the key factors of the effect without the limitations of experimental disturbances.

In compressively strained QW structures of thin TEM samples, a bulging of the QW region on the surface can be found, due to elastic relaxation of the material. The amount of this effect depends on the sample thickness *t*, the QW thickness *d* as well as on the strain between substrate and QW material.

First, this contribution focuses on the dependencies of the bulging on the parameters *d* and *t* for a given material combination. Furthermore, the influence of this bulging effect in binary and ternary materials on simulated STEM HAADF images is investigated and quantified. This also gives a value for the error one makes when neglecting strain relaxation of the sample in quantitative analysis, especially at interfaces between materials.

Several GaAs QW structures embedded in GaP buffers were modelled varying *d* and *t* systematically. The structures were designed and relaxed with the software COMSOL Multiphysics [1] to take into account the strain and the elastic relaxation of the compressively grown structure, respectively. Afterwards STEM HAADF images of the relaxed TEM samples were simulated with the help of the STEMsim [2] code. For investigating what difference the influence of the bulging makes on the images, also reference simulations were performed without the elastic relaxation of the sample. After stabilizing the method on the binary compound GaAs/GaP, nitrogen atoms were added to the GaAs QW. The N-content was chosen to be between 2% to 7% to match existing samples The nitrogen was distributed either statistically or at specific locations in the structure to investigate the influence of surface bending combined with static atomic displacements evoked by nitrogen atoms also in dependence on its arrangement in the QW.

Figure 1 shows a simulated STEM image of the modelled interface between the GaP buffer on the left and the Ga(NAs) QW on the right without and with bulging (fig.2). Also the difference of the two images is displayed in figure 3. The simulated images show that the bulging has a significant effect on the atom positions as well as on the intensities of the atom columns.

This contribution will discuss the influence of the strain relaxation of thin TEM samples on quantitative evaluation of STEM HAADF images with a specific focus on accurate atom position resolution and composition quantification at interfaces.

1. Multiphysics (MP) software 4.3 (COMSOL Inc., Palo Alto, CA)
2. A. Rosenauer, M Schowalter, Microsc. of Semicond. Materials 2007, Springer Proceedings in Physics Vol 120, pp 170-172

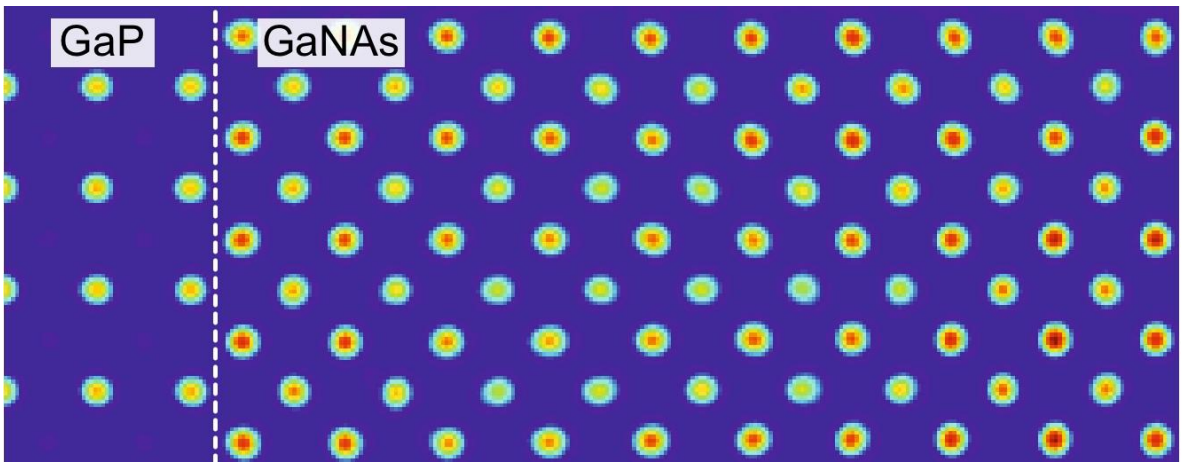

Figure 1. Simulated STEM HAADF image of modelled GaP/GaNAs interface with bulging.

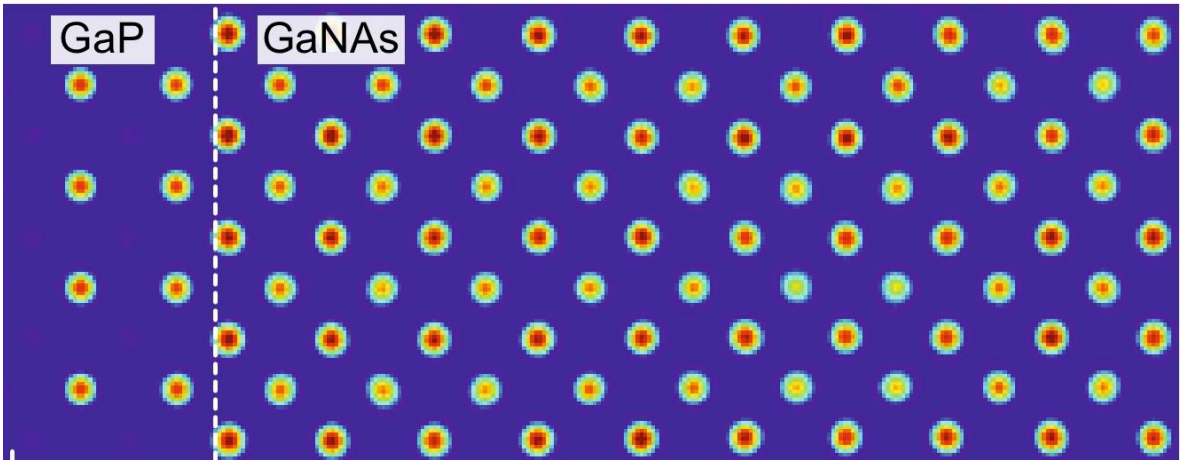

Figure 2. Simulated STEM HAADF image of modelled GaP/GaNAs interface without bulging.

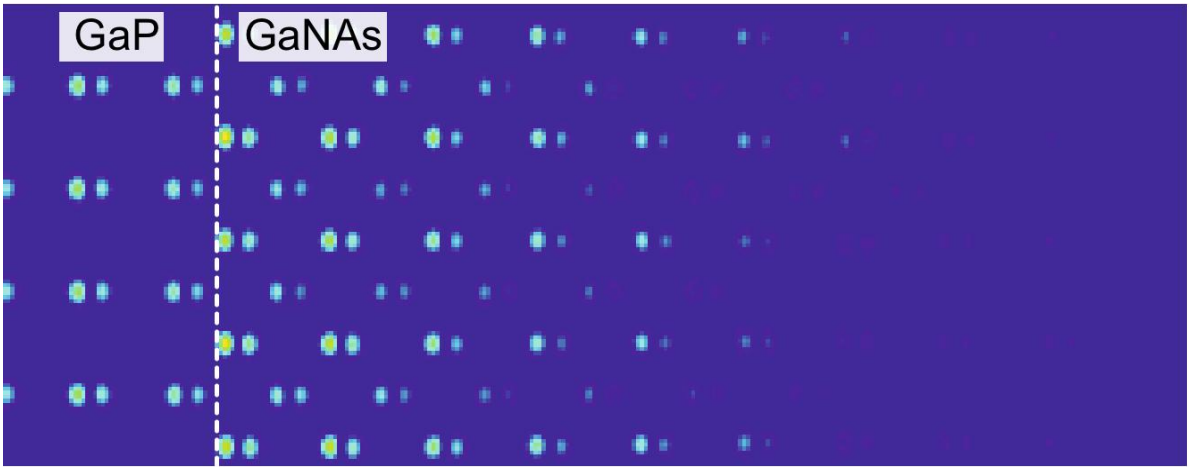

Figure 3. Intensity difference between figure 1 and figure 2.

Quantitative Techniques and Image Simulation in TEM/STEM, SEM and Diffraction

IM2.P073
Matching HRTEM micrographs with calculations

T. Niermann[1], M. Lehmann[1]

[1]Technische Universität Berlin, Institut für Optik und Atomare Physik, Berlin, Germany

niermann@physik.tu-berlin.de

With modern aberration corrected transmission electron microscopes it is possible to resolve structures at atomic resolution on an everyday basis. Depending on the concrete method used, different signals can be measured at this resolution. Even when concentrating only the coherent signals, different kinds of interference patterns can be recorded, revealing different aspects of the problem under study. Here, we will limit ourself to focal-series of HRTEM images and wave functions as reconstructed by off-axis holography. The later case has the advantage of a linear information transfer, it has the disadvantage of a rather noisy signal. Focal series are less noise-limited, however, they have the drawback of non-linear contrast formation, and thus requires multiple images with different transmission properties in order to record the full information resolvable by the microscope and lack of low spatial frequency transfer. Furthermore, this comes along with a higher sensitivity to microscope parameters like envelope functions and aberrations, which by themselves are only known to a certain degree.

Eventually the goal is a comparison of structure models with experimental data obtained with these fine microscopes. Within such an evaluation scheme, the precision of the structure parameters will depend on the amount and kind of noise in the data and the influence of the uncertainties in exactly these imaging parameters. The estimation of the imaging parameters can be done in image regions of known structure via matching these with image calculations [1].

For this estimation we combined exit-wave calculations by the Blochwave method (as shown in Fig. 2) and Multislice method (not shown here) and image calculations with a multi-parameter fit. Optimizable parameters include structural parameters, like specimen tilt, specimen thickness, and strain and microscope parameters like initial electron flux, aberrations, and image spread. We will discuss the precision of these parameters by observing the variations across different choices of initial guesses and investigated areas. Additionally instabilities like specimen drift between exposures as well as biprism drifts/instabilities in the case of off-axis holography must be fitted.

A comparison between experimental focal series and calculation in the case of a 3.2 nm thick ScN crystal alongdirection is shown in Figures 1 and 2. The full series consisting of 20 micrographs was used for the fit, only a subset of the series is shown. For most focus values a good match is achieved. However, small deviations can be noticed for those focal values, which result in a weak transfer of the {111} beams (e.g. at -0.9 nm). The contrast in these micrographs is more dependent on higher order beams, and thus is more sensitive to higher order aberrations and envelope functions.

1. G. Möbus, Structure Determination by Quantitative HRTEM, in High-Resolution Imaging and Spectrometry of Materials, Springer (2003)
2. Support by the DFG within SFB 787 is kindly acknowledged.

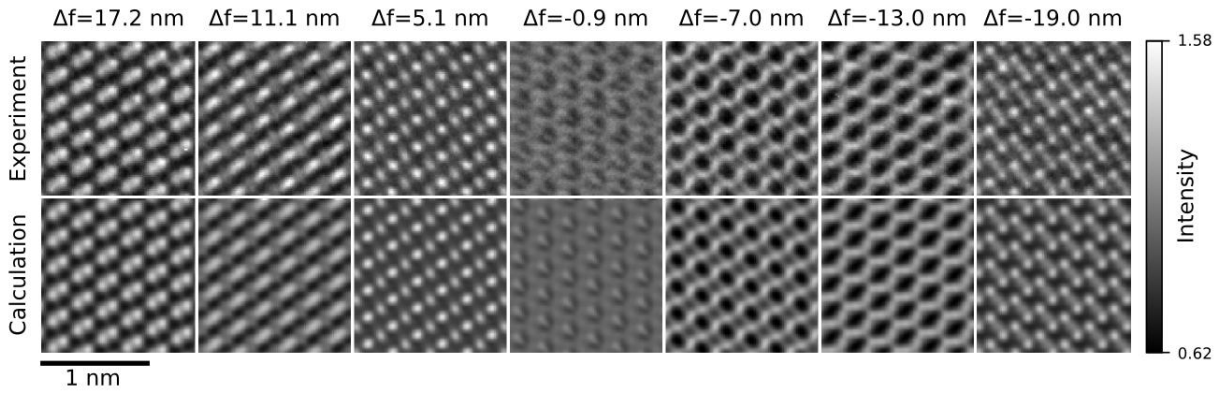

Figure 1. Comparison between experimental HRTEM focal series and calculation of a ScN crystal along direction. The positions of the individual atom columns is easily noticeable in the image with 5.1 nm defocus, where the brighter dots correspond to the Sc columns, while the less bright dots correspond to the N columns. Due to specimen drift the image regions are slightly shifted with respect to each other.

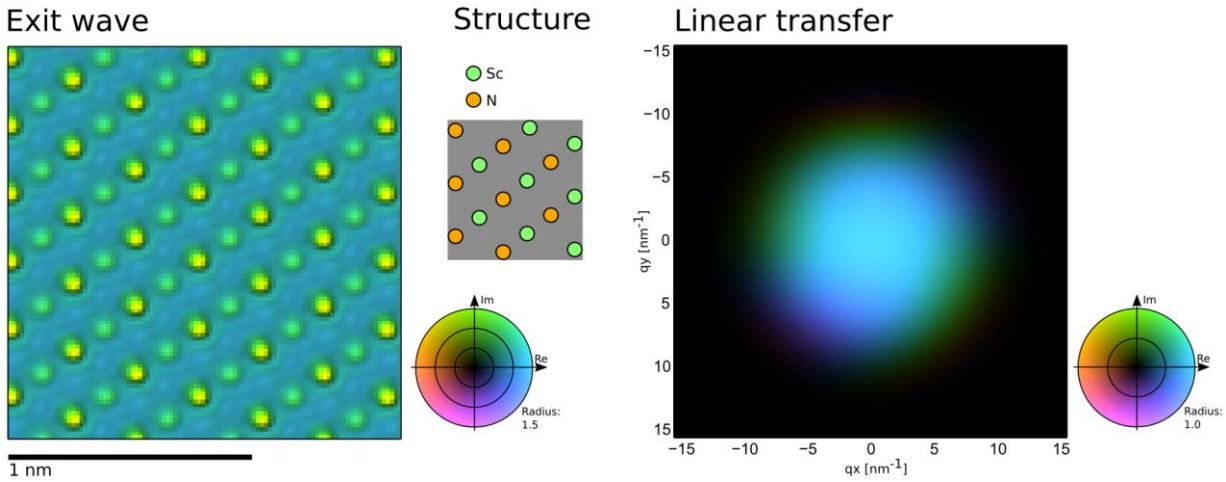

Figure 2. Left: exit wave for the above ScN focal series (3.2 nm thickness, specimen is tilted by 8.4 mrad around the vertical and by 10.9 mrad around the horizontal). Center: A sketch of the ScN structure (rock-salt structure). Right: Linear transfer function according to fit parameters (without defocus). Note, that the calculations were done integrating the full TCC via Gaussian-Hermite quadrature and not by linear imaging.

Quantitative Techniques and Image Simulation in TEM/STEM, SEM and Diffraction

IM2.P074
SEM image simulation of 3D samples

P. Cizmar[1], C. G. Frase[1]

[1]Physikalisch-Technische Bundesanstalt, 5.2, Braunschweig, Germany

Petr.Cizmar@ptb.de

Scanning-electron-microscope (SEM)imaging of three-dimensional (3D)samples has recently been gaining importance due to emerging applications in science and industry. Proper application of any metrological technique usually requires thorough evaluation of its accuracy. This surely applies to techniques using SEM images as an input as well. Appropriate assessment needs to investigate various influences, that usually appear at SEM image acquisition, e. g. edge-effect, drift, or noise. Solely using real SEM images is not satisfactory, since the amounts of the SEM-related effects in the images are unknown. On the other hand, amounts of these effects in simulated images are not only known, but also deterministically tunable. This renders application of simulated SEM images very useful. In various cases, like 3D photogrammetry with SEM images or contour metrology, consideration of the 3D character of the sample may be essential. Monte-Carlo-based techniques, e.g. MCSEM [1] developed by the PTB can very accurately carry out such simulations. Besides, methods based exclusively on calculation of the signal from the surface slope [2] provide another alternative, which work significantly faster. However, the latter technique does not cover all necessary effects, especially edge- and proximity-effects. The novel technique presented in this work is significantly faster than Monte-Carlo simulation and supports edge- and proximity-effects as well as it complies with all other necessary requirements for assessment of 3D-considering methods.

Image simulation starts with a three-dimensional model of the sample. Such model can be created in any 3D computer graphics software. All samples processed in this work and displayed in the figures have been created in a CAD software. As the first step, sample objects are divided into tetrahedral sections. The simulation algorithm of SEM image calculates the signal (usually represented by a grey level) corresponding to each image pixel. Parametrized beam originates in a source point and proceeds to the sample. Finding the point of interaction, which is the point where the beam hits the first tetrahedron representing the sample, requires testing of all surface triangles.

After calculation of the point of interaction, the algorithm deploys a signal source. In the first version, it is represented by a set of 870 points evenly distributed throughout a spherical volume. This sphere dips into the material of the sample leaving a minor part of it reaching somewhat above the point of interaction. (See Fig. 1.) Currently, the size and shape of the signal source as well as its dip depth and density functions are set based on a Monte-Carlo calculations. The points that are positioned out of the sample body contribute to the signal, while the ones inside do not. This principle suffices to simulate edge effects and proximity effects. (See Fig. 2.) Rest of the disturbances usually present in SEM images (e.g. drift and vibration, noise, and beam- profile-related blur) are modeled using ARTIMAGEN, which is a two-dimensional artificial SEM image generator [3].

This Monte-Carlo-less 3D SEM Image Simulation technique has been used to evaluate a photogrammetric 3D surface reconstruction techniques. For this application, calibration of the grey-levels has not been necessary, because the photogrammetric techniques are based on cross-correlation. Although the new technique is less accurate, it is many orders (over 100,000x, depending on the sample complexity) faster than Monte-Carlo-based techiques.

1. K-P Johnsen, CG Frase, H Bosse and D Gnieser, SEM image modeling using the new Monte Carlo model MCSEM, SPIE Proceedings 7638 (2010)
2. A Seeger and H Haussecker, Shape-from-shading and simulation of SEM images using surface slope and curvature, Surf. Interface Anal. 37 (2005), p. 927.
3. P Cizmar, AE Vladar and MT Postek, Scanning 30 (2008), p. 381.

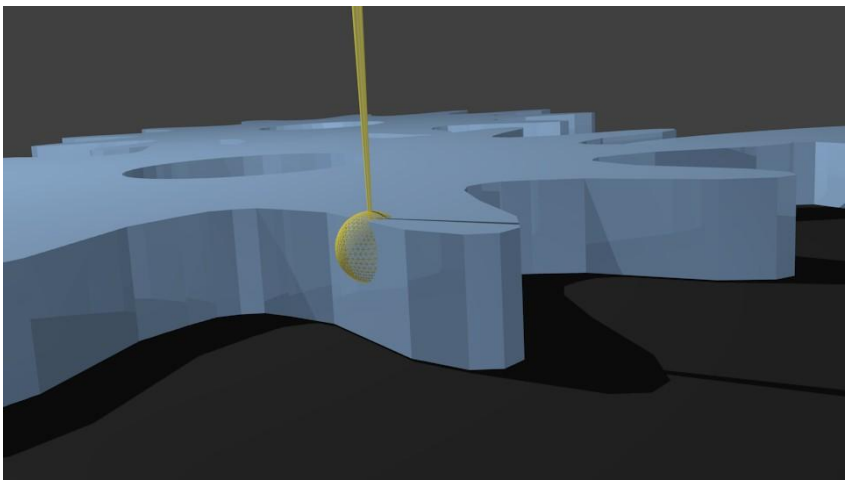

Figure 1. Visualization of the SEM image simulation principle at a point near the edge.

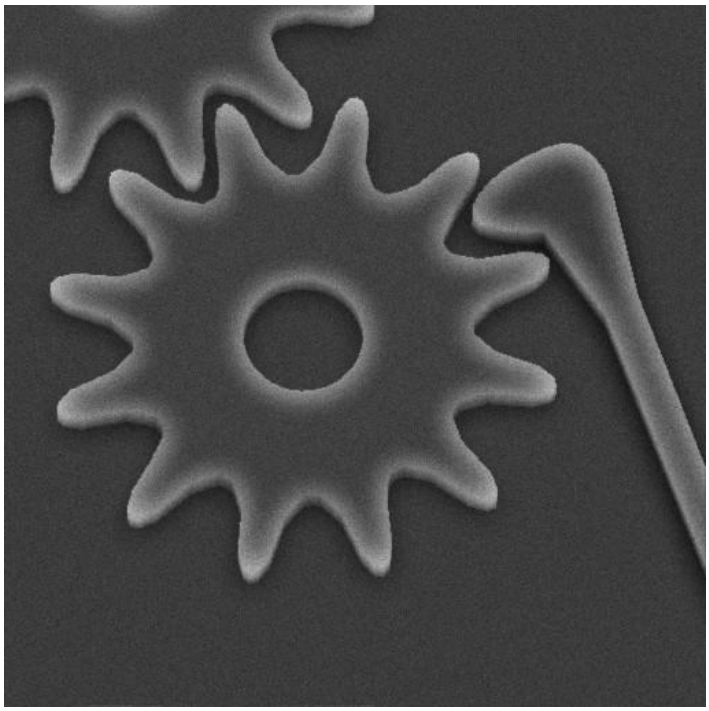

Figure 2. Simulated SEM image of a MEMS-like semiconductor structure exhibiting both edge and proximity effect.

Quantitative Techniques and Image Simulation in TEM/STEM, SEM and Diffraction

IM2.P075
Observation and simulation of parasitic signals during electro-optical investigation of ensembles of three dimensional microstructures by SEM

J. Ledig[1], C. G. Frase[2], J. Hartmann[1], A. Waag[1]

[1]Technische Universität Braunschweig, Institute of Semiconductor Technology and Laboratory for Emerging Nanometrology, Braunschweig, Germany
[2]Physikalisch-Technische Bundesanstalt, AG 5.24 Modellierung Rastermikroskopie, Braunschweig, Germany

j.ledig@tu-bs.de

Three dimensional (3D) nano- and microstructures (NAMs) are attracting a lot of attention and are discussed regarding several applications, especially in optoelectronics and semiconductor technology. The related research is also generating a request for characterization of local electro-optical properties with a high spatial resolution on single structures as well as in ensembles. However, the straightforward adaption of conventional techniques (e.g. Hall effect, capacitance-voltage) to 3D geometries is not possible or at least challenging. Thus, the characterization of NAMs is a substantial problem. Usually, electron microscopy is employed to investigate the geometry and properties of such 3D-NAMs and for mapping of vertical features by conventional signals in an SEM a certain sample tilt (e.g. about 30°) is needed.

For example GaN based 3D light emitting diodes (LEDs) with a core-shell geometry are supposed to have substantial advantages over conventional planar LEDs[1]: The active area along the sidewalls of hexagonal GaN pillars can considerably be increased by high aspect ratios - leading to a lower current density inside the InGaN quantum well (QW) at the same operation current per substrate area.

Investigation of single 3D-LEDs by electron beam induced current (EBIC) using an SEM based manipulator setup proves the presence of a pn-junction and doping type of the core and shell, while cathodoluminescence (CL) gives an insight to the optical properties of the QW. But in contrast to SEM on planar regions the interactions of the electron probe are significantly affected by the 3D geometry and the surrounding of the NAMs - as inclined facets or edges which are influencing the signal by affecting the yield (SE, BSE) and generation rate (CL, EBIC). In addition we observed local charging as well as parasitic effects resulting from interactions with neighbor structures of the ensemble and the substrate, e.g. signals are shadowed (SE, BSE, CL) and BSEs scattering into another surface generates similar signals as the primary electrons (CL, EBIC). As signals are generated quite close to the original region of the interaction, most SEM detectors cannot separate them from the original source.

For a quantitative interpretation of CL and EBIC measurement values and image contrasts, the physical modeling of SEM images and spatially resolved energy transfer by a probe spot is necessary. This is performed using the SEM simulation program MCSEM [2], which was developed at the Physikalisch-Technische Bundesanstalt (PTB). It models the different stages of SEM image formation and generates SEM grey level images of complex NAM shapes, in a first test Si was used for the modelled material (c.f. Figure 1). Aspects of the simulation are the electron probe formation, a 3D model of the specimen structure, the interaction of electron probe and solid state, the emission of secondary electrons, and different types of electron detectors. The specimen model is realized by methods of constructive solid geometry (CSG), combined with the possibility to include two-dimensional height maps. The Monte Carlo simulation of electron diffusion in solid state is based on tabulated elastic Mott scattering cross sections by Salvat and Mayol [3] and the Bethe continuous slowing down approximation in the modification of Joy and Luo [4]. Detector models include an in-lens SE detector based on secondary electron ray tracing calculations plus BSE and Transmission SEM (TSEM) detectors.

1. Mandl, M. *et al.* Group III nitride core-shell nano- and microrods for optoelectronic applications. *Phys. Status Solidi RRL - Rapid Res. Lett.* **7,** 800-814 (2013).
2. Frase, C. G., Gnieser, D. & Bosse, H. Model-based SEM for dimensional metrology tasks in semiconductor and mask industry. *J. Phys. D. Appl. Phys.* **42,** 183001 (2009).
3. Salvat, F. & Mayol, R. Elastic scattering of electrons and positrons by atoms. Schrödinger and Dirac partial wave analysis. *Comput. Phys. Commun.* **74,** 358-374 (1993).

4. Joy, D. C. & Luo, S. An empirical stopping power relationship for low-energy electrons. *Scanning* **11,** 176-180 (1989).

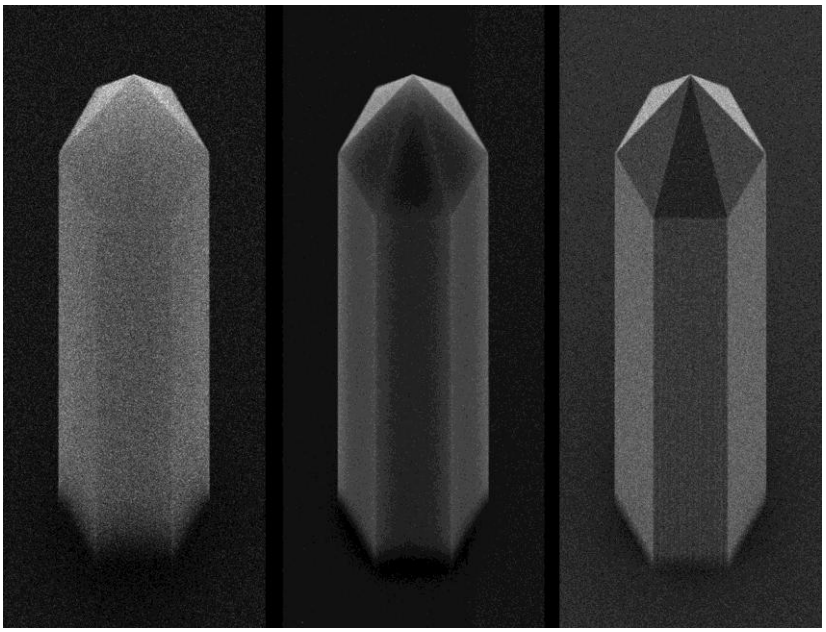

Figure 1. Simulated SE images (FOV = 4 µm, tilt of 35°) of a hexagonal silicon column using an electron probe with a diameter of 15 nm, an aperture of 10 mrad and different energies of 15 keV, 7.5 keV and 1 keV, from left to right, respectively.

Quantitative Techniques and Image Simulation in TEM/STEM, SEM and Diffraction

IM2.P076
Tool box for construction of supercells

J. Thomas[1], T. Gemming[1], J. Eckert[2]

[1]IFW Dresden, Micro- and Nanostructures, Dresden, Germany
[2]IFW Dresden, IKM, Dresden, Germany

j.thomas@ifw-dresden.de

One of the recently most discussed questions to explain the bone growth is the arrangement of calcium phosphates around the organic bone parts which are built by collagen triple helices. The understanding of this process of biomineralization is important for better chances of healing of bone fractures especially for elder persons.

One of the published details of arrangements is the combination of triclinic octacalcium phosphate (OCP) and hexagonal hydroxy apatite (HAP). Following Brown et al. [1] and Fernandez et al. [2] there are two variants which are distinguished revolving the octacalcium phosphate cell adjacent to a hydroxy apatite cell by an angle of 180° around the a- axis (x direction in figure 1). Another point is how additional cells can be arranged using this basic principle. The transmission electron microscopy can make an important contribution to determine the correct model. To do so, the ideas for such arrangements should be used for calculating the expected electron microscopic high-resolution images or diffraction patterns.

This is the point for our tool box. It is a computer program running under Windows and allowing an arrangement of cells by a model kit. The components are freely programmable, insofar the use of the tool box is not limited to biomineralization. Each last added cell can be shifted and tilted by three axes and angles in the space to construct the wanted arrangement. The composition of the components is synchronously observable in four directions: in the x-y plane, in the x-z plane, in the y-z plane, and in a perspectival direction. Similar to the single cells the complete construction can be shifted and tilted for better visualization. This is demonstrated by the screen snapshots in figure 2.

The tool box allows to image and to change the supercell construction in an easy way and is helpful for the creation of models for transmission electron microscopic image simulations.

1. W.E. Brown, J.P. Smith, J.R. Lehr, A.W. Frazier: “Octacalcium phosphate and Hydroxy apatite”, Nature, 196 (1962), 1048 - 1054
2. M.E. Fernandez, C. Zorrilla-Cangas, R. Garcia-Garcia, J.A. Ascencio, J. Reyes-Gasga: “New model for the hydroxyapatite-octacalcium phosphate interface”, Acta Cryst. B59 (2003), 175 – 181
3. We gratefully acknowledge funding by the Deutsche Forschungsgemeinschaft (DFG) via the Collaborative Research Centre SFB/TRR 79, project Z2.

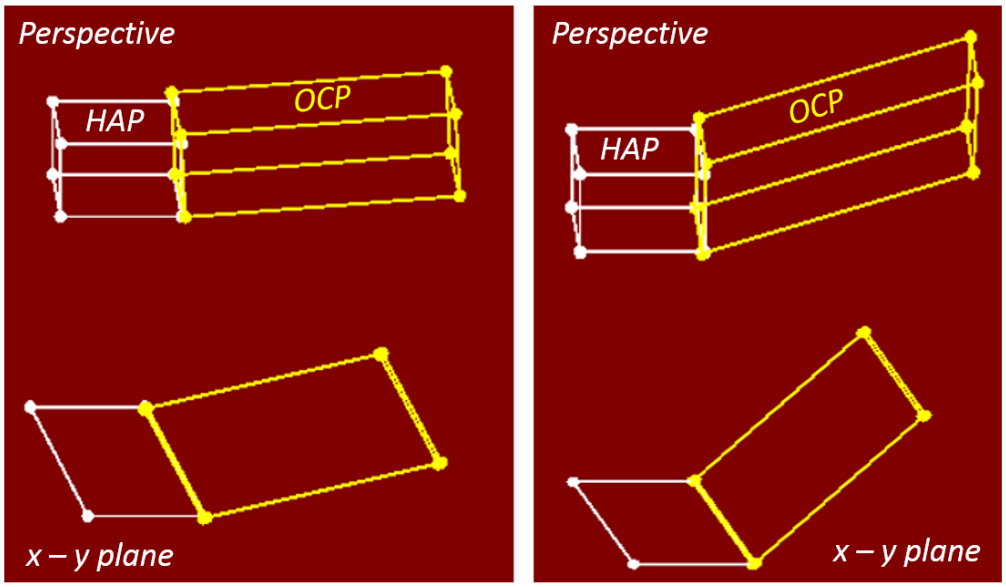

Figure 1. Combination of HAP and OCP cells following the models by Brown et al. (left) and Fernandez et al. (right)

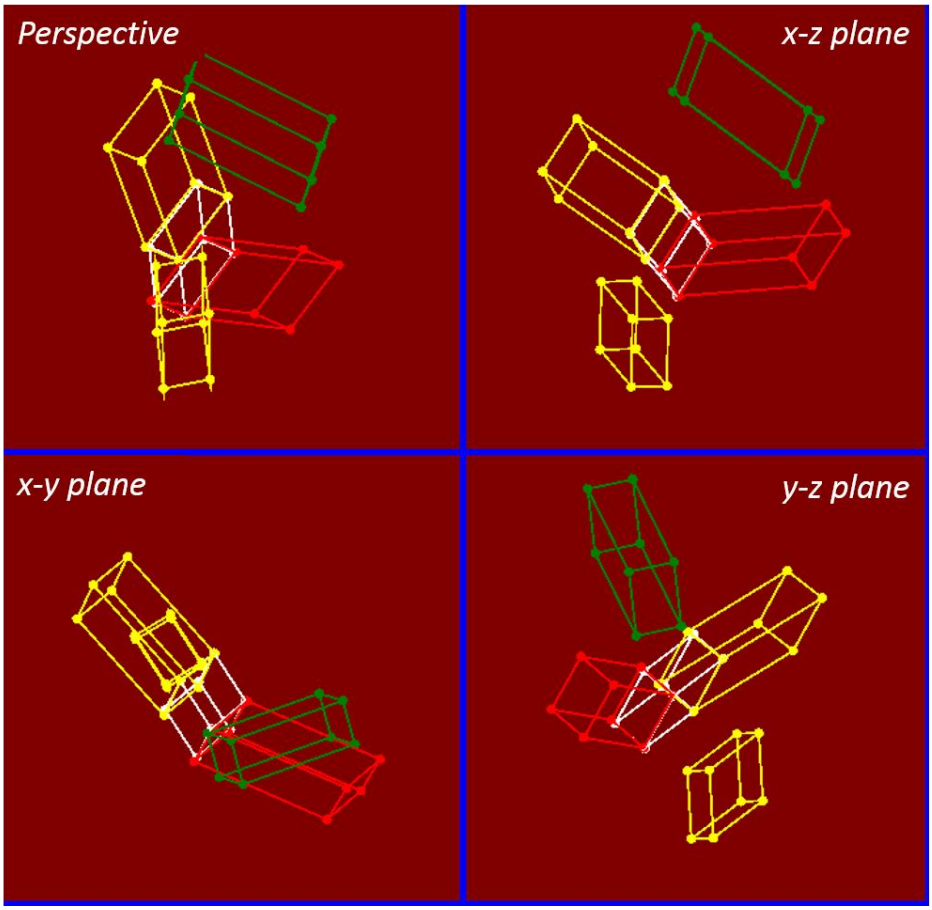

Figure 2. Arrangement of five shifted and tilted single cells observed in four directions

Quantitative Techniques and Image Simulation in TEM/STEM, SEM and Diffraction

IM2.P077
Influence of the delocalization of inner-shell excitations on atomic-resolution elemental maps

M. Y. Park[1], S. Majert[1], R. Roß[1], H. Kohl[1]

[1]Westfälische Wilhelms-Universität Münster, Physikalisches Institut, Münster, Germany

parkmi@uni-muenster.de

In an aberration corrected scanning transmission electron microscope (STEM) the elemental distribution in a specimen can be investigated with atomic resolution using energy dispersive x-ray spectroscopy (EDX). For a better interpretation of the experimental results it is necessary to compare them with calculations in order to distinguish specimen properties from imaging artifacts. We investigate the influence of channelling and of the delocalized excitation of inner-shell electrons on elemental maps.

The behaviour of electrons passing through the specimen is described using the multislice method [1]. The intensity of characteristic x-ray quanta of an EDX experiment is proportional to the electron beam intensity near the respective specimen atoms. In a first approximation the atoms are approximated as being point-shaped. This corresponds to an extremely localized excitation which can be described by a δ-distribution. To improve this localized approximation we consider the atoms' excitation probabilities and replace the δ-distribution with a delocalized excitation function [2].

We compare the results of both approximations with each other and with experimental results to estimate the influence of an atom excitation probability on elemental maps.

Two samples serve as examples of our calculations: An interface between a zinc crystal and a bismuth crystal and an interface between a zinc crystal and a lead crystal. The first results of the simulation, calculated using the localized approximation, and the dark field image are shown in figure 1. For this calculation we assumed a sample thickness of 12 nm (10 slices), an acceleration voltage of 300 kV, a 34 mrad aperture semiangle, and an aberration corrected STEM.

The results show that the position of the boundary can be clearly discerned from the simulated STEM-image.

Currently we investigate how the elemental map changes when considering a delocalized excitation function in the simulation. These results will be compared with experimental data.

1. Earl J. Kirkland “Advanced Computing in Electron Microscopy” (Plenum Press, New York, 1998) p. 157
2. D. Von Hugo, H. Kohl, and H. Rose, Optik **79** (1988) p. 19

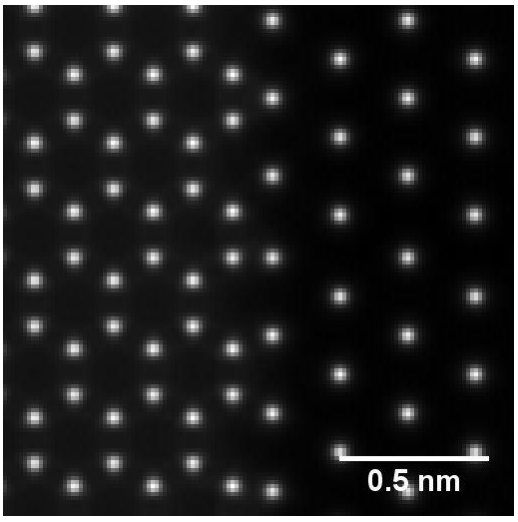

Figure 1. Simulated dark filed image of a Zn/Bi interface in [001]-orientation.

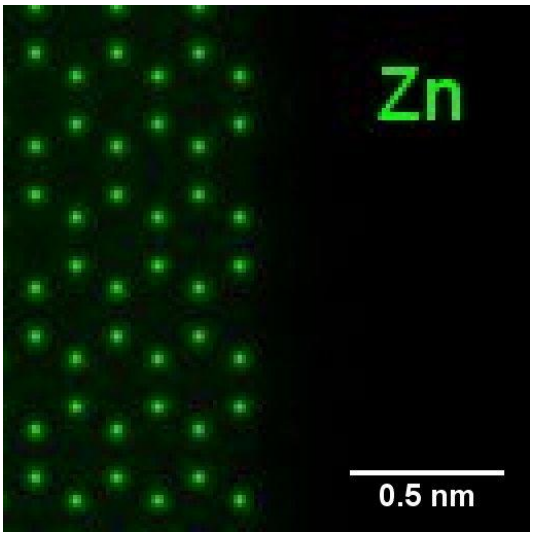

Figure 2. Simulation of the Zn-signal in an elemental map of 10 slices (≈12 nm) of a Zn/Bi interface simulated with localized approximation.

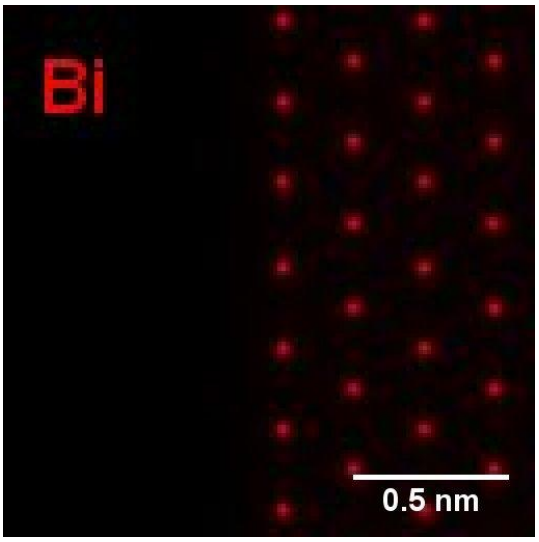

Figure 3. Simulation of the Bi-signal in an elemental map of 10 slices (≈12 nm) of a Zn/Bi interface simulated with localized approximation.

Quantitative Techniques and Image Simulation in TEM/STEM, SEM and Diffraction

IM2.P078
Correlation of strain evolution with dislocations distribution in metamorphic InGaAs/GaAs heterostructures observed by combination of diffraction techniques

D. Kirilenko[1], A. Sitnikova[1], S. Sorokin[1], G. Klimko[1], I. Sedova[1], S. Ivanov[1]

[1]Ioffe Institute, St. Petersburg, Russian Federation

zumsisai@gmail.com

Growth of metamorphic layers is a perspective direction of semiconductor technology development. Metamorphic buffers allow to combine conventional substrates with materials presenting better functional characteristics. The goal of creating a metamorphic layer is to get a defect-free material possessing a certain lattice parameter which is severely mismatched with the underlying substrate. Variation of the lattice parameter during epitaxial growth occurs by generation of elongated defects such as dislocations, which reduce the accumulated strain. Study of the strain variation versus depth and distribution of the dislocations is important for understanding the metamorphic layers growth.

In this work we present the results obtained by combination of electron diffraction and diffraction contrast techniques implemented in a transmission electron microscope (TEM), which allow one to trace the variation of strain tensor components with changes in dislocations distribution. The electron diffraction techniques including CBED and SAED allow measuring the variation of lattice parameters with the accuracy better than 0.1%. This, in turn, allows observation of even minor distortions of the unit cell and monitoring the chemical composition of the ternary InGaAs alloy with the accuracy about 1 at.%. Simultaneously, the conventional diffraction contrast imaging is used to study the defect structure of the material and its variation through the layer depth.

The studied metamorphic buffers are linearly graded InGaAs layers of about 1-μm in thickness, which were grown by molecular beam epitaxy using the procedure similar to that described in [1,2]. The 1-μm-thick top $In_xGa_{1-x}As$ layer of constant composition x=0.3, grown over the metamorphic buffer, has been found to be almost defect-free (the treading dislocation density is well below 10^6 cm^{-2}), that is in accordance with the theory of metamorphic layers growth [e.g. 3,4]. However, investigation of the sample series shows that the layer may possess a set of tetragonal distortions which correlate with the observed variations of the share of dislocations bent to the growth plane. Decrease of such "misfit" dislocations density causes elevation of the strain, which after some accumulation leads to increase of the dislocations density and elimination of the strain. The observed variation lasts till the stop of the layer relaxation, which occurs earlier than the graded layer growth. After the stop of the relaxation, the lateral lattice parameter remains unchanged and the residual tetragonal distortion is seen in the strain profiles.

Thus, combination of electron diffraction and diffraction contrast techniques has revealed the strain evolution in InGaAs metamorphic layers. Measuring the lattice parameters enable one to observe with the high accuracy fine details in strain profiles acquired with high lateral resolution achievable in TEM. Their combination with the conventional diffraction contrast imaging gives an opportunity to correlate the measured strain with variations of the defects distribution in the material.

1. I. Tångring, S.M. Wang, X.R. Zhu, A. Larsson, Z.H. Lai, and M. Sadeghi, Appl. Phys. Lett. 90, 071904 (2007).
2. I. Tångring, Y. X. Song, Z. H. Lai, S. M. Wang, M. Sadeghi, and A. Larsson, J. Cryst. Growth 311, 1684 (2009)
3. D.J. Dunstan et al., Appl. Phys. Lett. 59, 3390 (1991)
4. A. Sacedón, F. González-Sanz, E. Calleja, E. Muñoz, S.I. Molina, F.J. Pacheco, D. Araújo, R. García, M. Lourenco, Y. Yang, P. Kidd, and D. Dunstan, Appl. Phys. Lett. 66, 3334-36 (1995).
5. The work has been supported by Ministry of Education and Science of RF (projects #14.604.21.0008, ID RFMEFI60414X0008 and #14.621.21.0007 ID RFMEFI62114X0007). The TEM studies has been carried out at the Joint Research Centre "Material Science and Diagnostics in Advance Technologies" (St-Petersburg, Russia).

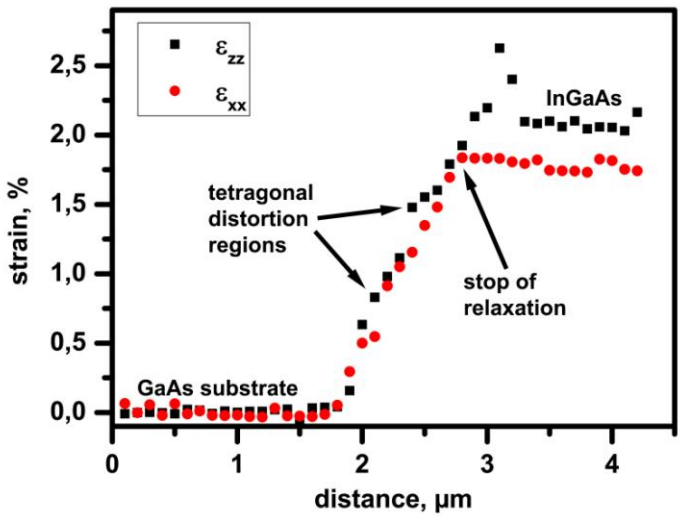

Figure 1. Plots of vertical and lateral strain tensor components along growth direction. Areas with tetragonal distortion in the graded InGaAs layer are observed, which correlate with lower "misfit" dislocations density. Stop of the layer relaxation corresponds to the absence of dislocations in the following part of the layer.

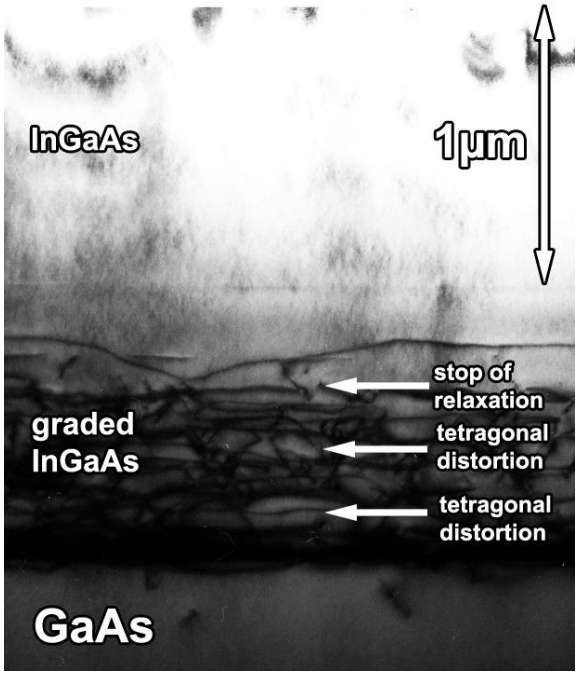

Figure 2. TEM brigth-field image showing the features of dislocation distribution which correspond to the observed details in the mesured strain profile.

Quantitative Techniques and Image Simulation in TEM/STEM, SEM and Diffraction

IM2.P079
Dislocation density determination in plastically deformed materials with HR-EBSD and X-ray diffraction

S. Kalácska[1], I. Groma[1], C. Maurice[2], A. Borbély[2], P. Ispánovity[1]

[1]Eötvös Loránd University (ELTE), Department of Materials Physics, Budapest, Hungary
[2]École des Mines, Saint-Étienne, France

kalacska@metal.elte.hu

Cross-correlation based analysis of electron backscatter diffraction (HR-EBSD) patterns is often carried out to map plastic strain variations in deformed polycrystalline samples [1]. In this work this method is applied to characterize the evolution of dislocation structures and corresponding distortion fields in Cu single crystals compressed to different levels. We aim at developing a statistical method that can be used to measure the total dislocation density in the specimen.

The distortion maps of the specimen are computed with the cross-correlation technique. This method is capable of detecting changes of the crystal orientation to higher accuracy, than the commercial software provided for standard EBSD devices that analyze each EBSD pattern individually. The distribution of distortions shows broadening with increasing load and a slow decay. To give a more detailed evaluation of the microstructure the measurements are complemented with the analysis of broadened X-ray diffraction (XRD) peaks. The total dislocation density and its fluctuation within the sample are determined by the variance method [2,3]. The good qualitative agreement found between the two methods indicate that the cross-correlation method is capable of giving a statistical characterization of the dislocation structure.

In the last part of the talk EBSD measurements on thin foils are presented, where the cellular dislocation structure can be directly observed by transmission electron microscopy. These results demonstrate the advantage of the EBSD method compared to XRD analysis, namely, that the former is not only capable of determining the dislocation density but also yields the spatial distribution of dislocations.

1. T.B. Britton and A.J. Wilkinson, High resolution electron backscatter diffraction measurements of elastic strain variations in the presence of larger lattice rotations. Ultramicroscopy 114 (2012) 82-95.
2. I. Groma, X-ray line broadening due to an inhomogeneous dislocation distribution. Phys. Rev. B. 57 (1998) 7535-7542.
3. F. Székely, I. Groma and J. Lendvai, Changes in the dislocation density fluctuations during plastic deformation. Scripta Mat. 45 (2001) 55-60.

Environmental, Time-Resolved and InSitu SEM/TEM

IM3.080
Imaging of materials dynamics in liquids using TEM

H. Zheng[1,2]

[1]Lawrence Berkeley National Laboratory, Materials Sciences Division, Berkeley, United States
[2]University of California, Berkeley, Berkeley, United States

hmzheng@lbl.gov

An understanding of how materials grow and transform in their working environments is essential to the development of functional materials for a variety of applications. We develop and apply liquid cell transmission electron microscopy to the imaging of crystal growth in solution, precipitation and dissolution at the electrode-electrolyte interfaces during electrochemical processes, and other materials processes in liquids at the nanometer or atomic scale. In this talk, I will first show an example on the study of shape evolution of nanocrystals. Our direct observation reveals unique growth mechanisms. We found that the shape controlling rules applied to bulk systems break down at the nanoscale. Nanocrystal growth is dominated by kinetic processes and strongly influenced by the surface ligand absorption. I will further show the growth of large dendritic structures. Crystallization at the reaction front and the branching mechanisms will be discussed. At the end, I will present our recent study on electrochemical processes using electrochemical liquid cells. Perspectives on in situ TEM study of electrode-liquid electrolyte interfaces for battery applications and discussions on electron beam effects and control will be provided.

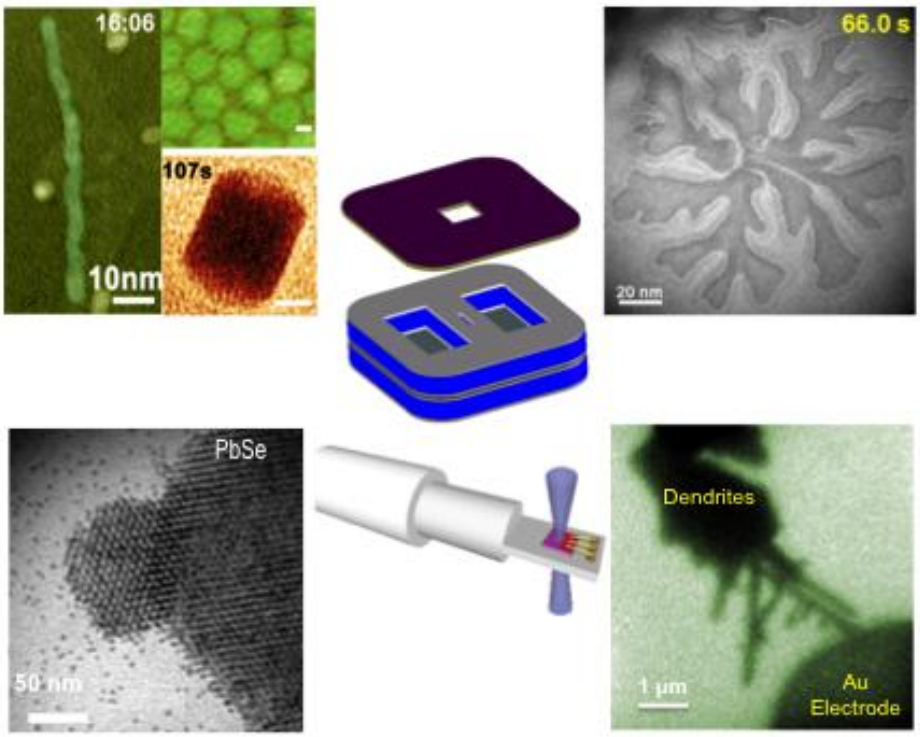

Environmental, Time-Resolved and InSitu SEM/TEM

IM3.081
Growth of colloidal Pt-Pd nanoalloys in liquid and their behavior in gas environment by in situ TEM techniques

A. De Clercq[1,2], O. Margeat[1], G. Sitja[1], C. R. Henry[1], S. Giorgio[1]

[1]Aix-Marseille Université-CNRS, CINAM UMR 7325, Marseille, France
[2]Aix-Marseille Université-CNRS, Madirel UMR 7246, Marseille, France

declercq@cinam.univ-mrs.fr
Keywords: nanoparticle growth, liquid TEM, environmental TEM, Pt-Pd, colloidal synthesis

The ability to image the growth of nanoparticles directly in the liquid phase by HRTEM has received increased attention. With this technique, the decomposition of dissolved metal precursors is initiated directly by the electron beam radiation. Most of these studies in liquid use microfabricated silicon cells, limiting the resolution. With the development of the graphene liquid cell [1], the start was given for atomic scale imaging of the nucleation of nanoparticles in the liquid phase.

In this study, we use a similar graphene oxide liquid cell as a straightforward liquid encapsulation technique. We show that the growth of spherical Pt-Pd nano-alloys, stabilized with oleylamine ligands, does not follow the same mechanism as pure Pt [2]. Their growth rate was found to be compatible with a Lifshitz−Slyozov−Wagner (LSW) mechanism in the limiting case of a reaction limited process, without coalescence (fig 1).

Next, we also studied the growth of a thin Pt layer on different Pd seeds. As such, the nucleation and growth of a very thin shell of Pt on a spherical Pd core could be imaged (fig 2). Since the colloidal synthesis method is characterized by a specific control over the particle morphology, we also studied the growth of Pt shells on cubic Pd cores (fig 3).

Finally, similar nanoparticles (alloyed spherical and core-shell cubic) were synthesized ex situ through a colloidal method in a standard reactor. The influence of oxidizing and reducing gasses (around 1 mbar) on these controlled nanostructures was then studied in situ with a HRTEM with environmental E-cell [3]. This technique can demonstrate not only shape changes, but also the possible segregation in nanoalloys under influence of the different gasses [4].

These results will show the value of the recent evolutions of in-situ TEM for the development of controlled nanostructures that can be obtained through colloidal methods [5].

1. J. M. Yuk, J. Park, P. Ercius, K. Kim, D. J. Hellebusch, M. F. Crommie, J. Y. Lee, A. Zettl, and A. P. Alivisatos, SCIENCE, 336 (2012), p. 61-64
2. A. De Clercq, W. Dachraoui, O. Margeat, K. Pelzer, C. R. Henry, and S. Giorgio, J. Phys. Chem. Lett. 5 (2014), p. 2126-2130
3. S. Giorgio, S. Sao Joao, S. Nitsche, D. Chaudanson, G. Sitja, and C. R. Henry, Ultramicroscopy, 106-6 (2006), p. 503-507
4. L. Delannoy, S. Giorgio, J. G. Mattei, C. R. Henry, N. El Kolli, C. Méthivier, and C. Louis, ChemCatChem, 5 (2013), p. 2707-2716
5. We want to thank the Région PACA for the financial support of the PhD Thesis of A. De Clercq

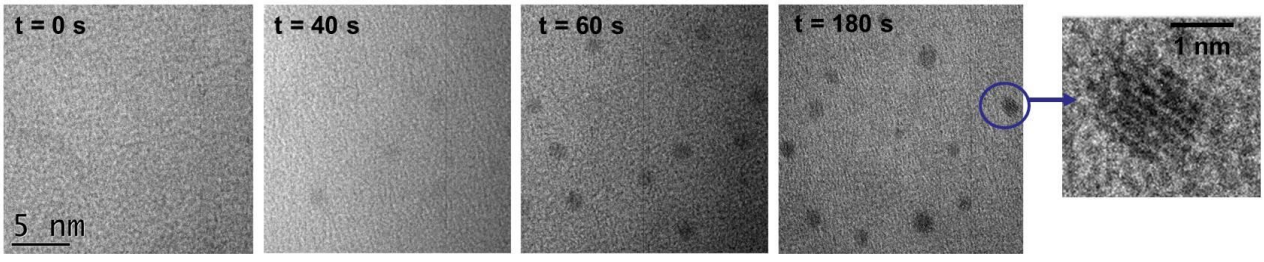

Figure 1. TEM images of the in-situ growth of small spherical Pt-Pd nanoalloys (2-3 nm) in a liquid graphene oxide cell, with the appearance of a facetted particle after 180 s.

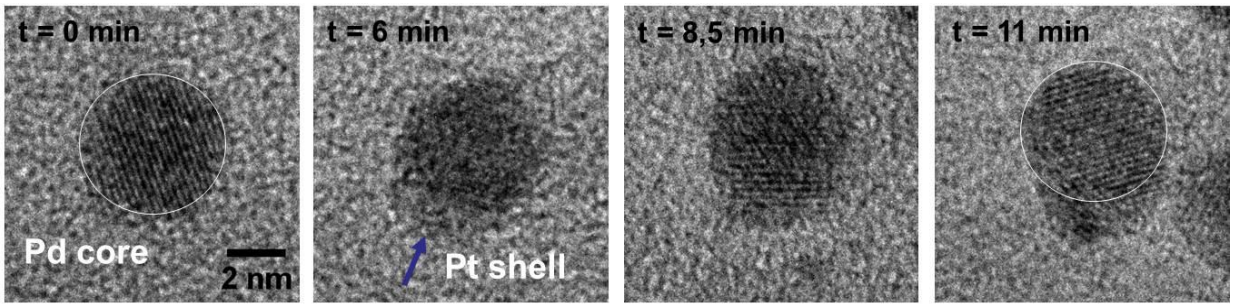

Figure 2. TEM images of the in-situ growth of a Pt shell on a Pd spherical core in a liquid graphene oxide cell

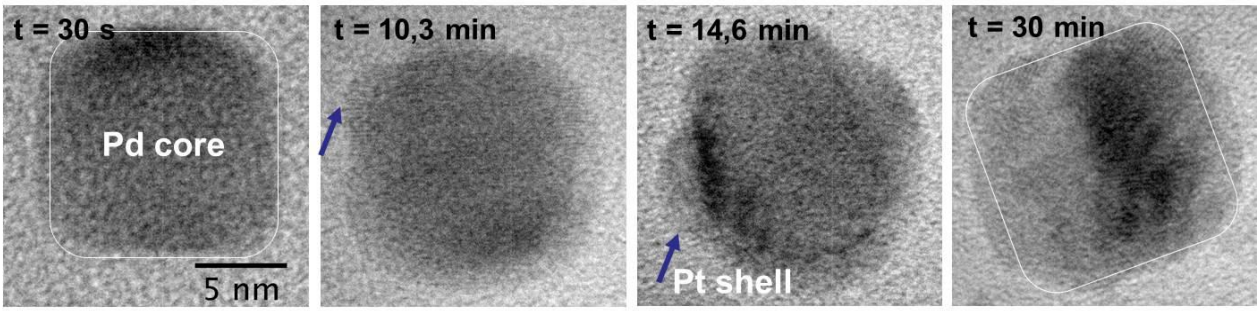

Figure 3. Growth of a Pt shell on a Pd cubic core observed in-situ in a liquid graphene oxide cell

Environmental, Time-Resolved and InSitu SEM/TEM

IM3.082
Microstructural changes in Pd thin films upon H_2 loading studied by in-situ electron microscopy

V. Roddatis[1], V. Burlaka[1], M. Bongers[1], A. Pundt[1]

[1]Institut für Materialphysik, Universität Göttingen, Göttingen, Germany

vroddatis@material.physik.uni-goettingen.de

Metal-Hydrogen (M-H) systems are interesting from both fundamental and practical points of view. Nowadays, M-H nanomaterials are suggested as promising candidates for hydrogen energy storage applications because of the fast loading and unloading times due to the intrinsically small diffusion lengths. The high mobility of hidrogen is also used to probe the defects in metals. Nobel metals are widely used as catalysts [1]. The interaction of hydrogen with metals can be studied using model systems, such as thin films grown on different substrates. In such experiments the desired microstructure can be adjusted beforehand and the hydrogen loading/unloading can be controlled in-situ via an external chemical potential changing from zero to high concentrations. Hereby, hydrogen can interact with defects (e.g. dislocations, GB, vacancies) present in the sample. Depending on the experimental conditions (hydrogen pressure, exposure time, and temperature), this interaction may activate some hydrogen assisted annihilation processes or, opposite, generate defects and irreversible microstructural changes resulting in preferential hydrogen trapping. As the influence of hydrogen has a significant effect on the microstructure and thereby on the material properties, it has to be well understood.

Here we report on the microstructure changes in thin Pd films stimulated by H_2 gas loading. The evolution of microstructure of two different model systems was studied: 1) Pd films with the thickness up to 200 nm grown on TiO_2 (110) substrate and prepared by use the reactive magnetron sputtering; 2) Pd thin film of 15 nm thickness (110) Nb-capped (11-20) sapphire substrates prepared by use the cathode ion-beam sputtering. Epitaxial Nb layers of 15 nm and of 50 nm thickness allow for substantially different out-of-plane expansion and surface roughening upon hydrogen uptake.[2] Specimens for the ETEM measurements were prepared by use of the focused ion beam (FIB) technique as well as by use of mechanical thinning followed by Ar^+ ion milling. The structure of samples was studied using a FEI environmental transmission electron microscope (ETEM) Titan 80-300 equipped with C_s-image corrector. During the ETEM experiments the hydrogen pressure was increased stepwise from $1 \cdot 10^{-6}$ mbar to 5 mbar. In this pressure range, hydrogen absorption in the Pd-film is known to be very small.[1] Between the measurements and during the pressure increase the electron beam was blanked to minimize its influence on the structure of analyzed films.

For the Pd-films on TiO_2 substrates exposed to hydrogen pressures, displacement and subsequent disappearance of dislocations was observed (Figure 1). The presence of the Nb-layer allows to actively change the interface morphology applied to the Pd-films: the exposure to hydrogen pressures of up to $p_{H=}$0.8mbar results, for the 15 nm Nb film, in only small surface modifications.[2] For this sample, we found that all investigated Pd films undergo significant structural changes. In general, the number of defects in Pd thin films after H_2 gas loading and unloading was significantly reduced, thus allowing to conclude that such a treatment favors for defect healing in thin Pd films. For the 50 nm Nb film, the exposure to hydrogen pressures results in lattice expansion and strong surface roughening in the two-phase region [2]. These changes also affected the Pd top-layer: in the areas placed above the locally expanded Nb film, the appearance of new defects was observed.

1. Pundt A, Kirchheim R, Annual Review Materials Research 36 (2006) 555-608
2. Burlaka V, Wagner S, Pundt A, JALCOM (2015), doi:10.1016/j.jallcom.2014.12.103.

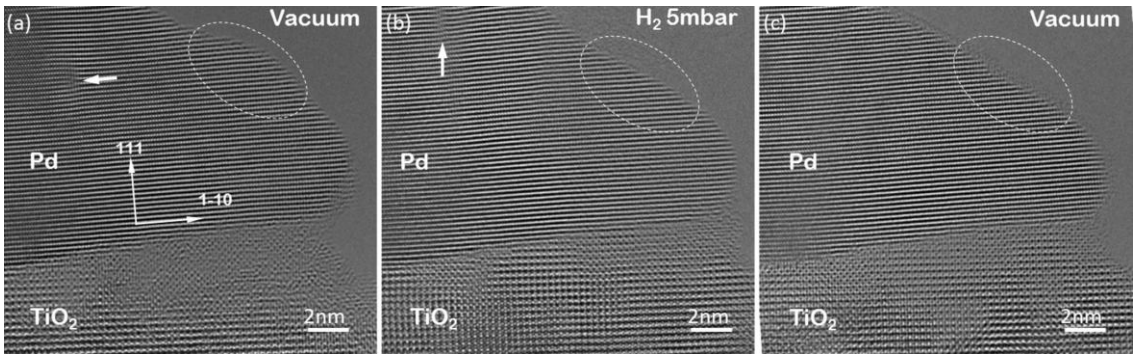

Figure 1. High resolution TEM images: (a) as prepared Pd film on TiO_2 substrate, an individual dislocation is marked with a white arrow; (b) the same part of the film as in (a) showing a displacement of the dislocation position; (c) hydrogen unloaded Pd film. A part of the surface where significant morphology changes appeared during the experiment is marked with the white contour.

Environmental, Time-Resolved and InSitu SEM/TEM

IM3.083
Direct observation of CVD graphene growth and gas-phase induced surface dynamics of active metal catalysts by In-situ scanning electron microscopy

Z.- J. Wang[1], J. Cao[1], G. Weinberg[1], R. Schlögl[1], M. G. Willinger[2]

[1]Fritz-Haber-Institut der Max-Planck-Gesellschaft, Anorganische Chemie, Berlin, Germany
[2]Max-Planck-Institut für Chemische Energiekonversion, Mühlheim (Ruhr), Germany

willinger@fhi-berlin.mpg.de

Due to the focus on ever increasing resolution during the last years, the potential of in-situ scanning electron microscopy has largely been overlooked by the community. Especially for the observation of chemical dynamics, where fast atomic motion prevents atomic scale imaging, intermediate scale observation can provide relevant statistical information about collective phenomena.

During the last three years, we have modified the set-up of a conventional scanning electron microscope in order to enable the observation of catalyst surface dynamics under controlled atmosphere and temperature. Online gas analysis allows relating the observed dynamics with catalytic conversion. Using this instrument, we have investigated chemical vapor deposition (CVD) growth of graphene on different metal catalysts. The instrument allows imaging the formation and growth of single layer graphene at temperatures of up to 1000°C [1]. At the same time, surface dynamics of the active metal catalyst can be observed and directly related to the catalytic activity. Due to the high sensitivity of the secondary electron signal to changes in the work function and charge transfer at the surface, we are able to visualize different degrees of graphene-substrate coupling [2]. The observations highlight the dynamic nature of catalysts and reveal the sensitive response of the surface to changes in the chemical potential of the gas phase. In-situ scanning electron microscopy furthermore covers the spatial resolution of complementary in-situ techniques that provide spectroscopic information, such as ambient pressure X-ray and Raman spectroscopy. It completes the spectroscopic data with visual information and spatially resolved chemical dynamics.

1. Zhu-Jun Wang et al., ACS Nano, **2015**, 9 (2), 1506-1519
2. Piran R. Kidambi et al., Nano Lett., **2013**, 13 (10), 4769-4778

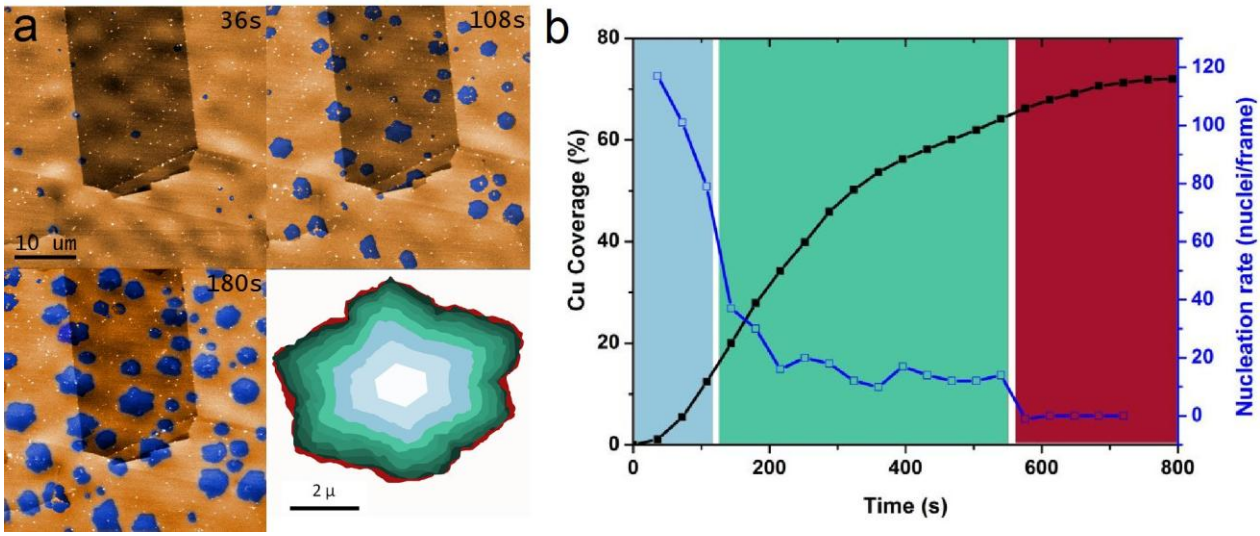

Figure 1. a) shows colorized snapshots taken during low-pressure CVD growth of graphene on copper at 1000°C. The growth and nucleation behaviour can directly be abstracted from the recorded images as shown in b).

Environmental, Time-Resolved and InSitu SEM/TEM

IM3.084
In-situ analysis of PES microfiltration membrane degradation in the ESEM

M. Nachtnebel[1], H. Fitzek[1], B. Chernev[2], P. Poelt[1]

[1]Graz University of Technology, Institute for Electron Microscopy and Nanoanalysis, Graz, Austria
[2]Graz Centre for Electron Microscopy, Graz, Austria

peter.poelt@felmi-zfe.at

Microfiltration is an important procedure for waste water treatment and for filtration of particles in the beverage industry. The basic material of the respective membranes is often polyethersulfone (PES), modified by additives such as poly(N-vinyl pyrrolidone) (PVP) to enhance hydrophilicity. Often such membranes consist of a rather thin separation layer, responsible for the filtration, and a backup layer which provides sufficient mechanical stability. The separation layer is located inside the backup layer and thus the pore size of the membrane can vary substantially across the cross section of the membrane. The structure of two different membranes can be seen in Fig. 1. Cleaning agents can degrade the performance of such membranes [1] and it might be interesting to know whether the degradation is homogeneous across the whole cross section or whether it happens preferentially in one of the layers.

Wetting and drying experiments of cooled membranes in the environmental scanning electron microscope (ESEM) provide on the one hand information about the structure of the membranes and enable on the other hand the investigation of the dynamics of the system “liquid (water) - solid (membrane) - gaseous (water vapor)” [2]. Direct observation of the membrane surface in the ESEM gives both the structure of the surface and the time duration until the surface has dried. The additional measurement of the temperature changes at the membrane surfaces during drying reveals the inner structure of the membranes. Finally by the combination of all these results the interaction mechanisms between pore surfaces and water can be elucidated. A comprehensive description of the experimental setup and the functional principle can be found in [2].

Fig. 2 shows the temperature - time diagrams for a pristine membrane and for two membranes treated with different chemical agents. The step at around -100 seconds in these diagrams indicates the start of the drying of the separation layer. The drying time for the separation layer seems to be the same for all membranes, irrespective of their treatment. On the contrary, the time for the drying of the surface layers (only that of the roll side is shown) is strongly dependent on the treatment of the membranes. Thus, degradation seems to happen preferentially at the surface and in the backup layer. Observation of the drying in the microscope confirmed that the drying time for the surface varied with varying membrane treatment. Moreover, mapping of the PVP concentrations at cross sections of the membranes by Fourier transform infrared spectroscopy also proved that degradation occurred mainly in the backup layer. But because of the low PVP concentrations these measurements have to be regarded with care. They have also been performed at just one cross section. Thus the *in situ* measurements are much more reliable, because they comprise a large sample volume.

1. B. Pellegrin, E. Gaudichet-Maurin, C. Causserand, Water Sci. & Technol.: Water Supply 13.2 (2013), 541-551
2. H. Reingruber, A. Zankel, C. Mayrhofer, P. Poelt, J. Membr. Sci. 399-400 (2012), 86-94

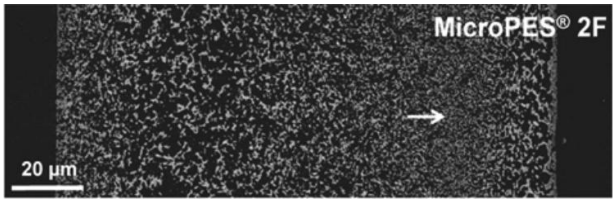

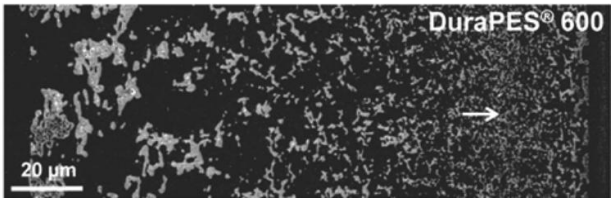

Figure 1. SEM images of the cross section of the membranes MicroPES® 2F and DuraPES® 600 embedded in resin. The bright areas correspond to the membrane material. The arrows mark the position of the separation layer. The surface at the left is always the roll side, that at the right the air side.

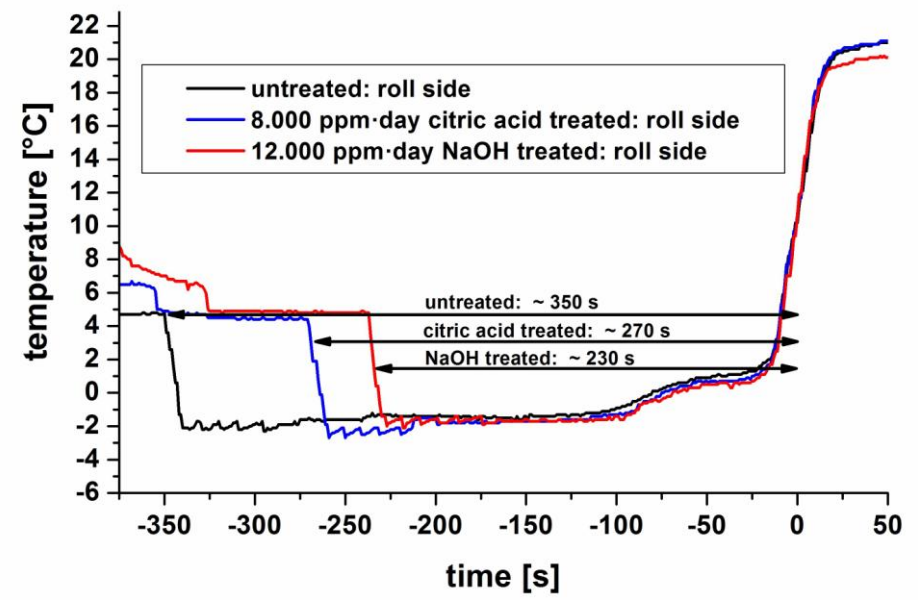

Figure 2. The temperature at the surface (roll side) of the membrane MicroPES® 2F as a function of time during the drying of the wet membrane and as a function of the membrane pretreatment. The drying of the membrane starts at the temperature drop caused by evaporation heat. The zero point of the time axis is always shifted to the end of the drying process.

Environmental, Time-Resolved and InSitu SEM/TEM

IM3.085
Combined statistical and microscopic study on solid-state dewetting of metallic thin films

F. Niekiel[1,2], S. M. Kraschewski[1,2], P. Schweizer[1,2], B. Butz[1,2], E. Spiecker[1,2]

[1]Universität Erlangen-Nürnberg, Lehrstuhl für Mikro- und Nanostrukturforschung, Erlangen, Germany
[2]Universität Erlangen-Nürnberg, Center for Nanoanalysis and Electron Microscopy (CENEM), Erlangen, Germany

florian.niekiel@fau.de

Dewetting describes the transition of a thin film into an energetically favorable set of droplets or particles, as this reduces the total energy balance of surface and interface energies. With the ongoing focus on nanotechnology it has been observed, that for sufficiently thin films (in the order of 100 nm) this transition can occur at temperatures well below the melting temperature of the bulk material, which is thus denominated as solid-state dewetting [1].

The phenomenon of solid-state dewetting is seen from two contrary sides in applications. On the one hand it poses a degradation mechanism to thin films in electronic, magnetic and optic devices. On the other hand dewetting is recently exploited to produce nanoparticle arrays, with elaborated techniques to control size, ordering, shape and composition. Despite the importance for applications the underlying mechanisms are still under discussion [1-3].

In this work [4] we present a combined statistical and microscopic approach to study the solid-state dewetting behavior of metallic thin films on ceramic substrates. We apply complementary microscopy techniques comprising scanning transmission electron microscopy (STEM), conventional transmission electron microscopy (CTEM), electron diffraction (ED) and high-resolution transmission electron microscopy (HRTEM) in combination with state-of-the-art *in situ* heating equipment (MEMS-based). Besides directly imaging the process of single dewetting events across length scales, statistical information is derived to quantitatively evaluate the dewetting behavior of the thin film.

Following examples have been taken from Au thin films dewetting *in situ* on silicon nitride membranes in the TEM. Figure 1 shows subsequent *in situ* high-angle angular dark field (HAADF) STEM images of a 22 nm thick Au film undergoing an isothermal heating experiment at 450 °C. The process of dewetting is clearly visible and temporally resolved in the acquired image series. The HAADF-STEM signal is dominated by a mass-thickness contrast and thus allows following the transport of material. An intermediate magnification is chosen, on the one hand, to image each dewetting event with sufficient spatial resolution, but on the other hand, to get an overview of several of such processes to allow statistical evaluation, e.g. for quantification of the dewetting kinetics.

Figure 2 depicts the results of a CTEM post-characterization on a prominent particle/island that formed during the above described isothermal heating experiment. Electron diffraction revealed an almost perfect [111] orientation with respect to the substrate and showed that small angle grain boundaries subdivide the grain (indicated by red labels). Texture evolution is expected to play an essential role during such a dewetting process.

In figure 3 subsequent *in situ* HRTEM images of a Au thin film dewetting at 300 °C are shown. Imaging on the atomic scale allowed to observe the retraction of surface steps (indicated by red label) to be one of the active mechanisms leading to shrinkage of the observed Au interconnection.

1. C. Thompson, Annu. Rev. Mater. Res. 42 (2012), pp. 399-434
2. O. Kovalenko, J. Greer, E. Rabkin, ActaMater. 61 (2013), pp. 3148-3156
3. D. Amram, L. Klinger, N. Gazit, H. Gluska, E. Rabkin, Acta Mater. 69 (2014), pp. 386-396
4. F. Niekiel, P. Schweizer, S.M. Kraschewski, B. Butz, E. Spiecker, Acta Mater. 90 (2015), pp. 118-132
5. Financial support by the DFG via the Research Training Group GRK 1896 “In situ microscopy with electrons, X-rays and scanning probes” and the cluster of excellence EXC 315 "Engineering of Advanced Materials" is gratefully acknowledged.

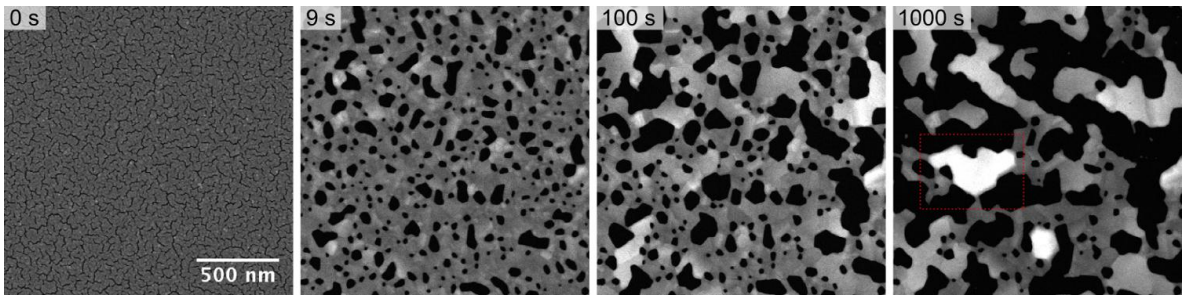

Figure 1. *In situ* HAADF STEM images of a 22 nm thick Au film dewetting at 450 °C, experiment time as indicated. Particle shown in figure 2 is highlighted by a red frame.

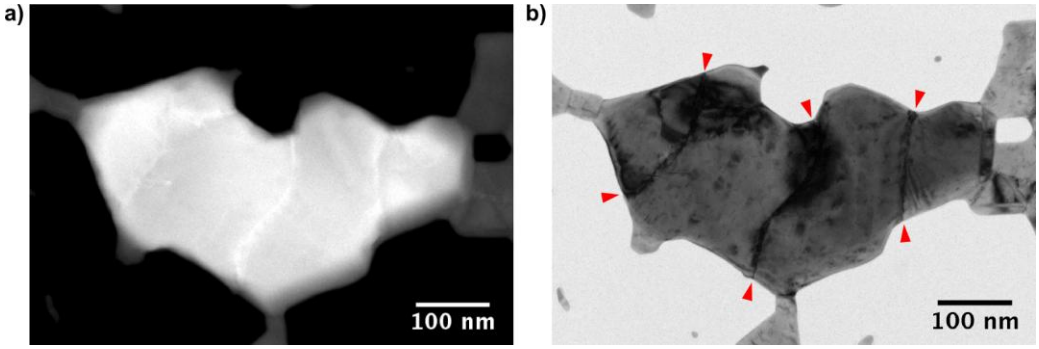

Figure 2. HAADF-STEM image (a) and CTEM bright field image (b) of a prominent particle evolving during the dewetting experiment shown in figure 1 (the sample has seen 450 °C for 4000 s). Small angle grain boundaries indicated by red labels.

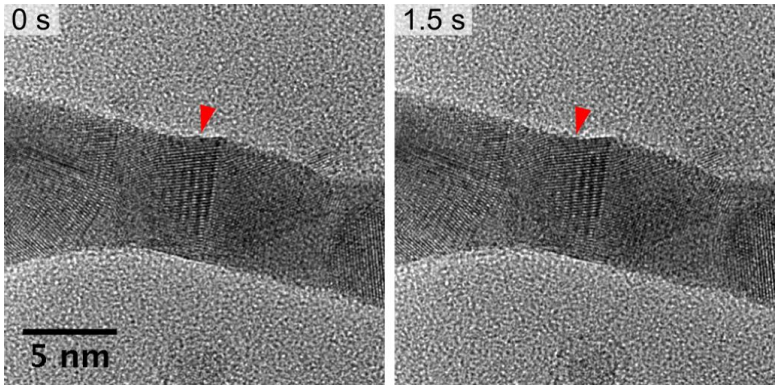

Figure 3. *In situ* HRTEM images of a Au thin film dewetting at 300 °C. Times indicated give relative time between the images. Red label highlight the retraction of a surface step.

Environmental, Time-Resolved and InSitu SEM/TEM

IM3.086
Mechanical quenching of nanoscale silica spheres - an in situ TEM approach

M. Mačković[1], F. Niekiel[1], E. Spiecker[1]

[1]Lehrstuhl für Mikro- und Nanostrukturforschung & Center for Nanoanalysis and Electron Microscopy, Erlangen, Germany

mirza.mackovic@fau.de

As functional materials and part of today's modern technologies oxide glasses have to feature mechanical reliability, besides their specific function in a device [1]. It was shown that the tensile strength of oxide glass fibers can be increased by applying axial stress during fiber drawing [2]. The increased strength is attributed to structural anisotropy of the glass network resulting from the axial stress during glass formation [2]. Brückner [3] proposed that structural anisotropy can be achieved by cooling of glass melts under load below the glass transition temperature, e.g. by uniaxial compression of glass melts and subsequent cooling to room temperature (RT) [4]. However, little is known on the impact of compression-induced structural anisotropy on the mechanical properties of oxide glasses.

Here we present a novel approach to perform mechanical quenching experiments on nanoscale amorphous silica (a-SiO_2) inside the transmission electron microscope (TEM) and to subsequently mechanically test the generated structure *in situ*. Nanoscale a-SiO_2 is known to reveal superplastic behavior when illuminated by high-energy electrons under appropriate conditions [5]. We exploit this phenomenon for athermal mechanical quenching in beam on/off experiments. Thereby, a-SiO_2 spheres (synthesized according to [6] and [7]) are compressed in the TEM by using a PI95 TEM Picoindenter^{TM} (Hysitron, Inc.). As known from our previous work [8], moderate electron-beam (e-beam) irradiation densifies such a-SiO_2 spheres removing free volume resulting from the synthesis route. To account for this and exclude the effect of densification on the mechanical properties, all spheres are exposed to an identical e-beam current dose prior to compression. In order to quench the a-SiO_2 spheres under load, during compression the e-beam is switched off and further compression is carried out without e-beam (see experiment (A) in Fig. 1). In experiment (B) additionally a holding segment is introduced into the displacement profile (see red data in Fig. 1), during which the material relaxes (clear drop in the load signal), followed by beam off compression. In difference to a classical quenching experiment (heating up to high temperature and rapid cooling to RT [3]), we use moderate e-beam irradiation and stay at/near RT. After switching off the e-beam and upon further compression, clear differences in the load-displacement (L-D) response are observed. The spheres from experiment (A) show higher maximum load and stiffness values, as indicated by green and blue arrow in Fig. 1, respectively, and evaluated for ten spheres for each experiment (see Fig. 2). Finite element method (FEM) simulations point on differences in the Young's modulus (not shown here). We propose and discuss that structural anisotropy is the reason for the surprising phenomena observed in the present work.

1. L. Wondraczek et al., *Adv. Mater.* 2011;23:4578.
2. M.D. Lund, Y. Yue, *J. Am. Ceram. Soc.* 2010;93:3236.
3. R. Brückner, *Glas. Berichte Glas. Sci. Technol.* 1996;69:396.
4. J. Wu et al., *J. Chem. Phys.* 2009;131:104504.
5. K. Zheng et al., *Nat. Commun.* 2010;1:24.
6. W. Stöber et al., *J. Colloid Interface Sci.* 1968;26:62.
7. M. Hanisch, M. Mačković, N. Taccardi, E. Spiecker, R.N. Klupp Taylor, *Chem. Commun.* 2012;48:4287.
8. M. Mačković, F. Niekiel, L. Wondraczek, E. Spiecker, *Acta Mater.* 2014;79:363.
9. Financial support by DFG via the SPP 1594 "Topological Engineering of Ultra-Strong Glasses", research training group GRK1896 "In situ microscopy with Electrons, X-rays and Scanning Probes" and Cluster of Excellence EXC 315 "Engineering of Advanced Materials" is gratefully acknowledged. We thank M. Hanisch and R.N. Klupp-Taylor for providing the silica spheres and E. Bitzek for fruitful discussions.

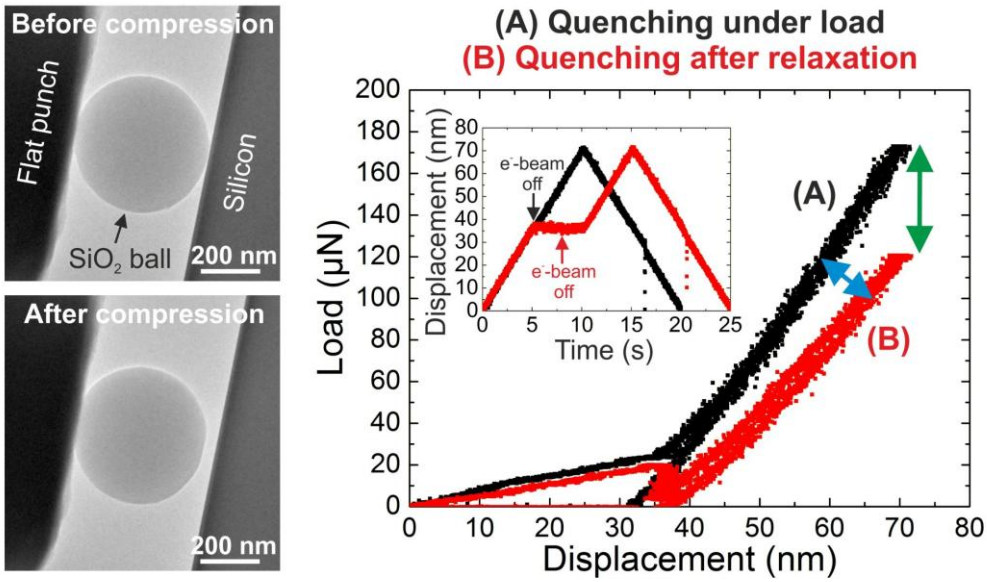

Figure 1. TEM images of a a-SiO_2 sphere before and after compression (experiment A) and L-D response of a-SiO_2 spheres for both experiments (A) and (B).

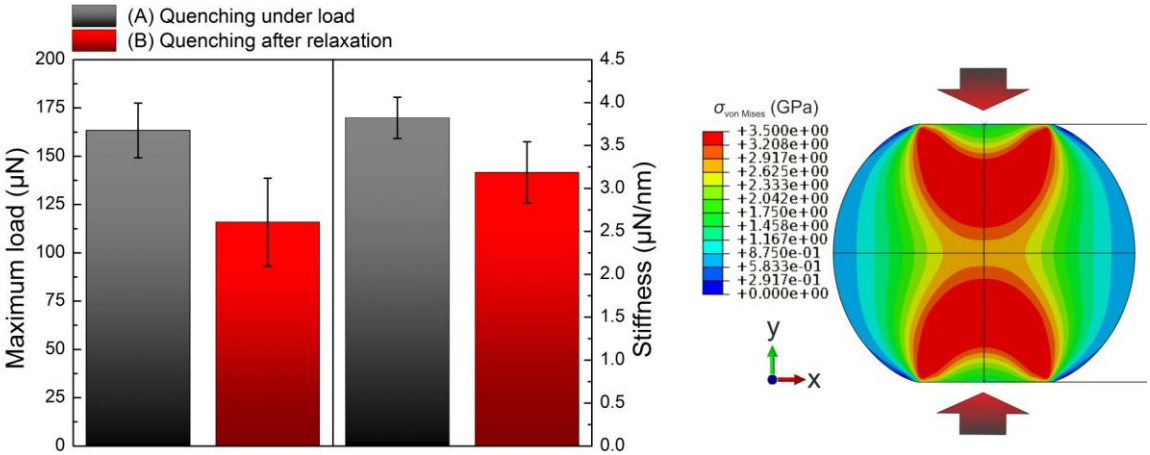

Figure 2. Maximum load and stiffness values of ten a-SiO_2 spheres for each experiment (A) and (B), and FEM model of von Mises stresses inside a a-SiO_2 sphere.

Environmental, Time-Resolved and InSitu SEM/TEM

IM3.P087
In situ ultramicrotomy in the variable pressure/environmental scanning electron microscope for the assessment of polymeric materials

A. Zankel[1,2], M. Nachtnebel[1,2], T. Müllner[3], P. Pölt[1,2]

[1]Graz University of Technology, Institute for Electron Microscopy and Nanoanalysis, NAWI Graz, Graz, Austria
[2]Graz Centre for Electron Microscopy, Graz, Austria
[3]Philipps-Universität Marburg, Department of Chemistry, Marburg, Germany

armin.zankel@felmi-zfe.at

In situ ultramicrotomy in the variable pressure/environmental scanning electron microscope (VP-ESEM) [1] was introduced by Denk and Horstmann in 2004 [2] as serial block face scanning electron microscopy (SBFSEM) utilizing an ultramicrotome in the specimen chamber of a variable-pressure SEM (VPSEM) or of an environmental scanning electron microscope (ESEM) which provides a low vacuum mode. The automated slice and view process enables three dimensional (3D) reconstructions of specimens.

The present results were achieved with an ESEM Quanta 600 FEG (FEI, Eindhoven, the Netherlands) and the serial block-face sectioning and imaging tool, 3View™ of Gatan, Inc. (Pleasanton, CA, USA) which is controlled by the software Digital Micrograph™. To image with backscattered electrons (BSE) a specially designed detector by Gatan, Inc. was used, which is optimized for low electron energies.

SBFSEM was invented for the investigation of neuronal tissues and is a well established method in life science. However, several papers are recently dealing with materials science investigations mainly concerning soft matter, although even SBFSEM investigations on aluminum samples were performed [3].

Concerning polymers, different properties can be assessed by applying SBFSEM. The *consistency* of a material can be investigated by e.g. the 3D-reconstruction of the distribution of polymer particles in a blend or the distribution of talcum particles in a polymer matrix. Additionally, interfaces between a polymer and other materials can be monitored [4].

Furthermore, the *functionality* of a polymeric product can be investigated. Figure 1 shows the reconstruction of a hypercrosslinked poly(styrene-co-divinylbenzene) monolith. The structure represents an about 120 µm long segment of this microfluidic component over the whole diameter of 100 µm. This large-volume reconstruction allows the unambiguous evaluation of the morphology [5], and is also a well-laid foundation for application-targeted simulations, especially for the simulation of advective-diffuse transport and the depending dispersion properties.

As a third aspect the *failure analysis* of polymers using SBFSEM is discussed, to achieve a deeper insight into fundamental properties, like the fracture behaviour of polymer blends. Therefore, 3D-reconstructions of cracks in polypropylene (PP) modified with ethylene propylene rubber (EPR) were obtained. Via SBFSEM it is possible to get image stacks with high resolution in all three dimensions, to create detailed models of the position of cracks related to the EPR filler particles inside the PP matrix. The 3D-reconstruction (see Figure 2) gives detailed information about the fracture formation, the propagation of the cracks within the filler particles, the distribution of both, the particle size and distance and furthermore the cracks' surface and shape.

1. Stokes, D.J.: Principles and Practice of Variable Pressure/Environmental Scanning Electron Microscopy (VP-ESEM). John Wiley & Sons, Ltd (2008)
2. Denk, W., Horstmann, H.: Serial block-face scanning electron microscopy to reconstruct three-dimensional tissue nanostructure. PLoS Biol. 2 (11) (2004) 1900-1909
3. Zankel, A., Wagner, J., Poelt, P.: Serial sectioning methods for 3D investigations in materials science. Micron 62 (2014) 66-78
4. Zankel, A., Kraus, B., Poelt, P., Schaffer, M., Ingolic, E.: Ultramicrotomy in the ESEM, a versatile method for materials and life sciences. Journal of Microscopy 233 (1) (2009) 140-148
5. Müllner, T., Zankel, A., Svec, F., Tallarek, U.: Finite-size effects in the 3D reconstruction and morphological analysis of porous polymers. Materials Today 17 (8) (2014) 404-411

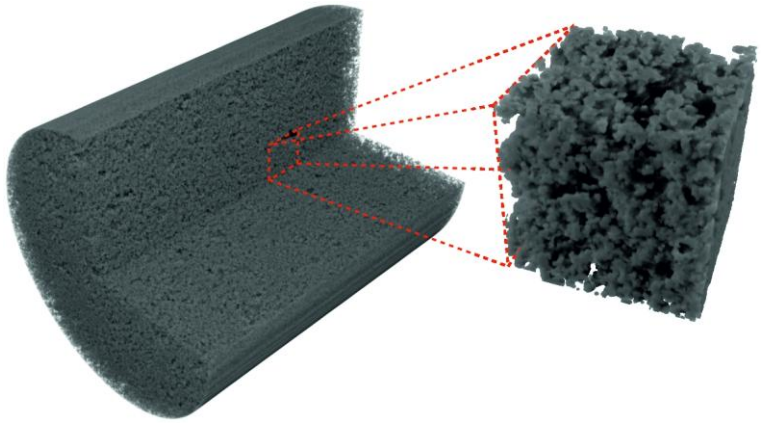

Figure 1. 3D-reconstruction (diameter: 100 µm, length: about 120 µm; edge length of the cube: 15 µm) of a hypercrosslinked poly(styrene-co-divinylbenzene) monolith

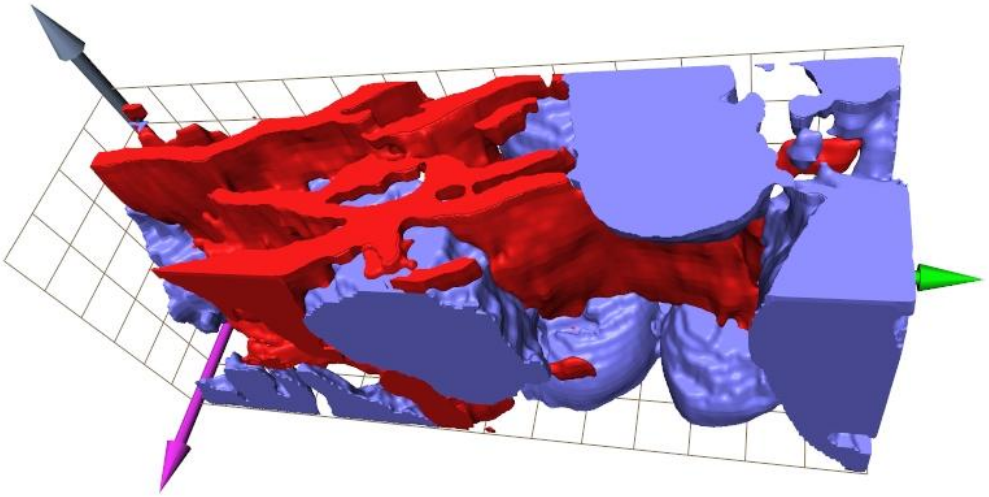

Figure 2. 3D-reconstruction of EPR-particles (blue) and cracks (red) in a PP specimen (reconstructed volume: 2 x 7 x 3 µm³, unit length 0.5 µm)

Environmental, Time-Resolved and InSitu SEM/TEM

IM3.P088
Atomic-scale evidence for the nucleation sites of multilayer graphene and its dynamic evolution to a carbon nanotube

L. Zhang[1], M. He[2], J. B. Wagner[1]

[1]Technical University of Denmark, DTU Cen, lyngby, Denmark
[2]ONERA-CNRS, Laboratoire d´Étude des Microstructures,, Châtillon CEDEX, France

lilizha@dtu.dk

In situ environmental transmission electron microscopy (ETEM) is of great importance to provide direct experimental evidence of structural dynamics of nanomaterials in a reactive gas at elevated temperature [1, 2]. Here, the catalytic nucleation of carbon nanostructures from nanoparticles are recorded with aberration-corrected high-resolution TEM studies. Figure 1. shows the surface-bounded graphene on a certain facet of the particle stacks layer by layer, meanwhile, the disordered region inside the particle expands deeply along the interface of particle and support, suggesting a bulk diffusion path of carbon. However, the appearance of the gas-absorbed interface on the other facet of the particle allows assembling a graphene layer on its partial surface via surface diffusion. The evolution of the particle morphology then results in an increased number of layers and a tube-like structure. Overall, this work provides an improved understanding of nucleation mechanism of graphene and carbon nanotubes.

1. Hansen, T. W.; Wagner, J. B. *ACS Catal.* **2014**, *4*, 1673.
2. He, M.; Kauppinen, E. I. et al. *Sci. Rep.* **2013**, *3*.

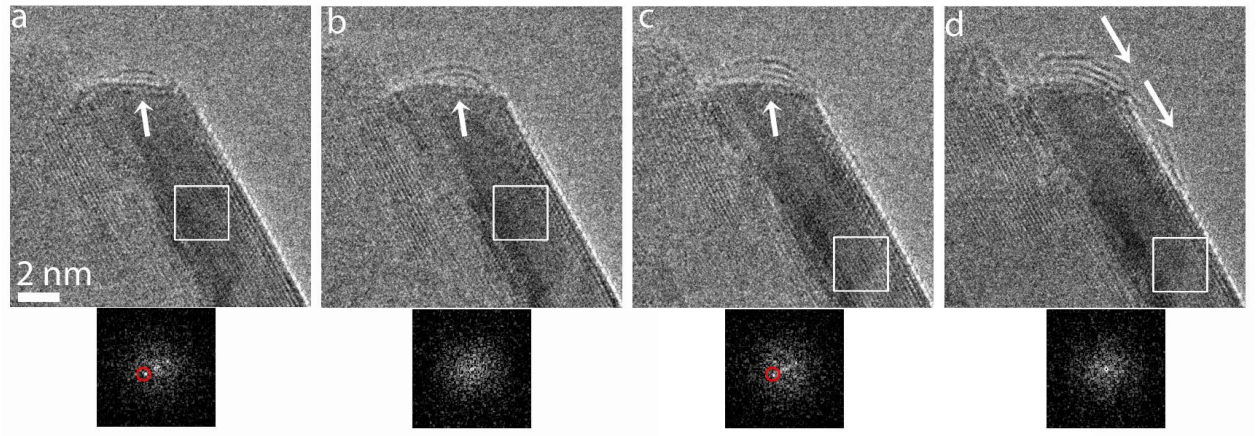

Figure 1. A series of high-resolution TEM images showing the nucleation processes of multilayer graphene. (a-c) A stack of graphene on one facet of the nanoparticle. (d) A graphene layer assembles on the other facet of the particle. Fast fourier transforms (FFTs) from the squares showing the expanded disordered region inside the particle.

Environmental, Time-Resolved and InSitu SEM/TEM

IM3.P089
Mechanical anisotropy of the MAX-phase Nb_2AlC at the nanometer and micrometer scale studied by means of in situ electron microscopy

N. Schrenker[1], Y. Kabiri[1], M. Mačković[1], J. Müller[1], P. Schweizer[1], F. Niekiel[1], B. Hoffmann[2], S. Christiansen[2,3], E. Spiecker[1]

[1]Friedrich-Alexander Universität Erlangen-Nürnberg, Lehrstuhl für Mikro- und Nanostrukturforschung & Center for Nanoanalysis and Electron Microscopy, Erlangen, Germany
[2]Max Planck Institute for the Science of Light, Erlangen, Germany
[3]Helmholtz Centre Berlin for Materials and Energy, Berlin, Germany

nadine.schrenker@fau.de

MAX phases are layered crystals with ternary or quaternary chemical composition. Due to their unique set of properties, which is a combination of metallic and ceramic attributes, they are an intriguing class of materials. They are excellent electric and thermal conductors, oxidation resistant as well as machinable and damage tolerant [1]. As a result of the layered nature of MAX phases, they behave plastically anisotropic. Depending on the orientation the deformation occurs by a combination of delamination of individual grains, formation of shear and kink bands. Moreover, Barsoum et al. [1] proposed the model of incipient kink bands to describe the observed fully reversible hysteresis loops in cyclic compression tests. In contrast to a kink band an incipient kink band does not dissociate into mobile dislocation walls. However, there are recent studies which propose that the reversible hysteresis loops of MAX-phases in compression tests of polycrystals are a result of an insufficient number of soft slip systems to accommodate the deformation [2] and microstructure anisotropy, which generate strong variations in microstrains [3]. Hence, the precise nucleation mechanism of dislocation walls and kink bands is not yet known.

By means of *in situ* indentation experiments in the electron microscope we investigate the anisotropic mechanical behavior of the MAX-phase Nb_2AlC. The preparation of pillars was performed with a Focused Ion Beam (FIB). In the transmission electron microscope pillar compression tests revealed nucleation and propagation of dislocations on the basal planes with 1/3 type Burgers vector (Fig. 1a). Deformation by basal slip was possible, as the basal planes were inclined to the pillar axis, which is depicted in the post mortem SEM image in Fig. 1b.

In addition, compression tests of submicron pillars with different orientations, determined by EBSD, were conducted in the scanning electron microscope. The EBSD map in Fig. 1e depicts the crystal orientations perpendicular to the surface. Single crystal pillars where the compression axis is parallel to the orientation of the layers are in a constrained deformation state. This is the case for the pillar cut at position 1 according to the EBSD map of Fig. 1e, where the orientation is close to [210]. The layers are forced to delaminate and bend. Post mortem SEM images show that the curvature of bending is high and reveal slip traces along the basal planes (Fig. 1c). In addition, pillars containing a grain boundary revealed the incompatibility of deformation of grains with different orientations, which is a result of the lack of five independent slip systems. Fig. 1d depicts a post mortem SEM image of a pillar containing a grain boundary between a grain in [001] and [210] direction, which was cut at position 2 according to the EBSD map.

Moreover, the measured compressive strength exceeds the strength of a bulk material. One possible mechanism is that dislocation sources get pinned at the surface and become single arm sources. The critical resolved shear stress is expected to increase with decreasing source length (source truncation) [4]. Furthermore, reaction of nucleated dislocations with preexisting dislocations or FIB induced defects can cause paucity of available dislocation sources (exhaustion hardening) [4].

It is believed that a constrained deformation state is required to form kink bands. For this reason further investigations on configurations with a constrained deformation state, for instance by introducing an obstacle like a grain boundary in the indentation zone, are thought to provide additional insights.

1. M.W. Barsoum et al., Annu. Rev. Mater. Res., 41(1):195-227, 2011.
2. N.G. Jones et al., Acta Mater., 69:149-161, 2014.
3. A. Guitton et al., Appl.Phys. Lett., 104(24):241910, 2014.
4. S.I. Rao et al., Acta Mater., 56(13):3245-3259, 2008.

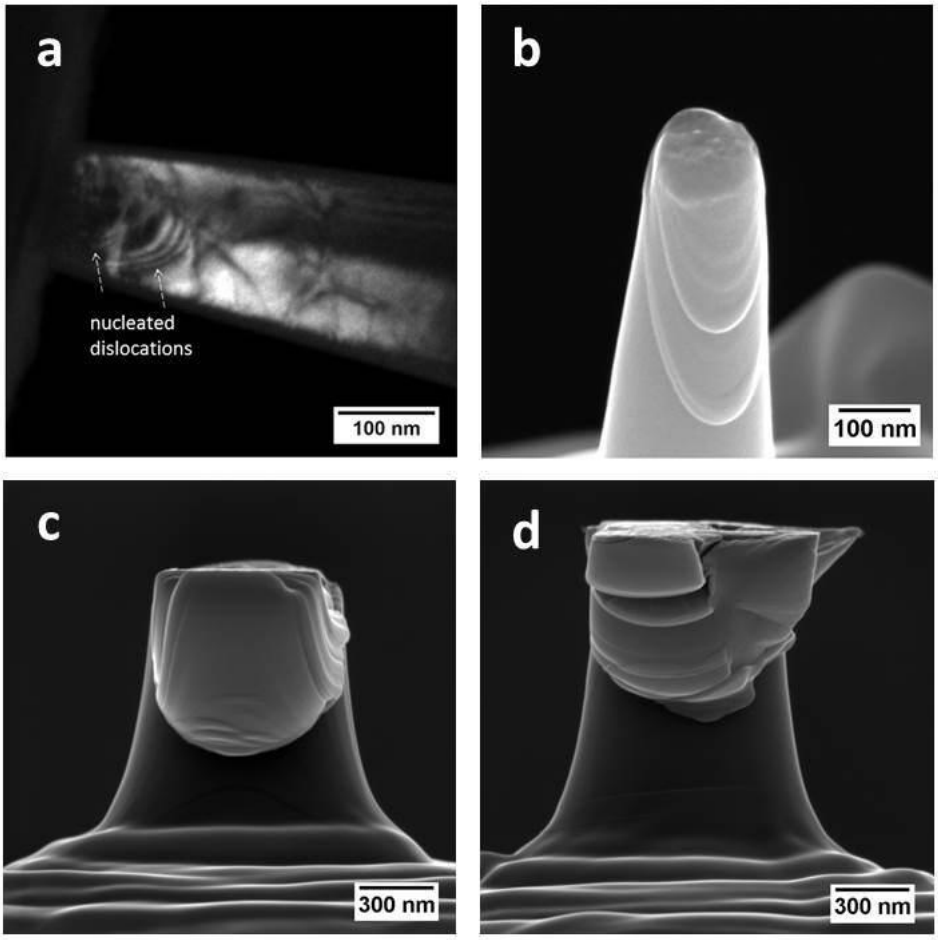
a
nucleated
dislocations
100 nm
b
100 nm
c
300 nm
d
300 nm
e
1
2
20 µm
[001]
Nb2AlC
[110]
[210]

Environmental, Time-Resolved and InSitu SEM/TEM

IM3.P090
In situ micromechanical testing and local strain analysis of nanoporous gold inside the scanning electron microscope

E. Thiess[1], T. Przybilla[1], F. Niekiel[1], B. Winter[1], M. Mačković[1], E. Spiecker[1]

[1]Institute of Micro- and Nanostructure Research & Center for Nanoanalysis and Electron Microscopy (CENEM), Department of Materials Science and Engineering, Friedrich-Alexander-Universität Erlangen-Nürnberg, Erlangen, Germany

erich.thiess@studium.fau.de

In situ micromechanical testing of nanoporous gold (np-Au) offers insights into deformation mechanisms of nanoscale metal foams. Au ligaments act together as a three-dimensional open porous network of interconnected nanostruts resulting in high mechanical strength under compression and nanoindentation [1, 2]. With decreasing ligament size stresses close to the theoretical shear strength of Au have been reported [2-4]. As the material is easy to process and the ligament size can be tailored within the nm-µm range without changing the relative density of the foam itself, np-Au can be regarded as a model material for studying size effects on nanoscale porous structures [5].

In this work we study the deformation behaviour of np-Au foams in micropillar compression experiments performed *in situ* in the scanning electron microscope (SEM). Therefore np-Au micropillars are prepared by focused ion beam milling. The nanoporous material itself is produced by the well-known process of (electro-) chemical dealloying [5]. In the present work an $Au_{23}Ag_{77}$ solid solution is etched in nitric acid. By variation of the acid concentration, immersion time, as well as the post annealing treatment, the diameter of the Au ligaments is tailored within the range of 10-70 nm (cf. Fig. 1a-b). In order to determine the degree of porosity, scanning transmission electron microscopy (STEM) tomography is performed on a suitable pillar (cf. Fig. 1c). Taking the porosity into account the dependency of the yield stress (acting in single Au ligaments) on the ligament diameter is evaluated using the foam scaling law by Gibson and Ashby [6]. To study the deformation behaviour of np-Au foams in more detail, the local strain is mapped from *in situ* SEM experiments by image correlation techniques modelling the displacement field using Bézier surfaces (cf. Fig. 2). Thereby local strain gradients are identified allowing a correlation between local and macroscopic strain values. Further experiments will focus on the combination of *in situ* pillar compression inside the transmission electron microscope combined with 360° STEM tomography to characterize the three-dimensional deformation behaviour of nanoscale metal foams.

1. C. A. Volkert, E. T. Lilleodden, D. Kramer, J. Weissmüller, Appl. Phys. Lett., 89, 2006.
2. A. M. Hodge, J. Biener, J. R. Hayes, P.M. Bythrow, C. A. Volkert, A. V. Hamza, Acta Mater., 55, 2007.
3. J. Biener, A. M. Hodge, J. R. Hayes, C. A. Volkert, L. A. Zepeda-Ruiz, A. V. Hamza, F. F. Abraham, Nano Lett., 6, 2006.
4. M. Hakamada, M. Mabuchi, Scr. Mater., 56, 2007.
5. E. Seker, M. L. Reed, M. R. Begley, Materials, 2, 2009.
6. L. J. Gibson, M. F. Ashby, Cellular Solids: Structure and Properties, (2nd ed.) Cambridge University Press, Cambridge, 1997.
7. The authors gratefully acknowledge the financial support of the German Research Foundation (DFG) within the research training group GRK 1896 “In-situ Microscopy with Electrons, X-rays and Scanning Probes” and the Cluster of Excellence EXC315 “Engineering of Advanced Materials”. They further thank Dr. Colin Ophus (NCEM, Berkeley) for helpful discussion on Bézier surface fitting.

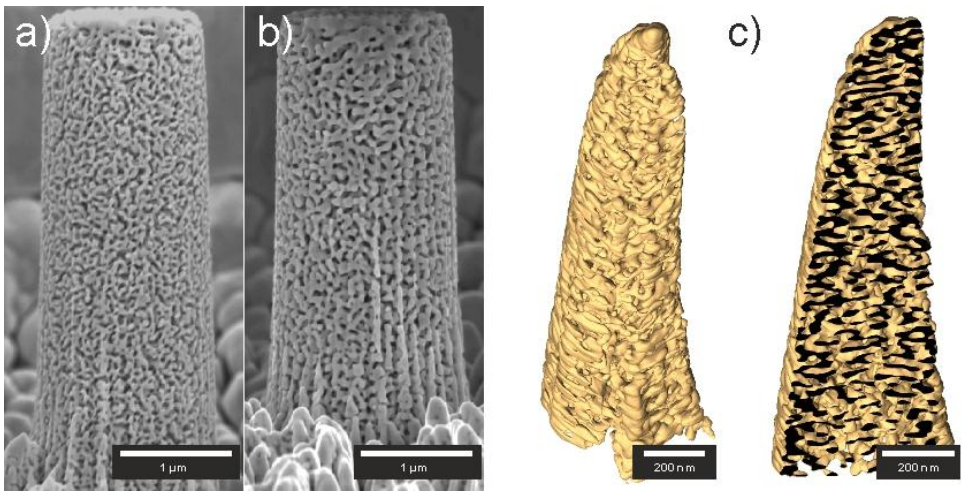

Figure 1. SEM micrographs of np-Au micropillars with ligament sizes of (a) 23 and (b) 68 nm. (c) 3D reconstruction (STEM tomography) of a np-Au micropillar - surface rendering of the full reconstructed volume (left), a cut (black surface represents the cut gold phase) through the reconstructed volume (right).

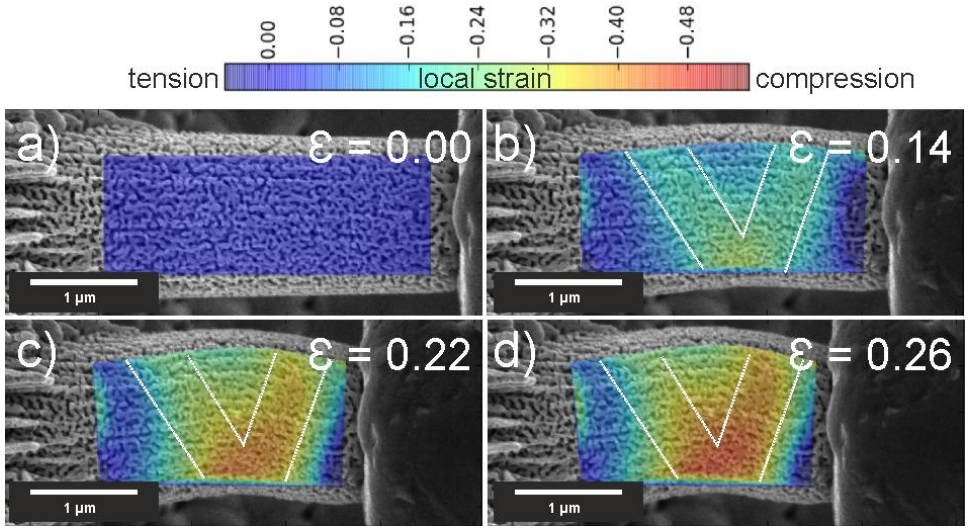

Figure 2. Local strain mapping (inset in SEM micrographs) during pillar compression at the corresponding macroscopic strain ϵ in direction of pillar axis: a) shows the undeformed state, while b)-d) show localization of pillar deformation in two discrete bands (indicated by dotted lines), which alternate in activity during compression.

Environmental, Time-Resolved and InSitu SEM/TEM

IM3.P091
In-situ TEM of phase transitions in TiNiCu based shape memory alloys

T. Wuttke[1], C. A. Volkert[1]

[1]Institute of Materials Physics, Göttingen, Germany

twuttke@ump.gwdg.de

Shape Memory Alloys (SMA) are known for their ability to recover plastic deformation upon heating and thus are being developed as actuators for application in various industrial, scientific and medical fields [1, 2]. The key mechanism responsible for this behavior is a reversible diffusionless solid-state phase transition between a highly twinned martensitic state and an untwinned austenitic phase of higher crystal symmetry [3].

We study here the martensitic phase transition of TiNiCu alloys utilizing in-situ TEM techniques.Both commercially available wires and samples prepared with vacuum arc melting were used. All samples were annealed at 600°C for 1.5h to promote grain growth and impede the nucleation of intermediate phases. This treatment also ensures that the phase transition takes place between RT and 100°C thus making it easily accessible in the TEM.

Figure 1 shows one complete phase transformation cycle taking place in a $Ti_{50}Ni_{30}Cu_{20}$ shape memory alloy when the temperature is initially increased from 40°C to 60°C and then lowered back down to 40°C. During the heating stage, the twins retreat as the orthorhombic martensite transforms into cubic austenite. At 60°C the phase transition is complete and there are no more twins remaining. Subsequent cooling reverses this process and leads to the reformation of martensite twins and transformation back to the orthorhombic state. The experiment has been carried out using a Gatan heating holder where the speed of transformation is mainly limited by heat diffusion and less so by intrinsic kinetic effects of the phase transformation. Still, it is possible to distinguish between two modes of transformation:

1. slow and steady movement of the austenite-martensite interface
2. jerky motion of the interface indicating that thermal activation is required to overcome an energy barrier

In-situ diffraction imaging has been carried out to further verify that the movement of twins is indeed based upon the expected orthorhombic to cubic phase transformation. Figure 2 shows SAD images which were recorded during heating and cooling of the TiNiCu sample without further tilting of the sample holder. At 40°C, the martensite shows a <211> zone axis which changes into <110> of cubic austenite once 60° is reached. Finally, the structure changes back to <211> as the sample is again cooled down to 40°C. The elongated diffraction spots in the martensite images are due to the twinning of the sample. It is also evident that the twins must have changed their orientation since the elongation of the diffraction spots has a different orientation before and after transformation.

Figure 3 shows the microstructure of a TiNiCu sample after several completed phase transformation cycles. The cycling has been performed using a Nanofactory STM-holder which uses current pulses to locally increase the sample temperature near the STM tip. During the first 10 cycles only slight shifts in the position of the twins has been observed. Higher cycle counts (up to 10 3) will be a part of future experiments and allow us to directly observe phase transition fatigue.

1. Jan Van Humbeeck, Non-medical applications of shape memory alloys, Materials Science and Engineering: A (1999)
2. N.B Morgan, Medical shape memory alloy applications—the market and its products, Materials Science and Engineering: A (2004)
3. K. Otsuka and X. Ren, Physical metallurgy of Ti-Ni-based shape memory alloys, Progress in Materials Science (2005)

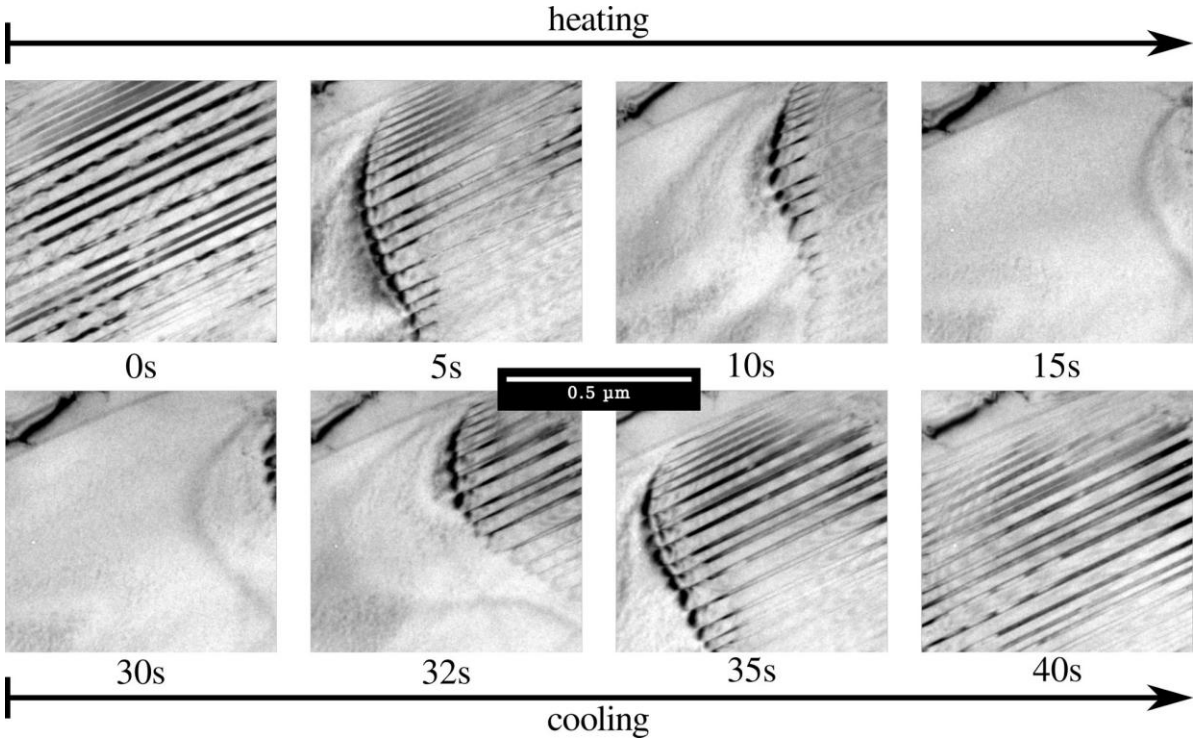

Figure 1.Shown is a complete phase transformation cycle taking place in a Ti50Ni30Cu20 shape memory alloy. During the first 15 seconds the sample is getting heated up to 60 °C which results in the slow withdrawal of the twins. After 15s the sample consists only of cubic austenite without any twins. Subsequent cooling down to RT results in twin reformation as the austenite turns again into orthorhombic martensite.

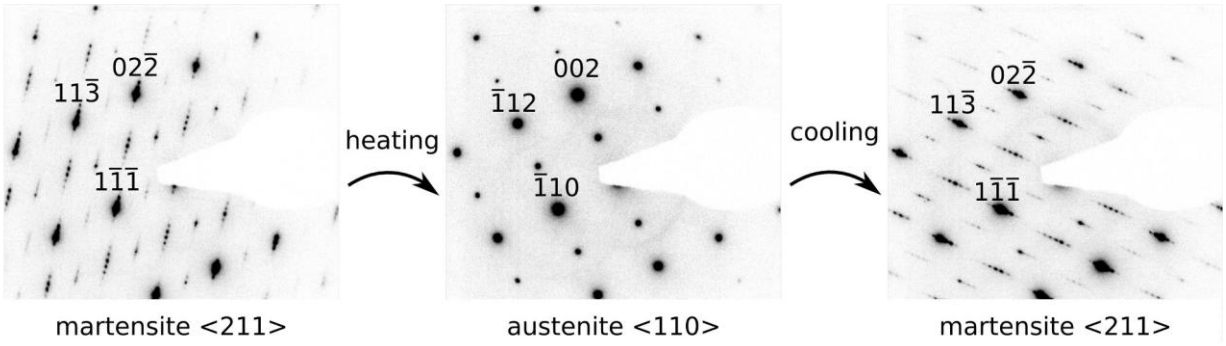

Figure 2. In-situ SAD imaging of zone axes during heating and cooling. The shown zone axes convert directly into each other without any tilting of the sample.

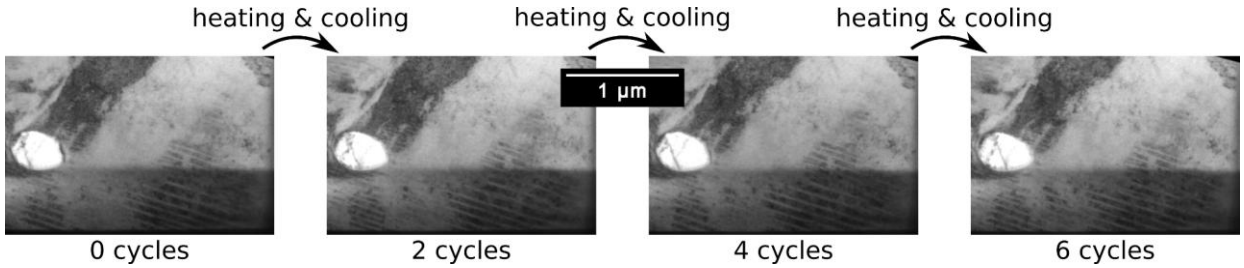

Figure 3. Several cycles using pulsed heating to study the effect of phase transition fatigue. During ~10 cycles only slight deviations regarding the position of twins have been observed. Higher cycle counts (~103) will be a part of future experiments.

Environmental, Time-Resolved and InSitu SEM/TEM

IM3.P092
Miniaturised multi-detector unit with a coaxial ion micro-source for 3D imaging in VP/E SEM

W. Slówko[1], A. Wiatrowski[1]

[1]Wroclaw University of Technology, Faculty of Microsystem Electronics and Photonics, Wroclaw, Poland

witold.slowko@pwr.edu.pl

A multi-detector method of three dimensional (3D) imaging shows some disadvantages [1,2] in relation to standard stereoscopic methods, but offers the capability of 3D imaging of very smooth and weakly modulated surfaces frequently seen at biological samples (Fig.1). This suggests application of this method in VP/E SEM as an instrument especially dedicated for investigations of wet samples. The multi-detector method of 3D imaging implies computer processing of signals acquired from four directional backscattered electron (BSE) detectors, i.e. detectors which collect electrons emitted from the sample in strictly defined directions. As the semiconductor quadruple BSE detectors cannot work properly at high water vapour pressures (approaching 10 hPa) demanded for samples of this kind, the combined directional electron detector system employing ionisation mechanisms was designed and first time presented at MC2013 in Regensburg [3,4]. This solution won the Gold Medal Award of Merit at INPEX 2014 in Pittsburgh, but it still showed too large dimensions that limit both the minimum working distance (WD) to approximately 15 mm, and obtainable resolution of images. Thus, deep miniaturisation of the detector unit should be done without loss of its electrical parameters. It was not an easy task because minimal dimensions of the electric discharge space depend mainly on the electron mean free path length in gas which is about 20 mm at BSE energy of 10 keV and water pressure of 1 hPa. Finally, dimensions of the detector unit containing four sector BSE detectors have been reduced to 10 mm in its length and 6 mm in diameter, as it is shown in Fig. 2. The detector unit is small enough in diameter to be placed inside the bore in a lower pole-piece of the objective lens (it is immersed in magnetic field). In this position the detector unit does not limit a minimum WD at all and therefore WD may be reduced even to zero. The magnetic field in the objective lens bore is too weak to influence highly energetic BSE efficiently, but can elongate trajectories of low energy environmental electrons which increases their multiplication in an ionisation avalanche. As the result the detector produces satisfying output signal for water pressures exceeding 2 hPa. The upper pressure limit approaches 10 hPa and is caused both by scattering the primary electron beam and BSE stream on their gas path lengths (GPL) to the sample which cannot be reduced much below 3 mm, because according to the method assumptions, maximum BSE detection angles should be possibly small to reduce a so called shadowing error. An axial part of the detector tube is occupied by a three segment pipe operating primarily as the throttling aperture extension and secondly as an ionisation secondary electron (SE) detector or a discharge chamber of the coaxial ion micro-source. The above described system should be sealed in the objective lens bore to close the intermediate vacuum space in the objective lens typical for VP/E SEM.

The described system can also be used in a classic high vacuum SEM. In this case it is combined with a differential pumping unit and a movable vacuum-detector head containing both the detector set and the intermediate vacuum chamber necessary for environmental applications. The capability of 3D imaging of the surface topography can be extended to the bulk 3D by a local surface sputtering with use of the coaxial ion micro-source arranged in the throttling aperture extension. This can be done in a form of 3D images (Fig. 3) made at several depths.

1. L. Reimer, R. Bongeler, V. Desai, Scanning Microscopy 1(3), 1987, p. 963.
2. J. Paluszyński, W. Słówko, J. Microsc. 233/1, 2009, p. 10.
3. W. Slówko, M. Krysztof, Proc. MC2013 Regensburg, p. 142-144.
4. W. Slówko, European patent application EP2672504 (A2).
5. Electronic parts of the system have been designed by Mr. J. Brach.

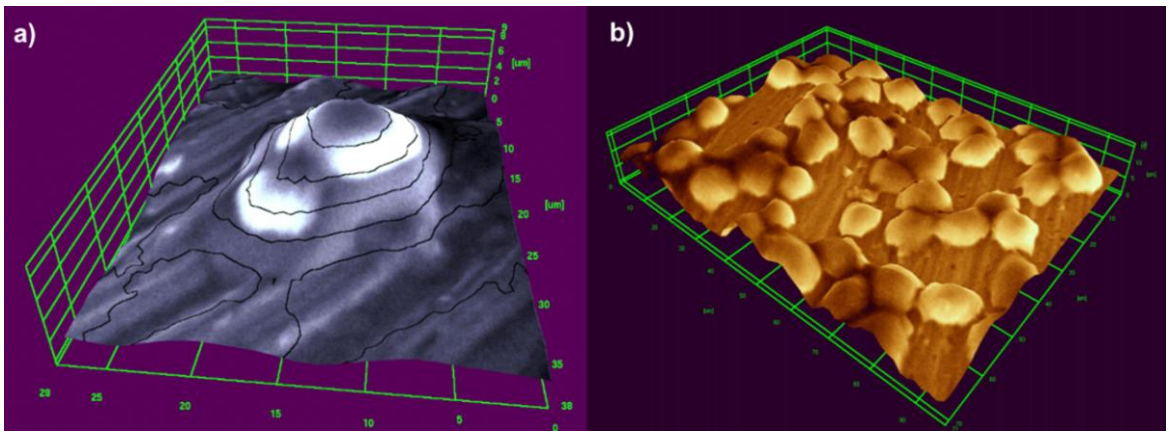

Figure 1. Spherical forms of stem cells: a) partly covered with mucus, b) after additional washing.

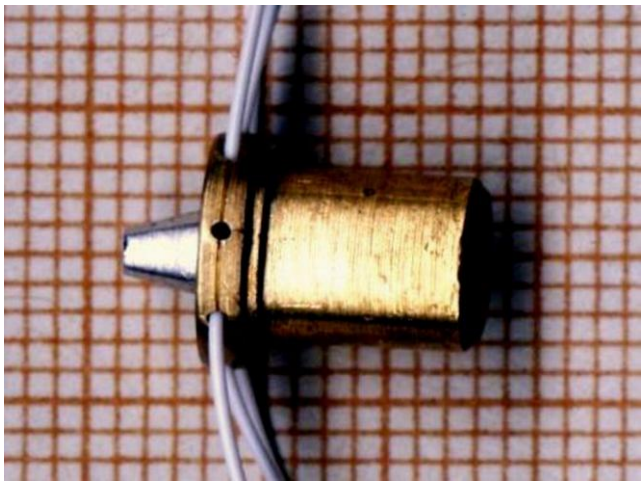

Figure 2. Miniaturized multi-detector unit.

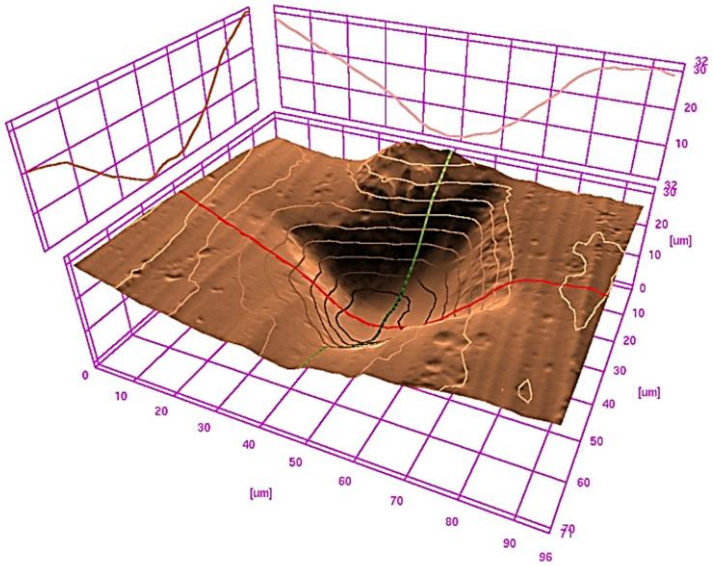

Figure 3. Cavity in a bronze foil made by ion bombardment.

Environmental, Time-Resolved and InSitu SEM/TEM

IM3.P093
Coaxial ion micro-source for 3D VP/E SEM

W. Slówko[1], A. Wiatrowski[1]

[1]Wroclaw University of Technology, Faculty of Microsystem Electronics and Photonics, Wroclaw, Poland

witold.slowko@pwr.edu.pl

Nowadays Scanning Electron Microscopy (SEM) has much to do with ion techniques and their marriage gets closer every day. Most SEM dedicated applications are based on the phenomenon of surface erosion under ion bombardment. In a SEM only a surface features of a sample are visible. To gain information on features below the surface in regions of interest it is possible to use a Focused Ion Beam (FIB), to strip away layers of material [1]. Combinations of FIB and SEM frequently called a Dual Beam present unique capabilities in nanotechnology or biomedical investigations and they may be used for ion machining with 10 - 100 nm resolution. Unfortunately, they belong to most sophisticated instruments in this branch and may cost a few times more than standard SEMs. On the other wing of ion instruments there are so called Broad Ion Beam (BIB) systems [2], offered as autonomous stations destined for preparing sample surfaces by ion milling and polishing usually with beams of a few mm in diameter. Such instrument for sample preparation to be further investigated in a SEM is relatively expensive because it must be equipped in autonomous electrical and vacuum systems. Thus a solution positioned in the middle of the mentioned systems, presenting an ion beam of medium resolution (about 10 µm), placed inside the SEM sample chamber and based on standard SEM equipment, seems very welcome as an universal in use and cheap instrument. To meet these requests the coaxial ion micro-source has been designed and combined with the multi-detector 3D system for a Variable Pressure/Environmental SEM (VP/E SEM). The main part of the source is a discharge chamber (Fig. 1) positioned at the electron optical axis of the SEM column instead of so called Pressure Limiting Aperture (PLA) extension usually present in a microscope of that kind. The discharge chamber is feed with Argon at pressure about 1 hPa while the sample chamber is kept in much better vacuum (< 10 Pa). It is possible to extract up to 10% of the discharge chamber current (< 100 µA) in the form of an ion beam which can be accelerated to the energy range of 0.5 keV to 3 keV. Distribution of the ion current density roughly resembles the Gaussian one with the skirt cut at the diameter close to the diameter of an extracting aperture. Estimated half width of the distribution can be reduced to some 20 µm for the extracting aperture of 200 µm in diameter. Preliminary experiments with the source were conducted on JSM 840 microscope equipped with an original detector-vacuum system extending capabilities of this old instrument to 3D VP/E SEM features. The source is too small to contain a beam deflecting system which is usually present in standard FIBs. As our JSM 840 microscope has no computer controlled stage such equipment is being designed. Then our investigations are limited to ion milling with stationary beam. In Fig. 2, Fig. 3 and Fig. 4 three stages of ion milling conducted on a 50 µm thick beryllium bronze foil are shown for example. Fig. 2 prepared as a 3D reconstruction illustrates an initial stage of the ion drilling and reveals main directions of the material texture. The next one (Fig. 3) shows a rhombic window in the foil with size of 10 µm at a lesser side. A small straw screened the foil from milling and an original material remained under this particle. The window seen in Fig. 4 is about 20 µm and a lesser magnification reveals the maximum beam diameter (about 200 µm) with a PLA vignette. The micro-source was designed mainly for a kind of 3D tomography obtainable classically by stripping layers of material or by drilling it in chosen point and making 3D images like this in Fig. 2 at a row of depths.

1. Ch. Parmenter, Imaging & Microscopy, 4, 2013, p. 12.
2. G. Desbois at al., Journal of Microscopy,249, 2013, p.215.
3. Electronic parts of the system have been designed by Mr. J. Brach.

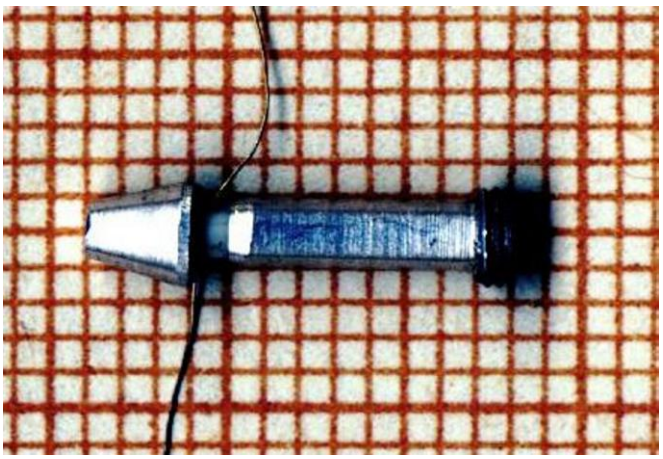

Figure 1. Discharge chamber of the micro-source.

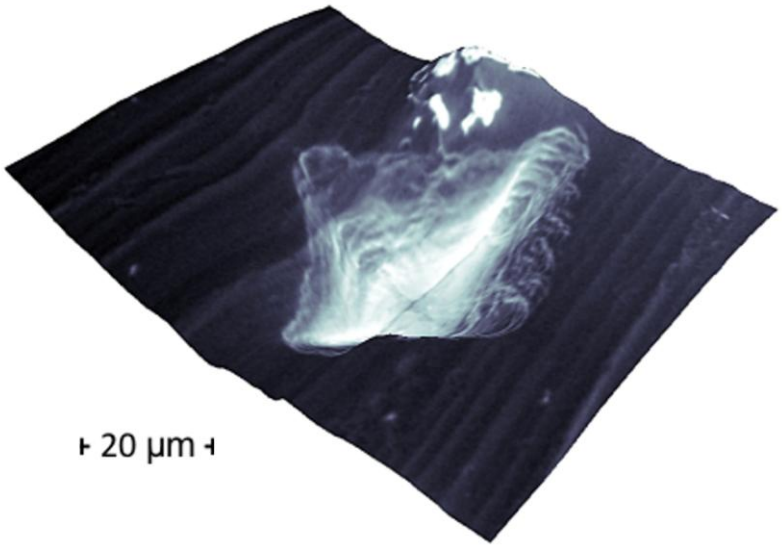

Figure 2. 3D view of the cavity in a 50 µm thick beryllium bronze foil obtained after 10 minutes of ion beam milling.

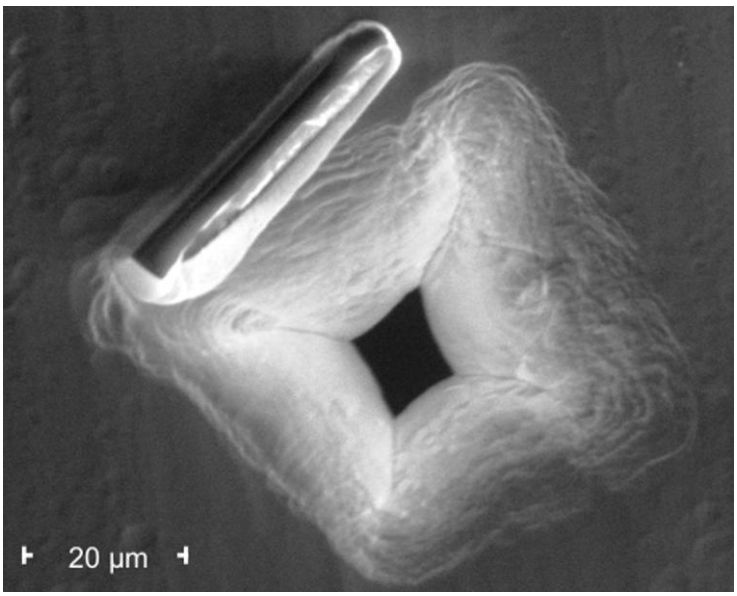

Figure 3. Rhombic window in the foil from Fig. 2 obtained after 20 min. of milling.

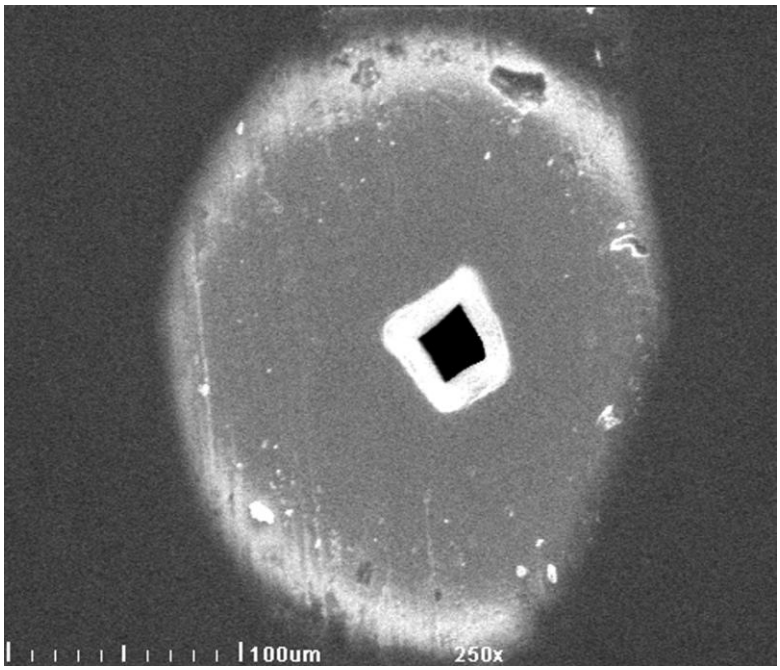

Figure 4. View of the foil surface with a PLA vignette after 30 min. of milling.

Environmental, Time-Resolved and InSitu SEM/TEM

IM3.P094
Surface morphology and water wettability of Aquilegia vulgaris studied by environmental scanning electron microscopy (ESEM)

M. Koch[1]

[1]INM - Leibniz Institute for New Materials, Physical Analytics, Saarbrücken, Germany

marcus.koch@inm-gmbh.de

Many plants in nature show superhydrophobic water wetting behaviour reflected by a contact angle of Θ > 150° between the water droplet and the leaf surface [1]. This wetting behaviour is caused by epicuticular wax crystals with different morphologies that are found on top of the leaf surfaces [2]. For the lotus plant (*Nelumbo nucerifa*) the extraordinary water repellency was named “Lotus effect” [3] and the self-cleaning properties have found technical applications. Generally, the combination of surface chemistry and surface topography in the sub-micron scale determines superhydrophobicity [4] and ESEM is capable of resolving surface features under dynamic water wetting conditions [5].

For a detailed analysis of the wetting phenomena on a superhydrophobic plant leaf we chose *Aquilegia vulgaris,* a plant with similar surface topography compared to the lotus plant (see Fig. 1). The wetting experiments were performed using an environmental scanning electron microscope at 276 K and a water vapour pressure range of 700-1000 Pa. Secondary electron images were captured at an accelerating voltage of 10 kV and 30 µs dwell time. After initiating water droplet formation on the leaf surface by increasing the water vapour pressure up to 1000 Pa, the droplet size was controlled by changing the water vapour pressure inside the SEM chamber.

Water droplet formation started both on the wax covered asperities and on the wax covered wrinkles of the leaf surface and grew as described by Rykaczewski (microdroplet growth mechanism, see [6]). By reducing the pressure inside the chamber, the water droplets collapsed and water patches are left on the surface. It is assumed that the diameter of these patches is equivalent to the droplet base. The maximum and minimum droplet diameters were analysed using the model of Extrand [7] and the contact angles for the asperity part and the wrinkle part were determined. After complete evaporation of the water droplets, the underlying wax crystals can be analysed regarding their contact line length. By means of the droplet base and the contact line length, the contact line density is determined and correlated with the maximum water droplet diameter.

It is found that the contact line density of the wax crystals on top of the leaf surfaces is a quantitative criterion for the contact angle between the water droplet and the leaf surface. The influence of the contact line density and the wetting behaviour for different leaf surfaces is discussed.

1. C. Neinhuis and W. Barthlott, *Annals of Botany* 79 (1997) 667.
2. K. Koch and H.-J. Ensikat, *Micron* 39 (2008) 759.
3. W. Barthlott and C. Neinhuis, *Planta* 202 (1997) 1.
4. R. Fürstner, W. Barthlott, C. Neinhuis and P. Walzl, *Langmuir* 21 (2005) 956.
5. M. Koch and N. de Jonge, *Advances in Imaging and Electron Physics*, 179 (2013) 193.
6. K. Rykaczewski, *Langmuir* 28 (2012) 7720.
7. C.W. Extrand, *Langmuir* 22 (2006) 8431.
8. I would like to thank Prof. Arzt for ongoing support.

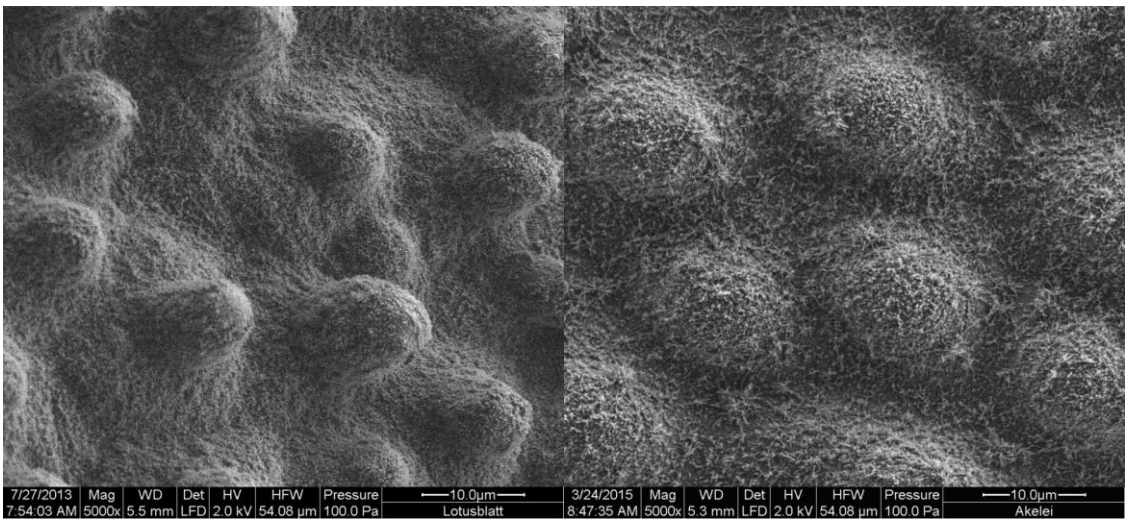

Figure 1. Secondary electron image of *Nelumbo nucerifa* (left) and *Aquilegia vulgaris* (right) at 2 kV accelerating voltage and 100 Pa water vapour pressure after 10° sample tilting. Small wax crystals cover both the asperities and the wrinkle part of the surface.

Environmental, Time-Resolved and InSitu SEM/TEM

IM3.P095
In-situ observation of catalyst splitting in vapor-liquid-solid growth kinetics

X. Huang[1], Z. Wang[1], G. Weinberg[1], X. Meng[2], R. Schlögl[1], M. G. Willinger[3]

[1]Fritz-Haber-Institut der Max-Planck-Gesellschaft, Inorganic Chemistry, Berlin, Germany
[2]Technical Institute of Physics and Chemistry of Chinese Academy of Sciences, Beijing, China
[3]Max-Planck-Institut für Chemische Energiekonversion, Mühlheim (Ruhr), Germany

xinghuang@fhi-berlin.mpg.de

In situ electron microscopy has been demonstrated to be a versatile and powerful technique for investigating kinetics of crystal growth,[1.] phase transition,[2.] and catalytic reaction.[3.] In this work, we report *in situ* observations during VLS growth of semiconductor nanowires in the chamber of an environmental scanning electron microscopy (ESEM). The instrument is equipped with an FEI heating stage and a gas-feeding system. Thus the chamber of the ESEM can be used as an *in situ* chemical vapor deposition (CVD) system that simultaneously enables electron microscopic investigation of the growth dynamics. For nanowire growth, a powder mixture of CdS and ZnS was used as source material and silver nanoparticles as metal catalyst. Through tracing growth kinetics of nanowires, we found that nanowires with a relatively bigger catalyst droplet pinned on the tip grow faster. Intriguingly, we also found that the growth of nanowires could involve in a direct catalyst splitting: while majority of catalyst would remain at the tip of nanowire and continuously assist the growth of nanowire as before, partial catalyst would stay at the position where the splitting occurred and later induce the growth of additional nanowire branch, after its diffusion and condensation processes. To the best of our knowledge, this is the first time that catalyst splitting was observed experimentally *in situ*. It may reside in the instability of catalyst droplet ascribed from the volume increase in the dynamic process. This observation also implies that the traditional mechanism proposed for growth of branched or hyperbranched nanowires may be oversimplified. So far it is assumed that it is the deposition and condensation of catalyst on the preformed nanowire which induces the nucleation and growth of nanowire branch. The composition and structure of resulting nanowires were examined with transmission electron microscopy (TEM), which indicates that the obtained nanowires are pure ZnS with a WZ structure. The absence of Cd in the nanowires can be ascribed to the complete substitution of Zn^{2+} for Cd^{2+} during growth. *In situ* growth inside the ESEM may enrich our understanding on the metal-catalyzed VLS growth kinetics and open up opportunities for morphology controlled synthesis of 1D semiconductor nanowires.

1. Wu, Y. Y.; Yang, P. D.Direct observation of vapor-liquid-solid nanowire growth, *J. Am. Chem. Soc.* **2001,** 123, (13), 3165-3166.
2. In, J.; Yoo, Y.; Kim, J. G.; Seo, K.; Kim, H.; Ihee, H.; Oh, S. H.; Kim, B.In Situ TEM Observation of Heterogeneous Phase Transition of a Constrained Single-Crystalline Ag_2Te Nanowire, *Nano Lett.* **2010,** 10, (11), 4501-4504.
3. Vendelbo, S. B.; Elkjaer, C. F.; Falsig, H.; Puspitasari, I.; Dona, P.; Mele, L.; Morana, B.; Nelissen, B. J.; van Rijn, R.; Creemer, J. F.; Kooyman, P. J.; Helveg, S.Visualization of oscillatory behaviour of Pt nanoparticles catalysing CO oxidation, *Nat. Mater.* **2014,** 13, (9), 884-890.

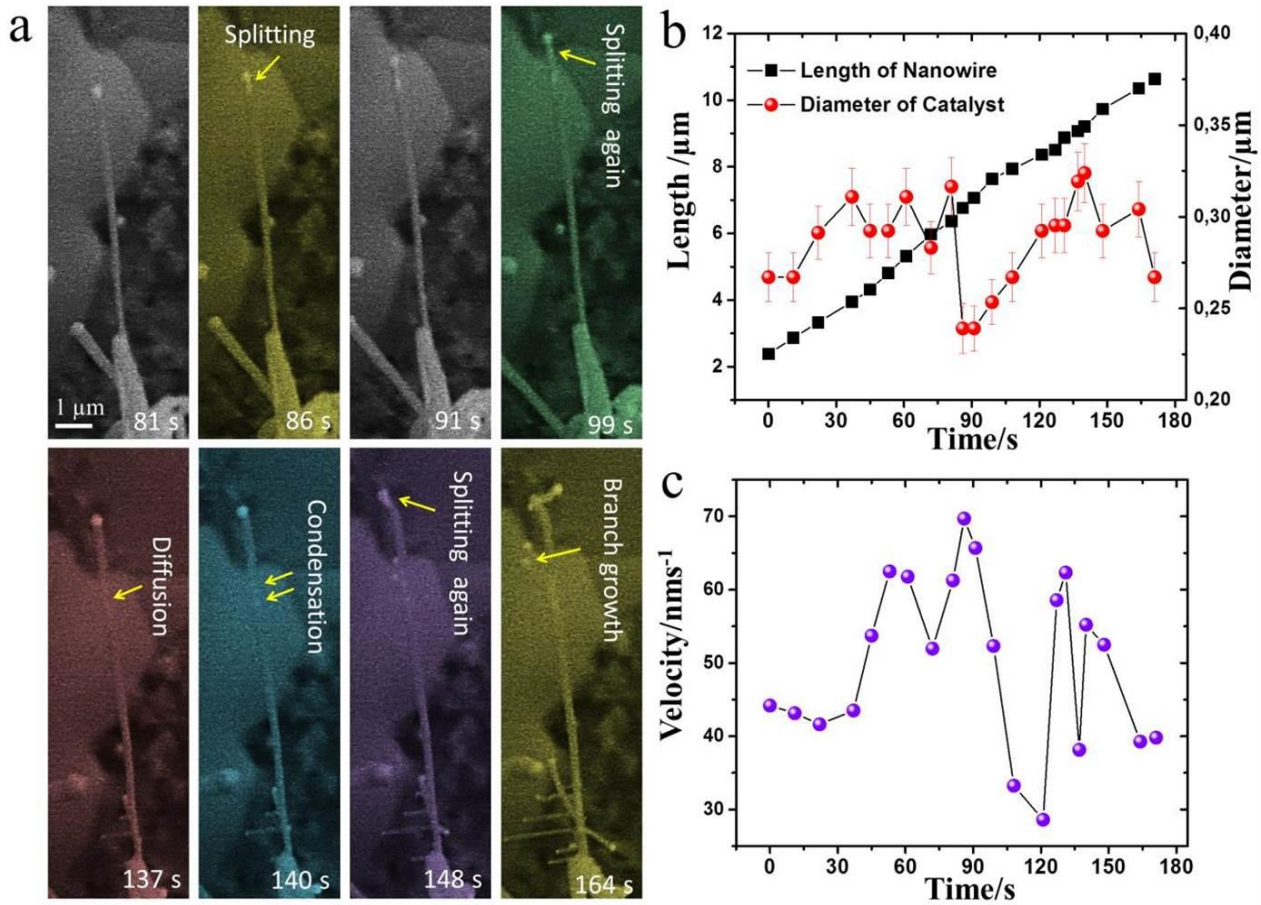

Figure 1. Kinetics of catalyst splitting: (a) *In situ* SEM observation of the catalyst splitting in the growth of branched nanowire; (b) Length of nanowire and diameter of catalyst as a function of time; (c) Velocity of nanowire as a function of time.

Environmental, Time-Resolved and InSitu SEM/TEM

IM3.P096
Marine in Industrial biotechnology: biosorption by Sargassum glaucescens brown algae nanoparticle at new membrane reactor

A. Esmaeili[1], A. Aghababai Beni[1]

[1]North Tehran Branch, Islamic Azad University, Department of Chemical Engineering, Tehran, Iran

akbaresmaeili@yahoo.com

In this study, a new membrane reactor with a volume of 1.5 liter was made to remove nickel and cobalt. In this process, initially wastewater was entered into a settling tank. Tthe liquid phase was separated and entered into a stalactite column in order to remove suspended particles. The biosorption reaction in the reactor was studied in the presence of nanobiosorbents in different conditions of pH, biosorbent dose, and temperature and retention time. Finally, the concentration of heavy metals was investigated after the fluid had passed through the membrane system. Algae nanobiosorbent was prepared using a planetary ball mill; Scanning Electron Microscope and Brunauer-Emmert-Teller tests showed an average diameter of 95.75 nm and specific surface area of 11.25 m^2g^{-1}, respectively. Maximum biosorption efficiency equal to 93% and 91% was achieved for nickel and cobalt at pH 6, temperature 35 °C with a retention time of 80 min, at biosorbent doses of 8 and 4 g. The kinetic data fitted well by pseudo-first-order model and equilibrium data of metal ions could be described well with the Langmuir and Dubinin-Radushkevich isotherm models. The calculated thermodynamic parameters showed that metal ion biosorption is feasibile, endothermic and naturally spontaneous.

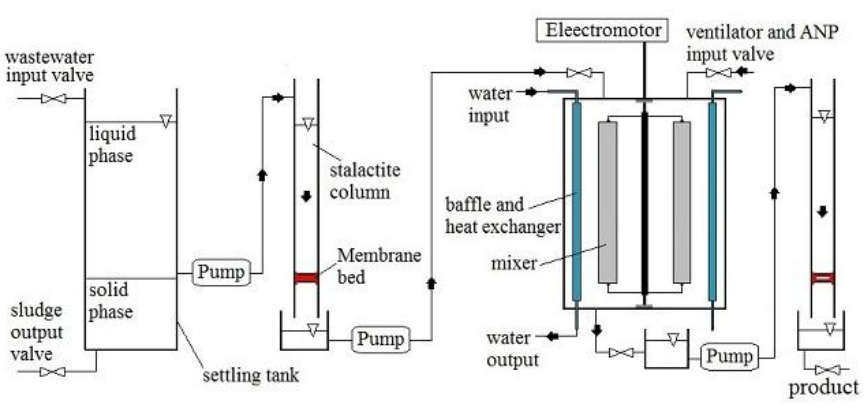

Spectroscopic TEM/STEM, EELS, EFTEM

IM4.098
Vibrational phonon spectroscopy of boron nitride polymorphs in the electron microscope: a comparison between theory and experiment

Q.M. Ramasse[1], F.S. Hage[1], R. Nicholls[2], J. Yates[2], D. McCulloch[3], T.C. Lovejoy[4], N. Dellby[4], O.L. Krivanek[4] and K. Refson[5,6]

[1] Department of Materials, University of Oxford, Parks Road, Oxford, UK
[2] SuperSTEM Laboratory, STFC Daresbury Campus, Keckwick Lane, Daresbury, UK
[3] School of Applied Sciences, RMIT University, Melbourne, Australia
[4] Nion Company, 11511 NE 118th St., Kirkland, WA 98034, USA
[5] STFC Rutherford Appleton Lab., Harwell Science and Innovation Campus, Didcot, UK
[6] Department of Physics, Royal Holloway, University of London, UK

QMRamasse@superstem.org
Keywords: STEM, EELS, phonons, vibrational spectroscopy, 2D materials

The increased energy resolution of a new generation of electron microscopes has made exploring the phonon region of the EELS spectrum possible [1]. To fully interpret the extra information available it is important to be able to compare the data to theoretical calculations so that we can extract physically meaningful results.

Here we use different polymorphs of boron nitride and in particular the cubic (c-BN) and hexagonal (h-BN) phases, as well as other BN-containing complex engineering materials, to compare experimental phonon spectroscopy results in the scanning transmission electron microscope to theoretical calculations. Both cubic and hexagonal boron nitride samples were prepared by simple drop casting onto lacey carbon grids. Imaging and EELS core loss and phonon spectrum imaging were carried out on the different BN polymorphs using a monochromated Nion UltraSTEM100MC 'HERMES' microscope [2] installed at the SuperSTEM Laboratory. Atomic resolution images and core loss chemical maps of the regions of interest were obtained in order to fully characterize them prior to phonon spectroscopy. For the high energy resolution experiments, the instrument was subsequently adjusted to provide a zero-loss peak (ZLP) full width at half-maximum (FWHM) of approximately 15 meV for a probe size of 2.5 Á. The microscope was operated at 60 kV in order to minimize any damage to the samples.

Typical phonon spectra are shown in figure 1: all spectra were normalized to the maximum of the zero-loss peak (ZLP) to account for total signal variations as the probe was moved into the rather thick BN flakes. Several very striking features can be observed. For h-BN, the main phonon peak appears at 183 meV (note that the difference with previously reported values [1] could be due flake size effects or to slight energy calibration differences). Interestingly, a small energy shift is observed as the probe moves from aloof geometry into the sample. The FWHM of the peak also increases within the sample. By contrast, the main phonon for c-BN appears at a lower energy of 147 meV. A small shoulder at ~100 meV appears only when the beam goes through the sample: its origin is being investigated.

Phonon modes are a property of the material and several techniques exist to calculate them including finite-displacement methods and perturbation theory. The intensity with which the modes appear in an experimental spectrum depends on the type of experiment and experimental set up. Several ab initio codes are able to compute phonon modes in solids together with IR and Raman intensities. We use the density functional theory code CASTEP [3] to calculate the phonon modes for the different BN polymorphs using a linear response method [4] and compare these to the experimentally observed spectra. One of the in-plane optical modes of h-BN is shown in Figure 2.

1. O.L. Krivanek, T.C. Lovejoy, N. Dellby et al., Nature 514 (2014), pp. 209-212.
2. O.L. Krivanek, J.P. Ursin, N.J. Bacon et al., Phil. Trans. Roy. Soc. 367 (2009), pp. 3683-3697.
3. S.J. Clark, M.D. Segall, C.J. Pickard et al., Z. Kristallog. 220 (2005), pp. 567-570.
4. K. Refson, S.J. Clark and P.R. Tulip, Phys. Rev. B 73 (2006), 155114.
5. SuperSTEM is funded by the UK Engineering and Physical Sciences Research Council (EPSRC).

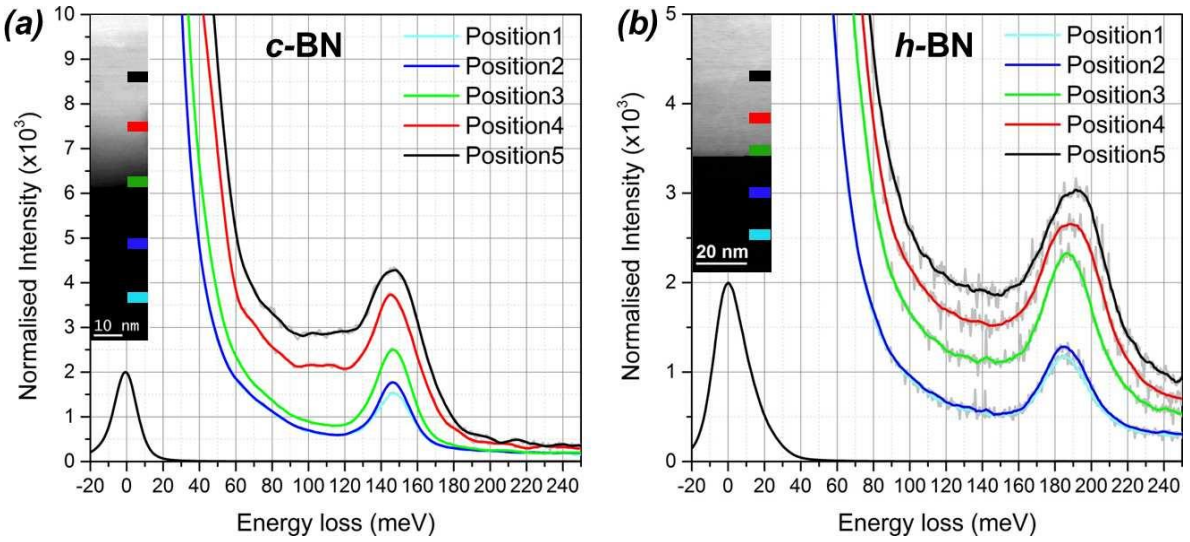

Figure 1. Position-resolved low loss EEL spectra taken at the edge and into (a) c-BN and (b) h-BN flakes. HAADF images, inset, show the exact location of the EELS acquisition with respect to the flake edge. 100 frames of 8ms (resp. 100 frames of 5ms) exposure each were averaged to improve the signal-to-noise for the c-BN (resp. h-BN), after careful alignment to their maximum. The full ZLP is shown for comparison, scaled by a factor of 1000 (a) (resp. 500, (b)).

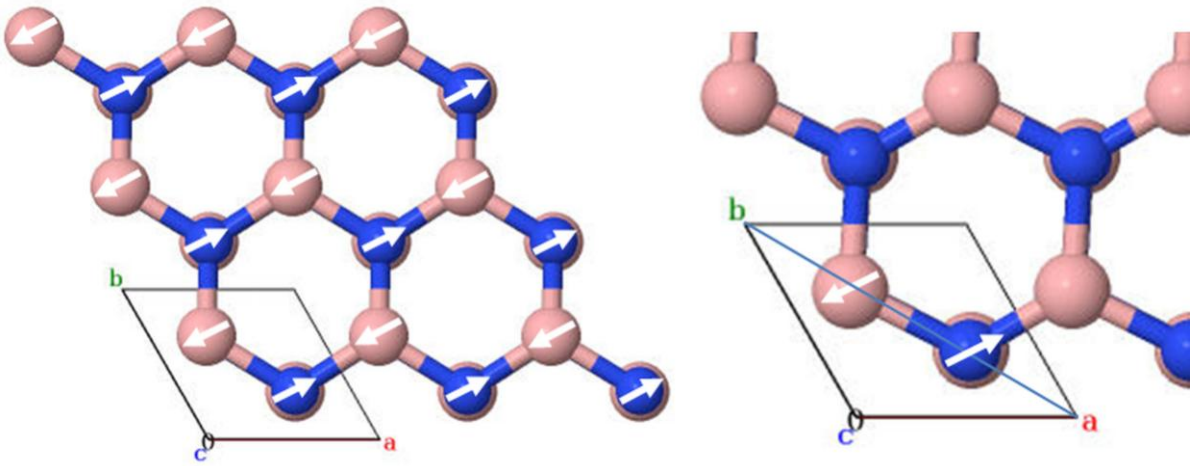

Figure 2. Simulated in-plane optical phonon mode for h-BN. Each column of atoms moves as a whole and, within each layer, the carbon-nitrogen bond oscillates.

Spectroscopic TEM/STEM, EELS, EFTEM

IM4.099
The quest for quantitative figures on atomic resolution inelastic STEM images

G. Kothleitner[1], N. R. Lugg[2], M. J. Neish[3], S. D. Findlay[4], W. Grogger[1], F. Hofer[1], L. J. Allen[3]

[1]Graz University of Technology, FELMI Inst. f. Electron Microscopy and Nanoanalysis, Graz, Austria
[2]The University of Tokyo, Institute of Engineering Innovation, Tokyo, Japan
[3]University of Melbourne, School of Physics, Parkville, Australia
[4]Monash University, School of Physics and Astronomy, Clayton, Australia

gerald.kothleitner@felmi-zfe.at

Locating atoms, identifying atoms, and revealing their bonding are fundamental goals in modern materials characterization and analysis. C_S-aberration corrected microscopy, as carried out in a scanning transmission electron microscope (STEM), has given access to atomic resolution and, accompanied by improvements in detecting X-ray (EDXS) and energy-loss (EELS) signals, analytical investigations now allow for a correlation of structural and chemical information [1-6].

Quantification of atomic resolution chemical maps on an absolute scale (i.e. in units of atoms/nm^3), however remains a challenge. First of all, the conversion of analytical intensities into concentration numbers for a particular quantification scheme often requires extra parameters, such as sample densities, absolute thicknesses, theoretical ionization cross-sections, zeta-factors etc. These can sometimes only be approximated, introducing errors. A recently described analysis concept that connects EDX and EELS signals in a common analysis framework helps reduce the need for estimates [7]. Secondly, the complex physics of scattering of the electron probe along aligned atomic columns produces a nonlinear relation between signal and composition and there is no longer a simple relationship between the observed analytical intensities from the projected atomic positions.

Experimental data from a 61 nm thick strontium titanate sample taken in [001] zone axis orientation, as shown in fig. 1, discloses big deviations that are either larger or smaller than the actual values for an element (in this case oxygen), when averaged over the full image. The spatial variation is also revealing. That the O K shell EDX signal on the Sr columns is almost equal to that on the pure O columns should not be interpreted to mean that the O concentration in these two columns is similar, but rather that, as a consequence of the elastic and thermal scattering of the electron probe, the electron probe can trigger about the same number of O K shell ionization events regardless of which of these two columns it is positioned upon.

To recover the true concentrations, different approaches to compensate for channeling can be taken. With the use of the so-called quantum excitation of phonons (QEP) model [8], a calculation of the underlying elastic and thermal diffuse scattering is possible and quantitative comparisons between experiment and quantum mechanical calculations for both EDXS and EELS can be made. By implementing an inversion process, the correct numbers can approximately be recovered [9, 10]. Other possibilities to reduce the effects of channeling are tilting or precessing the beam [11], and will also be discussed in this paper.

1. AJ D'Alfonso, B Freitag, DO Klenov and LJ Allen, *PRB* **81** (2010) 100101.
2. J LeBeau, SD Findlay, LJ Allen and S Stemmer, *PRL* **100** (2008) 206101.
3. PG Kotula, DO Klenov and HS Von Harrach, *Microsc Microanal* **18** (2012) 691.
4. HL Xin, C Dwyer and DA Muller, *Ultramicroscopy* **139** (2014) 38.
5. HS von Harrach et al., *Journal of Physics: Conference Series* **241** (2010) 012015.
6. A Gubbens et al., *Ultramicroscopy* **110** (2010) 962.
7. G Kothleitner et al., *Microsc. Microanal.* **20** (2014) 678.
8. BD Forbes et al., *Phys. Rev. B* **82** (2010) 104103.
9. NR Lugg et al. *APL* **101** (2012) 183112.
10. G Kothleitner et al. *PRL* **112** (2014) 085501.
11. NR Lugg, G Kothleitner, N Shibtata and Y Ikuhara, *Ultramicroscopy* **151** (2015) 150.
12. The substantial help of Bernd Kraus, Paul Thomas, and Ray Twesten from Gatan, as well as Meiken Falke and Ralf Terborg from Bruker and Dmitri Klenov from FEI, in setting up this particular analytical hardware configuration is acknowledged.
13. This research has received funding from the European Union within the 7th Framework Programme [FP7/2007-2013] under Grant Agreement no. 312483 (ESTEEM2)

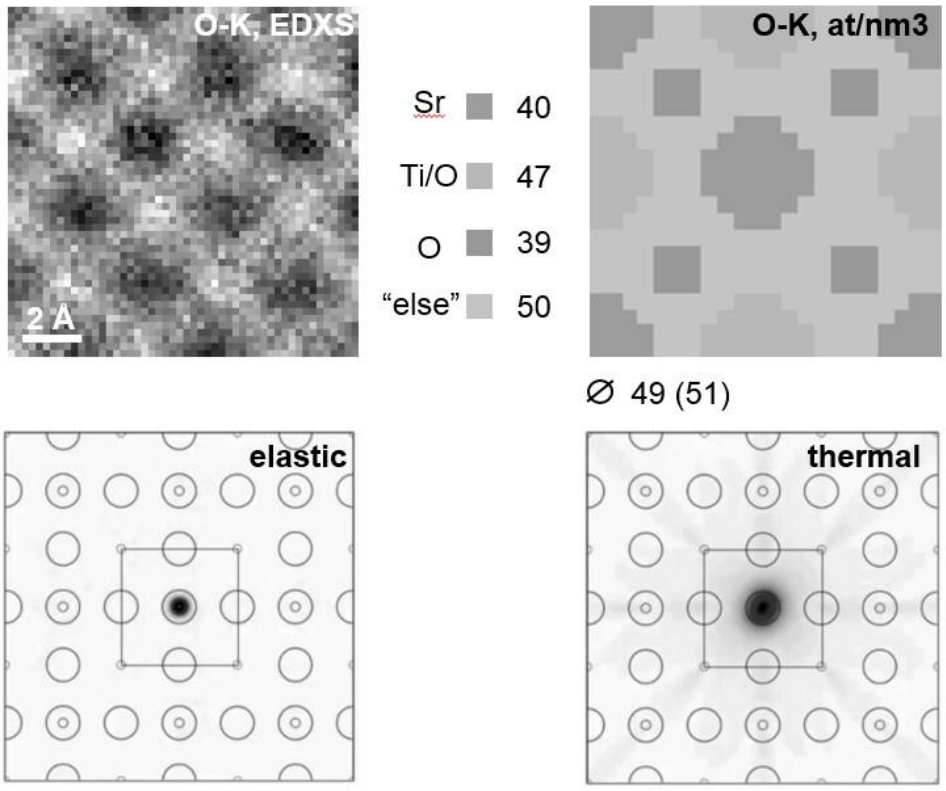

Figure 1. shows X-ray absolute volumetric concentrations for oxygen in strontium titanate [001] (upper row) together with QEP simulations (lower row), showing the elastic and thermal (scaled by x10) scattering components [10].

Spectroscopic TEM/STEM, EELS, EFTEM

IM4.100
Laterally resolved EELS of organic solar cells - optimizing spatial and energy resolution to localize charge transfer states with TEM

A. K. Kast[1,2,3], M. Oster[1], M. Pfannmöller[1,4], L. Veith[5], I. Wacker[5], G. Benner[6], W. Kowalsky[2,3], R. R. Schröder[1,2,5]

[1]Universitätsklinikum Heidelberg, CryoEM, CellNetworks, BioQuant, Heidelberg, Germany
[2]Innovationlab GmbH, Heidelberg, Germany
[3]TU Braunschweig, Institut für Hochfrequenztechnik, Braunschweig, Germany
[4]University of Antwerp, EMAT, Antwerp, Belgium, Belgium
[5]Universität Heidelberg, Centre for Advanced Materials, Heidelberg, Germany
[6]Carl Zeiss Microscopy GmbH, Oberkochen, Germany

anne.kast@bioquant.uni-heidelberg.de

Understanding the morphology of organic bulk heterojunction (BHJ) solar cells can greatly help in improving device efficiencies. While we know that domain sizes of donor and acceptor materials need to be around the exciton diffusion length so that electron and hole can be separated before recombination, we do not yet fully understand what is happening at the interfaces of the two materials where the separation occurs. Reports of so called charge transfer states, which show electronic features that neither of the two materials have, suggest interaction of the two materials.

Electron Energy-Loss Spectroscopy (EELS) in Transmission Electron Microscopy (TEM) has the necessary energy resolution to resolve such charge transfer states, occurring at low energies (for example below 2 eV for F_4TCNQ doped P3HT[1]) but spatial limitations due to large aperture sizes impede localisation and even confirmation of these states in BHJs. While we were able to visualize a third electronic state present at the interface of P3HT and PCBM using Electron Spectroscopic Imaging (ESI) [2], this method does not have the needed energy resolution to confirm the presence of a charge transfer complex.

Since these carbon-based materials are extremely prone to beam damage, especially from focussed probes with high beam currents[3], spatial spectral mapping using EELS in conventional scanning mode is not an option. To achieve both, spatial and energy resolution as it is obtainable from aberration corrected imaging energy filters we implement an automated scheme, which involves scanning the image of a slit aperture in the illumination beam path across the sample. Additional correction algorithms need to be applied to eliminate residual image distortion in the EEL spectrum to enable analysis and interpretation.

First measurements implementing Laterally Resolved EELS (LREELS) were performed using a sample of a perovskite solar cell prepared by focussed ion beam (FIB) milling[4]. The characteristic signals in the EEL spectra of the TiO_2 scaffold and the methylammonium lead iodide (MAPbI) absorber proved stable during electron irradiation, thus making this a suitable sample to test this approach.

Figure 1a shows a scanning TEM image of a FIB prepared cross section of such a solar cell. The placement of the slit aperture is indicated in red. It includes the so-called capping layer of pure MAPbI on top of the TiO_2/MAPbI layer. In figure 1b the acquired raw data of the low-loss region, without the zero-loss peak, can be seen. The raw spectral data was corrected for distortion and six spectra, equally spaced were extracted, as illustrated in figure 2. Starting at the bottom of the raw EELS data, spectrum 1 only contains information from a pure TiO_2 region. Spectrum 6 (yellow), from the capping layer, does not show the TiO_2-characteristic excitation around 48 eV, thus only containing MAPbI, as was expected. The spectra in-between show signals from both materials.

The application of such automated laterally resolved EEL spectroscopy (LREELS) as described here allows spatial mapping of high-resolution spectra in two dimensions at low-dose conditions. This is crucial for our understanding of organic BHJ solar cells.

1. P. Pingel & D. Neher. *Phys. Rev. B* **87,** 115209 (2013).
2. M. Pfannmöller, et al*. Nano Lett.* **11,** 3099-3107 (2011).
3. R.F. Egerton. *Micron* **43,** 2-7 (2012).
4. D. Nanova & A.K. Kast, et al. *Nano Lett.* **14,** 2735-2740 (2014).

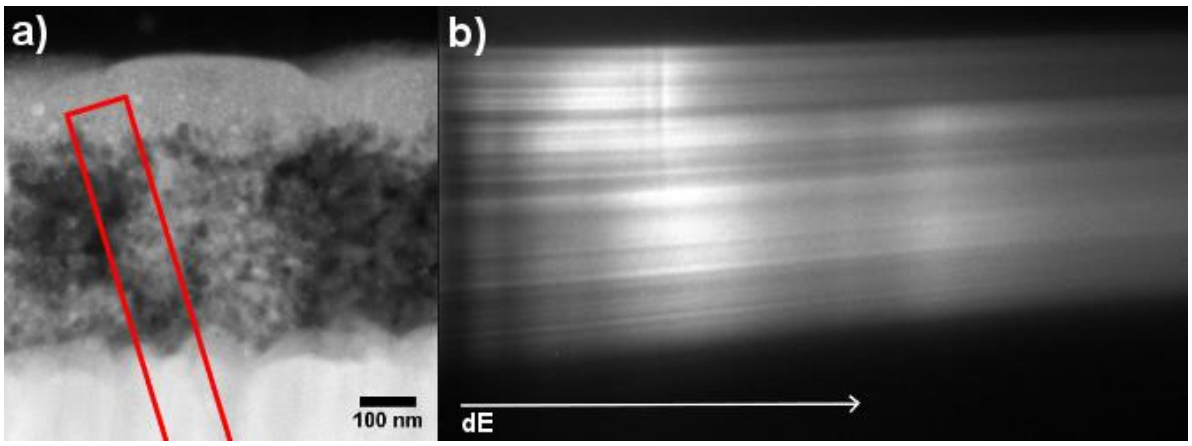

Figure 1. a) Scanning TEM image of a cross-section of a perovskite solar cell, prepared with FIB. LREELS measurements of the MAPbI filled TiO_2 scaffold and the overlying capping layer of pure MAPbI were performed, which is indicated by the red outline representing the slit aperture. b) Acquired LREEL spectrum, without the zero-loss peak, before distortion correction and analysis. The direction of energy dispersion is indicated.

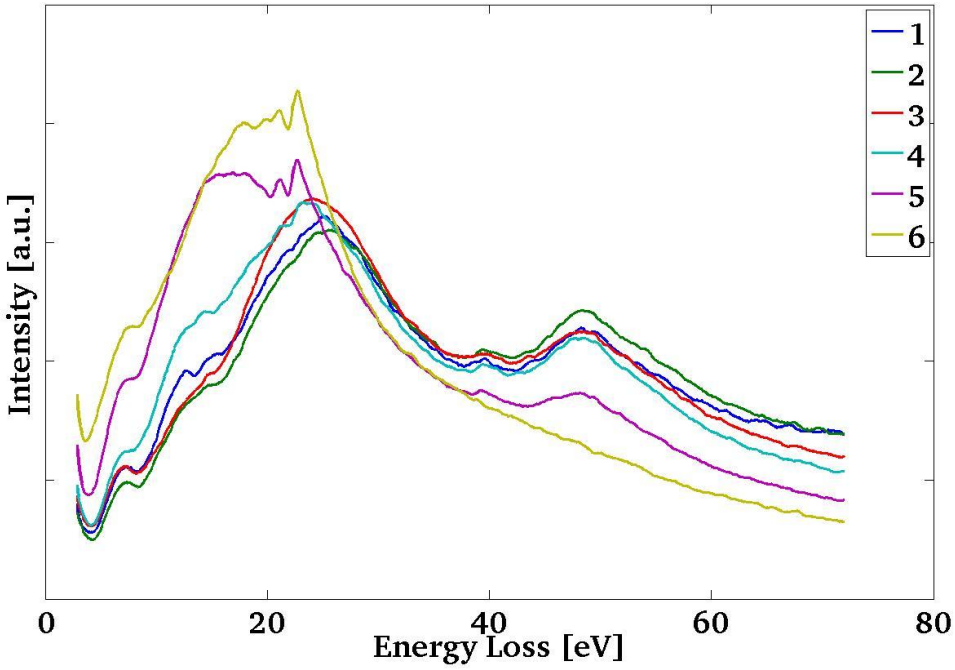

Figure 2. Spectral information extracted from the raw data shown in Fig. 2b. Six spectra, equally spaced, were extracted from the raw data after distortion correction starting at the bottom of the spectrum in Fig. 1b. This means spectrum 6 (yellow) came from the pure MAPbI layer, thus not showing the typical TiO_2 excitation around 48 eV.

Spectroscopic TEM/STEM, EELS, EFTEM

IM4.101
Low loss and core loss angular resolved EELS in anisotropic materials

F. Fossard[1], L. Schué[1], F. Ducastelle[1], A. Loiseau[1]

[1]Laboratoire d'Etude des Microstructures, CNRS/ONERA, Chatillon, France

frederic.fossard@onera.fr

Energy loss function and spectroscopies of an anisotropic crystal are highly orientation dependant and their measurements require to study their anisotropy behaviour. On one hand, X-rays measurements offer the finest energetic and angular resolution but a limited spatial resolution and require synchrotron facilities. On the other hand, electron energy losses (EELs) are highly related to both energy and momentum transferred to the material. Most of the time, EEL spectra are integrating a solid angle around the incident beam direction. Nevertheless, it has been demonstrated that core-loss EELS can be performed in order to obtain angular information in anisotropic materials [1].

Among anisotropic materials, 2D-materials (graphene, h-BN, MoS_2,…) present several peculiar properties. These layered material have strong in-plane bonds forming a compact lattice whereas layers are weakly bound by Van Der Waals forces. These materials, either semimetallic or semiconductors, exhibit a rich footprint in the low energy loss region (

We will present results on other peculiar anisotropic materials such as MAX phases which exhibit an hexagonal structure and anisotropic properties in the plasmonic region.

We used a Libra 200 equipped with an electrostatic monochromator operating at 80 kV. The achievable energetic resolution is 100 meV. We operate in the reciprocal space. Thanks to the in-column filter, energy loss signal is recorded as a function of both the energy and the momentum in a datacube, with the resolution of the exit slit of the filter. Each slice consists in a diffusion pattern indicating the momentum of the scattering for a given lost energy.

Angular Resolved EELS has been performed on foils cut in a HPHT h-BN single crystal along crystallographic orientations using a focused ion beam (FIB). We performed Energy Filtered TEM in diffraction mode to obtain diffusion pattern at given lost energies.

In order to achieve a better energetic resolution, we placed a dedicated slit in the entrance of the filter to select a specific crystallographic direction in the reciprocal space and disperse it perpendicularly (Fig1). In this way, we can link the losses to their angular dependence with an optimized resolution either in E and q [3]. This so-called “ω-q map” technique consists of a cartography of the losses (ω) in a specific direction of the reciprocal space (q).

The ω-q map extracted from the datacube along the (00l) q-direction near the B-K edge is presented in the figure 2. The difference in the dispersion of the excitation to π* and σ* states is dramatically revealed. Since initial state is an isotropic s state (K edge), the map directly reveals the symmetry of the final p-like state. We proceeded in the same way in the low loss region and we show that by gathering spectra in the high symmetry directions, we can probe the whole Brillouin zone and represent the plasmon dispersion as a function of the q momentum transferred to the h-BN layers.

We have studied the angular dependance of the Electron Energy Loss in anisotropic materials . Thanks to our experimental setup, we are able to disperse a part of the diffraction pattern in order to get Energy and momentum resolved maps of the losses. These maps, in the core-loss regime, allow to have a clear representation of atomic orbitals. In the low loss regime, we present raw determination of the plasmon dispersion in the different directions of the Brillouin zone.

The research leading to these results has received partial funding from the European Union Seventh Framework Programme under grant agreement n°604391 Graphene Flagship

1. R. Arenal et al, APL 90 (2007) 204105
2. A. Pierret et al., Phys. Rev. B 89 (2014) 035414
3. P. Wachsmuth et al., Phys. Rev. B 88, 075433 (2013)

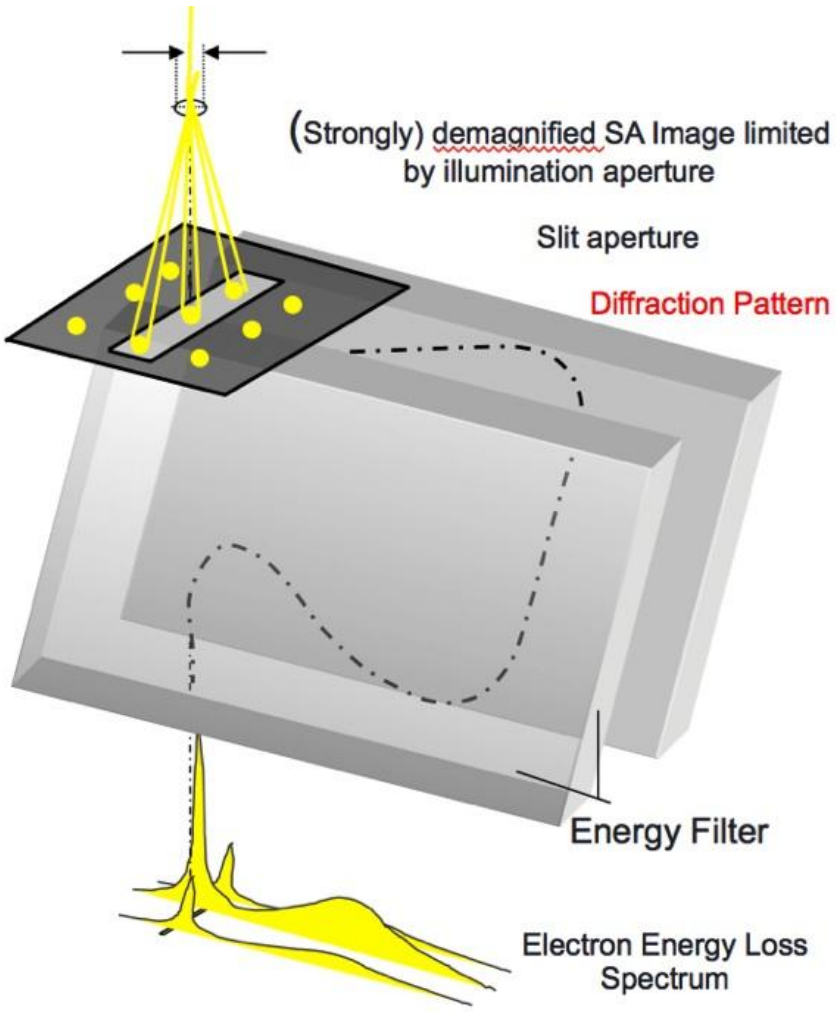
(Strongly) demagnified SA Image limited by illumination aperture
Slit aperture
Diffraction Pattern
Energy Filter
Electron Energy Loss Spectrum

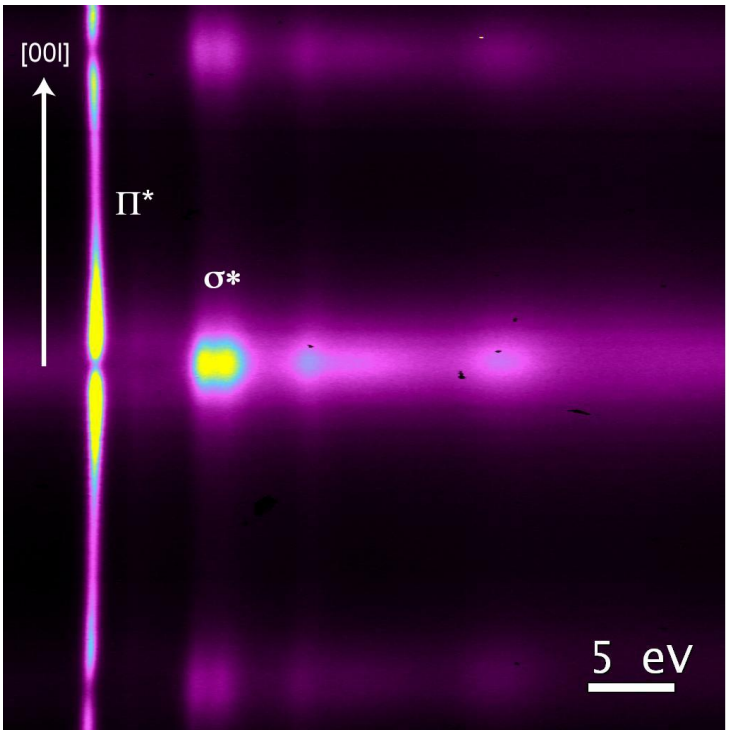
[00l]
Π*
σ*
5 eV

Spectroscopic TEM/STEM, EELS, EFTEM

IM4.102
DFT simulations: modelling EELS spectra for complex materials

P. Agrawal[1], M. D. Rossell[1], D. Passerone[2], R. Erni[1]

[1]Empa, Swiss Federal Laboratories for Materials Science and Technology, Electron Microscopy Centre, Dübendorf, Switzerland
[2]Empa, Swiss Federal Laboratories for Materials Science, Nanotech@surfaces laboratory, Dübendorf, Switzerland

piyush.agrawal@empa.ch

Recent advances in electron energy-loss spectroscopy (EELS) triggered the implementation of aberration correctors and novel spectrometers which have enabled atomic resolution and single atom sensitivity. The energy-loss near-edge structure (ELNES) in core-loss EELS provides insight into the electronic structure of individual atomic species containing information about their bonding characteristics such as, e.g., oxidation state, charge transfer and site coordination. Yet the electronic structure information is buried in the spectral fine structure which can be regarded as a “fingerprint” of the atom’s bonding characteristics. In order to overcome this shortcoming of a purely experimental approach, the ELNES of core-loss EELS ionization edges can be obtained from first-principles electronic structure calculations.

BiFeO3 (BFO) is a multiferroic perovskite that exhibits antiferromagnetism coupled with ferroelectric order. Because of their astounding electromechanical properties, BiFeO3 thin films are promising candidates for the replacement of lead-based ceramics in microelectromechanical system devices. With focus on the oxygen *K*- and the iron *L*-edges Calculations were performed on two different BFO phases (R and T) with the help of WIEN2k [1]. DFT core-hole calculations were performed on the geometry of two phases which were determined experimentally [2] previously along with energy loss spectra. Fig. 1 shows the comparison between DFT+U calculated energy loss near-edge structure of the oxygen *K*- and Fe *L*-edges in BFO with newly recorded experimental EELS data. Important conclusions can then be drawn that help understanding the site coordination and structural differences between the two phases.

Looking at the promising results for the complicated bulk BFO structure, another study is performed where dislocations in BFO close to the interface are analyzed. Based on the experimentally obtained energy loss spectra close to dislocations, a theoretical model is benchmarked. Most of the calculations in this particular study were performed on FEFF [3] which is a real space multiple scattering code. These results reveal the electronic structure and local bonding close to the dislocation and how it differs from the bulk structure. This study also provides valuable insights in order to understand how certain defects in this system affect its electronic properties.

[1] P. Blaha, K. Schwarz, G. Madsen, D. Kavasnicka, and J. Luitz, *WIEN2k, An Augmented Plane Wave + Local Orbitals Program for Calculating Crystal Properties* (Karlheinz Schwarz, Technische Universität, Wien, Austria, 2001).
[2] M. D. Rossell, R. Erni, M. P. Prange, J.-C. Idrobo, W. Luo, R. J. Zeches, S. T. Pantelides, and R. Ramesh, Phys. Rev. Lett. **108**, 047601 (2012).
[3] J. J. Rehr, J. J. Kas, F. D. Vila, M. P. Prange, and K. Jorissen, Phys. Chem. Chem. Phys. **12**, 5503 (2010).

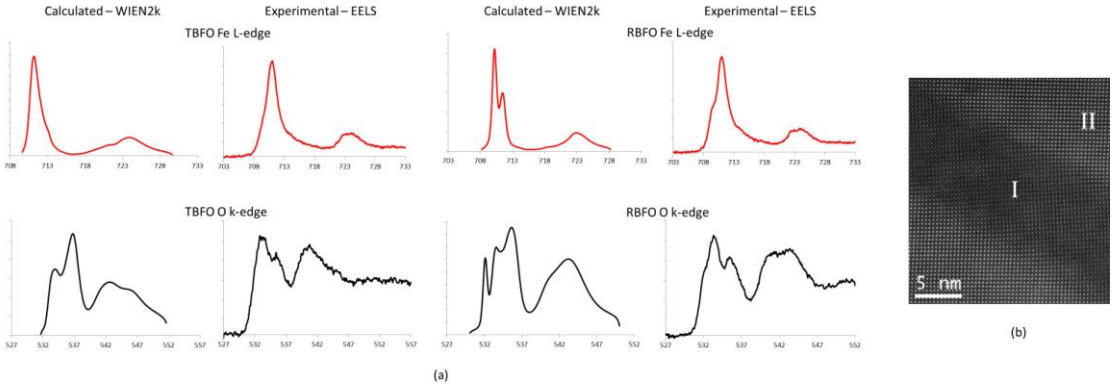

Figure 1. (a) Shows the experimentally and theoretically calculated Fe L-edge and O K-edge EELS spectra for both the phases. (R phase - RBFO, T phase - TBFO). (b) HRSTEM image of BFO (region I: T-phase, region II: R-phase)

Spectroscopic TEM/STEM, EELS, EFTEM

IM4.103
EMCD as a probe for magnetic phase transitions

W. Hetaba[1,2], S. Löffler[3,4], M. Stöger-Pollach[5], A. Hütten[6], G. Parkinson[7], P. Schattschneider[5,4]

[1]Vienna University of Technology, Vienna/Austria, Germany
[2]Fritz-Haber-Institut der Max-Planck-Gesellschaft, Berlin, Germany
[3]McMaster University, Department of Materials Science and Engineering, Hamilton, Canada
[4]Vienna University of Technology, Institute of Solid State Physics, Vienna, Austria
[5]Vienna University of Technology, University Service Centre for Transmission Electron Microscopy, Vienna, Austria
[6]Bielefeld University, Department of Physics, Bielefeld, Germany
[7]Vienna University of Technology, Institute of Applied Physics, Vienna, Austria

hetaba@fhi-berlin.mpg.de

Energy-loss magnetic chiral dichroism (EMCD) is a versatile technique to investigate magnetic properties on the nanoscale [1]. When performing EMCD experiments, electron energy-loss spectra (EELS) are acquired at two different scattering conditions. The two measurements are then compared in order to determine the element specific magnetic moment. In this work, we investigated the magnetic properties across phase transitions using EMCD and demonstrated the power of this method on two technologically important materials, Heusler-alloys and magnetite.

Heusler-alloys are promising systems in the field of spintronics. They show a magneto-caloric effect (MCE), which is related to a structural transformation [2]. Current research projects investigate multilayer Heusler systems, consisting of layers with different MCEs, which can be used for ferroic cooling applications. An austenitic-martensitic phase transition is present in these alloys (figure 1), where the transition temperature depends on the actual elemental composition. To investigate the changes of the magnetic properties at different temperatures we performed in-situ EMCD measurements. The experimental results are in good agreement with simulations. These simulations are crucial as dynamical diffraction strongly affects the intensity of the measured EMCD signal (figure 2), bringing the sample thickness and orientation into the game. By combining theory and experiments, this study paves the way for tailoring the magnetic phase transition of materials for the use in spintronics.

Magnetite is of interest in heterogeneous catalysis due to its surface chemistry. It shows a Verwey transition at about 120 K [3], in which the structural, electronic and magnetic properties of the material change. We used EMCD to investigate the change of the magnetic moments due to the Verwey transition (figures 3 and 4).

In both cases, the wide variety of analytical techniques available in a TEM, combined with EMCD, provide insight into the mechanism of the magnetic phase transition on a nanometer-scale.

1. P. Schattschneider et al., “Detection of magnetic circular dichroism using a transmission electron microscope”, Nature, 441, 2006, pp.486-488
2. A. Planes et al., “Magnetocaloric effect and its relation to shape-memory properties in ferromagnetic Heusler alloys”, J. Phys.: Condens. Matter, 21, 2009, p.233201
3. F. Walz, “The Verwey transition - a topical review”, J. Phys.: Condens. Matter, 14, 2002, p.R285-R340
4. WH thanks A. Steiger-Thirsfeld and J. Gruber for the preparation of the TEM-samples. The Austrian Science Fund (FWF) is acknowledged for financial support under grant numbers F4501-N16 (FOXSI) and I543-N20 (OMG). The German Research Foundation (DFG) is acknowledged for funding under grant SPP 1599 (Ferroic Cooling).

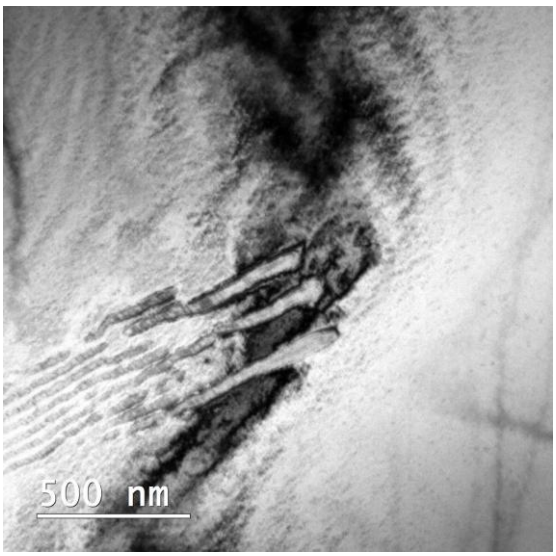

Figure 1. NiMnIn Heusler showing some transformed (martensitic) regions.

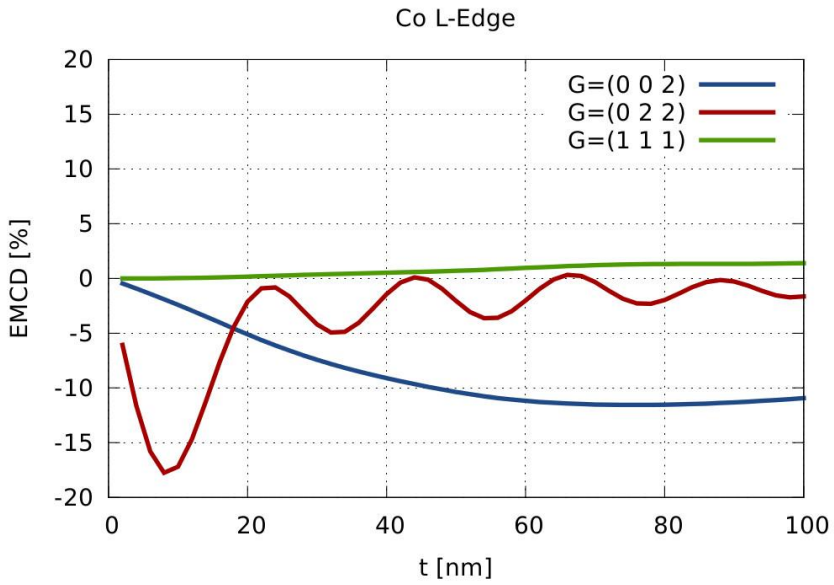

Figure 2. Simulation of the EMCD effect at the Co L-edge of a CoMnSi Heusler in its austenitic phase for an incident 200 keV plane wave as a function of sample thickness and scattering conditions.

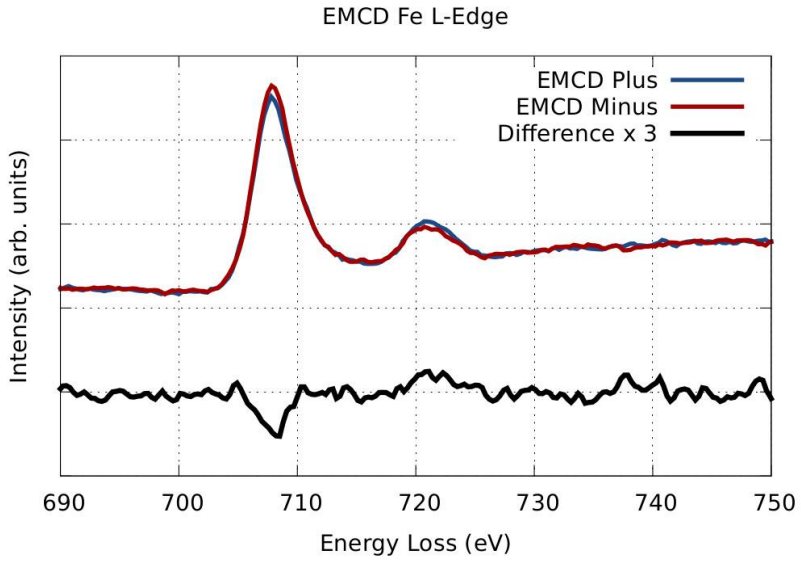

Figure 3. Measured EMCD effect in magnetite before the Verwey transition. The effect is clearly visible in the non-transformed magnetite (ca. 13.5 %).

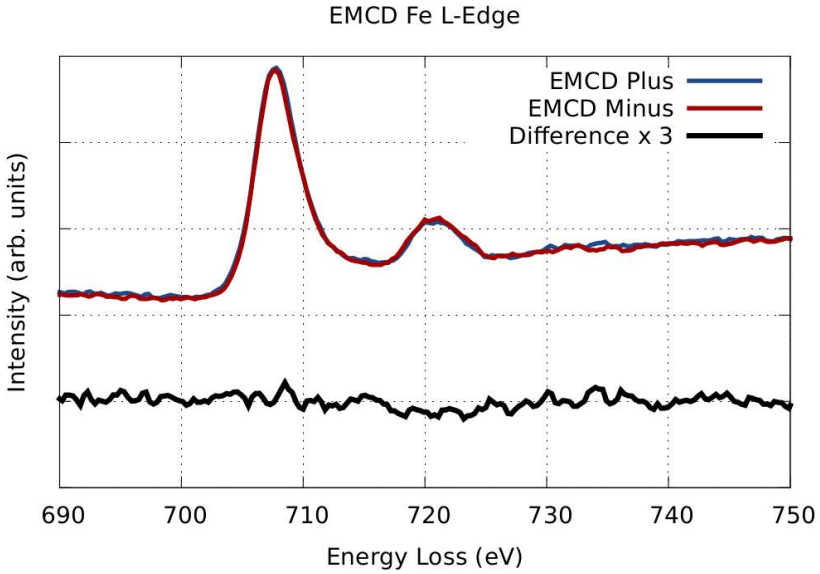

Figure 4. Measured EMCD effect after the Verwey transition. It can be seen that the EMCD effect has vanished.

Spectroscopic TEM/STEM, EELS, EFTEM

IM4.P104
Electron energy losses at interfaces

S. Löffler[1], G. A. Botton[1]

[1]McMaster University, Department of Materials Science and Engineering, Hamilton, Canada

st.loeffler@gmail.com

Electron energy loss spectrometry (EELS) in a transmission electron microscope (TEM) is a very versatile technique for studying material properties down to the atomic scale [1]. Ranging from chemical analyses with single atom sensitivity, valence determination, and bonding information over optical properties to magnetic properties, EELS and TEM have proven indispensable for a wide variety of fields including physics, chemistry, material sciences and biology.

It is well known from high-resolution TEM (HRTEM) and scanning TEM (STEM) that elastic scattering effects can have a large influence on the measured signal [1]. For EELS, the situation is further complicated by the fact that apart from the inelastic scattering, elastic scattering effects, both before and after the inelastic interaction, have to be taken into account simultaneously. Thus, to keep the computational effort manageable and to simplify data interpretation, core-loss EELS is typically performed on single-crystalline samples in practice.

However, many technologically relevant properties such as composition, electronic states, or diffusivity can change dramatically in the vicinity of surfaces, interfaces, and defects. Because many technologically relevant processes are determined by the material properties close to interfaces, such as grain boundaries or at defects, an extension of the existing core-loss EELS techniques to those complex situations is of utmost importance.

In this work, the applicability of standard core-loss EELS techniques close to interfaces is evaluated. As an example, fig. 1 shows simulations of an AlN/GaN interface. As can readily be seen, dynamic diffraction effects severely influence the EELS signal: the N signal seems to originate from an Al columns, the (constant) N content gives rise to different signal strengths across the interface, and there is Al signal even in the Al-free GaN layer. All these artifacts can give rise to a seriously wrong interpretation of measured data.

By using state-of-the-art multislice simulations [2] to treat elastic scattering effects and the mixed dynamic form factor (MDFF) formalism [3] to accurately model the inelastic scattering, it is possible to predict the dependence of the EELS signal on many parameters such as thickness, orientation, defocus, or chemical composition and to find conditions for the direct interpretability of experimental maps. Furthermore, the quality of these predictions is assessed by comparison with key experiments.

Interfaces are the key to new developments across many fields, including the development of new functionalized materials and of catalysts. The extension of the well-known core-loss EELS technique and its interpretation to interfaces will pave the way for new possibilities in the design of such novel materials [4].

1. D.B. Williams & C.B. Carter, Plenum Press 1996.
2. E.J. Kirkland, Plenum Press 1998.
3. P. Schattschneider et al., Micron 31 (2000) 333.
4. The author acknowledges financial support by the Austrian Science Fund (FWF; grant numbers I543-N20, SFB F45 FOXSI) and the University Service Centre for Electron Microscopy of the Vienna University of Technology.

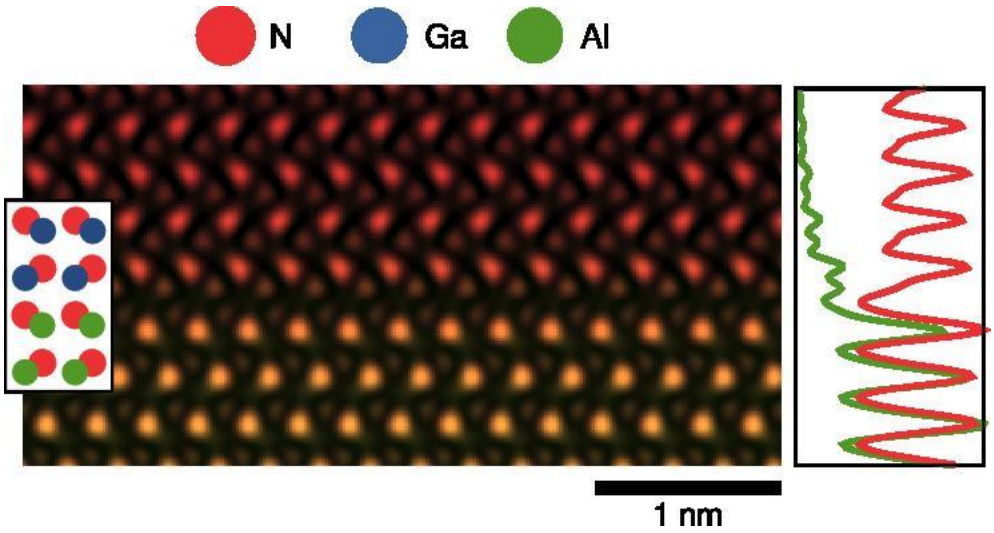

Figure 1. Superimposed simulated normalized energy-filtered maps of an AlN-GaN interface for an 80 keV beam incident along [100] on a 20 nm thick sample. The Al L-edge signal is shown in green and the N K-edge signal in red. The image is RGB color-coded. The inset shows the crystal structure around the interface and the line graphs show the intensity profiles. The appearance of yellowish columns in the lower half of the image is caused by a shift of the red N signal peaks to the green Al columns.

Spectroscopic TEM/STEM, EELS, EFTEM

IM4.P105
Simultaneous high-speed dualEELS and EDS acquisition at atomic level across the $LaFeO_3$ / $SrTiO_3$ interface

P. Longo[1], T. Topuria[2], P. Rice[2], A. Aitouchen[1], P. Thomas[1], R. Twesten[1]

[1]Gatan, Inc., Pleasanton, CA, United States
[2]IBM Research Division, San Jose, CA, United States

plongo@gatan.com

Lanthanum ferrite $LaFeO_3$ (LFO) is an antiferromagnetic perovskite oxide and has been investigated with great interest due to its potential applications in computer hard drives as read heads. LFO films are typically grown on $SrTiO_3$ (STO) substrates due to the well matched lattice constants and the effects of chemistry, morphology and strain at the LFO / STO interface on the magnetic and electrical properties of the system.Hence, the study of the chemistry and elemental distribution at the atomic scale is important in order to understand the properties of these films. EELS and EDS in a STEM microscope have proven to be valuable tools for characterizing such materials.

Here we show an approach where the simultanous high-speed acquisition of EELS and EDS spectra with an atomic scale probe allows the possibility to carry out a full compositional and chemical characterization of the LFO / STO interface. The analysis was carried out using a relatively short exposure time to reduce the effects of beam damage and sample drift which can be more pronounced when the data acquisiton is carried out at atomic level. To achieve efficient and fast joint EELS / EDS data acquisition, we have linked the STEM scan system with the EELS and EDS detectors via a single clock mastered off the EELS detector to ensure all the systems are in exact synchrony.

Data were acquired at IBM San Jose, CA, USA using a probe-corrected, C-FEG STEM operating at 200 kV. A GIF Quantum ER EELS system equipped with DualEELS capability was used for the acquisition of energy-loss data and a large area (~1 sr) EDS detector was used to acquire the EDS data. EELS data were acquired in DualEELS mode and the low-loss (0 eV to 500 eV) and core-loss (400 eV to 900 eV) EELS spectra were acquired nearly simultaneously with 10 µs transition time between exposures. The low-loss spectrum provides an accurate energy reference allowing absolute chemical shift measurements. The spectrometer was set up for moderate energy resolution analysis with a dispersion of 0.25 eV / channel yielding a measured energy resolution of 0.75 eV with 500 eV energy range in the spectrum. By looking at the shape of the near edge structure in the EELS spectrum, it is possible to extract information on the oxidation state, coordination state and much more. EELS data were used to analyze chemical state information and generate elemental maps of the O, Ti, Fe and La. In the EELS spectrum, the main signals for the Sr are the $M_{4,5}$ at 130 eV and the Sr $L_{2,3}$ at 1940 eV. The M-edges have a poor peak-to-background ratio due their low energy while the L-edges are out of the energy range for this experiment (0 eV to 900 eV). The EDS data were acquired simultaneously with the EELS data and can be used to generate a Sr elemental map that can be combined with those obtained by EELS. Since the EDS signal does not provide any chemical information, only composition can be studied for Sr at the experimental conditions used in this paper.

Figure 1 shows a colorized elemental map of Ti, Fe and La obtained using EELS and Sr using EDS. The color map suggests intermixing between Fe and Ti. Such intermixing can be confirmed and further investigated using EELS by looking at the fine structure of the edges across each atomic column. Figures 2a-c show EELS spectra of Ti L, O K and Fe L edges extracted from the selected regions in Figure 1. Changes can be observed in every spectrum although they are notable in the case of the O and Fe in Figures 2b,c with the Fe showing a chemical shift towards higher energy moving into the $LaFeO_3$. This is a clear indication of a change in the oxidation state. The interface was also analyzed using STEM diffraction where diffraction patterns are taken point by point across the interface. This gives a further insight into the structure across the interface and information about strain and crystal distortion can be revealed.

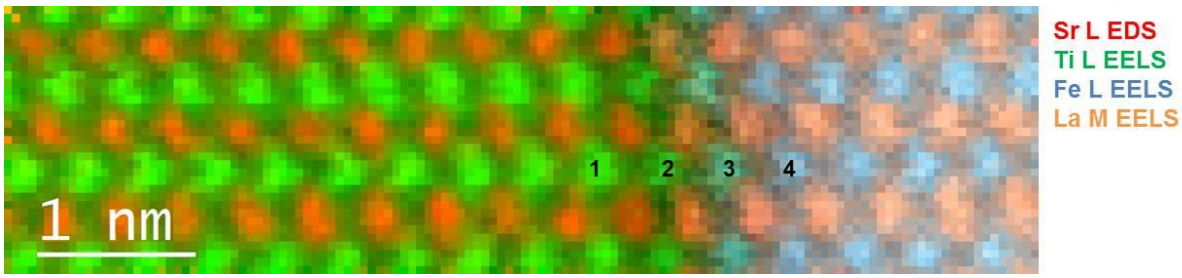

Figure 1. Color maps of Ti L at 456 eV in green, La M at 832 eV in orange and Fe L at 708 eV in light blue obtained using EELS and Sr L at 1.81keV in red obtained using EDS. The numbers 1 - 4 correspond to the selected region where the EELS spectra in Figures 2a-d were extracted.

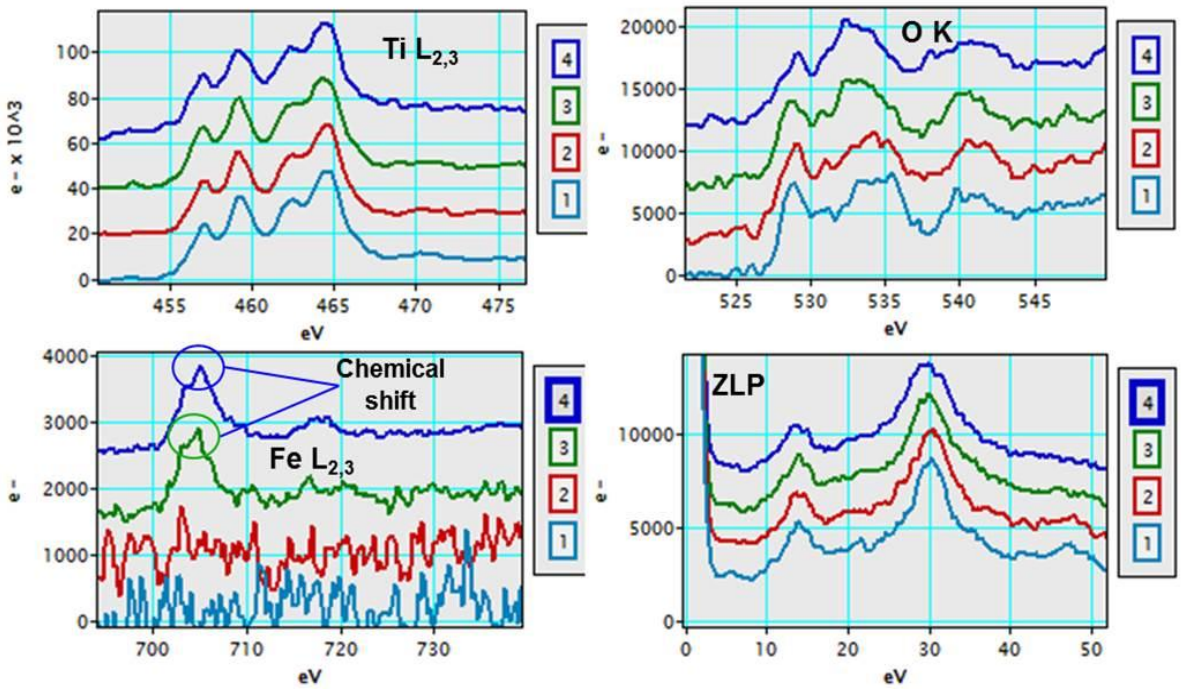

Figure 2. EELS spectra extracted from the selected region in Figure 1; a) Ti $L_{2,3}$-edges at 456eV; b) O K-edge at 532 eV; Fe $L_{2,3}$-edges at 708 eV; d) Low-Loss region.

Spectroscopic TEM/STEM, EELS, EFTEM

IM4.P106
ELNES measurement of graphitization on Li-S batteries by sp^2 hybridization

U. Golla-Schindler[1], H. Maria Joseph[2], A. R. Munnangi[2], M. Fichtner[2], U. Kaiser[1]

[1]Group of Electron Microscopy of Material Science, Ulm, Germany
[2]Helmholtz Institute Ulm (HIU), Ulm, Germany

ute.golla-schindler@uni-ulm.de

Rechargeable lithium-ion batteries are promising system for the storage of energy in many applications. There lithium-sulfur batteries are one candidate especially for high energy storage devices with potential cost-effectiveness. On technical issue to solve on the road to the commercial realization is the reduced cycle life associated with the formation of electrolyte soluble higher order polysulfides (Li_2S_x, x = 4-8). The use of a specific ultramicroporous carbon-sulfur composite cathode based on coconut shell carbon enables the direct transformation of sulfur to Li_2S_2/Li_2S in lithium-sulfur batteries [1].

Transmission electron microscopy (TEM) was used to characterize the as-synthesized coconut shell carbon (CNSC) and the uptake of sulfur into the coconut shell carbon sulfur composite material (CNSC-S). The TEM image of CNSC Figure1a) delivered carbon loops at the rim of the sample (loop size e.g. 4 and 5 Å). DFT calculations using isotherms of N_2 adsorption/desorption of CNSC yield predominantly ultra micropores with a pore size of 5 Å, which agrees nicely with the loop size of carbon loops at the rim of the sample. For further understanding of the structural and electronic properties of the composite material, electron energy-loss spectroscopy (EELS) was performed. Figure 1b) and 1d) show the raw data spliced EELS of the as-synthesized CNSC and CNSC-S composite, respectively. In the spectrum of the CNSC solely the C-K edge is detectable, whereas in the spectrum of CNSC-S the S-L edges can be recognized in addition. The power-law background-subtracted EELS are shown in Figure 1c) (CNSC), Figure 1e) and 1f) (CNSC-S). In both C-K edge spectra two characteristic peaks are detectable, a sharp peak at 285 eV dedicated to the 1s → Π* transition and a broader peak approximately at 292 eV corresponding to the 1s → σ* transition (Figure 1g). An increase in sharpness and height of the transition in the anti-bonding Π* and σ* states at the C-K edge is observed for CNSC-S (Figure 1e) in comparison to the empty CNSC (Figure 1c). Carbon is capable of forming many allotropes due to its valency. The common crystalline form of carbon is graphite. In graphite the sp^2 bonding corresponds to the hybridization of the atom's 2s orbital with $2p_x$ and $2p_y$ orbitals and results in a system of three planar s-bonds forming an angle of 120°. The remaining $2p_z$ orbital, which is perpendicular to the plane of the σ-bonds forms a Π-bond. Related to these bonding states are the unoccupied anti-bonding states σ* and Π* that play an important role in the interpretation of excitation spectra like EELS, see the figure 1g) which shows the reference spectrum of pure graphite [2]. Therefore the Π* peak increment represents an increase in sp^2 hybridization (graphitization) after sulfur incorporation and the σ* peak increment either indicates the increase in g or can be correlated to an additional contribution originating from C-S bonds. In the background corrected EELS of CNSC-S figure 1f) two peaks are detectable one at 165,7 eV corresponding to the S-$L_{2,3}$ edge and the second at 228,7 eV related to the S-L_1 edge. Those peaks confirm the presence of sulfur in the CNSC-S composite. The TEM and EELS studies were performed using an image-side Cs corrected FEI-TITAN equipped with a GIF Quantum 965 energy filter adjusted at 80 kV to avoid knock-on damage and increase the energy resolution [3].

1. Maria Joseph, H. et al (2015) submitted
2. Hamon, A.L., et al (2004) J. Mater. Chem. 14
3. Kaiser, U., (2011) Ultramicroscopy 111
4. This work is funded by the BMBF "Li-EcoSafe" joint research project (FKZ: 03X4636A)

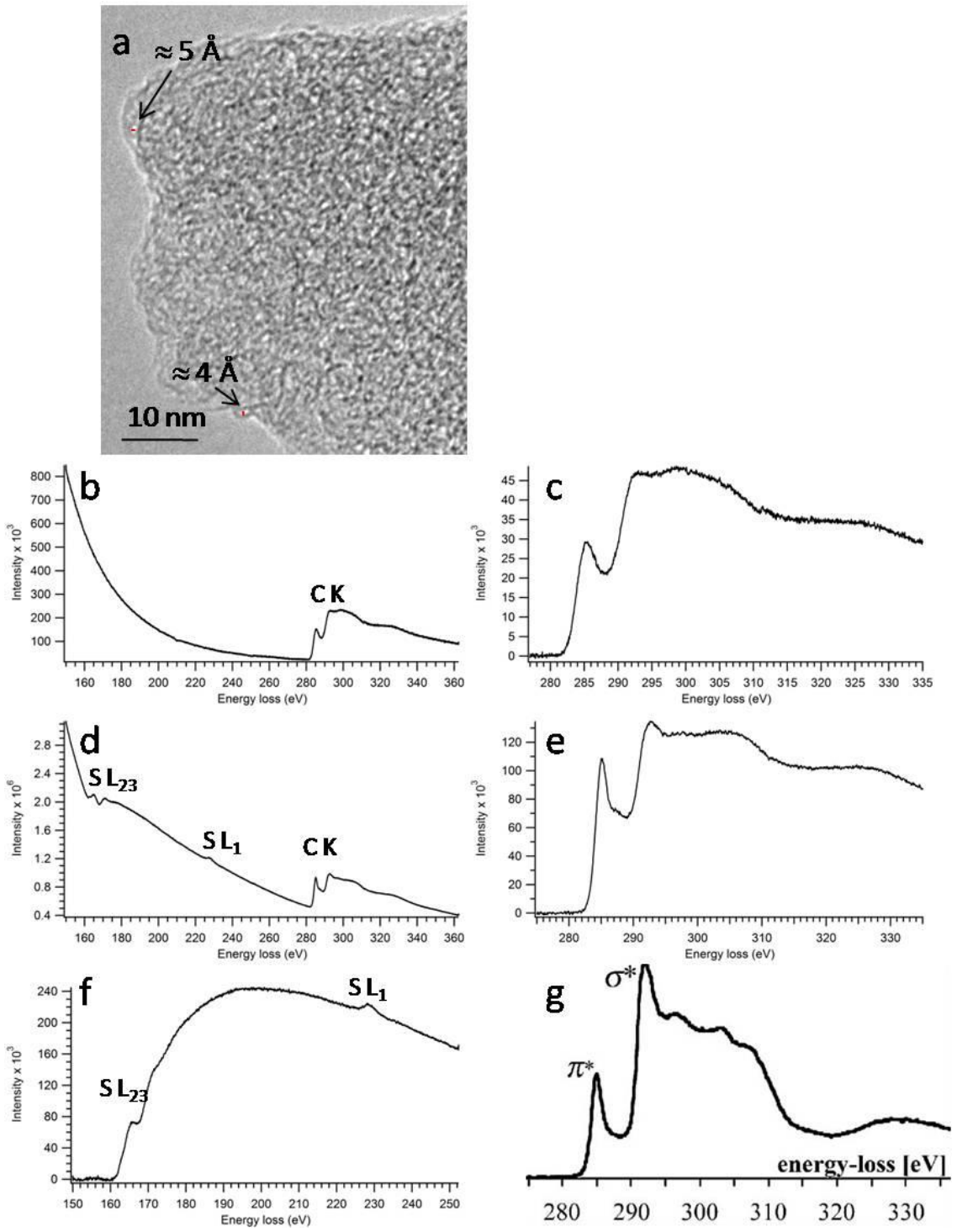

Figure 1.TEM study of synthesized coconut shell carbon and coconut shell carbon sulfur composite a) characteristic TEM image b) spliced EELS of the synthesized coconut shell carbon and c) background corrected corresponding C-K edge d) spliced EELS of the coconut shell carbon sulfur composite e) background corrected corresponding C-K edge and f) S-L edge g) reference spectra of graphite [2].

Spectroscopic TEM/STEM, EELS, EFTEM

IM4.P107
Monitoring of Ti atoms pathway at nano-scale in joined ceramics by electron microscopy

O. Tunckan[1], H. Yurdakul[1], S. Turan[1]

[1]Anadolu University, Airframe and Powerplant Maintenance , Eskisehir, Turkey

orkun.tunckan@gmail.com

Joining is great importance in materials science to make complex shape products. Many different methods serve for this purpose. Among them, capacitor discharge joining comes to the fore with its fascinating properties, e.g. superfast and explosion occurrence. However, the scientific mysteries behind the reactions during capacitor discharge process have not so far unraveled. Here, we report a nano-scaled study of Ti atoms' behavior across the grain boundaries, interfaces and lattices in Si_3N_4-SiAlON/Ti capacitor discharged joint ceramics as a function of temperature through electron microscopy.

Firstly, to make a bulk joint material with ceramic and metal foil, the experimental setup and design were organized. Later, samples were heat-treated in elevated temperatures between 900 and 1200°C under atmospheric conditions. Afterwards, electron transparent specimens from the special regions including Si_3N_4-SiAlON grains and Ti foil were prepared by using focused ion beam (FIB) lift-out method. Finally, the investigations of resulting samples were carried out by the use of different scanning and transmission electron microscopes (SEM and TEM).

Based on the electron energy loss (EEL)-spectrum imaging (SI) results that acquired in energy filtering transmission electron microscopy (EFTEM) and scanning transmission electron microscopy (STEM) modes, the intense movement of Ti atoms toward to Si_3N_4-SiAlON grains was observed. This gives rise to a new type of nano-scaled phase formations in metal-ceramic interface and within foil by the combination of Si and N atoms' diffusion arising from the Si_3N_4-SiAlON grains. The chemical compositions of these phases are well convenient with Ti_3N_2, Ti_3N, Ti_2N and $Ti_5Si_3N_x$. More interestingly, depending on the heat-treatment temperature, the morphology of the phases varies from the dendritic- to flower-type. Furthermore, Ti-rich cathodoluminescence (CL), energy dispersive X-ray (EDX), electron backscatter diffraction (EBSD), EFTEM-3 window and EELS elemental maps at grain boundaries and Si_3N_4-SiAlON grains revealed the nano-scale pathway of Ti atoms. Thus, we now thermodynamically make a clarification on the reactions that occur during the capacitor discharge process. These sequential ones will be also presented.

Spectroscopic TEM/STEM, EELS, EFTEM

IM4.P108
Spatially resolved EELS with an in-column Omega filter - from distorted recordings to corrected results

M. Entrup[1], H. Kohl[1]

[1]Westfälische Wilhelms-Universität Münster, Physikalisches Institut, Münster, Germany

michael.entrup@wwu.de

Spatially resolved EELS (SR-EELS) [1] is a technique to preserve spatial information when recording EEL spectra. Using SR-EELS, many EEL spectra are recorded in parallel as a function of one spatial coordinate, perpendicular to the energy dispersive direction. This method is useful for investigating specimens like interfaces and layer systems. We will show that the used in-column Omega filter [2] introduces distortions to the SR-EELS images and we present a work flow to entirely correct these distortions.

As a test specimen we have used an iron chromium layer system on silicon oxide with a layer thickness of about 12 nm. Figure 1a shows the combination of three elemental maps of this specimen. A slit aperture at the filter entrance plane (see fig. 1b) is used for performing SR-EELS. Compared with a round aperture the intensity along the lateral axis is uniform, but we loose intensity as the slit is narrower. We operate the microscope in EELS mode, which means that the 2nd projector system images the energy dispersive plane onto the camera.

Using the default parameters for the energy filter excitations we obtain an SR-EELS image as shown in figure 1c. One distortion is clearly visible: the lateral extend decreases with increasing energy loss. A second distortion is harder to see: The lateral magnification decreases towards the top and the bottom of the spectrum. This results in a higher intensity at the borders. We can reduce the magnitude of these distortions by tuning the excitation of the last hexapol corrector of the energy filter. The second distortion can be removed almost completely. Additionally the lateral extend of the spectrum is increased and therefore the lateral resolution.

The final result is shown in figure 1d. The excitation was optimised and the remaining distortions have been corrected by software processing. The software processing requires to perform a characterisation measurement: The small filter entrance aperture is shifted along the lateral axis. At several positions a SR-EELS dataset is recorded. For each energy channel of these datasets we can extract the position of the curved aperture borders. Polynomials of 2nd and 3rd order are fitted to the data points. They are used to describe and correct both distortions. Detailed information about the characterisation and the correction can be found at [3].

High spatial resolution is possible using SR-EELS. The interfaces of the 15 nm thick layers are clearly resolved. Additionally we obtain a high energy resolution without the difficulty of correlating the obtained spectra with the investigated area, as in conventional EELS or STEM-EELS.

1. L. Reimer et al., Ultramicroscopy 24 (1988) 339-354.
2. S. Lanio, PhD thesis (1986), TH Darmstadt.
3. EFTEMj is available on GitHub: https://github.com/EFTEMj/EFTEMj/tree/master/MC2015

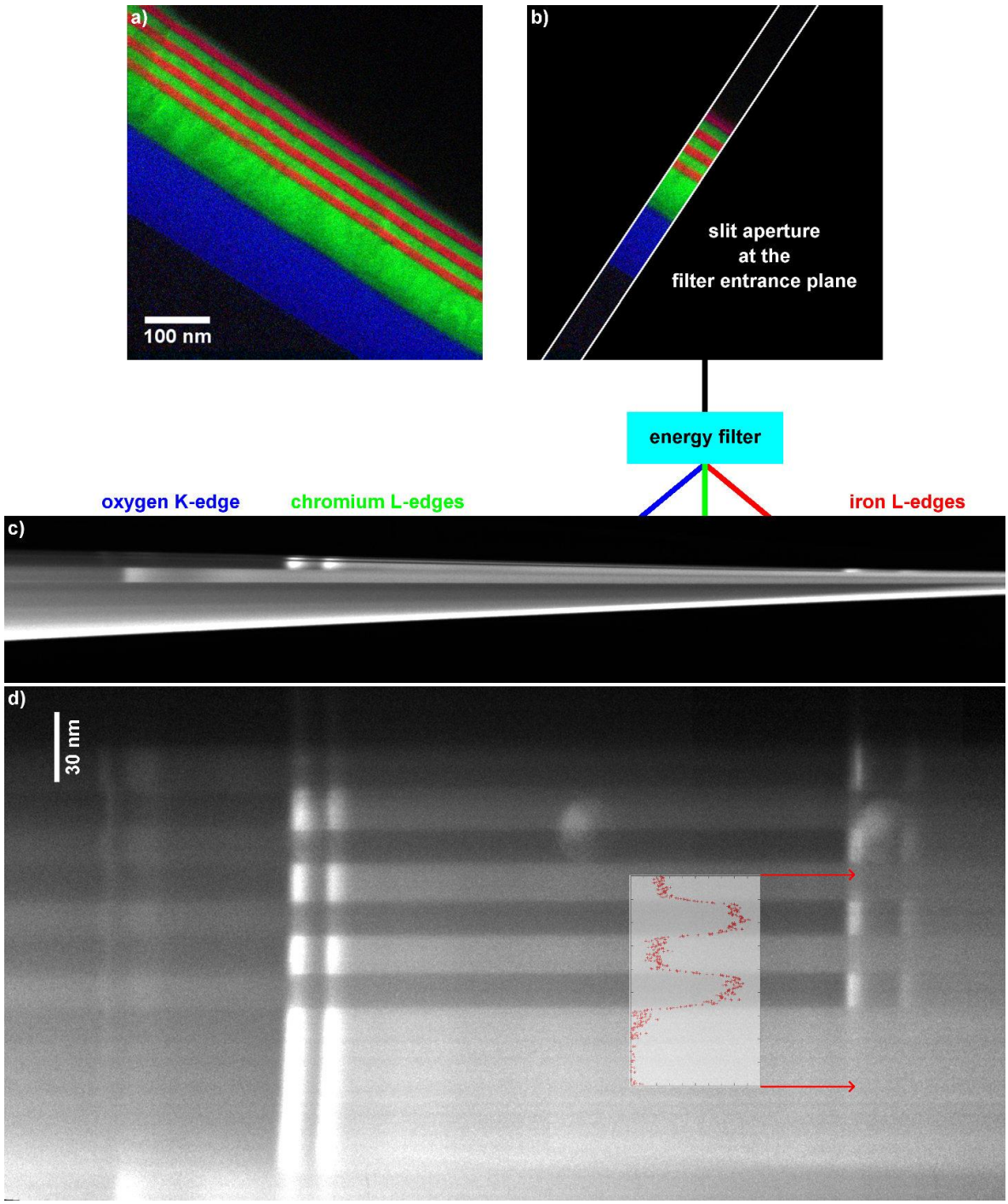

Figure 1. a) A combination of three elemental maps that shows the specimen (iron in red, chromium in green and oxygen in blue) used for SR-EELS measurements. b) This images shows how the specimen has to be aligned to perform a SR-EELS measurement. A slit aperture at the filter entrance plane is useful but not necessary. c) A SR-EELS measurement with default parameters for the energy filter excitations. The low lateral resolution and strong distortions are visible. d) The final SR-EELS image after optimising the energy filter excitations and post-processing of the recorded dataset with EFTEMj [3]. The inset shows the background subtracted iron L_3-edge signal. For a high resolution image visit [3].

Spectroscopic TEM/STEM, EELS, EFTEM

IM4.P109
SPARC: a cathodoluminescence platform for nanoscale spectroscopy in a scanning electron microscope

T. Coenen[1], J. J. de Boer[1], S. den Hoedt[1]

[1]DELMIC BV, Delft, Netherlands

coenen@delmic.com

Recently, electron-beam spectroscopy techniques have emerged as powerful probes in nanoscience due to their ability to generate, probe, and control light at length scales far below the diffraction limit of light. Spatially-resolved cathodoluminescence (CL) spectroscopy, in which the electron-beam-induced radiation is collected inside an electron microscope, is one of these techniques that holds great potential for nanoscience. For a long time CL spectroscopy was mainly used in geology to analyze and identify minerals, but in the past two decades its scope has expanded significantly. Recently it has been used to study fundamental optical properties of a myriad of metallic, semiconductor, and dielectric (nano)materials in the fields of materials science and nanophotonics, including plasmonics and metamaterials. We have developed a special version of CL spectroscopy in which we can both effectively measure the emitted spectrum as well as the angular emission distribution (SPARC) [1-2].

The SPARC system is integrated with a standard commercially available scanning electron microscope (SEM). SEMs are relatively easy to operate and do not require electron-transparent samples. Additionally, the vacuum chamber is more spacious providing more flexibility. As a result SEM-CL is widely applicable and easy to use. Innovations in the SPARC CL-system include an improved light collection with a piezo-controlled parabolic mirror and the development of angle-resolved CL, which have further expanded the possibilities. In Figure 1(a) we show a photograph of the SPARC CL collection system. The piezoelectric positioning of the paraboloid mirror enables efficient light collection which is critical in plasmonic studies where CL signals are typically very low (10^{-4} photons/electron). Furthermore, by measuring the CL beam profile from the paraboloid with a 2D camera we are able to measure the angular profile, as every transverse point in the beam corresponds to a unique emission angle. In Figure 1(b) an illustration is shown of how the angle-resolved measurements are performed.

The demonstrate the capabilities of the system we study the optical response of single gold nanoparticles. For small nanoparticles (< 50 nm) the resonant features are relatively easy to determine as they are predominantly dipolar. However, for larger particles this can be more challenging due to retardation effects which lead to the presence of higher order multipoles (magnetic dipoles, electric quadrupoles etc.). In Figure 2(a) we show the CL spectrum of a gold nanoparticle (180 nm diameter, 80 nm high) on a silicon substrate as measured with a spectrometer. The spectrum is averaged over all scanning pixels that fell within the particle (5 nm pixel). As inset we show the spatial profile at the peak wavelength which a distinct doughnut pattern. Figure 2(b) shows the angular profiles collected at different excitation positions on the particles. Clearly the particle acts as an efficient antenna and beams light away from the excitation position in a non-dipolar pattern. The CL spectrum, the nanoscale excitation distribution as well as the angular profiles provide valuable insights into the resonant behaviour of such particles [3].

1. T. Coenen, E. J. R. Vesseur, and A. Polman, *Appl. Phys. Lett.* **99**, 143103 (2011).
2. T. Coenen, E. J. R. Vesseur, A. Polman, and A. F. Koenderink, *Nano Lett*. **11**, 3779 (2011).
3. T. Coenen, F. Bernal Arango, A. F. Koenderink, and A. Polman, *Nat. Commun*. **5**, 3250 (2014).

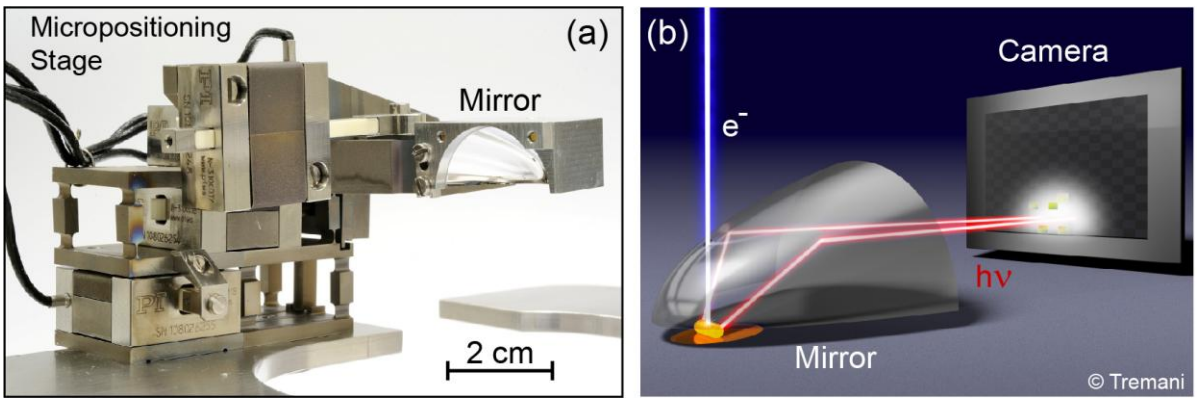

Figure 1. (a) Piezo-controlled mirror manipulator system for efficient light collection (e) Graphical representation of angle-resolved detection of CL where light coming from a parabolic mirror is projected onto a 2D silicon camera.

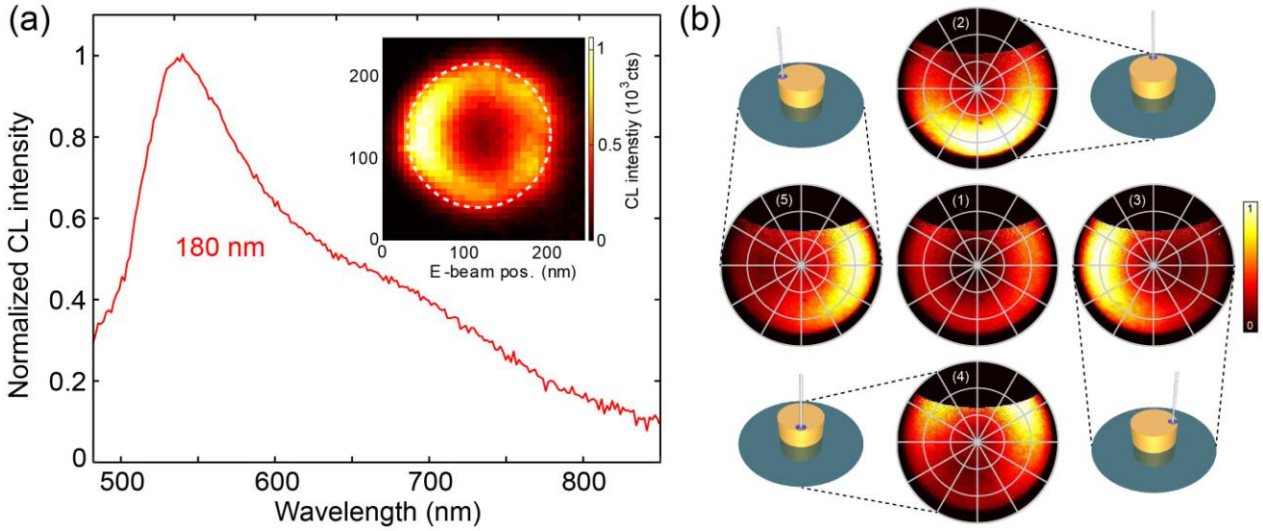

Figure 2. (a) Average CL spectrum for a 180 nm diameter gold particle on a silicon substrate. The inset shows the spatial profile at the peak wavelength (550 nm) where the white dashed line indicates the geometrical edge of the particle. (b) Angular emission profiles measured at 600 nm showing CL intensity as function of azimuthal and zenithal emission angles. for the same particle for central excitation (1) and four edge excitation positions (2-5) [3].

Spectroscopic TEM/STEM, EELS, EFTEM

IM4.P110
Acquiring momentum-resolved energy loss spectroscopy from thin nickelate layers at high spatial resolution

M. Kinyanjui[1], G. Benner[1], G. Pavia[1], F. Boucher[1], H.- U. Habermeier[1], B. Keimer[1], U. Kaiser[1]

[1]Ulm University, Electron Microscopy in Materials Science, Ulm, Germany

michael.kinyanjui@uni-ulm.de

Recent progress in electron energy loss spectroscopy (EELS) methods has lead to a tremendous improvement in the method's ability to acquire spectra at very high spatial (sub-nm) and energy resolutions (sub 0.1 eV). This has made EELS a method of choice when very high spatial resolution is required. However, the ability to obtain spectra both at high spatial and momentum resolutions has remained difficult. Momentum-resolved electron energy loss spectroscopy (MREELS) probes the momentum (q) dependence (dispersion) of energy losses from characteristic excitations such as excitons, plasmon, and interband excitations thus probing bandstructures, indirect excitations, and dipole-forbidden excitations. [1-5]

We present an experimental approach that enables the acquisition of momentum resolved spectra at a high spatial resolution of down to 2 nm using a nano-beam electron diffraction approach. Using this approach we have obtained momentum resolved spectra from individual, differently-oriented nano-domains in an ultra thin (12 nm) $PrNiO_3$ layer as well as spectra from different positions in $LaNiO_3$ thin film (70 nm). Figure 1(a) displays a Z-contrast image of the $PrNiO_3$ 12 nm thick layer. The nano-beam electron diffraction pattern from a [110] oriented domain in the $PrNiO_3$ is shown in Figure 1(b). Figures 1(c) and (d) show the Z-contrast image and nano-beam diffraction pattern from a LaNiO3 respectively. A selecting slit (showed by the dotted rectangle) is used to select a pair of diffraction spots allowing electrons that have been scattered to certain scattering angles into the spectrometer. The resulting spectra show energy loss as function of momentum (ω-q map) for various directions in the reciprocal space. Figures 1(e) and (f) present the momentum resolved EELS spectra showing energy loss (horizontal axis) as a function of momentum (vertical axis) for (e) $PrNiO_3$ // [002] direction (g) $LaNiO_3$ // [022] direction.We have characterized the acquired spectra with the help of calculated dielectric and energy loss functions**.**

The presented approach will enable the acquisition of momentum resolved spectra from nano-structured materials, thin films, interfaces, surfaces, and heterostructures at high spatial, energy, and momentum resolutions.

1.K. Zeppenfeld, Z. Phys. 243, 229(1971)
2. R. D. Bringans, and W. Y. Liang, *J. Phys. C: Solid State Phys.* 14, 1065 (1981).
3. M. K. Kinyanjui, C. Kramberger, T. Pichler, J. C. Meyer, P. Wachsmuth, G. Benner and U. Kaiser, Europhys. Lett. 97, 57005 (2012)
4. P. Wachsmuth, R. Hambach, M. K. Kinyanjui, M. Guzzo, G. Benner, and U. Kaiser, Phys. Rev. B 88, 075433 (2013)
5. F. S. Hage, Q. M. Ramasse, D. M. Kepaptsoglou, Ø. Prytz, A. E. Gunnaes, G. Helgesen, and R. Brydson, Phys. Rev. B 88, 155408 (2013)

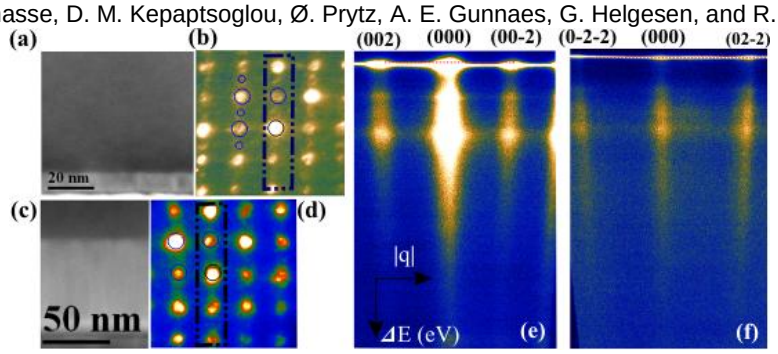

Figure 1. (a) Z-contrast image of (a) $PrNiO_3$ (12 nm) layer (b) A nano-beam electron diffraction pattern of a [110] oriented domain in the $PrNiO_3$ layer. The position of the slit used to select a set of diffraction spots is shown by the dotted rectangle(c) Z-contrast image of a $LaNiO_3$ layer (70 nm). (d) A nano-diffraction pattern from the $LaNiO_3$ layer along the [100] pseudo-cubic direction. (e)Momentum resolved EELS spectra direction showing energy loss (horizontal axis) as a function of momentum (vertical axis) for (e) $PrNiO_3$ // [002] direction (g) $LaNiO_3$ // [022] direction

Spectroscopic TEM/STEM, EELS, EFTEM

IM4.P111
A mechanistic study with microscopic techniques: enhanced curcumin uptake and retention in prostate cancer cells using a polymeric nano-bioenhancer system

M. Dwivedi[1]

[1]CSIR-National Botanical Research Institute. India, Lucknow, India

monika.nbri@gmail.com

The multidrug resistance (MDR), is a major impediment of current chemotherapy for cancer. The development of simultaneous resistance consequences in amplifying the doses of toxic drugs used in chemotherapy to many folds. A major cause of MDR is the efflux mechanism oftransporter protein P-gp. This draws the attention towards the elaborated researches on drug transport barriers for effective cell uptake of drug. Also, the co-delivery of P-gp inhibitors with the anticancer drug holds a contemprerary resolution for the problem by a P-gp inhibitory effect. Curcumin (CUR) has multifunctional anticancer properties, but its clinical use has been limited by poor solubility. Present study was emphasized on the cell internalization of drug in nano-bioenhancer system: curcumin (CMN) and its combination with natural bioenhancer (CPPn) using polymer poly (lactide-co-glycolide) (PLGA) by nanoprecipitation method. Curcumin incorporated in PLGA nanospheres using stabilizer tween 80 was found to have comparatively high encapsulation (70%) with particle size 216.2±4.6 nm and zeta potential of -20.6±1.6 mv. The characterization of the formulation was done using Transmission Electron Microscopy. This delivery system produced nanosphere with high cell uptake with a high encapsulation efficiency, good stability, and slow release of CMN. CPPn nanospheres had cytotoxic effect on prostate cell-line PC3 about 2.5 times more than CMN alone. The cytotoxic effect was correlated by cytoskeletal visualization of the PC-3 cell line in presence of CMN and CPPn using fluorescent microscopy. The mechanism behind the cell structural changes were also explored with nuclear and cell morphology visualization of the PC-3 cell line in presence of CMN and CPPn using confocal microscopy. The ROS mediated cell apoptotic was monitored by evaluating the ROS intracellular content by means of dichlorodihydrofluorecein dictate labelling and ROS accumulation was studied by fluorescence microscopy.

1. Wilken R, Veena MS, Wang MB, Srivatsan ES. Curcumin: A review of anti-cancer properties and therapeutic activity in head and neck squamous cell carcinoma. Molecular cancer,10:12.(2011)
2. Oyagbemi AA, Saba AB, Ibraheem AO. Curcumin: from food spice to cancer prevention. Asian Pacific journal of cancer prevention : APJCP,10:963-7.(2009)
3. Aggarwal BB, Kumar A, Bharti AC. Anticancer potential of curcumin: preclinical and clinical studies. Anticancer research,23:363-98.(2003)
4.Anand P, Nair HB, Sung B, Kunnumakkara AB, Yadav VR, Tekmal RR, et al. Design of curcumin-loaded PLGA nanoparticles formulation with enhanced cellular uptake, and increased bioactivity in vitro and superior bioavailability in vivo. Biochemical pharmacology,79:330-8.(2010)
5. Martindale, J.L. and N.J. Holbrook, Cellular response to oxidative stress: signaling for suicide and survival. J Cell Physiol, 192(1): p. 1-15. (2002)
6. Cen, D., et al., Disulfiram facilitates intracellular Cu uptake and induces apoptosis in human melanoma cells. J Med Chem, 47(27): p. 6914-20. (2004)

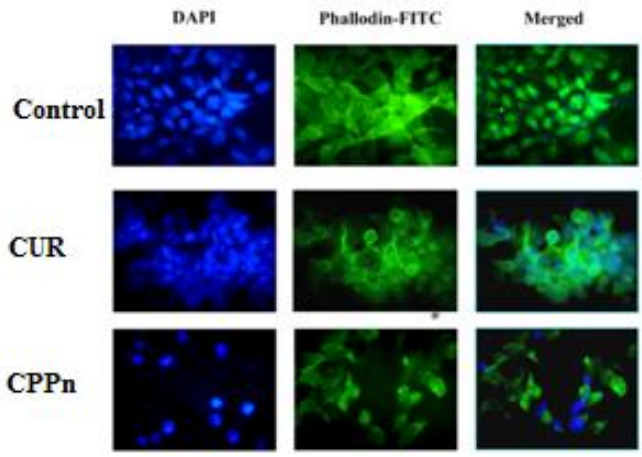

Figure 1. Cytoskeletal visualization of the PC-3 cell line in presence of CMN and CPPn using fluorescent microscopy.

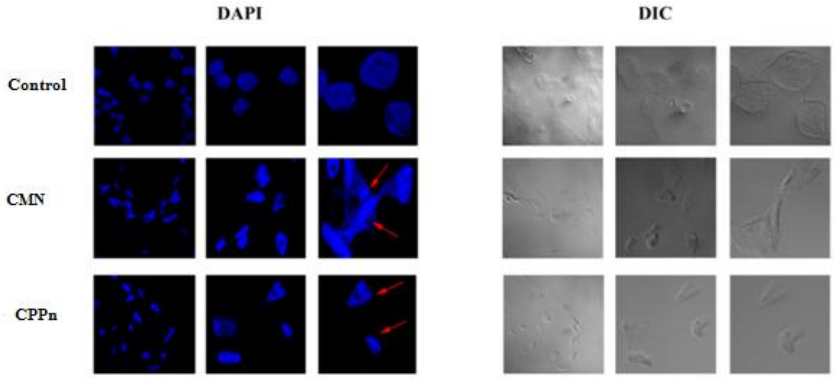

Figure 2. Nuclear and cell morphology visualization of the PC-3 cell line in presence of CMN and CPPn and vehicle (control) using confocal microscopy.

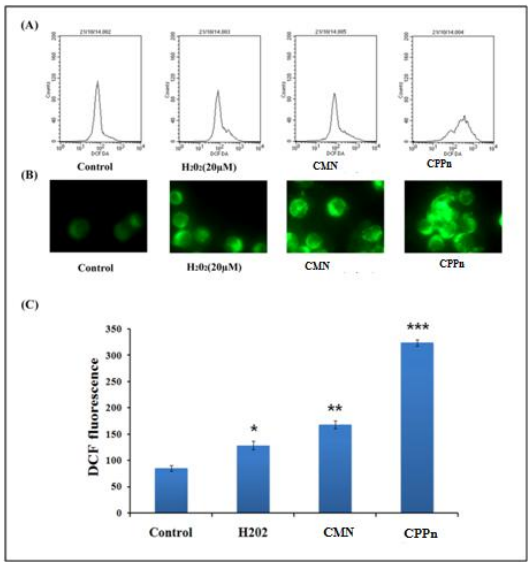

Figure 3 a Representative cytograms indicating increase in ROS accumulation by CMN and CPPn in PC-3 cells. ROS intracellular content was evaluated by means of dichlorodihydrofluorecein diacetate labelling; b Detection of ROS accumulation (indicated by green fluorescence) by fluorescence microscopy; c Representative histogram indicating increase in ROS accumulation by CMN and CPPn in PC-3 cells; Significant difference from control (vehicle) is indicated as ***P < 0.001; **P < 0.01; *P < 0.05.

Spectroscopic TEM/STEM, EELS, EFTEM

IM4.P113
Ideal EELS references by ex-situ sample treatment in combination with inert-gas transfer

B. Butz[1], M. Stark[1], F. Niekiel[1], E. Spiecker[1]

[1]Universität Erlangen-Nürnberg, Institut für Mikro- und Nanostrukturforschung, Erlangen, Germany

benjamin.butz@fau.de

The extreme and in this respect disadvantageous surface area/inner volume ratio makes high-quality TEM samples sensitive to oxygen, water vapor or hydrocarbons from air. Nevertheless, for most investigations it is a prerequisite to preserve the original microstructural and chemical state. This particularly applies to oxidation-state or chemical bond-state analyses by quantitative electron energy-loss spectroscopy (EELS). Necessarily, the fundamental question, which has to be answered, is how such properties can be conserved for microscopic investigation. How can we impede oxidation of nanoparticulate/-structured but also bulk metals or semiconductors? Are there appropriate alternatives to much more demanding environmental TEM?

For many applications, optimized sample handling in inert-gas environment is ideally suited. In a first step we successfully established sample transfer between an inert-gas glove box (Ar, 3 mbar overpressure) and our aberration-corrected FEI Titan Themis[3] 300 by the use of a commercial transfer holder (Gatan 648) (Fig. 1). However, this just allows for simple handling of freshly prepared TEM samples, e.g., from particle solutions. Our objective was to go one substantial step further, meaning, to develop an approach to tailor ideal metallic and metal-oxide reference samples for EELS analyses or even to conduct *ex situ* experiments like environment-dependent solid-state dewetting or structure formation prior to TEM evaluation. Our rather exotic but very efficient and convenient approach is to adapt a gas reactor to our glove box (Fig. 1 left). By the use of that setup, most different types of materials can be treated in defined environments like N2, Ar, O_2, H_2 or high vacuum at temperatures up to 1000 °C prior to the transfer into our microscope. As most carbon-based TEM support grids withstand reducing conditions even at temperatures as high as 800 °C, a simple approach to generate purely metallic, nm-sized EELS reference particles is to deposit metal-oxide/surface-oxidized metal nanoparticles onto such a substrate prior to gas-phase reduction.

As one scientific example, Fig. 2a-c depicts the oxidation-state analysis of Ni precipitates at a grain boundary of a ceramic fuel-cell electrolyte [1, 2]. Here, Ni-$L_{2,3}$ EELS reference spectra (Fig. 2b) from such ideal references were employed. Figure 2a shows the purely metallic Ni nanoparticles after *ex situ* reduction and transfer. By complementary techniques comprising high-resolution imaging, electron diffraction and EELS, the excellent quality of those Ni metal particles was proven. Within the detection limitations of the applied methods, no indication for oxidation was found even studying particles with diameters of only a few nm. In this presentation, methodical aspects as well as the advantages and limitations of our approach will be discussed using further materials science examples.

1. B. Butz et al., Acta Mater. 57 (2009) 5480-5490
2. B. Butz et al., Solid State Ionics 214 (2012) 37-44
3. We acknowledge financial support by the DFG within the framework of the SFB953, the GRK1896 and the Cluster of Excellence EXC 315. The authors thank Martin Stark, M.Sc. for fruitful discussions and technical realization.

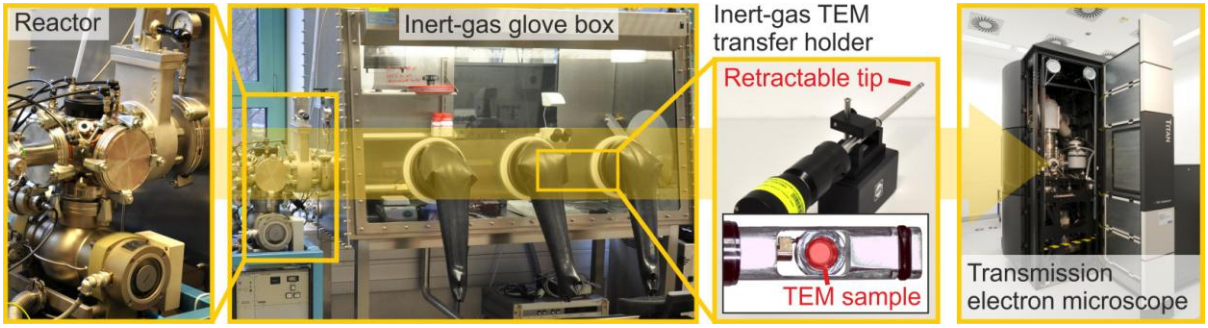

Figure 1. Reactor: sample treatment in various environments at temperatures up to 1000 °C → Direct transfer into inert-gas glove box → Mounting sample intoTEM transfer holder: 3 mbar Ar overpressure ensures minimal indiffusion of air and water during transfer → Introduction into microscope: holder tip is released at total pressure $<5 \cdot 10^{-8}$mbar.

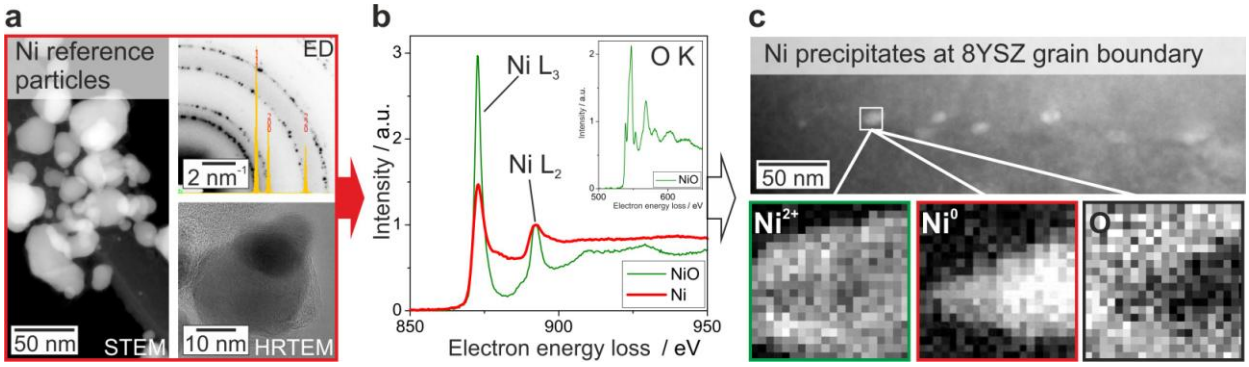

Figure 2. Metallic Ni nanoparticles as reference for oxidation-state analysis of Ni precipitates in an 8.5 mol% yttria-stabilize zirconia (8YSZ) fuel-cell electrolyte: a) Characterization of reference particles by STEM, electron diffraction (ED) (simulation of cubic Ni phase) and HRTEM → No indication for oxidation within detection limitations was found. b) EEL spectra from metallic Ni/NiO particles. c) Use of a)+b) for oxidation-state analysis of Ni precipitates at a grain boundary of a real fuel-cell electrolyte.

Spectroscopic TEM/STEM, EELS, EFTEM

IM4.P114
Surface plasmon polariton mediated coupling in submicron double-slit systems investigated by STEM-EELS

S. Fritz[1], R. Walther[1], R. Schneider[1], D. Gerthsen[1], T. Maniv[2], H. Cohen[3], C. Matyssek[4], K. Busch[4,5]

[1]Karlsruher Institut für Technologie, Laboratorium für Elektronenmikroskopie, Karlsruhe, Germany
[2]Technion - Israel Institute of Technology, Schulich Faculty of Chemistry, Haifa, Israel
[3]Weizmann Institute of Science, Department of Chemical Research Support, Rehovot, Israel
[4]Humboldt-Universität zu Berlin, Institut für Physik, AG Theoretische Optik & Photonik, Berlin, Germany
[5]Max-Born-Institut, Berlin, Germany

stefan.fritz@kit.edu

Surface plasmon polaritons (SPPs) and associated cavity modes (CMs) in rectangular submicron slits in thin Au- and Ag-films were recently analyzed by scanning transmission electron microscopy combined with electron energy loss spectroscopy (STEM-EELS) [1] and by energy-filtered TEM [2]. The characteristics of the CMs are determined by their structural dimensions. In comparison to a single slit, a strong enhancement of the CMs was observed upon introduction of a neighboring slit [3]. Such nanostructures were extensively studied by optical methods because they exhibit extraordinary optical transmission, as a result of strong photon-SPP coupling [4]. However, STEM-EELS provides a higher spatial resolution than any optical method and is therefore well suited to investigate in detail the field distribution within slits, in particular their variation under interaction between neighboring slits.

In this work, EEL spectra were acquired in a FEI Titan³ 80-300 equipped with a Wien-filter monochromator and a Gatan Tridiem 865 HR imaging energy filter. At a high voltage of 300 kV, an energy resolution of 0.12 eV is achieved under monochromated conditions with a probe size of 1 nm. Double-slit systems with different slit lengths and different widths of the metal bar between the two slits were prepared in a 200 nm thick Au film by focused-ion-beam milling. Numerical simulations of the EEL spectra were performed on basis of the Discontinuous Galerkin Time Domain method [5].

Figure 1a shows EEL spectra of the fundamental CM acquired at 10 nm distance from the inner wall of double-slit systems with a slit length of 535 nm and different metal bar widths d between d=90 nm and d=1120 nm. The beam position is marked by a white dot in the high-angle annular dark-field (HAADF) STEM image in the inset. For the smallest bar width only one peak at 0.80 eV is visible which is slightly red-shifted compared to the single-slit energy at 0.84 eV (dashed black line). With increasing bar width the red shift increases and the peak intensity decreases. For larger bar widths, a blue-shifted peak (compared to the single-slit energy) arises which increases in intensity and becomes dominant for d>535 nm. Figure 1b shows the corresponding simulated spectra which agree very well with the experiments. The red- and blue-shifted modes show energy shifts and intensity variations under increasing bar width: a decrease in intensity of the red-shifted mode and an increase in intensity of the blue-shifted mode.

Figure 2a shows the energies of the red- and blue-shifted modes for three different measurement series with slit lengths of 535 nm, 645 nm and 1330 nm. The coupling seems to be independent of the slit length and depends only on the ratio d/λ of the metal bar width between the two slits and the wavelength λ of the propagating SPP. Moreover, the energy values reveal mode splitting with avoided level crossing due to the strong coupling of the hybridized SPP-CMs. The intensity of the modes normalized with respect to the intensity of the zero-order beam is shown in Figure 2b. For $d/\lambda<0.5$ the red-shifted mode is dominant, whereas the blue-shifted mode is dominant for $d/\lambda>0.5$.

1. I. Carmeli et al., Phys. Rev. B **85** (2012)
2. B. Ögüt et al., ACS Nano **5**, 6701 (2011)
3. R. Walther et al., J. Phys. Chem. C **118** (2014)
4. F.J. Garcia-Vidal et al., Rev. Mod. Phys. **82**, 729 (2010)
5. C. Matyssek et al., Photonics Nanostruct. **9**, 367 (2011)
6. Funding by the German Research Foundation (DFG) within project Bu 1107/7-2 is acknowledged by KB and CM.

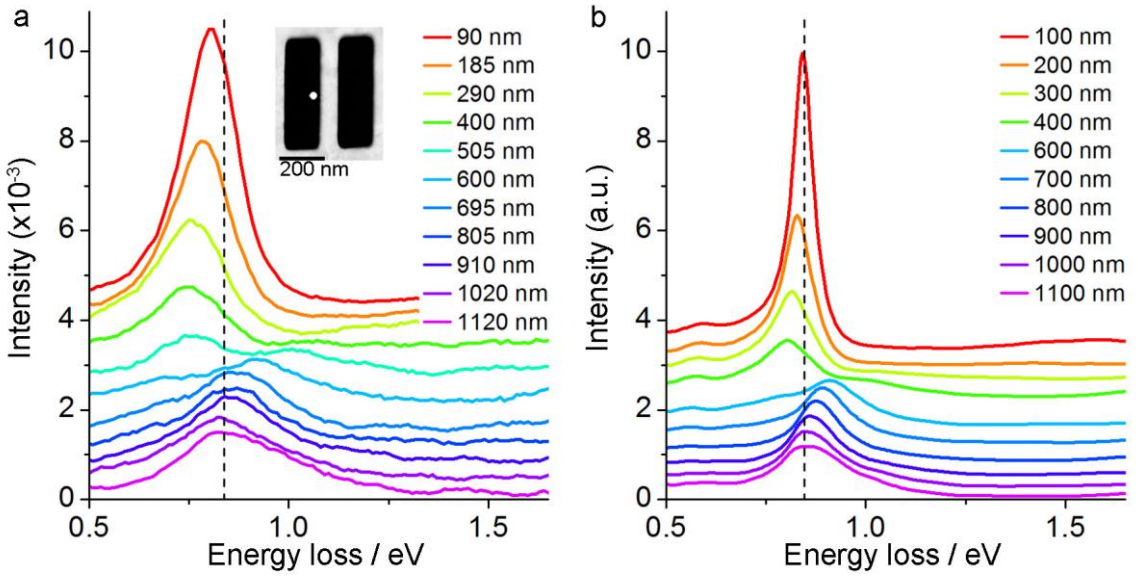

Figure 1. a) Experimental and b) simulated EEL spectra at the inner wall in double-slit systems with 535 nm slit length (cf. HAADF-STEM image in inset for position of the electron beam) and different bar widths. The dashed black line represents the energy of a single slit with identical slit length.

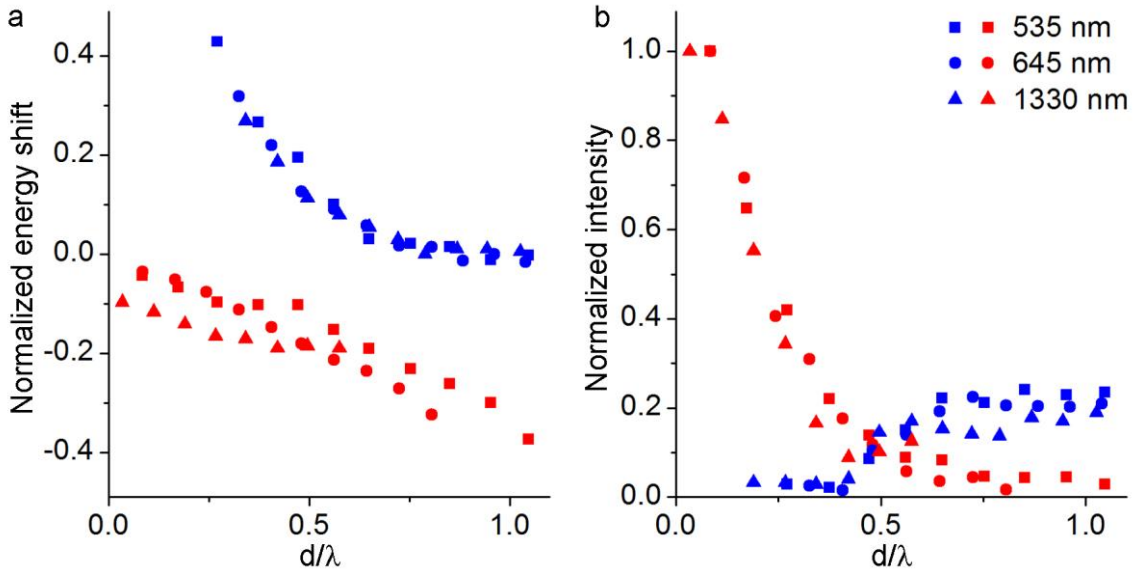

Figure 2. a) Normalized energy shift and b) normalized intensity of the experimental blue- and red-shifted modes (blue and red symbols) for three different double-slit systems (slit length of 535 nm, 645 nm and 1330 nm) with different bar widths.

Spectroscopic TEM/STEM, EELS, EFTEM

IM4.P115
The influence of the self-interaction correction on the calculation of differential cross-sections

F. Schröder[1], H. Kohl[1]

[1]Westfälische Wilhelms-Universität Münster, Physikalisches Institut, Münster, Germany

f_schr15@uni-muenster.de

Electron energy loss spectroscopy (EELS) allows to determine the chemical composition of a specimen quantitatively, if the ionization cross section is known. These are calculated via transition matrix elements between atomic bound and free electron wave functions. Using the approximation of a spherical symmetric atomic potential these wavefunctions can be separated into a radial and an angular part [1]. The latter can be determined analytically, whereas the radial part is challenging. A numerical calculation of the radial electron wave function has already been performed by Frigge [2] using a program to solve the Kohn-Sham equation within the linear density approximation to obtain the radial wave functions. Due to the exponential behavior of the central potential within the standard LDA approach one can describe the asymptotic behavior of the final free electrons wave functions by a combination of Bessel and Neumann functions.

To avoid this unphysical exponential decay of the potential, we have used a self-interaction correction in the Kohn-Sham potential [3]. This potential shows the physically correct decay proportional to -1/r in the outer region. In order to normalize the free electron one now has to fit the function to regular and irregular Coulomb wave functions, which are the correct radial functions for a free charged particle in a Coulomb potential. This procedure leads to a non-negligible phase shift of the free electron wave function.

The modification of the atomic potential due to the self interaction correction is even more significant in the inner atomic region. The correction results in a potential being by far more attractive than the standard one. This is particularly important for the free electrons with an orbital angular momentum l>0. Here the difference of the Kohn-Sham potential results in a shift of the centrifugal barrier around the center of the atom [Fig. 1]. This leads to a drastic shift and a change in amplitude of the free wave function [Fig. 2]. Due to the strong overlap to bound electron wave functions in this region this also has an effect on the differential cross section.

1.R.D. Leapman, P. Rez, D.F. Mayers, J. Chem. Phys., 72 (1980), 1232
2. M. Frigge: “Numerische Berechnung von Wirkungsquerschnitten im Zentralfeldmodell”, Diplomarbeit, Westfälische Wilhelms-Universität Münster, 2011
3 J.P. Perdew and A. Zunger, Phys. Rev. B 23 (1981), 5048
4. We thank Prof. Dr. Peter Krüger (Institut für Festkörpertheorie, Universität Münster) for valuable discussions and for providing the program to calculate the self interaction corrected Kohn-Sham potentials.

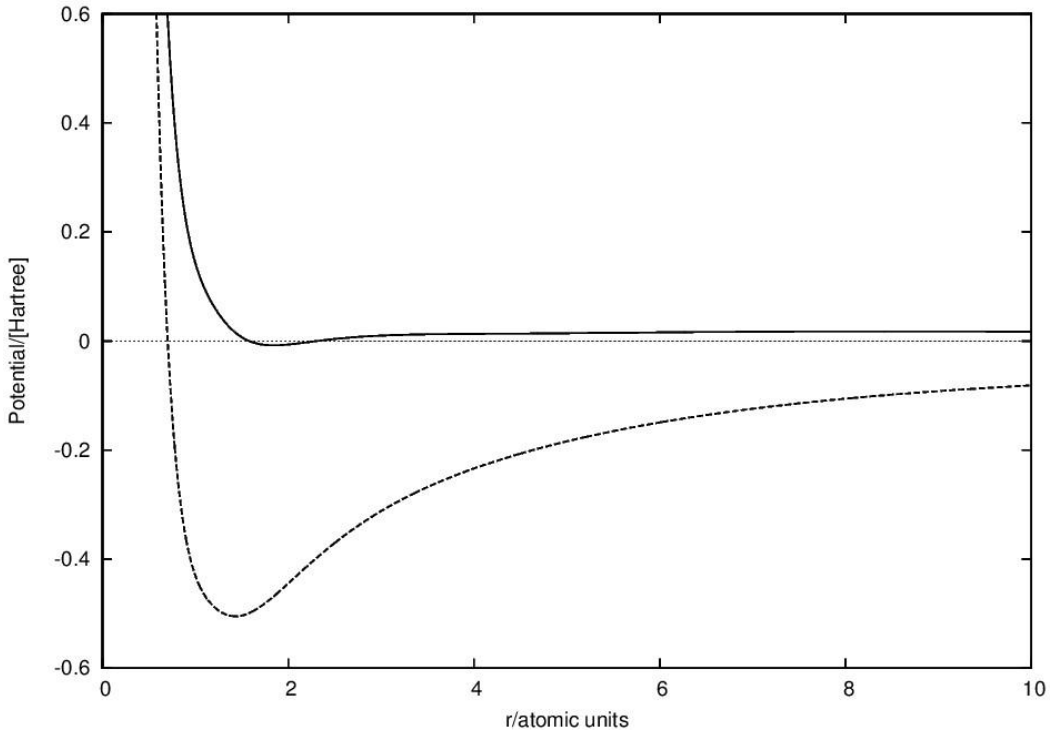

Figure 1. Effective potential calculated within standard LDA (solid line) and self interaction correction (dashed line)

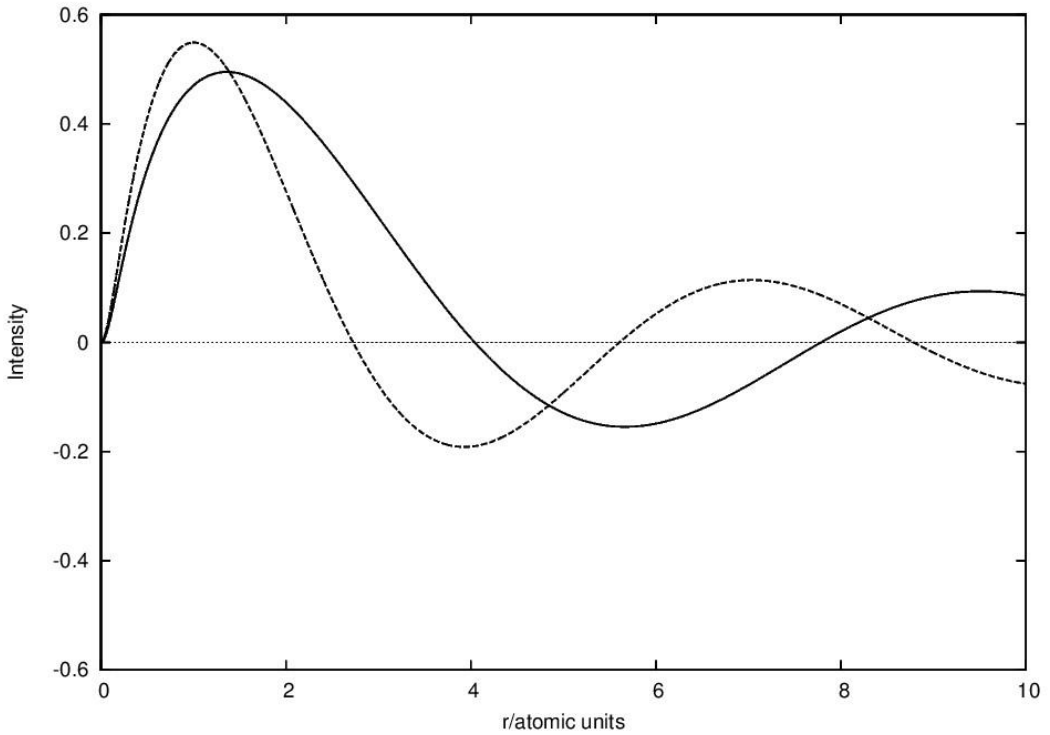

Figure 2. Free electron wave function (l=2,E=10eV) for a standard LDA (solid line) and a self interaction corrected (dashed line) potential

Spectroscopic TEM/STEM, EELS, EFTEM

IM4.P116
Energy resolution enhancement of EELS data by use of the Richardson-Lucy algorithm

S. Fritz[1], R. Walther[1], R. Schneider[1], D. Gerthsen[1]

[1]Karlsruher Institut für Technologie, Laboratorium für Elektronenmikroskopie, Karlsruhe, Germany

stefan.fritz@kit.edu

The energy resolution is one of the most important parameters to obtain high-quality electron energy loss spectroscopy (EELS) data. Especially if weak signals at low energy losses, e.g. surface plasmon polariton (SPP) cavity-modes are analyzed [1]. In this particular case the energy losses range between 0.2 eV and 2.4 eV with very weak intensities (~10^{-3}) compared to the zero-loss peak (ZLP). Even state-of-the-art electron microscopes equipped with electron gun monochromators are often unable to provide the needed energy resolution. Further improvement of the energy resolution can be obtained by numerical methods like the Bayesian-based iterative Richardson-Lucy (RL) deconvolution algorithm [2,3]. The algorithm has been successfully applied to image restoration in other scientific fields, in particular in restoration of Hubble space telescope images, but it can also be adapted for EELS [4,5]. The RL algorithm sharpens EEL spectra by deconvolution with the point-spread function of the microscope and the spectrometer. As this function is usually not known, a reference spectrum without a specimen inserted can be used.

In this work, EEL spectra were acquired in a FEI Titan³ 80-300 equipped with a Wien-filter monochromator and a Gatan Tridiem 865 HR imaging energy filter. Under monochromated conditions at 300 kV, an energy resolution of 0.12 eV (FWHM of the ZLP) with a probe size of 1 nm is achieved. To increase the signal-to-noise ratio 50 EEL spectra were acquired with the binned-gain averaging method [6]. The samples are 200 nm thick Au films containing rectangular double-slit systems with different slit lengths and inter-slit distances prepared by focused-ion-beam milling.

Figure 1a shows raw EELS data (black curve) taken in a slit at half of the slit length at 10 nm distance to the metal bar in a 950 nm long double-slit system (cf. white dot in the HAADF STEM image in Figure 1a). The effects of the RL algorithm with different number of iterations on the ZLP are clearly visible. The raw data with an energy resolution of 0.12 eV is normalized to the height of the ZLP. With increasing number of iterations the spectrum becomes sharper and the energy resolution is improved to 0.03 eV for 500 iterations. The RL algorithm has also a strong influence on the SPP cavity-modes as shown in Figure 1b. Prior to deconvolution, the fundamental and the 3rd harmonic mode at 0.52 eV and 1.52 eV are obstructed by the tail of the ZLP, whereas the peaks are clearly visible after several iterations. However, at large iteration numbers, the algorithm is limited by noise amplification (cf. green spectrum in Figure 1b). Therefore a compromise between sharpening and noise amplification is required. In the best case, peak intensities (which increase for larger number of iterations) should be identical to the raw data after background subtraction of a bi-exponential fit to the tail of the ZLP (cf. Figure 2). The EEL spectrum processed with 7 iterations (red line) and raw data (black line) are almost identical in intensity, for both the fundamental and the 3rd harmonic mode. Thus, reliable evaluation of the intensity of all peaks between 0.4 eV and 2.4 eV is achieved with 7 iterations of the RL algorithm.

1. R. Walther et al., J. Phys. Chem. C **118** (2014)
2. W.H. Richardson, J. Opt. Soc. Am. **62** (1972)
3. L.B. Lucy, Astronomical Journal **79** (1974)
4. J.M. Zuo, Microsc. Res. Technol. **49** (2000)
5. A. Gloter et al., Ultramicroscopy **96** (2003)
6. M. Bosman and V.J. Keast, Ultramicroscopy **108** (2008)

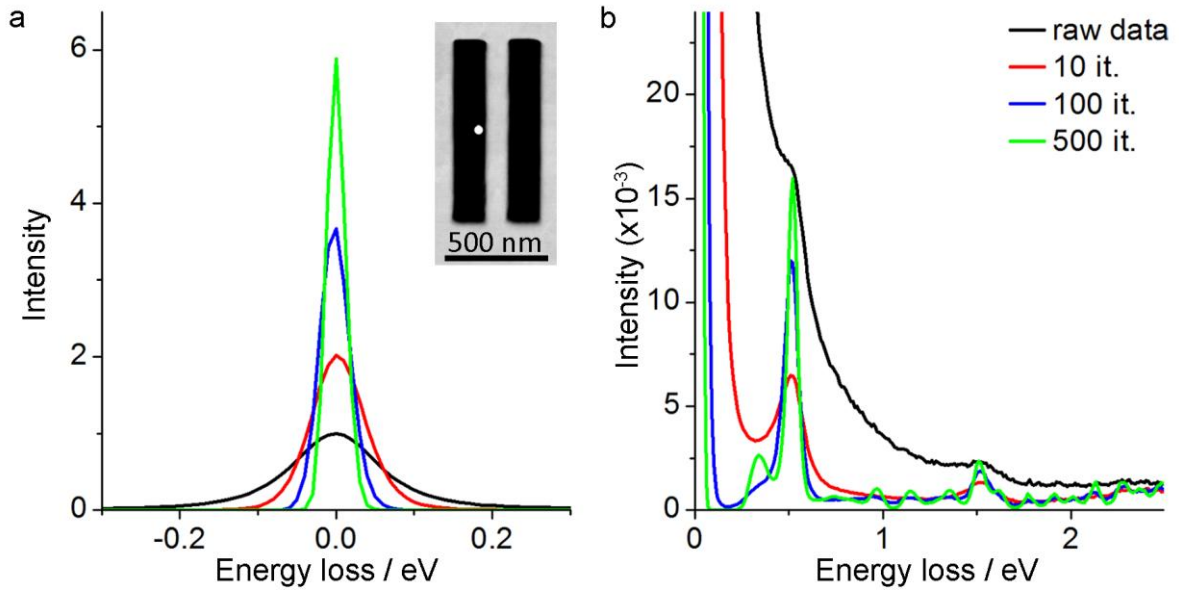

Figure 1. Effects of the RL algorithm on a) the ZLP and b) the energy loss region of the SPP cavity-modes. Raw data was acquired at half of the slit length at 10 nm distance to the metal bar in a 950 nm long double-slit system (white dot in the HAADF STEM image) and is normalized with respect to the height of the ZLP.

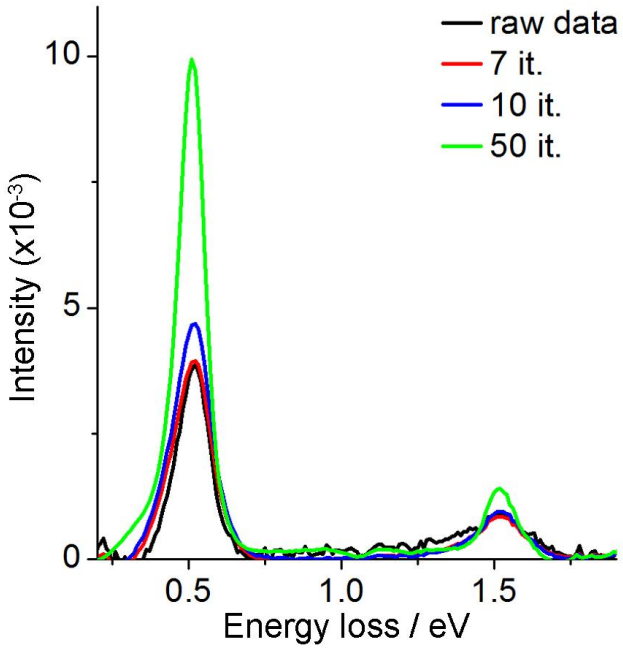

Figure 2. EEL spectra after bi-exponential background subtraction for different number of iterations. Raw data is almost identical to data after 7 iterations.

Spectroscopic TEM/STEM, EELS, EFTEM

IM4.P117
EM study of FeTe(Se,S) superconductors

M. Presniakov[1], A. Vasiliev[1,2], V. Bondarenko[1], I. Makarova[2]

[1]NRC "Kurchatov Institute", Moscow, Russian Federation
[2]Shubnikov Institute of Crystallography of the Russian Academy of Sciences, Moscow, Russian Federation

mpresniakov@gmail.com

Modern technology of superconducting manufacturing based on Nb_3Sn and NbTi for high magnetic field applications is close to the limit of critical current (j_c) capabilities and for further improvement the utilization of novel superconducting materials is necessary. The search for new materials pointed to the new copper-free superconductors $Fe_{1+y}Ch_x$ where Ch - S, Se, Te [1]. The transition temperature (T_c) in compounds $Fe_{1+y}Se_xTe_{1-x}$ at $x \approx 0.5$ is close to 15 K at atmospheric pressure and in $FeSe_{0.82}Te_{0.18}$ at 7 GPa T_c=37 K [2,3]. The crystal structure (Fig.1) was detemined in [4]: S.G. *P4/nmm, a=3.8242(1) Å, c = 6.2771(2) Å.*

Overall study of $Fe_{1+y}Te_{1-x}(S, Se)_x$ single crystals and thin films, prepared by pulse laser deposition method on MgO and $LaAlO_3$ substrates, includes HR TEM, HR STEM and EDXS was performed to get the correlation between the structure and physical properties. All samples were prepared by FIB (Helios 600, FEI, US) and studied in probe Cs corrected Titan 80-300 TEM/STEM (FEI, USA)

HAADF HR STEM investigations of $Fe_{1.1}Te$ (Fig. 2 (a)) demonstrated that Fe1 atoms occupied staggered position. Image simulations (JEMS, P.Stadelmann) did not show such deviation from the position obtained by X-ray study (Fig.2 (b)). That could point that symmetry of the crystal should be reconsidered.

Fe2 (10% occupation) mostly regroup together, which is visible in the intensity profiles taken along the line from HR STEM images. More clear these atomic groups are visible in 2D intensity profile Fig.3.

HRTEM of $FeTe_{0.9}S_{0.1}$ single crystals indicated the partial substitution of Te by S with the uprising of the additional reflections in hk0 position (where h and k are odd) on FFT patterns and SADP. These reflections could not appeared due to double diffraction, and that was demonstrated by EDP simulations. The areas where the space doubling were observed were 4-5 nm in size.

To reveal the possible influence of the stress, emerged during films formation due to film-substrate lattice mismatch, the interfaces of $Fe_{1.1}Te$ films on MgO and LaAlO3 substrates on Tc the cross sections of these heterostructures were studied.

The cross sectional HAADF HR STEM image of $Fe_{1.1}Te$/MgO reveal the misfit dislocations, located at the interfaces. These dislocations could release the stress in the $Fe_{1.1}Te$ layers, thus leave the relaxed structure of the film and Tc value unaffected.

The cross sectional BF TEM investigations of $FeTe_{0.5}Se_{0.5}$ /$LaAlO_3$ interfaces showed the presence of the intermediate layer which also release the stress in the $FeTe_{0.5}Se_{0.5}$ layers, thus leave the Tc unaffected. Some areas

1. Mizuguchi Y., Takano. J. Phys. Soc. Jpn. 2010. V. 79. P. 102001.
2. Margadonna S., et al. Phys. Rev. B 2009. V. 80. P. 064506.
3. Yeh K.W., et al. EPL. 2008. V. 84. P. 37002

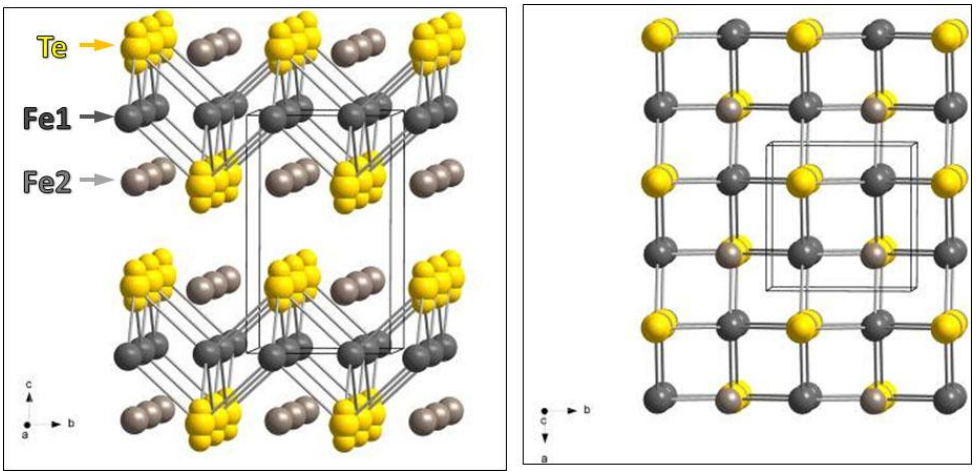

Figure 1. Crystal structure of$Fe_{1.1}Te$. The occupancy of Fe1 is 100% and Fe 2 - 10%.

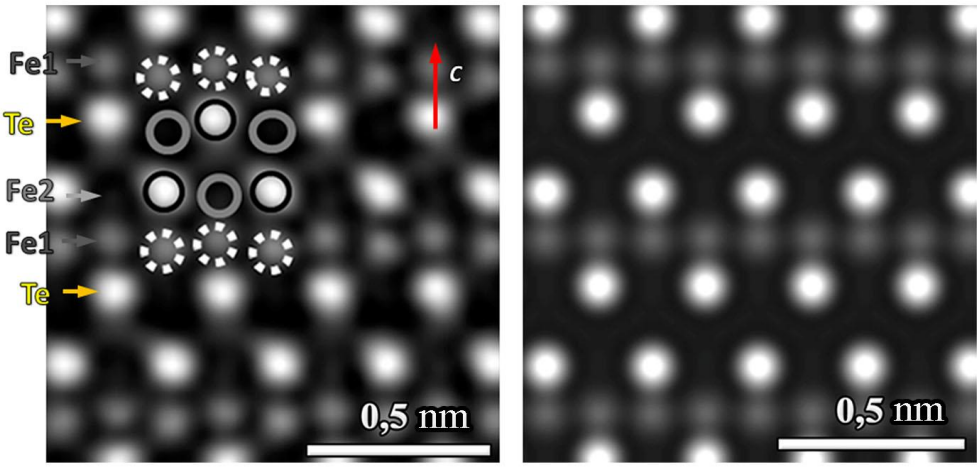

Figure 2. a) HAADF HR STEM image of FeTe single crystal in [010] zone axis; b) Simulated HAADF HR STEM image of FeTe single crystal in [010] zone axis.

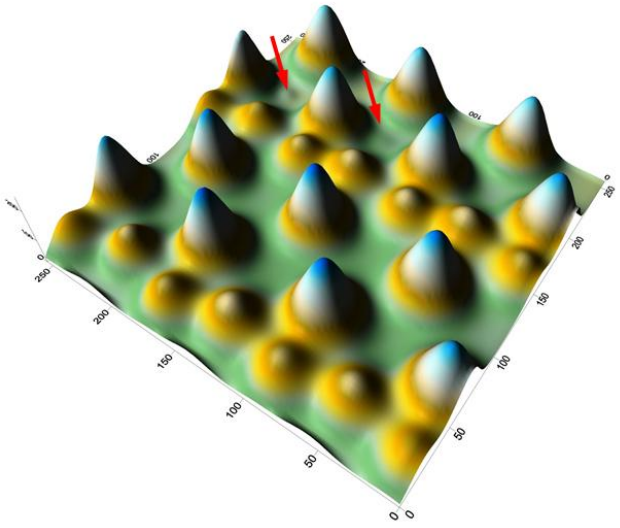

Figure 3. 2D intensity profiles of HAADF HR STEM image of FeTe single crystal in [010] zone axis. Red arrows pointed the groups of Fe2 atoms

Spectroscopic TEM/STEM, EELS, EFTEM

IM4.P118
Monochromated and angular resolved low loss EELS studies on a Titan Themis

T. Dennenwaldt[1], C. Hébert[1]

[1]EPFL, CIME, Lausanne, Switzerland

teresa.dennenwaldt@epfl.ch

The electronic structure of materials can be studied in depth at a high spatial and energy resolution with electron energy loss spectroscopy (EELS) in the transmission electron microscope (TEM). With low loss EELS (< 50 eV) physical parameters like the dielectric function or the band gap of materials can be determined. In this regime, plasmons and inter-and intraband transitions are excited and give rise to the solid state behavior of the material. Angular resolved low loss EELS allows analyzing the momentum transfer q, an additional dimension of the loss function [1]. The advantage compared to optical absorption is that EELS is not limited to momentum transfer q = 0.

We investigated the dynamical electronic response of polycrystalline Pd and single crystalline Si at very low energy losses with a high energy resolution with angular resolved low loss EELS. As the energy resolution of the angular resolved EELS is amongst others limited by the energy resolution of the microscope we conducted the experiments on the recently installed double-corrected Titan Themis (equipped with a monochromator and a GIF) at the Center for Integrated Electron Microscopy (CIME) at EPFL. We performed the experiments in diffraction mode and used the entrance aperture as well as the objective aperture to create a slit to select a line between the diffraction spots and record directly an “E-q” diagram”. The experimental results are compared to theoretical calculations.

1. C. Hébert et al., Eur. Phys. J. Appl. Phys. 54 (2011) 33510.

Spectroscopic TEM/STEM, EELS, EFTEM

IM4.P119
Momentum-resolved electron energy-loss spectroscopy of 2D heterostructures

M. Mohn[1], R. Hambach[1], P. Wachsmuth[1], U. Kaiser[1]

[1]Ulm University, Electron Microscopy Group of Materials Science, Ulm, Germany

michael.mohn@uni-ulm.de

By means of momentum-resolved electron energy-loss spectroscopy, dielectric properties of 2D materials can be accessed for different in-plane momentum transfers *q*. With regard to high-energy plasmons in layered heterostructures, the formation of low-loss EEL spectra cannot be easily explained in terms of spectra of the constituent monolayers. We address this problem by direct comparison of our experimental results and corresponding ab-initio calculations. Eventually, we want to evaluate the prospects of investigating highly beam-sensitive MoS_2 layers with EELS in TEM by encapsulating them between graphene [1].

Our measurements have been performed at an acceleration voltage of 40 kV in a Zeiss Libra 200 based TEM prototype ("SALVE I" [2,3]) equipped with a monochromator and an Ω-type in-column energy filter. They cover energy losses in the range up to 50 eV and momentum transfers within the Brillouin zone, along the ΓM and ΓK direction.

For the individual monolayers, separate ab-initio calculations have been performed as follows: For the ground-state calculations, the density functional theory (DFT) software abinit [4] has been used with pseudopotentials and the local-density approximation (LDA). Linear response was then calculated using the dp-code [5], within random-phase approximation (RPA).

Based on these simulations, we employ model calculations in order to describe the EEL spectra of graphene and MoS_2 heterostructures. Thereby, we take into account Coulomb interactions between the layers. Whereas the spectra of few-layer graphene can be accurately described within the layered electron gas (LEG) model [6,7], we find that it fails to describe heterostructures with MoS_2. By accounting for the finite thickness of the MoS_2 layers in more sophisticated calculations, we attempt to simulate the EEL spectra of a graphene/MoS_2/graphene sandwich structure more precisely.

Moreover, in this paper, we also illuminate several pitfalls and general limitations of momentum-resolved EELS: Depending on the exact setup, spatial, energy and momentum resolution may be very different. In addition, we highlight that contamination and beam damage have to be weighed against low signal-to-noise ratio for high *q*.

1. G. Algara-Siller et al., Appl. Phys. Lett. 103, 203107 (2013)
2. U. Kaiser et al., Ultramicroscopy 111, 1239-1246 (2011)
3. P. Wachsmuth et al., Phys. Rev. B 88, 075433 (2013)
4. X. Gonze et al., Comp. Mat. Sci. 25, 478 (2002)
5. V. Olevano, L. Reining, F. Sottile, http://www.dp-code.org (1998)
6. V. Borka Jovanović et al., Phys. Rev. B 84, 155416 (2011)
7. P. Wachsmuth et al., Phys. Rev. B 90, 235434 (2014

Spectroscopic TEM/STEM, EELS, EFTEM

IM4.P120
Investigation of plasmonic modes of gold tapers by EFTEM and EELS

S. Guo[1], N. Talebi[1], W. Sigle[1], M. Esmann[2], S. Becker[2], R. Vogelgesang[2], C. Lienau[2], P. van Aken[1]

[1]Max Planck Institute for Solid State , StEM, Stuttgart, Germany
[2]Carl von Ossietzky Universität Oldenburg, Oldenburg, Germany

s.guo@fkf.mpg.de

Surface plasmons are collective oscillations of conduction electrons at the surfaces of metals. The coupling of plasmons and light and the propagation of surface plasmons at the surfaces have been so far intensively studied in the literature. A very interesting application of surface plasmons is the localization of optical energies in metallic nanostructures at the nanometer scale by utilizing so-called nanoantennas.

Electron energy-loss spectroscopy (EELS) has been among the first methods for investigating surface plasmons through their coupling with relativistic electron beams. Only recently, by enormously improving the EELS technology, such as aberration-corrected magnetic lenses and monochromated electron guns, it has become possible to investigate the optical modes at the single nanoparticle level with a huge band-width [1]. Moreover, theoretical advancements have also shown that the EELS signal can be interpreted as the local density of optical modes projected along the electron trajectory [1].

We report the application of energy-filtering transmission electron microscopy (EFTEM) and EELS in investigation of localized surface plasmon (LSP) modes at apices of gold tapers with different apexes and opening angles. Due to the high performance of the employedZeiss SESAM electron microscope [2], more fine details at taper apices are rendered with both high energy and high spatial resolution.

EFTEM can be exploited to map real-space distribution of a selected energy range in a reasonably short time. As directly visualized in Fig.1, a smoothly tapered gold apex supports a broadband LSP resonance with a bandwidth up to 2.0 eV. More details of the broadband local density of optical states at the taper apex are indicated by an EELS line scan (with the electron beam focused and scanned along the red arrowstowards taper apex in Fig.1). A very exciting feature obvious in this experiment is the higher order resonances forming an interference-like pattern with a hyperbolic-like dispersion becoming apparent in the energy-distance map. In order to understand the physics behind such resonances, we have theoretically calculated the EELS spectra using the three-dimensional finite-difference time-domain technique with an embedded electron source [3]. Our calculations demonstrate that the higher-order resonances are due to the excitation of whispering gallery modes of the structure. We further benchmark our observations with theoretical calculations of the EELS spectra from rods and spheres, which also sustain similar whispering gallery modes. [4]

1. F.J. García de Abajo: *Optical excitations in electron microscopy*. Reviews of Modern Physics **82** (2011) 209-275.
2. C.T. Koch, W. Sigle, R. Höschen, M. Rühle, E. Essers, G. Benner, M. Matijevic: *SESAM: Exploring the Frontiers of Electron Microscopy*. Microscopy and Microanalysis **12** (2006) 506-514.
3. N. Talebi: *A directional, ultrafast and integrated few-photon source utilizing the interaction of electron beams and plasmonic nanoantennas*. New J. Phys. **16** (2014) 053021.
4. The research leading to these results has received funding from the European Union Seventh Framework Programme [FP7/2007-2013] under grant agreement n°312483 (ESTEEM2).

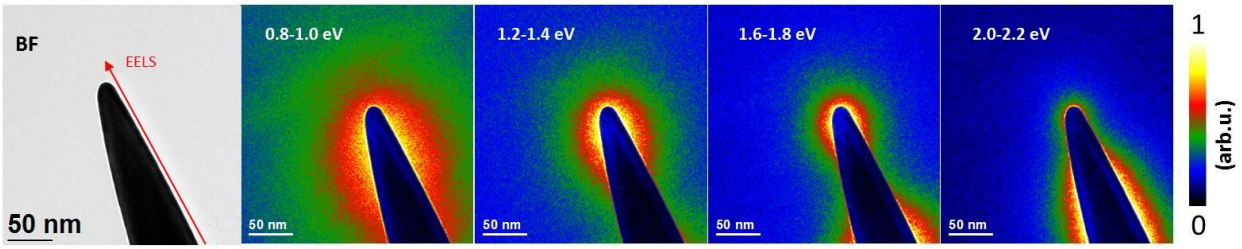

Figure 1. Bright-field image and EFTEM images of a conical Au taper in the energy-loss interval from 0.8 to 2.2 eV. The color bar on the right symbolizes the energy-loss probability which is a measure of the *z*-component of the excited electric field.

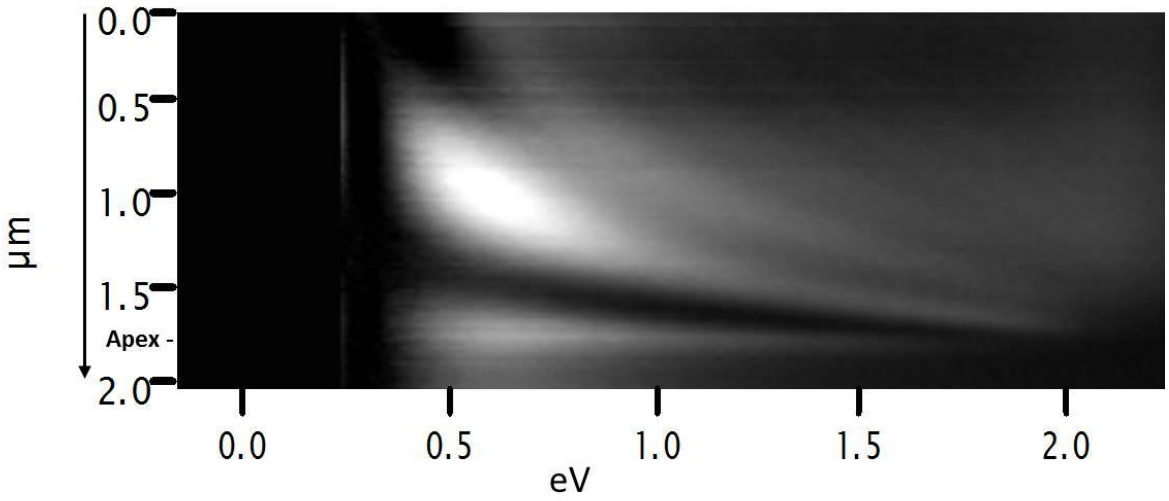

Figure 2. Zero-loss extracted EELS spectra as a function of energy loss and impact location along the taper shaft for the gold taper shown in Fig.1. Zero-loss peaks were removed by applying a power-law fit to the peak tail and the residual signals were extracted.

Spectroscopic TEM/STEM, EELS, EFTEM

IM4.P121
Measurements of the lateral quantitative resolution of electronprobe microanalysers with field emission source

J. Nissen[1], D. Berger[1]

[1]Technical University Berlin, Center for Electron Microscopy (ZELMI), Berlin, Germany

joerg.nissen@tu-berlin.de

High resolution electron microprobe analysers (EPMA) use field emission electron sources (FEG) that provide highly focused electron beams even at low acceleration voltages below 7 kV. The resulting interaction volume of the electron inside the specimen is laterally small, thus the sources volume of generated x-rays, and therefore a high spatial resolution is obtained in elemental analysis using EDX- and WDX-detectors. In the context of element analysis it is necessary to distinguish between quantitative and qualitative spatial resolution. It has already experimentally been proofed [1] that precipitates with sizes well below 100 nm might be recognized using the WDX-signal - this refers to the so called qualitative lateral analytical resolution. Obviously, a precise element quantification of this small precipitates is impossible since the interaction volume of the electrons exceeds the size of the precipitates.

The aim of the present work is to determine the lateral analytical resolution of a FEG-EPMA, i.e. the minimum thickness of a layer, for which a precise element quantification is still possible. A first estimation is given by Monte Carlo (MC) simulations (program Casino v2.48) of the interaction volume in pure gold at 15, 8, 5, and 3 keV electron energies (Fig. 1). The lateral diameter of the interaction volume decreases from about 500 nm at 15 keV to about 150 nm at 5 keV. Following the simulation, a significant further decrease is not expected when the electron energy is further decreased to 3 keV.

For the experimental verification, test specimens with sputtered gold layers with different thicknesses (140, 335, 450, 1100 nm) on SIGRADUR glassy carbon substrate were produced. To avoid fluorescence effects in the WDX-signal of the Au-layer, all specimens were covered with an additional 400 nm silver layer The cross sectional preparation of the specimen were done first by cleaving and then by polishing with a focused Ga-ion beam (FEI Helios Nano Lab600 FIB) requiring protection layer consisting of Ga, Pt and C (Fig. 2). The MC simulations are based on the reduced density of sputtered gold which was measured to be about 17.6 g/cm^3.

Figure 3 summarized the results of the element quantification of the gold layer using different electron energies and the WDX-signal of the Au-Ma- (PET-) and Au-La-lines (LIF-crystal) respectively. A quantification result of (100.0 +/- 0.2) % indicates that the source volume of the generated X-rays is completely inside the Au-layer. Using the 1100 nm Au-layer, no signal from the surrounding carbon and silver is detected even at 15 keV, therefore it is applied as reference standard for the quantification (indicated by 100.00 in table 1). The 450 nm-layer is resolved with the Au-Ma-signal for electron energies 8 and 5 keV only. The source volume of the higher energy Au-Lais found to be smaller than the thickness of the 450 nm-layer even at 15 keV (low overvoltage condition [2]). The 335 nm-layer might be quantified precisely at 8 and 5 keV using the Au-Ma-signal, while the 140 nm-layer is not even resolved at 5 keV. The results of table 1 are in good agreement with the MC simulations of Fig.1.

Following the simulated and measured results, it seems to be feasible to get a lateral quantitative resolution of about 150 nm in WDX element quantification using a FEG-EPMA. For the future, further specimens with layer-thicknesses between 150 and 200 nm will be examined. In the next step, measurements of the depth-resolution in WDX element quantification are of interest.

1. Berger D and Nissen J 2014 *IOP Conf. Ser.: Mater. Sci. Engng.* 55 012002.
2. McSwiggen P 2014 *IOP Conf. Ser.: Mater. Sci. Engng.* 55 012009.

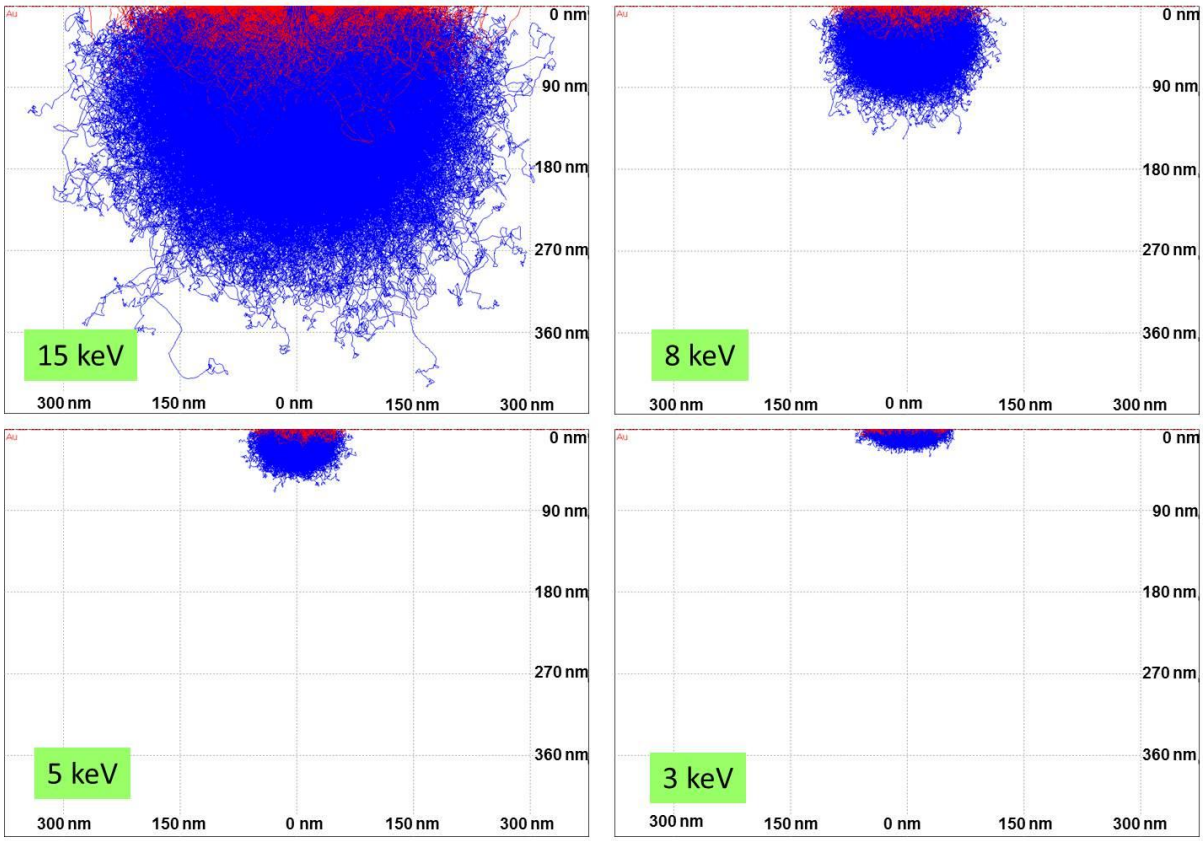

Figure 1: Monte Carlo simulations (Casino v2.48) for gold with 15, 8, 5 and 3 keV electron energy.

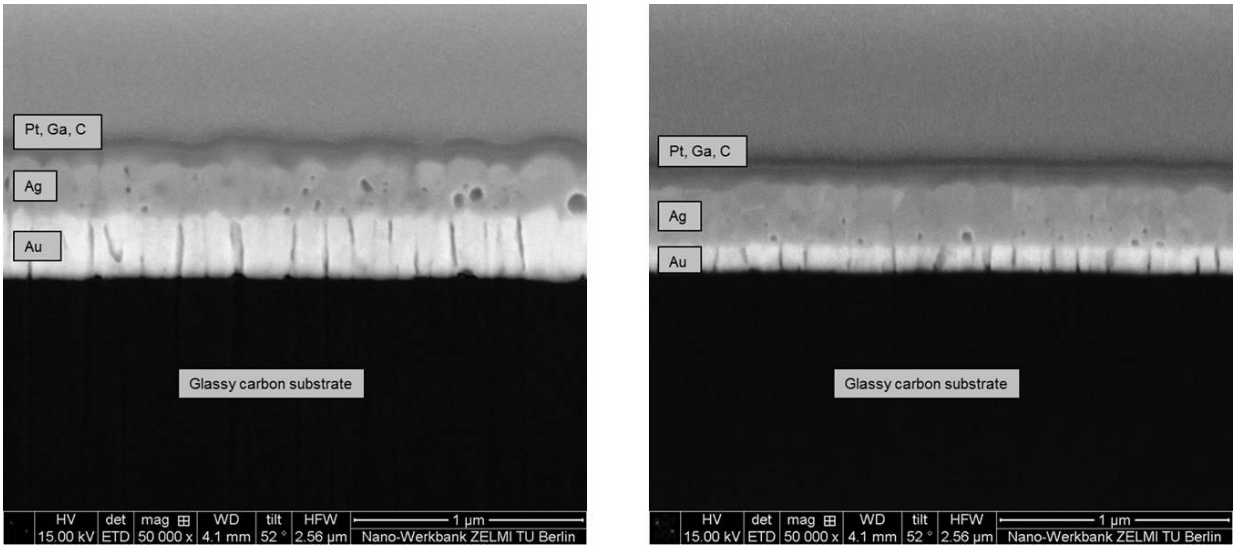

Figure 2: SE images of the 335 nm (left) and the 140 nm (right) gold layer in cross-section.

Au layer thickness [nm]	15 kV (AuMα)	15 kV (AuLα)	8 kV (AuMα)	5kV (AuMα)
1000 (Reference)	100.00	100.00	100.00	100.00
450	92.04	99.95	99.93	99.89
335	/	/	99.81	99.82
140	/	/	/	91.04

Figure 3. Results of the quantitative measurements of the gold layers (in wt% Au)

Spectroscopic TEM/STEM, EELS, EFTEM

IM4.P122
Optimization of energy resolution for EELS measurements in diffraction mode

H. Zschiesche[1], A. Mogilatenko[1,2], H. Kirmse[1]

[1]Humboldt University of Berlin, Department of Physics , Berlin, Germany
[2]Ferdinand-Braun-Institut, Leibniz-Institut für Höchstfrequenztechnik, Berlin, Germany

hannesz@physik.hu-berlin.de

Electron energy loss spectroscopy (EELS) can be used to obtain chemical, optical and electronic information. In particular, information on the density of states of the atoms can be determined from the energy loss near edge structure (ELNES). Atomic-site specific analysis can be done by analysing the fine-structure of energy loss by channelled electrons (ELCE) [1]. To see the characteristics and compare them with simulations, it is indispensable to have an optimum energy resolution with a signal intensity as high as possible. Here we present the results of a systematic analysis of the impact of all relevant microscope parameters.

The measurements were performed on a TEM JEOL JEM 2200FS (200 kV) which is equipped with a field emission gun, in-column energy filter and 1k x 1k slow-scan CCD camera (Gatan). For defined ELCE conditions the diffraction mode was chosen with a camera length of 150 cm for highest selectivity in reciprocal space. To ensure sharp diffraction spots a parallel incoming beam was adjusted. The acquisition time was always set to 0.05 s in order to protect the detector against beam damage.

The measurements were organized according to the three main items influencing the spectrum quality: setting of condenser lens system, of apertures and of the detector system (CCD camera).

Changes in spot size, beam convergence angle and brightness modify the shape of the zero loss peak (ZLP). While the full width at half maximum (FWHM) of the ZLP, and thereby the energy resolution, does not depend on the spot size (see Fig.1), the intensity increases with a smaller spot-number (Fig.2). Hence, for core losses a smaller spot size is favourable. From Fig. 1 & 2 it is also obvious that different condenser lens aperture (CLAp) and different high contrast aperture (HCAp) settings neither change the energy resolution nor the intensity. But, there are restrictions with respect to beam convergence angle and brightness for ensuring sharp diffraction spots.

With respect to the aperture setting it was found that for different aperture combinations the beam-limiting aperture changes. This aperture determines both, the FWHM (see Fig.3) and the intensity (not shown). In addition, a small selected area aperture (SAAp) and HCAp/filter entrance aperture ensure selection of a small sample area and a good reciprocal space resolution, respectively. For the aperture size setting installed in the JEOL 2200FS, the smallest HCAp is the most sensitive aperture for the reciprocal space.

A small dispersion of the EEL spectrum detector (CCD camera) increases the FWHM artificially (see Fig.4). On the other hand, the highest dispersion limits the energy range detected by the CCD camera. Hence, good compromise is found at about 200 µm/eV.

Summing up all findings, the following recipe can be given: select the intensity by the spot size, use a small SAAp for selecting a small sample area, use the smallest HCAp for good reciprocal space sensitivity and set a large dispersion for optimum energy resolution at the detector.

1. W. Hetaba, S. Löffler, M.-G. Willinger, M. E. Schuster, R. Schlögel, P. Schattschneider, Micron **63** (2014) 15

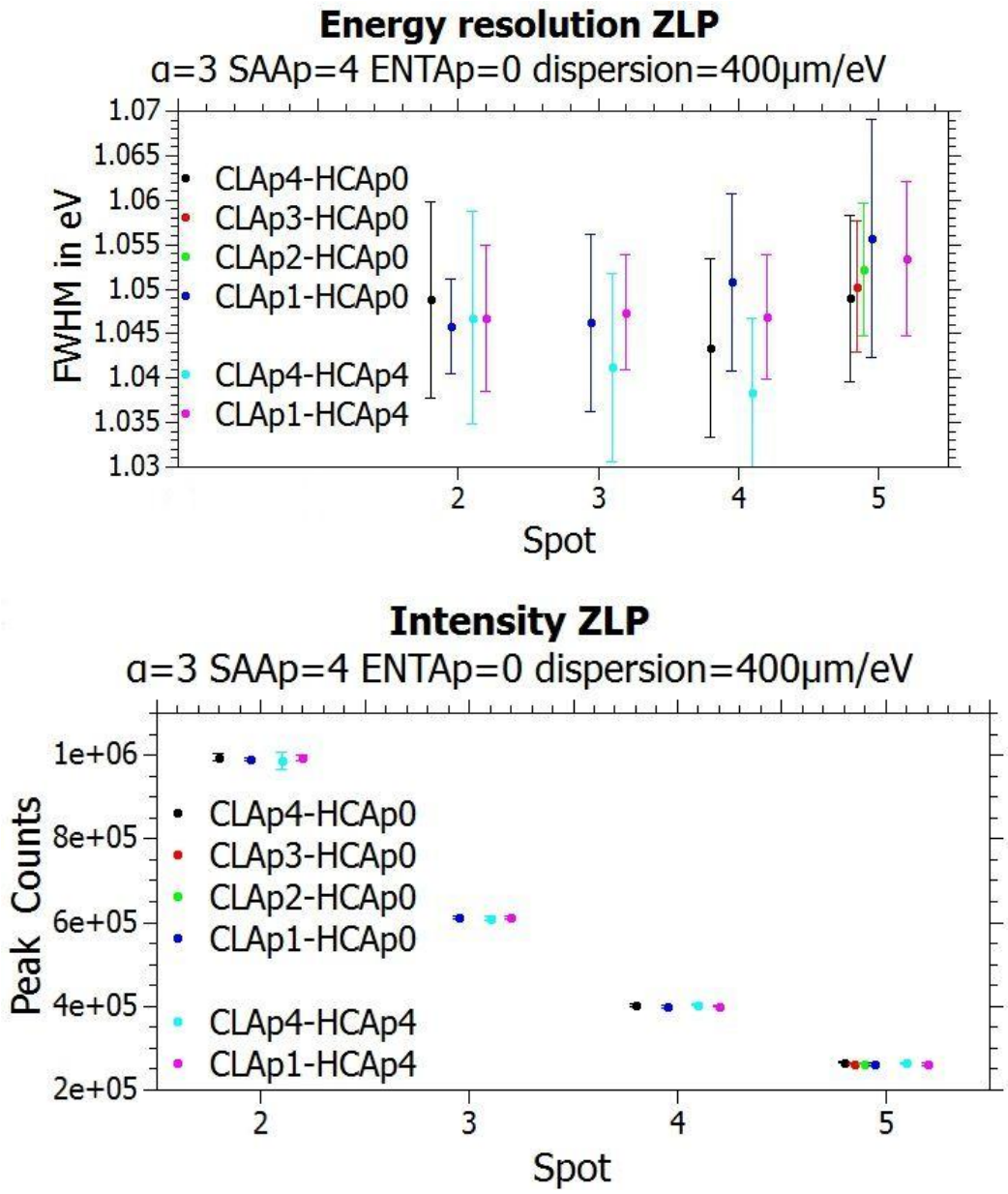

Figure 1. & Figure 2. Influence of the spot-number (as higher as larger the spot) on the FWHM of the ZLP (1) and on the intensity (2) analysed for different condenser lens aperture (CLAp) and high contrast aperture (HCAp) settings. There is no effect on the FWHM (see 1), but the intensity increases with smaller spot number (see 2). The aperture settings have no effect.

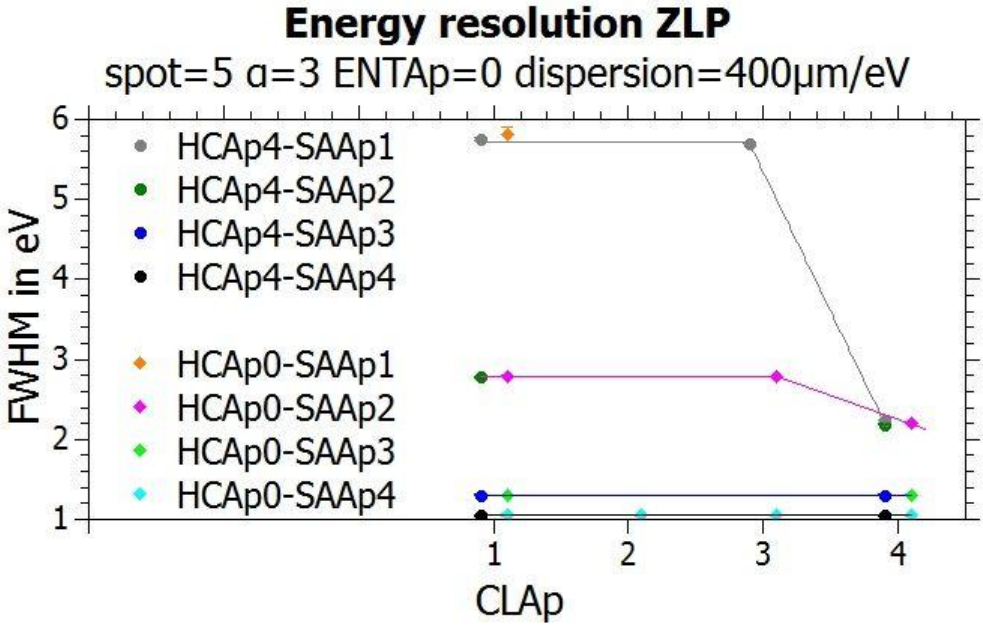

Figure 3. Investigation of the influence of the condenser lens aperture (CLAp) and different settings of the high contrast aperture (HCAp) and the selected area aperture (SAAp) on the energy resolution. Only the beam-limiting apertures (SAAp or CLAp) affects the FWHM.

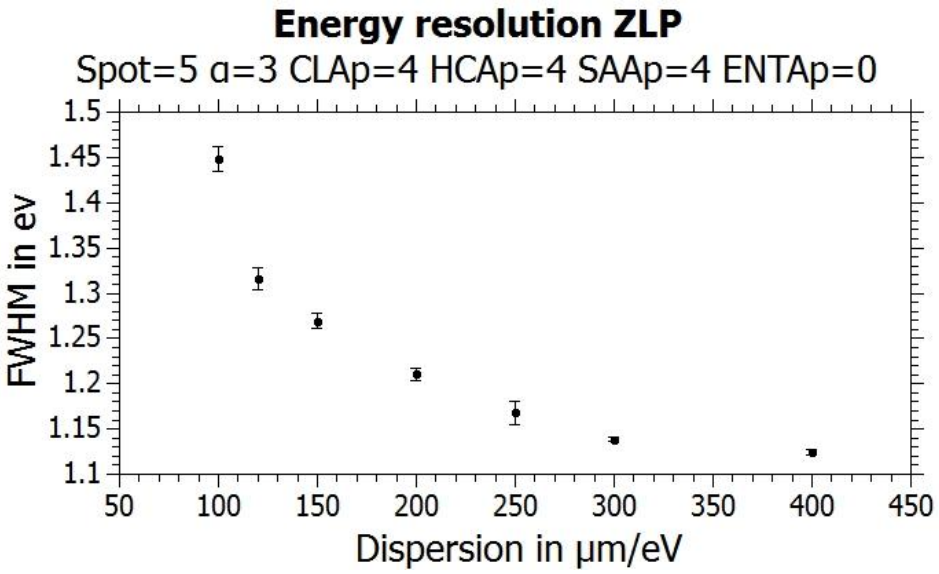

Figure 4. Influence of the dispersion on the FWHM of ZLP. Increasing dispersion results in a lower FWHM and thus a higher energy resolution. Up to 300 µm/eV the energy resolution is limited by the pixel size of the CCD camera.

Spectroscopic TEM/STEM, EELS, EFTEM

IM4.P123
Electron microscopy of surface layers from thermally, mechanically and electro-chemically processed samples in order to develop process signatures

L. Ehle[1], B. Kolkwitz[2], S. Harst[3], S. Schneider[3], J. Mayer[1]

[1]RWTH Aachen, Central Facility of Electron Microscopy, Aachen, Germany
[2]University Bremen, Institut für Werkstofftechnik, Bremen, Germany
[3]RWTH Aachen, Werkzeugmaschinenlabor, Aachen, Germany

ehle@gfe.rwth-aachen.de

Reproducible properties of surface layers, such as residual stress, are in high demand in industrial production processes. So far these have been developed by determining appropriate boundary and process conditions by means of several time-consuming iterative procedures. Since these boundary and process conditions only refer to the examined process and it's specific process parameters, it's not possible to transfer these conditions to other production processes in order to achieve the same surface layer properties. Therefore a new energy based approach called Process Signatures was established, which describes the relationship between material loads from the production process and material modification of the generated surface layers. Because of the energy based approach the Process Signatures allow a comparison of different processes with the same physical working principle. For the development of such Process Signatures it is necessary to characterize the surface layers before and after the processing. This way, the change of material properties (e.g. structure modification or dislocation density/ movement/ arrangement) can be determined according to the predominant working principle of the used production process.

In this work scanning electron microscopy (SEM) and transmission electron microscopy (TEM) are used to characterize the surface layers of samples which are processed by grind hardening (GH), electrochemical machining (ECM) and electro-discharge machining (EDM). Therefore the predominant working principles of these processes are thermo-mechanical, chemical and thermal leading to different surface modifications. SEM and TEM analysis of the different processed samples show a wide range in the thickness of the generated surface layers with more than 1000 µm for samples processed by grind hardening, less than 4 µm for EDM processed samples and no distinctive surface layer for ECM processed samples. The surface zones of the GH and the EDM processed sample show a similar surface modification according to the thermal working principle (see Figure 1 right and Figure 2 left). So a first step for the development of Process Signatures has been done that will achieve comparability for different processes with same physical working principle.

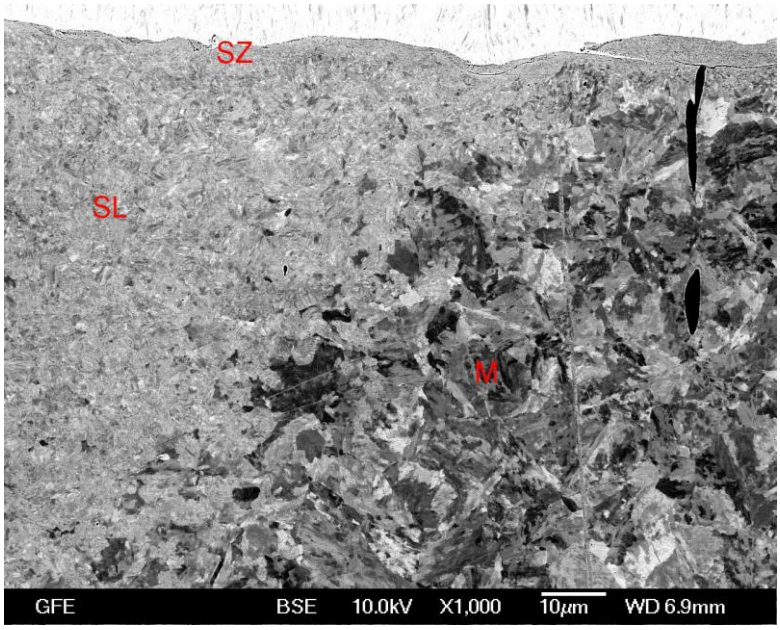

Figure 1. SEM image of a sample processed by grind hardening; left: surface layer (SL) and matrix (M); right: SL and surface zone (SZ).

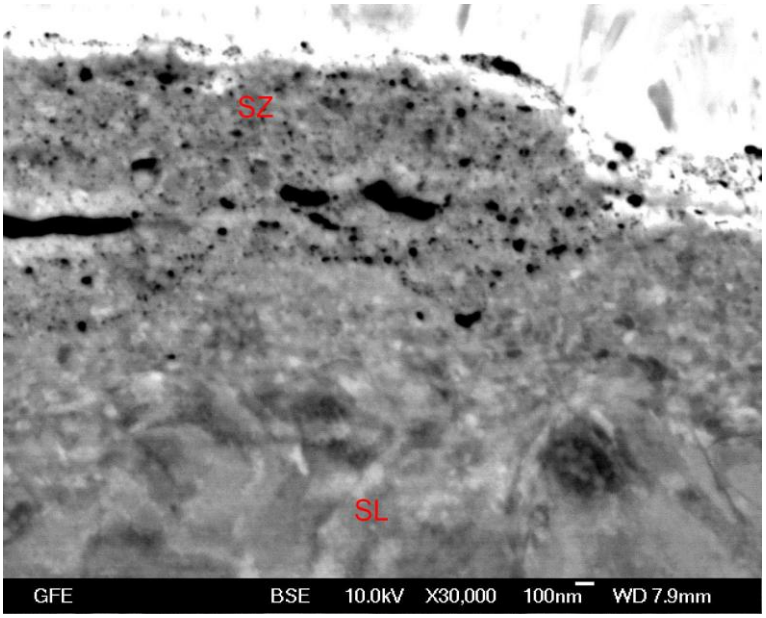

Figure 2. left: SEM image of a sample processed by EDM; right: TEM image of a sample processed by ECM.

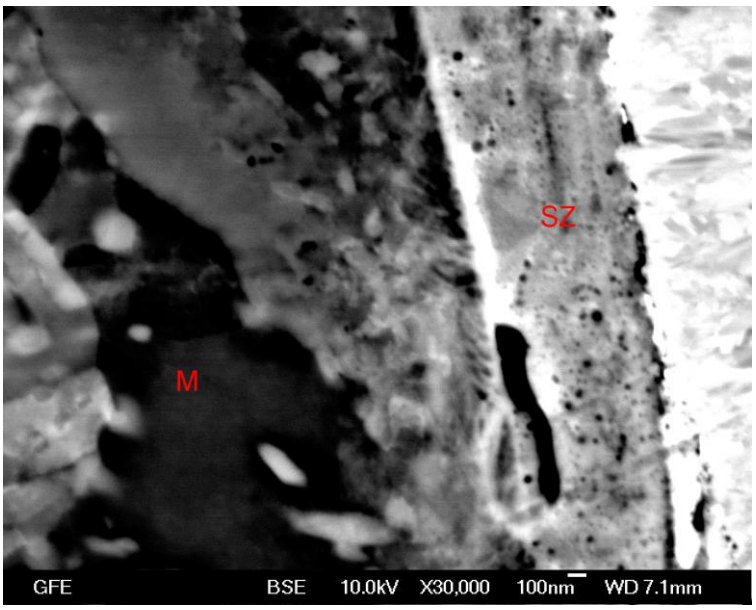
SZ
M
GFE BSE 10.0kV X30,000 100nm WD 7.1mm

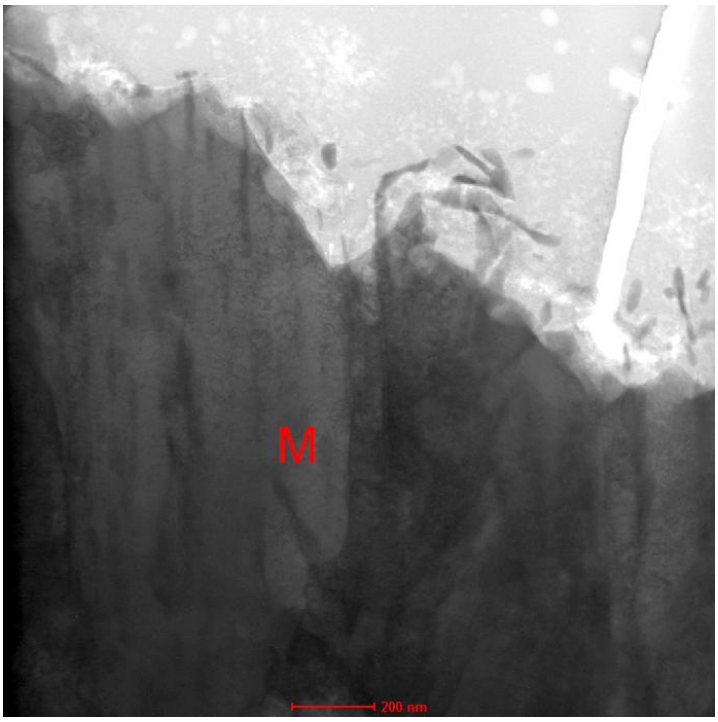
M
200 nm

Spectroscopic TEM/STEM, EELS, EFTEM

IM4.P124
Site occupancy determination of a dopant substituting for multiple sites using beam-rocking TEM-EDX and statistical analysis

M. Ohtsuka[1], S. Muto[2], K. Tatsumi[2]

[1]Nagoya University, Graduate School of Engineering, Nagoya, Japan
[2]Nagoya University, EcoTopia Science Institute, Nagoya, Japan

m-ohtsuka@nucl.nagoya-u.ac.jp

Fast incident electrons can propagate preferentially along particular atomic sites, depending on the incident beam direction with respect to the crystal. Two-dimensional X-ray spectral mapping as a function of the incident angle by beam-rocking is a microanalysis based on such channelling phenomena, frequently called high-angular resolution electron channelling X-ray spectroscopy (HARECXS). This is an extension of conventional atom-location by channeling-enhanced microanalysis (ALCHEMI), and the intensity map of the characteristic X-ray peak, called the ionization channelling pattern (ICP), reflects the occupancy site and concentration of the element of interest. This method enables us to analyse a trace element. ICP is a directional projection of the crystal symmetry about the element of interest, so that we can obtain statistically sufficient information of a trace element by collecting the signal widely distributed over the rocking angle. The method provides quantitative and three dimensional information, in contrast to the atomic scale analysis using the state-of-the-art scanning transmission electron microscopy, corresponding to two-dimensional projection of particular atomic columns in real space.

If a trace dopant element substitutes for particular atomic sites of host elements, the ICP of a dopant element can be approximately described by a linear combination of ICPs of the host elements. We can thus obtain the occupancy sites and concentration of a dopant quantitatively by applying the statistical ALCHEMI/HARECXS method [1, 2]. However, this method is not applicable to the cases where a host element occupies crystallographically inequivalent multiple sites, because it requires to separate the signal of an element sitting on the multiple sites into ones from the individual sites.

We propose here a scheme to decompose such a mixed ICP into site-specific ICPs corresponding to the different individual sites, utilizing precise theoretical simulations based on dynamical elastic/inelastic electron diffraction theories. By the statistical analysis combined with this scheme, we have analyzed M-type strontium ferrite $Sr_{0.8}La_{0.2}Fe_{11.4}Co_{0.2}O_{19}$, where doped Co occupies the five different Fe sites, 2a, 2b, $4f_1$, $4f_2$, and 12k sites in Wycoff's notation, and doped La occupies the Sr site, to improve the magneto-crystalline anisotropy. Figure 1 shows the electron channeling pattern (ECP) and X-ray ICPs for O-K, Fe-K, Co-K, Sr-L and La-L lines, respectively. While La-L ICP is very similar to Sr-L ICP, Co-K ICP does not well reproduce Fe-K ICP. This implies that La occupies the Sr site alone, whereas Co occupies the five Fe sites with different weights. Figure 2 shows decomposed site-specific Fe-K ICPs for the five different sites. As a result of statistical analysis, the optimized linear combination of decomposed Fe-K ICPs reproduced Co-K ICP well as shown in Fig. 3. From the optimized fitting parameters, we obtained a quantified result that Co preferentially occupies $4f_1$ and 12k sites. This result is consistent with the most probable model by neutron diffraction/Rietveld analysis, and is also supported by the energetics based on *ab initio* calculations.

1. Rossouw *et al*., *Philos. Mag. Lett.*, **60**, 225-232 (1989).
2. Fujimichi *et al*., *J. Solid State Chem.*, **183**, 2127-2132 (2010).

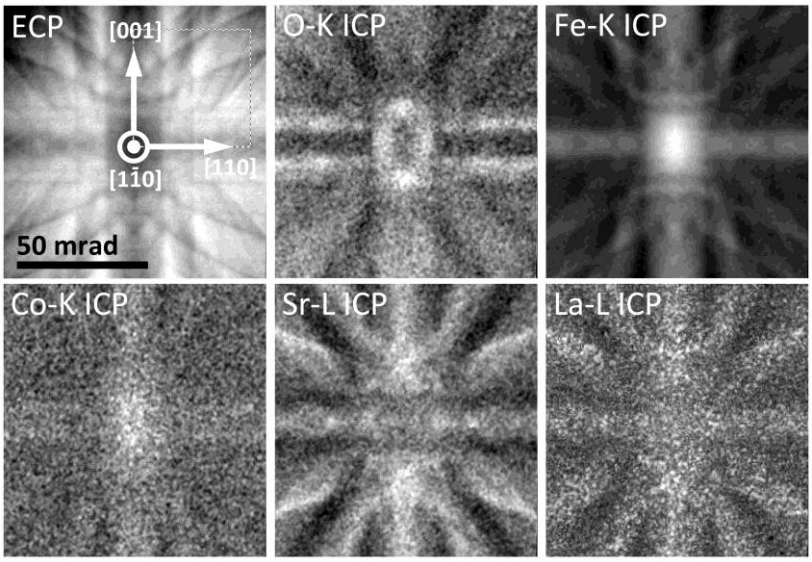

Figure 1. Experimental ECP and X-ray ICPs of O-K, Fe-K, Sr-L, and La-L lines, respectively, around [110]-orientation of $Sr_{0.8}La_{0.2}Fe_{11.4}Co_{0.2}O_{19}$.

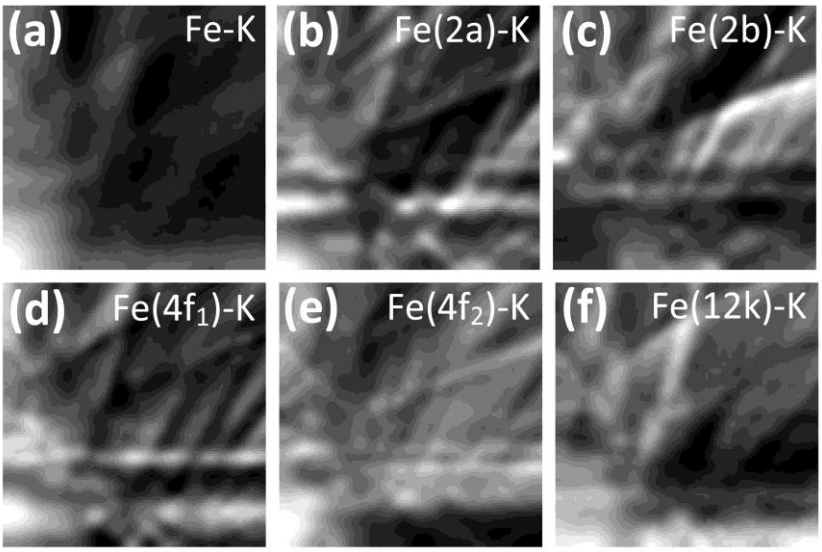

Figure 2. (a) Fe-K ICP extracted from upper-right half region of Fe-K ICP shown in Fig. 1 and (b-f) decomposed Fe-K ICPs for 2a, 2b, $4f_1$, $4f_2$ and 12k sites.

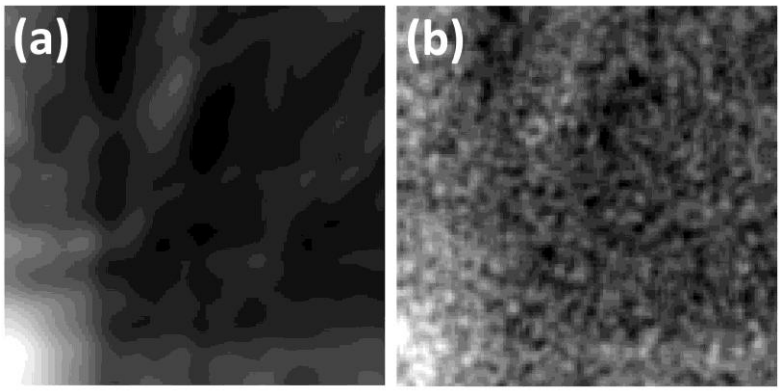

Figure 3. (a) Optimized linear combination of decomposed site-specific Fe-K ICPs, and (b) corresponding experimental Co-K ICP.

Phase-Related Techniques and Holographic Beam Shaping (inc. phase plates, DPC, vortices, electric and magnetic field imaging...)

IM5.125
State of the art electron holographic tomography at the nanoscale

A. Lubk[1], D. Wolf[1], P. Prete[2], N. Lovergine[3], T. Niermann[4], H. Lichte[1]

[1]TU Dresden, Triebenberg Laboratory, Dresden, Germany
[2]IMM-CNR, Lecce, Italy
[3]Università del Salento, Lecce, Italy
[4]Technische Universität Berlin, Berlin, Germany

axel.lubk@triebenberg.de

Electrostatic potentials in nanostructures mirror their chemical composition and electronic properties. Therefore, the distribution of these potentials in three dimensions provides access to the internal structure, space charge regions or band pinning and hence the functionality of modern nanomaterials. Electron holographic tomography (EHT) in the transmission electron microscope is unique in its capability to provide this data with nanometer resolution [1].

Here, we report on our recent progress in the development of EHT towards a versatile measurement technique by overcoming several limitations and significantly extending the amount of the reconstructed information. In particular, we tomographically reconstruct the complete holographic dataset - intensity, interference amplitude and phase - to obtain the three-dimensional distribution of the electrostatic potential as well as elastic and inelastic attenuation coefficients in the material [2]. The crucial phase unwrapping is performed taking into account the information of the complete tilt series. The tomographic reconstruction is performed on optimally sampled polar grids taking into account symmetry and other spatial constraints of the sample [3]. Reconstructed 3D distributions are investigated as a function of different regularization levels, allowing to estimate the signal-to-noise level of the results. Additionally, we show how a deliberate restriction of the tomographic reconstruction to the exterior of the NWs can be used to quantitatively reconstruct very weak stray fields invisible in the standard reconstruction [4].

The improved performance and prospects of EHT are displayed at the example of a GaAs-AlGaAs core-shell nanowire. The NW was grown by metal-organic vapor phase epitaxy (MOVPE) using Au nanoparticles as metal catalyst. We demonstrate 5 nm spatial and 0.2 V signal resolution by reconstructing various potential details, such as localized Al segregation or modulated nanofacets of the core. The three tomographic datasets allow distinguishing between drift-diffusion potentials and composition changes in the various parts of the NW. We furthermore show the electrostatic stray field around the NW produced by the charging of the NW within the electron beam.

The improved performance of EHT opens new avenues for characterizing materials. For instance, weak magnetic stray fields around nanowires or the screened Coulomb potential of ionized dopants in semiconductors may be studied in three dimensions by EHT, thereby contributing to the development of magnetic sensors or electronic devices.

1. Wolf, D.; Lubk, A.; Röder, F. & Lichte, H. Current Opinion in Solid State and Materials Science , 2013, 17, 126 - 134.
2. Lubk, A.; Wolf, D.; Kern, F.; Röder, F.; Prete, P.; Lovergine, N. & Lichte, H., Applied Physics Letters, 2014, 105.
3. Lubk, A.; Wolf, D.; Prete, P.; Lovergine, N.; Niermann, T.; Sturm, S. & Lichte, H. Phys. Rev. B, 2014, 90, 125404
4. Lubk, A.; Wolf, D.; Simon, P.; Wang, C.; Sturm, S. & Felser, C., Applied Physics Letters, 2014, 105.

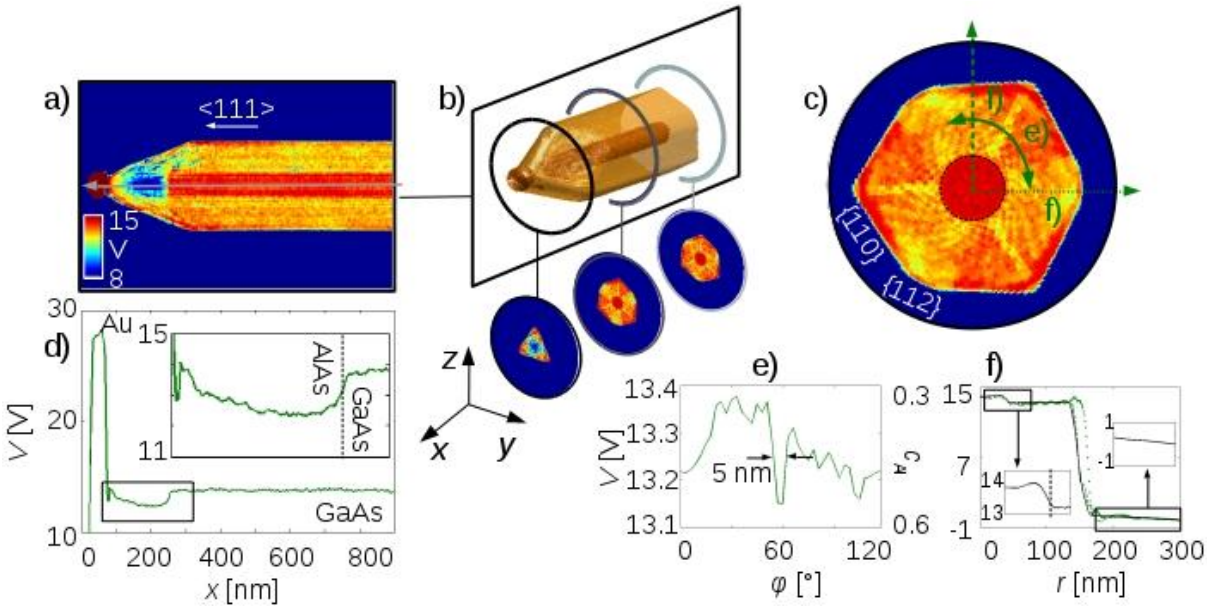

Figure 1. Reconstructed 3D potential of GaAs-AlGaAs core shell NW: The isosurfaces (b) at 9 and 13.75 V illustrate the core-shell morphology. The zx -plane (a) with corresponding linescan (d) on the left shows the sequence Au, AlAs and GaAs unraveled through their different MIPs. The projected yz -plane (c) with corresponding linescans in azimuthal (e) and radial (f) direction shows the core-shell structure with local Al accumulation identified through a characteristic potential reduction in the azimuthal scan. Here, the corresponding Al concentration c_{Al} determined from Vegard's Law is shown on the right y-scale.

Phase-Related Techniques and Holographic Beam Shaping (inc. phase plates, DPC, vortices, electric and magnetic field imaging...)

IM5.126
Towards model-based electron holographic tomography of magnetic vector fields in ferromagnetic nanostructures

P. Diehle[1], J. Caron[1], A. Kovács[1], J. Ungermann[2], R. E. Dunin-Borkowski [1]

[1]Forschungszentrum Jülich, Ernst Ruska-Centre for Microscopy and Spectroscopy with Electrons and Peter Grünberg Institute , Jülich, Germany
[2]Forschungszentrum Jülich, Institute for Energy and Climate Research, Jülich, Germany

p.diehle@fz-juelich.de

The development of an experimental technique that allows the three-dimensional magnetic state of a nanoscale object to be measured quantitatively is of great importance for fundamental and applied research in nanomagnetism. Off-axis electron holography is a powerful technique that can be used to record the phase shift of an electron wave that has passed through a specimen in the transmission electron microscope (TEM) [1]. The phase shift is, in turn sensitive to the in-plane component of the magnetic induction within and around the specimen projected in the electron beam direction. A combination of electron holography with backprojection-based tomographic reconstruction algorithms has been used to recover three-dimensional information about the magnetic flux density within and around materials [2, 3]. Such experiments typically require the acquisition of orthogonal tilt series of electron holograms and the separation of the magnetic from the mean inner potential contribution to the phase shift at each specimen tilt angle.

Figure 1 shows experimental and simulated magnetic induction maps of a GaAs/CoFeB core/shell nanowire. The magnetic induction maps shown in Figs. 1a and 1b were recorded at 300 kV using electron holography in an aberration-corrected FEI Titan TEM operated in Lorentz mode. They are taken from a tilt series of induction maps recorded over ±60º in 5º steps on a 2k x 2k charged coupled device camera. The acquisition time for each hologram was 16 s and the biprism voltage was 99.8 V, resulting in a holographic interference fringe spacing of 3.3 nm and a fringe contrast of 19.4 % in vacuum. Figures 1c and 1d show corresponding simulated magnetic induction maps derived, which are from finite element micromagnetic simulations and suggest that such nanowires can support a mixed magnetic state consisting of uniform magnetisation along their axis and vortices towards their ends [4].

We are currently developing a model-based approach to magnetic vector field tomography that can be applied to results such as those shown in Figs. 1a and 1b. The approach, which is described schematically in Fig. 2, involves using an iterative reconstruction algorithm to obtain the three-dimensional magnetization distribution in a specimen from a series of recorded phase images by the repeated application of a forward model to calculate phase images based on simulated magnetization distributions. We are also developing a tomographic holder that will allow a conventional 3-mm-diameter specimen to be rotated by 360º inside the electron microscope. The holder is equipped with an inclinometer, which allows the specimen tilt angle to be measured to a precision of 0.1°.

We are grateful to J. Arbiol, A. Fontcuberta i Morral, D. Grundler, R. Speen, T. Duden and A. Kákay for valuable contributions to this work and to the European Commission for financial support.

1. M. Lehmann and H. Lichte, “Tutorial on Off-Axis Electron Holography”, Microsc. Microanal., 8, 447, 2002.
2. T. Tanigaki, Y. Takahashi, T. Shimakura, T. Akashi, R. Tsuneta, A. Sugawara and D. Shindo, “Three-dimensional observation of magnetic vortex cores in stacked ferromagnetic discs”, Nano Letters, 15, 1309, 2015.
3. A. Lubk, D. Wolf, P. Simon, C. Wang, S. Sturm and C. Felser, “Nanoscale three-dimensional reconstruction of electric and magnetic stray fields around nanowires”, Appl. Phys. Lett., 105, 173110, 2014.
4. P. Landeros, O.J. Suarez, A. Cuchillo and P. Vargas, “Equilibrium states and vortex domain wall nucleation in ferromagnetic nanotubes”, Phys. Rev. B, 79, 24404, 2009.

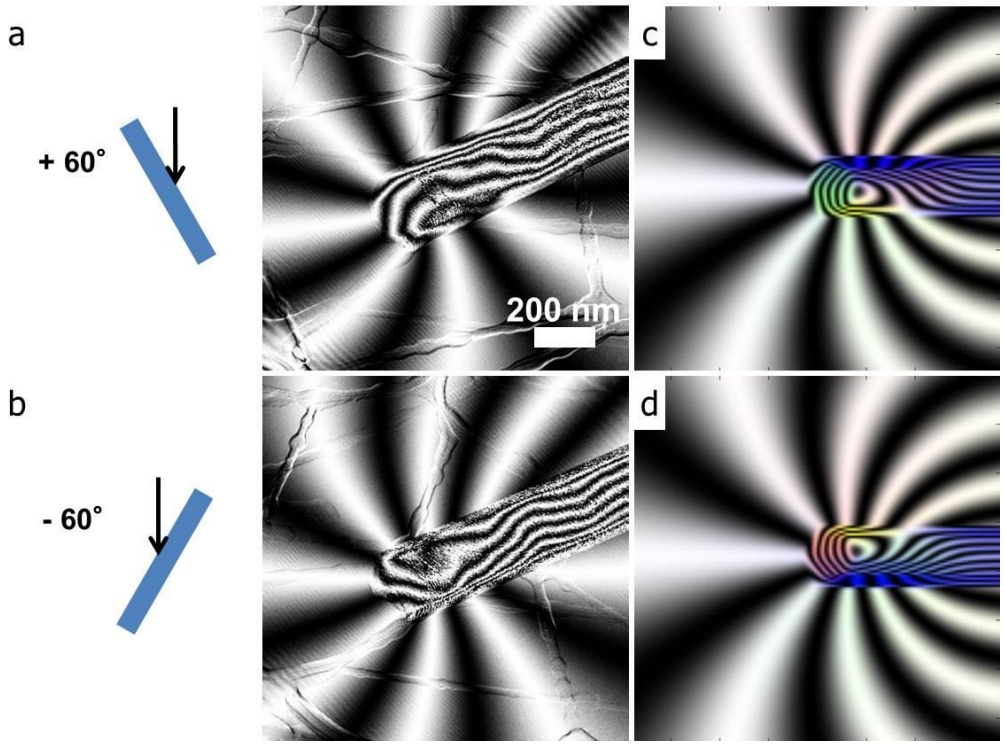

Figure 1. (a, b) Experimental magnetic induction maps recorded at specimen tilt angles of +60° and -60°. The phase contour spacing is π radians. (c, d) show corresponding simulated magnetic induction maps based on micromagnetic simulations.

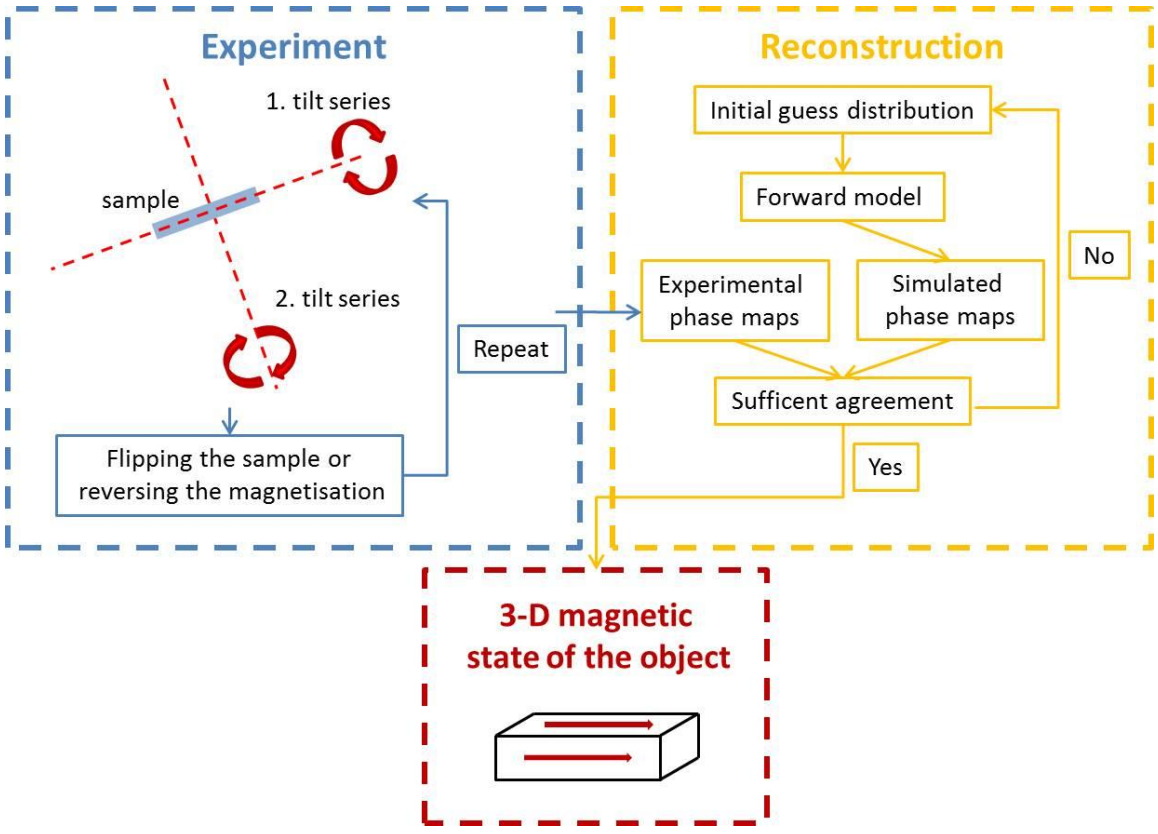

Figure 2. Schematic diagram showing the steps in hologram acquisition and model-based reconstruction used to retrieve the three-dimensional magnetic state of an object.

Phase-Related Techniques and Holographic Beam Shaping (inc. phase plates, DPC, vortices, electric and magnetic field imaging...)

IM5.127
Quantum mechanical interpretation of electron picodiffraction reveals atomic electric fields

K. Müller-Caspary[1,2], F. F. Krause[1], A. Beche[3], M. Schowalter[1,2], V. Galioit[4], S. Löffler[5,6], J. Verbeeck[3], J. Zweck[4], P. Schattschneider[5,6], A. Rosenauer[1,2]

[1]Universität Bremen, Bremen, Germany
[2]Center of Excellence for Materials and Processes, Bremen, Germany
[3]EMAT, University of Antwerp, Antwerp, Belgium
[4]Universität Regensburg, Regensburg, Germany
[5]Vienna University of Technology, Inst. of solid State Physics, Vienna, Austria
[6]University Service Centre for TEM, Vienna, Austria

mueller@ifp.uni-bremen.de

A prominent scanning TEM (STEM) technique for studying atomic-scale electric fields is differential phase contrast (DPC) microscopy. Conventionally, segmented ring detectors as in Fig. 1a are utilised to record portions of the ronchigram [1], which is assumed to be homogeneously filled and shifted as a whole by electric fields in the specimen.

We firstly investigate the reliability of these assumptions by simulating diffraction patterns for 1.3nm thick GaN in [11-20] orientation using multislice with the projected Coulomb potential shown in Fig. 1b. For the two indicated positions ronchigrams are shown in Fig. 1c: Both exhibit rich intensity variations already for this extremely thin crystal even when the STEM probe is at interstitial position 1. In particular, the dominant effect of the atomic electric field on an aberration-corrected STEM probe at position 2 is a complex redistribution of intensity inside the ronchigram. This explains why segmented DPC detectors yield high contrast at atomic sites whereas a quantification of electric fields in terms of ronchigram shifts is prone to errors.

We secondly give a quantum mechanical interpretation of DPC. The ronchigram is recorded in the Fraunhofer diffraction plane which is related to the specimen exit plane by Fourier transform which, in quantum theory, corresponds to switching between real- and momentum space representation. According to the axioms of quantum mechanics, the local ronchigram intensity I(**p**) is thus proportional to the probability density for the lateral momentum vector **p** to occur. Hence the expectation value <**p**> for the momentum is calculated by a centre-of-gravity-type summation, relating the rich details of the ronchigram to a single vector with fundamental physical meaning in a direct and simple manner. The momentum <**p**> is drawn in Fig. 1c, indicating no average deflection of the STEM probe at interstitial position 1 but an average momentum transfer <**p**>=(3.32, 0.65) h/nm (h: Planck constant) towards the positively charged Ga nucleus for beam position 2.

Finally Ehrenfest's theorem is applied to relate the expectation value for the electric field to that of the momentum transfer via a proportionality factor determined by the electron charge, its speed and the specimen thickness. We find that the measured electric field is the convolution of the true field with the STEM probe intensity for thin specimen.

Thirdly, we demonstrate the power of this concept in a comprehensive simulation study of GaN and an experiment with $SrTiO_3$ employing an aberration-corrected STEM as shown in Fig. 2. From simulated diffraction patterns at a regular probe raster in the red area of Fig. 1b we obtain the electric field in Fig. 2a. Obviously, atom cores are sources of the electric field with strengths of up to 2V/pm near Ga and 0.7V/pm near N due to the different nuclear charges. Note the decreasing field strength at the direct vicinity of atomic sites due to the finite probe size. In addition, the inset depicts ronchigrams and momentum transfers near Ga from which the electric field was calculated. Except for typical STEM artefacts such as scan noise and sample drift, the experimental result for $SrTiO_3$ in Fig. 2b exhibits complete analogy to the simulations with heavy Sr and Ti/O columns as strong, light O columns as weak sources of the electric field. The result in 2b is verified quantitatively by simulations [2].

Our contribution closes with prospects as to the mapping of charge- and electron densities by virtue of Maxwell's equations.

1. Shibata et al., Nat.Phys. 8, p611 (2012)
2. Müller et al., Nat.Comm. 5, p5653, (2014)

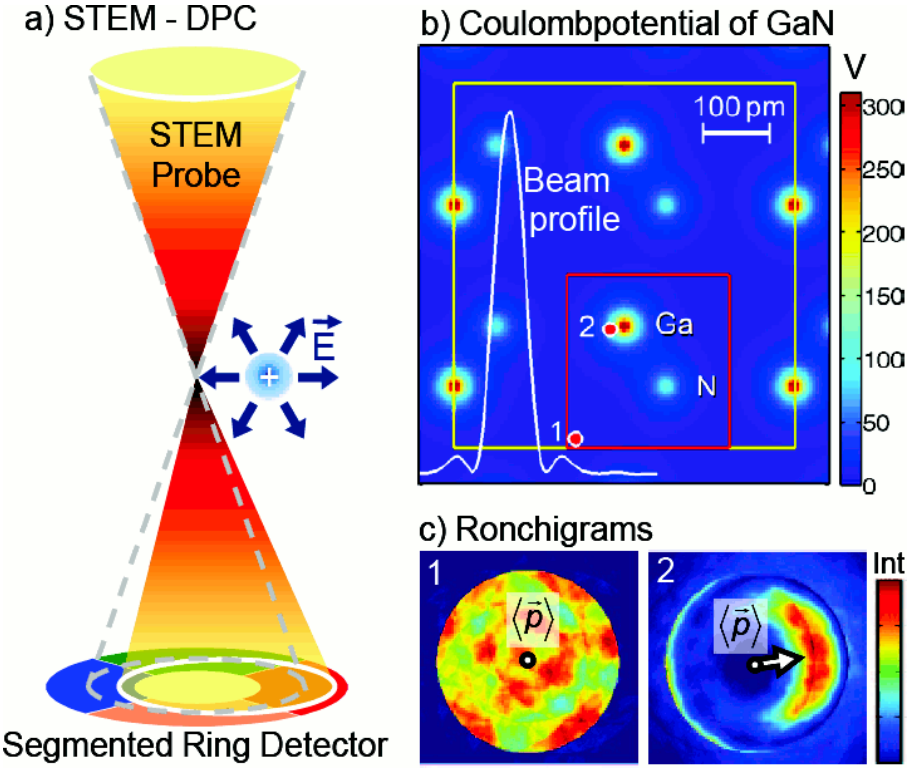

Figure 1. a) Deflection of the STEM probe by atomic electric fields and conventionally used detectors. b) Coulomb potential of GaN with probe profile. c) Simulated diffraction patterns ("ronchigrams") for positions marked in b.

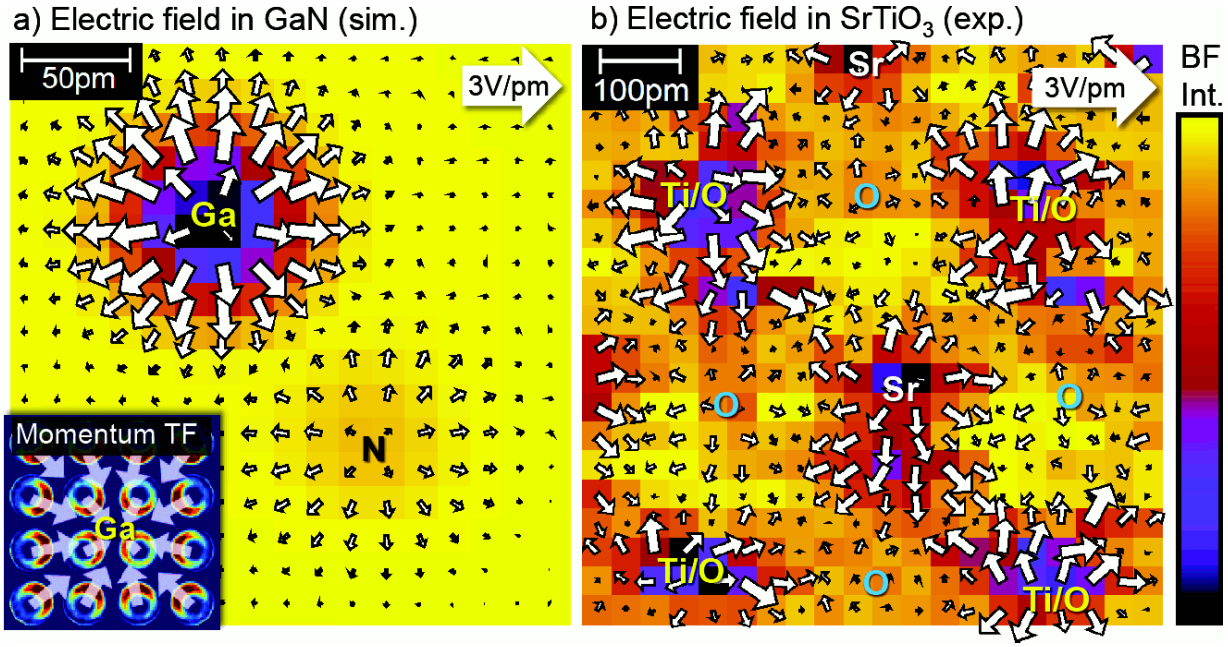

Figure 2. Electric field for a) GaN and b) $SrTiO_3$ determined from the momentum transfers calculated from ronchigrams, exemplarily shown in the inset of a). Arrows top right are legends for the field strength. The STEM bright field (BF) intensity is shown colour-coded, also visualising atomic sites.

Phase-Related Techniques and Holographic Beam Shaping (inc. phase plates, DPC, vortices, electric and magnetic field imaging...)

IM5.128
Construction of a programmable electron vortex phase plate

J. Verbeeck[1], A. Béché[1], G. Guzzinati[1], L. Clark[1], R. Juchtmans[1], R. Van Boxem[1], G. Van Tendeloo[1]

[1]University of Antwerp, EMAT, Antwerp, Belgium

jo.verbeeck@uantwerpen.be

Electron vortex beams form part of an interesting class of electron wavefunctions, as their spiralling wavefronts carry orbital angular momentum along the propagation direction. Many different methods of creating such waves in the transmission electron microscope have been devised, each providing unique advantages and disadvantages [1]. Potential applications range from mapping magnetic fields on the atomic scale [2], detecting chirality in crystals [3], to mapping chiral plasmons [4].

All of these applications have in common that only a relatively small part of the signal depends on the vorticity of an incoming vortex wave, making the technique susceptible to noise and especially systematic errors.

To overcome this issue we developed a dynamically controllable vortex beam which can change from left- to right-handed vortices by an external control. In this way, all parameters can be kept identical while only the vorticity of the wave is changed, cancelling sources of systematic errors. We demonstrate an early prototype based on a microscopic solenoid placed in the center of a condenser aperture. Driving a current through the solenoid and creating a magnetic flux equal to one flux quantum leads to the formation of a vortex beam with either a left or right handed character, depending on the direction of the current. Preliminary results show that this concept works after solving charging issues but the required high current densities in the solenoid remain problematic.

A second prototype uses a ferromagnetic single domain microscopic needle that is magnetized in the external magnetic field of a macroscopic solenoid attached around the condenser aperture rod. This allows for the rapid switching between left- and right-handed vortices by sending a short current pulse through the solenoid and relying on the remanent magnetization of the needle to form a spiral phase plate. This setup works exceptionally well and is capable of producing atomic sized vortices that can be switched in the microsecond regime. Synchronizing the vortex switching to the STEM scan engine allows the recording of STEM-EELS spectra with alternating left and right handed vorticity.

Preliminary experimental results on magnetic materials will be discussed.

The authors acknowledge financial support from the EU under the Seventh Framework Program (FP7) under a contract for an Integrated Infrastructure Initiative, Reference No. 312483-ESTEEM2. JV, AB, GG and LC acknowledge funding from the European Research Council under the FP7, ERC Starting Grant 278510 VORTEX. RVB and RJ acknowledge funding from the FWO as PhD. Fellows.

1. Verbeeck, J., Guzzinati, G., Clark, L., Juchtmans, R., Van Boxem, R., Tian, H., Béché, A., Lubk, A., Van Tendeloo, G. , *Comptes Rendus Physique* 15 (2-3) 190-199 (2014)
2. Schattschneider, P., B. Schaffer, I. Ennen, and J. Verbeeck. *Physical Review B* 85 (13) 134422 (2012)
3. Juchtmans R., Béché A., Abakumov A, Batuk M. and Verbeeck J., Phys. Rev. B 91, 094112 (2015)
4. A. Asenjo-Garcia and F. J. García de Abajo, Phys. Rev. Lett. 113, 066102 (2014)
5. Béché A., Van Boxem R., Van Tendeloo G. and Verbeeck J., Nat. Phys. 10, 26 (2014)

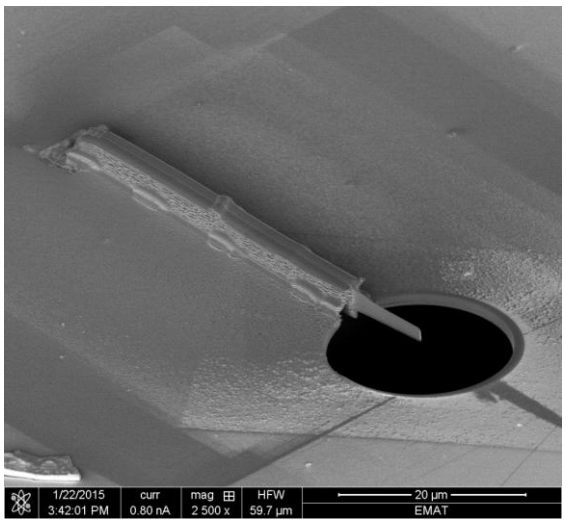

Figure 1. Ferromagnetic Ni needle mounted with its tip at the center of a condenser aperture.

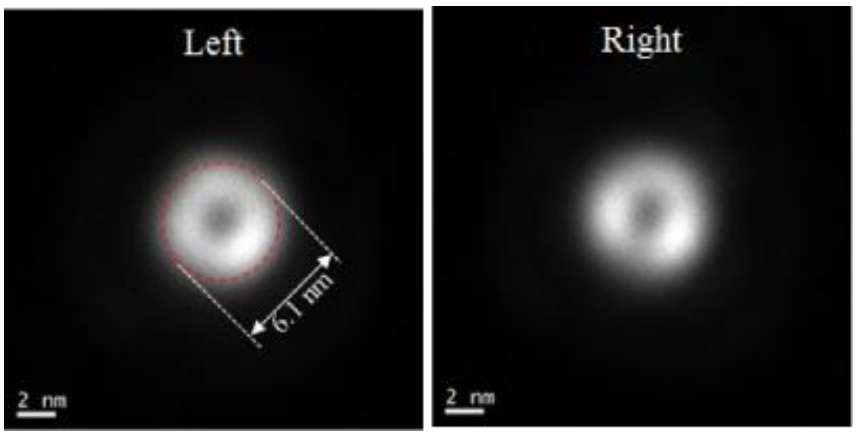

Figure 2. Image of the resulting vortex beam in TEM mode for opposite magnetization of the needle

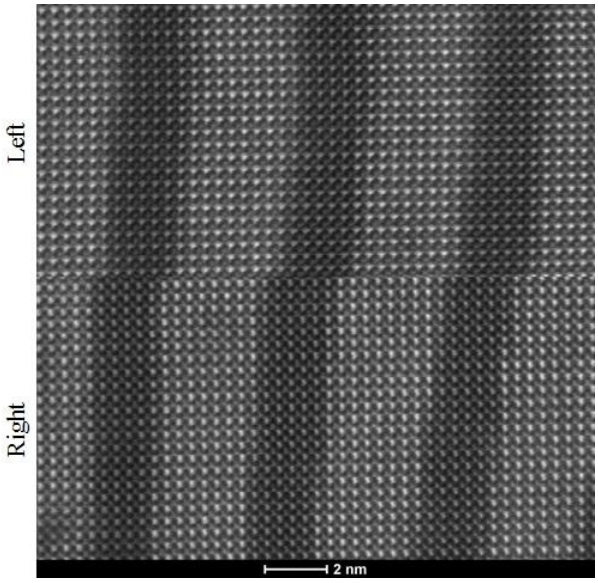

Figure 3. Atomic resolution HAADF image obtained with the vortex aperture set to either left-handed (top) or right-handed (bottom).

Phase-Related Techniques and Holographic Beam Shaping (inc. phase plates, DPC, vortices, electric and magnetic field imaging...)

IM5.129
Holographic generation of highly twisted electron beams

V. Grillo[1], G. C. Gazzadi[1], E. Mafakheri[1], S. Frabboni[1], E. Karimi[1], R. Boyd[1]

[1]CNR, IMEM, Parma, Canada

vincenzo.grillo@unimore.it

Free electrons can possess an intrinsic orbital angular momentum upon free-space propagation [1][2].

Beams with a high number of twists are of particular interest because they carry a high magnetic moment about the propagation axis. Using electron holographic plates obtained by FIB patterning of SiN membranes we generated a beam with an orbital angular momentum up to 200ħ in the first order of diffraction: the biggest ever demonstrated so far [3].

Using EFTEM mapping in a JEOL 2200 FEG TEM microscope operated at 200KeV we carried on a detailed experimental analysis of the thickness pattern in the holographic plate in order to evaluate the introduced phase effect and therefore the wavefunction right at the exit of the hologram. By simple propagation we were able to know the wavefunction at different planes: The intensity pattern was found to be in agreement with the experiments at different focal planes.

Fig 1a shows indeed the comparison of the intensity pattern as calculated by propagation and the experiment at Fraunhofer, it is evident a very good agreement.

The knowledge of the wavefunction permits to decompose it in different values of Orbital angular momentum (OAM). The OAM spectrum (fig 1b) is evaluated by transforming the calculated electron wave function into polar coordinates and performing the Fourier transform in the azimuth coordinates.

It is easy to verify that when the OAM is written with respect to the geometric center of one of the vortexes the correct average OAM number of about L=200ħ is recovered. The broadening of the distribution is due to the loss of intensity at very high frequencies induced by hologram imperfections.

In fact an eigenvalue of OAM should have no azimuthal localisation.

We were also able to locate the positions of the each singularity: in fig 1c we highlighted in red the singularity centres and superimposed them to the intensity. Singularities are mainly located on the periphery of the dark region and spatially decomposed probably as an effect of the interference of the 0th order beam that cannot be completely spatially separated.

An in depth analysis of the radial profile also reveals a large number of ripples outside the main ring, a detailed analysis indicates that the generated beam has a large spectrum decomposition in terms of Laguerre-Gauss Eigenfunctions especially with respect to the radial number p. These characteristic can be tight down to the hard aperture used to limit the hologram. In fig 1d we fitted for sake of example the wavefunction at a given plane using a “minimal” set of Laguerre Gauss states about L=200 ħ and p=0-50 but it is worth recalling that the actual radial decomposition depends sensibly on the actual electron optics, on the hologram details and on hologram illumination conditions.

We expect to apply these beams to interact with magnetic field and to couple with Landau states in the microscope but it is important to take into account the above limitations to plan future experiments.

1. J. Verbeeck, H. Tian, and P. Schattschneider, Nature 467, (2010) p 301.
2. B. J. McMorran, A. Agrawal, I. M. Anderson, A. A. Herzing, H. J. Lezec, J. J. McClelland, and J. Unguris, Science 331, 192 (2011).
3. V. Grillo, G. C. Gazzadi, E. Mafakheri, S. Frabboni, E. Karimi and R W. Boyd Phys. Rev.Lett 114, (2015) 034801

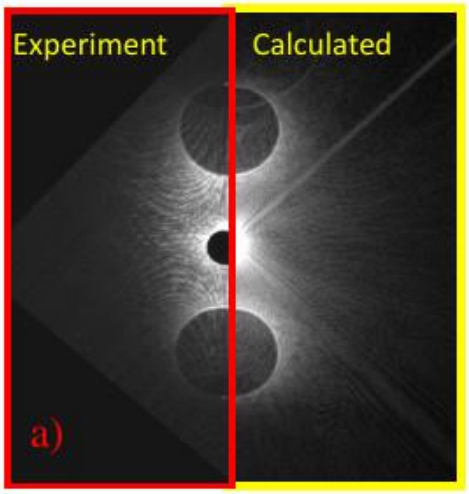
Experiment
Calculated
a)

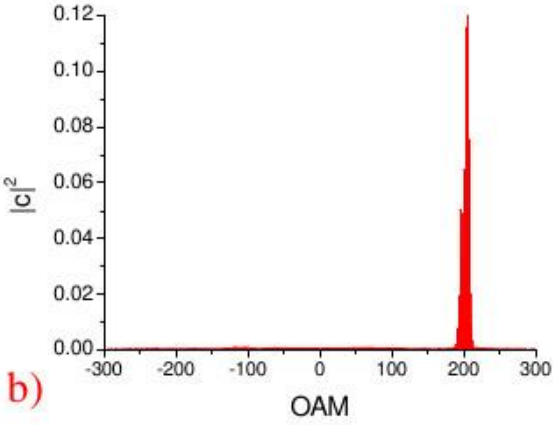
0.12
0.10
0.08
0.06
0.04
0.02
0.00
|c|²
-300
-200
-100
0
100
200
300
OAM
b)

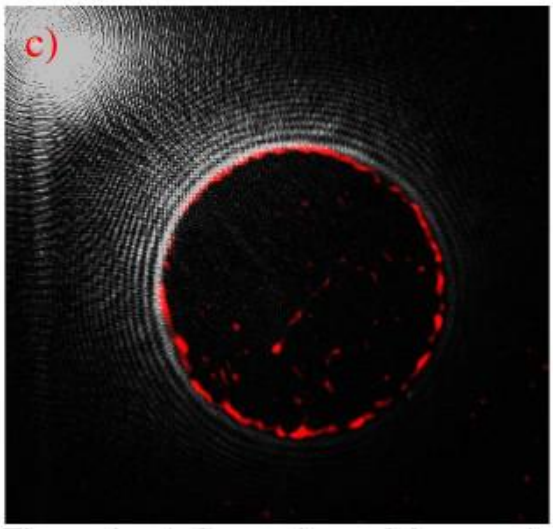
c)

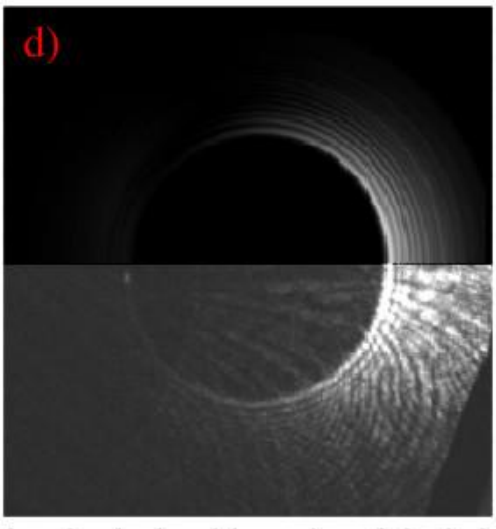
d)

Phase-Related Techniques and Holographic Beam Shaping (inc. phase plates, DPC, vortices, electric and magnetic field imaging...)

IM5.130
Bessel beams with high OAM: prospects for unconventional electrodynamics

T. Schachinger[1,2], A. Steiger-Thirsfeld[2], M. Stöger-Pollach[2], P. Schattschneider[1,2]

[1]TU Vienna, Solid State Physics, Vienna, Austria
[2]TU Vienna, University Service Centre for Electron Microscopy, Vienna, Austria

thomas.schachinger@tuwien.ac.at

By placing holographic masks (HM) in the condenser system of a TEM it is possible to shape the electrons' wavefront such that it carries orbital angular momentum (OAM) quantized in units of ħ, as well as magnetic moment [1].

It has been shown that such electron vortex beams (EVBs) represent free electron Landau states (LS) in the objective lens field of a TEM under certain conditions [2]. According to QED calculations [3] there should be transitions between the different LS levels in the form of spontaneous photon emission. As the photon energy in the case of a LS transition with an OAM change of 1 ħ and a magnetic field of 1.9 T is of the order of 160 µeV one has to dramatically increase the EVBs' OAM in order to push the transition energy into the IR/visible light regime. Then it could be detected using a cathodoluminescence holder, at least in theory. Additionally, the rotational energy of EVBs could become resolvable in EELS for EVBs carrying OAM larger than ~ 625 ħ, corresponding to an electron energy loss of ~ 100 meV [2].

Focused ion beam (FIB) milling is a robust and reliable technique to produce HMs. These masks create a series of EVBs where the different diffraction orders are linearly arranged according to their magnetic quantum number. The EVB radii increase with increasing OAM and thus juxtaposed vortex orders tend to overlap. The separation distance between neighboring orders is inversely proportional to the grating period of the HM and as such poses a technical limit to the generation of beams carrying high OAM. Nevertheless, EVBs up to OAM = 200 ħ have been generated [4]. There, a small central region of the HM, where the feature size could not be resolved anymore by the FIB instrument, was excluded from the FIB milling processes. By extending this Ansatz such that only a small outer ring of the whole HM pattern is milled and by giving up the non-overlapping condition, Bessel beams with even higher OAM values can be generated.

Traditionally the HM are placed in the C2 aperture holder (or in C3 where it applies) of a TEM such that no further manipulation of the EVB is possible. Placing the HM in the C1 (or in C2 where it applies) aperture holder opens up the possibility to separate the overlapping vortex orders by using sub micrometer ring apertures. First tests show that, using optimized milling paths, we can produce HMs allowing OAM = 250 ħ in the first diffraction order, see Fig. 1. With such a mask, placed in the C1 aperture holder, we have observed EVBs up to the 5th diffraction order, carrying OAM = 1250 ħ, see Fig. 2, and a huge magnetic moment of 1250 Bohr magnetons.

This is interesting for the above mentioned detection of LS transitions. Moreover theoretical investigations suggest that asymmetries in the transition radiation of electrons passing conductive surfaces could be detected if the EVBs' magnetic moment is of the order of 1000 Bohr magnetons [5]. Thus EVB with high OAM could become a novel tool in the physics of electromagnetic radiation.

1. J. Verbeeck, H. Tian and P. Schattschneider, 2010. Nature 467, 301.
2. P. Schattschneider, T. Schachinger, M. Stöger-Pollach et al.,2014. NatCommun 5, 4586.
3. I. Kaminer, M. Mutzafi, G. Harari et al., 2014. CLEO: QELS_Fundamental Science, DOI: 10.1364/CLEO_QELS.2014.FM3D.6 and private communication with I. Kaminer.
4. V. Grillo, G. C. Gazzadi, E. Mafakheri et al., 2014. PRL 114, 034801.
5. I. P. Ivanov and D. V. Karlovets, 2013. PRA 88, 043840.
6. TS and PS acknowledge financial support by the Austrian Science Fund (FWF) under grant number I543-N20.

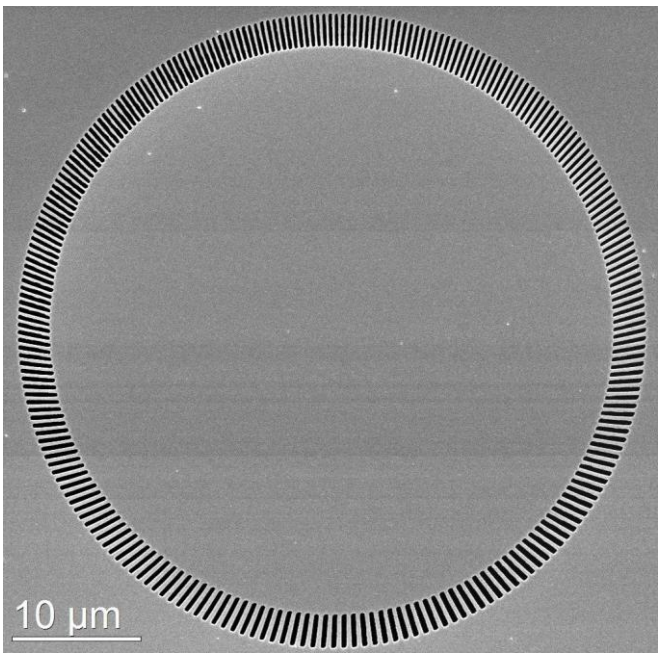

Figure 1. SEM image of the OAM = 250 ħ HM placed in the C1 aperture holder of a TF20.

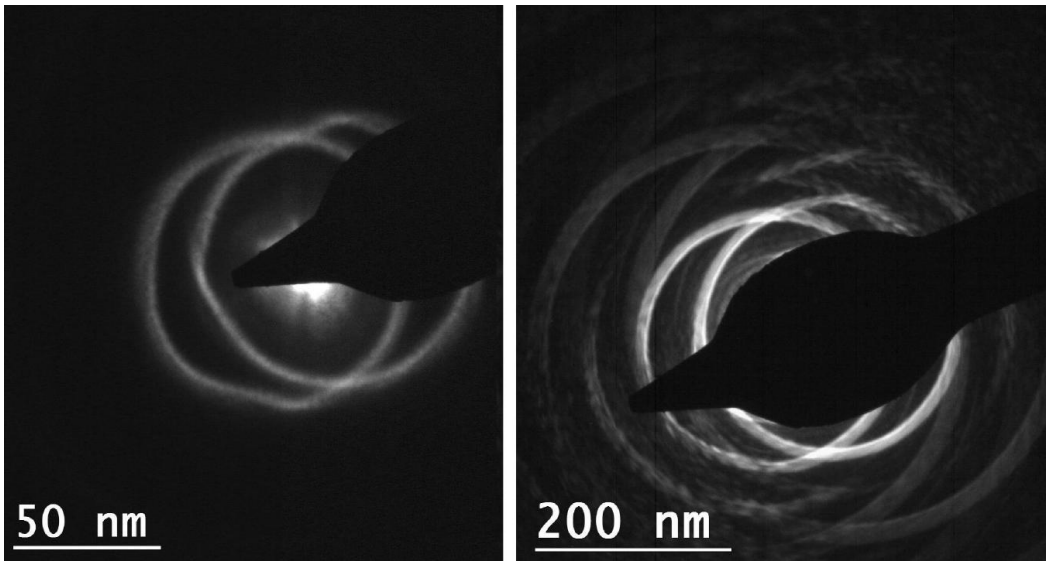

Figure 2. Resulting far field images of the HM shown in Fig. 1. Left: First diffraction orders carrying an OAM of ±250 ħ, right: higher diffraction orders, with the brightest being the ±3rd diffraction orders carrying an OAM of ±750 ħ.

Phase-Related Techniques and Holographic Beam Shaping (inc. phase plates, DPC, vortices, electric and magnetic field imaging...)

IM5.P131
High-resolution transmission electron microscopy with Zach phase plate

S. Hettler[1], M. Dries[1], T. Schulze[1], M. Oster[2], C. Wacker[2], R. R. Schröder[2], D. Gerthsen[1]

[1]Karlsruhe Institut für Technologie, Laboratorium für Elektronenmikroskopie, Karlsruhe, Germany
[2]Universität Heidelberg, BioQuant CellNetworks, Heidelberg, Germany

simon.hettler@kit.edu

Physical phase plates (PP) for transmission electron microscopy (TEM) provide contrast enhancement of weak-phase objects by introducing a relative phase shift between scattered and unscattered electrons. Several experimental realizations have been proposed [1] with thin-film PPs being the most frequently used concept up to now [2]. However, scattering of electrons by the thin film of the PP induces a damping of the phase contrast transfer and reduces the resolution of the microscope. In contrast, the electrostatic Zach-PP generates a strongly localized electrostatic potential to induce the phase shift and is not affected by this effect [3]. In this work, the application of a Zach-PP for high-resolution (HR) TEM is investigated by studying a crystalline Si-sample.

The Zach-PP (Fig. 1) consists of a single rod with an Au electrode which is surrounded by insulating and shielding electrically conductive layers. If a voltage is applied to the electrode, an inhomogeneous potential emerges at the PP tip which generates a phase shift in the back-focal plane. The experiments were performed in a Zeiss 923Ω transmission electron microscope equipped with a field-emission gun operated at 200 kV and a 4k TVIPS CCD-camera. For PP TEM imaging, the tip is usually positioned close to the zero-order beam to minimize the cut-on frequency and enhance the contrast of weak-phase objects up to 10 nm size [4]. For HR PP TEM in this work, the cut-on frequency is of minor importance and the PP was positioned at an increased distance to the zero-order beam to reduce charging effects.

The results obtained with a single-crystalline Si-sample in [110] zone-axis orientation are presented in Fig. 2 and Fig. 3. Fig. 2a shows a HR PP TEM image in an overview perspective which was acquired without applied voltage. Si-oxide formation and amorphization during sample preparation causes the relatively thick amorphous region at the sample edge. The marked area is displayed enlarged in Fig. 2b where (111)-type lattice fringes are clearly resolved. The four (111)-type and the (002)-reflections as well as the PP rod are revealed in the power spectrum of the HR PP TEM image (Fig. 2a) in Fig. 3a. Acquiring an image series with a variation of the PP voltage from -5 V to + 5 V allows the analysis of the influence of the phase shift on the reflection intensity. The intensity of the (111)-reflections in the corresponding power spectra is plotted in Fig. 3b, where the blue and red crosses are the averaged intensities from the reflections marked in Fig. 3a. Theory predicts a $\sim|\cos(\varphi_{PP}+\theta)|$ dependence of the reflection intensity on the phase shift φ_{PP}, where the phase θ comprises the wave aberration function and the phases of the zero-order beam and the corresponding (111)-type reflection. The experimental data is well fitted by a respective function which shows that the electrostatic Zach-PP does not reduce the resolution of the microscope and is suitable for HR TEM applications.

1. R. M. Glaeser, Rev. Sci. Instrum. **84** (2013), 111101.
2. R. Danev, K. Nagayama, Ultramicroscopy **88** (2001), p. 243-252.
3. K. Schultheiss *et al*, Microsc. Microanal. **16** (2010), p. 785-794.
4. N. Frindt *et al*, Microsc. Microanal. **20** (2014), p. 175-183.
5. Financial support by German Research Foundation (DFG) under contract Ge 841/16 and Sch 424/11.

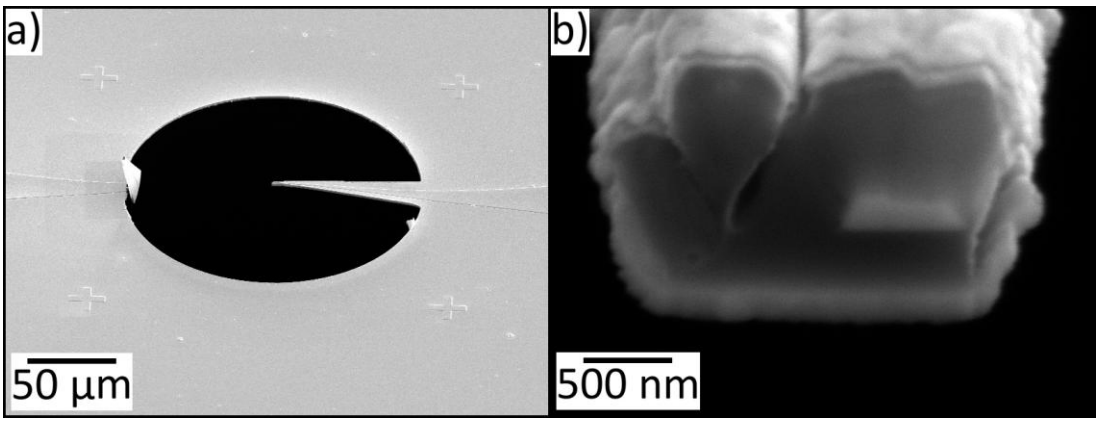

Figure 1. Scanning electron microscopy images of the Zach-PP used in the experiments. (a) The PP aperture has a diameter of 90 µm. (b) The image of the PP tip shows the layer system of central electrode, surrounding insulating layers and shielding metal layers.

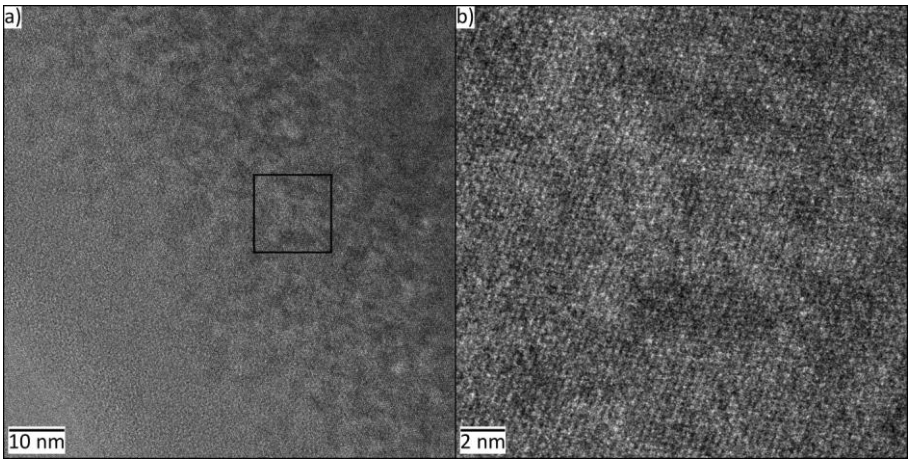

Figure 2. (a) Overview HR PP TEM image of the Si-sample in [110] zone-axis orientation. (b) Detail image of the area marked by a black frame in (a).

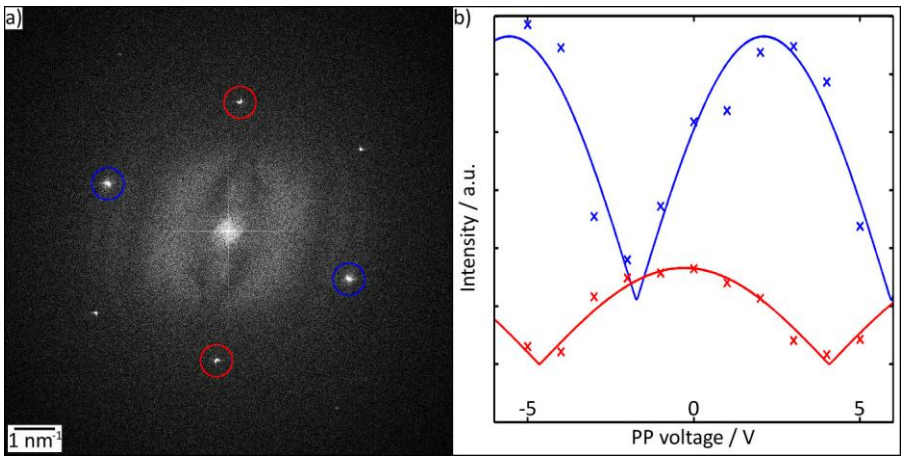

Figure 3. Analysis of the reflection intensity. (a) Power spectrum of the image in Fig. 2a with (111)-reflections marked by the red and blue circles and unmarked (002)-reflections. (b) Plot of the averaged reflection intensity of the four (111)-type reflections marked blue and red in (a) as a function of the applied voltage. Solid lines represent fits with a $|\cos(\varphi_{PP}+\theta)|$ behavior.

Phase-Related Techniques and Holographic Beam Shaping (inc. phase plates, DPC, vortices, electric and magnetic field imaging...)

IM5.P132
A development of two types of amorphous carbon thin film phase plate

Y. Konyuba[1], H. Iijima[1], N. Hosogi[1], Y. Abe[2], I. Ishikawa[1], Y. Ohkura[1]

[1]JEOL Ltd., Tokyo, Japan
[2]Yamagata Research Institute of Technology, Yamagata, Japan

ykonyuub@jeol.co.jp

Phase contrast transmission electron microscopy (PC-TEM) with the phase plate attracts much attention in cryo-TEM applications such as cryo-tomography, single-particle analysis and single image cryo-EM, because it enables us to obtain high contrast resulting in increased signal to noise ratio of the images of samples, which are composed of light elements such as biological samples and polymer samples.

So far, many types phase plates for TEM have been proposed [1]. Among them, thin film type phase plate has gotten promising results [2-3]. However, it had a few serious problems such as reliability, life time (due to charging and ageing) and cost (due to craft production). To solve the above problems, we also have tried to develop thin film phase plate using Micro Electro Mechanical Systems (MEMS) technology. Thereby, we could improve the stability of the thin film phase plate and the manufacturing yield. Presently, we plan to provide two types of amorphous carbon thin film phase plate.

First is a thin film Zernike phase plate (ZPP). Figure.1 shows configuration of the amorphous carbon thin film ZPP. In the center of each square window, there is a small hole which is nearly perfect circles drawn by electron beam lithography system. Thin thickness of the film is approximately 30 nm that gives π/2 phase shift for an accelerating Voltage of 200kV. Thus, our amorphous carbon thin film ZPP offers increased contrast at low spatial frequencies.

The other one is a hole-free phase plate (HFPP) [4-5]. Figure.2 shows configuration of the HFPP (prototype model). The HFPP consists of 15 nm amorphous carbon thin film with no hole. The HFPP usage is similar to that of the thin film ZPP. It is also positioned at the back focal plane of the objective lens. The incident beam passing through the thin film of HFPP generates secondary electrons. And they in turn lead to an electrostatic charging (potential). It causes a phase shift and gives high contrast image at low spatial frequencies.

In order to improve two types of amorphous carbon thin film phase plates, we have established a fabrication method [6]. Furthermore, we also have adjusted carbon thin film characters (thickness, crystalline, electro resistibility, flatness and others). In addition, amorphous carbon thin film ZPP and HFPP were formed in same outer shape, therefore they can be installed in common phase plate holder. Thus, the advantages (quantitative phase shift, alignment necessity, interference fringes, lifetime, and others) of each phase plate were drawn out by utilizing MEMS technology. Consequently, the phase contrast images were obtained with these phase plates.

1. RM.Glaeser, Review of Scientific Instruments 84.11 (2013), p.111101.
2. R.Danev et al, Ultramicroscopy, 88, (2001), p. 243.
3. W.Dai et al, Nature protocols 9, (2014), p. 2630.
4. M.Malac et al, Ultramicroscopy 118 (2012), p. 77.
5. M.Malac et al, U.S. Patent US 8,785,850.
6. H.Iijima, Y.Konyuba, US Patent 8,829,436. EP 2750160. JP 2014-130715.

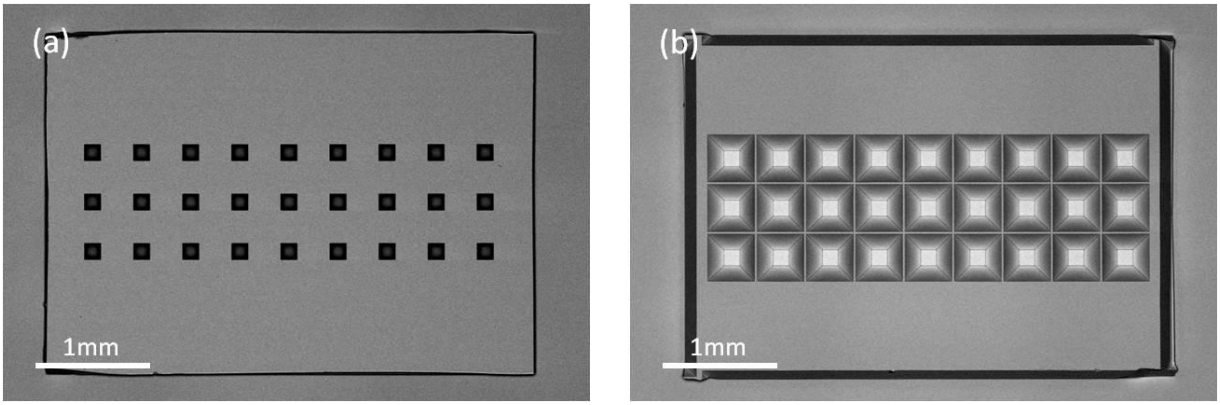

Figure 1. SEM images of the amorphous carbon thin film Zernike phase plate array. (a) top side (b) bottom side.

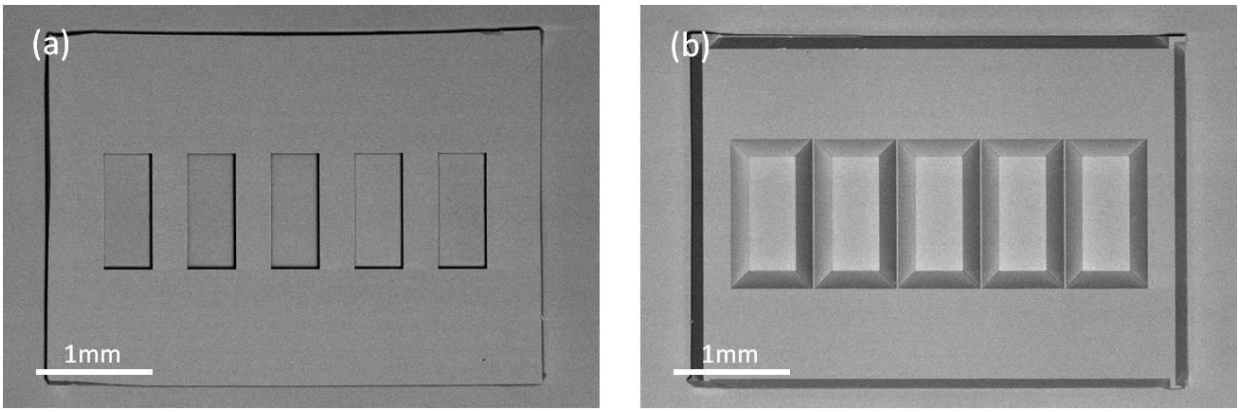

Figure 2. SEM images of the hole-free phase plate array (prototype model). (a) top side (b) bottom side.

Phase-Related Techniques and Holographic Beam Shaping (inc. phase plates, DPC, vortices, electric and magnetic field imaging...)

IM5.P133
A gradient flipping regularized solution to the transport of intensity equation(GFTIE)

A. Parvizi[1], C. T.Koch[1], J. Mueller[1]

[1]Ulm University, Experimental Physic, Ulm, Germany

amin.parvizi@uni-ulm.de

Over the past two decades the well known transport of intensity equation (TIE), owing to its simple mathematical formulation and convenient experimental implementation, has attracted enormous attention from many research communities such as transmission elec- tron microscpy, X-ray and optical microscopy, neutron imaging, etc.. The TIE is a second order, elliptical, none-separable partial differential equation which relates the variation of the intensity along the optical axis of an optical system to a Laplacian-type derivative of the phase information carried by the wavefront to be analyzed. Input to the TIE is the variation of the detected intensity along the optical axis z. The solution of this equation in Fourier space is widely used due to its deterministic nature and computational speed when implemented by FFT [1]. However, the periodic boundary conditions inherent to this Fourier-domain approach may introduce low spatial frequency artifacts in the case of none-periodic objects. We developed an algorithm to generate boundary conditions for the TIE in such a way that the gradient of the retrieved phase as sparse as possible while still consistent with the experimental data. To accomplish this regularization scheme, we combine the TIE with the charge flipping algorithm [2], which was originally developed to solve the crystallographic phase problem in X-ray crystallography. However, instead of flipping the charge we flip the gradient of the phase, iterating back and forth between the experimental data linked to the phase via the TIE, and the gradient of the phase. In this manner the boundary conditions are updated at each iteration until either the convergence criterion is satisfied, i.e. changes in the phase between successive iterations become negligible. The reconstruction starts by estimating the variation of the intensity via the finite difference method. This intensity derivative is then padded with zeros. The FFT approach is then applied to solve the TIE to reconstruct an intermediate phase. In order to minimize the total variation of the gradient of the retrieved phase, the charge flipping algorithm is exploited. However, instead of flipping the phase we first compute the gradient of the phase and then flip each of the components of this gradient where the gradient is small. Just as in the original charge flipping algorithm, the result is that the recovered phase becomes sparse in the gradient domain. Afterwards a new estimate of the intensity derivative is computed by computing the divergence of the processed gradient. Now the experimentally obtained intensity derivative is used where it is available, but in the padded region the just computed divergence of the gradient is used. From this intensity derivative with modified boundary conditions we can now again compute the phase according to the TIE. Repeating the process a few times leads to a converged result as shown in Fig.1c. A simple optical setup serves to investigate the performance of the proposed algorithm. Fig.1a and Fig.1d illustrate the experimental under-focused image and the intensity variation estimated by finite difference method and further more, the reconstructed phase of a fly's wing by means of the proposed algorithm (Fig.1c) and the FFT method (Fig.1b) for the same experimental data. As is shown clearly, the FFT based phase retrieval approach suffers from serious low-frequency artifacts due to the inherent periodicity of the boundary conditions. The phase reconstructed by the proposed algorithm has a lot less of these low spatial frequency artifacts. It worth mentioning that the line profile across the reconstructed phases clearly mirrors the fact that the phase experiences a steep slope in the free area in the FFT-based approach (Fig.1e) while that of proposed algorithm is reasonably constant (Fig.1f).

1. D. Paganin and K. A. Nugent, "Noninterferometric phase imaging with partially coherent light," Physical review letters, vol. 80, no. 12, p. 2586, 1998.
2. G. Oszl´anyi and A. S¨uto, "The charge flipping algorithm," Acta Crystallographica Section A: Foundations of Crystallography, vol. 64, no. 1, pp. 123-134, 2007.
3. The authors acknowledge funding from the Carl Zeiss Foundation.

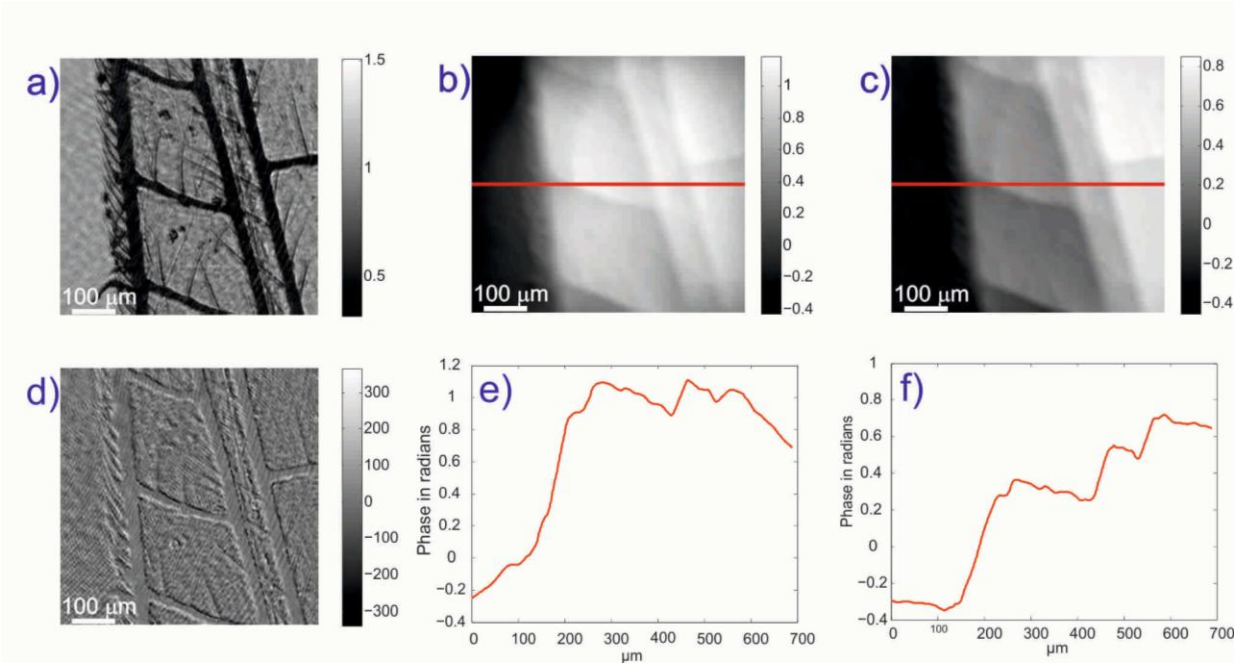

Figure 1. a)Under-focused experimental image b)Finite difference estimation of intensity varia-tion. Reconstructed phase b)conventional FFT approach c)proposed algorithm. The line profile across the retrieved phase e)FFT approach f)proposed algorithm.

Phase-Related Techniques and Holographic Beam Shaping (inc. phase plates, DPC, vortices, electric and magnetic field imaging...)

IM5.P134
A proposal for the holographic correction of incoherent aberrations by tilted reference waves

F. Röder[1], A. Lubk[1]

[1]Institut für Strukturphysik / TU Dresden , Triebenberg-Labor, Dresden, Germany

falk.roeder@triebenberg.de

Off-axis electron holography is an interferometric transmission electron microscope (TEM) technique facilitating the reconstruction of electron waves elastically scattered at an object (see e.g. [1,2]). The interference pattern (hologram) in the image plane is formed by superimposing an object modulated wave and a plane reference wave, which have been mutually inclined by the action of the Möllenstedt biprism [3]. Limited ensemble coherence of the electron beam in combination with the geometric aberrations of the objective lens leads to an attenuation of large spatial frequencies in the reconstructed wave up to the information limit (Fig. 1). To describe this effect, we recently derived a general transfer theory for off-axis electron holography [3]. Here, we propose a new approach for reconstructing the electron wave beyond the conventional information limit. It is based on concerted tilts of the reference wave only, keeping the object wave invariant. This allows shifting the transferred spatial frequency range even beyond the information limit without changing the scattering on the object [4] (Fig.2). The latter allows to linearly synthesize an effective aperture (Fig.3) for the reconstructed object wave with a broader bandwidth compared to conventional off-axis electron holography. To supplement our theoretical considerations, we present an experimental proof-of-principle. The proposed method permits a correction of incoherent aberrations in transmission electron microscopy. By the same token, tilting the reference wave with respect to an unmodulated plane wave can be used to measure the coherent and incoherent aberrations of a TEM without requiring an object. Furthermore, a tilted reference wave is expected to improve the signal-to-noise ratio in dark-field off-axis electron holography [6,7]. Thus, the presented approach is beneficial for a variety of TEM techniques. The development of an electron optical device facilitating a controlled tilt of the reference wave into large is underway.

1. H. Lichte and M. Lehmann, Rep. Prog. Phys. 71, 016102 (2008).
2. M. R. McCartney and D. J. Smith, Annu. Rev. Mater. Res. 37, 729 (2007).
3. G. Möllenstedt, H. Düker, Z. Phys. 145 (1956) 377-397.
4. F. Röder, A. Lubk, Ultramicroscopy 146 (2014) 103-116.
5. F. Röder, A. Lubk, Ultramicroscopy 152 (2015) 63-74.
6. K.-J. Hanszen J. Phys. D, Appl. Phys. 19 (1986) 373-395.
7. M. Hÿtch, F. Houdellier, F. Huë, E. Snoeck, Nature 453 (2008) 1086-1089.

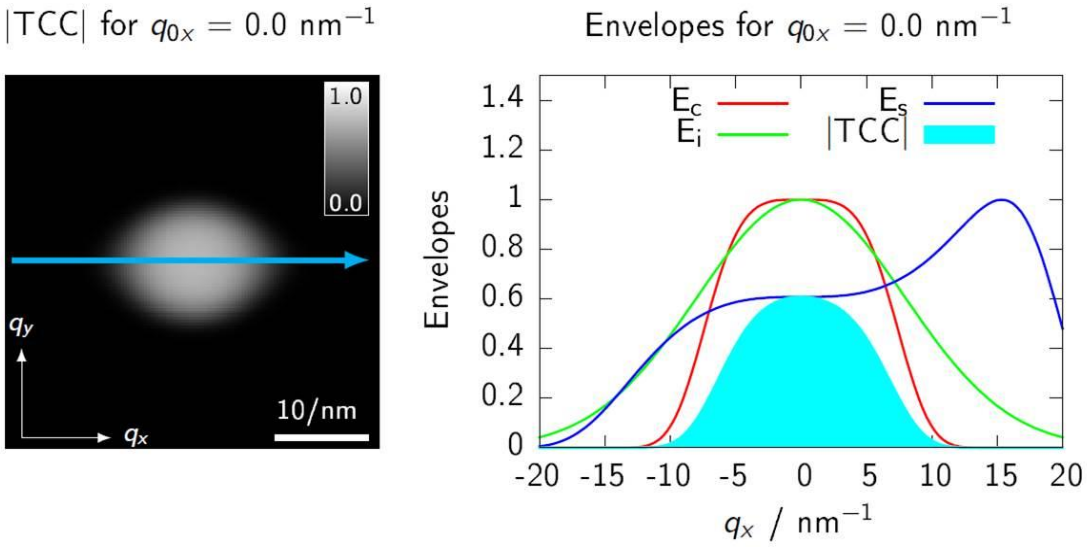

Figure 1. Transfer envelopes for the holographic sideband for an uncorrected TEM (C_s=1.4mm, C_c=1.4mm, energy width=1eV (FWHM), illumination aperture 0.1 mrad, illumination aspect ratio = 20, image spread = 20 pm, biprism oriented in y-direction, shear = 80nm). Profiles of transfer envelope (blue arrow): E_c chromatic envelope (red), E_i image spread envelope (green), E_s spatial envelope (blue) and TCC: transmission cross coefficient.

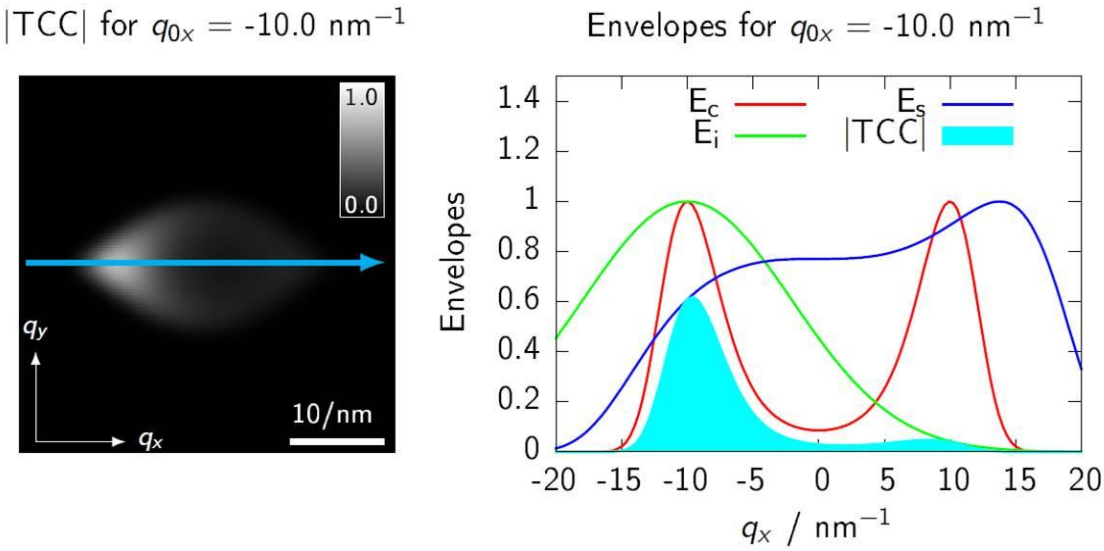

Figure 2. Transfer envelopes for the holographic sideband for an uncorrected TEM (same parameters as Fig. 1) for a reference wave tilted in x direction by means of the wave vector q_{0x}=-10/nm. (Legend see Fig. 1).

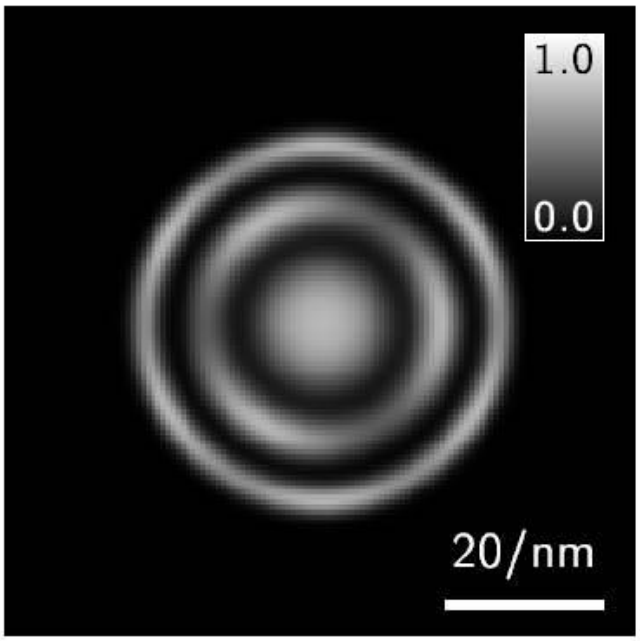

Figure 3. Sideband aperture synthesized by means of linear superposition of the transmission cross coefficients for different tilts of the reference wave (C_s-corrected case) providing an improved spatial resolution. The inner band corresponds to the TCC of an conventional off-axis electron hologram, the next ring to azimuthally rotated tilt vectors of 15/nm magnitude and the outer ring to tilt vectors of 22.5/nm.

Phase-Related Techniques and Holographic Beam Shaping (inc. phase plates, DPC, vortices, electric and magnetic field imaging...)

IM5.P135
Exploiting orbital angular momentum in transmission electron microscopy to detect the chirality of crystals

R. Juchtmans[1], A. Béché[1], A. Abakumov[1], M. Batuk[1], J. Verbeeck[1]

[1]University of Antwerp, Physics, Antwerp, Belgium

roeland.juchtmans@uantwerp.be

Electron vortex beams in cylindrical coordinates have the form $\Psi(r, \varphi,z)=\exp(im\varphi)\psi(r,z)$, where m is called the topological charge of the vortex. Being an eigenstate of the angular momentum operator $L_z=-i\hbar\partial/\partial\varphi$, they possess a series of remarkable properties such as a well-defined angular momentum of $m\hbar$ per electron as well as a magnetic moment of $m\mu_B$. On top of that, vortex beams are chiral, in contrast to normal beams they are fundamentally different from their mirror image. Indeed mirroring a vortex with TC m=1 will return a vortex with TC m=-1. It is this property that makes them a valuable tool to study chiral materials. We have shown that diffraction of electron vortices is sensitive to the chirality of the scattering object [1] and in some specific cases the chirality of a crystal can be seen from the symmetry in the diffraction pattern. This way dynamical simulations for which prior knowledge about the thickness of the sample has to be known [2-5] can be avoided. In this lecture we will show where this symmetry comes from and present simulations and experimental results (see fig. 2).

The vortices we use, are generated by placing a magnetized needle in the condensor plane, as described by Béché et al. [6]. However, when placing such a needle in the diffraction plane, it acts as a spiral phase plate adding orbital angular momentum to the scattered wave *after* interacting with the sample. We will show how images of chiral crystals obtained with such phase plate possess features that reveal the screw axis symmetry, independent from the thickness of the sample. We will explain why these features are present and evidence this with numerical simulations. Advantages of such a technique and experimental feasibility will be discussed.

This research was supported by an FWO PhD fellowship grant (Aspirant Fonds Wetenschappelijk Onderzoek - Vlaanderen). The authors acknowledge financial support from the EU under the Seventh Framework Program (FP7) under a contract for an Integrated Infrastructure Initiative, Reference No. 312483-ESTEEM2. JV acknowledges funding from the European Research Council under the FP7, ERC Starting Grant 278510 VORTEX.

1. Juchtmans R., Béché A., Abakumov A., Batuk M. and Verbeeck J. 094112. (2015)
2. Goodman P. and Johnson A. W. S., Acta Cryst. A33, 997-1001. (1977)
3. Goodman P. and Secomb, T. W., Acta Cryst. A33, 126-133. (1977)
4. Johnson A. and Preston A., Ultramicroscopy 55, 348. (1994)
5. Inui H., Fujii A. and Tanaka K., Acta Cryst. B, 802. (2003)
6. Béché A., Van Boxem R., Van Tendeloo G. and Verbeeck J., Nat. Phys. 10, 26. (2014)

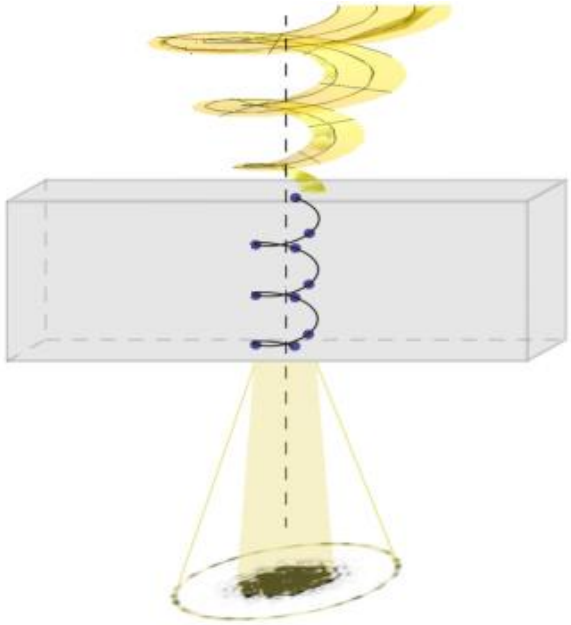

Figure 1. Schematic illustration of a focused vortex beam scattered on a 3-fold screw axis with only one heavy atom in its vicinity.

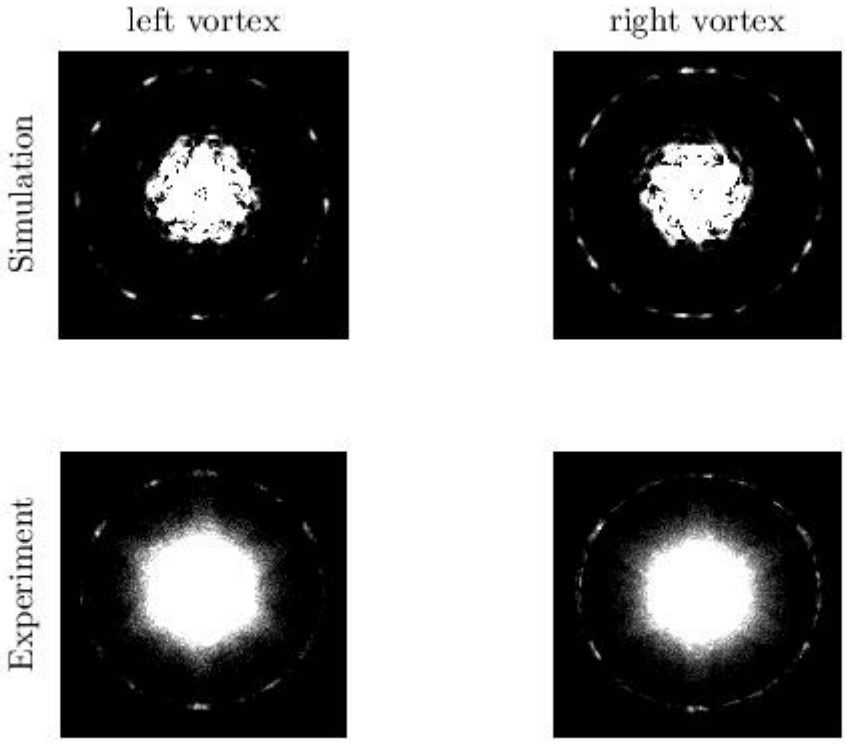

Figure 2. Simulated (top) and experimental (bottom) diffraction pattern of a left and a right handed vortex scattered on a 3_1-screw axis in $Mn_2Sb_2O_7$.

Phase-Related Techniques and Holographic Beam Shaping (inc. phase plates, DPC, vortices, electric and magnetic field imaging...)

IM5.P136
Full-resolution high-contrast imaging of phase objects by gradient-flipping-assisted focal series reconstruction

C. Ozsoy-Keskinbora[1], W. Van den Broek[2], A. Parvizi[2], X. Jiang[2], C. Boothroyd[3], R. E. Dunin-Borkowski[3], P. van Aken[1], C. T. Koch[2]

[1]Max Planck Institute for Solid State Research, Stuttgart, Germany
[2]Ulm University, Ulm, Germany
[3]Ernst Ruska-Centrum und Peter Grünberg Institut, Julich, Germany

ozsoycigdem@gmail.com

When considering elastic electron scattering by thin samples in the transmission electron microscope (TEM) (e.g., by applying zero-loss energy filtering), samples that consist of light elements (e.g., almost all thin samples investigated by cryo TEM) affect mostly the phase of the probing electron wave function and produce very little absorption contrast. However, the phase component of the image is lost during conventional imaging processes. Fresnel fringes visible in defocused images as a result of the interference of the wave scattered by the sample and the forward-transmitted wave can be used to reconstruct this phase information. Such Fresnel fringes are very efficient in retrieving high spatial frequency information. However, in order to reliably recover lower spatial frequencies (within the lateral coherence length of the illumination), highly defocused images are needed. There exist many iterative reconstruction algorithms that are based on approaches such as the transport of intensity equation (TIE)[1], the weak phase object approximation[2] and maximum likelihood optimization[3]. Although they each have their strengths, none of them is fully capable of reliably recovering very low spatial frequencies[4], especially in the case of limited spatial coherence. Here, we present results obtained by using a modified flux-preserving focal series reconstruction algorithm[5]. The modification consists of flipping the gradient of the recovered phase every few iterations where its absolute value is below a certain threshold. Such a procedure is known to favor solutions that are sparse in the domain where the flipping is applied[6]. In order to test this approach, both off-axis electron holograms and focal series of images of the same sample were acquired. The off-axis holography experiment was carried out using round illumination and a biprism voltage of 89.4 V in an FEI Titan 80-300 TEM equipped with two electron biprisms and a Gatan imaging filter with a 2048 × 2048 pixel charge-coupled device camera. For focal series acquisition, the conditions were kept the same, with the exception that the biprism was retracted. Iron-core/carbon-shell nanoparticles were used as a test sample. The reconstruction results show that the new in-line reconstruction approach is able to recover both high and also very low spatial frequency components of the phase, except for a few extremely low spatial frequencies (Fig. 1). This remaining discrepancy may be in part due to imperfect zero-loss filtering. While similar noise levels are determined for both approaches (0.063 for the improved reconstruction algorithm and 0.058 for the conventional algorithm), the signal to noise ratio is approximately 300 times higher for the conventional algorithm and 12 times higher than for the off-axis case. [7]

1. Teague, M. R., Deterministic Phase Retrieval: A Green's Function Solution. *Journal of the Optical Society of America* 1983, 73, 1434-1441.
2. Kirkland, E., The Transmission Electron Microscope. In *Advanced Computing in Electron Microscopy*, Springer US: 2010; pp 5-27.
3. Coene, W. M. J.; Thust, A.; Op de Beeck, M.; Van Dyck, D., Maximum-likelihood method for focus-variation image reconstruction in high resolution transmission electron microscopy. *Ultramicroscopy* 1996, 64, 109-135.
4. Koch, C. T., Towards full-resolution inline electron holography. *Micron*.
5. Koch, C. T., A flux-preserving non-linear inline holography reconstruction algorithm for partially coherent electrons. *Ultramicroscopy* 2008, 108, 141-150.
6. Oszlanyi, G.; Suto, A., Ab initio structure solution by charge flipping. *Acta Crystallographica Section A* 2004, 60, 134-141.
7. The research leading to these results has received funding from the European Union Seventh Framework Programme [FP7/2007-2013] under grant agreement n°312483 (ESTEEM2). W. V. d. B. acknowledges the Carl Zeiss Foundation.

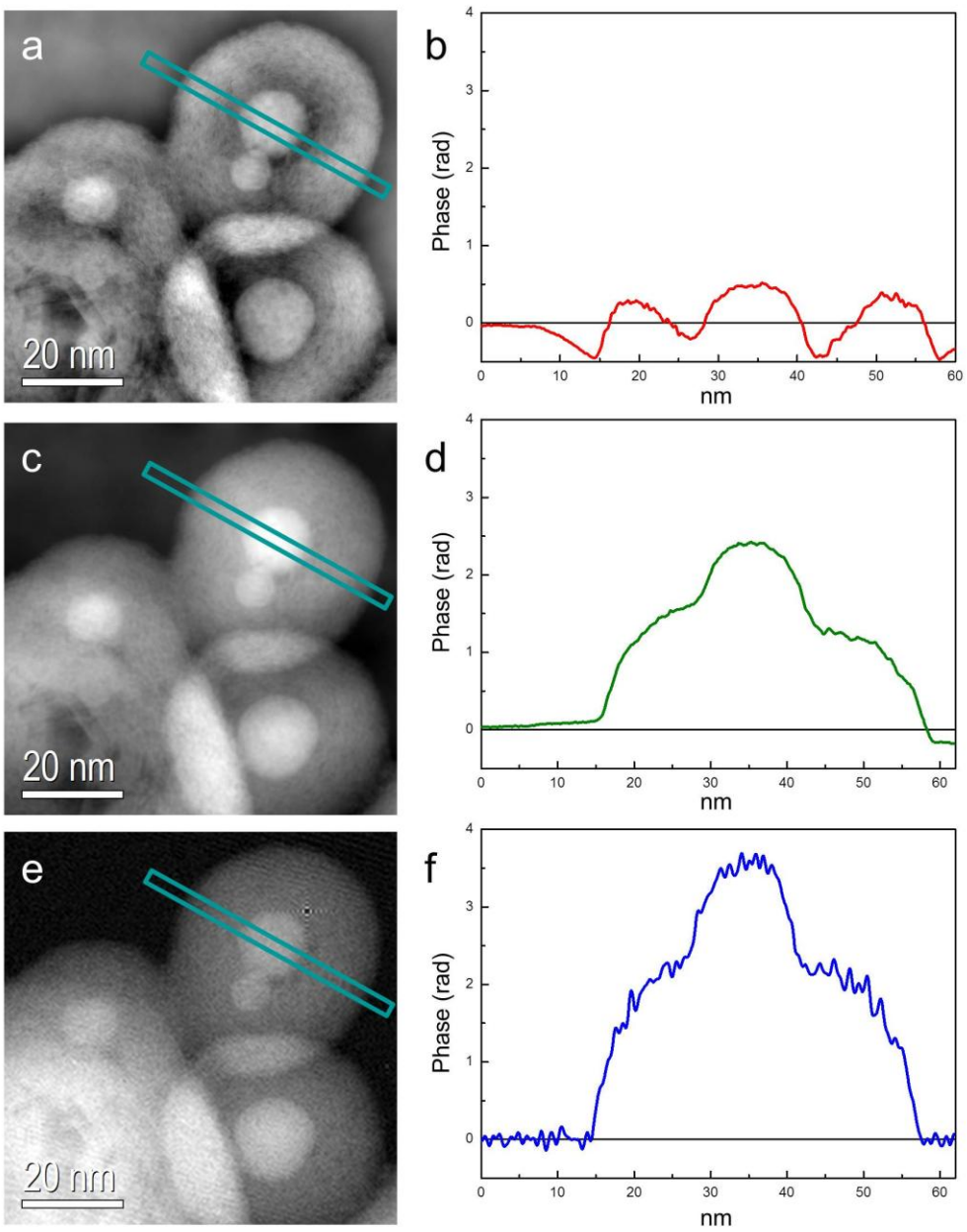

Figure 1. (a, c, e) Phase images and (b, d, f) corresponding line profiles across a feature within them. (a, b) Phase retrieved using conventional focal series reconstruction[5]. (c, d) Phase retrieved using gradient-flipping-assisted focal series reconstruction. (e, f) Phase retrieved using off-axis electron holography.

Phase-Related Techniques and Holographic Beam Shaping (inc. phase plates, DPC, vortices, electric and magnetic field imaging...)

IM5.P137
Thin-film based phase plates for transmission electron microscopy fabricated from metallic glasses

M. Dries[1], T. Schulze[1], S. Hettler[1], W. Send[1], E. Müller[1], R. Schneider[1], D. Gerthsen[1], Y. Luo[2], K. Samwer[2]

[1]Karlsruher Institut für Technologie (KIT), Laboratorium für Elektronenmikroskopie (LEM), Karlsruhe, Germany
[2]Universität Göttingen, I. Physikalisches Institut, Göttingen, Germany

manuel.dries@kit.edu

The development of physical phase plates (PPs) for transmission electron microscopy (TEM) was driven by the poor or even vanishing contrast of organic objects in biology and medicine. This led to considerable progress in the field of PP TEM during the past decade. Since the experimental realization of electrostatic PPs remains a challenging task, research has focused on thin-film PPs, which are typically fabricated from amorphous carbon (aC)-films. Impressive results have been obtained by the application of aC-film based PPs [1]. However, the illumination with high-energy electrons initiates a steady, irreversible degeneration of the aC-film, which reduces the lifetime of aC-film based PPs [2]. Hence, recent investigations concentrated on the search of alternative materials with an improved material stability [3,4].

This study, for the first time, presents thin-film PPs fabricated from metallic glass alloys, which are characterized by a high electrical conductivity and an amorphous structure. The zirconium-based alloy $Zr_{65.0}Al_{7.5}Cu_{27.5}$ (ZAC) was chosen, which is expected to remain in the amorphous state even under intense electron illumination as long as the temperature stays below the crystallization temperature of 437 °C [5].

In this work, Hilbert PPs (HPPs) were fabricated, which consist of a micro-structured thin film located in the back focal-plane (BFP) of the objective lens [6]. The ZAC-film was sputtered on mica-substrates and floated on Cu-grids. Using a focused-ion-beam system, rectangular windows were structured into the ZAC-film. The Cu-grid was implemented in the BFP of a Philips CM200 FEG/ST. At an electron energy of 200 keV, a ZAC-film of 24 nm thickness induces a phase shift close to π. The phase shift is imposed on electrons in one half of the diffraction pattern except for the zero-order beam. This results in an overall phase shift of π/2 for all spatial frequencies above the cut-on frequency.

Oxidation of the surface of the ZAC-film could not be avoided, which leads to electrostatic charging upon electron exposure in the transmission electron microscope. Hence, a 4 nm thin aC-coating was applied on both sides of the ZAC-film. Fig. 1a shows the power spectrum of a PP TEM image of an amorphous test object, which verifies the desired phase-shifting properties. The power spectrum is subdivided in a central stripe (red) and outer regions (green) with Thon-rings shifted by π/2. Moreover, the Thon-ring intensity at high spatial frequencies is comparable in the red and green regions of Fig. 1a. This indicates that the coherence loss due to inelastic scattering in the ZAC-film is surprisingly low. Plasmon scattering was investigated by electron energy loss spectroscopy (EELS). The EELS spectra of a 24 nm thick ZAC- and a 49 nm thick aC-film are shown in Fig. 1b. Both films induce a phase shift close to π due to their different inner potentials. The low intensity of the ZAC plasmon signal at an energy loss ΔE of 18 eV clearly indicates less inelastic scattering compared to the aC-film with its plasmon peak at 24 eV. The ZAC signal at 42 eV corresponds to the Zr-N2,3 ionization edge and is not related to plasmon scattering.

The low probability for plasmon scattering and the comparatively small reduction of the information limit make the ZAC-alloy a promising material to improve the performance of thin-film PPs for PP TEM [7].

1. R. Danev et al., PNAS 111 (2014) 15635-15640
2. R. Danev et al., Ultramicroscopy 109 (2009) 312-325
3. M. Marko et al., J. Struct. Biol. 184 (2013) 237-244
4. M. Dries et al., Ultramicroscopy 139 (2014) 29-37
5. R. Rambousky et al., Z. Phys. B 99 (1996) 387-391
6. R. Danev, K. Nagayama, J. Phys. Soc. Jpn. 73 (2004) 2718-2724
7. Financial support by the Deutsche Forschungsgemeinschaft (DFG)

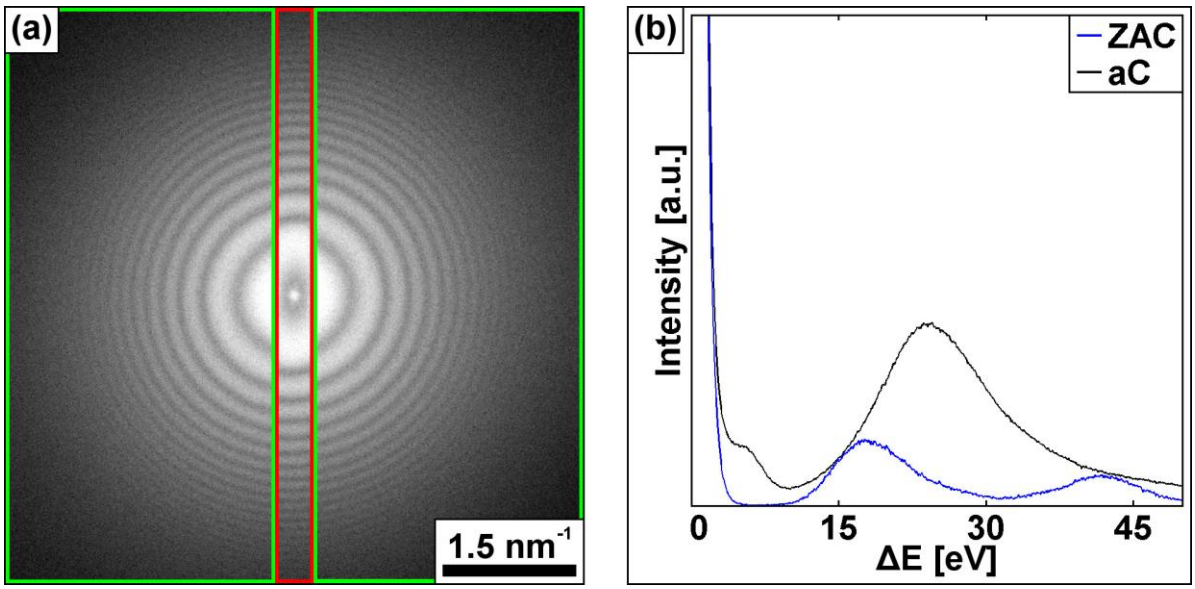

Figure 1. (a) Phase-shifting properties of the aC-coated ZAC-film based HPP. Power spectrum of a PP TEM image of an amorphous test object. (b) EELS spectra of a 24 nm thick ZAC- and a 49 nm thick aC-film.

Phase-Related Techniques and Holographic Beam Shaping (inc. phase plates, DPC, vortices, electric and magnetic field imaging...)

IM5.P138
Probing magnetic properties on the nm scale: EMCD on individual FePt nanocubes

S. Schneider[1,2], D. Pohl[1], S. Löffler[3], T. Schachinger[3], P. Schattschneider[3,4], L. Schultz[1,2], B. Rellinghaus[1]

[1]IFW Dresden, Institute for Metallic Materials, Dresden, Germany
[2]Technische Universität Dresden, Institut für Festkörperphysik, Dresden, Germany
[3]Vienna University of Technology, USTEM, Vienna, Austria
[4]Vienna University of Technology, Institute of Solid State Physics, Vienna, Austria

sebastian.schneider@ifw-dresden.de

Skyrmions and topological insulators are “hot topics” of current research in solid state physics. Although a lot of success was achieved in the research of the origin and properties of these phenomena, today there is still no method to probe such phenomena in the volume with atomic resolution. X-ray magnetic circular dichroism (XMCD) satisfies all the prerequisites for such studies, but can only reach lateral resolutions, which are one magnitude higher than the length scale of these exotic states. Recently, electron energy-loss magnetic chiral dichroism (EMCD), which is the electron wave analogue of XMCD, was proposed as a candidate to overcome this lack of resolution. It offers the possibility to study magnetic properties at the nanoscale in a transmission electron microscope (TEM) [1]. In a “classical” EMCD setup, the sample is illuminated with an electron plane wave and acts as a beam splitter. Although this method is meanwhile well established, so far only very few EMCD spectra were obtained from individual nanoparticles [2, 3].

We report on “classical” EMCD measurements on individual FePt nanocubes (cf. Fig. 1 and Fig. 2) and compare our experimental findings with simulations. $L1_0$ ordered FePt is a particularly important material, since it offers the highest magneto-crystalline anisotropy among the oxidation-resistant hard magnets. It is therefore a promising materials candidate for media in future high density magnetic data storage. $L1_0$ ordered FePt nanocubes were prepared by inert gas condensation. Prior to the spectroscopic measurements the samples were exposed to an external magnetic field of H_{ext} = 7.5 T applied perpendicular to the film plane. Hereby, all cubes with [001] zone axis orientation should give a maximum dichroic response (and with the same sign for all particles), since the magnetization is then (anti)parallel to the electron beam.

The dichroic signals at the iron L_3 and L_2 edges are expected to be as small as just 10 % of the total absorption. Due to these small intensity differences in the electron energy loss spectra (EELS), a proper microscope alignment, a good reproducibility, a sufficiently stable sample, and a decent signal-to-noise (S/N) ratio pose extreme experimental demands. The experiments were performed on a FEI Titan^3 80-300 microscope equipped with an image C_S corrector, and binned-gain acquisition of the EEL spectra was used to optimize the S/R ratio [4]. Particular attention was paid to the analysis of the EEL spectra. A pathway is presented, which allows for the extraction of a dichroic signal despite a non-optimal S/R ratio in the recorded spectra. Our experiments are supported by simulations off EEL spectra utilizing the WIEN2k program package [5], based on which FePt cubes with an optimal thickness were chosen for highest EMCD signals [6]. The likewise conducted experiments indeed reveal a small, but reproducible dichroic signal that agrees well with the results of the theoretical calculations.

1. P. Schattschneider et al., Nature **441** (2006), p. 486.
2. J. Salafranca et al., Nano Lett. **12** (2012), p. 2499.
3. Z.Q. Wang et al., Nature Comm. **4** (2013), p. 1395.
4. M. Bosman and V. J. Keast, Ultramicroscopy **108** (2008), p. 837.
5. K. Schwarz and P. Blaha, Computational Materials Science **28** (2003), p. 259.
6. S. Löffler and P. Schattschneider, Ultramicroscopy **110** (2010), p. 831.

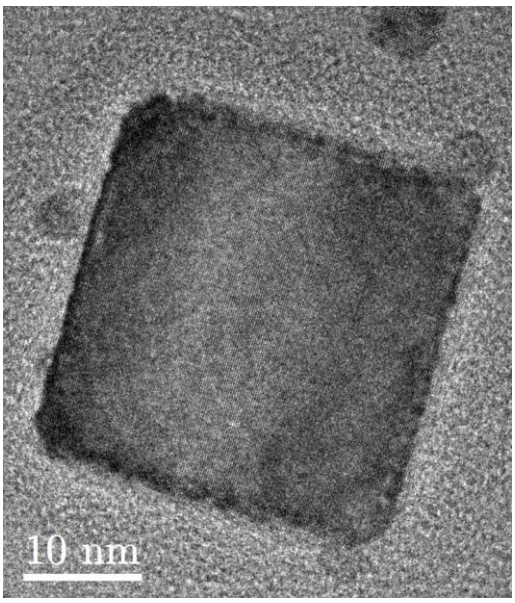

Figure 1. TEM image of FePt nanocube with a thickness of approximately 30 nm.

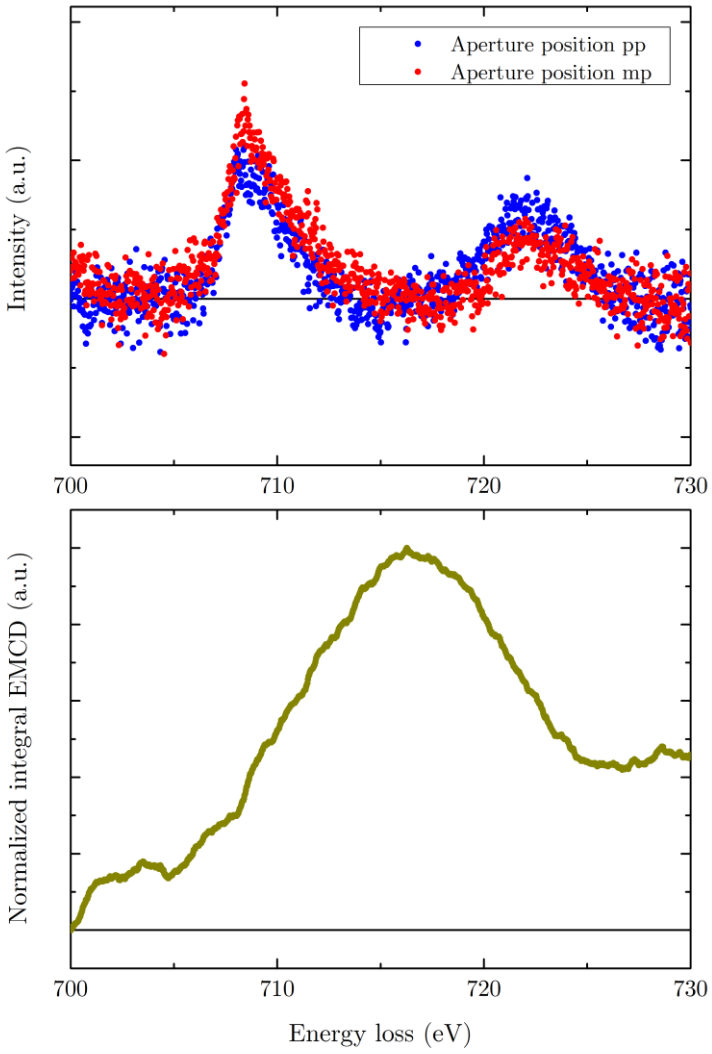

Figure 2. EEL spectra (above) of the nanoparticle in Fig1. at the Fe L_3 and L_2 edges for the two detector positions in EMCD geometry. Integrated EMCD signal (below) as derived from these spectra.

Phase-Related Techniques and Holographic Beam Shaping (inc. phase plates, DPC, vortices, electric and magnetic field imaging...)

IM5.P139
Automatic Zernike phase plate alignment and its use to eliminate cut-on artifacts

M. Oster[1], R. R. Schröder[1]

[1]Universitätsklinikum Heidelberg, CellNetworks Bioquant CryoEM, Heidelberg, Germany

marco.oster@bioquant.uni-heidelberg.de

Phase contrast microscopy using physical phase plates has proven to provide superior contrast, especially for frozen-hydrated biological samples [1]. However, for Zernike type thin film phase plates their successful application imposes highest demands on the precise alignment of the phase plate hole relative to the zero order beam. This renders routine image acquisition time consuming and tedious [1].

Here we present our approach on enabling optimal imaging solution for beam sensitive specimen by automating the acquisition process. Custom software has been integrated into the Leginon [2] framework, which aligns the phase plate at minimal dose. The use of predefined microscope settings in a specified order also minimizes lens hysteresis and the likelihood of accidentally damaging the phase plate film with an intense beam. Combined with target identification at lower magnifications and high defocus, and the possibility of focusing the objective lens and aligning the phase plate at a specimen position away from the region of interest, this enables automated phase contrast microscopy even on beam sensitive specimen.

Besides ease of operation, automation enables to remedy imaging artifacts inherently present in thin film hole phase plates, which suffer from a non zero cut-on frequency, due to a finite aperture hole. This results in typical low-frequency fringing artifacts (Fig. 2a) as a result of the sharp spatial frequency onset. Furthermore, any phase contrast information with a spatial frequency smaller than the cut-on frequency is not transferred into object contrast at all. This effect could in principle be reduced by downsizing the phase plate hole, which on the other hand would be even less forgiving in terms of phase plate alignment errors.

As long as the objective lens is well focused, it is possible to allow for small deviations of the angle of the illuminating beam during the image acquisition time, since there is no detectable image shift for moderate resolution. Therefore, the relative position of the phase plate hole can be controlled by a small variation of the illumination tilt, which is useful for fine alignment (Fig. 1a). This can further be exploited by applying a dynamic offset, which scans the zero order beam along the perimeter of a phase plate hole during the image integration time on the camera (Fig. 1b). This beam precession significantly lowers the effective cut-on frequency and allows for averaging of the phase noise stemming from film roughness [3] and other local imperfections in the phase shifting film material. The radius of the scanning trajectory can be maximized for perfect alignment, which pushes the cut-on frequency close to zero.

A direct comparison between conventional and precessing technique is shown in Fig. 2.

1. Dai W et al.: N. Protocols 9 2630-2642
2. Suloway C et al.:J Struct Biol. 151 41-60
3. Dries M et al.: Ultramicroscopy 139 29-37
4. We thank Götz Hofhaus for sample preparation
5. Discussions, sharing ideas and hardware with the KonTEM team are acknowledged
6. This work was funded by the DFG under the grant Sch 424/11

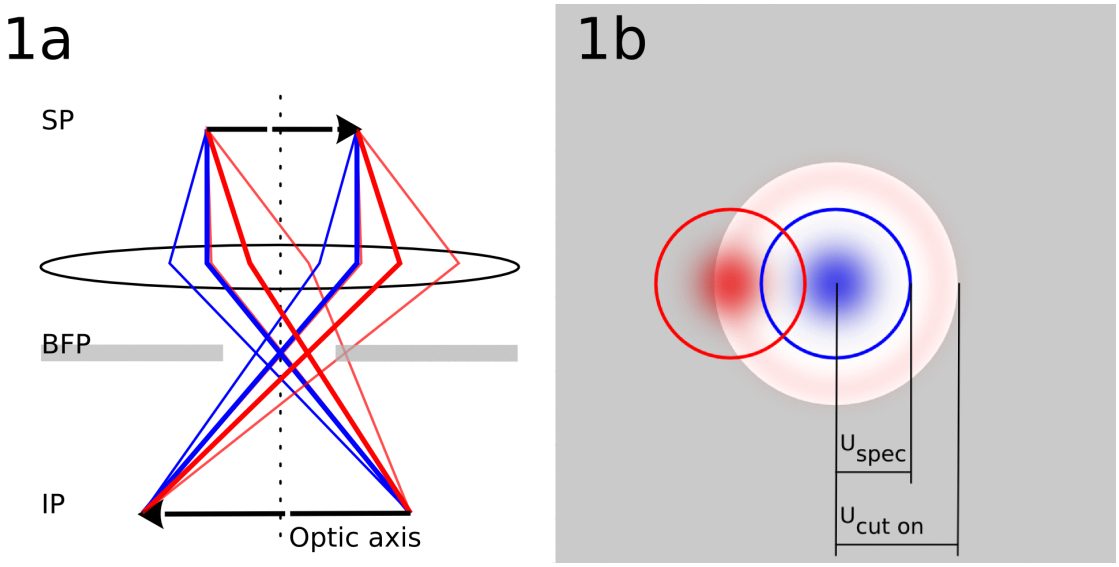

Figure 1. a shows the transfer of zero order (thick lines) and diffracted beams (thin lines) for untilted (blue) and tilted (red) illumination from the specimen plane SP to the image plane IP. Fig. 1b shows a top view of the phase plate in the back focal plane BFP with corresponding positions of diffracted beams of one particular spatial frequency u_spec smaller than u_cuton. In case of an untilted illumination (blue), this spatial frequency does not benefit from an additional phase shift and is thus not transferred. For the tilted illumination (red), a fraction of the spatial frequencies u_spec is transferred with the intended additional phase shift. For different azimuthal beam positions, corresponding fractions are transferred, which result in full contrast transfer.

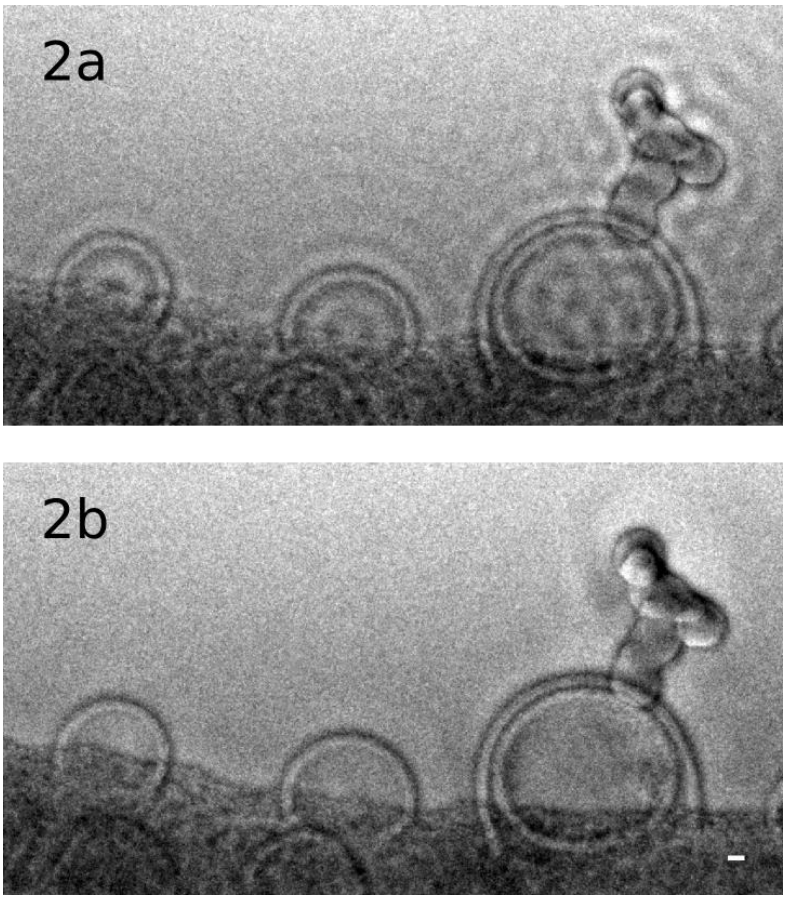

Figure 2. a shows an in-focus image of frozen-hydrated liposomes [4] with a Zernike phase plate. Note the excessive fringing artifacts especially prominent in the ice. Fig. 2b taken with the same dose as Fig. 2a shows the image without fringing artifacts. Scale bar is 10 nm.

Phase-Related Techniques and Holographic Beam Shaping (inc. phase plates, DPC, vortices, electric and magnetic field imaging...)

IM5.P140
Differential phase contrast: a method to improve contrast in biological samples?

E. Müller[1], E. Poghosyan[1], J. Zweck[2]

[1]PSI, EMF, Villigen, Switzerland
[2]University Regensburg, Regensburg, Germany

elisabeth.mueller@psi.ch

Differential phase contrast (DPC) imaging is a scanning transmission electron microscopy (STEM) technique which uses a dark field and possibly a bright field STEM detector which is split into quadrants. This allows to detect asymmetric angular distribution of the scattered electrons in scanning mode. Such detectors are common already long time in scanning electron microscopy. In transmission electron microscopy, this technique has been used since 1978 [1], but was used exclusively to image magnetic domain structures at intermediate or low resolution by only a small community. -Recently, for polar materials [2,3], (sub-)atomic resolution has been demonstrated. Both material classes belong to the field of materials science.

Totally unexpectedly, there appears to exist a third type of materials, which can benefit from this method. We have applied DPC imaging to unstained biological specimens such as microtubules and axoneme, both, at room temperature as well as under cryo-conditions. In order to increase contrast, conventional room temperature TEM of biological samples involves staining with heavy atoms such as sodium silicotungstate, uranyl acetate or ammonium molybdate. However, the granularity of the staining material brings additional limitation in resolution and dehydration during stain drying, causing flattening or shrinkage artifacts. To cope with the above mentioned problems, rapid freezing is used, where biological samples are preserved in frozen hydrated or native state. Nevertheless, these specimens are known to suffer from very weak image contrast, because they consist of only light elements in non-crystalline arrangement. Therefore there is only weak phase contrast, while they can neither benefit from strong mass- nor from diffraction contrast.

Amazingly, the signal of these materials appears to cause a strong enough difference in opposed quadrants of the DPC detector to give image contrast. Two different aspects of the sample contribute to this effect: On one side, differences in sample thickness and on the other side, differences in the mean inner potential appear to cause sufficiently large asymmetry in the distribution of scattered electrons to give rise to clearly recognizable image contrast.

1. J.N. Chapman and P.E. Batson and E.M. Waddell and R.P. Ferrier, The direct determination of magnetic domain wall profiles by differential phase contrast electron microscopy , Ultramicroscopy **3** p. 203-214 (1978)
2. N. Shibata et al., J. Electr. Micr. **59** (2010) 473 and Nature Physics, (2012) 611
3. Mueller, Knut and Krause, Florian F. and Béché, Armand and Schowalter, Marco and Galioit, Vincent and Löffler, Stefan and Verbeeck, Johan and Zweck, Josef and Schattschneider, Peter and Rosenauer, Andreas, Atomic electric fields revealed by a quantum mechanical approach to electron picodiffraction, Nat Commun (2014) **5** p 5653 http://dx.doi.org/10.1038/ncomms6653

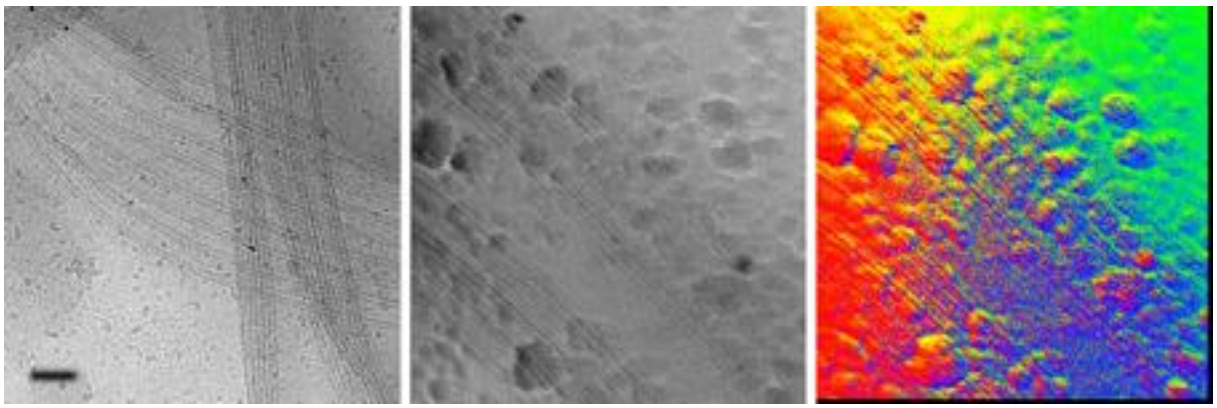

Figure 1. a) plunge frozen axonemes imaged in cryo at large defocus in BF TEM mode (left). The same type of cryo-sample imaged in focus with differential phase contrast imaging (middle: difference image, right: reconstructed DPC image). Here, both causes for contrast can be recognized: little hillocks on the ice and differences in local mean inner potential due to the axoneme. Please note that the intense colours (red-blue-green-yellow) are due to a descan artefact. Nontheless, the axoneme are clearly visible. (scale bar 100nm)

Phase-Related Techniques and Holographic Beam Shaping (inc. phase plates, DPC, vortices, electric and magnetic field imaging...)

IM5.P141
Calibration and characterization of a DPC system

F. Schwarzhuber[1], J. Wild[1], M. Lohr[1], R. Schregle[1], B. Bauer[1], J. Zweck[1]

[1]University Regensburg, Institute of Experimental and Applied Physics, Regensburg, Germany

felix.schwarzhuber@ur.de

Differential phase contrast microscopy (DPC) in a scanning transmission electron microscope (STEM) is a well known method to measure microscopic magnetic and/or electric field distributions inside a specimen. This technique was proposed 1977 by H. Rose [1] and realized at first in 1978 by J.N. Chapman [2] to investigate magnetic domain wall profiles. Later it has been shown that it is also possible to measure internal electrostatic fields e.g. in GaN/InGaN quantum well structures [3] and GaAs nanowires with DPC [4].

When the electron probe of the STEM is scanned over an area containing intrinsic magnetic or electric fields the beam gets deflected by an angle ε due to the Lorentz or Coulomb force. This leads to a shift of the diffraction disk in the detector plane. The shift is proportional to the strength and parallel to the field's direction. To detect this shift a four segmented ring detector is used. By subtracting the signals of opposing segments an orthogonal coordinate system is defined and the movement of the diffraction disk can be measured (fig. 1).

The aim of this work was to determine how different microscope modes (STEM, LMSTEM) and measurement parameters (camera length) affect the achievable sensitivity for a deflection by an angle ε of the DPC system and to find the ideal parameters for a given task. For promising settings a calibration factor κ has been determined which permits quantitative DPC measurements.

To achieve this we use a custom built TEM holder [5] with a parallel plate capacitor on its tip. The well known plate geometry allows to generate defined electric fields to deflect the electron beam. For different combinations of parameters we recorded the difference signals of the detector as a function of the variation of the electric field. Figure 2 shows the linear dependence of the difference signals to the voltage applied to the capacitor. From the slopes $S_{12\text{-}6}$ and $S_{3\text{-}9}$ in the graph we calculate the calibration factor $\kappa=(S_{12\text{-}6}{}^2 + S_{3\text{-}9}{}^2)^{1/2}$ relating the change in DPC signal to the change of the field. Larger values of κ give rise to better field sensitivities.

These measurements show a great dependence of the DPC signal on the camera length of the microscope, the C2 aperture used, determining the size of the diffraction disk and the intensity of the electron beam on the detector.

In addition to the microscope parameters the sensitivity also depends on the noise of the setup's dwell time. Looking at the time evolution of the single measurement values (10 µs dwell time each) and their average over time (fig. 3) we are able to determine the measurement time needed to obtain statistically reliable measurements for a certain confidence level.

As can be seen in Fig. 3, for averaging over less than about 80 single measurements the curve shows significant variation. This has to be considered in the quantitative evaluation of DPC measurements and we will present approaches to deal with these shortcomings.

1. H Rose, “Nonstandard imaging methods in electron microscopy”, Ultramicroscopy 2 (1976-1977), p. 251-267
2. J N Chapman et al, “The direct determination of magnetic domain wall profiles by differential phase contrast electron microscopy”, Ultramicroscopy 3 (1978), p. 203-214
3. M Lohr et al, “Differential phase contrast 2.0 — Opening new ‘‘fields’’ for an established technique ”, Ultramicroscopy 117 (2012), p. 7-14
4. B Bauer et al, "Direct detection of spontaneous polarization in wurtzite GaAs nanowires", Applied Physics Letters 104, 211902 (2014)
5. R Schregle, “Kalibrierung eines DPC-Detektors mit Hilfe eines speziell erstellten Probenhalters ”, Diplomarbeit (2011)

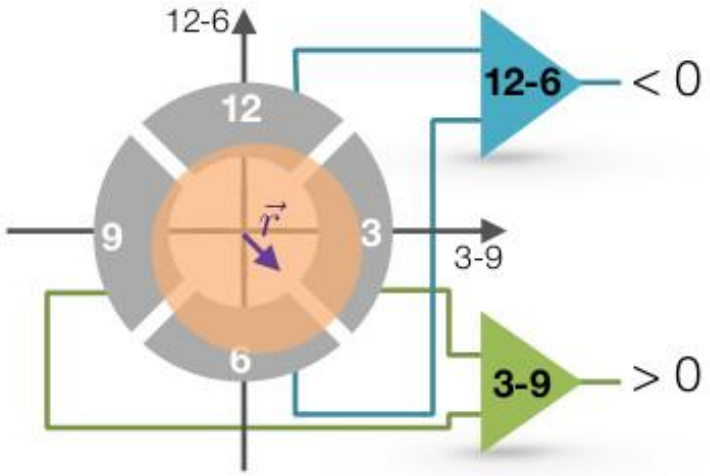

Figure 1. Scheme of the DPC detector (four grey sectors). The components of the shifting vector ($r_{3\text{-}9}$, $r_{12\text{-}6}$) of the diffraction disk is proportional to the difference signals 12-6 and 3-9.

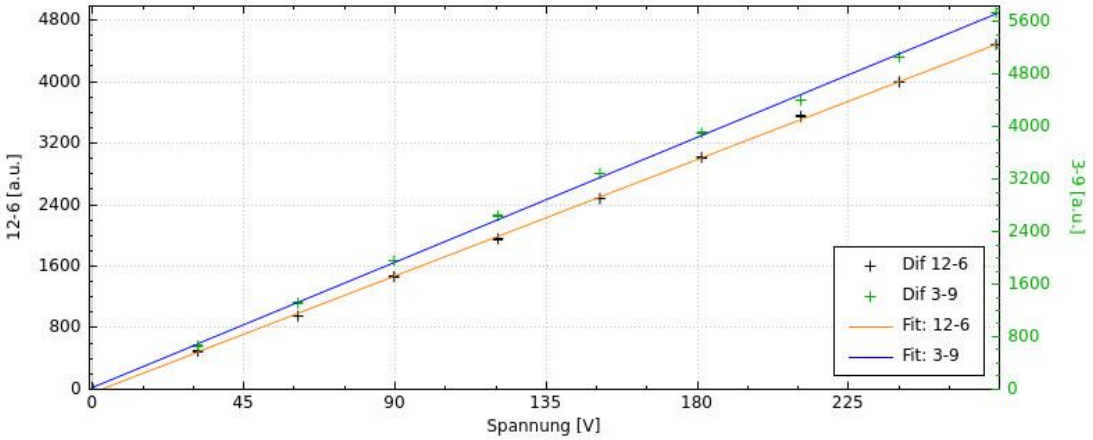

Figure 2. Fitted result of a measurement with the capacitor holder. The difference signals 12-6 and 3-9 show a linear behavior.

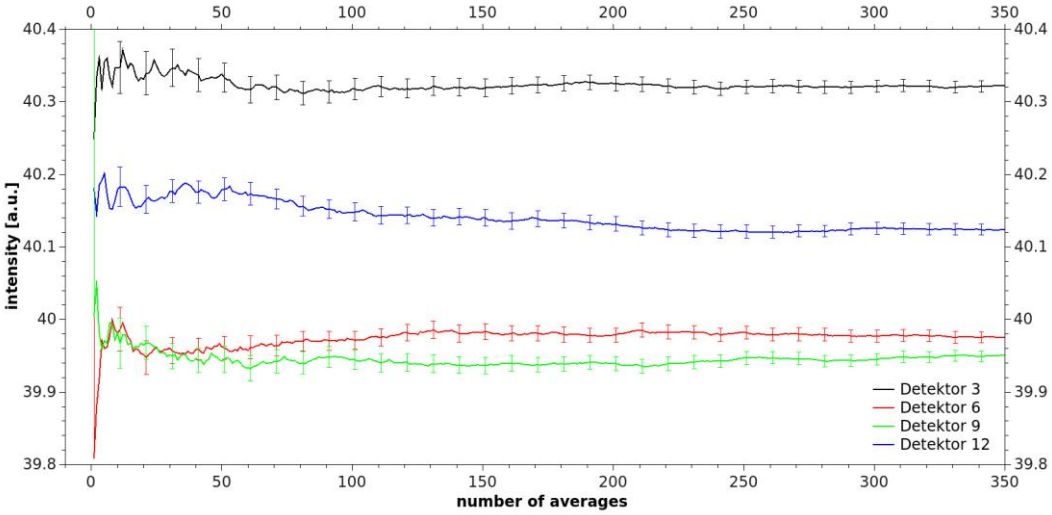

Figure 3. Dependence of the mean values of the detector signals to the number of averages with corresponding standard errors.

Phase-Related Techniques and Holographic Beam Shaping (inc. phase plates, DPC, vortices, electric and magnetic field imaging...)

IM5.P142
Study of the coherence of the primary beam in the low energy scanning electron microscope

T. Řiháček[1], F. Mika[1], M. Matějka[1], S. Krátký[1], I. Müllerová[1]

[1]ASCR, Institute of Scientific Instruments, Brno, Czech Republic

rihacek@isibrno.cz

Coherence of an electron beam is an important characteristic in a transmission electron microscope (TEM). It can be measured simply by analyzing the interference fringes in a diffraction pattern. On the other hand, the coherence of the beam is usually not important for standard applications of a scanning electron microscope (SEM). Nevertheless it can be of importance for some specific cases. The aim of this experiment is to find out whether the coherence of our SEM beam is high enough to enable us to perform a diffraction experiment at low energies (E = 350 - 2000 eV) which would enable us to create an electron vortex beam with of tens of keV.

Some complications with the visualization of a diffraction pattern arise because SEM does not allow observing the pattern directly because of the scanning of the electron beam. Therefore the usual TEM diffraction techniques cannot be used. One way to get the resulting intensity profile is proposed in [1]. We therefore make use of an experimental setup similar to that used in [1] which is depicted in Figure 1.

Our experiment was adapted for the SEM microscope FEI Magellan 400. The grating is carried by the retractable mechanism of a CBS detector which is placed below the pole piece of the objective lens where the diffraction of the primary beam takes place while the beam itself is focused to the specimen plane. The imaging of a diffraction pattern is achieved by scanning the beam across a specimen which consists of a contrasting vertical stripe on a dark background. For this purpose we have chosen a golden stripe on a carbon substrate. Secondary electrons are then collected with the standard side Everhart-Thornley (ET) detector.

For the preparation of the nitride membrane patterned with grating structure, high resolution electron beam lithography was used. A process we developed, using electron beam lithography (EBL), reactive ion etching (RIE) and other techniques, enables us to fabricate a free standing grating in the thin membrane of silicon nitride with periodicity 300 nm. One of these gratings is shown in Figure 2.

The contrasting golden stripe on a carbon background was created by EBL method using e-beam writer Vistec EBPG5000+ ES (100 kV system) for exposing the stripe pattern. Several stripes of different widths (from 250 nm to 4 μm) were prepared. We are therefore allowed to choose an appropriate stripe to obtain a signal strong enough without significant deformation of a pattern.

Coherence of the beam can be then estimated by analyzing the number of visible intensity maxima and comparing them to the simulated model. In a simulated diffraction pattern both the chromatic and spherical aberrations of the objective lens are taken into account. These aberrations turn out to have a small influence on the final pattern, as well as having a finite source size. The intensity profile of course strongly depends upon the actual size of the slits and bars in a grating. In Figure 3 we show an example of an intensity profile of a simulated diffraction pattern for a grating with the slits and bars of equal width (200 nm).

1. McMorran B. et al, Ultramicroscopy **106** (2006) 356 - 364.
2. We acknowledge the financial support from the project TE01020118 of the Technology Agency of the Czech Republic (Competence centre: Electron Microscopy). We thank Michal Lenc for valuable discussions.

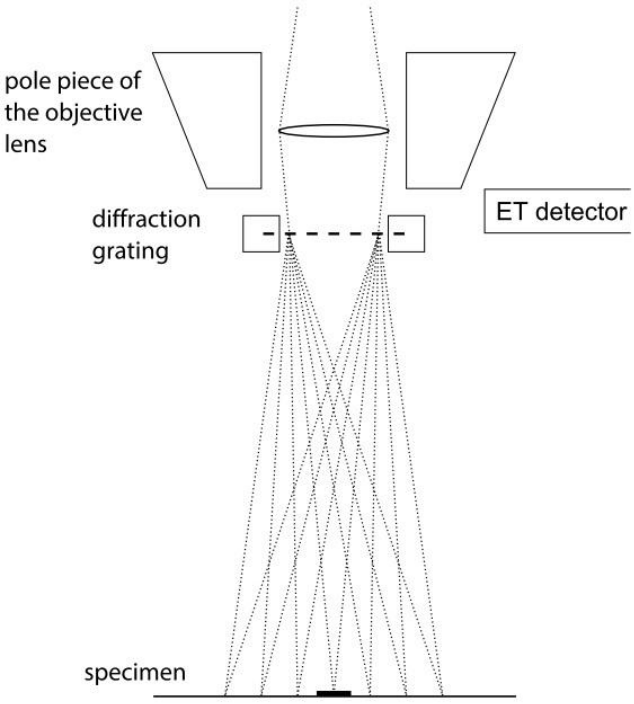

Figure 1. Scheme of the diffraction experiment.

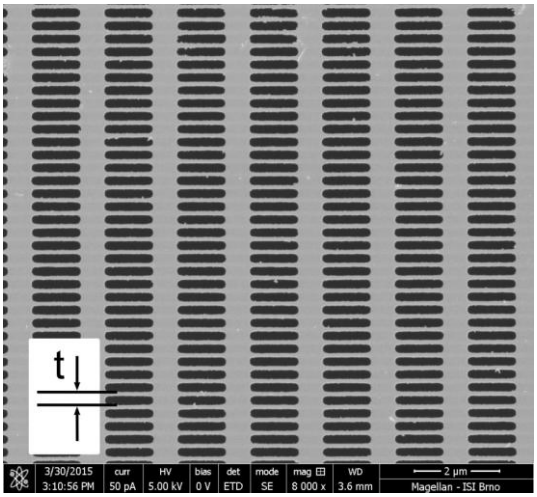

Figure 2. Diffraction grating, period t = 300 nm.

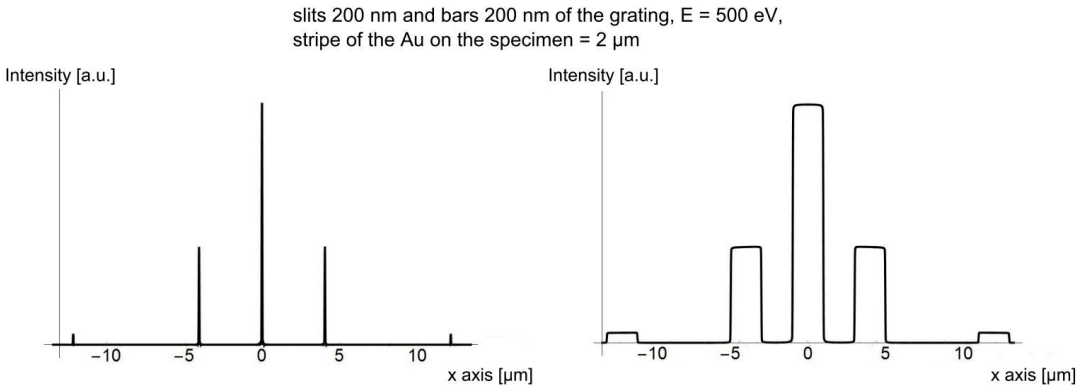

Figure 3. Left - intensity profile, right - intensity profile modulated by the specimen stripe.

Phase-Related Techniques and Holographic Beam Shaping (inc. phase plates, DPC, vortices, electric and magnetic field imaging...)

IM5.P143
Topological analysis of paraxially scattered electron vortex beams

A. Lubk[1], L. Clark[2], G. Guzzinati[2], J. Verbeeck[2]

[1]TU Dresden, Triebenberg Laboratory, Dresden, Germany
[2]University of Antwerp, EMAT, Antwerp, Belgium

axel.lubk@triebenberg.de

Electron vortex beams carrying orbital angular momentum (OAM) [1], experimentally created by dedicated apertures in the TEM, hold promise for atomic resolution mapping of magnetic states in materials by means of Electron Magnetic Circular Dichroism (EMCD) [2]. Such beams must contain a phase singularity, which adds a new flavour to the electron wave. Topological concepts can be used to precisely define that singularity in terms of topological charges thereby characterizing the electron wave. However, for the particular case of highly-localized electron vortex beams scattering at atomic potentials, little is known about their vortex behaviour upon propagation.

Thus, we analyze the fabric of vortex lines occurring in a vortex beam upon propagation through an atomic lattice with respect to general topological information. Our study is mainly based on scattering simulations utilizing the Multislice approximation to paraxial electron scattering and we employ $SrTiO_3$ as test structure. The following features could be distinguished [3]:

(I) A Rankine like vortex structure with significantly reduced diffusion of the vortex beam compared to a non-vortex beam, when centered on an atomic column (Fig. 1). Therefore vortex beams hold the promise to significantly improve atomic resolution STEM-EELS techniques, where the ubiquitous delocalization of the probe upon propagation systematically obscures the atomic information.

(II) A systematic deflection of vortex lines from amplitude and phase perturbations leading, e.g., to a circulation of vortex lines around atomic columns depending on the sign of the vorticity.

(III) Symmetry dependent splitting of m-order vortex beams. We show that combining topological concepts (conservation of total winding number) and symmetry allows predicting the vortex line structure of the beam without solving the scattering equations at all. In particular one can predict which high-order vortex beam will maintain a centered topologically protected zero under certain rotational symmetries.

(IV) The appearance of vortex-antivortex pairs corresponding to not-knotted vortex loops predominantly attached to atomic columns. That observation is important for the design of phase unwrapping algorithms for electron holography, where the linking of phase singularities represents the major obstacle.

In total, we reveal the significance of the topological structure, i.e. the vortex line fabric, for the elastic electron wave propagation through an atomic lattice. The obtained results are particularly important for setting up optimal scattering geometries for probing magnetic fields both elastically or inelastically via electron vortex beams.

1. Uchida, M., Tonomura, A., 2010, 464, 737-739. Verbeeck, J.,Tian, H., Schattschneider, P., Nature, 2010, 467, 301-304.
2. Schattschneider, P. et al., Nature, 2006, 441, 486-488.
3. Lubk, A.; Clark, L.; Guzzinati, G. & Verbeeck, J., Phys. Rev. A, American Physical Society, 2013, 87, 033834.

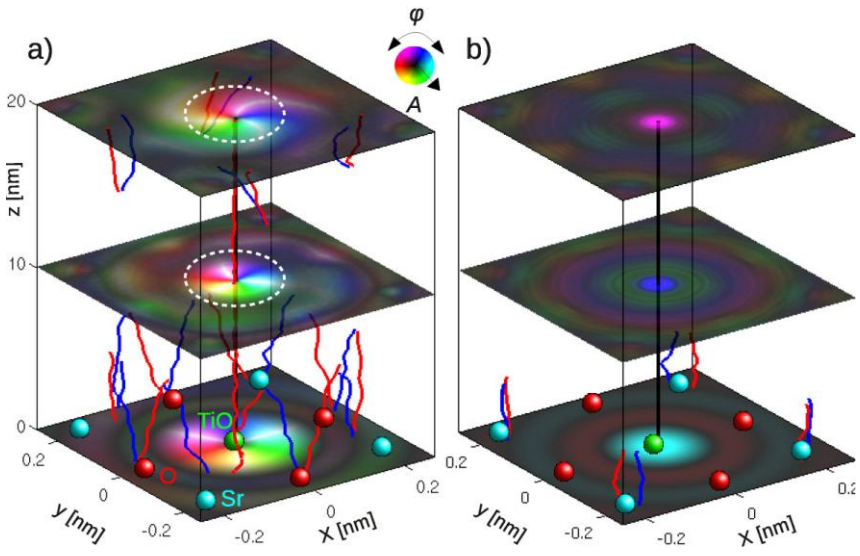

Figure 1.) m=1 vortex and b) m=0 conventional beam. The wave function at different z -planes are displayed domain coloured. m=1(-1) vortex lines are blue (red). The center of mass line is black. The atomic columns of $SrTiO_3$ are indicated at the bottom plane. The undisturbed vortex region is indicated by a white circle in a).

Tomographic Techniques (electron tomography, atom probe tomography, atom counting tomography)

IM6.144
STEM-based tomography: new opportunities and challenges

P.A. Midgley[1]

[1]Department of Materials Science and Metallurgy, University of Cambridge, 27 Charles Babbage Road, Cambridge, UK

pam33@cam.ac.uk

Over the past 15 years, electron tomography has become an increasingly popular method to discern the structure of nanoscale materials in three dimensions. Combining tomography with scanning transmission electron microscopy (STEM) offers a number of advantages: STEM high angle annular dark field (HAADF) image contrast is easily interpreted and the intensity varies monotonically with thickness (at least for reasonable mass-thickness levels); the HAADF signal is sensitive to atomic number and provides a measure of the local composition; it can be combined easily with analytical techniques such as energy-dispersive x-ray spectroscopy (EDX), electron energy loss spectroscopy (EELS), and electron diffraction. It is this last advantage that will be explored in this paper.

STEM-EELS or EDX tomography provides spectral information at every 3D real space location (voxel). Many modern electron microscopes are fitted with large solid angle x-ray detectors and when symmetrically disposed around the optic axis, taking into account the shadowing of detectors when the sample is titled, offer an efficient means to record EDX spectrum-images as a function of tilt to build up a 4D data set, see Fig. 1 [1]. From that data set, 3D elemental-, or phase-, specific maps may be reconstructed. Likewise, EELS tomography enables 3D compositional maps to be reconstructed (using core loss data) and 3D optical / dielectric maps (using low loss spectra), see Fig 2 [2]. We have recently developed a new technique, scanning precession electron tomography (SPET), which uses a scanned beam to record a precession electron diffraction (PED) pattern at every real space pixel to form a 4D 'diffraction-image'. By acquiring a tilt series, both real and reciprocal spaces can be reconstructed for every phase in the volume of interest [3].

In each of these techniques, mixed signals (spectra or diffraction patterns) need to be 'unmixed' in an objective fashion. We use multivariate statistical analysis to decompose each raw signal into a linear sum of signal components (e.g. spectral modes or distinct diffraction patterns) weighted by a loading (spatial distribution map) [4].

This paper will present a number of examples using decomposition techniques applied to EELS, EDX and diffraction-based tomography to illustrate the opportunities and challenges afforded by STEM-based tomography [5].

1. C.S.M. Yeoh, D. Rossouw, Z. Saghi, P. Burdet, R.K. Leary and P.A. Midgley (2015) *Microscopy and Microanalysis* doi.10.1017/S1431927615000227.
2. O. Nicoletti, F. de la Peña, R.K. Leary, D.J. Holland, C. Ducati, P.A. Midgley (2013) *Nature* **502** 80-84.
3. A.S. Eggeman, R. Krakow and P.A. Midgley, (2015) *Nat Commun* (in press)
4. *http:/hyperspy.org*
5. The research leading to these results was funded by the European Research Council under the European Union's Seventh Framework Program (FP7/2007–2013)/ERC grant agreement 291522-3DIMAGE.

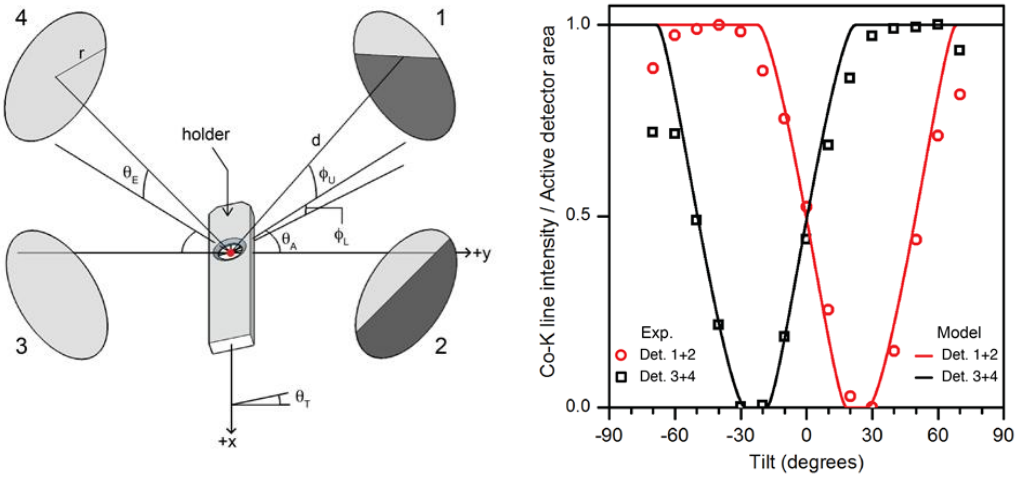

Figure 1. (left) Schematic figure indicating the partial shadowing of EDX detectors by a tilted holder; (right) Integrated Co-Kα intensity from a Co-rich nanoparticle fitted with a model based on the geometry indicated on the left [1].

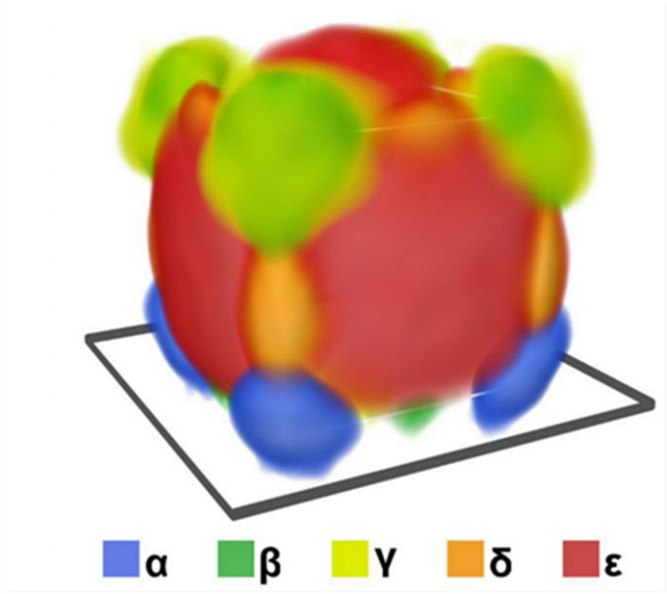

Figure 2. (b) 3D rendering of five surface plasmon modes of a silver nanocube (100nm in size), reconstructed using STEM-EELS tomography, multivariate statistical analysis and compressed sensing electron tomography [2].

Tomographic Techniques (electron tomography, atom probe tomography, atom counting tomography)

IM6.145
3D atomic scale characterization of twin boundaries in Au nanocrystals

B. Goris[1], T. Altantzis[1], G. Van Tendeloo[1], S. Bals[1]

[1]EMAT, University of Antwerp, Antwerp, Belgium

bart.goris@uantwerpen.be

A precise three dimensional (3D) characterization of the atomic lattice in nanocrystals is crucial for a thorough understanding of their physical properties. Indeed, defects and small displacements at the atomic scale may have major impact on the catalytic properties of nanoparticles. Electron tomography is a technique to obtain 3D information based on a tilt series of 2D projection images and recently, different approaches have enabled the extension of the resolution up to the atomic scale. [1-3]

Here, we characterize the atomic structure near planar defects such as twin boundaries in 3D. Therefore, we applied a tomographic reconstruction technique which is based on compressive sensing (CS). [3] During the reconstruction, no prior knowledge about the crystal lattice is exploited enabling us to measure small deviations from a perfect crystal lattice. In this manner, we investigated Au nanodumbbells containing twin boundaries perpendicular to a [111] direction. Figure 1a presents a high resolution high angle annular dark field (HAADF) scanning transmission electron microscopy (STEM) projection image of a Au nanodumbbell. A more detailed image of the region surrounding the twin boundary is presented in Figure 1b. In order to obtain a 3D reconstruction of the atomic arrangement around the twin boundary, different high resolution HAADF-STEM projection images are acquired. For each projection, the Au dumbbell was oriented along a [110] zone axis by tilting the specimen over 60º around a tilt axis perpendicular to the twin boundary. The projection images are then used as an input for the CS based reconstruction algorithm. A visualization of the 3D reconstruction of the Au nanodumbbell is presented in Figure 1c**.** Three orthogonal slices through the reconstruction, clearly demonstrating the atomic lattice, are displayed in Figure 1d**.** A more detailed analysis of the twin boundary can be obtained from the magnified region of the stacking sequence as displayed in Figure 1e, indicating that the twin boundary indeed acts as a mirror plane. In addition, it can be observed that the twin boundary is apparent through the volume of the crystal and, as a result, it separates two similar crystals with mirror symmetry between them.

Although a 3D reconstruction is obtained from a Au nanodumbbell having one twin boundary, it is expected that the applied methods can be extended for the 3D characterization of multiply twinned nanoparticles as well, yielding a complete understanding of the connection between the 3D displacement field at the atomic scale and the catalytic properties of multiply twinned nanoparticles.

1. S. Van Aert et al., Nature 470 (2011) 374-377
2. M.C. Scott et al., Nature 483 (2012) 444-447
3. B. Goris et al., Nature Materials 11 (2012) 930-935
4. The authors acknowledge support from the European Research Council (ERC Grants # 24691-COUNTATOMS and #335078-COLOURATOMS) and from the Flemish Fund for Scientific Research.

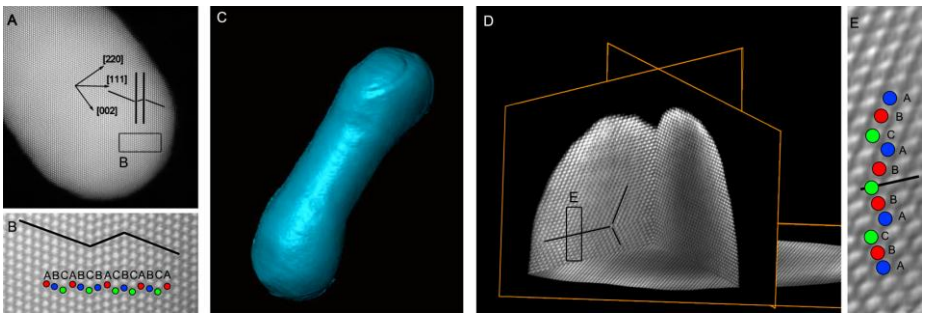

Figure 1. (A) HAADF-STEM projection image of Au nanodumbbell containing two parallel twin boundaries. (B) Magnified region showing the lattice stacking near the twin boundaries. (C) Visualization of the 3D reconstruction of such a Au nanodumbbell. (D) Three orthogonal slices through the 3D reconstruction revealing the atomic lattice. (E) Magnified region as indicated in (D) displaying the stacking sequence in 3D.

Tomographic Techniques (electron tomography, atom probe tomography, atom counting tomography)

IM6.146
Compressed sensing approaches for multi-dimensional electron microscopy

Z. Saghi[1], M. Benning[2], R. Leary[1], P. Midgley[1]

[1]University of Cambridge, Department of Materials Science and Metallurgy, Cambridge, United Kingdom
[2]University of Lübeck, Institute of Mathematics and Image Computing, Lübeck, Germany

saghizineb@gmail.com

Electron tomography (ET) coupled with dynamic and/or spectroscopic dimensions has recently gained considerable interest thanks to the advent of microscopes with unprecedented analytical and in-situ capabilities [1-3]. These information-rich imaging modes are however often subject to long acquisition times and electron dose, and smart scanning strategies and reconstruction algorithms have to be employed.

In this work, we explore novel acquisition and recovery strategies for ET experiments with random STEM pixel subsampling and reduced number of tilt series projections. An organic/inorganic CoPC/ZnO core-shell nanowire (NW) was used as a test object. The sample was dispersed on a commercial TEM grid possessing a 5 nm-thick carbon film on a thicker 30 nm holey carbon film (Pacific Grid Tech). Using a probe-corrected TITAN microscope (FEI) operating at 300 kV, a NW oriented parallel to the rotation axis was selected, and a HAADF-STEM tilt series was acquired from -70˚ to +68˚ with 2˚ increment. Random subsampling patterns were generated following Bernoulli distribution, and used as masks over the fully sampled projections. Experimentally, this set-up simulates a reduction in dose (and acquisition time) per image, without altering the signal-to-noise ratio of the sampled pixels. Total Variation (TV) inpainting [4] was then employed to restore the images, and tomographic reconstruction using a limited number of projections was performed by CS-ET [5]. A reliable reconstruction from data constituting a dose reduction of 10x was successfully achieved, corresponding to a 30% image downsampling and a 6˚ tilt increment [6].

The combination of these novel acquisition schemes and image recovery strategies provides new avenues to reduced-dose and high-speed imaging, and encourages the practical implementation of random STEM pixel subsampling [7].

1. P.A. Midgley and J.M. Thomas. **Angew. Chem. Int. Ed.** 2014, 53 (33), 8614-8617.
2. G. Haberfehlner, A. et al. **Nanoscale** 2014, **6,** 14563-14569.
3. O.-H. Kwon and A.H. Zewail. **Science** 2010, 328 (5986), 1668-1673.
4. X. Zhang et al. S. **J. Sci. Comput.** 2011, 46(1), 20-46.
5. R. Leary et al. **Ultramicroscopy** 2013, 131, 70-91.
6. Z. Saghi et al., **Adv struct chem imaging** 2015, *accepted.*
7. The research leading to these results has received funding from the European Union Seventh Framework Programme under Grant Agreement 312483 - ESTEEM2 (Integrated Infrastructure Initiative-I3), as well as from the European Research Council under the European Union's Seventh Framework Programme (FP/2007-2013)/ERC grant agreement 291522 - 3DIMAGE.

Tomographic Techniques (electron tomography, atom probe tomography, atom counting tomography)

IM6.147
Crystallite and particle shape of επ-Fe_2O_3: comparison of results obtained from diffraction and tomography

P. Brazda[1], L. Palatinus[1], C. Kübel[2], M. Klementova[1]

[1]Institute of Physics of the Czech Academy of Sciences, v. v. i., Department of structure analysis, Prague, Czech Republic
[2]Karlsruhe Institute of Technology, Karlsruhe Nano Micro Facilty, Eggenstein-Leopoldshafen, Germany

petr.brazda@seznam.cz

ε-Fe_2O_3 crystallizes in an orthorhombic crystal system and its structure is described in the space group P*na*2_1 [1]. This ferric oxide polymorph is interesting due to its 2 T coercivity at room temperature [2]. The phase is stable only on nanoscale. The most frequent preparation method uses a confinement of the ε-Fe_2O_3 nanocrystals within amorphous SiO_2 matrix. Using pure SiO_2 matrix is reported to produce nearly spherical crystals (2D projections in TEM images) [3, 4], while doping with Sr or Ba leads to rod-like particles elongated along *a*-axis [2]. Profile analysis of the diffraction maxima of the X-ray powder diffraction data obtained on our samples lead to the conclusion that the crystallites adopt disc-like rather than spherical shape with aspect ratio of about 1.5 [5]. We have also discovered using HR-TEM technique that the ε-Fe_2O_3 nanoparticles contain structural defects.

Therefore, we have performed tomography measurements, which were supposed to give us the information about the physical dimensions of the particles, their size distribution and a mean size, which we could compare with the average length of the coherently diffracting domain obtained from the XRPD experiments. The chosen sample was Fe_2O_3/SiO_2 nanocomposite with 30 wt. % of Fe_2O_3. The phase composition obtained from XRPD data was 90(2) % of ε-Fe_2O_3, 1(1) % of α-Fe_2O_3, 3(1) % of β-Fe_2O_3, and 6(1) % of γ-Fe_2O_3. The coherently diffracting domain lengths of the polymorphs were 20(1) nm for ε-Fe_2O_3 and below 5 nm for γ-Fe_2O_3. Those of the α-Fe_2O_3 and β-Fe_2O_3 were fixed to 37 nm during the Rietveld refinement.

The reconstruction of the density from the tomographic data was done using Simultaneous iterative reconstruction technique (SIRT) and the alignment of tilt series was done with a help of fiducial markers (Au particles with diameter of 6 and 15 nm). The SIRT reconstructed density generally suffers from the missing wedge artefacts (in our case the elongation ratio was 21 %) and a density increase towards the centre of the reconstructed object with the largest problems at the surface of the object (Figure 1). These artefacts prevented us from the extraction of the desired information from the reconstructed density by setting a general density threshold. Therefore, we decided to write a programme, which uses a gradient map for the estimation of the border of the Fe_2O_3 particles. The algorithm searches for the surface of the particles by locating the gradient maxima closest to the user-provided particle seed (point in the gradient map, which lies within a particle). Generally, setting the particle seed is the only human interference with the evaluation process. More serious problem represents the elongation due to the missing wedge. Using the gradient map for the evaluation, the elongation ratio was reduced twice - from 21% to about 10 %. This is, however, just an estimation, and comparison with simulated data will be necessary to exactly quantify the improvement. Advantage of this approach is that the results are not biased by human interference. The most outstanding advantage of the use of the gradient map is the removal of the "increasing density artefact", which prevents setting the real particle boundaries using density threshold.

The shape of the particles is more or less flattened disc, *i.e.* similar to the shape of the crystallites obtained from XRPD data. The volume-weighted diameter of the particles was 26.4 nm (calculated as $d = (\pi V/6)^{1/3}$ and corrected for the elongation artefact). With the sphere approximation, this corresponds to the length of the coherently diffracting domain of 19.8 nm, which is in very good agreement with the length obtained from XRPD (20(1) nm). We may then conclude that the defects in e-Fe_2O_3 have no significant effect on the length of the coherently diffracting domain.

1. E. Tronc et al. *J. Solid State Chem.*, **139** (1998) 93-104
2. J. Jin et al. *Adv. Mater.* **16(1)** (2004) 48-51
3. P. Brázda et al. *J. Sol-Gel Sci. Technol.*, 51 (2009) 78-83
4. M. Gich et al. *Faraday Discuss.* **136** (2007) 345-354

5. P. Brázda et al. to be published in 2015
6. The work was supported by CSF, project number P204/10/0035.

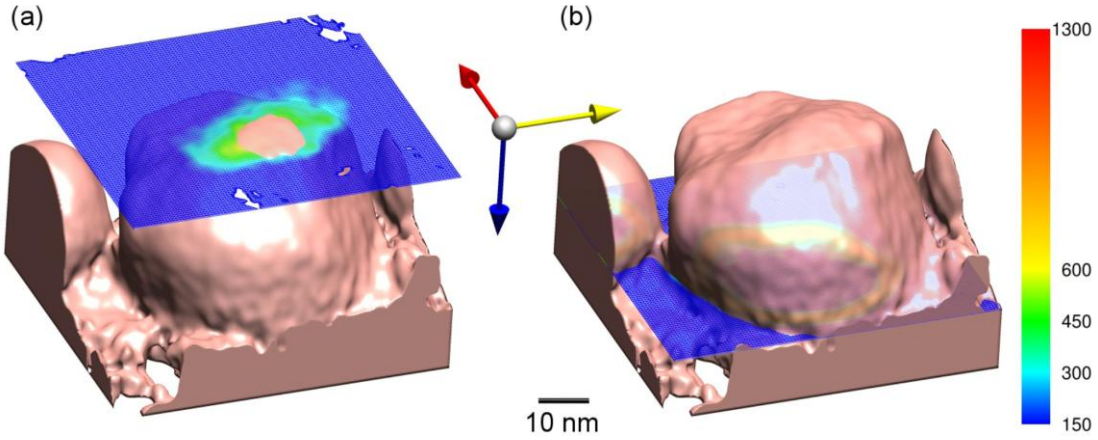

Figure 1. Comparison of threshold (pink) and gradient (sections, colour scale on the right) definition of iron oxide particle boundaries. (a) Threshold is set to coincide with gradient boundary at the surface of nanocomposite. (b) Divergence of the two boundary definitions when moving inside the nanocomposite. Blue arrow coincides with electron beam direction and red arrow represents tilt axis.

Tomographic Techniques (electron tomography, atom probe tomography, atom counting tomography)

IM6.148
Tomographic reconstruction of thick sections from biological samples in Cs/Cc corrected TEM

R. R. Schröder[1]

[1]Cryo EM, CellNetworks, BioQuant, Universitätsklinikum Heidelberg, Heidelberg, Germany

Imaging of whole cells at electron microscopic resolution and obtaining their 3D reconstruction has been a long standing driving force for testing novel and unconventional TEM and STEM imaging modalities [1,2]. Recent studies used C_s/C_c corrected TEMs to obtain 3D reconstructions of the cellular ultrastructure from thick plastic sections of cells [3] or the distribution of nano-particles in whole mount cells [4]. Both these studies made use of all scattered electrons to record images, i.e. it is expected, that elastic as well as inelastic scattering events contribute to sample contrast. This is of particular interest as the ratio of elastic to inelastic and also multiple scattering will change from image to image in the recorded tilt series. This should affect the image formation processes as well as the coherence of the imaging electrons. It is therefore not trivial to interpret object contrast quantitatively and at present conventional reconstruction algorithms may not yield high-resolution 3D reconstructions. In fact it is unclear what level of resolution can be obtained for such samples and first results may be interpreted in such a way that resolution will deteriorate depending on sample thickness and position of the object in the sample [4].

To complicate things the real interest for whole cell TEM imaging in biology derives from the perspectives to image and to reconstruct cryo-fixed cells [5]. In contrast to the studies mentioned above using C_s/C_c correction for imaging of heavy metal stained samples or metal nano-particles, cryo-samples rely solely on phase contrast. Taking into account results from electron holography [6], it might – however - not be impossible to retrieve the phase contrast signal from C_s/C_c corrected images.

To better understand this novel imaging process we analyze in detail image formation in the case of elastic-inelastic multiple scattering. Examples of the differences between corrected and uncorrected imaging of thick samples will be discussed. First data will be shown on phase contributions to the contrast of objects embedded in thick plastic layers and imaged at typical Plasmon loss energies.

1. McEwen et al. PNAS 83 (1986) 9040.
2. Sousa et al. J Struct Biol 174 (2011) 107.
3. Wacker et al. Microsc Microanal 16(Suppl2) (2010) 972.
4. Baudoin et al. Microsc Microanal 19 (2013) 814.
5. Medalia et al. Science 298 (2002) 1209.
6. Röder & Lichte, Eur J Phys Appl Phys 54 (2011) 33504.
7. The contribution will review the recent advances in this area rather than focus on one particular study. The author therefore acknowledges the contribution of a large number of collaborators, in particular B. Kabius and N. Zaluzec as the scientists operating the Cs/Cc-corrected TEM at Argonne National Laboratory, Argonne, USA.

Figure 1. X,y-slices through a tomographic 3D reconstruction volume of a 600 nm thick plastic section of conventionally embedded tissue material (mouse neuromuscular junction) recorded at 80 keV primary electron energy. Slices are 2.5nm thick in z-direction (incident electron direction), the field of view is about 5x5 μm^2, cf [3].

Tomographic Techniques (electron tomography, atom probe tomography, atom counting tomography)

IM6.149
Cryo-STEM tomography of intact vitrified cells provides morphological and analytic information simultaneously

S. G. Wolf[1], P. Rez[2], D. Kirchenbuechler[3], Y. Mutsafi[4], B. Horowitz[4], L. Houben[1], D. Fass[4], M. Elbaum[3]

[1]Weizmann Institute of Science, Chemical Research Support, Rehovot, Israel
[2]Arizona State University, Department of Physics, Tempe, United States
[3]Weizmann Institute of Science, Department of Materials and Interfaces, Rehovot, Israel
[4]Weizmann Institute of Science, Department of Structural Biology, Rehovot, Israel

sharon.wolf@weizmann.ac.il

Tomography of intact, vitrified cells and tissues is an integral part of a multidimensional approach to structure/function studies in cell biology. Tomography using zero-loss energy-filtered transmission electron microscopy (zl-cryoTEM) allows for 3D imaging of vitrified tissue with sample thickness below ~400 nm. This limitation is due primarily to inelastic scattering, which causes a severe loss of signal at the energy filter for specimens thicker than the inelastic mean free path. Low dose conditions essential to work with delicate biological specimens preclude compensation with higher exposure.

We recently demonstrated that cryo-scanning transmission electron tomography (CSTET) provides tomographic reconstructions of vitrified cells with superior information transfer at high tilts and for thicker specimens than defocus phase contrast (Wolf *et al.*, 2014). In the STEM mode there are no image forming lenses after the electron beam passes through the sample. Detection is incoherent and the contrast loss due to inelastic scattering is not substantial. This is especially important for the light elements whose inelastic scattering cross-section is larger than the elastic. Electron dose is used more efficiently to achieve high signal-to-noise reconstructions. Moreover dynamic focusing of the rastered beam provides in-focus imaging even far from the tilt axis.

Figure 1 shows a comparison between zl-cryoTEM and CSTET reconstructions of *Agrobacterium tumefaciens*. It is clear from the figure that the CSTET provides enhanced contrast without the need for low-pass filtering, nor does it contain the fringing that characterizes far-from-focus conditions needed for cryoTEM imaging of thick vitrified specimens. The very dark dense bodies seen in the cells are poly-phosphate bodies (PPBs), which store inorganic phosphorous. The STEM modality allows for selection of data collection from specific scattering angle ranges, and thus it is possible to highlight phosphorous or other heavy atoms embedded in biological specimens, and indeed even to quantify the amount of that element (Wolf *et al.*, 2015), similar to Z-contrast imaging used by materials scientists. By selection of detector angle specific for phosphorous scattering, ribosomes are highlighted in tomographic reconstructions of intact vitrified fibroblast cells (Figure 2). Cell hierarchal structure is revealed in these tomograms (Kirchenbuechler *et al.*, 2015), and it is expected that dual-axis data collection will significantly improve the data quality.

1. Kirchenbuechler, D., Mutsafi, Y., Horowitz, B., Fass, D., Wolf, S. G. & Elbaum, M. (2015) Cryo-STEM tomography of intact vitrified fibroblasts. *submitted*.
2. Wolf, S. G., Houben, L. & Elbaum, M. (2014) Cryo-scanning transmission electron tomography of vitrified cells. *Nat Methods,* **11,** 423-428.
3. Wolf, S. G., Rez, P. & Elbaum, M. (2015) Phosphorus detection in vitrified bacteria by cryo-STEM annular dark field analysis. *submitted*

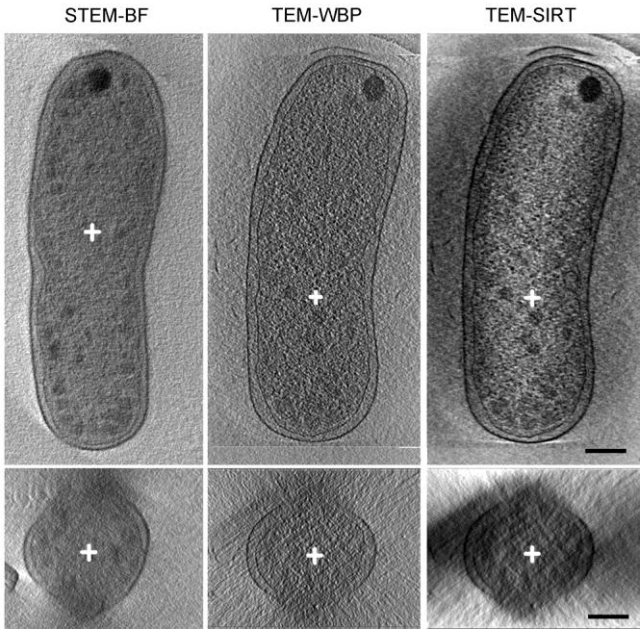

Figure 1. Comparison of CSTET and zl-cryoTEM tomographic reconstructions of *Agrobacterium tumefaciens* cells taken on a Tecnai F20 Twin microscope at 200kV. Left: 20-nm-thick reconstructed xy and xz sections of tilt series of 84 images taken to ±65° using the BF detector. Sampling at 4.0 nm/pixel, total cumulative exposure 115 electrons/Å^2. Middle and right panels: 20-nm-thick sections of a zl-cryoTEM reconstruction. The dataset had 81 images, each with exposure 1 electron/Å^2, over a range of ±62°, sampling 2.6 nm/pixel, cumulative exposure 80 electrons/Å^2. Reconstructions were done by weighted back-projection (WBP) (middle panel) and SIRT (right panel) techniques. White crosses indicate identical positions in the xy and xz sections. Scale bar, 200 nm.

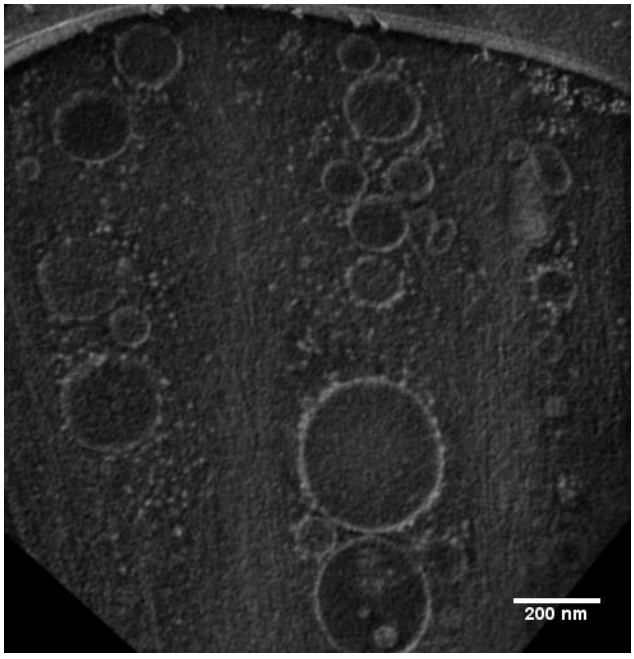

Figure 2. CSTET tomographic reconstruction of a vitrified human fibroblast cell. Tilt series recorded to ±70° using a BF detector (intensity inversed for display purposes). Sampling at 2.9 nm/pixel, and total cumulative exposure 103 electrons/Å^2. Volume rendering of 25 slice sections (73 nm thick) of the cell parallel to the substrate.White dots are identified as ribosomes, with enhanced intensity due to high phosphorous content. Scale bar 200 nm.

Tomographic Techniques (electron tomography, atom probe tomography, atom counting tomography)

IM6.P150
From macropores to mesopores: three-dimensional morphology of hierarchical porous solids by combination of FIB slice&view and STEM tomography

D. Stoeckel[1,2], C. Kübel[3], B. Smarsly[2], U. Tallarek[1]

[1]Philipps-University, Department of Chemistry, Marburg, Germany
[2]Justus-Liebig-University, Institute of Physical Chemistry, Giessen, Germany
[3]KIT, INT, Eggenstein-Leopoldshafen, Germany

christian.kuebel@kit.edu

Hierarchical porous silica monoliths have for some time been used in chromatography and heterogeneous catalysis as an alternative to other fixed bed structures. Their distinctly bimodal pore size distribution is essential to the performance of the silica monoliths as solid support. A continuous network of macropores (~2 µm) enables liquid transport at high flow rates without necessitating high pressures, while the nanometer-sized mesopores provide a high surface area for sufficient contact between chemicals and the stationary phase (for separation or catalysis) immobilized on the fixed bed.

The porous structure of the monoliths are typically characterized using bulk techniques such as mercury intrusion porosimetry and nitrogen physisorption to provide pore size information, which however can only be interpreted accurately if a good model is known for the pore network. The structure of the disordered macroporous network has been started to be accessed by confocal laser scanning microscopy [1], but no accurate description of the mesoporous structure has been obtained so far. This provides a major challenge for tailoring the morphological properties of the mesoporous adsorbents for their intended use in catalysis or separation.

Here we demonstrate the 3D reconstruction and characterization of the complete morphology of a silica monolith, from macropores to mesopores, by advanced electron microscopy techniques. The 3D macropore space has been imaged by FIB slice & view techniques and the 3D mesoporous structure has been reconstructed from HAADF-STEM tomography tilt-series. Based on the three-dimensional reconstructions, we performed a comprehensive statistical analysis to extract the cord length distribution and pore tortuosity/coordination number as key structural parameters relevant to mass transport at the macropore and mesopore level (Fig. 1) [2]. The reconstructed model is also the starting point for simulations of flow, mass transport [3], sorption and reaction which aim at a fundamental understanding of the morphology-transport relationships of hierarchically structured, disordered materials. This approach has been systematically applied to a series of monoliths to study the correlation between synthesis conditions, domain size and structural homogeneity (Fig. 2) [4].

1. S. Bruns, T. Hara, B. M. Smarsly, U. Tallarek, J. Chromatogr. A 2011, 1218, 5187-5194.
2. D. Stoeckel, C. Kübel, K. Hormann, A. Höltzel, B.M. Smarsly, U. Tallarek, Langmuir, 2014, 30, 9022-9027
3. D. Hlushkou, K. Hormann, A. Höltzel, S. Khirevich, A. Seidel-Morgenstern, U. Tallarek, *J. Chromatogr. A* 2013, 1303, 28-38.
4. D. Stoeckel, C. Kübel, M. Loeh, B. Smarsly, U. Tallarek, Langmuir, 2015, online; DOI: 10.1021/la5046018.

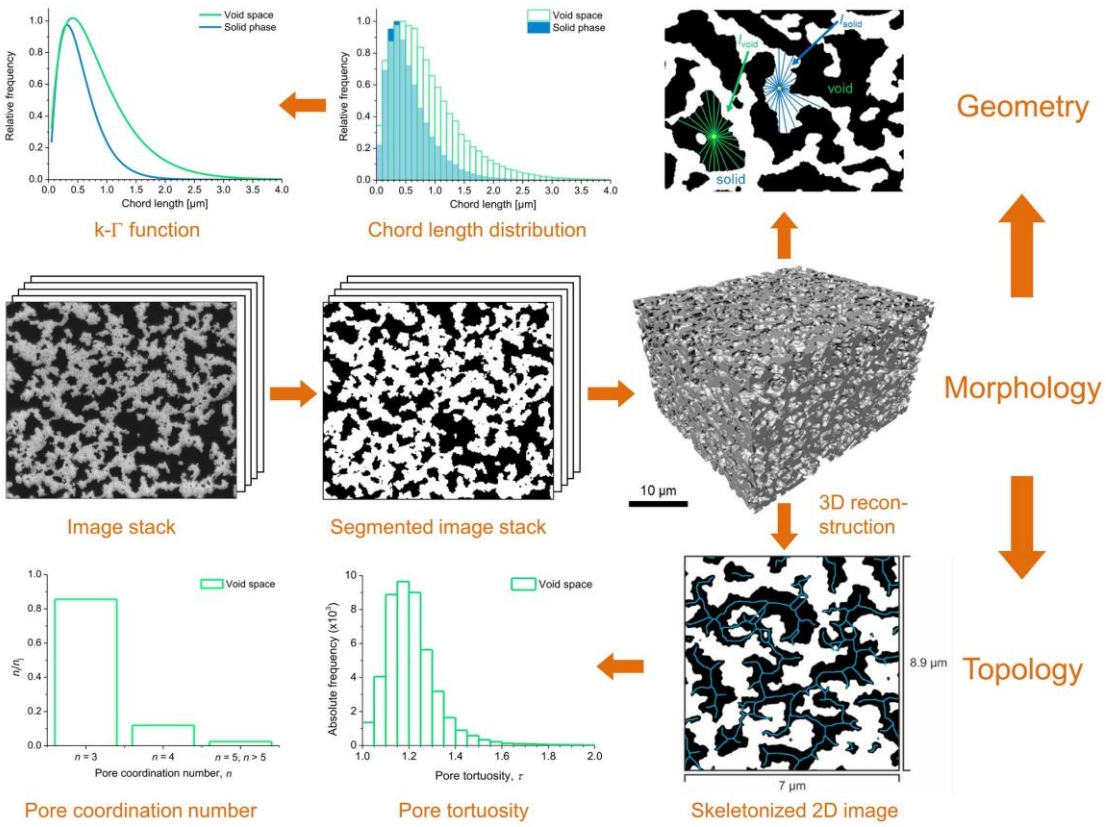

Figure 1. Illustration of the analytical work flow for a quantitative description of the macro- and mesoporous structure (from Ref [4]).

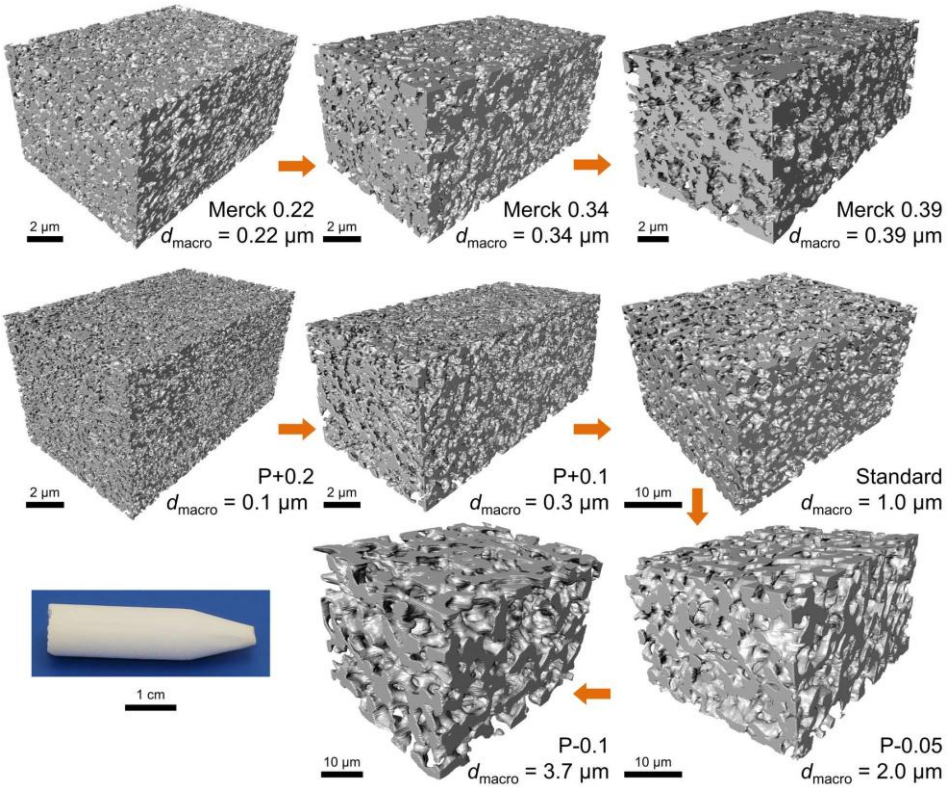

Figure 2. Three-dimensional reconstruction of the macropore space of various silica monolith samples with decreasing average macropore size (from Ref [4]).

Tomographic Techniques (electron tomography, atom probe tomography, atom counting tomography)

IM6.P152
Unscrambling mixed elements in HAADF STEM imaging

K. H. W. van den Bos[1], P. D. Nellist[2], S. Van Aert[1]

[1]University of Antwerp, Department of Physics, Antwerp, Belgium
[2]University of Oxford, Department of Materials, Oxford, United Kingdom

karel.vandenbos@uantwerpen.be

High angle annular dark field scanning transmission electron microscopy (HAADF STEM) imaging is a popular material's characterisation technique, sensitive to both chemical and structural information. A powerful tool for the quantitative evaluation of these images is the so-called scattering cross-section; corresponding to the total intensity of scattered electrons in each atomic column [1-4]. The use of this performance measure has enabled the visualisation of 3D atomic structures of monotype crystalline structures [2,4]. Applications in hetero-nanostructures are currently limited because of the lack of methods to quantitatively unscramble mixed elements. In order to help solving this problem, a model has been derived for predicting scattering cross-sections of mixed columns.

For monotype crystalline structures the 3D atomic structure can be reconstructed by determining the number of atoms for each atomic column [2,4]. Here, the monotonic increase of scattering cross-sections with atomic column thickness is used. For hetero-nanostructures containing mixed columns counting the number of atoms is more complicated due to the presence of coherent effects. As a result, scattering cross-sections depend on the specific configuration of mixed columns [5], such as the depth location of an impurity atom in a column (Fig. 1). To quantitatively extract the composition, and possibly even the configuration, experimental images need to be compared with image simulations of each column configuration. Since such image simulations are time-consuming, the availability of a model to predict scattering cross-sections as a function of composition, configuration and thickness is desirable. In the simplest model the scattered intensity of an atomic column is written as the sum of the scattered intensities of the individual atoms constituting this column. Therefore, channelling is neglected in this model leading to large deviations (Fig. 2). Furthermore, it also neglects the information about the configuration of the column. A more accurate prediction is obtained based on the principles of the channelling theory in which it is assumed that each atom acts as a lens focussing the electrons on the next atom [6]. Here, the lensing factors of the individual atoms in monotype atomic columns are calculated to predict the scattering cross-sections of mixed columns. This new approach leads to a significant improvement in the prediction of scattering cross-sections which is not restricted to number of atom types (Fig. 2) or detector angles (Fig. 3).

In conclusion, scattering cross-sections of mixed columns can be accurately predicted which opens up new possibilities to unscramble the 3D arrangement of atoms in complex hetero-nanostructures.

1. Van Aert *et al*., Ultramicroscopy **109** (2009), p. 1236
2. Van Aert *et al*., Nature **470** (2011), p. 374
3. E *et al*., Ultramicroscopy **133** (2013), p. 109
4. Jones *et al.*, Nano Letters **14** (2014), p. 6336
5. Martinez *et al.* Ultramicroscopy **137** (2014), p. 12
6. Van Dyck *et al.* Ultramicroscopy **64** (1996), p. 99
7. The authors acknowledge financial support from the Research Foundation Flanders (FWO,Belgium) through project fundings (G.0393.11N, G037413N, G.036915N and G.036815N) and a Ph.D. research grant to K.H.W. van den Bos. The research leading to these results has also received funding from the European Union Seventh Framework Programme [FP7/2007- 2013] under Grant agreement no. 312483 (ESTEEM2).

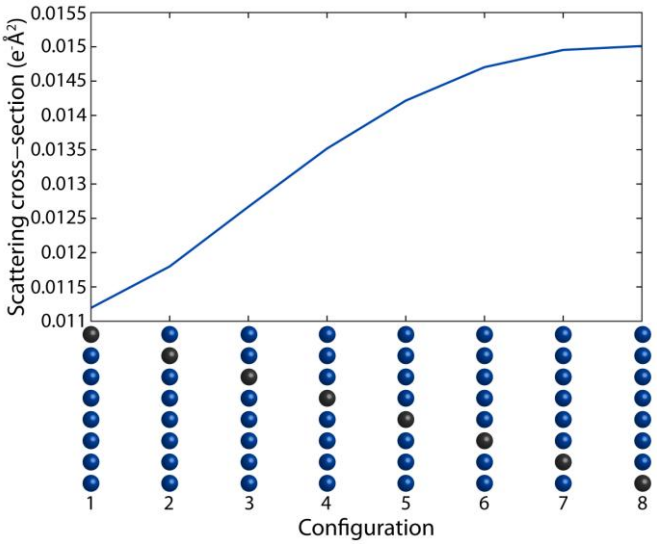

Figure 1. The scattering cross-section scales with the depth location of a single Pt impurity atom in an atomic column ofCo.

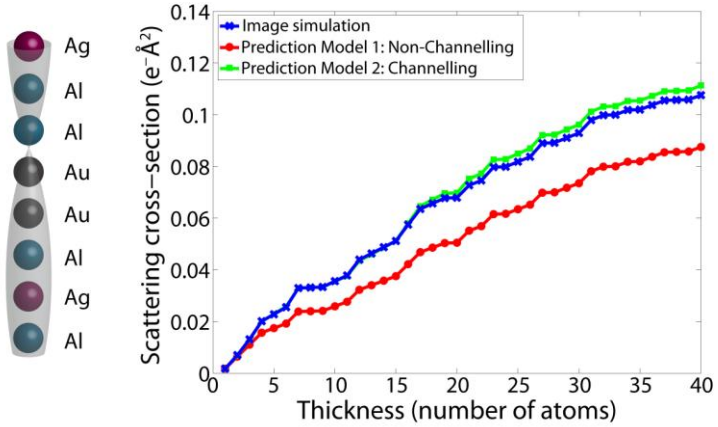

Figure 2. Scattering cross-sections of a column containing Al, Ag and Au atoms in a random ordering are calculated by using image simulations, a non-channelling and a channelling based model.

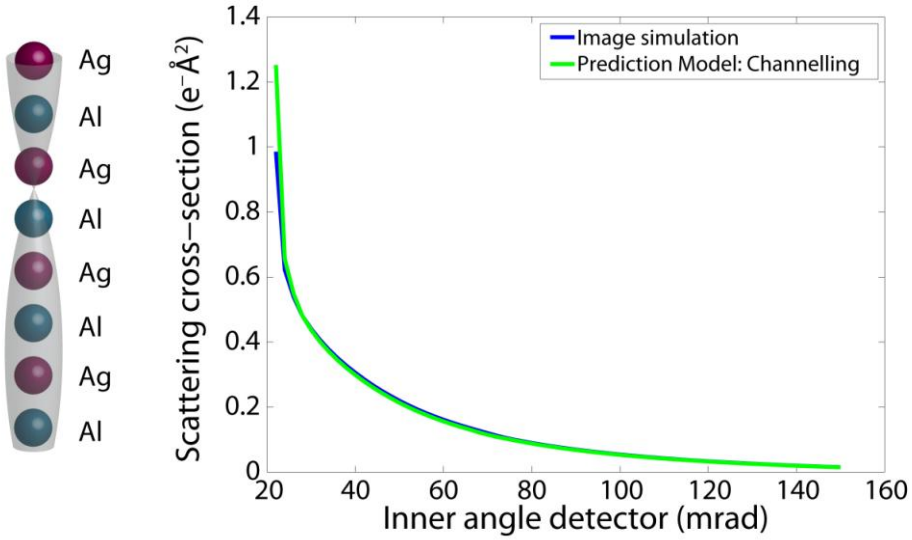

Figure 3. Scattering cross-sections of a column of 50 atoms containing alternating Ag and Al atoms are calculated for an inner detector angle varying from 22 to 150 mrad. The outer angle was kept constant at 200 mrad.

Tomographic Techniques (electron tomography, atom probe tomography, atom counting tomography)

IM6.P153
3D atomic electron tomography for CeO_2 nano-crystal

L.- G. Chen[1], A. I. Kirkland[2], D. V. Dyck[3], F.- R. Chen[1]

[1]National Tsing Hua University, Engineering and System Science, Hsinchu, Taiwan
[2]University of Oxford, Materials , Oxford, United Kingdom
[3]University of Antwerp, Physics, Antwerp, Belgium

liu31448@gmail.com

Transmission electron microscopy (TEM) has been well recognized for its power in spatial resolution to the sub-Å level, especially, with aberration-corrected optics [1,2]. However, the ultimate goal of electron microscopy is not only to obtain nice images but also to advance materials science. This means that EM has to evolve from describing to understanding materials properties. It is well-known that all the structure-property relations are encoded in the positions of the atoms and the shape of particle, specially, in the case of catalysts and biological species. The future EM is then to be considered as a communication channel between object and observer and the images as data planes from which the 3D atom positions and the shape of the sample can be extracted quantitatively. Although, with the newest generation of Cs corrected EM's the resolution is sufficient to resolve the individual atoms and to refine their position with picometer precision. The drawbacks of high resolution TEM are two folds. First, it gives only 2D projected structural information. And second, the passband of the lens transfer at the low spatial frequencies is very poor and such that the information about shape is lost.

In this report, we intend to determine the three-dimensional structure of a nanocrystalline object-Cerium oxide at atomic resolution. For nanocrystalline object, there are two levels of coupled structural signal in exit wave, the shape and the atomic structure, which are the targets to be retrieved in order to correlate the structure-property of the nano-object. The exit wave of CeO_2 is reconstructed from a focal series of HRTEM images. The modulus of the reconstructed exit wave is shown in Fig.1. By back / forward propagating the wave through the space with sub-angstrom defocal steps, the position of atomic columns can be determined. Wave back propagation method describes the fact that the propagated intensities decreases with the distance away from the exact focus position. The maximum intensity occurs at the exact in-focus position, so that intensity distribution along defocal axis forms "cigar" shape (Fig.2). The atomic column's vertical position of thick specimen therefore can be traced out by wave back propagation method. The Big-bang theme [3] is then applied to refine defocus of surface.

The thickness of atomic columns could be carried out by phase value of wave. The mass of each atomic column can be calibrated by the mean inner potential and the vacuum wave. Based on these methods, the three dimensional reconstructed model with atomic resolution is proposed.

The preliminary results of reconstructed CeO_2 tomogram is shown in the Fig.3.

1. Haider, M., et al., A spherical-aberration-corrected 200 kV transmission electron microscope. Ultramicroscopy, 1998. **75(**1): p. 53-60.
2. Urban, K., et al., A way to higher resolution: spherical-aberration correction in a 200 kV transmission electron microscope. Journal of Electron Microscopy, 1999. **48(**6): p. 821-826.
3. Van Dyck, D., J.R. Jinschek, and F.R. Chen, 'Big Bang' tomography as a new route to atomic-resolution electron tomography (vol 486, pg 243, 2012). Nature, 2012. **489(**7416): p. 460-460.

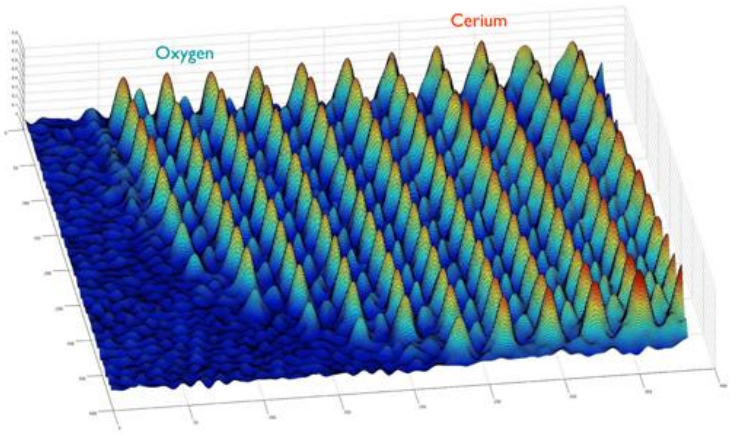

Figure 1. Modulus of reconstructed exit wave of CeO_2. The Exit wave is reconstructed from a focal series of TEM images .

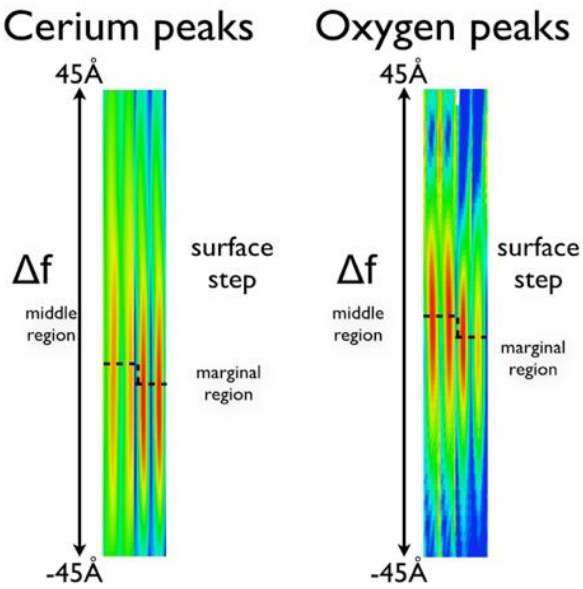

Figure 2. Cigar plot for nanocrystal.

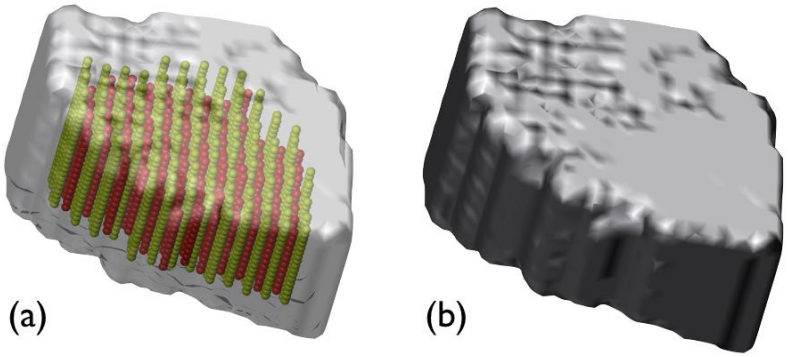

Figure 3. The preliminary reconstructed CeO_2 tomogram, (a) atomic model (b) shape and surface morphology of nano-crystal.

Tomographic Techniques (electron tomography, atom probe tomography, atom counting tomography)

IM6.P154
Incorporating fresnel propagation into electron holographic tomography

J. Krehl[1], A. Lubk[1]

[1]TU Dresden, Triebenberg Laboratory, Dresden, Germany

jonas.krehl@triebenberg.de

Electron Tomography (ET), combined with the multitude of signals available in Transmission Electron Microscopy (TEM), makes for a versatile technique, able to reconstruct local quantities from projections and with that the three-dimensional distributions and structures. The capabilities of ET have been demonstrated in a variety of applications from cell structures to nanoparticles. Its resolution, however, is currently limited due to the approximations in the reconstruction methods. There are ongoing efforts to develop new methods in order to reach atomic resolution.

In essence, tomographic methods invert the scattering process (which maps the object information to a measurable signal) so that the object can be reconstructed from the given signal. The information of a single image is usually insufficient and multiple measurements with varying parameters (e.g. by tilting the specimen) are needed. Mathematically, this is an inverse problem, which are rather difficult to treat. It is advantageous to have a linear model for the signal, as linear inverse problem theory offers general theorems for crucial characteristics, like the stability of the reconstruction, which are not available in the nonlinear case.

Electron Holographic Tomography (EHT) is commonly based on an approximation that the phase of the exit wave is given by an integral of the electric potentials along straight paths. This Phase Grating Approximation (PGA) is, therefore, a linear mapping, but equates to neglecting any propagation effects during transmission through the specimen. As the Fresnel Propagator scales with (propto k^2) ((k) being the lateral spatial frequency) this neglection becomes critical whereever high scattering angles are significant (as is the case in high-resolution and low-order zone-axes imaging). In consequence, while the PGA has proven to be an adequate approximation at medium resolution, it causes artifacts in atomic-resolution imaging [1], rendering it unusable.

These considerations raise the question wether linear approximations which incorporate the propagation of the wave can be found. We propose and compare such approximations, where the potential is integrated over an extended kernel (see figure), related (at least in analogy) to the convolution formulation of Fresnel Propagation. As we demand linearity in the specimen potentail, these models must neglect mutliple scattering, which makes them inappropriate in low-order zone-axes.With the extended kernel it is also no longer possible to separate the three-dimensional problem along the tilt axis into a stack of two-dimensional problems, making the reconstruction computationally much more challenging than conventional methods.

Using the Direct Algebraic Reconstruction Technique and a conjugate gradient method on a cylindrical grid we are able solve problems of practical dimensions on a fairly standard computer. We will compare several approximations in terms of their derivation, implementation and performance using simulated tilt series. From these deliberations we estimate the quality required of holographic tilt series in practical applications as that is the ultimate goal.

1. J. Krehl und A. Lubk. Ultramicroscopy 150 (2015).

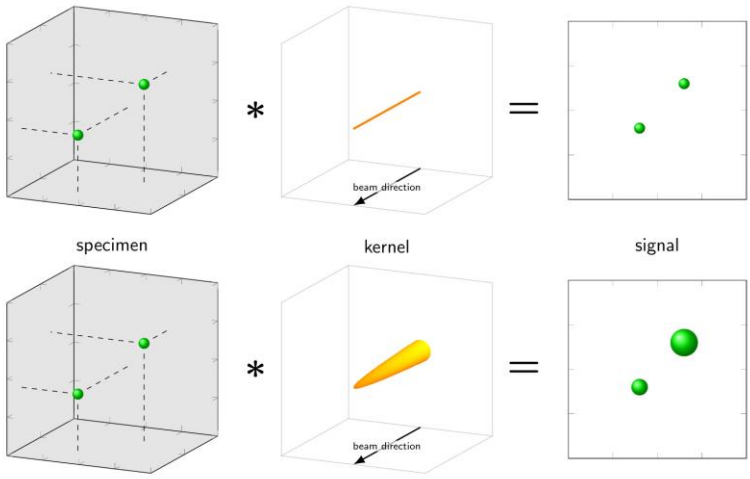

Figure 1. Signal formation model, as used in tomography, with a ray kernel (upper) and an extended kernel (lower), at a specimen made up of two “atoms”, for a single specimen orientation. Here, the conical hape of the extended kernel causes a sense of depth in the signal.

Tomographic Techniques (electron tomography, atom probe tomography, atom counting tomography)

IM6.P155
Transfer of individual micro- and nanoparticles for 360° electron tomography

T. Przybilla[1], B. Winter[1], A. M. Beltrán[1], A. G. Machoke[2], A. Inayat[2], B. Butz[1], W. Schwieger[2], E. Spiecker[1]

[1]Institute of Micro- and Nanostructure Research & Center for Nanoanalysis and Electron Microscopy (CENEM), Department of Materials Science and Engineering, Friedrich-Alexander-Universität Erlangen-Nürnberg, Erlangen, Germany
[2]Institute of Chemical Reaction Engineering, Friedrich-Alexander-Universität Erlangen-Nürnberg, Erlangen, Germany

thomas.przybilla@fau.de

Particles with sizes in the nm- and µm-range are used in diverse fields of research and application such as catalysis, drug delivery, sensing or optoelectronics [1]. As the particle design rises in complexity, a detailed characterization of their properties like crystallinity, chemistry/phase distribution or morphology becomes indispensable in order to understand and prospectively design functionality. Complementary to other electron-microscopic techniques, 360° electron tomography (ET) enables a high precision 3D analysis of micro- and nanoparticles without so-called "missing wedge" artefacts known from conventional ET [2]. This technique necessitates rod-like specimens enabling a 360° rotation with constant projected thickness and therewith imaging conditions. Concerning the preparation of individual nanoparticles, this sample geometry was realized by, e.g., cutting thin pillars out of embedded [3] or covered [4] nanoparticulate samples using focused ion beam (FIB) milling, or by dispersion of particles in solution onto tips [5]. The drawbacks of these techniques are that no particular particle can be chosen for the later analysis and that there is usually the need for embedding material or protective layers for protection against ion beam irradiation during pillar preparation.

In this work, a methodological approach is presented that provides a general recipe to *in situ* transfer of individually selected, specific micro-/nanoparticles onto tailored tips for 360° ET investigation using a dual-beam FIB instrument or even a simple scanning electron microscope (SEM) equipped with a suitable micromanipulator. A dedicated, electron-transparent tomography tip with a plateau diameter matching the respective particle, which was beforehand milled by FIB, is used to pick a selected particle from a suitable sample grid directly by a "stamping" method (cf. Fig. 1). The tomography tip with the particle is then used to acquire a full tilt-angle range series in the transmission electron microscope.

The transfer technique and subsequent 360° ET are demonstrated for two classes of particles with different orders of magnitude - micro- and macroporous zeolite (MFI-type) particles with sizes in the µm-range (cf. Fig. 2) [6] and mesoporous alpha-hematite nanoparticles exhibiting particle sizes of 50-100 nm. The proposed method is applicable using every FIB/SEM instrument and enables a damage- as well as contamination-free preparation (no protective layer needed) of samples. Especially the latter aspect is advantageous not only for 360° ET but also for other complementary characterization techniques like atom probe tomography, optical near field measurements or, more general, applications which address the measurement of physical properties of individually selected micro- or nanoparticles.

The authors gratefully acknowledge the financial support of the "Deutsche Forschungsgemeinschaft" (DFG) within the framework of the SPP 1570 (project DFG SP 648/4-1 ''3D analysis of complex pore structures using ET and high-resolution TEM'') and the graduate school GRK 1896 ("*In situ* Microscopy with Electrons, X-rays and Scanning Probes") as well as through the Cluster of Excellence ''Engineering of Advanced Materials'' at the Friedrich-Alexander-Universität Erlangen-Nürnberg (Germany).

1. T. Wang et al., New J. Chem. 2014, 38, 46-49.
2. V. Novák et al., Chem. Eng. J. 2014, 248, 49-62.
3. X. Y.Wanget al.,Ultramicroscopy2012, 113, 96-105.
4. M.Hayashidaet al.,Ultramicroscopy2014, 144, 50-57.
5. K. Jarausch et al., J. Electron Microsc. 2009, 58, 175-183.
6. A. G. Machoke et al., Adv. Mater. 2015, 27, 1066-1070.

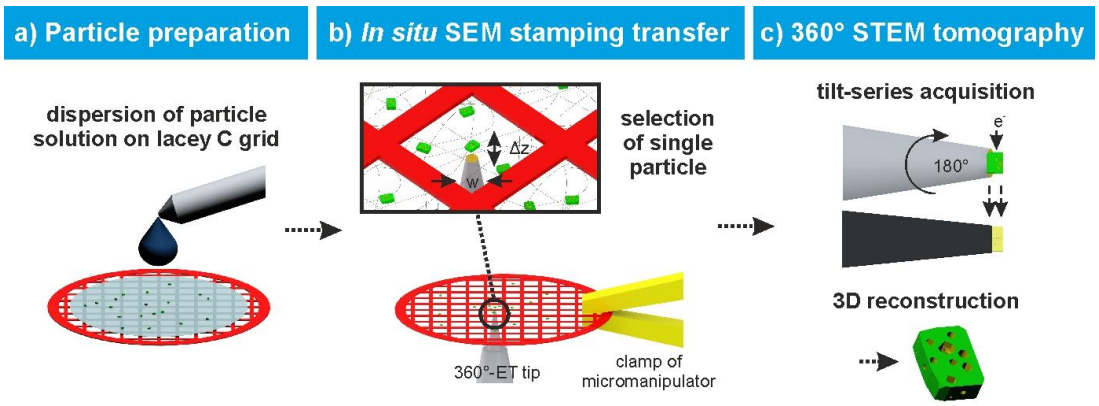

Figure 1. Scheme illustrating preparation and selective *in situ* transfer technique for 360° ET of individually selected micro-/nanoparticles enabling high precision 3D-analysis. Tip width *w* is tailored to fit the particle size and distance *Δz* is reduced to approach the particle with the tip.

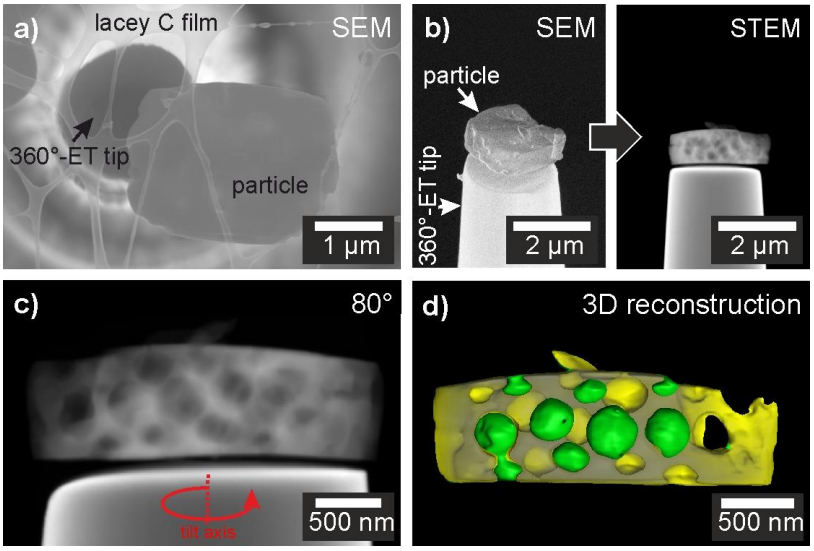

Figure 2. (a-b) Experimental flowchart of the particle transfer technique in the SEM and (b-c) 360° STEM tomography of a single selected micro- and macroporous zeolite particle. (d) Slice through the 3D reconstruction (surface rendering - surface facing towards the pore space in green and the particle in yellow).

Tomographic Techniques (electron tomography, atom probe tomography, atom counting tomography)

IM6.P156
Correlating genomics, proteomics and function through 3-D cryo-TEM of intact environmental microbial cells

L. R. Comolli[1], B. Luef[2]

[1]ALS-Molecular Biology Consortium, ALS-LBNL, Berkeley, CA, United States
[2]University, Biotechnology, Trondheim, Norway

lrcomolli@lbl.gov

Although cryogenic transmission electron microscopy (cryo-TEM) has been available for many years, it has rarely been applied to environmentally-relevant organisms. This in part due to the difficulty in preparing cryogenic TEM samples from microorganisms that cannot be cultured. Cryo-TEM has already changed our view of microbial cell architecture, and cryogenic electron tomography (cryo-ET) is becoming a more widely used technique worldwide. Consequently, there is a potential interest in using this technology as an approach to study environmental microbial systems. These systems are challenging because they are often remote, not possible to culture, difficult to transport artifact-free and intact, and "dirty" of minerals and nanoparticles although such particles contribute to their interest. Here we demonstrate that these obstacles can be overcome. Our results include unprecedented cryo-TEM and cryo-ET image data on intact cells and microbial communities from environmental sites for which genomics and proteomics data are available. Correlative high resolution imaging of intact microbial communities integrated with metagenomics and proteomics data can help us understand metabolic states, inter-species relationships, the role of bacteriophage infections and the adaptive responses to external stress. We have established unprecedented interactions and cytoplasmic connections across species in the well characterized AMD community. These first successful applications of cryo-TEM to microorganisms within the in-situ context of their mutual interactions and extracellular minerals open the way to similar studies in many other relevant model and environmental systems in microbial ecology, Geomicrobiology, and plant or biomedical microbial communities.

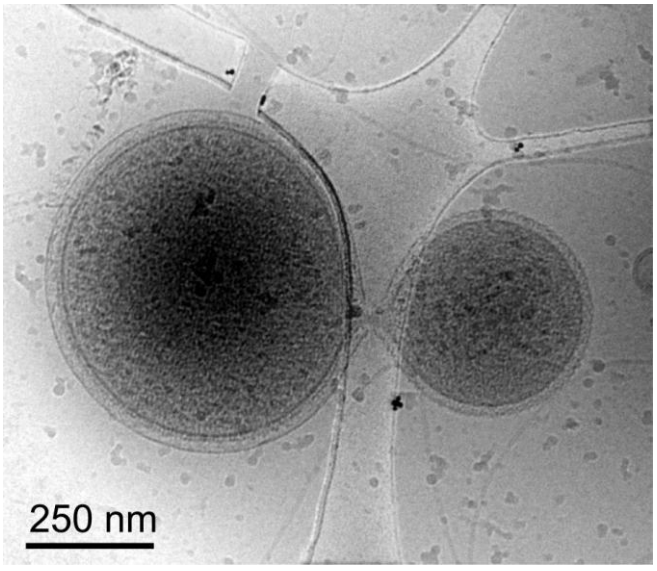

Figure 1. *Inter-species interaction between ARMAN and a Thermoplasmatal cell through a cytoplasmic bridge or synapse-like connetion.* 2D cryo-TEM projection showing a "synapse-like" structural connection between an ARMAN cell, left (gram negative-like cell wall), and a *Thermoplasma* "bud" with an S-layer-like outer surface surrounding the plasma membrane.

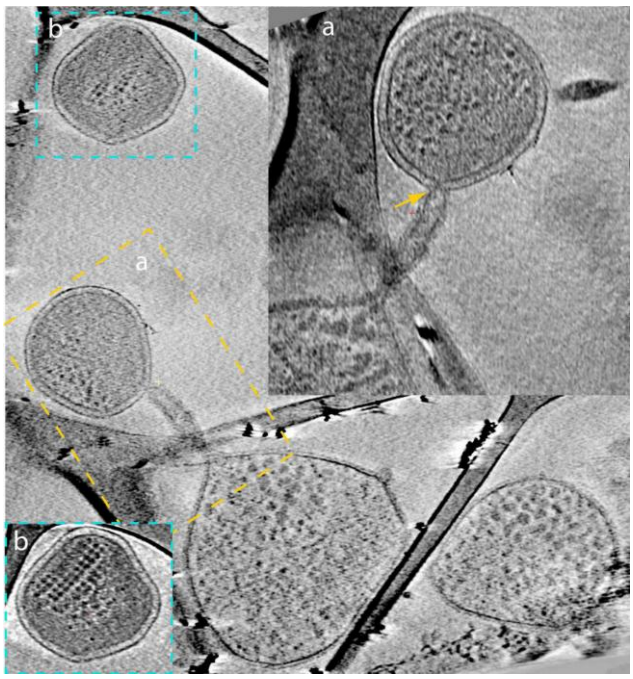

Figure 2. *ARMAN - Thermoplasmatales inter-species associations and viral infection processes. Slices from a 3D cryo-ET reconstruction.* A *Thermoplasmatal* cell and an ARMAN cell -enclosed within the dash yellow box, are connected through a remarkable tubular appendage; the region within the dash yellow box is magnified as inset (a) in a slice at a different angle. The cell within the blue box has very regular ladder-like series of high contrast elements, putative polysomes.

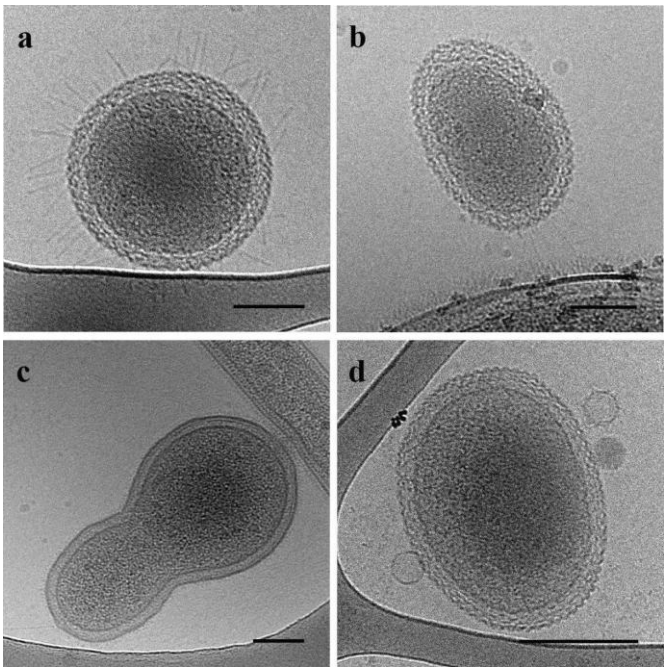

Figure 3. *Cryo-TEM images (2D) documenting the size and some morphological features of ultra-small bacteria.* The cell wall has a novel architecture, with a remarkable and distinct surface layer. Two types of pili are discernible: numerous radiating pili cover the surface of the cells in **a)** and **b**), apparently connecting it to an adjacent bacterium (only top surface shown). **c**) A dividing ultra-small bacterium in contact with a Spirocheate cell. Three bacteriophages are associated with the surface of the cell in (**d**). Scale bars are all 100 nm.

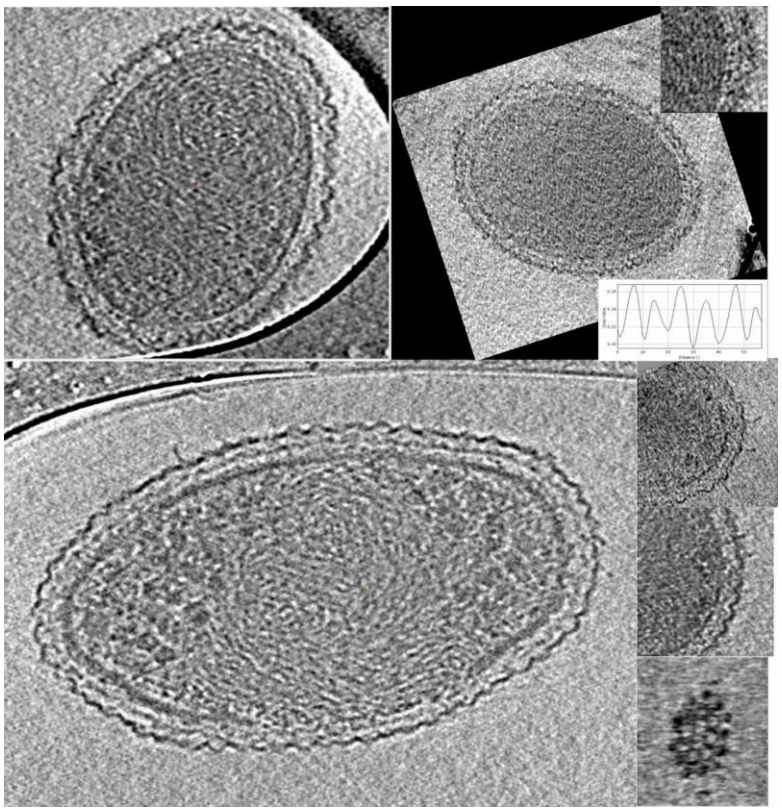

Figure 4. *Cryo-electron tomography (cryo-ET) 3D reconstructions of nanobacteria.* All panels are slices from 3D reconstructions, revealing a very dense cytoplasmic compartment and a complex cell wall enveloped by a periodic surface layer. The high contrast sub-cellular bodies in left, top and bottom panels are putative ribosomes. The 3D slice shown in the top right panel contains a feature of periodic line densities at 5.6 nm consistent with a toroidal genome. Bottom right small panels show the appendages covering the cell surface and the hexagonal pattern of the surface layer. See prior and next images for scales.

Tomographic Techniques (electron tomography, atom probe tomography, atom counting tomography)

IM6.P157
Characterization of $LiMn_2O_4$ with laser assisted atom probe tomography

B. Pfeiffer[1], J. Arlt[1], J. Maier[1], C. Nowak[1]

[1]Georg-August-University Göttingen, Institute of Materials Physics, Göttingen, Germany

bpfeiffer@ump.gwdg.de

Manganese dioxides are extensively studied as cathode material for Li-ion batteries. Understanding ionic conductivity and the detailed mechanisms of phase transitions is crucial to obtain further insights into the conversion between electrical and chemical energy in Li-ion batteries. Current experimental data is often obtained with methods characterizing transport on a macroscopic scale or as ensemble property, but particularly along with phase transitions transport can be strongly localized. In order to meet these requirements, atom probe tomography (APT) and related techniques can be used to obtain spatially resolved information on the chemical composition and ionic transport with sub nm resolution [1, 2].

Especially in connection with APT, due to the ionic conductivity of lithiated manganese dioxide, the influence of the measurement parameters has to be considered. Temperature and the electrostatic field present during analysis can have a crucial effect on the mobility of lithium within the manganese dioxide framework. This can lead to a change in local composition or even, due to the positive electrostatic potential of the sample during analysis, to in-situ delithiation of specimens. Therefore, the choice of parameters not only affects the result of the experiment but can determine the kind of the experiment itself and two limiting cases are conceivable: either lithium is completely immobile and the atom probe measurement takes place as usual or pure delithiation occurs and only lithium will be field evaporated, while the framework of manganese and oxygen remains unchanged.

Here, we present laser assisted APT studies on $LiMn_2O_4$. Modifying the experimental conditions (e.g. sample temperature, laser intensity and evaporation rate) strongly affects the mobility of lithium. This enables to select parameter sets where delithiation dominates the measurement or where lithium shows only limited mobility in the Mn_2O_4 framework and the material is characterized. The transition between these two regimes, possible reaction mechanisms and the reliability of the results will be discussed.

1. G. Schmitz et al., *Z. Phys. Chem.* **224**, 1795 (2010).
2. C. Escher et al., *Phys. Rev. Lett.* **97**, 136601 (2006).

Tomographic Techniques (electron tomography, atom probe tomography, atom counting tomography)

IM6.P158
Determination of the Ga penetration during FIB machining using atom probe tomography and ToFSIMS

U. Muehle[1], J. Huang[2], M. Loeffler[2], A. Than[2], L. Kwakman[3], H. Mulders[3], E. Zschech[1,2]

[1]Fraunhofer IKTS-MD, Micro- and nanoevaluation, Dresden, Germany
[2]Technische Universität Dresden , Dresden Center for Nanoanalysis (DCN), Dresden, Germany
[3]FEI Inc., Building AAE, Eindhoven, Netherlands

uwe.muehle@ikts-md.fraunhofer.de

Typical features in leading-edge semiconductor devices, like FET gate lengths, are decreasing currently below 20nm [1]. Process development and control in semiconductor industry require cross-section analysis of such nano-devices using Transmission Electron Microscopy (TEM). Due to the required target preparation, Focused Ion Beam technique (FIB) is the way to prepare the TEM lamellae. However, material damage has to be mitigated [2]. Damage phenomena are structural damage and complete amorphization in a near-surface range of the TEM lamellae up to 20nm for silicon, when applying an acceleration voltage of Ga ions of 30kV [3]. This penetration of Ga-ions into the material changes the materials properties significantly [4]. The reduction of the acceleration voltage during the final preparation steps leads to a significant reduction of the thickness of this damaged layer.

Atom Probe Tomography (APT), as one of the methods to determine elemental distributions on base of direct detection of implanted atoms, was applied to study the depth profile of the Ga concentration. The samples for APT were also prepared using FIB, applying parameters in terms of angle, currents, etc,which are close to the final steps of the preparation applied at a semiconductors analysis with advanced requirements [5]. The 3D-distribution of Ga-atoms (figure 1) enables to extract depth profiles at different locations (figure 2). The concentration profile of Ga in Si is shown at the edge up to a depth of about 10 nm, where the concentration decreases about 1.5 orders of magnitude.

Time-of-Flight Secondary Ion Mass Spectroscopy (ToFSIMS) was applied to study the Ga penetration for a larger area [6]. An extended field of view of 50 µm x 70 µm improves the counting statistic, reduces the influence of the shape of the ion trajectories and enlarges the depth profile up to 4 orders of magnitude. The effect of different acceleration voltages at the final FIB polish step is shown in figure 3.

The results of both approaches are in a good agreement for the near-surface region, where APT provides reliable results. The results are in coincidence with the predictions of simulations using an advanced TRIDYN [7] approach [8].

1. ITRS-Roadmap;http://www.itrs.net/ITRS%201999-2014%20Mtgs,%20Presentations%20&%20Links/2013ITRS/2013TableSummaries/2013ORTC_SummaryTable.pdf; last call: 24.03.2015
2. Giannuzzi, L.A., Stevie, F.A.; Introduction to Focused Ion Beams - Instrumentations, Theorie, Techniques and Practice; Springer Science + Business Media, Inc.; 2005
3. Engelmann, H.-J., Volkmann, B., Ritz, Y., Saage, H., Stegmann, H., de Robilfard, Q., Zschech, E.;, Microscopy Today 11 (2003) issue 2, 22-24
4. Lenk, A., Muehle, U., Lichte, H.; Why does a p-doped area show a higher contrast than a n-doped area of same dopant concentration?; Microscopy of Semiconducting Materials XIV 2005; Oxford/UK; Springer Proceedings in Physics Volume 107 (2005), 213-216
5. Huang, J., Loeffler, M., Muehle, U., Moeller, W., Mulders, H., Kwakman, L., Zschech, E.; A Study of Gallium FIB induced Silicon Amorphization using TEM, APT and BCA Simulation; Microscopy & Microanalysis; Portland (OR) 2015; submitted
6. Mühle, U., Steinhoff, J., Hillmann, L.; Influence of FIB-acceleration Voltage on Lateral Damage of Silicon based TEM-samples; Poster zur Microscopy Conference 2007; 2.- 7.9.2007 Saarbruecken
7. Moeller, W., Eckstein, W., Biersack, J.P., Computer Physics Communications 51 (1988), 355-368
8. Huang, J. et al; in preparation

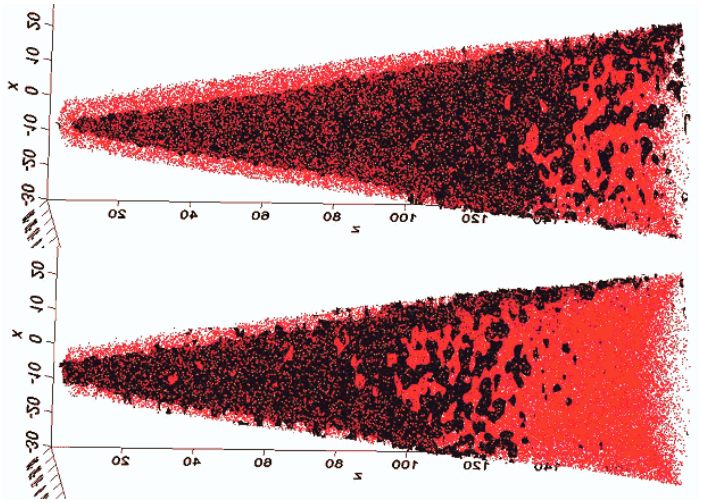

Figure 1. Visualistion of Ga-distribution in an APT-needle of Si as plot of isoconcentration surface of 0.5% Ga (up) and 1.5 % Ga (low)

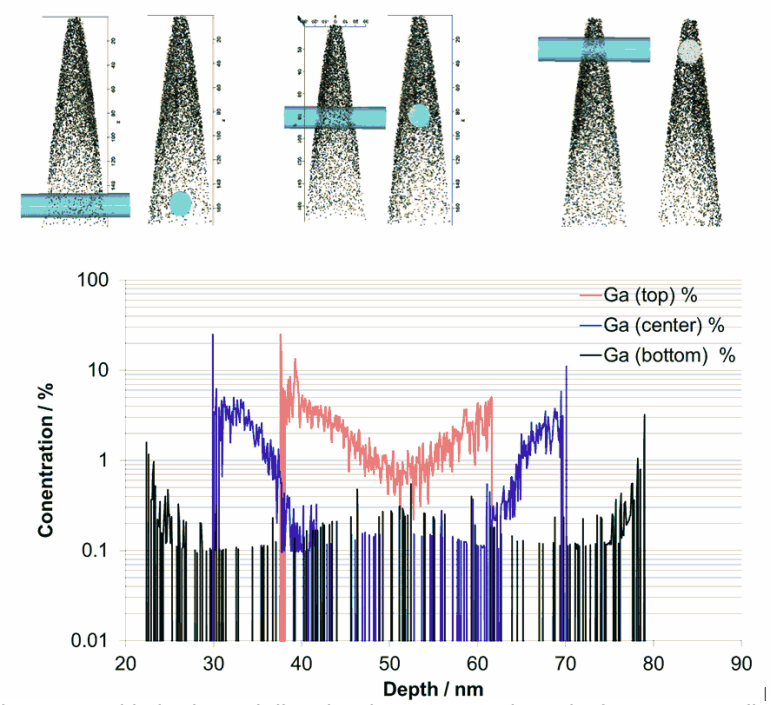

Figure 2. Ga depth profile extracted in horizontal direction (see upper scheme) of an APT needle-shape sample

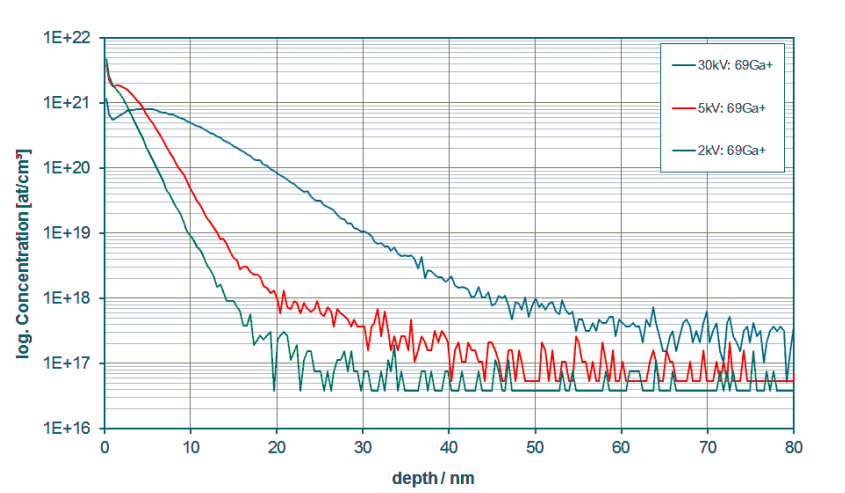

Figure 3. Lateral Ga penetration due to FIB milling for several acceleration voltages, measured by ToFSIMS

Tomographic Techniques (electron tomography, atom probe tomography, atom counting tomography)

IM6.P159
Structure and composition study of steel alloys by atom probe

A. Savenko[1], U. Breuer[1]

[1]Forschungszentrum Jülich (FZJ), Zentralinstitut für Engineering, Elektronik und Analytik, Jülich, Germany

a.savenko@fz-juelich.de

Atom probe tomography (APT) is a powerful method to observe distribution of atoms within a small volume of the analyzed sample. Positions of atoms can be determined with precision about 1 nm in lateral direction and 0.5 nm in longitudinal direction of the sample. Recent instrument developments significantly improved performance of APT method. Detection efficiency increased to 80%, that is the fraction of ions that reach detector in respect to all evaporated ions from the sample. Application of 355 nm UV laser helps to localize heating at the apex of the sample and to increase energy absorption efficiency for many materials. Larger field of view (up to 150 nm depending on the material) is capable for analysis of bigger volumes of the sample. All these improvements resulted in the latest instruments of LEAP 5000 series from Ametek Inc. However presented work was carried out at LEAP 4000X HR setup that is equipped with reflectron for mass spectrometry at higher resolution (HR).

Application of APT towards steel research is capable to provide important information that is not achievable by other analytical methods. FeCr steel alloy available at the market as Crofer22H was investigated in this work. It may contain up to 15 additional elements according to specification. The main of which are Si and W. The areas of interest were precipitates and inhomogeneous inclusions of other phases that differ from the matrix material in composition and crystal structure. These inclusions are formed during fabrication and/or exploitation of the steel and influence on properties (creep resistance, oxidation, etc.). APT was used to determine concentrations of chemical elements within precipitate and matrix, to calculate profiles of elements distribution. Ultimately the combination with complementary methods (e.g. SIMS, SEM, TEM, EDX, WDS and EELS) often provides a “bridge” to chemical and structural parameters at sub-atomic scale as well as macro scale.

APT samples were prepared in the shape of needle with tip radius about 30-40 nm and shank half angle 7-11°. Focused ion beam setup Helios 600i equipped with Omniprobe was utilized for preparation. Microtips were mounted onto a standard silicon coupon with flat-top posts. The length of the piece of the sample was about 2 mm. Only top conical part 100-500 nm long can be analyzed that is limited by the too high electric field reached during measurement.

Placing of the precipitate inside the fabricated microtip is not a trivial task, considering the fact that the size of precipitates was 0.1-2.0 mm and imaging contrast in SEM during sample preparation is not very strong. Back scattered electron detector was used to determine location of inclusions, while later a regular secondary electron detector was used to track position of inclusion during sample fabrication. Preliminary FIB cross-sections were very helpful to determine orientation of inclusion inside the volume and to select appropriate region the most interesting for analysis.

Nonhomogenities in sample composition result in variation of evaporation conditions during the APT measurement. For example W inclusions require significantly higher evaporation field comparing to Fe, namely 52 V/nm versus 33 V/nm. Thus conditions for ions formation at the surface of microtip are varied during the measurement. Such variations cause difficulties in 3D reconstruction of the measured volume and create regions with higher/lower density of detected ions. Usually special data treatment procedures are applied to the data set to smoothen the density. Manual control and tuning of measurement conditions (i.e. evaporation field) was considered as an opportunity to mitigate this problem as well as to reduce background noise and improve detection limit for low concentrations.

Better understanding of Croffer22H steel structure was attained within conducted research. Basing on the functional role of each chemical element within alloy a future improvement of exploitation qualities and optimization of steel fabrication is expected to be achieved.

Tomographic Techniques (electron tomography, atom probe tomography, atom counting tomography)

IM6.P160
Distribution of layered-silicate nanocomposites in polyamide fibers revealed by electron tomography

N. Wirch[1], R. Stolz[2], T. Vad[2], T. Gries[2], T. Weirich[1]

[1]University RWTH Aachen, GFE (Central Facility of Electron Microscopy), Aachen, Germany
[2]University RWTH Aachen, Institut für Textiltechnik, Aachen, Germany

wirch@gfe.rwth-aachen.de

Polymer nanocomposites based on layered silicates (clay) - *polymer layered-silicate nanocomposites (PLSN)* - have gained the most importance due to their nontoxic and environmental compatible nature of the nanoparticles.

In the present study we investigated cross-sections of elongated PA6 PLSN fibers containing different amounts of dispersed nanoclay particles by employing conventional TEM and electron tomography in order to link processing parameters with nanoparticle distribution and orientation.

Examination of the samples was carried out by either conventional TEM bright-field imaging or by recording tilt series succeeded by 3D volume reconstruction (electron tomography).

All of the results presented stem from a series of fibers with varying nanoclay concentration between 0.1 and 5 wt%. A detailed analysis of the images recorded from different regions across the fiber proves that the distribution of the nanoparticles is homogeneous along the fibers.

However, the orientation of the layered silicates within the cross-section clearly depends on the region within the fiber and is seemingly an indicator of the laminar streaming profile during the solidification of the fiber, *i.e.* particles near the fiber surface are oriented in radial direction while particles close to the core region are oriented more randomly and appear disordered (Fig. 1).

1. Financial support by DFG (Deutsche Forschungsgemeinschaft e.V.) within the project ‘Fiber Sage‘ is gratefully acknowledged. We thank Mrs. N. Fasold (ITA) and Mrs. M. Rohs (ITA) for TEM sample preparation and Mr. F. Mariano (GFE) for recording REM images.

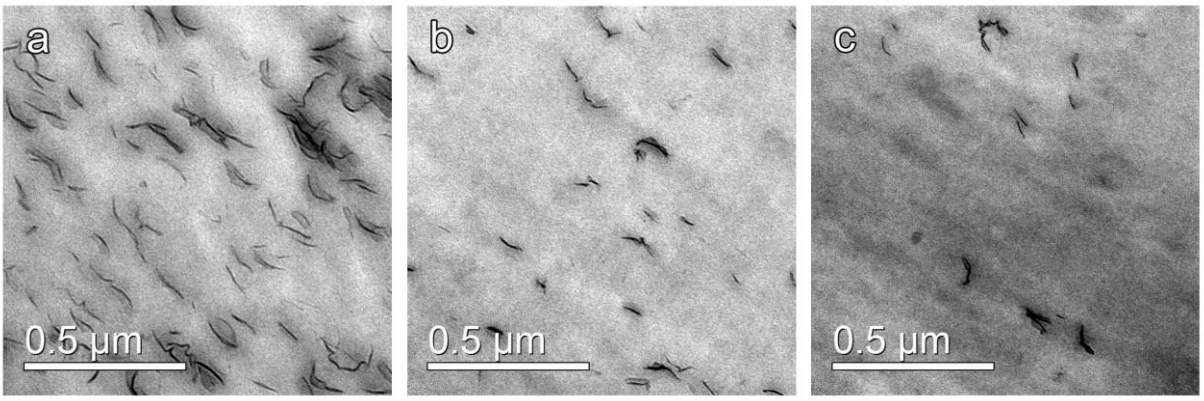

Correlative Microscopy in Life and Material Sciences (combination of several microscopy techniques)

IM7.161
Moving towards a single microscope for 3D light microscopy and 3D electron microscopy of cells and tissues

L. M. Collinson[1]

[1] Electron Microscopy Unit, Francis Crick Institute, London, UK

lucy.collinson@crick.ac.uk

Correlative light and electron microscopy (CLEM) combines the benefits of fluorescence and electron imaging, revealing protein localisation against the backdrop of cellular architecture. CLEM is usually performed by growing cells on gridded coverslips, imaging the cells (live or fixed) using confocal microscopy, preparing the cells for electron microscopy, relocating the cell position and plane for electron imaging of the fluorescent structure, selecting and modeling the 3D data in both modalities, and overlaying the two datasets to identify the structure of interest. This process usually requires collaboration with expert electron microscopists, and has sufficient steps and complexity to deter many researchers. Nevertheless, for those who commit to the process, there are rich rewards in the understanding of biological processes. Our recent work has focused on improving the speed, accuracy and accessibility of CLEM.

To image rare events in cells, tissues and whole model organisms, we developed Correlative Light and Volume EM (CLVEM), which combines correlative workflows with microscopes that automatically collect large stacks of high resolution images. The Serial Block Face Scanning Electron Microscope (SBF SEM) consists of a miniaturised ultramicrotome mounted inside the SEM chamber, which cuts resin-embedded samples using a diamond knife prior to imaging the exposed surface with the electron beam. Thousands of images can be aquired over a single day. This fast automated data acquisition allows us to move towards high throughput quantitative CLEM at a rate of one whole cell per day.

During this development work, it became clear that the technical challenges associated with CLEM are exaggerated when working in 3D. To increase protein localisation precision, we developed an 'In-Resin Fluorescence' (IRF) protocol that preserves the activity of GFP and related fluorophores in resin-embedded cells and tissues. The sample preparation is relatively fast, and also introduces electron contrast so that cell structure can be visualised in the electron microscope. Once the resin blocks have been cut into ultrathin sections, out-of-plane fluorescence is removed resulting in physical 'super-resolution' light microscopy in the axial direction, which increases the accuracy of the LM-EM overlays. Localisation precision is further increased by imaging the IRF sections *in vacuo* in the next generation of commercial integrated light and electron microscopes (ILEM). We are seeking to further improve accuracy by developing integrated super resolution light and electron microscopy, and implementing automated 3D imaging for 3D functional and structural analysis of whole cells and tissues at the nanoscale.

Correlative Microscopy in Life and Material Sciences (combination of several microscopy techniques)

IM7.162
Correlative microscopy with a laser-plasma soft X-ray microscope and a fluorescent microscope for biological imaging of live hydrated cells

M. Kado[1], M. Kishimoto[1], S. Tamotsu[2], K. Yasuda[2], M. Aoyama[2], S. Tone[3], K. Shinohara[4]

[1]Japan Atomic Energy Agency, Kyoto, Japan
[2]Nara Women's University, Nara, Japan
[3]Kawasaki Medical School, Okayama, Japan
[4]Tokai University, Kanagawa, Japan

kado.masataka@jaea.go.jp

A laser-plasma soft X-ray microscope which is combination of a highly intense laser-plasma soft X-ray source and contact microscopy has been developed. We have proposed a correlative microscopy with the laser-plasma soft X-ray microscope and a fluorescent microscope that is to observe the same biological cells with the both microscopes at the same time. Live hydrated biological cells and various cellular organelles of them have been observed with the correlative microscopy. Using the information of the cellular organelles obtained with the fluorescence microscope, inner structures obtained with the soft X-ray microscope are exactly identified. Since the spatial resolution of the soft X-ray microscope is much higher than that of the fluorescent microscope, fine structures of the cellular organelles of the live biological cells have been visualized with the correlative microscopy.

Shown in Fig.1 were a soft X-ray image (a) and a fluorescent image (b) of the live Leydig cells of mouse testis labeled with mito-tracker, DAPI and Phalloidin. Structures appearing in red color are mitochondria, blue are chromatin and green are actin filaments in the fluorescent image. Comparing the soft X-ray image to the fluorescent image of the same biological cells, cellular organelles such as mitochondria, chromatin and actin filaments in the soft X-ray image were exactly identified and fine structures of the cellular organelles were acquired. Shown in Fig.2 were the soft X-ray image (a) and the fluorescent image (b) of one of the cells in the Fig.1. In the both images nucleus and chromatin structure were clearly seen and the nucleus was surrounding by the bright structures in the soft X-ray image and red colored structures in the fluorescent image. Comparing both images those structures surrounding the nucleus in the soft X-rat image were identified as mitochondria and the mitochondria in the soft X-ray image appeared to be web-like structures. This result showed that the correlative microscopy with a laser-plasma soft X-ray microscope coupled with a fluorescent microscope had a potential to image fine structures of cellular organelle in a live biological cell without any artificial treatments.

1. M. Kado, M. Ishino, S. Tamotsu, K. Yasuda, M. Kishimoto, M. Nishikino, Y. Kinjo, and K. Shinohara, AIP Conf. Proc. 1365 (2011) 391.
2. M. Kado, M. Kishimoto, M. Ishino, S. Tamotsu, K. Yasuda, and K. Shinohara, AIP Conf. Proc. 1465 (2012) 246.
3. M. Kado, M. Kishimoto, S. Tamotsu, K. Yasuda, and K. Shinohara, J. of Phys.: Conf. Series 463 (2013) 012056-1.

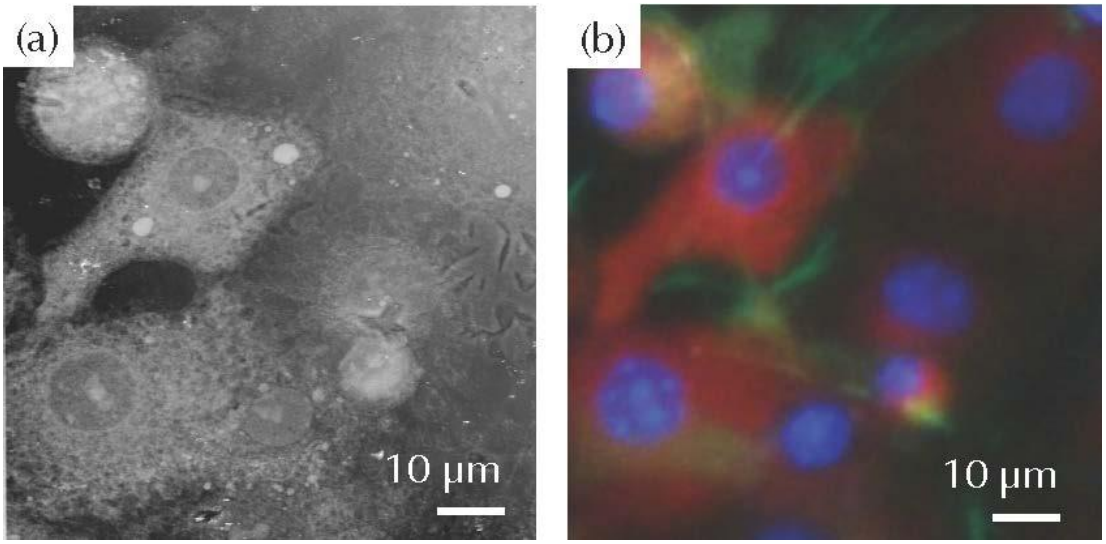

Figure 1. Soft X-ray image (a) and fluorescent image (b) of the live hydrated biological cells. Structures appearing in red color are mitochondria, blue are chromatin and green are actin filaments.

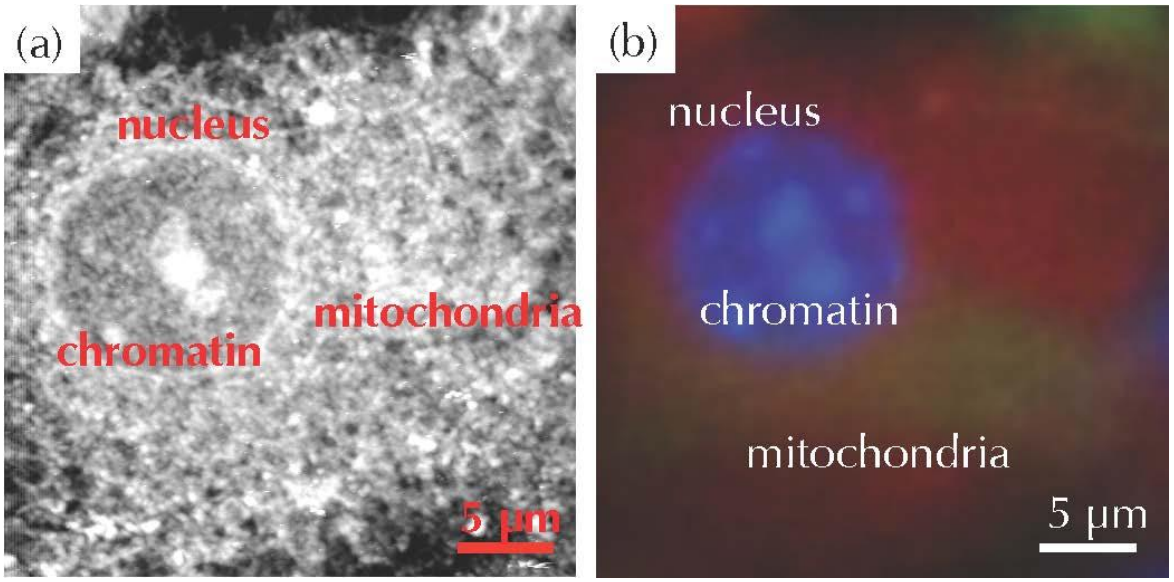

Figure 2. Soft X-ray image (a) and fluorescent image (b) of a live biological cell. In the both images nucleus and chromatin structure were clearly seen and the nucleus was surrounding by mitochondria.

Correlative Microscopy in Life and Material Sciences (combination of several microscopy techniques)

IM7.163
Ultrastructural analysis of insulin secretory granule ageing by super resolution and transmission electron microscopy

A. Müller[1], A. Ivanova-Cederström[1], C. Münster[1], T. Kurth[2,3], J.- M. Verbavatz[4], M. Solimena[1,4]

[1]Paul Langerhans Institute Dresden of the Helmholtz Zentrum München at TU Dresden, Molecular Diabetology, Dresden, Germany
[2]Center for Regenerative Therapie Dresden (CRTD), Dresden, Germany
[3]Biotechnology Center of the TUD, Dresden, Germany
[4]Max Planck Institute of Molecular Cell Biology and Genetics, Dresden, Germany

andreas.mueller8@mailbox.tu-dresden.de

Pancreatic beta cells store insulin within secretory granules (SGs). Hyperglycemia elicits beta cells to release insulin in two phases: a short and rapid first phase followed by a sustained second phase. Lack of the first phase of insulin secretion is a hallmark of type 2 diabetes. Notably, newly synthesized insulin SGs are preferentially released, but the molecular reasons for this phenomenon remain unclear. Thus, the characterization of SGs poised for exocytosis during the first phase of insulin secretion is of particular interest for understanding the physiology of healthy and diabetic beta cells.

We labeled insulin SGs of different age in beta cells of pancreatic islets isolated from SOFIA (Study ofinsulin aging) mice, in which an insulin2-SNAP allele had been knocked-in in the *Ins2 locus*. Isolated islets were kept in standard culture medium containing 5.5 mM glucose and labeled 24 hours after isolation for the detection of SG pools with ages ranging from several hours to 5 days. Combining structured illumination microscopy (SIM) and transmission electron microscopy (TEM) for correlative light-electron microscopy (CLEM) we precisely tracked age-distinct insulin SGs in Tokuyasu sections of beta cells. Since each beta cell contains ~ 5-6 $x10^3$ insulin SGs and in TEM sections 1-2 $x10^2$ SGs per cell can be seen, the precise correlation achieved here was pivotal for discriminating labeled from unlabeled SGs.

We have previously shown that a fusion construct between insulin and the SNAP tag is a reliable reporter for fluorescent labeling of age-distinct insulin secretory granules (SGs). In insulinoma Ins1 cells transiently transfected with hIns-SNAP we could demonstrate the preferential release of young insulin SGs (Ivanova et al., 2013) and the degradation of old SGs into multigranular bodies (MGBs) (Hoboth et al., 2015). Accordingly, we found a significant decrease in the number of labeled SGs starting from 3 days of age with a reduction of ~60% at an SG age of 5 days in primary beta cells. This reduction was accompanied by the detection of SNAP-fluorescence in MGBs showing the intracellular degradation of old SGs.

This approach allows for quantitative and topographic analyses of age-distinct insulin SGs in relationship to their life cycle in different metabolic conditions such as high glucose or the presence of free fatty acids. Combination with immunogold labeling could further enable the identification of molecular signatures associated with SG aging and degradation. Our CLEM approach may be applicable to a wide variety of cell biological questions beyond the research field on beta cells and diabetes, especially when the focus of interest is on subcellular features of small cell populations embedded in complex tissues (e.g. stem cells, dissipated endocrine cells). The use of EM sections in combination with super resolution microscopy would also allow the use of other EM preparation techniques that retain the initial fluorescence of the sample, e.g. high pressure freezing (HPF) followed by freeze substitution (FS) and embedding in lowicryl resin. Hence our method is easily adaptable to different biological systems and experimental conditions.

1. Ivanova, A., Kalaidzidis, Y., Dirkx, R., Sarov, M., Gerlach, M., Schroth-Diez, B., Müller, A., Liu, Y., Andree, C., Mulligan, B., Münster, C., Kurth, T., Bickle, M., Speier, S., Anastassiadis, K., and Solimena, M. (2013). Age-dependent labeling and imaging of insulin secretory granules.Diabetes, 62(11):3687-3696.
2. Hoboth, P., Müller, A., Ivanova, A., Mziaut, H., Dehghany, J., Sönmez, A., Lachnit, M., Meyer-Hermann, M., Kalaidzidis, Y., Solimena, M. (2015). Aged insulin granules display reduced microtubule-dependent mobility and are disposed within actin-positive multigranular bodies. *Proc. Natl. Acad. Sci. U.S.A.*, 112(7):E667-76.

Correlative Microscopy in Life and Material Sciences (combination of several microscopy techniques)

IM7.164
Correlative electron and X-ray spectro-microscopy of nanoparticles

A. Goode[1], S. Tay[1], J. Nelson Weker[2], A. Cruickshank[1], S. Heutz[1], A. Hart[1], M. Toney[2], D. McComb[3], A. Porter[1], M. Ryan[1]

[1]Imperial College London, Materials, London, United Kingdom
[2]Stanford University, Menlo Park, United States
[3]The Ohio State University, Columbus, United States

aeg08@ic.ac.uk

With recent advances in instrumentation, the opportunities for performing chemical analysis in the transmission electron microscope are developing rapidly. Concurrently, enhancements in X-ray microscopy optics have improved the spatial resolution of soft X-ray instruments to ~ 15 nm. Here we will present results of correlative electron and X-ray microscopy studies on the characterisation of inorganic nanoparticle systems. We correlate between two complementary high resolution spectro-microscopy methods: electron energy-loss spectroscopy in the scanning transmission electron microscope (STEM-EELS) and X-ray absorption spectroscopy in the (scanning) transmission X-ray microscope ((S)TXM-XAS), which provide spatially resolved quantitative information at different spatial and spectral resolutions.

Firstly, the chemical form of nanoscale wear debris from cobalt-chromium metal-on-metal (MOM) hip replacements was studied. This debris is associated with a local inflammatory response, and eventual failure of the prosthesis. Surprisingly, spatially resolved X-ray spectroscopic analysis of debris within explanted hip tissue reveals only trace concentrations of cobalt, even though the alloy contains cobalt, chromium and molybdenum at 60, 30 and 7 at% respectively. Analysis of the O K- and Cr $L_{2,3}$-near edge structure indicates that the majority of chromium is present as octahedrally coordinated Cr^{3+}, most likely in the form of $Cr(PO_4)$. STEM-EELS provides higher spatial resolution elemental mapping across individual debris nanoparticles, whilst focussed ion beam scanning electron microscopy (FIB-SEM) was used to characterise the three-dimensional morphology of the debris (figure 1).

Secondly, the versatility of these techniques is demonstrated by imaging the growth of ZnO nanostructured films *in situ* at a hard X-ray transmission X-ray microscope. By developing a custom-built electrochemical cell, we image, in real time, the growth of ZnO nanostructures, as well as transient events which occur during electrodeposition, and correlate X-ray microscopy to subsequent morphological analysis in the SEM. These examples demonstrate the power of a correlative approach in more completely characterising the morphology and chemistry of nanoparticle systems, during growth and after corrosion.

*CoCrMo experiments were performed at the soft X-ray Spectromicroscopy beamline 10ID-1 at the Canadian Light Source.
** ZnO experiments were performed at the hard X-ray TXM beamline 6-2c at the Stanford Synchrotron Radiation Laboratory

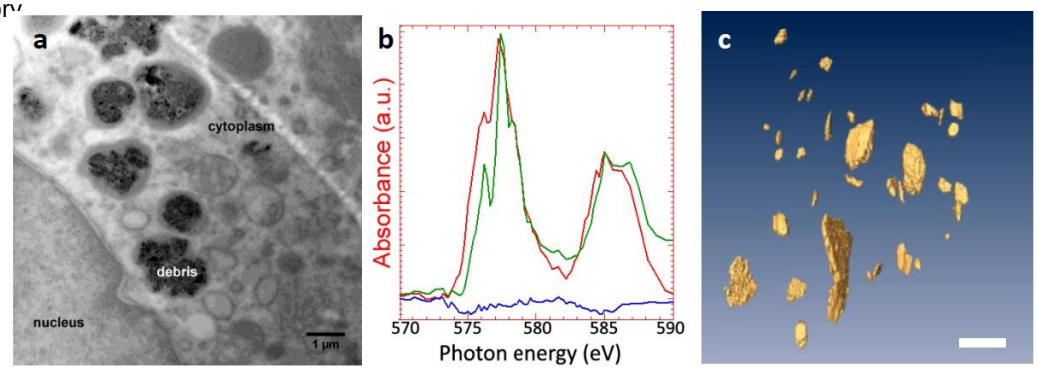

Figure 1. Correlative micro-spectroscopy analysis of wear particles created from metal-on-metal hip prostheses. (a) TEM image of nanoparticles located within a macrophage cell, (b) XAS analysis at the Cr $L_{2,3}$ edge shows variation in the amount of Cr^{3+} between different nanopartices, and (c) 3D morphology of wear particles determined using FIB-SEM. Scale bars 1 µm.

Correlative Microscopy in Life and Material Sciences (combination of several microscopy techniques)

IM7.165
Fluorescence confocal scanning correlated high resolution transmission electron microcopy

S. Ghosh[1], H. Schuhmann[2], M. Seibt[2], N. Karedla[1], A. Chizhik[1], A. Chizhik[1], J. Enderlein[1]

[1]University of Goettingen, III. Physics, Göttingen, Germany
[2]University of Goettingen, IV. Physics, Göttingen, Germany

siddharth.ghosh@phys.uni-goettingen.de

We present a single-photon-emitter sensitive correlative atomic resolution microscopy approach where fluorescence confocal scanning microscopy (FCSM) is correlated with high resolution transmission electron microcopy (HRTEM). The insight of atomic structure of the emitter is unavailable in any standalone fluorescence microscopy, even considering super-resolution florescence microscopy techniques. The motivation behind this correlative microscopy study was to understand the insight of photoluminescence behaviour of single carbon nanodots (CNDs) [1].

In this method, as a first step of correlation, the position markers of standard TEM grid were utilized to observe the same nanoparticles using fluorescence microscopy and HRTEM (figure 1). And to avoid any electron beam induced radiation damage, FCSM was performed prior to study the same C-dots under HRTEM. As a final step of correlation, the photon emitting regions were well overlapped with electron density of carbon lattices. Finally, this correlative investigation allows to extract the atomic parameters needed for any photophysical ab-intio calculations.

1. Ghosh, et al. Nano Lett. 2014, 14, 5656.

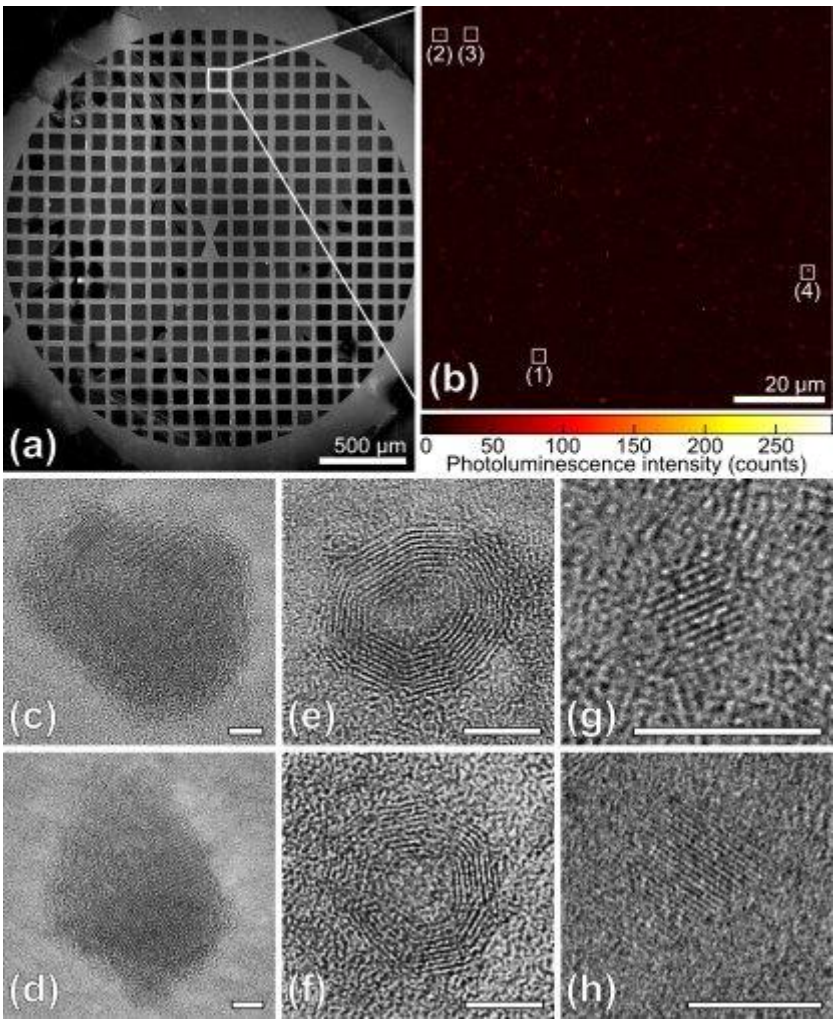
(a)
500 μm
(b)
(1)
(2) (3)
(4)
20 μm
0 50 100 150 200 250
Photoluminescence intensity (counts)
(c)
(d)
(e)
(f)
(g)
(h)

Correlative Microscopy in Life and Material Sciences (combination of several microscopy techniques)

IM7.166
Correlative TEM in-situ ion and electron spectrometry: low Z elemental analysis

L. Yedra[1], S. Eswara Moorthy[1], D. Dowsett[1], H. Q. Hoang[1], T. Wirtz[1]

[1]Luxembourg Institute of Science and Technology (LIST), Advanced Instrumentation for Ion Nano-Analytics (AINA), MRT Department, Belvaux, Luxembourg

lluis.yedra@list.lu

To address the demands of increasing complexity and size reduction of devices in materials science research, there is an urgent need for accurate characterization at high-spatial resolution and high-chemical sensitivity. Transmission Electron Microscopy (TEM) can offer sub-Å spatial information combined with electron spectroscopies yielding chemical and electronic information. However, the analytical TEM retains some limitations that make it unsuitable for applications requiring distinguishing isotopes, detecting trace elements below 0.1 at.% concentration or characterization of very light elements such as hydrogen, lithium or boron [1,2]. By contrast, Secondary Ion Mass Spectrometry (SIMS) has superior sensitivity (ppm range) and is capable of distinguishing isotopes and detecting light elements, but suffers from an inherent fundamental limitation in spatial resolution. By correlating TEM with SIMS in-situ, it is possible to overcome their individual limitations and obtain information at high-resolution and high-sensitivity simultaneously.

In order to push the analytical limits of the TEM, a dedicated, compact, high-performance SIMS system that was developed in-house, together with a Ga^+ focused ion beam (FIB) column have been fitted in a modified FEI Tecnai F20 pole piece. A special sample holder which can be biased to high-potential (±5 kV) was also developed to create an electric field above the specimen for an optimized collection of the secondary ions. This unique prototype (Fig. 1), dedicated to parallel ion-electron spectrometry (PIES) combines all the conventional TEM information, scanning TEM, energy dispersive X-ray spectroscopy (EDX) and mass spectrometry, therefore allowing for correlative TEM imaging and ion-electron spectrometry. The main advantage of the in-situ approach is its capability to analyse the same area of interest of any sample without need of changing the instrument. Moreover, the artefacts and sample modifications related to transfer between instruments are avoided.

In this preliminary work, we focus on the case studies of materials containing very low atomic number elements, namely H, Li or B. These elements are known to be extremely difficult or impossible to study by conventional EDX. The subjects of the case studies are (a) Hydrogen diffusion and trapping in the microstructure of structural steels, which plays a major role in durability [3], (b) Lithium incorporation to battery nanostructures, which is the key factor in higher capacity energy storage and battery lifetime extension [4] and (c) Boron in semiconductors, found as a dopant in very low concentrations whose, as structures shrink, characterisation becomes more important. Here we demonstrate the ability of the PIES instrument to map these elements (Fig. 2) and study the best approach for correlating TEM and SIMS results.

1. Reimer,L, & Kohl, H., *Transmission Electron Microscopy: physics of image formation* (Springer, New York, 2008).
2. Egerton, R.F., *Electron Energy-Loss Spectroscopy in the Electron Microscope* (3rd edition), (Springer, New York, 2011).
3. Kanezaki, T., *Effects of hydrogen on fatigue crack growth behavior of austenitic stainless steels*, 33 (2008) 2604-2619
4. Tarascon, J.M. et al., *Issues and challenges facing rechargeable lithium batteries*, Nature 414 (2001) 359-367

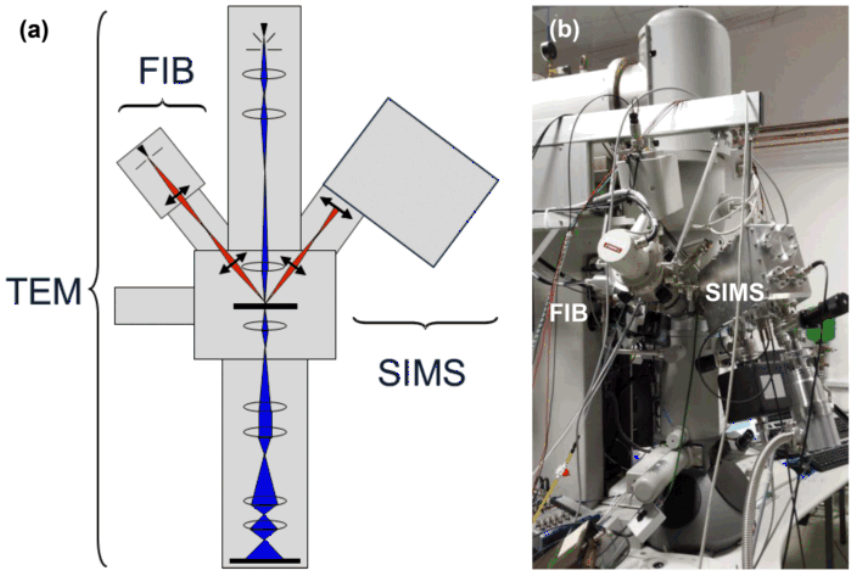

Figure 1. (a) Schematic of the modified Tecnai F20 and (b) actual image of the prototype instrument. The EDX spectrometer is found opposite of the FIB column

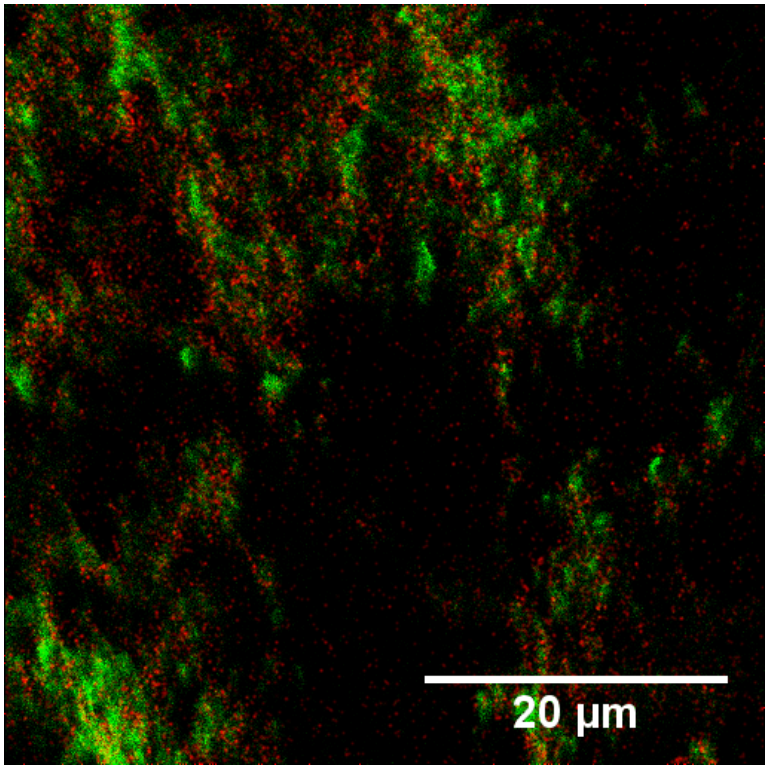

Figure 2. SIMS image obtained in the PIES of the $^{7}Li^{+}$ (in green) and $^{11}B^{+}$ (in red) ions in a sample mixture of lithium titanate and boron nitride nanoparticles.

Correlative Microscopy in Life and Material Sciences (combination of several microscopy techniques)

IM7.P167
CLEM of immunolabeled sections to find the needle in the haystack

T. Kurth[1], S. Kretschmar[1]

[1]TU Dresden / CRTD, EM/Histology Facility, Dresden, Germany

thomas.kurth@crt-dresden.de

Correlative microscopy combines the large field of view of the fluorescence microscope (FLM) with the high spatial resolution of the electron microscope (EM). Regarded as state-of-the-art technology, many CLEM-protocols are dependent on technical skills and/or sophisticated instrumentation [e.g. 1-4]. However, simultaneous on-section labeling of resin or Tokuyasu-cryo-sections with fluorochrome-coupled antibodies and gold probes are versatile and fast methods for CLEM of cells and tissues [5-9], especially when rare cell types or events are to be characterized in complex tissues.

Here, we describe fast and simple labeling protocols for correlative immunofluorescence and immunogold labeling on resin- and Tokuyasu cryo-sections (Fig. 1A). Ultrathin tissue sections are mounted on EM-grids and stained simultaneously with fluorescent and gold markers. The samples are analyzed at the fluorescence microscope (FLM), demounted from the microscope slide, stained with uranyl acetate and subsequently imaged in the transmission electron microscope (TEM). This way, fluorescent signals are correlated to the corresponding subcellular structures and corresponding immunogold signals in the area of interest (Fig. 1B-H). The two approaches will be illustrated with different tissue and cell culture samples containing genetically modified cell types, cell and progenitor cells, and other rare cells populations.

1. P Verkade, J. Microsc. **230** (2008), 317-328.
2. M Grabenbauer, WJC Geerts, J Fernandez-Rodriguez, A Hoenger, AJ Koster, and T Nilsson, Nat. Methods **2** (2005), 857-862
3. C van Rijnsoever, VM Oorschot, and J Klumperman, Nat. Methods **5** (2008), 973-980
4. AV Agronskaia, JA Valentijn, LF van Driel, CT Schneijdenberg, BM Humbel, PM van Bergen en Henegouwen, AJ Verkleij, AJ Koster, and HC Gerritsen, J Struct. Biol. **164** (2008) 183-189
5. H Schwarz and BM Humbel, Methods Mol. Biol. 1117 (2014), p. 559-592.
6. T Takizawa and JM Robinson, Methods Mol. Med. **121** (2006), p. 351-369.
7. G Vicidomini, MC Gagliani, M Canfora, K Cortese, F Frosi, C Santangelo, PP Di Fiore, P Boccacci, A Diaspro, and C Tacchetti, Traffic **9** (2008), p. 1828-1838.
8. G Fabig, S Kretschmar, S Weiche, D Eberle, M Ader, and T Kurth, Methods Cell Biol. **111** (2012), p. 75-93.
9. T Santos-Ferreira, K Postel, H Stutzki, T Kurth, G Zeck, and M Ader, Stem Cells **33** (2015), p. 79-90.

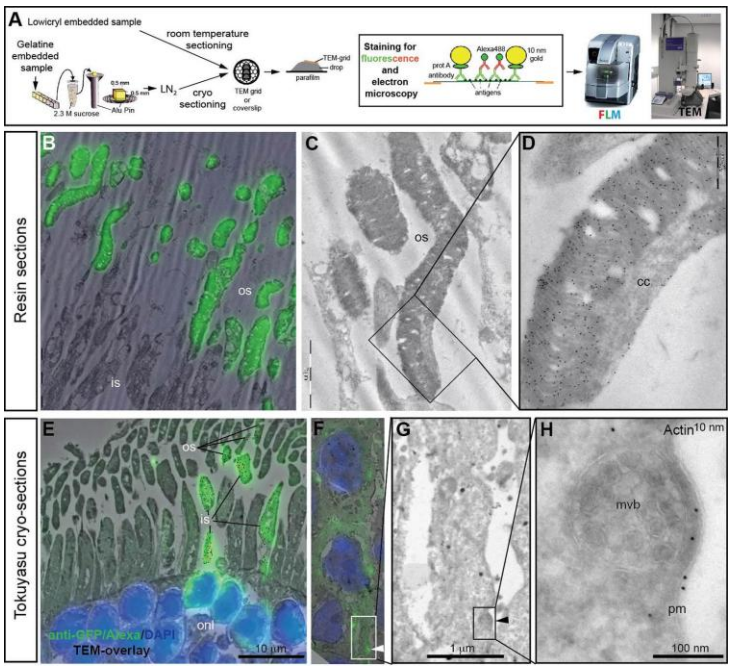

Figure 1. A Overview of sample preparation for on-section CLEM. **B-D** Labeling of a Lowicryl K4M section through mouse retina with mouse-anti-Rhodopsin (detected by rabbit-anti-mouse, goat-anti-rabbit Alexa488, and protein A gold). Outer segments (os) of the rod photoreceptor cells are labelled; is, inner segment; cc, connecting cilium. **B** Overlay FLM and low-mag TEM-image. **C** enlarged outer segments in the TEM, the region indicated by the square is shown in C at higher magnification. **D** further enlarged outer segment with gold-labeled membrane stacks. **E** Labeling of a Tokuyasu-cryosection through mouse retina with transplanted cone-like cells (marked by GFP), labeling with rabbit-anti-GFP, goat-anti-rabbit Alexa488, and protein A gold. The black dots indicate the positions of gold particles in the transplanted cells. **F-H** Tokuyasu-cryosection through a pellet of HEK293T cells expressing JAK3-eGFP, labeling with anti-actin and protein A gold. **E** Overlay of GFP fluorescence and a low mag TEM-image. The area of interest (submenbraneous speckle) is indicated by an arrowhead. The square indicates the region displayed in F. **F** Higher magnification, an electron dense structure in the area of interest is indicated by an arrowhead. The boxed region is displayed in G at higher magnification. **G** The fluorescent speckle highlighted in E is identified as a multivesicular body, cortical actin in the vicinity is labeled with gold.

Correlative Microscopy in Life and Material Sciences (combination of several microscopy techniques)

IM7.P168
Correlative imaging of large volumes across scales

R. Schröder[1], H. Blank[2], A. Schertel[2], M. Thaler[2], A. Orchowski[2], I. Wacker[3]

[1]Universität Heidelberg, Cryo EM, CellNetworks, BioQuant, Heidelberg, Germany
[2]Carl Zeiss Microscopy GmbH, Oberkochen, Germany
[3]Universität Heidelberg, Cryo EM, Centre for Advanced Materials, Heidelberg, Germany

rasmus.schroeder@bioquant.uni-heidelberg.de

Integrated workflows allowing shuttling of samples between different imaging modalities are a prerequisite for correlative imaging of large volumes. In principle X-ray microscopy (XRM) can bridge the gap between macroscopic and microscopic world. To gain comprehensive information about biological samples extended in 3D we have started to assess how XRM, light microscopy (LM) and electron microscopy (EM) might be combined to reach that goal.

Fluorescence LM is commonly used in CLEM, correlated LM and EM, to define a certain functional state. This state is then put into structural context using EM. For XRM a comparable approach has been shown for single cells grown on TEM grids, plunge frozen, and analyzed by cryo-XRM [1]. Since samples thicker than 200 micrometers cannot be vitrified such an approach is not possible for tissue. Here a different workflow is needed, starting with a chemical fixation. Samples may then be imaged directly in aqueous medium in LM and XRM, the latter being able to yield voxel sizes down to 350 nm. However, XRM has to be complemented by EM if ultrastructural resolution in the range of few nanometers is required. To achieve that for large volumes [2] several options are available, based on SEM imaging such as serial blockface or focussed ion beam scanning electron microscopy (SBFSEM or FIBSEM) or array tomography (AT). When whole brains are imaged at high resolution as is the case in connectomics, SBFSEM is optimal. Questions in other areas of cell and developmental biology may rather call for imaging of only a minute part of the whole sample because only there the target structure is present. To avoid creation of huge amounts of unnecessary data identification of this target is very important. For two examples, the formation of an immunological synapse (IMS), a rare event in a cell population, and the neuromuscular junction (NMJ), a rare structure within a large volume, we employ XRM combined with a dedicated software package for targeting. The new solution ZEISS Atlas 5 (Carl Zeiss Microscopy GmbH) contains modules for automated SEM imaging of large areas and crossbeam (XB) nanotomography, thus offering a sample centric correlative environment, which fuses all available 2D and 3D data of the sample from various modalities. First a large volume XRM dataset is created where features of interest are identified and then Crossbeam technology is used for nanometer scale analysis of features buried below the sample surface. Typical workflows for large volume samples such as muscle tissue or cell pellets are illustrated in Figure 1. Definition of a reference framework inherent to the samples of interest is important. Fast and accurate navigation of the sample in 3D is possible when this “sample coordinate system” is mapped seamlessly from one imaging technique to the next.

1. Hagen et al., J Struct Biol **177** (2012) 193-201; Chicon et al., J Struct Biol **177** (2012) 202-211.
2. I Wacker, RR Schröder, J Microscopy **252** (2013) 93-99.
3. The authors acknowledge C Bartels and L Veith for technical support, C Grabher for samples, BMBF for NanoCombine grant FKZ 13N11401 and MorphiQuant grant FKZ 13GW0044.

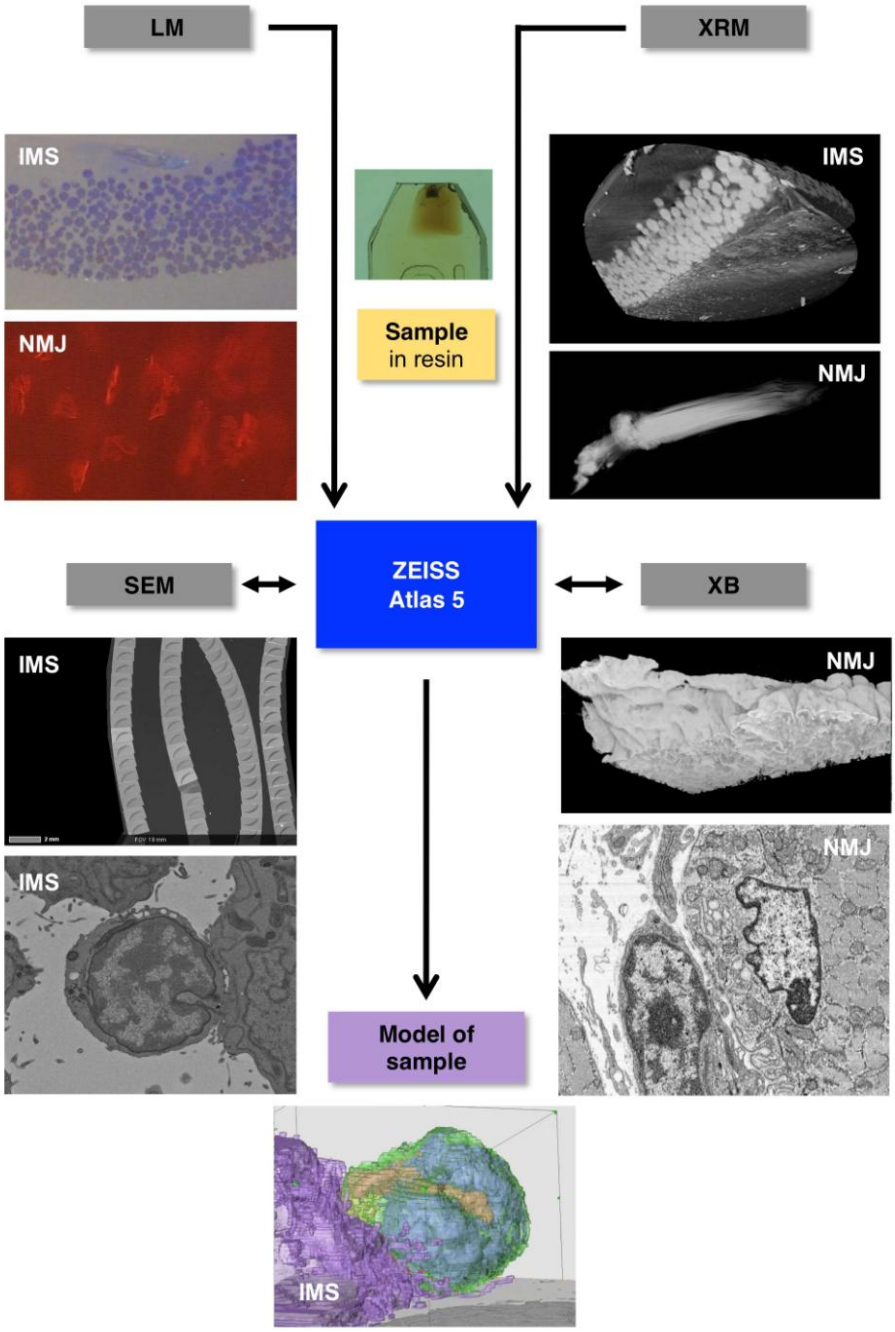
LM
XRM
IMS
NMJ
Sample
in resin
IMS
NMJ
SEM
ZEISS
Atlas 5
XB
IMS
IMS
NMJ
NMJ
Model of
sample
IMS

Correlative Microscopy in Life and Material Sciences (combination of several microscopy techniques)

IM7.P169
Correlative SEM and SERS imaging of plasmonic nanostructures

R. Váňa[1], M. Kocman[1], L. Štolcová[2], J. Proška[2], J. Jiruše[1]

[1]TESCAN Brno, s.r.o., Brno, Czech Republic
[2]Faculty of Nuclear Sciences and Physical Engineering, Czech Technical University in Prague, Prague, Czech Republic

rostislav.vana@tescan.cz

Surface Enhanced Raman Spectroscopy (SERS) is becoming still more popular due to its ability to overcome the major disadvantage of Raman spectroscopy, the low Raman cross-sections. The enhancement of the signal is caused by the excitation of localized surface plasmon resonancesand the corresponding increase in the intensity of the local electromagnetic field. The highest enhancement occurs usually in the gaps, crevices, or sharp nanoscale features of metallic nanostructures called, hot spots', whose size varies between a few and several hundred nm. Visualization of exactly the same area of the SERS substrate in SEM and Raman is very challenging in two stand-alone systems since the plasmonic nanostructures on substrates are usually periodically arranged and are similar to each other. However, we were able to visualize hot spots using a recently developed correlative Scanning Electron (SEM) and Confocal Raman (CRM) microscopy [1] we call RISE. The unique configuration of the RISE system lies in the direct navigation between SEM image and corresponding area for Raman spectra acquisition. Figure 1 shows overlaid SEM and Raman images of a silver SERS substrate with corresponding SERS spectra of mercaptopyridine. Different intensities of the Raman signal of mercaptopyridine can be seen due to variance of the plasmonic nanostructures on the periodically ordered, plasma etched, and silver-coated polystyrene spheres [2].

The RISE system comprises a high-resolution SEM and CRM integrated into the vacuum chamber. The CRM is equipped with a green excitation laser (532 nm) which provides a lateral resolution of 360 nm and depth resolution of 750 nm, respectively. Thus the resolution of CRM is comparable with stand-alone Raman instruments and it is not compromised by integration with the SEM. The electron microscope used here comprises the immersion magnetic optics with a resolution of 1.4 nm at 1 kV and 1 nm at 15 kV [3], however, other types of electron columns are possible as well. The high resolution at low electron acceleration voltages makes it suitable for beam-sensitive samples.

1. J Jiruše *et al,* Journal of Vac. Sci. Technol. B **32** (2014), 06FC03.
2. L Štolcová *et al*, Proceedings of Progr. in Elmag. Res. Symp. (PIERS), Stockholm (2013), 426.
3. J Jiruše *et al*, Microsc. Microanal. **19** Suppl. 2 (2013), 1302.
4. The research leading to these results has received funding from the European Union 7th Framework Program [FP7/2007-2013] under grant agreement n°280566, project UnivSEM and from the Czech Science Foundation grant No. P205/13/20110S (J.P.).The authors would like to thank Maria Domonkos (IOP, AS CR)for performing RIE of the polystyrene spheres.

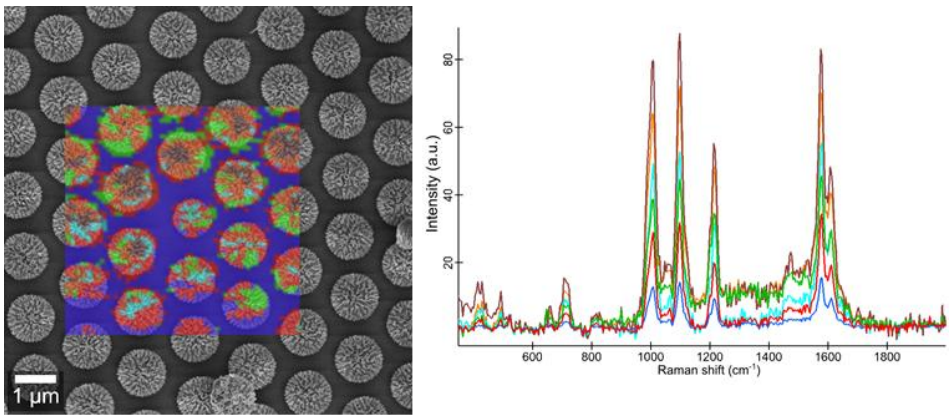

Figure 1. A detailed view of SERS substrate with correlative SEM-Raman imaging. Left: Overlaid SEM and Raman micrographs, Right: Corresponding Raman spectra showing characteristic peaks of mercaptopyridine. Various colors correspond to the different enhancement factor of the spectra caused by variance of the plasmonic structures on polystyrene spheres.

Correlative Microscopy in Life and Material Sciences (combination of several microscopy techniques)

IM7.P170
How to achieve a 50 nm overlay accuracy in CLEM without fiducial markers

M. van der Haar[1], L. M. Voortman[2], S. den Hoedt[2]

[1]Delft University of Technology, Delft, Netherlands
[2]DELMIC, Delft, Netherlands

mischavanderhaar@gmail.com

Correlative light and electron microscopy (CLEM) encompasses a wide variety of techniques and hardware, and is used to achieve a very diverse set of goals. But whether CLEM is used to trace neurons over large distances, or to identify unknown ultrastructural changes, one of the essential challenges of CLEM is to achieve an unbiased and accurate overlay.

The difficulty of this overlay, resides in the unavoidable difference in contrast between fluorescence and electron microscopy. And even though doing an overlay of fluorescence and electron images 'by hand' can work for some cases, this is definitely not the way to answer unresolved biological questions.

A better approach is to add correlative fiducials which are clearly visible in both the optical microscope and electron microscope. The main difficulty of this approach is that inserting the right concentration of fiducials in the sample adds to a typically already difficult sample preparation. Furthermore, for some samples it might be impossible to add fiducials because of known, or unknown interference with the biological system.

Here we propose to use an integrated correlative microscope to bridge information in different microscopes. The key to our approach is that correlating fluorescence to fluorescence data, or from one electron microscope to another, can be achieved with an accuracy better than the resolution limit of said microscope.

We make use of a proprietary alignment method developed by DELMIC to correlate fluorescence and electron images. This method uses temporary fiducial markers created by cathodoluminescence. In an integrated microscope, the optical microscope can detect the light generated by the electron beam impinging on the specimen substrate.

Our approach allows us to start at an optical microscope of choice, use the integrated correlative microscope as a 'correlation bridge' and continue in a TEM for high resolution tomography.

Correlative Microscopy in Life and Material Sciences (combination of several microscopy techniques)

IM7.P171
A modern correlative microscopy environment to connect data across length scales, dimensions, and modalities

A. Merkle[1], L. Lechner[1], A. Steinbach[1], J. Gelb[1], W. Harris[1], F. Perez-Willard[2], M. Phaneuf[3], D. Unrau[3]

[1]Carl Zeiss X-ray Microscopy, Inc., Pleasanton, CA, United States
[2]Carl Zeiss Microscopy, GmbH, Oberkochen, Germany
[3]Fibics Incorporated, Ottawa, Canada

arno.merkle@zeiss.com

Modern microscopy tools have been developed to offer a remarkable range of imaging modalities spanning orders of magnitude in length scale, from the macro level to the sub-nanometer scale. Examples of such modern tools and methods include industrial and medical CT, high resolution X-ray microscopy (XRM), confocal light microscopy, 3D SEM imaging methods including FIB-SEM and serial block face SEM, TEM, atomic force microscopy, and more. While each tool has emerged with specific advantages and strengths, many scientific characterization challenges require incorporation of data from multiple imaging tools to properly address the range of structural features and parameters that dictate the sample properties or performance. As such, a new challenge has emerged regarding how to best handle massive data sets, acquired on multiple platforms, in an efficient and convenient manner to make these types of correlative microscopy studies both manageable and powerful. [1]

Here we present the major development of a new tool for streamlining correlative microscopy studies over a range of modalities, scales, and dimensions. ZEISS Atlas 5, a new software environment released in 2015, serves the dual role of an advanced, automated SEM and FIB-SEM acquisition system, as well as an environment for the combination of data sets acquired across multiple instruments (SEM, LM, FIB-SEM, XRM, etc.), serving as the common hub central interface between the various experiments. Atlas 5 empowers the user by providing a visualization environment to co-locate, calibrate and register multiple datasets, simplifying the correlation workflow as well as guiding future data acquisition at specific targeted regions and volumes of interest. By incorporating 3D data from methods such as FIB-SEM and XRM tomography, the platform extends beyond the traditional 2D correlation approach, offering new opportunities to explore complex structures and sub-surface features.

We demonstrate efficient correlative workflows in the context of examples from Materials Research and Life Science. In Materials Science, 3D XRM data collected on an Al 7075 aluminum alloy (Figure 1) is used to locate inclusions and pores buried below the material surface. The XRM data is used to drive the FIB-SEM to perform high resolution serial sectioning at these specific, targeted regions of interest to characterize the features in greater detail [2]. In Life Sciences, XRM presents a unique opportunity to bridge the length scales between light and electron microscopy (Figure 2), easing the 'needle in a haystack' navigation problem for locating the same region of interest using multiple microscopes [3].

1. Burnett T., et. al. Correlative Tomography, Scientific Reports (2014).
2. A. P. Merkle et al., Automated Correlative Tomography Using XRM and FIB-SEM to Span Length Scales and Modalities in 3D Materials, Microscopy and Analysis, 28 (2014), p. S10-S13
3. E. Bushong et al., X-Ray Microscopy as an Approach to Increasing Accuracy and Efficiency of Serial Block-Face Imaging for Correlated Light and Electron Microscopy of Biological Specimens, Microscopy and Microanalysis (2014).

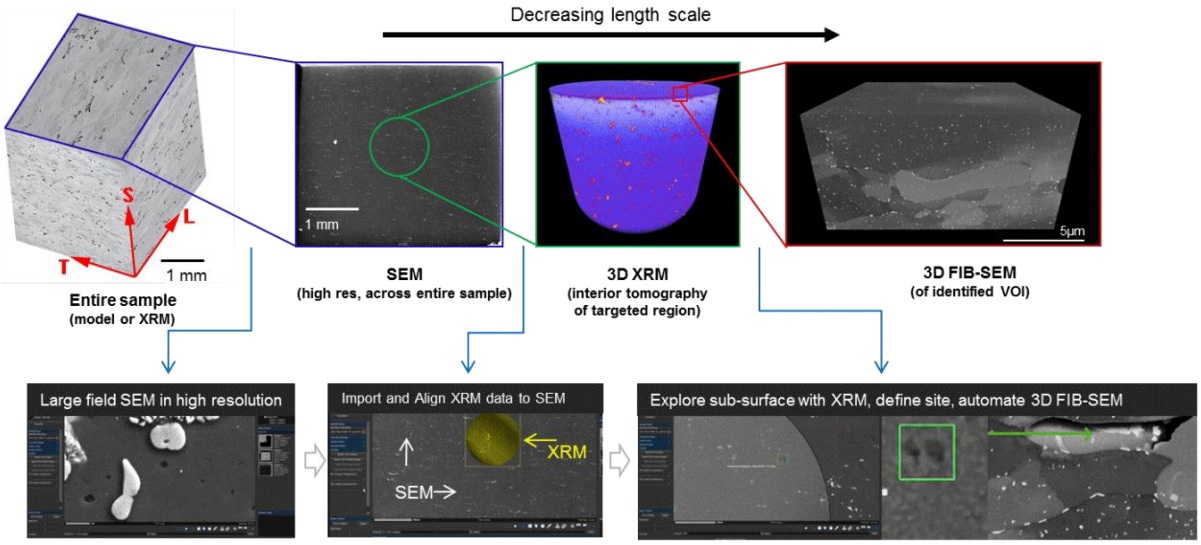

Figure 1. A 3D automated correlative study on an Aluminum 7075 alloy to access information about inclusions, voids, precipitates and the Al matrix grain structure. In collaboration with N. Chawla and S. Singh of Arizona State University.

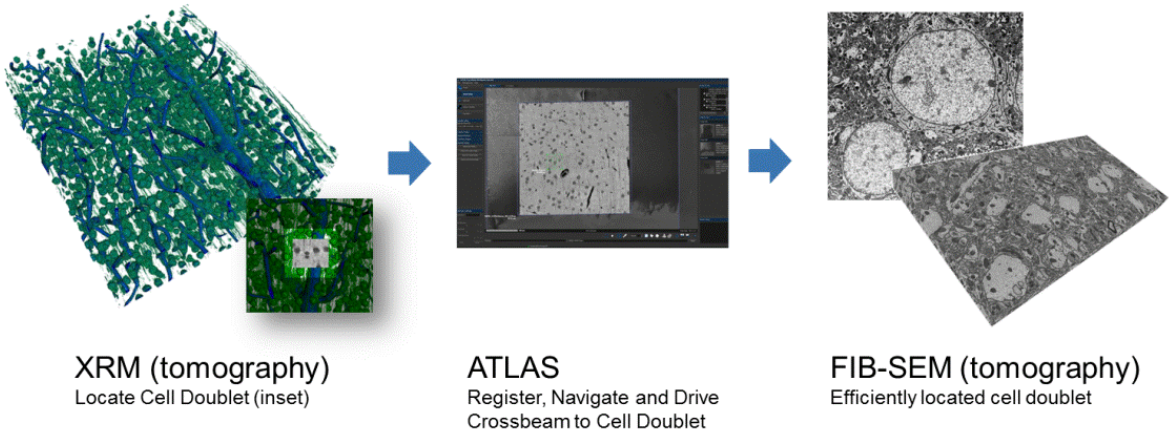

Figure 2. XRM dataset of stained (for EM) mammalian brain tissue, used to navigate to specific subsurface volumes of interest quickly, thereby multiplying the efficiency of 3D EM techniques. In collaboration with NCMIR at the University of California San Diego.

Correlative Microscopy in Life and Material Sciences (combination of several microscopy techniques)

IM7.P172
Easy cell CLEM: eC-CLEM a plugin to register correlative data easily

X. Heiligenstein[1], P. Paul-Gilloteaux[2], J. Salamero[2], G. Raposo[1]

[1]Institut Curie, UMR144-Structure and membrane comparments, Paris, France
[2]Institut Curie, UMR144-Spatio-temporal modeling Imaging and cellular dynamics, Paris, France

xavier.heiligenstein@curie.fr

Melanin biosynthesis occurs in melanocytes, a specialized cell dedicated to melanin pigment production and responsible for tissue pigmentation. Skin melanocytes exploit their endosomal system and associated machineries to generate a Lysosome Related Organelle (LRO), the melanosome, where melanin is synthesized and stored. Melanosome originates from early sorting endosome and matures through a sequential supply of melanogenic cargoes. Using Alexa-labelled transferrin and GFP-tagged proteins involved in formation of endosomal carriers, we decipher the mechanism of cargo delivery to melanosomes that underlie the pathophysiology of albinism (Delevoye et al., 2014).

Melanosome biogenesis is addressed in vivo in skin melanocytes and in reconstructed human epidermis using our advanced Correlative light and electron microscopy (CLEM) workflow (Heiligenstein et al., 2014). CLEM is taking an increasing part in imaging for electron microscopy laboratories and many approaches are developed to address a large variety of biological specimen and phenotypes. Yet, aligning the light microscope images with the electron micrographs remains common to all CLEM approaches. We have developed easy Cell CLEM (eC-CLEM) as a new and intuitive plugin to allow any scientist to align its CLEM images without any image processing prerequisite or mathematical background. We rely on the user expertise to identify corresponding landmarks between the different images to align the two registered images. Our plugin functions for two or three dimension datasets and contains some internal routines to pre-process the data and improve the signal to noise ratio, thereby facilitating the user's task.

No mathematical background is required to manipulate the plugin and the code is open source to allow increasing the plugin improvement on a long term.

A simple GUI

To design the plugin, we used the open-source software Icy (de Chaumont et al., 2012). The intuitive interface with several display controls at hand makes the images manipulation very rapid and user-friendly. We simplified the graphical user interface (GUI) to the strict minimum to avoid distracting the user or disturb him with complex mathematical parameters (figure 1).

The graphical user interface offers to work in two dimensions (2D) or in three dimensions (3D), and options appear accordingly. We supposed that most application would require registering fluorescent images on electron micrographs, but the choice is left to the user. Applying a previously computed transformation allows to align large datasets (time course, multichannel for example) according to the chosen image. This saves a significant processing time when large datasets are meant to be registered.

Registration error calculation

The registration is based on landmarks seeding by the user (figure 2). Each supplementary fiducial is used to recalculate the localization accuracy of all landmarks (Fitzpatrick and West, 2001). Thereby, it becomes possible to locally assign the alignment accuracy of a pin-pointed feature (figure 2). A global error map can also be calculated to illustrate the global alignment accuracy of the image. It may be extrapolated to the deformation induced to the specimen between the various transformation steps between the light and the electron microscope.

We have created a simple plugin, dedicated to image registration for non image-analysts. Our goal was to keep the biological expertise into the scientist hands, without requiring advance image processing knowledge. The plugin is freely available on the Icy website.

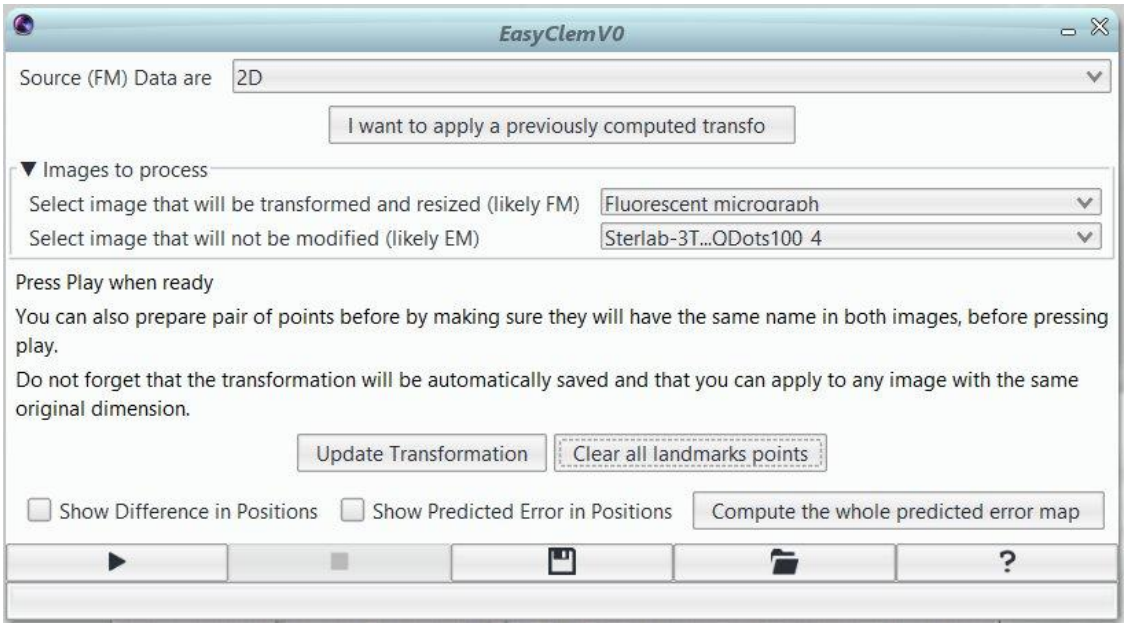
EasyClemV0
Source (FM) Data are
2D
I want to apply a previously computed transfo
▼ Images to process
Select image that will be transformed and resized (likely FM)
Fluorescent micrograph
Select image that will not be modified (likely EM)
Sterlab-3T...QDots100 4
Press Play when ready
You can also prepare pair of points before by making sure they will have the same name in both images, before pressing play.
Do not forget that the transformation will be automatically saved and that you can apply to any image with the same original dimension.
Update Transformation
Clear all landmarks points
Show Difference in Positions
Show Predicted Error in Positions
Compute the whole predicted error map

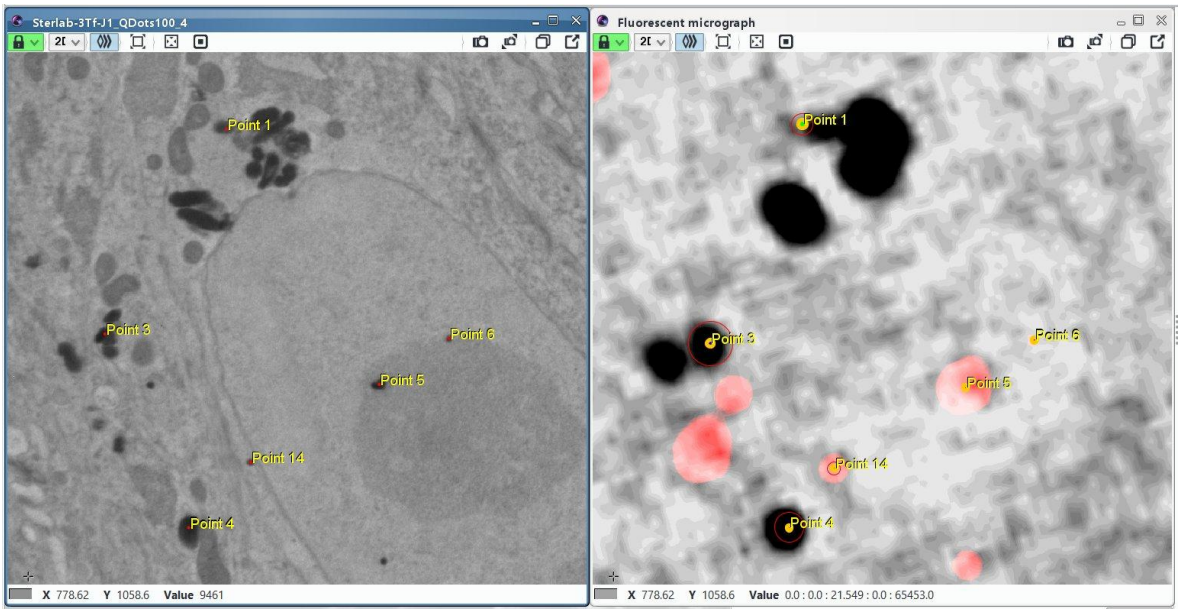
Sterlab-3Tf-J1_QDots100_4
Point 1
Point 3
Point 6
Point 5
Point 14
Point 4
X 778.62 Y 1058.6 Value 9461
Fluorescent micrograph
Point 1
Point 3
Point 6
Point 5
Point 14
Point 4
X 778.62 Y 1058.6 Value 0.0 : 0.0 : 21.549 : 0.0 : 65453.0

Correlative Microscopy in Life and Material Sciences (combination of several microscopy techniques)

IM7.P173
Correlative microscopy at ProVIS - centre for chemical microscopy

M. Schmidt[1], H. Stryhanyuk[1], H. H. Richnow[1], N. Musat[1]

[1]Helmholtz-Zentrum für Umweltforschung, Isotope Biogeochemistry, ProVIS, Leipzig, Germany

matthias.schmidt@ufz.de

The Helmholtz-Centre for Environmental Research Leipzig (UFZ) has established the ProVIS centre for chemical microscopy recently. ProVIS aims to visualise biochemical processes on cellular level. The centre comprises equipment for sample preparation, a number of different microscopes - fluorescence, scanning electron (SEM) and helium ion microscopes (HIM) - as well as mass spectrometers, for instance nanoSIMS and ToFSIMS with imaging option. In order to investigate the morphology of a particular microbe as well as its metabolism the different imaging techniques are combined in a correlative way.

We will present a correlative microscopy study of a soil sample collected from the Davidschacht mine tailings in Saxony, Germany, as an example. The sample was at first chemically fixed, then sonicated to remove microbial cells from the soil particles followed by filtration of the supernatant on Pd/Au sputter-coated filters. Further the filters containing fixed microbial cells were hybridized using a fluorescence in situ hybridization standard protocol and were analysed in a correlative manner.

In order to identify and mark the positively hybridized bacteria on the filter, a laser microdisection system and fluorescence microscopy were employed. Thereby the regions of interest (ROIs) were laser-marked. Subsequently, the sample was analysed by SEM, in particular the morphology of positively hybridized bacteria detected by FISH was investigated. In addition, in order to obtain information on the chemical composition of both, mineral particles and microbial cells energy dispersive X-ray spectroscopy (EDX) was conducted. Further, for a high-resolution investigation of the cell-surfaces the sample was investigated by HIM. Using HIM a lateral resolution significantly better than 5nm can be achieved whilst in addition advantage is taken of the instrument's surface sensitivity (information stems from approximately 1nm below the surface). Finally, more detailed chemical information of the ROIs was obtained by focussed ion beam secondary ion mass spectroscopy (nanoSIMS). Compared to EDX, nanoSIMS is more sensitive to low element concentrations and yields, due to ion-sputtering, a depth-profile of the analysed ions. The results obtained by the different methods were correlated using the ImageJ-plugin CORRELIA which was coded at ProVIS. The software allows overlaying different microscopy images by calculating the corresponding transformation matrix from user-defined features in the images. Furthermore false-colours can be attributed to EDX/nanoSIMS intensity maps. The overlay of microscopy images obtained by different techniques with different resolution and chemical composition maps allows to draw conclusions on morphology, composition and metabolism of bacteria or eukaryotic cells.

Correlative Microscopy in Life and Material Sciences (combination of several microscopy techniques)

IM7.P174
3D Raman imaging meets AFM, SNOM, profilometry, and SEM

U. Schmidt[1], P. Ayasse[1], J. Englert[1], O. Hollricher[1]

[1]WITec GmbH, Ulm, Germany

ute.schmidt@witec.de

Knowledge about the morphology and chemical composition of heterogeneous materials on a sub-micrometer scale is crucial for the development of new material properties for highly specified applications. Each analytical measuring technique however faces limitations, which can be overcome only by their combination. Recently after its invention, confocal microscopy has been used to reconstruct three-dimensional images of micro-objects by using a spatial pinhole to eliminate out-of focus light in specimens thicker than the focal plane. Raman spectroscopy on the other hand is known to be used to unequivocally determine the chemical composition of a material. The confocal Raman microscope combines the chemically sensitive Raman spectroscopy with high resolution confocal microscopy. The discrimination of out of focus information used in confocal microscopy is particularly beneficial for confocal Raman imaging since it reduces the volume from which the Raman spectrum is collected. This leads to a diffraction limited resolution in chemical imaging of samples. Due to the confocal principle, depth information from transparent materials can be easily obtained, leading to full three dimensional chemical reconstructions of the materials composition.

However, the high confocality always results in high focus sensitivity. Therefore, Confocal Raman imaging of rough opaque samples was so far very challenging and time consuming, due to the inability to keep the samples in focus. True surface microscopy, a new imaging technique developed for measurements on rough surfaces over large areas, allows confocal Raman imaging guided by the surface topography obtained by an integrated non-contact optical profilometer. Large-area topographic coordinates from the chromatic confocal profilometer measurements can be precisely correlated with the large area confocal Raman imaging data. This allows true surface Raman imaging on heavily inclined or rough surfaces, with the true sample surface held in constant focus, while maintaining highest confocality.

Nanometer scale samples are most commonly investigated using Scanning Probe Microscopy (SPM) or Scanning Electron Microscopy (SEM) techniques. SPM´s use mechanical probes (cantilever-tips) to trace the surface topography on the nanometer scale. By investigating the tip-sample interaction, one can obtain not only the high resolution topographic structure of the surface but also information about the local mechanical properties of the sample components. If the standard AFM cantilever is replaced by a micro-machined SNOM cantilever optical images with resolution below the diffraction limit can be acquired as well. An even more complete characterization of materials can be achieved if the chemical information is linked to the high resolution SPM images. This can be realized by combining SPM and confocal Raman microscopy (Fig. 1).

The newest achievement in microscopy is the combination of confocal Raman microscopy and SEM in one instrument - the RISE microscope. With this new instrument the structures observed with an SEM can be directly linked to the molecular composition of the sample (Fig. 2).

In summary, the combination of confocal Raman microscopy with SPM, true surface microscopy and SEM (RISE) allows the characterization of materials at high, submicron resolution, as well as on mm-rough surfaces across large areas. Examples from various fields of applications will be presented.

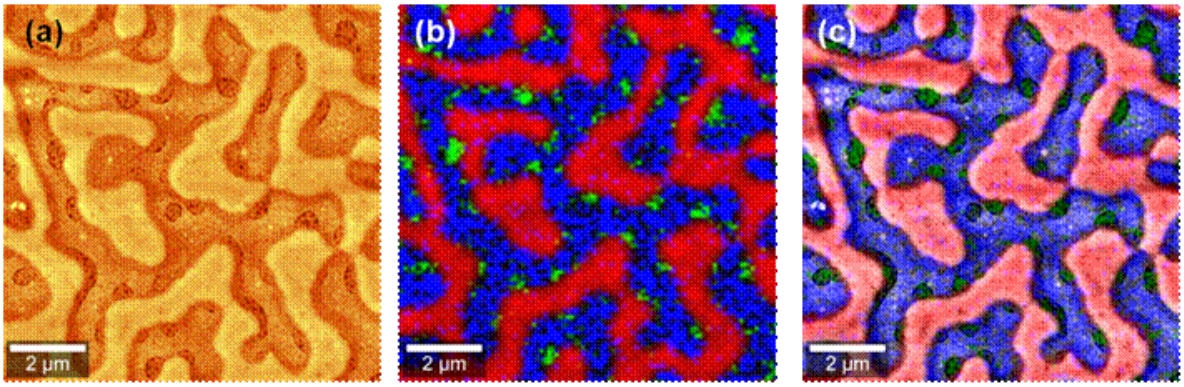

Figure 1. Correlative Raman-AFM image of a three component polymer blend consisting of PS-SBR_EHA: AFM phase image (a), confocal Raman image (b), and correlated Raman-AFM image (c).

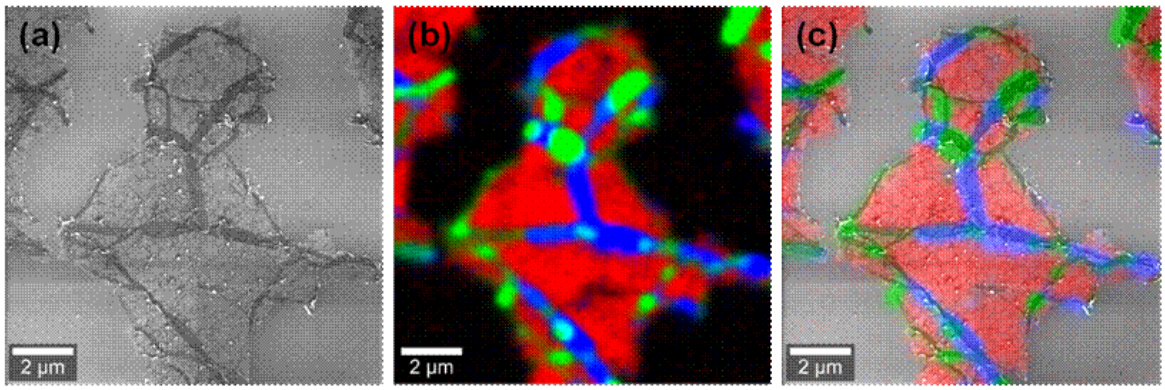

Figure 2. Correlative Raman-SEM imaging of CVD graphene: SEM (a), Raman (b) and RISE image (c).

Correlative Microscopy in Life and Material Sciences (combination of several microscopy techniques)

IM7.P175
Far-field Raman and tip-enhanced Raman spectroscopy (TERS) on B-site ordered double perovskite $A_2BB'O_6$ (A=La, Pr, Sm; B=Co, Ni; B'=Mn) thin films

C. Meyer[1], H. Ehlers[1], S. Hühn[1], M. Jungbauer[1], S. Merten[1], B. Damaschke[1], K. Samwer[1], V. Moshnyaga[1]

[1]Georg-August-Universität Göttingen, I. Physikalisches Institut, Göttingen, Germany

christoph.meyer@phys.uni-goettingen.de

B-site cation ordered double perovskites $A_2BB'O_6$ (A=La, Pr, Sm; B=Co, Ni; B'=Mn) with monoclinic $P12_1/n1$ structure can be derived from a perovskite ABO_3 by alternating layers of B^{2+} and B'^{4+} on the B-site. They are promising materials for spintronic applications due to ferromagnetic ordering, magnetodielectric coupling and multiferroic behavior. Since the performance is strongly affected by the degree of B-site ordering, we applied Raman spectroscopy to correlate the phonon spectra with the B-site ordering as well as with the A-cation influence. Saturation magnetization and temperature dependent magnetization measurements were additionally accomplished for indirect quantification. A study of the far-field Raman and tip-enhanced Raman spectroscopy (TERS) of the ordered double perovskite thin films on SrTiO3(100), SrTiO3(111) and MgO(100) substrates, grown by metalorganic aerosol deposition (MAD) technique, was performed. Polarization dependent TERS was carried out to determine the contributions for enhancement due to surface plasmon polariton (SPP) excitation within the tip, incident field depolarization and their interplay; they were set in relation to the far-field Raman spectra for quantification. Due to long-range B-site cation ordering, the spectra exhibit a strong high-frequency mode with A_g symmetry in the 600-700 cm^{-1} range, generated by octahedral $(B/B')O_6$ stretching vibrations, and largest TERS contrast of 60-100 in the crossed polarization configuration. A tip-induced depolarization of the incident light and a significant intensity enhancement for all observable modes due to general field amplification were observed. Therefore double perovskites provide an excellent test system to study TERS phenomena on oxide surfaces. Because TERS enhances also the spatial resolution approximately to the tip apex size (20-50 nm), local sensitivity at the nanoscale can be potentially achieved. First results on $CaMnO_3$ and highly doped $La_{1-x}Ca_xMnO_3$ thin films reveal a strong A_g mode at 642 cm^{-1}, which can be observed only with TERS in the parallel polarization configuration. Since this mode can be attributed to the existence of small Hausmannite (Mn_3O_4) precipitations on the surface, it shows the possibility of successful local TERS microscopy on our setup.

1. Financial support by the DFG via project SFB 1073/B04 is gratefully acknowledged.

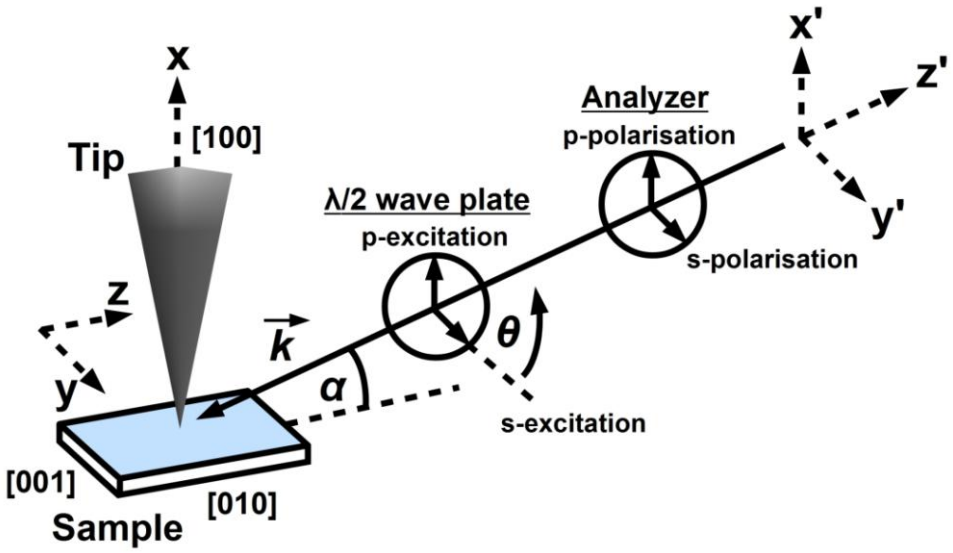
x
[100]
Tip
z
y
[001]
[010]
Sample
Analyzer
p-polarisation
s-polarisation
x'
z'
y'
λ/2 wave plate
p-excitation
s-excitation
α
θ
k

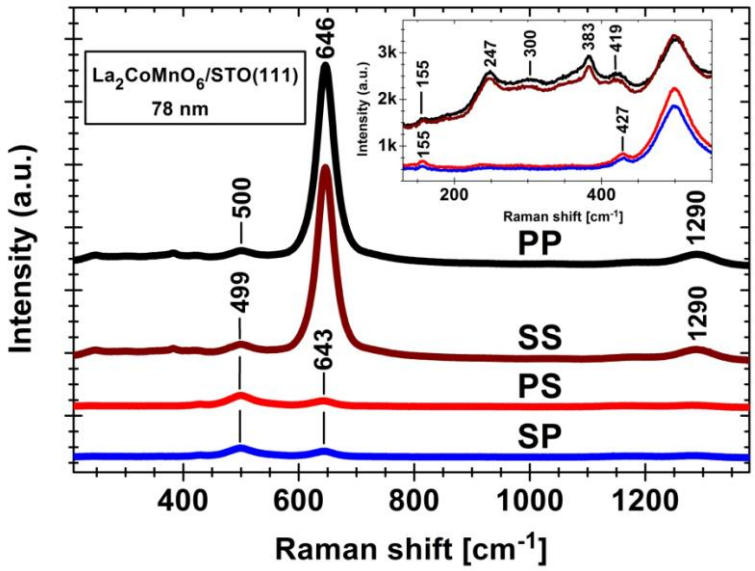
La2CoMnO6/STO(111)
78 nm
646
500
499
643
1290
1290
PP
SS
PS
SP
Intensity (a.u.)
Raman shift [cm-1]
247
300
383
419
155
155
427

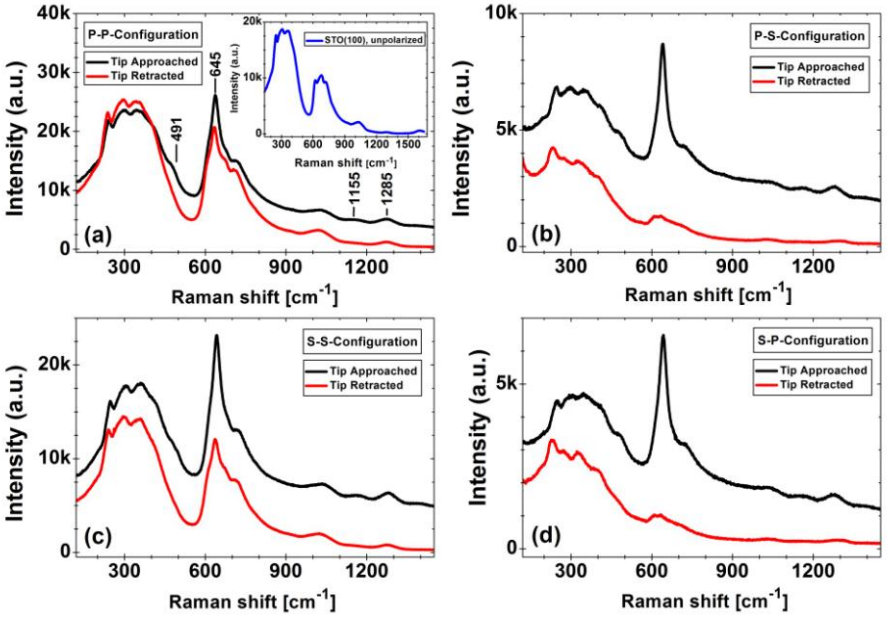
P-P-Configuration
Tip Approached
Tip Retracted
STO(100), unpolarized
645
491
1155
1285
(a)
P-S-Configuration
(b)
S-S-Configuration
(c)
S-P-Configuration
(d)
Intensity (a.u.)
Raman shift [cm-1]

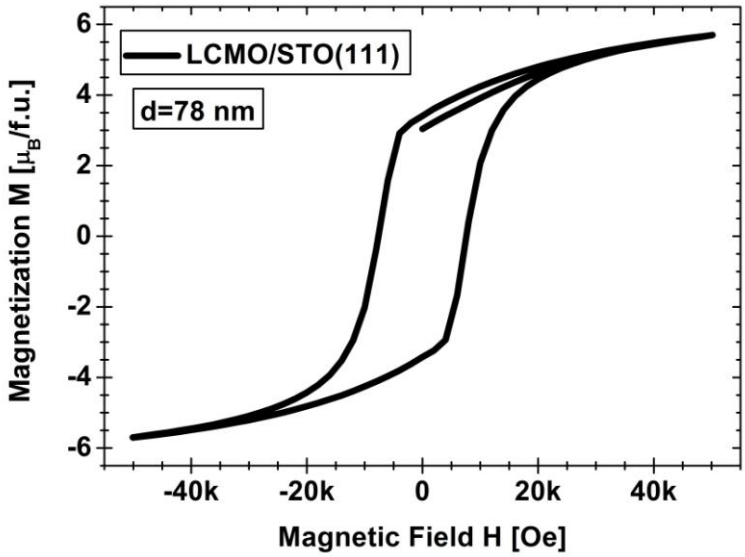
LCMO/STO(111)
d=78 nm
Magnetization M [μB/f.u.]
Magnetic Field H [Oe]
6
4
2
0
-2
-4
-6
-40k
-20k
0
20k
40k

Correlative Microscopy in Life and Material Sciences (combination of several microscopy techniques)

IM7.P176
Correlative microscopy based on secondary ion mass spectrometry for high-resolution high-sensitivity nano-analytics

D. Dowsett[1], T. Wirtz[1], S. Eswara Moorthy[1]

[1]Luxembourg Institute of Science and Technology, Advanced Instrumentation for Ion Nano-Analytics (AINA), Belvaux, Luxembourg

david.dowsett@list.lu

As analysis volumes shrink, higher and higher demands are placed on imaging and analytical techniques. New characterisation tools need to anticipate these research trends, but as more and more techniques approach their fundamental limits it is only by combining multiple techniques that disruptive advances may be made.

While techniques such as Electron Microscopy, Helium Ion Microscopy and Scanning Probe Microscopy are commonly used for high-resolution imaging, they do not provide the highest sensitivity analytical information. Both EDX and EELS have limited sensitivity, neither can distinguish isotopes and both have difficulty with light elements. While analytical techniques such as secondary ion mass spectrometry (SIMS) offer extremely high chemical sensitivity, they typically suffer from poor lateral resolution due to the interaction volume of the analytical beam with the sample. However, by combing high resolution microscopy techniques with high sensitivity analytical techniques, these intrinsic drawbacks may be overcome.

In order to obtain chemical information with both the highest possible sensitivity and the highest possible lateral resolution we have investigated combining SIMS with several microscopy techniques and developed three corresponding prototype instruments:

TEM -SIMS : FEI Tecnai F20 equipped with a Ga+ FIB column and dedicated SIMS extraction optics, mass spectrometer and detectors (figure 1)

HIM - SIMS : Zeiss ORION Helium Ion Microscope with dedicated SIMS extraction optics, mass spectrometer and detectors [1,2]

SPM - SIMS : Cameca NanoSIMS 50 with integrated AFM/SPM [3-5]

In order to reach good detection limits when probing very small voxels in imaging applications, the ionization probability of the sputtered atoms and molecules needs to be maximized. When using primary ion species such as Ga (as is the case on the integrated TEM - SIMS instrument) or noble gases (HIM - SIMS instrument), the intrinsic yields are low compared to the ones found in conventional SIMS. However, the yields may be drastically increased by using reactive gas flooding during analysis. Our results show that both negative and positive ion yields obtained with Ga+ bombardment are increased by up to 4 orders of magnitude when using such reactive gas flooding. This optimization of secondary ion yields leads to detection limits varying from 10^{-3} to 10^{-6} for a lateral resolution between 10 nm and 100 nm (figure 2).

Each of these three combinations offers unique advantages in terms of correlative microscopy combining both high special resolution structural and high sensitivity chemical information. We will present the latest results and perspective for each of these combinations.

1. T. Wirtz et al., Appl. Phys. Lett. 101 (2012) 041601
2. L. Pillatsch et al., Appl. Surf. Sci. 282 (2013) 908
3. T. Wirtz et al., Surf Interface Anal. 45 (1) (2013) 513-516
4. T. Wirtz et al., Rev. Sci. Instrum. 83 (2012) 063702
5. C. L. Nguyen et al., Appl. Surf. Sci. 265 (2013) 489-494

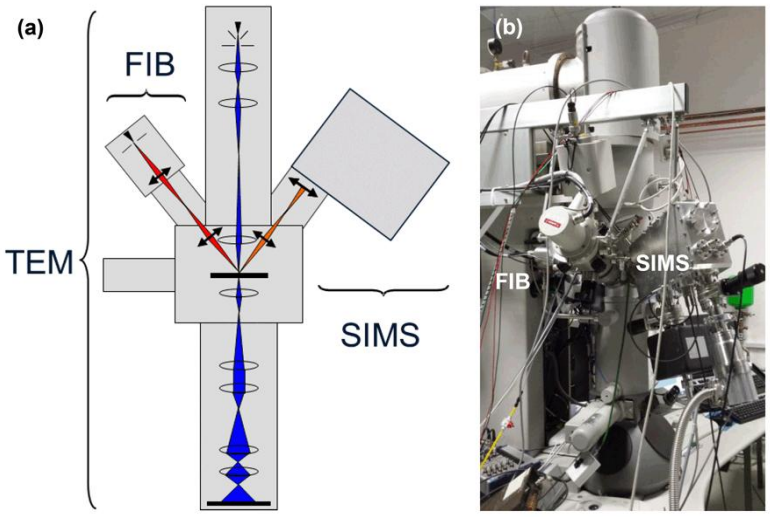

Figure 1. Prototype of a combined TEM-SIMS instrument: modified Tecnai F20 equipped with a Ga+ gun and dedicated SIMS column.

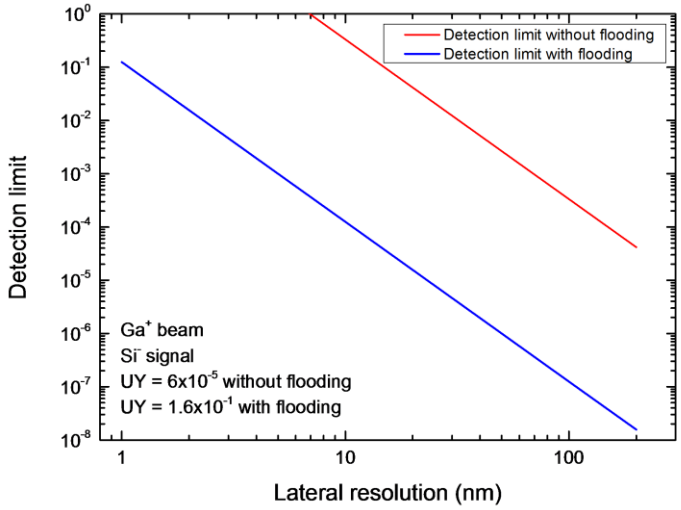

Figure 2. Detection limit using a Ga+ FIB with and without Cs^0 flooding vs. minimum feature size: example for the detection of Si^-.

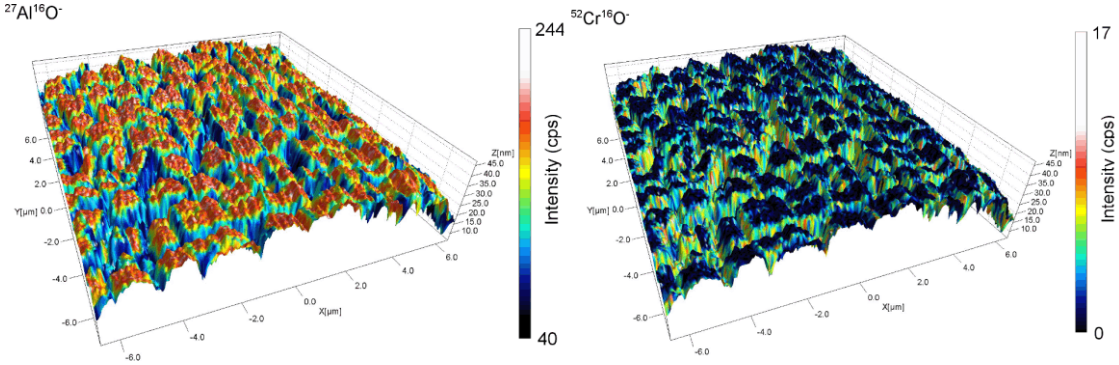

Figure 3. Combined SIMS-SPM 3D reconstruction of a nickel-based super-alloy: Al distribution (left), Cr distribution (right)

Correlative Microscopy in Life and Material Sciences (combination of several microscopy techniques)

IM7.P177
Targeted 3D-CLEM workflow on cultured cells

A. Steyer[1], N. Schieber[1], N. Duishoev[1], R. Pepperkok[1], Y. Schwab[1]

[1]EMBL Heidelberg, CBB, Heidelberg, Germany

anna.steyer@embl.de

Correlative light and electron microscopy (CLEM) experiments uniquely provide an accurate link between the imaging of individual living cells and their 3D ultrastructure. However, they generally suffer from a low throughput. The major hurdles include tracking the object throughout the different imaging modalities, the tedious procedures for sample preparation and the lack of automation in the data acquisition by electron microscopy. Our workflow is developed and tested on cultured cells and employed in a study of the Golgi apparatus organization. We visualize, at the ultrastructural level, how specific mutations (revealed in a genome-wide siRNA screen (1)) influence the morphology of the Golgi apparatus. Fluorescence microscopy is utilized to screen for specific phenotypes and electron microscopy to look at the corresponding ultrastructure. By combining CLEM and automated serial imaging, we intend to dramatically improve the throughput of CLEM experiments. On one hand CLEM allows for addressing highly heterogeneous populations, and optimizes the data volume by targeting image acquisition to sub-cellular regions. On the other hand focused ion beam-scanning electron microscopy (FIB-SEM) fully automates the serial sectioning of the embedded cells and the acquisition of 3D image stacks.

1. Simpson J. C., et al. (2012). "Genome-wide RNAi screening identifies human proteins with a regulatory function in the early secretory pathway" Nat Cell Biol 14(7): 764-774.

Correlative Microscopy in Life and Material Sciences (combination of several microscopy techniques)

IM7.P178
The rapid freezing system and advanced cryo-stage for direct correlative live-cell microscopy and cryo-electron tomography

S. Jun[1], E. Lee[2], H. S. Jung[1], M. S. Seok[1], S.- M. Jin[2]

[1]Korea Basic Science Institute, Daejeon, Korea
[2]Chungnam National University, Daejeon, Korea

smjun@kbsi.re.kr

Cryo-electron tomography (cryoET) allows 3D visualization of cellular structures at molecular resolution in a close-to-physiological state [1,2]. However, direct visualization of individual viral complexes in their host cellular environment with cryoET is challenging [2,3], due to the infrequent and dynamic nature of viral entry, particularly in the case of HIV-1. While time-lapse live-cell imaging has yielded a great deal of information about many aspects of the life cycle of HIV-1 [4-8], the resolution afforded by live-cell microscopy is limited (~ 200 nm). My work was aimed at developing a correlation method that permits direct visualization of early events of HIV-1 infection by combining live-cell fluorescent light microscopy, cryo-fluorescent microscopy, and cryoET. In this manner, live-cell and cryo-fluorescent signals can be used to accurately guide the sampling in cryoET [9,10]. Furthermore, structural information obtained from cryoET can be complemented with the dynamic functional data gained through live-cell imaging of fluorescent labeled target.

In here, the rapid freezing system and advanced cryo-stage are described as new tools for correlative microscopy. In visualization of HIV-1 infection using the correlative microscopy, the live cell imaging work of the experiment is crucial to determine the dynamic behavior of the particles with a time resolution of a few seconds. Although it is possible to correlate the last fluorescence confocal image in a live-cell series with cryoET for stationary viral particles, the time lapse of about 2-5 min between the last confocal live-cell image and plunge-freezing might be long enough for the position of the fluorescent particle to change due to the movement of either the cell or the particle itself. Therefore, to facilitate cryoET data acquisition for high-resolution 3D structure analysis, we designed and built both the rapid freezing system for the subsequent freezing within a few seconds and advanced cryo-fluorescence light microscopy stage for imaging frozen-hydrated samples. Using the rapid freezing system, the sample grid is frozen within several seconds immediately after preforming live-cell imaging to achieve the ‘direct’ correlation and get a ‘real’ image of nature. In addition, the advanced cryo-stage allows both light and electron microscopies to be performed on the same EM cryo-holder (in this poster, Gatan 626 cryoholder) without specimen transfer. In future works, we will apply the new tools for the correlative microscopy to investigate cell signaling events and many other cellular processes and also develop the freezing system to reduce the transfer time from the live-cell microscopy to the cryo-fixation.

1. Leis, A. et al. Trends Biochem Sci 34, (2009) 60-70.
2. Jun, S. et al. J Anal Sci Tech 3, (2012) 202-208.
3. Maurer, U.E. et al. Proc Natl Acad Sci U S A 105, (2008) 10559-10564.
4. McDonald, D. et al. J Cell Biol 159, (2002) 441-452.
5. Arhel, N. et al. Nat Methods 3, (2006) 817-824.
6. Gousset, K. et al. PLoS Pathog 4, (2008) e1000015.
7. Jouvenet, N. et al. Nature 454, (2008) 236-240.
8. Koch, P. et al. Retrovirology 6, (2009) 84.
9. Jun, S. et al. Structure 19, (2011) 1573-1581.
10. Jun, S. et al. J Vis Exp 76, (2013) e50386.

Correlative Microscopy in Life and Material Sciences (combination of several microscopy techniques)

IM7.P179
Development of epithelial and mesenchymal compartments in the lung air-sac system of the embryonic chicken: a light- and electron microscopic study

A. Greulich[1], E. Hempel[1], M. Frank[1]

[1]University Medicine Rostock, Medical Biology and Electron Microscopy Centre, Rostock, Germany

marcus.frank@med.uni-rostock.de

The construction of the avian respiratory system is unique and provides the most efficient gas exchange among vertebrates with a continuous unidirectional air-flow across the respiratory epithelium. In the bird lung, a parallel array of epithelial tubes, the parabronchial system, is ventilated by accessory structures, the air-sacs, emerging anterior and posterior from the lung tissue. Thus, lung development and branching morphogenesis in the bird differs largely from the well-studied situation in the mammalian lung. In the embryonic chicken, lung development starts at embryonic day E4.5 with lung bud formation and continues until hatching (E21) after three weeks of incubation.

In our study, we have examined the epithelial and mesenchymal differentiation during formation of parabronchi and expansion of air-sacs in more detail with immunocytochemistry, transmission- and scanning electron microscopy. Antibodies for E-cadherin (a marker of the epithelial compartment) and smooth muscular actin (SMA, a marker of the mesenchymal compartment), as well as for Sox2, a transcription factor involved in lung epithelial morphogenesis were used with a focus on developmental stages E8 to E18.

We find that anti-E-cadherin immunostaining in paraffin sections precisely outlines the epithelial compartment of the parabronchi and is especially useful to illustrate the invasion of epithelial cells into the mesenchyme during the formation of atrial openings and during differentiation of the gas exchange tissue. This process starts around E12 from the parabronchi and continuously proceeds into the surrounding mesenchyme with the exception of small interparabronchial septa (Fig. 1 A). On electron microscopic level, E-cadherin immunoreactivity is frequently observed at apical junctional complexes visible in thin sections of LR-White embedded lung tissue (Fig.1 B).

The parallel differentiation of the mesenchyme, e.g. of smooth muscles forming around the atrial openings and in the wall of blood vessels, was visualized by anti-SMA immunostaining. We observed strong Sox2 immunoreactivity in the proximal airway epithelium, e.g. in the primary and secondary bronchi as well as in the epithelium lining the air-sacs. Sox2 and E-cadherin labeling allowed us to visualize the sprouting and bilateral extension of anterior air-sacs into thoracic and cervical regions from E10 onwards. In the differentiating parabronchi of the lung, Sox2 expression is lower and found in epithelial as well as in underlying mesenchymal cells, both in nuclear and non-nuclear distribution.

Taken together, the combined use of immunocytochemistry at light and electron microscopic level allowed us to monitor the complex epithelial-mesenchymal interactions during chick lung development in more detail, complementing previous morphological observations on bird lung morphogenesis.

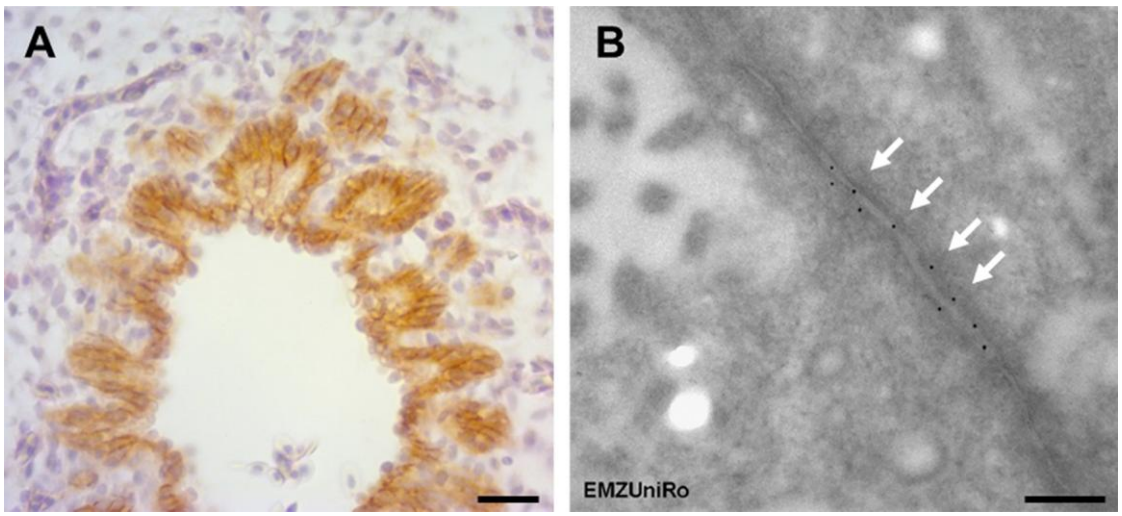

Figure 1. Parabronchial epithelium of E16 embryonic chicken lungs stained with anti-E-cadherin antibodies using biotinylated secondary antibodies / streptavidin peroxidase on paraffin sections (A) or using 10nm gold-coupled secondary antibodies on thin sections of LR-White resin in post-embedding staining protocol (B). Note the localization of E-cadherin to the junctional complex (arrows). Scale bars are 20µm and 200nm.

Correlative Microscopy in Life and Material Sciences (combination of several microscopy techniques)

IM7.P180
Characterization of blue laser diodes by X-ray computer tomography and correlative microscopy

T. Ogbazghi[1], B. Willeke[2], C. Thomas[1]

[1]Hamm-Lippstadt University of Applied Sciences, Micro- and Nanotechnology, Lippstadt, Germany
[2]HELLA Hueck KGaA & Co., L-LAB, Lippstadt, Germany

christian.thomas@hshl.de

Development of new lighting systems in automotive industry has been accelerating within the last years. The rapid replacement of halogen and high-intensity discharge (HID) lamps in car lighting systems by Light Emitting Diodes (LED) is not only based on lower production costs but also due to longer lifetime, higher efficiency and better reliability [1,2]. After introduction and implementation of LEDs in headlight systems the focus nowadays shifts to the field of laser diodes. which may outperform the LEDs in the near future [2].

A typical wavelength of commonly used semiconductor lasers for headlight systems is 450 nm with an optical output power between 500mW to 1,6W. Similar to the blue LEDs used for white color lighting, the blue Laser light is converted by a ceramic phosphor plate into white light. The difference in this approach is that the light converting inorganic phosphor is not directly mounted to the light emitting source but beyond laser diode and lens. Therefore, the laser light is focused onto the phosphor resulting in an emission of white light as a mix of converted yellow light and scattered blue light [3].

Due to their application in automotive tasks the demands on laser diodes with respect to reliability and stability are quite high over the whole lifetime of each device. Especially large temperature gradients and mechanical vibrations should not influence the performance of the laser. Therefore, reliability tests and failure analysis are essential for the development of laser headlight systems.

A promising approach for precise failure analysis of laser diodes is the combination of X-ray Computer Tomography (CT) and Correlative Light and Electron Microscopy (CLEM) which will be presented in this contribution. The combination enables a fast and reliable workflow for precise failure analysis. CT gives a non-destructive 3D overview of the device with its internal structure down to the sub-µm range. This allows exact localization of defects for target preparation. After preparation the defects can be investigated by CLEM combining light (LM) and scanning electron microscopy (SEM) characterization in the same location [4, 5]. Thereby the diode can still be in active operation. This enables a direct correlation of functional and structural information on the microscale with the different techniques [6]. Thus, failure characteristics can be precisely investigated.

Fig.1 exemplarily shows a laser diode in the original TO56 package removed from the headlight system. The complete device is characterized by CT measurement with 3µm voxel size. After reconstruction and rendering 3D volume information is obtained. This is depicted in Fig.2 as a 3D image. Possible defects can be extracted from this information for further characterization. Figs. 3 and 4 show a grinded and polished cross section of the laser diode under active biasing. Distribution of light emission can be shown in the LM without additional illumination (Fig.3), whereas the SEM shows the microstructure of the device by SE imaging. The overlay of both images (Fig.4) allows correlation of functional behavior and structure to analyze defects as it will be shown in this contribution.

1. M. Löffler-Mang, Optische Sensorik, Vieweg 2012, p.98
2. F. Tappe, J. Meyer, 10th Intern. Symposium on Automotive Lightning, Volume 15 (2013), p.150
3. R. Hying, A. Nauen, Th. Reiners, S. Haneder, Th. Dobbertin, 10th Intern. Symposium on Automotive Lightning, Volume 15 (2013), p.112-114.
4. Ch. Thomas, M. Edelmann, C. Hafner, T. Bernthaler, G. Schneider, Microsc. Microanal. 16, Suppl. 2 (2010), p.784
5. A.F. Elli, Ch. Thomas, Ch. Böker, M. Wiederspahn, Optik & Photonik 7, no.1 (2012), p.32
6. T. Ogbazghi, Ch. Thomas, Imaging & Microscopy 3/2014 (2014), 32-34

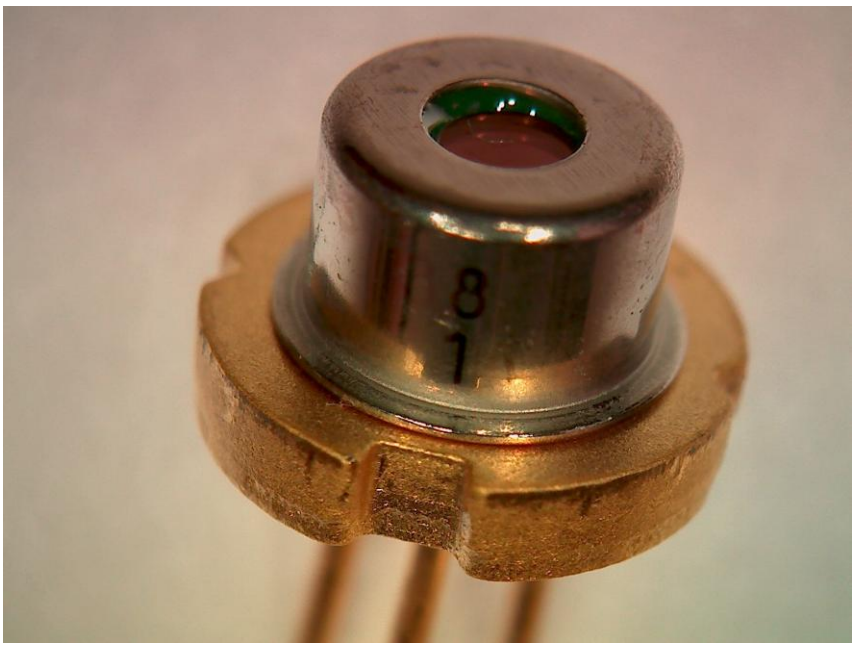

Figure 1. Packaged laser diode

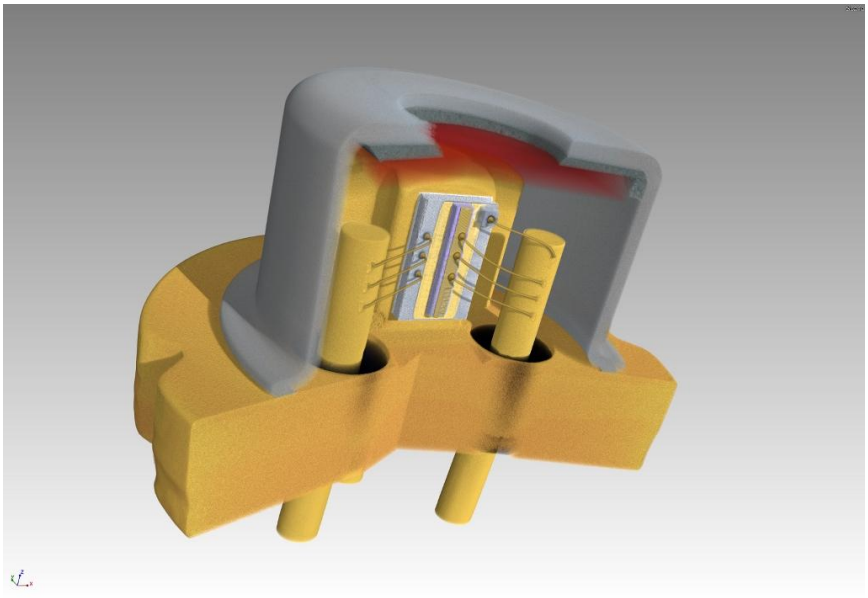

Figure 2. 3D reconstruction of internal structures obtained in CT

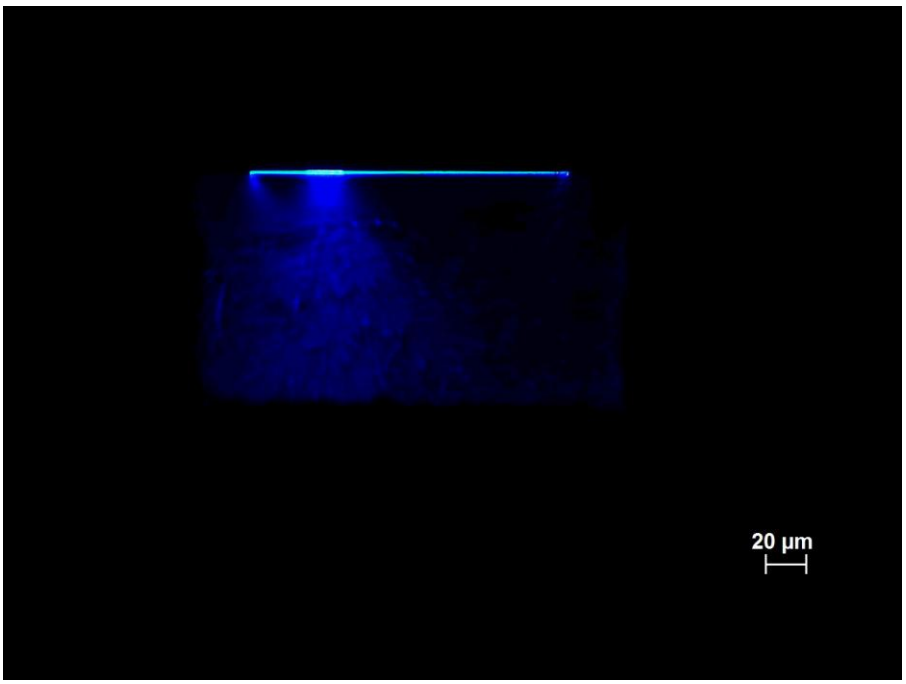

Figure 3. LM image showing distribution of light emission in the diode

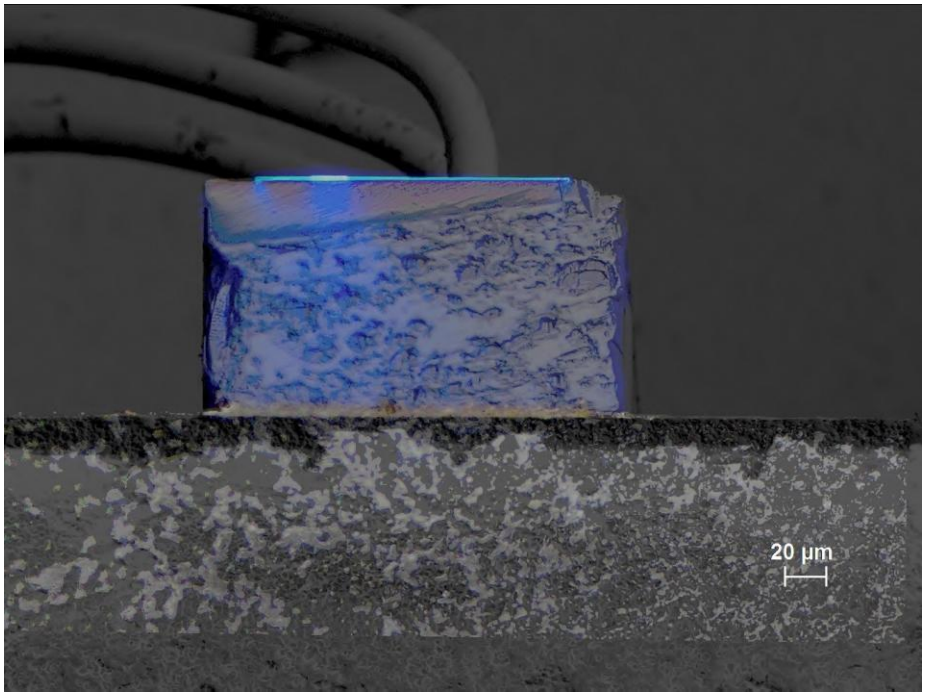

Figure 4. Overlay of function and structure by CLEM

Neurobiology

LS1.001
Structural plasticity of mossy fiber synapses in the hippocampus

M. Frotscher[1]

[1]Institute for Structural Neurobiology, Center for Molecular Neurobiology Hamburg (ZMNH), Hamburg, Germany

michael.frotscher@zmnh.uni-hamburg.de

The granule cells of the dentate gyrus give rise to thin unmyelinated axons, the mossy fibers. Their endings form giant boutons on the large complex spines on proximal dendrites of CA3 pyramidal cells and mossy cells in the hilus of the dentate gyrus. Mossy fiber (MF) synapses are easily recognized by light- and electron microscopy allowing the investigator to study an identified central synapse. We aim at determining functional and structural changes associated with MF synaptic plasticity. By using high-pressure freezing for electron microscopy (HPF/EM) we found that the induction of chemical long-term potentiation (cLTP) resulted in a decreased number of synaptic vesicles in MF boutons associated with an increased perimeter of MF bouton profiles, suggesting the fusion of abundant vesicles as a result of the stimulation. On the postsynaptic side we observed the formation of finger-shaped small spines, emanating from the large complex spines on CA3 pyramidal cell dendrites. Accordingly, the number and area of spine profiles per area of bouton profiles was significantly increased following the induction of cLTP. These newly generated spines were endowed with synaptic contacts as revealed by quantifying the number of active zones per bouton area. Quantitative immunogold studies for phospho-cofilin pointed to cLTP-induced reorganization of the actin cytoskeleton. Synaptic plasticity of individual MF synapses was induced by pairing the stimulation of single MF boutons with back-propagating action potentials in the target neuron and monitoring calcium transients in the postsynaptic spine. Having established protocols for HPF/EM and the induction of synaptic plasticity at single MF synapses, we are now going to determine the molecular players underlying the functional and structural changes associated with MF synaptic plasticity.

Neurobiology

LS1.002
Correlative optical and isotopic super-resolution imaging

S. Rizzoli[1]

Universitätsmedizin Göttingen, Abteilung für Neuro- und Sinnesphysiologie, Göttingen, Germany

srizzol@gwdg.de

Studying the long-term metabolism and atomic composition of cells has become an important avenue of research, especially since it can be performed *in situ* by secondary-ion mass spectrometry (SIMS). This method, however, is limited to investigating whole cellular areas – it cannot reveal specific organelles or protein complexes. This type of problem has been solved in the optics field by the introduction of genetic encoding of green fluorescent proteins, or by specific immunostaining. We followed a comparable strategy for SIMS imaging. First, we established protocols for correlative optical and isotopic nanoscopy (COIN), in which we first image biological samples in super-resolution fluorescence microscopy, and then in SIMS. Second, we generated isotopic probes, containing several ^{19}F or ^{15}N atoms, which we link to specific proteins by genetic code expansion and click chemistry. These probes are also fluorescently labelled, thus enabling dual optical and isotopic imaging. This second method, which we termed specific protein isotopic labeling, or SPILL, enables now the investigation of the isotopic composition of cells, organelles and protein complexes, in any biological system that is compatible with genetic code expansion. Such systems include all cell culture systems, from bacteria and yeast cells to mammalian cultures, as well as small model organisms like *C. elegans* and *Drosophila*. Thus, SPILL opens a gate into a previously unexplored field of science: the molecular and atomic organisation of organelles or cellular sub-compartments.

Neurobiology

LS1.003
In vivo calcium imaging in E13-E15 mouse embryos connected to the mother

M. Yuryev[1], C. Pellegrino[2,3], V. Jokinen[4], S. Khirug[1], L. Khiroug[1], C. Rivera[1,2,3]

[1]University of Helsinki, Neuroscience Center, Helsinki, Finland
[2]INSERM, INMED, Marseille, Finland
[3]Aix-Marseille Université, Marseille, Finland
[4]Aalto University, School of Chemical Technology, Espoo, Finland

mikhail.yuryev@helsinki.fi

While calcium activity is being extensively studied *in vivo* in the adult brains in rodents, the thorough investigation of calcium events in the pre-natal stage of development has been obstructed by the lack of *in vivo* measurements methods. Most of the information on the calcium dynamics in the mammalian embryonic brains has been obtained using *in vitro* and *ex vivo* preparations such as acute slice imaging. Different patterns of calcium activity have been shown such as singular events, synchronized coupled rises in neighboring cells and calcium waves. However, the temporal and spatial dynamics of these events has never been confirmed in the *in vivo* conditions. Here, we present the method of *in vivo* two-photon calcium imaging in the mouse embryos at the age E13-E15 while still connected to the mother.

To measure calcium the cells were loaded with acetomethyl ester forms of different calcium dyes in utero. The embryos were immobilized in a custom made chamber that allowed keeping the embryos connected to the anesthetized mother through the umbilical cord. The chamber was filled with artificial cerebro-spinal fluid.

Using the system developed spontaneous calcium events were observed under isoflurane anesthesia of the mother while they were absent under ketamine/xylazine anesthesia. To study the intercellular connectivity properties we stimulated calcium waves using the high power laser emission and show the significant increase in the number of the cells involved in the wave propagation after injection of caffeine to the embryos while the waves were suppressed by injection of non-selective ATP-receptors blocker suramin.

Altogether, the data demonstrates the capabilities of the *in vivo* imaging method for investigation of calcium dynamics in the mouse embryos.

Neurobiology

LS1.004
Zooming in on synapses: visualizing and clasifying dendrite spines with super resolution microscopy

C. Fitzsimons[1], P. Bielefelf[1], M. Schouten[1], D. Alatriste Gonzalez[1], F. Verbeek[1,2], E. Manders[1,2,3]

[1]University of Amsterdam, Center for Neuroscience, Swammerdam Institute for Life Research, Amsterdam, Netherlands
[2]Leiden University, Imaging & BioInformatics, Leiden Institute of Advanced Computer Science, Leiden, The Netherlands, Netherlands
[3]University of Amsterdam, van Leeuwenhoek Centre for Advanced Microscopy, Swammerdam Institute for Life Sciences, Amsterdam, Netherlands

c.p.fitzsimons@uva.nl

Dendritic spines are protrusions that emerge from the dendrite of a neuron and represent the primary postsynaptic targets of excitatory inputs in the brain. Technological advances have identified these structures as key elements in neuron connectivity and synaptic plasticity. Several brain functions are thought to rely on spine plasticity, including learning and memory. Additionally, whereas many psychiatric and neurological disorders are accompanied by alterations in spine morphology and synapse numbers, the quantitative analysis of spine morphology remains an essential problem. Dendritic spines can be readily identified by confocal laser-scanning fluorescence microscopy. However, measuring subtle changes in the shape and size of spines is difficult because spine dimensions other than length are usually smaller than what conventional optical systems can reliably resolve. Up to now, several recently developed “super-resolution” techniques have been used to image dendritic spines. Thus there’s still a need for an imaging technique that combines spatial resolution, speed and large fields of view. Here we apply super resolution structured illumination microscopy (SIM) to the imaging of dendritic spines in primary hippocampal neuron cultures. We transfected these cultures with different fluorescent proteins and use specialized software to automatically trace and reconstruct dendrites and spines in 3 dimensions from confocal and SIM image stacks. Using machine-learned data mining techniques we plan to extract structural parameters from 3D dendritic spine images that cannot be quantified by conventional confocal microscopy techniques. These parameters will improve and accelerate standardized classification of dendritic spine morphologies. Finally, we expect this new classification for dendritic spine morphology and dynamics can assist in the development of an innovative, high throughput screening method for the discovery of new compounds with potential application in psychiatric and neurologic disorders.

1. This work was financed by a VIDI NWO grant: H64.09.016 and ISAO Grant: 14533 to CPF.

Neurobiology

LS1.005
High-resolution localization of the F-BAR domain protein syndapin I at membranes of hippocampal neurons

E. Seemann[1], K. Schneider[1], M. Westermann[2], M. M. Kessels[1], B. Qualmann[1]

[1]Jena University Hospital, Institute of Biochemistry, Jena, Germany
[2]Jena University Hospital, Electron Microscopy Center, Jena, Germany

eric.seemann@med.uni-jena.de

F-BAR domain proteins like syndapins are dimeric, lipid-binding proteins that associate with cellular membranes. They induce membrane curvature by partial membrane insertion and by imposing their curved shape onto the lipid bilayer [1]. Syndapin I is a predominantly neuronal protein shown to play a role in vesicle formation processes and actin cytoskeletal dynamics [2, 3, 4].

Using the freeze-fracture replica immunolabeling technique (FRIL) we achieved large and detailed ultrastructural views of the topology of cellular membranes in the transmission electron microscope combined with the immunolocalization of membrane-attached proteins. We furthermore established a method to grow primary hippocampal neurons on sapphire discs to preserve the neuronal network during freeze-fracturing.

When applying the FRIL technique chemically unfixed cellular samples are rapidly cryofixed in their natural environment. In a second step the samples are fractured, replicated and immobilized by a platinum/carbon evaporation followed by a careful SDS treatment. After the “SDS-digestion” [5] molecules like membrane proteins or lipids that are in direct contact with the platinum-carbon replica keep bound to the replica film and are accessible to immunolabeling [6]. This “SDS-digestion” allowed us to explicitly study membrane-associated, endogenous syndapin I at high resolution in membranes of neurons.

In this work we show the localization of endogenous syndapin I at the plasma membrane of primary hippocampal neurons grown on sapphire discs by using the FRIL technique. Syndapin I was detected at the protoplasmic fracture face of the plasma membrane and membrane-associated syndapin I preferentially occurred in dendritic spines (Figure 1). Syndapin I was not evenly distributed at spine membranes, our analyses revealed that syndapin I was enriched in spine heads in all examined types of spines (Figure 2). Additionally we could show that syndapin I accumulates in form of nanoclusters at the plasma membrane of the head region of dendritic spines [7].

In summary, the freeze-fracture replica immunolabeling technique showed that plasma membrane-associated syndapin I in dendritic spines is enriched in spine heads and forms nanodomains, which act as important spatial cues and organizing platforms, shaping dendritic membrane areas into synaptic compartments. Our data are an excellent example for studying membrane-associated proteins in terms of localization and function at the ultrastructural level using FRIL.

1. Qualmann B, Koch D, Kessels MM, EMBO Journal. **30** (2011), 3501-3515
2. Qualmann B, Roos J, DiGregorio PJ, Kelly RB, Molecular Biology of the Cell **10** (1999), 501-513
3. Kessels MM, Qualmann B, EMBO Journal **21** (2002), 6083-6094
4. Koch D, Spiwoks-Becker I, Sabanov V, Sinning A, Dugladze T, Stellmacher A, Ahuja R, Grimm J, Schüler S, Müller A, Angenstein F, Ahmed T, Diesler A, Moser M, Tom Dieck S, Spessert R, Boeckers TM, Fässler R, Hübner CA, Balschun D, Gloveli T, Kessels MM, Qualmann B, EMBO Journal **30** (2011), 4955-4969
5. Fujimoto K, Journal of Cell Science **108** (1995), 3443-3449
6. Westermann M, Steiniger F, Richter W, Histochemistry and Cell Biology **123** (2005), 613-620
7. Schneider K, Seemann E, Liebmann L, Ahuja R, Koch D, Westermann M, Hübner CA, Kessels MM, Qualmann B, The Journal of cell biology **205** (2014), 197-215

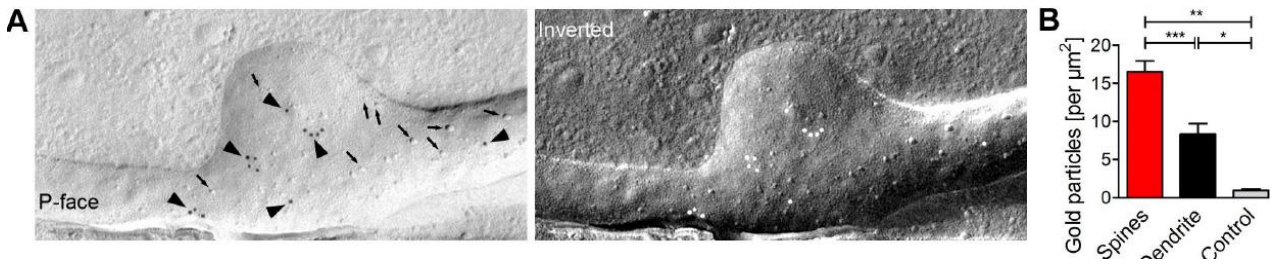

Figure 1. (modified from [7]. A) Electron micrograph of an anti-syndapin I immunogold labeled (arrowheads) replica of a dendrite section of rapid-frozen, freeze-fractured primary rat hippocampal neurons (DIV 16). Examples of intramembrane particles (arrows) identifying the P-face. Right, inverted image (light = C/Pt shadowing direction). Scale bar 200nm. B) Quantitation of anti-syndapin I labeling densities in spine, dendrite, and control areas. *, P < 0,05; ** P < 0,01; *** P < 0,001. Data represent mean ± SEM (error bars)

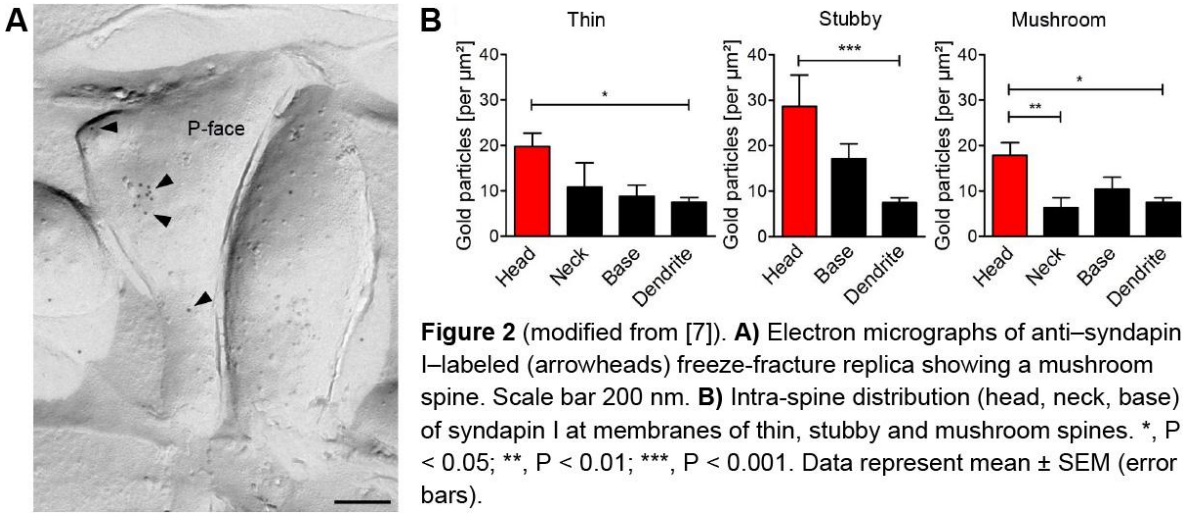

Figure 2 (modified from [7]). **A)** Electron micrographs of anti–syndapin I–labeled (arrowheads) freeze-fracture replica showing a mushroom spine. Scale bar 200 nm. **B)** Intra-spine distribution (head, neck, base) of syndapin I at membranes of thin, stubby and mushroom spines. *, P < 0.05; **, P < 0.01; ***, P < 0.001. Data represent mean ± SEM (error bars).

Figure 2. (modified from [7]. A) Electron micrographs of anti-syndapin I-Labeled (arrowheads) freeze-fracture replica showing a mushroom spine. Scale bar 200nm. B) Intra-spine distribution (head, neck, base) of syndapin I at membranes of thin, stubby and mushroom spines. * P < 0,05; ** P < 0,01; *** P < 0,001. Data represent mean ± SEM (error bars).

Neurobiology

LS1.006
Molecular mechanism of myelin disassembly

M.- T. Weil[1], W. Möbius[1], T. Ruhwedel[1], A. Winkler[2], C. Stadelmann-Nessler[2], S. Frey[3], P. Kursula[4], M. Kerschensteiner[5], M. Simons[1]

[1]MPI for experimental medicine, Göttingen, Germany
[2]University Medical Center, Institute for Neuropathology, Göttingen, Germany
[3]Max Planck Institute for Biophysical Chemistry, Department of Cellular Logistics, Göttingen, Germany
[4]University of Bergen, Department of Biomedicine, Bergen, Norway
[5]Medical Center of the LMU Munich, Institute of Clinical Neuroimmunology, Munich, Germany

weil@em.mpg.de

Myelin is a specialized membrane produced by oligodendrocytes, which ensheaths axons enabling fast signal conduction. Myelin is a major target of autoimmune diseases, such as multiple sclerosis. However, the mechanisms of myelin damage and disassembly are poorly understood.

Myelin is characterized by the stacking of multiple layers of membranes compacted by myelin basic protein (MBP). This naturally unstructured protein has a high positive charge at physiological pH and hence, binds negatively charged lipids. The binding of MBP to the membranes leads to its self-assembly and the compaction of the leaflets.

Our studies could show that phenylalanines within the amphipathic helices are crucial for the membrane binding and self-interaction of MBP. With the help of this knowledge, we could identify the QD9 antibody that recognizes an epitope within an amphipathic helix of MBP and stains MBP in a “disassembled state” where it is not bound to the membrane or each other. Hence, we showed that changes in the membrane environment, such as antibody binding to myelin surface epitopes, depletion of lipids or changes in the ion homeostasis lead to the unmasking of this epitope. Upon treatment, MBP detached from the membrane, had a decreased self-interaction and led to decompaction of primary oligodendrocytes.

As MBP is the only determinant for the compaction of the myelin sheath, our current investigations suggest that the unmasking of the QD9 epitope is an early marker for the loss of compact myelin in early stages of demyelinating diseases. We hypothesize that loss of membrane binding and self-interaction of MBP leads to a sequence of changes in the myelin ultrastructure before demyelination. In order to test this hypothesis, we used several animal model of demyelinating diseases, such as the lysolecithine and cuprizone model, toxin-based models of demyelination, or the experimental autoimmune encephalomyelitis (EAE), intracerebral injections of MOG or Aquaporin 4 antibodies as models of inflammatory demyelination. Interestingly, the temporary sequence of myelin fragmentation in all demyelinating conditions starts with a vacuolization of the innermost lamellae proceeded by vacuolization of the whole myelin sheath. After the myelin sheath is completely degenerated, it is ultimately degraded.

Our data therefore shed light on the mechanisms of changes in myelin ultrastructure prior to demyelination and might prove useful in understanding how myelin is affected in several, yet incurable diseases, like multiple sclerosis.

Neurobiology

LS1.P007
Nicotine impact on the structure of adult rat auditory cortex

S. Elgayar[1], O. Hssein[1], A. Abdelhafez[1], H. Thabet[1]

[1]Assiut University, Faculty of Medicine, Histology, Assiut, Egypt

selgar1@hotmail.com

A growing body of evidence suggests chronic cigarette smoking alone causes detrimental effects on brain blood flow, neurophysiology, neurochemistry and morphology. Nicotine binds to and interacts with nicotinic acetyl choline receptors which normally modulate the effects of the neurotransmitter acetylcholine within the auditory system.

Aim of work: to study the structural changes in primary auditory cortex region (Layer V), under the influence of nicotine.

Material and Methods: fifteen male guinea pigs were classified into two groups: group I (control) and group II (nicotine treated group). Group II was further subdivided into two subgroups; IIA and IIB according to the dose of nicotine (3 mg/kg and 6 mg/kg, respectively). The brain was sectioned and specimens from the area of the primary auditory cortex were processed for transmission electron microscopy microscopy.

Results: nicotine treated group revealed structural changes which extended to involve almost all the structural components of the primary auditory cortex (Layer V), in a dose dependent manner. Numerous neurons revealed variable degrees of degenerative changes with disorganization of microtubules and myelin degeneration of their processes. All types of neuroglia revealed marked reactivity, whereas the blood capillaries revealed contraction, irregular lumen and thickened basal lamina.

Nicotine has a dramatic effect on the integrity of the auditory cortex.

Neurobiology

LS1.P008
Sensilla coeloconica as a tool of host-seeking in biting midges (Diptera: Ceratopogonidae)

A. Urbanek[1], M. Kapusta[1]

[1]University of Gdańsk, Invertebrate Zoology and Parasitology, Gdańsk, Poland

aleksandra.urbanek@biol.ug.edu.pl

The distribution and morphology of antennal sensilla coeloconica of parasitic and predaceous biting midges were studied. It is a grooved peg chemoreceptor with a ring of microtrichia. The peg is sunk in the deep pit whereas the microtrichia encircling it form a picket fence so as to maintain a higher level of humidity, which facilitates the capture and transport of odour molecules through the channels in the peg wall. This specific olfactory receptors serve as food detectors in crepuscular / nocturnal biting midges, during the night or in the evening, when the light is weak and the air humidity high. Sensilla coeloconica with a ring of microtrichia evolved several times independently among crepuscular or nocturnal moths (Lepidoptera) and nematocerous flies (Diptera). In moths their role is to locate carbohydrate food, whereas in dipterans they are used to search for a protein-rich meal - blood or haemolymph. In biting midges the distribution of sensilla coeloconica correlates with the evolution of feeding habits.

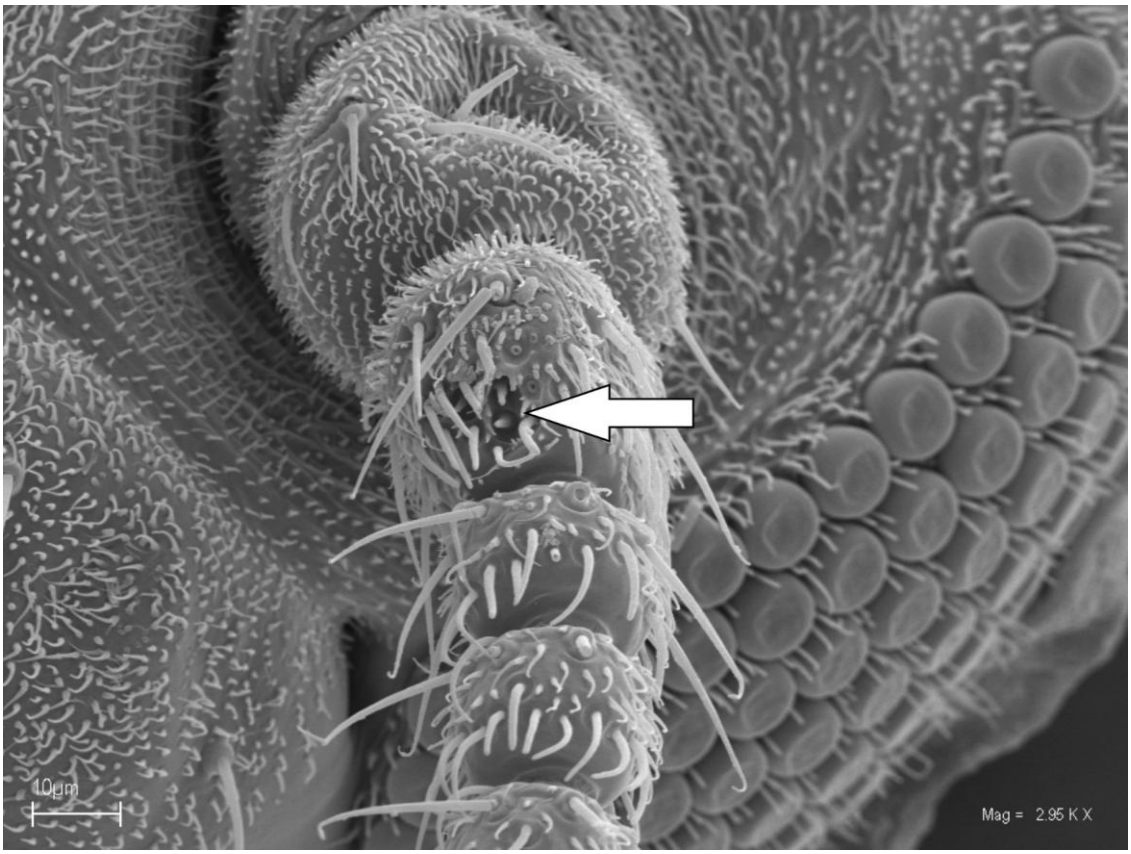

Microbiology, Virology

LS2.009
A closer look at Gemmata obscuriglobus; a gram-negative bacterium with a developed endomembrane system.

R. Santarella-Mellwig[1], S. Pruggnaller[1], N. Roos[2], I.W. Mattaj[1], D.P. Devos[3]

[1]European Molecular Biology Laboratory, Heidelberg, Germany
[2]Department of Molecular Biosciences, University of Oslo, Oslo, Norway
[3]Centro Andaluz de Biologia del Desarollo (CABD), Universidad Pablo de Olavide, Seville, Spain

santarel@embl.de

The development of an endomembrane system and how cellular space is organized and divided into compartments has been an open question for decades. Members of the bacterial superphylum Planctomycetes-Verrucomicrobia-Chlamydiae (PVC) have been of keen interest for a long time, as they possess features that differentiate them from classical Gram-negative (G-) bacteria. Here we have focused on Gemmata *obscuriglobus*, a member of the phylum Planctomycetes. Using electron tomography we have examined two types of cells that are likely to represent the major stages of the cell cycle in G. *obscuriglobus*. One population displays extensive invaginations of the inner membrane inside the cytoplasm. The others have increased periplasmic volume populated by vesicle-like structures. We have found that the organization of cellular space is similar to that of a classical G- bacterium, modified by the presence of large invaginations of the inner membrane inside the cytoplasm or towards the periplasm[1]. 3D reconstruction of whole Gemmata cells revealed that these bacteria are not compartmentalized, as the membranes are all interconnected. Moreover, we have shown that the vesicles in the second cell population are interconnected and form a network of tubules and vesicles or a tubulovesicular network (TVN) inside the periplasm of these cells[2]. In addition, we have shown that proteins structurally related to the eukaryotic proteins involved in endomembrane system maintenance are present in those bacteria and localize in close proximity to the periplasmic vesicles[3]. It has also been shown that this bacterial endomembrane system is involved in external compound internalization and degradation in the periplasm[4]. This most likely occurs through the TVN, indicating subfunctionalization and filtering before cytoplasmic internalization; a process reminiscent to endocytosis in eukaryotes.

There is still no direct evidence that G. obscuriglobus and eukaryotic endomembrane systems are related. Nevertheless, they provide an excellent opportunity to examine the endomembrane organization in a non-eukaryotic system without the complexity found in eukaryotes.

1. Santarella-Mellwig R, Pruggnaller S, Roos N, Mattaj IW, Devos DP. Three-dimensional reconstruction of bacteria with a complex endomembrane system. PLoS Biol. 2013;11(5):e1001565.
2. Acehan D, Santarella-Mellwig R, Devos DP. A bacterial tubulovesicular network. J Cell Sci. 2014 Jan 15;127(Pt 2):277-80.
3. Santarella-Mellwig R, Franke J, Jaedicke A, Gorjanacz M, Bauer U, Budd A, Mattaj IW, Devos DP. The compartmentalized bacteria of the planctomycetes-verrucomicrobia-chlamydiae superphylum have membrane coat-like proteins. PLoS Biol. 2010 Jan 19;8(1):e1000281.
4. Lonhienne TG, Sagulenko E, Webb RI, Lee KC, Franke J, Devos DP, Nouwens A, Carroll BJ, Fuerst JA. Endocytosis-like protein uptake in the bacterium Gemmata obscuriglobus. Proc Natl Acad Sci U S A. 2010 Jul 20;107(29):12883-8.

Microbiology, Virology

LS2.010
Make yourself at home: host remodeling to accommodate nidovirus and enterovirus replication

R.W.A.L. Limpens[1], B. van der Hoeven[1], H.M. van der Schaar[2], A.H. de Wilde[3], C.E. Melia[1], F.J.M. Kuppeveld[2], A.J. Koster[1], E.J. Snijder[3], M. Bárcena[1]

[1]Department of Molecular Cell Biology, Leiden University Medical Center, Leiden, The Netherlands
[2]Department of Infectious Diseases and Immunology, Utrecht University, Utrecht, The Netherlands
[3]Department of Medical Microbiology, Leiden University Medical Center, Leiden, The Netherlands

m.barcena@lumc.nl
Keywords: positive-strand RNA viruses, viral replication, 3D-EM,

All viruses, as obligate intracellular parasites, depend on the infrastructure and metabolism of the host cell to replicate and have evolved strategies to manipulate the intracellular environment. One of the most striking examples is the severe remodelling of intracellular membranes into specific structures that support the replication of positive-stranded RNA (+RNA) viruses. Although the exact role of these membranous structures remains to be elucidated, the accumulated evidence invariably points to a key role in viral RNA synthesis. These compartmentalization could be advantageous for +RNA virus replication by providing a way to concentrate the components required for viral RNA synthesis, shielding the intermediates of this process from the host defence system, and by helping to spatially separate and coordinate different processes in the virus life cycle [1]. Different viruses manipulate different intracellular membranes but, in terms of morphology, certain virus-induced membranous structures appear to be recurrent themes in +RNA virus infection. Accordingly, +RNA viruses studied so far can be classified into two classes: those inducing membrane invaginations and those inducing double-membrane vesicles (DMVs) [1]. Our research focuses on the DMV-inducing viruses and, specifically, on coronaviruses and arteriviruses (families of the order *Nidoviridae*), and on picornaviruses of the enterovirus genus. Using advanced preservation techniques (high-pressure freezing and freeze-substitution) in combination with electron tomography we have uncovered the three-dimensional (3D) architecture of the membrane modifications induced along infection by SARS-CoV (Severe Acure Respiratory Syndrome coronavirus), the arterivirus EAV (equine arteritis virus), and the enterovirus CVB3 (coxsackievirus B3) [2,3,4]. These 3D characterizations, together with similar studies performed by others with other DMV-inducing viruses [5,6,7], have made apparent fundamental differences among these type of viruses in terms of the architecture and topology of the DMVs as well as a large variety of additional membranous structures that these viruses induce (e.g. convoluted membranes for beta-coronaviruses, single-membrane tubules in enterovirus infection). In the complex scenario that these studies reveal, multiple new questions arise about how this variety of structures and topologies are exploited by viruses and what is their origin and dynamics. We are currently investigating these and other aspects using a variety of microscopy techniques (e.g. autoradiography, light microscopy and correlative light-electron microscopy) together with molecular biology approaches. We will present our latest results towards the localization of the actual site of viral RNA synthesis and the elucidation of the biogenesis mechanism(s) that give raise to the membrane alterations and will lay out future venues for the investigation of these remarkable structures.

1. D. Paul and R. Bartenschlager, World Journal of Virology 2 (2013), p. 32.
2. K. Knoops, M. Kikkert, S.H.E. van den Worm, J.C. Zevenhobbe-Dobbe, Y. van der Meer, A.J. Koster, A.M. Mommaas and E.J. Snijder, PLoS Biology 6 (2008), p. e226.
3. K. Knoops, M. Bárcena, R.W.A.L. Limpens, A.J. Koster, A.M. Mommaas, E.J. Snijder, Journal of Virology 86 (2012), p. 2474.
4. R.W.A.L. Limpens, H.M. van der Schaar, D. Kumar, A.J. Koster, E.J. Snijder, F.J.M. van Kuppeveld and M. Bárcena, mBio 2 (2011), p. e00166.
5. G.A. Belov, V. Nair, B.T. Hansen, F.H. Hoyt, E.R. Fischer and E. Ehrenfeld, Journal of Virology 86 (2012), p. 302.
6. I. Romero-Brey, A. Merz, A. Chiramel, J.-Y. Lee, P. Chlanda, U. Haselman, R. Santarella-Mellwig, A. Habermann, S. Hoppe, S. Kallis, P. Walther, C. Antony, J. Krijnse-Locker and R. Bartenschlager, PLoS Pathogens 8 (2012), p. e1003056.
7. H.J. Maier, P.C. Hawes, E.M. Cottam, J. Mantell, P. Verkade, P. Monaghan, T. Wileman and P. Britton, mBio 4 (2013), p. e00801.
8. We acknowledge the financial support of this research by the Netherlands Organization for Scientific Research (NWO) through grants NWO-CW-TOP-700.57.301 to E.J.S. and A.J.K, NWO-VENI-863.12.005 to H.M.V.D.S., NWO-ALW-820.02.018 and NWO-VICI-91812628 to F.J.M.V.K., and NWO-MEERVOUD-863.10.003 to M.B.

Microbiology, Virology

LS2.011
3D analysis of HCMV induced nuclear membrane structures by FIB/SEM tomography: novel insight into their formation and function

P. Walther[1], C. Villinger[1,2], G. Neusser[3], C. Kranz[3], T. Mertens[2]

[1]Ulm University, Central Facitlity for Electron Microscopy, Ulm, Germany
[2]Ulm University, Institute of Virology, Ulm, Germany
[3]Ulm University, Institute of Analytical and Bioanalytical Chemistry, Ulm, Germany

clarissa.villinger@uni-ulm

We analyzed the three-dimensional structure of a large segment (dimensions 6.4 µm x 5.5 µm x 10 µm) of a nucleus infected with the beta-herpesvirus human cytomegalovirus (HCMV) by using focused ion beam/scanning electron microscopy (FIB/SEM) tomography. Samples were prepared by high-pressure freezing and freeze substitution. Together with acquisition of the secondary electron signal we gained a resolution comparable to the resolution of conventional TEM [1]. This allowed detailed examination of the morphology of the large nuclear infoldings which have been previously described based on a two-dimensional study [2]. The previous findings suggest that nuclear egress of HCMV capsids occurs by budding of the capsids into these intranuclear membrane structures. Their lumen corresponds to the perinuclear space (PNS). The budding process provides the capsids with an envelope.

By three-dimensional investigation we observed that the infoldings form a much more complex network of interlaced membrane structures than assumed before: The infoldings (1st order) contained in all cases further invaginations. The lumen of 2nd order infoldings corresponded to the nucleoplasm, the lumen of 3rd order infoldings again to the PNS. 2nd order invaginations were either open towards the nucleoplasm on one side or were closed on both sides. This proofed that the 2nd order infoldings originated from invagination into 1st order infoldings. Enveloped HCMV capsids were only found in 1st order infoldings (PNS) and non-enveloped capsids only in 2nd order infoldings. We assumed that only enveloped capsids in 1st order infoldings can reach the cytoplasm by de-envelopment at the outer nuclear membrane.

Surprisingly, we found only one infolding clearly connected to the inner nuclear membrane. Furthermore, 2nd and 3rd order infoldings seemed to block free movement of enveloped capsids through the infoldings.

The infoldings facilitate capsid budding, since they are not covered by a lamin layer [2]. Our findings do, however, not support the hypothesis that the infoldings provide an obstacle-free route from the nucleoplasm to the cytoplasm, thus questioning the proposed function of the infoldings for efficient nuclear egress of HCMV capsids.

1. Villinger, C.; Gregorius, H.; Kranz, C.; Höhn, K.; Münzberg, C.; Wichert, G.; Mizaikoff, B.; Wanner, G.; Walther, P. FIB/SEM tomography with TEM-like resolution for 3D imaging of high-pressure frozen cells. *Histochem. Cell Biol.* **2012**, *138*, 549-556.
2. Buser, C.; Walther, P.; Mertens, T.; Michel, D. Cytomegalovirus Primary Envelopment Occurs at Large Infoldings of the Inner Nuclear Membrane. *J. Virol.* **2007**, *81*, 3042-3048.

Microbiology, Virology

LS2.012
Polarized macrophages use veiled surface structures to ingest HIV particles

H. Mostafa[1], P. Walther[2], O. Zirafi[3], J. Muench[3], M. Schneider[1]

[1]University Hospital, Section Experimental Anaesthesiology, Ulm, Germany
[2]Ulm University, Central Facility for Electron Microscopy, Ulm, Germany
[3]Ulm University, Institute of Molecular Virology, Ulm, Germany

haouraa-1.mostafa@uni-ulm.de

We established a culture system to characterize the inflammatory immune response of monocytes and dendritic cells in various diseases such as severe sepsis, diabetes type 2, autoinflammatory disorders such as macrophage activation syndromes (MAS), and from conditions with major tissue repair activities following trauma. After in vivo exposure to local growth factors, pro-inflammatory cytokines, and microbial compounds, these cells differentiate into macrophages and dendritic cells (Tacke and Randolph 2006). While these monocytes play a key role in eliminating invading bacteria, viruses, fungi, and protozoans, they can also play a role in the pathogenesis of inflammatory and degenerative diseases. In the present investigation we studied virus-uptake mechanisms by in vitro cultures macrophages and dendritic cells derived from patients. We used recombinant HIV-particles enriched from HEK-cell cultures and simultaneously tested the effect of a novel albumin-derived peptide, EPI-X4 (Mohr et al. 2015).

Methods:In vivo activated antigen presenting cells were enriched by cell culture and subjected to novel culture conditions in the presence of absence of 2% human serum albumin. Before cell culture in 1µ-slide IV IBIDI dishes, the 14-28 day cultured cell preparations were characterized by flow cytometric analysis to distinguish inflammatory macrophages (designated M1, M2a-M2c) and anti-inflammatory macrophages termed M2d. After 72h, the cell cultures were inoculated with HEK derived HIV-1 particles. After 48h, the cell cultures were examined by standard fluorescence microscopy and then subjected to standard transmission electron microscopy.

Results:Different macrophages and dendritic cell subtypes derived from the different diseases and disease states were all similar regarding a unique virus uptake structure characteristic for dendritic cells and composed of a pattern of veiled plasma membrane leaves. These protrusions were preferentially used as virus uptake machinery and remained intact when ingested into the phagocytic cell. Remnants of the extracellular fluid in the cytoplasm were regularly observed which indicates a mechanism described as macropinocytosis. When HSA-treated cultures (Fig. C-D) were compared with non-treated cultures (Fig. A-B), the amount of morphologically identifiable particles was in all cases reduced. Most pronounced effects by HSA-treatment were observed in M2d type macrophage cultures (Fig. A-D).

Conclusion:The current investigations suggest a novel virus specific uptake mechanism in macrophages and dendritic cells by macropinocytosis and defined veiled surface structures. Further studies address the role of EPI-X4 in either blocking CXCR4 specific entry or competition by the HSA-derived peptide in solution.

1. Tacke, F., Randolph, G. J. 2006. Migratory fate and differentiation of blood monocyte subsets. *Immunobiology* 211:609-618.
2. Mohr, K. B., O. Zirafi, M. Hennies, S. Wiese, F. Kirchhoff, and J. Munch. 2015. Sandwich enzyme-linked immunosorbent assay for the quantification of human serum albumin fragment 408-423 in bodily fluids. *Analytical biochemistry* 476:29-35.

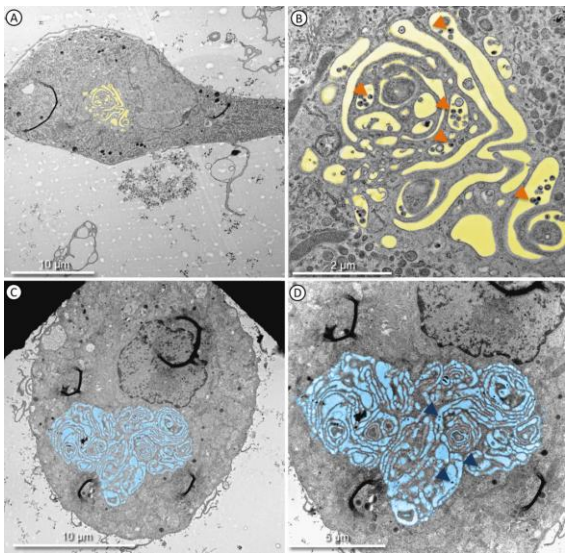

Figures. 1. Control macrophage (M2d differentiation type) infected with rhHIV1; **B:** Enlarged insert area, note abundant virus particles (arrows) in ingested veiled membrane protrusions, fluid from extracellular medium has been colored in yellow; **C:** Human serum albumin- (HSA-) treated macrophage (M2d differentiation type) infected with rhHIV-1; **D**: Enlarged insert area, note the sparse virus particles (arrows) in ingested veiled membrane protrusions, fluid from extracellular medium has been colored in blue.

Microbiology, Virology

LS2.014
Effects of human neutrophil peptide-1 on ultrastructure of Fusobacterium nucleatum: a TEM study

A. Musrati[1], D. Fteita[1], J. Paranko[1], E. Könönen[1], U. Gursoy[1]

[1]University of Turku, Turku, Finland

ahsamu@utu.fi

The ability of certain periodontitis-associated bacteria to evade the oral host defense is multifaceted. Although recent evidences showed that *Fusobacterium nucleatum* seems to have the capability of protecting its cellular integrity against the action of α-defensins (human neutrophilic peptides, HNPs), the morphological mechanisms remain unclear. The aim of this work was to assess the cellular morphological changes of *F. nucleatum* as defense mechanisms against the effect of HNP-1.

The type strain of *F. nucleatum* (ssp. *nucleatum* ATCC 25586) and two clinical strains (ssp. *polymorphum* AHN 9910 and ssp. *nucleatum* AHN 9508) were cultured and incubated with four different test concentrations of recombinant human HNP-1 (1, 5, 10 and 20 µg/ml) and one control group in (0 µg/ml) in anaerobic conditions for 24 hours. A sample of bacterial pellet from each concentration was fixed and processed for TEM imaging. From the same bacterial suspensions of the four different defensins concentrations, planktonic growth was assessed quantitatively by colony forming unit method.

TEM images revealed corrugated rough surface of bacterial outer membrane in the control group of strain AHN-9508, while, with increasing HNP-1 concentrations, the roughness started to fade-off the cell membranes. In higher concentrations of HNP-1, bacterial cells of AHN-9910 showed thicker outer membranes with a number of associated rough vesicles attached to the outer layer, while in the control group such membrane vesicles were seldom found. In the third strain, i.e., ATCC-25586, the treated bacterial cells contained increased numbers of intracellular granules. Planktonic growth of the two clinical strains AHN 9910 and AHN 9508 were significantly increased (P<0,001) with gradually increased concentrations of HNP-1. However, the opposite was found with the type strain ATCC 25586 at HNP-1 concentrations of 1-10 µg/ml. With the highest concentration of HNP-1 (20 µg/ml) the bacterial growth showed the highest peak value among the three study strains.

F. nucleatum seems to undergo morphological changes in order to withstand the lethal effects of HNP-1 in a strain-dependent pattern.

Microbiology, Virology

LS2.015
The DNA of dormant bacterial spores is localized in crystalline core regions to avoid DNA damage during dormancy

C. Dittmann[1], H. Han[2], M. Grabenbauer[3], M. Laue[1]

[1]Robert Koch Institute, Advanced Light and Electron Microscopy (ZBS 4), Berlin, Germany
[2]Max-Planck-Institute for Molecular Physiology, Department of Systems Cell Biology, Dortmund, Germany
[3]University of Heidelberg, Institute for Anatomy and Cell Biology, Heidelberg, Germany

lauem@rki.de

Spores of the endospore forming *Bacillus* and *Clostridium* genera are involved in the transmission of diseases, like anthrax or botulism. This is mainly due to the extraordinary resistance of the spores against various environmental stresses, such as heat, aridity, disinfection. A couple of molecular and structural factors are responsible for this resistance [1]. The core membrane provides an efficient barrier even for small molecules and the core is almost dry, packed with calcium-dipicolinic acid. However the most important protection is provided by the binding of small acid soluble proteins (SASP) to the DNA. While this association has been deduced from various experiments, e.g. by providing the x-ray structure of crystallized bound DNA and SASP fragments [2], the structural arrangement *in vivo* is still unknown. In our presentation, we show that the DNA is localized in core regions of dormant spores which possess a highly ordered, crystalline arrangement (Figure 1). These ordered core regions correspond to the so-called nucleoid, a region of the cytoplasm which contains the DNA. Spores which are deficient of producing the major SASPs are devoid of crystalline nucleoids, which underlines that the association of SASPs is necessary to form the crystalline structures. During germination the crystalline arrangement is lost at an early stage and transformed into bundles of filaments. At this stage of germination, water is taken up by the spore, calcium-dipicolinic acid is released and the spores lose their resistance against dry heat and UV. Since calcium-dipicolinic acid deficient spores retain a significant resistance, presence of SASPs is the major molecular factor providing resistance. Our results imply that this resistance is due to a highly ordered crystalline arrangement of the SASP/DNA assemblies which is the most stable supramolecular structure to avoid molecular movements induced by heat or radiation thereby reducing the risk of DNA-strand breaks.

To investigate the core structures of the spores, we needed to apply various methods of ultrastructural research, basically because dormant spores are difficult to prepare and some of them are infectious. We have used self-pressurized rapid freezing and CEMOVIS [3] to describe the core structures. Immunogold labeling and comparative studies using spores from a variety of species were done using microwave-assisted chemical fixation and plastic embedding [4]. High-pressure freezing and plastic embedding was used to follow the germination of spores. Phase-contrast light microscopy, life cell imaging and measurement of calcium content (by X-ray microanalysis) were used to check physiological properties of the spores. Part of our presentation will focus on the various difficulties encountered in the sample preparation of spores and how we have solved them.

1. P. Seltow, Trends Microbiol. 15 (2007), p. 172
2. K.S. Lee, D. Bumbaca, D., J. Kosman, P. Setlow, M.J. Jedrzejas, PNAS, 105 (2008), p.2806.
3. H. Han, J. Huebinger, M. Grabenbauer, J. Struct. Biol. 178 (2012), p. 84
4. M. Laue, B. Niederwöhrmeier, N. Bannert, J. Microbiol. Meth. 70 (2007), p.45

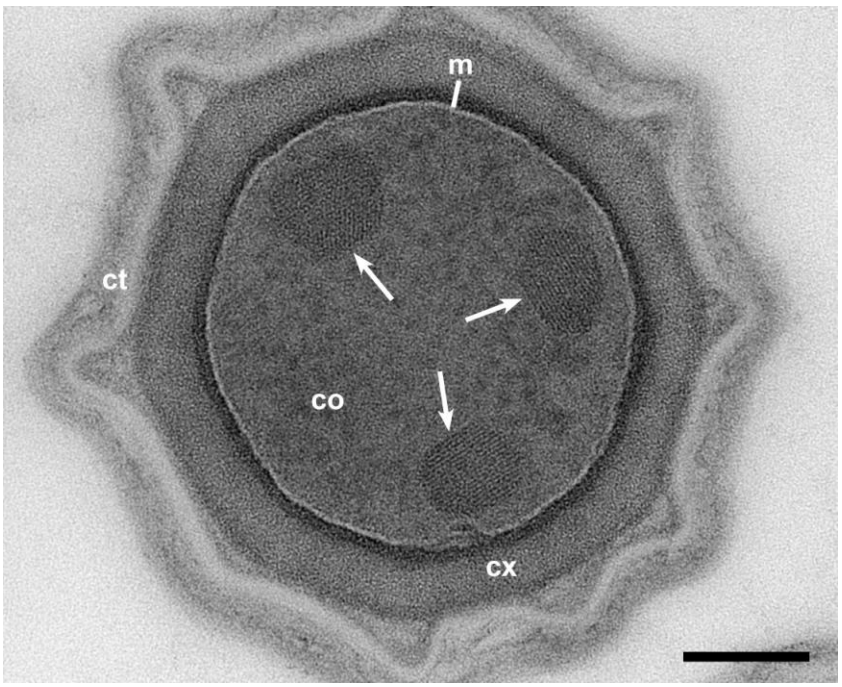

Figure 1. Transmission electron microscopy of a cross section through a dormant spore of *Bacillus subtilis*. In this case, spores were chemically fixed (microwave-assisted) and embedded in LR White. The particular section staining by uranyl acetate/methyl cellulose provided a mixture of negative and positive staining allowing visualization of crystalline core regions (arrows) which were initially found using CEMOVIS. (*co*) core, (*ct*) coat, (*cx*) cortex, (*m*) core membrane. Bar = 100 nm.

Microbiology, Virology

LS2.016
Structural and functional compartmentalization in a hyperthermophilic prokaryote

J. Flechsler[1], T. Heimerl[2], R. Rachel[1]

[1]University of Regensburg, Center for EM, Regensburg, Germany
[2]University Marburg, Cell Biology, Marburg, Germany

reinhard.rachel@biologie.uni-regensburg.de

In most prokaryotic cells, there is a clear and usually simple compartmentalization: as the cells do not possess any membrane-bound organelles as eukaryotic cells, the dominating part of biomass is contained within the cytoplasm. It covers the by far greatest part of the cell volume; in this compartment, DNA and ribosomes are found, as well as all enzymes for biosynthetic, metabolic and catabolic pathways, including for information processing and energy conservation.

Ignicoccus hospitalis is a hyperthermophilic, chemolithoautotrophic crenarchaeon [1]. The cells exhibit an extraordinary ultrastructure. In addition to the cytoplasmic membrane, there is an outer cellular membrane, which encases an intermembrane compartment (IMC). The IMC contains membrane-surrounded tubes and vesicles, derived from the cytoplasm. Altogether, the ultrastructure is reminding of the eukaryotic endogenous membrane system [2].

Autotrophic prokaryotes have developed at least five different ways of CO_2 fixation which are assumed to be located in the cytoplasm [3]. In *Ignicoccus* cells, however, CO_2 fixation is proceeds via the unique dicarboxylate/4-hydroxybutyrate cycle [4]. One unusual feature of *Ignicoccus* cells is the location of the ATP synthase, its only complex synthesizing chemical energy in form of ATP; it is exclusively found in the outer cellular membrane of *Ignicoccus*. This lets us assume that large quantities of ATP are available in the IMC [5].

The compartmentalized cell structure of *Ignicoccus* and the unique location of the ATP synthase in the outer cellular membrane raise questions about the subcellular distribution of other metabolic pathways which depend on the availability of ATP, e.g. different steps of the CO_2 fixation pathway. To address this question we used a variety of methods for 3D electron microscopy (serial sectioning, electron tomography) in combination with immunolabelling of cryo-immobilized, freeze substituted cells. Immuno-EM revealed that the Acetyl-CoA synthetase, an enzyme that catalyzes the initial step of the CO_2 fixation, is located in the IMC, associated with the outer cellular membrane. Additionally, we were able to detect e.g. the Crotonyl-CoA hydratase and the PEP carboxylase in the IMC of *Ignicoccus*. The results obtained so far show a unique example of functional compartmentalization in an unusual prokaryotic cell.

1. Huber et al., Antonie van Leeuwenhoek **102** (2012) p 203-219
2. Heimerl, 2012, EMC 2012 proceedings (2012).
3. Fuchs, Annu Rev Microbiol.**65** (2011), p 631-58.
4. Jahn *et al.,* J Bacteriol **189** (2007), p. 4108.
5. Küper *et al.*, PNAS **107** (2010), p. 3152.
6. This research was supported by grants from the DFG (Germany)

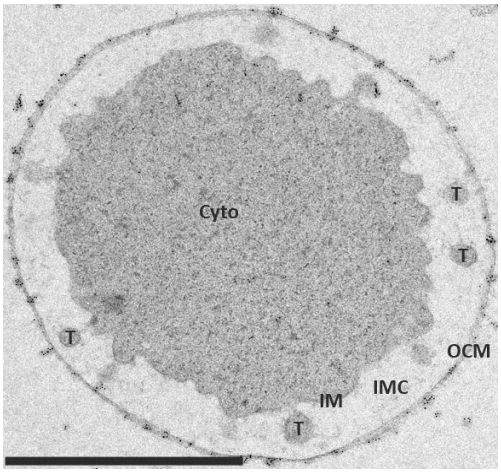

Figure 1. Ultrathin section of *Ignicoccus*, highlighting the essential features of the cell's ultrastructure. Cells were cryo-fixed by high-pressure freezing, freeze-substituted, and embedded in Epon. Cyto, cytoplasm; IM, inner membrane; OCM, outer cellular membrane; IMC, inter-membrane compartment; T, cross-section of tubes in the IMC. Section was labeled with antibodies directed against the hydrogen sulfur oxidoreductase. Bar, 1 µm

Microbiology, Virology

LS2.P017
Xanthomonas campestris pv. vesicatoria secretes predicted proteases and xylanases via outer membrane vesicles and the type II secretion system

G. Hause[1], A. Rother[1], M. Sole[2], F. Scheibner[2], N. Hartmann[2], A.- K. Hoffmeister[2], M. Lautier[3], M. Arlat[3], D. Büttner[2]

[1]Martin-Luther-University Halle-Wittenberg, Biocenter, Halle, Germany
[2]Martin-Luther-University Halle-Wittenberg, Genetics, Halle, Germany
[3]INRA, LIPM, Castanet-Tolosan, France

gerd.hause@biozentrum.uni-halle.de

Many plant pathogenic bacteria utilize type II secretion (T2S) systems to secrete degradative enzymes into the extracellular milieu. We previously reported that the Xps-T2S system from the tomato and pepper pathogen *Xanthomonas campestris* pv. *vesicatoria* contributes to virulence, extracellular xylanase and protease activity. The analysis of candidate T2S substrates led to the identification of two predicted xylanases, a putative protease and a lipase as substrates of the Xps-T2S system. Mutant studies revealed that the identified T2S substrates contribute to bacterial virulence and *in planta* growth. Notably, however, reduced amounts of the identified T2S substrates were still secreted in T2S mutants, suggesting the contribution of an additional Sec-dependent transport system to secretion. Interestingly, immunoelectron microscopy led to the detection of predicted extracellular proteases and xylanases in outer membrane vesicles, suggesting that they provide an alternative transport route for secreted virulence factors of *X. campestris* pv. *vesicatoria*. For this purpose the bacteria were high pressure frozen, freeze substituted and embedded in Lowicryl (HM20). The c-Myc epitope-tagged proteins were immunolabelled with monoclonal antibodies against the epitope-tag.

Microbiology, Virology

LS2.P018
Antimicrobial activity of the saponin extract of Sansevieria trifasciata var. Golden Hahnii

W. F. Dewatisari[1]

[1]University, Biology, Bandar Lampung, Indonesia

dewatisari@whika.web.id

Sansevieria trifasciata used as an ornamental plant. It also used as a traditional medicine for influenza, cough and inflammation of the respiratory tract. The roots and leaves of *S. trifasciata* contains many secondary metabolites such as saponins that efficacious as a cough remedy, to treat sprains, injuries hit, venomous snake bites, ulcers, cough, inflammation of the respiratory tract and hair growth. (Stover, 1983). Microbes are used to seeing the antibacterial saponins activity of of *S. trifasciata* are *Escherichia coli* and *Staphylococcus aureus*. The main reason for used these microbes because *E. coli* is a bacterium that causes diarrhea and *S. aureus* is one of the bacteria that cause cough in humans. Plants were used *S. trifasciata* var. Golden Hahnii. Based on research by Dewatisari (2008), states that the variety had the highest saponin content of *S. trifasciata* is Golden Hahnii among other varieties and the parts that had the highest saponin was in its roots.This article aims to explain quantitatively the effectiveness of saponin compounds from the roots of *S. trifasciata* var. Golden Hahnii as antimicrobials in inhibiting the growth of bacteria *S. aureus*, and *E. coli*. Methods of data collection were sample preparation, a preliminary test, the extraction of saponins, antibacterial activity test, and isolate compound separation by TLC (Thin layer Chromatography). In this study, the extraction of the active compounds in the roots of *S. trifasciata* by maceration with methanol 90%. Separation of the active compound was conducted by TLC. Eluent used was chloroform; methanol; water with various concentration (13: 4: 1), (65; 50: 10), (20: 60: 4), 20: 60: 10). Antibacterial test conducted by the disc diffusion method against *S. aureus* and *E. coli*. Identification of test compounds triterpenoid saponins using foam and Liebermann-Burchard color test (LB). The results showed that the extract of the roots has potential as antibacterial. The extract was able to inhibited the growth of *E. coli* and *S. aureus*. At the optimum concentration of 200 ppm produced inhibition zone was 26.5 mm to 20.2 mm for *S. aureus* and *E. coli*. Best eluent to separate the triterpenoid saponins in root extracts of *S. tifasciata* was chloroform; methanol; water at a concentration (20: 60: 4) with 3 separate visible stains are : 0.135; 0.85; 0,815 .Mechanism root extract as an antibacterial *S. trifasciata* was synergistic. It was seen from the inhibition zone, for *E. coli* isolates the I = 5.52 mm and 2.50 mm isolates II =, for *S. aureus* isolates I = 1.52 mm and isolates II = 0.58 mm, while the isolates III is not effective as an anti-bacterial.

Microbiology, Virology

LS2.P019
Detection of endophytic entomopathogenic fungi in crop plants with microscopical, histochemical and immunological methods

C. Ullrich[1], C. Matecki[1], J. Schäfer[1], T. Burkl[1], F. Rabenstein[2], E. Koch[1], R. G. Kleespies[1]

[1]Julius Kühn-Institut, Institute for Biological Control, Darmstadt, Germany
[2]Julius Kühn-Institut, Institute for Epidemiology and Pathogen Diagnostics, Quedlinburg, Germany

regina.kleespies@jki.bund.de

Entomopathogenic fungi are efficiently used in biological control of economically important herbivorous insects. Since several years, efforts have been made to establish entomopathogenic fungi directly in crop plants and finally in their seeds to control both insect pests and plant pathogens. However, apart from grasses and coniferous trees, the establishment and unequivocal detection of systemically growing endophytes in most dicots is still problematic.

In the present study, experimental plants, *Brassica napus* L., *Cucumis sativus* L., and *Vicia faba* L., were treated with *Beauveria bassiana* Naturalis ATCC74040, *Isaria fumosorosea*, *Lecanicillium muscarium* and *Metarhizium anisopliae*. Suspensions were applied to the plants, either by infiltration of blastospores from submerged cultures into leaves or stems with a syringe or by spraying on leaves and flowers; or conidiospores from MPA were directly applied after needle wounding in *B. napus* cotyledons. Between 4 hpi and 27 dpi, plant samples were taken and submitted to various staining methods.

Here, we report on our results on the optimisation of histochemical detection and on immunofluorescence localization of the applied fungi in plant sections. The IgG fraction of polyclonal antibodies raised against *B. bassiana* in rabbit was used in combination with FITC-labelled goat anti rabbit secondary antibodies.

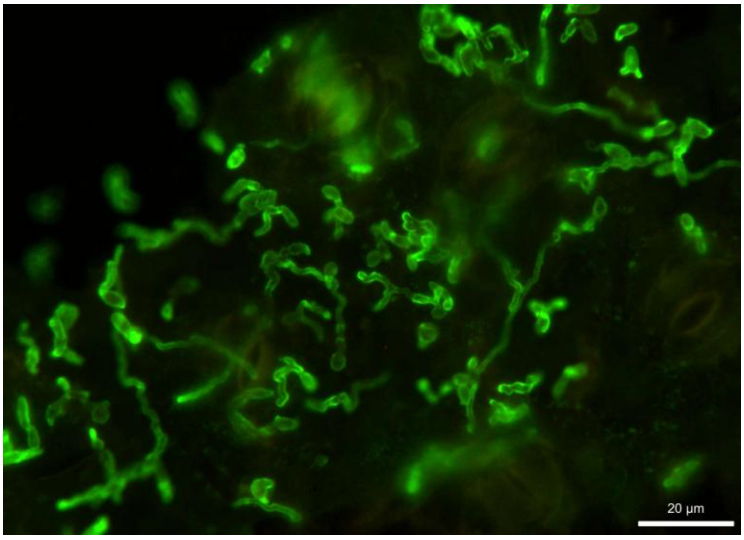

Figure 1. *Beauveria bassiana* Naturalis ATCC74040 on an oilseed rape leaf (5 dpi), detected with polyclonal antibodies (IgG)/FITC.

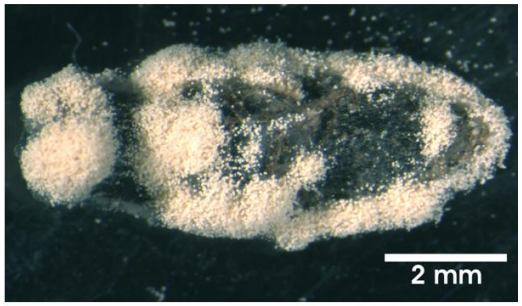

Figure 2. *Agriotes gallicus* infected by *Beauveria bassiana.*

Microbiology, Virology

LS2.P020
Viral determinants required to build up the HCV replication factories

I. Romero Brey[1], C. Berger[1], S. Kallis[1], D. Paul[1], V. Lohmann[1], R. Bartenschlager[1]

[1]University of Heidelberg, Infectious Diseases- Molecular Virology, Heidelberg, Germany

ines_romero-brey@med.uni-heidelberg.de

Like all positive-strand RNA viruses, hepatitis C virus (HCV) extensively reorganizes intracellular membranes to allow efficient RNA replication. We have recently shown that HCV infection induces ER-derived double membrane vesicles (DMVs) that represent the major constituent of the cytoplasmic replication factory within the host cell. Formation of this factory requires a concerted action of nonstructural proteins (NS) 3, 4A, 4B, 5A and 5B. Moreover, we found that the sole expression of NS5A was sufficient to induce DMV formation, albeit at low efficiency. In the present study we dissected the determinants within NS5A responsible for DMV formation.

Transmission electron microscopy (TEM), correlative-light electron microscopy (CLEM) and Western blot. We found that the RNA binding domain 1 (D1) as well as the amino-terminal membrane anchor are indispensable for this process. In contrast, deletion of NS5A D2 or D3 did not affect DMV formation, but completely disrupted RNA replication and virus assembly, respectively. To identify cis- and trans-acting factors of DMV formation we established a trans-cleavage assay. We found that induction of DMVs requires full length NS3 whereas a mutant lacking the helicase domain was unable to trigger DMV formation in spite of efficient polyprotein cleavage. Importantly, a mutation accelerating cleavage kinetics at the NS4B-5A site diminished DMV formation, while the insertion of an internal ribosome entry site (IRES) mimicking constitutive cleavage at this boundary completely abolished this process. These results suggest that regulated polyprotein cleavage is essential for efficient DMV biogenesis.

These results identify novel determinants governing the biogenesis of the HCV replication factory with possible implications for our understanding of how this central compartment of positive-strand RNA viruses is formed.

Microbiology, Virology

LS2.P021
Scanning electron microscopy and Raman spectroscopy of microorganisms related to biofuels and biopolymer production

K. Hrubanova[1], O. Samek[1], S. Obruca[2], A. Haronikova[2], V. Krzyzanek[1]

[1]Institute of Scientific Instruments of the ASCR, v. v. i., Brno, Czech Republic
[2]Brno University of Technology, Centre for Material Research, Brno, Czech Republic

hrubanova@isibrno.cz

Red yeast strains such as *Rhodotorula spp., Cystofilobasidium spp.* and *Sporobolomyces spp.* are well known due to their potential applications in the field of biofuel generation and food industry [1]. In order to utilize biomass for efficient industrial production, the optimal cultivation parameters have to be determined which in turn lead to high production of desired substances such as oil and carotenoids in the selected cell line.

In this project we have studied, using scanning electron microscopy (SEM) and Raman spectroscopy techniques, how different cultivation conditions influence production of oil and carotenoids. Raman spectroscopy can be used for the determination of the oil present in the biomass and also for the determination of carotenoids as the intensity ratios of specific, selected Raman bands [2]. SEM uses focused electron beam to gain information about morphology of cells (biomass structure) which is very important factor to study cells response on the applied stress.

In our experiments we have observed different morphology when employing SEM to study cells of *Cystofilobasidium capitatum* which was cultivated in media with different carbon to nitrogen (C/N) ratios per one day at temperature 37°C. Cells suspensions were processing by chemical fixation: 2 hours in 2.5 % glutaraldehyde in PBS and 30 min in 1 % OsO4, dehydrated by acetone series and dried in HDMS on the glass slides [3]. The image of prepared sample was scanned without any metal coating at electron beam energy 1 kV and beam current 3.1 pA in SEM Magellan (FEI). Corresponding Raman spectra is also shown (Figure 1).

The main aim of our investigations concerning polyhydroxyalkanoates (PHA) study is to utilize combination of the two modern methods - electron and Raman microscopy in the complex study on changes in physico-chemical properties of bacterial cells and cell cytoplasm with respect to intracellular content of PHA. For this purpose, we have utilized following bacterial strain *C. necator* H16 and also its PHA none-producing mutant *C. necator* PHB-4. Raman spectroscopy seems to be very efficient tool for direct analysis of intracellular PHA content of bacteria and, furthermore as mentioned above, can be combined with SEM imaging to make it possible to measure/follow nutrient dynamics and metabolism of the cells. Moreover, with this type of sensing one may detect variability of polymers contained within the cells which could help in elucidating different morphological features during the process of cryo scanning electron microscopy (cryo-SEM) technique (Figure 2). All Raman micro-spectroscopic experiments with above mentioned cells were carried out using inVia Renishaw system.

We believe that our study will be of significant assistance to research group being involved in study of microorganisms for biofuels, food, and biopolymer production. Our results are convincing enough to warrant more extensive investigations with larger sets of yeast/bacterial strains to evaluate combination of Raman spectroscopy and SEM/cryo-SEM.

1. O. Samek, A. Jonas, Z. Pilat, P. Zemanek, L. Nedbal, J. Triska, P. Kotas, M. Trtilek, Sensors, 2010, 10, 8635-8651.
2. Z. Pilat, S. Bernatová, J. Ježek, M. Sery, O. Samek, P. Zemanek, L. Nedbal, M. Trtilek, J. Appl Phycol, 2012, 24, 541-546.
3. K. Dobranska, et al., (EMC 2012 Proceedings, Manchester) 2012, p. 671.
5. The research was supported by the Grant Agency of the Czech Republic (GA14-20012S, GA15-20645S), MEYS CR (LO1212), its infrastructure by MEYS CR and EC (CZ.1.05/2.1.00/01.0017).

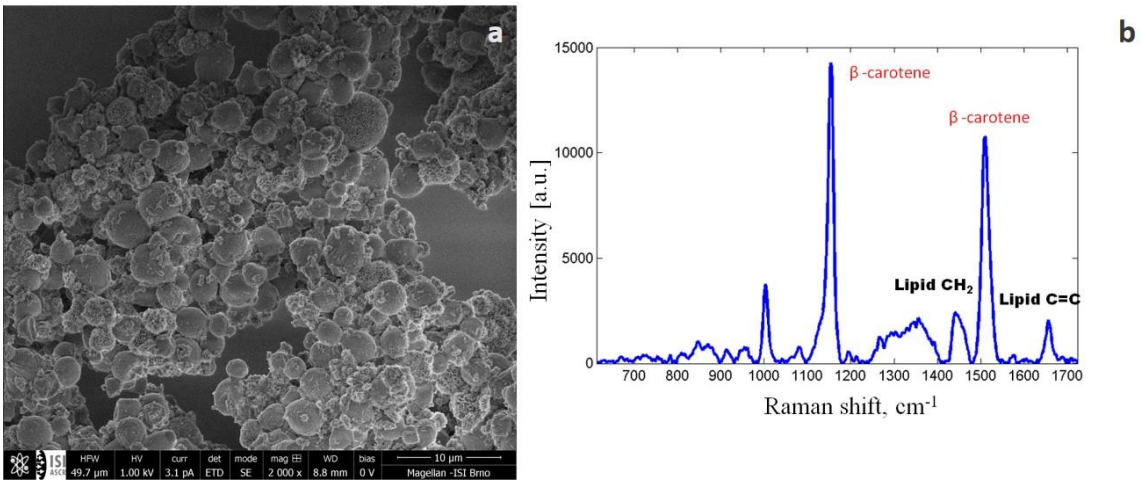

Figure 1. a) SEM image of *C. capitatum*; b) Raman spectra of *C. capitatum* cultivated in medium which contributes to increased lipid production.

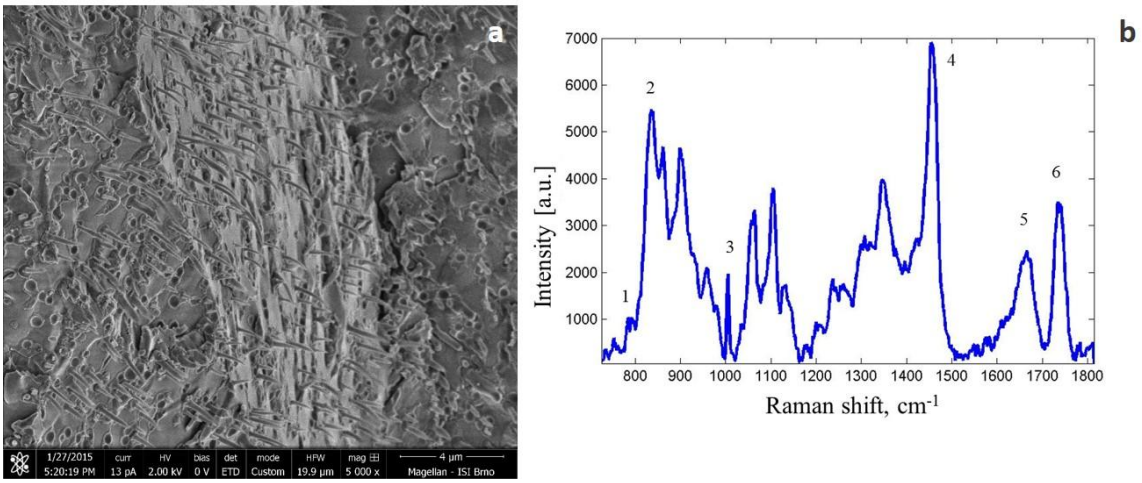

Figure 2. a). Cryo-SEM image of *C. necator* H16. Needle-type deformations can be clearly seen on the fractured sample surface. b) Raman spectra of *C. necato*r H16. The most prominent contributions are (1) DNA, (2,4,6) PHB, (3) Phenylalanine, (5) lipids.

Microbiology, Virology

LS2.P022
Ultrastructural changes in protein morphology of Cheddar cheese during manufacture and aging

A. Vollmer[1], N. Youssef[1], D. McMahon[1]

[1]Utah State University, Western Dairy Center, NDFS, Logan, UT, United States

almut.vollmer@usu.edu

Rheological studies indicate that there are changes in the physical properties of Cheddar cheese that take place during manufacture and aging. These include the change from elastic after manufacture to brittle after a few months in storage.

We are testing our hypothesis that changes in the ultrastructure of the protein component of the cheese correspond with the documented textural changes.

Cheddar cheese was made using 16 kg of milk and stored for up to 3 months at 6°C. Samples of curd and cheese were taken at various time points and immediately processed for transmission electron microscopy.

The addition of rennet to milk caused individual casein micelles to aggregate into loose clusters forming a fine-stranded soft gel, the curd. During the subsequent steps of cheese making and concomitantly with whey expulsion, the network strands coalesced into thicker, irregular strands in which individual casein micelles could not be discerned but the protein network retained a particulate appearance. After 3 days of cold storage, a secondary, more dispersed protein arrangement of flocculent protein was observed adjacent to the protein matrix. After 7 days, the protein matrix became the continuous phase in which pockets of fat and whey were distributed. With further storage, the protein matrix changed from mostly uniformly dense to coarsely granulated. After 3 months in storage, there were no discernable whey pockets and the secondary protein network structure was no longer apparent.

Changes in ultrastructure in Cheddar cheese corresponded with known physiochemical changes that occur after manufacture when cheese is cooled: (1) the individual curd particles continue to knit together and the protein matrix becomes the continuous phase producing the elastic structure, (2) this occurs as the level of protein-bound calcium is reduced and the extent of water entrapped within the protein network is increased, (3) with continued storage the less protein-dense regions that provide flex points to the matrix structure contain more protein, becoming part of the overall protein matrix, and (4) a more rigid protein matrix structure is observed after 3 months that correspond with the cheese becoming harder and more brittle.

Microbiology, Virology

LS2.P023
Structure of geminiviral replication initiation protein complexes

M. Paul[1], H. Jeske[1], K. Hipp[1]

[1]University of Stuttgart, Molecular Biology and Plant Virology, Stuttgart, Germany

martin.paul@bio.uni-stuttgart.de

Geminiviruses, small plant viruses with circular single-stranded DNA, infect many different economically important crops such as cotton, bean, sweet potato, tomato, sugar beet and cassava. They possess characteristic and unique twin capsids, that are formed by two incomplete icosahedra (Böttcher *et al.* 2004). African cassava mosaic virus (ACMV) has caused severe economic damages in cassava, which is the main starchy food for more than 500 million people worldwide.

The genome of ACMV consists of two components, named DNA A and DNA B. The replication initiation Protein (Rep, AC1), which is required for rolling circle replication, is encoded on the complementary strand of DNA A and is the only viral protein indispensable for replication while replication itself relies on host polymerases (Hanley-Bowdoin *et al.* 1990; 2004).

Although the mode of replication initiated by Rep has been described (Jeske *et al.* 2001) and the required activities have been demonstrated (Laufs *et al.* 1995; Clérot and Bernardi 2006), the exact mechanisms and the potentially different oligomeric states for each functional complex of Rep are still unknown.

In order to determine the conditions, which lead to formation of complexes, we are using purified protein expressed in *Schizosaccharomyces pombe*. The complexes will be identified and characterized by size exclusion chromatography and transmission electron microscopy. Subsequently the structure of the complexes will be resolved by single particle reconstruction using negatively stained as well as vitrified samples.

1. Böttcher, B.*, et al.,* 2004. Geminate structures of African cassava mosaic virus. *Journal of virology,* 78 (13), 6758-6765.
2. Clérot, D., and Bernardi, F., 2006. DNA helicase activity is associated with the replication initiator protein rep of tomato yellow leaf curl geminivirus. *Journal of virology,* 80 (22), 11322-11330.
3. Hanley-Bowdoin, L., Elmer, J.S., and Rogers, S.G., 1990. Expression of functional replication protein from tomato golden mosaic virus in transgenic tobacco plants. *Proceedings of the National Academy of Sciences of the United States of America,* 87 (4), 1446-1450.
4. Hanley-Bowdoin, L., Settlage, S.B., and Robertson, D., 2004. Reprogramming plant gene expression: a prerequisite to geminivirus DNA replication. *Molecular plant pathology,* 5 (2), 149-156.
5. Jeske, H., Lütgemeier, M., and Preiss, W., 2001. DNA forms indicate rolling circle and recombination-dependent replication of Abutilon mosaic virus. *The EMBO journal,* 20 (21), 6158-6167.
6. Laufs, J.*, et al.,* 1995. Identification of the nicking tyrosine of geminivirus Rep protein. *FEBS letters,* 377 (2), 258-262.

Microbiology, Virology

LS2.P024
Morphological features of the ammonia-oxidizing archaeon Nitrososphaera viennensis sp. nov.

M. Stieglmeier[1], N. Leisch[2], C. Schleper[2], A. Klingl[1]

[1]Plant Development & Electron Microscopy, Department I - Botany, Planegg-Martinsried, Germany
[2]University of Vienna, Department of Ecogenomics and Systems Biology, Vienna, Austria

michaela.stieglmeier@biologie.uni-muenchen.de

Ammonia-oxidizing archaea are widespread and abundant in Nature and are thus considered to impact the global nitrogen cycle. However, only few organisms have so far been cultivated or enriched. Among these, *Nitrososphaera viennensis* represents the first organism from a soil habitat that is amenable to detailed investigations because it can be grown in pure laboratory cultures. We studied the ultrastructure and S-layer of *N. viennensis*, to obtain general information on this first type strain of the novel class *Nitrososphaeria* within the novel phylum Thaumarchaeota of the domain Archaea [1].

Ultra-thin sections of chemically fixed and high pressure frozen cells were prepared and analyzed by TEM to get insights into the ultrastructure. For the investigation of the S-layer purified S-layer sheets were negatively stained and freeze-fracturing/ freeze-etching was performed. TEM images of these samples were used for correlation averaging to get information about the S-layer symmetry and lattice constants.

N. viennensis cells are small, irregular shaped cocci with a diameter of about 0.78 ± 0.13 µm. Cells are motile and possess appendages like archaella (archaeal flagella) and pili. The analyses of the ultra-thin sections revealed distinct intracellular features like tubule-like structures, small inclusions with high and low electron density and a clearly discernable, cytoplasmic, larger area. This area might represent a storage compartment for polyhydroxyalkanoate produced by *N. viennensis* cells. *N. viennensis* has an S-layer with p3-symmetry, which was until now thought to be specific to *Sulfolobales*. Thus, the irregular coccoid shape common to *N. viennensis* and *Sulfolobales* cells might result from the p3-symmetry of the S-layer.

The characterization of *N. viennensis* extends the knowledge about the morphology of Thaumarchaeota and reveals interesting intracellular features, which have to be investigated further to understand their structure and function for e.g. cell stability or metabolism.

1. Stieglmeier M. et al. (2014). *IJSEM* **64**(8):2738-52

Microbiology, Virology

LS2.P025
Cationically fabricated lipid nanocarriers of a potent chemotherapeutic agent for enhanced antileishmanial efficacy: a cost effective approach

P. Tripathi[1], P. R. Mishra[1]

[1]CSIR-Central Drug Research Institute, Lucknow, India

priyankampharma@gmail.com

The current increase in Visceral leishmaniasis throughout the world to epidemic proportion coupled with increasing incidence of the disease as a severe opportunistic infection among people with HIV-1 infection have created an urgency to provide novel, efficient, target oriented, cost effective and industrially feasible drug delivery system for this disease. Here, an effort has been made to develop novel cationically fabricated lipid nanocarriers (NLC) of AmB to increase therapeutic efficacy and reduce toxicity with the use of microfluidizer.

Visceral leishmaniasis (VL), a vector-borne disease that infects a million people living in subtropical and tropical areas, is caused by intramacrophage trypanosomatid protozoa of the genus Leishmania. VL is manifested by hematological and hepatosplenic abnormalities and is usually fatal if not treated properly. Despite the availability of several chemotherapeutic drugs, successful management of VL has not yet been attained. Indeed, Amphotericin B (AmB) is used as a prototype antileishmanial agent due to its excellent efficacy, with great commercial success but it is challenging because of its severe and potentially lethal nephrotoxicity, hepatotoxicity and emerging incidence of resistance. Therefore, there is an urgent need of novel, leishmanicidal drug carriers for safe and effective management of VL. Cationic chitosan modified nanoparticles could be used for effective delivery of biopharmaceuticals into the macrophages because of better accumulation in macrophage rich organs when compared with other colloidal systems due to their preferential phagocytosis. Therefore, we have developed and evaluated cationic novel AmB lipid nanocarriers as cost effective and target oriented alternative.

Various formulations were developed with the use of microfluidizer (optimized by varying pressure and number of cycles) and characterized for various parameters (particle size, zeta potential, % entrapment efficiency, morphology, stability, *in vitro* release and toxicity). The chitosan concentration was optimized by measuring the change in zeta potential, particle size, and stability.

The AmB-NLC and Chi-AmB-NLC, characterized for % entrapment efficiency (94.2 % and 92.3%), particle size (144±7.2nm and 161.8±6.4nm), zeta potential [(-29±1.6mv and +31±2.1mv) Fig.1] and *in vitro* drug release [(68% and 65% within 24 hrs) Fig 2] were found stable for >3 months. The morphological characterization was done using TEM (Fig. 3). The toxicity profile showed the permissible range of haemolysis and cytotoxicity (Fig. 4).

Chitosan-coated nanocarriers with an oily core have a great affinity for macrophage uptake due to easy electrostatic interaction of cationic particles with negatively charged surfaces of macrophages by ionic adsorption, promoting subsequent cellular uptake leading to passively targeted drug delivery. The findings suggested that it would be preferable to deliver AmB through chitosan anchored lipid nanocarriers for better and cost effective management of visceral leishmaniasis.

1. Murray, H.W.; Berman, J.D.; Davies, C.R. and Saravia, N.G. *Lancet.* **2005**, 366, 1561-1577.
2. Wang, J.J.; Sung, K.C.; Hu, O.Y.; Yeh, C.H. and Fang, J.Y. *J. Control. Release*. **2006**, 115, 140-9.
3. Hu FQ, Zhang Y, Du YZ, Yuan H. *Int J Pharm.* **2008**, 348, (1-2), 146-152.
4. Kansal, S.;Tandon, R.; Dwivedi, P.; MisraP.; Verma, P.R.P.; Dube, A. and Mishra, P.R. *J. Antimicrob. Chemother*. **2012**, 67, (11), 2650-60.
5. Dwivedi, P.; Kansal, S.; Sharma, M.; Shukla, R.; Verma, A.; Shukla, P.; Tripathi, P.; Gupta P.; Saini D.; Khandelwal K.; Verma R.; Dwivedi, A.K. and Mishra, P.R. *J. Drug Target.* **2012,** 20, (10), 883-96.
6. Asthana, S.; Jaiswal, A. K.; Gupta, P. K.; Pawar, V. K.; Dube, A.; Chourasia, M. K. *Antimicrobial Agents and Chemotherapy.* **2013**, 57, (4), 1714-1722.

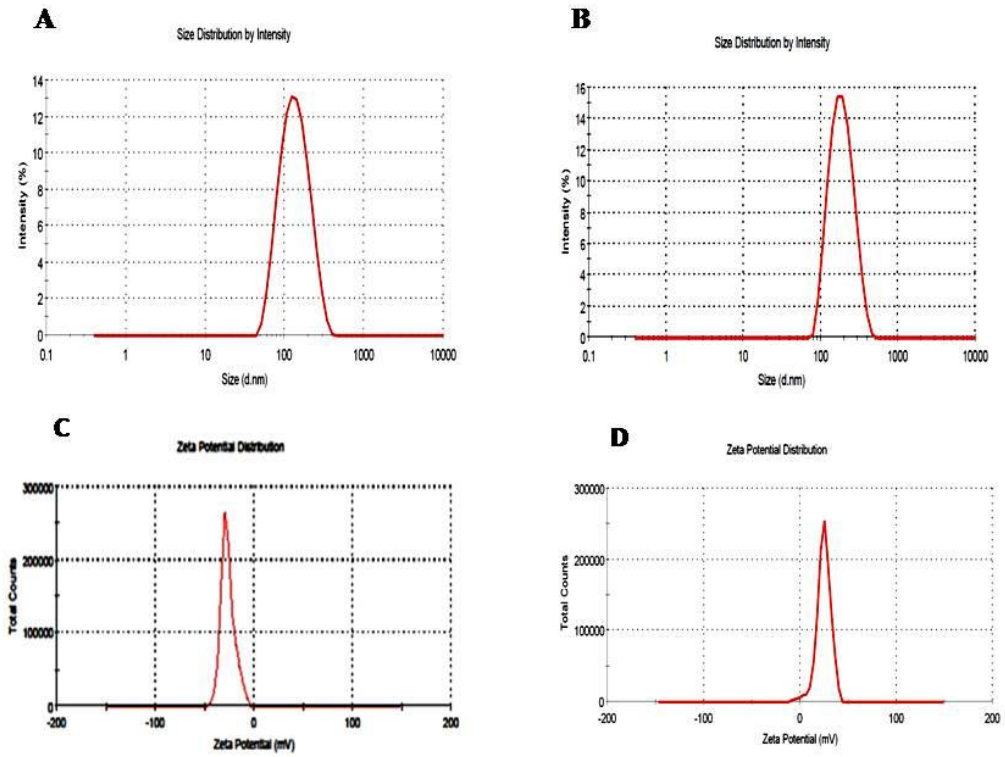

Figure 1. Average particle size of (A) AmB-NLC and (B) Chi-AmB-NLC; and zeta potential distribution of (C) AmB-NLC and (D) Chi-AmB-NLC

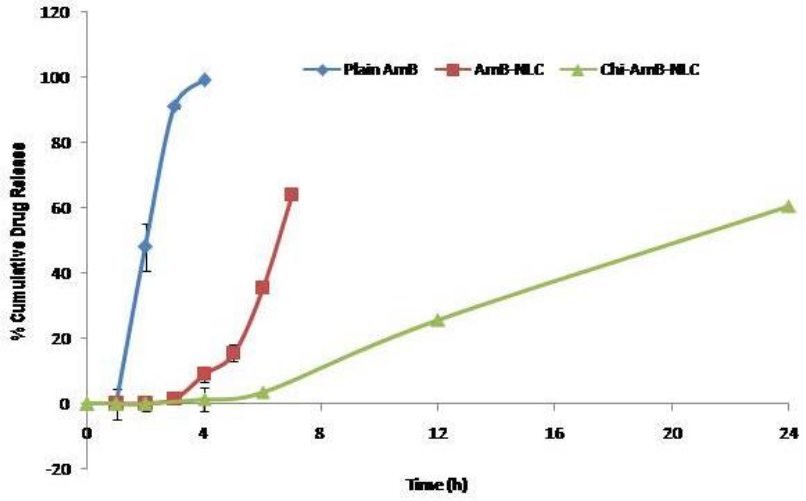

Figure 2. *in vitro* **drug release profile**

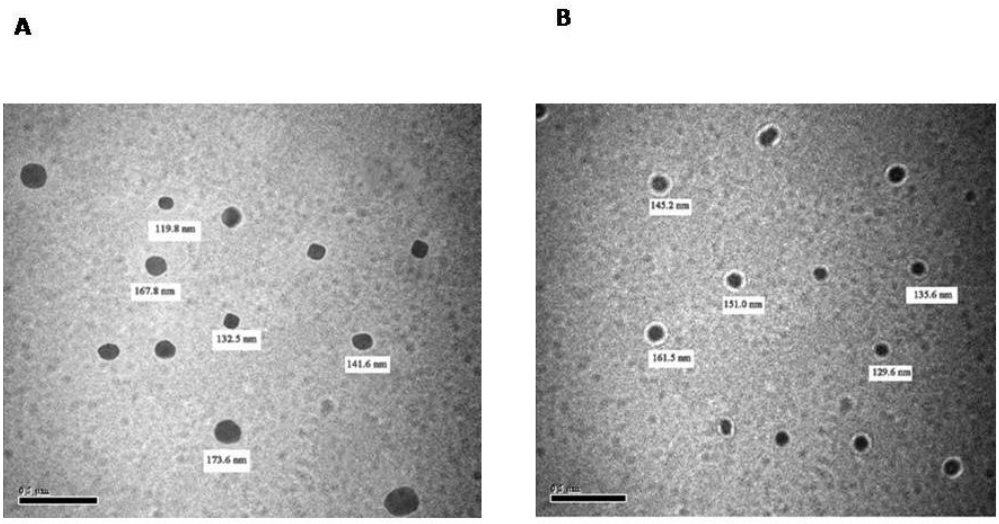

Figure 3. TEM microphotographs of NLCs (A) AmB-NLC and (B) Chi-AmB-NLC

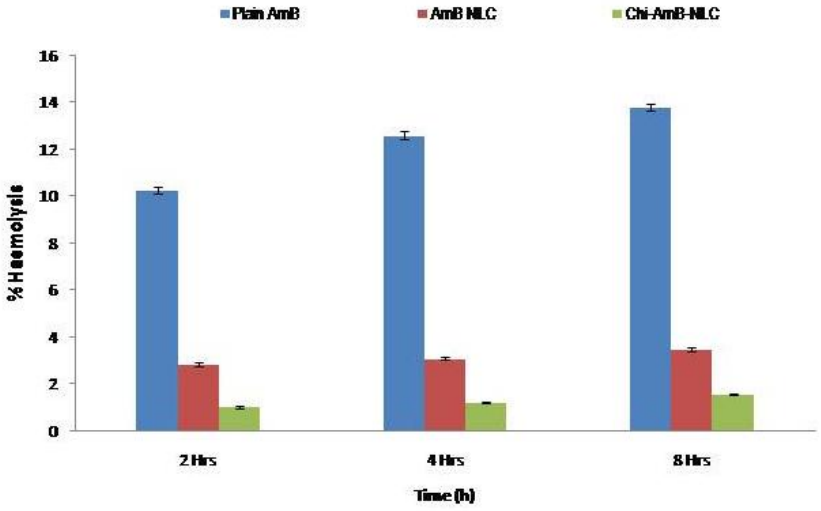

Figure 4. % Haemolysis

Pathology, Diagnostic EM, Medicine

LS3.026
The ultrastructural diagnosis of primary ciliary dyskinesia

H. Omran[1]

[1]University Hospital Münster, Department of Pediatrics, Münster, Germany

labor-omran@ukmuenster.de

Primary ciliary dyskinesia (PCD) is a rare congenital disorder of the cilia, which usually manifests itself in the respiratory system. If the presence of PCD is suspected, especially when screening markers such as reduced nasal nitric oxide (NO) levels are positive, then patients should promptly undergo further diagnostic measures. High-speed video microscopy analysis (HVMA) of ciliary beating should be the initial diagnostic measure to support or exclude PCD; in hospital centers where HVMA is available, an additional test to measure nasal NO is not mandatory. With an abnormal HVMA test result, additional tests including transmission electron microscopy (TEM) and high-resolution immunofluorescence microscopy (IFM) can directly assay abnormalities in cilia. At least two congruent pathological findings from HVMA, TEM and IFM analyses are obligatory for the diagnosis of PCD. If a PCD variant shows no ultrastructural ciliary defect by TEM analysis, then an identical ciliary beat pattern by HVMA must be confirmed by three independent test measurements. After collecting evidence for a PCD diagnosis by HVMA, TEM and IFM analyses, genetic evaluation should be pursued. A unique genetic finding can also confirm the diagnosis of PCD.

Originally, Transmission electron microscopy (TEM) analysis was the sole gold standard for the diagnosis of PCD. However, it is now recognized that many PCD variants have no detectable ultrastructural changes in cilia by TEM analysis despite a ciliary beating defect observed by HVMA, as in the case of *DNAH11* mutations. Certain genetic mutations (*HYDIN*) that affect the composition of the central pair complex in cilia are only detectable by electron microscopy tomography, but this method is too expensive for routine diagnostic use. Other mutations (e.g., *CCDC164*) that affect the DRC or Nexin Link complex in cilia result in very subtle ultrastructural defects that are often overlooked and missed by TEM analysis. Furthermore, some genetic mutations (e.g., *KTU*) result in only regional defects of the cilia and can also be overlooked by TEM analysis. As a rule, certain ultrastructural abnormalities observed by TEM such as “compound cilia” or “axonemal blebs” are nonspecific artifacts of secondary nature and are not pathognomonic for PCD. IDAs are a component of cilia that are difficult to resolve by TEM due to their low electron density. Up to 30% of biopsy material obtained during examination is not useful for diagnosis due to the presence of metaplasia or excessive mucus and inflammatory cells. In 3-5% of PCD cases involving *situs inversus* (Kartagener Syndrome) or dextrocardia the ultrastructure of cilia is normal by TEM analysis, and these require further characterization by HVMA analysis. To ensure that adequate quality standards are maintained for PCD diagnosis, only specialized centers with extensive experience in ciliary assessment should be commissioned.

Pathology, Diagnostic EM, Medicine

LS3.027
Detection of Newly Recognized Viruses by Using Tissue Culture and Electron Microscopy

C. Goldsmith[1]

[1]Centers for Disease Control and Prevention (CDC), Mailstop G32, Atlanta, United States

cgoldsmith@cdc.gov

The technique of isolating viruses in cell culture allows for the biological amplification of virus particles to levels where they can be detected by electron microscopy (EM). If the viral isolate cannot be recognized by other detection methods (ELISA, PCR, IFA, etc.), then EM is an ideal method because it can give an “open view” (term coined by Hans Gelderblom) to morphologically classify the isolate to a specific virus family. Once the family is known, molecular and immunologic techniques can be employed to elucidate which virus genus/species has been isolated.

An example of an unknown isolate being identified by EM was during the SARS coronavirus outbreak. Here, an isolate grown in cell culture was examined by thin section EM and identified as a coronavirus. This finding was rapidly confirmed by negative stain EM, immunohistochemistry, PCR, serology, and genomic sequencing. In other words, once the family of the virus became known, the other virus-specific tools for identification (antibodies, known pan-coronavirus PCR primers) could be applied.

There are several other examples which will be given where an isolated virus was first identified by thin section EM: i) Nipah virus, a paramyxovirus, was isolated in Malaysia during an outbreak of encephalitis among more than 100 pig farmers. ii) Four transplant-associated transmissions of lymphocytic choriomeningitis virus, an arenavirus, were identified in 2003. iii) A previously healthy man in North Carolina became extremely ill and eventually died. An orthobunyavirus, Cache Valley virus, was isolated from blood, serum and cerebrospinal fluid. iv) West Nile virus was isolated from the skin of a fatal case of hemorrhagic fever. v) During attempts to isolate *Ehrlichia chaffeensis* from blood samples from patients in Missouri, USA, a bunyavirus, designated as Heartland virus, was isolated from two people.

Two other recent examples of where EM helped in the characterization of newly recognized viruses will be given. Akhmeta virus, a member of the genus *Orthopoxvirus*, was recently detected in two cattle farmers in the country of Georgia. In addition, Bourbon virus, a tick-borne virus in the family *Orthomyxovirus*, was isolated from a patient with febrile illness and death in Kansas, USA.

Virus isolation and electron microscopy in combination are powerful tools in the identification of viral illnesses of undetermined cause. This can become particularly important during outbreaks of unknown origin.

Pathology, Diagnostic EM, Medicine

LS3.028
Impact of electron microscopy in diagnosis of juvenile liver diseases

J. Schröder[1], H. Siegmund[1], C. Grafe[1], B. Knoppke[2], J. Vermehren[2], M. Melter[2], F. Hofstädter[1]

[1]University Hospital Regensburg, Pathology, Central EM-Lab, Regensburg, Germany
[2]University Hospital Regensburg, Paediatric and Juvenile Medicine, Regensburg, Germany

josef.schroeder@ukr.de

This contribution focuses on the use of electron microscopy (EM) as adjunct tool in diagnostic hepatology [1] of mainly congenital, infectious, and storage diseases of juvenile patients (often candidates for liver transplantation) examined in the recent 8 years in our departments.

We receive mostly small primary Karnovsky-fixed parts of liver biopsies (adequate tissue preservation is a crucial methodical prerequisite for a reliable results interpretation) and peripheral blood samples (cases of suspected storage disease). Samples were automated processed and embedded in EPON-resin (in urgent cases microwave-assisted), tissue blocks were semithin (for light-microscopic orientation and block trimming) and ultrathin sectioned, and EM-examined. We demonstrate EM findings of selected cases of above mentioned diseases and the impact of telemicroscopy via Internet for second opinion retrieval and expert consultation [2].

In the heterogeneous group of progressive familial intrahepatic cholestasis (PFIC) diseases EM shows distinct bile characteristics (coarsely granular texture = ”Byler bile”, amorphous/filamentous, presence of cholesterol crystals) and bile canaliculus alterations pathognomonic for FIC1-, BSEP-, and MDR3-deficiency, respectively. In an Alagille syndrome patient, EM revealed numerous bile inclusions in the dilated intercellular space, in alpha-1-antytrypsin deficient patient typical amorphous accumulations in distended RER-cisternae are visible (Figure 1).

Two children with congenital glycogenosis condition displayed by EM in the hepatocytes non-membrane bound intracytoplasmic deposits of abnormal filamentous glycogen (d=8 nm) with sparse normal glycogen rosettes in their periphery (Andersen disease). Additionally, in the peripheral blood a fraction of leucocytes showed multiple vacuoles containing similar abnormal glycogen particles. PCR analyses identified one boy to be a compound heterozygous carrier of two mutations in exon 12 of the chromosome 3p14. In the other child two mutations were found in exon 6 and 13 encoding of the GBE-1 gene, respectively. In a fatal virus hepatitis of a transplanted child multiple adenovirus particles were detected (Differential Diagnosis: in early disease stages > CMV-hepatitis, GvHD, drug intoxication). Another not trivial pathologic light-microscopy diagnosis seems to be the Gaucher and Niemann-Pick storage diseases - EM reveals the pathognomonic cell inclusions (Figure 2).

Ultrastructural examination of liver biopsies reveals significant information for the final diagnosis, in case of storage diseases EM of peripheral blood leukocytes provides the rationale for the enzymatic and genomic mutation analysis. We conclude that EM is still a very valuable tool for diagnosis in rare diseases of the liver [3].

1. Phillips MJ, et al. The Liver. An Atlas and Text of Ultrastructural Pathology. Raven Press, New York 1987.
2. Schroeder JA. Ultrastructural Pathology Today - Paradigm Change and the Impact of Microwave Technology and Telemicroscopy. In: Stirling JW, Curry A, and Eyden B., Diagnostic Electron Microscopy. Wiley & Sons Ltd, Chichester 2013. Chapter 15.
3. Cheville NF. Ultrastructural Pathology. The Comparative Cellular Basis of Disease. Wiley-Blackwell, Ames 2009. Second edition.

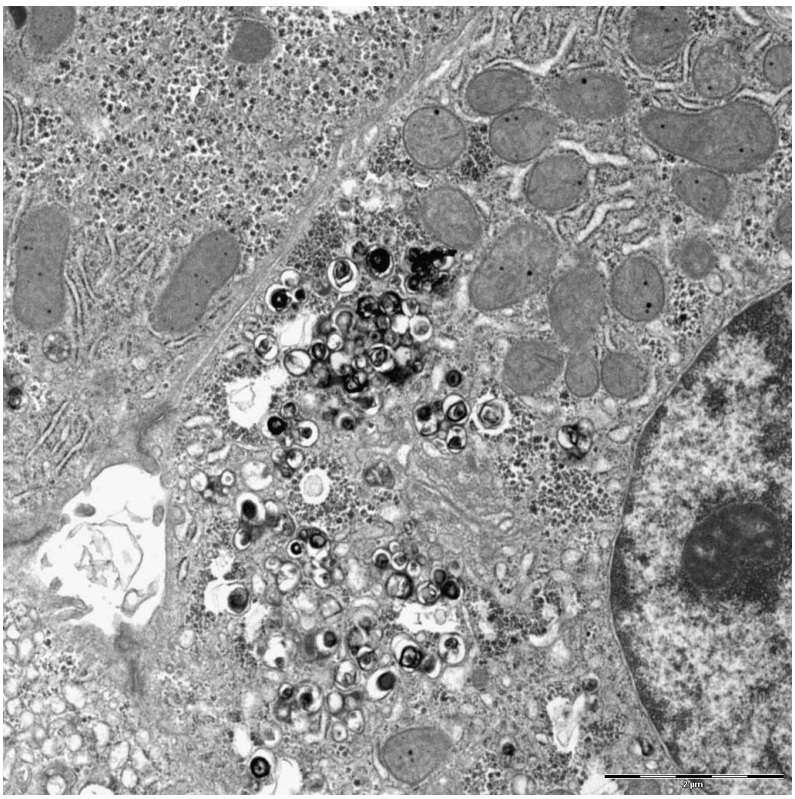

Figure 1: The image displays typical peribiliary dark inclusions representing cholestasis in the liver of a patient suffering of arteriohepatic dysplasia (Alagille Syndrome). Bar = 2 µm.

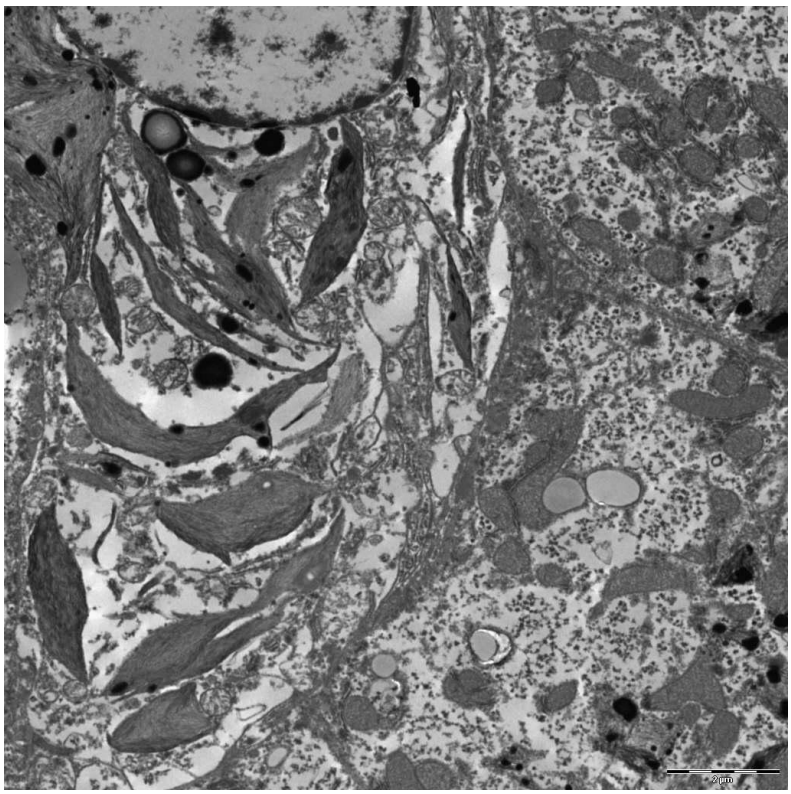

Figure 2: Note the numerous dark angular lysosomes containing multiple long tubular inclusions in Gaucher cells of an unclear case of hepatosplenomegaly (EM diagnosis: sphingolipid storage disease, Morbus Gaucher). Bar = 2 µm.

Pathology, Diagnostic EM, Medicine

LS3.029
Fulminant cowpox infection in an immunocompromised patient

W. Van Hecke[1], J. C. Sinnige[2], M. Tersmette[3], O. de Weerdt[4], J. L. Murk[2]

[1]University Medical Center Utrecht, Department of pathology, Utrecht, Netherlands
[2]University Medical Center Utrecht, Department of Medical Microbiology, Utrecht, Netherlands
[3]St. Antoniusziekenhuis, Department of Medical Microbiology and Immunology, Nieuwegein, Netherlands
[4]St. Antoniusziekenhuis, Department of Haematology, Nieuwegein, Netherlands

w.vanhecke@umcutrecht.nl

In the summer of 2014 a 44 year old female who lived on a farm in the Netherlands was presented at the emergency department with fever and redness and swelling of her labia. The previous year she was diagnosed with non-Hodgkin lymphoma, for which she received chemotherapy and an autologous stem cell transplantation in March 2014. After this, her disease was in remission. Her genital condition was diagnosed as erysipelas and antibiotics were promptly started. However, her condition deteriorated and she subsequently developed blisters in the genital region and over the rest of her body. With viral culture, electron microscopy and PCR an infection with cowpoxvirus was diagnosed. Unfortunately, by the time the diagnosis was made the patient had died.

Pathology, Diagnostic EM, Medicine

LS3.030
Postmortem ultrastructural analysis of a cornea transplanted with descemet membrane endothelial keratoplasty

M. Bruinsma[1], E. Livny[1], J. Parker[1], M. van der Kaaij[1], E. Haasdijk[2], J. van der Wees[1], G. Melles[1]

[1]Netherlands Institute for Innovative Ocular Surgery, R&D, Rotterdam, Netherlands
[2]Erasmus Medical Center Rotterdam, Department of Neuroscience, Rotterdam, Netherlands

bruinsma@niios.com

Fuchs endothelial dystrophy is a corneal disorder resulting in reduced visual function, characterized by "guttae," collagenous excrescences extending from the Descemet membrane. Currently, cornea transplantation (keratoplasty) is the only treatment option for this disease. In recent years, surgical treatment has shifted from conventional penetrating keratoplasty, where all layers of the cornea are replaced by that of a donor, to posterior lamellar techniques that specifically replace only the diseased posterior layers. In the last decade, we have introduced various endothelial keratoplasty techniques for the management of corneal endothelial diseases. Our latest state-of-the art technique, Descemet membrane endothelial keratoplasty (DMEK), is a surgical procedure in which only an isolated donor Descemet membrane (DM) and its endothelial layer are transplanted. By replacing only the affected inner layers of the cornea with the same layers of healthy donor tissue, the anterior corneal surface is not compromised, minimizing the risk of surgery-induced anterior corneal surface irregularities and providing faster and more complete visual rehabilitation. Clinically, corneas operated with DMEK appear "normal": their natural anatomy seems restored. However, in our experience, removing a failed DMEK-graft is frequently more challenging than removing DM in a "virgin" eye. In general, the donor DMEK-graft seems "stickier," more adherent, and more difficult to remove. This observation raised the questions of whether DMEK really does return the eye to its natural state or whether the adherence between the graft and the posterior stromal surface is of a fundamentally different sort? The answer is critical because graft detachment remains the main complication after DMEK and determining the nature of this interaction may suggest new strategies for either treatment or prevention. Therefore, the aim of this study was to describe the ultrastructure of the host-donor interface in the eye of a recently deceased patient, who underwent DMEK.

In 2010, a 76-year-old female received a DMEK in her right eye at our institute for treatment of Fuchs endothelial dystrophy. Informed consents for operation, study inclusion, and postmortem tissue donation were obtained from the patient. DMEK was performed using our standard surgical technique. Postoperative courses were unremarkable. Two years after the surgery, the patient passed away. Less than 36 hours postmortem, both globes were enucleated, decontaminated, and sectioned to produce 2 corneo-scleral buttons (1 per eye). Since only one eye received a DMEK, only this corneo-scleral button was cut into 4 quadrants, and processed for transmission electron microscopy evaluation. Healthy donor corneo-scleral buttons which were not eligible for transplantation were used as controls.

Transmission electron microscopy revealed close attachment of the donor's Descemet membrane to the host's stroma and projection of stromal collagen fibers into the interfacial matrix, resembling a normal "virgin" corneal architecture.

Ultrastructurally, an attached DMEK-graft closely resembles that of an un-operated, healthy eye with no appreciable adventitious or missing structures.

Pathology, Diagnostic EM, Medicine

LS3.031
Models for heritable skin diesases: morphological phenotypes correlated to molecular data

I. Hausser[1]

[1]University Hospital Heidelberg, EM Lab, Institut of Pathology, Heidelberg, Germany

ingrid.hausser-siller@med.uni-heidelberg.de

Some of the rare monogenetic genodermatoses are characterized by specific ultrastructural markers enabling classification or diagnosis including identification of causing canditate genes (or exclusion, respectively) and some insights in pathogenetic backgrounds. Examples are heritable bullous diseases (epidermolysis bullosa), keratinization disorders (e.g. ichthyoses) and connective tissue disorders (Ehlers-Danlos syndrome, cutis laxa. The molecular genetic causes of several human forms remain unknown, however, and to date only symptomatic therapies are available. Various types of animal models and organotypic cell cultures have been established to further investigate the distinct pathology and for evaluating novel therapeutic procedures. The challenge is to reproduce human disease (morphological) phenotype. Constitutive and conditional knockout mice for 12r-LOX and elox3 could be shown to express differential skin barrier defects and compensatory hyperkeratosis. A skin-humanized mouse model faithfully recapitulates transglutaminase 1 (TG1)-deficient lamellar ichthyosis, including expressing the ultrastructural marker (cholesterol clefts); this long-term model seems in some respects advantageous to organotypic cell cultures and was successfully used for an enyzyme substitution therapy with TG1-containing liposomal preparations. In an interdisciplinary study a new gene involved in autosomal recessive congenital ichthyosis (ARCI) pathology was identified by investigating a Golden retriever breed spontaneously affected by a lamellar ichthyosis. Homozygous PNPLA1 mutations revealed characteristic morphological aberrations, and subsequently six individuals with ARCI of two families were identified with PNPLA1 mutations and similar morphology with vacuolic structures in granular cells and their remnants in horny lamellae. Functional studies are in progress and localization of the gene product showed its presence in the upper epidermis but not in lamellar bodies. A spontaneous mouse model for recessive dystrophic epidermolysis bullosa shows considerable decrease in anchoring fibrils at the dermoepidermal junction as in respective human patients. A therapy based on bone marrow derived mesenchymal stromal cells (MSCs) revealed secretion of collagen VII and higher anchoring fibril formation than in untreated areas. These examples point to the merits of applying monogenetic disease models with specific ultrastructural disease markers.

Pathology, Diagnostic EM, Medicine

LS3.P033
Ameliorative potentials of a combination of Fenugreek and α-tocopherol on cadmium induced testicular toxicity: an ultrastructural study

H. N. Mustafa[1], A. M. Hussein [1], M. H. Badawoud [1]

[1]King Abdulaziz University, Anatomy, Jeddah, Saudi Arabia

hesham977@hotmail.com

The current study aimed to elucidate the protective role of combined fenugreek and α-tocopherol against cadmium induced histopathological changes in the testes.

Thirty adult male albino rats divided into three equal groups 10 rats each. Group I is the control group. Group II received 5 mg/kg/day cadmium chloride. Group III received 5 mg/kg/day cadmium chloride and 150 mg/kg/day fenugreek and 100 mg/kg/day of α-tocopherol. The treatment of all groups were done by oral gavage for 60 consecutive days. The testes were subjected to histopathological and ultrastructure study.

Rats exposed to cadmium showed severe histopathological changes in the spermatogenic series, many vacuoles and multinucleated giant cells. Treatment with fenugreek and α-tocopherol partially improved the morphological changes, reduced tissue damage and rebuilt of the spermatogonia layer.

Fenugreek and α-tocopherol might represent a promising medicinal combination to ameliorate the toxic effects of cadmium exposure.

	Body weight (g)	**Testis weight (g/100 g)**
Control (N=10)	210.40±3.062	0.73±0.036
$CdCl_2$ (N=10)	199.5±.028* P<0.001	0.61±0.084* P<0.001
Combined fenugreek and α-tocopherol with $CdCl_2$ (N=10)	208.10±0.994 P<0.128	0.68±0.030 P<0.139

Table 1. Mean testes weight and body weight by grams

	Control (n = 200)	CdCl2 (n = 200)		Combined fenugreek and α-tocopherol (n = 200)
Tubular Diameter **(MSTD) (µm)**	253.427±17.536	240.256±29.926 **P < 0.0001***		246.223±34.145 **P < 0.029***
Seminiferous epithelium Height (µm)	76.502±5.549	70.066±8.319 **P < 0.0001***		73.333±7.962 **P < 0.0001***

Table 2. Mean Diameter of Seminiferous Tubules (MSTD) and Germinal Epithelial Height by µm.

	Control (n = 10)	$CdCl_2$ (n = 10)	Combined fenugreek and α-tocopherol (n = 10)
CD3 Area %	0.031±0.027	0.090±0.049 **P < 0.014***	0.056±0.060 P < 0.553
CD20 Area %	0.050±0.022	0.091±0.040 **P < 0.033***	0.060±0.026 P < 0.692
CD68 Area %	0.058±0.028	0.139±0.080 **P < 0.034***	0.106±0.073 P < 0.213

Table 3. Mean area percentage of CD3, CD20, and CD68 immunostaining.

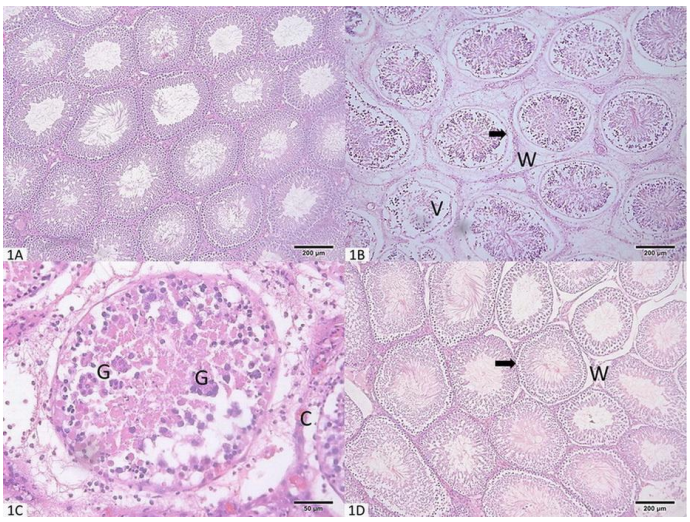

Figure 1 (1A). control group. **Fig. (1B):** $CdCl_2$ showed vacuolation (V) with spermatogonia separated from the basal lamina (↑). **Fig. (1C):** Higher magnification showed multinucleated giant cells (G). **Fig. (1D):** $CdCl_2$ and combined fenugreek and α-tocopherol showed restoration of the spermatogonia near the basal lamina (↑) and a decrease of the widening.

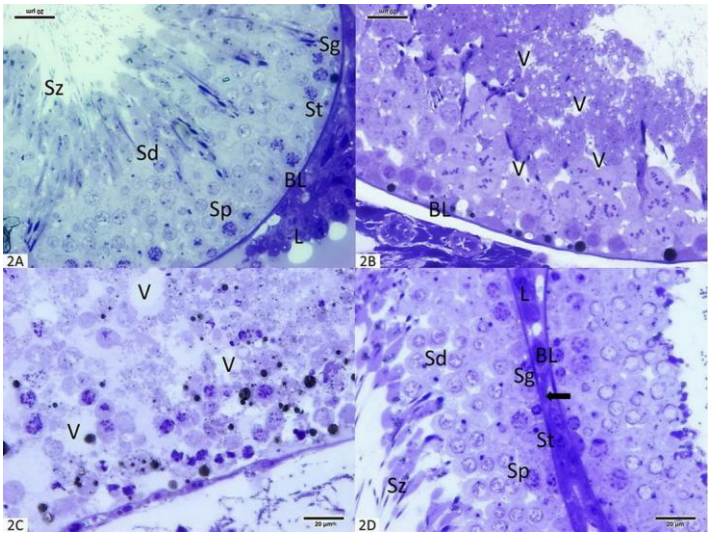

Figure 2 (2A). Control group. **(2B)** $CdCl_2$ showed vacuolations (V). **(2C)** showed depletion, extensive vacuolization (V) of the germinal epithelium. **(2D)** combined fenugreek and α-tocopherol with $CdCl_2$ shows improvement of the epithelial layers.

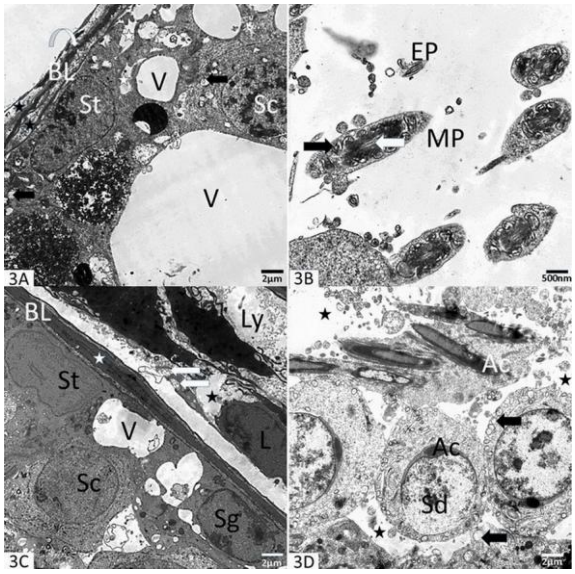

Figure 3. $CdCl_2$ treated group. **Fig. (3A).** Sertoli cell (St) and primary spermatocyte (Sc) is separated by spaces (white star) and vacuolated mitochondria (black arrows). Vacuoles (V) and thickened basal lamina (BL) containing collagen (black star) and a myoid cell (curved arrow). **Fig. (3B).** Mid-piece of the sperm (MP) with swollen mitochondria (black arrow) surrounds the central axoneme (white arrow). End pieces (EP). **Fig. (3C).** Leydig cell (L), vacuoles (V), an empty space (black star), lymph vessels (Ly) and vacuolated mitochondria (white arrow). The spermatogonia (Sg) and the Sertoli cell (St) and thickened basal lamina (BL) with a myoid cell (star), primary spermatocyte (Sc). **Fig. (3D).** Spermatids (Sd) with mitochondria with lost cristae (black arrow) and acrosomal cap (Ac). Empty spaces (star) are all around.

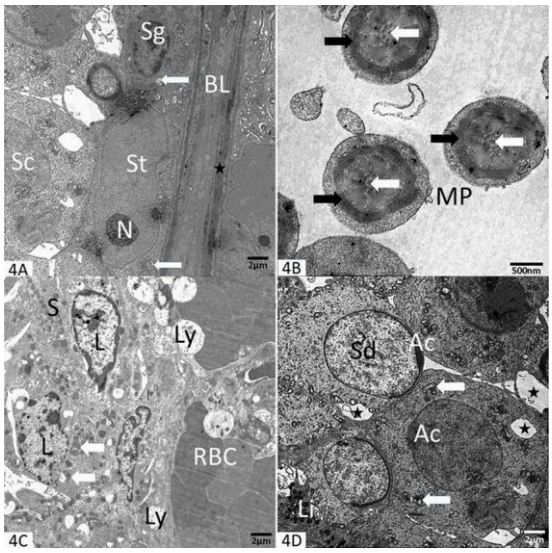

Figure 4. combined fenugreek and α-tocopherol and $CdCl_2$ **Fig. (4A).** Sertoli cell (St) with a nucleolus (N) and the spermatogonia (Sg) on the thickened basal lamina (BL) with myoid cell (black star). Mitochondria (arrow) and primary spermatocyte (Sc) noticed. **Fig. (4B).** Mid-pieces (MP) with axoneme (white arrow) and a mitochondrial sheath (black arrow). **Fig. (4C).** Leydig cells (L), multiple lysosomes (S) and mitochondria (arrow) and Lymph vessels (Ly). **Fig. (4D).** The Spermatids (Sd) with mitochondria with preserved cristae (arrow) and acrosomal cap (Ac). Minimal empty spaces (star) in the affected intercellular bridge and lipid droplets (Li).

Pathology, Diagnostic EM, Medicine

LS3.P034
Electron microscopic investigation of the in vitro cytotoxicity of crystallized bee venom and melittin

A. C. Bolundut[1], A. Florea[1], O. Soriţău[2], A. Câmpian[2], H. V. Matei[1]

[1]"I. Hatieganu" University of Medicine and Pharmacy, Cell and Molecular Biology, Cluj-Napoca, Romania
[2]"Prof. Dr. Ion Chiricuţă" Oncology Institute , Radiotherapy, Tumor and Radiobiology Laboratory, Cluj-Napoca, Romania

alex.bolundut@yahoo.com

Finding new strategies to fight against malignant cells is a topic of tremendous importance in the context of the increasing number of patients suffering of various types of cancers. The side effects of chemotherapeutic drugs and of radiotherapy are among the factors that direct the research towards alternative approaches, less harmful for the human body. We tested here the cytotoxic effect of bee venom (BV - collected by us and lyophilized) and melittin (MLT - HPLC purity, purchased from Sigma Aldrich), a 28 amino-acid cationic peptide and the main component of BV, known to interact non-specifically with cell membranes. The both BV and MLT were reconstituted in 150 mM NaCl, 5.5 mM glucose, and 5 mM HEPES at pH 7.4. Three cell lines were tested: 1) a Michigan Cancer Foundation-7 (MCF7) breast cancer cell line; 2) a line of malignant stem cells established from human glioblastoma multiforme (GM1), and 3) a line of normal mesenchymal stem cells isolated from dental follicle (DFSC), used as reference. MTT test was performed 24 h after the treatment of cells with different increasing doses of BV and MLT (starting with 1 µg/ml) in order to find the most adequate doses for further investigation. Then, the effects of BV and MLT, in dose of 30 µg/ml for both (that inhibited statistically significant the cell proliferation), were assessed at 24 h and 48 h respectively. Pellets of cells were prefixed with 2.7% glutaraldehyde, postfixed with 1.5% osmium tetroxide, dehydrated and embedded in Epon 812. Ultrathin sections, cut with glass knifes and double contrasted with uranyl acetate and lead citrate, were examined with a Jeol JEM 1010 transmission electron microscope. Cells in the control group remained unmodified, displaying the same normal ultrastructure after 24 and 48 h. The BV applied for 24 h partially affected the cells from all three lines. Despite the fact that in all lines most of the cells were totally disorganized, in MCF-7 and DFSC cultures, intact, almost normal cells were still found, displaying only limited cytoplasmic lesions. In GM1 line, all the cells suffered significant degrees of ultrastructural alterations. After 24 h of MLT exposure, the cells in all lines were completely destroyed, showing disrupted plasma membranes, cytoplasmic debris (in which swollen mitochondria with abnormal cristae could be identified), and nuclear ghosts (nuclear envelopes devoid of chromatin, but with 1-3 nucleoli still attached to a discontinued rim of heterochromatin). The 48 h treatment with BV strongly affected the cells in all lines. However, in MCF-7 and DFSC rare intact cells, but obviously damaged, were noted. The 48 h MLT treatment resulted in total destruction of cells in the three lines: only the nuclear ghosts were observed on the sections, along with debris resulted from disorganization of cellular organelles. Both BV and MLT had important cytotoxic effects upon all three types of cells used in our study, mainly due to changes produced at the level of all cellular membranes. Their effects were time-dependent and the ultrastructural changes induced by MLT were more accentuated than those triggered by the BV. Among the three types of cells, GM1 line showed the highest sensitivity to BV and MLT. Since no specificity of BV and MLT for malignant cells was observed in our study, further studies are required to find ways to direct selectively the molecules towards the cancer cells only.

Pathology, Diagnostic EM, Medicine

LS3.P035
Melatonin limits er stress in the obese mice liver through Sirtuin 1

A. Stacchiotti[1], G. Favero[1], A. Lavazza[2], M. Aleksic[3], I. Golic[3], A. Korac[3], R. Rezzani[1]

[1]Brescia University, Dept.Experimental and Clinical Sciences, Brescia, Italy
[2]Istituto Zooprofilattico Sperimentale della Lombardia ed Emilia-Romagna, Brescia, Italy
[3]University of Belgrade, Faculty of Biology Center of Electron Microscopy, Belgrade, Serbia

alessandra.stacchiotti@unibs.it

Obesity represents the fifth leading cause of death in industrialized countries and is considered an epidemic condition linked to sedentary style of life, fat diet, abnormal metabolism [1]. Melatonin (N-acetyl-5-methoxytryptamine), the pleiotropic product of the pineal gland with antioxidant and anti-inflammatory properties, has been successfully tested against the metabolic syndrome and diabetes [2]. Leptin-deficient heterozygous mice (*ob/ob*) are a translational model of early non alcoholic fat liver disease (NAFLD) with obesity but without inflammation [3]. In these mice we recently demonstrated a beneficial role of melatonin against vascular and renal mitochondria alterations [4-5]. Sirtuin 1 (Sirt1), a conserved NAD+-dependent class III histone deacetylase enzyme, is the main regulator of reduced fatty liver upon caloric restriction in vivo and protects hepatoma cells against ER stress in vitro [6]. In leptin-deficient and high fat diet-induced obese liver, altered ER-mitochondria crosstalk and abnormal ER homeostasis were recently demonstrated [7].

So, considering that obesity may impact different intracellular targets and their energetic pathways, we performed the present study by light and TEM microscopy. We analysed by histopathology and immunohistochemistry the hepatic localization of Sirtuin 1, ER stress and metabolic markers in leptin-deficient mice fed a normal rodent diet but drinking or not melatonin. Lobular distribution of glycogen and steatosis and the localization of sirtuin 1, ER resident chaperones (GRP78 and GRP94), beta catenin and retinol binding protein 4-RBP4 were assessed. Moreover by ultrastructural analysis (TEM Tecnai G2 Spirit and CM12-FEI), qualitative and quantitative changes of mitochondria, ER and lipid droplets in lean and *ob/ob* mice receiving or not melatonin at 100 mg/kg in drinking water for 8 weeks were acquired.

No statistically significant differences were detected in C57BL6 mice receiving or not melatonin, so we referred to these last as lean group. By contrast, in *ob/ob* mice Sirt1 was barely detectable, but became evident in the nuclei of *ob/ob* mice plus melatonin in the pericentral zone 3 almost similar to lean group (Figure 1). GRP78 and GRP94 immunosignals located within the periportal and mid-portal area in ob/ob mice, decreased significantly after melatonin intake. C/EBP homologous protein (CHOP), a downstream pro-apoptotic signal of ER stress, undetectable in lean mice, was moderate in *ob/ob* mice but reduced after melatonin supplementation. Beta catenin and RBP4 immunostainings in *ob/ob* mice were reorganized and restricted mainly to the pericentral area after melatonin treatment. Regular rough ER, round and small mitochondria were prevalent features in hepatocytes in *ob/ob* mice drinking melatonin vs *ob/ob* group.

Our results suggest that in this animal model, melatonin might be a useful adjuvant treatment in obesity, able to orchestrate a cascade of events like Sirt1 expression, so ameliorating mitochondria and ER homeostasis and leading to reduced steatosis.

1. Malik V, Willet W, Hu F. Nature Reviews Endocrinology 9 (2013), 13-27; 2. Mozdan M et al Arch Med Sci 10 (2014), 669-675; 3. Kozirog M et al. J Pineal Res 50 (2011), 261-266; 4. Favero G et al. Acta Histochem 115 (2013), 783-788;5. Stacchiotti A et al. PlosOne 9 (2014), e 111141;6. Li X et al. FASEB J 25 (2011), 1664-1679;7. Arruda A et al. Nature Medicine 20 (2014) 1427-1435.

#

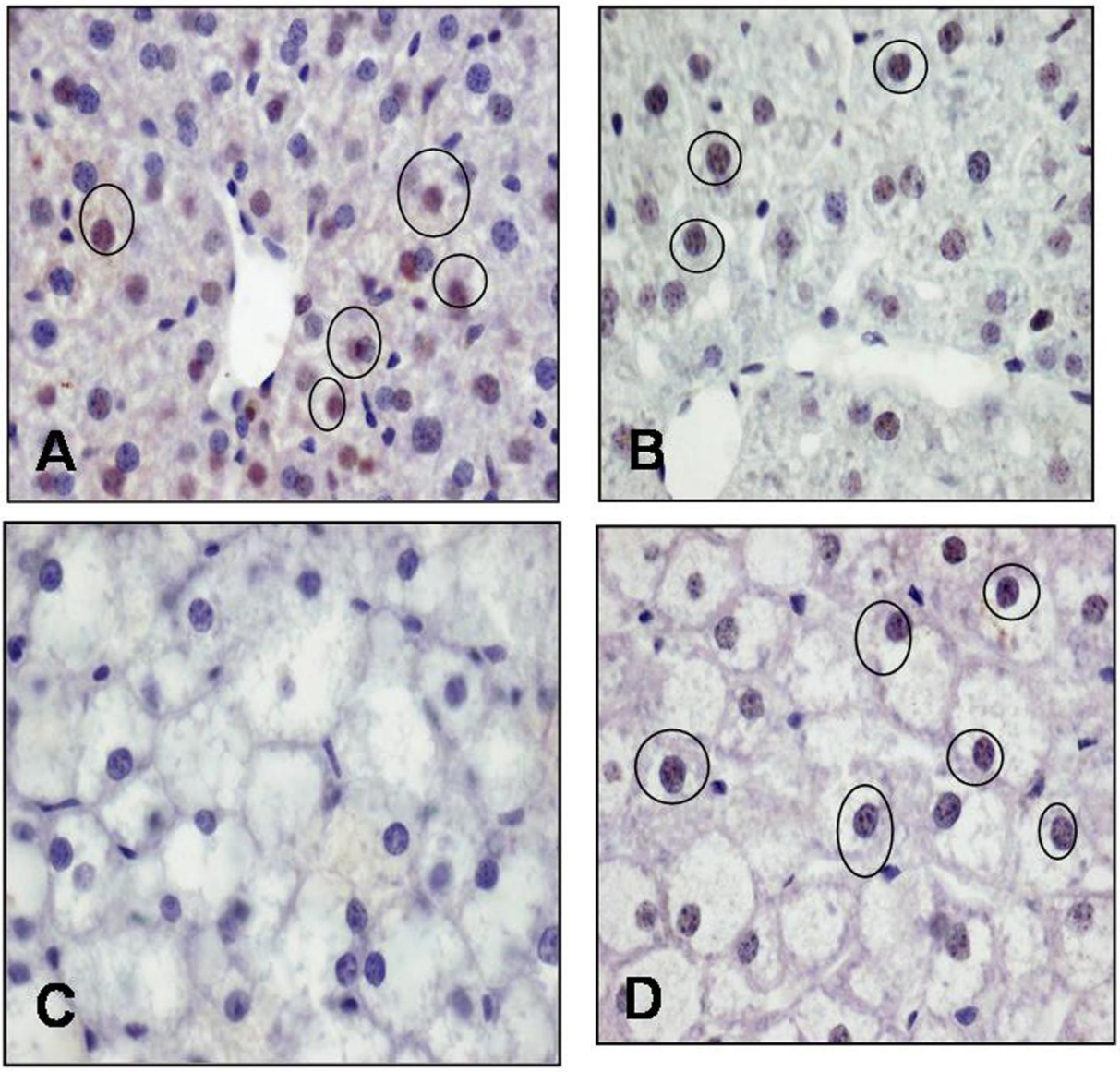

Figure 1. Sirtuin1 immunostaining in mice liver drinking or not melatonin (MEL) at 100 mg/kg for 8 weeks. **A**= Lean (C57BL6), **B**= Lean plus MEL, **C**= Leptin-deficient obese (*ob/ob*) mice, **D**= *ob/ob* plus MEL. Nuclei positive encircled. Original magnification 40x

Pathology, Diagnostic EM, Medicine

LS3.P036
Increased number of small blood vessels and capillaries in the uninvolved rectal mucosa 10 cm away from the malignant tumor

S. Despotović[1], I. Lalic[1], N. Milicevic[1], Z. Milicevic[1]

[1]University of Belgrade, School of Medicine, Institute of Histology and Embryology, Belgrade, Serbia

sanjadesp@gmail.com

Despite the wealth of data regarding the interactions between tumor cells and tumor-associated stromal elements in the progression of malignant disease (1,2), no attention has been devoted to the studies of uninvolved stromal tissue in the remote surrounding of the tumor. Recently we have demonstrated structural alterations of the mucosa 10 cm and 20 cm away from the rectal adenocarcinoma. They consisted of reduced cellularity and tissue edema accompanied by disorganized extracellular matrix of the lamina propria (3). Small blood vessels and capillaries seem to appear more frequently in the lamina propria of rectal mucosa 10 cm and 20 cm away from the malignant tumor in comparison with healthy controls and the aim of our study was to quantify those changes using an objective morphometric approach.

Morphometric study of rectal mucosa was performed in samples taken 10 cm and 20 cm away from the malignant tumor during endoscopic examination of patients with rectal adenocarcinoma. The samples of rectal mucosa obtained from healthy persons subjected to diagnostic rectoscopy during active screening for asymptomatic cancer were used as control. Tissue sections were stained immunohistochemically for CD34. Microphotographs were acquired with a digital camera Leica DFC295 (Leica, Hüllhorst, Germany) connected to a light microscope (Leica, Hüllhorst, Germany). Measurement of the number of blood vessels and capillaries in the lamina propria (per 0,1 mm^2 of the tissue) was performed using an open/source software Fiji. Measurements were performed at 10 fields per slide at magnification x200. Results were statistically analyzed with Student T-test.

At the distance of the 10 cm away from the tumor lesion a significant increase in the number of blood vessels and capillaries was observed (64,48±14,26 per mm^2) in comparison with healthy controls (54,24±14,93 per mm^2). At the distance of the 20 cm away from the tumor lesion an increase in the number of blood vessels was also observed (61,88±22,88 per mm^2), but without statistical significance.

There is increased number of small blood vessels and capillaries in the remote, uninvolved lamina propria of rectal mucosa 10 cm away from the malignant tumor.

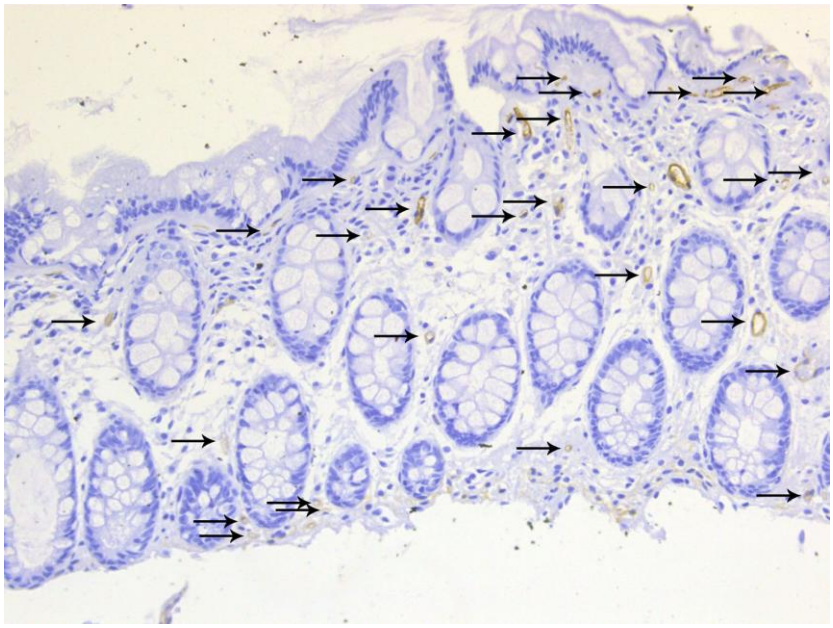

Figure 1. Rectal mucosa of healthy person stained with CD34. Small blood vessels and capillaries are indicated by arrows. (x200)

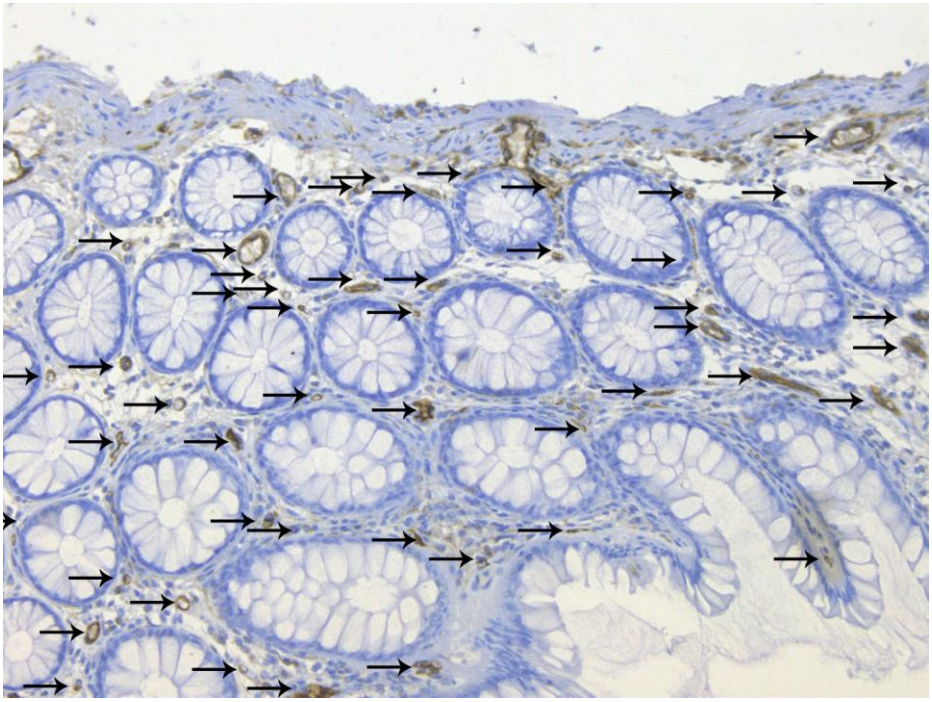

Figure 2. Rectal mucosa 10 cm away from the malignant tumor stained with CD34. Small blood vessels and capillaries are plentiful (indicated by arrows). (x200)

Pathology, Diagnostic EM, Medicine

LS3.P037
Implantation of human glioblastoma cells into the brain of zebrafish embryos for the in vivo study of tumour invasion

M. Vittori[1], B. Breznik[1], H. Motaln[1], T. T. Lah[1]

[1]National Institute of Biology, Department of Genetic Toxicology and Cancer Biology, Ljubljana, Slovenia

milos.vittori@nib.si

Zebrafish (*Danio rerio*) and their transparent embryos are becoming an increasingly popular tool for studying tumour biology [1]. The xenotransplantation of fluorescently labelled mammalian cancer cells into zebrafish embryos enables relatively low-cost and high-throughput *in vivo* analyses and has an unprecedented potential for the real-time visualisation of processes involved in cancer progression at single-cell resolution. The implantation of brain tumour cells into the yolk sac of zebrafish embryos has previously been utilized to study tumour cell invasion and tumour-induced angiogenesis [2,3]. The implantation of brain tumour cells, such as glioblastoma multiforme (GBM) cell lines, into the embryonic brain might offer some advantages over implantation into the yolk sac, as the zebrafish embryonic brain more closely resembles the microenvironment of brain tumour cells *in situ*. In our approach, we used GBM cell lines U87 and U373 that stably express the fluorescent proteins DsRed and eGFP, respectively, for implantation into the brain of zebrafish embryos 2 days after fertilization. The xenotransplanted cells were then monitored during three days of incubation in order to quantify tumour cell invasion *in vivo*. We demonstrated that the implanted GBM cells survive within the brain and invade the spinal cord. The frequency of invasion into this structure is higher in U87 cells (35% ± 5%) than in U373 cells (20% ± 5%). This indicates that GBM cell implantation into the brain of zebrafish embryos represents a promising approach to study GBM invasion within the central nervous system *in vivo*. We applied this approach to study the effects of the mesenchymal stem cells (MSCs) on the invasion of GBM cells *in vivo*. MSCs are known to migrate towards the tumour site and become a part of the GBM microenvironment. Still, their role within GBM remains poorly understood [4]. We aimed to evaluate the effect of a direct interaction between GBM cells and MSCs on the invasion of GBM cells by implanting a mixture of eGFP-expressing U373 GBM cells and DiI-labelled MSCs into the brain of zebrafish embryos 2 days after fertilization. For the quantification of U373 cell's invasion, individual embryos were imaged at two time points, 24 h and 72 h after the implantation of the cell mixture. We used computer image analysis to evaluate the relative increase of the dispersion distance of eGFP-expressing U373 cells at these time points. Witht this we demonstrated that the direct interaction of MSCs with U373 cells at the implantation site enhances the invasion of U373 cells. We confirmed that xenotransplantation into the brain of zebrafish embryos can be successfully applied to study brain tumour cell heterogeneity and the interactions between tumour cells and their microenvironment.

1. Konantz et al. (2012). Ann N Y Acad Sci 1266:124-37
2. Yang et al. (2013). Plos One 8: e61801
3. Yang et al. (2014). Plos One 9: e85759
4. Schichor et al. (2012).Exp Neurol.234: 208-19

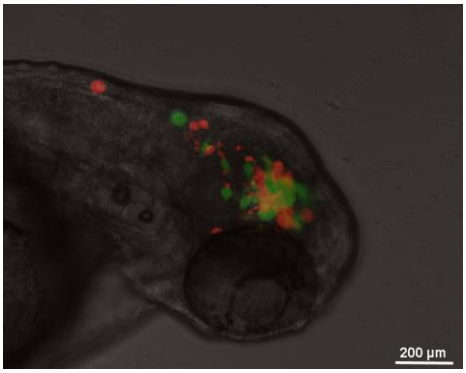

Figure 1. Implanted eGFP-expressing U373 glioblastoma cells (green) and DiI-labelled mesenchymal stem cells (red) in the brain of a zebrafish embryo 1 day after implantation.

Pathology, Diagnostic EM, Medicine

LS3.P038
Electron microscopy of leptospirosis in humans - a fast and reliable tool supporting molecular biological and bacteriological diagnostics

S. Richter[1], M. Müller[1], R. Posch[1], A. Steinrigl[1], F. Schmoll[1]

[1]AGES-Inst. for Veterinary Disease Control Moedling, Moedling, Austria

susanne.richter@ages.at

Leptospirosis, caused by *Leptospira interrogans,* is a zoonotic, worldwide distributed disease that affects humans and animals. Almost every mammal can serve as a carrier of leptospires, harboring the spirochete in the proximal renal tubules of the kidneys, leading to urinary shedding. *L. interrogans* can also survive outdoors under favorable conditions. Mice and rats serve as the major sources in most human leptospirosis cases, excreting high concentrations of leptospires. Important transmitters are also canids, cattle, pigs, horses, sheep and goats. Transmission of the pathogen to human occurs either through direct contact with infected animals, or through contact with soil or water that have been contaminated by animal urine. Especially in the livestock industry the disease can be a serious problem. Persons at risk are people predominately handling livestock and livestock products e.g. farmers, veterinarians and butchers. Leptospirosis can cause a wide range of symptoms in humans, some of which may be mistaken for other diseases. The disease can range from very mild and symptomless to a more serious, even life threatening form, that may be associated with kidney and liver failure, meningitis, respiratory distress, and even death.

For cultivation methods a large amount of liquor from infected persons is necessary for diagnosis. For detection of leptospiral DNA in clinical samples real-time quantitative PCR, for example targeting the *lipL32* gene that is only present in pathogenic leptospires, is in our institute the method of choice. All tested *Leptospira* strains, belonging to a variety of pathogenic *Leptospira* serovars and genomospecies are correctly identified with this qPCR. Despite excellent technical performance of the assay, testing of clinical samples reveals a problem because of the presumably low number of bacteria in the clinical sample, especially in human liquor. Cultivation from clinical samples (in the form of inoculated liquid cultures) is important but complicated. Thus, ultrastructural metal shadow cast preparations and negative staining, which are fast and reliable detection methods for bacteria in body liquids, can support cultivation methods and molecular biological tests by providing additional information and can help to confirm the diagnosis. However, their spiral confirmation and great length-to wide ratio make leptospires difficult to examine by ultrastructural techniques. For diagnostic purposes, special care in fixation and sample preparation must be taken. In good condition, leptospires are thin, helically coiled, motile spirochetes usually 6-20µm in length (Fig. 2a-b). The hooked bacterial ends, giving its distinctive question-mark shape in light microscopy, are rarely seen in negative staining. The bacterium consists of a homogeneous protoplasm and two periplasmic flagella (Fig. 1b), which arise from each end of the bacterium. Small spherical bodies can be randomly positioned along the bacterial wall (Fig. 1c). The bacterial-wall in some cases is distended to large, globular formulations measuring 0,5-1,8 µm in diameter, with the body of the leptospira passing diametrically through them (Fig. 1b). In young cultures, part of the organism can be rolled up within such an end bulb, giving the appearance of a partly encysted spirochete (Fig. 1a). In degenerated bacteria, detected in liquor of successfully treated patients or in dead cultures, the cytoplasmic mass is virtually absent; the bacteria resemble multilayered thread-like structures (Fig. 2c-d).

1. Evangelista, K.V.; J. Coburn, J. (2010): Leptospira as an emerging pathogen: a review of its biology, pathogenesis and host immune responses. Future Microbiol. 5(9): 1413.

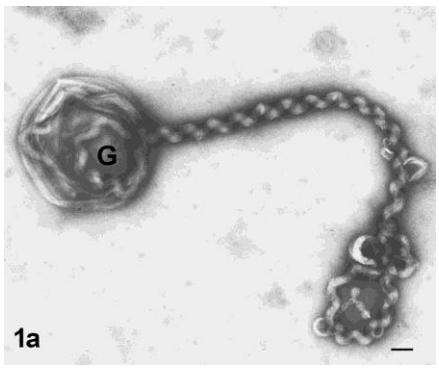

Figure 1. *Leptospira interrogans* serovar Bratislava in culture (Medium: EMJH, source: human liquor) a) bacterium with globular end formation (G), b) globular formation (G), periplasmic flagella (F) c) small spherical bodies (S), bar: 250nm

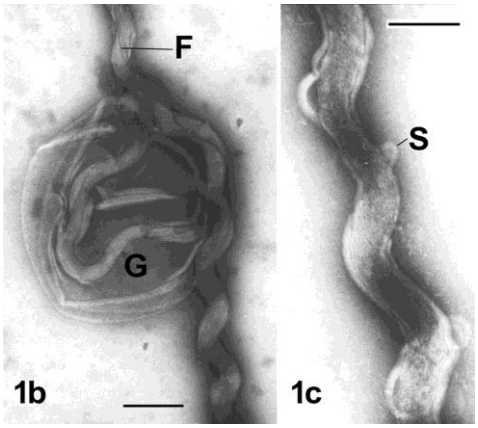

Figure 2. *L. interrogans* Bratislava: a) bacteria from liquid culture (EMJH medium, source human liquor), b-d: from human liquor: b) at the beginning of the disease, c-d) after medical treatment: degenerated bacteria resembling multilayered thread-like structures, bar: 1µm

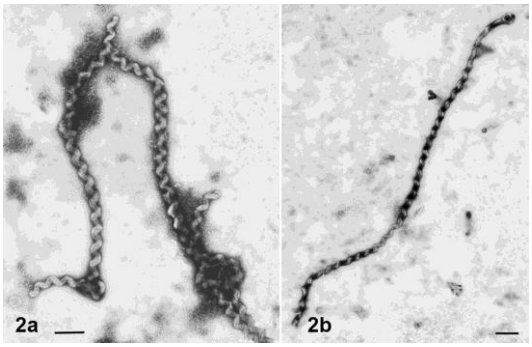

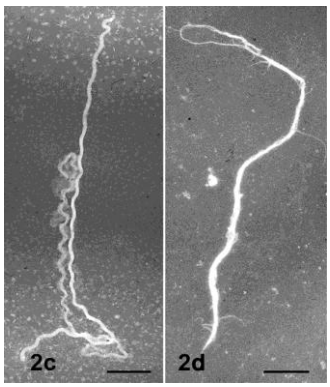

Pathology, Diagnostic EM, Medicine

LS3.P039
Electron microscopy structural studies of the myosin thick filament from human heart muscle

H. AL-Khayat[1], M. Yacoub[1]

[1]Qatar Foundation, Doha, Qatar

halkhayat@qf.org.qa

All muscles involve the interaction between two sets of filamentous proteins, actin and myosin, that leads to muscle contraction and force production mediated by the hydrolysis of ATP (Adenosine triphosphate).

The myosin filaments are formed from complicated arrangements of myosin molecules and accessory proteins [e.g. myosin binding protein C (MyBP-C) and Titin]. The aim of this project is to study and compare the arrangement of the myosin molecules and the accessory proteins in the human heart muscle myosin filaments and how these arrangements change in diseased human heart muscles, suffering from either hypertrophic or dilated cardiomyopathies.

Mutations in cardiac muscle myosin and its associated proteins are known to be associated with a number of cardiomyopathies which change the proteins involved in producing and regulating heart muscle contraction. In order to understand the effect of myosin-associated heart disease, it is important to understand the three-dimensional (3D) structure of myosin filaments in both the normal as well as in the diseased human heart muscles.

A laboratory method to isolate myosin filaments from normal undiseased human cardiac muscle has already been developed. This led, for the first time, to the detailed analysis of the 3D structure of myosin filaments from normal human heart muscles by electron microscopy, single particle image analysis, 3D reconstruction and structural interpretation (AL-Khayat *et al*., 2013, Proc. Natl. Acad. Sci., USA, **110**, 318-323). Knowledge of this 3D structure serves as the starting point from which myosin filaments isolated from human cardiomyopathic samples will be studied (AL-Khayat, 2013, Global Cardiology Science and Practice, 36, http://dx.doi.org/10.5339/gcsp.2013.36).

By direct comparison of the 3D structure of myosin filaments from diseased human heart muscle to that from normal undiseased human cardiac muscle, would eventually permit the structural effects of known myosin filaments-associated mutations to be investigated in detail as well as to relate structure-to-function-to-the overall disease process. Detailed understanding of the disease process would then allow us to design possible therapeutic interventions for patients suffering from such genetic myosin-related cardiomyopathies.

Pathology, Diagnostic EM, Medicine

LS3.P040
RANK/RANKL/OPG signaling pathways and VEGF/BSP expression analyses in necrotic jaw bone from bisphosphonate-treated subjects

M. De Colli[1], V. L. Zizzari[1], G. D. Marconi[1], C. Di Nisio[1], G. Tetè[1], M. Falconi[2], G. Teti[2], A. Cataldi[1], S. Zara[1]

[1]University "G. d'Annunzio", Department of Pharmacy, Chieti-Pescara, Italy
[2]University Alma Mater Studiorum, Dipartimento di Scienze Biomediche e NeuroMotorie (DiBiNeM), Bologna, Italy

marianna.decolli@libero.it

Bisphosphonates (BPs), synthetic analogues of pyrophosphate compounds, showing direct anti-tumor capabilities, are currently administered as anti-resorptive medications to treat several bone diseases.

Osteonecrosis of the jaw (ONJ) is a chronic complication affecting long-term bisphosphonate-treated subjects, clinically defined as an area of exposed bone in the maxilla or in the mandible that has failed to heal within a period of six to eight weeks. The pathophysiological mechanism underlying ONJ has not been fully elucidated and its spontaneous occurrence suggests a multifactorial pathogenesis.

The aim of the present study was to investigate the role of RANK/RANKL/OPG signaling pathway along with angiogenic and matrix mineralization response in jaw bone necrotic samples obtained from bisphosphonate-treated subjects with established ONJ.

Necrotic bone samples and native bone samples were processed for Field Emission in Lens Scanning Electron Microscope (FEISEM) morphological analysis. Light microscopy was applied for both haematoxylin-eosin staining and for Vascular Endothelial Growth Factor (VEGF) and Bone Sialoprotein (BSP) immunohistochemical detections. Real-Time RT PCR was performed to investigate TNFRSF11A (RANK), TNFSF11 (RANKL) and TNFRSF11B (OPG) gene expression. Morphological analyses performed by light microscope and FEISEM show empty osteocytic lacunae and alteration of lamellar organization with degradation of mineralized bone matrix in necrotic bone samples. A significant increase in TNFRSF11A, TNFSF11, TRAF6 and NFAT2 gene expression and a reduction of TNFRSF11B gene transcription level are also showed in necrotic bone compared to control samples. No significant difference of VEGF expression between necrotic and control samples is detected , while lower BSP expression in necrotic bone compared to healthy samples is found.

Even if the pathogenesis of bisphosphonate associated ONJ remains unknown, a link between oral pathogens and its development seems to exist. We suppose that lipopolysaccharide produced by bacteria colonizing and infecting necrotic bone and the surrounding viable area could trigger RANK/RANKL/OPG signaling pathway. Moreover osteoclasts activation could be considered as a protective strategy carried out by the host bone tissue to delimitate the necrotic area and to counteract infection. Furthermore even if the expression of VEGF is similar in control and necrotic bone samples, indicating that the vascular support of the area does not modify, BSP lower expression could be related to a reduction in osteoblastic activity in the necrotic area, upon osteoclast activation, and in general to an impairment of the remodeling phenomena.

Pathology, Diagnostic EM, Medicine

LS3.P041
A comprehensive case study of regional odontodysplasia including electron microscopy

S. Nietzsche[1], S. Junge[2], R. Heinrich-Weltzien[2]

[1]University Hospital Jena, Center for Electron Microscopy, Jena, Germany
[2]University Hospital Jena, Department of Preventive and Pediatric Dentistry, Jena, Germany

sandor.nietzsche@med.uni-jena.de

Investigation of the ultra-structural abnormalities of dental hard tissues obtained from a recent case of Regional Odontodysplasia (RO).

Clinical, radiographic and histological findings of RO in a 3-year old German boy were presented. The anomaly affected all maxillary deciduous and permanent tooth germs of the right quadrant. One of the affected deciduous teeth could be preserved for scanning electron microscopic examination. After embedding, cutting, and polishing backscattered electron imaging and energy dispersive X-ray spectroscopy were performed.

In this study many different methods were combined to get a comprehensive sight on an individual case of RO. Furthermore, it was possible to follow the progression of the anomaly over more than two years. The electron microscopic examination revealed several kinds of disturbed hard tissue and different grades of mineralization. Based on the microscopic structure of the hard tissue new aspects of the development of the anomaly are suggested.

The RO-related disturbances in the dental development start during pregnancy. Very early parts of the teeth are mineralized normally. The development of the disturbed hard tissue is correlated to the vascularization of the enamel organ and the dental follicle. Finally, a proposal for the therapeutic treatment of the presented case is discussed.

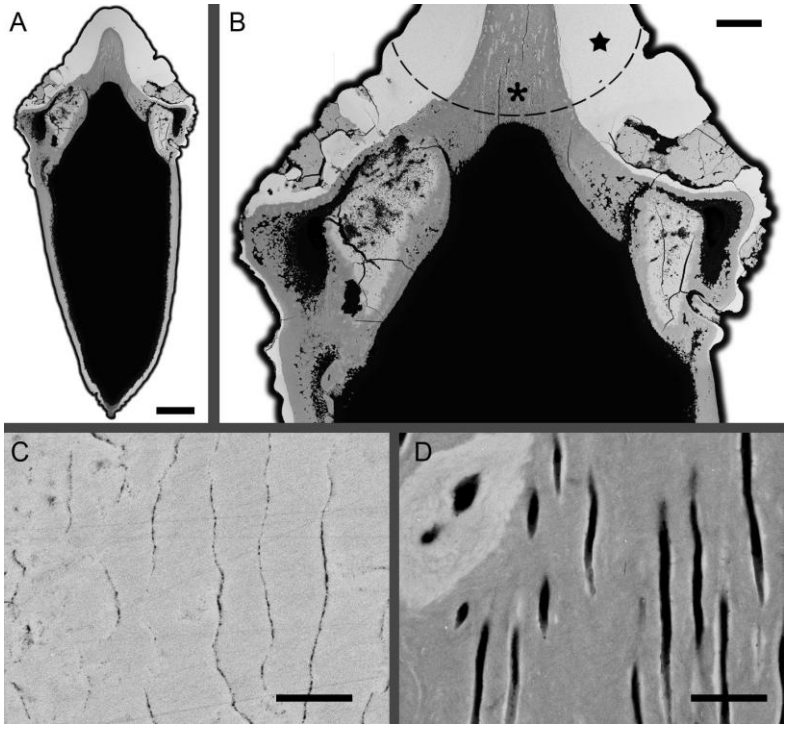

Figure 1. Scanning electron micrograph (BSE mode) of a cross section of the RO affected primary canine 53; A) overview of the tooth showing a huge cavity inside (scale bar 500 µm); B) detailed view of the middle part revealing the different mineralization grades corresponding to the local grey level, normal enamel and dentine is depicted above the dashed line whereas all other parts are mostly abnormal (scale bar 100 µm); C) close view of the normal enamel (star) showing a typical pattern of the prismatic structure (scale bar 5 µm); D) close view of the normal dentine (asterisk) showing a typical tubular structure (scale bar 10 µm).

Pathology, Diagnostic EM, Medicine

LS3.P042
Ultrastructural characterization of malathion induced granulosa cell apoptosis in caprine antral follicles

J. K. Bhardwaj[1], P. Saraf[1]

[1]Kurukshetra University, Reproductive Physiology Laboratory, Department of Zoology, Kurukshetra, India

jkbkuk@gmail.com

Reproductive toxicology aims at establishing exposure- risk correlation between a toxicant and reproduction within living organisms. Malathion, an organophosphate pesticides, used abundantly against ticks, bugs etc., is a potent reproductive toxicant that increases the incidence of follicular atresia by bringing the demise of granulosa cells through a programmed cell death mechanism, termed as apoptosis. The loss of ovarian follicle, at all developmental stages, by granulosa cell apoptosis interfere the normal ovarian physiology, directly affecting the fertility of an organism. Thus, the present study aims to employ histological analysis, ultrastructural technique, fluorescence assay, apoptosis quantification, TUNEL assay and antioxidant enzyme analysis for assessing the cytotoxicity and oxidative stress generated in granulosa cells of caprine antral follicles due to malathion toxicity at nanomolar concentrations (1nM, 10 nM and 100 nM) with different exposure durations.

Classic histological studies exhibited the occurrence of apoptotic attributes within malathion induced granulosa cells like condensed and marginated chromatin with fragmented nucleus, pyknosis, loss of membrane integrity, increased empty spaces and vacuolization in time and dose dependent manner. Transmission electron microscopy too revealed detailed cytological alterations within cytoplasmic and nuclear structure namely, presence of indented nuclear membrane with blebbing, pyknotic crescent shaped nuclei, fragmented nuclei with apoptotic body, degenerating mitochondria, increased vacuolization and degenerating homogenous osmophilic lipid droplets at 100 nM malathion concentration whereas at 10 nM, prominent association of nucleus, ER, mitochondria and lipid droplets; nucleus invagination into lipid droplets, apical localization of lipid bodies, occurrence of autophagic body were observed. Granulosa cells exhibited diminished cell-cell contact and cellular integrity, presence of crescent shaped nucleus, chromatin condensation and pyknosis with nuclear membrane folding, accumulation of lipid droplets with occurrence of cytoplasmic protrusions at lowest selected dose of malathion i.e. 1 nM. Furthermore, EB/AO fluorescence staining and apoptosis quantification demonstrated a significant increase in incidence and percentage of apoptosis after malathion exposure ($p<0.001$), both between and within the groups. Cytogenetic toxicity assessed via TUNEL assay revealed a higher rate of DNA fragmentation due to malathion exposure in comparison with control. Malathion was found to increase the oxidative stress within granulosa cells of healthy antral follicles by declining the antioxidant enzymes activity namely catalase and superoxide dismutase, that also established a negative correlation between the apoptosis incidence and the level of antioxidant enzymes activity, superoxide dismutase ($r= -0.73$ $p<0.01$) and catalase ($r= -0.80$ $p<0.01$) post malathion treatment.

Thus, the study unveiled the role of malathion as a reproductive toxicant, highlighting the role of altered membrane permeability, steroidogenesis and organelle's membrane potential; DNA fragmentation and increasing oxidative stress that induced cytotoxic and genotoxic alterations within granulosa cells of antral follicles bringing its apoptosis, thereby, affecting the overall fertility.

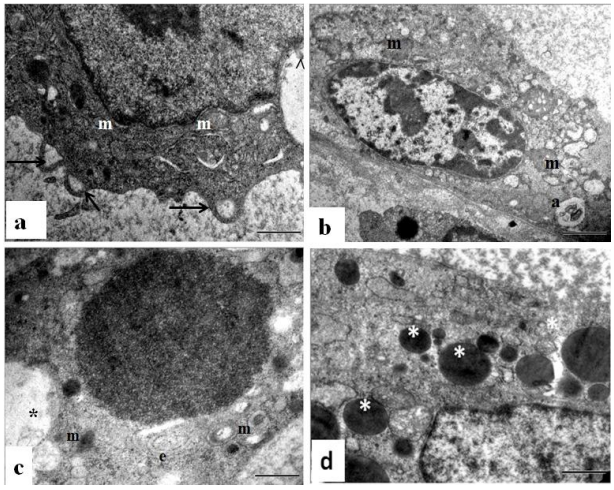

Figure 1. Electron micrograph of malathion treated apoptotic granulosa cells showing: (a) apoptotic characterises along with extensive membrane ruffling and cytoplasmic protrusions (arrow); presence of lipid (*) droplets with nucleus invaginating lipid droplet (arrow head); (b) chromatin condensation and margination, existence of degenerated mitochondria and autophagic body (a); (c) close association of ER (e), mitochondria (m), lipids droplets and nucleus with degenerated mitochondria; (d) increased presence of large and fragmented lipid droplets (*) at 1 nM (a,b), 10 nM (c) and 100 nM (d) doses concentration.

Pathology, Diagnostic EM, Medicine

LS3.P043
TEM study on nano-toxicology of metal oxide nanoparticles intratracheally instilled in rat lung

K. Yamamoto[1], T. Yoshida[1], T. Hayashida[1], H. Izumi[2], Y. Morimoto[2]

[1]National Institute of Advanced Industrial Science and Technology (AIST), National Metrology Institute of Japan, Tsukuba, Japan
[2]University of Occupational and Environmental Health, Kitakyushu, Japan

k-yamamoto@aist.go.jp

Industrial applications of nanoparticles were reported in many fields recently. Particles less than 100nm with one of three dimensions were defined as nanomaterials. However, the toxicity of these nanoparticles for the human was not clear, so the toxicity study of nanoparticles is important. The gold standard test to estimate the harmful effect of respirable chemical is inhalation studies. Inhalation studies can provide reliable and informative data for the effect on human body because of the reproduction of similar human exposure style. However it is difficult to examine the hazard and risk evaluation of lots of nanoparticles using inhalation studies because of expensive cost, and necessity of specific apparatus and experts. On the other hand intratracheal instillation studies, of which chemicals was inserted into trachea or pharyngeal cavity, have been used for dose-dependency of pulmonary toxicity and the mechanism of lung disorder due to exposure of chemicals with known quantity. In this study, intratracheal instillation studies of metal oxide nanoparticles using rats were performed, and TEM observations of lung tissues were examined.

The NiO and TiO_2 nanoparticles were examined in this study. The nanoparticle was suspended with 0.4 ml distilled water, and 0.2 mg (0.8 mg/kg) or 1 mg (4 mg/kg) of NiO and TiO_2 was intratracheally instilled once to rats (12 weeks old). The negative control groups received distilled water. Animals were dissected at 3 days, 1 week, 1 month, 3 months, and 6 months after the instillation. Lung tissues after the instillation tests were observed by TEM. The lung tissues were fixed using a perfusion system using a 4%paraformaldehyde solution, and were then post-fixed using a 1% osmium tetroxide solution. They were subsequently dehydrated in ethanol, followed by embedding in epoxy resin. Ultrathin sections were cut with a diamond knife using microtomy. Thin sectioning specimens were stained with a 2% uranyl acetate solution and a mixed solution of 0.3% lead nitrate and 0.3% lead acetate, all at room temperature. Conventional TEM observation was performed with H-7600 (Hitachi, Japan) at an accelerating voltage of 80kV.

Figure 1(a) shows TEM image of alveolar macrophage in high dose NiO instillation group lung tissue 3 days after exposure. Large mounts of black particles were observed in cytoplasm. As aggregate size of NiO in instilled suspensions was between 20 and 100 nm shown in Figure1 (a), NiO particles make larger aggregates in macrophage. Figure 1(b) shows TEM image of alveolar macrophage in high dose TiO_2 instillation group lung tissue 3 days after exposure. Many phagosomes containing TiO_2 particles were observed. TEM image of high dose NiO instillation group lung tissue 6 months after exposure was shown in Figure 2 (a), and high dose TiO_2 instillation group 6 months after exposure was shown in Figure 2 (b). In TiO_2 instillation group, a small amount of TiO_2 is observed in the alveolar macrophages (Figure 2 (b)), however most of the alveolar macrophages are not containing TiO_2. In NiO instillation group, accumulation of alveolar macrophage taken up NiO particles is observed in Figure 2 (a). Both of NiO and TiO_2 instillation groups 3 days after exposure took up much mounts of instilled particles (Figure1(a)-(b)). On the other hands, uptaken particles in macrophages was decreased after 6 months (Figure2(a)-(b)). Therefore, we think that clearance of instilled NiO and TiO_2 particles is occurred. As NiO was observed more frequently in macrophages compared with TiO_2 after 6 months, we think that clearance of NiO is more delayed than that of TiO_2.

1. This work is partially supported by “Development of innovative methodology for safety assessment of industrial nanomaterials" by Ministry of Economy, Trade and Industry (METI) of Japan.

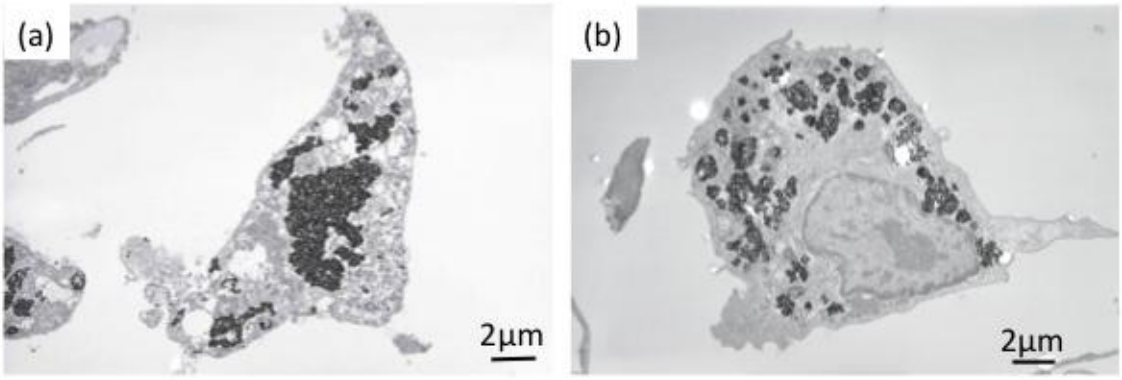

Figure 1. Lung tissue TEM images of high dose group of 3 days after NiO instillation (a), and TiO_2 instillation (b).

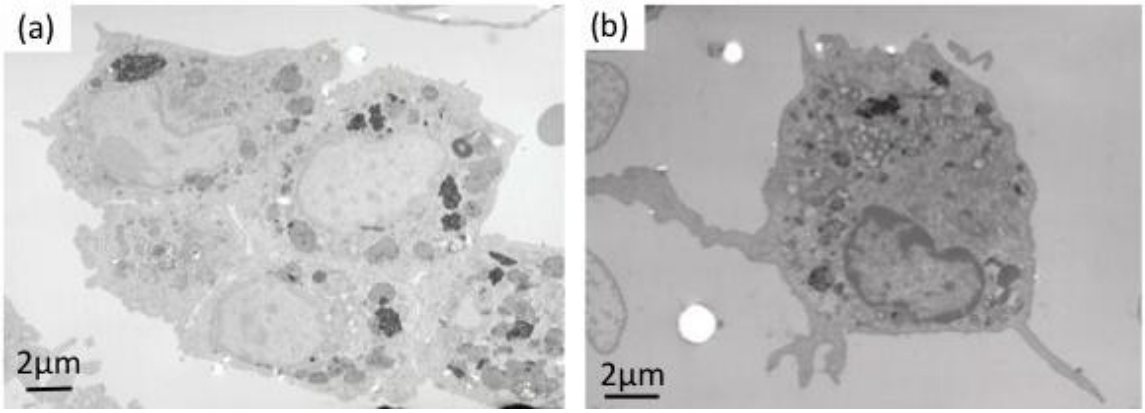

Figure 2. Lung tissue TEM images of high dose group of 6 months after NiO instillation (a), and TiO_2 instillation (b).

Pathology, Diagnostic EM, Medicine

LS3.P044
Enhancement of the therapeutic efficacy of anticancer drug using magnetic gold nanocarriers

M. Fathy[1]

[1]Cairo University , Biophysics , Giza, Egypt

mohammed.elasal@gmail.com

Treatment of approximately 50% of human cancers includes the use of chemotherapy. The major problem associated with chemotherapy is the inability to deliver pharmaceuticals to specific site of the body without inducing normal tissue toxicity. Consequently, the efficiency of chemotherapy could potentially be improved by the development of a targeted drug nanocarriers that would enhance the effective water solubility of hydrophobic anticancer drugs as well as the selective delivery of drugs to malignant tissues. Thereby increasing the curative effectiveness of the cancer treatment while sparing normal tissues from the side effects of the chemotherapeutic agent.

In this study, we were focused on designing a biocompatible magnetic drug delivery system (magnetic gold nanoparticles MGNPs) to be used as nanocarriers of the anti-cancer drug doxorubicin (DOX) for *in vivo* and *in vitro* applications. Therefore, MGNPs were prepared and functionalized with thiol-terminated polyethylene glycol (PEG), and then loaded with DOX. The physicochemical properties of the prepared nanoparticles (NPs) were investigated using different techniques. Transmission electron microscopy (TEM) revealed the spherical mono dispersed nature of MGNPs with size about 22 nm which was confirmed by Dynamic light scattering (DLS) measurements. Energy Dispersive X-ray Spectroscopy (EDX) assured the existence of both iron and gold elements in the prepared MGNPs. The optical properties of the prepared NPs were investigated using UV-vis spectroscopy. Fourier transform infrared spectroscopy (FTIR) assessment revealed that PEG and DOX molecules were successfully loaded on the MGNPs surfaces, and the amine group of DOX is the active attachment site to MGNPs. Superparamagnetic properties of the MGNPs were assessed using vibrating sample magnetometer (VSM). DOX loading profile demonstrated that the maximum drug loading efficiency was 100 µg DOX/mg MGNPs. DOX release profile performed at pH 5.5 showed higher drug release over that at pH 7.5. *In vitro* studies elucidated that DOX loaded MGNPs (MGNPs-DOX) have more potent therapeutic effect than free DOX against MCF-7 cancer cells. *In vivo* studies proved that magnetic targeted drug delivery (MTD) can provide a higher accumulation of drug throughout tumor compared with that delivered by passive targeting. This clearly appeared in tumor growth inhibition assessment, biodistribution of DOX concentrations in body organs and histopathological examinations of Ehrlich carcinoma. To assess the *In vivo* toxic effect of the prepared formulations, several biochemical parameters such as aspartate aminotransferase (AST), alanine transaminase (ALT), Lactate dehydrogenase (LDH), creatine kinase MB CK-MB, urea, uric acid and creatinine were measured.

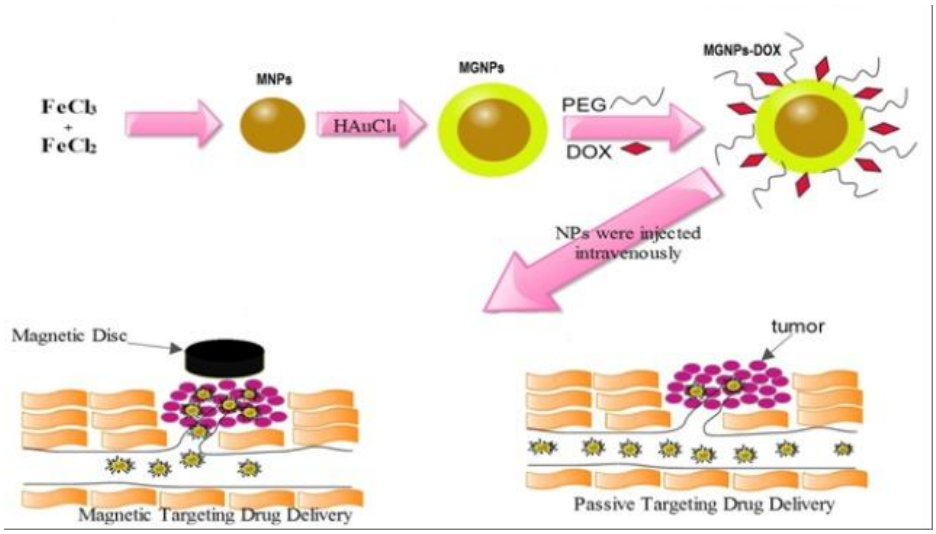

Pathology, Diagnostic EM, Medicine

LS3.P045
Scanning electron microscopic evaluation of material-dentinal interface using adhesive systems

S. Masudi[1], N. Sukminingrum[1]

[1]School of Dental Sciences USM, Restorative Dentistry, Kubang Kerian, Malaysia

sam@usm.my

An essential attribute of a good bond is the ability of the restorative material to wet and infiltrate the dentinal tubules. The technique, so-called “Sandwich” of dentin replacement materials, glass ionomer, dental adhesive and composite resin was proposed as an effective technique as a means for pulpal protection from the acid-etch and a mechanism for sealing the cavity in the absence of good dentin adhesion. SDR® - Smart Dentine Replacement (Dentsply, USA), simplifies the procedure for placing adhesive posterior composite fillings. SDR can be applied in increments of up to 4 mm without layering, facilitating safe and fast lining. Recently a nano-filled resin composite and glass ionomer were introduced that exhibit a high initial polish while retaining this over time combined with excellent physical properties (Mitra *et al*., 2003).

To compare dentinal interface characterization on nano glass ionomer, with or without surface pre-treatment and dentin replacement materials (SDR) by means of SEM.

Caries-free second premolars (n=12) with were selected and class I cavity were prepared on occlusal surface and randomly assigned into four groups of 3 teeth (n=3). Samples in group 1 were treated with Dentin Conditioner (Polyacrylic acid) and Nano glass ionomer (Ketac N100, USA). Samples in group 2 were treated with Ketac N100 Primer + Nano glass ionomer-Ketac N100. Group 3 were treated with acid etching using 37% phosphoric acid for 10 seconds; bonding agent and dentin replacement material (SDR). Control group was treated with Nano glass ionomer -Ketac N100 only. After filling with composite resin, the crowns were sectioned to obtain dentin discs of 3mm thick using Exakt Cutting System (Exakt, Germany). The samples were washed and immersed into a glutaraldehyde solution (2.5%) in sodium cacodilate (0.1M) buffer with a 7.4 pH, for 12 hours at 4°C. After being fixed, the samples were cleaned by ultrasonic cleaner (Branson 5510, USA) for ten minutes. The samples were cleaned in distilled water, dried and finally dehydrated in increasing ethanol series, and then immersed in hexamethyldisilazane (HDMS) for 10 minutes. The specimens were metalized with a fine gold overlay and were viewed under SEM (FEI Quanta FEG 450, USA) and qualitatively analyzed at different sections.

Control group showed a gap (40-80nm) between the Ketac Nano/dentin interfaces, with smear layer. Group 1 showed smaller gap interface (10-40nm) with present of smear layer. Group 2 showed a gap (5-10nm) without smear layer and dentinal tubules were closed. Group 3 showed formation of adhesive layer at SDR®-dentin interface and no smear layer present and dentinal tubules were exposed. This results are in agreement with study by Burgess and Munoz (2012); Pfefferkorn (2013), which stated that SDR has greatly simplified the restorative treatment of posterior teeth. In this study, it was verified that pre-treating the surface with either dentin conditioner or primer improves the material/dentin interaction. Pre-treatment with primer yields better result in term of smear layer removal.

Group 3 (SDR) showed the best dentinal interface characterization, followed by Group 1 and Group 2 (Ketac Nano) where Group 2 showed better smears layer removal. Control group showed the worst dentinal interface characterization.

1. Mitra, S.B., Wu D. and Holmes B.N. 2003. An application of nanotechnology in advanced dental materials. *J. Am. Dent. Assoc***.** 134(10):382-1390,
2. Burgess, J and Munoz, C. 2012.The 36-month data from a prospective clinical study*. www.dentsply.co.uk.*
3. Pfefferkorn, F. 2013. What is smart dentin replacement? *www.dentistry.co.uk*.:68.
4. SEM images of dentinal interface characterization between Control Goup, Group 1, Group 2 and Group 3

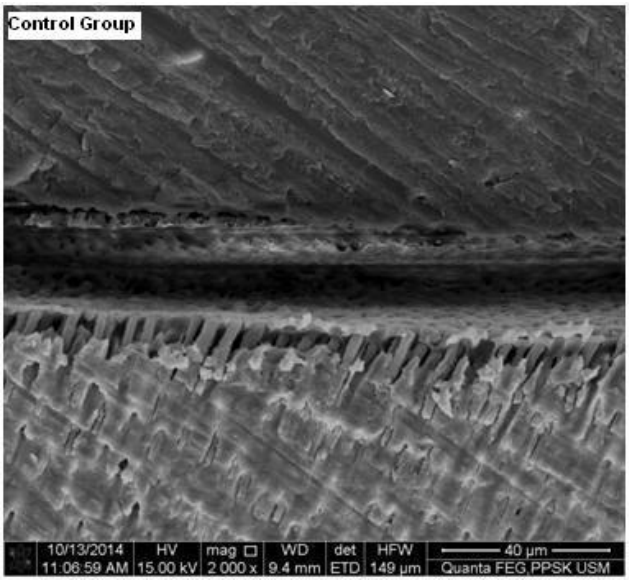
Control Group
10/13/2014 11:06:59 AM
HV 15.00 kV
mag 2 000 x
WD 9.4 mm
det ETD
HFW 149 µm
40 µm
Quanta FEG,PPSK USM

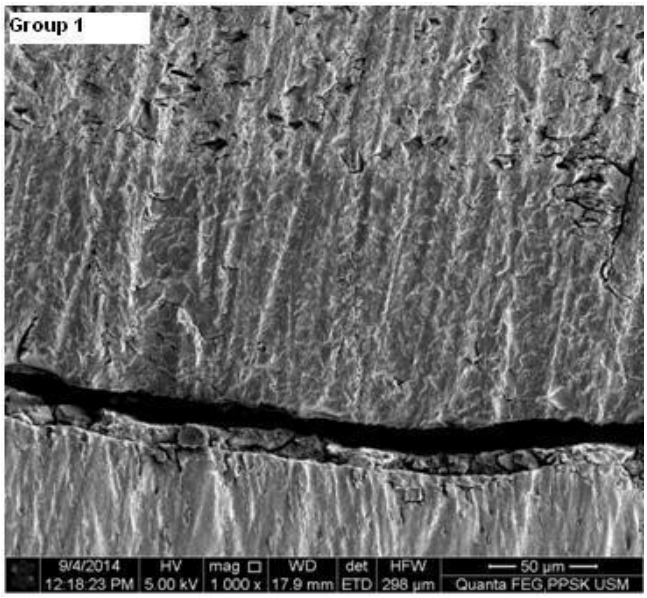
Group 1
9/4/2014 12:18:23 PM
HV 5.00 kV
mag 1 000 x
WD 17.9 mm
det ETD
HFW 298 µm
50 µm
Quanta FEG,PPSK USM

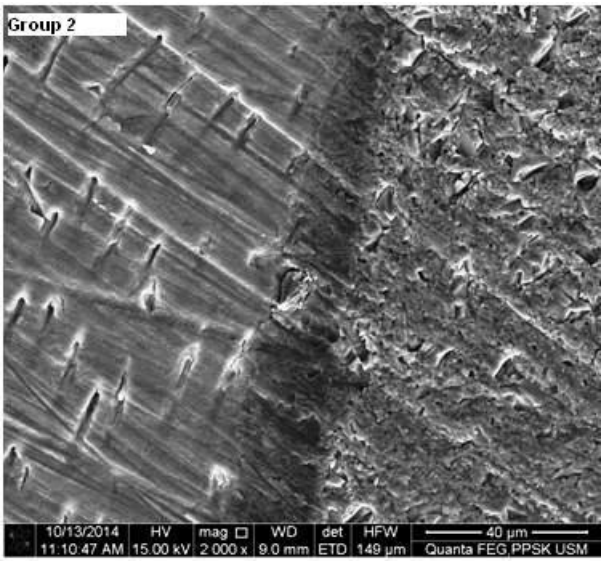
Group 2
10/13/2014 11:10:47 AM
HV 15.00 kV
mag 2 000 x
WD 9.0 mm
det ETD
HFW 149 µm
40 µm
Quanta FEG,PPSK USM

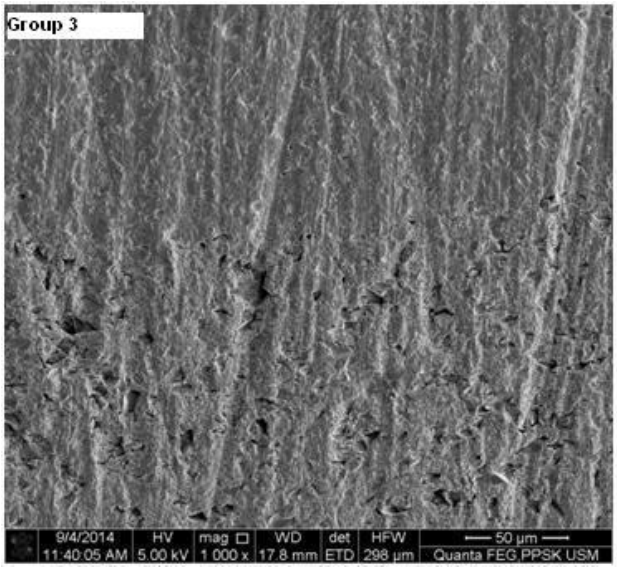
Group 3
9/4/2014 11:40:05 AM
HV 5.00 kV
mag 1 000 x
WD 17.8 mm
det ETD
HFW 298 µm
50 µm
Quanta FEG,PPSK USM

Pathology, Diagnostic EM, Medicine

LS3.P046
Surface roughness of nanofilled tooth-colored restorative materials after tooth whitening

S. Masudi[1], N. Sukminingrum[1]

[1]School of Dental Sciences USM, Restorative Dentistry, Kubang Kerian, Malaysia

sam@usm.my

Tooth whitening has gained considerable acceptance among dentists and patients as a simple, effective and safe procedure to lighten discolored teeth. The principle of tooth whitening is degrading of peroxides from hydrogen peroxide or its compounds such as carbamide peroxide (CP) into unstable free radicals. These radicals are further broken down into large pigmented molecules either through oxidation or reduction reaction (Costa *et al*., 2009). This process changes the chemical structure of the interacting organic substances of the tooth, which results in the change in color.

This *in vitro* study was conducted to evaluate the effect of tooth whitening on the surface roughness of dental restorative filling materials using atomic force microscopy (AFM).

Two-nano hybrid and micro hybrid resin composites and one nano-ionomer, were used in the present study. Samples were fabricated in 2 mm thick plexiglass with a circular opening of 6 mm. A total of 30 samples were prepared, thirty samples (n=10) for each test material. Group I (n=10), was filled with Filtex Z350 XT nano hybrid composites (3M-ESPE, USA); Group II (n=10) with Estelite Σ micro-hybrid composites (Tokuyama, Japan); and Group III (n=10) with Ketac N100 nano ionomer cements (3M-ESPE, USA). All samples were light-cured from the top and bottom using an Elipar Freelight-2, according to the manufacturer's instructions. The nano ionomer cement after placement was light-cured for 20 s, while the resin composite materials light-cured for 20 seconds each increment. All samples were then polished using Sof-Lex and a slow-speed hand piece. After polishing, the samples were cleaned ultrasonically using a Sonica 2200 ETH for 5 minutes and then stored in distilled water at 37° C for 24 hours prior to the bleaching treatment. The specimens were subjected to bleaching agent following the manufacturers' instructions. Samples in subgroup A (control group) were not bleached but stored in a vibrating distilled water bath for 14 days at 37° C. Samples in subgroup B were subjected to Opalescence home bleaching PF a 20% CP four hours per day, for 14 days. Samples from each group were subjected to surface roughness evaluation using AFM. The mean surface roughness was assessed with a contact mode. Five different randomly selected areas were scanned with an area of 40 Å~ 40 µm and resolution of 512 Å~ 512 pixels to obtain surface roughness values (Ra). Ra analysis was done by Scan Atomic SPM control software. Then, three-dimensional (3D) images with 10 Å~ 10 µm sizes were acquired for each group of materials.

There was no statistically significant change in roughness for all three materials tested after 14 days of bleaching with 20% CP compared to the control group. The AFM method senses any irregularities on the surface of the specimen and in this study no significant differences between the materials were recorded. This is in agreement with findings of de A Silva *et al.* (2006). However, our data contradicts Hafez *et al.* (2010), who reported an increased surface roughness of composites resin, which they determined, depended on the bleaching agent as well as the type of material tested.

It can be concluded that 20% CP home bleaching did not cause changes in surface roughness of the three tested materials. The AFM evaluation of surface roughness observed in the 3D images proved to be an effective technique.

1. Costa S.X., Becker A.B., Rastelli A.N., Loffredo L.C., Andrade M.F., Bagnato V.S. 2009. Effect of four bleaching regimens on color changes and microhardness of dental nanofilled composite. *Intern J Dent E pub*, Nov 12, 313845.
2. de A Silva M.F., Davies R.M., Stewart B., DeVizio W., Tonholo J., da Silva Junior J.G., Pretty I.A. 2006. Effect of whitening gels on the surface roughness of restorative materials in situ. *Dent Mat*, 22, 919-924.
3. Hafez R., Ahmed D., Yousry M., El-Badrawy W., El-Mowafy O. 2010. Effect of In-Office Bleaching on Color and Surface Roughness of Composite Restoratives. *Eur J Dent*, 4, 118-1127.

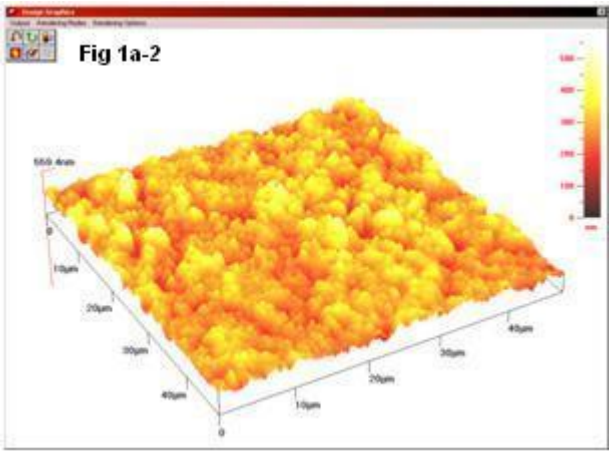

Figure 1a. 3D AFM images showing the topography of Ketac N100 nanoionomer b. Filtek Z350XT and c. Estelite Sigma Quick after tooth whitening application

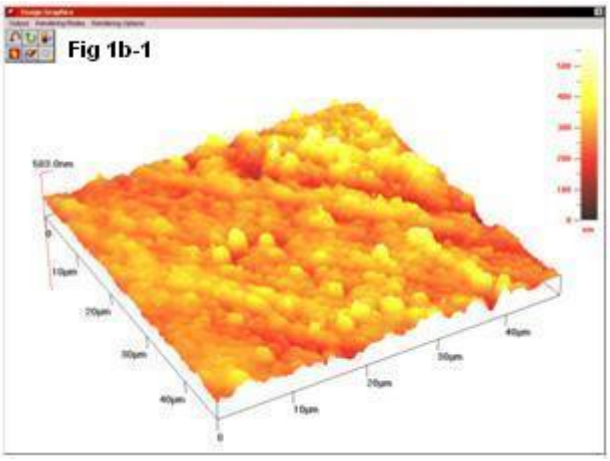

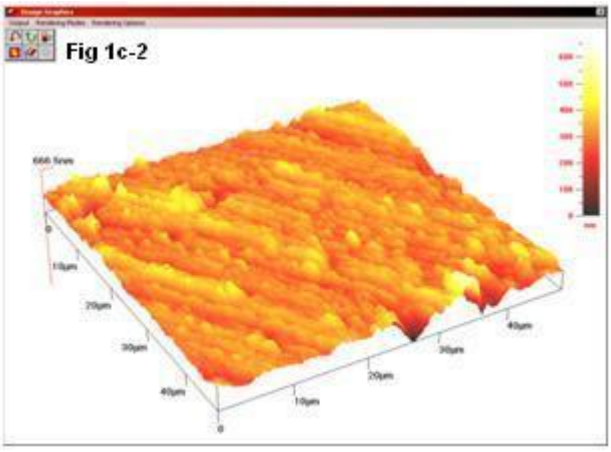

Pathology, Diagnostic EM, Medicine

LS3.P047
Comparison of the Kato-Katz and FLOTAC techniques for the diagnosis of soil-transmitted helminth infections

K. Habtamu[1,2]

[1]Health Science College, Med.Laboratory Technology, Addis Ababa, Ethiopia
[2]Menelik II Health Science College, Medical Laboratory Technology, Addis Ababa, Ethiopia

kasshabt@fastmail.fm

Decisions on individual or community treatment and evaluation of chemotherapy based control programs depend on parasitological diagnostic techniques.

The principal purpose of this study was to compare the accuracy of a single Kato-Katz thick smear and a single FLOTAC for the determination of the prevalence and intensity of soiltransmitted helminth infections.

A total of 271 faecal specimens were collected from schoolchildren in Ethiopia, and microscopically examined using the Kato-Katz method (41.7mg stool per slide) and the FLOTAC technique.

The combined results from the Kato-Katz and FLOTAC methods were used as diagnostic 'gold' standard for reference in the analysis. Agreement between the two methods showed kappa values of 0.74, 0.73 and 0.28 for *Ascaris lumbricoides*, *Trichuris trichiura* and hookworm, respectively. A single FLOTAC revealed significantly more infections than a single Kato-Katz for each of the three soil-transmitted helminths ($p<0.01$). The sensitivities of a single Kato-Katz for diagnosis of *T. trichiura*, *A. lumbricoides* and hookworm infections were 76.6%, 67.8% and 19.6%, respectively, while the sensitivity of FLOTAC was 100% for all the three soil-transmitted helminth species. A single Kato-Katz yielded considerably higher mean faecal egg counts (FECs) (729.1, 145.2 and 60.7 eggs per gram of stool (EPG) for *A. lumbricoides*, *T. trichiura* and hookworm, respectively) compared with a single FLOTAC (142.5, 54.5 and 14.6 EPG, respectively) ($p<0.05$).

Our study confirms that a single FLOTAC is more sensitive than a single Kato-Katz for the diagnosis of soil-transmitted helminth infections, but results in lower FECs.

Further standardization and validation are still required in different epidemiological settings with varying levels of intensity of infections before recommending FLOTAC for large-scale community diagnosis.

Molecular Microscopy

LS4.048
Structure of mitochondrial ATP synthases and their role in shaping cristae membranes

K. M. Davies[1], M. Allegretti[1], T. Blum[1], B. Daum[1], A. Mühleip[1], C. Anselmi[2], J. D. Faraldo-Gomez[2], W. Kühlbrandt[1]

[1]Department of Structural Biology, Max Planck Institute of Biophysics, and Cluster of Excellence 'Macromolecular Complexes', Goethe university, Frankfurt am Main, Germany;
[2]Theoretical biophysics, National heart blood and lung institute, Bethesda, Maryland, USA

karen.davies@biophys.mpg.de

Mitochondria are the powerhouses of eukaryotic cells and the main site of ATP synthesis in cells performing aerobic respiration. Located in the cristae membranes, the ancient nano-machine, ATP synthase, uses the energy stored in an electrochemical gradient of protons to catalyses the conversion of ADP and inorganic phosphate to ATP. The mechanism of proton-coupled ATP synthesis has remained poorly understood for decades due to the lack of structural information on the membrane-embedded subunits of this complex. By single-particle cryo-EM analysis, we have revealed a bundle of long horizontal, membrane intrinsic helices adjacent to the rotor ring of a mitochondrial ATP synthase thereby providing a structural basis for understanding how proton movement across a membrane drives ATP synthesis. Moreover, by electron cryo-tomography and subtomogram averaging we have shown that mitochondrial ATP synthases play a major role in shaping cristae, which in turn affects cellular fitness.

Molecular Microscopy

LS4.049
Cotranslational protein translocation and membrane insertion studied by subtomogram analysis

S. Pfeffer[1], Y. Chen[1], P. Unverdorben[1], F. Foerster[1]

[1]Max Planck Institut of Biochemistry, Martinsried, Germany

foerster@biochem.mpg.de

Cryoelectron tomography (CET) allows visualizing the three-dimensional (3D) structures of macromolecular complexes in their native environment. The resolution of cryo-tomograms is typically sufficient to distinguish large macromolecular complexes and computational extraction of subtomograms, their alignment to a common coordinate system and averaging allows unraveling further structural details. We present computational methodology for subtomogram analysis that we use to elucidate the structure of the endoplasmic reticulum (ER) and mitochondria co-translational translocation *in situ* using this approach. The workflow, which is part of the PyTom package, involves 3D reconstruction of the sample from its projections, localization and identification of recurrent structural features in these volumes, coherent averaging of the respective subtomograms, as well as classification of different conformations underlying the subtomograms. Application of this workflow to tomograms of isolated yeast mitochondria reveals detailed insights into the supramolecular organization of the mitochondrial translation machinery and its association with the inner membrane in translation-competent mitochondria. Subtomogram analysis of the ER-associated translocation machinery from dog pancreatic microsomes reveals its subnanometer structure in its native membrane. A surprising result is that the structure of the Sec61 protein-conducting channel in the native membrane differs from that in the presence of detergence, highlighting the importance of structural investigations *in situ*.

Molecular Microscopy

LS4.050
The structure of the COPI coated vesicles by cryo-electron tomography and subtomogram averaging

S. Dodonova[1], P. Diestelkoetter-Bachert[2], W. Hagen[1], A. von Appen[1], M. Beck[1], F. Wieland[2], J. Briggs[1]

[1]EMBL, Structural and Computational Biology Unit, Heidelberg, Germany
[2]Heidelberg University, Biochemistry Center, Heidelberg, Germany

dodonova@embl.de

The COPI membrane coat protein complex mediates formation of coated vesicles that transport material between cellular compartments. We determined the structure of the assembled COPI vesicular coat at 13 Å resolution by cryo-electron tomography and subtomogram averaging. By combining this structural information with cross-linking/mass-spectrometry we were able to derive a complete molecular architecture of the COPI coat. We found that the COPI coat building block, the “triad”, has an intrinsically curved membrane-interaction surface, while the inter-triad connections are mediated by mobile protein domains. These findings indicate that clustering of triads on the membrane rather than formation of a polygonal protein scaffold promotes curvature generation during COPI vesicle formation. The COPI coat appears to be a highly interconnected assembly, whose architecture is not consistent with prevailing models in which coats can be functionally subdivided into adaptor- or cage-like subcomplexes. Based on great differences of the coat assembly of COPI and clathrin coated vesicles, but at the same time on the high similarity of the protein domain architecture, we speculate that the possible ancient protocoatomer function was to distribute membrane bending proteins and cargo binding sites over the membrane surface, while the global coat stabilization could be reached by oligimerization or clustering of proteins on the membrane.

Molecular Microscopy

LS4.051
Studying growth factor receptor proteins in whole cells in liquid using scanning transmission electron microscopy

N. de Jonge[1,2], U. Korf[3], D. Peckys[1]

[1]INM - Leibniz Institute for New Materials, Saarbrücken, Germany
[2]Saarland University, Physics Department, Saarbrücken, Germany
[3]German Cancer Research Center, Division of Molecular Genome Analysis, Heidelberg, Germany

niels.dejonge@inm-gmbh.de

We have pioneered scanning transmission electron microscopy (STEM) of cells in liquid [1,2], so-called Liquid STEM, to study protein complex subunits in whole cells in their native liquid environment. Eukaryotic cells were grown on silicon microchips with silicon nitride (SiN) membrane windows, and incubated with specific protein labels consisting of fluorescent nanoparticles, quantum dots (QDs). The samples were first studied with fluorescence microscopy. Subsequently, the cells were fixed, and transferred into a cooled water environment. The cells were then imaged using environmental scanning electron microscopy (ESEM) with STEM detection [3] (Fig. 1). On account of the atomic number (Z) contrast of the STEM detector, the QDs of high-Z material were detected within the background signal produced by the low-Z material of the cell and surrounding liquid. A spatial resolution of 3 nm was achieved in the flat parts of the cells.

Liquid STEM was used to study individual proteins of the receptor tyrosine kinase HER2 in intact SKBR3 breast cancer cells. Fluorescence microscopy revealed a considerable heterogeneity of HER2 expression patterns, differing between membrane ruffles and flat areas. Correlative ESEM-STEM was then employed to image the labels in selected cellular regions. The high resolution and the close proximity between the QD and the membrane protein achieved with a short linker enabled visualizing the stoichiometry of individual protein complexes, and distinguishing between monomers, dimers, and higher order clusters. Data analysis, based on calculating the pair correlation function from QD-label positions, revealed the stoichiometric state of a selected area. The sample preparation for Liquid STEM was similar in complexity as for standard fluorescence microscopy. Since extensive sample preparation common to biological electron microscopy was altogether avoided, it was possible to acquire data of thousands of labels on dozens of cells. We thus obtained sufficient statistics to distinguish characteristic stoichiometric distributions between cells and even between specific functional membrane regions.

A key result of our study is the finding that HER2 homodimers were present with the highest concentration in membrane ruffles, associated with invasive behavior and metastasis in cancer cells. Moreover, the dimers were mostly absent from a small sub-population of cells lacking membrane ruffles. From the difference in cell morphology compared to the average SKBR3 cell we deduce a functional difference of this sub-population. Our method enables microscopic studies of cancer cells that include the examination of selected, rare cell sub-populations, for example, cancer stem cells, and may provide additional information about the mechanisms involved with cancer drugs and a difference in effectiveness for subgroups of the same cell type.

1. de Jonge, N., et al. Proc Natl Acad Sci 106, 2159-2164, 2009.
2. de Jonge, N., Ross, F.M., Nat Nanotechnol 6, 695-704, 2011.
3. Peckys, D.B., et al., Sci. Rep. 3, 2626: 1-6, 2013.

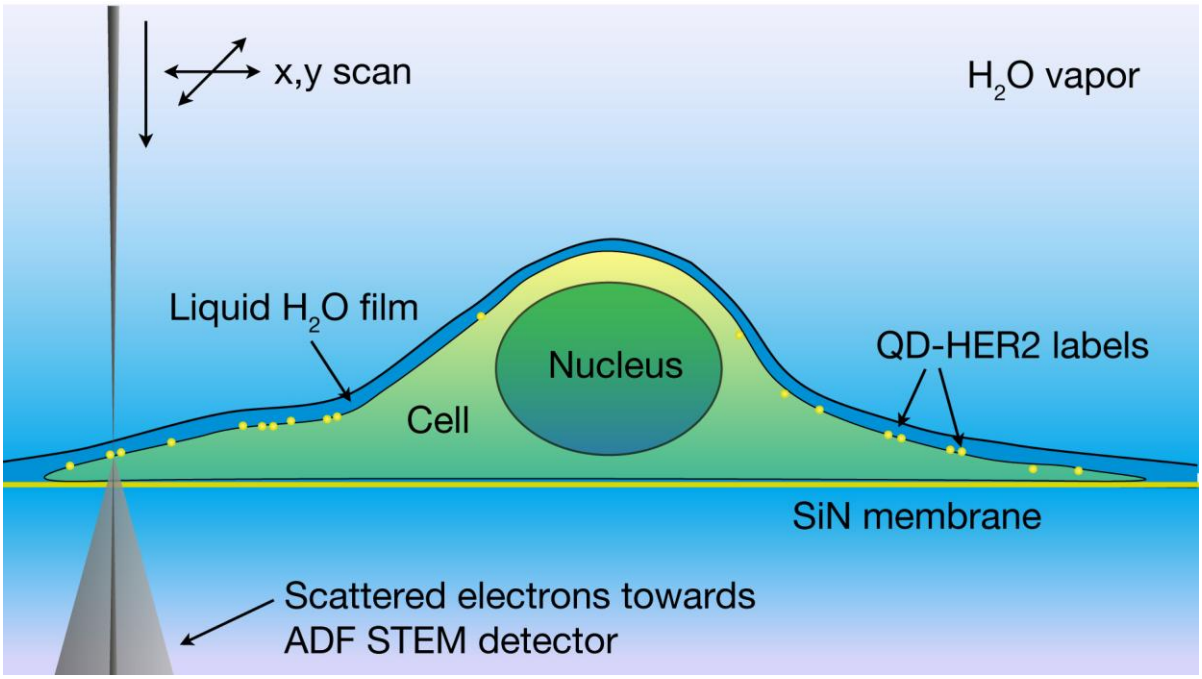

Figure 1. Principle of Liquid STEM. A eukaryotic cell is grown on a supporting SiN membrane. HER2 proteins labeled with QDs nanoparticles reside in the plasma membrane. An image is obtained by scanning a focused electron beam over the cell. Transmitted electrons are recorded with the STEM detector located beneath the sample. The cell is maintained in a saturated water vapor atmosphere, while a thin layer of water covers the cell for Liquid STEM using ESEM.

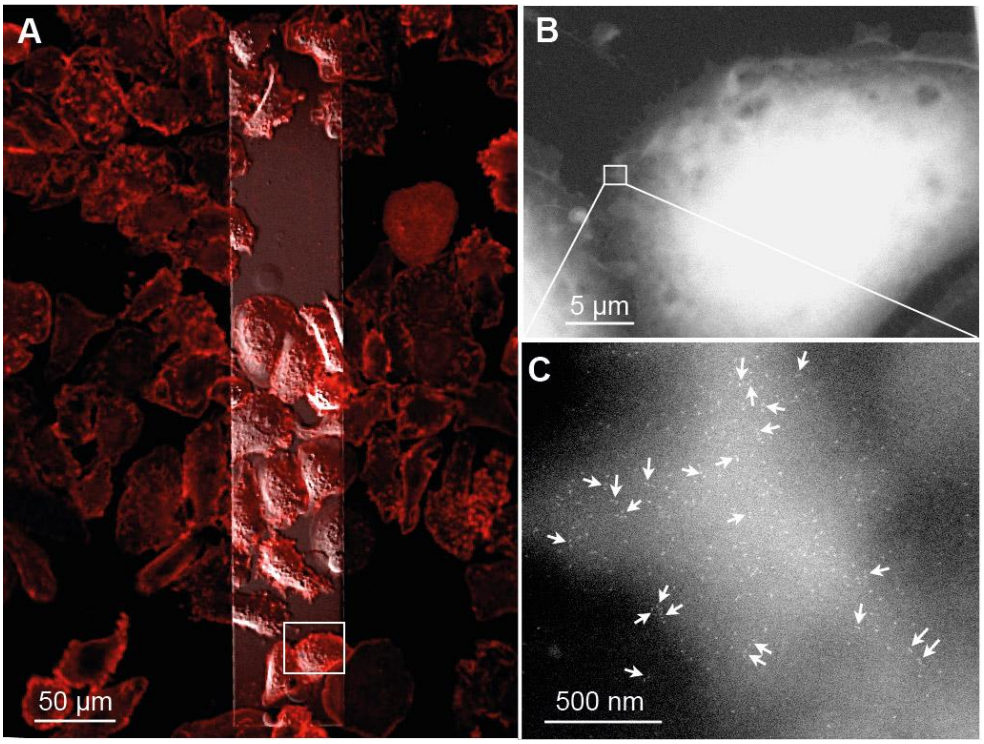

Figure 2. Correlative images of QD-labeled HER2 on SKBR3 cells. (A) Overlay of fluorescence and differential interference contrast (DIC) image of SKBR3 breast cancer cell showing a large heterogeneity in membrane HER2 concentration. (B) ESEM-STEM overview image of the same cells marked in A. (C) High resolution ESEM-STEM image, taken at the position marked in B. The HER2-bound QDs emerge as bright elongated pots. Many paired QDs, indicating homo-dimers, can be seen (see arrows).

Molecular Microscopy

LS4.052
Atomic resolution structure of the mammalian mitochondrial ribosome

D. Boehringer[1], B. Greber[1], M. Leibundgut[1], P. Bieri[1], N. Ban[1]

[1]ETH Zurich, Inst. f. Molekularbiologie u. Biophysik, Zurich, Switzerland

boehringer@mol.biol.ethz.ch

Mammalian mitochondrial ribosomes have undergone massive structural changes compared to bacterial ribosomes to adopt for the specific requirements of mitochondrial protein biosynthesis. Several mitochondrial-specific ribosomal proteins have been acquired during evolution of the mitochondrial ribosome with specialized functions. Here we determined the structure of the mammalian mitochondrial ribosome at 3.8 angstrom resolution using single particle EM. The reconstruction allowed us to build the atomic structure of the ribosomal RNA and most ribosomal proteins. For the refinement of the atomic coordinates in the EM-reconstruction we employed a novel Fourier shell correlation based weighting scheme of the map phases. The structure reveals the inter-subunit contacts of the ribosomal subunits, the conformational dynamics of the mitochondrial ribosome during the translational cycle and provides insight into the highly specialized mechanism of mRNA recruitment to the 28S subunit. Furthermore, the structure contributes to a mechanistic understanding of side effects of aminoglycoside antibiotics.

Molecular Microscopy

LS4.053
Structure of the E. coli ribosome-EF-Tu complex at <3 Å resolution by Cs-corrected cryo-EM

N. Fischer[1], P. Neumann[2], A. L. Konevega[3,4], L. V. Bock[5], R. Ficner[2], M. V. Rodnina[4], H. Stark[1,6]

[1]Max-Planck-Institute for Biophysical Chemistry, 3D Electron Cryomicroscopy Group, Goettingen, Germany
[2]Georg-August Universität Göttingen, Abteilung Molekulare Strukturbiologie, Göttingen, Germany
[3]B.P. Konstantinov Petersburg Nuclear Physics Institute of National Research Centre 'Kurchatov Institute', Molecular and Radiation Biophysics Department, St. Petersburg, Russian Federation
[4]Max-Planck-Institute for Biophysical Chemistry, Department of Physical Biochemistry, Göttingen, Germany
[5]Max-Planck-Institute for Biophysical Chemistry, Department of Theoretical and Computational Biophysics, Göttingen, Germany
[6]Georg-August Universität Göttingen, Department of 3D Electron Cryomicroscopy, Göttingen, Germany

niels.fischer@mpibpc.mpg.de

Single particle electron cryomicroscopy (cryo-EM) has recently made significant progress in high-resolution structure determination of macromolecular complexes due to improvements in electron microscopic instrumentation and computational image analysis. However, cryo-EM structures can be highly non-uniform in local resolution and all structures available to date have been limited to resolutions above 3 Å. We have determined the cryo-EM structure of the *Escherichia coli* 70S ribosome in complex with elongation factor Tu, aminoacyl-tRNA and the antibiotic kirromycin at 2.65-2.9 Å resolution using spherical aberration (C_S)-corrected cryo-EM. Overall, the cryo-EM reconstruction at 2.9 Å resolution is comparable to the best-resolved X-ray structure of the *E. coli* 70S ribosome (2.8 Å), but provides more detailed information (2.65 Å) at the functionally important ribosomal core. The cryo-EM map elucidates for the first time the structure of all 35 rRNA modifications in the bacterial ribosome, explaining their roles in fine-tuning ribosome structure and function and modulating the action of antibiotics. We also obtained atomic models for flexible parts of the ribosome such as ribosomal proteins L9 and L31. The refined cryo-EM-based model presents the currently most complete high-resolution structure of the *E. coli* ribosome, which demonstrates the power of cryo-EM in structure determination of large and dynamic macromolecular complexes.

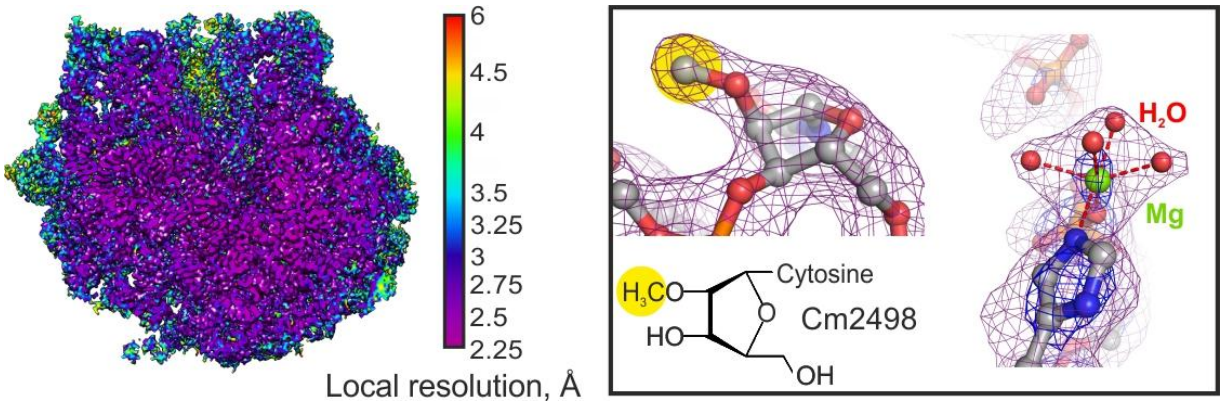

Figure 1. | High-resolution structure of the *E. coli* 70S ribosome by Cs-corrected cryo-EM. The structure has broken the 3 Ångstrom resolution barrier in single particle cryo-EM for the first time and is in many regions much better resolved (left). As a consequence, the cryo-EM structure visualizes ions, water molecules and the functional important modifications of the ribosomal RNA as shown exemplary on the right (Cm: 2'-O-methylcytidine; yellow mark: RNA modification; magenta mesh: cryo-EM density).

Molecular Microscopy

LS4.P056
Morphological and molecular biological characterization of Pleistophora aegyptiaca sp. nov. infecting the Red Sea fish Saurida tumbil.

R. Abdel-Gaber[1], F. Abdel-Ghaffar[1], K. Said[1]

[1]Cairo University, Zoology, Giza, Egypt

rewaida_rewaida@yahoo.com

One hundred three out of 225 (45.8%) of the Red Sea fish Saurida tumbil were infected with microsporidian parasites. The infection was recorded as tumor-like masses (whitish macroscopic cysts) or xenomas often up to 2 cm in diameter and embedded in the peritoneal cavity. Generally, the infection was increased during winter 63.8% (86 out of 135) and fall to 18.9% (17 out of 90) in summer. Light microscopic study revealed that xenomas were encapsulated by a fibrous layer encircling numerous sporophorous vesicles filled with mature spores measuring 1.7 ± 0.6 (1.5-2.7 µm) × 1.5 ± 0.3 µm (1.2-1.8 µm) in size. Ultrastructural microscopic study showed the presence of smooth membranes of the sarcoplasmic reticulum forming a thick, amorphous coat surrounding various developmental stages of the parasite. The various recognizable stages of the parasite were uninuclear, binucleated, and multinucleated meronts followed by detachment of the plasmalemma of the sporont from the sporophorous vesicle producing sporoblasts. Mature spores consist of a spore coat and spore contents. The spore contents consist of the uninucleated sporoplasm and a posterior vacuole located at the posterior end. The polar tube consists of a straight shaft and a coiled region (26-32 coils) arranged in many rows along the inside periphery of the spore. Molecular analysis based on the small subunit rDNA gene was performed to determine the phylogenetic position of the present species. The percentage identity between this species and a range of other microsporidia predominantly from aquatic hosts demonstrated a high degree of similarity (>92%) with eight Pleistophora species.

Molecular Microscopy

LS4.P057
Heteroleptic tris-chelate Ruthenium(II) complexes of *N*,*N* disubstituted-*N´*-acylthioureas: synthesis, structural studies and cytotoxic activity

J. Barolli[1], J. Moreira[2], P. Maia[3], L. Colina-Vegas[1,3], R. Mocelo[4], A. Plutin[4], V. Deflon[5], M. Cominetti[1], M. Camargo-Mathias[2], A. Batista[1]

[1]UFScar, Chemistry, São Carlos, Brazil
[2]Institute of Biosciences/UNESP, Biology, Rio Claro, Brazil
[3]UFTM, Chemistry, Uberaba, Brazil
[4]Universidad de La Habana, Chemistry, La Habana, Cuba
[5]USP, Chemistry, São Carlos, Brazil

janesmoreira@yahoo.com.br

New six heteroleptic ruthenium(II) complexes with general formulae [Ru(L)(bipy)(dppb)]PF_6, (**1-6**) where L: *N*,*N*-disubstituted-*N´*-acylthiourea, dppb: 1,4-bis(diphenylphosphino)butane and bipy: 2,2'-bipiridine were synthesized and characterized by elemental analysis, IR, NMR (^{1}H, $^{13}C\{^{1}H\}$ and $^{31}P\{^{1}H\}$) spectroscopies, molar conductivity and X-ray diffraction. Heteroleptic trischelate Ru(II) complexes containing acylthiourea ligands can be prepared in high yields and purity. The IR and NMR data suggest the coordination of the ligands to the Ru(II) metal center through the thiocarbonyl and carbonyl groups and the X-ray structures of the new complexes (Figure 2) were confirmed. The *N*,*N*-disubstituted-*N´*-acylthioureas and their Ru(II) complexes were tested for *in vitro* activity against MCF-7 (human breast cancer cells ATCC HTB-26), DU-145 (human prostate cancer cells ATCC HTB-26), and L929 (health fibroblasts from mouse ATCC CCL-1) by MTT assay (Figure 1). The results indicate that the combination of Ru(II) and acylthiourea in a single molecule results in complexes that are more cytotoxic than the individual organic components alone, displaying in all cases lower IC_{50} values and high selectivity indexes. Apoptosis was confirmed by the action of compound **2**, [Ru(L^2)(dppb)(bipy)]PF_6**,** on actin filaments, as shown in the confocal images, in which the filaments are constituents of the cytoskeleton (Figure 3 D-F). These results are similar to the rhodium complexes in lung cancer cells (A549). The changes of peripheral groups R1 and R2 of the thiourea moiety influences the degree of cytotoxicity of the acylthioureas and the complexation with Ru(II) metal center increases their activity, indicating that the metal center plays a key role on the activity of the complexes. Further experiments are necessary to comprehend the observed results.

1. DYSON, P. J. & SAVA, G. Dalton Trans, 16:1929, 2006.
2. KELLAND, L. Nat. Rev. Cancer, 7(8): 573, 2007.
3. PIZARRO, A. M. & SADLER, P. J. Biochimie, 91(10):1198, 2009.
4. RONCONI, L. & FREGONA, D. Dalton Trans. 48:10670, 2009.
5. REEDIJK, J. Eur. J. Inorg. Chem, 1303, 2009.
6. The authors gratefully acknowledge the financial support provided by CAPES/MES, CNPq, FAPEMIG and FAPESP (Grants 2009/54011-8 and 2011/16380-1). J.P. Barolli thanks FAPESP for a Post-Doc fellowship (Grants number 2013/21611-8 and 2011/21033-9) and Electron Microscopy Laboratory of UNESP Rio Claro-São Paulo, Brazil.

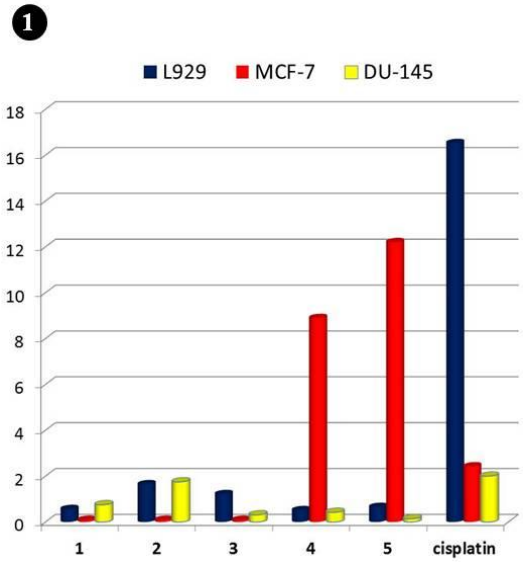

Figure 1. Inhibitory concentration of 50% of cell growth for ruthenium complexes against tumor and health cell lines;

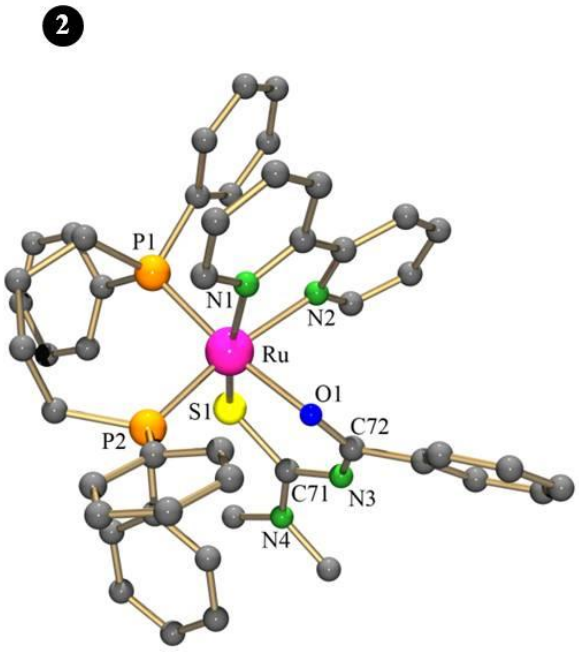

Figure 2. ORTEP structure of complex [Ru(L^2)(dppb)(bipy)]PF_6 (**2**). Hidrogen atoms are omitted for clarity;

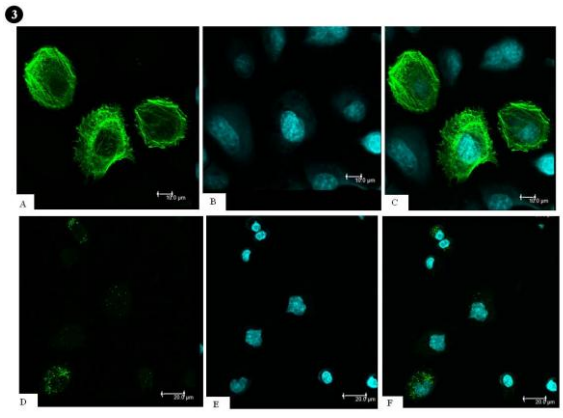

Figure 3. Confocal fluorescence images of Actin -F (Alexa Fluor® 488 Phalloidin) in green + DAPI (nuclear stain) blue of 24h of incubation in controls cells (A-C) and cancer cells treated with **2** (D-F).

Molecular Microscopy

LS4.P058
Morphology and iron storage in ferritin by aberration-corrected HAADF STEM

N. Jian[1], M. Dowle[1], R. Palmer[1]

[1]University of Birmingham, School of Physics & Astronomy, Birmingham, United Kingdom

nxj203@bham.ac.uk

Iron plays an important role in the body for cellular respiration, oxygen transport and DNA synthesis.[1] As the major iron storage protein, ferritin stores and releases iron to maintain the balance of iron in animals, plants, bacteria and other species.[2] Disorders in the storage of iron induce many diseases like haemochromatosis and Friedreich's ataxia. So a better understanding of the morphology and iron loading of ferritin is valuable for public health.

Here we present an investigation of the morphology and iron loading of ferritin from equine spleen by using aberration-corrected HAADF STEM. Atom counting with size selected Au clusters was employed to determine the number of iron atoms in each ferritin clusters.[3] The protein shell thickness was obtained by HAADF intensity profiling and the separation of ferritn cores within close-packed networks, suggesting a protein shell thickness of ~0.5nm. The quantitative analysis of ferritin's iron loading shows that the iron nuclearity in the protein varies from a few hundred Fe atoms to around 5000 Fe atoms. A relationship between the iron loading and iron core morphology is established. This relationship may contribute to a better understanding of the mechanism of iron storage and release from the protein shell.

1. A. Lewin, G. Moore, and N. Le Brun, *Dalt. Trans.*, 2005, 3597-3610.
2. Y. H. Pan, K. Sader, J. J. Powell, A. Bleloch, M. Gass, J. Trinick, A. Warley, A. Li, R. Brydson, and A. Brown, *J. Struct. Biol.*, 2009, **166**, 22-31.
3. J. Barton and L. Bertoli, *Nat. Med.*, 1996, **2**, 394-395.
4. T. Karlberg, U. Schagerlöf, O. Gakh, and S. Park, *Structure*, 2006, **14**, 1535-1546.
5. N. Jian, C. Stapelfeldt, K.-J. Hu, M. Fröba, and R. E. Palmer, *Nanoscale*, 2015, **7**, 885-888.

Molecular Microscopy

LS4.P059
Segmentation of individual cells at phase contrast microscopy images

J. Soukup[1,2,3]

[1]Charles University in Prague, Faculty of Mathematics and Physics, Prague, Czech Republic
[2]Czech Academy of Sciences, Institute of Information Theory and Automation , Prague, Czech Republic
[3]University of South Bohemia in České Budějovice, Faculty of Fisheries and Protection of Waters, České Budějovice, Czech Republic

jindra@matfyz.cz

Time-lapse microscopy imaging is a commonly used modern method for observing the dynamics of cells and tissues. A large number of images that time-lapse microscopy generates is difficult to evaluate manually, and computer methods of image processing would be highly advantageous. Quantifying of mammalian cancer cell images captured by phase contrast microscopy is especially challenging. Cancer cells have irregular shapes that change over time and the mottled background pattern is partially visible through the cells. In addition, the images contain artifacts such as white areas around the cell edges - so called halos.

Phase contrast microscopy is often used in the study of mammalian cancer cells to assess biotoxicity of materials in vitro. A common approach in biotoxicity assessment is measuring cell growth rate or counting the number of living cells. Phase contrast microscopy provides a nearly natural environment for cells due to small invasiveness and a low-level of exposure.

We developed a novel algorithm for segmentation of individual cells. First part separate the cells from the background and it is based on the differences in time between consecutive images and a combination of sophisticated thresholding, blurring, and morphological operations. It is fast and precise. The second part of our algorithm separates individual cells in the clusters. It uses the halos between cells (thresholding and modified skeletonization) and fills the missing parts by connecting the hanging branches of the skeleton via Dijkstra algorithm.

We tested the algorithm on images of four cell types acquired by two different microscopes, evaluated the precision of segmentation against manual segmentation performed by a human operator.

We created the software which implements our segmentation method. We added the possibility to modify the resulting segmentation. User can modify the result by merging or splitting the cell regions that was found by out algorithm.

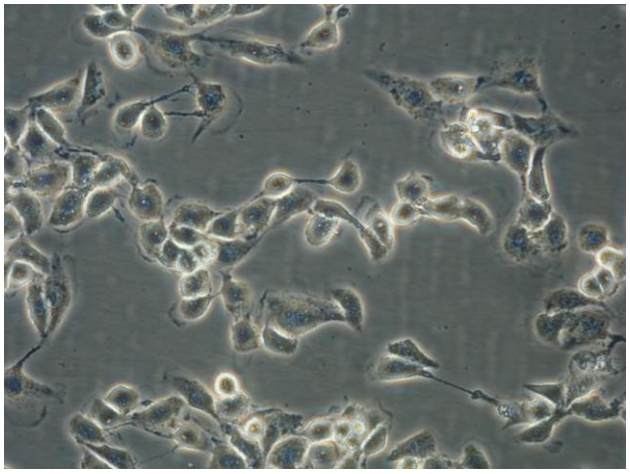

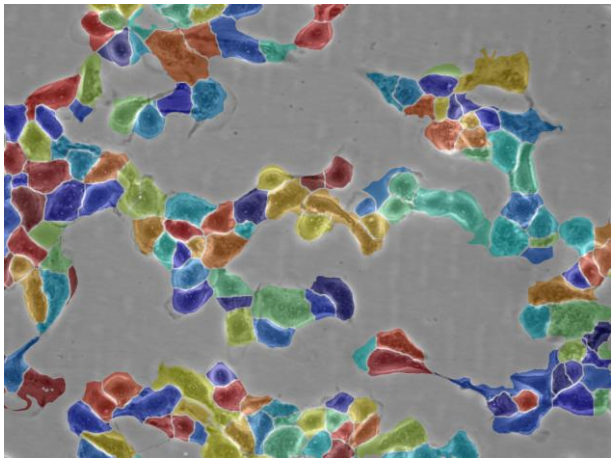

Molecular Microscopy

LS4.P060
Practical aspects of construction of high-resolution bright-field optical microscope with particular software

R. Rychtarikova[1], T. Nahlik[1], D. Malakhova[1], D. Stys[1]

[1]University of South Bohemia in Budweis, FFPW and CENAKVA, Inst. of Complex Systems, Nove Hrady, Czech Republic

rrychtarikova@frov.jcu.cz

Bright-field microscopy is the simplest of all the optical microscopy observation techniques. It is also non-destructive and, theoretically, enables to observe any type of biological phenomenon at microscale, from the shapes of observed organelles and cells to tracking dynamical objects inside the living cell.

During the experiment, rays ofwhite lightfrom a light source are transmitted through the sample and contrast in the sample is caused mainly by three mechanisms:

1) by absorbance of a part of the transmitted light in optical dense areas of the sample,
2) by diffraction at the interfaces of the observed objects and
3) by emission from autofluorescent objects

The diffracted light interferes to create a diffraction pattern of the observed object, which is consequently distorted by the incidence of the lenses (including aberrations and other types of non-idealities). Intensities projected on the digital camera chip have a multifractal character due to the fact that similar objects located at different levels project according to different, but similar, rules. Intensities reaching the camera chip are finally discretized and stored in the computer.

The contribution will aims to describe practical aspects of a technical construction of the body of the bright field optical microscope as well as particular software designed to retrieve as much information about the experiment on a live cell as possible, down to the level of an elementary diffracting objects. Among the principles analysed in the software are the physical assumptions mentioned above, use of information difference entropy which accounts for the anticipated multifractality and simple image subtraction for segmentation. The resulting least distorted, but still phenomenological, 3D image of the living cell is verified by highlighting the image contrast, classification of image pixels and collation with other imaging methods, namely the atomic force microscopy.

This analysis resulted in a construction of a high-resolution optical microscope for observation of a spatio-temporal change and topology of an unlabelled live cell.

Molecular Microscopy

LS4.P061
Ultrastructural changes associated with cryopreservation in tomato (Lycopersicon esculentum Mill.) shoot apices

A. Halmagyi[1], A. Coste[1], S. Tripon[2], C. Craciun[2]

[1]Institute of Biological Research, Experimental Biology, Cluj-Napoca, Romania
[2]Babeş-Bolyai University, Electron Microscopy Center, Cluj-Napoca, Romania, Romania

adela.halmagyi@icbcluj.ro

Conservation of plant genetic resources is essential not just to maintain biodiversity, but also to support plant biotechnology and breeding programmes. Cryopreservation (-196ºC) is an important tool for long-term conservation of the genetic pool of plant species. Vitrification based cryopreservation methods were used to cryopreserve complex, heterogeneous tissues (such as shoot apices) and involves removal of most or all freezable water by osmotic dehydration of explants followed by rapid freezing (4, 5). The damages as a consequence of metabolic stresses induced at each successive stage of the cryopreservation protocol may predispose the tissue to further damage or even loss of viability (2). The degree of damages caused by cold stress may vary, depending on the tolerance of plant material to low temperatures (3, 1).

In the present study the ultrastructural responses and the severity of damages in the cells of different layers of tomato (*Lycopersicon esculentum* Mill., cv. 'Darsirius') shoot tips exposed to osmotic dehydration, cryoprotection, liquid nitrogen storage, and recovery following low temperature storage have been evaluated.

The following sample variants were prepared for transmission electron microscopic (TEM) observations: (a) control shoot tips from in vitro grown tomato plants; (b) shoot tips after preculture in sucrose and 20 min dehydration in plant vitrification solution 2 (4); (c) shoot tips after rewarming; (d) shoot tips regenerated after cryopreservation.

Ultrastructural observations of the apical dome subjected to cryopreservation are a powerful source of information necessary to understand the responses of cells to stress induced by cryoprotective treatments or due to the freezing process itself. Cryopreservation allowed survival of small areas of cells located in the meristematic dome which have retrieved their original features after transfer to recovery medium. An intact cell structure with many organelles, dense cytoplasm, the presence of nuclear associated bodies, amyloplasts, indicated that osmotic dehydration did not cause significant damages to the cells, whereas the dehydration with the plant vitrification solution and the cryopreservation treatment indicated an increased number of vacuoles, cells with plasmolysis leading to reduced matrix density, a rarefied cytoplasm with numerous vacuoles, clearly exhibiting a greater vacuole/cytoplasm ratio and invaginated plasma membrane (Fig. 1a-c). Cells of the apical dome recovered from low-temperature storage showed that the meristematic zone have retrieved their original features (Fig. 1d).

Although, the majority of cells in the layers under the dome were injured after cryopreservation, some cells located in the meristematic dome could undergo normal cell division and they could recover after subculture.

1. Benson EE, Bremner D (2004) in *Life in the Frozen State,* Fuller BJ, Lane N, Benson EE (eds.), CRC Press, Boca Raton, Florida, USA, pp 205-241.
2. Engelmann F (2004) *In Vitro Cell Dev Biol-Plant* 40, 427-433.
3. Pritchard HW, Grout BWW, Short KC (1986) *Ann of Bot* 57, 41-48.
4. Sakai A, Kobayashi S, Oiyama I (1990) *Plant Cell Rep* 9:30-33.
5. Wilkinson T, Wetten A, Prychid C, Fay MF (2003) *Ann of Bot* 91, 65-74.
6. This study has been supported by a grant of the Romanian National Authority for Scientific Research, CNCS-UEFISCDI, Project nr. PN-II-ID-PCE-2011-3-280.

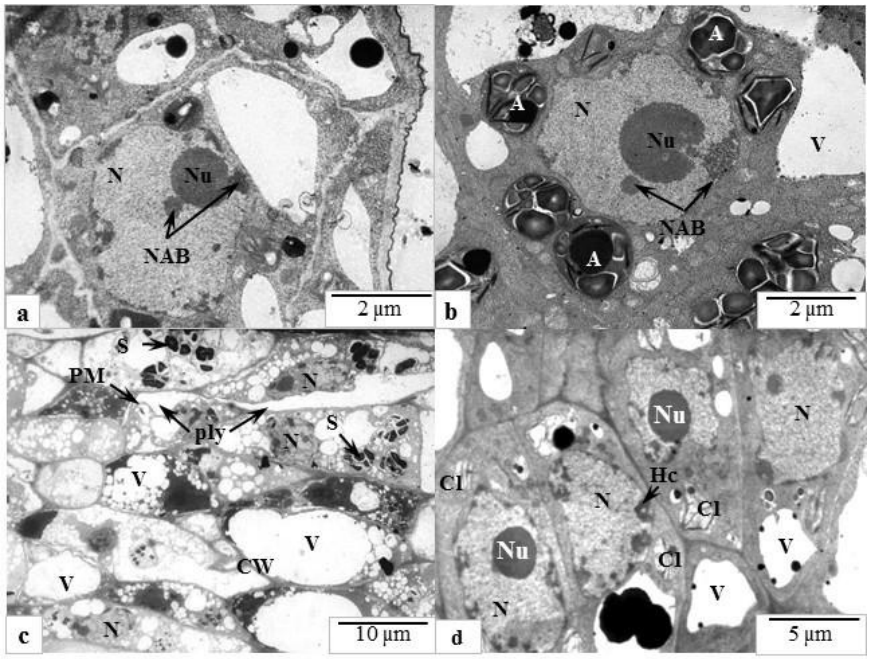

Figure 1. Ultrastructure of tomato meristematic cells subjected to cryopreservation. **(a)** apical dome intact cell structure of control cells with prominent nucleus and nucleolus with associated bodies; **(b)** cells of the upper layers of the meristematic dome with amyloplasts after preculture in sucrose; **(c)** cells of the basal region of the meristematic dome showing high vacuolization and signs of plasmolysis **(ply)** immediately after thawing following liquid nitrogen storage; **(d)** lower primordial cells of the meristematic dome showing that the cells recovered their characteristics. *Letters represent:* **A** amyloplast, **Cl** chloroplast, **CW** cell wall, **Hc** heterochromatin, **G** grana, **N** nucleus, **Nu** nucleolus, **NAB** nucleolus associated body, **P** plastids, **PM** plasma membrane, **S** starch grain, **V** vacuoles.

Molecular Microscopy

LS4.P062
Ultrastructural study of the thyroid gland of the domesticated adult greater cane rats (Thryonomis swinderianus, Temminck 1827

C. Igbokwe[1], B. Onoja[2]

[1]University of Nigeria, Nsukka, Nigeria
[2]University of Nigeria, Veterinary Anatomy, Nsukka, Nigeria

casmir.igbokwe@unn.edu.ng

Thyroid glands obtained from adult male greater cane rats, aged from 10-14 month were used to study its general histo-architecture, ultrastructural features of the follicular and parafollicular cells. The histological observations showed a well-developed capsule, interfollicular connective tissue and varying sizes of follicles similar to that of several mammals. Various forms of follicular cells that varied from squamous (flattened) to cuboidal shape were identified. Occasionally, low columnar cells were evident in some follicles. Flattened follicular cells appeared to be predominant over cuboidal cells and were poor in cytoplasmic organelles including microvilli. No cilia were identified in the thyroid follicular cell of this adult animal Highly dilated cisternae of rough endoplasmic reticulum (RER) commonly observed in adult follicular cells of some mammals were absent in this study. The parafollicular cells (C cells) were distributed throughout the gland singly or in cluster of 2-3 cells. The RER of parafollicular cells was frequently seen in form of concentric whorls and enclosed small cytoplasmic island. Electron-dense granules were in abundance as in several mammals. The parafollicular has some features commonly present in rodents like the tree shrews and guinea pigs. The present study of thyroid of great cane rats showed some similarities to that of other rodents. It also suggests that the variability of thyroid morphology is in response to several factors that include species, age, climate, feeding and environmental factors.

1. Abdel-Magied EM, M Taha. and AB Abdalla. 2000. Light and electron microscopic study of the thyroid gland of the camel *(Camelus dromedaries*), Anat Histol Embryol, 29: 331-336.
2. Adebayo AO and SA Olurode. 2010. The morphology and morphometry of the epididymis in the geater cane rat *(Thryonomys swinderianus*, Temminck), Folia Morphol. 64 (4): 246-252.
3. Adeyeye EI, O Olaofe and RE Ogunjana. .2012. Lipid profiles of skin, muscle and liver of greater cane rats *(Thryonomys swinderianus)*; dietary implications, Elixir Food Sci. 53: 11749-11756.

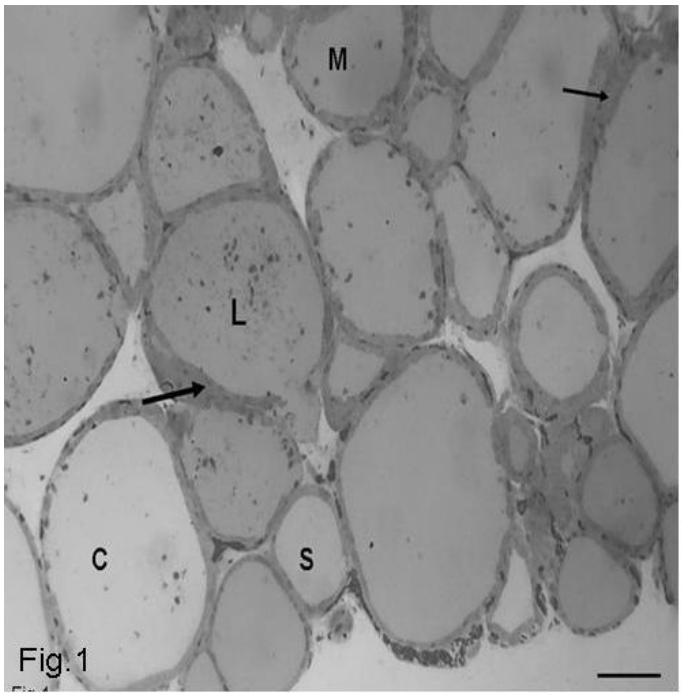

Fig. 1

Figure 1. Light micrograph of the thyroid gland showing small (S) and large-sized (L) follicles. The follicles are filled with colloid (C), and surrounded by interfollicular connective tissue (arrows). Bar = 45µm: Toluidine stain

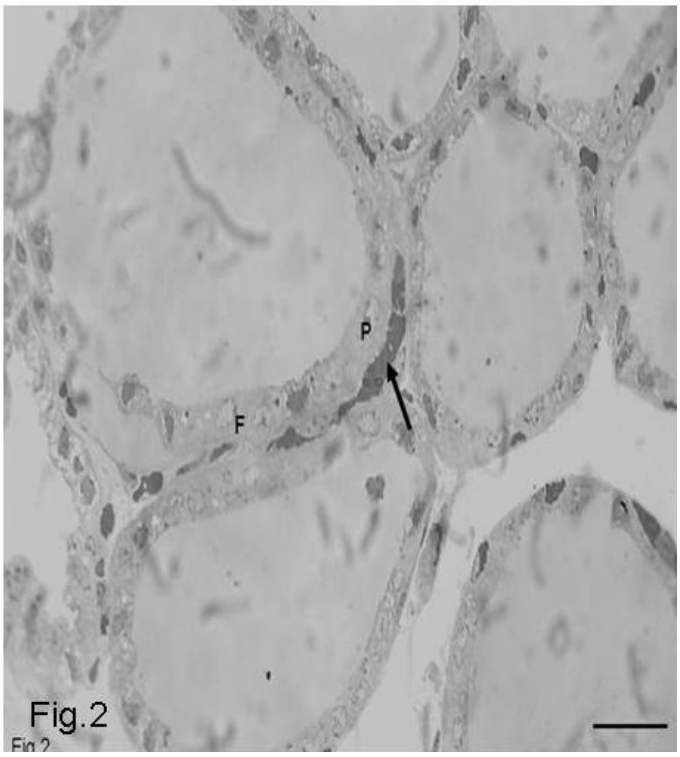

Figure 2. Higher magnification of light micrograph showing well-vascularsed interfollicular connective tissue (arrow), Follicular cells (F) and parafollicular cells (P). Bar 15µm: Toluidine stain)

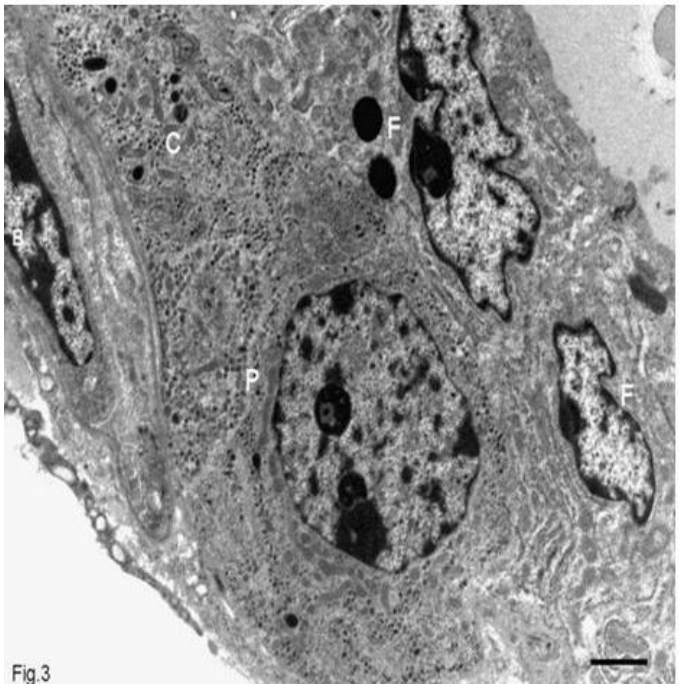

Figure 3. Electron microscopic photograph of follicular epithelium of greater cane rat thyroid showing flattened follicular cells (F) with indented nuclei and larger parafollicular cells (P) with some slender cytoplasmic extensions (C), fibroblast (B). Bar 2µm

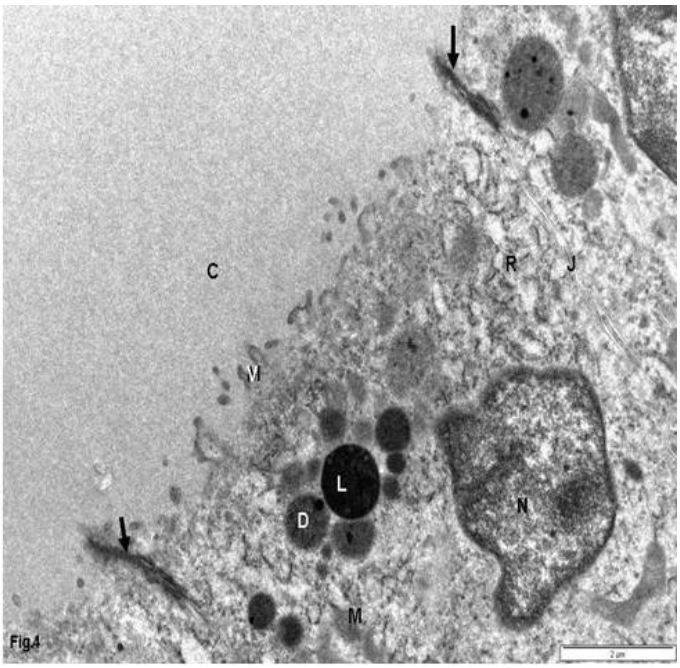

Figure 4. Apical cytoplasm of cuboidal follicular cells showing profiles of RER (R), nucleus (N), mitochondria (M), short microvilli (V), primary lysosomes (L), collod (C) and colloid droplets (D) . Note the well-developed tight junction (arrow) of the junctional complex (J) . Bar 2µm

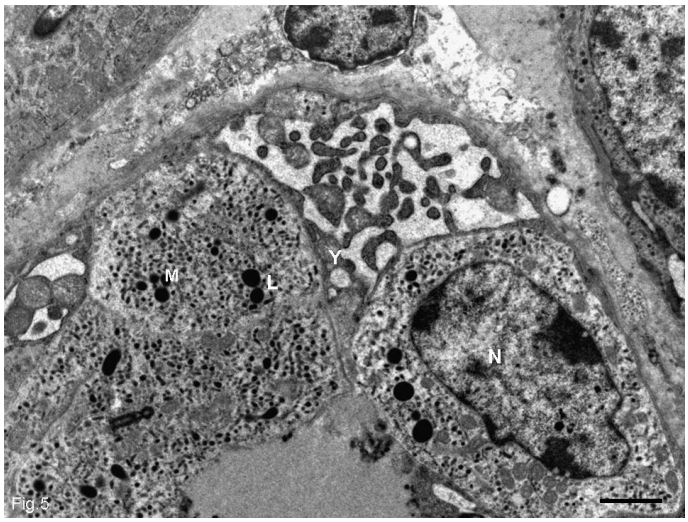

Figure 5. Micrograph of thyroid gland of greater cane rats showing apposed parafollicular cells with nucleus (N) in with intercellular spaces between them with protrusions of cyplasm resembling microvilli (Y) opening into it. Note abundant electron dense granules in these cells. Lysosome-like bodies (L) and multivesicular bodies are present (M). Bar 2µm

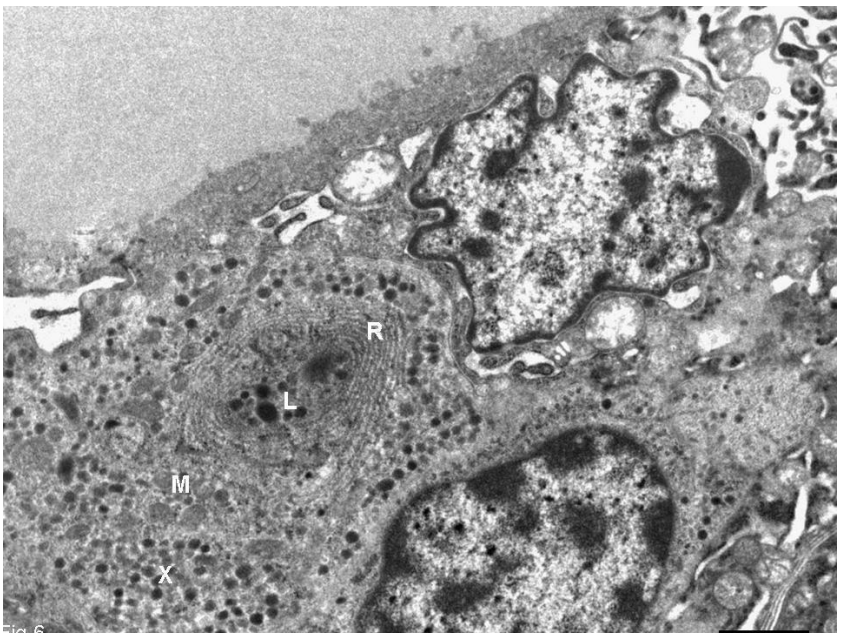

Figure 6. Electron micrograph of parafollicular cell showing well-developed RER in concentric whorls (R) enclosing small cytoplasm. Note abundance of electron dense secretory granules (X), mitochondria (M) and lysosome-like dense granules (L). Bar 2µm

Molecular Microscopy

LS4.P063
Optical evaluation of cellular dynamics of ChR2 expressing HEK293 cells induced by light control

L. Stanica[1,2], M. Gheorghiu[1], E. Gheorghiu[1,2]

[1]International Centre of Biodynamics, Bucharest, Romania
[2]University of Bucharest, Faculty of Biology, Bucharest, Romania

lstanica@biodyn.ro

We advance a cellular platform integrating electro-optical assessment under controlled light stimulation of genetically modified HEK293 cells that express channelrhodopsin-2 (ChR2), K+ channels for swift recovery of the membrane potential after light induced depolarization and yellow fluorescent protein (YFP) towards development of cell based biosensing platforms.

Real-time, sensitive evaluation of dynamic cellular processes upon light stimulation on optogenetically modified cells was realized using microscopy techniques as Differential Interference Contrast (DIC) Microscopy and Fluorescence Microscopy, Total Internal Reflection Fluorescence Microscopy (TRIFM) in parallel with impedance spectroscopy assays. Quantitative evaluation of optical data provide time series of morphological and cell-substrate interface parameters consistent with dynamic extension and contraction of lamellipodia as well as bleb formation in response to light pulses. For this automatic evaluation we rely on ImageJ and related analysis modules adapted for DIC and fluorescence data. Moreover, based on TIRFM observations, we assayed modifications in cell-cell junctions and cell-substrate adherence upon light actuation, changes traditionally overlooked in classical optogenetic studies. These results were confirmed by complementary electrical impedance experiments which enabled monitoring with high temporal resolution the alterations occurring within the cell layer, especially at the cell-substrate level. The multiple well cell growth platforms developed within ICB to enable advanced optical assays (including TIRF and DIC) in conjunction with electrical evaluation were compared with commercially available ECIS optical sensors and demonstrate significant improvements.

The results of real-time noninvasive evaluation of cellular dynamics upon light stimulation on ChR2 expressing cells demonstrate the capabilities of the proposed analytical platform for both basic and applied research.

3D Imaging of Organisms, Tissues and Cells

LS5.064
Electron tomography of the archaeum Pyrococcus furiosus

V. Heinz[1], A. Bellack[2], R. Wirth[2], R. Rachel[1]

[1]University of Regensburg, Center for EM, Regensburg, Germany
[2]University of Regensburg, Microbiology, Regensburg, Germany

reinhard.rachel@biologie.uni-regensburg.de

The hyperthermophilic, strictly anaerobic euryarchaeum *Pyrococcus furiosus* has emerged as an excellent model system for a number of studies of archaeal cell and molecular biology. In particular, *P. furiosus* is attractive because a shuttle vector-based transformation system is available, making it genetically tractable (Waege et al 2010). The slightly irregular cocci exhibit up to 50 flagella, several µm in length. They have been proven to mediate cell motility, adhesion to various surfaces, and formation of cell-cell connections, as visualized by swimming studies (Herzog and Wirth, 2012) and by SEM/TEM (Näther et al, 2006). The major protein of the flagella was determined to be FlaB0; this protein is not yet included in the published genome, as the gene is difficult to clone into *E. coli* using standard approaches (Näther-Schindler et al 2014).

As *P. furiosus* can withstand and handle harsh environmental conditions, its cellular architecture (e.g., composition of the cell envelope, organisation of the S-Layer, insertion of the flagella, cytoskeleton) is of great interest. We employed various electron microscopical methods (Rachel et al, 2010) to study the cell ultrastructure. In particular, TEM tomography of 300nm thin sections of high-pressure frozen, freeze-substituted and resin-embedded *P. furiosus* cells was performed in order to get a 3D view into the structure of the cytoplasm and the cell wall. Additionally, STEM tomography datasets of 600nm sections were recorded to reach a higher content of information (reduction of focus gradient due to a greater depth of focus in STEM mode), while investigating a larger volume of the cell (Yakushevska et al, 2007). All datasets were reconstructed using 3Dmod (using WBP and SIRT), and finally segmented and visualized in AMIRA.

Tomography turned out to be an excellent means for investigating the architecture of a complete *P. furiosus* cell. Several yet undescribed features, like the partial withdrawal of the S-Layer in certain areas, or structures associated with the cell wall, could be visualized.

For a proper comparison, the generation of FIB-SEM datasets is planned, in order to obtain an overview of the architecture of a whole cell. For high-resolution investigation of ultrastructural details, cryo-tomography is planned to be performed in the near future.

1. Herzog and Wirth, 2012: Swimming behavior of selected species of Archaea. Appl Environ Microbiol 78: 1670-1674
2. Näther et al, 2006: Flagella of *Pyrococcus furiosus*: Multifunctional organelles, made for swimming, adhesion to various surfaces, and cell-cell contacts. J Bacteriol 188: 6915-6923
3. Näther-Schindler et al, 2014: *Pyrococcus furiosus* flagella: biochemical and transcriptional analyses identify the newly detected *flaB0* gene to encode the major flagellin. Front Microbiol, in press
4. Rachel et al, 2010: Analysis of the ultrastructure of Archaea by electron microscopy. Meth Cell Biol 96: 47-69
5. Yakushevska et al, 2007: STEM tomography in cell biology. J Struct Biol 159: 381-391
6. Waege et al, 2010: Shuttle vector-based transformation system for *Pyrococcus furiosus*. AEM 76: 3308-3313

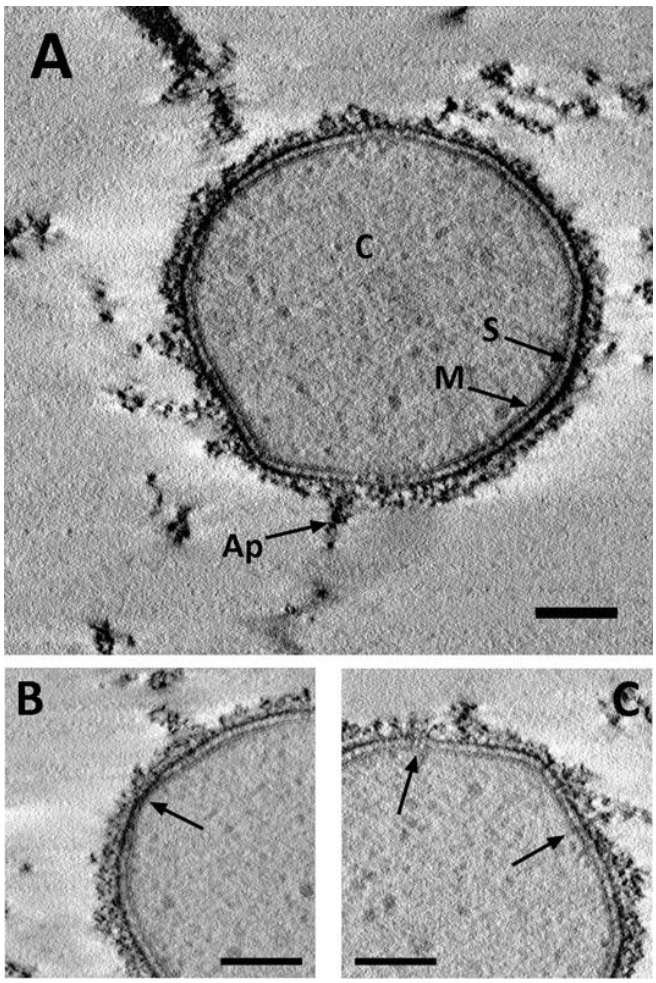

Figure 1. A: 2nm slice of a 300nm thick section of Epon-embedded *P. furiosus* cells; C = cytoplasm, M = membrane, S = S-Layer, Ap = cell appendages; bar = 200nm. B: Close-up view of an area where membrane and S-Layer appear to fuse (arrow); bar = 200nm. C: Structures crossing membrane and / or S-Layer (arrows); bar = 200nm.

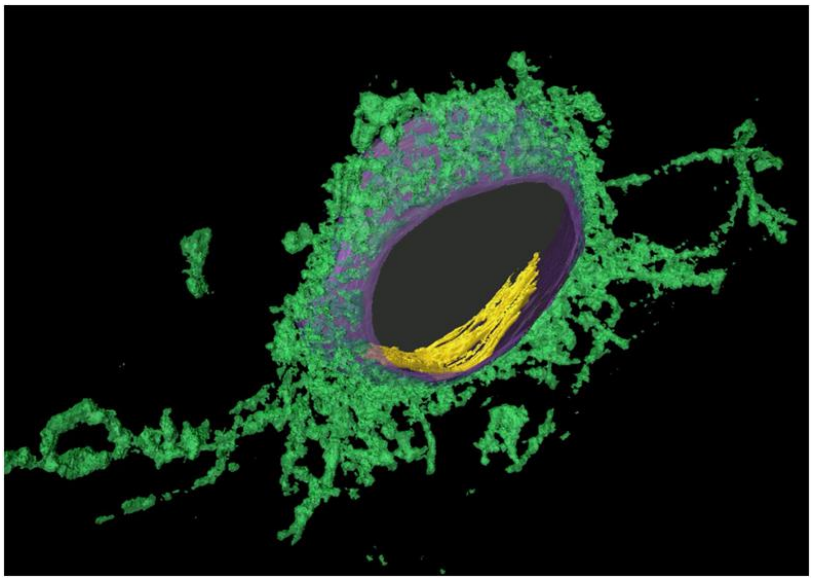

Figure 2. 3D visualization of the *P. furiosus* cell shown in fig. 1A. The model was obtained by combined manual and semi-automated segmentation of the SIRT image stack in AMIRA. Color code: green = cell appendages, purple = S-Layer, yellow = electron-dense layer.

3D Imaging of Organisms, Tissues and Cells

LS5.065
Caught in the Act: high-resolution 3D imaging of single tumor cells invading mouse tissue

M. Karreman[1], L. Mercier[2], N. Schieber[1], G. Solecky[3], B. Ruthensteiner[4], G. Allio[2], F. Winkler[3], J. Goetz[2], Y. Schwab[1]

[1]EMBL Heidelberg, Cell Biology and Biophysics, Heidelberg, Germany
[2]INSERM U1109, Strasbourg, France
[3]German Cancer Research Center (DKFZ), Heidelberg, Germany
[4]Zoologische Staatssamlung München, Munich, Germany

karreman@embl.de

Metastasis is the main cause of cancer mortality, but its underlying mechanisms are poorly understood *in vivo*. Crucial steps in the spreading of cancer include extravasation, exiting the blood vessel at a secondary site, and invasion of the surrounding tissue. Here, we employ established mouse model systems to study the ultrastructure of invasive tumor cells and their microenvironment. In order to capture extravasation, tumor cells were intracardially injected into living mice. Tumor cells that were arrested in the vasculature of the brain were captured with intravital 2-photon excitation microscopy (2PEM) through a cranial window. The regions of interest was marked by near-infrared branding, dissected and processed for electron microscopy (EM). To facilitate the retrieval of these single cells with EM, the sample was imaged by microscopic x-ray computed tomography (microCT). MicroCT scans revealed the outline of the resin block, the brain biopsy and the blood vasculature therein. Using the vasculature as a reference, the 2PEM dataset could be registered in the microCT volume, allowing precise mapping of the position of the tumor cell within the resin block. This enables quick and accurate trimming of the resin block to expose the tumor cell for 3D electron microscopy. Using focused ion beam scanning electron microscopy (FIB-SEM) the tumor cell was imaged in full at high resolution in 3D, revealing unprecedented views of its complex architecture and its interactions with the endothelial cells lining the blood vessel. The process of invasion was studied by intravital 2PEM imaging of fluorescent tumor cells xenotransplanted in mouse ear skin tissue. Following EM processing of skin biopsy, invasive cellular protrusions were quickly targeted as described above and imaged at high resolution by serial TEM and electron tomography. Here, we demonstrate the power and necessity of 3D EM imaging in the study of metastasis. Using our newly developed correlative approach, *in vivo* observed tumor cells could quickly and efficiently be targeted and imaged in full at high resolution. This method opens up new avenues for high-throughput studies revealing tumor cell behavior at the ultrastructural level.

3D Imaging of Organisms, Tissues and Cells

LS5.066
FIB-SEM tomography of freeze-substituted biological samples

C. Kizilyaprak[1], D. De Bellis[1], J. Daraspe[1], B. M. Humbel[1]

[1]University of Lausanne, Lausanne, Switzerland

caroline.kizilyaprak@unil.ch

Three-dimensional (3-D) spatial distribution of organelles within cells at nanometer resolution is essential to better understand cellular processes and functions. Currently, FIB-SEM tomography provides a promising technology to generate volume data with nanometer resolution (Bushby et al., 2011;Heymann et al., 2009;Knott et al., 2011;Villinger et al., 2012;Wei et al., 2012). A FIB-SEM microscope is a scanning electron microscope (SEM) combined with a focused ion beam (FIB) where both beams coincide at their focal points. This combination enables to locally section bulk embedded-resin samples by ion milling, creating a fresh surface for subsequent imaging with the electron beam. This process is repeated automatically to generate 3-D information of relatively large volumes with a field of view of several micrometers.

Ultrastructural preservation and stability of the biological sample are important issues for 3-D analyses. Typically, any fixed and embedded resin samples prepared for TEM examination can be used for FIB-SEM tomography. However, considerations have to be given to artefacts induced by sample preparation, FIB milling and SEM imaging (Drobne et al., 2007). To preserve the ultrastructure of the sample as closely as possible to the native state, we combine high pressure freezing (HPF) with freeze-substitution (FS) and resin embedding. A wealth of different substitution protocols exists but they were not systematically investigated for FIB-SEM tomography. To improve data acquisition during FIB-SEM tomography, we have to find the best compromise between ultrastructure preservation and high contrast of cellular components in order to increase the signal/noise ratio, decrease the charging effect and decrease acquisition time.

In this study, mouse liver samples were cryo-immobilized and freeze-substituted using different FS cocktail. The addition of water in organic solvent during FS reveals the bilayer structure of membranes (Buser and Walther, 2008), addition of uranyl acetate and methanol is used to increase contrast in mitochondria (Ichimura and Hashimoto, 1988), addition of glutaraldehyde and osmium results in high contrast and excellent visibility of subcellular components and membrane bilayer (Schwarz and Humbel, 1989). After FS, the samples were embedded in Hard-Plus resin that has the best stability in the ion and electron beam (Kizilyaprak et al., 2015). The contrast quality of the different FS protocols was evaluated in the TEM (Figure1) and the most promising preparations were investigated using FIB-SEM tomography.

In conclusion, we propose a biological sample preparation protocol that can serve as starting point in order to visualize cells in 3-D with the best compromise between ultrastructural preservation, contrast and dimensional integrity at nanometer resolution using FIB/SEM tomography.

1. Buser, C., Walther, P., 2008. Journal of Microscopy 230, 268-277.
2. Bushby, A.J., P'Ng K, M., Young, R.D., Pinali, C., Knupp, C., Quantock, A.J., 2011. Nat Protoc 6, 845-858.
3. Drobne, D., Milani, M., Leser, V., Tatti, F., 2007. Microsc Res Tech 70, 895-903.
4. Heymann, J.A., Shi, D., Kim, S., Bliss, D., Milne, J.L., Subramaniam, S., 2009. Journal of structural biology 166, 1-7.
5. Ichimura, T., Hashimoto, P.H., 1988. J Neurocytol 17, 3-12.
6. Kizilyaprak, C., Longo, G., Daraspe, J., Humbel, B.M., 2015. Journal of structural biology 189, 135-146.
7. Knott, G., Rosset, S., Cantoni, M., 2011. J Vis Exp, e2588.
8. Schwarz, H., Humbel, B.M., 1989. Scanning Microsc Suppl 3, 57-63; discussion 63-54.
9. Villinger, C., Gregorius, H., Kranz, C., Hohn, K., Munzberg, C., von Wichert, G., Mizaikoff, B., Wanner, G., Walther, P., 2012. Histochem Cell Biol 138, 549-556.
10. Wei, D., Jacobs, S., Modla, S., Zhang, S., Young, C.L., Cirino, R., Caplan, J., Czymmek, K., 2012. Biotechniques 53, 41-48.

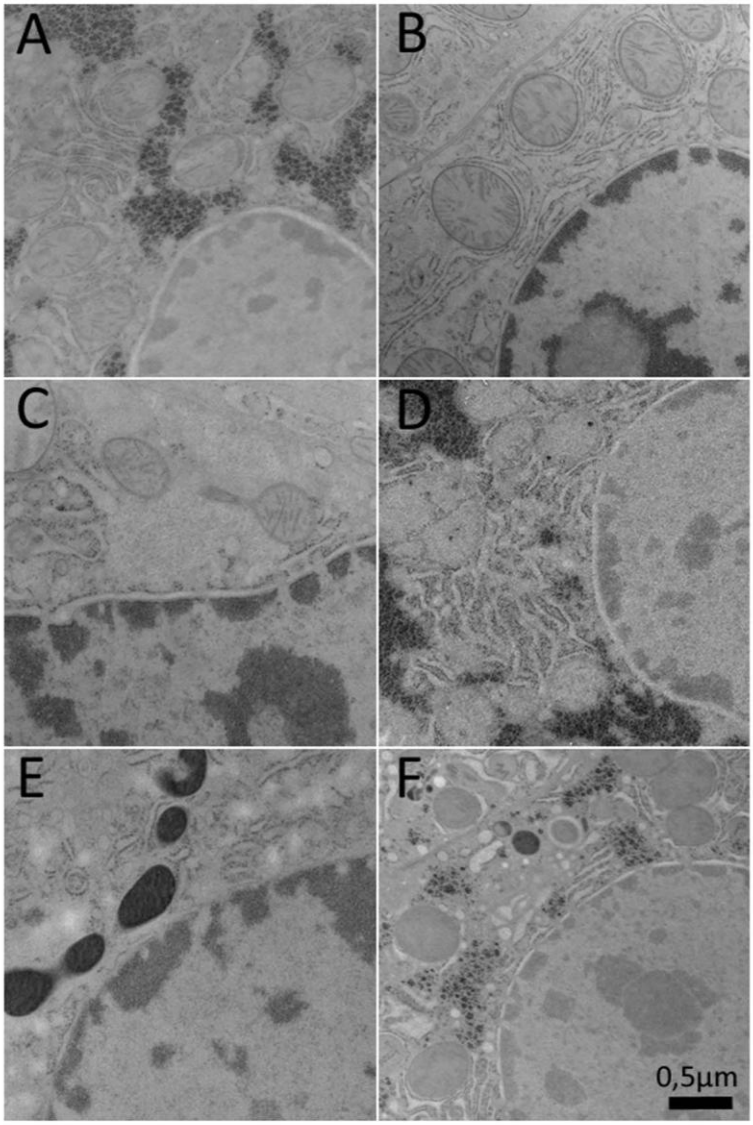

Figure 1. Transmission electron micrographs of high pressure frozen mouse liver freeze-substituted with different FS medium: A- FS in acetone with 2 % Osmium tetroxide. B- FS is acetone containing 2% osmium tetroxide and 2,5 % water. C- FS is acetone containing 2 % osmium tetroxide and 3% glutaraldehyde. E- FS is acetone containing 2% osmium tetroxide following by an incubation in methanol containing 2,5% uranyl acetate. F-FS in acetone containing 2% osmium tetroxide, 3% glutaraldehyde and 2,5% methanol.

3D Imaging of Organisms, Tissues and Cells

LS5.067
New tools for array tomography: approaching large volumes in LM and SEM

I. Wacker[1], W. Spomer[2], A. Hofmann[2], U. Gengenbach[2], M. Thaler[3], L. Ness[4], P. Brey[4], R. Schröder[5]

[1]Universität Heidelberg, Cryo EM, Centre for Advanced Materials, Heidelberg, Germany
[2]Karlsruhe Institute of Technology, Institute for Applied Computer Science, Karlsruhe, Germany
[3]Carl Zeiss Microscopy GmbH, Oberkochen, Germany
[4]RMC Boeckeler, Tucson, Arizona, USA, United States
[5]Universität Heidelberg, Cryo EM, CellNetworks, BioQuant, Heidelberg, Germany

irene.wacker@bioquant.uni-heidelberg.de

A number of methods are available to reconstruct large volumes at ultrastructural resolution [1]. Focussed ion beam or serial blockface scanning electron microscopy (FIBSEM or SBFSEM) are inherently destructive: The sample will eventually be gone after the many alternating cycles of blockface imaging and subsequent removal of a thin layer of material. Array tomography (AT) [2] on the other hand has the greatest potential for correlative imaging because it offers the possibility of imaging at different resolutions and with different techniques, such as (fluorescence) light microscopy (LM) and SEM.

A high degree of automation during both, sample preparation and imaging procedure is desirable when aiming at large volumes. The ATUMtome [3] was introduced as one way to automate the generation of the thousands of serial sections necessary for brain mapping. It is now commercially available for early adopters (RMC Boeckeler). Epifluorescence LM may be possible because the sections are collected on carbon-coated Kapton tape, but super-resolution LM methods [4] do not work on such non-transparent tape.

We have developed a novel device for reliable collection of long ribbons of serial sections (cf Spomer et al., this conference) onto silicon wafers for SEM imaging. The special construction of our device also allows deposition of serial sections on ITO-coated glass coverslips, a super-resolution LM-compatible solid substrate thus overcoming the limitations of the Kapton tape.

Samples are embedded in epoxide after either classical aldehyde-based chemical fixation or cryofixation and freeze substitution. Lowicryl embedding is preferred if fluorescence signals have to be preserved or for post-embedding immuno-labeling. To stabilize the ribbons during handling trimmed blocks are coated with a thin layer of glue on the leading and trailing edges. After hydrophilization by glow discharge substrates are immersed into the boat of a Jumbo knife (Diatome) using the novel substrate holder. Several ribbons are attached to the substrate (Fig. 1A) and gently lifted from the water. Sections can be from ultrathin (down to 50nm) to semithin (up to 3mm). Large numbers of sections can reproducibly be deposited on ITO-coated glass coverslips (Fig. 1A, B, ca 100 sections) or silicon wafers (Fig. 1C, ca 100 sections).

Staining of sections may be done with fluorescent dyes or antibodies for LM or with uranylacetate and lead citrate for SEM imaging. High resolution SEM imaging is possible without further coating with sections up to 200nm thickness, using either secondary or back-scattered electrons.

Automation of the imaging process is necessary to image large numbers of sections. Repeated imaging of the sample at increasing resolution is possible with the newly released product ZEISS Atlas 5 Array Tomography (Carl Zeiss Microscopy GmbH). First an overview of the whole substrate (Fig. 2A) is recorded with a pixel size of several 100nm. Regions of interest (ROI), for example individual sections or parts thereof (Fig. 2B) are then recorded with intermediate pixel sizes. Single cells (Fig. 2C) can finally be selected and imaged automatically over large numbers of sections at pixel sizes down to 2-5nm to reconstruct whole cells at nanoscale resolution.

1. I Wacker, RR Schröder, J Microscopy **252** (2013), p93-99.
2. KD Micheva, DJ Smith, Neuron **55** (2007), p25-36. Erratum in: Neuron **55** (2007), p. 824.
3. KJ Hayworth et al., Front Neural Circuits **8** (2014), article 68, p1-18.
4. S Nanguneri, et al., PLoS One **7** (2012), e38098.
5. The authors acknowledge C Bartels and L Veith for technical support, C Grabher for samples, BMBF for NanoCombine grant FKZ 13N11401 and MorphiQuant grant FKZ 13GW0044, and HEiKA for initial funding of the substrate holder development.

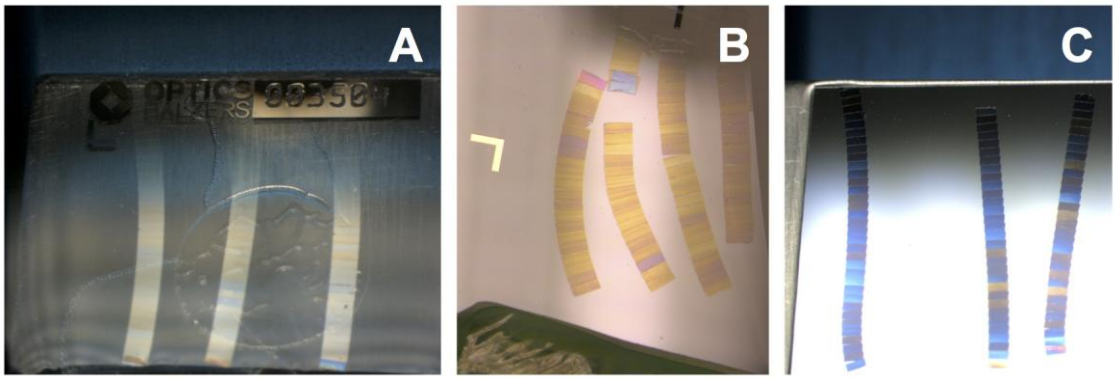

Figure 1. Production of arrays of serial sections: A) Three ribbons floating in knife boat, attached to ITO-coated glass coverslip by their lower ends. B) Ribbons on an ITO-coated glass coverslip after lift-out and drying. C) Three ribbons (100 consecutive sections in total) on surface of silicon wafer.

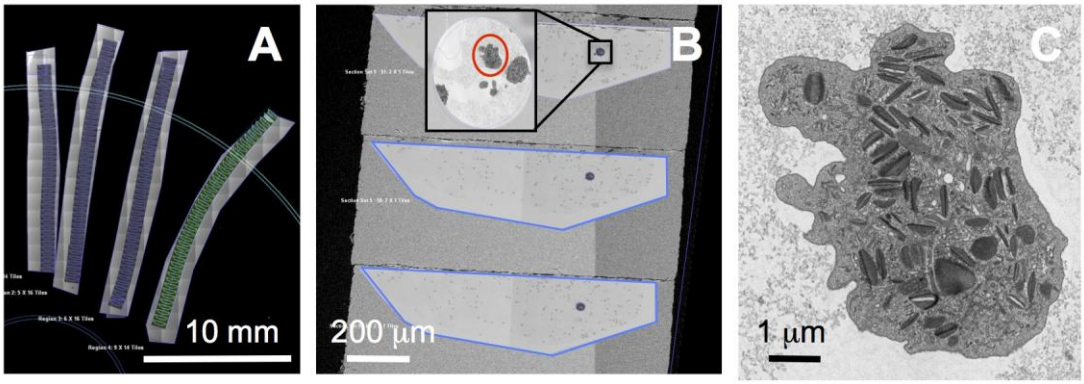

Figure 2. Automatic imaging of arrays using ATLAS 5 Array Tomography software: A) Images of four ribbons, ROIs already imaged are marked in blue, ROIs not imaged yet in green B) individual sections with cell pellets (blue outline) imaged at 50nm pixel size, inset imaged at 5nm pixel size, D) individual cell marked by red circle in C)

3D Imaging of Organisms, Tissues and Cells

LS5.068
3D FIB-SEM tomography of neuronal cells on microelectrode arrays (MEA)

B. Schroeppel[1], S. Roehler[1], R. Samba[1], B. Stamm[1], C. J. Burkhardt[1]

[1]NMI Natural and Medical Sciences Institute, Reutlingen, Germany

birgit.schroeppel@nmi.de

In drug discovery and basic research, microelectrode arrays (MEA) are used in vitro and in vivo for electrical recording and stimulation of tissue and cells (e.g. brain tissue, neurons, cardiomyocytes) [1]. The electrodes well-established today are typically fabricated from metal based materials and show ideally low electrical impedance to the surrounding tissue or cells and high charge transfer capacitance. For further improvement of MEA systems new electrodes are developed based on non-metal materials. Two promising candidates are carbon nanotube (CNT) electrodes [2, 3] and PEDOT-CNT electrodes [4]. Beside electrochemical and electrophysiological measurements indicating the advantageous properties of these electrodes a morphological study of the biological technical interface with high spatial resolution showing the connection of the cells to the microelectrode is important for understanding the different behaviour. Therefore a 3D FIB-SEM tomography study is performed on three different types of electrodes consisting of (i) TiN, (ii) CNT and (iii) PEDOT-CNT.

For 3D microscopy analysis, conventional EM preparation methods for cell based samples are applied. Chemical fixation with formaldehyde and glutaraldehyde, staining with osmium tetroxide and uranyl acetate, dehydration and embedding in epoxy resin are used on the biological technical system consisting of the MEA and neuronal cells grown on the MEA. This results in a compact and fixed sample. To get access to the electrode cell interface, which is hidden some tens of microns inside the embedding, the sample has to be assembled via diamond wire saw and by appropriate grinding and polishing methods commonly applied to material science samples. Thereby a thin sample composed of the actual electrode array, the cells and the embedding layer is obtained to enable FIB-SEM analysis of the biological technical interface. As this preparation method comprises all electrodes, the ones showing particular good signals in recording or stimulation can be selected for 3D microscopy analysis. Light microscopy is used to get an overview of the region of interest. By manually correlating the light microscope images and the images obtained by the SEM this region of interest can be relocated in the FIB-SEM instrument.

FIB-SEM serial sectioning tomography [5-7] is accomplished on a crossbeam instrument (Zeiss Auriga 40) equipped with a gallium FIB and a low voltage SEM. The gallium FIB produces a series of cross sections containing the interface electrode to cell. Each cross section is imaged by the low kV SEM using the energy selected backscattered (EsB) electron detector for image acquisition. This yields to images with good contrast due to the heavy metal staining.

In this manner, a stack of 2D images is acquired. The software package Fiji is used to perform 3D reconstruction including image processing, alignment, segmentation and representation of the results obtained. The resulting 3D reconstruction helps to analyse morphological aspects of the complex electrode cell interface on a nanometre range. In comparing three different types of electrodes, better insight into the process of coupling and connection of cells to the electrode materials is achieved which is particularly crucial for electrical recording and stimulation.

1. M. Fejtl et al, Advances in Network Electrophysiology, Springer, New York, 2006, pp.24-37.
2. B. Stamm et al, Carbon nanotube electrodes for neuronal recording and stimulation, MEA Meeting.
3. K. Schneider et al, Chemical vapor deposition grown carbon nanotubes on recessed contacts of flexible polyimide MEAs, MEA Meeting 2014.
4. R. Samba et al, J. Neural Eng. 12 (2015) 016014.
5. L. Holzer *et al*, J. Am. Ceram. Soc., 89, 2006, p. 2577-2585.
6. C. Villinger et al, Histochem. Cell Biol (2012) 138:549-556.
7. G. Knott, S. Rosset, M. Cantoni, J. Vis. Exp. (53), e2588.
8. Acknowledgement: Thanks to Elvina Houas and Paulo Cesare for cell culturing and sample preparation.

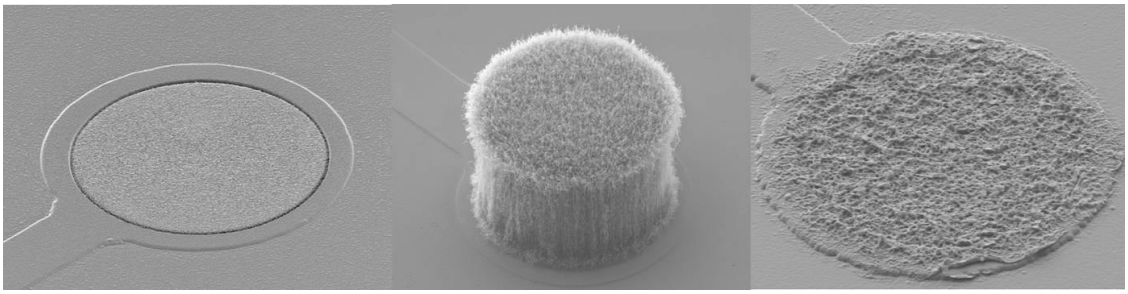

Figure 1. SEM images of three different types of electrodes: (i) Titanium nitride (ii) carbon nanotube (iii) PEDOT-CNT.

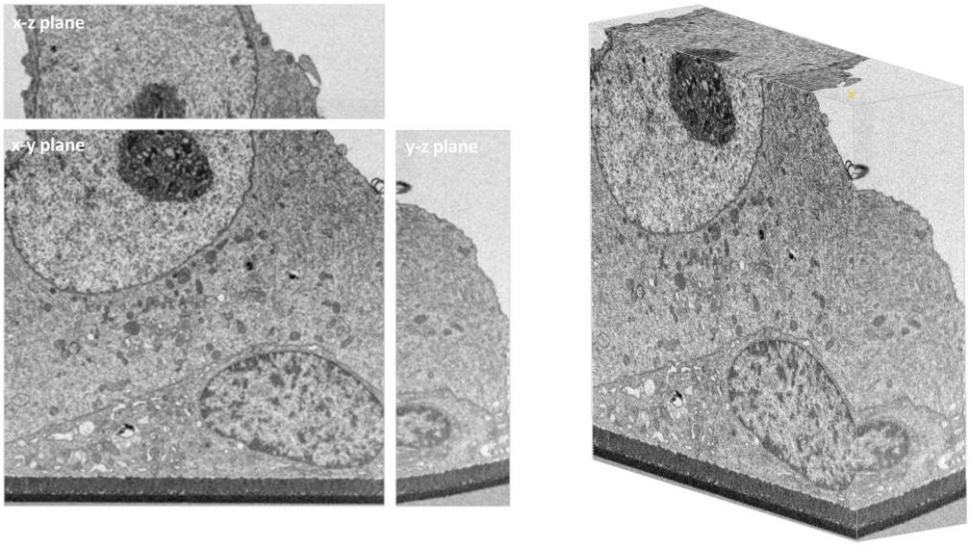

Figure 2. FIB-SEM tomography of electrode cell interface for neuronal cells on TiN electrode showing good alignement in y and z, pixel size is 30nm.

3D Imaging of Organisms, Tissues and Cells

LS5.069
Bone-stromal cells up-regulate tumourigenic markers in a tumour-stromal 3D model of prostate cancer.

L. Windus [1], T. Glover[1], V. Avery[1]

[1]Eskitis Institute , Brisbane, Australia

l.windus@griffith.edu.au

The cellular and molecular mechanisms that mediate interactions between tumour cells and the surrounding bone stroma are to date largely undetermined in prostate cancer (PCa) progression. The purpose of this study was to evaluate the role of alpha 6 and beta 1 integrin subunits in mediating tumour-stromal interactions using novel 3D co-culture *in vitro* assays.

Utilising 3D in vitro assays in conjunction with 3D imaging acquisition and reconstruction we evaluated and compared 1. Monocultures of prostate metastatic PC3, bone stromal derived HS5 and prostate epithelial RWPE-1 cells and 2. Tumour-stromal co-cultures (PC3 + HS5) to ascertain changes in cellular phenotype, function and expression of metastatic markers.

In comparison to 3D monocultures of PC3 or HS5 cells, when cultured together, these cells displayed up-regulated invasive and proliferative qualities, along with altered expression of epithelial-to-mesenchymal and chemokine protein constituents implicated in metastatic dissemination. When co-cultured, HS5 cells were found to re-express N-Cadherin and chemokine receptor CXCR7. Alterations in N-Cadherin expression were found to be mediated by soluble factors secreted by PC3 tumour cells, while chemokine receptor re-expression was dependent on direct cell-cell interactions. We have also shown that integrins beta 1 and alpha 6 play an integral role in maintaining cell homeostasis and mediating expression of E-Cadherin, N-Cadherin and vimentin, in addition to chemokine receptor CXCR7.

Collectively our results suggest that both PC3 and HS5 cells provide a "protective" and reciprocal milieu that promotes tumour growth. As such 3D co-cultures may serve as a more complex and valid biological model in the drug discovery pipeline.

3D Imaging of Organisms, Tissues and Cells

LS5.070
SRμCT of mineral distribution and its changes during the moult cycle of the terrestrial crustacean Porcellio scaber

A. Ziegler[1], F. Neues[2], J. Janáček[3], M. Epple[2]

[1]University of Ulm, Central Facility for Electron Microscopy, Ulm, Germany
[2]University of Duisburg-Essen, Inorganic Chemistry, Essen, Germany
[3]Academy of Sciences of the Czech Republic, Institute of Physiology, Prague, Czech Republic

andreas.ziegler@uni-ulm.de

The terrestrial isopod *P. scaber* moults first the posterior and less than 24 hours later the anterior half of the body (Fig. 1 A,B). This biphasic moult cycle allows for shifts of calcium carbonate between the anterior and posterior half of their exoskeleton during moult related storage and recycling of amorphous calcium carbonate [1]. We used synchrotron radiation microcomputer tomography at a voxel size of 3.8 µm to obtain serial images from resin embedded specimens of *P. scaber* in the intermoult stage and various moulting stages. Segmentation of skeletal elements was performed using the minimal cut module implemented in the Ellipse (ViDiTo) image analysis software. The relative degree of mineralisation for distinct anterior and posterior skeletal elements was calculated from the number and grey levels of voxels above a threshold value. Greylevels in air as well as head width of the animals were used to normalize the data.

The results show that in intermoult animals the degree of mineralisation is similar and highest in the head, antenna, and tergites (Fig. 1 A, B) cuticle, whereas the mineralisation of the ventral cuticle is less than 75% and that of the pereopods (walking legs) less than 55% of that in the antenna. Since *P. scaber* has long legs and can run fast to prevent predation, less mineralized and thus lightweight cuticle in pereiopods likely serves to lower energy consumption during escape behaviour.

Comparison of relative changes of the mineral distribution in cuticle from different stages before moulting confirm the general decrease of mineral in the posterior, and increase in the anterior cuticle. Most pronounced is the increase of more than 100% in the anterior sternites (ventral cuticle), which serve as calcium carbonate reservoirs (Fig. 1 C). For the other anterior skeletal elements the increase is highest, with about 40%, in the head and anterior pereopods. Mineral within the hepatopancreas after moult suggests uptake of calcium carbonate from the exuviae that is ingested after the moult (Fig. 1 B). Maximum loss of mineral by 46% for the anterior and 43% for the posterior cuticle was derived from the values for the intermoult cuticle and exuviae. The highest decrease of 86% was observed for the anterior sternites; in anterior and posterior tergites and posterior pereopods the decrease was between 54 and 37%. Interestingly, the mineral in the anterior pereiopods decreases by 25% only, likely to maintain stability of the legs to allow for locomotion until moult of the anterior half of the body takes place. Differential demineralisation was observed in the head cuticle, in which the cornea of the complex eyes remains completely mineralised. After the posterior moult, the decrease of mineral in the anterior half of the cuticle is accompanied by an increase in the posterior cuticle. The time course of remineralisation of the cuticle suggests that part of the mineral from the anterior half is stored and recycled in the posterior cuticle. Differential mineralisation occurs within the new cuticle of the mandibles, which are partially mineralised before the old cuticle is demineralised and shed (Fig. 1 D). Likely this increases the stability of the new mandibles that are required to cut the old exuviae that is ingested immediately after moult.

1. Neues, F., Hild, S., Epple, M., Marti, O., Ziegler, A., 2011. Amorphous and crystalline calcium carbonate distribution in the tergite cuticle of moulting *Porcellio scaber* (Isopoda, Crustacea). J. Struct. Biol. 175, 10-20.
2. Supported by the DFG within the priority program SPP 1117, Zi 368/4-3 and Ep 22/16-3. We thank the HASYLAB and DESY for generous allocation of beamtime.

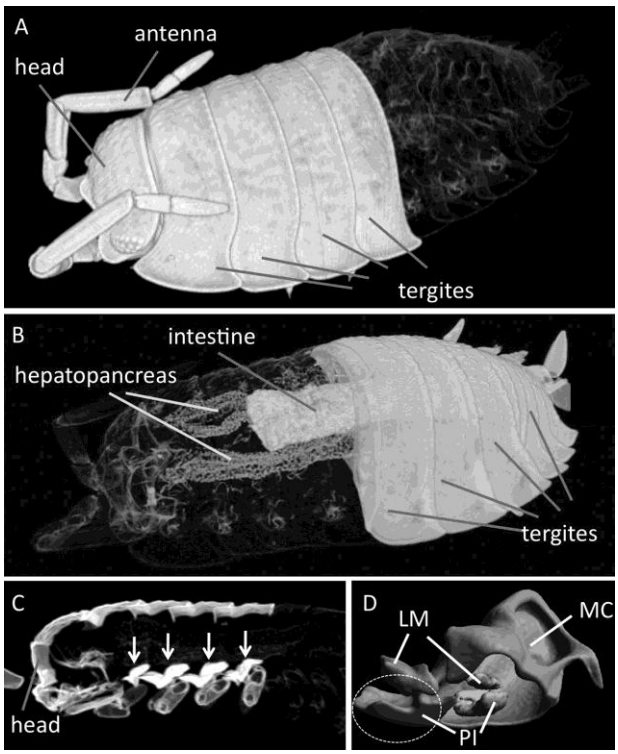

Figure 1. SRµCT of mineral distribution in the cuticle of *Porcellio scaber* after the posterior (A) and anterior (B-D) moult. (C) The anterior sternites (white arrows) serve as transitory calcium carbonate reservoirs. Before the anterior moult the new incisive edge (Pars incisive, PI) and the new lacinia mobils (LM) are mineralised within the old mandible corpus (MC).

3D Imaging of Organisms, Tissues and Cells

LS5.P071
3D reconstruction of the living cell interior from core information content of the brigheld optical microscopy

D. Stys[1], R. Rychtáriková[1], T. Náhlík[1]

[1]University of South Bohemia, Faculty of Fishery and Water Protection, Institute of Complex Systems, Nové Hrady, Czech Republic

stys@jcu.cz

The observation of "sub-resolution " objects using brightfield optical microscopy has been reported since late 1960 . The problem of definition of such objects in complex structures such as the living cell is our ability to discriminate these objects from the rest of the image. We use the topological definition of discriminability. Two objects are discriminable if there is an open sentence that is satised by at least for one of the elements of the one object and not by at least one of the element of the other object. Two objects are distinguishable if there is at least one open sentence which is satised for all elements of one of the objects and not satised for all elements of the other object.

We report here methods by which the location of the object is found by detailed analysis of consecutive images in the z-stack.We examine the change of the information in the image caused by the replacement of each of the pixels by a corresponding pixel from the next image. In the case that the information is unchanged, the point/object spread function indicates position of a large and homogeneous object. To the opposite the maximal information change, i.e. case when a large object gives place to a large object in the next image, usually indicates movement of an organelle. Any other combinations of intensities are typical indices of the point spread function behaviour. The approach may thus be understood as resolution of spatial discriminability of elementary diffracting objects in the living cell.

Detected objects may be placed in the space which gives rise to 3D model of the living cell. Separate use of colour channels of the camera brings also information about differences in optical properties of detected objects. Auto fluorescent objects are detected and analysed separately.

We shall describe technical hurdles accompanying the use of the method in a standard microscope and briefly inform about a new construction. There will be reported also technical differences between the optical microscope using modern lense optics and prototype microscope using reflector objective.

1. This work was partly supported by the Ministry of Education, Youth and Sports of the Czech Republic { projects CENAKVA (No. CZ.1.05/2.1.00/01.0024) and CENAKVA II (No. LO1205 under the NPU I program), by Postdok JU CZ.1.07/2.3.00/30.0006, and GAJU Grant (134/2013/Z 2014 FUUP).

Figure 1. By subtraction of consecutive images in the z-scan series may be obtained points whose position, diffraction properties and response at the camera screen remains the same between two positions in the optical path. Not necessary such information is obtained in the neighbourhood of the focus. The figure shows summary of such occasions. It reveals that objects of the size of one camera pixel - i.e. 35 nm in the given case - may be discriminated.

3D Imaging of Organisms, Tissues and Cells

LS5.P072
A new integrated solution for volume reconstruction of biological samples

M. Hovorka[1], F. Boughorbel[2], P. Potocek[2], P. Cernohorsky[1], L. Hekking[2], R. van den Boogaard[2], T. Janocko[1], E. Korkmaz[2], M. Langhorst[2], B. Lich[2]

[1]FEI, Brno, Czech Republic
[2]FEI, Eindhoven, Netherlands

milos.hovorka@fei.com

The Teneo VS SEM represents a new integrated solution for SEM (scanning electron microscopy) volume data acquisition based on a refined SBFSEM (Serial Block-Face SEM) technique [1]. A combination of hardware and software components allows for automatic data acquisition from selected regions of interest in resin embedded samples stained with heavy metals. The volume information is revealed by physical and/or virtual slicing depending on the required depth resolution and sample conditions. The pure SBFSEM mode is based on alternate slicing and backscatter imaging of the block-face. For virtual slicing a series of images of the exposed block-face is acquired using different accelerating voltages. By their proper selection different backscatter depth emission profiles are created. The collected images may serve as the input for a deconvolution algorithm that computes several subsurface layers. This approach is based on the MED-SEM (multi-energy deconvolution SEM) which is a non-destructive technique capable of high-resolution reconstruction of the top layers of the sample [2]. In the case of physical slicing the minimal slice thickness, and thus the depth resolution, is limited. Virtual slicing is capable of extending it towards the nanometer range and hence high-resolution isotropic datasets can be generated.

The Teneo SEM, in addition to a newly developed in-situ microtome and the reconstruction software form the key components of the workflow used to automatically acquire and process volume data on the different regions of interest. Data throughput depends on sample properties, the desired resolution, as well as on the detection module of the microscope. The Teneo SEM serves as the host tool providing high-resolution backscatter images both in HiVac and LoVac. The backscatter electron signal can be detected by in-column detectors or by a newly developed below the lens detector dedicated to LoVac operation. A compact automated ultramicrotome equipped with a diamond knife is mounted directly on the stage inside the SEM chamber. Easy switching between the dedicated tool and a normal SEM mode is straightforward. The complete workflow is controlled using a software package with a single user interface for setting up and monitoring the 3D acquisition process. Improved ease of use is facilitated through a set of advanced auto-functions for electron column alignment ensuring optimal image quality during data acquisition. These auto-functions include automated focus, contrast-brightness, stigmator, and position alignments for easy image registration etc.

1. B. Titze & W. Denk, Journal of Microscopy, vol. 250(2), pp. 101-110 (2013).
2. F. Boughorbel et al., SEM Imaging Method, Patent US 8,232,523 B2, 31st July 2012.

3D Imaging of Organisms, Tissues and Cells

LS5.P073
Differences between Arabidopsis thaliana chloroplast structures in lipid mutants and related ecotypes

J. Skupień[1], Ů Kowalewska[1], R. Mazur[2], J. Obrębska[1], M. Garstka[2], A. Mostowska[1]

[1]Univeristy of Warsaw, Faculty of Biology, Department of Plant Anatomy and Cytology, Warsaw, Poland
[2]Univeristy of Warsaw, Faculty of Biology, Department of Metabolic Regulation, Warsaw, Poland

j.skupien@biol.uw.edu.pl

The subject of this investigation is to find structural differences between chloroplasts of *Arabidopsis thaliana* mutants with a distorted lipid biosynthesis pathway, which is important for the formation and maintaining of plastid membranes, with the corresponding wild type Arabidopsis ecotypes. The aim of this work is to show the places of disturbance in thylakoid membranes which point the role of the relevant lipid. It is known that two classes of glycoglycerolipids: monogalactosyldiacylglycerol (MGDG), which constitutes around 50% of the total membrane lipids and digalactosyldiacylglycerol (DGDG) - around 30% of the total membrane lipids, are necessary for photosynthesis [1]. The mutant lacking MGDG, one of the most important lipid in the chloroplast membrane development, accumulates large amounts of DGDG and shows a strong defect in the chloroplasts biogenesis [1]. The analysis of the *mgd1* mutant as well as *dgd1* can shed light on their role in the grana formation. We choose the *mgd1* mutant and the *dgd1* for the structural reconstruction of the real membrane changes and compared them with the relevant ecotypes. Among 750 of *A. thaliana* ecotypes, which differ between each other with growth rate, grain size or susceptibility to light, the most common in the laboratory work is the Columbia variety and among it the *Col-0* and *Col-2* ecotypes used to construct the mutant *mgd1* and *dgd1* respectively. The reconstruction and the spatial models of chloroplasts in the fully developed leaves of both mutants and wild type *Arabidopsis thaliana* will be crucial in finding the places of disturbance. Three-dimensional structure of the thylakoid membrane arrangement was performed before on different species using both electron tomography and 3D CLSM modeling [2, 3].

For our investigation we took classical TEM pictures of the mesophyll chloroplasts of *mgd1* (Fig. 1) and *dgd1* (Fig. 2) mutants and the relevant ecotypes*: col 0* (Fig. 3) for *mgd1* and *col2* (Fig. 4*)* for *dgd1.* CLSM data were obtained using isolated living plastids. Collected image stacks were deconvolved and subsequently processed using a 3D imaging software to visualize the native structure of the chloroplast membranes. Structural changes were correlated with selected photosynthetic protein levels and chlorophyll-protein complexes composition.

Thylakoid membranes of chloroplasts of the *mgd1* mutant exhibit a strong disturbance of the grana and stroma thylakoids; swelling of the grana external thylakoids is the most pronounced feature (Fig. 1). The chloroplast images resemble chloroplasts affected by an oxidative stress. As opposed to the *mgd1* chloroplasts the *dgd1* chloroplasts (Fig. 2) seem to have a normal ultrastructure with well-preserved grana and stroma thylakoid membranes as well as the chloroplast envelope membranes, also they resemble chloroplasts of the appropriate control ecotype (Fig. 4).

This study reports a part of larger investigation aimed to find the structural role of the relevant lipids and their interactions in mature chloroplasts and during the chloroplast biogenesis.

1. Kobayashi K. et al. Plant J., 73 (2013) 250-261
2. Austin J.R., and Staehelin A. Plant Physiol., 155 (2011) 1601-1611
3. Daum B. and Kuhlbrandt W. J. Exp. Bot. 62 (2011) 2393-2402
4. The project granted on the decision number DEC-2014/13/B/NZ3/00413 by the National Science Centre.
5. TEM images were performed in the Laboratory of Electron Microscopy, Nencki Institute of Experimental Biology on JEM 1400 (JEOL Co. Japan) electron microscope. This equipment was installed within the project sponsored by the EU Structural Funds: Centre of Advanced Technology BIM - Equipment purchase for the Laboratory of Biological and Medical Imaging.

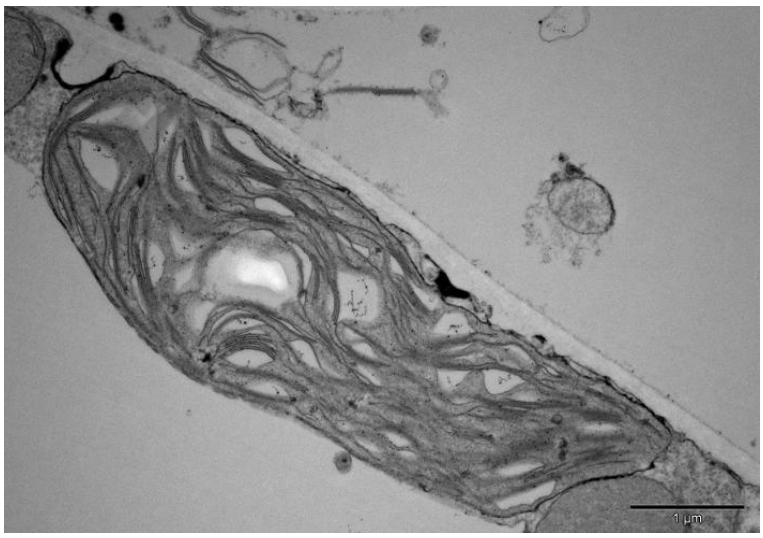
1 µm

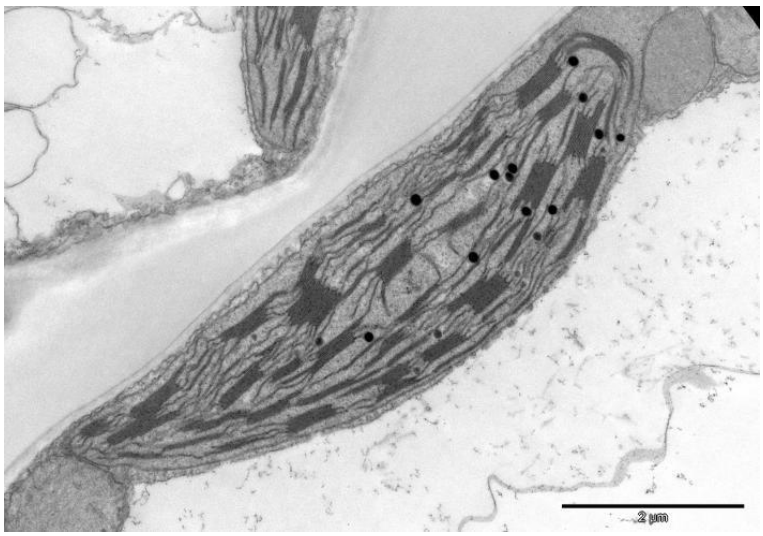
2 µm


1 µm

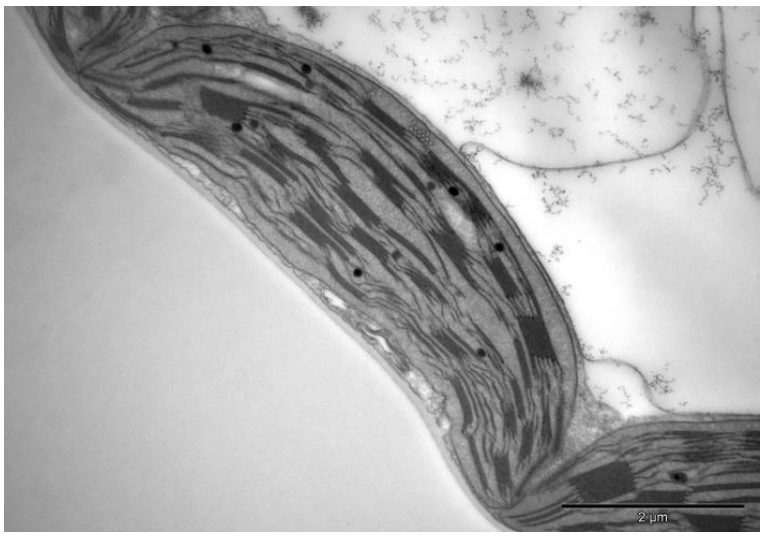

Figures 1 - 4. TEM images of mesophyll chloroplasts of *mgd1 (*Fig. 1) *and* of *dgd1* (Fig. 2) mutants and of the relevant ecotypes*: col 0* (Fig. 3) for *mgd1* and *col2* (Fig. 4*)* for *dgd1.*

3D Imaging of Organisms, Tissues and Cells

LS5.P074
Using serial block face scanning electron microscopy (SBF-SEM) to investigate maturation and heterogeneity of inner hair cell ribbon synapses

S. Michanski[1], R. Chakrabarti[1], C. Fischer[2], C. Wichmann[1]

[1]Institute for Auditory Neuroscience & InnerEarLab, Göttingen, Germany
[2]Johann-Friedrich-Blumenbach Institute for Zoology, Göttingen, Germany

susann.michanski@gmail.com

Hearing in mammals relies on cochlear inner hair cells (IHCs) that are specialized for detecting mechanical vibration of their stereocilia deflection, caused by sound pressure waves, and for converting this mechanical stimulus into an electrical signal by ribbon-typed synapses. Synaptic ribbons are electron dense structures that tether numerous synaptic vesicles (SVs) and transmit signals by Ca^{2+}-dependent exocytosis of glutamate at the presynaptic active zone (AZ) to spiral ganglion neurons (SGNs). The position of individual synapses within a single IHC has been suggested to be of great importance: as indicated for the cat, synapses containing large or even multiple ribbons seem to drive low spontaneous rate neurons, localized mainly at the neural side of IHCs, whereas small synapses are preferentially situated at the abneural side and are most likely driven by high spontaneous rate neurons [1]. Interestingly in mouse IHCs, heterogeneous excitatory postsynaptic current (EPSC) shapes and amplitudes were described. Several candidate mechanisms for release have been proposed: the variability might be a result of multi- or, as it has been recently introduced, uniquantal release of SVs at IHC ribbon synapses [2,3].

Synaptic ribbons undergo several morphological and functional changes upon maturation. Before the onset of hearing IHCs fire spontaneous Ca^{2+}-dependent action potentials, while mature IHCs generate graded receptor potentials in response to sound stimuli [4]. This stimulation of the auditory pathway in the immature stage is supposed to be essential for the Ca^{2+}-sensitivity and normal ribbon development [4,5]. Structurally, ribbon synapses increase in size, while their number decreases. Further, the ribbon shape strikingly changes from round before onset of hearing to predominantly oval after hearing onset and ribbons become more connected to the AZ [6].

For mice, a detailed analysis of the correlation between position and morphology of ribbon synapses within one individual IHC is still lacking. Moreover, it is still not well understood, how such a heterogeneity is established during development.

We use serial block face scanning electron microscopy (SBF-SEM) combined with transmission electron microscopy (TEM) and pre-embedding immunogold labeling to investigate heterogeneity and maturation of IHC ribbon synapses. Here, we will present first 3D reconstructions of the basal region of IHCs and their SGNs using SBF-SEM to systematically correlate between the location of SGNs and attributes like the fiber diameter, postsynaptic density (PSD) and ribbon size as well as number of ribbons per AZ. Furthermore, we present a detailed ultrastructural analysis of IHC ribbon maturation by examining different developmental stages before and after onset of hearing.

1. Merchan-Perez A & Liberman MC (1996) Ultrastructural differences among afferent synapses on cochlear hair cells: correlations with spontaneous discharge rate. J Comp Neurol, 371(2):208-21.
2. Chapochnikov NM et al. (2014) Uniquantal Release through a Dynamic Fusion Pore Is a Candidate Mechanism of Hair Cell Exocytosis. Neuron, 83(6):1389-403.
3. Glowatzki E & Fuchs PA (2002) Transmitter release at the hair cell ribbon synapse. Nature Neuroscience, 5:147-54.
4. Johnson SL et al. (2013) Presynaptic maturation in auditory hair cells requires a critical period of sensory independent spiking activity. PNAS, 110(21):8720-25.
5. Safieddine S, El-Amraoui A, Petit C (2012) The Auditory Hair Cell Ribbon Synapse: From Assembly to Function. Annual Review of Neuroscience, 35(1):509-28.
6. Wong AB et al. (2014) Developmental refinement of hair cell synapses tightens the coupling of Ca^{2+} influx to exocytosis. TheEMBOJournal, 33(3): 247-64.

3D Imaging of Organisms, Tissues and Cells

LS5.P075
Comparative study of SEM based 3D imaging methods on heart tissue: FIB-SEM tomography versus EsB imaging of serial sections versus STEM imaging of serial sections

B. Schroeppel[1], S. Röhler[1], P. Fallier-Becker[2], G. Frommer-Kaestle[2], R. Knittel[2], U. Kraushaar[1], C. J. Burkhardt[1]

[1]NMI Natural and Medical Sciences Insititute, Reutlingen, Germany
[2]University of Tuebingen, Institute of Pathology and Neuropathology, Tuebingen, Germany

birgit.schroeppel@nmi.de

3D imaging methods in light and electron microscopy are gaining more and more importance for life science application [1, 2]. To obtain such 3D datasets in electron microscopy, different approaches evolved over the last few years. The methods available for serial electron imaging of stained embedded biological samples in an SEM are FIB-SEM tomography [3, 4], serial thin sectioning and imaging in backscattered image mode, progressively automated regarding sectioning and / or imaging [5-7] or high-precision microtomes within a scanning electron microscope enabling serial block face imaging [8]. They developed due to the capabilities of modern scanning electron microscopes. These instruments provide good resolution in the nm range in low kV mode and new detectors for energy selected backscattered electron images to achieve a good contrast on heavy metal stained biological samples.

Conventional thin sectioning and imaging in a TEM still provides higher resolution, but is much more time consuming, especially for larger areas and volumes. A compromise between achievable resolution and necessary effort is the combination of conventional thin sectioning via microtome and imaging in transmission mode via STEM detector in a SEM [9]. Compared to 3D imaging methods based on backscattered electron images, transmission mode in a SEM offers better resolution due to higher primary electron energy (e.g. 30keV) and small working distances obtainable (e.g. 1mm). Additionally, navigation and orientation on the sample is easier in a SEM compared to a TEM and the number of grids that can be loaded to the SEM chamber at once is higher as in a TEM. As the STEM detector in a SEM offers bright field and dark field imaging mode, the images obtained are similar to conventional TEM images.

Compared to blockface based 3D imaging methods like FIB-SEM tomography or cutting with a microtome within a SEM, serial thin sectioning methods are not destructive. Thus archiving of the samples and re-imaging and analysing if necessary is possible. Furthermore, serial thin sectioning and mounting on an appropriate holder provides the opportunity of post-staining of the sections increasing the obtainable contrast.

In this study, three methods for 3D image acquisition are performed to compare the achievable results. (i) FIB-SEM tomography, (ii) serial thin sectioning, mounting on a conductive but electron opaque holder and imaging in low kV mode using backscattered electrons and serial thin sectioning and (iii) mounting on conventional TEM grids and imaging in transmission via STEM are all processed on a Crossbeam platform (Zeiss Auriga 40) enabling direct comparison of the methods. Therefore, heart tissue (mouse and rat) is chemically fixed, stained and embedded in a conventional way. 3D image stacks are taken by the methods and 3D volumes are reconstructed by Fiji. The pros and cons of the different methods are discussed regarding parameters like resolution and achievable volume size but also taking into account practical criterion such as time requirements, handling and costs.

1. J. M. Lucocq et al, Trends in Cell Biology, February 2015, Vol. 25, No.2
2. J.L. Morgan, J.W. Lichtman, Nat. Methods 2013, 10(6): 494-500
3. C. Villinger et al, Histochem. Cell Biol 2012, 138:549-556
4. G. Knott et al, J. Vis. Exp. (53), e2588
5. M. Lucas et al, Methods Cell Biol. 2012, 11: 325-356
6. R. Schalek et al, Micros. Microanal. 17 (Suppl. 2), 2011
7. K.J. Hayworth et al, Frontiers in Neural Circuits, 2014, 8, 68
8. W. Denk, H. Horstmann, PLOS Biology, 2004, 2(11), e329
9. M. Kuwajima et al, PLOS ONE, 2013, 8(3)

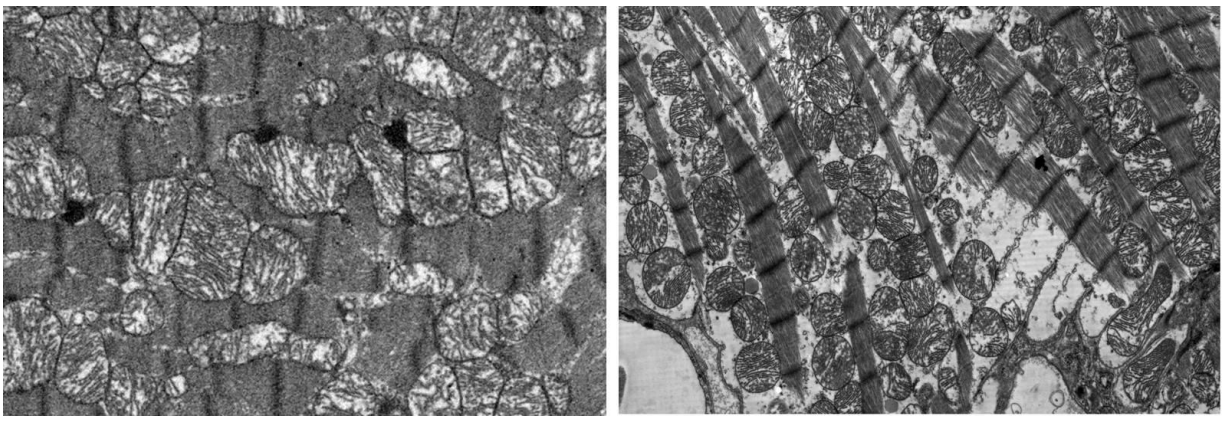

Figure 1. FIB-SEM blockface image (EsB detector, left side) and thin setion image (STEM detector, right side) aquired in a Crossbeam instrument with a pixel size of 15nm respectively 11nm; for comparison the EsB image was inverted and contrast and brightness were enhanced.

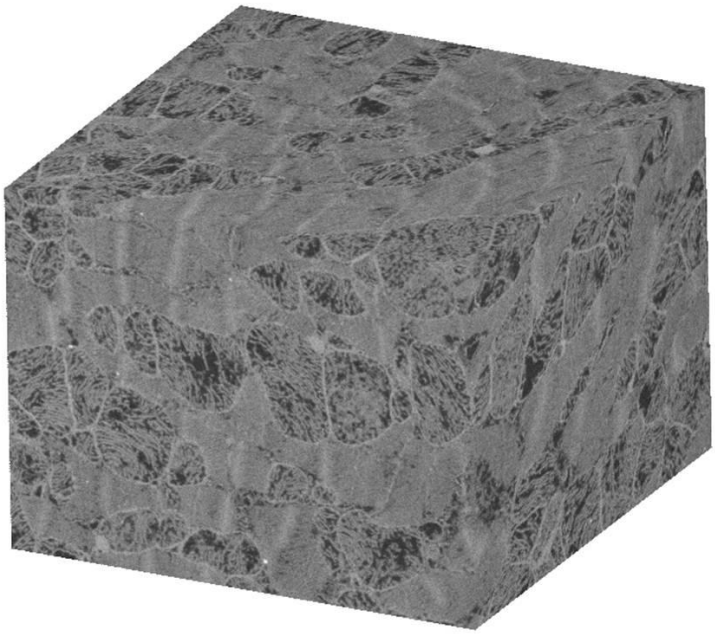

Figure 2. 3D FIB-SEM tomography of mouse heart tissue showing regular voxel size and good alignement in x,y and z direction.

3D Imaging of Organisms, Tissues and Cells

LS5.P076
Using optical projection tomography for 3D visualization of nerve microarchitecture

E. Cvetko[1], M. Capek[2], B. Radochova[2], M. Damjanovska[3], T. Stopar Pintaric[3], M. A. Reina[4], I. Erzen[1]

[1]Institute of Anatomy, Faculty of Medicine, University of Ljubljana, Ljubljana, Slovenia
[2]Institute of Physiology CAS, Prague, Czech Republic
[3]Clinical Department of Anaesthesiology and Intensive Therapy, University Medical Centre Ljubljana, Ljubljana, Slovenia
[4]Department of Clinical Medical Sciences and Applied Molecular Medicine, CEU San Pablo University School of Medicine, Madrid, Spain

erika.cvetko@mf.uni-lj.si

Nerve injury resulting from a peripheral nerve block is a rare but serious complication which can result in permanent neuropathy[1]. Intraneural injections are considered a major risk factor, however, not all intraneural injections lead to neurological complications[2]. The reason may be related to the microarchitecture of the peripheral nerve.

Up to now, nerve structure has been studied using histological methods. Their major limitation was the use of 2D imaging techniques for the reconstruction and evaluation of 3D nerve structures. This is time-consuming, difficult and has not been performed on the peripheral nerve to date.

The more recent development of optical projection tomography (OPT)[3] has provided a novel platform for studying microstructures in 3D. The method requires the tissue to be optically cleared[4] in order to allow light to pass through the object. It is based on acquiring sets of optical projections of the specimen within a scope of view of 360° and the subsequent calculating of the 3D image using tomographic reconstruction.

The objective of this study was to evaluate the ability of optical projection tomography to discern the nerve microarchitecture and injection injury in 3D. Five piglets were studied, whose median and lingual nerves were, post mortem, unilaterally injected with pre-set volumes of local anaesthetic, excised and subsequently cleared with BABB and finally captured in 3D. The same contralateral nerves were used as controls.

For acquisition of specimens we used a custom-made OPT machine which was developed in cooperation with the Politecnico di Milano, Italy and installed in the Institute of Physiology CAS in Prague. The specimens were acquired using an excitation wavelength of 405 nm and emission wavelengths from 550 nm with a high pass filter. 3D reconstructions were created using NRecon and analyses were done using DataViewer sw, both of which are available online (skyscan.be).

Using OPT we were able to visualize the outer and inner epineurium, the fascicles with their interconnections, and the perineurium. The fascicles were found loosely packed in the median nerve (Fig. 1A) and more densely so in the lingual (Fig. 1B). The inner epineurium was abundant in the median nerve and scant in the lingual. In the lingual nerve, the perineurium of most of the fascicles was in close contact and attached to the outer epineurium whereas, in the median nerve, the fascicles were separated from the outer epineurium by the inner epineurium. Therefore, using OPT, we confirmed the differences between the two nerves in their diameters, number and the diameter of their fascicles, as well as in the ratio of neural to non-neural tissue, as seen in Figure 2.

Five nerve specimens from the injected median and lingual nerves were analysed in order to test the ability of OPT to discern the injection injury. Immediately after injection, the median nerve was found to have expanded extensively, with its diameter approximately twice the size of that before injection. The OPT demonstrated the fascicles were only displaced with the consequent distension of the outer epineurium. The needle entry point and path were not demonstrated (Fig. 3A). In the lingual nerve, however, we could clearly identify the needle entry point and path, and the disruption to the fascicles with the focal disruption of the outer epineurium (Fig. 3B).

Thus, we conclude that OPT can be used with advantage for studying nerve microarchitecture topography and its tolerance to injection injury.

Supported by the Czech Science Foundation (13-12412S), AMVIS (LH13028), the Slovenian Research Agency (N° P3 0043) and the tertiary funds (N° 20110329) of the Clinical Department of Anaesthesia and Intensive Therapy, University Medical Centre Ljubljana.

1. Brull R, McCartney CJ, Chan VW, El-Beheiry H. *Anesth Analg.* 2007; **104**: 965-74.
2. Morau D, Levy F, Bringuier S, et al. *Reg Anesth Pain Med.* 2010; **35**: 559-64.
3. Sharpe J. *J Anat.* 2003; **202**: 175-81.
4. Zhu D, Larin KV, Luo Q, Tuchin V. *Laser Photonics Rev.* 2013; **7**: 732-757.

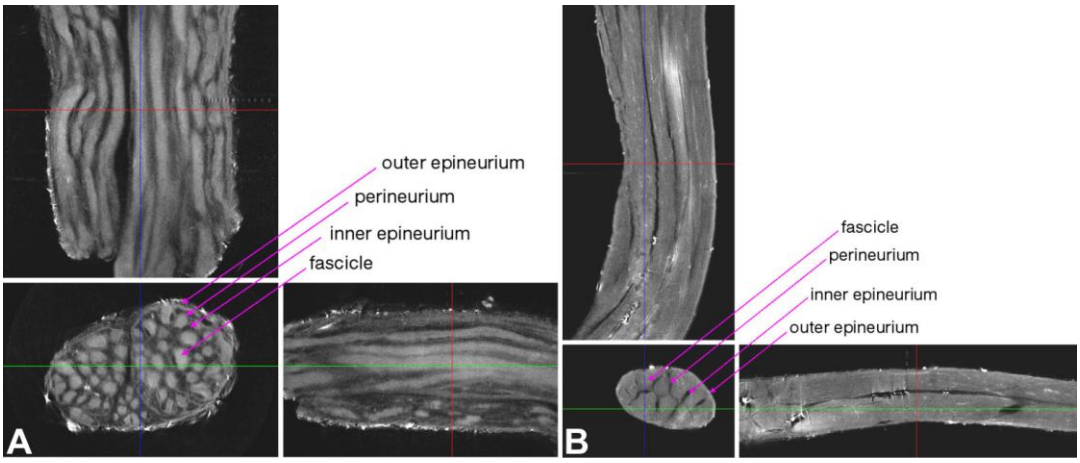

Figure 1. Microarchitectures of the non-injected median (A) and lingual nerve specimen (B), respectively, as seen in x-z, x-y and z-y planes.

	Area of neural tissue		Number of fascicles		Fascicle diameter	Nerve diameter	
	Absolute (mm^2)	Relative (%)	Mean ±SD	Range	mean±SD (mm)	mean±SD (mm)	Range (mm)
Median nerve	2.27±0.77	23.0	46.0±14.0	27-61	0.24 ±0.05	2.99 ±0.49	2.29-3.06
Lingual nerve	1.46±0.36	75.6	16.4.±16.1	7-45	0.40 ±0.10	1.56 ±0.15	1.48-1.83

Figure 2. Absolute and relative cross-sectional area of neural tissue, number (N) of the fascicles, diameter of the fascicles and nerve diameter in non-injected (control) median (N=5) and lingual nerve (N=5), respectively.

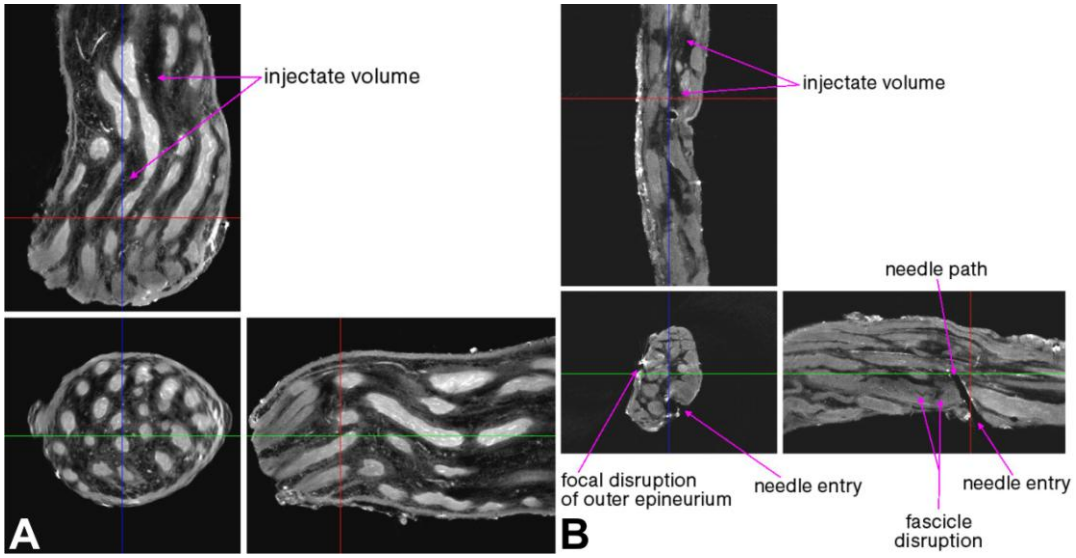

Figure 3. Microarchitectures of the injected median (A) and lingual nerve specimen (B), respectively, as seen in x-z, x-y and z-y planes.

3D Imaging of Organisms, Tissues and Cells

LS5.P077
Morfofunctional aspects of biological materials used in cardiovascular surgery

P. Karakozov[1], I. Baibekov[1], B. Ibadov[1]

[1]Center of surgery, pathology, Tashkent, Uzbekistan

baibekov@mail.ru

A number of native and preserved biological materials used in clinical and experimental cardiovascular surgery have been examined **(**in vitro**)**. The pericardium, diaphragm, broad fascia, dura mater, liver capsule, atriums walls, latisimus dorsi muscle, heart valves, main vessel walls of adults and fetuses of human and animals, used as free plasty or neuro-vascular pedicle flaps, were studied. Interaction between biological materials and biological tissues in various periods after their implantation into man's and experimental animal's cardiovascular system (in vivo) were also studied. The methods of scanning and transmission electron microscopy, light microscopy of stained histological and half-thin sections were used.

The research showed considerable differences in structure and spatial orientation of connective tissue framework as well as microrelief of their surface which represented by folds consisting of furrows and ridges of various sizes, shapes and directions. At the same time folds of three types are found: type I are formed by connective tissue constructions; type II are formed by endothelial and methoteial layers; type III folds are formed by nuclei and microvilli of endotheliocytes and methoteliocytes. Each of the studied biological materials has its specific morfofunctional characteristics which change in the process of sterilization and preservation. It affects the microrelief, influencing on the local blood flow after the biological material implanted into the cardiovascular system. These differences in the considerable range determine different results of biomaterials usage, with or without complications typical for implants. Alteration of the local hemodynamic of the reconstruction zone leads to thrombosis or microthrombosis of biological tissue. Thrombi organization contributes to disorganization of used biological tissue and further to its fibrosis and sclerosis. Accordingly, biological prosthesis microrelief must maximally correspond with microrelief of surrounding tissues, being reconstructed.

Initial morfofunctional characteristic of biological materials, their embryological origin and correspondence to the new conditions of existence and the level of preservation of all structural components after implantation are the maim factors affecting the biological grafting results. The distinct interconnection between three-dimensional histological architecture and the biological material function was revealed. Along with this, the more structural organization of spatial architectonic of biological tissue, including its surface microrelief, is close to the such in the reconstructed areas of cardiovascular system, the better are the results of intervention and the less specific complications ensue.

Thereby the structural peculiarities of the biological tissues are one of the determining factors of their adequate functioning and must be taken into consideration in selecting biological materials for using them in cardiovascular surgery. Meeting these requirements will prevent from disorganization of connective tissue structures and extend the adequate functioning period of biological prostheses, to reduce the level or risk of clinical complications specific of implants, including disturbance of local hemodynamic, thrombosis or microthrombosis.

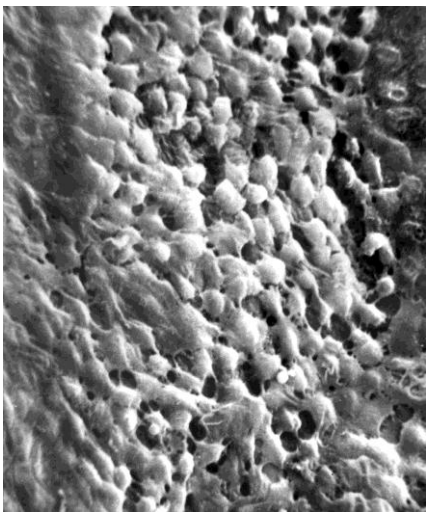

Figure 1. Origin human diaphragm tedious part. Abdominal surface. SEM. x200.

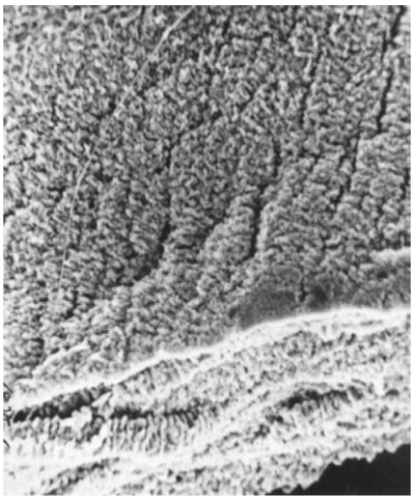

Figure 2. Origin bovine pericardium inner surface. SEM. x 60

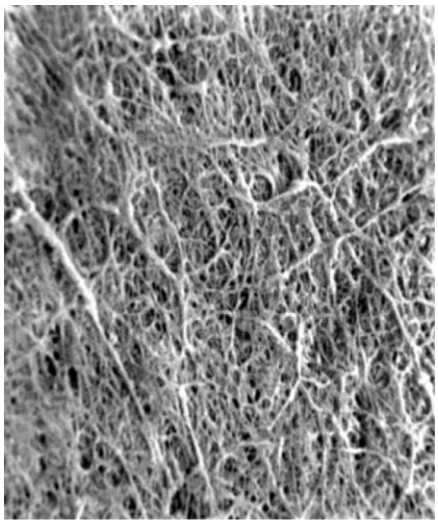

Figure 3. Bovine glutaraldehyde preserved pericardium inner surface. 14 days after implantation in man's interatrial position (ASD repair). SEM.x100.

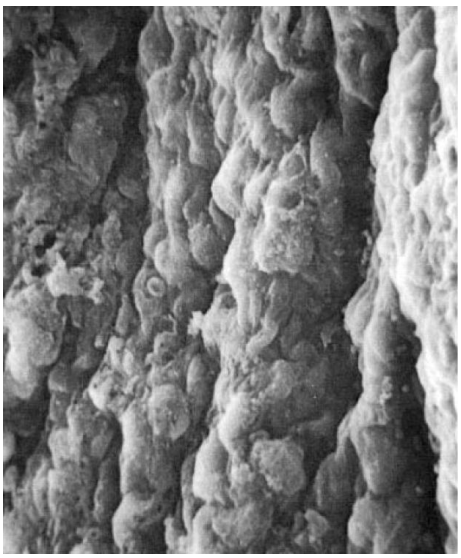

Figure 4. Bovine glutaraldehyde preserved pericardium inner surface. 7 days after implantation in man's interventricular position (VSD repair). SEM.x1000.

3D Imaging of Organisms, Tissues and Cells

LS5.P078
The name-bearing ghosts from the past

P. Dominiak[1], M. Rychłowski[2]

[1]University of Gdańsk, Department of Invertebrate Zoology & Parasitology, Gdańsk, Poland
[2]Intercollegiate Faculty of Biotechnology UG-MUG, Intercollegiate Faculty of Biotechnology UG-MUG, Gdańsk, Poland

patrycja.dominiak@biol.ug.edu.pl

The types, the most precious and most important specimens are at heart of taxonomic investigation. These name bearing specimens, usually kept in the museum collections, are highly desirable and staple in many taxonomical research, especially those concerning redescription of the species and determination of the valid names. However, sometimes the type specimens cause troubles. Many unfortunate things can happen to the types. They can be lost, destroy or they can just get... invisible.

Our study concerned the type materials of various species of biting midges (Diptera: Ceratopogonidae) described by J. J. Kieffer in 1915, and housed in the collection of the Zoological Museum, University of Copenhagen (Denmark). Presently, the taxonomic status of most of them is still unclear and the species should be revised and redescribed. However, it is impossible because of very bad condition of the type specimens. The materials examined were cleared in potassium hydroxide or solution of phenol and absolute alcohol, and subsequently mounted on microscope slides in the mixture of Canada-balsam and phenol. It is a standard procedure but appeared to be insufficient in this case. All of these type materials were teneral specimens, killed shortly after the adults emerged, and stored in alcohol for over 100 years. What are the consequences of such treatment? The morphological structures are barely visible because of the presence of muscles and fat body which could not be removed, or in the contrary, whole specimens are totally transparent and nearly ‘invisible’ on the slides. We investigated the usefulness of a confocal laser scanning microscopy (CLSM) for the study of the type specimens difficult to identify using a light microscopy. The fully three dimensional reconstructions allow to capture of morphology of the structures of diagnostic value, including important characters in male genitalia. The CLSM has been successfully used in insect taxonomy for many years, also for examining the museum specimens. We tried to apply this technique for the type specimens in very poor condition, not stained, and already mounted on the microscope slides.

3D Imaging of Organisms, Tissues and Cells

LS5.P079
Visualization of vascular bed of human normal heart

P. Karakozov[1], I. Baibekov[1], B. Ibadov[1]

[1]Center of surgery, pathology, Tashkent, Uzbekistan

baibekov@mail.ru

The microrelief of inner surface of normal human heart coronary vessels has been studied. The methods of scanning electron microscopy, light microscopy of stained histological and half-thin sections were used. The microvessels basins of both coronary arteries of man's normal heart with the zones of blood supplying of atria, ventricles, atrial and ventricular septa have been also studied. The method of scanning electron microscopy of corrosion preparations was used.

Our research showed that heart coronary arteries and veins microrelief was represented by folds of various size and shape, located mainly along the long axis of the vessels. The microrelief components are formed by endothelial layer of intima and its connective tissue elements. The connective tissue constructions and muscle fibers of media take partial part in microrelief formation. At the same time folds of three types are found: type I are formed by curves of connective tissue constructions of intima and media; type II are formed by endothelial and subendothelial layers; type III folds are formed by the nuclei of endotheliocytes. The microrelief nature considerably changes according to the vessels caliber and their type, while its spatial orientation remains unchanged. The differences of endothelial layers and type endotheliocytes, and to the grater extent the nature of underlying structures determine the differences in the microrelief of heart coronary arteries and veins. Plenty of chiomicrons of various sizes and at different integration level can be defined on the endothelial surface, in the intercellular fissures and deeper located parts of vessels. It reflects intensive myocardial metabolism.

Spatial orientation and microrelief features determine local hemodynamics in these parts, which in turn, determines the corresponding morphological structure.

It was found that microcirculatory bed significantly differs in various parts of heart. First of all it concerns the quantity of microvessels in a unit of volume, the quantity of anastomoses among them, the nature and spatial orientation of network formed by them. The caliber of microvessels is less variable, though microvessels of various calibers can be found in same zone. Walls of heart ventricles are the most rich in microvessel networks having large and small loops, oriented along their long axis and having multiple anastomoses. The networks of thick vessels are more abundant in the sinus parts of ventricles. The microcirculatory bed is poorer with the less quantity of anastomoses in the outflow tracts. In the left atrium microcirculatory bed is more definite than in the right one. Orientation of the microvascular nets in the free walls of atrium corresponds to the long axis of atria. A lot of blindly ended microvessels can be found in the atrial auricles. Ventricular and atrial septa are characterized by nets having small loops without distinct orientation, with moderate quantity of anastomoses and microvessels blindly ended.

Every part of man's myocardium is distinguished with peculiar, specific microcirculatory bed connected in a more or less degree with the rest parts of heart. The spatial orientation of microcirculatory bed depends on functional peculiarities of a particular part of heart.

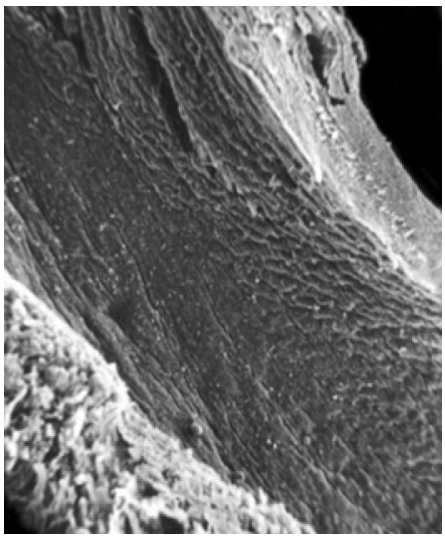

Figure 1. The main left coronary artery wall inner surface. SEM. x500.

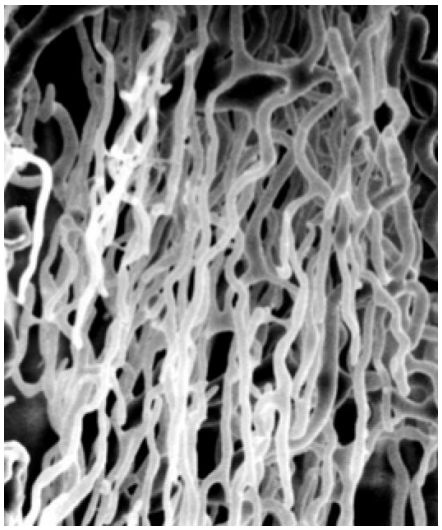

Figure 2. The left ventricle free wall microvessels.. Corrosion preparation. SEM. x500

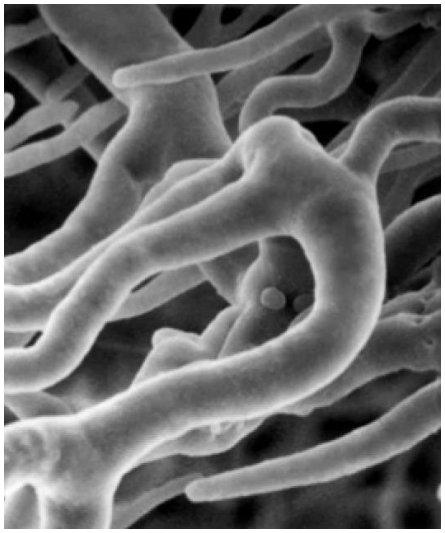

Figure 3. The left atrium free wall microvessels. Corrosion preparation. SEM. x1000.

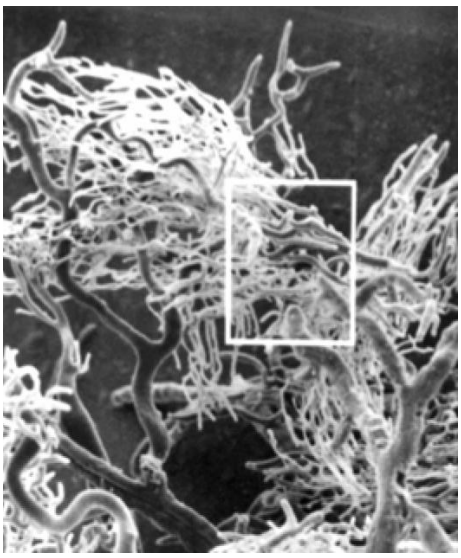

Figure 4. The left ventricle wall microvessels. Transition zone of sinus to outflow part. Corrosion preparation. SEM. x250.

3D Imaging of Organisms, Tissues and Cells

LS5.P080
3D visualization of TEM image data - beech chloroplasts size and shape variability

B. Radochova[1], J. Janacek[1], M. Capek[1], Z. Lhotakova[2], L. Kubinova[1], J. Albrechtova[2]

[1]Institute of Physiology CAS, Department of Biomathematics, Prague, Czech Republic
[2]Faculty of Science, Charles University in Prague, Department of Experimental Plant Biology, Prague, Czech Republic

b.radochova@seznam.cz

Chloroplasts are semiautonomous organelles characteristic for plant cells. In the process called photosynthesis they harvest light and convert CO_2 to organic carbon while producing oxygen from water. In seed plants, chloroplasts are usually disk-shaped and measure between 4 and 6 µm in diameter [1]. They can be observed easily in light microscopes, but their inner structure is usually examined using transmission electron microscopy (TEM). For TEM analysis, ultrathin sections (usually 70-100 nm) are used, which limits the extent of three-dimensional (3D) structural information gathered from them. Therefore to visualize chloroplasts in 3D, several microscopy techniques are used, including serial sectioning. The serial sectioning technique is based on the acquisition of TEM images from serially cut standard ultrathin sections that are subsequently aligned and visualized. Even though the resolution in the z-axis is limited, this method is useful for visualization of both chloroplast shape and rough spatial organization of its internal structures.

In the present study, we used the serial sectioning technique for 3D visualization of the chloroplasts from beech (Fagus sylvatica L.) leaves sampled at the experimental site Bílý kříž (Beskids Mts., Czech Republic). Samples were chemically fixed, processed using microwave tissue processor and embedded into Spurr´s epoxy resin. Images from 60 serial sections were acquired from the same part of palisade parenchyma tissue, using JEOL JEM-1010 microscope. At first the images were registered by rigid motions minimizing correlation of subsequent images. Than the general nonrigid registration procedure using facultative discontinuous correspondence between images [2] was applied. Rigid registration and manual correction were implemented in PC program ImagReg1 and surface rendering and nonrigid registration was implemented as plug-in modules of program Ellipse (ViDiTo, Slovakia).

Chloroplasts and some parts of their inner structure (starch, plastoglobuli) were traced in registered series of images by interactive segmentation.

The present study revealed a great variability in size and shape of beech chloroplasts. The chloroplasts had irregular shapes and often formed chloroplast protrusions. Two main forms of these protrusions were found: first, they formed rather shallow pocket-like structures often containing mitochondria or microbodies; second, they occurred in form of thin sheet like structures, thus enhancing chloroplast surface area. Chloroplasts protrusions never contained thylakoids or starch, but sometimes small vesicles of inner envelope were seen.

This work was supported by the Czech Science Foundation (P501/10/0340 and 13-12412S) and by the Czech Academy of Sciences (RVO:67985823).

1. K. Esau, in “The Protoplast: Plasma Membrane, Nucleus, and Cytoplasmic Organelles”, R. F. Evert, Esau´s Plant Anatomy 3rd Ed, 2006, Wiley, New Jersey, pp. 15-43.
2. J. Janácek, in “Image registration by discontinuous correspondence calculated iteratively using graph cuts,” M. A. Pabst and G. Zellnig, Eds., Microscopy Conf. 2009, Graz, Austria, vol. 2, pp. 417-418.

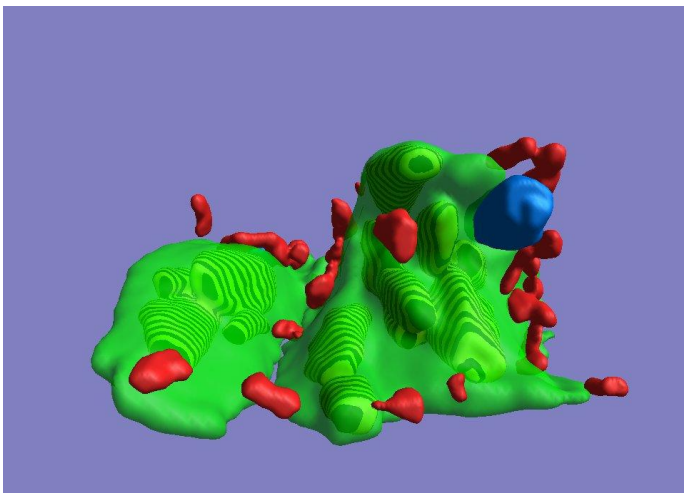

Figure1. 3D visualization of two chloroplasts from beech (Fagus sylvatica). Chloroplasts in green, mitochondria in red, microbodies in blue. Starch grains are visualized as hatched yellow structures inside of chloroplasts. (59 consecutive sections, 100nm thick.)

3D Imaging of Organisms, Tissues and Cells

LS5.P081
Three-dimensional microscopy of biopsies with a handheld confocal microscope

W. Piyawattanametha[1], S. Pattanasak[2]

[1]King Mongkut's Institute of Technology Ladkrabang, Electronics Engineering, Bangkok, Thailand
[2]Valaya Alongkorn Rajabhat University, Faculty of Science and Technology, Pathumthani, Thailand

wibool@gmail.com

Intravital single-axis confocal (SAC) microscope is a versatile tool in disease diagnosis enabling high-resolution three-dimensional (3-D) capability for imaging biological tissues. Its unique features are derived from a high numerical aperture (NA) lens to achieve high lateral resolution, and its optical sectioning property from a pinhole placed in front of the detector to reject out of focus light. Therefore, a high-resolution 3-D image from highly scattering media can be reconstructed by successively scanning each 2-D focal imaging plane. Nonetheless, SAC microscopes have trade-offs among resolution, field of view (FOV), and an objective size, since a high NA objective is needed for sufficient resolution, and a long focal length is needed for a large FOV and working distance (WD). The dual-axis confocal (DAC) microscope architecture has been proposed utilizing two low NA objectives providing overlapping long working beams circumventing above tradeoffs [1, 2].

Because of DAC post-objective configuration, it offers several advantages over the SAC architecture such as long WD, balance in all spatial resolutions (x-y-z), and enhancing both detection sensitivity and dynamic range [3]. Previously, MEMS-scanner-based DAC microscopes have been demonstrated in a tabletop setup [4], v-groove packaging mount [5], and clinical setup [6]. In this work, we present a handheld MEMS-scanner-based DAC microscope capable of 3-D real-time imaging for biopsy imaging. Figure 1a shows a 3-D schematic drawing of handheld DAC microscope.

The laser source is coupled into an input fiber collimator focused by a parabolic mirror and reflected outside packaging by a MEMS scanner. The scattered light from the sample returns to another side of a MEMS scanner and coupled back into a fiber collimator, which is fed to a data acquisition system with real-time display. Figure 1b shows a photograph of a mounted a two-dimensional MEMS scanner on a printed circuit board. The MEMS scanner scans the focused laser beam over an *en face* FOV.

All images are captured at 5-10 Hz with approximate maximum FOV of 700 x 260 mm^2. The acquired image in Figure 2a shows a US Air Force (USAF) resolution target of Group 7-6. It is also used as a sample to measure the image resolutions and FOV. The FWHM of transverse and axial resolutions are 5 um and 7 um, respectively. Figure 2b show a 3-D rendered image of a human colon biopsy.

We demonstrated a 3-D microscopy with a handheld confocal microscope in 10 mm diameter package for biopsy imaging. When coupled with fluorescence markers targeted against a variety of diseases, the handheld microscope will enable *in vivo* optical biopsy for early and accurate detection of cancer.

1. T. D. Wang, M. J. Mandella, C. H. Contag, and G. S. Kino, "Dual-axis confocal microscope for high-resolution *in vivo* imaging," *Opt. Lett.,* vol. 28, pp. 414-416, 2003.
2. T. D. Wang, C. H. Contag, M. J. Mandella, N. Y. Chan, and G. S. Kino, "Dual-Axes confocal microscopy with post-objective scanning and low coherence heterodyne detection," *Opt. Lett.,* vol. 28, pp. 1915-1917, 2003.
3. J T.C. Liu, M. J. Mandella , S. Friedland, R. Soetikno, J. M. Crawford, C. H. Contag, G. S. Kino, and T. D. Wang, *J. Biomed. Opt. 2006*;11:054019-1-10.
4. H. Ra, Y. Taguchi, D. Lee, W. Piyawattanametha, and O. Solgaard, "Two-Dimensional MEMS scanner for Dual-Axes Confocal *In Vivo* Microscopy," *MEMS 2006, IEEE Int. Conf. on Micro Electro Mechanical Systems*, Turkey, 2006, pp. 862-865.
5. W. Piyawattanametha, J. T. C. Liu, M. J. Mandella, H. Ra, L. K. Wong, P. Hsiung, T. D. Wang, G. S. Kino, and O. Solgaard, "MEMS Based Dual-Axes Confocal Reflectance Handheld Microscope for *in vivo* Imaging," in *IEEE Int. Conf. on Opt. Micro. Electro. Mech. Sys.*, Montana, Aug 21-24, 2006, pp.164-165.
6. W. Piyawattanametha, H. Ra, M. J. Mandella, K. Loewke, T. D. Wang, G. S. Kino, O. Solgaard, and C. H. Contag, "3-D Near Infrared Fluorescence Imaging using a MEMS-based Miniature Dual-Axes Confocal Microscope," IEEE JSTQE, vol. 15, no. 5, pp. 1344-1350, 2009.

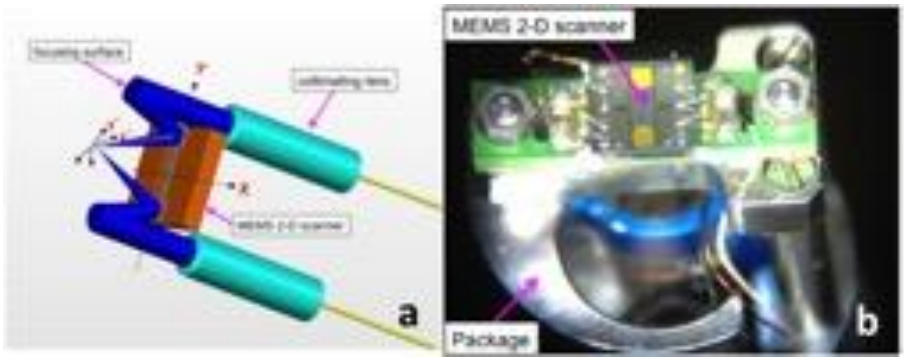

Figure 1.*a) A 3-D schematic drawing of DAC configuration. B) MEMS scanner mounted on a PCB on top a 10-mm package.*

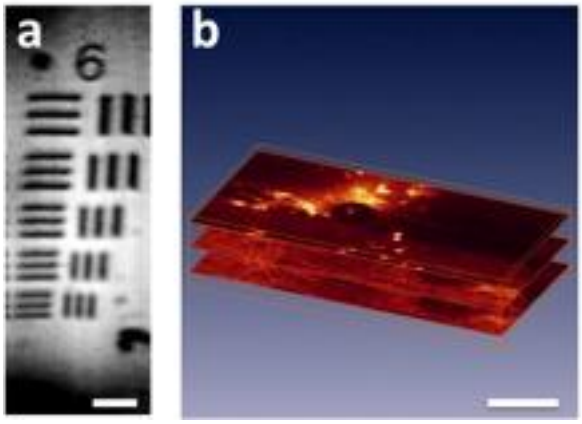

Figure 2. *a) A cropped 7-6 of USAF resolution target image with no frame averaging (scale bar 5 mm). b) A 3-D rendered image of a human colon biopsy tissue (scale bar 100 mm).*

3D Imaging of Organisms, Tissues and Cells

LS5.P082
The new Zeiss GeminiSEM Meets the needs of challenging biological applications

I. Angert[1], C. Berger[1], R. Kirmse[1], M. Edelmann[1], A. Thesen[1]

[1]Carl Zeiss Microscopy GmbH, Oberkochen, Germany

isabel.angert@zeiss.com

For studying structural properties and context of cells and tissue modern field emission scanning electron microscopy (FE-SEM) techniques get increasingly important. Widely used applications are imaging of tissue by serial block face or array tomography methods (AT) [1,2]. In serial block face imaging a thin layer of the embedded sample is removed either mechanically or with a focused ion beam. Afterwards the fresh block face is imaged. In contrast for AT serial sections of the sample are produced in advance and mounted on. silicon wafer or glass. The individual sections are investigated in the FE-SEM afterwards. The imaging modes can vary from secondary electrons (SE) and back scattered electrons (BSE) detection to scanning transmission electron microscopy (STEM). Optimum resolution and contrast, surface sensitivity, control of sample charging as well as optimizing the data acquisition for high-throughput imaging are prerequisites for biological imaging with best performance.

The new ZEISS GeminiSEM500 meets these challenges with an improved low kV performance offering optimal resolution across the entire voltage range and a new variable pressure (VP) concept for using in-lens detection. In addition GeminiSEM features a broad detector portfolio covering efficient parallel in-lens SE and energy selective backscattered (EsB) detection, backscatter detection on a five sector diode detector and STEM detection on a diode based detector with real annular design (aSTEM).

Here we show a variety of application examples that highlight the benefits of the new system. The new low kV lens in the GeminiSEM 500 enables optimum resolution without biasing the stage (e.g 1.1 nm @ 1 kV, 1.2 nm @ 500V). Lower electron energies are particularly important for blockface imaging or nano-tomography to avoid beam damage of deeper layers that will be exposed next. Using the new Zeiss backscattered detector even at 1.5 kV enables the detailed structural investigation of biological tissue with optimal contrast (Fig. 1A). Even at 50 V surface structures can be resolved in great details as shown at the example of an uncoated moth wing (Fig. 1B). Using such extremely low energies even the most challenging non-conductive samples can be investigated without charge accumulation. At higher beam energies structures below the surface can be reached. With the new NanoVP mode the pressure in the specimen chamber can be adjusted from 1 to about 150 Pa and a differential pumping aperture reduces the scattering of the electrons in the gas allowing in-lens detection (Fig. 1C) without considerable loss of resolution and increasing VPSE detection efficiency.

Transmission imaging mode in the scanning electron microscope (STEM) is a widely applied method for imaging transmissible samples often resulting in higher resolution than classical SE or BSE imaging mode [3]. The ZEISS aSTEM detector provides excellent contrast and dynamic range (Fig. 1D) and allows bright-field (BF), annular dark-field (DF) and high-angle annular dark-field (HAADF) detection. The detail that can be obtained in STEM mode is close to the limit in the amount of detail that can be expected from conventionally prepared, chemically fixed and plastic embedded samples.

1. P Schneider et al. Bone 49 (2011) p. 304-311.
2. M Kuwajima et al., PLoS One 8(3): e59573. (2013)
3. KD Micheva and SJ Smith, Neuron 55 (2007) p. 25-36.

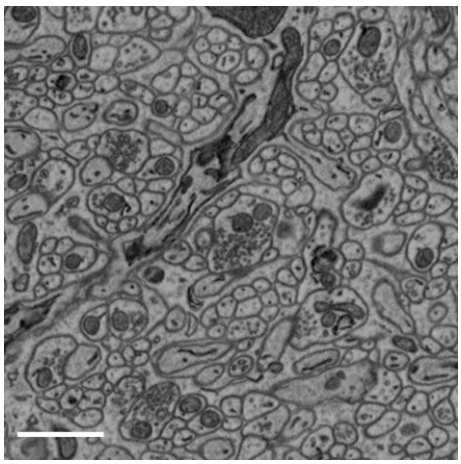

Figure 1. Image of brain tissue with a backscattered detector at 1.5 kV primary energy with 10 nm pixel size, scale 1µm.

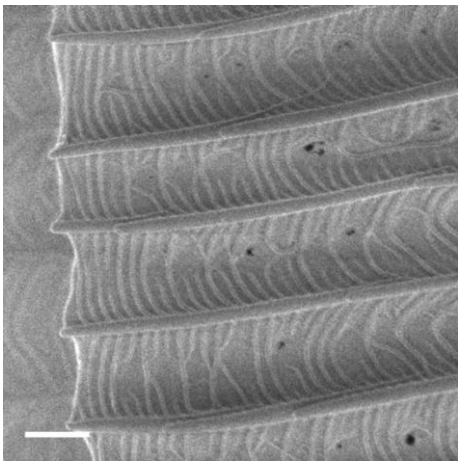

Figure 2. Uncoated moth wing imaged at 50 eV with in-lens detection. This shows highest surface sensitivity and imaging of non-conductive samples, scale 1µm.

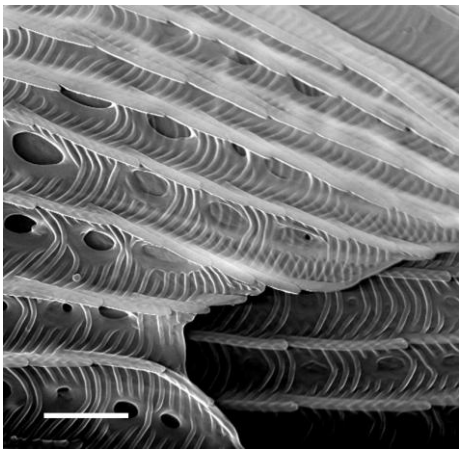

Figure 3. Uncoated moth wing imaged at 20 keV with in-lens detection. With the nanoVP mode the pressure at the sample was set to 100 Pa, scale 1 µm.

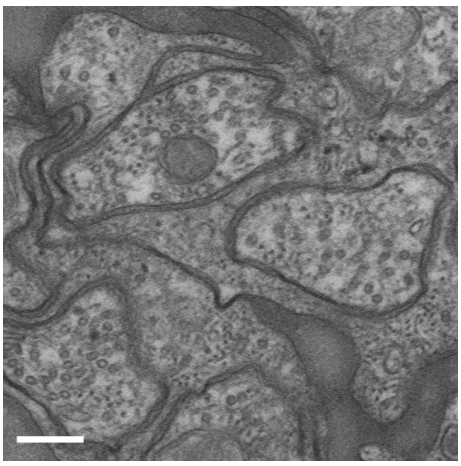

Figure 4. STEM image of brain tissue at 28 kV in BF mode, scale 200 nm.

3D Imaging of Organisms, Tissues and Cells

LS5.P083
Structural characterisation of the silk of two-spotted spider mite Tetranychus urticae Koch (Acari: Tetranychidae)

S. Doğan[1], î Çırak[2], M. Çağlar[1], B. Çağlar[1,3]

[1]Erzincan University, Biology, Erzincan, Turkey
[2]Erzincan University, Physics, Erzincan, Turkey
[3]Erzincan University, Chemistry, Erzincan, Turkey

salihdogan_tr@yahoo.com

Two-spotted spider mite, *Tetranychus urticae* Koch, is amongst of the most damaging of mite pests of ornamental plants, vegetables and many fruit trees. *T. urticae* silk roles are relatively better studied, but its physical and chemical features are poorly known, and silk web architecture is still unexplored. Some structural properties of the silken threads produced by *T. urticae* individuals in different gender are examined by using the atomic force microscope (AFM), scanning electron microscope (SEM) and energy dispersive X-ray spectrophotometer (EDX) in this study. This work contributes to define some physical and chemical features of *T. urticae* silk.

1. Clotuche, G., Goff, G.L., Mailleux, A.-C., Deneubourg, J.-L., Detrain, C., Hance, T. 2009. How to visualize the spider mite silk? Microscopy Research and Technique, 72, 659-664.
2. Hudson, S.D., Zhurov, V., Grbić, V., Grbić, M., Hutter, J.L. 2013. Measurement of the elastic modulus of spider mite silk fibers using atomic force microscopy. Journal of Applied Physics, 113 (154307), 1-7.
3. Shatrov, A.B. 2014. Phenomenon of silk production in water mites (Acariformes, Hydrachnidia). In: Microscopy: advances in scientific research and education (Méndez-Vilas, A. (Ed.). Formatex, 538-544.
4. Siri, S., Maensiri, S. 2010. Alternative biomaterials: Natural, non-woven, fibroin-based silk nanofibers of weaver ants (*Oecophylla smaragdina*). Int. J. Biol. Macromol. 46, 529-534.

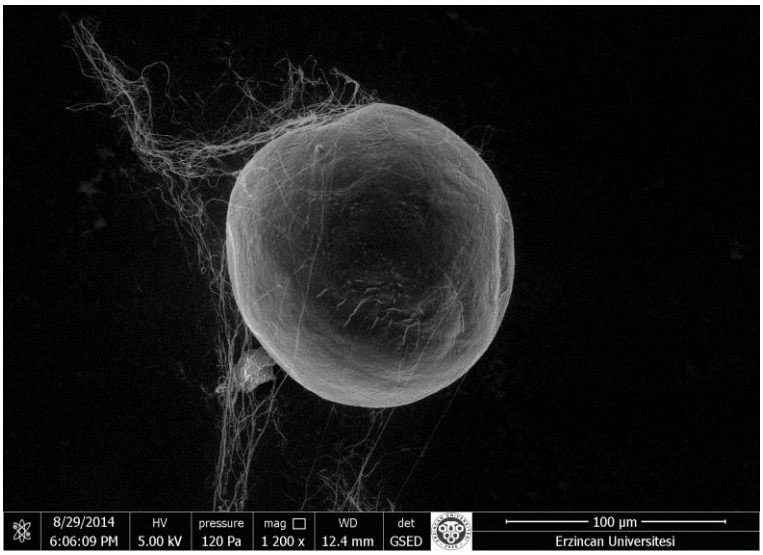

Figure 1. Scanning electron micrograph of *Tetranychus urticae* egg and silk.

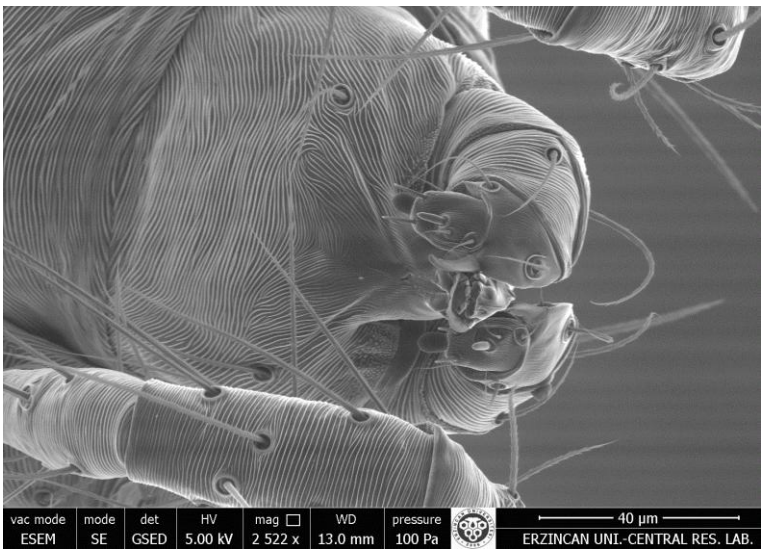

Figure 2. *Tetranychus urticae* Koch (female). Scanning electron micrograph of palp.

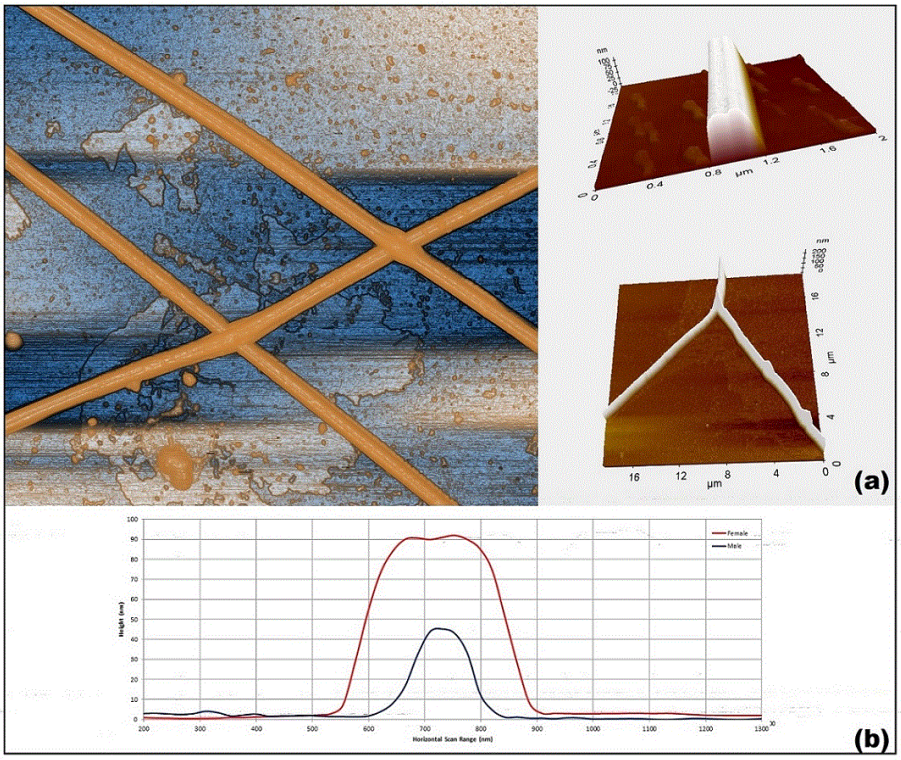

Figure. 3. (a) 2D/3D AFM images of female *Tetranychus urticae* silk fibre; **(b)** Topographic plots of the female and male mites silk.

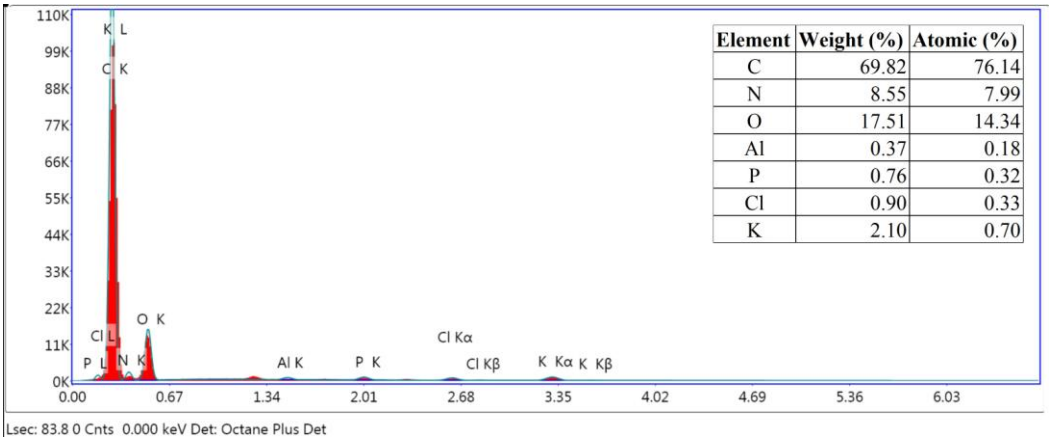

Element	Weight (%)	Atomic (%)
C	69.82	76.14
N	8.55	7.99
O	17.51	14.34
Al	0.37	0.18
P	0.76	0.32
Cl	0.90	0.33
K	2.10	0.70

Figure 4. EDX analyse of *Tetranychus urticae* silk.

3D Imaging of Organisms, Tissues and Cells

LS5.P084
3D-imaging and analysis of neural networks using combined 3D-EM approaches

M. Scheungrab[1], P. Guder[1], K. Schulze[1], K. Boergens[2], A. Gour[2], M. Helmstaedter[2], G. Wanner[3], M. Heß[1]

[1]Biozentrum LMU Munich, Biology II, Planegg-Martinsried, Germany
[2]Max Planck Institut für Hirnforschung, Frankfurt, Germany
[3]Biozentrum LMU Munich, Biology I, Planegg-Martinsried, Germany

maximilian.scheungrab@campus.lmu.de

The vertebrate retina - area sensor as well as imaging computer - opens up the window to the photic environment and thus it is an organ essential for survival for visually oriented organisms. Notwithstanding detailed knowledge about its principal architecture since Cajal (~1900), the complete structural elucidation of a representative volume of interest (VOI) of the neural network got possible only recently (see e.g. Helmstaedter et al. 2013, Nature 500: 168). Not until the consequent application of 3D electron microscopy (3D-EM) combined with computer-aided segmentation and surface rendering data sets can be created, that allow for the acquisition of all cells contained in the VOI over their entire extend (many µm) with a resolution that reveals even the finest dendritic ramifications and synaptic fine structures in the cable mess of plexiform layers (few nm/px). Perfectly aligned 3D-EM data - if necessary combined from different imaging methods - permit the isolation of any cell, morphotype classification, analysis of areal abundance, shape of dendritic fields, (co)stratifications, cell-type specific synaptic contacts (i.e. wiring rules), and display in any perspective and constellation.

We investigated the retina of the European anchovy (2-channel polarization vision instead of color vision) with a most regular pattern of cone pedicles in the outer plexiform layer (OPL). The tissue was stained either with Os and U (standard for TEM, satisfactory for FIB) or additionally with Fe and Pb (OTO-staining for 3View) and embedded in epoxy resin. The cell axes were oriented appropriately (Mesa technique) and cut/imaged with three different 3D-EM methods: classical serial sectioning transmission electron microscopy (ssTEM Jeol JEM1230, 140 slices, VOI 60 x 125 x 10 µm) and two modes of serial block-face scanning electron microscopy (BFSEM), based on (A) focused ion beam milling (FIB Zeiss Auriga, 5600 planes, VOI 24 x 20 x 145 µm) and (B) mechanical sectioning (3View + FEI Quanta, 1003 planes, VOI 60 x 155 x 30 µm). Combined approaches (FIB + ssTEM or 3View) were undertaken with cutting planes oriented 90° to each other. The TEM images were elastically aligned using Fiji: (a) compensation of lens aberration with the module bUnwarpJ and (b) block matching with the module TrakEM2. All data stacks were aligned, manually segmented (partly for months) and surface rendered with Amira®.

All three 3D-EM techniques provided gapless fine structural data sets in generic quality: (1) ssTEM - best contrast and XY-resolution (5 nm/px), Dz = 70 nm, large VOI, serious image distortions, extremely time-consuming; (2) FIB - standard EM staining yields sufficient contrast, XY-resolution 8 nm/px, best Z-resolution: 8 nm, small VOI, no distortions. (3) 3View - special contrasting required for reasonable contrast and minimization of charging, XY-resolution 12 nm/px, Dz = 30 nm, large VOI, no distortions. Detailed reconstruction of the OPL was only possible using FIB data, numerous bipolar and some horizontal cells were contained in the VOI. Most amacrines and ganglion cells, however, exceeded the boundaries of the small FIB VOI (single field of view). These cells can be entirely covered by the larger VOIs of ssTEM and 3View, both allowing the stitching of several neighboring scanning fields.

A comprehensive analysis of neural networks showing all cells involved and considering all (or most) of their synaptic contacts is possible using 3D-EM, whereas the advantages of BFSEM by far outmatch ssTEM. For extremely fine neuropils FIB with its isotropic resolution of down to 5 nm/px is the means of choice. The small field of view could be overcome by the Zeiss Atlas system - limited access, high scanning costs and limited long time scanning stability remain problematic. Scanning of larger VOIs can be managed best with 3View (or comparable machines) if a XY-resolution of 10-12 nm/px and Z-resolution of 25-30 nm is not undercut. In the case of the inner retina it became apparent that a combined approach is most expedient, scanning the OPL with FIB and the more vitreal parts with 3View.

Sample Preparation Methods and Strategies

LS6.085
Large-scale EM ("nanotomy") and correlative microscopy

B. N.G. Giepmans[1]

[1]Dept. Cell Biology, University Medical Center Groningen, The Netherlands

b.n.g.giepmans@umcg.nl

Microscopy has gone hand in hand with the study of living systems since van Leeuwenhoek observed living microorganisms and cells in 1674 using his light microscope. A spectrum of dyes and probes now enable the localization of molecules of interest within living cells by fluorescence microscopy. With electron microscopy (EM), cellular ultrastructure has been revealed. Bridging these two modalities, correlated light microscopy and EM (CLEM) opens new avenues [1]. The first focus will be on recent developed labeling strategies for molecules that allow CLEM. These include particles (gold, quantum dots) to highlight endogenous proteins, but also genetically-encoded probes [2], as well as traditionally used stains for light microscopy that aid in EM-analysis of samples. Probes that can only be detected in a single modality, and require image overlay, as well as combinatorial probes that can be visualized bot at LM and EM will be discussed.

In addition, new approaches for large scale EM ("nanotomy"), either TEM-based [3] or S(T)EM-based [4,5], to visualize macromolecules and organelles in the context of organized cell systems and tissues will be highlighted. Matching the areas of acquisition in CLEM and EM will not only increase understanding of the molecules in the context, but also is a straight forward manner to combine the LM and EM image data. Covering a wide variety of probes and approaches for image overlay will help to enable (new) users to implement CLEM to better understand how molecules (mal)function in biology.

1. De Boer et al. (2015) CLEM: Ultrastructure lights up! *Nature Methods* 12:503
2. Kuipers et al. (2015) FLIPPER for CLEM. *Cell & Tissue Research* 360:61
3. Ravelli et al. (2013) Destruction (…) in T1D rats at macromolecular resolution. *Scientific Reports* 3:1804
4. Sokol et al. (2015) Nanotomy of blistering diseases. J*. Investigative Dermatology* 135:1763
5. Kuipers et al. (2015) Sample prep for SEM-based immunolabelling and nanotomy. *Exp. Cell Res. in press*
www.nanotomy.org

Sample Preparation Methods and Strategies

LS6.086
Dedicated (cryo) sample preparation for 3D SEM life science applications

R. Wepf[1], M. Lucas[1], A.-G. Bittermann[1], M. Günthert[1], F. Lucas[1], P. Gasser[1]

[1]ETH Zurich ScopeM, Zurich, Switzerland

roger.wepf@scopem.ethz.ch

In the EM-community, it is generally accepted that the quality of the sample, the sample preparation history, has a direct impact on the quality, validity and value of the microscopy and microanalysis results. Nevertheless, many of us struggle with their specific sample or local available instrumentation to follow the best possible so-called “silver bullet” pure cryo-solutions.

Most sample preparation methods for cellular and molecular structural biology have been originally developed for small volume (cryo) TEM investigation. With the improvement over the last 15 years in SEM technology, e.g in resolution, detection efficiency and extension to real manipulating workstation, there is a strong tendency to adapt such protocols for HR-(FIB)SEM structure research applications. Mainly since SEM offers much more flexibility to automatize imaging and investigate structures at a much larger 3D volume then TEM does.

In this review we will focus on the discussion of sample preparation workflows, their impact on the final structure, their advantage, limitations and potentials for 3D structure research by high-resolution SEM investigations. We will also discuss novel approaches towards optimizing and standardizing sample preparation, such as semi-automatic sample handling by microfluidic techniques, MEMS based techniques and others, for macromolecular as well as for cellular and tissue 3D-SEM investigations.

Time for evaluating the quality of sample preparation, the image quality, content and finally the extraction of meaningful structural data have become as important and more time consuming as the time spent for sample preparation and imaging. Accepting the limitations of sample preparation methods and hence their applications area calls for an open and general discussion of the quality of these methods within the community to enhance our validity and acceptance among structural biologist. The time of “artifact” research, myth of interpretation and expertise, has to be overcome for the next generation of microscopist by establishing an “open-source” repository for protocols. This has become even more of importance, since modern publisher/Journal strategies avoid such discussions and exposure of “best practice” and “tips&tricks” in an open user discussions format, as it is well know by the “Wipkipedia” publishing concept.

Sample Preparation Methods and Strategies

LS6.087
Advanced tool for ultramicrotomy: substrate holder and multi-axis manipulator

W. Spomer[1,2], A. Hofmann[1,2], I. Wacker[3,2], L. Ness[4], P. Brey[4], R. R. Schröder[5,2], U. Gengenbach[1,2]

[1]Karlsruhe Institute of Technology (KIT), Institute for Applied Computer Science, Karlsruhe, Germany
[2]HEiKA, Heidelberg Karlsruhe Research Partnership, Heidelberg, Germany
[3]Universität Heidelberg, Cryo EM, Centre for Advanced Materials, Heidelberg, Germany
[4]RMC Boeckeler Instruments, Tucson, Arizona, United States
[5]Universitätsklinikum Heidelberg, Cryo EM, Centre for Advanced Materials, Heidelberg, Germany

spomer@kit.edu

For reconstructing the nano-scale structure of large volumes array tomography (AT) is an established method. Compared to other methods it preserves sample sections and thus enables correlative imaging: The same sample can be examined by different imaging modalities, such as light microscopy (LM) and electron microscopy (EM) [1].
Applying correlative imaging requires the substrate to be conductive (for EM) and also transparent (for LM) like glass coverslips coated with indium tin oxide (ITO). Before imaging the samples are cut in ultrathin sections and collected as ribbons floating on the surface of a water filled knife trough. While sectioning is done by the ultramicrotome the collecting step is still a tedious, manual handling process and requires a human operator. Generally the user holds the substrate in one hand while manipulating the ribbon with the other. Substrates being held by hand may be affected by tremor - a major difficulty for perfectly aligned ribbons. This also prevents placing more than one ribbon on the substrate. The first concepts to support the operator in this task were described in literature as early as the 1960s [2]. From time to time several devices holding the substrate are presented, one of the latest is described in [3]. Unfortunately these concepts do not allow adapting to all desired knife orientations because they are lacking the required degrees of freedom. As the sample is very rarely mounted in parallel with the knife edge nowadays microtomes offer a yaw axis for knife rotation to align the block-face. This enables to produce usable sections right from the beginning of the sectioning process. The substrate, held by a fixed holder, remains in its orientation while the knife is rotated with respect to the microtome. This is critical for substrates using the full width of the knife trough: If the knife is being realigned the substrate may collide with the sides of the trough. Thus a substrate holder with an adaptation for rotated knifes is desirable.

Once the sections have been pinned to the substrate surface another aspect becomes important: the lift-up movement of the substrate from the trough. A lift-up trajectory actuating several axes simultaneously reduces ribbon damage. In these two aspects the substrate holders proposed so far fall short.

To overcome these limitations and increase reliability we developed a novel, multi-axis device, which supports the operator in transferring the sections onto a solid substrate such as ITO glass or silicon wafer respectively. Its seven degrees of freedom (Fig. 1A) allow positioning the substrate in different orientations, using the lower axes, as well as different lift-up movements, using the upper axes (Fig. 1B). For coarse adjustment the substrate holder provides two axes in x/y-direction and for the rotation about the z-axis a rotary stage to fit rotated knifes. For smooth movements with minimal water turbulence lift-up involving two axes at the same time avoids ribbon drift and ribbon breaking. There are micro-positioning stages for fine positioning and height adjustment. Thousands of ribbons have been collected with the device presented here, even on challenging substrates with rough surface such as ITO-coated glass (Fig. 1C, cf. Wacker et al., this conference).

The authors acknowledge C. Bartels, L. Veith and R. Scharnowell for technical support, as well as the Heidelberg Karlsruhe Research Partnership (HEiKA) for initial funding.

1. K. D. Micheva, D. J. Smith, Neuron 55 (2007), p. 25-36.
2. O. Behnke, J. Rostgaard, Biotechnic & Histochemistry 39 (1964), p. 205-208
3. H. Horstmann et al., PLoS ONE 7 (2012), p. e35172

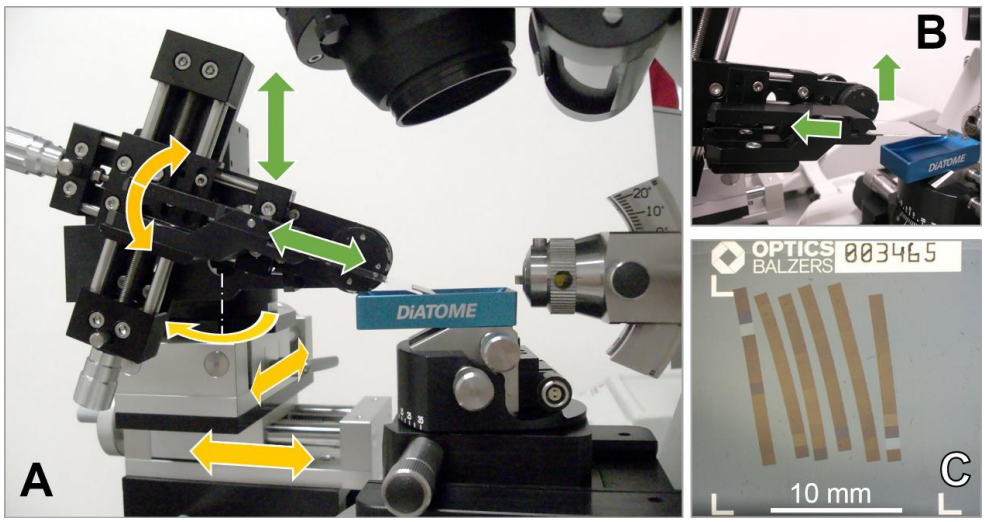

Figure 1. Typical ultramicrotome setup with substrate holder mounted in front of it, Arrows showing the adjustable axes for positioning (orange arrows) and lift up (green arrows) (A); Different possible lift-up movements (B); Ribbons on an ITO-coated glass coverslip collected with the device presented here (cf. Wacker et al., this conference) (C)

Sample Preparation Methods and Strategies

LS6.088
The HPM light µ: from live cell imaging to high pressure freezing in less than 2 seconds

X. Heiligenstein[1], J. Heiligenstein[2], M. Frei[3], M. Belle[2], C. Delevoye[1], I. Hurbain[1], J. Salamero[4], G. Raposo[1]

[1]Institut Curie, UMR144-Structure and membrane comparments, Paris, France
[2]CryoCapCell, Paris, France
[3]ABRA Fluid, Widnau, Switzerland
[4]Institut Curie, UMR144-Spatio-temporal modeling Imaging and cellular dynamics, Paris, France

xavier.heiligenstein@curie.fr

Correlative light and electron microscopy (CLEM) takes an increasing part in biological studies since a decade. The recent methodological developments have given the chance to most electron microscopists to step towards light microscopy and create the bridge between both modalities. Concomitantly, light microscopists express an increasing desire to connect with electron microscopy with the emergence of super-resolution approaches. The sample preparation becomes thereof the concern to unite both world. Electron microscopy long investigated the power of cryo-immobilization to prepare the sample in a close to native state. Out of all the solutions employed, High Pressure Freezing (HPF) has been acknowledge as the most suitable to cryo-immobilize bulk samples up to 400 µm. The CryoCapsule® (Heiligenstein et al., 2014) was developed to ease all sample manipulation required to conduct HPF sample preparation and is now routinely used in many groups. One critical step to conduct CLEM experiment using HPF remains unsolved: the sample transfer between the light microscope and the High Pressure Freezing machine. In order to correlate living specimens with the corresponding ultrastructure in the electron microscope the delay between light microscopy and freezing is critical.

We have developed a new High Pressure Freezer, associated to a state of the art light microscope that transfers the specimen automatically within less than 2 seconds to get as close as possible to the live specimen in a fully reproducible manner: the HPM Light µ. We collaborated with the manufacturer ABRA Fluid to design a new High Pressure Freezer based on the well proven core of the HPM010 (previously BalTec). Exploiting the CryoCapsule® as an advanced sample transfer shuttle, we designed an automated arm that maintains the specimen above the light microscope. At the end of the live cell data recording, the specimen is automatically transferred into the High Pressure chamber to be vitrified. The process happens in less than 2 seconds making it the fasted CLEM system in the world to date.

We will use this approach to investigate the process of pigmentation occuring in epidermal melanocytes, a specialized cell dedicated to melanin pigment production and responsible for skin pigmentation. Melanocytes exploit their endosomal system and associated machineries to generate a Lysosome Related Organelle (LRO), the melanosome, where melanin is synthesized and stored. Melanosome originates from early sorting endosome and matures through a sequential supply of melanogenic cargoes. The cargo delivery is a fast process that occurs within a few seconds (Delevoye et al., 2009). Using Alexa-labelled transferrin and GFP-tagged proteins involved in formation of endosomal carriers, we address the mechanism of cargo delivery to melanosomes that underlie the pathophysiology of albinism (Delevoye et al., 2014).

1. Delevoye, C., Hurbain, I., Tenza, D., Sibarita, J., Uzan-Gafsou, S., Ohno, H., Geerts, W.J.C., Verkleij, A.J., Salamero, J., Marks, M.S., et al. (2009). AP-1 and KIF13A coordinate endosomal sorting and positioning during melanosome biogenesis. J. Cell Biol. 187, 247–264.
2. Delevoye, C., Miserey-Lenkei, S., Montagnac, G., Gilles-Marsens, F., Paul-Gilloteaux, P., Giordano, F., Waharte, F., Marks, M.S., Goud, B., and Raposo, G. (2014). Recycling Endosome Tubule Morphogenesis from Sorting Endosomes Requires the Kinesin Motor KIF13A. Cell Rep. 6, 445–454.
3. Heiligenstein, X., Heiligenstein, J., Delevoye, C., Hurbain, I., Bardin, S., Paul-Gilloteaux, P., Sengmanivong, L., Régnier, G., Salamero, J., Antony, C., et al. (2014). The CryoCapsule: Simplifying Correlative Light to Electron Microscopy. Traffic 15, 700–716.

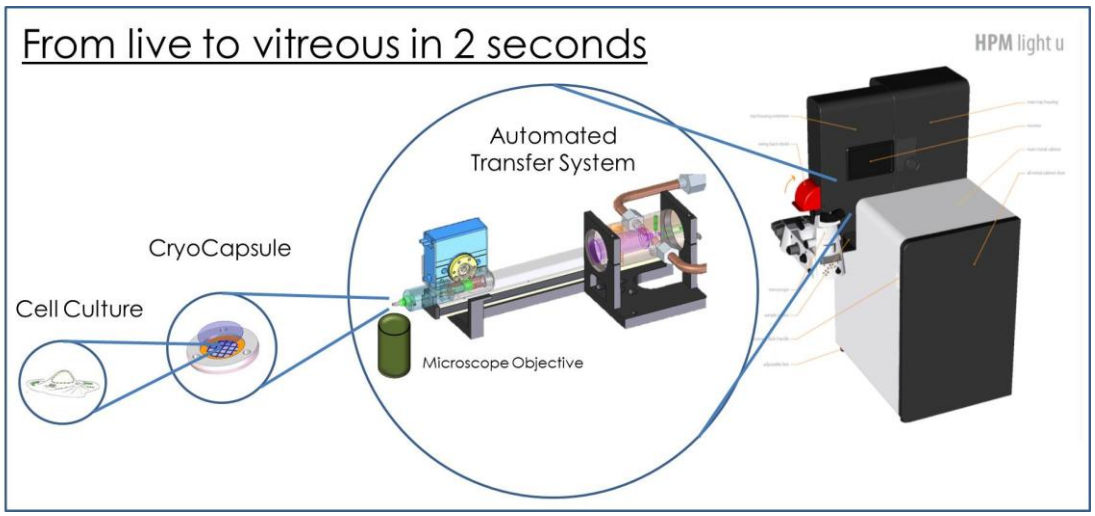
From live to vitreous in 2 seconds
HPM light u
Automated
Transfer System
CryoCapsule
Cell Culture
Microscope Objective

Sample Preparation Methods and Strategies

LS6.P071
Comparative sample preparation using focused ion beam and ultramicrotomy of human dental tissues for TEM imaging and analysis

K. Witzke[1], M. Frank[2], O. Specht[3], C. Lurtz[4], D. Behrend[4], P. Ottl[1], M. Warkentin[4]

[1]University Medicine Rostock, Department of Prosthodontics and Materials Science, Rostock, Germany
[2]University Medicine Rostock, Electron Microscopy Centre, Rostock, Germany
[3]Institute for Implant Technology and Biomaterials e.V., Rostock, Germany
[4]University of Rostock, Department of Material Science and Medical Engineering, Rostock, Germany

katharina.witzke@uni-rostock.de

There is an increasingly need to develop dental filling materials with structural compatibility to its corresponding human dental tissues. To obtain highest possible native structure information a cutting procedure of electron transparent samples without artifacts is necessary. Mineralized human dental tissues are highly filled biological composites, consisting of hydroxylapatite crystals forming nanofibrills, embedded in an organic matrix containing type-I collagen [1, 2]. In this methodological study TEM-sections prepared by Focused Ion Beam and Ultramicrotomy were systematically compared in detail by a combination of various microscopic examination methods.

Recently extracted intact maxillary and mandibular premolars without any carious lesions or fillings were examined. An interdisciplinary developed guideline in preparing mineralized human enamel and dentine for electron-microscopic visualization is presented. Data for evaluating TEM sample preparation were obtained by scanning acoustic microscopy (SAM), confocal laser scanning microscopy (CLSM), scanning electron microscopy (SEM) and transmission electron microscopy (TEM).

We demonstrate an In-Situ FIB Lift-Out specimen preparation of human dental tissues to produce high quality TEM-sections showing the ultrastructural configuration in detail. In addition ultramicrotome-induced artefacts are illustrated.

The described proceeding has strong potential for preparing mineralized biomaterials for TEM imaging and analysis.

1. Behrend, D.; Warkentin, M.; Specht, O.; Schmidt, W.; Rosentritt, M.; Ottl, P. (2011): Materialographical Investigations of Dental Materials. In: *Practical Metallography* 48 (1), S. 8-16. DOI: 10.3139/147.110115
2. Marshall, G. W. Jr.; Marshall, S. J.; Kinney, J. H.; Balooch, M. (1997): The dentin substrate: structure and properties related to bonding. In: *J Dent* 25 (6), S. 441-458.

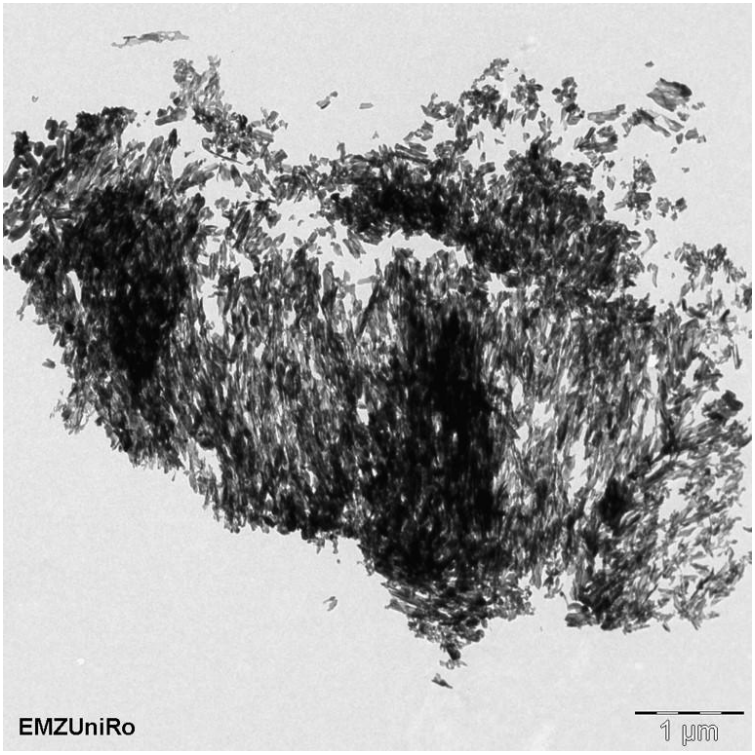

Figure 1. TEM micrograph of an ultramicrotome prepared enamel-section (scale 1 µm)

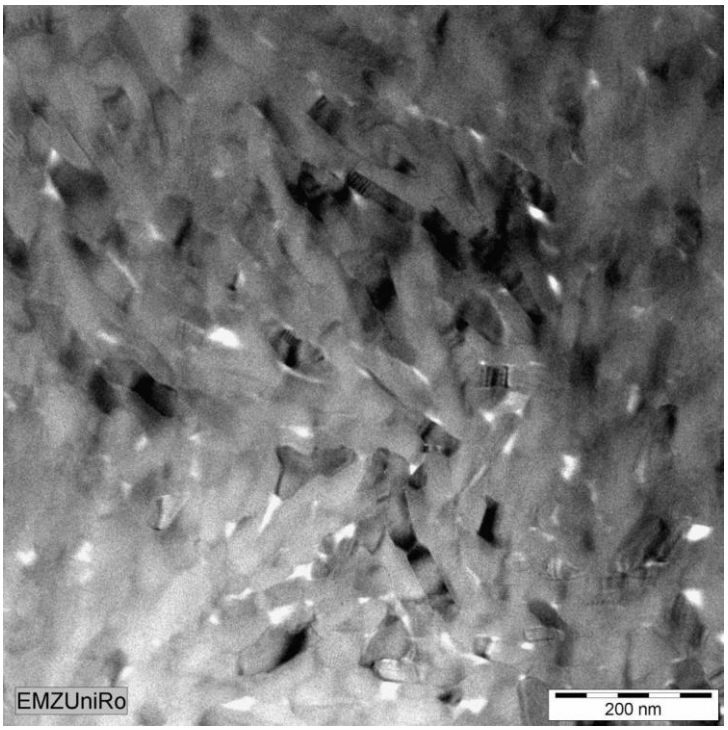

Figure 2. TEM image of In-Situ FIB Lift-Out prepared enamel (scale 200 nm)

Sample Preparation Methods and Strategies

LS6.P072
Effect of microtubule inhibitors on motility of 3T3 fibroblasts in the wound healing assay: high-throughput microscopic approach.

S. Kauanova[1], A. Balabiyev[1], I. Vorobjev[2]

[1]Nazarbayev University Research and Innovation System, Astana, Kazakhstan
[2]M.V. Lomonosov Moscow State University, Moscow, Russian Federation

skashikova@nu.edu.kz

Collateral evolution of computers, image acquisition equipment and microscopy techniques provide tools for highly effective data collection. It is now possible to collect data on living cells within hour and days with precise automated control for numbers of samples running simultaneously. In the current study we applied high-throughput automated microscopy to the study of fibroblast motility.

Nocodazole, taxol and vinorelbine are chemotherapy drugs widely used in clinics and experimental trials for their capability to change cell behavior through suppression of microtubule dynamics by three different mechanisms of drug-tubulin interactions. The effect of these drugs is widely studied on the model of wound healing, when cells grown on the adhesive substrate move into the scratched area. It was shown that microtubule inhibitors applied in nanomolar concentrations slowdown cell migration. However there is still lack of data on the comparison of effects of different drugs, especially for low doze effect.

3T3 cells were grown up to monolayer then experimental wound was made. Time-lapse observation was performed on Zeiss Cell Observer inverted microscope with temperature incubation module, motorized *XYZ* stage and CMOS camera. Stage was calibrated before each experiment. Wound healing assay was performed in 24 well plates, where 4 non-adjacent regions were selected for recording resulting in total of 96 regions per plate using DIC with PlanApo x10/0.45 objective. Each region was XYZ adjusted, frames step for each position was 15-20 min. Each plate was used to run all three drugs at different concentrations with 2-3 control wells. Collected movies were analyzed by ZEN and ImageJ software tools.

Cells move into the experimental wound in asynchronous way (Fig.1). After 10-12 h individual cells start randomly migrating in the wound area (Fig.1, E-F). Thus rate of cell migration was determined during first 10 h as average for a large number of cells (encircled within 1 square mm, Fig.1), and we found that cell extension occurs in the linear way for up to 10 h (Fig.2): $V= (S(t_0)- S(t_n))/(2 * 1000)$ μm/h, where ***V*** - average speed of edge, ***S*** - wound area at ***t*** time, 1000 μm - ROI side length.

We further compared the rate of cells extension for taxol, vinorelbine and nocodazole had been applied in the range of concentrations of 1-300 nM. Nocodazole and taxol at a concentration as low as 1 nM significantly slowdown cell migration, while vinorelbine has effect only starting from 3 nM. All three inhibitors show S-shaped curve of dose-response effect (Fig.3). At a concentration >50 nM all inhibitors slowdown migration approximately 4 times and higher concentrations result in the same effect. Comparing the action of different inhibitors it should be stated that at high concentrations (50-300 nM) taxol that was less effective compared to nocodazole and vinorelbine, while at a concentration of 6-10 nM taxol was the most potent inhibitor.

During experiments we gained total ~500k images, for total ~4k hours of ~200 independent samples which were analyzed to obtain statistically significant data. Parallel recording made us possible to test hypothesis on the constant rate of cell motility and to normalize data not only for each concentration, but also against control in each independent experiment providing more robust statistics. Obtaining large enough data sets it was possible to determine subtle changes in cell behavior that occur under the action of each microtubule inhibitor at a concentration of 1-3 nM.

We conclude that nocodazole, taxol and vinorelbine show similar effect on the fibroblast motility and suggest this effect results from the slowdown of the dynamic instability of microtubules and does not depend on the particular molecular mechanism of drug-tubulin interaction.

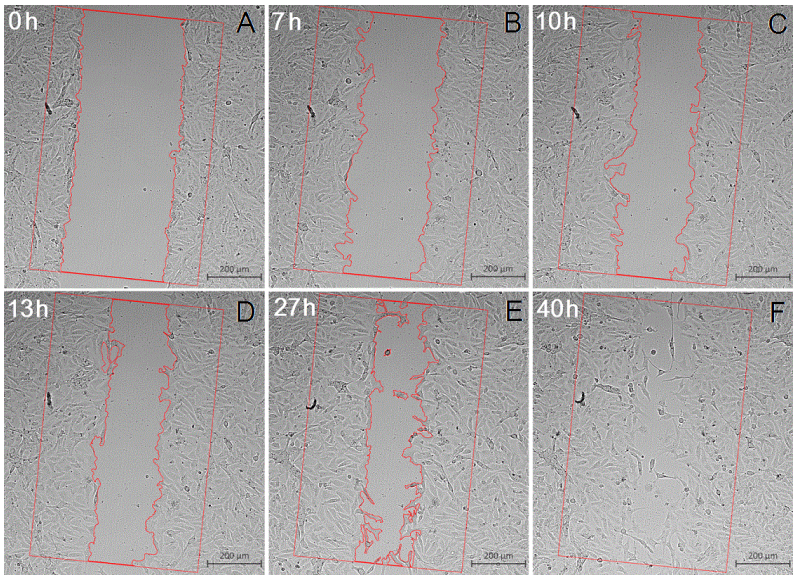

Figure 1. Consecutive frames from the time-lapse.

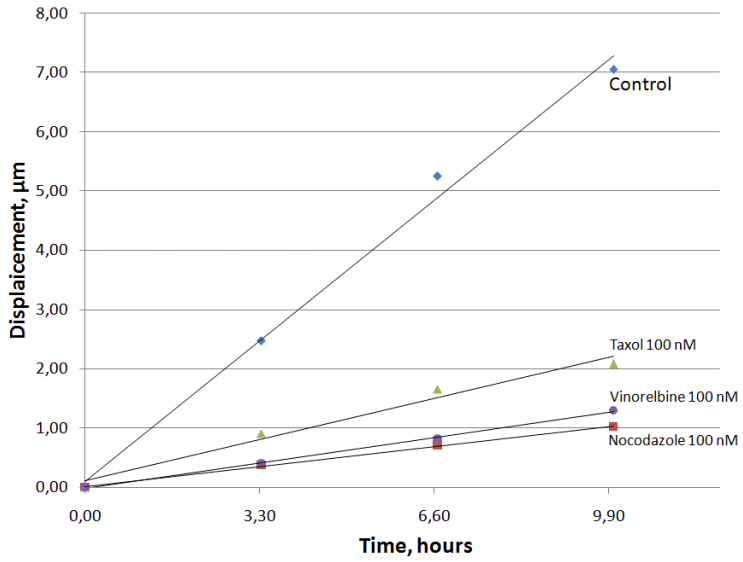

Figure 2. Linear regression analysis of cell motility.

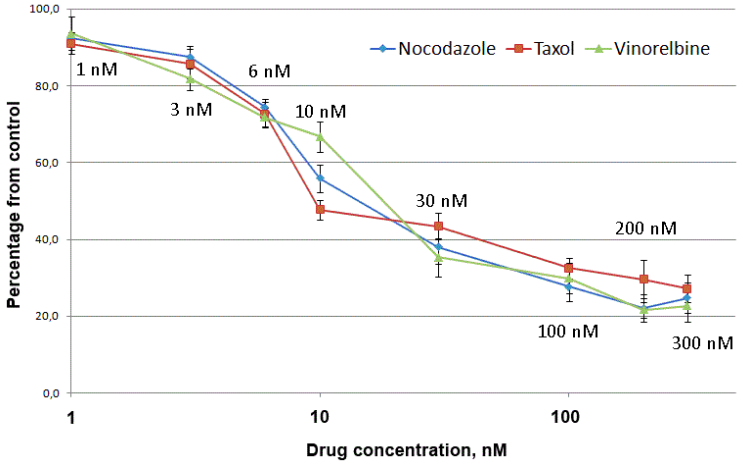

Figure 3. Effect of nocodazole, taxol and vinorelbine on 3T3 cell motility. X axis is presented at logarithmic scale.

Sample Preparation Methods and Strategies

LS6.P073
Scanning electron microscopy for morphology and membrane damage characterization of E.coli

R. V. Mateiu[1], B. Mojsoska[2], H. Jenssen [2], J. Birkedal Wagner[1]

[1]Technical University of Denmark, Center for Electron Nanoscopy, Kgs Lyngby, Denmark
[2]Roskilde University, Department of Science, Roskilde, Denmark

ram@cen.dtu.dk

Within the last decade, bacterial resistance to conventional antibiotics has increased considerably. The increased resistance correlates with an increased consumption of antibiotics. Modifying already existing drugs is not always efficient as the action mechanism does not change compared to that of the parent drug, resulting in quick resistance development. Therefore, antimicrobial peptides and their synthetic analogues, which target directly the bacteria membrane, present a promising novel antimicrobial drug class. The 3-dimentional view of surfaces produced by the scanning electron microscope (SEM) makes it a powerful tool for this particular development. The SEM can be used not only for visualizing the actual membrane damage but also for quantification of morphology modifications that accompanies the administration of drugs.

The method we present is suited for E.coli characterization. The first step in the sample preparation is fixation in 3% glutaraldehyde, pH adjusted to that of the culture, at 4°C for 16h. The sample is next stained with 1% OsO_4 at 4°C for 16h. Next again, the sample is dried in ethanol series at 25°C for 10 minutes for each ethanol step (30%, 50%, 70%, 80%, 90% and 100% ethanol). Finally the 100% ethanol is replaced with acetone in three 10-minutes steps: first with 30% acetone, second with 50% acetone and third with 100% acetone. After the acetone step, the sample is further dried in a Leica EM CPD300 on a silicon disc substrate. The silicon substrate offers a smooth, conducting substrate that contrasts the specimen. We have diced our silicon disks by laser laser micromaching. The silicon substrate with the dried sample is attached onto an aluminum stub with carbon tape and the sample is coated with 2 nm Pt in a Cressington 208HR High Resolution Sputter Coater. The sample is now ready for imaging in the SEM.

We have successfully applied the above mention protocol to two different independent studies, which indicates that the method is reliable.

For the morphology characterization we use ImageJ, which allows us to measure cells lengths, widths and curvatures for healthy and damaged cells.

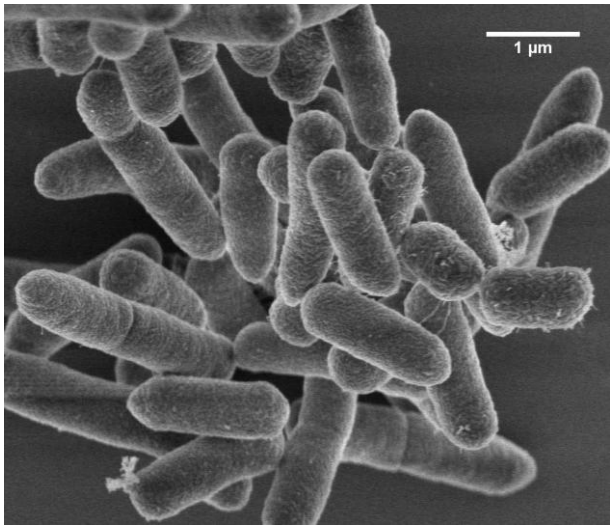

Figure 1. Control Sample showing healthy *E.coli*.

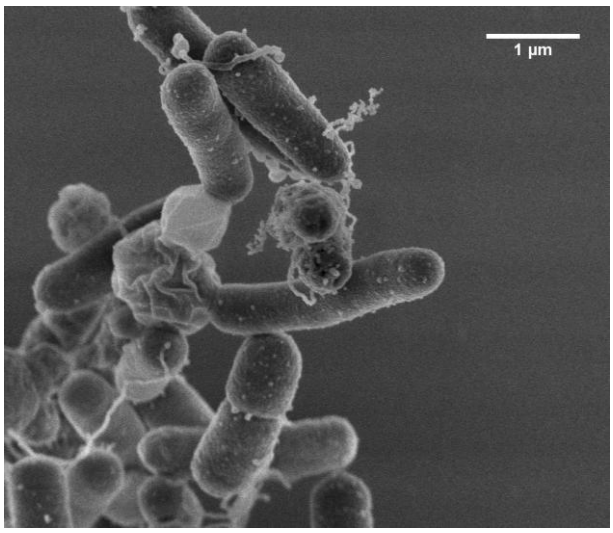

Figure 2. *E.coli* treated with 1xMIC peptoid 1.

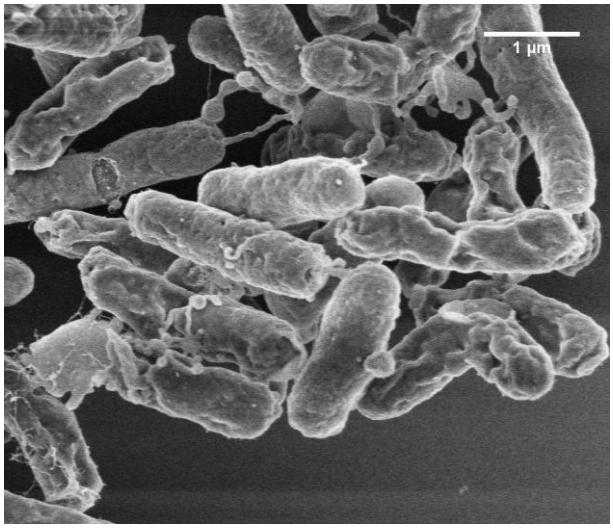

Figure 3. *E.coli* treted with 4 x MIC peptoid 1.

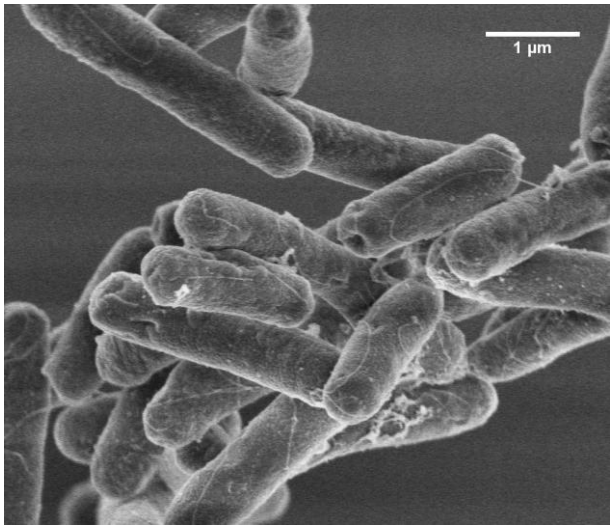

Figure 4. *E.coli* treated with 1 x MIC peptoid 2.

Sample Preparation Methods and Strategies

LS6.P074
Effects of different preparation techniques on the microstructure of potato tissue for scanning electron microscopy: comparison of preservation of cell morphology and dimensions

S. Yoneji[1], E. Ahmadi[1], M. Khaninour[2], S. Azami[3], J. Karcz[4]

[1]Buali Sina University, Biosystem Engineering, Hamedan, Iran
[2]Buali Sina University, Material Engineering, Hamedan, Iran
[3]Buali Sina University, Para-Veterinary Sciences, Hamedan, Iran
[4]Silesia, Katowice, Poland

s.yoneji@basu.ac.ir

Potato tissue is built of thin cell walls and the sample preparation for scanning electron microscopy by chemical fixation without critical point drying results in shrinkage of cell walls. We investigated to identify a protocol that would preserve cell morphology and dimensions better than standard chemical fixatives and dehydration regimes. This paper compares different preparation techniques of potato tissue to study of the cellular structures by image analysis. The methods of fixatin and dehydration were 100% methanol fixation and 100% methanol dehydration, 100% methanol fixation and 100% ethanol dehydration, 100% ethanol fixation and 100% ethanol dehydration, FAA fixation and dehydration ethanol series, 2.5% glutardialdehyde fixation (5 min, 1 h and 2 h) and dehydration ethanol series and fresh unprocessed sample. Also the methods of drying the specimens; air drying, freeze drying, (HMDS) Hexamethyldisilasane (5 min, 15 min and over night) and compositoin of ethanol and HMDS (3:1, 1:1 and 1:3- 15 min each) were tested on potato tissue. Results show that the method of 100% ethanol fixation and 100% ethanol dehydration was the best for preservation rather than 100% methanol and FAA protocol. Air drying and freeze drying altered tissue dimensions. However, HMDS drying samples showed strong differences to the other samples. This study shows that 2.5% glutardialdehyde fixation (2 h) and dehydration ethanol series followed by HMDS alcohol (over night) results in better preservation of dimensions and morphology of potato tissue than other fixation, dehydration and drying methods, especially for thicker or larger samples.The importance is that HMDS is suitable replacement of critical point drying for preparation of Potato tissue for scaning electron microscopy.

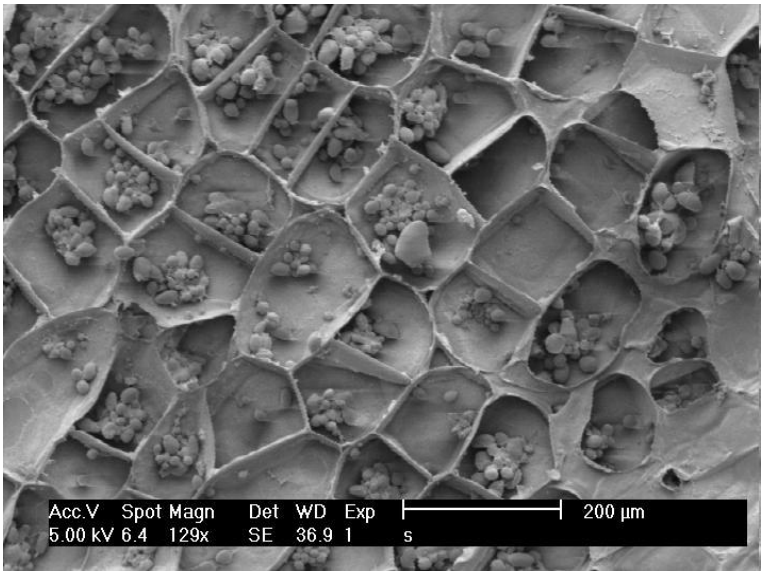

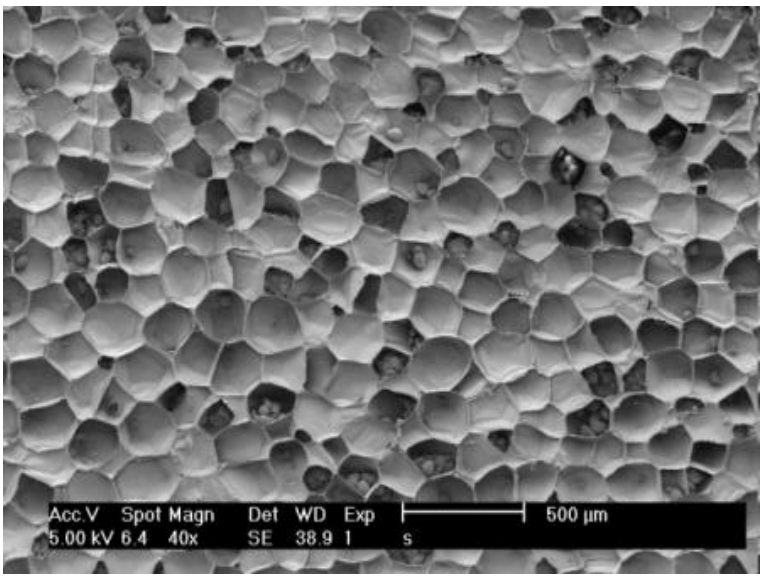
Acc.V Spot Magn Det WD Exp
5.00 kV 6.4 40x SE 38.9 1 s
500 µm

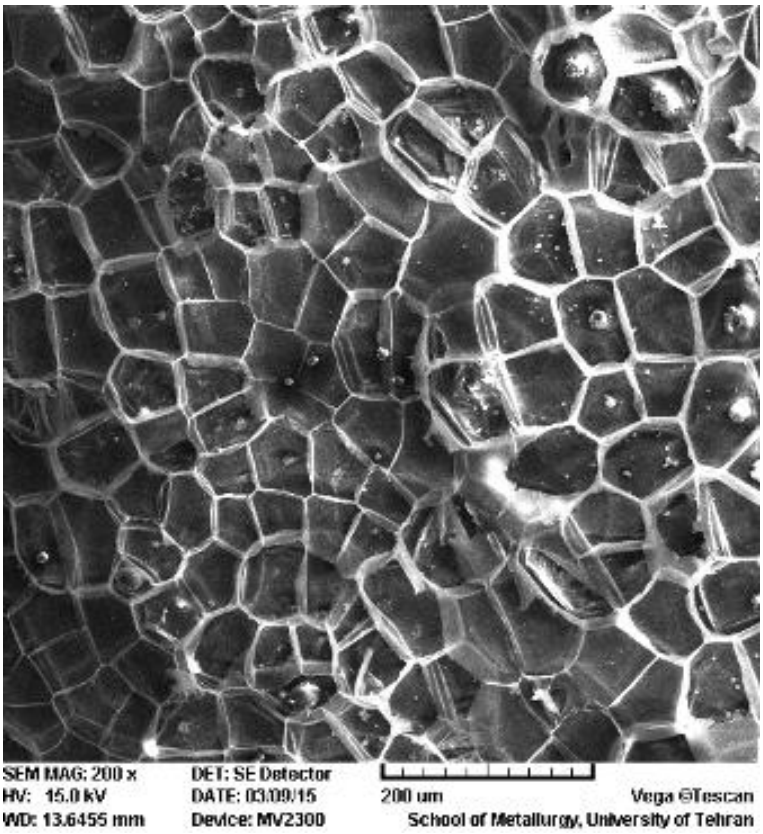
SEM MAG: 200 x
HV: 15.0 kV
WD: 13.6455 mm
DET: SE Detector
DATE: 03/09/15
Device: MV2300
200 um
Vega ©Tescan
School of Metallurgy, University of Tehran

Sample Preparation Methods and Strategies

LS6.P075
Microscopic analysis adapted to segmented-flow technology

R. Römer[1], J. Schemberg[1], K. Lemke[1], G. Gastrock[1]

[1]Institute for Bioprocessing and Analytical Measurement Techniques e.V., Bioprocess Engineering, Heilbad Heiligenstadt, Germany

robert.roemer@iba-heiligenstadt.de

To overcome the disadvantages (e.g. evaporation) of well-established bioassays based on microwell plates or “hanging drop” technology, a novel pipe based system called “pipe based bioreactors (*pbb*)” was developed at the Institute for Bioprocessing and Analytical Measurement Techniques in Heilbad Heiligenstadt. The principle of this platform bases on segmented-flow technology. Thereby a main carrier fluid (typically oil) is immiscible with the sample medium (aqueous solution) and may be used as a gas reservoir for the sample (Figure1). Droplets of volume sizes from 60 nL to 20 µL can be applied as bioreactors and used in a wide range of biological and chemical applications by means of microchips or a specific probe [1,2,3]. Depending on the application the following types of droplet operations can be implemented with specific microfluidic modules; (i) droplet generation, (ii) droplet incubation; (iii) droplet dosage, (iv) droplet merging, (v) medium exchange, (vi) droplet switching, and (vii) cell or droplet detection (via microscope or optical fibre systems). Regarding to the application the challenges of the adaption of microscopic analysis to this *pbb*-platform as single cell and / or as 3D cell culture analysis techniques will be presented; (i) the rapid detection of food borne pathogens, and (ii) the embryoid body formation of stem cells including the following cell proliferation.

For the first example the aim was to detect every single microorganism in a 150 nL droplet in a micro channel of a glass chip by fluorescence microscopy. For this purpose the food pathogen was first specific isolated by biomagnetic separation from the food sample and was subsequently labelled by fluorescence microcapsules for microscopic detection [4,6]. Appropriate kinetic measurements by means of grey scale values of ‘‘Regions of Interest’’ (ROI) were performed by creating a video sequence following by the transfer of the grey scale value into a diagram versus time (Figure 2).

For the second example the cultivation of murine embryonic stem cells was monitored microscopically for several days in the droplets of the *pbb*-platform under non-adherent conditions in a highly controlled microenvironment. Coming from a cell suspension these stem cells reproducible formed embryoid bodies by self-assembling within one day (Figure 3). The formation of this 3D cell culture structure is essential for further stem cell differentiation. Afterwards the cell proliferation could be determined by the measurement of the increase of the embryoid body´s diameter or cross-sectional area directly in the droplet by means of the microscope [5,6]. Therefore the platform will have the potential to be broadly applied for several bioassays or long term cultivation protocols.

1. K. Martin *et al*., Lab Chip 3 (2003), p. 202.
2. K. Lemke *et al*., Deutsches Patent (2008), DE 10 2008 039 117.4-41; Anmeldedatum: 21.08.2008.
3. G. Gastrock *et al*., Deutsches Patent (2009). DE 10 2009 020 449.0; Anmeldedatum 05.06.2009.
4. J. Schemberg *et al*., Eng.Life Sci. 9 No.5 (2009), p.391.
5. K. Lemke *et al*., J. Biotechnol. (2015), http://dx.doi.org/10.1016/j.jbiotec.2014.11.040.
6. We kindly acknowledge AIF within ZUTECH-program (“LÖBISENA”, research project no. 217 ZBR) and the European Commission (“HYPERLAB”, grant agreement no. FP7-223011) for funding.

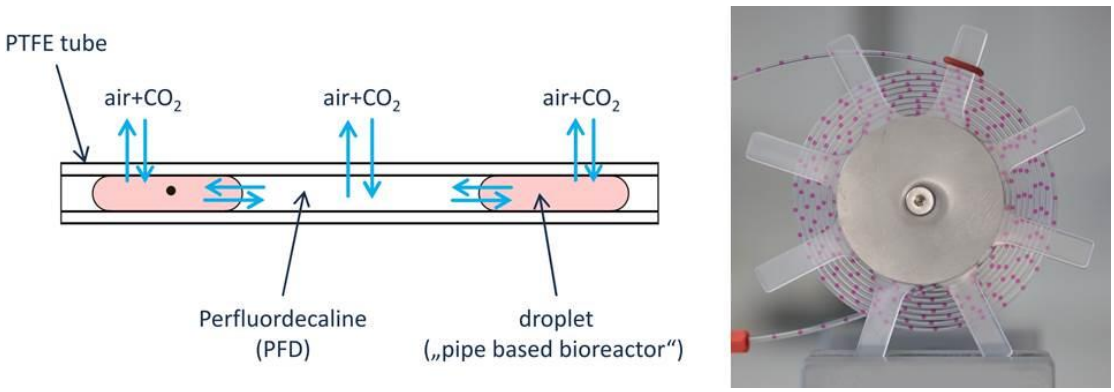

Figure 1. Principle of the “pipe based bioreactor (*pbb*)”-platform and its gas transport and 800 nL droplets in a 1 mm tube (from left to right).

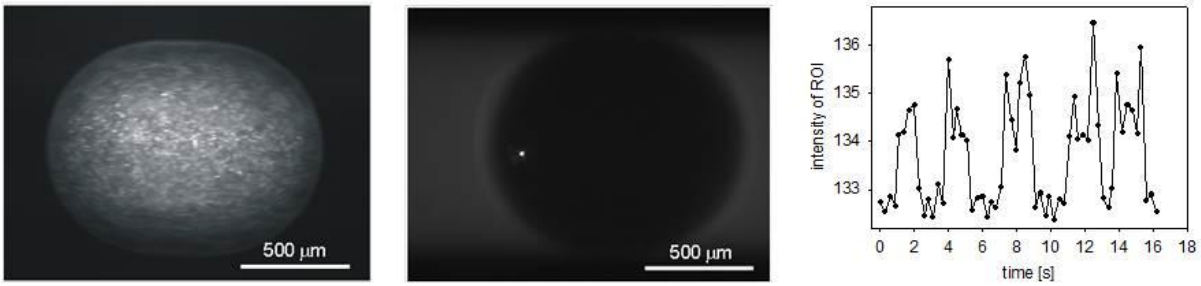

Figure 2. Microscopic detection of one droplet with approx. 6000 fluorescence microcapsules (Ø = 600 nm, left) and one microcapsule (Ø = 910 nm, right) within a micro channel of a glass chip (IPHT, Jena), and the measurement by means of grey scale values of “Regions of Interest” (ROI) of five droplets (from left to right).

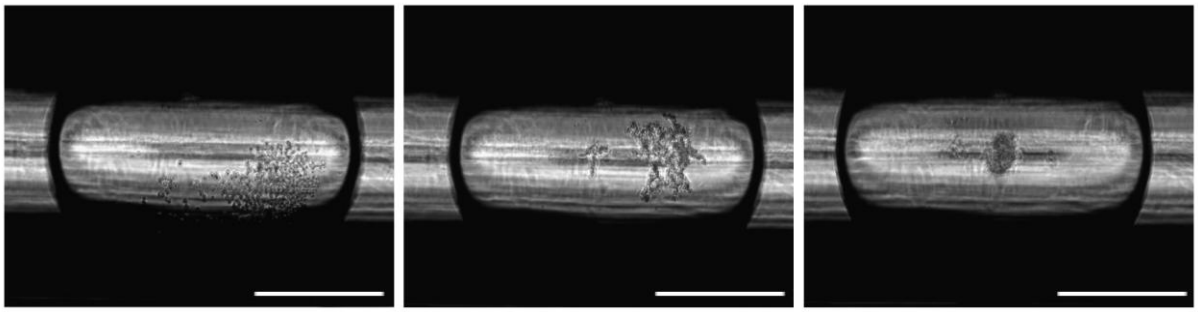

Figure 3. Embryoid body formation of murine embryonic stem cells in a 800 nL droplet; cell suspension at the beginning, after 6 h of incubation, and the already formed embryoid body after 24 h of incubation (scale bar was 500 µm, from left to right).

Sample Preparation Methods and Strategies

LS6.P076
Influence of ultrathin resin section aging and its reduction for imaging in the low voltage STEM

V. Krzyzanek[1], R. Skoupy[1], K. Hrubanova[1], L. Kocova[2], J. Nebesarova[2]

[1]Institute of Scientific Instruments of the ASCR, v.v.i., Brno, Czech Republic
[2]Biology Centre of the ASCR, Institute of Parasitology, Ceske Budejovice, Czech Republic

krzyzanek@isibrno.cz

A scanning transmission electron microscope (STEM) is a useful device combining features of scanning and transmission electron microscopes [1]. Nowadays, low voltage STEM - here we mean a transmission mode in a SEM [2] that uses, in respect to a commercial STEM, much lower voltages - is increasingly used also for imaging of ultrathin sections. However, many TEM operators consider STEM as a significant source of radiation damage for observation of ultrathin sections (for typical examples see Figure 1); two main features caused by beam damages are the mass loss and the contamination. Both types of damages depend on the used electron energy and the electron dose applied to the sample. In general, the mass loss depends on the sample composition and the contamination results mainly from the poor vacuum in the specimen chamber of the SEM and cleanness of the sample surface. Here, we focus on quantitative investigations of the mass loss of embedding media ultrathin sections in specific aging conditions. Moreover, we discuss our results and propose reduction of the damage for imaging in the low voltage STEM.

For simplicity, in our feasibility study we have used for estimation of the mass loss of ultrathin sections pure Epon resin that is one of the most often used resins for embedding biological samples for investigations in TEM. We collected bright-field (BF) images of the same area at the sample. Consequently, an overview of the scanned area taken after multiple scans at a half magnification shows already the increase of the signal due to the mass loss (Figure 2a). The Figure 2b shows the relative mass loss of the measured sections to the total dose of electrons for the 6 weeks old Epon resin sections of the thickness of 60 nm imaged with 30 keV electrons at different conditions: (i) pure Epon sections showing high mass loss, (ii) sections coated from one side or both sides by 3 nm thick Carbon layer shortly after cutting, and (iii) coating from both sides of the old sections. The experiments have been performed using SEM Magellan 400L (FEI) at 30 kV and the lowest probe current of 1.6 pA, so that the dose of one scan was about 60 electrons/nm^2.

Our preliminary results show that the mass loss at 30 keV can be high even at relatively low doses for the section which is older (sections showed here are 6 weeks old). We show that even very thin coating of carbon can considerably reduce the mass loss, even if the coating is applied on the old section immediately before imaging. Thus, in the next step we plan to perform our experiments with real sections of biological samples.

1. Adv. Imaging & Electron Phys. 159 (2009), pp. 101-121 & 357-386.
2. A Bogner et al, Micron 38 (2007) p. 390.
3. The authors acknowledge the support by the grants 14-20012S (GACR) and TE01020118 (TACR).

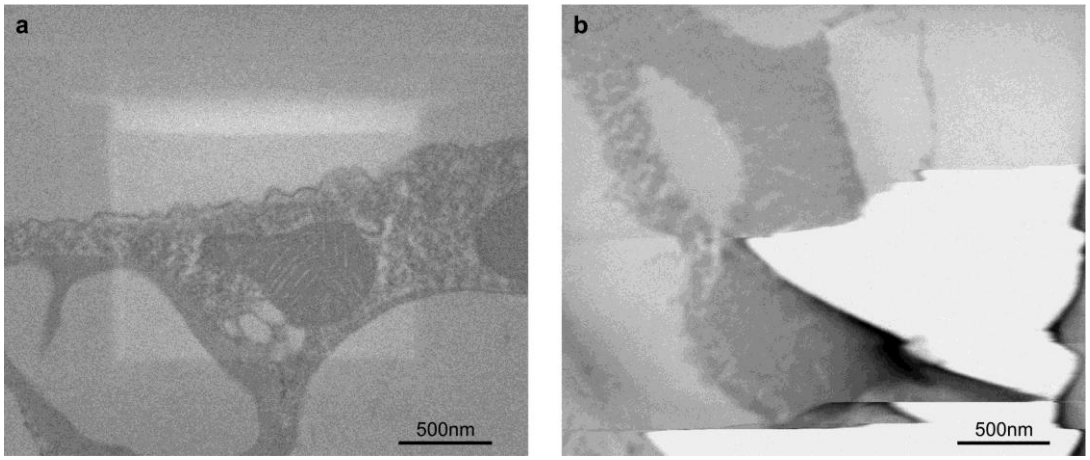

Figure 1. BF micrographs of 30 nm section of *Euglena gracilis* without any staining imaged at 30 keV; (a) mass loss in the central part from the previous scan at higher magnification, (b) burning out.

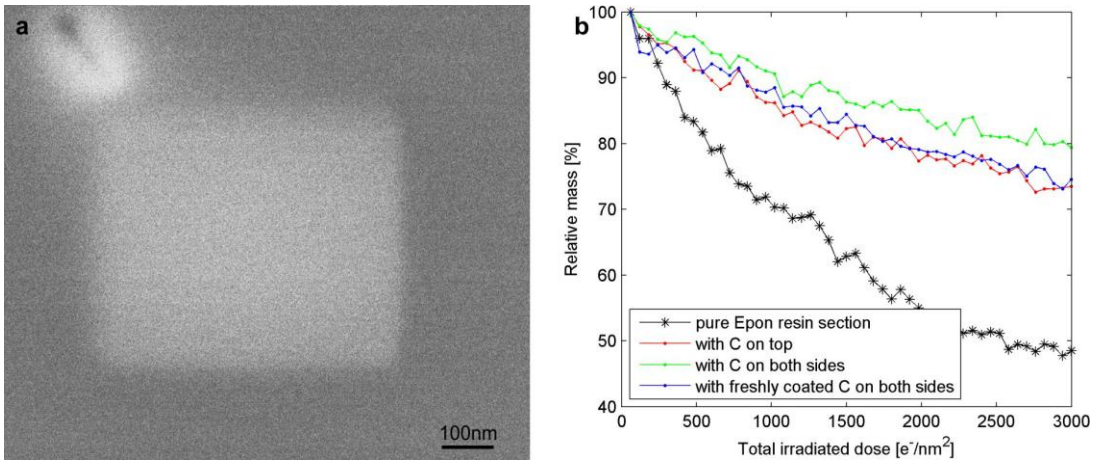

Figure 2. (a) BF micrographs showing an overview of the multiple scanned area of the 60 nm thick Epon resin section at a half magnification. (b) Plot showing relative mass vs. total irradiated dose for the 60 nm thick Epon resin section at 30 keV; the decrease of the curves shows directly the mass loss.

Sample Preparation Methods and Strategies

LS6.P077
TEM-imaging of collagen fibrils in mineralized human dental enamel using in-situ FIB lift-out preparation technique

K. Witzke[1], M. Frank[2], O. Specht[3], C. Lurtz[4], D. Behrend[4], P. Ottl[1], M. Warkentin[4]

[1]University Medicine Rostock, Department of Prosthodontics and Materials Science, Rostock, Germany
[2]University Medicine Rostock, Electron Microscopy Centre, Rostock, Germany
[3]Institute for Implant Technology and Biomaterials e.V., Rostock, Germany
[4]University of Rostock, Department of Material Science and Medical Engineering, Rostock, Germany

katharina.witzke@uni-rostock.de

Human dental enamel is the most highly filled and hardest biological composite in the human body, consisting of 96 wt.% inorganic minerals embedded in a matrix of 1 wt.% organic proteins and 3 wt.% water [1]. The presence of collagen within the organic matrix is controversially discussed in literature [2, 3]. Until now, no reports are available on detecting collagen in human enamel by using transmission electron microscopy (TEM). In this in vitro study the first TEM-Imaging of collagen microfibrils in human mineralized and mature enamel is presented using In-Situ FIB Lift-Out preparation technique.

Recently extracted intact maxillary and mandibular premolars without any carious lesions or fillings were examined. An interdisciplinary developed guideline in preparing mineralized human dental enamel for TEM-visualization is presented.

We demonstrate an In-Situ FIB Lift-Out specimen preparation of human enamel to produce high quality TEM-sections showing the ultrastructural configuration in detail. High magnification reveals fibrous aggregations embedded in hydroxylapatite crystallites that are reminiscent of collagen microfibrils.

The present study suggests that mineralized human enamel has a collagen-based organic matrix. In-Situ FIB Lift-Out preparation is a powerful preparation technique of mineralized biomaterials for TEM-imaging.

1. Ten Cate, A. R; Dale, A. C. (1980): Oral histology. Development, structure, and function. St. Louis: Mosby.
2. Fearnhead, R. W. (1979): Matrix - Mineral Relationships in Enamel Tissues. In: Journal of Dental Research 58 (2 suppl), S. 909-921. DOI: 10.1177/00220345790580024501
3. Acil, Y.; Mobasseri, A. E.; Warnke, P. H.; Terheyden, H.; Wiltfang, J.; Springer, I. (2005): Detection of mature collagen in human dental enamel. In: Calcif Tissue Int 76 (2), S. 121-126. DOI: 10.1007/s00223-004-0122-0

Figure 1. TEM micrograph of a FIB prepared enamel-section (scale 2µm)

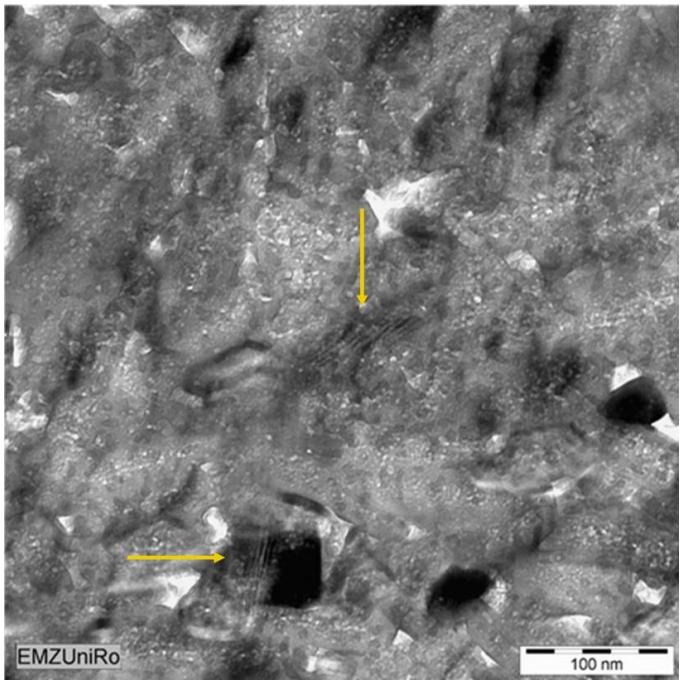

Figure 2. TEM image of In-Situ FIB Lift-Out prepared enamel (scale 100 nm). The arrow indicates the presence of collagen microfibrils.

Sample Preparation Methods and Strategies

LS6.P078
Studies on microscopic feature of foetal and adult ovaries and uteri in white fulani cattle (Bos indicus)

I. Nwaogu[1], C. Egejuru[1], K. Okorie[1], C. Abiezute[1]

[1]University of Nigeria, Nsukka, Veterinary Anatomy, Nsukka, Nigeria

nwaoguinnocent@gmail.com

In this work we studied the microscopic features of 45 foetal and 15 adult ovaries and uteri obtained from slaughtered white Fulani cows in Nsukka abattoir, Enugu State, Nigeria. The age of the adult were determined by dentition and that of fetuses by crown rump length methods. The foetal and adult ovaries and uteri were divided into four (4) groups using specific age intervals as gestation day (GD) 90-152, 153-215, 216-278 and adults. For microscopic studies the ovaries and uteri were fixed in Bouin's fluid, processed and routinely stained with Hematoxylin and Eosin. The ovarian follicles were classified into five types according to granulosar cell layers surrounding the oocytes. The endometrial and myometrial thickness were also determined. The ovary of GD 90-152 had no distinct cortex and medulla. Types 1 and 1A primordial follicles were present. By GD 153-215, the ovaries contained types 1, 1A, 2, 3 and 4 follicles, and GD 216-278 had type5 follicles in addition. The adult ovaries contained types 2, 3, 4 &5 follicles as well as corpus albicans while very few type1 follicles were observed. Precursors of uterine glands in form of shallow invaginations of luminal epithelium into the endometrium were observed by GD 90-152. These invaginations deepened further by GD 153-215 and became clusters of cells by GD 216-278. The adult uterus exhibited the mocroscopic features characteristic of ruminants. The endometrial and myometrial wall thickness of the adults were significantly ($p<0.05$) larger than those of the foetuses. These results provide baseline information on ovarian development and uterine adenogenesis in the white Fulani cattle.

Sample Preparation Methods and Strategies

LS6.P079
Optimization of preparation steps for 2D-materials - transfer, cleaning and sandwiching

T. Lehnert[1], R. Leiter[1], G. Algara-Siller[1], U. Kaiser[1]

[1]Universität Ulm, ZE Materialwissenschaftliche Elektronenmikroskopie, Ulm, Germany

tibor.lehnert@uni-ulm.de

Since the first layer of graphene was fabricated with the micromechanical cleavage in 2004[1], 2D-materials camestronglyinto the field of interest. In addition to theirremarkable properties, the 2D-materials are also promising candidates foratomic structureinvestigations inhigh-resolutiontransmission electron microscopy, where thin samples are necessary. For this purpose,optimalpreparationstepsare required.

Free-standing 2D-materials can be obtained either from their 3D counterparts by breaking the Van-der-Waals bond between the layers, applying the well-known scotch-tape method[1], or via the chemical vapor deposited (CVD) growth process[2]. Although exfoliated 2D materials usually contain much less defects, CVD-grown layers are much larger [2] and therefore suitable for device applications.

To get a2D-layer on arbitrary surfaces,includingquantifoil gridsfor TEM investigations, most oftenpolymethyl methacrylate (PMMA) is used. The disadvantage is that PMMA-residues remain on the sample surface[3]. This undesired contaminationmakes HRTEM imagingdifficult or impossible and also may alter the current-voltage characteristics of a 2D based transistor. Therefore in this paper we demonstrate how to get a 2D layer on an arbitrary surface without the use of PMMA. Instead of PMMA, we use just a droplet ofwater or isopropanol and wait until the liquid is evaporated. Afterwards we proceed in the well-known way; we etch away the substrate, for SiO_2-substrate, potassium hydroxide or hydrofluoric acidis used andforcopper-substrate we useammonium peroxydisulphate.

Moreover, we briefly demonstrate the optimization of two other important 2D-material preparation steps: cleaning and sandwiching. We found that dry-cleaning of graphene with activated carbon results in a cleaniness ofthe surface of about 95%[6]. For this purpose we use a special furnace which is shown in the figure below. We show in addition how to stack 2D materials using a micromanipulator.

1. K.S. Novoselov, A.K. Geim, S.V. Morozov, D. Jiang, Y. Zhang, S.V. Dubonos, I.V. Grigorieva, A.A. Firsov, Science, 306, 666-669 (2004)
2. Y. Zhang, L. Zhang, C. Zhou; Acc. Chem. Res., 2013, 46 (10), pp 2329-2339
3. A. Reina, H. Son, L. Jiao, B.Fan, M.S. Dresselhaus, Z.Liu, J.Kong; J. Phys. Chem. C, 2008, 112 (46), pp 17741-17744
4. J.C. Mayer, A.K. Geim, M.I. Katsnelson, K.S. Novoselov, T.J. Booth, S. Roth; Nature 446, 60-63 (2007)
5. G. Algara-Siller, S. Kurasch, M. Sedighi, O. Lehtinen, U. Kaiser; Appl. Phys. Lett. 103, 203107 (2013)
6. G. Algara-Siller, O.Lehtinen, A. Turchanin, U. Kaiser; Appl. Phys. Lett. 104,153115 (2014)
7. We acknowledge financial support by the German Research Foundation (DFG) and the Ministry of Science, Research and the Arts (MWK) of Baden-Württemberg in the frame of the SALVE project and by the DFG in the frame of the SPP 1459 “Graphene” project.

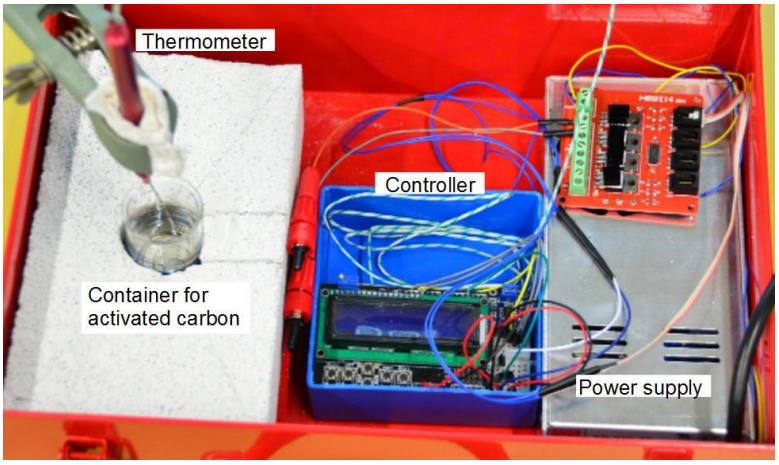

Figure 1. *Setup of the furnace for dry-cleaning of graphene*

Sample Preparation Methods and Strategies

LS6.P080
Effect of different adjuvants on the cuticle of Diaphorina citri (Kuwayama) (Hemiptera: Liviidae) - an important citrus pest

A. Arnosti[1], I. Delalibera Jr.[2], M. I. Camargo-Mathias[1], M. R. Conceschi[2], K. C. S. Furquim[1]

[1]Biosciences Institute-UNESP, Biology Department, Rio Claro, Brazil
[2]College of Agriculture Luiz de Queiroz -Esalq-USP, Entomology and Acaralogy Department, Piracicaba, Brazil

andre_arnosti@hotmail.com

The insect *Diaphorina citri* is one of the most important citrus pest, once it is the vector of the bacterial pathogens '*Candidatus* Liberibacter americanus' and '*C.* Liberibacter asiaticus' agents of the disease "Huanglongbing" (HLB), popularly known as "Citrus Greening". Considering the difficulty in controlling this insect, the use of adjuvants is a promising tool, presenting synergic effect when added to either synthetic or biological control methods. The effects of the adjuvants on the insect have not been clarified; therefore, further research on this topic is needed. The cuticle of the arthropods in general is a physical-chemical barrier against several external agents, isolating and protecting the internal organism. Thus, this study had the objective to evaluate the effect of the following adjuvants: a) 0.01% of Tween 80 USP (Oxiteno®, Brazil) (Control); b) 0.075% of KBRAdj (unregistered composition) and c) 0.025% of Silwet L-77 (Momentive Performance Materials Industry of Silicon LTDA®, Brazil) on the cuticle of *D. citri* adult individuals. In this study, 10 adult individuals were kept under controlled conditions in the Laboratory of Pathology and Microbial Control of Insects of the Agriculture College "Luiz de Queiroz", Piracicaba/SP (Brazil). After being collected, the insects were anesthetized with CO_2, pulverized with 2mL/plate of each adjuvant in "Potter Tower" system with a pressure of 15 PSI. After 72 hours of exposition, the specimens were collected, fixed and processed for Scanning Electron Microscopy (SEM). Then they were examined and documented under scanning electron microscope Hitachi TM3000. The results of the ultramorphological analysis showed that the application of the adjuvants KBRAdj and Silwet-L77 caused the cuticle disruption in the individuals analyzed. This result was evidenced by the presence of more electron-dense regions (indicated by arrows). The adjuvant Tween 80 did not affect the cuticle structure (Fig.1A-D and D1). In the group exposed to adjuvant KBRAdj the ventral region was more affected (Fig.1 E-G). The dorsal region remained intact (Fig.1 H and H1). The same result was found for the adjuvant Silwet-L77, which caused more alterations on the ventral (Fig. 1I-K) than on the dorsal cuticle (Fig. 1L e L1). Thus, these findings clearly showed that the adjuvants evaluated in this study affected the ventral cuticle of the insects, modifying the structure and consequently causing morphophysiological alterations on this important physical barrier. In addition, it was demonstrated that the control methods had their efficiency enhanced by the application of the adjuvants KBRAdj and Silwet-L77.

1. CHAPMAN, R.F. 1998. **The insects: Structure and function**. The English Universities Press, New York. 1998.
2. CHAVAN, V.M.; A.S. SUMMANWAR.1993.Population dynamics and aspects of the biology of citrus psylla, *Daiphorina citri* Kuw., in Maharashtra. In: Navarro, L., J.V da Graça ; L.W. Timmer (Eds), **Proceedings Conference of the International Organization of Citrus Virologists**, 12., Riverside: University of California. p.286-290.
3. Financial support by FAPESP (Grant n.2014/19240-4) and CNPq

FIGURE 1

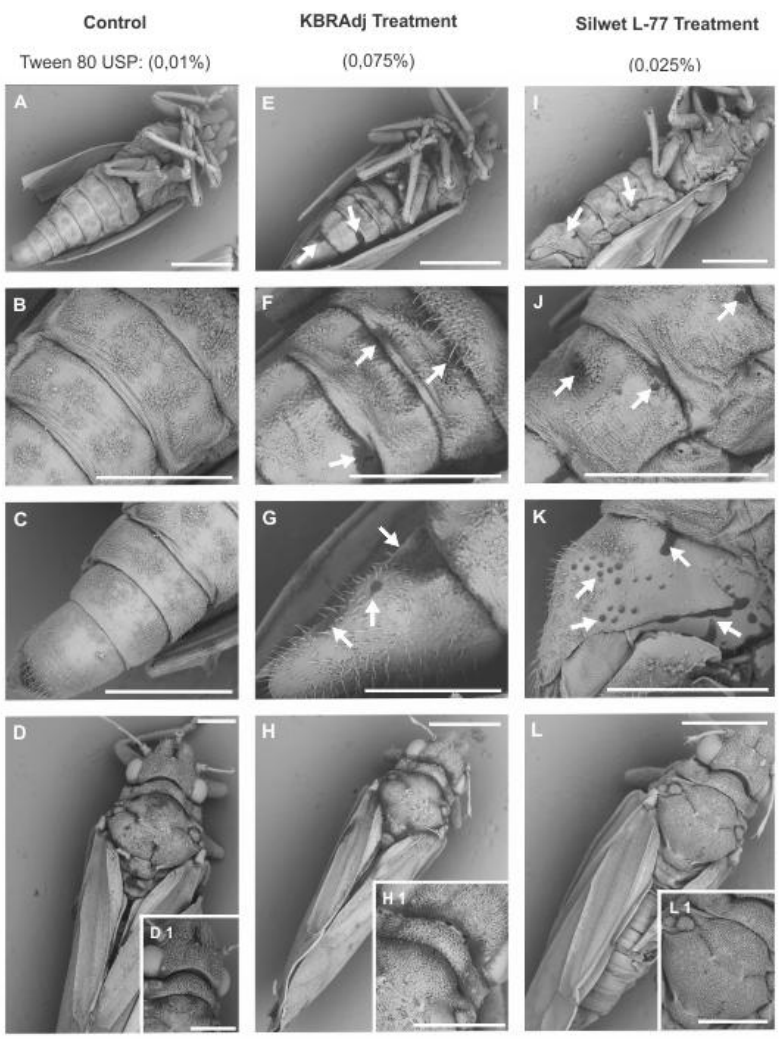

Figure 1. Electron Scanning Micrographies of the ventral (A-C, E-G and I-K) and dorsal (D, D1, H, H1 and L1) regions of Diaphorina Citri adult individuals subjected to different adjuvants. The affected regions (areas of cuticle degradation) mainly the ventral region, are indicated by arrow. BAR: A, D, E, H, I e L: 500µm; B, C, F, J e K: 300µm; G: 400µm; D1, H1 e L 1:250 µm.

Fundamental Cellular Processes: Cell Division, Endo-, Exocytosis, Remodeling of Cytoskeleton, Membrane Trafficking

LS7.081
Current approaches for cellular electron microscopy: lessons from resin-embedded samples

K. McDonald[1]

[1]University of California, Berkeley, USA

klm@berkeley.edu

While imaging in vitreous ice is clearly the gold standard for cellular EM, a lot can be learned by imaging in resins if the cells and tissues are prepared carefully. A useful compromise is to use cryo-immobilization and low temperature dehydration/fixation combined with resin embedding. Samples prepared in this way can compare favorably with vitrified cells at all but the highest levels of resolution. Once cells and tissues are in resin, there are many imaging options for the electron microscopist. At the most basic level, there are thin sections viewed in the TEM, or 3-D analysis of thicker sections using electron tomography. In addition, high-resolution SEM can be used on resin-embedded specimens for serial blockface (SBF) or focused ion beam (FIB) imaging. Resin-embedded material lends itself quite well to correlative LM-EM studies using a variety of techniques including array tomography, preservation of fluorescence in resin, and on-section immunolabeling, to mention a few. Finally, there is a size constraint beyond which cryo-processing is not possible, e.g., for the reconstruction of a whole *Drosophila* or mouse brain, where embedding in resin becomes the method of choice. These and other examples will be presented and discussed.

LS7.082
The use of cryo-electron microscopy to study the mechanisms of flagellar/ciliary assembly and function

G. Pigino[1]

[1]MPI of Molecular Cell Biology and Genetics, Dresden, Germany

pigino@mpi-cbg.de

Modern biology is increasingly addressing phenomena bridging multiple scales. One such phenomenon is the assembly of large functional machines out of proteins and protein complexes. The cilium (or eukaryotic flagellum) is a great example of a sophisticated and large cellular machine that assembles out of many interacting multi-protein complexes. Although best known for their role in cellular motility, cilia also serve a multitude of sensory and signaling functions, which are essential for organ development, tissue homeostasis, and maintenance. All types of cilia share a common microtubule-based structure, the axoneme, which is composed of more than 600 different proteins. Today we do still not know the role and often not even the localization of many of those proteins. Also we do not know much about how they assemble into a functioning cilium. However, if the correct assembly of cilia is compromised, cilia-related pathologies (ciliopathies) occur. We look closely at several aspects of axonemal assembly and maintenance processes in *Tetrahymena* and *Chlamydomonas* cilia, using methods for cryo-electron tomography and 3D image analysis. In this way we show the three-dimensional architecture of axonemal protein complexes. Thanks to a new generation of electron detectors, latest improvements of other microscope components, and the development of new image processing strategies, we are now able to visualize the 3D architecture of non-repeating structures of the axoneme -- structures such as the ciliary tip. Based on our structural and biochemical findings we can now start reasoning about biological processes at these important structures.

Fundamental Cellular Processes: Cell Division, Endo-, Exocytosis, Remodeling of Cytoskeleton, Membrane Trafficking

LS7.083
Branching properties of single keratin filaments in keratinocytes visualized by high resolution scanning electron microscopy

S. Nafeey[1], P. Walther[1], E. Felder[2]

[1]University Ulm, Central Facility for Electron Microscopy, Ulm, Germany
[2]university, Institute for General Physiology, Ulm, Germany

soufi.nafeey@uni-ulm.de

The cytoskeleton of most metazoan cells encompasses three different types of filament systems: actin filaments, microtubules and the intermediate filament (IF) network. In the human genome approximately 70 genes encode for the large, tissue specific protein family of the IFs [1]. Although the IF proteins play an important role not only in providing mechanical stability to the cells, but also in protecting cells and tissues from external mechanical forces [2], there is only little known about their branching properties. In this project we investigated whether branching occurs on the level of single filaments.

In a previous project we were able to show branching points using STEM tomography of high pressure frozen and freeze substituted keratinocytes [3]. In the present work we wanted to measure the filament diameters for a better understanding of the branching properties. This turned out to be difficult with STEM due to the insufficient signal to noise ratio in the images. Therefore we choose high resolution SEM of detergent extracted cells as the method of choice, because the thin filaments provide a high secondary electron emission [4].

We defined the filament with the largest diameter of a branching point as the mother filament M. The other two filaments emerging from M are defined as the daughter filaments D1 and D2 (Fig. D). We calculated the sum of the cross section areas D1 and D2 and divided it by M, as shown in the formula of Fig. E. When all three filaments had the same cross-section area, the quotient would be 2. (This is, e.g. the case in actin branches.) In the intermediate filament branches of this study, however, this was rarely the case. A quotient of 1 is expected, when the cross-section area of the mother filament is divided up into the two daughter filaments. This was indeed found frequently. In most cases the sum of the cross-section areas of both daughter filaments was larger than the cross-section area of the mother filament. The highest peak was reached at a value of 1.6. This indicates, that branching of intermediate filaments is very different from branching of actin and is heterogeneous.

1. Hesse, M., Magin, T. M. & Weber, K. J. Cell Sci. 114, 2569-75 (2001).
2. Goldman, R. D., Cleland, M. M., Murthy, S. N. P., Mahammad, S. & Kuczmarski, E. R. J. Struct. Biol. 177**,** 14-23 (2012)
3. S. Nafeey, E Felder, C. Schmid, M. Sailer, P. Walther. Proceedings of the Microscopy Conference (2013), Regensburg, p. 286.
4. M. Sailer, K. Höhn, S. Lück, V. Schmidt, M. Beil and P. Walther, Microsc. Microanal. 16 (2010), 462-471

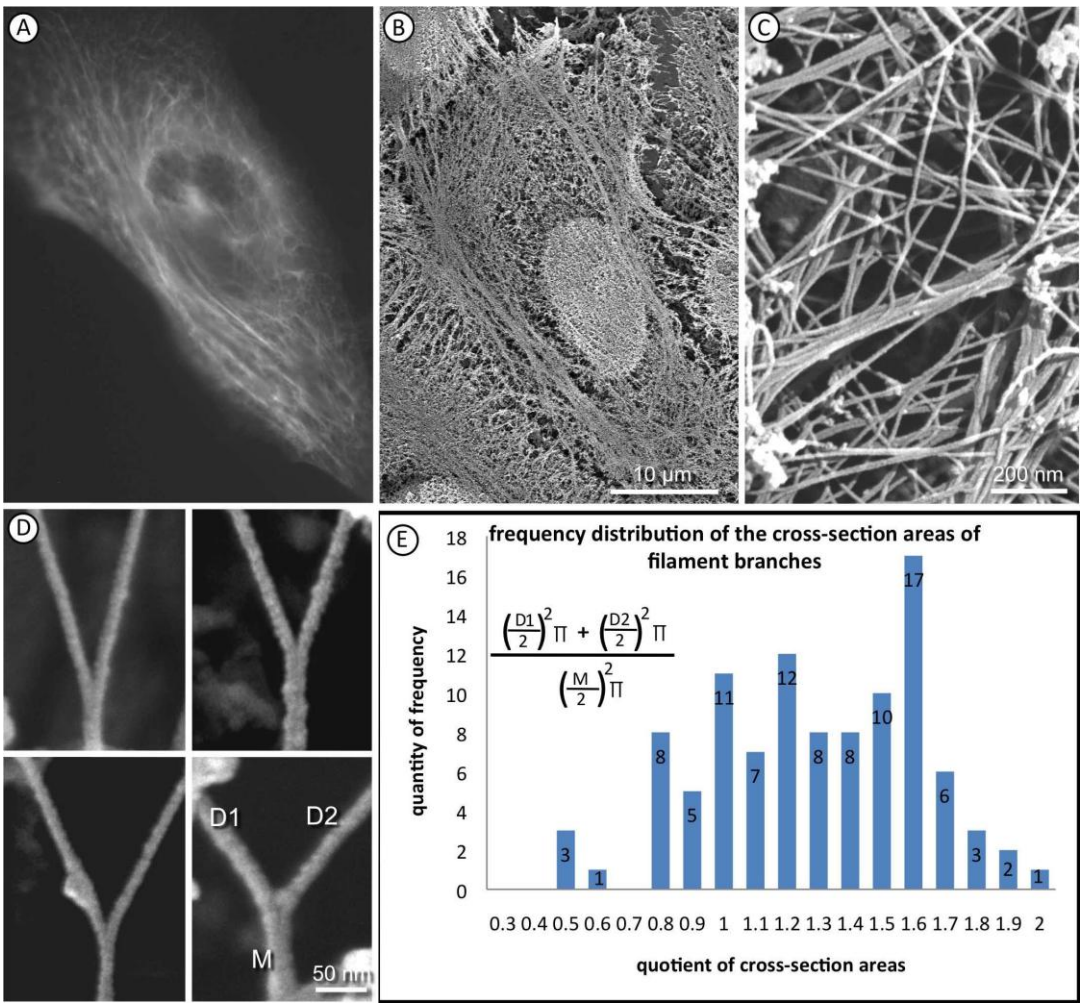

Figure 1. In Fig. A keratin was GFP labeled and the cell was imaged in the fluorescence light microscope. A network of filaments and filament bundles can be observed. Fig B was a similar cell but detergent extracted and imaged in an SEM. Also in this representation different bundles of filaments are visible. The very general structure regarding thickness and arrangement of filament bundles of both images was comparable, indicating that the same keratin structures are highlighted. At higher magnification (Fig. C) it is visible that the bundles are constituted from filaments. Figure D shows branches at the level of single filaments. In Fig. E the results of diameter measurements and their calculated cross-section area proportions are shown. The majority of the proportions are between 1 and 2 whereat a maximum can be observed at the value 1.6. indicating that branching of intermediate filaments is different from actin branching.

Fundamental Cellular Processes: Cell Division, Endo-, Exocytosis, Remodeling of Cytoskeleton, Membrane Trafficking

LS7.084
Three-dimensional reconstruction of the first mitotic spindle in C. elegans reveals different populations of microtubules with distinct properties

S. Redemann[1], J. Baumgart[2], N. Lindow[3], A. Kratz[3], S. Prohaska[3], T. Müller-Reichert[1]

[1]Technische Universität Dresden, MTZ, Dresden, Germany
[2]Max Planck Institute for the Physics of Complex Systems, Dresden, Germany
[3]Zuse Institut, Berlin, Germany

stefanie.redemann@mailbox.tu-dresden.de

Upon entering mitosis, the microtubule cytoskeleton of any eukaryotic organism undergoes a fundamental reorganization to form a bipolar spindle, which first aligns the condensed chromosomes on the metaphase plate and then segregates the chromatids to the forming daughter cells. Despite the fact, that bipolar spindles are composed of the same building blocks and conduct the same function, there is a huge variety in spindle size, assembly and architecture across eukaryotic species. In order to understand spindle architecture, it is essential to understand the detailed 3D ultrastructure of a mitotic spindle and to quantitatively study the key features. We generated full 3D reconstructions of the first mitotic spindle in *C. elegans* during metaphase and anaphase using serial-section electron tomography. In addition, we applied light microscopy to analyze the dynamics of spindle microtubules. This combined analysis provided us with detailed information on the number and length distribution of spindle microtubules, including those microtubules attaching to the holocentric kinetochore. To our surprise, the percentage of kinetochore microtubules within the *C. elegans* spindle is very small, only about 5%. In addition, our data revealed a population of relatively stable kinetochore microtubules with minus ends detached from the spindle poles. Currently, we favor a model in which putative kinetochore microtubules grow out from the centrosome and detach from the spindle pole once the microtubule plus end has connected to the kinetochore, while the plus-end is stabilized on the kinetochore. We will compare our results to published results obtained in other systems.

Fundamental Cellular Processes: Cell Division, Endo-, Exocytosis, Remodeling of Cytoskeleton, Membrane Trafficking

LS7.085
Adhesion process of a virulent and non-virulent ameba studied by transmission electron microscopy and atomic force microscopy

D. Talamás-Lara[1], L. Salazar-Villatoro[1], R. Fragoso-Soriano[1], A. González-Robles[1], B. Chávez-Munguía[1], P. Talamás-Rohana[1], A. Martínez-Palomo[1]

[1]CINVESTAV, Infectomic of pathogenesis molecular, México, D.f., Mexico

daniel_talamas@hotmail.com

Entamoeba histolytica is a significant cause of morbidity and mortality in developing countries. *E. histolytica* is a potent pathogen capable of invading the intestinal mucosa and spreading to other organs, mainly the liver; due to this, *E. histolytica* is able to degrade extracellular matrix (ECM) components during invasion of the intestinal mucosa. Specific adhesion of *E. histolytica* trophozoites to fibronectin (FN) substrate has been previously reported, showing that a specific receptor for FN exists in the amoeba and when this receptor binds to FN it induces the activation of signal pathways that will impact on the actin cytosqueleton structure (Flores-Robles et al., 2003; Sengupta, et al., 2009). The description of the noninvasive *Entamoeba dispar* as a different species has raised the question as to whether the lack of pathogenic potential of this ameba correlates with a weak adhesion and a limited cytoskeleton restructuring capacity. We have therefore compared the process of adhesion to FN in both species.

To analyze the ultrastructural morphology of *E. histolytica* and *E. dispar* during the adhesion process to FN.

Entamoeba histolytica HM1-IMSS and *Entamoeba dispar* SAW 760 RR strains were used. Trophozoites from both species were incubated in petri dishes coated with fibronectin (FN) at 60 min. Parasites were fixed with 2.5% glutaraldehyde and processed for conventional transmission electron microscopy technique (TEM). The same samples were analyzed by atomic force microscopy (ATM).

E. dispar and *E. histolytica* present different adhesion patterns as well as unequal cytoskeleton reorganization when binding to FN. Whereas *E. dispar* binds weakly and without a marked reorganization of the actin cytoskeleton, *E. histolytica* binds in a stronger manner and inducing a notorious structuration of the actin cytoskeleton towards the host-parasite interface. We also observed by TEM and ATM that *E. histolytica* plasma membrane is more intimately attached to the substrate and produced focal adhesions points in the tightest contact sites. In contrast, *E. dispar* plasma membrane shows an irregular profile and less intimately attached to fibronectin. By means of atomic force microscopy using “error signal” we highlighted structures at the contact sites in *E. histolytica* while in *E. dispar* these were not present.

Although these amoebae are morphologically and genetically very similar, there is a clear structural difference in the adhesion process between the virulent and the non-virulent strain when binding to FN. This could be related with the invasive character of *E. histolytica*.

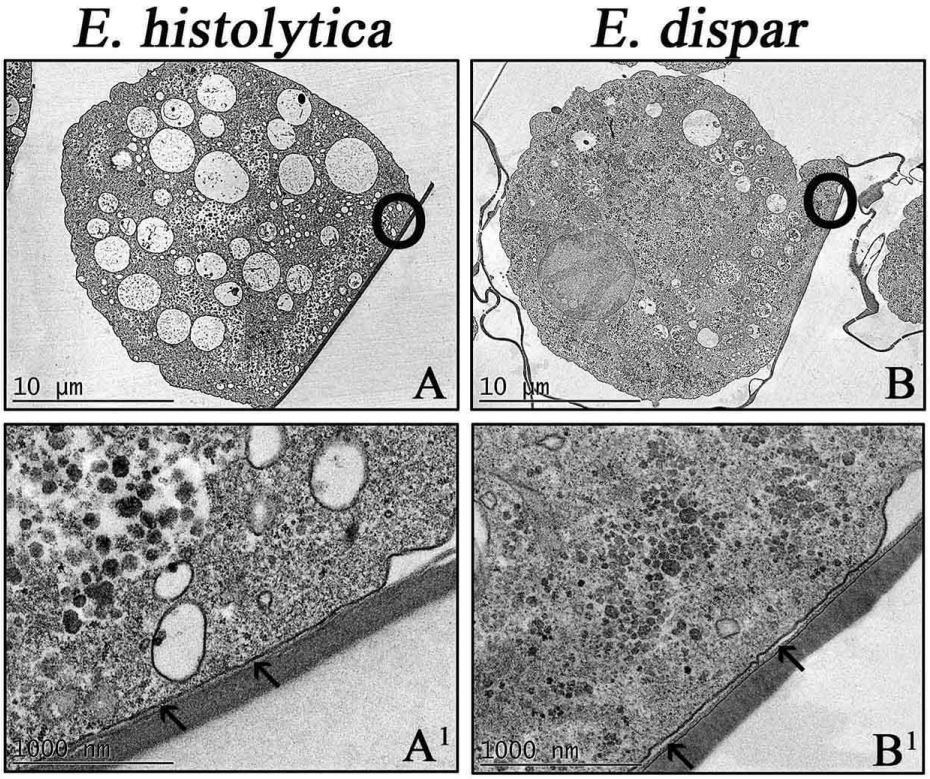

Figure 1. Comparison of intimate adhesion to fibronection of E. histolytica and E. dispar by transmission electron microscopy. A) A complete E. histolytica trophozoite, an B) a complete E. dispar trophozoite adhered to FN are shown; the circles refer to increased areas presented in images A^1 and B^1 respectively. A^1) The plasma membrane is closely adhered to the substrate (arrows). B^1) The plasma membrane is adhered discontinuously and even there are some spaces that have no contact between them (arrows).

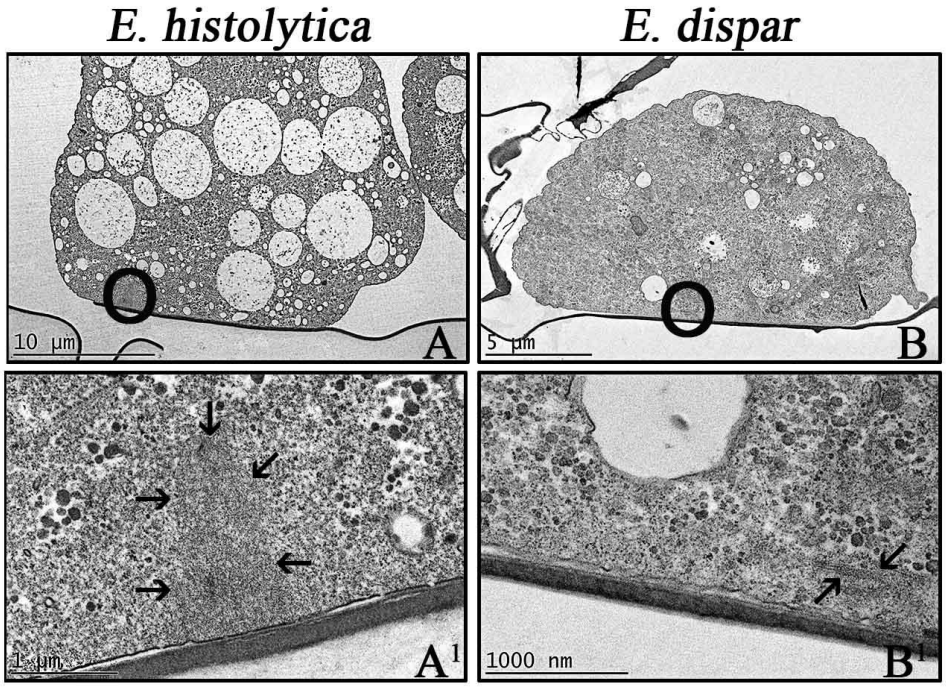

Figure 2. Comparison of the actin cytoskeleton rearrangement in E. histolytica and E. dispar by transmission electron microscopy. A) A complete E. histolytica trophozoite, and B) a complete E. dispar trophozoite adhered to FN are shown; the circles refer to increased areas presented in images A^1 and B^1 respectively. A^1) This image displays a focal adhesion with a strong cytoskeletal rearrangement in the most intimate area of the membrane bound tot the substrate (arrows). B^1)

This image also displays a cytoskeletal rearrangement, however it is located in a cytoplasmic portion of the cell and not near the site of contact with the substrate (arrows).

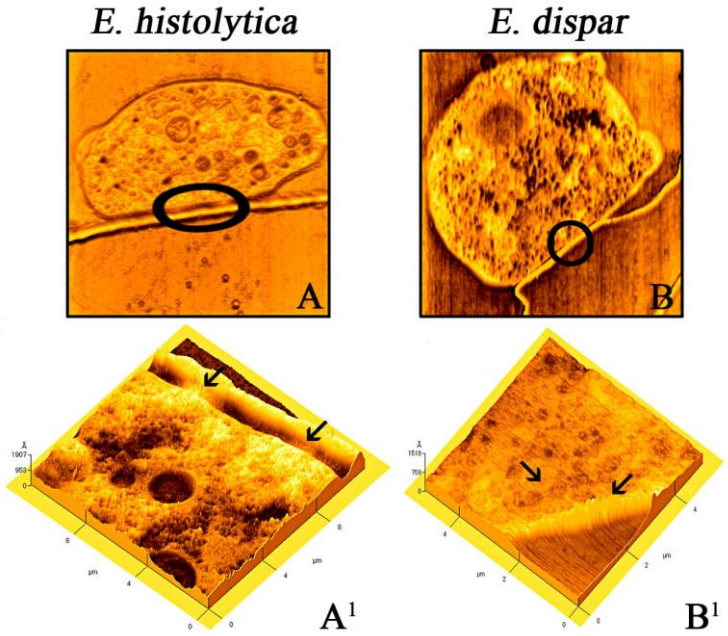

Figure 3. Topographic analysis, by atomic force microscopy, of a site of contact with FN in E. histolytica and E. dispar. A) A complete E. histolytica trophozoite, and B) a complete E. dispar trophozoite adhered to FN are shown; the circles refer to increased areas presented in images A^1 and B^1 respectively. A^1) This image displays two focal adhesions and how there seems to be extended membrane adhering strongly to the substrate (arrows). B^1) This image displays the site of contact, however, there is not a characteristic change or alteration in the contact site and the cytoplasm is observed homogeneous (arrows).

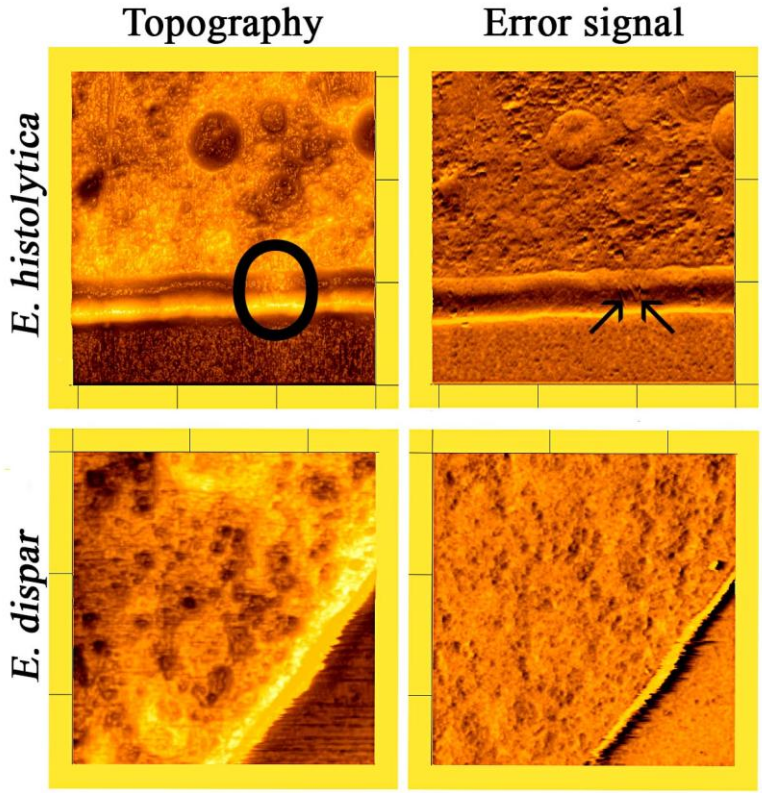

Figure 4. Comparison using topography and error signal mode by atomic force microscopy, of the site of contact in E. histolytica and E. dispar. Topographic image of E. histolytica shows a pronounced focal adhesion (circle) which then, when analyzed using the error signal, displays filamentous structures oriented toward the substrate (arrows); otherwise topgraphic and error signal images in E. dispar demonstrate that these structures are not present at the contact site.

Fundamental Cellular Processes: Cell Division, Endo-, Exocytosis, Remodeling of Cytoskeleton, Membrane Trafficking

LS7.P086
Comparative morphological study of the actin cytoskeleton rearrangement in amoebae of the genus Entamoeba (E. histolytica and E. dispar)

D. Talamás-Lara[1], L. Salazar-Villatoro[1], B. Chávez-Munguía[1], A. González-Robles[1], P. Talamás-Rohana[1], A. Martínez-Palomo[1]

[1]CINVESTAV, Infectomic of pathogenesis molecular, México, D.f., Mexico

daniel_talamas@hotmail.com

Different species of *Entamoeba* perform similar functions such as adherence, cytolysis, and phagocytosis. For example, *E. histolytica* and *E. dispar* share the same processes although the former is pathogenic while the second is non-pathogenic. Systematic comparison between both is an important research area to identify and analyze factors that may be related to pathogenicity. The ability to ingest microorganisms and target cells is associated with amoebic pathogenesis, and in this process, the binding of the parasite to the target cell is mediated initially by electrostatic forces and then, mechanisms that involve surface molecules begin to engage (Sateriale, A., et al., 2012). This binding leads to the activation of signaling pathways that promote reorganization of the actin cytoskeleton (Talamás-Rohana, P. and Ríos A., 2000).

To analyze the dynamics of the actin cytoskeleton between *E. histolytica* and *E. dispar*.
Entamoeba histolytica HM1-IMSS and *Entamoeba dispar* SAW 760 RR strains were used. Trophozoites from both species were incubated on coverslips coated or uncoated with fibronectin (FN) for 60 min. Parasites were fixed with 2.5% glutaraldehyde to view morphological differences using a Jeol JSM-7100F scanning electron microscope. Also the parasites were fixed with 4% paraformaldehyde, permeabilized, and stained with antibody against fibronectin coupled with FITC and rhodamine-conjugated phalloidin; phalloidin, which specifically binds to polymerized actin, is a toxin derived from the fungus *Amanita falloides* (Wehland, J., et al., 1977). Tracking of the restructuring of the actin cytoskeletal in both species was done by confocal microcopy using a Carl Zeiss LSM 700 microscope.

Actin polymerization of *E. histolytica* begins at early times. The formation of lamellipodia in *E. histolytica* is more evident than in *E. dispar*. The non-pathogenic amoeba presents a more limited morphology as well as slower polymerization process. The structuring of actin in *E. histolytica* is induced in areas extremely close to the site of contact with the substrate, showing nucleation points, stress fibers, phagocytic structures and a complete degradation in the part where the amoeba was positioned, besides the FN shows a clear distribution in the cell membrane. In comparison, *E. dispar* shows a limited structuration of the actin cytoskeleton, as the fluorescent label is observed as amorphous clusters distributed throughout the cell volume, without specific locations; furthermore the substrate remains homogeneous without relocation. Z-stack analysis, ortho-cuts, and quantification of fluorescence intensity allowed delimitation of specific sites where the re-structuring of filamentous actin is occurring in both species. To show with more detail the actin structures formed as well as their location within the cell, we processed all optical images from “Z” cuts to achieve a three-dimensional animated reconstruction.

Manifestation of the pathogenic behavior requires cytoskeletal dynamics as this allows parasite movement and tissue penetration. Therefore, results obtained in this work let us conclude that variation in the efficiency of polymerization and subcellular localization of polymerized actin between the strains studied, could explain the aggressive behavior of *E. histolytica*.

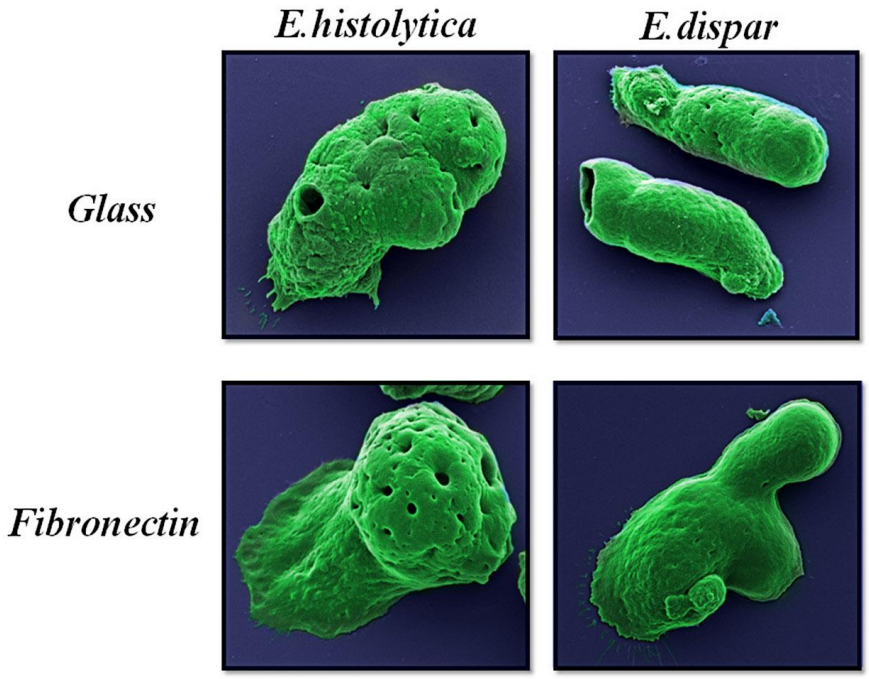

Figure 1. Morphological comparison between Entamoeba histolytica and Entamoeba dispar adhered to glass and fibronectin. Entamoeba histolytica as Entamoeba dispar being adhered to glass, seem to have no morphological changes except for the differences in the roughness of the plasma membrane, however, when these two species adhere to fibronectin, a clear change is observed in Entamoeba histolytica, showing the formation of a prominent lamellipodia, while Entamoeba dispar does not show a significant change in morphology.

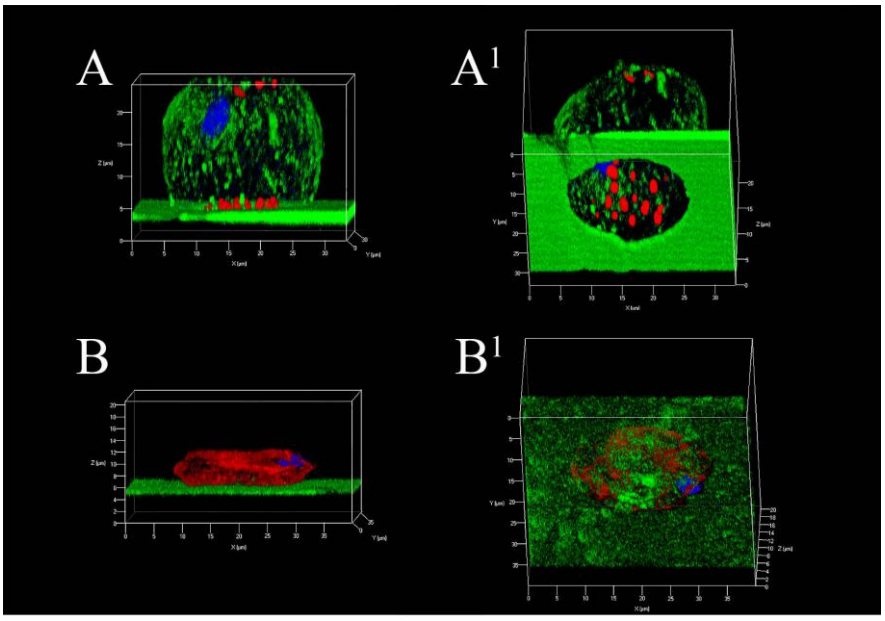

Figure 2. Polymerized actin rearrangement in Entamoeba histolytica and Entamoeba dispar in the adhesion process to fibronectin. A) Three-dimensional reconstruction of Entamoeba histolytica cuts in confocal analysis in Z stack viewed horizontally and A^1) another angle showin actin polymerization as well as degraded substrate. B) Three-dimensional reconstruction of Entamoeba dispar cuts in confocal analysis in Z stack viewed horizontally and B_1) another angle showing actin poymerization and undegraded substrate.

Fundamental Cellular Processes: Cell Division, Endo-, Exocytosis, Remodeling of Cytoskeleton, Membrane Trafficking

LS7.P087
Ultrastructure of wound healing in LED irradiation

A. Butaev[1], J. Mardonov[1], I. Baybekov[1]

[1]Center of surgery, pathology, Tashkent, Uzbekistan

azazello78uz@gmail.com

The use of LED irradiation has increased in medicine, including its application in the phototherapy of wounds. This necessitates research of the comparative effectiveness of different lengths of LED.

The effects of LED radiation of the following diapasons: blue λ - 470 nm with infrared - λ -940 nm (Barva - Flex / BIR), and green - λ -525 nm with infrared - λ -940 nm (Barva - Flex / GIR) on the morphology of the healing of standard dermatome wounds with a diameter of 0.9 cm, reproduced in Wistar rats, as well as the influence of LED irradiation on red blood cells in peripheral blood and around wounds were studied. Wounds were irradiated for 2 min daily during 10 days. Studies were carried out on the 3, 5, 7 and 10 days after the dermatomy. Samples were studied by light, transmission and scanning electron microscopy and morphometry.

During traumatic inflammation stage, the density of neutrophil infiltration increases and the volume fraction of cell-free zones decrease. More rigorous grows of microvessels, predominantly vertically oriented, were observed in the stage of granulation tissue formation, due to increased proliferation of fibroblasts and endothelial cells. The stage of epithelial regeneration was also characterized by active mitotic activity.

Significant differences of wounds are detectable on the day 3 of the study upon visual assessment. Wounds in control had greater area than in LED irradiation. At this period the bottom of wounds contain granulation tissue with a layer of vertical microvessels, which is more mature in the irradiated group. The formed granulation tissue serves as the basis for “crawling” of the epithelial bands on them and epithelialization of wounds. This process too was more pronounced in irradiated animals (Fig. 6,7). In epithelial strands, LED stimulates proliferation of epithelial cells, and especially the so-called intercalary epidermal growth that is seen from increased numbers of mitotic figures.

SEM shows that the tongues of epithelium from the wound edges with a large number of hair rods climb onto granulation tissue, where hair and other appendages of skin are absent. In irradiated animals, these tongues are much wider. The ultrastructural changes in the cells under the influence of LED point to marked intensification of differentiation of newly formed cells and epithelialization of the wound surface. The number of pathological forms of erythrocytes (PFE) was increased in the samples of peripheral blood and blood taken from the areas of wounds. Exposure to the LED result in the normalization of ratio discocytes and PFE both in the peripheral blood and blood from the area of wound defects.

Studies have shown that the effects of different wavelengths of LED irradiation on the wound healing is practically similar, which is concluded in acceleration of all stages of wound healing. However, studies suggest that exposure to LED Barva - Flex / BIR is more effective.

In the stage of traumatic inflammation this type o LED-therapy reduces the manifestations of edema and exudation, accompanied by an increase of the density of neutrophils and their functional activity.

In the stage of granulation tissue formation specific phototherapy intensifies proliferative activity of fibroblasts, endothelial cells and pericytes. Morphologically, it appears as an increase of the number of fibroblasts and increases of the density of newly formed microvessels, especially apparent at period when vertical capillaries are formed [1].

Experimental studies have shown that the LED matrix stimulates proliferation of both connective tissue and epithelial cells. This ensures the effectiveness of their use in treatment of various pathological conditions of the skin. The simplicity of exploitation, high reliability and affordability make the use of LED matrix Barva - Flex a promising method in management of wounds.

Fundamental Cellular Processes: Cell Division, Endo-, Exocytosis, Remodeling of Cytoskeleton, Membrane Trafficking

LS7.P088
Ultrastructural evaluation of the influence of LED douche on reparative processes

A. Butaev[1], A. Baybekov[1], B. Ibadov[1]

[1]Center of surgery, pathology, Tashkent, Uzbekistan

azazello78uz@gmail.com

Total laser irradiation of small animals, the so-called “laser shower” or “laser douche” has a high stimulating effect on the processes of physiological and reparative regeneration of skin, gastro - intestinal tract and bone marrow. Matrices of Light Emitting Diode-LED can simplify the implementation of “photo-douche”. There is scarce data giving experimental-morphological substantiation of their use.

Structural skin changes in dermatome wounds and changes in bone marrow were studied after exposing body surfaces of Wistar rats to LED at blue (λ -470 -12 nm), green (λ -525 nm-12), and infrared (λ -940 -12 nm) ranges. Transmission and scanning electron microscopy - TEM and SEM with light microscopy of semi-thin epon-araldite sections were used for study. Changes, occurring in rats with standard dermatome wounds and in intact rats were compared. Rats were exposed to radiation for 2 minutes daily during 10 days. The radiation power of each LED was equal to 5mW. The control group was not exposed to photoradiation.

Besides the local manifestations of the inflammatory reactions, dermatome wounds change the ratio between normal erythrocytes-discocytes and pathological forms - echinocytes, stomatocytes, erythrocytes with crests. This is accompanied by an increase in the number of abnormal forms of erythrocytes in bone marrow. LED “douche” of control animals causes ultrastructural changes in cells of skin, bone marrow, colon and stomach after 2-3 sessions, representing intensification of specific cellular functions. The most pronounced changes which justify above mentioned occur to connective tissue with increasing growth of microvessels to provide rising demand for microcirculation. Epithelial and connective tissue cells of stomach, intestines and skin increase their proliferative activity. In the bone marrow, along with an increase of mitotic activity and accelerated differentiation of cells of erythroid and myeloid series, of significantly increases the migration of mature cells to the sinusoidal capillaries and in the circulation. The phagocytic activity of all types of phagocytes becomes increased.

In animals with dermatome wounds, LED douche accelerates all stages of wound healing. It reduces the manifestations of edema and exudation during traumatic inflammation and increases the density of neutrophils and their functional activity.

Ultrastructural studies has shown that increased cell proliferation is accompanied by intensification of differentiation processes. In the bone marrow, peripheral blood, and blood samples from wound area showed shifting of the ratio to normal red blood cells- discocytes.

Structural changes in the cells of organs points at fact that LED douche can be an alternative to laser douche. Possibility of using the LED irradiation on large surfaces of body determines extreme importance of this type of phototherapy in injuries of large surfaces of skin, in particular, for burns.

Fundamental Cellular Processes: Cell Division, Endo-, Exocytosis, Remodeling of Cytoskeleton, Membrane Trafficking

LS7.P089
Electron microscopic study of the effects of laser radiation on the interaction of synthetic meshes with biological tissues

I. Baybekov[1], N. Sadikov[2], S. Yigitaliev[2]

[1]Center of surgery, pathology, Tashkent, Uzbekistan
[2]Center of surgery, surgery, Tashkent, Uzbekistan

baibekov@mail.ru

Various meshes of synthetic materials are widely used for plastics of hernias.

Implantation of any foreign material into body causes development of inflammatory-reparative processes, which are manifestations of defense reactions of tissues.

One of the most powerful modern means of providing anti-inflammatory effect, is a low-intensity laser radiation - LILI

A study of the characteristics of these interactions and the effect of LILI on them would recommend the best options for the use of synthetic prostheses and modes of laser exposures when used in hernia repair. This determined the essence of this piece of work.

For morphological study with scanning electron SEM and light microscopy, tissue fragments were excised at days 7, 14 and 30 after implantation of PTFE, PROCEED, and PROLEN meshes. The animals of control group were not exposed to laser irradiation. Experimental group was irradiated with magnet-infrared laser “Mustang” on a daily basis during the period of observation.

PTFE meshes have the most complex laminated structure. It consists of three layers, with different structure, as shown by SEM. Outside it was formed by consistently ribbed surface resembling furrows plowed field. The core located between two outer layers, in turn, is formed by several layers, which are formed of closely intertwined short fibers.

PROLEN represents a mesh formed by the interweaving of homogeneous filaments.

PROCEED, in addition to the filaments, is formed by irregularly shaped plate-like structures.

Studies of the interactions of meshes with tissues showed that with structural integrity of their surfaces, they do not cause significant pathological reactions in tissues.

Well developed connective tissue complexes start to appear after 14 days on the surface of the PROCEED meshes. Frequently, erythrocytes are visible on the surface PROCEED meshes together with connective tissue cells.

SEM shows that at day 14, red blood cells and connective tissue cells are determined in all layers of PTFE meshes, which is clearly visible on lateral surfaces of their pores. On the surface itself, the layers of connective tissue contain erythrocytes.

Application of laser irradiation in implanting all types of meshes leads to a significant decrease in the manifestation of inflammation, especially in early stages, at 7-14 days of observation, formation on surfaces of grids softer capsules.

On the 14th day of interaction of PROLEN mesh with tissues the filament of meshes are seen as smooth flat surface, with absence of any superpositions. Filaments themselves did not have defects or tears.

On day 30 PTFE meshes are coated with homogenous layer of connective tissue.

PROLEN meshes also contain single red blood cells on their smooth surface 14 days after implantation and laser therapy.

The fragments of PROCEED meshes, also, did not contain any superpositions on the 14 and 30 days in their depth after laser therapy.

PTFE mesh does not cause connective tissue proliferation between it and the adjacent tissues; only thin layers of connective tissue are detectable on the surface between PTFE mesh and adjoining to it tissue.

Laser irradiation of the wound area, after implantation meshes, reduces expression of alterative inflammation phase and is completed by the formation of subtle connective tissue capsule on the surface of meshes. It also contributes to reduction of hemorrhagic foci in the area of surgical sutures.

Fundamental Cellular Processes: Cell Division, Endo-, Exocytosis, Remodeling of Cytoskeleton, Membrane Trafficking

LS7.P090
Visualization of plastoglobules isolated from plants with different chilling tolerance.

J. Wójtowicz[1], J. Grzyb[2], J. Skupień[1], A. Mostowska[1], K. Gieczewska[1,3]

[1]Warsaw University, Department of Plant Anatomy and Cytology, Faculty of Biology, Warsaw, Poland
[2]Polish Academy of Sciences, Institute of Physics, Warsaw, Poland
[3]Maria Curie-Sklodowska University in Lublin, Department of Biophysics, Institute of Physics, Lublin, Poland

j.wojtowicz@biol.uw.edu.pl

Chloroplasts are organelles present in plant cells and some eukaryotic organisms. Chloroplasts have a highly developed membrane system consisting of: the outer membrane, the inner membrane and the thylakoid system where the photosynthesis process occurs. Plastoglobules are lipoprotein particles inside chloroplasts. Composed of an outer polar lipid monolayer containing lipids (mainly prenylquinones, triacylglycerol, and carotenoids), studded with harbor proteins are believed to play a biosynthetic function in chloroplast development. Plastoglobule unique spatial relationship to thylakoid membranes is probably due to their extensive function in plant response to stress by accumulating antioxidants [1] and various methabolic pathways such as vitamin K, tocopherol, and carotenoids synthesis. It has been observed that the size and number of these small structures is regulated in correlation with the fitness of the thylakoid membranes [2]. Therefore, appears to be essential to characterize the arrangement and conformation of plastoglobules in the thylakoid membrane environment, their spatial distribution as well as topography and physical properties.

Studies were carried out on two species of plants with different response to chilling stress, chilling sensitive bean (Phaseouls vulgaris L.) and chilling tolerant pea (Pisum sativum L). Our previous research demonstrated that the mature chloroplasts of these plants differ in the

thylakoid organization [3], which affects the plastoglobule formation and composition. Moreover, we showed that plastoglobules isolated from pea and bean chloroplasts differ in lipid composition and significantly vary in shape and size. To further investigate the topography and physical properties of these structures contact and non-contact mode of AFM microscope, TEM and CLSM microscopy was used.

1. C.Brehelin, F. Kessler, The plastoglobule: a bag full of lipid biochemistry tricks. Photochem Photobiol 84 (2008) 1388-1394.
2. C. Besagni, F. Kessler, A mechanism implicating plastoglobules in thylakoid disassembly during senescence and nitrogen starvation. Planta 237 (2013) 463-470.
3. Rumak, I. *et al.* (2012) Correlation between spatial (3D) structure of pea and bean thylakoid membranes and arrangement of chlorophyll-protein complexes. *BMC Plant Biology* 12: 72
4. Presented work was financed by SONATA grant no 2013/09/D/NZ3/02399 from National Science Centre, Poland (KG).

Fundamental Cellular Processes: Cell Division, Endo-, Exocytosis, Remodeling of Cytoskeleton, Membrane Trafficking

LS7.P091
Detection of Wnt/β-catenin signaling in spermatogonia by different microscopic techniques and activation of spermatogenesis by β-catenin in ex vivo testis explants from double transgenic medaka

F. Pfennig[1], T. Kurth[2], M. Ullrich[1], M. Kotte[1], A.- C. Stuhr[1], M.- R. Weise[1], M. Kluge[1], O. Borsch[1], A. Froschauer[1], H. O. Gutzeit[1]

[1]Institute of Zoology, TU Dresden, Dresden, Germany
[2]CRTD/Biotec, TU Dresden, EM facility, Dresden, Germany

frank.pfennig@tu-dresden.de

Wnt/β-catenin signaling plays a pivotal role during differentiation and proliferation of stem cells. The canonical Wnt pathway is characterized by nuclear localization of β-catenin. Furthermore, membrane-associated β-catenin is a typical feature of a stem cell niche. Recent reports indicate an involvement of canonical Wnt signaling in the regulation of mouse spermatogonial stem cells (SSCs). Histological data about the role of Wnt signaling in development of SSCs in fish testis are limited and therefore in focus of our studies.

We analyzed the β-catenin localization with reference to the expression of established stem cell- and germ line markers in the testis of the Japanese medaka (*Oryzias latipes*) by immunofluorescence and confocal laser scanning microscopy. Proliferation was detected by incorporation of the thymidine analogon Click-It®Edu and PCNA antibody staining. The subcellular localization of β-catenin was confirmed by preembedding immunogold labeling and electron microscopy. Our experiments revealed that nuclear β-Catenin accumulated in the *oct4*-expressing SSCs (type A spermatogonia) and that membrane bound- and cytoplasmic β-Catenin was enriched preferentially in these undifferentiated spermatogonia.

For functional proof of a role of β-Catenin/Wnt signaling in fish spermatogenesis we developed an *ex vivo* organ culture system that allows the interference with developmental processes by specific inhibitors. By the use of Gsk3β-inhibitors (causing stabilization of cytoplasmic β-Catenin) we have induced spermatogonial proliferation. The results suggest the involvement of β-Catenin in the regulation of SSC proliferation and differentiation in a non-mammalian vertebrate model organism.

Fundamental Cellular Processes: Cell Division, Endo-, Exocytosis, Remodeling of Cytoskeleton, Membrane Trafficking

LS7.P092
Structural changes in domestic cat ovarian tissue after the needle immersed vitrification method

M. Demirel[1], D. Baki Acar[2], F. Topal Çelikkan[3], B. Ekim[4], S. Özkavukçu[5], H. Kanca[6], E. Atabenli Erdemli[3], A. Başţan[6]

[1]Gazi University, Faculty of Farmacy, Laboratory Animal Care and Research Unit, Ankara, Turkey
[2]Afyon Kocatepe University, Faculty of Veterinary Medicine, Department of Obstetrics and Gynecology, Afyonkarahisar, Turkey
[3]Ankara University Medicine Faculty, Histology and Embryology, Ankara, Turkey
[4]Gazi University, Life science Research and Application Center, Ankara, Turkey
[5]Ankara University, Assisted Reproduction Center, School of Medicine, Ankara, Turkey
[6]Ankara University, Faculty of Veterinary Medicine Department of Obstetrics and Gynecology, Ankara, Turkey

ferdatopal@gmail.com

In recent years, cryopreservation of ovarian tissue is opening new horizons for fecundity preservation and overcoming infertility. Moreover, in veterinary medicine, cryopreservation of oocyte and ovarian tissue is crucial to protect the race for species that are in danger of extinction.

Some of the studies showed that vitrification seems a more useful, cheap and rapid method for ovarian cryopreservation. In this study we investigate the structural effects of NIV method in domestic cat ovarian tissue As it is known Turkish Ankara and Van cats are in danger of extinction so that good preservation of the ovarian tissue will contribute to increase the population size of this domestic species.

Domestic feline ovarian tissues were used for this study. All animal procedures were approved by the Ethics Comittee of Ankara University (No: 2012-5-30). Ovaries were collected from cats undergoing routine ovariohystrectomy (aged 10-24 month, n: 25). To vitrify, tissues were cut very small fragments (1 mm^3) and immersed L-15 medium. Then, tissue pieces were placed in an acupuncture needle equilibrated in gradually increasing concentrations of CPA (cryoprotectant agent) (DMSO, EG, sucrose). After equilibration, tissues were plunged directly into liquid nitrogen and put into cryovials. After one week, vitrified ovarian tissues were transferred through a series of gradually decreasing concentrations of CPA. Tissues were washed in DPBS and transferred to Bouins' and 2% glutaraldehyde solution.

Paraffin slides were stained with Hematoxylen-Eosin, anti-caspase3 and observed under a brightfield microscope (CarlZeiss Axioskop,Germany). TUNEL) method was used to assess the apoptosis and for ultrastructural observations, after conventional tissue processing, semi-thin and ultra-thin sections were cut and observed by TEM (LEO 906 E TEM, 60 kV; Zeiss,Jena,Germany) and photographed.

In control group, follicles were examined in normal appearance. Oocytes had regular architecture with euchromatic nuclei. Follicle cells which surrounding oocytes were observed as uniform shapes (fig 1a). In vitrified group, oocytes were observed as degenerated with eosinophilic cytoplasm and condense nuclei. In atretic follicles, oocytes and follicle cells were shrinkaged in vitrified tissues. Irregullar oolemma and ZP were also seen. Vacuolisation was evident between oocyte and follicle cells and in interstitial tissue (fig 1b). TUNEL and anti-caspase-3 staining in vitrified group were more frequent than in control group (fig 2b, 2c, 3b, 3c).

In thin sections, oocyte nuclei and the distribution of the chromatin were intact in non-degenerated follicles in control group. The junctions between the follicle cells were preserved in this group. In vitrified group, oocyte organelles were condensed and gathered in the particular side of cytoplasm. Vacuolisation was obvious between oocyte and follicle cells. Loosely interstitium and necrotic interstitial cells with karyolytic nucleus were observed in this group (fig 4a, 4b, 4c, 4d).

Vitrification with NIV method caused degeneration on feline ovarian follicle. This technique is needed to be improved for diminishing the damage. Before the transplantation, tissue structure should be checked to promote tissue viability.

1. This study was supported by Turkish Scientific and Technical Research Council-TUBITAK (Project Number: 112O811.

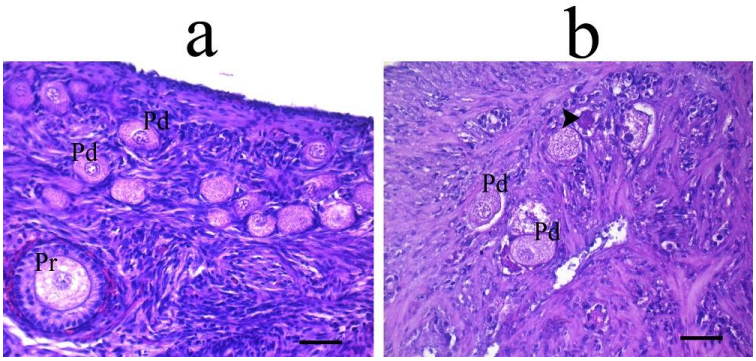

Figure 1. a) Control group, b) Vitrification group. Pd: primordial follicle, Pr: primary follicle. Arrow head: degenerated follicle. Hematoxylen-Eosin, scale bar: 50 µm.

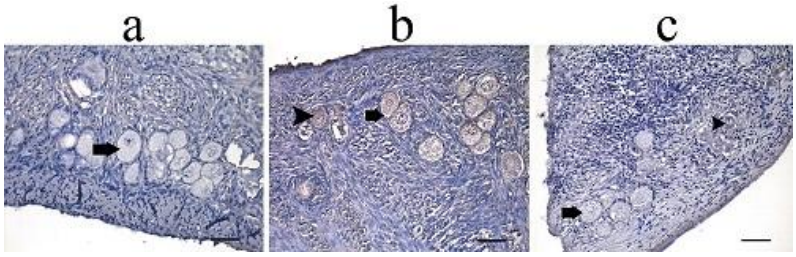

Figure 2. a) Negative control staining b) Control group, c) Vitrification group. Arrow head: stained oocyte with anti-caspase-3, thick arrow: unstained oocyte with anti- caspase-3. Scale bar: 50 µm.

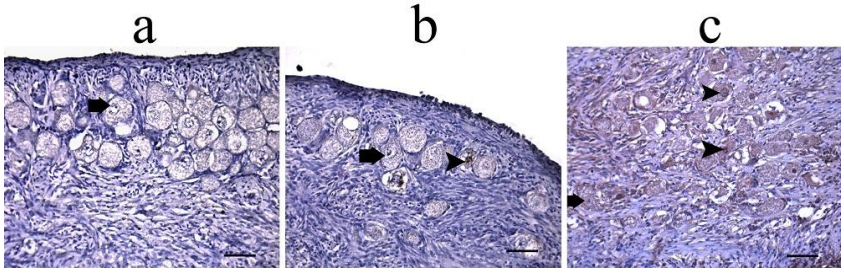

Figure 3. a) Negative control b) Control group, c) Vitrification group. Arrow head: unstained oocyte with TUNEL, thick arrow: positive staining with TUNEL. Scale bar: 50 µm.

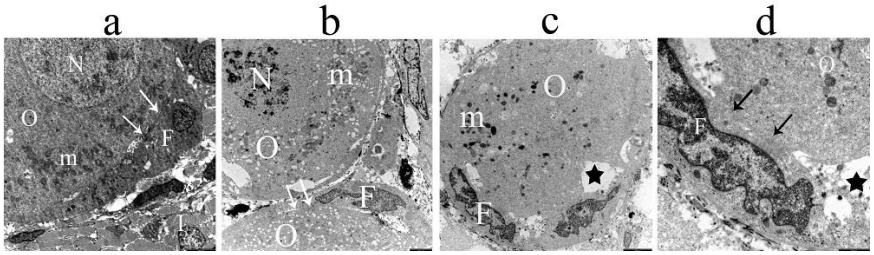

Figure 4. a) Control group, b, c, d) Vitrification group. O: oocyte, N: nucleus of oocyte, m: mitochondrion, F: follicle cell, I: interstitium, thin arrows: junction between oocyte-follicle cell, aster: vacuolization.

Fundamental Cellular Processes: Cell Division, Endo-, Exocytosis, Remodeling of Cytoskeleton, Membrane Trafficking

LS7.P093
The human submandibular gland: immunohistochemical analysis of SNAREs and cytoskeletal proteins

M. Stoeckelhuber[1], E. Q. Scherer[2], K.- P. Janssen[3], J. Slotta-Huspenina[4], D. Loeffelbein[1], M. R. Kesting[1]

[1]Technische Universität München, Department of Oral and Maxillofacial Surgery, Munich, Germany
[2]Technische Universität München, Department of Otorhinolaryngology, Munich, Germany
[3]Technische Universität München, Department of Surgery, Munich, Germany
[4]Technische Universität München, Institute of Pathology, Munich, Germany

stoeckelhuber@mkg.med.tum.de

Submandibular acinar glands secrete numerous proteins such as digestive enzymes and defense proteins on the basis of the exocrine secretion mode. Exocytosis is a complex process, including a soluble NSF attachment protein receptor (SNARE)-mediated membrane fusion of vesicles and target membrane and the additional activation of cytoskeletal proteins. Relevant data are available predominantly for animal salivary glands, especially of the rat parotid acinar cells. The aim of our study was to elucidate the participation of actin, myosin II, cofilin, profilin, SNAP-23, syntaxin-2, syntaxin-4, VAMP-2, and septin-2 in the exocytosis mechanism in the human submandibular gland.

Immunohistochemistry and immunofluorescence

We investigated the secretory molecular machinery of acinar (serous) cells in the human submandibular gland and found diverse proteins associated with exocytosis for the first time. SNAP-23, syntaxin-2, syntaxin-4, VAMP-2 were localized at the luminal plasmamembrane, syntaxin-2 and septin-2 were expressed in vesicles in the cytoplasm. Double-staining of syntaxin-2 and septin-2 revealed a colocalization on the same vesicles. Lactoferrin and alpha-amylase served as marker for secretory vesicles and were labeled positively together with syntaxin-2 and septin-2 in doublestaining procedures. Cytoskeletal components like actin, myosin II, cofilin and profilin are concentrated at the apical plasma membrane of acinar submandibular glands.

This study reveals the participation of actin, myosin II, cofilin, profilin, SNAP-23, syntaxin-2, syntaxin-4, VAMP-2, and septin-2 in the complex exocytosis mechanism of the human submandibular gland.

Dynamic microscopy of energy conversion processes

JS-SFB.01
Cooperative atomic motion probed by ultrafast transmission electron diffraction

J. Demsar[1]

[1]Institute of Physics, Johannes Gutenberg-University Mainz, Germany

demsar@uni-mainz.de

In solids, exhibiting broken symmetry ground states, the changes in the electronic (spin) structure often result in modulation of the underlying crystal structure. Examples of such are charge and spin density wave systems [1], magnetic shape memory alloys, or multi-ferroics. Femtosecond time-resolved techniques recently contributed many important insights into the origin of their ground states, and the interplay between the electronic (spin) and lattice degrees of freedom, by tracking their dynamics using ultrashort light pulses ranging from THz to UV [2,3,4]. To gain direct access into the accompanying changes in the crystal lattice femtosecond X-ray methods have been a method of choice [5,6,7]. In the last decade or so, however, ultrafast electron diffraction and microscopy techniques have been put forward [8,9,10].

Here we present studies of light-induced structural dynamics in quasi two-dimensional charge density wave systems utilizing ultrafast transmission electron diffraction. Since intensities of the super-lattice diffraction peaks are in the first approximation proportional to the square of the periodic lattice distortion (PLD) amplitude, their temporal evolution provides direct access to the order parameter dynamics. The light induced cooperative atomic motion takes place on a 100 femtosecond timescale, corresponding to a fraction of a period of the corresponding lattice vibration [6,7,9,11]. However, since energy transfer from the excited electronic system to the lattice takes place on a comparable, sub-picosecond, timescale [9,11], contribution of the incoherent lattice motion on diffraction intensities is not negligible and has to be taken into account, when trying to extract the order parameter trajectory.

Here we demonstrate that, using an ultrafast transmission electron diffraction, relative changes in individual diffraction peaks of less than 1% can be studied. Taking a prototype two-dimensional charge density wave system 1T-TaS_2 as an example, we demonstrate, that by simultaneously tracking the dynamics of intensities in super-lattice peaks, lattice peaks and of the incoherent background over multiple diffraction orders, the two processes, order parameter dynamics and the incoherent electron-phonon thermalization, can be effectively disentangled, providing direct access to the dynamics of the order parameter.

*In collaboration with M. Eichberger, S. Liebermann, C. Klose, M. Obergfell, R. Birmuske, J. Sutter, M. Krumova, and H. Berger

1. G. Grüner, *Density waves in solids*, Addison-Wesley, 1994.
2. H. Schaefer et al., Phys. Rev. Lett. 105, 066402 (2010).
3. K.W. Kim, et al., Nature Mat. 11, 497 (2012).
4. M. Porer et al., Nature Mat. 13, 857 (2014).
5. K. Sokolowski-Tinten, et al., Nature 422, 287 (2003).
6. E. Vorobeva, et al., Phys. Rev. Lett. 107, 036403 (2011).
7. T. Huber et al., Phys. Rev. Lett. 113, 026401 (2014).
8. B. Siwick, et al., Science 302, 13 (2003).
9. M. Eichberger, et al., Nature 468, 799 (2010).
10. M. Gulde, et al., Science 345, 200 (2014).
11. N. Erasmus, et al., Phys. Rev. Lett. 109, 167402 (2012).

Dynamic microscopy of energy conversion processes

JS-SFB.02
Unraveling heterogeneous structural dynamics using ultrafast electron microscopy

O.- H. Kwon[1,2]

[1]Ulsan National Institute of Science and Technology, Department of Chemistry, Ulsan, Korea, Republic of
[2]Institute for Basic Science, Center for Soft and Living Matter, Ulsan, Korea, Republic of

ohkwon@unist.ac.kr

With advances in spatial resolution reaching the atomic scale, 2 and 3 dimensional (D) imaging in transmission electron microscopy (TEM) has become an essential methodology in various fields of research providing *static* structural information. Now it has become possible to integrate the ultrahigh temporal resolution (fourth dimension) to the 3D spatial resolution of TEM.[1,2] Here, presented is the concept of time-resolved imaging in ultrafast electron microscopy (UEM).

Here, we demonstrate the selectivity and sensitivity of the technique by visualizing the structural *dynamics* of single nanocrystals, whether isolated[3] or crowded,[4] in real and reciprocal space. Their behavior were observed to be distinct from that imaged by averaging over ensembles of heterogeneous nanoparticles and dependent on their size.

Finally, also presented is an ongoing effort at UNIST to upgrade UEM operating in both modes of stroboscopy (repetition of a pair of pump and probe) and single-shot measurements (single pump and multiple probes).

1. B. Barwick, H. S. Park, O.-H. Kwon, J. S. Baskin, A. H. Zewail, *Science* 322 (2008) 1227.
2. O.-H. Kwon, A. H. Zewail, *Science* 328 (2010) 1668.
4. R. van der Veen, O.-H. Kwon, A. M. Tissot, A. Hauser, A. H. Zewail, *Nature Chem.* 5 (2013) 395.
H. Liu, O.-H. Kwon, J. Tang, A. H. Zewail, *Nano Lett.* 14 (2014) 946.

Dynamic microscopy of energy conversion processes

JS-SFB.03
Design of a new ultrafast transmission electron microscope

K. Bücker[1], M. Picher[1], J. P. Derouet[2], G. Brunetti[2], T. Lagrange[3], B. W. Reed[4], D. Masiel[4], F. Banhart[1]

[1]IPCMS, DSI, Strasbourg, France
[2]JEOL (Europe) SAS, Croissy-sur-Seine, France, France
[3]Interdisciplinary Center for Electron Microscopy, Ecole Polytechnique Fédérale de Lausanne, Lausanne, Switzerland
[4]Integrated Dynamic Electron Solutions Inc., (IDES), Pleasanton CA, USA, United States

kerstin.buecker@ipcms.u-strasbg.fr

In the past decades, spatial resolution of Transmission Electron Microscopes (TEM) has been improved down to the sub-Angstrom range. More recently, studies have begun to focus on *in-situ* experiments for imaging a variety of dynamic processes at the atomic scale. However, most of the nanoscale processes occur at very short time scales, in the micro- to femtosecond domain. Studies on such processes are limited by the acquisition frequency of the TEM detectors (~few milliseconds), thus missing the salient details of the sample dynamics, e.g. defect processes, phase transformations, or nucleation phenomena.For such studies, a much higher temporal resolution is required.

This can be obtained using short electron pulses in a pump-probe approach. After excitation (pump) the sample is probed with an electron packet at a variable time delay with respect to the excitation. Repeating this process at different delays allows time-resolved studies.

These pulsed electron imaging studies can be carried out in two different operating modes:

- Single shot mode, required for studying irreversible processes, using high intensity pulses with a sufficient number of electrons ($>10^8$) to capture single-shot images of transient states in the material on nanosecond to microsecond timescales.

- Stroboscopic mode allows imaging and spectroscopy of reversible processes with high spatial and energy resolution through the accumulation of millions of low-intensity electrons pulses (1-100 electrons) at MHz repetition rates.

In this contribution, we present the setup and the first results of the new Ultrafast Transmission Electron Microscope (UTEM) developed at the IPCMS (Strasbourg, France). The microscope is the first instrument designed to operate in both stroboscopic and single-shot modes. At the present time, the microscope operates in stroboscopic mode, while the single-shot mode is under development.

The equipment is based on a JEOL 2100 transmission electron microscope combined with a femtosecond fiber laser. The initial infrared laser beam (1030 nm, pulse length 370 fs) is split into two beams. The pump beam is focused onto the specimen and excites the material. The probe beam is frequency-quadrupled to ultra-violet (257 nm) and then focused onto the filament of the TEM gun to generate electron pulses via photoemission. The delay between both pulses is controlled by tuning the path length of one laser beam with respect to the other, using a high-precision optical delay line. A new condenser lens (C_0 lens) was integrated for focusing the electron beam above the conventional condenser lens system, thus increasing the beam current.

In the present configuration (stroboscopic mode) the high repetition rate of the laser (1 kHz - 40 MHz) generates a continuous train of pulses that illuminates the TEM sample, allowing picosecond events to be investigated in imaging, diffraction and spectroscopy modes. The repetition rate of the laser is set such that the sample relaxes to its ground state between the pulses. Images and spectra are generated through the integration of millions of pump-probe events.

The first results show comparable image resolution (0.23 nm) for thermionic and photoelectron modes, while the energy resolution for EELS (< 0.7 eV) is much improved in the photoelectron mode (Figs. 1a and b). Detailed characterization of the electron pulses (duration and intensity distribution) as a function of UTEM parameters is done through the Photon-Induced Near-Field Effect (PINEM). This effect is based on the photon-electron interaction in the near-field of nanoscale objects, i.e. electrons coinciding with the photon pulse at the specimen loose or gain entire quanta of photon energy which is visible in the electron energy-loss spectrum (Fig. 1c).

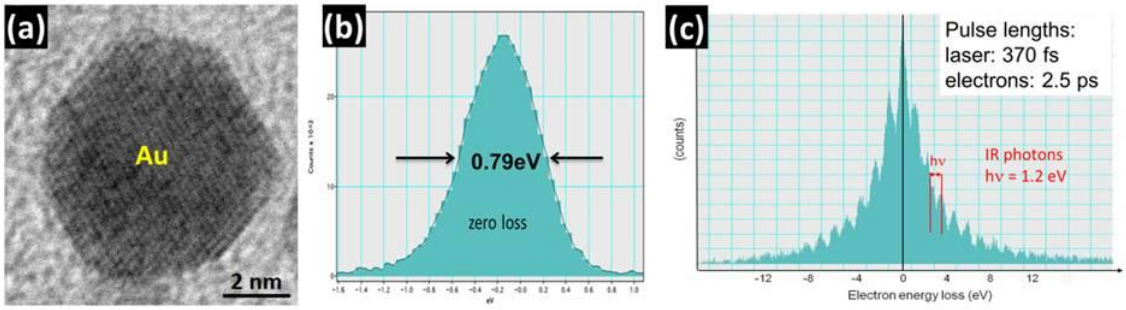

Figure 1. Spatial resolution in the photoelectron imaging mode, without laser on the specimen **(a),** zero-loss peak showing the EELS resolution in the photoelectron mode **(b),** broadening of the zero-loss peak in the PINEM spectrum **(c).**

Dynamic microscopy of energy conversion processes

JS-SFB.04
Ultrafast transmission electron microscopy based on a laser-driven Schottky field emitter

A. Feist[1], K. E. Echternkamp[1], R. Bormann[1], N. Rubiano da Silva[1], M. Möller[1], J. Schauss[1], S. V. Yalunin[1], S. Schäfer[1], C. Ropers[1]

[1]Universität Göttingen, IV. Physikalisches Institut, Göttingen, Germany

feist@ph4.physik.uni-goettingen.de

Ultrafast transmission electron microscopy (UTEM) is a promising technique, which utilizes sub-picosecond electron pulses to resolve ultrafast laser-induced processes on a nanometer length scale (Fig. 1a) [1, 2]. In UTEM, a pulsed electron beam of sub-picosecond duration is employed to stroboscopically probe ultrafast laser-driven dynamics with the imaging and diffraction capabilities of electron microscopy. The potential of this approach crucially depends on the implementation of high-brightness laser-driven electron sources within the constraints of a functional electron microscope

Here, we present recent developments and first applications of the Göttingen UTEM instrument, which is based on the custom modification of a JEOL 2100F Schottky field emission TEM. The laser-triggered nanoscopic electron source [3] employs localized single-photon photoemission from a tip-shaped ZrO/W(100) emitter. Highly coherent ultrashort electron pulses with a normalized emittance of 4 nm·mrad are generated, enabling ultrafast electron imaging with phase-contrast (Fig. 1b) and time-resolved local probing. Specifically, in the sample plane, we obtain electron focal spot diameters down to 3 nm, with a temporal pulse width of 300 fs (full-width-at-half-maximum) and a spectral bandwidth of 0.6 eV (cf. Figs. 1c-e, Fig 2d).

In a first application, we utilize the nanoscopic probing capabilities of our microscope to investigate the inelastic scattering of free electrons with confined light (Fig. 2a) [4,5]. Specifically, the energy spectrum of electrons traversing an optical near-field develops a comb of spectral side-bands, corresponding to the absorption and emission of multiple photons, with the interaction strength governed by the local near-field amplitude (Fig. 2b).

We experimentally demonstrate the quantum-coherence of this process by observing Rabi oscillations in the populations of spectral side-bands as a function of the amplitude of the optical driving field (Fig. 2c) [2]. Such an interaction constitutes a coherent optical phase-modulation of the incident electron wave function, and we discuss its application for the longitudinal manipulation electron densities on attosecond time scales.

In conclusion, we characterize the performance of nanoscale photoemitters in time-resolved transmission electron microscopy and present first results on free electron pulses interacting with intense optical near-fields.

1. A. H. Zewail, Science **328**, 187 (2010).
2. A. Feist et al., Nature, accepted for publication (2015).
3. M. Gulde et al., Science **345**, 200 (2014).
4. B. Barwick et al., Nature **462**, 902 (2009).
5. F. J. García de Abajo et al., Nano Lett. **10**, 1859 (2010).

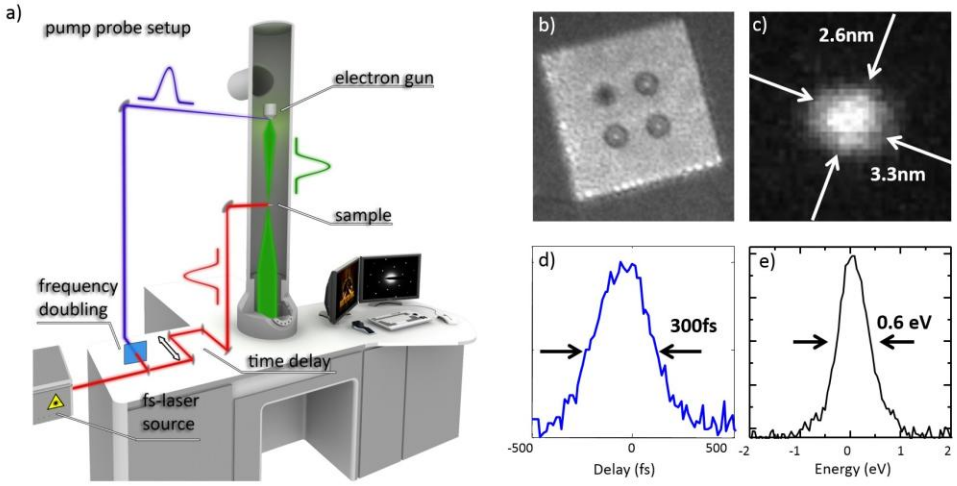

Figure 1. (a) General principle of UTEM. Pulses illustrate the stroboscopic laser-pump/electron-probe scheme. (b) Lorentz image of a magnetic nanostructure acquired with ultrashort electron pulses (image edge length: 4 µm). (c) Minimum electron focal spot size and (d,e) temporal/spectral electron pulse properties for localized single photon-photoemission from a ZrO/W(100) emitter, enabled by the Schottky effect.

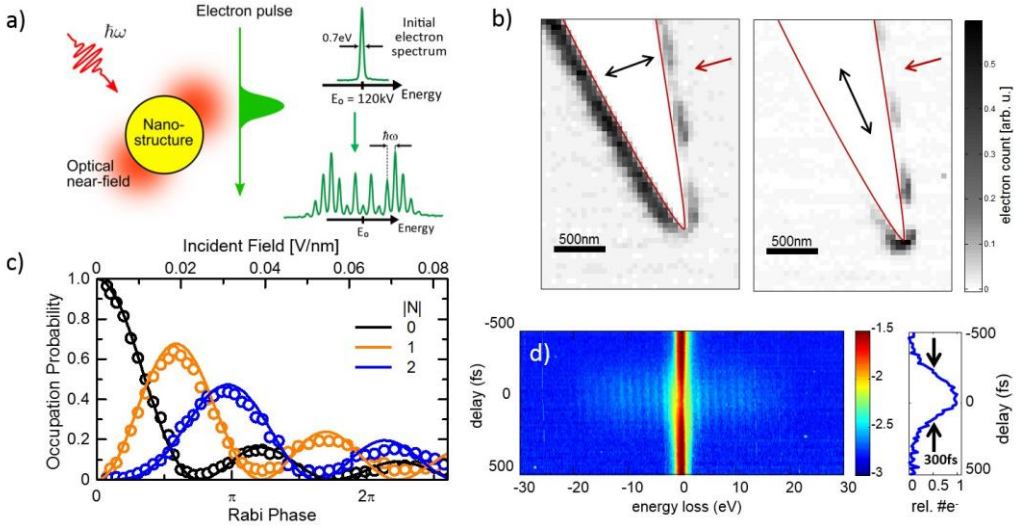

Figure 2. (a) Electrons traversing an intense optical near-field experience a loss or gain of multiples of the photon energy, which is forbidden in the case of propagating light, due to a mismatch of the respective dispersion relations. (b) Spatial maps of inelastic electron near-field scattering in close vicinity to an illuminated gold nanotip (shape indicated by red line), obtained by raster scanning the electron focus across the nanostructure and recording the gain-scattered electron count. Arrows denote direction (red) and polarization (black) of the optical driving field. (c) Occupation probability of individual side-bands depending on incident laser field strength. Pronounced Rabi oscillations in free electron momentum states are observed. (d) Electron energy spectrum after near-field interaction (logarithmic scale) as a function of the time delay between the arrival of the electron bunch and the optical driving pulse (left panel). Right panel: An electron pulse duration of about 300 fs is obtained.

Dynamic microscopy of energy conversion processes

JS-SFB.05
Imaging optically induced magnetization dynamics by Lorentz microscopy

M. Möller[1], N. Rubiano da Silva[1], J. G. Gratzmann[1], A. Feist[1], V. Zbarsky[2], M. Münzenberg[3], C. Ropers[1], S. Schäfer[1]

[1]University Göttingen, 4th Physical Institue, Göttingen, Germany
[2]University Göttingen, 1st Physical Institute, Göttingen, Germany
[3]Greifswals University, Institut für Physik, Greifswald, Germany

moeller@ph4.physik.uni-goettingen.de

Lorentz microscopy is an established technique for the nanoscale mapping of magnetization structures in thin films and nanostructures [1,2]. In particular the in-plane magnetization can be quantitatively reconstructed from through-focus image series [2]. While Lorentz microscopy has been widely applied to study static magnetic domains and domain boundaries, its adaptation to time-resolved in-situ imaging offers fascinating prospects for the investigation of fast and ultrafast magnetization dynamics [3,4].

Here, we present two approaches to access ultrafast magnetization dynamics with Lorentz microscopy. In a first approach, we employ Lorentz microscopy with in-situ femtosecond optical excitation. We demonstrate that in homogeneous iron thin films, intense single optical pulses induce a dense network of magnetic vortices and antivortices with typical correlation lengths on the order of 500 nm (cf. Fig. 1). Using optical pulse pairs with variable delay, we find an enhanced generation of vortices for pulse pair delays below about 5 ps, indicating the importance of ultrafast processes for the creation of the observed vortex-antivortex network.

In a second approach, we aim for a combination of Lorentz microscopy with ultrafast transmission electron microscopy (UTEM) in a laser-pump/electron probe scheme [5]. The Göttingen UTEM instrument is ideally suited for this type of experiment, as the implemented pulsed electron source provides highly coherent electron pulses, enabling ultrafast electron imaging with phase contrast. In Fig. 2, we present Lorentz images of permalloy nanoislands recorded with sub-picosecond electron pulses. Shape-induced magnetic vortices and adjacent domain walls can be mapped with high contrast. In a next step, we plan to investigate optically induced reversible magnetization dynamics in such type of structures.

1. M. Schneider, H. Hoffmann, and J. Zweck, “Lorentz microscopy of circular ferromagnetic permalloy nanodisks”, Applied Physics Letters **77**, 2909-2911 (2000)
2. M. De Graef, “Magnetic imaging and its applications to materials”, Academic Press **36** (2000)
3. S.D. Pollard, L. Huang, K.S. Buchanan, D.A. Arena and Y. Zhu, “Direct dynamic imaging of non-adiabatic spin torque effects”, Nature communications **3,** 1028 (2012)
4. A.H. Zewail, “Four-Dimensional Electron Microscopy” Science **328**, 187-193 (2010)
5. H.S. Park, J.S. Baskin and A.H. Zewail, “4D Lorentz Electron Microscopy Imaging: Magnetic Domain Wall Nucleation, Reversal, and Wave Velocity” Nano Lett.**10,** 3796-3803 (2010)

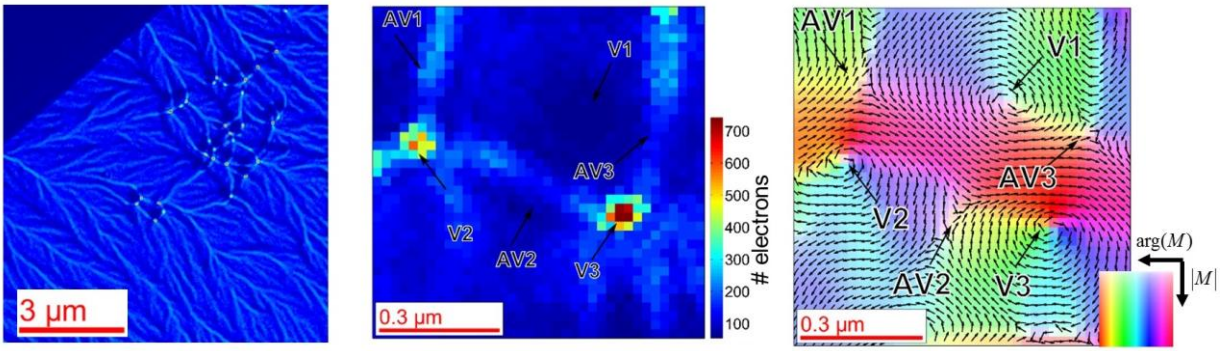

Figure 1. (left) Lorentz image of an optically induced magnetic vortex-antivortex (V/AV) network in an iron thin film after applying a single intense laser pulse. (center/right) Lorentz image and reconstructed in-plane magnetization of V/AV network at small length scales demonstrating the interwoven network structure.

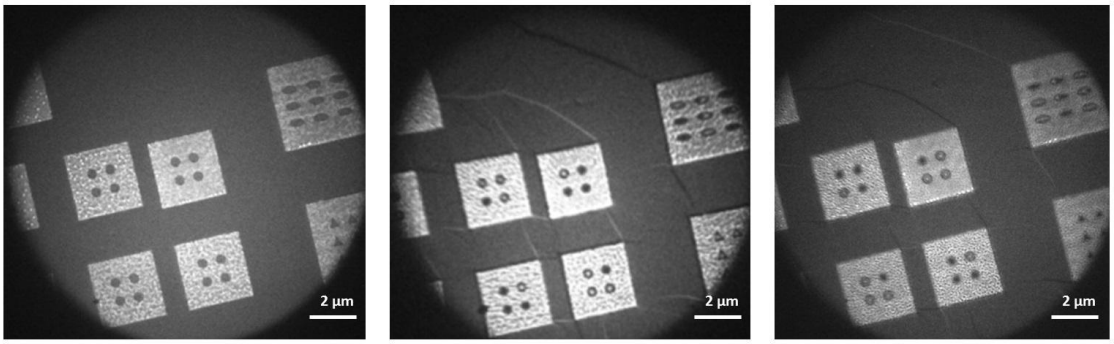

Figure 2. Lorentz images acquired with ultrashort electron pulses of a nano-patterned permalloy thin film on a silicon-nitride membrane. In-focus image (left) and out-of-focus images with $\Delta f > 0$ (center) and $\Delta f < 0$ (right). Domain boundaries and vortices within the nanostructures are visible with high contrast. Imaging conditions are: 1.5 e^-/pulse, 250 kHz rep. rate, 60 s exposure time.

Dynamic microscopy of energy conversion processes

JS-SFB.06
How to image vibrating spatial MEMS structures?

M.- A. Schröter[1], M. Ritter[2], M. Holschneider[3], H. Sturm[1,4]

[1]Federal Institute of Materials Research and Testing (BAM), Nanotribology and Nanostructuring of Surfaces, Berlin, Germany
[2]Hamburg University of Technology (TUHH), Electron Microscopy Unit, Hamburg, Germany
[3]University of Potsdam, Department of Mathematics, Potsdam, Germany
[4]Technische Universität Berlin, Faculty V, Berlin, Germany

maria-astrid.schroeter@bam.de

The presentation shows the development and verification of a theory, with which the results of a newly developed measuring method (DySEM technique) can be described [1].

The term "DySEM" (Dynamic Scanning Electron Microscopy) denotes an experimental procedure for measuring the vibrational dynamics of a microscale oscillator using a scanning electron beam.

In addition to the classical secondary electron (SE) signal, the dynamic part of the signal can be obtained using a lock-in amplifier synchronized to the excitation frequency. The DySEM technique enables the direct observation of freely vibrating structures, including several modes in the normal and torsional direction as well as their higher harmonics.

Thanks to the precise local definition of electron beam and to lock-in technique the vibration images can exhibit high spatial resolution (< 20nm). Additionally, measurements of very small amplitudes of oscillations (< 20pm) can be performed. Thus, this technique is a tool of modal analysis of microscale structure in oscillation, which is frequently used in micro- and nanoelectromechanical systems (MEMS and NEMS) and where an optimization of the design parameters often only can be achieved by imaging the vibration. Additionally, the DySEM images contain characteristic amplitude-dependent image features that need to be understood theoretically [2]. So, we analyse silicon cantilevers as a simplified mechanical model of such much more complex systems.

The new theoretical model of imaging generating mechanism relates the experimental images to the spatio-temporal interaction between electron beam and periodically vibrating microstructure. So, for the first time the detailed interpretation of the experimental results was possible [3].

In addition, local properties (material properties) of the micro-oscillator are important. Similarly, the contributions of energy loss mechanisms must be considered for imaging.

To explicitly derive the imaging equations, the mathematical analysis is limited in this presentation to the adoption of a free oscillating unilaterally clamped oscillator without interaction with matter, as it is approximated in DySEM experiment by imaging in high vacuum.

Simulated images show very good qualitatively and quantitatively correspondence to the experimental data.

First the theoretical model of the imaging process makes it possible to use the DySEM technique as a quantitative analysis tool. Without such an understanding of the relationship between image contrast and interaction geometry, a quantitative interpretation of the DySEM images is hardly possible. The advantage of DySEM technique is the ability to distinguish between artefacts based on the imaging process and features which carry relevant information (i.e. nonlinear mechanical behavior of the micro-oscillator). The analysis of the imaging of oscillating microstructures by means of scanning electron microscopy is thereby achieved as a combination of experiment, theory and simulation.

1. M.-A. Schröter, Untersuchung schwingender Mikrostrukturen mittels dynamischer Rasterelektronenmikroskopie: Experiment und Theorie, Dissertation(2014), urn:nbn:de:kobv:83-opus4-58836
2. M.-A.Schröter, M. Holschneider, H. Sturm, Analytical and numerical analysis of imaging mechanism of dynamic scanning electron microscopy, Nanotechnology 23 (2012) 433501
3. M.-A. Schröter, H. Sturm, M.Holschneider, Phase and amplitude patterns in DySEM mappings of vibrating microstructures, Nanotechnology 24 (2013) 215701

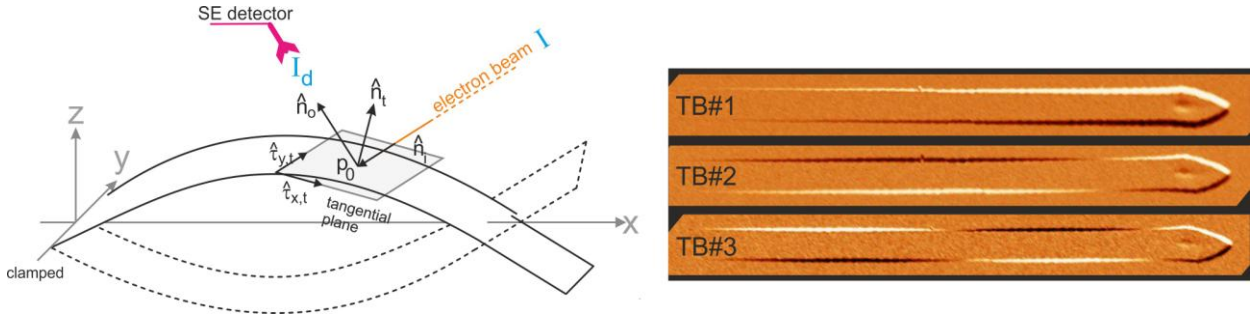

Figure 1. Left: Theoretical model of the geometric relationship between electron beam and vibrating cantilever. Right: Representation of the real part measurements of the first three flexural modes of the cantilever.

Dynamic microscopy of energy conversion processes

JS-SFB.07
In situ dynamic environmental TEM of energy conversion processes at the atomic scale.

S. Takeda[1], Y. Kuwauchi[1], H. Yoshida[1], K. Soma[1]

[1]Nanoscience and Nanotechnology Center, Institute of Scientific and Industrial Research (ISIR), Osaka University, Ibaraki, Osaka, Japan

takeda@sanken.osaka-u.ac.jp

Among the various microscopy methodologies, in situ transmission electron microscopy (TEM) has recently advanced with technological developments such as aberration correction of lenses, fast digital cameras, and miniaturized specimen containers with various functions. These advances have enabled observation of a variety of phenomena in materials and devices at higher spatial and temporal resolution, especially in gases. Given the recent advances in TEM technology, it is now possible to investigate the essential static and dynamic characteristics of materials and devices by quantitative in situ environmental TEM (ETEM) at the atomic scale.

We briefly summarize our recent in situ ETEM studies of catalyst materials in reaction conditions [1, 2]. The catalytic activity of supported metal nanoparticles such as gold and platinum depends on their size, shape, surface and interface structure. It was found that the majority of Au nanoparticles in the Au/CeO_2 and Au/TiO_2 catalysts changed surface structures systematically depending on gas environments. This change is reversible in gas environments. Aberration-corrected ETEM can capture the finite movement of an Au nanoparticle in the Au/CeO_2 catalyst in a reaction environment. The Au nanoparticles were displaced and rotated step-wisely during ETEM observation. The nanoparticles did not move on the substrate surface continuously. The analyses leaded to a conclusion that the activation sites of oxygen molecules at room temperature locate at the perimeter interface between an Au nanoparticle and a metal oxide support. Furthermore, the atomic structure at the perimeter interface, or the most probable reaction sites of the catalysts, is not structurally rigid in reaction conditions. The observation results on the Au catalysts are compared with those on Pt/CeO_2.

To investigate an energy converting process of batteries, advanced methodology is needed for elucidating dynamic structural properties in charging and discharging processes. We will present a recent development toward in situ dynamic TEM of batteries [3].

In electron-irradiation-sensitive materials and devices, intrinsic phenomena may be masked by electron irradiation. It is helpful to systematically acquire in situ TEM data as a function of electron current density, electron dose, and electron energy. In several applications, the intrinsic phenomena and/or structures can be deduced by systematically acquiring in situ TEM data. For quantitative in situ ETEM of time-dependent phenomena in a energy conversion process, quantitative evaluation and removal of the electron-irradiation-induced phenomena is required.

1. S. Takeda, Y. Kuwauchi, H. Yoshida, Ultramicroscopy, 151 (2015) 178.
2. H. Yoshida, Y. Kuwauchi, J. R. Jinschek, K. Sun, S. Tanaka, M. Kohyama, S. Shimada, M. Haruta, S. Takeda, Science335 (2012) 317.
3. K. Soma et al., unpublished (2015).

Dynamic microscopy of energy conversion processes

JS-SFB.08
Stimulated dynamic electron microscopy

J. B. Wagner[1]

[1]Center for Electron Nanoscopy, Technical University of Denmark, Denmark

jakob.wagner@cen.dtu.dk

Monitoring the dynamic nature of nanostructured materials under various stimuli offers the opportunity for studying the dynamic structure-functionality relationship leading to insight and understanding of relevant phenomena for tailor-made materials.

Electron microscopy combined with various stimuli, that being gas exposure, heating, light, biasing, indentation, etc. is a unique tool for such monitoring. Both structural and compositional characterization of materials in active environments are becoming more and more accessible throughout laboratories around the Globe.

Here, a few examples on how stimulated dynamic electron microscopy has shed light on the nature of the nanomaterial dynamics, are discussed - mainly focusing on gas exposure, heat, and visible light treatment.

The redox behavior of nanostructured nickel is of great importance in a variety of applications, including solid oxide fuel cells. Here, the Ni serves as an active part of the anode placed on the fuel side of the cell in form of sub-micron sized grains co-sintered with a ceramic material. During operation at elevated temperature, failure and severe irreversible destruction of the anode will happen due to oxidation of the Ni if exposed to non-reducing conditions. In Fig. 1 the morphological and chemical development of the redox treatment of Ni(O) is shown. The initial NiO agglomerates are reduced in 130 Pa H_2 followed by an oxidation in 320 Pa O_2, both at 600˚C. Furthermore, co-sintered Ni-ceramic matrices are treated at similar conditions in the environmental transmission electron microscope (ETEM) in order to elucidate the possible effect of the ceramic on the redox behavior of Ni. [1,2]

Photocatalysts for solar fuel production are subject to intensive investigation as they constitute one viable route for solar energy harvesting. Cuprous oxide (Cu_2O) is a working photocatalyst for hydrogen evolution but it photocorrodes upon light illumination in an aqueous environment. In Fig. 2 the morphological and chemical evolution of Cu_2O cubes are followed by means of ETEM. The presence of H_2O (500 Pa) and visible light (405 nm) results in development of metallic copper grains in the cubes as confirmed by electron energy-loss spectroscopy. The water-light treatment are performed with the electron beam blanked due to electron beam effects. [3]

A few other examples will serve as a teaser for the vast opportunities stimulated electron microscopy in general and environmental transmission electron microscopy in particular gives researchers within the field of energy conversion processes.

1. Q. Jeangros, A. Faes, J.B. Wagner, T.W. Hansen, U. Aschauer, J. Van herle, A. Hessler-Wyser, R.E. Dunin Borkowski, Acta Materialia 58 (2010) 4578.
2. Q. Jeangros, T.W. Hansen, J.B. Wagner, Acta Materialia 67 (2014) 362.
3. F. Cavalca, A.B. Laursen, J.B. Wagner, C.D. Damsgaard, I. Chorkendorff, T.W. Hansen, Chemcatchem 5 (2013) 2667.

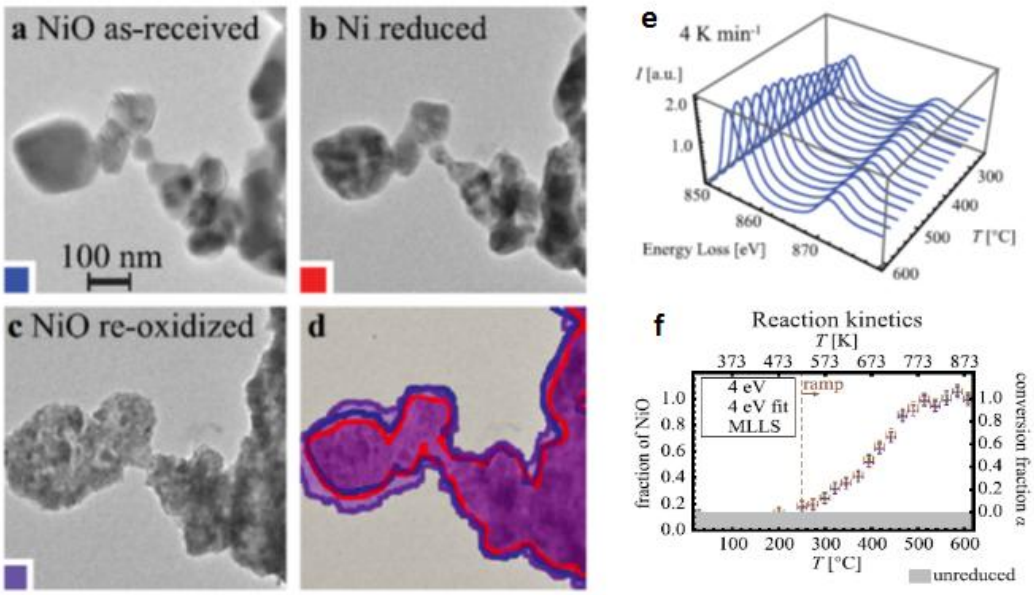

Figure 1. Structural and compositional changes in a set of NiO particles (initial structure shown in (a)) observed after (b) reduction and (c) re-oxidation. The projected areas of (a–c) are superimposed in (d). e) Background-subtracted EEL spectra acquired as a function of temperature for a 4 K min^{-1} ramp (normalized to unity at L_2). NiO and Ni experimental reference spectra were used to determine the oxidation kinetics (f).

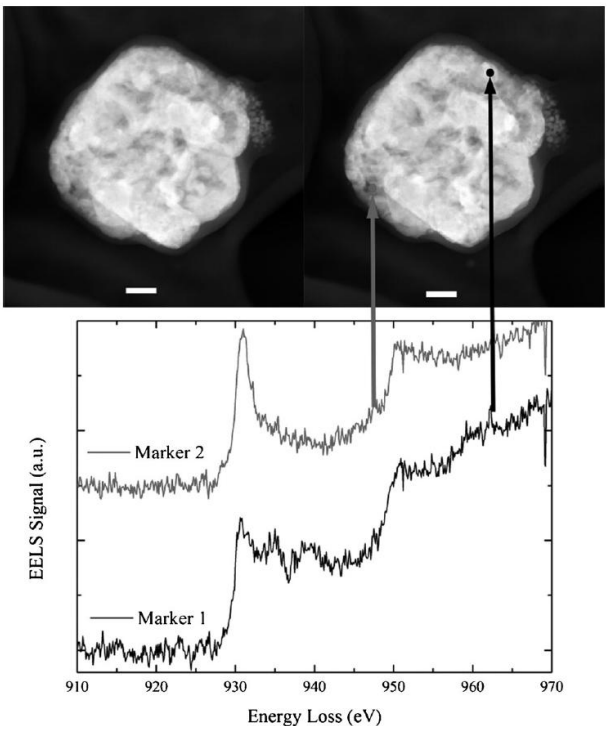

Figure 2. HAADF-STEM images of a Cu_2O nanocube during exposure to H_2O and light. The images show how reduced crystals nucleate and grow within the particle body. STEM EELS on the marked positions is used to investigate the chemical phase of individual grains. The plot shows that a predominantly reduced phase at position 1 and an oxidized phase at position 2 coexist in the particle after 45 min exposure. Scale bar 50nm.

Dynamic microscopy of energy conversion processes

JS-SFB.09
Benefit and challenge of in-situ ETEM experiments - electron beam induced potentials

S. Mildner[1], D. Mierwaldt[1], J. Ciston[2], T. Kasama[3], S. Yazdi[3], M. Beleggia[3,4], J. B. Wagner[3], T. W. Hansen[3], Y. Zhu[5,6], C. Jooss[1]

[1]University of Goettingen, Institute for Materials Physics, Göttingen, Germany
[2]Lawrence Berkeley National Laboratory, National Center for Electron Microscopy, Berkeley, United States
[3]Technical University of Denmark, Center for Electron Nanoscopy, Kongens Lyngby, Denmark
[4]Helmholtz-Zentrum Berlin for Materials and Energy, Berlin, Denmark
[5]Brookhaven National Laboratory, Department of Condensed Matter Physics, Upton (NY), United States
[6]Brookhaven National Laboratory, Center for Functional Nanomaterials, Upton (NY), United States

sraabe@ump.gwdg.de

Environmental TEM (ETEM) represents a powerful tool for atomic resolution studies of materials in selected gas atmosphere. It enables, for example, the in-situ investigation of catalytic materials in their active state and, equipped with EELS, allows for observation of the atomic and electronic surface structure during reactions. However, the interpretation of such investigations also poses a great challenge in terms of comparability with conventional (ex situ) experiments: Inter alia, the question how the electron beam affects catalytic activity needs to be addressed.

In this contribution, the electron beam driven oxygen evolution at a $Pr_{0.68}Ca_{0.32}MnO_3$ manganite electrode in water vapor atmosphere is analyzed where oxygen evolution has been monitored by means of a side reaction of a sacrificial substance with evolved oxygen (Fig.1). Using a sample holder equipped with an STM tip, we present a bias-controlled ETEM experiment at $Pr_{0.05}Ca_{0.95}MnO_3$ in contact with water vapor where an electron beam initiated degradation process has been stopped by applying an electric potential. The role of the electron beam as the driving force for chemical reactions in the ETEM is investigated in the framework of electron beam induced electric potentials caused by secondary electron emission (Fig. 2). A quantification of these potentials on the basis of off-axis electron holography experiments combined with electrostatic modeling as well as a theoretical consideration of the secondary electron yield is presented. The impact of the gas species and pressure on beam induced potentials is addressed.

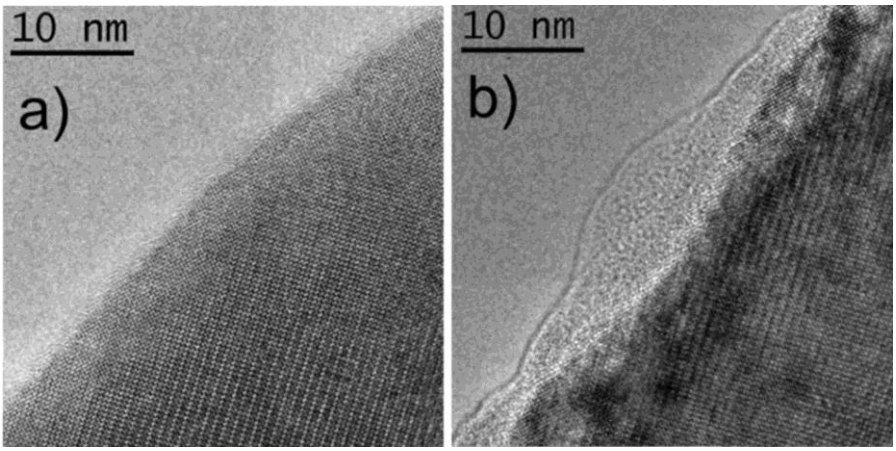

Figure 1. Crystalline PrCaMnO3 TEM sample (a) in the initial state and (b) after 120 s in 0.3 mbar $He_2/H_2O/SiH_4$ gas under electron flux of 11000 e/Å^{2}s. Electron irradiated sample regions are covered by amorphous SiO_2 which originates from the side reaction of SiH4 with the evolved oxygen [S. Mildner et al., J. Phys. Chem. C 119 (2015)].

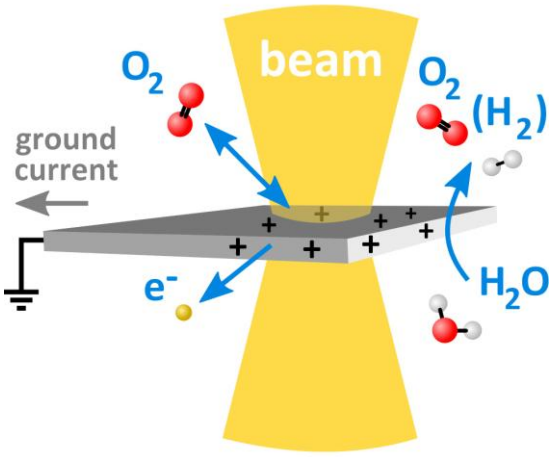

Figure 2. Scheme of TEM sample charging and potential buildup by secondary electron emission as the driving force for water splitting reaction in the ETEM [S. Mildner et al., J. Phys. Chem. C 119 (2015)].

Dynamic microscopy of energy conversion processes

JS-SFB.10
Transmission electron microscopy study of novel 3D hierarchical $Nb_3O_7(OH)$ superstructures; performing in-situ heating experiments and tomography reconstruction

S. Betzler[1], J. Ciston[2], A. Wisnet[1], D. Ulrich[2], C. Scheu[3]

[1]Ludwig Maximilians University Munich, Munich, Germany
[2]National Center for Electron Microscopy, Molecular Foundry, Lawrence Berkeley National Laboratory, Berkeley, United States
[3]Max-Planck-Institut für Eisenforschung, Düsseldorf, Germany

sophia.betzler@cup.uni-muenchen.de

Decreasing fossil fuel resources enforce the development of renewable energy sources. Photocatalytic splitting of water to hydrogen and oxygen gas allows the conversion of solar power to storable energy, as hydrogen gas can be used in fuel cells and for the synthesis of energy dense materials.

Novel $Nb_3O_7(OH)$ superstructures have promising properties for this task, as they combine a band gap of 3.2 eV with a large surface area (55 m^2/g) and high crystallinity. These superstructures form self-organized in a one-step hydrothermal synthesis approach [1]. Scanning electron microscopy (SEM) images show their cubic morphology and hollowness (Fig. 1a) and transmission electron microscopy (TEM) reveals that their walls consist of a highly ordered nanowire network (Fig. 1b). A combination of site-selective thickness measurements using electron energy-loss spectroscopy and 3D tomography was applied to elucidate the nanowire arrangement in the network to get further insights into the stabilization of these superstructures. These investigations were carried out for network fragments and reveal two different junction types as well as no interpenetration of the nanowires at the junctions (Fig. 1c).

The superstructures show promising hydrogen production rates, however modifying their properties by doping or calcination can further improve their performance. Ex-situ TEM heating experiments reveal a phase transformation from $Nb_3O_7(OH)$ to Nb_2O_5 at 850 °C, which goes a long with a morphologic change of the nanowires resulting in a collapsing of the superstructures (Fig. 2a,b). In-situ TEM heating experiments show the generation of pores within the crystal lattice at temperatures above 500 °C, which serve as a pattern for the formation of small nanocrystals at temperatures above 900 °C (Fig. 2c,d). These nanocrystals increase in size at temperatures above 1000 °C. Networks heated in-situ in the absence of the electron beam show a similar behavior as observed for ex-situ heated ones and no pores are formed in these regions. This indicates that the pore-formation is induced by a combination of the electron beam-matter interaction and the heat.

1. S. B. Betzler, A. Wisnet, B. Breitbach, C. Mitterbauer, J. Weickert, L. Schmidt-Mende and C. Scheu, *Journal of Materials Chemistry A*, **2014**, *2*, 12005-12013.

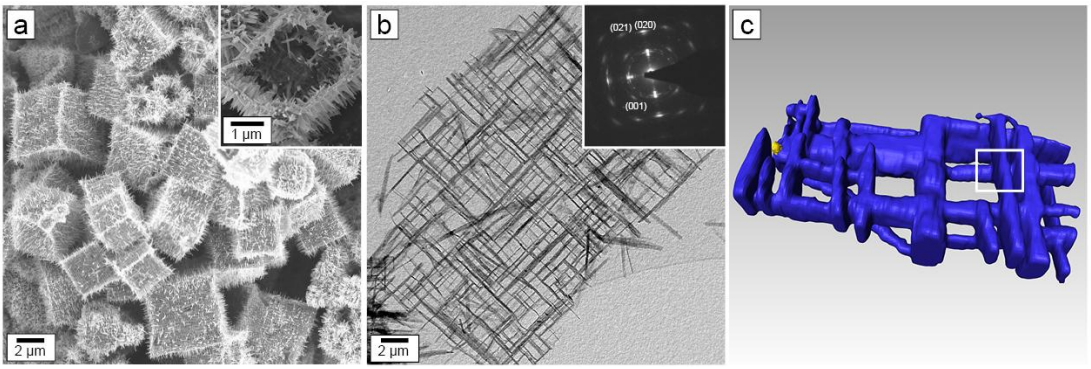

Figure 1. Scanning electron microscopy image of the cubic superstructures, the inset shows a fragment of one single cube (a). b) Bright field image of a network fragment, which consists of a highly ordered nanowire network. The high

degree of ordering reflects in the diffraction pattern given in the inset. c) 3D tomogram of the network allowing a detailed view on the nanowire arrangement.

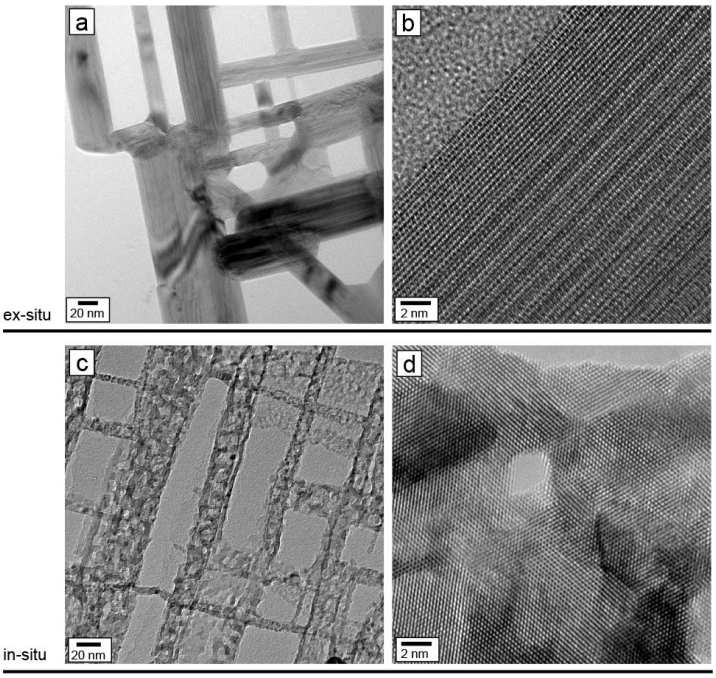

Figure 2. a)TEM image of a nanowire network after calcination in the open air at 850 °C. b) HRTEM image of one single crystal. c) TEM image of a nanowire network during an in-situ experiment at 900 °C. d) HRTEM image showing the formation of nanocrystals, which express the same crystal orientation.

Dynamic microscopy of energy conversion processes

JS-SFB.11
In-situ TEM study of $LiMn_2O_4$ lithiation

T. Erichsen[1], C. A. Volkert[1]

[1]University of Göttingen, Institute of Materials Physics, Göttingen, Germany

terichsen@ump.gwdg.de

Lithium ion batteries are currently the most widely used portable and rechargeable electrochemical storage systems due to their high energy density. While there are many different Li-based cathode materials in use or being considered for use, spinel-type $LiMn_2O_4$ (LMO) provides a good model system to study electrochemical processes at a local scale. It has a strong coupling between structural and electronic/valence properties and is phase separating for higher contents of Li. This creates a solid/solid interface which allows both sides of an electrochemical reaction to be studied inside a high-resolution transition electron microscope (TEM). In combination with energy-loss spectroscopy (EELS) this makes a powerful tool to characterize sample structure, valence state and Li content at the atomic scale. Previous TEM studies on LMO have been limited to post-mortem characterization and to in-situ diffraction studies of the lithiation of LMO-wires [1] and have only provided limited information about phase nucleation at internal interfaces.

We attempt to perform in-situ high resolution studies of the dynamics of LMO lithiation. Our experimental setup consists of a Nanofactory STM-TEM-holder that is used to bring Li into contact with a FIB-prepared, polycrystalline LMO lamella (i.e. a solid electrolyte half-cell) and to apply a voltage to drive the electrochemical reaction. We use an image-corrected FEI Titan microscope to perform high-resolution imaging, electron diffraction and EELS at different stages of the lithiation process. This allows us to gain access to structural and chemical information of the LMO when it is transformed by lithiation as well as giving us the possibility to look at local defects and interface structures.

Preliminary tests have been performed and show that we are able to drive and observe an electrochemical reaction in the LMO TEM specimen (see Figure 1). First results show that a lamellar structure is formed in the LMO (Figure 2) and EELS confirms the presence of Li. The lamellar structure suggests that the phase transformation may occur by spinodal decomposition. We are currently performing high resolution characterization of the lithiated specimen. Furthermore, we have been able to confirm that the stability of the test setup is sufficient for high resolution imaging and will attempt this in our next in-situ experiments.

1. S. Lee, et al., J. Phys. Chem. C 117 (2013)

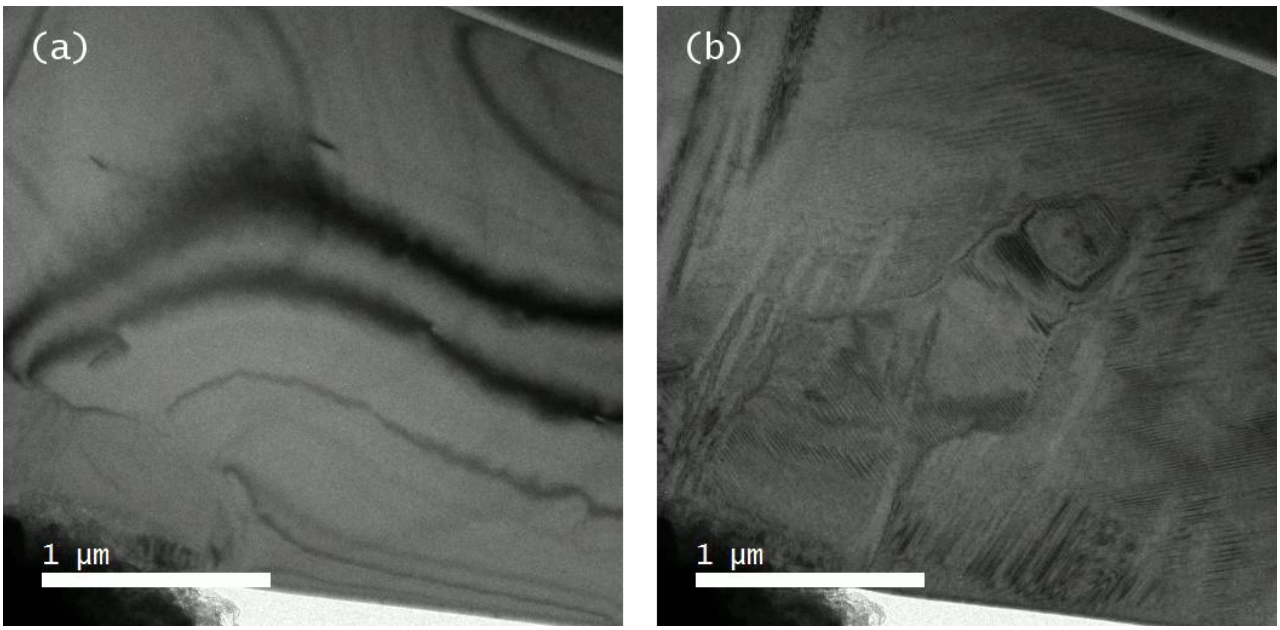

Figure 1. Bright field images from a video taken during lithiation of LMO at an applied voltage of -5V. Image (a) shows the initial state of the lamella after contact with the tip (visible in the lower left corner) but before applying the voltage. (b) was taken 180 seconds after applying the voltage. Besides bending contours moving through the lamella, structural changes in the LMO can also be observed.

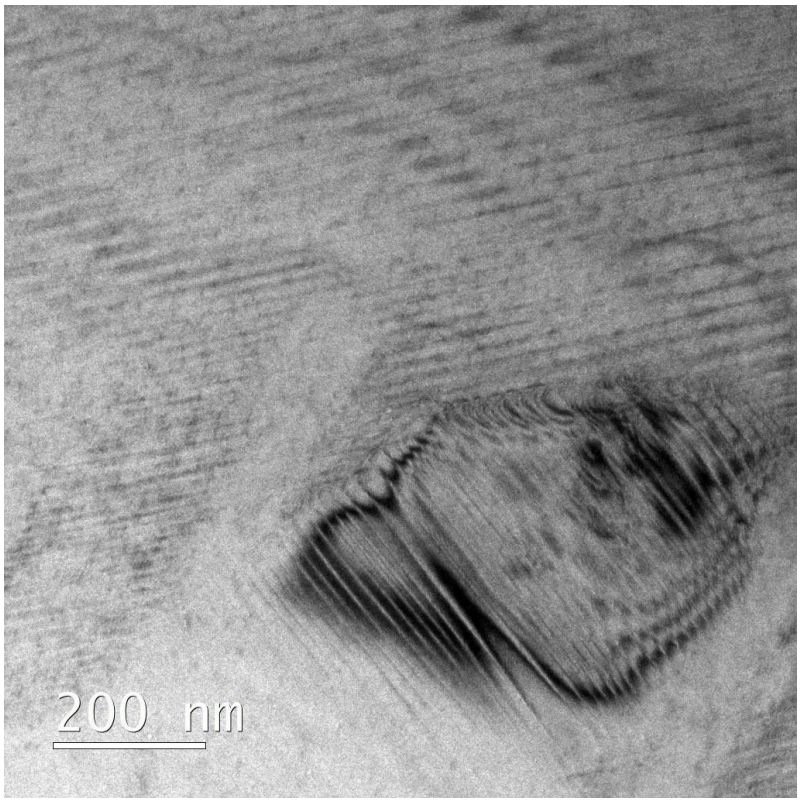

Figure 2. Bright-field image taken after the video series in Fig. 1 showing the formation of lamellar structures during lithiation.

Dynamic microscopy of energy conversion processes

JS-SFB.12
Exploring the friction between atomic layers in VSe_2 by *In situ* SEM compression and shearing tests

P. Schweizer[1], F. Niekiel[1], E. Spiecker[1]

[1]Center for Nanoanalysis and Electron Microscopy, Erlangen, Germany

peter.schweizer@fau.de

Layered crystals have experienced a surge of attention in materials science in recent years due to their quasi two-dimensional structure which gives rise to a plethora of outstanding properties. Certainly a lot of that interest came with the rise of graphene, which is the basic building block of the most well-known example for a layered crystal: graphite. A class of materials which is very similar in structure to graphite are the transition metal dichalcogenides, which show many intriguing properties such as semiconductivity, superconductivity or the formation of charge density waves[1]. Like graphite these materials can be exfoliated into stable single layers, which promise to be highly useful for electronic applications. Besides the electronic properties, the mechanical properties of layered crystals are highly intriguing because they show an extreme case of anisotropy. The strong inner-layer bonds are in stark contrast with the weak van-der-Waals type interlayer bonds, which on the one hand results in serious strength for single layers, as it was shown for graphene and MoS_2 while on the other hand making a bulk sample comprised of many layers very deformable. Due to these properties layered crystals have long been used as solid lubricants[2]. With the discovery of superlubricity, a tribological regime where all static friction vanishes, a closer look has to be taken at the interactions of the atomic layers when they slide against each other.

In this work we present a method that enables us to measure frictional forces between two atomic layers of a layered crystal using vanadium diselenide (VSe_2) as an exemplary material. We start with a modified version of the well-established micro-pillar compression tests, which uses the inclination angle of the pillars to achieve the desired crystallographic orientation of the sample in relation to the compression axis (see Figure A below). Additionally a cap made of platinum enables a defined contact between indenter and pillar. During compression slip along a single atomic interface is achieved consistently (see Figure B). After slip has been initiated the friction of the interface is tested using a custom built manipulator tip (see Figure C) which shears off the top of the pillars. To measure the force during shearing the sample is placed on a soft spring table. Using image correlation the relative displacement of the sample can be measured and together with the known spring constant the friction force can be calculated. By correlating the contact area of the interface with the force needed to induce slip intrinsic properties can be extracted that characterize that tribological system (see Figure D). Further analysis includes transmission electron microscopy (TEM) of thin lamellae prepared in plan-view and cross-section geometry to learn more about the defects generated during slip at the interface, especially dislocations networks.

Future work will expand these tests to other materials like graphite or MoS_2. Additionally by inducing a controlled rotation after slip has been induced these tests may also enable us to test incommensurate configurations which may show the effect of superlubricity.

Financial support by the DFG via the research training group GRK 1896 "In situ microscopy with electrons, X-rays and scanning probes" is gratefully acknowledged.

1. Wang, Q. H. Kalantar-Zadeh, K. Kis, A. Coleman, J. N. & Strano, M. S. Electronics and optoelectronics of two-dimensional transition metal dichalcogenides, Nature Nanotech 7, 699-712 (2012).
2. Winer, W. O. Molybdenum disulfide as a lubricant: A review of the fundamental knowledge, Wear 10, 422-452 (1967).

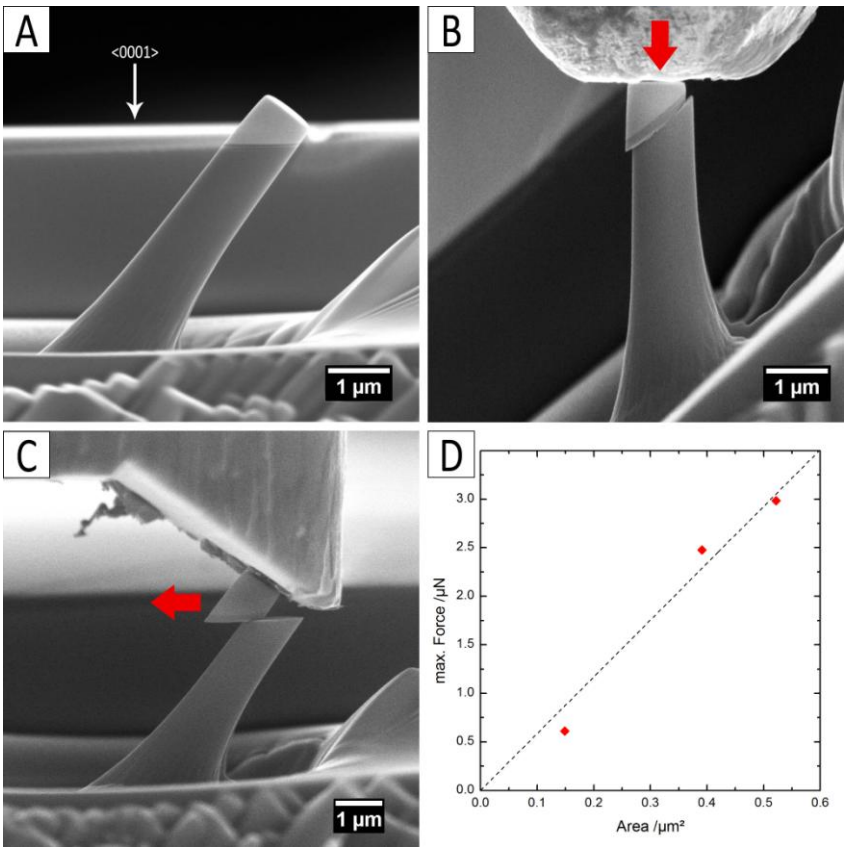

Figure 1. A) The as-prepared Pillars with an inclination angle of 52°. B) During the compression of the pillars slip is achieved along a single atomic interface. C) Using a custom-built manipulator-tip the pillar can be sheared along the interface. D) To initiate slip a certain maximum force has to be applied, which can be correlated to the interface area to extract intrinsic properties of the tribological system.

Dynamic microscopy of energy conversion processes

JS-SFB.P13
In-Situ TEM electrochemical studies of all solid-state fluoride ion battery

M. Hammad[1], V. S. K. Chakravadhanula[2,1,3], T. Scherer[1,3], C. Rongeat[1], A. R. Munnangi[2,1], F. Maximilian[2,1], H. Hahn[2,1], C. Kübel[2,1,3]

[1]Karlsruhe Institute of Technology, Institute for Nanotechnology, Eggenstein-Leopoldshafen, Germany
[2]Karlsruhe Institute of Technology, Helmholtz Institute Ulm for Electrochemical Energy Storage, Eggenstein-Leopoldshafen, Germany
[3]Karlsruhe Institute of Technology, Karlsruhe Nano Micro Facility, Eggenstein-Leopoldshafen, Germany

cvskiran@kit.edu

The increasing demand for energy storage resulted in improving the performance of Lithium ion batteries (LIB) and a continuing search for alternative battery technologies. Many alternative technologies are being developed, based on different chemistries, such as Na, Mg, F, Cl as charge transfers ions. Reversible batteries based on a fluoride anion shuttle (fluoride ion battery) are an interesting alternative to LIBs [1]. Fluoride ion batteries can theoretically achieve a high-energy density compared to LIBs, above 5000 $Wh.L^{-1}$ (50% above the theoretical capacity of the Li air cell) [2]. However, research in the field of fluoride ion batteries is at an early stage of development needing large improvement to meet the requirements for application. Understanding the electrochemical reaction occurring at the battery electrodes during cycling is essential to improve the performance and cyclic stability of fluoride ion batteries.

Battery research groups worldwide, demand the direct observation of the structural and chemical evolution of battery components and its correlation with the corresponding ex-situ battery cycling. In-situ analysis comprises complex sample environment systems, requiring careful development of experimental aspects to enable correlation with the true operating conditions. In-situ TEM is one of the few techniques that can provide direct structural and compositional information of micron-sized batteries during cycling. As these in-situ studies probe the specimens close to true operating conditions, they often necessitate unique sample preparation techniques. An additional aspect is electron beam damage of battery materials, complicating the data interpretation. The components used in fluoride ion batteries are generally stable under the electron beam, making it suitable for in-situ electrochemical studies inside the TEM.

In this study, ball milling of a mixture of $(1-y)LaF_3$ and $yBaF_2$ was employed to prepare a $La_{0.9}Ba_{0.1}F_{2.9}$ electrolyte. This electrolyte was initially studied for its structure, composition and stability towards the electron beam. A mixture of Cu (90%), as an active material, and C (10%) was used as a cathode. The anode, in the case of half-discharged-state, was prepared from a mixture of Mg, MgF_2, $La_{0.9}Ba_{0.1}F_{2.9}$ (for ionic conductivity), and C (for electronic conductivity). Cathode, anode and electrolyte were pressed together to form a pellet. A focused ion beam system was used to prepare a lamella and electrically contacted on an MEMS based device at the edge of the electrodes (Fig. 1a). For electrochemical measurements, an Aduro sample holder was used in the Titan 80-300 TEM.

Variations in morphology, structure and composition of the electrodes, electrolyte and their interfaces were characterized using TEM, STEM, and SAED during electrochemical cycling (Fig. 1b). The HRTEM images, SAED studies and STEM-Map of the cathode at the interface indicate the formation of CuF_2 phase after charging (Fig. 1c,d), which was not present in the as-prepared state. The sample preparation, and the changes in the morphology, structure and composition of the La, Ba/ $La_{0.9}Ba_{0.1}F_{2.9}/BiF_3$ and the Mg/ $La_{0.9}Ba_{0.1}F_{2.9}/CuF_2$ systems will be presented and discussed.

1. M. Anji Reddy & M. Fichtner - J. Mater. Chem. 43 (2011) 17059.
2. Carine Rongeat, M. Anji Reddy, Raiker Witter, and Maximilian Fichtner, J. Phys. Chem. C, 117 (2013) 4943−4950.

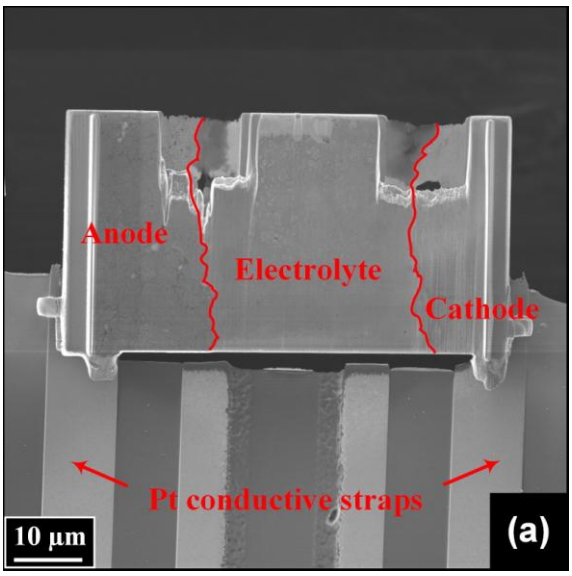

Figure 1. (a) Lamella on MEMS-device through FIB preparation, (b) I-V curve during charging, (c) HRTEM micrograph depicting formation of CuF_2, (d) Line profiles of diffraction patterns before and after cycling, showing peaks of Cu and CuF_2 distinctly.

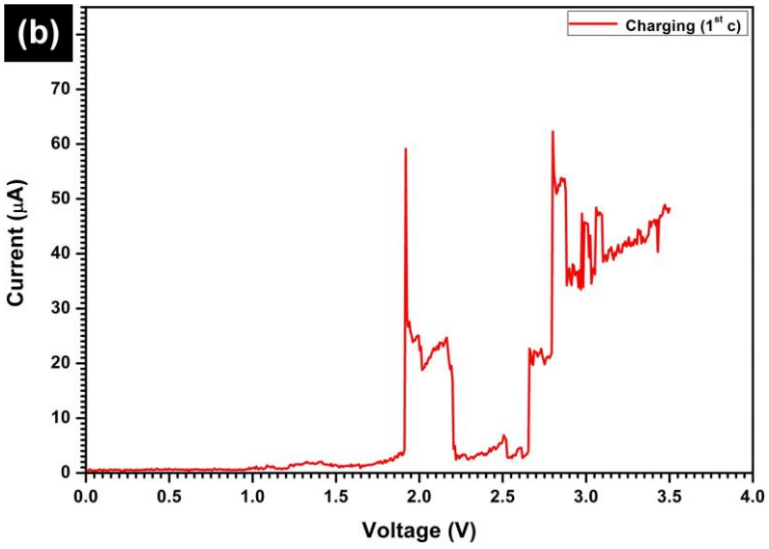

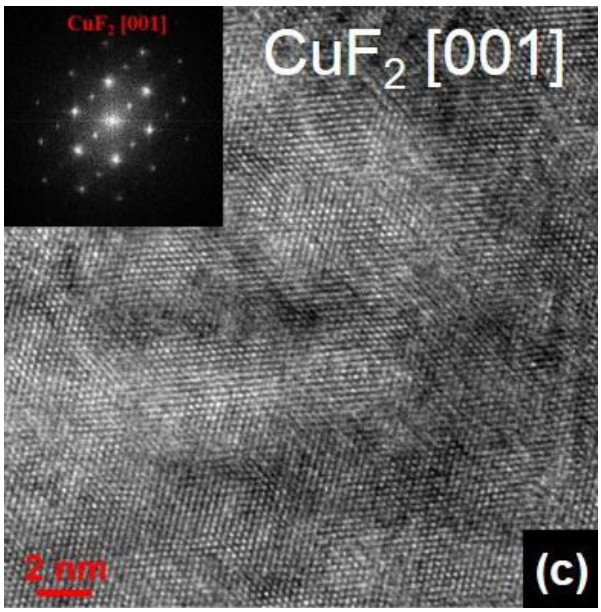
CuF2 [001]
CuF2 [001]
2 nm
(c)

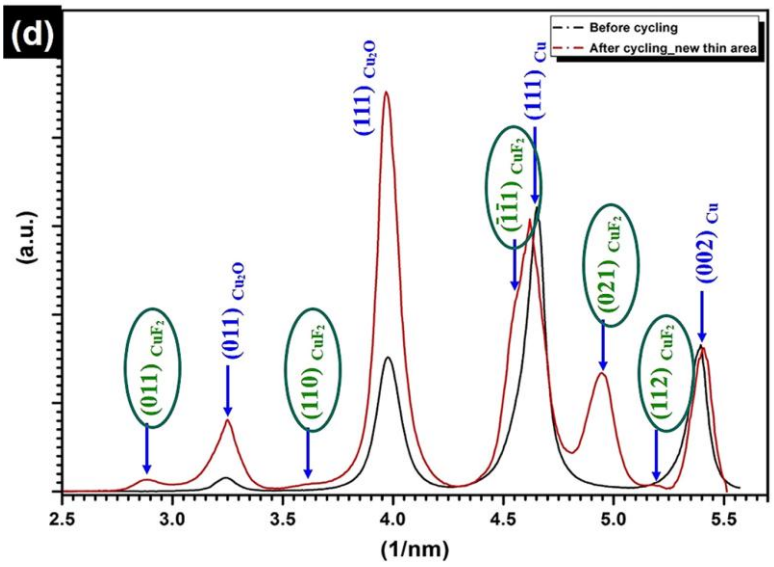
(d)
Before cycling
After cycling_new thin area
(a.u.)
(1/nm)
2.5
3.0
3.5
4.0
4.5
5.0
5.5
(011) CuF2
(011) Cu2O
(110) CuF2
(111) Cu2O
(111) CuF2
(111) Cu
(021) CuF2
(112) CuF2
(002) Cu

Dynamic microscopy of energy conversion processes

JS-SFB.P14
Environmental TEM and in situ XANES/XPS study of doped manganese perovskite catalysts for OER

D. Mierwaldt[1], S. Mildner[1], V. Roddatis[1], R. Arrigo[2], A. Knop-Gericke[2], C. Jooss[1]

[1]Georg-August-Universität, Institut für Materialphysik, Göttingen, Germany
[2]Max-Planck-Gesellschaft, Fritz-Haber-Institut, Berlin, Germany

dmierwaldt@ump.gwdg.de

We present a study on epitaxial manganite perovskite thin films ($Pr_{1-x}Ca_xMnO_3$) active for the oxygen evolution reaction (OER) from electro-catalytic water splitting. These A-site doped materials have been chosen as a model system for studying fundamental aspects of the cooperative multi-electron transfer under OER conditions. They have been studied by Environmental Transmission Electron Microscopy (ETEM) as well as in situ X-Ray Absorption Near-Edge Spectroscopy (XANES) and X-Ray Photoelectron Spectroscopy (XPS). These in situ techniques allow interesting insights into the structure and electronic states of the active catalyst surface. In particular, changes in Mn valence states, surface structure and surface defect chemistry can be studied in the active state, which is important in order to have progress in understanding the mechanisms of water oxidation.

ETEM experiments using an aberration corrected FEI Titan have revealed significant changes in morphology, atomic structure and electronic configuration of samples stimulated by electron beam irradiation in water vapor. Surface properties depend on vapor pressure as well as beam dose. Oxygen evolution was ex situ observed by mass spectrometry and indirectly visualized in the TEM by the oxidation of silane by the evolved O_2 [2]. First steps towards bias-control of catalysis and catalyst formation in ETEM using a Nanofactory STM-TEM sample holder as well as a self-developed TEM sample holder are presented.

In situ XANES has revealed significant changes of the Mn valence state within the first few nanometers below the catalyst surface at positive sample bias in water vapor at near-ambient pressure. Surprisingly, the formation of the active catalyst in this oxidative environment results in a reduced Mn^{2+} surface species, which coexists with the formal $Mn^{(3+x)+}$ valence state of the bulk. Full reversibility of this self-formation is observed after post reaction annealing at 120°C in O_2 atmosphere. In Situ XPS has been performed for further investigation of the active catalyst surface [1].

Ex situ cyclic voltammetry (CV) and chrono-amperometry at controlled electrochemical potentials have revealed doping-dependent trends in catalytic activity and stability. The combination of in situ XANES/XPS with post reaction TEM analysis of samples measured by ex situ CV and in situ ETEM experiments allow us to distinguish between self-formation of the active catalyst during OER and corrosion processes at the $Pr_{1-x}Ca_xMnO_3$-H_2O interface as well as to evaluate the role of point defects like oxygen vacancies for catalyst formation.

1. Mierwaldt D, Mildner S, Arrigo R, Knop-Gericke A, Franke E, Blumenstein A, Hoffmann J, Jooss Ch, accepted for publication in *Catalysts*
2. Raabe S, Mierwaldt D, Ciston J, Uijttewaal M, Stein H, Hoffmann J, Zhu Y, Blöchl P, Jooss Ch. *Adv. Funct. Mater.* 2012; 22; 3378-3388.

Dynamic microscopy of energy conversion processes

JS-SFB.P15
Optical phase modulation of free electrons in an ultrafast transmission electron microscope

A. Feist[1], K. Echternkamp[1], J. Schauss[1], S. Yalunin[1], S. Schäfer[1], C. Ropers[1]

[1]Georg-August-Universität Göttingen, IV. Physikalisches Institut, Göttingen, Germany

feist@ph4.physik.uni-goettingen.de

Ultrafast transmission electron microscopy (UTEM) is a promising laser pump/electron probe technique, enabling the investigation of ultrafast processes on the nanometer length scale [1]. Modifying a Schottky field emission TEM (JEOL JEM-2100F), we have recently implemented the first UTEM that operates with a nanoscale laser-driven photocathode. We obtain electron pulses as short as 300 fs, focusable down to a spot size of 3 nm, and with a kinetic energy spread of 0.6 eV.

Here, we employ the advanced beam properties of the UTEM to study quantum coherent electron-light interactions. In our experiments, we focus the electron beam close to a surface of a nanostructure. The optically excited near-field of the nanostructure is highly spatially confined and therefore allows for an otherwise forbidden coupling between the free electrons and photons. This causes the generation of optical sidebands in the electron kinetic energy spectra, in very close agreement to theoretical computations [2,3]. Strong field-dependent Rabi oscillations in the populations of different sidebands demonstrate the quantum coherence of the process [4].

Based on numerical computations, we predict that free propagation over several mm behind the near-field interaction reshapes the electron wave function into a train of attosecond pulses. The focal distances are in an experimentally accessible range, and we anticipate these pulse trains to enable the study of attosecond phenomena and optical phase-resolved imaging of polarizations in electron microscopy.

In conclusion, we characterized the performance of nanoscale photoemitters for ultrafast transmission electron microscopy and studied the interaction of swift electrons with intense optical near-fields as a first application.The observed quantum coherent manipulation of free-electron momenta may allow for a variety of further applications in electron interferometry, metrology or free-electron laser and accelerator science.

1. A. H. Zewail, “Four-Dimensional Electron Microscopy”, Science 328, 187 (2010).
2. F. J. García de Abajo, A. Asenjo-Garcia and M. Kociak, “Multiphoton Absorption and Emission by Interaction of Swift Electrons with EvanescentLight Fields”, Nano Lett. 10, 1859-63 (2010).
3. S. T. Park, M. Lin, and A. H. Zewail, “Photon-induced near-field electron microscopy (PINEM): theoretical and experimental”, New J. Phys. 12, 123028 (2010).
4. A. Feist, K. E. Echternkamp, J. Schauss, S. V. Yalunin, S. Schäfer, and C. Ropers, “Quantum coherent optical phase modulation in an ultrafast transmission electron microscope”, Nature, accepted for publication (2015).

Dynamic microscopy of energy conversion processes

JS-SFB.P16
Micro- and nanoscale observations of gas-solid interactions using in situ SEM and TEM techniques: a case study of CNTs growth on nickel

R. Farra[1], A. Rinaldi[1], M. G. Willinger[2], R. Schlögl[1]

[1]Fritz Haber Institute of the Max Planck Society, Inorganic Chemistry, Berlin, Germany
[2]Max-Planck-Institut für Chemische Energiekonversion, Mühlheim (Ruhr), Germany

farra@fhi-berlin.mpg.de

The conventional approach of characterizing solid catalysts under static conditions, i.e., before and after reaction, does not provide sufficient insight on the physicochemical processes occurring under dynamic conditions. Furthermore, recent studies have demonstrated that the active surface evolves dynamically under reaction conditions[1,2]. Hence, improving and implementing new *in situ* characterizing techniques with the potential of being used under relevant catalytic reaction conditions is highly desirable.

In situ Scanning Electron Microscopy (SEM) and Transmission Electron Microscopy (TEM) have proven to be powerful techniques for the study of atmosphere and temperature induced morphological or compositional changes of catalysts at micro- to atomic resolution scale[3,4].

In situ SEM and TEM can be used as complementary methods from the point view of applicable pressure range and the obtainable resolution. Hence, pressure gap impact on the catalyst's activity can be assessed using these techniques. On the other hand, collective (SEM) and individual (TEM) phenomena on the surface of active catalysts in the micro- to nanometer scale can be compared and correlated to the reactivity. The growth of carbon nanotubes on nickel serves as our example.

We have investigated the conditions for carbon nanofiber growth on commercial Ni foams at low pressure. Using *in situ* SEM it was found that surface nano-structuring during oxidative and reductive treatment is required in order to prevent bulk diffusion of carbon and to enhance the yield of carbon nanofiber growth at low pressure (x10Pa). At higher pressures (x1000Pa), the *in situ* TEM observation impressively demonstrated that metallic Ni readily decomposes during the exposure to ethylene and forms nanoparticles that lead to carbon nanofiber growth. The differences in the CNTs growth rate and the quality of the CNTs performed in the *in situ* SEM and *in situ* TEM will be highlighted. In this contribution we will outline how the implementation of complementary *in situ* electron microscopy techniques can enrich our understanding of the dynamic behaviour of the active catalysts.

1. T. Lunkenbein, J. Schumann, M. Behrens, R. Schlögl, M. G. Willinger, *Angew. Chem. Int. Ed.* **2015**, DOI: 10.1002/anie.201411581
2. S. Piccinin, S. Zafeiratos, C. Stampfl, T. W. Hansen, M. Hävecker, D. Teschner, V. I. Bukhtiyarov, F. Girgsdies, A. Knop-Gericke, R. Schlögl, et al., *Phys. Rev. Lett.* **2010**, *104*, 035503.
3. Z.-J. Wang, G. Weinberg, Q. Zhang, T. Lunkenbein, A. Klein-Hoffmann, M. Kurnatowska, M. Plodinec, Q. Li, L. Chi, R. Schloegl, et al., *ACS Nano* **2015**, *9*, 1506-1519.
4. S. B. Vendelbo, C. F. Elkjær, H. Falsig, I. Puspitasari, P. Dona, L. Mele, B. Morana, B. J. Nelissen, R. van Rijn, J. F. Creemer, et al., *Nat. Mater.* **2014**, *13*, 884-890.

Dynamic microscopy of energy conversion processes

JS-SFB.P17
Electron beam induced current investigations on a complex oxide pn-junction

P. Peretzki[1], B. Ifland[2], C. Jooss[2], M. Seibt[1]

[1]Faculty of Physics, Georg August University Goettingen, IV. Physical Institute, Goettingen, Germany
[2]Faculty of Physics, Georg August University Goettingen, Institute of Material Physics, Goettingen, Germany

peretzki@ph4.physik.uni-goettingen.de

The perovskite material $Pr_{0.67}Ca_{0.33}MnO_3$ (PCMO) combined with $SrTi_{0.998}Nb_{0.002}O_3$ (STNO) is presently explored as a model system for manganite-based pn-heterojunctions where PCMO is p-doped and STNO is n-doped. In this system, it is expected [1] that the rapid thermalization of low-energy photoexcited charge carriers can be quenched by making use of hot polaron-type correlated states with long lifetimes [2]. However, how polaron lifetimes convert into a diffusion length is presently not well understood, since the polaron mobility strongly depends on the excited state. Success in decrease of polaron thermalization would open the possibility of converting the photon energy of a broad range of the solar spectrum into electric energy. PCMO can be epitaxially grown on STNO and atomic scale PCMO-STNO interface design is expected to be crucial for controlling the charge transfer across the interface and thus photovoltaic properties.

Illumination- and temperature-dependent photovoltaic response has already been measured in the system. [1, 3] Electron beam induced current (EBIC) measurements provide a method for mapping the short-circuit current, from which the carrier diffusion length can be extracted. [4] To investigate the carrier diffusion length in PCMO-STNO samples, we measure EBIC in different geometries by combining SEM-based EBIC with Focused Ion Beam preparation in a dual beam instrument. We report a diffusion length in the nanometer range in the PCMO-STNO junction.

EBIC is resolution-limited because of the SEM probe size and the carrier generation volume, increasing with the electron beam energy. This is important especially in cross-section EBIC measurements around the PCMO/STNO interface as all relevant length scales are in the order of 1 to a few 10nm and, consequently, usual approximations do not hold. To encounter this situation, we interprete our results by comparison to Monte Carlo simulations. Furthermore, we perform EBIC measurements in thin TEM lamellae of the junction in order to reduce the generation volume. This allows simplifying the data evaluation and increasing the spatial resolution.

1. G. Saucke et al., Phys. Rev. B 85 (2012) 165315.
2. P. Grossmann et al., Rev. Sci. Instrum. 83 (2012) 053110.
3. A. Sawa et al., App. Phys. Lett. 86 (2005) 112508.
4. H. J. Leamy, J. App. Phys. 53(6) (1982) R51-R80.
5. We thank the German Research Society for funding through CRC1073

Index

C

H

T

U